

REPORT DOCUMENTATION PAGE				Form Approved OMB No. 0704-0188	
<small>Public reporting burden for this collection of information is estimated to average 1 hour per response, including the time for reviewing instructions, searching data sources, gathering and maintaining the data needed, and completing and reviewing the collection of information. Send comments regarding this burden estimate or any other aspect of this collection of information, including suggestions for reducing this burden to Washington Headquarters Service, Directorate for Information Operations and Reports, 1215 Jefferson Davis Highway, Suite 1204, Arlington, VA 22202-4302, and to the Office of Management and Budget, Paperwork Reduction Project (0704-0188) Washington, DC 20503.</small>					
PLEASE DO NOT RETURN YOUR FORM TO THE ABOVE ADDRESS.					
1. REPORT DATE (DD-MM-YYYY) 24-06-2002		2. REPORT TYPE Final		3. DATES COVERED (From - To) 15-4-2001 -- 31-3-2002	
4. TITLE AND SUBTITLE 2001 Workshop on Nonneutral Plasmas				5a. CONTRACT NUMBER	
				5b. GRANT NUMBER N00014-01-1-0729	
				5c. PROGRAM ELEMENT NUMBER --	
6. AUTHOR(S) Driscoll, C. Fred (Workshop Chair)				5d. PROJECT NUMBER --	
				5e. TASK NUMBER --	
				5f. WORK UNIT NUMBER --	
7. PERFORMING ORGANIZATION NAME(S) AND ADDRESS(ES) University of California at San Diego Office of Contract and Grant Administration 0934 9500 Gilman Drive La Jolla CA 92093-0934				8. PERFORMING ORGANIZATION REPORT NUMBER --	
9. SPONSORING/MONITORING AGENCY NAME(S) AND ADDRESS(ES) Office of Naval Research Ballston Centre Tower One 800 North Quincy Street Arlington VA 22217-5660				10. SPONSOR/MONITOR'S ACRONYM(S) ONR	
				11. SPONSORING/MONITORING AGENCY REPORT NUMBER	
12. DISTRIBUTION AVAILABILITY STATEMENT Approved for Public Release; distribution is Unlimited.					
13. SUPPLEMENTARY NOTES					
14. ABSTRACT Proceedings: Non-Neutral Plasma Physics IV; Workshop on Non-Neutral Plasmas, San Diego CA 2001 (AIP Conf. Proc. Vol. 606); F. Anderegg, L. Schweikhard and C.F. Driscoll, editors; AIP, New York, 2002 (738 pages). The preface summarizes workshop content and activities. The 89 scientific articles describe current non-neutral plasma research in the areas of antimatter plasmas, strongly coupled plasmas, beams, waves, transport, 2D fluids, general theory, experimental devices, and toroidal systems.					
15. SUBJECT TERMS Non-neutral Plasmas, Anti-matter, Beams, 2D Fluids					
16. SECURITY CLASSIFICATION OF:			17. LIMITATION OF ABSTRACT	18. NUMBER OF PAGES	19a. NAME OF RESPONSIBLE PERSON
a. REPORT	b. ABSTRACT	c. THIS PAGE			C. Fred Driscoll
UC	UC	UC	UC	1	19b. TELEPHONE NUMBER (Include area code) 858-534-2489

NON-NEUTRAL PLASMA PHYSICS IV

20020701 087

Previous Proceedings in the Series of Workshops on Non-Neutral Plasma Physics

	Year	Publisher	ISBN
III	1999	AIP Conference Proceedings 498	1-56396-913-0
II	1994	AIP Conference Proceedings 331	1-56396-441-4
I	1988	AIP Conference Proceedings 175	0-88318-375-7

Other Related Titles from AIP Conference Proceedings

- 595** Radio Frequency Power in Plasmas: 14th Topical Conference
Edited by Tak Kuen Mau and John deGrassie, November 2001, 0-7354-0038-5
- 563** Plasma Physics: IX Latin American Workshop
Edited by Hernán Chuaqui and Mario Favre, May 2001, 1-56396-999-8
- 547** Atomic Processes in Plasmas: Twelfth Topical Conference
Edited by Roberto C. Mancini and Ronald A. Phaneuf, December 2000, 1-56396-976-9
- 537** Waves in Dusty, Solar, and Space Plasmas
Edited by F. Verheest, M. Goossens, M. A. Hellberg, and R. Bharuthram,
October 2000, 1-56396-962-9
- 521** Synchrotron Radiation Instrumentation: Eleventh US National Conference
Edited by Piero Pianetta, John Arthur, and Sean Brennan, May 2000, 1-56396-941-6
- 485** Radio Frequency Power in Plasmas: 13th Topical Conference
Edited by Stefano Bernabei and Franco Paoletti, September 1999, 1-56396-861-4
- 457** Trapped Charged Particles and Fundamental Physics
Edited by Daniel H. E. Dubin and Dieter Schneider, January 1999, 1-56396-776-6
- 443** Atomic Processes in Plasmas: Eleventh APS Topical Conference - 1998
Edited by Eugene Oks and Michael S. Pindzola, September 1998, 1-56396-802-9
- 426** Superstrong Fields in Plasmas: First International Conference
Edited by M. Lontano, April 1998, 1-56396-748-0

To learn more about these titles, or the AIP Conference Proceedings Series, please visit the
webpage <http://proceedings.aip.org>

NON-NEUTRAL PLASMA PHYSICS IV

Workshop on Non-Neutral Plasmas

San Diego, California 30 July–2 August 2001

EDITORS

François Anderegg

University of California, San Diego

Lutz Schweikhard

Ernst-Moritz-Arndt-Universität, Greifswald, Germany

C. Fred Driscoll

University of California, San Diego

SPONSORING ORGANIZATIONS

U.S. Office of Naval Research

National Science Foundation

U.S. Department of Energy

Institute for Pure and Applied Physical Sciences - UCSD

**AMERICAN
INSTITUTE
OF PHYSICS**

Melville, New York, 2002

AIP CONFERENCE PROCEEDINGS ■ VOLUME 606

Editors:

François Andereg
University of California at San Diego
Institute for Pure and Applied Physical Sciences
9500 Gilman Drive
La Jolla, CA 92093-0360
USA
E-mail: fanderegg@ucsd.edu

Lutz Schweikhard
Ernst-Moritz-Arndt-Universität
Institut für Physik
Dormstrasse 10a
D-17487 Greifswald
GERMANY
E-mail: Lutz.Schweikhard@physik.uni-greifswald.de

C. Fred Driscoll
University of California at San Diego
Department of Physics
9500 Gilman Drive
La Jolla, CA 92093-0319
USA
E-mail: fdriscol@ucsd.edu

The articles on pp. 63-72, 121-126, 127-134, 151-163, and 209-217 were authored by U.S. Government employees and are not covered by the below mentioned copyright.

Authorization to photocopy items for internal or personal use, beyond the free copying permitted under the 1978 U.S. Copyright Law (see statement below), is granted by the American Institute of Physics for users registered with the Copyright Clearance Center (CCC) Transactional Reporting Service, provided that the base fee of \$19.00 per copy is paid directly to CCC, 222 Rosewood Drive, Danvers, MA 01923. For those organizations that have been granted a photocopy license by CCC, a separate system of payment has been arranged. The fee code for users of the Transactional Reporting Service is: 0-7354-0050-4/02/\$19.00.

© 2002 American Institute of Physics

Individual readers of this volume and nonprofit libraries, acting for them, are permitted to make fair use of the material in it, such as copying an article for use in teaching or research. Permission is granted to quote from this volume in scientific work with the customary acknowledgment of the source. To reprint a figure, table, or other excerpt requires the consent of one of the original authors and notification to AIP. Republication or systematic or multiple reproduction of any material in this volume is permitted only under license from AIP. Address inquiries to Office of Rights and Permissions, Suite 1N01, 2 Huntington Quadrangle, Melville, N.Y. 11747-4502; phone: 516-576-2268; fax: 516-576-2450; e-mail: rights@aip.org.

L.C. Catalog Card No. 2001099228
ISBN 0-7354-0050-4
ISSN 0094-243X
Printed in the United States of America

CONTENTS

Preface.....	xiii
Sponsors and Organizing Committee	xvii
Group Photo.....	xix

SECTION 1: ANTIMATTER PLASMAS AND RECOMBINATION

The Creation of High Quality Positron Beams Using Traps	3
R. G. Greaves	
Practical Limits on Positron Accumulation and the Creation of Electron-Positron Plasmas.....	10
R. G. Greaves and C. M. Surko	
Low-Energy Positron-Matter Interactions Using Trap-Based Beams.....	24
S. J. Gilbert, J. P. Sullivan, J. P. Marler, L. D. Barnes, P. Schmidt, S. J. Buckman, and C. M. Surko	
Recent Progress on the ATHENA Positron Accumulator	35
L. V. Jørgensen, D. P. van der Werf, T. L. Watson, M. Charlton, and M. J. T. Collier	
Electron Plasma for Antiproton Cooling in the ATHENA Experiment.....	45
M. Amoretti, C. Carraro, V. Lagomarsino, G. Manuzio, G. Testera, and A. Variola	
Cold Antimatter Plasmas, and Aspirations for Cold Antihydrogen.....	51
G. Gabrielse, J. N. Tan, N. S. Bowden, P. Oxley, C. H. Storry, M. Wessels, A. Speck, J. Estrada, P. Yesley, T. Squires, D. Grzonka, W. Oelert, G. Schepers, T. Sefzick, and J. Walz	
A Laser-Cooled, High Density Positron Plasma.....	63
B. M. Jelenković, A. S. Newbury, J. J. Bollinger, T. B. Mitchell, and W. M. Itano	
Two-Stream Instabilities in Guiding-Center Plasmas for Antihydrogen Recombination Schemes.....	73
R. Stowell and R. C. Davidson	
Design and Test of a Beam Line for Extraction of Slow Antiprotons from a Multi-Ring Electrode Ion Trap	79
K. Y. Franzen, H. Higaki, T. Ichioka, M. Hori, Z. Wang, N. Kuroda, S. Yoneda, H. A. Torii, K. Komaki, and Y. Yamazaki	
Spectroscopy of Rydberg Atoms in Non-Neutral Cold Plasmas.....	89
D. Feldbaum, N. V. Morrow, S. K. Dutta, and G. Raithel	
Ultracold Neutral Plasmas.....	96
T. C. Killian, M. J. Lim, S. Kulip, and S. L. Rolston	
Numerical Simulation of Ultracold Neutral Plasmas.....	102
S. G. Kuzmin and T. M. O'Neil	

SECTION 2: STRONGLY COUPLED PLASMAS, HIGHLY CHARGED IONS, AND DUSTY PLASMAS

Experimental Dynamics of Stressed, Strongly Correlated Magnetized Plasmas	111
T. B. Mitchell, J. J. Bollinger, W. M. Itano, and D. H. E. Dubin	
Laser-Induced Wakes in Ion Crystals	121
J. M. Kriesel, J. J. Bollinger, T. B. Mitchell, L. B. King, and D. H. E. Dubin	
Specific Heat and Latent Heat in Finite and Infinite One-Component Plasmas.....	127
J. P. Schiffer	
Ion Coulomb Crystals and Some Applications.....	135
M. Drewsen, L. Hornekær, N. Kjærgaard, K. Mølhave, A. M. Thommesen, Z. Videsen, A. Mortensen, and F. Jensen	
Coulomb Crystals in a Pulse-Excited Linear Paul Trap.....	145
N. Kjærgaard, K. Mølhave, and M. Drewsen	
Trapped Highly Charged Ion Plasmas.....	151
E. Takács and J. D. Gillaspay	
Cold Highly Charged Ions in a Penning Trap: Experiment and Simulation	164
J. P. Holder, L. Gruber, D. A. Church, and D. Schneider	
EBIT in the Magnetic Trapping Mode: Mass Spectrometry, Atomic Lifetime Measurements, and Charge Transfer Reactions of Highly Charged Atomic Ions	174
L. Schweikhard, P. Beiersdorfer, and E. Träbert	
Structure and Madelung Energy of Coulomb Clusters.....	181
H. Totsuji, T. Kishimoto, C. Totsuji, and K. Tsuruta	
Formation and Structural Transitions of 3D Coulomb Crystals in Dusty Plasmas	191
Y. Hayashi	
Dusty Plasmas under Microgravity	201
H. Totsuji, C. Totsuji, T. Kishimoto, and K. Tsuruta	

SECTION 3: CHARGED PARTICLE BEAMS AND FREE-ELECTRON LASERS

Kinetic Effects in High Gain Free-Electron Lasers.....	209
B. Hafizi and C. W. Roberson	
Self-Compensation for the Axial Velocity Spread in a Wiggler Field	218
D. F. Gordon, B. Hafizi, C. W. Roberson, and P. Sprangle	
An Experiment to Transfer Angular Momentum from a Helical Low Energy Proton Beam to a Trapped Electron Plasma	223
D. S. Todd and R. E. Pollock	
Intrabeam Scattering and Halo Formation in Intense Ion Beams.....	229
N. Uhlmann and G. Zwicknagel	
Crystalline Ion Beams in the RF Quadrupole Storage Ring PALLAS.....	235
U. Schramm, T. Schätz, and D. Habs	

Multiple Coulomb Ordered Strings of Ions in a Storage Ring	245
R. W. Hasse	

SECTION 4: COLLECTIVE MODES

Thermal Excitation of Trivelpiece-Gould Modes in a Pure Electron Plasma	253
F. Anderegg, N. Shiga, J. R. Danielson, D. H. E. Dubin, C. F. Driscoll, and R. W. Gould	
Thermal Excitation of Modes in a Non-Neutral Plasma	263
R. W. Gould	
Using the Plasma Noise Spectrum to Measure the Parallel Temperature in a Non-Neutral Plasma	271
M. T. Nakata, G. W. Hart, and B. G. Peterson	
Trapped Particle Asymmetry Modes in Non-Neutral Plasmas	277
A. A. Kabantsev, C. F. Driscoll, T. J. Hilsabeck, T. M. O'Neil, and J. H. Yu	
Simulations of the Instability of the $m=1$ Self-Shielding Diocotron Mode in Finite-Length Non-Neutral Plasmas	287
G. W. Mason and R. L. Spencer	
Large Amplitude $m=1$ Diocotron Mode Measurements in the Electron Diffusion Gauge Experiment	298
T. G. Jenkins, K. A. Morrison, R. C. Davidson, and S. F. Paul	
$m=1$ Diocotron Mode Damping in the Electron Diffusion Gauge (EDG) Experiment	305
S. F. Paul, K. A. Morrison, R. C. Davidson, and T. G. Jenkins	
Magnetic Shear Stabilization of Diocotron Instability	311
S. Kondoh, T. Tatsuno, and Z. Yoshida	
$l=1$ Diocotron Instability of Single Charged Plasmas in a Cylindrical Penning Trap with Central Conductor	317
M. Romé, A. V. Arefiev, I. A. Kotelnikov, and R. Pozzoli	
Rigorous Fluid Model for 3D Analysis of the Diocotron Instability	323
G. G. M. Coppa, A. D'Angola, G. L. Delzanno, and G. Lapenta	
Diocotron Spectrum with Compression Effects	329
G. L. Delzanno, V. I. Pariev, G. Lapenta, and J. M. Finn	
Modes in a Non-Neutral Plasma Column of Finite Length	335
S. N. Rasband and R. L. Spencer	
Interacting Solitons in a Non-Neutral Plasma	341
G. W. Hart and B. G. Peterson	
Experimental Observation of Fluid Echoes in a Non-Neutral Plasma	347
J. H. Yu and C. F. Driscoll	
Landau Damping of Electron Plasma Waves in the Linear and Trapping Regimes	353
J. R. Danielson, F. Anderegg, N. Shiga, K. Rigg, and C. F. Driscoll	
Collective Motional Resonances and Instabilities of an Electron Cloud Stored in a Penning Trap	360
D. Biswas, P. Paasche, T. Valenzuela, C. Angelescu, S. Ananthamurthy, and G. Werth	

SECTION 5: TRANSPORT

Amplitude Scaling of Asymmetry-Induced Transport	369
D. L. Eggleston and B. Carrillo	
Quadrupole Induced Resonant Particle Transport in a Pure Electron Plasma	378
E. P. Gilson and J. Fajans	
Shear Reduction of 2D Point Vortex Diffusion.....	388
D. H. E. Dubin and C. F. Driscoll	
Shear-Limited Test Particle Diffusion in 2-Dimensional Plasmas	401
F. Anderegg, C. F. Driscoll, and D. H. E. Dubin	
Classical Collisional Diffusion in the Annular Penning Trap.....	407
Q. Quraishi, S. Robertson, and B. Walch	
Investigation of the Expansion Rate Scaling of Plasmas in the Electron Diffusion Gauge Experiment.....	416
K. A. Morrison, R. C. Davidson, S. F. Paul, and T. G. Jenkins	
Decay of the Diocotron Rotation and Transport in a New Low-Density Asymmetry-Dominated Regime	422
E. Sarid, E. Gilson, and J. Fajans	
Breaking the Azimuthal Symmetry—Jumping Off-Axis or Staying Away from the Axis?	433
E. Sarid, C. Teodorescu, P. Marcus, and J. Fajans	

SECTION 6: 2D FLUID DYNAMICS

Two-Dimensional Vortex Dynamics with Background Vorticity	443
D. A. Schecter	
Continuously Injected Plasma Columns	453
T. Pasquini and J. Fajans	
Experimental and Numerical Study of Asymmetric Vortex Merger in a Pure Electron Plasma	459
M. Amoretti, D. Durkin, J. Fajans, R. Pozzoli, and M. Romé	
Interaction of Electron Vortices under the Influence of Background Vorticity Distribution	464
Y. Kiwamoto, K. Ito, A. Sanpei, Y. Soga, T. Yuyama, and T. Michishita	
Electron Vortex Dynamics and Two-Dimensional Field Analysis.....	474
K. Ito, A. Sanpei, and Y. Kiwamoto	
Characteristics and Generation Mechanism of Holes in an Extended Electron Vortex	480
A. Sanpei, K. Ito, Y. Soga, and Y. Kiwamoto	
Nonlinear PIC Simulation in a Penning Trap	486
G. Lapenta, G. L. Delzanno, and J. M. Finn	

SECTION 7: GENERAL THEORY

Energy Loss of Ions by Collisions with Magnetized Electrons.....	499
G. Zwicknagel and C. Toepffer	
Floquet Theory of the Quantum Dynamic Kingdon Trap	509
R. Blümel	
Kinetic Description of a Degenerate, Rotating, Non-Neutral Electron Plasma in External Magnetic Fields in the Framework of the Thomas-Fermi-Dirac Theory.....	513
V. G. Molinari, F. Rocchi, and M. Sumini	
Analytic Potentials for Realistic Electrodes	519
S. E. Barlow, A. E. Taylor, and K. Swanson	
Image Charge Forces inside Conducting Boundaries	525
M. D. Tinkle and S. E. Barlow	
Non-Collisional Kinetic Model for Non-Neutral Plasmas in a Penning Trap: General Properties and Stationary Solutions.....	531
G. G. M. Coppa and P. Ricci	
Forms and Oscillations Modes of Ion Cloud in the Linear RF-Only Quadrupole Traps and in Ion Traps	537
A. A. Vedenov and E. N. Nikolaev	
Charge Sign Effect on the Coulomb Logarithm for a Two-Component (e.g., Antihydrogen) Plasma in a Penning Trap	544
J. R. Correa, Y. Chang, and C. A. Ordonez	
Two-Temperature Equilibration Rate for a Two-Component (e.g., Antihydrogen) Plasma in a Penning Trap	550
Y. Chang and C. A. Ordonez	
Confinement Properties of Non-Neutral and Neutral Plasmas in an Axially Symmetric System.....	556
T. Tamano and I. Katanuma	

SECTION 8: EXPERIMENTAL DEVICES AND TECHNIQUES

Synchronization Effect in an Ion Trap Resonator	565
H. B. Pedersen, B. Amarant, O. Heber, M. L. Rappaport, and D. Zajfman	
Paul Trap Simulator Experiment (PTSX) to Simulate Intense Beam Propagation through a Periodic Focusing Quadrupole Field.....	576
R. C. Davidson, P. C. Efthimion, E. Gilson, R. Majeski, and H. Qin	
A Magnetic Trap for Simultaneous Confinement of Neutral Atoms and a Non-Neutral Plasma	582
D. H. E. Dubin	
Possible Antihydrogen Trapping Field and Non-Neutral Plasma Density Limits.....	590
C. A. Ordonez and D. D. Dolliver	
Ion Trapping in the Virtual Cathode of the Penning Fusion eXperiment-Ions	596
M. M. Schauer, D. C. Barnes, and K. R. Umstadter	

Status of the Eltrap Project.....	603
M. Amoretti, G. Bettega, F. Cavaliere, M. Cavenago, F. De Luca, R. Pozzoli, and M. Romé	
Bunching and Cooling of Radioactive Ions with REXTRAP.....	609
F. Ames, D. Beck, G. Bollen, O. Forstner, D. Habs, G. Huber, K. Reisinger, and P. Schmidt	
SHIPTRAP: A Capture and Storage Facility on Its Way Towards a RIB-Facility.....	615
G. Marx, J. Dilling, H.-J. Kluge, M. Mukherjee, W. Quint, S. Rahaman, D. Rodriguez, G. Sikler, M. Tarisien, C. Weber, and the SHIPTRAP Collaboration	
Development of an RF Ion Guide for Trapping Energetic Radioactive Nuclear Ions.....	625
M. Wada, Y. Ishida, T. Nakamura, N. Oshima, Y. Nakai, T. M. Kojima, Y. Kanai, H. Ohyama, T. Kambara, Y. Yamazaki, A. Yoshida, T. Kubo, Y. Matsuo, Y. Fukuyama, K. Okada, K. Noda, S. Ohtani, H. Kawakami, and I. Katayama	
System of Slow Highly Charged Ion Beam Generation Using a Cold Positron Plasma Trap at RIKEN.....	634
A. Mohri, T. M. Kojima, N. Oshima, M. Niigaki, and Y. Yamazaki	
Proposed Non-Neutralized Two-Fluid Plasma Experiment.....	641
H. Himura, Z. Yoshida, M. Fukao, J. Morikawa, and Y. Ogawa	
Quadrature Detection for the Separation of the Signals of Positive and Negative Ions in Fourier Transform Ion Cyclotron Resonance Mass Spectrometry.....	647
L. Schweikhard, J. J. Drader, S. D.-H. Shi, C. L. Hendrickson, and A. G. Marshall	
Charge-Changing Reactions and Their Influence on the Ion Motion in a Penning Trap.....	652
A. Herlert, L. Schweikhard, and M. Vogel	

SECTION 9: TOROIDAL GEOMETRY

Flowing Electron Plasmas as Modified Current Source.....	661
H. Himura, C. Nakashima, H. Saito, Z. Yoshida, J. Morikawa, and M. Fukao	
Electron Plasma Confinement in a Partially Toroidal Trap.....	671
M. R. Stoneking, P. W. Fontana, R. L. Sampson, and D. J. Thuecks	
Comparative Experimental Study of Large-Scale Fluctuations in a Toroidally Magnetized Low-β Plasma.....	681
O. Grulke, F. Greiner, T. Klinger, and A. Piel	
Design of a Toroidal Device with a High Temperature Superconductor Coil for Non-Neutral Plasma Trap.....	691
Y. Ogawa, J. Morikawa, H. Nihei, D. Ozawa, Z. Yoshida, T. Mito, N. Yanagi, and M. Iwakuma	

**Injection of Electrons into a Toroidal Trap Using Chaotic Orbits near
Magnetic Null697**
C. Nakashima, Z. Yoshida, H. Himura, M. Fukao, J. Morikawa, and
H. Saitoh

Relaxed States in Plasmas—Non-Neutral and Diamagnetic Plasmas703
Z. Yoshida and H. Saitoh

NNP-2001 Roundtable Discussion713

List of Participants725

Author Index735

Preface

This Proceedings volume incorporates most of the scientific presentations at the Workshop on Non-Neutral Plasmas, held at the University of California at San Diego, from July 30 to August 2, 2001. This meeting was the sixth in a series which includes Washington DC (1988) [1], Irvine CA (1992), Berkeley CA (1994) [2], Boulder CO (1997), and Princeton NJ (1999) [3].

Historically, non-neutral plasma research began with investigations of collective effects in the equilibria, modes and instabilities of energetic particle beams [4-6]. In the 1970's and early 80's, experiments and theory at Maryland, UCLA, and UCSD began to focus on relatively low energy, *trapped* clouds of electrons or ions. The 1988 meeting at the National Academy of Sciences in Washington was organized by Chuck Roberson of the Office of Naval Research to give focus to the new community of researchers working on trapped non-neutral plasmas. A later study by the NAS included the research potential in non-neutral plasmas [7]. The 2001 Workshop, with about 110 participants, shows that non-neutral plasma physics is now a mature, healthy sub-field of physics.

In simplest terms, these plasmas are rotating clouds of 1 to 1 billion charged particles, all with the same sign of charge, suspended in vacuum by simple magnetic and electric fields [8]. The motion of these particles can be accurately diagnosed, allowing the collective "plasma" interactions to be studied in detail. Because of their simplicity, non-neutral plasmas are a natural focus for basic research which is driven by the internal logic of the science rather than by the demands of particular applications. In a sense, these simple systems of N identical charged particles in near-thermal-equilibrium states are the classical physics analog of liquid Helium (or today's Bose-Einstein condensate), with opportunities for fundamental research advances which can then be applied to multi-species plasmas in more complex configurations.

Today, non-neutral plasma research ranges from basic plasma physics to sophisticated technical applications; and much of the success of the field depends on the continuing close interplay between theory and experiment. In basic research, the fact that non-neutral plasmas can be contained in near-thermal-equilibrium states means that first-principles theories can be directly and quantitatively compared to experiments. On the harder problems, such as particle and heat transport, several iterations between theory and experiment may be required; but the system is simple enough that the process inevitably leads to a deeper understanding of fundamental plasma physics. This "enabling science" supports the "applied" technical applications which now range from antimatter containment to quantum computing; but even the most sophisticated experiments continue to be closely coupled to basic theory.

Section 1 in this Proceedings contains papers on the exciting topics of Antimatter Plasmas and Recombination. Containment of positrons at high densities and low temperatures now enables positron beam probes of molecular bonds and of solid surfaces. At the CERN accelerator, antiprotons are being trapped and cooled, both to form beams for spectroscopic and collision studies, and (more ambitiously) to generate antihydrogen from antiprotons trapped together with positrons. Recombination in ultracold neutral matter plasmas is also being investigated, with fundamental theory questions as to the meaning of particle correlations.

Section 2 describes some of the stunning experiments on crystallized ions at milli-Kelvin temperatures, including work on “earthquakes”, phonon wakes, and multi-species effects. Crystallized ions have now been created in a variety of geometries, including linear Penning and Paul traps and circular storage rings, with possible applications ranging from quantum computing to microprobes. The “EBIT” experiments can trap highly stripped ions for precise spectroscopy in the X-ray wavelengths. The theory of crystallization in infinite and finite-sized systems is well developed, and has much in common with “dusty plasmas”.

Section 3 presents connections to the large and varied field of beam physics. Kinetic and collisional effects are important for the electron beams driving free-electron lasers, and (in a more unusual application) for proton beams impacting electron plasma targets. With modern laser cooling techniques, ion beams can form crystalline strings in storage rings, with important dynamical effects in precision mass determinations.

In Section 4, we turn to the basic plasma physics of collective waves and instabilities in trapped electron plasmas. Electron plasmas in thermal equilibrium are among the simplest many-body systems known, and received plasma waves can be used as a plasma thermometer. On the other hand, the $\mathbf{E} \times \mathbf{B}$ drift (or “diocotron”) modes pose many challenges with regard to trapped particles, damping, and instabilities in realistic finite-geometry plasmas. Here, the level of understanding obtained from the combination of theory, simulation, and experiments is truly impressive.

Section 5 presents several perspectives on the transport of particles and energy across the magnetic field. Plasma expansion and loss due to “external” effects such as trapping field asymmetries or collisions with neutral background gas can limit the plasma lifetime; here, experiments agree with theory in many regimes, but further development is needed in other regimes. In contrast, research on transport towards the confined thermal equilibrium state due to “internal” particle collisions has had more success: theory and experiments have definitively mapped out the particle diffusion, heat diffusion, and viscosity coefficients due to “long-range” collisions, most recently including the reduction of diffusion due to shear in the plasma flow velocity. Moreover, these transport processes may be applicable to neutral plasmas in a variety of regimes.

The papers in Section 6 are motivated by the striking correspondence between high temperature electron plasmas and fluids such as water in 2-dimensional flows. Experiments on vortex dynamics and on the free relaxation of fluid turbulence have been exceptionally “clean”, and have led to further advances from theory and

computer simulation. Here again, many results are directly applicable to $\mathbf{E} \times \mathbf{B}$ drift vortices in neutral plasmas.

Section 7 contains a variety of General Theory papers, ranging from classical potential theory and classical particle kinetics to quantum effects in esoteric non-neutral plasmas. In all these systems, the theory analyses are well connected to the possibility of experimental verification.

The papers in Section 8 discuss a wide variety of sophisticated non-neutral plasma devices and techniques developed in the pursuit of physics goals ranging from ion spectroscopy to beam physics to fusion physics to antimatter containment. Here, connections are made to the wide community of physicists who *use* non-neutral plasmas in the many-particle limit where the collective interactions become important.

Section 9 presents research venturing from the relative simplicity of cylindrical geometry to the complexities of toroidal confinement systems, with strong scientific connections to the $\mathbf{E} \times \mathbf{B}$ flows arising from local charge separation in neutral plasmas. Here, the single species experiments are advantageous in that the electric field is directly related to the particle density, simplifying the comparisons between theory and experiment.

Finally, the Roundtable Discussion offers perspectives from past Workshop chairmen on the past, present and future of non-neutral plasma research. These perspectives and the papers presented in this Proceedings all suggest a healthy research program, with core research on basic physics questions supporting a wide range of sophisticated and important technical applications and applied science.

REFERENCES

1. C.W. Roberson and C.F. Driscoll, Eds., *Non-Neutral Plasma Physics*, AIP Conf. Proc. No. 175 (AIP, New York, 1988).
2. J.R. Fajans and D.E. Dubin, Eds., *Non-Neutral Plasma Physics II*, AIP Conf. Proc. No. 331 (AIP, New York, 1995).
3. J.J. Bollinger, R.L. Spencer and R.C. Davidson, Eds., *Non-Neutral Plasma Physics III*, AIP Conf. Proc. No. 498 (AIP, New York, 1999).
4. R.C. Davidson, *Theory of Nonneutral Plasmas* (Addison-Wesley, Redwood City, CA, 1974).
5. R.C. Davidson, *Physics of Nonneutral Plasmas* (Addison-Wesley, Redwood City, CA, 1990).
6. R.C. Davidson and H. Qin, *Physics of Intense Charged particle Beams in High Energy Accelerators* (World Scientific Publishing Co, to appear, Winter 2001).
7. *Plasma Science: From Fundamental Research to Technological Applications* (National Academy Press, Washington, D.C., 1995).
8. T.M. O'Neil, *Physics Today* **52** (No. 8), 24 (1999).

C. Fred Driscoll
Chair, NNP-2001 Workshop

2001 Workshop on Non-Neutral Plasmas

July 30-August 2, 2001
University of California, San Diego
La Jolla, California USA

Sponsored by
US Office of Naval Research
National Science Foundation
US Department of Energy
Institute for Pure and Applied Physical Sciences - UCSD

Organizing Committee

C. Fred Driscoll, Chair
University of California, San Diego

Ron Davidson, Vice Chair
Princeton Plasma Physics Laboratory

Dan Barnes
Los Alamos National Laboratory

John Bollinger
National Institute of Standards and Technology

Dan Dubin
University of California, San Diego

Joel Fajans
University of California, Berkeley

John Goree
University of Iowa

Jeff Hangst
University of Aarhus

Yasuhito Kiwamoto
Kyoto University

Robert Pollock
Indiana University

Roberto Pozzoli
University of Milan

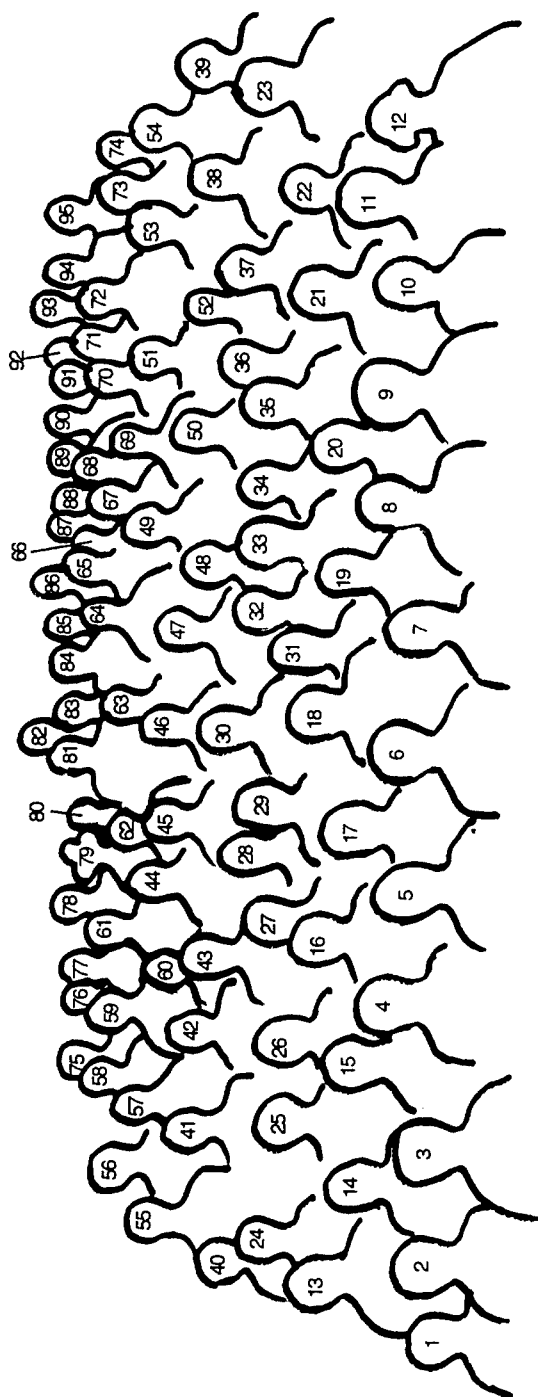
Charles Roberson
Office of Naval Research

Dieter Schneider
Lawrence Livermore National Lab.

Lutz Schweikhard
Ernst-Moritz-Arndt-Universität

Matthew Stoneking
Lawrence University

Cliff Surko
University of California, San Diego



- 1) A. Mohri 2) C. Nakashima 3) K. Ito 4) Z. Yoshida 5) A. Sanpei 6) Y. Hayashi 7) T. Nakata 8) G. Otto 9) H. Himura 10) J. Christina
- 11) N. Kuroda 12) R. Blumel 13) S. Kondo 14) J. Schiffer 15) A. Vedenov 16) L. Schweikhard 17) M. Zuzic 18) R. Quinn 19) J. Ellsworth
- 20) D. Bahr 21) J. Holder 22) T. Tamano 23) D. Zajfman 24) T. Pasquini 25) H. Totsuji 26) R. Gould 27) D. Dubin 28) K.Y. Franzen
- 29) S. Kuzmin 30) T. Killian 31) K. Meyer 32) T. Mitchell 33) S. Paul 34) T. Ichioka 35) C.F. Driscoll 36) G. Raithel 37) T. O'Neil
- 38) C. Roberson 39) T. Schatz 40) Y. Kiwamoto 41) K. Rigg 42) G. Zwicknagel 43) U. Eisenbarth 44) J. Danielson 45) L. Barnes
- 46) C. Surko 47) U. Schramm 48) E. Sarid 49) M. Drewsen 50) F. Rocchi 51) R. Hasse 52) M. Amoretti 53) N. Kjaergaard
- 54) S.N. Rasband 55) K. Morrison 56) M. Wada 57) J. Kriesel 58) T. Hilsabeck 59) J. Yu 60) J. Marler 61) N. Shiga 62) R. Greaves
- 63) M. Stoneking 64) G. Marx 65) G. Hart 66) Q. Quraishi 67) F. Anderegg 68) S. Barlow 69) M. Rome 70) W. Manheimer 71) D. Barnes
- 72) D. Eggleston 73) T. Jenkins 74) R. Stowell 75) J. Bollinger 76) D. Schecter 77) R. Pozzoli 78) D. Todd 79) M. Tinkle 80) F. Ames
- 81) R. Pollock 82) L. Jorgensen 83) P. Schmidt 84) G. Lapenta 85) O. Grulke 86) E. Takacs 87) G. Mason 88) S. Robertson
- 89) B. Peterson 90) G. Bollen 91) P. Ricci 92) G.L. Delzanno 93) D. Goldbeck 94) J. Goree 95) R. Davidson



SECTION 1

ANTIMATTER PLASMAS

AND RECOMBINATION

The Creation of High Quality Positron Beams Using Traps

R. G. Greaves

First Point Scientific, Inc., 5330 Derry Avenue, Suite J, Agoura Hills, CA91301

Abstract. High quality positron beams are currently used for a variety of applications in science and technology. One of the most demanding applications is as analytical tools for surface and materials science, where ultra-short positron pulses (<200 ps) and microscopic beams (<1 micron in diameter) are desirable. Positron traps offer a qualitatively new method for beam formation and manipulation that has significant advantages in efficiency, flexibility, and cost over current beam conditioning techniques. One important capability is brightness enhancement by radial compression of the positron plasma using the rotating wall technique developed for electron and ion plasmas. A second capability is the production of ultra-short positron pulses required for positron annihilation lifetime spectroscopy. This can be accomplished using a trap by means of the simple technique of quadratic potential bunching, thus avoiding multiple stages of rf bunching currently used to produce pulsed positron beams.

INTRODUCTION

Over the past 30 years low-energy positron beams have been developed for a variety of scientific and technological applications. These include fundamental studies of atomic physics phenomena [1], mass spectrometry [2], and the analysis of surfaces and solids [3,4]. During this period, positron beam fluxes have increased by at least six orders of magnitude, while techniques have been developed for producing pulse widths of less than 100 ps and beams with diameters of less than $1\text{ }\mu\text{m}$. Many of the developments in positron beam conditioning have been adapted from electron beam technology, and the limits of these techniques have now been reached. Further advances must therefore involve the development of stronger positron sources or must appeal to different approaches.

One of the most promising new approaches to the creation of high quality positron beams is the use of positron traps. These devices have been extensively employed for studies of positron-molecule interactions [5,6], mass spectrometry [2], electron-positron plasma experiments [7], and astrophysical simulations [8]. They have also been applied to a limited extent for beam condition on LINACS [9]. More recently a positron trap was used to create an ultracold positron beam [10] and this beam has been used for ground breaking studies of positron-molecule interactions in a previously inaccessible low-energy regime [11, 12].

However, these experiments have exploited only a fraction of the potential capabilities for beam conditioning using traps. In this paper, we present some of these capabilities, including the potential for producing ultrashort positron pulses and microbeams.

POSITRON TRAPPING

Trap-based positron beams assume that the positrons have been accumulated in a Penning trap. A variety of techniques have been proposed or developed for trapping positrons, including trapping by collisions with a buffer gas [13], trapped ions [14] or trapped electrons [15], trapping by electronic damping [16], chaotic orbits and field ionization of Rydberg positronium atoms [17]. Of these, only the buffer gas technique has the efficiency to be usable for high throughput beam systems, although trapping using ions has the potential to achieve similar high efficiencies.

For the buffer-gas approach, the trap has three stages of successively lower pressure, established by differential pumping, and electrostatic potential. Radial confinement is by an axial magnetic field [18, 19]. Positrons from a conventional positron source are trapped by collisions with a buffer gas, usually nitrogen, in the high pressure region and accumulate and cool in the low pressure region. Trapping efficiencies of $> 30\%$ have been achieved, and up to 3×10^8 positrons have been accumulated in eight minutes from a 70-mCi ^{22}Na source. This system is tolerant of low-quality positron beams of the type obtained from rare gas moderators, which makes it suitable for high flux systems.

POSITRON BEAM TECHNOLOGY

Positron Beam Applications

Positron beams have been widely exploited as diagnostics of surfaces and solids [3]. These techniques involve the injection of a positron beam onto a surface, and measuring the particles or photons that are emitted. A variety of properties can be measured, including the surface composition, crystal structure, and concentration and distribution of vacancy type defects. In some cases, positron beam techniques provide similar information to their electron-beam analogues. For example, Low-Energy Positron Diffraction (LEPD) is analogous to Low-Energy Electron Diffraction (LEED), and Positron Annihilation Induced Auger Electron Spectroscopy (PAES) is analogous to Electron Auger Spectroscopy (AES). In other cases, positron based techniques provide information not available using electron beams. In particular, techniques based on the annihilation and positronium formation channels, which are not available for electrons, can provide unique information. For example, Positron Annihilation Spectroscopy (PAS), which measures the Doppler broadening of the 511 keV annihilation line, and Positron Annihilation Lifetime Spectroscopy (PALS), which measures the lifetime of positrons in materials, provide the most sensitive measure available of the size distribution and concentration of vacancy type defects.

Furthermore, even in cases where the same information is available using electrons, the analogous positron technique often has significant advantages. For example, in contrast to AES, PAES is carried out using low energy positron beams and can provide spectra that are essentially free from background secondary electrons [20].

One of the most important areas of current research using PAS and PALS is the characterization of the low- k dielectrics that are being used to increase the clock speeds

of integrated circuits [21]. Using PAS it is possible to measure the dielectric constant of these films in a non-destructive way [22], thus providing a potential quality control tool for IC production lines. The techniques also provide sensitive measurements of crystal lattice damage from ion implantation. Another important area is the measurements of aging and other properties in polymers [23].

Positron Beam Requirements

Each positron-based technique has its own particular beam requirements. In general, maximum beam flux is desirable. For some applications such as time-of-flight PAES and PALS, ultrashort positron pulses (< 200 ps) are desirable. For atomic physics experiments, ultracold positron beams are useful. Many techniques benefit if they are implemented using scanning microbeams ($< 1 \mu\text{m}$ in diameter) so that spatially resolved information can be obtained.

Current technology uses complex rf bunchers and choppers for producing short pulse beams, while the inefficient technique of remoderation brightness enhancement [24] is used to produce microbeams. As described below, positron traps can be used to perform both of these functions with the potential advantages of improved efficiency, simplicity and reduced cost.

Beam Bunching

A variety of techniques have been developed for producing pulsed positron beams. The most advanced of these have the capability for producing subnanosecond positron pulses. One of these techniques is the harmonic potential buncher developed by A. P. Mills [25]. This applies a harmonic potential over the flight path of the positrons, thus producing a spatio-temporal focusing effect at the point of lowest potential. This technique has been applied to beams in flight, but it can be implemented in a much simpler and more effective way using trapped positrons, because the effect is strongest when applied to a pulse of positrons that is much shorter than the flight path. This can be easily accomplished using trapped positrons, and moreover, the trapping electrode structure can be used to provide the harmonic potential.

Brightness Enhancement

Several positron applications require microbeams, which can be produced using traps by a combination of two techniques, namely plasma compression prior to beam extraction, and extraction of positrons from the center of the plasma.

The smallest diameter to which a positron beam can be focused is determined by the relation [26]:

$$d_{\min} \simeq \frac{\varepsilon}{\alpha\sqrt{E}}, \quad (1)$$

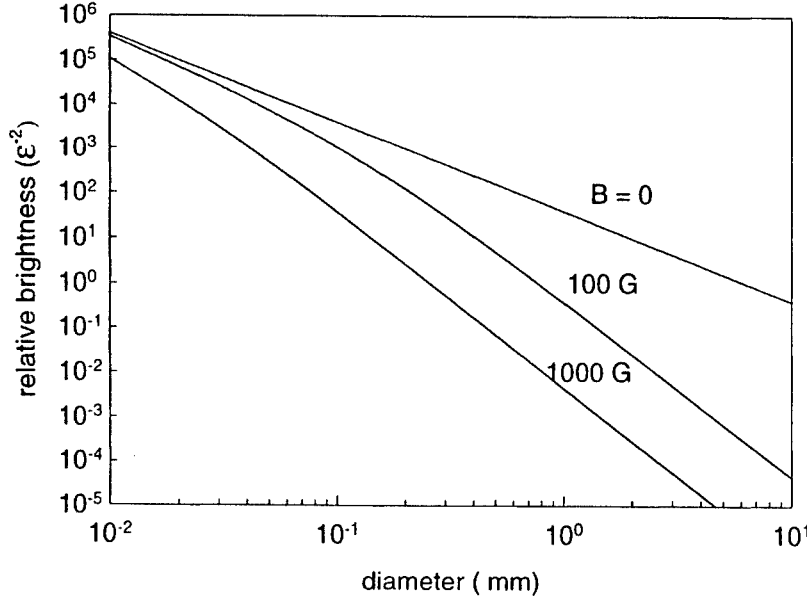


FIGURE 1. Relative brightness of a positron beam as a function of beam diameter for $E_{\perp} = 0.025$ eV.

where α and E are the convergence angle and energy of the beam at the focus and ϵ is the beam emittance. For a beam extracted from a magnetic field B , the emittance is given by [27]:

$$\epsilon \simeq d\sqrt{\Delta E_{\perp}} + \frac{1}{2\sqrt{2}}\sqrt{\frac{e}{m}}d^2B. \quad (2)$$

Figure 1 shows the dependence of the relative brightness, $1/\epsilon^2$, on beam diameter for various values magnetic field strength. From this figure it can be seen that the magnetic field has the effect of reducing the brightness of the beam, but considerable brightness enhancement is possible by compressing the plasma radially. It also illustrates the importance of working at as low a magnetic field as possible.

Plasma compression is achieved by applying a rotating electric field to the plasma [28]. This is accomplished by applying suitably phased sine waves to azimuthally segmented confining electrodes. Figure 2 shows the development of radial distribution of a positron plasma in time during the application of a rotating electric field [29, 30]. These data were obtained in a relatively low magnetic field using a buffer gas to cool the plasma during compression. This proof-of-principle experiment demonstrated that significant radial compression (~ 20 increase in central density) and rapid compression ($dN/dN \sim 15 \text{ sec}^{-1}$) could be obtained in a good vacuum environment ($p \sim 10^{-8}$ torr) where the annihilation is negligible ($\tau_a > 1000$ s). As described below, this technique is being refined and implemented in an advanced trap-based positron beam system.

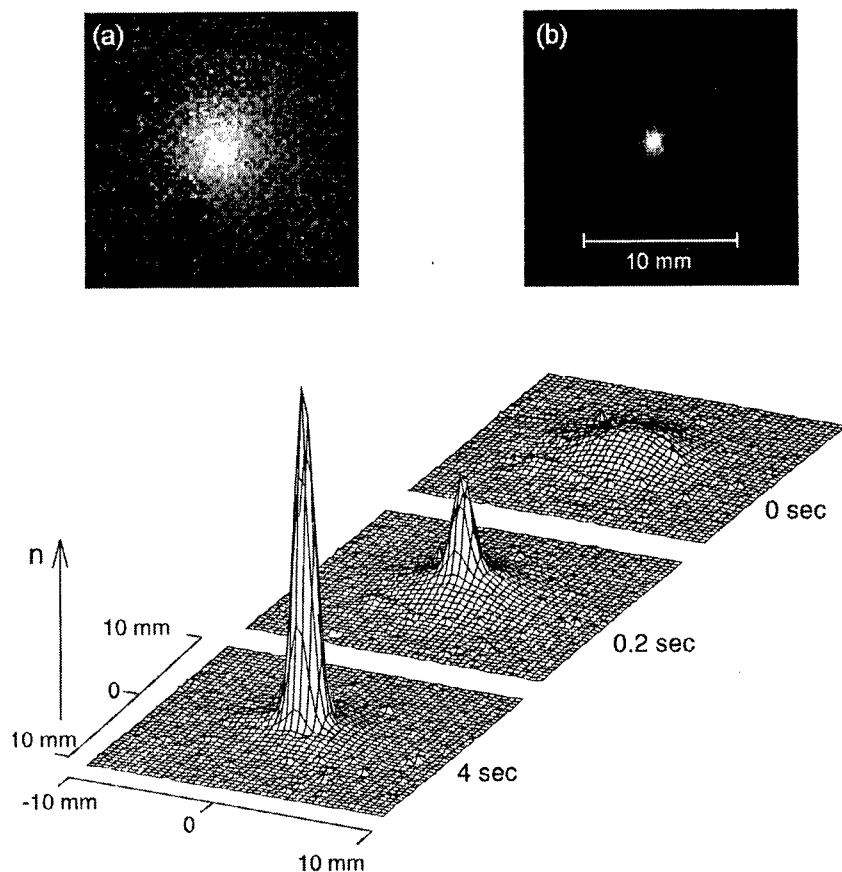


FIGURE 2. (a) and (b): CCD images of positron plasmas at $t = 0$ and $t = 4$ s respectively. (c) Radial profiles of a positron plasma with $N_{\text{tot}} = 10^7$ positrons, $f_w = 2.5$ MHz, $A_w = 56$ mV, and 2×10^{-8} torr of CF_4 .

ADVANCED TRAP-BASED POSITRON BEAM SYSTEMS

First Point Scientific, Inc. (FPSI) is currently developing an Advanced Positron Beam Source (APBS) based on a two-stage buffer gas trap. This system features a compact, low-cost design and the capability for producing subnanosecond positron pulses using a harmonic potential buncher. FPSI is also developing a separate, differentially-pumped third stage, the Positron Trap Beam Source (PTBS), featuring a rotating electric field and advanced extraction system for producing microbeams. The layout of these systems is shown in Fig. 3.

Features of the systems include the capability of producing pulse widths of < 200 ps (for a stand alone APBS system), and ultracold (< 8 meV energy spread), small diameter ($\sim 10 \mu\text{m}$) beams for the APBS/PTBS system in the magnetic field. After extraction from the field and focusing, it is expected that microbeams can be obtained by focusing.

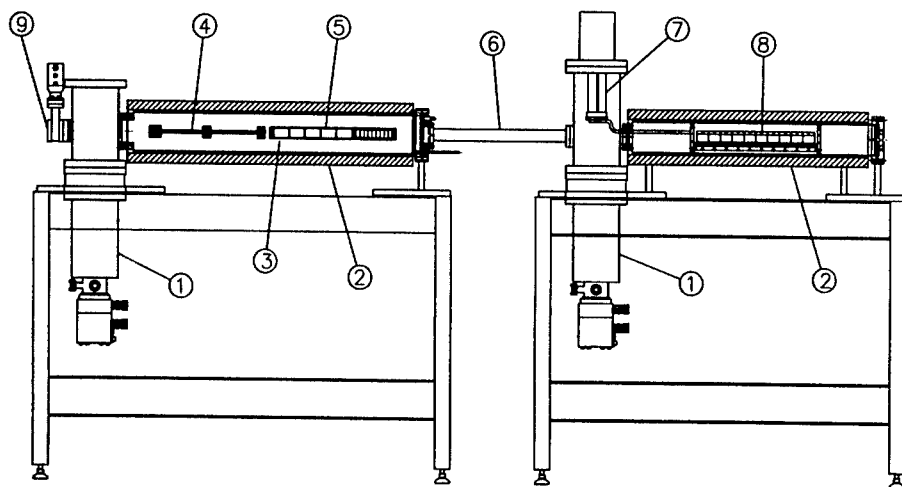


FIGURE 3. Layout of the APBS (left) and the PTBS (right) showing: 1. Cryopumps; 2. Solenoid magnets; 3. Confining electrodes; 4. High pressure section; 5. Intermediate pressure section; 6. Differential pumping section; 7. Cold head; 8. Confining electrodes in lower pressure region including rotating wall section; and 9. Entry port for positron beam.

Throughput is expected to be 30–40% of the incident beam.

These systems are expected to form the basis of a new generation of trap-based positron beam systems with advantages of lower cost, greater compactness and improved performance over existing systems.

CONCLUSION

A new generation of positron beam systems is being developed based on positron trapping techniques. These systems will have unique capabilities for producing bright, ultracold, pulsed positron beams with a variety of applications in scientific research and in industry.

ACKNOWLEDGEMENTS

The author acknowledges helpful conversations with C. M. Surko and J. R. Bayless. This work is supported by Office of Naval Research, Grant No. N00014-00-C-0710, and the National Science Foundation, Grant No. DMI-0078468.

REFERENCES

1. W. E. Kauppila and T. S. Stein, *Advances in Atomic, Molecular, and Optical Physics* **26**, 1 (1990).
2. L. D. Hulett, Jr. *et al.*, *Chemical Physics Letters* **216**, 236 (1993).
3. P. J. Schultz and K. G. Lynn, *Reviews of Modern Physics* **60**, 701 (1988).
4. R. H. Howell *et al.*, *Applied Surface Science* **116**, 7 (1997).
5. K. Iwata *et al.*, *Physical Review A* **51**, 473 (1995).
6. K. Iwata, R. G. Greaves, and C. M. Surko, *Physical Review A* **55**, 3586 (1997).
7. R. G. Greaves and C. M. Surko, *Physical Review Letters* **75**, 3846 (1995).
8. B. L. Brown, M. Leventhal, A. P. Mills, Jr, and D. W. Gidley, *Physical Review Letters* **53**, 2347 (1984).
9. D. Segers, J. Paridaens, M. Dorikens, and L. Dorikens-Vanpraet, *Nuclear Instruments and Methods in Physics Research A* **337**, 246 (1994).
10. S. J. Gilbert, C. Kurz, R. G. Greaves, and C. M. Surko, *Applied Physics Letters* **70**, 1944 (1997).
11. S. J. Gilbert, R. G. Greaves, and C. M. Surko, *Physical Review Letters* **82**, 5032 (1999).
12. J. Sullivan, S. J. Gilbert, and C. M. Surko, *Physical Review Letters* **86**, 1494 (2001).
13. C. M. Surko, M. Leventhal, and A. Passner, *Physical Review Letters* **62**, 901 (1989).
14. D. J. Wineland, C. S. Weimer, and J. J. Bollinger, *Hyperfine Interactions* **76**, 115 (1993).
15. A. Mohri, these proceedings.
16. L. Haarsma, K. Abdullah, and G. Gabrielse, *Physical Review Letters* **75**, 806 (1995).
17. J. Estrada *et al.*, *Physical Review Letters* **84**, 859 (2000).
18. T. J. Murphy and C. M. Surko, *Physical Review A* **46**, 5696 (1992).
19. R. G. Greaves and C. M. Surko, *Physics of Plasmas* **4**, 1528 (1997).
20. A. Weiss *et al.*, *Physical Review Letters* **61**, 2245 (1988).
21. A. P. Knights, F. Malik, and P. G. Coleman, *Applied Physics Letters* **75**, 466 (1999).
22. M. P. Petkov *et al.*, *Applied Physics Letters* **74**, 2146 (1999).
23. L. D. Hulett, Jr. *et al.*, *Applied Surface Science* **85**, 334 (1995).
24. A. P. Mills, *Applied Physics Letters* **37**, 667 (1980).
25. A. P. Mills Jr., *Applied Physics* **22**, 273 (1980).
26. A. P. Mills, Jr., *Experimental Methods in the Physical Sciences* **29A**, 39 (1995).
27. V. W. Hughes *et al.*, *Physical Review A* **5**, 195 (1972).
28. F. Anderegg, E. M. Hollmann, and C. F. Driscoll, *Physical Review Letters* **81**, 4875 (1998).
29. R. G. Greaves and C. M. Surko, *Physical Review Letters* **85**, 1883 (2000).
30. R. G. Greaves and C. M. Surko, *Physics of Plasmas* **8**, 1879 (2001).

Practical Limits on Positron Accumulation and the Creation of Electron-Positron Plasmas

R. G. Greaves* and C. M. Surko[†]

*First Point Scientific, Inc., 5330 Derry Avenue, Suite J, Agoura Hills, CA 91301

[†]Department of Physics, University of California, San Diego, CA 92093

Abstract. The tasks of accumulating large numbers of positrons, creating high-density positron plasmas, and confining electron-positron plasmas present a number of technical challenges. Some practical considerations and limitations of common confinement schemes are discussed. A novel design for a multi-cell Penning-Malmberg trap is proposed for the accumulation of large numbers of positrons (e.g., $> 10^{12}$ and $T \sim 0.5$ eV). A method is described to create a low-density, electron-positron plasma (e.g., $n \sim 10^7$ cm⁻³) for basic plasma physics studies that uses a combination of radio-frequency and magnetic confinement. The possibilities for confinement of a hot (e.g., $T > 10$ keV) electron-positron plasma in a magnetic mirror are also discussed.

INTRODUCTION

Positrons are now used routinely for a wide range of applications, including the study of atomic and molecular physics [1], antihydrogen formation [2], plasma physics [3], and the characterization of materials and surfaces [4]. Further progress in many of these areas will be limited by improvements in positron sources and the ability to manipulate and cool large collections of antiparticles. In this paper we explore the possibilities for, and limitations on the accumulation of large numbers of positrons and the generation of high density positron plasmas.

There are a number of interesting phenomena that might be studied if one could create and confine neutral positron-electron plasmas. However, this is likely to be exceedingly challenging as compared with the study of single-component positron plasmas. We discuss briefly motivations for electron-positron plasma experiments and some relevant practical considerations. A scheme is proposed to create a low density, low temperature electron-positron plasma using a combination of radio frequency and magnetic confinement. Another scheme is described that could, in principle, permit confinement of a hot electron-positron plasma. While much more difficult, the latter experiment could enable studies of relativistic electron positron plasmas, an area which has been considered extensively theoretically and is important in a number of astrophysical contexts, but one in which there have been no experiments to date.

POSITRON TRAPPING

Low energy positrons are obtained from either radioisotope sources [5] or from LINAC sources [6]. Radioisotope sources are currently limited to positron fluxes of $< 10^8$ slow positrons per second, while LINAC sources have the potential for positron fluxes greater than 10^9 s^{-1} .

There are a number of methods that have either been used or proposed for trapping low-energy positrons [7]. These include trapping by collisions with trapped ions [8, 9], trapped electrons [10], neutral gas [11], by stochastic orbits [12], in a magnetic mirror configuration [13], by electronic damping [14], and by field ionization of Rydberg positronium atoms [15].

The buffer-gas trapping scheme is by far the most efficient of any method used to date to accumulate and cool large numbers of positrons [7, 11]. Typically, $\sim 1\%$ of positrons from a ^{22}Na source are slowed to a few electron volts using a solid neon moderator. They are then injected into a Penning-Malmberg trap in the presence of a buffer gas and an applied magnetic field $\sim 0.1 \text{ T}$. The accumulator has three stages, each at successively lower gas pressure and electrostatic potential. As many as 30% of the incident positrons become trapped in the third stage of the accumulator where they cool to room temperature in $\sim 0.1 \text{ s}$ [16] using a mixture of N_2 and CF_4 . Using this technique, 3×10^8 positrons have been accumulated in 8 minutes from a 70-mCi ^{22}Na source.

A separate cryogenic UHV trap is currently being constructed at UCSD [17]. Positrons from a buffer gas trap will be stacked into the UHV trap. This device is expected to enable the accumulation of large numbers of positrons ($> 10^{10}$), and the confinement of high density ($> 10^{10} \text{ cm}^{-3}$) cryogenic plasmas ($T < 10 \text{ K}$) with long lifetimes (e.g., days to weeks).

All positron trapping to date has been conducted in Penning traps. For certain applications, however, trapping using rf fields (e.g., as in a Paul trap) or a magnetic mirror may be useful. One of the most attractive features of the Paul trap is its ability to trap both signs of charge simultaneously. This feature has already been demonstrated for plasmas consisting of both positive and negative ions [18]. This principle has also been applied in a hybrid Penning-Paul trap for the confinement of proton-electron plasmas [19]. Below we propose a similar configuration for the containment and study of a cool low-density electron-positron plasma. Paul trap is achieved using the ponderomotive force in a oscillating electric field.

CONFINEMENT OF SINGLE-COMPONENT POSITRON PLASMAS

In this section, we briefly discuss considerations involved in confining large numbers of positrons for long times. Besides the usual loss processes due to transport, annihilation on neutral background gas present in the vacuum system must also be considered.

Annihilation on neutral gas

Positron annihilation rates on a variety of atomic and molecular gases are well documented. They are conventionally expressed by comparison with annihilation on an uncorrelated electron gas

$$\Gamma = \pi r_0^2 c n_n Z_{\text{eff}}, \quad (1)$$

where r_0 is the classical radius of the electron, and n_n is the number density of the neutral gas molecules. In general, for atoms, small molecules, and fluorocarbon molecules, Γ is of the order of that corresponding to the uncorrelated electron gas limit with $Z_{\text{eff}} \sim Z$. For hydrocarbon molecules, on the other hand, Z_{eff} can exceed Z by many orders of magnitude. Table 1 presents the annihilation time for a selection of gases. These data show that positron annihilation can, in practice, be made negligible by maintaining a hydrocarbon free vacuum environment, e.g., by placing the electrodes in a cryogenic environment in the vacuum chamber.

TABLE 1. Annihilation times, τ_{ann} for a selection of gases typically found in vacuum systems, each at a partial pressure of 10^{-10} torr.

Gas	Formula	τ_{ann}
Helium	He	121 days
Nitrogen	N ₂	17.4 days
Butane	C ₄ H ₁₀	1 hour
Sebacic acid dimethyl ester	C ₁₂ H ₂₂ O ₄ *	5.5 seconds

*A common constituent of diffusion pump oil.

Radial Transport

For single component plasmas (SCP), cross-field transport will be the same for positrons as for electrons, and it is well documented that electron SCP's have excellent confinement properties [20]. At sufficiently low neutral gas pressure, electron transport is found empirically to scale as $\kappa(L/B)^2$, where L , is the length of the plasma, B is the magnetic field strength, and κ is a device-dependent constant. With careful experimental design, confinement times of hours or even days are attainable [21]. Transport rates also have a dependence on plasma density and temperature, although these are not as easily characterized [22]. Recently, it has been demonstrated that applying a rotating electric field ("rotating wall") to a single component plasma can counteract radial transport, and even lead to significant inward transport [23,24]. Thus it now appears that radial transport is less likely to be a major obstacle to the confinement of high density positron plasmas.

Brillouin Density Limit

The maximum density of positrons that can be confined by a magnetic field, B , is given by the Brillouin limit [25],

$$n_B = \frac{B^2}{8\pi mc^2}. \quad (2)$$

For example, for a 1 tesla magnetic field, $n_B \simeq 5 \times 10^{12} \text{ cm}^{-3}$. Several schemes have been proposed for exceeding the Brillouin limit using non-uniform magnetic fields [26]. The factors that can be achieved, however, are only of the order of two, so the Brillouin limit remains a fundamental constraint on the storage of unneutralized plasmas. We note in passing that Eq. 2 is equivalent to the requirement that the energy in the magnetic field must always exceed the rest mass energy of the confined particles, so energy storage by accumulating unneutralized antimatter in the form of an SCP is not practical, regardless of whether positrons or antiprotons are used.

Space Charge Limit

The space charge at the center of a column of charged particles of radius R_p , confined within a cylindrical electrode of radius R_w , is given by

$$V_s \simeq 1.4 \times 10^{-7} \frac{N_t}{L} \left[1 + 2 \log_e \left(\frac{R_w}{R_p} \right) \right], \quad (3)$$

where V_s is in volts, N_t is the total number of positrons, and L is the length of the plasma in centimeters. To confine a positron SCP in a Malmberg-Penning trap, one must apply a confining potential in excess of V_s on the end electrodes, and this is an important constraint on the maximum achievable value of N_t/L . For example, for $N_t = 3 \times 10^{12}$, $L = 10 \text{ cm}$, and $R_w/R_p = 2$, $V_s \simeq 100 \text{ kV}$.

A MULTICELL TRAP FOR STORAGE OF LARGE NUMBERS OF POSITRONS

For many applications, the accumulation of large numbers of positrons is desirable. As can be seen from Eqs. 2 and 3, the space charge limit is likely to be reached before the Brillouin limit. Since applying confining potentials greater than a few kilovolts in vacuum becomes technologically difficult, especially if they must be switched on a short timescale, it is desirable to develop geometries for accumulating large numbers of positrons with reduced space potential. One possible scheme is suggested by Eq. 3, which shows that the space charge of the plasma depends only on charge per unit length, and on the size of the plasma *relative* to the confining electrodes. The key point is that subdividing the plasma into n separate plasma columns using a multicell trap reduces the space charge potential by a factor of n .

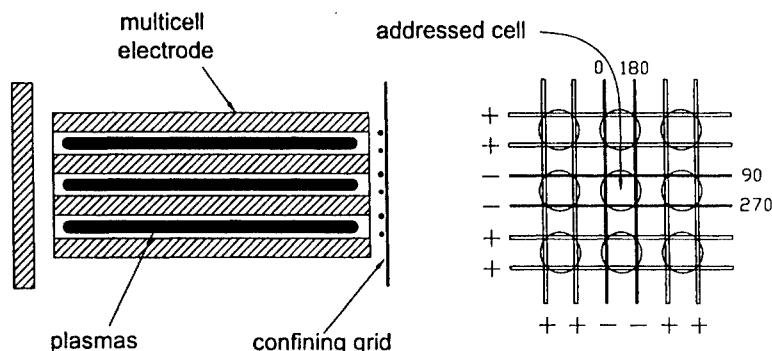


FIGURE 1. Possible multicell configuration for confining large numbers of positrons.

A possible geometry for accomplishing this is shown in Fig. 1. Here the main confining electrode is penetrated by multiple cylindrical openings to form a multicell array [27]. The confining potential at one end is applied using a plate electrode. In order to access the cells separately, individual cylindrical gate electrodes could be provided for each cell. An alternative to this approach could be to use a grid of wires that can be biased individually, as shown in Fig. 1. By reducing the potentials on the four wires adjacent to a particular cell, the potential barrier for that cell could be lowered selectively, thus permitting positrons to be loaded or unloaded. Capacitive coupling of phase-shifted sine waves to the wires, as shown in the figure for one cell, could be used to apply a "rotating wall" confining field.

One potential application of this device would be for use in a portable trap for positrons that could be used in place of a radioactive source. For example, an array of 10 cells by 10 cells, each 3 mm in diameter, and 10 cm long, containing plasmas 1 mm in diameter would be able to contain 10^{12} positrons with a confining potential of < 500 V. Such a trap would be able to supply a beam of 10^6 cold positrons per second (typical for laboratory positron beam systems) for more than 10 days before it would need to be refilled at a positron production facility, such as a LINAC. This approach would have the advantage of eliminating the radioactive source and associated moderating equipment, leading to improved safety, reduced cost, greater versatility, and higher beam quality.

ELECTRON-POSITRON PLASMAS

In this section we consider the factors relevant to the confinement of electron-positron plasmas. The problem is even more challenging than that of overcoming the transport problems associated with neutral electron-ion plasmas. In particular, one must also overcome positron loss due to annihilation of the positrons with the plasma electrons and the formation and subsequent loss of positronium atoms.

Motivation for electron-positron plasma experiments

Electron-positron plasmas are an example of equal-mass plasmas, whose behavior is fundamentally different than that of conventional electron-ion plasmas. They are important in astrophysical environments, such as pulsar magnetospheres and active galactic nuclei. Plasmas of this type have been studied theoretically [28–42]. We briefly discuss some motivations for laboratory studies:

Plasma confinement. The confinement of neutral plasmas by a magnetic field is fundamentally different from that of single-component plasmas, which are well-known to exhibit remarkably good confinement. Very long confinement times of single-component plasmas (i.e., hours or days) have been obtained by careful experimental design [43]. For two-species plasmas, however, unlike-particle collisions lead to cross-field transport many orders of magnitude larger than that observed in single component plasmas. It should be possible to study continuously the transition from a single-component positron plasma to a completely neutralized e^+/e^- plasma, thus providing new insights into (turbulent) transport processes in partially neutralized and neutral plasmas.

Plasma wave studies. The linear modes of electron-positron plasmas are similar to those in conventional plasmas [37]. However, in a seminal paper, Tsytovich and Wharton showed that the nonlinear processes in e^+/e^- plasmas are dramatically different [44]. For equal temperatures and equal densities of positrons and electrons, three-wave coupling vanishes identically, and so quasilinear relaxation of a beam-plasma instability is absent. Furthermore, because of the equal masses of both particle species, ordinary nonlinear Landau damping (NLLD) is larger by the ion-to-electron mass ratio. Consequently, nonlinear growth can overwhelm linear growth, and quasilinear relaxation is replaced by very strong nonlinear Landau damping. In one step, energy can be coupled directly into the bulk of the particle distribution.

Electron-positron vortices. Two-dimensional fluid vortex phenomena have been studied in electron plasma experiments. For a strongly magnetized electron plasma, the electron density is the exact analog of vorticity in a two-dimensional fluid, and electron plasmas closely approximate the ideal case of an inviscid fluid. A variety of interesting phenomena such as vortex merger, and vortex crystals have been studied with a precision not possible in ordinary fluids [45, 46]. In electron-positron plasmas, the more general case of a fluid with two signs of vorticity could be studied.

CONFINEMENT LIMITS FOR ELECTRON-POSITRON PLASMAS

In this section we discuss relevant confinement issues, and then propose two possible schemes for confinement of electron-positron plasmas. We note in passing that one might ask, for example, if this could be a way to store large numbers of positrons by avoiding the space charge limit. As we discuss below, the answer is ‘no’ due to the relatively poor confinement achievable for neutral plasmas.

Annihilation

In addition to annihilation on neutral gas, discussed above in the section on single component positron plasmas, two additional annihilation channels are present in electron-positron plasmas, namely annihilation on plasma electrons, and the formation (and subsequent annihilation) of positronium atoms. In an electron-positron plasma annihilation will occur at a rate given by:

$$\Gamma = \pi r_0^2 c n_e, \quad (4)$$

where r_0 is the classical radius of the electron, c is the speed of light, n_e is the electron density. The annihilation time, $\tau_a = 1/\Gamma$ is plotted in Fig. 2 as a function of plasma density in the range of interest. From these data, it is clear that electron-positron annihilation is negligible at low plasma densities. For higher densities, experiments are still possible provided that the phenomena of interest can be studied on short timescales, and high positron throughput is possible.

Positronium Formation

In addition to direct annihilation, positrons can be lost from an electron-positron plasma by positronium formation. The most likely process is three-body recombination at a rate, Γ_{Ps} , given by [47]:

$$\Gamma_{Ps} \simeq A n b^2 v_{th} (n b^3) \quad (5)$$

where $v_{th} = \sqrt{k_B T/m}$ is the thermal velocity of the particles, $b = e^2/k_B T$ is the distance of closest approach, and $A \simeq 0.07$. This is an upper limit, including the formation of weakly bound high-Rydberg states. Figure 2 shows the dependence of direct annihilation and positronium formation on plasma density for three values of plasma temperature. From this Figure, it is clear that positronium formation is not a problem for either the low density electron-positron plasma or the high density relativistic plasmas described below. However, positron annihilation is likely to be a problem in low-temperature, high-density electron-positron plasmas.

Radial Transport

Radial transport in an electron-positron plasma will be qualitatively different from an SCP and is expected to scale as in a neutral plasma. The smallest rate that might be expected is that due to Coulomb collisions between the two species. In this case the diffusion coefficient is [48]:

$$D_c = \frac{4}{3} \sqrt{\pi} n v_{th} b^2 \rho^2 \ln \left(\frac{\rho}{b} \right) \quad (6)$$

where ρ is the gyroradius. For a plasma of radius R , the typical confinement time will be

$$t_c \sim \frac{R^2}{2D_c}. \quad (7)$$

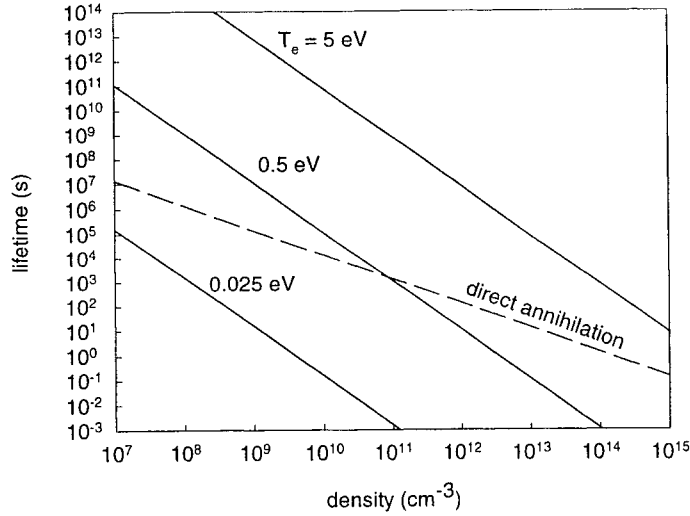


FIGURE 2. Electron-positron plasma lifetime due to direct annihilation (dashed line) and positronium formation (solid lines) as a function of plasma density.

In practice, however, diffusion rates are generally found to be larger than those predicted by this classical picture. As an upper bound, (e.g., for transport due to plasma turbulence) one can take the phenomenological Bohm diffusion coefficient

$$D_B = \frac{ckT}{16eB}. \quad (8)$$

In this case,

$$t_c \sim R^2/2D_B. \quad (9)$$

We note that many practical confinement schemes exhibit values of τ_c larger than Eq. 9 (i.e., confinement better than Bohm), so Eq. 9 is likely to be a lower bound on τ_c .

Plotted in Fig. 3 are values of τ_c predicted by Eqs. 7 and 9 as a function of plasma density. These results indicate that, for a neutral electron-positron plasma, cross-field transport is likely to be a serious concern.

NEAR-TERM POSSIBILITIES FOR EXPERIMENTS

The techniques described above to accumulate large numbers of positrons from a radioactive source in a Penning trap have enabled us to perform the first electron-positron plasma experiments by transmitting an electron beam through a stored positron plasma [3, 49]. These experiments deliberately avoided the problem of simultaneous confinement of electrons and positrons by introducing the electrons in a transient manner in the form of a beam. However in order to study phenomena in plasmas where there is no relative drift between the two charge species, simultaneous confinement of electrons and

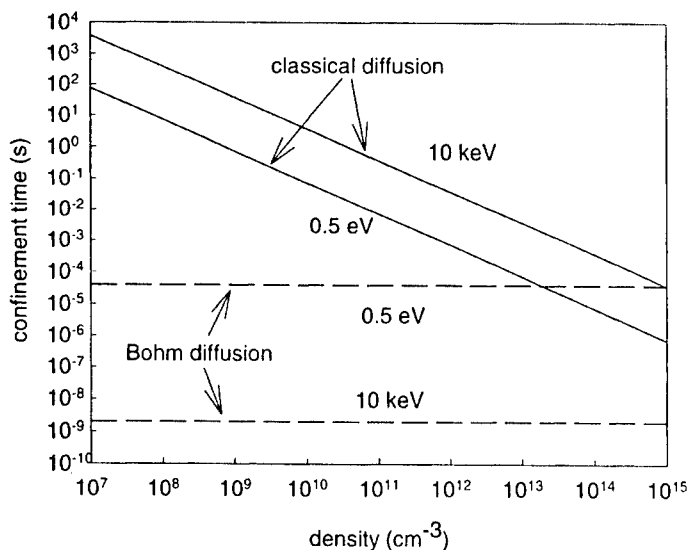


FIGURE 3. Calculated confinement times for 0.5-eV and 10-keV electron-positron plasmas, 0.5 cm in diameter, at $B = 1$ kG.

positrons is required. Since one can expect relatively poor confinement of the positrons in a neutral plasma, even under the best circumstances, being able to exploit a high-intensity positron facility for such studies (e.g., using a LINAC) would be a great advantage.

The design of such an experiment is “nontrivial”. Unfortunately, the electrostatic confinement scheme of the Penning trap (which has been the basis of positron plasma experiments to date) is suitable for confining only one sign of charge. “Nested” potential wells cannot be used to achieve simultaneous confinement of electron and positron plasmas in the direction of a confining magnetic field, since overlap of the charge clouds can be achieved in this geometry only if one species is not in the plasma limit. This is due to the fact that, in the nested wells, overlap of the plasmas will occur only if one species has a Debye screening length large compared with the size of the other plasma, in which case the hotter species is not in the plasma limit.

Magnetic geometries such as mirrors (discussed below) and toruses are subject to relatively rapid losses, but might be usable at a high-intensity beam facility.

Combined trap for low-density electron-positron plasmas

We envision that the difficulties in simultaneous confinement of both charge species can be overcome by the use of a Paul trap, which confines charged particles by means of radio frequency (rf) fields. Because the confinement is dynamic in nature, particles of both signs of charge can be confined. Paul traps have already been used to confine quasi-neutral plasmas of positive and negative ions [18]. More recently, the simultaneous

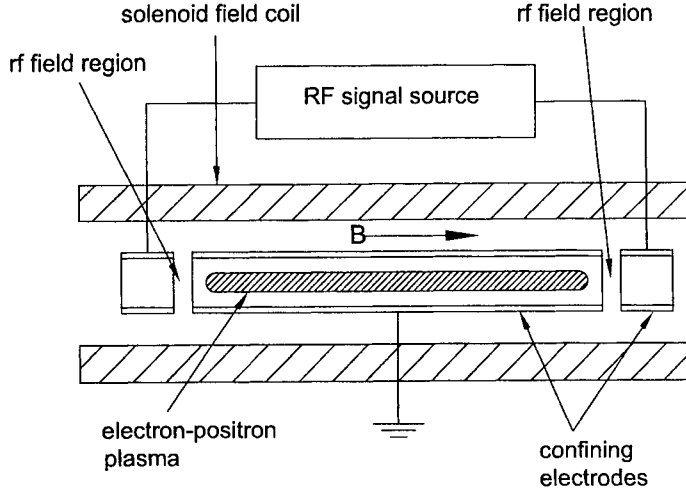


FIGURE 4. Possible combined Penning-Paul trap for studying electron-positron plasmas.

confinement of protons and electrons was demonstrated in a trap in which the electrons were confined by rf fields and the protons were confined in an overlapping Penning trap [19].

A natural extension of these experiments would be to use a combined trap to confine an electron-positron plasma. We envision that this might be done using a hybrid Penning-Paul trap where radial confinement is provided by a magnetic field, as in a Penning trap, but with the confinement at the ends provided by rf fields, in place of the electrostatic potentials of the Penning design. Heating of the species by the rf is a potential problem. We suggest that this might be overcome using the cooling provided by small amounts of a suitably chosen molecular gas, similar to the operation of the buffer-gas positron accumulator described above.

A possible geometry for such an experiment is shown schematically in Fig. 4. The design parameters of the experiment are given in Table 2. The depth of the potential well achievable using the Paul trapping technique is limited by practical considerations to a few electron Volts, thereby placing limits on the plasma temperature and acceptable amount of charge imbalance. For these experiments, the advantage of using an intense positron source would be that the experiments could be conducted with a rapid cycle time, even if confinement is poor (which is likely).

The heating rate in this trap can be estimated by balancing the heating of the particles, $\dot{\epsilon}_{\text{rf}}$, due to the rf field with the cooling, $\dot{\epsilon}_{\text{col}}$, due to electron-molecule and positron-molecule collisions. We find for the heating rate,

$$\dot{\epsilon}_{\text{rf}} \simeq 2m\nu_c \overline{(\delta v)^2} \quad (10)$$

where ν_c is the Coulomb collision frequency and $\delta v = eE_{rf}/m\Omega$ is the particle velocity due the rf field at frequency Ω . It is useful to note that

$$\dot{\epsilon}_{rf} \propto U_{rf} = \frac{e^2 \overline{E_{rf}^2}}{m\Omega^2} \simeq m(\delta v)^2, \quad (11)$$

where U_{rf} is the rf trapping potential energy.

This heating rate must be spatially averaged over the trajectory of the particles in the potential well. For a cylindrical plasma of length L , confined by cylindrical electrodes of radius R_w at $z = 0$ and $z = L$, the rf potential on the axis will be

$$V(z) \simeq \frac{V_{rf}}{2} \left[\tanh\left(\frac{1.3z}{R_w}\right) - \tanh\left(\frac{1.3[z-L]}{R_w}\right) - 2 \right], \quad (12)$$

where V_{rf} is the applied rf voltage. We assume a trapping well depth, $U_{rf} = 5$ eV and a plasma temperature $kT = 0.5$ eV. The particles will be heated appreciably only near the ends of the plasma in a region of extent $\Delta z \sim 0.4R_w$. Here they experience an rf potential of strength $< kT/e$, but spend more time near these turning points than in other regions of the trap. Taking these factors into account and assuming $L = 30R_w$, we estimate the time-averaged heating rate to be,

$$\dot{\epsilon}_{rf} \simeq 0.05\nu_c kT \quad (13)$$

The collisional energy loss on molecules will be $\dot{\epsilon}_{col} \simeq -\nu_{col}\delta\epsilon_{col}$, where $\delta\epsilon_{col}$ is the average energy loss per collision and ν_{col} is the collision frequency. As an estimate, we assume cooling on CO_2 which has $\delta\epsilon_{col} = 0.3$ eV and a collision cross section $\sigma \sim 10^{-16} \text{ cm}^2$ [50]. With these assumptions

$$\nu_{col} = n_n \sigma \nu_{th} \simeq 15 \times 10^4 P \text{ s}^{-1}, \quad (14)$$

where n_n is the CO_2 number density and P is the pressure in mTorr. Thus

$$\dot{\epsilon}_{col} \simeq 5 \times 10^4 P \text{ eV s}^{-1}. \quad (15)$$

For balance, we require $\dot{\epsilon}_{rf} = \dot{\epsilon}_{col}$. Thus from Eqs. 13 and 15, we find

$$\nu_c \sim 2 \times 10^6 P \text{ s}^{-1}. \quad (16)$$

For $n = 10^7 \text{ cm}^{-3}$ and $T = 0.5$ eV, $\nu_c \simeq 2 \times 10^3 \text{ s}^{-1}$, requiring a CO_2 pressure of 1×10^{-6} torr.

At this pressure, the annihilation time is ~ 80 s, the diffusion time due to collisions with neutral gas is ~ 500 s, the diffusion time due to electron-positron collisions is ~ 200 s, and the Bohm diffusion time is $\sim 100 \mu\text{s}$. Thus the plasma can be expected to survive between $100 \mu\text{s}$ and several hundred seconds, depending on which transport process dominates. This is an interesting issue in its own right and would by its nature be the first phenomenon to be studied. Since the plasma frequency is ~ 30 MHz, plasma wave phenomena could be studied, even if the confinement time was as short as $100 \mu\text{s}$.

While this combined trap is suitable for low-density electron-positron plasma studies, it is not likely to be a viable geometry for confining higher density plasmas. This is due to plasma heating, which will increase with plasma density, and the unavailability of a sufficiently rapid cooling mechanism.

TABLE 2. Design parameters of an electron-positron experiment using a combined Penning-Paul trap.

Parameter	Approx. Value
density	10^7 cm^{-3}
plasma length	30 cm
plasma radius	0.5 cm
wall radius	1 cm
particle number	5×10^8
rf frequency	200 MHz
rf voltage	100 V _{rms}
rf potential well	5 V
cooling gas	CO ₂
CO ₂ pressure	1×10^{-6} torr
plasma temperature	0.5 eV

A mirror geometry to confine hot electron-positron plasmas

Experimental studies of relativistic electron-positron plasmas will be much more challenging. The plasma limit requires $n\lambda_D^3 \gg 1$, and $\lambda_D \ll L$. In these expressions, L is the characteristic dimension of the charge cloud, n is the plasma density, and λ_D is the Debye screening length. Thus, in order to have λ_D as small as 1 cm at $T_e > 200$ keV (i.e., a mildly relativistic plasma), a density $n = 10^{12} \text{ cm}^{-3}$ is required. At a minimum, we must have $L = 10\lambda_D$ (e.g., to study plasma wave phenomena), which in turn requires confining 10^{15} positrons. Beyond the challenge of accumulating such a large number of positrons, their confinement in a neutral plasma will be a great challenge.

One possible geometry for such an experiment is a magnetic mirror. Confinement in a mirror is better when the plasma is hot (i.e., thereby reducing the loss due to Coulomb collisions). In the mirror, it is also beneficial to arrange $T_\perp \gg T_\parallel$, where T_\perp and T_\parallel are the perpendicular and parallel temperatures of the particles. Both conditions can be achieved relatively easily for electron-mass particles by heating at the cyclotron frequency using microwave radiation. Confinement of the positrons could be further increased by placing electrodes on either end of the mirror, biased to as large a potential as possible. In this case, positrons exiting the usual "loss cone" in mirrors (i.e., particles with low values of T_\perp/T_\parallel are not confined by the mirror fields) would be reflected back into the magnetic mirror. One unwanted side effect of the hot plasma will be intense cyclotron emission from the hot particles.

SUMMARY

In this paper we have discussed two key topics concerning positron plasmas, the practical considerations associated with the accumulation of large numbers of positrons, and the prospects for creating (neutral) electron-positron plasmas in the laboratory. Penning-Malmberg traps are a relatively simple and useful way to confine single component plasmas with densities from 10^{12} to even 10^{15} cm^{-3} . The multicell trap arrangement

described here can potentially extend this upper limit by a few orders of magnitude. Since the largest densities achieved to date are $\sim 4 \times 10^9 \text{ cm}^{-3}$ [51], and the largest number of positrons confined are $< 10^9$, it is important to point out that these estimates are large extrapolations and should be regarded as a projection as to what might be possible rather than a certainty.

Possible schemes to avoid the Brillouin and space charge limits by neutralizing positron plasmas with electrons were discussed. They suffer from losses due to both annihilation and plasma transport. They do not appear to offer an advantage over positron SCP's in terms of achieving either high positron densities or large total numbers of positrons. The net result is that, while positrons can be accumulated and stored, in some cases for very long times (e.g., days to weeks), achieving very large particle numbers of antimatter in the laboratory is likely to be constrained for the foreseeable future by the considerations discussed above.

In contrast, with regard to creating and studying low density electron-positron plasmas in the laboratory, there are likely to be a number of potentially practical possibilities. Here we discussed only two of them, a combined trap, consisting of a linear magnetic field with rf confinement at the ends, and confinement in a magnetic mirror. The former scheme appears appropriate for confining and studying low-density, low temperature plasmas. The latter offers the possibility for confinement of a much hotter, high-density plasma (e.g., temperatures $> 10 \text{ keV}$). If either of these experiments were successful, they would permit study of a range of interesting topics associated with the unique and interesting electron-positron plasma system. As a practical note, however, judging from more than a half century of experience attempting to confine neutral plasmas, the first topic of study will most likely concern understanding the confinement of these unique, electron-mass, neutral plasmas.

ACKNOWLEDGEMENTS

The work at UC, San Diego is supported by the Office of Naval Research, Grant No. N000-14-97-1-0366. The work at First Point Scientific, Inc., is supported by the Office of Naval Research, Grant No. N00014-00-C-0710, and the National Science Foundation, Grant No. DMI-0078468. We also wish to acknowledge helpful conversations with Dan Dubin and Tom O'Neil.

REFERENCES

1. K. Iwata, R. G. Greaves, and C. M. Surko, *Physical Review A* **55**, 3586 (1997).
2. M. Charlton *et al.*, *Physics Reports* **241**, 65 (1994).
3. R. G. Greaves and C. M. Surko, *Physical Review Letters* **75**, 3846 (1995).
4. P. J. Schultz and K. G. Lynn, *Reviews of Modern Physics* **60**, 701 (1988).
5. A. P. Mills, Jr., *Experimental Methods in the Physical Sciences* **29A**, 39 (1995).
6. R. H. Howell, I. J. Rosenberg, and M. J. Fluss, *Applied Physics A* **43**, 247 (1987).
7. R. G. Greaves and C. M. Surko, *Physics of Plasmas* **4**, 1528 (1997).
8. D. J. Wineland, C. S. Weimer, and J. J. Bollinger, *Hyperfine Interactions* **76**, 115 (1993).

9. A. S. Newbury, B. M. Jelenkovic, J. J. Bollinger, and D. J. Wineland, *Physical Review A* **62**, 023405 (2000).
10. A. Mohri, these proceedings.
11. C. M. Surko, A. Passner, M. Leventhal, and F. J. Wysocki, *Physical Review Letters* **61**, 1831 (1988).
12. B. Ghaffari and R. S. Conti, *Physical Review Letters* **75**, 3118 (1995).
13. H. Boehmer, M. Adams, and N. Rynn, *Physics of Plasmas* **2**, 4369 (1995).
14. L. Haarsma, K. Abdullah, and G. Gabrielse, *Physical Review Letters* **75**, 806 (1995).
15. J. Estrada *et al.*, *Physical Review Letters* **84**, 859 (2000).
16. T. J. Murphy and C. M. Surko, *Physical Review A* **46**, 5696 (1992).
17. C. M. Surko, S. J. Gilbert, and R. G. Greaves, in *AIP Conference Proceedings no. 498, Non-Neutral Plasma Physics III*, edited by J. J. Bollinger, R. L. Spencer, and R. C. Davidson (AIP, Melville, New York, 1999), pp. 3–12.
18. J. P. Schermann and F. G. Major, *Applied Physics* **16**, 225 (1978).
19. J. Walz *et al.*, *Physical Review Letters* **75**, 3257 (1995).
20. T. M. O'Neil, *Physics of Fluids* **23**, 2216 (1980).
21. C. F. Driscoll, K. S. Fine, and J. H. Malmberg, *Physics of Fluids* **29**, 2015 (1986).
22. J. M. Kriesel and C. F. Driscoll, *Physical Review Letters* **85**, 2510 (2000).
23. F. Anderegg, E. M. Hollmann, and C. F. Driscoll, *Physical Review Letters* **81**, 4875 (1998).
24. R. G. Greaves and C. M. Surko, *Physical Review Letters* **85**, 1883 (2000).
25. L. Brillouin, *Physical Review* **67**, 260 (1945).
26. L. Turner, *Physics of Fluids B* **3**, 1355 (1991).
27. This concept was invented independently by one of the authors (R.G.) and K. Lynn; private communication, K. Lynn (2000).
28. V. I. Berezhiani and S. M. Mahajan, *Physical Review Letters* **73**, 1110 (1994).
29. Y. A. Gallant *et al.*, *Astrophysical Journal* **391**, 73 (1992).
30. T. Kitanishi, J. Sakai, K. Nishikawa, and J. Zhao, *Physical Review E* **53**, 6376 (1996).
31. U. A. Mofiz and A. A. Mamun, *Physics of Fluids B* **5**, 1667 (1993).
32. F. B. Rizzato, R. S. Schneider, and D. Dillenburg, *Physics Letters A* **133**, 59 (1988).
33. A. D. Rogava, S. M. Mahajan, and V. I. Berezhiani, *Physics of Plasmas* **3**, 3545 (1996).
34. P. K. Shukla, M. Y. Yu, and L. Stenflo, *Astrophysics and Space Science* **127**, 371 (1986).
35. L. N. Tsintsadze and P. K. Shukla, *Physical Review A* **46**, 5288 (1992).
36. A. S. Volokitin, V. V. Krasnosel'skikh, and G. Z. Machabeli, *Fizika Plazmy* **11**, 531 (1985).
37. G. P. Zank and R. G. Greaves, *Physical Review E* **51**, 6079 (1995).
38. N. Iwamoto, *Physical Review E* **47**, 604 (1993).
39. G. Machabeli, S. Vladimirov, and D. Melrose, *Physical Review E* **59**, 4552 (1999).
40. J. Sakai, M. Eda, and W. Shiratori, *Physica Scripta* **T75**, 67 (1998).
41. D. Gyobu *et al.*, *Journal of the Physical Society of Japan* **68**, 471 (1999).
42. V. Skarva, V. Berezhiani, and G. Carlini, *Physica Scripta* **57**, 456 (1998).
43. J. H. Malmberg and C. F. Driscoll, *Physical Review Letters* **44**, 654 (1980).
44. V. Tsytovich and C. B. Wharton, *Comments on Plasma Physics and Controlled Fusion* **4**, 91 (1978).
45. C. F. Driscoll and K. S. Fine, *Physics of Fluids B* **2**, 1359 (1990).
46. T. B. Mitchell and C. F. Driscoll, *Physics of Fluids* **8**, 1828 (1996).
47. M. E. Glinsky and T. M. O'Neil, *Physics of Fluids B* **3**, 1279 (1991).
48. D. H. E. Dubin, *Physics of Plasmas* **5**, 1688 (1998).
49. S. J. Gilbert, D. H. E. Dubin, R. G. Greaves, and C. M. Surko, *Phys. Plasmas*, in press (2001).
50. J. Sullivan, S. J. Gilbert, and C. M. Surko, *Physical Review Letters* **86**, 1494 (2001).
51. B. Jelenkovic and J. Bollinger, to be published.

Low-Energy Positron-Matter Interactions Using Trap-Based Beams

S. J. Gilbert, J. P. Sullivan, J. P. Marler, L. D. Barnes, P. Schmidt, S. J. Buckman,¹ and C. M. Surko

Department of Physics, University of California, San Diego, La Jolla CA 92093-0319

Abstract. We present an overview of nonneutral plasma techniques developed to study the interaction of low-energy positrons with atoms and molecules. Both scattering and positron annihilation experiments are described. The scattering experiments provide the first state-resolved cross sections for both vibrational excitation of molecules and electronic excitation of atoms and molecules by positron impact. The annihilation experiments provide the first energy-resolved measurements of positron annihilation. Extensions of these techniques are briefly discussed, including work to create a new generation of positron beams with milli-electron volt energy resolution and the development of methods to study atomic clusters and dust grains.

I. INTRODUCTION

Positrons are now used routinely for a wide range of applications, including the study of atomic and molecular physics [1], plasma physics [2, 3], experiments attempting to form antihydrogen [4], and the characterization of materials and material surfaces [5, 6]. Nevertheless, progress in many of these areas has been limited by the availability of cold, intense positron sources. The situation has changed qualitatively by the recent exploitation of nonneutral plasma physics techniques to produce antimatter plasmas and beams in new regimes of parameter space and to manipulate these collections of positrons for specific measurements [2, 7, 8]. Methods were developed to efficiently accumulate and cool positrons from a ^{22}Na radioactive source. This source of cold positrons led to the development of a new method to create a cold, bright positron beam, tunable from 50 meV upwards, having an energy resolution of 20 meV, FWHM [9, 10]. These developments in positron plasmas and beams have enabled new studies of the interaction of low-energy positrons with ordinary matter. They have been used to study aspects of atomic and molecular physics and plasma physics, and they have sparked efforts in other areas, including a promising approach

1. Permanent address: Australian National University, Canberra, ACT, Australia.

to the formation of neutral antihydrogen atoms [11] and new approaches to positron beam sources for the study of materials and material surfaces [12].

In this paper, we present an overview of recent studies of the interaction of positrons with atoms and molecules made possible by this technology. These advances have brought qualitative changes to the way in which positron scattering and annihilation experiments can be done. To put these developments into perspective, Fig. 1 shows the typical ranges of energies of important physical processes for positron interactions with atoms and molecules. The 20 meV resolution of the trap-based cold positron beam represents more than an order of magnitude improvement over conventional positron scattering experiments (e.g., with typical energy resolutions ≥ 400 meV). In the last two years, it has enabled the first measurements of cross sections for excitation of vibrational modes in molecules by positron impact [13, 14], the first state-resolved cross sections for electronic excitation [15], and the first energy resolved measurements of positron annihilation on atoms and molecules [16]. These results can be regarded as first steps in establishing a quantitative antimatter-matter chemistry, important not only in obtaining a fundamental understanding of nature, but also in using antimatter in the laboratory for science and technology.

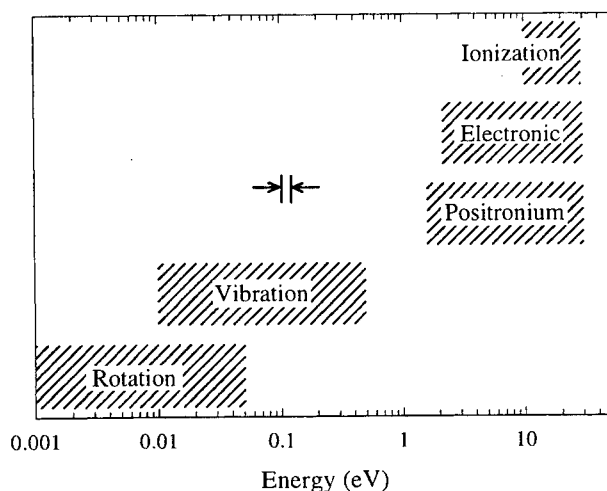


FIGURE 1. Representative energies of important processes in positron-matter interactions, including electronic excitation of atoms and molecules, vibrational and rotational excitation of molecules, positronium formation, and ionization. Annihilation (not shown) can occur at all energies. Vertical bars at 0.1 eV indicate the 20 meV energy resolution of the cold positron beam described here.

We describe here a new technique to make scattering measurements with the cold positron beam in the presence of an appreciable magnetic field (~ 0.1 tesla). This method is, in fact, superior to conventional positron and electron scattering techniques (e.g., using electrostatic beams) for a number of important measurements, such as energy-resolved cross sections for specific excitation processes integrated over scattering angle.

Annihilation is another important aspect of positron-matter interactions, and almost all positron annihilation studies to date have been done with a Maxwellian distribution at 300 kelvin. We describe very recent experiments that use the cold positron beam to make annihilation measurements as a function of positron energy. This technique, which is still in its infancy, provides important, target-specific information, such as the dependence of annihilation in molecules on the molecular vibrational modes.

In this paper we present an overview of these new methods to study positron scattering and annihilation processes -- techniques enabled by nonneutral plasma technology. We present examples of recent measurements made with these techniques and describe briefly future research directions. There are a wide range of problems in this area that can now be addressed, ranging from elucidating the mechanisms for positron annihilation in large molecules to understanding the fragmentation patterns of molecules following positron annihilation.

II. POSITRON ACCUMULATION AND COLD BEAM FORMATION

The buffer-gas trapping scheme is by far the most efficient of any method used to date to accumulate and cool large numbers of positrons [2, 17, 18]. Typically, $\sim 1\%$ of positrons from a ^{22}Na source are slowed to a few electron volts using a solid neon moderator. They are then injected into a Penning-Malmberg trap in the presence of a buffer gas and an applied magnetic field ~ 0.1 T. The accumulator has three stages, each at successively lower gas pressure and electrostatic potential. As many as 30% of the incident positrons become trapped in the third stage of the accumulator where they cool to room temperature in ~ 0.1 s [19, 20] on a mixture of N_2 and CF_4 . Using this technique, 3×10^8 e^+ have been accumulated in 8 minutes from a 90 mCi ^{22}Na source.

This trapping scheme was used to create a state-of-the-art cold positron beam (parallel energy spread ≤ 20 meV, FWHM) [9, 10], tunable over a wide range of energies, from ~ 0.05 eV upwards. This technique can be used to increase the brightness of a positron or electron beam and to create intense, short pulses of positrons with narrow energy spreads. In the case of positrons, it exceeds what has been done with other techniques in terms of energy resolution. In the case of electrons, while there are methods to generate much colder beams, this new method is likely to have advantages for specific applications such as study of the electron-beam positron-plasma instability [3, 21].

Cold beam formation is illustrated in Fig. 2. After the positrons are trapped and cooled, the potential of the bottom of the trap is raised, forcing the particles over a fixed-height potential barrier, V_B . The spread in parallel beam energies is measured using a retarding potential analyzer (RPA), by adjusting the voltage V_A in Fig. 2 (b). Using this technique, beams can be created with parallel energy spreads as small as 18 meV (FWHM). The perpendicular energy spread is comparable in magnitude (i.e. $\Delta E_{\perp} \sim k_B T = 25$ meV).

III. A NEW METHOD TO STUDY POSITRON SCATTERING

We have used the cold positron beam for a range of low-energy scattering studies [13, 14]. To do this, we developed a new technique to study scattering processes [22]. Since the positron plasmas and cold beam are in a magnetic field, it is convenient to also study the scattering in a magnetic field, in contrast to conventional atomic physics scattering experiments which are conducted with *electrostatic* beams in field-free collision environments. This new technique exploits the adiabatic properties of the positron's motion in the field -- a principle well known in the plasma community but not fully exploited for atomic physics applications. This technique is likely to have additional uses beyond the specific application to positrons (e.g., for electron scattering studies).

The arrangement for the scattering experiments is shown in Fig. 2. The positron beam is guided magnetically through a gas cell containing the test gas, then analyzed using a retarding potential analyzer (RPA) [15, 22]. The principle of the technique is illustrated in Fig. 3. It relies on the fact that the positron orbits are strongly magnetized (\sim e.g., for $B \sim 0.1$ T, the particle gyroradii are $\leq 10 \mu$). In this case, the total energy of the positrons can be separated into a sum of a component, E_{\parallel} , parallel to the magnetic field, and a second component, E_{\perp} , representing the energy in the particle gyromotion in the plane perpendicular to B . With the exception of the short duration of the scattering

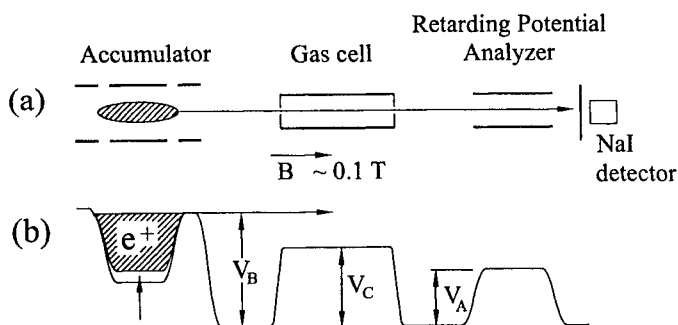


FIGURE 2. (a) Schematic diagram of the apparatus used to form a cold positron beam and to study scattering in a magnetic field; (b) the corresponding potential profile.

event, the quantity E_{\perp}/B is constant (i.e., an adiabatic invariant). The magnetic field in the scattering and analysis regions can be adjusted independently, and as we discuss below, this provides a convenient way of manipulating the perpendicular and parallel energy components of the positrons for specific measurements.

To date the positron beam and this scattering technique have been used for studies of total cross sections (TCS), differential elastic cross sections, and 'integral cross sections' (i.e., cross sections for *specific inelastic processes* integrated over angle). Here we present examples of the first measurements ever taken of integral cross

sections for both electronic and vibrational excitation of molecules by positrons [13-15]. Figure 4 shows data for a measurement of the vibrational excitation cross section of CO at 0.5 eV [13]. In Fig. 4(a) is shown an RPA curve when the ratio of fields, M , in the scattering and analysis region are the same. This corresponds to the situation illustrated in Fig 3(a) in which the RPA measurement is unable to distinguish the elastic and inelastic scattering components. In contrast, data taken at a field ratio $M = 35$ are shown in Fig. 4(b). This situation corresponds to that illustrated in Fig. 3(b). There is now a distinct separation of the inelastic and elastic scattering. This results in a sharp step at an RPA voltage corresponding to the *total* energy of a positron after an inelastic scattering event, while the elastic scattering is compressed in a small energy region near the beam cut-off. Note the expanded scale in (b), the good sensitivity, and the excellent discrimination of the inelastic process.

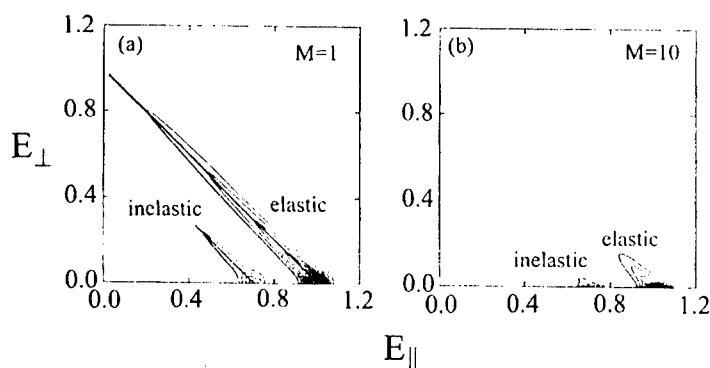


FIGURE 3. Simulation of the scattering of particles from a beam with energy $E_{\parallel} = 1.0 \gg E_{\perp}$, initially traveling parallel to the magnetic field. (a) Elastic and inelastic scattering. (b) For a magnetic field ratio of $M = 10$ between the scattering cell and the RPA, the spread in E_{\perp} is greatly reduced, so an RPA measurement can distinguish elastic and inelastic scattering.

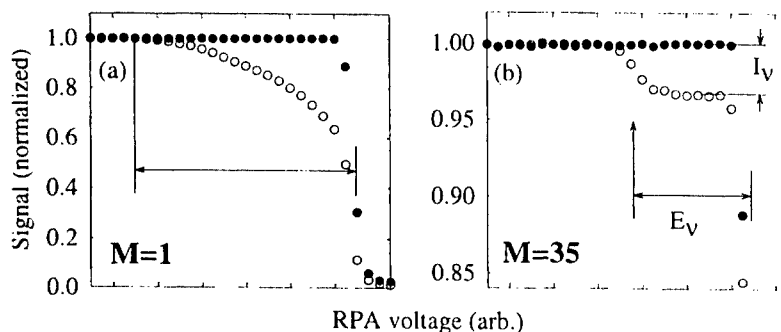


FIGURE 4. RPA measurement for CO using a 0.5 eV positron beam (open circles); no gas in cell (solid circles): (a) magnetic field ratio, $M = 1$, of the field in the scattering cell to that in the analysis region; (b) same measurement at $M = 35$. The step marked by the arrow in (b) corresponds to excitation of the vibrational mode in CO at $E_v = 0.27$ eV.

Figure 5 shows examples of measurements for vibrational excitation of molecules by positrons. Data for H_2 and CO_2 are shown together with available theoretical predictions [13]. Note that two modes are resolved in CO_2 , with the lowest having an energy of only 0.08 eV. Comparisons with theory are absolute, with no fitted parameters. Agreement with theory is very good considering this is the first time such a comparison was possible. Work is currently in progress to examine in more detail the behavior of the cross sections near threshold.

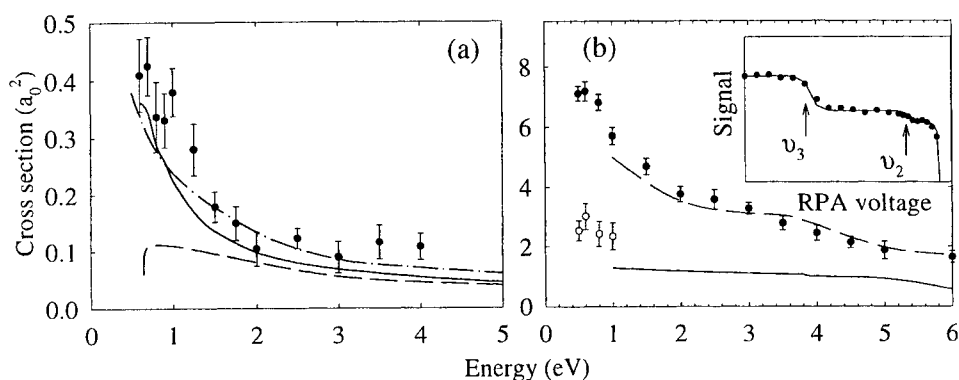


FIGURE 5. Cross sections for vibrational excitation as a function of positron energy: (a) the v_1 mode of H_2 at 540 meV, compared with theoretical predictions: solid line, Ref. [23]; dot-dashed line, Ref. [24]; and dashed line, Ref. [25]. (b) the v_2 and v_3 modes in CO_2 at 80 and 290 meV, respectively. The inset in (b) shows raw data and resolution of the 80 meV, v_2 excitation. The lines (except in the inset), are comparisons with the theory of Ref. [26].

Figure 6 shows examples of the first state-resolved cross sections for *electronic* excitation of molecules [15]. These measurements required resolving structure due to the vibrational manifolds of the excited electronic states; which was made possible because of the excellent energy resolution of the cold beam. The reader is referred to Ref. [15] for details.

To put these measurements in perspective, also shown in the figure are the only measurements of cross sections for excitation of these transitions by electron impact. Comparison of the two data sets indicates that the quality of the positron data are comparable to or better than the electron measurements. This is due to the fact that the electron measurements were done with an electrostatic beam, measuring the differential cross section at many angles and then integrating over angle. This procedure is relatively time consuming and error prone for this kind of measurement, as compared with the technique described here.

The data for H_2 strongly favor one of two competing theoretical calculations. There are no theoretical predictions presently available for N_2 . The sharp rise in the cross section in N_2 near threshold provides insight into the operation of the buffer-gas

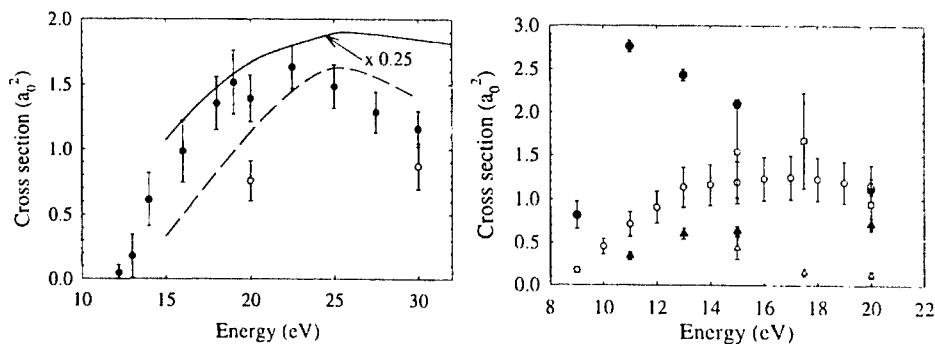


FIGURE 6. (a) Cross section for excitation of the $B^1\Sigma$ electronic state of H_2 , and absolute comparison with theory: solid line, Ref. [27] and dashed line, Ref. [28]. (b) Cross section for excitation of the $a^1\Pi$ and $a^1\Sigma$ states of N_2 are shown by the solid circles and triangles respectively. Open symbols are the available electron scattering data: (a) circles, Ref. [29]; (b) circles, Ref. [30], and squares and triangles, Ref. [31].

positron trap. Empirically, the buffer-gas trap works most efficiently on N_2 when the energy loss per stage is tuned to operate in this region (i.e., $\sim 9 - 10$ eV). In N_2 , positronium formation (which is the dominant loss process in the trap), begins at a threshold energy of 8.8 eV, increasing from zero at that point. The data in Fig. 6(b) indicate that the high trapping efficiency in N_2 is due to the very rapid increase in the cross section for electronic excitation in the region just above threshold where the loss due to positronium formation is relatively small.

IV. ENERGY RESOLVED ANNIHILATION MEASUREMENTS

The fate of all antimatter in our world is annihilation with ordinary matter. Thus understanding the details of these annihilation processes is both of fundamental importance and crucial for a range of applications. With the exception of experiments conducted in the buffer-gas trap varying the temperature of the positrons, studies of positron annihilation have been limited to room temperature. An outstanding problem for almost four decades is that positron annihilation on molecules can be orders of magnitude larger than expected from simple collisions. In order to address this problem, we recently began experiments using the cold beam to make high-resolution measurements of annihilation as a function of positron energy [16]. These measurements, which are the first of their kind, are difficult due to the fact that the annihilation cross section is typically several orders of magnitude smaller than the cross sections for typical scattering processes (i.e., those illustrated in Fig. 1).

The apparatus for the annihilation experiment is shown schematically in Fig. 7. In this experiment, 2 μs pulses of $\sim 5 \times 10^4$ cold positrons are passed through the annihilation cell. Annihilation is monitored from a 10 cm long region along the positron beam. In order to minimize the background signal that would arise if the

positrons were to strike a collector or other metal surface, the positrons are kept in flight, transiting the cell ~ 10 times during the time annihilation gamma rays are monitored. The detector consists of a relatively compact CsI crystal with integrated light pipe and photodiode surrounded by a lead shield. Typical background levels are one count per 10^9 positrons.

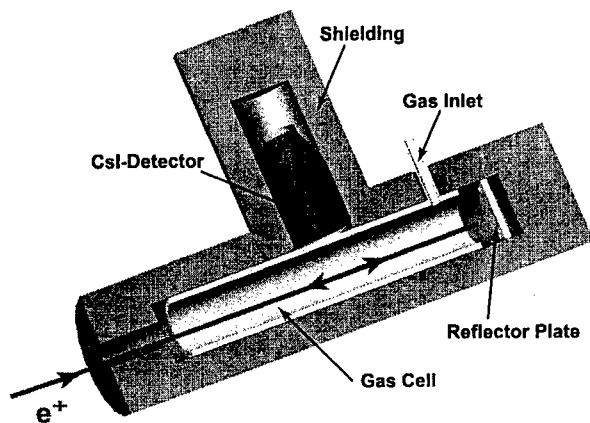


FIGURE 7. The apparatus used for energy-resolved positron annihilation measurements. Monoenergetic pulses of positrons transit the gas cell while the gamma ray signal is recorded.

Thus far we have studied annihilation from Xe atoms and several molecules (mostly hydrocarbons) ranging in size from acetylene (C_2H_2) to butane (C_4H_{10}) in the range of energies from 50 meV to ~ 500 meV. Selected studies have included higher energies, up to ~ 4 eV.

Shown in Fig. 8 are data for annihilation in butane from an energy of 50 meV to within 0.5 eV of the positronium threshold at 3.8 eV [16]. The annihilation rate is given in terms of the dimensionless parameter, Z_{eff} , defined in terms of the Dirac annihilation rate for a positron in an electron gas, assuming no correlation of the particles. If this simple model were correct, the annihilation rate would be $Z_{eff} = Z$, where Z is the number of electrons in the molecule.

The data for butane are typical of the alkane molecules studied (C_2H_6 , C_3H_8 , and C_4H_{10}), in that very large enhancements in the annihilation rate are observed when the incident positron energy is tuned to the range of the molecular vibrations, while Z_{eff} is ≤ 100 at energies above this region. In butane, the sharp peak observed at the C-H stretch mode (i.e., at ~ 0.36 eV) is 23,000, compared with the value of 10,500 measured with a Maxwellian distribution of positrons at 300 K.

While these experiments are in their infancy, a number of important results have already emerged. The data show clearly that it is vibrational resonances of the positron molecule complexes that lead to the large values of Z_{eff} . The resonances in larger molecules are downshifted tens of millivolts; this is interpreted as a measure of

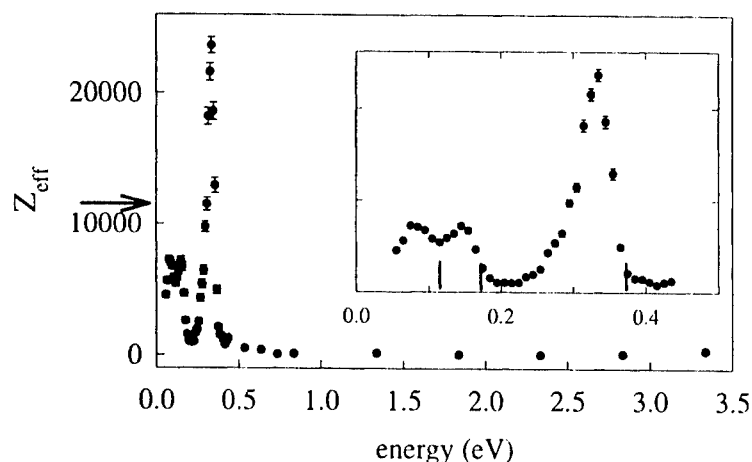


FIGURE 8. The first energy resolved measurements of positron annihilation rates. The normalized rate, Z_{eff} , is shown for butane (C_4H_{10}) as a function of positron energy, ϵ , in the range $50 \text{ meV} \leq \epsilon \leq 3.3 \text{ eV}$. The inset shows the same data in the range, $50 \leq \epsilon \leq 450 \text{ meV}$, on an expanded scale. The arrow on the ordinate indicates the value at room temperature. The vertical bars on the abscissa in the inset indicate the positions of the infrared-active vibrational modes.

the binding of positrons to molecules [16]. Finally, addition of fluorine atoms to hydrocarbons results in a decrease in Z_{eff} at the C-H stretch mode energy by a much larger factor than the change in the fraction of C-H bonds in the molecule. This tends to support the conjecture of Gribakin [32, 33] that fluorination of hydrocarbons can change the positron-molecule potential from attractive to repulsive, and turn off the resonant annihilation mechanism.

V. A LOOK TO THE FUTURE

There are several new experiments made possible by the positron scattering and annihilation techniques described here, and a number of potentially important extensions of these techniques are now possible. Experiments are currently in progress to study several aspects of positron scattering. We are interested in understanding the sharp threshold behavior in vibrational excitation of molecules, more complete measurements in energy and more detailed comparisons with theoretical calculations. The subject of electronic excitation by positron impact is even less mature, and our measurements have now motivated new theoretical efforts [34]. Questions of interest include obtaining a quantitative understanding of the cross sections and effects such as the threshold behavior of the $\text{A}^1\Pi$ excitation cross section in N_2 (c.f., Fig. 6). Another question of interest is whether positron impact can result in electronic excitations of targets involving a spin flip. Such transitions, which are common in electron scattering due to exchange, might occur via the spin-orbit interaction in the case of positrons. We have also searched briefly for resonances in

scattering in the range of energies of low-lying electronic excitations. Further studies of this phenomenon are planned.

There are a large number of open questions in the area of positron annihilation that can now be addressed by the new experiment described above. Our first experiments appear to confirm the model of Gribakin that large values of annihilation in molecules occurs *via* vibrational resonances of the positron-molecule complex. One can now make more detailed tests of the model. Questions of interest include the magnitude of the positron binding energy, the density of resonances as a function of energy, and the dependence of these resonances on molecular structure.

Several extensions of the work in a number of directions are now either in progress or are planned. As indicated in Fig. 1, good energy resolution is crucial in studying many important processes. We are currently building a positron trap having a 5 tesla magnetic field and walls cooled to 10 kelvin. The plasma will cool to 10 kelvin (equivalent to 1 meV) by cyclotron radiation. This device should, in principle, be capable of producing a positron beam with millielectron volt energy resolution which would enable a new regime of high resolution scattering and annihilation studies.

Other planned directions include study of the scattering and annihilation of positrons interacting with larger molecules (e.g., those with negligible vapor pressure at room temperature), atomic clusters and dust grains. Neutral large molecules and clusters can be studied in a gas cell at elevated temperature. Ionized species and ionized fragments produced *via* annihilation can be studied *in situ* in a Penning trap in the high field magnet.

VI. CONCLUDING REMARKS

The understanding of antimatter-matter interactions has lagged significantly compared with analogous studies involving ordinary particles. In the past few years, progress has been made in closing this gap by research efforts such as that described here, research that was driven in large part by novel applications of nonneutral plasma techniques. Many important questions in this area are either presently being studied or can now be addressed. Additional tools for these studies, such as a millielectron volt positron beam, are currently under development. This progress bodes well for achieving a fundamental understanding of broad classes of antimatter-matter interactions that can be used, in turn, for a range of scientific and technological applications.

ACKNOWLEDGEMENTS

We are pleased to acknowledge helpful conversations with Rod Greaves, Gleb Gribakin, and Jim Mitroy, and the technical assistance of Gene Jerzewski. This work is supported by the National Science Foundation, grant PHY 98-76894, and the Office of Naval Research, grant N00014-97-1-0366. One of us (SJB) gratefully acknowledges the support of the Australian-American Fulbright Commission.

REFERENCES

- [1] *New Directions in Antimatter Chemistry and Physics*, C. M. Surko and F. A. Gianturco, eds. Kluwer Academic Publishers, The Netherlands, 2001.
- [2] Greaves, R. G. and Surko, C. M., *Phys. Plasma* **4**, 1528-1543 (1997).
- [3] Gilbert, S. J., Dubin, D. H. E., Greaves, R. G., *et al.*, *Phys. Plasmas*, in press (2001).
- [4] Eades, J. and Hartmann, F. J., *Rev. Mod. Phys.* **71**, 373-419 (1999).
- [5] Schultz, P. J. and Lynn, K. G., *Rev. Mod. Phys.* **60**, 701-79 (1988).
- [6] *Positron Spectroscopy of Solids*, A. Dupasquier and A. P. Mills, Jr., eds. IOS Press, Amsterdam, 1995.
- [7] Murphy, T. J. and Surko, C. M., *Phys. Rev. A* **46**, 5696-705 (1992).
- [8] Surko, C. M., Gilbert, S. J., and Greaves, R. G., *Non-Neutral Plasma Phys. III*, edited by J. J. Bollinger, R. L. Spencer, and R. C. Davidson, American Institute of Physics, New York, 1999, pp. 3-12.
- [9] Gilbert, S. J., Kurz, C., Greaves, R. G., *et al.*, *Appl. Phys. Lett.* **70**, 1944-1946 (1997).
- [10] Kurz, C., Gilbert, S. J., Greaves, R. G., *et al.*, *Nucl. Instrum. Methods in Phys. Res.* **B143**, 188-194 (1998).
- [11] Holzscheiter, M. H., *et al.*, *Nucl. Phys. B* **56A**, 336-48 (1997).
- [12] Greaves, R. G. and Surko, C. M., *Non-Neutral Plasma Phys. III*, edited by John J. Bollinger, *et al.*, American Institute of Physics, Princeton, NJ, 1999, pp. 19-28.
- [13] Sullivan, J., Gilbert, S. J., and Surko, C. M., *Phys. Rev. Lett.* **86**, 1494-1497 (2001).
- [14] Gilbert, S. J., Greaves, R. G., and Surko, C. M., *Phys. Rev. Lett.* **82**, 5032-5035 (1999).
- [15] Sullivan, J. P., Marler, J. P., Gilbert, S. J., *et al.*, *Phys. Rev. Lett.* **87**, 073201-4 (2001).
- [16] Gilbert, S. J., Barnes, L. D., Sullivan, J. P., *et al.*, unpublished.
- [17] Surko, C. M., Leventhal, M., and Passner, A., *Phys. Rev. Lett.* **62**, 901-4 (1989).
- [18] Murphy, T. J. and Surko, C. M., *Phys. Rev. Lett.* **67**, 2954-2957 (1991).
- [19] Greaves, R. G. and Surko, C. M., *Phys. Rev. Lett.* **85**, 1883-1886 (2000).
- [20] Greaves, R. G. and Surko, C. M., *Phys. Plasmas* **8**, 1879-1885 (2001).
- [21] Greaves, R. G. and Surko, C. M., *Phys. Rev. Lett.* **75**, 3846-3849 (1995).
- [22] Gilbert, S. J., Sullivan, J., Greaves, R. G., *et al.*, *Nucl. Instrum. Methods in Phys. Res.* **B171**, 81-95 (1999).
- [23] Sur, S. and Ghosh, A. S., *J. of Phys. B* **18**, L715-L719 (1985).
- [24] Gianturco, F. A. and Mukherjee, T., *Phys. Rev. A* **64**, 024703 (2001).
- [25] Baille, P. and Darewych, J. W., *J. de Phys. Lett.* **35**, 243-45 (1974).
- [26] Kimura, M., *et al.*, *Phys. Rev. Lett.* **80**, 3936-3939 (1998).
- [27] Mukherjee, T., Sur, S., and Ghosh, A., *J. Phys. B* **24**, 1449-1454 (1991).
- [28] Lino, J. L. S., Germano, J. S. E., and Lima, M. A. P., *J. Phys. B* **27**, 1881-1888 (1994).
- [29] Khakoo, M. and Trajmar, S., *Phys. Rev. A* **34**, 146-156 (1986).
- [30] Mason, N. J. and Newell, W. R., *J. Phys. B* **20**, 3913-3921 (1987).
- [31] Campbell, L., Brunger, M. J., Nolan, A. M., *et al.*, *J. Phys. B* **34**, 1185-1199 (2001).
- [32] Gribakin, G., *Phys. Rev. A* **61**, 022720-1-13 (2000).
- [33] Iwata, K., Gribakin, G. F., Greaves, R. G., *et al.*, *Phys. Rev. A* **61**, 022719-1-17 (2000).
- [34] McEachran, R., private communication, 2001.

Recent Progress on the ATHENA Positron Accumulator

L. V. Jørgensen, D. P. van der Werf, T. L. Watson, M. Charlton
and M. J. T. Collier

Department of Physics, University of Wales Swansea, Singleton Park, Swansea SA2 8PP, United Kingdom.

Abstract. The Positron Accumulator for the ATHENA anti-hydrogen experiment at CERN, Geneva has recently been upgraded with a new 50 mCi ^{22}Na β^+ -radioactive source. Following this, rapid progress has been made in optimizing and characterizing the properties of the positron plasma. The rotating wall technique has also been implemented in the accumulation region and has been shown to lead to compression of better than a factor of 10 in density and markedly increased lifetimes, even when using the N_2 buffer gas as a cooling gas. Using these techniques we have routinely accumulated up to 2×10^8 positrons in a few minutes. The positron plasma has a FWHM of only 3-4 mm when using the rotating wall which compares with a FWHM of 15 mm without the rotating wall.

INTRODUCTION

The ATHENA anti-hydrogen experiment at CERN, Geneva aims to produce and trap anti-hydrogen for further studies including tests of CPT and the weak equivalence principle [1-5]. In such a quest to synthesize atomic low-energy anti-hydrogen there are many parameters to optimize. A few of these have to do with maximizing the number, density and lifetime of the constituent particles of positrons and anti-protons. In order to accumulate as many positrons as possible a positron accumulator based on the design of the Surko Group at the University of California San Diego [6-8] has been constructed over the past few years. In this accumulator we have trapped up to 2×10^8 positrons prior to transferring them across a low field region to the main ATHENA recombination trap situated inside a 3 T magnetic field.

EXPERIMENTAL

The positron accumulator traps and cools a continuous beam of slow positrons. The slow positrons injected into the accumulator are generated by moderating β^+ particles from a ^{22}Na radioactive source and guiding them into the trapping region using a

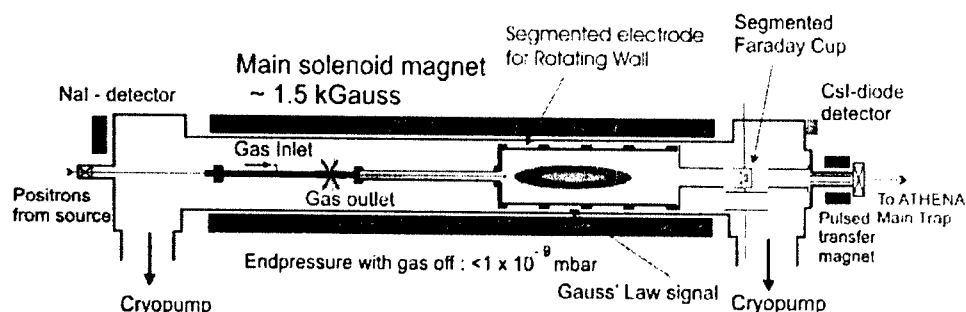


Figure 1. Schematic overview of the ATHENA Positron Accumulator, showing the electrodes used for the rotating wall and the electrode used to generate the Gauss' Law signal.

magnetic field. Recently the ATHENA Positron Accumulator has been fitted with a new 50 mCi ^{22}Na source from NAC in Cape Town, South Africa. A cryogenic cold head capable of reaching 5.5 K cools down the source and makes it possible to grow a solid neon moderator directly on the source. The new source has meant that a slight redesign was necessary as the dimensions of the new source are quite different from the old source. Details of the source end design as well as further details of the experimental set-up can be found elsewhere [9, 10]. Placing a NaI-detector close to the gate valve between the source end and the main trapping region made it possible to optimise the moderator growth. During moderator growth this gate valve would be closed and the positrons would annihilate on the closed valve. To calibrate the NaI signal to obtain the absolute beam strength a channeltron detector was briefly inserted here and coincidence measurements performed. The primary positron beam now has an intensity of 7×10^6 positrons per second.

The trapping scheme used is similar to that used in the new positron trap of the Surko Group [6] and utilizes nitrogen buffer gas to trap and cool the positrons. After trapping the axial confinement is provided by applying appropriate electric potentials to the electrode array while the radial confinement is provided by a 0.15 T axial magnetic field.

One of the trapping electrodes (see Fig. 1) is split into 6 segments, making it possible to use it to compress the plasma by applying a rotating electric field ('rotating wall') [11]. This method has been shown recently to work well also for positrons plasmas [12-13]. In our case the electrodes used have a significantly larger radius (~ 10 cm) than in earlier experiments but recent results have shown that we can still influence the positron plasma from that distance. Using a rotating wall will lead to heating of the plasma and since the magnetic field in our trap is too small to allow re-cooling using synchrotron radiation another means of cooling the plasma has to be present. We have so far used the nitrogen already present in the form of the buffer gas to cool the plasma again. However, it has been shown [13] that nitrogen is not a very efficient choice as cooling gas, so a CF_4 gas line is presently being commissioned. It should be noted though, that all the data presented in this paper were obtained using nitrogen as a cooling gas. Having the rotating wall present in the accumulation trap means that we

can use the rotating wall during accumulation and thus try to increase the lifetime of the positrons in the presence of the buffer gas. This in turn should increase the overall number of positrons we can accumulate, which will be very beneficial when trying to make anti-hydrogen.

The detection system used for our experiment consists of 3 detectors: (1) A segmented Faraday cup detector consisting of 9 plates to get information about the size and position of the plasma. The total size of the Faraday cup is 25 cm^2 and it is situated outside the main magnet in a region where the magnetic field is about a quarter of the field inside the trap. This means that the data obtained from the Faraday cups is 'magnified' compared to the actual sizes inside the magnet and to get the true sizes this magnification factor has to be taken into account. (2) A CsI-diode detector to detect the positron annihilation signal. (3) A 'Gauss' Law' signal from one of the confining electrodes caused by charge being induced on the electrode as the confined plasma is being dumped on the Faraday cup. The whole experimental set-up including the data acquisition from the detectors has been automated to make it possible to run the experiment remotely.

After trapping the positrons still need to be transferred to the 3 Tesla ATHENA main magnet where the antiproton capture trap and the recombination trap is situated. A special transfer section has been constructed for this purpose. This section consists of vacuum separation valve, a pumping restriction, a number of transfer electrodes as well as a transfer magnet capable of pulsing from 0 to 1 Tesla in 20 ms and staying at 1 Tesla for 1 s. This system has been installed and undergone preliminary testing.

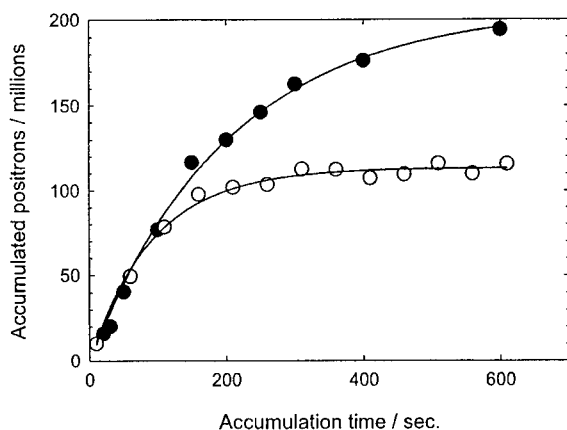


Figure 2. Accumulation of positrons. The open circles show accumulation of positrons without using the rotating wall technique, but with the bottom of the trap lowered by 4 V during the accumulation. The solid circles show accumulation while using the rotating wall technique. The rotating wall was on for the last 50% of the accumulation time. The frequency used was 500 kHz at an amplitude of 0.4 V. In this case the bottom of the trap was lowered by 6 V during accumulation. Using the rotating wall increases the lifetime by almost a factor of 2 while the accumulation rate remains about the same.

However, due to problems with the power supply for the magnet no data on the transfer will be presented in this paper.

RESULTS

Following the installation of the new source rapid progress has been made in optimizing and characterizing the accumulated positron plasma and in implementing the rotating wall technique. This rapid progress was made possible not only by the fact that a larger source means more positrons but also, as we shall see later, that when it is possible to accumulate more than a few tens of million of positrons many of the plasma parameters seem to become more stable. Since most of the data that will be presented here has been obtained recently a thorough analysis of the data has not yet been completed and parts of it are not yet understood in detail.

The increased number of positrons made available by the new source made it possible to optimise the electrode potentials and buffer gas better and also made a fine-tuning of the alignment of the magnetic field to the physical axis of the system possible simply by carefully analysing the data obtained. The better alignment in turn lead to an increase in the total number of positrons trapped since the lifetime of the positrons was increased. Figure 2 shows the end result of this fine-tuning. It was thus possible to accumulate more than 100 million positrons in a few minutes. When using

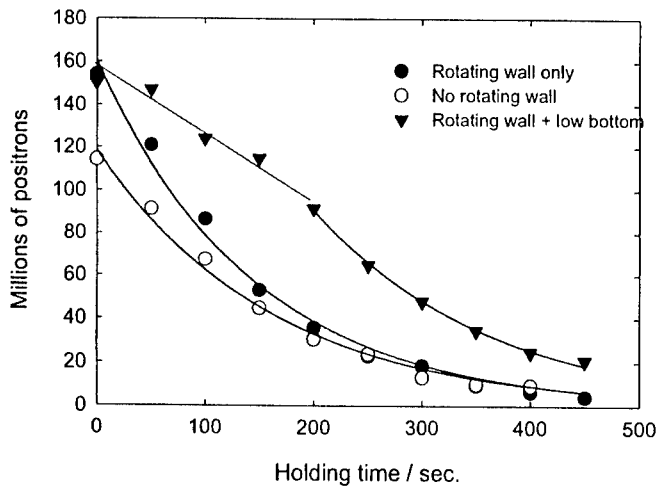


Figure 3. Decay of the positron plasma after the buffer gas is pumped out and the rotating wall is turned off. The frequency used for the rotating wall was 400 kHz and the amplitude used was 0.2 V. The rotating wall was on for the last 50% of the accumulation time. For the data when the rotating wall was used together with lowering of the bottom of the trap during accumulation, the trap bottom was lowered by 4 V.

a suitable (see later) frequency and amplitude for the rotating wall and applying the rotating wall for the last 50 % of the accumulation time it was possible to double the lifetime of the positrons in the presence of the buffer gas while maintaining the same accumulation rate and we therefore now routinely accumulate about 200 million positrons with such settings. The data using the rotating wall shown in Figure 2 yielded a lifetime of 200 seconds when fitted to the standard accumulation formula while the data without the rotating wall gave a lifetime of 95 seconds. It is important to stress that this is with the buffer gas present in the trap. The increase in the lifetime when using the rotating wall shows that under normal operation without using the rotating wall the plasma does not appear to be in the annihilation limit, i.e. the limit where annihilation on the rest gas (buffer gas) is the dominant loss. Rather it would indicate that there is still a large collisional cross-field drift to the electrode walls.

In order to try to accumulate as many positrons as possible we also tried to lower the bottom of the trap gradually during accumulation. This has been shown previously [6] to increase the number of accumulated positrons. However, no increase was found, possibly due to the fact that the trap is not filled to the space charge limit before the bottom is lowered.

Lowering the bottom of the trap gradually during accumulation did turn out to have one surprising effect though. It dramatically increased the lifetime of the positrons after the buffer gas was pumped out. Figure 3 shows the result of such a lifetime measurement. The data for accumulation with and without a rotating wall were both

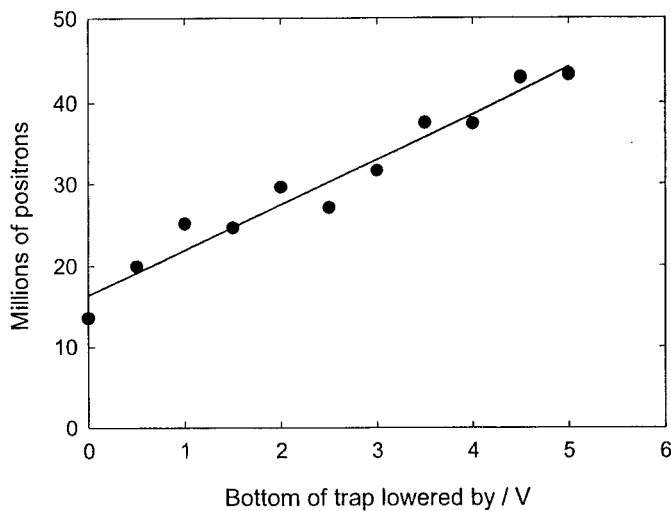


Figure 4. Effect on lifetime of lowering the bottom of the trap. Data shows the number of positrons left after 80 seconds of accumulation followed by 200 seconds of holding the positrons after the gas was pumped out. No rotating wall was used for these measurements. The line is a linear fit to the data with a slope of 5.7 million positrons per V.

fitted using a lifetime of 150 seconds, the main difference between the two sets of data being the increased number of positrons accumulated before the gas was pumped out when using the rotating wall. The data when the bottom of the trap was gradually lowered during accumulation exhibits an as yet unexplained slow linear fall-off up to about 200 seconds after which the data appears to follow an exponential fall off that again could be fitted with a 150 second lifetime.

To investigate this phenomenon further an experiment was performed looking at the number of positrons left in the trap after 80 seconds of accumulation without using a rotating wall and 200 seconds of holding without buffer gas as a function of how much the bottom of the trap was lowered during accumulation. This is shown in Figure 4 and reveals a linear dependence between the two quantities.

The rotating wall was optimised by mapping out the yield as a function of the frequency and amplitude of the applied rotating electric field. By yield we here mean the general effect it has on the plasma, both in increasing the total amount of positrons but also in centring them in the trap. The CsI diode detector monitored the total

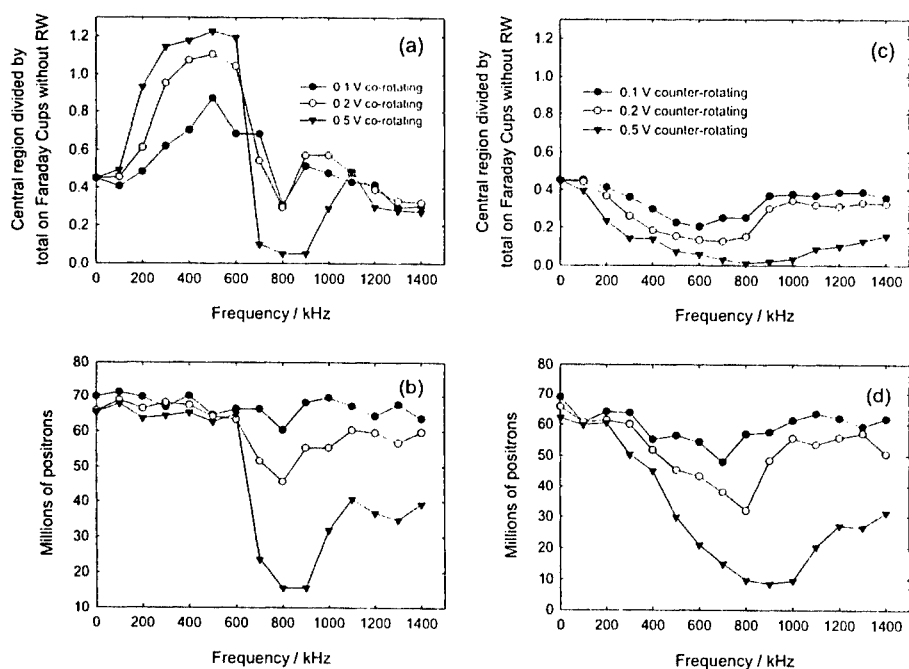


Figure 5. Optimisation of the rotating wall. (a) The number of positrons in the central region compared to the same number with no rotating wall. The data is for accumulation for 60 sec. and with the rotating wall on for the last 30 sec. of the accumulation. (b) CsI annihilation data for the same experiments. (a) and (b) are for a co-rotating electric field. (c) and (d) show the corresponding data for a counter-rotating field.

number of positrons while the segmented Faraday cup monitored the centering of the plasma. The centring could then be observed by looking at the increase in the signal on the central plates of the Faraday cup. Looking at various ratios between the the signals on the Faraday cup plates and fitting the data yielded information about positioning and absolute plasma sizes.

Figure 5 (a) and (c) show the ratio between the signal in a central region of the Faraday cup while using the rotating wall and the total signal on the Faraday cup with no rotating wall as a function of the applied frequency and amplitude of the rotating wall. The area of the central region constituted about 20 % of the total area of the Faraday cup. Figure 5 (b) and (d) show the total number of positrons for the same experiments as observed by the CsI diode detector. The data show how there appears to be a broad peak in the compression in the frequency range of 300-600 kHz and that the compression is increasing with increasing amplitude. Above 600 kHz there is an abrupt fall-off in the signal on the central plate coinciding with a quick drop-off in the total number of positrons. Note that up to 600 kHz the total number of positrons is very stable for all amplitudes and the fact that the ratio for the central region goes above unity must mean that parts of the positron plasma initially missed the Faraday cup altogether, but that the rotating wall has compressed even this outer lying part of the plasma into the central region. The data for the counter-rotating field ((c) and (d)) show a loss of positrons in the centre of the plasma coinciding with overall loss of positrons. The loss seem to increase with increasing amplitude of the rotating wall and also with increasing frequency, at least up to around 800-1000 kHz.

The data in Figure 5 seem to indicate a compression of a factor of about 2.5. However, the compression turns out to be even better than that. The central region of 20 % of the total area of the Faraday cups contains 5 individual plates. Of these only 3 were actually recording a signal when the rotating wall was being used. Unfortunately these 3 were not axisymmetric, meaning that the plasma was hitting the Faraday cup off-centre. This could possibly be attributed to the fact that our main magnet has had correction coils placed on the outside to make the field in the trapping regions sufficiently homogeneous and that these correction coils could probably induce a small dipole field at the end of the magnet. However, by looking at ratios between opposing plates and between central plates and the total on all plates and comparing this to similar data when the Faraday cup is moved slightly up or down (it is situated on a linear motion drive), it is possible to get absolute information about the position and size of the plasma. In this manner we found that the plasma had a FWHM of 15 mm when no rotating wall was being used and a FWHM of 3-4 mm when the rotating wall was being used. As the total number of positrons stayed constant or in some cases even increased this means that the central density increased by a factor of more than 10 and in quite a few cases even more than 20 when using the rotating wall. This compression ratio is much larger than that reported for N_2 previously [13] but this can possibly be attributed to the much larger pressures used. The pressure in the final stage of our trap, where the rotating wall electrode is situated, can be as high as a few times 10^{-6} mbar during accumulation. This is about two orders of magnitude higher than the pressure used in the earlier study [13].

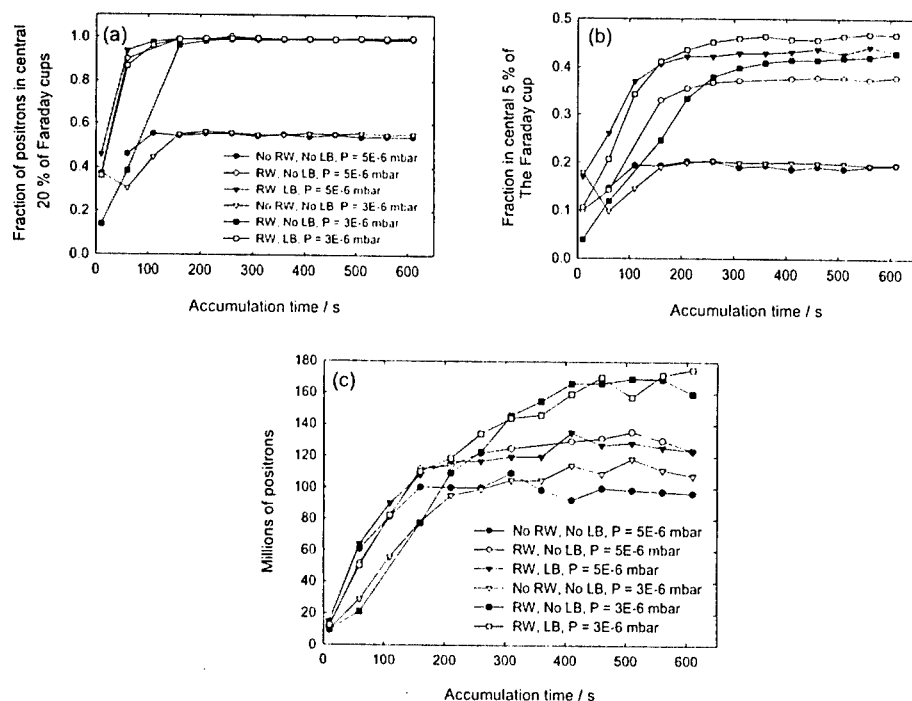


Figure 6. (a) The ratios of accumulated positrons within a central region constituting 20 % of the Faraday cups compared to the total on the Faraday cups. (b) A similar ratio for the central plate of the Faraday cup, constituting 5 % of the total area. (c) The number of accumulated positrons under the same conditions. Note how stable the ratios are for widely varying conditions. (RW = Rotating Wall, 500 kHz, 0.4 V; LB = Lowered Bottom of trap 4 V during accumulation).

One of the main features that made it possible to extract all this information from the ratios from the Faraday cup is that the signals from them were stable and reproducible. Figure 6 shows data of the ratio for the central 20 % of Faraday cup compared to the total (a) and for the single central plate constituting 5 % of the total area, again compared to the total signal on the Faraday cup (b) and the corresponding total positron numbers as observed by the CsI diode detector (c). The data contains 2 different accumulation pressures, with and without using the rotating wall and lowering of the bottom of the trap. It should be noted that the pressures mentioned are the pressures in the first pump-box before the electrode array. This pressure should have a direct linear relationship with the pressure inside the electrodes when in a steady state and is used for overall pressure stabilization.

The most remarkable thing about the data in Figure 6 is that the ratios are so reproducible even for very different total numbers of positrons and thus for very different densities. It would appear that if one can accumulate more than about 40-50

million positrons the plasma properties becomes very stable. This is obviously very important for the wider ATHENA experiment as it makes it possible to predict the size, density and position of the positron plasma prior to transferring it to the main ATHENA recombination trap. It has also made it possible within the last weeks to try to map the evolution of the plasma after the rotating wall is turned off and the buffer gas is pumped out. This is of importance to our experiment since it takes up to 20 seconds between beginning the gas pump-out and transferring the plasma. However, it is also of interest in order to try to understand how lowering of the bottom of the trap increases the lifetime of the plasma.

CONCLUDING REMARKS

The rapid progress recently in increasing the number of positrons trapped and the plasma density and characterization made possible by the upgrade of the positron source and the implementation of the rotating wall puts us a small step closer to making anti-hydrogen. Ongoing effort to transfer the positrons to the main recombination trap should allow us to deliver 100-150 million positrons to the ATHENA experiment every 5 minutes, the repetition rate being dictated by the cycle time for the pulsed transfer magnet. Optimising the transfer and recapture will be the main focus of our efforts over the next few months.

However, for the half of the year where there are no anti-protons available at CERN the Positron Accumulator could also act as a valuable reservoir of cold, well characterized pulses of low energy positrons for a variety of experiments making use of the traps and detection methods available at the ATHENA experiment.

ACKNOWLEDGEMENTS

We would like to thank the EPSRC (grant number GR/N65240/01) for its support of this project and the TMR-network EUROTRAPS (contract number ERBFMRXCT970144) for its funding of a postdoctoral position. We wish to thank K. S. Fine, M. Doser and R. Funakoshi for much needed help with hardware and software as well as many useful discussions. We would also like to thank Cliff Surko and Rod Greaves for providing helpful advice.

REFERENCES

1. Holzscheiter, M. H. *et al.*, *Nucl. Phys. B* **56A**, 336 (1997)
2. Fine, K. S., "The ATHENA Antihydrogen Experiment" in *Non-Neutral Plasma Physics III*, edited by J. J. Bollinger, R. L. Spencer and R. C. Davidson, AIP Conference Proceedings 498, New York, 1999, p. 40-47
3. Holzscheiter, M. H. and Charlton, M., *Rep. Prog. Phys.* **62**, 1 (1999)

4. Amsler, C., *et al.*, "Antihydrogen Production and Precision Spectroscopy with ATHENA/AD-1" in *The Hydrogen Atom, Precision Physics of Simple Atomic Systems*, edited by Karshenboim, S. G., *et al.*, Springer Lecture Notes in Physics, Berlin, 2001, p. 469-488
5. Fujiwara, M., *et al.*, "Producing Slow Antihydrogen for a Test of CPT Symmetry" in *Proc. Int. Conf. On Muon Catalysed Fusion and related exotic atoms*, Edited by K. Nagamine and K. Ishida, to be published in *Hyperfine Interactions*
6. Surko, C. M., Gilbert, S. J. and Greaves, R. G. "Progress in Creating Low-Energy Positron Plasmas and Beams" in *Non-Neutral Plasma Physics III*, edited by J. J. Bollinger, R. L. Spencer and R. C. Davidson, AIP Conference Proceedings 498, New York, 1999, p. 3-12
7. Murphy, T.J. and Surko, C.M., *Phys. Rev. A*, **46**, 5696 (1992)
8. Greaves, R. G., Tinkle, M. D., and Surko, C. M., *Phys. Plasmas* **1**, 1439 (1994)
9. Jørgensen, L. V., Collier, M. J. T., Fine, K. S., Watson, T. L., van der Werf, D. P. and Charlton, M., "A Positron Accumulator for Antihydrogen Synthesis" in *Positron Annihilation ICPA-12*, edited by W. Triftshäuser, G. Kögel and P. Sperr, Mat. Sci. Forum **363-365**, 2001, p 634-636
10. Collier, M. J. T., Jørgensen, L. V., Meshkov, O. I., van der Werf, D. P. and Charlton, M., "Development and Testing of a Positron Accumulator for Antihydrogen Production" in *Non-Neutral Plasma Physics III*, edited by J. J. Bollinger, R. L. Spencer and R. C. Davidson, AIP Conference Proceedings 498, New York, 1999, p.13-18
11. Huang, X., Anderegg, F., Hollmann, E. M., Driscoll, C. F. and O'Neil, T. M., *Phys. Rev. Lett.* **78**, 875 (1997)
12. Greaves, R. G. and Surko, C. M., *Phys. Rev. Lett.* **85**, 1883 (2000)
13. Greaves, R. G. and Surko, C. M., *Phys. Plasmas* **8**, 1879 (2001)

Electron Plasma for Antiproton Cooling in the ATHENA Experiment

M. Amoretti^{†*}, C. Carraro[†], V. Lagomarsino[†], G. Manuzio[†], G. Testera[†]
and A. Variola[†]

^{*}*INFN (U.d.R. Milano Università) and Dipartimento di Fisica, Università degli Studi di Milano,
Via Celoria 16, 20133 Milano, Italy*

[†]*INFN and Dipartimento di Fisica, Università degli Studi di Genova, Via Dodecaneso 33, 16164
Genova, Italy*

Abstract. The first phase of the ATHENA (AnTiHydrogEN Apparatus) experiment is devoted to the study of cold antihydrogen production.

The apparatus includes an antiproton capture trap designed to trap and to cool antiprotons coming from the CERN Antiproton Decelerator (AD). The antiproton cooling is achieved by means of the collisional interaction with a cold cloud of trapped electrons. The electron plasma is loaded in the trap before the antiproton capture by means of a small-size heated filament and cooled to sub-eV temperatures by cyclotron radiation.

We report some measurements devoted to the characterization of the electron plasma. The ATHENA apparatus design does not allow the use of complex diagnostic; therefore the plasma properties are obtained using electrostatic wall probes, radio-frequency diagnostic, and dumping the electrons onto a charge collector. A simple experimental method to obtain an estimate of the electron plasma radius is discussed.

INTRODUCTION

The aim of the ATHENA experiment [1, 2] is the cold antihydrogen production for high resolution laser spectroscopy studies. The first phase of the experiment is focused on the production of low temperature antihydrogen atoms from the interaction of several thousands antiprotons with a dense positron plasma. The two antihydrogen components are produced and accumulated in two different electromagnetic traps and then they are transferred in a nested-well plasma multi-ring trap.

The positron plasma is produced in a modified Penning-Malmberg trap based on the design described in Refs. 3 and 4 (see also Ref. 5).

The antiprotons are delivered by the Antiproton Decelerator (AD) [6] at CERN with a kinetic energy around 5 MeV. The AD antiprotons bunch pass through some degrader foils and up to $1.6 \cdot 10^4$ antiprotons are routinely caught in a high voltage trap. The trapped antiprotons are then cooled by the interaction with a cold dense electron plasma. Once antiprotons are cooled, they are transferred into the recombination trap.

In this work we will focus our attention on the electron plasma used to slow down the antiproton bunch. In the following, we present the structure of the antiproton catching trap and the electron plasma diagnostic system. We also report and discuss our experimental investigations on electron plasma properties.

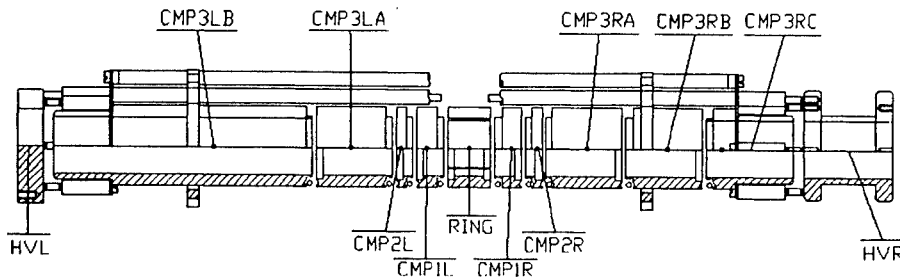


FIGURE 1. Configuration of the antiproton catching trap electrodes

ANTIPROTONS CATCHING TRAP

The antiproton catching trap is composed by 12 cylindrical electrodes (Fig. 1). The internal diameter of the electrodes is 2.5 cm while the electrodes lengths vary from 0.5 cm to 13 cm. The trap is mounted in a cryogenic ultra-high vacuum system placed in a magnetic field of 3 T.

The two external electrodes (HVR and HVL) are used to trap the antiprotons beam coming from the AD. Some foils acting as energy degraders are mounted in front of the HVL electrode and they are traversed by the antiproton beam. Among these foils there is a silicon sensor (67 μm thick) used as beam counter and a 80 μm aluminum foil closing the external side of the entrance electrode (HVL).

Before the antiprotons arrival, the far away electrode (HVR) is polarized applying up to -10 kV. After a suitable delay (few hundreds of ns) from the time when the antiprotons hit the silicon detector, the HVL voltage is rapidly (in a few tenths of ns) switched on and the particles exiting from the degrader and lying in tail of the energy distribution are captured into the trap.

The central section, composed by 10 electrodes, is used to confine the electron plasma and the cold antiprotons. The electrodes have different lengths and can be separately polarized in order to have a good flexibility in the external electrostatic field configuration. The applied potentials can be chosen in order to shape the trap region with harmonic or flat electrostatic field. The central electrode (RING) is sectorized in 4 azimuthal parts to detect and drive diocotron modes.

DIAGNOSTIC SYSTEMS

Two different kind of diagnostic are implemented [7]: a destructive diagnostic based on the dumping of the electrons on the degrader foil connected with HVL electrode, and a non-destructive diagnostic of the plasma collective modes.

The destructive diagnostic consists in dumping the electrons on the degrader and measuring the collected charge by means of an high-impedance low-noise amplifier. The measurement of the total number of the electrons extracted varying the confining

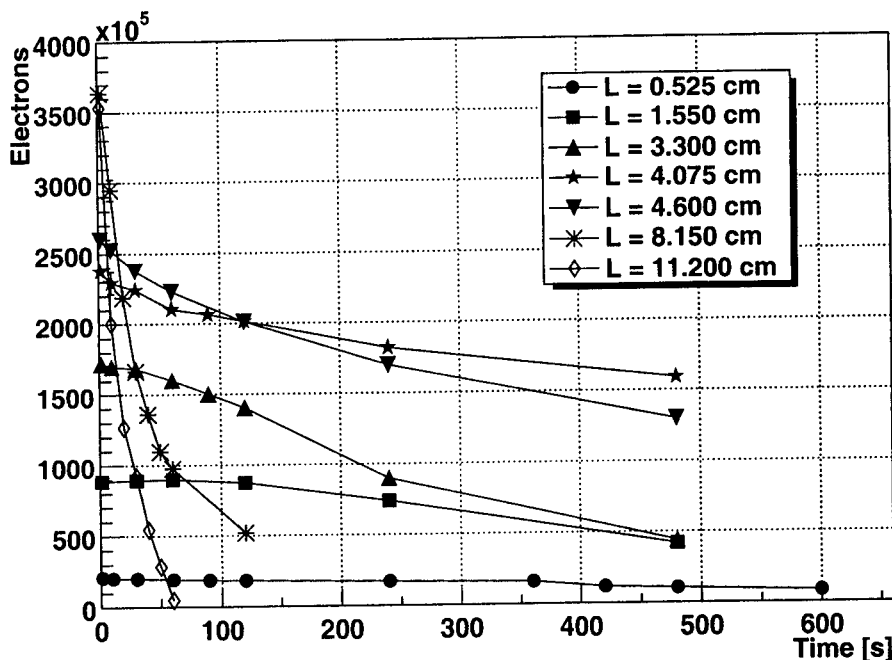


FIGURE 2. Example of the dependence of the number of loaded electrons on the confining time. The potential applied to the two confining electrodes is -35 V.

potential gives different information on the plasma. It can be used to measure the longitudinal plasma temperature [8] or, assuming a plausible temperature value, it is useful to have an indication of the radial extension of the plasma.

A fast rough estimate of the plasma radius can be obtained by the following procedure. Assuming a zero-temperature model, the electrons cloud shape is approximated by an infinite plasma column of radius R_p and constant line density $n_0 = N_i/L_T$, where L_T is the trap length. On the axis of the trap, the space charge potential $\Phi(N_i, R_p, L_T)$ is less than the external applied potential V_T and this condition assures the confinement of the plasma. If the confining potential is lowered by a suitable value ΔV , a small amount of particles leaves the trap on the axis, reducing the space charge potential until the confining condition is again satisfied. The number of escaping electrons N_e can be thought as the number of extracted particles necessary to leave an hollow cylinder charge distribution having, external radius R_p , internal radius $R_h = R_p(N_e/N_i)^{1/2}$, and a space charge potential on the trap axis $\Psi(N_i, N_e, R_p, L_T)$ equal to $V_T - \Delta V$. The measure of the total initial electrons number, and the detection of number of escaping particles as function of ΔV , combined with the analytic expression of $\Psi(N_i, N_e, R_p, L_T)$, permit to easily obtain the radius R_p and line density n_0 of the plasma.

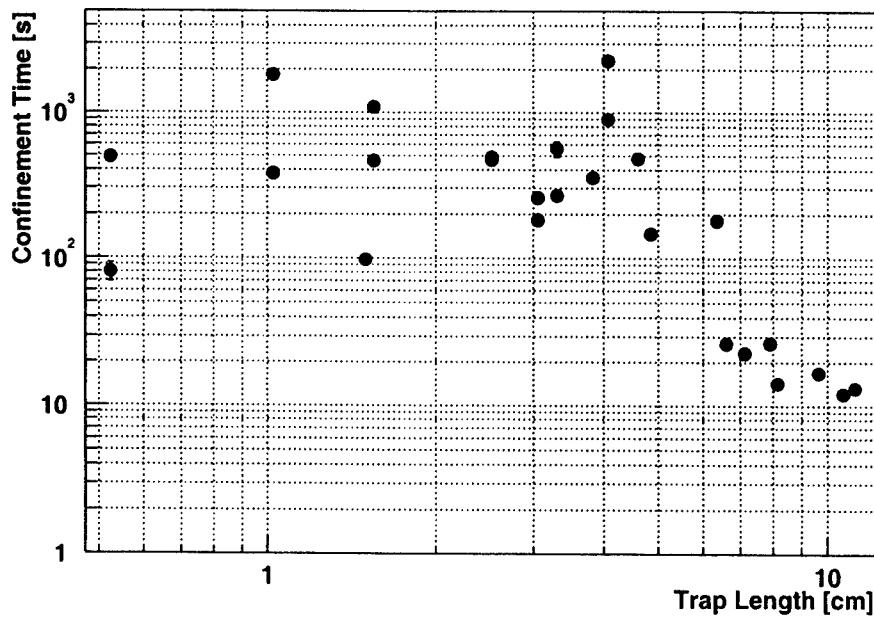


FIGURE 3. Dependence of confinement time on trap length. The confinement time is defined like the required time for one-half of the injected electrons to be lost.

The non-destructive diagnostic is based on the measure of the induced signals on electrodes due to electrons and/or antiprotons collective modes.

One of the collective modes monitored is the $m=1$ diocotron mode of the electron plasma. This diagnostic uses the sectors of the RING electrode. The wave is excited by applying a suitable pulse to two opposite sectors, the induced signals on the other two sectors gives the information on the frequency and the amplitude of the resulting mode. After the detection, the mode is damped by negative feedback [9]: the signal received on one wall sector is amplified, phase shifted and then applied to a second sector making the $m=1$ mode to damp.

When the confining electrostatic field is harmonic, it is possible to extract the total number of both the electrons and the antiprotons by detecting the center mass oscillation. In an harmonic trap, the particles motion along the axis is characterized by a fixed frequency ω_z , dependent on external applied fields. A center of mass oscillation can be excited by applying on one trap electrode a drive potential having frequency close to ω_z . The resulting collective oscillation is detected by a resonant circuit connected to another electrode. Two different resonant circuits, characterized by two different resonance frequencies (~ 14 MHz and ~ 1.4 MHz), are used for electrons and antiprotons. The amplitude of the induced voltage signal is proportional to the number of stored particles. An independent measure of the total number of particles is also given by the frequency shift between the collective mode and the single particle oscillation.

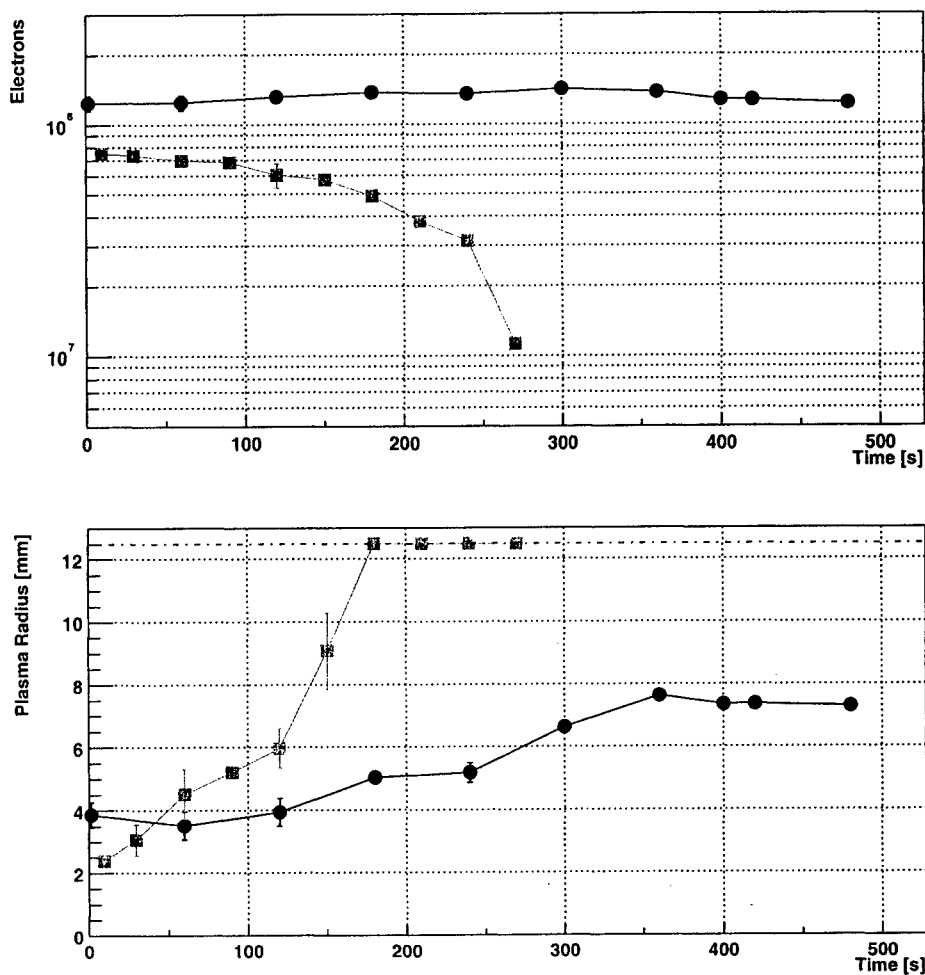


FIGURE 4. Time evolution of the total electron number and of the plasma radius for two different initial conditions.

ELECTRON PLASMA LOADING AND CONFINEMENT

The electrons are loaded in the trap using a small-size tungsten heated filament. The electron source is located about 2 m away from the antiproton trap in a low-magnetic field zone ($B \simeq 0.01$ T). To reach the antiproton trap the electron beam passes through several grounded cylindrical electrodes composing the nested-well multi-ring trap that will be used for the recombination studies [1, 2]. The typical source emitted current is about $200 \mu\text{A}$ while the electron current that reaches the aluminum foil is less than

20 μA . The loading procedure consists in preparing a potential well of variable depth (up to 50 V) and length and leaving the filament switched on for few seconds. Plasmas with different total number of electrons (up to 10^9) and radial extension (from few millimeter to the electrodes radius) can be loaded changing the intensity of the primary beam or the shape of the electrodes potentials (Figs. 2,3 and 4).

The plasma confinement time is short respect to the expected time due to the interaction with the residual gas (the typical working pressure is less than 10^{-12} mbar). As it has been observed in similar apparatus, the loss of the plasma is due to a radial expansion connected to system asymmetries. The measured dependence of the confinement time on the plasma length is shown in Figs. 2 and 3. The lifetime of the plasma does not follow a simple length scaling, different trap regions with similar lengths show very different containment times. Applying the method described in the previous section, it is also possible to follow the time evolution of the plasma radius (Fig. 4).

ACKNOWLEDGMENTS

The authors wish to thank all the ATHENA collaboration, in particular we thank Paul Bowe for his help and technical work on the apparatus. One of the author (M. Amoretti) also acknowledges the economical support of the Italian Ministry of University and Scientific Research (MURST "Young Researchers" Fund).

REFERENCES

1. ATHENA Collaboration (Holzscheiter, M. H., et al.), "Antihydrogen Production and Precision Experiments", *CERN SPSLC-96-47* (1996).
2. Holzscheiter, M. H., and Charlton, M., *Rep. Prog. Phys.*, **62**, 1 (1999).
3. Murphy, T. J., and Surko, C. M., *Phys. Rev A*, **46**, 5696 (1992).
4. Greaves, R. G., Tinkle, M. D., and Surko, C. M., *Phys. Plasmas*, **1**, 1439 (1994).
5. Jørgesen, L. V., et al., "Progress on the ATHENA Positron Accumulator", in these Proceedings.
6. Maury, S., *Hyperfine Int.*, **109**, 43 (1997).
7. Testera, G., et al., *Nucl. Inst. Meth. Phys. Research A*, **461**, 253 (2001).
8. Eggleston, D., et al., *Phys. Fluids B*, **4**, 3432 (1992).
9. White, W. D., and Malmberg, J. H., *Bull. APS*, **27**, 1031 (1982).

Cold Antimatter Plasmas, and Aspirations for Cold Antihydrogen

G. Gabrielse*, J.N. Tan*, N.S. Bowden*, P. Oxley*, C.H. Storry*, M. Wessels*, A. Speck*, J. Estrada*, P. Yesley*, T. Squires*, D. Grzonka†, W. Oelert†, G. Schepers†, T. Sefzick† and J. Walz**

*Dept. of Physics, Harvard University, Cambridge, MA 02138, USA

†IKP, Forschungszentrum Jülich GmbH, 52425 Jülich Germany

**CERN EP Division, 1211 Geneva 23, Switzerland

Abstract. Only our ATRAP Collaboration is yet able to accumulate and store 4.2 K antiprotons and positrons. The antiprotons come initially from the new Antiproton Decelerator facility at CERN. Good control of such cold antimatter plasmas is key to aspirations to produce and study antihydrogen atoms that are cold enough to confine by their magnetic moments. In the closest approach to cold antihydrogen realized to date, the cold positrons have been used to cool antiprotons, the first time that positron cooling has ever been observed. The Penning-Ioffe trap, one possibility for simultaneously confining antihydrogen and the cold ingredients from which it is formed, is introduced and discussed.

INTRODUCTION

Cold antiproton plasmas are required to make cold antihydrogen. A recent review [1] recounts the TRAP Collaboration's development and demonstration of slowing, trapping and electron-cooling antiprotons to thermal equilibrium at 4.2 K – an energy that is reduced by more than a factor of 10^{10} compared to the lowest energy antiprotons realized previously (Fig. 1). The slowed and cooled antiprotons reside within a small volume (of order mm^3) of an ion trap in a nearly perfect vacuum, better than 5×10^{-17} Torr. Their average kinetic energy is so low, less than 1 meV, that temperature units are often used. The energy “thermometer” of Fig. 1 represents the energy of antiprotons and protons in various giant storage rings at the top, with the lowest storage ring energies (for LEAR and the AD) near the middle. Towards the bottom, 10^{10} times lower in energy than has been realized in the lowest energy storage rings, is the new low energy frontier at only 4 degrees above absolute zero (4 K). Even lower antiproton temperatures should be possible as illustrated by the 70 mK temperatures some of us recently realized with trapped electrons [2].

In a series of three charge-to-mass ratio measurements, TRAP compared the cyclotron frequencies of an antiproton and a proton. Fig. 2 shows comparisons of the antiproton and proton as they improved in time, starting with the first observation of the antiproton. The final TRAP comparison, to 9 parts in 10^{11} , is the most accurate comparison of any baryon and antibaryon by almost a factor of

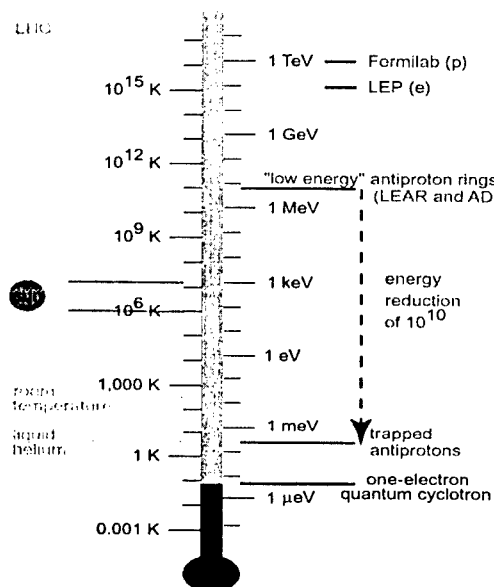


FIGURE 1. Particle energies

a million. An improved baryon CPT test (e.g. involving cold antihydrogen as we will discuss) should arguably improve upon this accuracy.

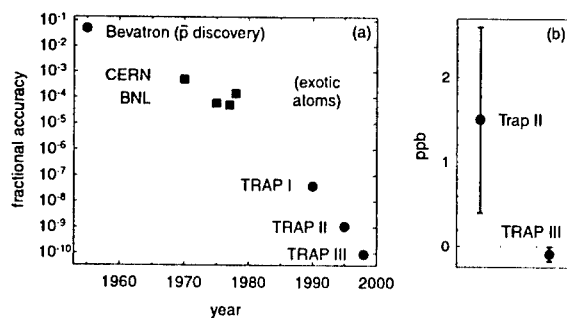


FIGURE 2. (a) Accuracy in comparisons of \bar{p} and p . (b) The measured difference between $|q/m|$ for \bar{p} and p (TRAP III) is improved more than ten-fold.

The TRAP techniques mentioned are being used by all three collaborations using CERN's new Antiproton Decelerator (AD). The AD delivers far fewer antiprotons per pulse of antiprotons sent to experiments than did its predecessor LEAR. However, the AD pulses come more often. Using the stacking techniques developed and demonstrated by TRAP, the experiments are left to accumulate as many antiprotons in a Penning trap as are desired. It is much less expensive to accumulate antiprotons in a small trap than in much larger storage rings.

QUEST FOR COLD ANTIHYDROGEN

Now TRAP has expanded to become ATRAP, and our goal is to produce and study cold antihydrogen atoms. As enunciated shortly after antiprotons were first trapped, the most attractive approach “would be to capture the antihydrogen in a neutral particle trap ... The objective would be to then study the properties of a small number of [antihydrogen] atoms confined in the neutral trap for a long time” [3]. As discussed in the next section, we believe that the laser spectroscopy of cold, trapped antihydrogen may yield even more precise tests of CPT invariance with baryons and leptons than have been realized so far.

The pursuit of cold antihydrogen thus began some time ago, long before others of us observed a few antihydrogen atoms traveling at nearly the speed of light [4], revealing great public interest in antimatter atoms. Unlike the extremely energetic antihydrogen, cold antihydrogen that can be confined in a magnetic trap for highly accurate laser spectroscopy offers the possibility of comparisons of antihydrogen and hydrogen at an important level of accuracy (Fig. 4). Interesting gravitational measurements can also be contemplated [5] since the antimatter atom is electrically neutral and hence somewhat insensitive to electric and magnetic forces.

Not only ATRAP is now pursuing cold antihydrogen. The competing ATHENA Collaboration has similar goals, and is using the techniques for accumulating cold antiprotons discussed above. The third collaboration working at the Antiproton Decelerator, ASACUSA, is not pursuing antihydrogen. However, they too have recently started to use the same techniques for trapping and cooling antiprotons.

SEEKING MORE STRINGENT CPT TESTS

Experimental tests have made physicists abandon earlier mistaken but widely held assumptions about fundamental symmetries – first, that reality is invariant under parity transformations (P) and then, that reality is invariant under CP transformations, where C stands for charge conjugation. The current assumption, that reality is invariant under CPT transformations with T indicating a time reversal operation, is based in large part upon the success of quantum field theories. These are invariant under CPT as long as reasonable assumptions (like causality, locality and Lorentz invariance) are made. Of course, this argument is not complete since gravity has not yet been fit into a quantum field theory. Theoretical investigations of possible CPT violations are thus now beginning to appear in the context of string theory [6, 7]. A theoretical model of possible Lorentz invariance violating extensions to the standard model [8] now allows quantitative comparisons of existing CPT tests and possible antihydrogen measurements.

Whether reality is invariant under CPT transformations is in the end an experimental question, and is one important motivation for experiments which compare either antiprotons and protons, or antihydrogen and hydrogen. A reasonable requirement for any new test is that it eventually be more stringent than existing tests with leptons and baryons (Table 1). Here the accuracy of the CPT test must

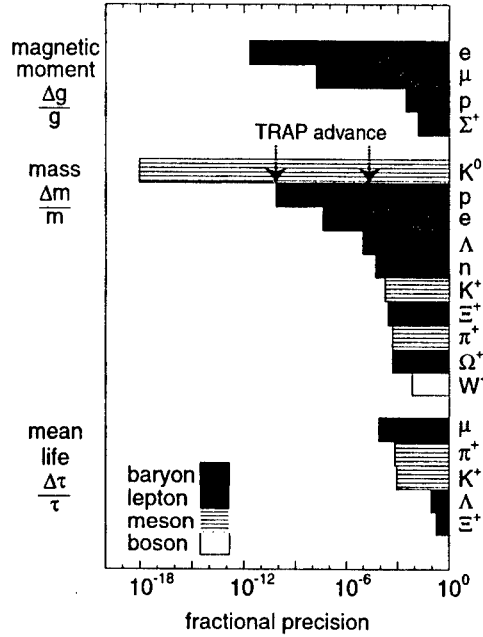


FIGURE 3. Tests of CPT Invariance (taken primarily from the Review of Particle Properties by the Particle Data Group). The particle-antiparticle pair is identified on the right. The shading indicates which species of particles (leptons, mesons or baryons) are involved in the test. The accuracy achieved in the comparison is indicated below. Charge-to-mass ratio comparisons are included in “mass” measurements.

be distinguished from the accuracy with which the relevant physical quantity must be measured since these can be very different. The most accurate baryon CPT test is the 9×10^{-11} (0.09 ppb) comparison of the charge-to-mass ratios of the antiproton and proton that some of us carried out [9] after developing the techniques to obtain 4 K antiprotons. For this measurement, as for the proposed antihydrogen/hydrogen comparison, the CPT test accuracy is the same as the measurement accuracy, requiring extremely accurate measurements.

Current CPT tests with leptons and mesons involve free enhancement factors that make the accuracy of the CPT test substantially greater than the corresponding accuracy needed in a measured quantity. The most accurate lepton CPT test is a 2×10^{-9} comparison of measured magnetic moment anomalies of electron and positron [10], interpreted as a comparison of magnetic moments at 2×10^{-12} . A meson CPT test is even more precise [11]. The delicately balanced nature of the unique kaon system makes it possible to interpret a measurement at an accuracy of only 2×10^{-3} as a comparison of the masses of the K_0 and \bar{K}_0 to an impressive 2×10^{-18} . (A recent theoretical speculation [6] suggests that quantum gravity could produce a CPT violation which is smaller by only a factor of 10.) The three most accurate tests of CPT invariance are represented in Table 1, and a summary of the

CPT tests listed by the Particle Data Group is in Fig. 3.

TABLE 1. Comparing the Accurate CPT Tests for the Three Species of Particles

	CPT Test Accuracy	Measurement Accuracy	Enhancement Factor
Mesons ($K_0\bar{K}_0$)	2×10^{-18}	2×10^{-3}	10^{15}
Leptons (e^+e^-)	2×10^{-12}	2×10^{-9}	10^3
Baryons ($p\bar{p}$)	9×10^{-11}	9×10^{-11}	1

In principle, the comparisons of antihydrogen and hydrogen could make possible a CPT test at the meson precision. We label this the “antihydrogen dream” in Fig. 4. The 1s-2s transition has an extremely narrow fractional linewidth of only 5×10^{-16} . With a measurement signal-to-noise ratio of 200, line splitting by this factor would allow a comparison at the kaon precision. There are serious obstacles to attaining this extremely high precision, including a 2.4 mK laser cooling limit, a second order Doppler shift, and possible Zeeman shifts depending on the configuration of the magnetic trap. Nonetheless, even a measurement at an accuracy of 10^{-13} , the level at which the difficulties mentioned seem manageable in the first traps [12], would give a substantially improved CPT test involving leptons and baryons.

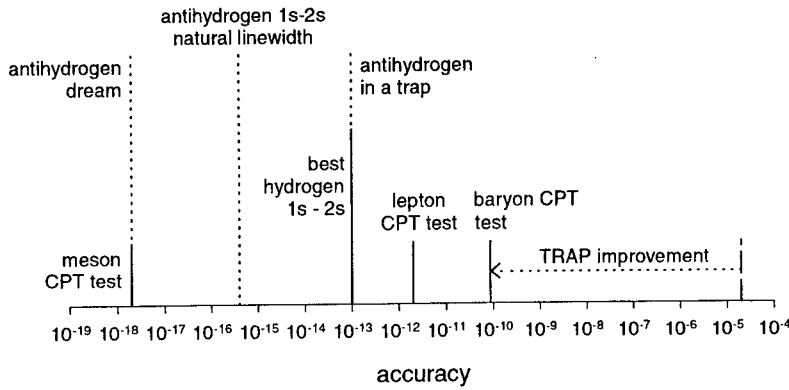


FIGURE 4. Accuracies for the precise 1s - 2s spectroscopy of antihydrogen are compared to the most stringent tests of CPT invariance carried out with mesons, leptons and baryons.

The most precise laser spectroscopy of hydrogen attained so far was obtained with a cold hydrogen beam by one group in our ATRAP collaboration [13]. The narrowest observed width is still much wider than the natural linewidth, but we expect that steady and substantial improvements in accuracy will continue as they have been for many years. If such a line were available for antihydrogen as well as hydrogen, the signal-to-noise ratio would be sufficient to allow the frequencies to be compared to at least 1 part in 10^{13} , a large increase in accuracy over the current tests involving baryons and leptons. The first use of cold trapped hydrogen

for 1s-2s spectroscopy [14], in an environment similar in many respects to that we hope to arrange for antihydrogen, already came close to this linewidth.

The ratio of the 1s-2s transition frequencies can be used to determine a ratio of Rydberg constants. It is instructive to express this ratio in terms of other fundamental constants (assuming the very long range Coulomb interaction to have the same form for \bar{H} and H),

$$\frac{R_{\infty}(\bar{H})}{R_{\infty}(H)} = \frac{m[e^+]}{m[e^-]} \left(\frac{q[e^+]}{q[e^-]} \right)^2 \left(\frac{q[\bar{p}]}{q[p]} \right)^2 \frac{1 + m[e^+]/M[\bar{p}]}{1 + m[e^-]/M[p]}.$$

The only ratios on the right that have been measured accurately are the electron-to-proton mass ratio and the ratio of the electron and proton charges. This CPT test comparison thus clearly involves fundamental lepton and baryon constants but in a combination which makes it difficult to simply interpret the comparison as a measurement of the electron-to-positron mass ratio, or any other such simple ratio. The comparison of 1s-2s transition frequencies measured for antihydrogen and hydrogen would be a test of CPT invariance that involves the charges and masses of leptons and baryons at an unprecedented precision. Fig. 4 illustrates the punch line. The accuracy scales for 1s - 2s spectroscopy of antihydrogen (mentioned above) are compared with the accuracies attained in existing CPT tests with leptons, mesons and baryons.

A second motivation for experiments which compare cold antihydrogen and hydrogen is the possibility to search for differences in the force of gravity upon antimatter and matter [15]. Making gravitational measurements with neutral antihydrogen atoms certainly seems much more feasible than using charged antiprotons, for which the much stronger Coulomb force masks the weak gravitational force. Members of the ATRAP Collaboration have considered the possibility of gravitational measurements with trapped antihydrogen [16], and routinely time the free fall of cold atoms released from a trap [17]. We are intrigued by the possibility of experimental comparisons of the force of gravity upon antihydrogen and hydrogen, and will pursue this direction when the techniques are sufficiently advanced to permit attaining an interesting level of precision.

ACCUMULATING COLD ANTIPROTONS

A 5.3 MeV pulse of antiprotons from the Antiproton Decelerator arrive at the ATRAP apparatus approximately once every two minutes. These are slowed in a thin beryllium window whose thickness has been chosen to slow as many of the antiprotons as possible to the lowest possible energy. Antiprotons which emerge with energies below 3 keV, in the original direction of antiproton propagation, are trapped by the sudden application of trapping potentials. Fig. 5 shows an example of the measured energy spectrum of 12,000 trapped antiprotons.

Electrons are preloaded into the trap before the antiprotons arrive. They rapidly cool via synchrotron radiation to the ambient temperature of the trap, 4.2 K. Trapped antiprotons oscillate back and forth through these cold electrons, with

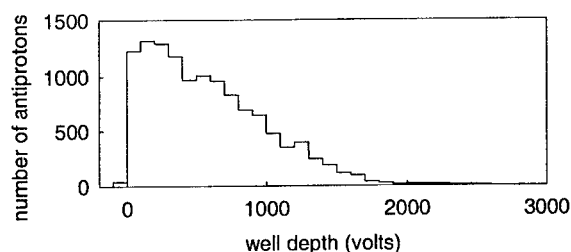


FIGURE 5. Energy of 12,000 of the first antiprotons trapped from a single pulse of AD antiprotons.

collisions cooling them down to 4.2 K. The antiprotons are cooled into the regions of the trap that contain the cooling electrons before another pulse of antiprotons arrives from the Antiproton Decelerator. The trap can be open in time for the next pulse of antiprotons to be trapped and cooled by the same electrons. Fig. 6 shows the measured energy spectrum of 106,000 antiprotons accumulated from successive pulses of antiprotons. Fig. 7 shows how the number cold antiprotons builds as a function of the number of pulses of antiprotons that are "stacked" into the trap.

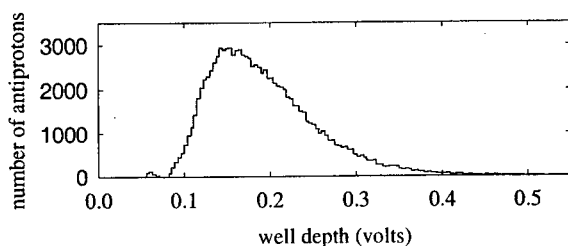


FIGURE 6. Energy of 106,000 of the first antiprotons electron-cooled and stacked at the AD.

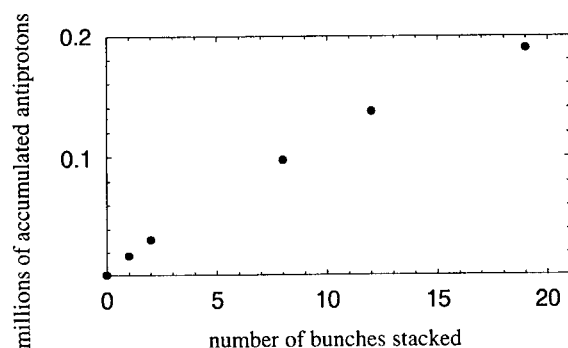


FIGURE 7. Stacking successive pulses of antiprotons.

ACCUMULATING COLD POSITRONS

Positrons accumulate in the upper trap region at the same time that antiprotons accumulate below. The new and efficient method for accumulating large numbers of 4.2 K positrons [18, 19] is the only one yet demonstrated. The positrons accumulate directly in a 6 Tesla field, and in the extremely good cryogenic vacuum.

The positrons originate in a 110 mCi ^{22}Na source that is lowered until it settles against the 4.2 K trap enclosure. They follow magnetic field lines and enter the trap vacuum through a thin Ti window. Some of them slow as they enter the trapping region through a 2 μm thick single crystal of tungsten. Others slow while turning around within a thick tungsten crystal that is rotated to the trap axis when the rotatable electrode is in its closed position.

Slow positrons emerging from the thin crystal pick up electrons while leaving the thin crystal form Rydberg positronium atoms. These atoms travel parallel to the axis of the trap until they are ionized by the electric field of the trap well, and captured. The frequency spacing of the two peaks in the electrical signal induced across an RLC circuit attached to the trap reveals the number of accumulated positrons. Fig. 8b shows approximately 2 million positrons accumulating in an hour [19], a 27-fold increased rate compared to the recent report [18] announcing the method.

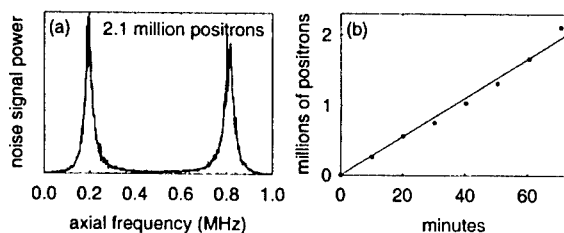


FIGURE 8. (a) Electrical signal from trapped positrons. (b) Positrons accumulate 27 times faster than reported in a recent introduction to the technique.

FIRST DEMONSTRATION OF POSITRON COOLING

The closest approach to cold antihydrogen so far is ATRAP's first demonstration of positron cooling [19]. Fig. 9 shows the trap electrodes that we used to simultaneously capture and confine antiprotons and positrons, and to make them interact. Surrounding scintillating fibers and plastic scintillators detect the annihilation signals from antiprotons released from the trap, and electrical circuits allow nondestructive detection of particles remaining within the trap.

The next step on the path to cold antihydrogen is to bring the cold ingredients together. Since the positrons and antiprotons have an opposite sign of charge, they cannot be confined in the same Penning trap well. Our "nested Penning trap", proposed for this purpose [20], was first tested with electrons and protons [21]. The motional energy of the trapped antiprotons is transferred to the lighter

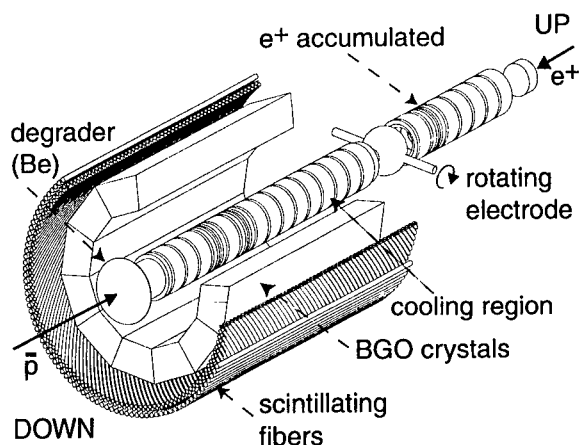


FIGURE 9. Outline of trap electrodes surrounded by annihilation detectors.

trapped particles by Coulomb collisions, and these lighter particles cool rapidly via synchrotron radiation. Fig. 10a-b contrast the energy spectra observed without and with positron cooling.

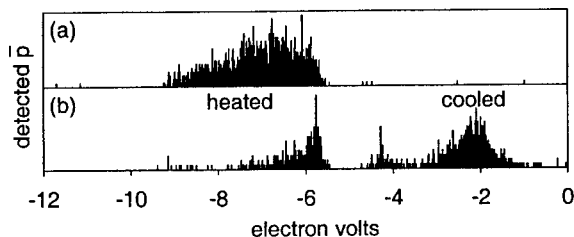


FIGURE 10. (a) Uncooled antiproton energy spectrum. (b) Energy spectra showing cooled antiprotons.

The cooled antiprotons have a low relative velocity with respect to the cold positrons that cooled them. A low relative velocity is one condition under which antihydrogen formation processes (e.g. radiative recombination and three body recombination) are expected to have their highest rates. These rates are nonetheless very small so that observing these processes will take much time and care. In addition, the electric fields of the trap will ionize any high Rydberg state produced by the latter process.

Much remains before cold antihydrogen is produced, stored and studied with precise laser spectroscopy. However, significant progress has been made. The cold ingredients are now readily available, and their interaction at low relative velocity has been clearly demonstrated.

PENNING-IOFFE TRAP

An intriguing question is whether it may be possible to trap cold antihydrogen atoms along with the charged antiprotons (\bar{p}) and positrons (e^+) from which they form. Fig. 11a shows a Penning-Ioffe trap configuration that has now been investigated theoretically [22] to see if a charged particle and a neutral atom could be confined at the same time. The Ioffe trap would confine the antihydrogen atoms, and the Penning trap would trap a charged ingredient. The stability of the trapped charge is crucial; the charged ingredients of antihydrogen must remain confined long enough for neutral atoms to form.

The simplest experimental realization (Fig. 11a) could direct the magnetic field of a solenoid (not pictured) along the axis of the stacked rings of an open-access Penning trap [23]. The Ioffe field would come from currents through vertical Ioffe bars and through "pinch coils" above and below. The latter can be away from the central region where charged particles are trapped, so only the leading term of the radial magnetic field from Ioffe bars are considered.

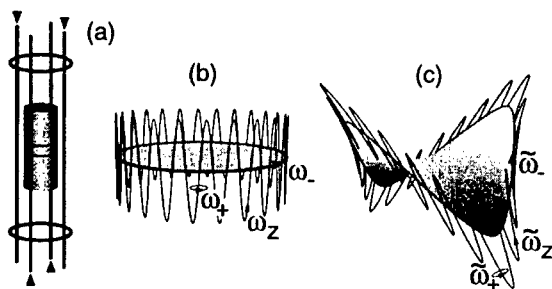


FIGURE 11. (a) Open access Penning trap electrodes, with vertical current bars and pinch coils of a Ioffe trap. Orbits for a charged particle in a Penning trap (b) without and (c) with a radial Ioffe field.

The theoretical analysis [22] of the Penning-Ioffe system, and the analysis of the motion of a charged particle within it, are simple and clean, yet nontrivial. Despite the breakdown of axial symmetry, and the loss of a confinement theorem [24], we find stable orbits (Fig. 11b) centered upon the intersection of an electrostatic potential and a force free sheet (Fig. 12a). The stable orbits are associated with adiabatic invariants, and occur within a central region of the trap (Fig. 12a). Expressions are given for their frequencies, and resonances that must be avoided are characterized. A guiding-center approximation [25], a perturbation expansion using the method of multiple time scales [26], and exact numerical calculations are compared and discussed.

Confining antiprotons and positrons in a nested version [21] of a Penning-Ioffe trap, along with cold antihydrogen atoms that are formed, now seems feasible for low particle densities. At a higher density, yet to be determined, collisions could break the adiabatic invariants, space charge could modify resonance frequencies, and collective plasma modes could be crucial. These effects may be more pronounced in a Malmberg-Ioffe trap [27] where oscillation frequencies are less well

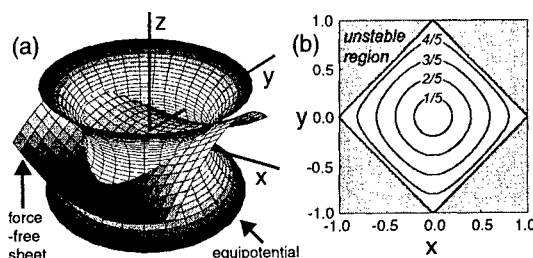


FIGURE 12. (a) The force-free sheet and an equipotential of the electrostatic quadrupole. (b) Projections of stable magnetron orbits upon the xy plane lie within a square.

defined. The relationship of density and stability for charged plasmas in a Penning-Ioffe trap remains to be investigated.

ACKNOWLEDGEMENTS

This work is supported by the NSF, AFOSR, the ONR of the US, and the German BMBF.

REFERENCES

1. G. Gabrielse, *Ad. in At., Mol. and Opt. Phys.* **45**, 1 (2000).
2. S. Peil and G. Gabrielse, *Phys. Rev. Lett.* **83**, 1287 (1999).
3. G. Gabrielse, in *Fundamental Symmetries*, edited by P. Bloch, P. Paulopoulos, and R. Klapisch (Plenum, New York, 1987), p. 59.
4. G. Baur, et al., *Phys. Lett. B* **368**, 251 (1996).
5. G. Gabrielse, *Hyper. Int.* **44**, 349 (1988).
6. J. Ellis, N. Mavroumatis, and D. Nanopoulos, *Phys. Lett.* **B293**, 142 (1992).
7. V. Kostelecky and R. Potting, *Phys. Rev. D* **51**, 3923 (1995).
8. D. Colladay and V. Kostelecky, *Phys. Rev. D* **55**, 6760 (1997).
9. G. Gabrielse, D. Phillips, W. Quint, H. Kalinowsky, G. Rouleau, and W. Jhe, *Phys. Rev. Lett.* **74**, 3544 (1995).
10. R.S. Van Dyck, Jr., P. Schwinberg, and H. Dehmelt, *Phys. Rev. Lett.* **59**, 26 (1987).
11. R. Carosi, et al., *Phys. Lett.* **B237**, 303 (1990).
12. C. Zimmerman and T. Hänsch, *Hyper. Int.* **76**, 47 (1993).
13. F. Schmidt-Kaler, C. Zimmermann, D. Leibfried, W. König, M. Weitz, and T. Hänsch, *Phys. Rev. A* **51**, 2789 (1995).
14. C. Cesar, D. Fried, T. Killian, A. Polcyn, J. Sandberg, I. Yu, T. Greytak, D. Kleppner, and J. Doyle, *Phys. Rev. Lett.* **77**, 255 (1996).
15. R. Hughes, *Hyper. Int.* **76**, 3 (1993).
16. G. Gabrielse, *Hyper. Int.* **44**, 349 (1988).
17. P. Lett, R. Watts, C. Westbrook, W. Phillips, P. Gould, and H. Metcalf, *Phys. Rev. Lett.* **61**, 169 (1988).
18. J. Estrada, T. Roach, J. Tan, P. Yesley, D. Hall, and G. Gabrielse, *Phys. Rev. Lett.* **84**, 859 (2000).
19. G. Gabrielse *et al.*, *Phys. Lett. B* **507**, 1 (2001).

-
20. G. Gabrielse, S. Rolston, L. Haarsma, and W. Kells, Phys. Lett. **A129**, 38 (1988).
 21. D. Hall and G. Gabrielse, Phys. Rev. Lett. **77**, 1962 (1996).
 22. T. Squires, P. Yesley, and G. Gabrielse, Phys. Rev. Lett. **86**, 5266 (2001).
 23. G. Gabrielse, L. Haarsma, and S. Rolston, Intl. J. of Mass Spec. and Ion Phys. **88**, 319 (1989), *ibid.* **93**, 121 (1989).
 24. T. O'Neil, Phys. Fluids **23**, 2216 (1980).
 25. B. Lehnert, *Dynamics of Charged Particles* (Wiley, New York, 1964).
 26. C. Bender and S. Orszag, *Advanced Mathematical Methods for Scientists and Engineers* (McGraw-Hill, New York, 1978), p. 544ff.
 27. E. Gibson and J. Fajans, in *Non-Neutral Plasma Physics III 498*, edited by J. Bollinger, R. Spencer, and R. Davidson (AIP Conference Proceedings, ADDRESS, 1999), p. 250.

A Laser-Cooled, High Density Positron Plasma[§]

B.M. Jelenković[†], A.S. Newbury^{*}, J.J. Bollinger, T.B. Mitchell[†] and
W.M. Itano

Time and Frequency Division, NIST, Boulder, CO 80305

Abstract. We present results on trapping and cooling of positrons in a Penning trap. Up to a few thousand positrons are trapped and sympathetically cooled through Coulomb collisions (sympathetic cooling) with laser-cooled ${}^9\text{Be}^+$ ions. By imaging the ${}^9\text{Be}^+$ laser-induced fluorescence, we observe centrifugal separation of the ${}^9\text{Be}^+$ ions and the positrons, with the positrons coalescing into a column along the trap axis. This indicates the positrons have the same rotation frequency and comparable density ($\sim 4 \times 10^9 \text{ cm}^{-3}$) as the ${}^9\text{Be}^+$ ions, and places an upper limit of approximately 5 K on the positron temperature of motion parallel to the magnetic field. The measured positron lifetime is > 8 days in our room temperature vacuum of 10^{-8} Pa.

[§] Contribution of NIST. Not subject to U.S. copyright.

I INTRODUCTION

This paper presents experimental results on the capture, storage and cooling of positrons in a Penning trap that simultaneously contains laser-cooled ${}^9\text{Be}^+$ ions. The experimental work follows previous discussions and simulations of trapping and sympathetic cooling of positrons via Coulomb collisions with cold ${}^9\text{Be}^+$ ions [1,2]. Similar and somewhat more detailed discussions are given in [3]. Cold positron plasmas are useful as a source for cold beams of high brightness [4,5]. In addition cold positron plasmas are useful for studies of positron-normal-matter interactions, such as the study of resonances in low-energy positron annihilation on molecules [4], for production of a plasma whose modes must be treated quantum mechanically [1,6], and for formation of antihydrogen by passing cold antiprotons through a reservoir of cold positrons [7,8].

Several groups have successfully trapped positrons in electromagnetic traps. Positrons have been trapped using resistive cooling of the positrons [9], by ramping the trap electrostatic potential [10], and in a magnetic-mirror configuration by electron cyclotron-resonance heating [11]. Recent experiments by Gabrielse and co-workers [8,12,13] have successfully trapped more than 10^6 positrons in a cryogenic trap in 1 hour through a method where positronium in a high Rydberg state created

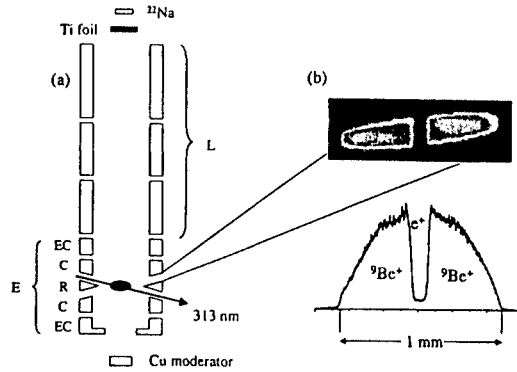


FIGURE 1. (a) Schematic diagram of the load and experimental cylindrical Penning traps; EC=end cap, C=compensation, R=ring of the experimental trap. (b) Two species ${}^9\text{Be}^+ - e^+$ plasma: camera image (top) and radial variation of fluorescence signal integrated over z (bottom).

on the surface of the moderator is field-ionized in the trap. Surko and co-workers [4,5,14–16], using a 90 mCi positron source, report the largest number of trapped positrons ($\sim 3 \times 10^8$) with a trapping rate of 3×10^8 positrons in 8 minutes and a trapping efficiency greater than 25 % of the moderated positrons. In these experiments trapping was achieved through collisions with a room-temperature buffer gas of N_2 . In this paper we discuss the results of simultaneously trapping and cooling positrons with laser-cooled ${}^9\text{Be}^+$ ions. We observe centrifugal separation of the positrons and ${}^9\text{Be}^+$ ions, which enables us to determine the positron density and place a rough upper bound on the positron temperature.

II EXPERIMENTAL SETUP

The Penning trap, along with the positron source and positron moderator are shown in Fig. 1(a). The stack of cylindrical electrodes (10 mm in diameter, 60 mm long) forms two Penning traps, in a 6 T magnetic field. The top, load (L) trap was used to create ${}^9\text{Be}^+$ ion plasmas by ionizing neutral ${}^9\text{Be}$ atoms sublimated from a heated ${}^9\text{Be}$ filament. The ${}^9\text{Be}^+$ ions are transferred to the lower, experimental (E) trap for experimentation. In a single load-transfer cycle we can store over one million ions. An axisymmetric, nearly quadratic trapping potential is generated by biasing the ring of the experimental trap to a negative voltage V_R and adjacent compensation electrodes to $V_C = 0.9 \times V_R$. For $V_R = -100$ V, and for the endcap voltage $V_{EC} = 0$ the single particle axial frequency for ${}^9\text{Be}^+$ ions is $\omega_z/2\pi = 870$ kHz, and the magnetron frequency is $\omega_m/2\pi = 35$ kHz.

The ions were cooled by a laser beam tuned ~ 10 MHz lower than a hyperfine-Zeeman component of the $2s^2S_{1/2} \rightarrow 2p^2P_{3/2}$ resonance in ${}^9\text{Be}^+$ at 313 nm [17]. The laser beam was directed through the trap, intersecting the ion plasma on

the side receding from the laser beam due to the plasma rotation. As shown in Fig. 1(a) the beam entered the trap between the upper compensation and ring electrodes, passed through the trap center, and exited through the gap between the ring and lower compensation electrode, making an 11° angle with the horizontal (x-y) plane. Based on measurements performed in previous experiments [17–19] we expect $T_\perp \leq T_\parallel \leq 100$ mK, where T_\perp and T_\parallel describe the velocity distributions in the direction perpendicular and parallel to the trap axis (z axis).

An ion plasma in thermal equilibrium at these cryogenic temperatures is a uniform-density plasma with a rigid-body rotation frequency ω_r in the range $\omega_m < \omega_r < \Omega - \omega_m$, where $\Omega = 10.2$ MHz is the ion cyclotron frequency. We used a rotating electric field perturbation to control ω_r [20]. The ion density is constant within the plasma and is given by $n_0 = 2\epsilon_0 m \omega_r (\Omega - \omega_r) / q^2$, where q and m are the charge and mass of an ion, and ϵ_0 is the permittivity of the vacuum. Since the trapping potential is quadratic near the trap center, the plasma has the shape of a spheroid whose aspect ratio, $\alpha = z_0/r_0$, depends on ω_r . Here $2z_0$ and $2r_0$ are the axial and radial extents of the plasma spheroid. Low rotation ($\omega_r \sim \omega_m$) results in an oblate spheroid of large radius. Increasing ω_r increases the Lorentz force due to the plasma rotation through the magnetic field, which in turn increases α and n_0 . At $\omega_r = \Omega/2$ (Brillouin limit) the ion plasma attains its maximum aspect ratio and density. For ${}^9\text{Be}^+$ ions at 6 T the maximum ion density is $1.1 \times 10^{10} \text{ cm}^{-3}$. Side-view images of the ${}^9\text{Be}^+$ plasma spheroid were produced by an f/5 imaging system that sends 313 nm photons scattered in a direction 11° above the $z = 0$ plane of the trap onto the photocathode of a photon-counting imaging detector.

The source for the positrons is a 2 mCi ${}^{22}\text{Na}$ source with an active diameter of ~ 1 mm. The source is placed just above the vacuum envelope, and positrons enter the trap through a Ti foil of $7\mu\text{m}$ thickness. Positrons travel along the axis of the Penning traps until they hit the moderator crystal placed below the lower end-cap of the experimental Penning trap. The positron current reaching the crystal was measured by an electrometer. At the beginning of our experiment the measured current was ~ 2 pA. For the method of trapping positrons discussed in [2], a room-temperature kinetic-energy distribution of moderated positrons is important. Room-temperature distributions of moderated positrons have been reported in the literature for a number of single-crystal metallic moderators. We chose a Cu(111) moderator crystal because of the expected narrow distribution of positrons [21,22], and because it can be annealed at a lower temperature ($\sim 900^\circ\text{C}$). However, for the experimental results discussed here the moderator crystal was heated only to 350°C during the vacuum bakeout.

III POSITRON DETECTION

In the experiment, the presence of trapped positrons was verified by three different methods. The positrons were detected by our (a) observing changes in the ${}^9\text{Be}^+$ ion fluorescence due to application of microwaves near the positron cyclotron

frequency, (b) detecting the absence of ${}^9\text{Be}^+$ ions in the plasma center in side-view images of the ${}^9\text{Be}^+$ ion fluorescence, and (c) detecting the annihilation radiation after pulsing the accumulated positrons onto the titanium foil above the trap.

The first evidence of positron accumulation was obtained through microwave excitation of the positron cyclotron resonance near 166 GHz. Waveguides carried the microwave radiation into the magnet bore close to the trap center. The microwaves heated the positrons by increasing their cyclotron energy. Through Coulomb interactions the positrons then increased the ${}^9\text{Be}^+$ ion energy which changed the level of the ${}^9\text{Be}^+$ ion fluorescence. The positron cyclotron resonance curve, obtained by sweeping the microwave radiation around 166 GHz, was ~ 200 kHz wide [3]. We believe this resonance width was probably caused by power broadening. Significant positron excitation was required [3] to observe the resonance because of the weak coupling between the positron cyclotron and the ${}^9\text{Be}^+$ ion motions and the low rate of energy transfer between the positron cyclotron and axial energies in the high magnetic field of our trap [23].

Due to the plasma rotation, ion species with different charge-to-mass ratios tend to centrifugally separate in a Penning trap [24,25]. With positrons and ${}^9\text{Be}^+$ ions, the positrons drift radially inward and the heavier ions outward until both species come to thermal equilibrium and rotate at the same ω_r as a rigid body [25]. In the limit of zero temperature, the edges of each plasma will be sharp (Debye length $\rightarrow 0$), and the plasmas will completely separate, with the positrons forming a column of uniform density along the trap axis. If the ${}^9\text{Be}^+$ plasma density is significantly below the Brillouin limit, the e^+ and ${}^9\text{Be}^+$ densities are approximately equal and the plasma separation is quite small [25].

Figure 1(b) shows an image of a ${}^9\text{Be}^+ - e^+$ plasma along with the radial dependence of the fluorescence signal. The ${}^9\text{Be}^+$ ion density n_0 is calculated from the rotation frequency ω_r set by the rotating wall. With approximately equal density for both species, the number of positrons in the "dark" column of the plasma image is $n_0 \times V$, where V is the volume of the "dark" region.

If any ions with a mass-to-charge ratio less than ${}^9\text{Be}^+$ are created during the positron accumulation, they will also centrifugally separate and contribute to the size of the non-fluorescing column in the plasma center. With the ${}^{22}\text{Na}$ source blocked, we deliberately created singly charged light-mass ions by ionizing background gas with a ~ 15 eV electron beam. From the volume of the central dark region as a function of time, the lifetime of the light-mass ions was measured to be less than 10 hours. Similar measurements were performed after accumulating positrons and are discussed in more detail in the next section. In this case very little change in the volume of the central dark region was observed after the ${}^{22}\text{Na}$ source was blocked for 12 hours. This indicates that most of the dark central region in Fig. 1(b) is due to positrons rather than impurity ions of light mass.

To further verify that the dark central column in Fig. 1(b) is due to accumulated positrons, we pulsed the $e^+ - {}^9\text{Be}^+$ plasma onto the $7\text{ }\mu\text{m}$ Ti foil located above the trap and detected the resulting positron annihilation radiation. The positron annihilation radiation was detected with a NaI scintillation crystal mounted 2.5 or

5 cm above the Ti foil. A light pipe coupled the output of the NaI crystal to a photomultiplier tube mounted a few feet above the magnet. The ^{22}Na source is removed from the magnet bore during this procedure.

We attempted to eject all the positrons rapidly compared to the rise time of the NaI crystal scintillation (~ 300 ns). In this way the scintillation crystal will produce a single pulse, free from background radiation, whose height is proportional to the number of annihilated positrons. The resulting annihilation pulse was recorded on a digital oscilloscope. For a fixed procedure for positron ejection the voltage peak of the output pulse was proportional to the amount of light-mass charge measured from side-view images such as Fig. 1(b). However, changing the ejection procedure by pulsing the positrons with different voltages, or by moving the positrons to the load trap for ejection, produced, in many cases, a different proportionality constant. For some conditions the output annihilation pulse was significantly longer than the scintillator single-event pulse and delayed beyond the scintillator and high-voltage pulse rise-times. This indicated that for these conditions not all the positrons were dumped simultaneously. We believe the reason for this is pick-up and ringing induced by the high-voltage pulse on different trap electrodes. Therefore, to estimate the number of trapped positrons, only annihilation procedures that produced single-event pulses were used.

The NaI crystal detection system was calibrated with a ~ 37 kBq ($1 \mu\text{C}$) ^{68}Ge source. Overall we estimate the uncertainty in determining the number of annihilated positrons from the peak of the annihilation pulse to be $\sim 25\%$. Figure 2 summarizes the results of positron annihilations done with several different experimental procedures. Systematic variation between the different procedures is

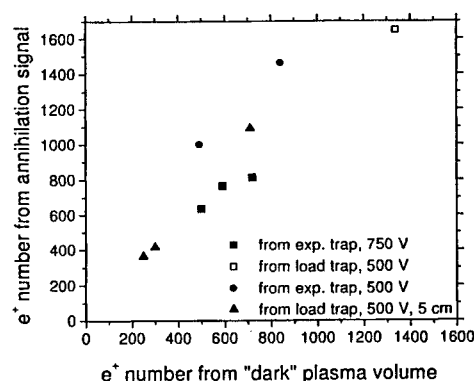


FIGURE 2. Comparison of the number of trapped positrons obtained from the calibrated annihilation signal with the number obtained from the volume of the "dark" plasma column. Measurements were taken with the positrons ejected from different traps, with different voltage pulse heights (500 - 750 V), and with the NaI crystal located 2.5 cm (squares and circles) and 5 cm (triangles) from the Ti foil.

observed. While we do not understand this variation, the positron number determined by the annihilation method should provide a lower limit for the number of trapped positrons. In all cases the positron number measured by annihilation is greater than the number calculated from the volume of the “dark” column. However, the $\sim 40\%$ difference is on the order of the combined uncertainty of these two positron measurement methods. Therefore we cannot determine with any certainty whether the number of trapped positrons is greater than indicated by the volume of the “dark” column. However the annihilation measurements do support our claim that most of the light-mass charges in images such as Fig. 1(b) are positrons that have centrifugally separated from the Be^+ ions.

Centrifugal separation implies that the positrons are rotating with the same rotation frequency as the Be^+ ions and are cold enough to have approximately the same density. We observed centrifugal separation of the positrons with rotation frequencies up to 1 MHz. For larger rotation frequencies, the radius of the positron column was too small to clearly see separation. In the 6 T magnetic field of this experiment $\omega_r \approx 2\pi \times 1$ MHz gives positron densities $\sim 4 \times 10^9 \text{ cm}^{-3}$. This is ~ 50 times greater than the highest positron density previously achieved [16].

IV POSITRON ACCUMULATION AND LIFETIME

Because of method’s simplicity, we initially attempted to load positrons by following, as much as possible, the method described in Ref. [13] of field ionizing high-Rydberg positronium. The basic idea is that in high magnetic field a fraction of the moderated positrons that leave the moderator crystal combine with an electron to form positronium in a very high Rydberg state at the moderator crystal’s surface. After leaving the crystal, the positronium travels into the trap as long as the electric fields between the moderator and trap are not large enough to field-ionize the Rydberg state. The trap potentials are adjusted to give a larger electric field inside the trap capable of field-ionizing the positronium and therefore capturing the positron.

By mimicking this method we were able to accumulate a few thousand positrons. However, our accumulation rate is approximately 3 orders of magnitude lower than that obtained in [13] and limited the total number of positrons loaded into the trap. While both experiments are performed in a high magnetic field (5.3 T in [13] and 6 T in our setup), there were substantial differences in the two setups. In particular, reference [13] used tungsten moderator crystals at cryogenic (4 K) temperatures, compared with the room-temperature Cu moderator used here. They observed that their accumulation rate depended sensitively on the gas adsorbed on the surface of the moderator crystal. Heating the moderator while the rest of the trap is at 4.2 K significantly reduced the accumulation rate. Our Cu moderator crystal was baked with the rest of the trap at 350 °C for about 2 weeks, which may have desorbed much of the adsorbed gases. We also plan to accumulate positrons by the method outlined in Ref. [2], where positrons are loaded through Coulomb collisions with

trapped ${}^9\text{Be}^+$ ions. Results of this method will be discussed in a future publication.

Figure 3 shows the measured lifetime of the positrons, ${}^9\text{Be}^+$ ions, and light mass impurity ions. The ${}^9\text{Be}^+$ ion and positron lifetimes were measured simultaneously on the same plasma by first accumulating positrons and then blocking the ${}^{22}\text{Na}$ source and measuring the number of ${}^9\text{Be}^+$ ions and positrons that remained after each day for a week. The trap voltage during the lifetime measurement was -40 V. When the ion and positron numbers were not being measured, the laser cooling and rotating electric field perturbation were turned off. The measured lifetime of the positrons was 8 days and is nearly identical to the measured ${}^9\text{Be}^+$ lifetime. This

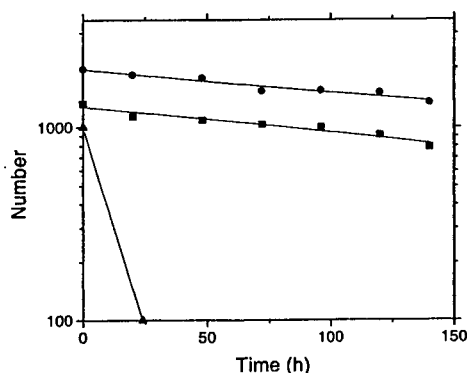


FIGURE 3. Life-time of positrons (solid circles), ${}^9\text{Be}^+$ ions (solid boxes, number shown = actual number \div 100) and light impurity ions (triangles)

indicates that the measured positron lifetime could be limited by the trapping lifetime of charged particles in our trap, rather than by annihilation with background gas. We measure the background pressure in our trap to be between 10^{-9} and 10^{-8} Pa. The trap was baked at 350°C for about 2 weeks and was pumped by a sputter-ion pump and a titanium sublimation pump. For comparison we also show the measured lifetime of light-mass impurity ions. These ions such as H_2^+ , H_3^+ or He^+ disappear relatively quickly due to reactions with background gas molecules.

V POSITRON TEMPERATURE ESTIMATE

Centrifugal separation of two-species ion plasmas has been observed and studied in ${}^9\text{Be}^+-\text{Hg}^+$ [24], ${}^9\text{Be}^+-{}^{26}\text{Mg}^+$ [26], ${}^9\text{Be}^+-\text{Cd}^+$ [27], and ${}^9\text{Be}^+-{}^{136}\text{Xe}^{q+}$ ($32 \leq q \leq 44$) [28] plasmas. In these experiments, laser-cooling of one ion species resulted in temperatures of less than ~ 1 K for the other ion species. However, the energy transfer in a $e^+-{}^9\text{Be}^+$ collision is ~ 1000 times weaker than in these previous sympathetic cooling studies. Because we could not find a more direct method, we used the centrifugal separation of the ${}^9\text{Be}^+$ ions and positrons to place an upper limit of about 5 K on the positron temperature of motion parallel to the magnetic field.

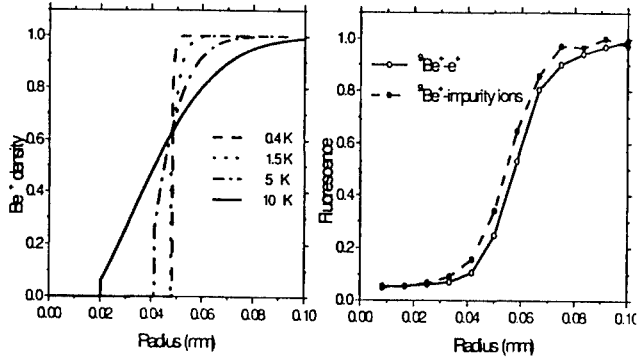


FIGURE 4. (a) Calculated radial variation of the ${}^9\text{Be}^+$ ion density for different positron temperatures, and (b) Measured radial dependence of the fluorescence of scattered laser light for ${}^9\text{Be}^+$ - impurity ion and for ${}^9\text{Be}^+-\text{e}^+$ plasmas.

In the 6 T magnetic field of the trap, the positron cyclotron motion is coupled to the room temperature walls (electrodes) of the trap with a ~ 100 ms time constant. In addition the positron cyclotron motion is collisionally coupled to the positron axial motion, but this coupling becomes exponentially weak when the Larmor radius is less than the distance of closest approach (the strongly magnetized regime). For a 10^9 cm^{-3} positron plasma this energy transfer rate is ~ 10 Hz for $T \sim 10$ K [23]. Therefore we anticipate T_{\perp} to be ~ 10 K and greater than T_{\parallel} , which is cooled by Coulomb collisions with the laser-cooled ${}^9\text{Be}^+$ ions.

Centrifugal separation has been discussed theoretically by O'Neil [25]. In this case the different charged species were assumed to have the same temperature as required in a global thermal equilibrium state. However, because of the weak thermal coupling between the positrons and ${}^9\text{Be}^+$ ions, the positrons could have a greater temperature than the ${}^9\text{Be}^+$ ions. In order to estimate the effect of the positron temperature on the centrifugal separation we calculated the positron and ${}^9\text{Be}^+$ radial density profiles for an infinitely long column assuming rigid rotation of the plasma but different temperatures. The ${}^9\text{Be}^+$ ions were assumed to be cold ($T_{\text{Be}^+}=0$) and the positron temperature non-zero ($T_{\text{e}^+} > 0$). Figure 4(a) shows the results of these calculations for conditions similar to some of the experimental measurements ($\omega_r = 2\pi \times 500$ kHz, positrons/length = $1.5 \times 10^5 \text{ cm}^{-1}$). For a given positron temperature, the ${}^9\text{Be}^+$ density makes a sharp jump to a non-zero density at a particular radius. This jump is then followed by a gradual increase at larger radii. As the positron temperature increases, the sharp jump becomes smaller and the subsequent increase in the ${}^9\text{Be}^+$ density more gradual.

We compare these calculations with the experimental profiles of the radial variation of fluorescence, or the ${}^9\text{Be}^+-\text{e}^+$ ion density (Fig. 4(b)). In the experimental measurements the plasmas had an axial extent that is typically smaller than the overall plasma diameter (see Fig. 1b)). However, the calculations, which are for an infinitely long column, should describe the separation of the species as long as the

diameter of the dark region in the $^9\text{Be}^+$ fluorescence is smaller than the axial extent of the plasma. We typically worked in this regime. Comparison of the profiles in Figs. 4(a) and (b) shows a measured separation that is significantly sharper than that calculated at 10 K and reasonably consistent with the 5 K separation. Also shown in Fig 4(b) is the measured separation between $^9\text{Be}^+$ ions and light mass ions for the same inner column size. From previous studies of sympathetic cooling [24,26–28] we expect the temperature of both species to be less than 1 K. However, because the sharpness of the separation is much worse than calculated for $T = 1$ K, we believe the profile measurements in Fig. 4(b) are limited by the resolution of the imaging-system optics.

We emphasize that this temperature limit is only for positron motion parallel to the magnetic field. This is because for a strongly magnetized plasma the perpendicular kinetic energy is constrained by a many-particle adiabatic invariant [23]. This modifies the particle distribution function (which is what we measure in Fig. 4(b)) with the result that the Debye length is determined by T_{\parallel} , not T_{\perp} [29].

VI DISCUSSION AND ACKNOWLEDGMENTS

The low accumulation rate limited to a few thousand the number of positrons that could be accumulated. This number needs to be significantly increased for most of the potential applications of cold positrons, such as a source for cold beams. This could be done by combining the sympathetic cooling technique with an established technique for accumulating positrons [12–16]. It is interesting to speculate about the maximum number of positrons that can be sympathetically cooled. A potential limit is the number of ions that can be directly laser-cooled. We can routinely load and laser-cool $\sim 10^6$ $^9\text{Be}^+$ ions to temperatures ≤ 10 mK. This ion number is limited by our loading technique rather than by the capabilities of laser-cooling. With a different loading technique non-neutral plasmas of $\sim 10^9$ Mg^+ ions have been laser-cooled to ~ 1 K temperatures [30]. Therefore $\sim 10^9$ positrons, comparable to the current largest number of trapped positrons, could possibly be sympathetically laser-cooled in a Penning trap. This would provide a useful, very cold source of positrons in a room-temperature vacuum system.

Support for this research was provided by the Office of Naval Research. The authors thank Brian Zimmerman and Bert Coursey at the NIST Ionizing Radiation Division for calibrating the activity of the ^{68}Ge source, and Robert Ristinen and Jeffrey Brack for discussion on detecting positron annihilation γ -rays. We thank David Wineland and Tom O’Neil for suggestions through out the experiment and for comments on the manuscript.

REFERENCES

- [†] Also at Institute of Physics, University of Belgrade, Yugoslavia.
- ^{*} Present address: Ball Aerospace, Boulder, CO 80301.

[†] Present address: Dept. of Physics and Astronomy, Univ. of Delaware, Newark, DE 19716.

1. D. Wineland, C. Weimer, and J. Bollinger, *Hyperfine Interac.* **76**, 115 (1993).
2. A. Newbury, B. M. Jelenković, J. Bollinger, and D. Wineland, *Phys. Rev. A* **62**, 023405 (2000).
3. B. Jelenković *et al.*, in *New Directions in Antimatter Chemistry and Physics*, edited by C. M. Surko and F. Gianturco (Kluwer Academic Publishers, Dordrecht, The Netherlands, 2001), in press.
4. R. G. Greaves and C. M. Surko, *Phys. Plasmas* **4**, 1528 (1997).
5. S. Gilbert, C. Kurtz, R. Greaves, and C. Surko, *Appl. Phys. Lett.* **70**, 1944 (1997).
6. J. Malmberg and T. O'Neil, *Phys. Rev. Lett.* **39**, 1333 (1977).
7. M. Glinsky and T. O'Neil, *Phys. Fluids* **B3**, 1279 (1991).
8. G. Gabrielse and the ATRAP Collaboration, *Phys. Lett. B* **507**, 1 (2001).
9. P. Schwinberg, R. V. Dyck, and H. Dehmelt, *Phys. Lett.* **81**, 119 (1981).
10. R. Conti, B. Ghaffari, and T. Steiger, *Nucl. Instr. Meth. Phys. Res. A* **299**, 420 (1990).
11. H. Boehmer, M. Adams, and N. Rynn, *Phys. Plasmas* **2**, 4369 (1995).
12. L. Haarsma, K. Abdullah, and G. Gabrielse, *Phys. Rev. Lett.* **75**, 806 (1995).
13. J. Estrada *et al.*, *Phys. Rev. Lett.* **84**, 859 (2000).
14. T. Murphy and C. Surko, *Phys. Rev. A* **46**, 5696 (1992).
15. C. Surko, S. Gilbert, and R. Greaves, in *Non-neutral Plasma Physics III*, edited by J. Bollinger, R. Spencer, and R. Davidson (AIP, New York, 1999), p. 3.
16. R. Greaves and C. Surko, *Phys. Rev. Lett.* **85**, 1883 (2000).
17. W. Itano, L. Brewer, D. Larson, and D. Wineland, *Phys. Rev. A* **38**, 5698 (1988).
18. J. Bollinger and D. Wineland, *Phys. Rev. Lett.* **53**, 348 (1984).
19. L. Brewer *et al.*, *Phys. Rev. A* **38**, 859 (1988).
20. X.-P. Huang, J. Bollinger, T. Mitchel, and W. M. Itano, *Phys. Rev. Lett.* **80**, 73 (1998).
21. C. Murray and A. M. Jr, *Solid State Commun.* **34**, 789 (1980).
22. R. Wilson, *Phys. Rev. B* **27**, 6974 (1983).
23. M. E. Glinsky, T. M. O'Neil, and M. N. Rosenbluth, *Phys. Fluids B* **4**, 1156 (1992).
24. J. Larson, J. Bergquist, W. Itano, and D. Wineland, *Phys. Rev. Lett.* **57**, 70 (1986).
25. T. O'Neil, *Phys. Fluids* **24**, 1447 (1981).
26. J. Bollinger *et al.*, *IEEE Trans. Instr. Measurement* **40**, 126 (1991).
27. H. Imajo *et al.*, *Phys. Rev. A* **55**, 1276 (1997).
28. L. Gruber *et al.*, *Phys. Rev. Lett.* **86**, 636 (2001).
29. D. H. Dubin and T. O'Neil, *Phys. Rev. Lett.* **60**, 511 (1988).
30. E. Hollmann, F. Anderegg, and C. Driscoll, *Phys. Rev. Lett.* **82**, 4839 (1999).

Two-Stream Instabilities in Guiding-Center Plasmas for Antihydrogen Recombination Schemes¹

Ronald Stowell and Ronald C. Davidson

Plasma Physics Laboratory, Princeton University, Princeton, NJ 08543

Abstract. Two-stream instabilities are studied analytically in the guiding-center kinetic regime, which is chosen in order that the results may be applied to the mixing of antiprotons and positrons preceding antihydrogen recombination. The guiding-center kinetic description is valid for a range of parameters which includes cases in which magnetic fields are 3–5 T; temperatures are 4–10 K; positron densities are $10^7 - 10^8 \text{ cm}^{-3}$; and antiproton densities are $10^4 - 2 \times 10^7 \text{ cm}^{-3}$. The species occupy long, cylindrical columns coaxial with an outer, conducting, cylindrical wall. Plasma column radii are between 0.05 and 0.3 wall radii. A constant, axial, externally generated magnetic field permeates the system. Linear stability of the plasma is studied as a function of the species' temperatures, densities and column radii; the mean antiproton velocity; and wavenumber. Drifting Maxwellian distribution functions are considered.

INTRODUCTION

For fifteen years, cold, stationary antihydrogen has been sought [1, 2] for use in fundamental experiments, including tests of the equivalence principle of general relativity [1] and the CPT symmetry of the standard model [3]. The protracted nature of this effort is the result of technical challenges, such as deceleration and cooling of the constituent species [4, 5] and, nonetheless, exceedingly slow recombination rates [6]. Only recently have cold antiprotons and positrons been allowed to interact, though no attempt has been made yet to detect recombined antihydrogen [7].

As the experimentalists successfully accumulate antimatter, collective descriptions of the interacting species will become more useful. Accordingly, plasma phenomena with which we are familiar in other contexts may appear. In particular, two-stream instabilities, manifest as the electron-proton (e-p) instability in proton storage rings [8], could occur in antihydrogen traps when the constituent species are mixed. There is free energy to drive this instability because the system is not in thermal equilibrium during mixing. The following describes preliminary research toward assessing the possibility of two-stream instabilities in cold antimatter plasmas and finding the regimes of stable operation of the traps.

¹ Research supported by the United States Department of Energy, and in part by the Office of Naval Research.

Currently there are two distinct collaborations seeking to synthesize cold antihydrogen at rest in the laboratory frame. Each group has its own scheme for inducing recombination. The ATHENA collaboration is considering a method described as follows. Antiprotons are sent into a cloud of positrons where the antiprotons are cooled by collisions with the positrons [9]. Escaping antiprotons would be caught electrostatically and sent back into the positron cloud. The ATRAP collaboration releases bunches of cold antiprotons from an electrostatic well into a positron cloud [7]. As long as ATHENA's antiproton densities are extremely low, a plasma description is not appropriate. However, this will change as ATHENA will ultimately seek to increase production of antihydrogen. A plasma model is already useful for ATRAP's parameters.

GENERAL THEORETICAL MODEL

It may be worrisome that the coupling parameter $\Gamma = [e^2/(4\pi n/3)^{-1/3}]/k_B T$ is only one or two orders of magnitude smaller than unity. Even a modest improvement in densities or temperatures will force the system into the regime of a Wigner liquid. However, for the parameters presently envisioned, a plasma description of the antimatter is valid.

The geometry considered is shown in Fig. 1. Two cylindrical, coaxial plasma columns of equal radius, composed of positrons and antiprotons, are coaxial with an outer, cylindrical, conducting wall. The antiprotons move through the cloud of positrons which are stationary on average. Some important approximations which are made to solve the problem mathematically are as follows. Bunches, or clouds, of particles of finite extent are treated as having infinite length. This is a valid approximation if we study the system on a scale much smaller than the bunch length. For the present purposes, the bunches are also treated as having the same radius, uniform density and Maxwellian unperturbed distribution functions f_{s0} . Our attention is restricted to azimuthally symmetric perturbed distribution functions f_{s1} . The externally generated part ϕ^{ext} of the electrostatic potential ϕ is assumed to be constant in space and time. Collisions are not included in the analysis.

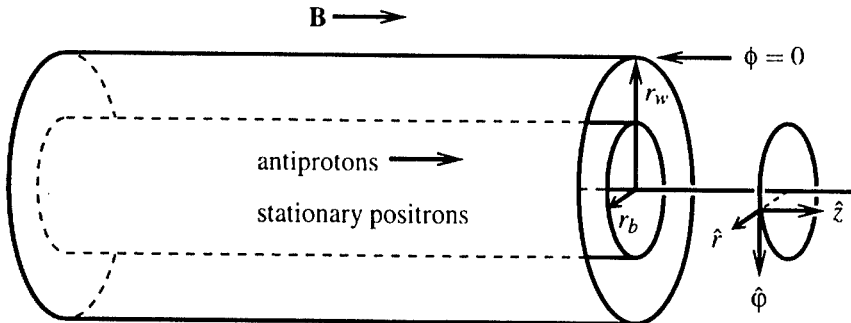


FIGURE 1. Geometry Considered.

From the values of the antihydrogen trap parameters in Nonneutral Plasma Physics

III² [10, 11, 12, 13], it can be seen that, for relevant temporal and spatial scales, the antimatter plasmas fall within the gyrokinetic regime, which is, by definition, the regime in which $\omega/\omega_{c\bar{p}}$, $(e\phi/T_{e+})(k_{\perp}\rho_{L\bar{p}})^2$, k_{\parallel}/k_{\perp} and ρ_{Ls}/L_{\perp} are small quantities [14, 15, 16]. Here ω is any frequency considered, ω_{cs} is the cyclotron frequency for species s , ϕ is the electrostatic potential, T_s is the temperature of species s , \mathbf{k} is any wavenumber considered, ρ_{Ls} is the Larmor radius for species s and L_{\perp} is the perpendicular length of the system. The subscripts “ \perp ” and “ \parallel ” indicate components perpendicular and parallel to the magnetic field \mathbf{B} , respectively. Furthermore, the plasmas are in the drift kinetic regime, which is, by definition, that part of the gyrokinetic regime in which $k_{\perp}\rho_{L\bar{p}} \ll 1$. The plasmas are in the guiding-center kinetic regime, which is, by definition, that part of the drift kinetic regime in which $\omega_{ps}^2/\omega_{cs}^2 \ll 1$ for each species, where ω_{cs} and ω_{ps} are the cyclotron and plasma frequencies, respectively, for species s .

From $\omega/\omega_{c\bar{p}} \ll 1$, it follows that the $\mathbf{E} \times \mathbf{B}$ drift is much greater than the polarization drift. Since $T_{e+}/e\phi \ll 1$, where ϕ is the electrostatic potential, the $\mathbf{E} \times \mathbf{B}$ drift is much greater than the curvature and ∇B drifts. The Banós drift [17, 18] is extremely small.

If the longitudinal and transverse waves are decoupled, we may further restrict attention to the electrostatic approximation,

$$\nabla \cdot \mathbf{E} = -\nabla^2(\phi^{\text{self}} + \phi^{\text{ext}}) = 4\pi \sum_{s \in \{e^+, \bar{p}\}} q_s \int d^3\mathbf{v} f_s. \quad (1)$$

Here ϕ^{self} and ϕ^{ext} are the parts of the electrostatic potential due to the plasma and external sources, respectively, q_s is the charge of species s , $f_s(\mathbf{r}, \mathbf{v}, t)$ is the distribution function for species s and \mathbf{v} is velocity. Since, for each species, the collision frequencies $\nu_{ss'}$ are small compared to the plasma frequencies ω_{ps} , collisions may be neglected.

The above approximations lead to the collisionless guiding-center kinetic equation

$$\frac{\partial f_s}{\partial t} + \left[\frac{c\mathbf{E} \times \mathbf{B}}{B^2} \right] \cdot \nabla_{\perp} f_s + v_{\parallel} \nabla_{\parallel} f_s + \frac{q_s}{m_s} E_{\parallel} \frac{\partial f_s}{\partial v_{\parallel}} = 0. \quad (2)$$

The distribution functions f_s have units of volume⁻¹ · velocity⁻³. The quantity m_s is the mass of species s . In cylindrical coordinates (r, ϕ, z) , with a constant, axial magnetic field $\mathbf{B} = B\hat{z}$ and ϕ^{ext} independent of position and time, Eqs. (1) and (2) may be simplified. Perturbing the result about an equilibrium solution $(f_{e+0}, f_{\bar{p}0}, \phi_0)$ which is independent of ϕ and z and applying the Fourier-Laplace transform $(F_s, \Phi) = (2\pi)^{-2} \int_{-\infty}^{\infty} dz \int_0^{2\pi} d\phi \int_0^{\infty} dt e^{-i(\ell\phi + k_z z - \omega t)} (f_{s1}, \phi_1^{\text{self}})$, where $\text{Im}[\omega] > 0$, to the three first-order equations for the perturbed solution $(f_{e+1}, f_{\bar{p}1}, \phi_1)$ yields an inhomogeneous initial-value problem. The corresponding homogeneous equation is

$$\left(\frac{1}{r} \frac{\partial}{\partial r} r \frac{\partial}{\partial r} - \frac{\ell^2}{r^2} - k_z^2 - \sum_s \frac{\omega_{ps}^2}{n_{s0}} \int d^3\mathbf{v} \frac{k_z \frac{\partial f_{s0}}{\partial v_z} + \frac{1}{\omega_{cs}} \frac{\ell}{r} \frac{\partial f_{s0}}{\partial r}}{\omega - \ell\omega_E(r) - k_z v_z} \right) \Phi = 0, \quad (3)$$

² The radius of ATRAP's positron bunch was estimated from Fig. 1 of reference [10] to be 0.15 mm. The radius and length of ATHENA's antiproton bunch and the radius of ATRAP's antiproton bunch were estimated from ASACUSA's data [11] to be 0.1 cm, 5.0 cm and 0.1 cm, respectively. All other data appears numerically in the appropriate articles [10, 12, 13].

where $\omega_E = -cE_0(r)/rB_0$ is the equilibrium $\mathbf{E} \times \mathbf{B}$ rotation frequency. Here the subscripts 0 and 1 indicate unperturbed equilibrium quantities and perturbed quantities, respectively. The boundary conditions are that Φ is zero at the wall, finite on the trap's axis and continuous at the plasma edge. The dispersion relation is obtained using the additional condition found by integrating Eq. (3) across the plasma edge.

APPLICATION TO COLD PLASMAS

By "cold," it is meant that both parallel thermal velocities are small compared to the average parallel velocity of the antiprotons. In this special case, which is a simple place to begin,

$$f_{s0} = n_{s0} H(r_b - r) G(v_\perp) \delta(v_z - u_{sz0}). \quad (4)$$

Here n_{s0} is the equilibrium density, which is constant in space; H is the Heaviside step function; r_b is the plasma radius, which is the same for both species; and $G(v_\perp)$ is an arbitrary distribution in perpendicular velocity space normalized according to $2\pi \int_0^\infty dv_\perp v_\perp G(v_\perp) = 1$. If (4) is used with $\ell = 0$, Eq. (3) may be simplified to

$$1 = \frac{k_z^2}{k_r^2 + k_z^2} \sum_s \frac{\omega_{ps}^2}{(\omega - k_z u_{sz0})^2}, \quad (5)$$

where k_r solves

$$k_z \frac{K_0(k_z r_w) I_1(k_z r_b) + K_1(k_z r_b) I_0(k_z r_w)}{K_0(k_z r_w) I_0(k_z r_b) - K_0(k_z r_b) I_0(k_z r_w)} + k_r \frac{J_1(k_r r_b)}{J_0(k_r r_b)} = 0. \quad (6)$$

Here, u_s is the average velocity of species s ; r_w is the wall radius; and I_n , J_n and K_n are Bessel functions. The transcendental equation (6) may be solved for $k_r(k_z)$, which, for any particular value of k_z , is quantized with a radial mode number n . The solutions for k_r , which are displayed in Fig. 2, are then substituted into (5).

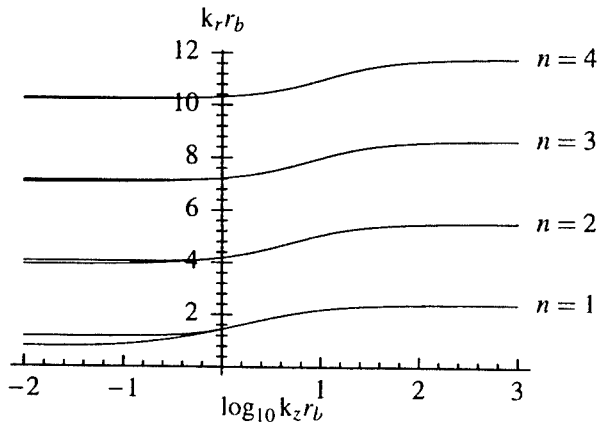


FIGURE 2. Solutions to (6). For a given radial mode number n , the upper and lower branches are for $r_b/r_w = 0.3$ and 0.05 , respectively, which bound the range of values of r_b/r_w of practical interest.

Using *Mathematica*[®], the quartic equation (5) for ω was solved both analytically and numerically with the same results. Eq. (5) has four roots. One root is unstable for a range of values of k_z . The unstable root, for physical values of the trap parameters, is shown in Fig. 3. The oscillation frequency $\text{Re}[\omega]/\omega_{pe+}$ and the growth rate $\text{Im}[\omega]/\omega_{pe+}$ are displayed as functions of $k_z u_{\bar{p}z0}/\omega_{pe+}$. As expected [19], for a cold plasma, the maximum growth rate scales as $\omega_{pe+}^{1/3} \omega_{p\bar{p}}^{2/3}$.

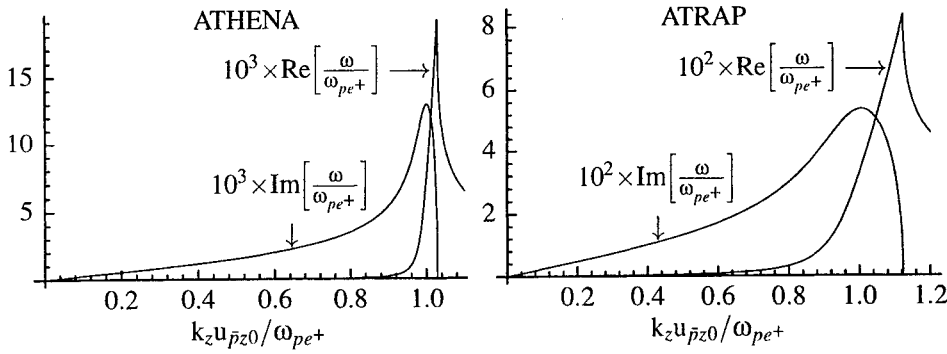


FIGURE 3. The unstable root of (5) for $n = 1$. The left and right plots are for ATHENA and ATRAP, respectively; r_h/r_w is 0.1 and 0.125, respectively; $\omega_{pe+}/\omega_{p\bar{p}}$ is 380 and 44, respectively; and $u_{\bar{p}z0}/(\omega_{pe+} r_h)$ is 5.8×10^{-4} and 8.4×10^{-4} , respectively.

APPLICATION TO DRIFTING MAXWELLIAN PLASMAS

Now the unperturbed distribution functions are allowed to have nonzero parallel thermal velocities v_{tsz} :

$$f_{s0} = \frac{n_{s0} H(r_b - r)}{v_{tsz} \sqrt{2\pi}} G(v_{\perp}) \exp \left[-\frac{(v_z - u_{sz0})^2}{2v_{tsz}^2} \right]. \quad (7)$$

If Eq. (7) is substituted into Eq. (3) with $\ell = 0$, Eq. (3) takes the form

$$-\sum_s \frac{1}{\lambda_{Ds}^2} \left(1 + i \sqrt{\pi} \frac{\omega - k_z u_{sz0}}{k_z v_{tsz} \sqrt{2}} \exp \left[-\left(\frac{\omega - k_z u_{sz0}}{k_z v_{tsz} \sqrt{2}} \right)^2 \right] \left(1 + \text{erf} \left[i \frac{\omega - k_z u_{sz0}}{k_z v_{tsz} \sqrt{2}} \right] \right) \right) = k_r^2 + k_z^2, \quad (8)$$

where $\lambda_{Ds} = v_{tsz}/\omega_{ps}$ is the Debye length for species s , $\text{erf}(z) = (2/\sqrt{\pi}) \int_0^z dt e^{-t^2}$ and k_r solves (6), exactly as for a cold plasma.

Using *Mathematica*[®], the transcendental equation (6) for $k_r(k_z)$ was solved numerically, and the result was substituted into the transcendental equation (8), which was also solved numerically. For ATHENA's and ATRAP's parameters, it is found that there is a critical average velocity for the antiprotons below which the system is stable. In these cases and in all others examined, it was found that the critical velocity of the antiprotons is the positron thermal velocity times a number of order unity. For both ATHENA's

and ATRAP's parameters, typical maximum growth rates are found to be of the order of $\omega_{pe}^{1/3} \omega_{p\bar{p}}^{2/3}$ when $u_{\bar{p}z0}/v_{tisz} \gg 1$.

In the second section, terms scaling like the collision frequencies were neglected in favor of terms scaling like the plasma frequencies. However, the growth rates can be comparable in size to $\omega_{pe}^{1/3} \omega_{p\bar{p}}^{2/3}$, which is about the same size as the largest collision frequency, the positron-positron collision frequency. This suggests that collisions play an important role in the damping or growth of the mode. Fortunately, to leading order, positron-positron collisions are described by O'Neil's collision operator [20, 21]. Inclusion of collisions is a logical next step in the calculations.

REFERENCES

1. Gabrielse, G., Fei, X., Helmerson, K., Rolston, S., Tjoelker, R., Trainor, T., Kalinowsky, H., Haas, J., and Kells, W., *Physical Review Letters*, **57**, 2504–2507 (1986).
2. Holzscheiter, M., and Charlton, M., *Reports on Progress in Physics*, **62**, 1–60 (1999).
3. Gabrielse, G., Fei, X., Haarsma, L., Rolston, S., Tjoelker, R., Trainor, T., Kalinowsky, H., Haas, J., and Kells, W., *Physica Scripta*, **T**, 36–40 (1988).
4. Surko, C., Greaves, R., and Charlton, M., *Hyperfine Interactions*, **109**, 181–188 (1997).
5. Lefevre, P., Mohl, D., and Plass, G., “The CERN Low Energy Antiproton Ring (LEAR) project”, in *11th International Conference on High-Energy Accelerators*, Birkhauser Verlag, 1980, pp. 819–823.
6. Gabrielse, G., Rolston, S., Haarsma, L., and Kells, W., *Hyperfine Interactions*, **44**, 287–294 (1988).
7. Gabrielse, G., First positron cooling of antiprotons, and prospects for simultaneous trapping of neutrals and charged particles (2001), poster presentation at the 2001 Workshop on Nonneutral Plasmas.
8. Neuffer, D., Colton, E., Fitzgerald, D., Hardek, T., Hutson, R., Macek, R., Plum, M., Thiessen, H., and Wang, T.-S., *Nuclear Instruments and Methods in Physics Research*, **A321**, 1–12 (1992).
9. Private communication with L. V. Jørgensen (2001), on August 1.
10. Gabrielse, G., Estrada, J., Peil, S., Roach, T., Tan, J., and Yesley, P., “Progress Toward Cold Antihydrogen”, in *Nonneutral Plasma Physics III* (AIP Conference Proceedings 498), edited by J. J. Bollinger, R. L. Spencer, and R. C. Davidson, American Institute of Physics, 1999, pp. 29–39.
11. Yamazaki, Y., “Trapping, Cooling and Extraction of Antiprotons, and the ASACUSA Project”, in *Nonneutral Plasma Physics III* (AIP Conference Proceedings 498), edited by J. J. Bollinger, R. L. Spencer, and R. C. Davidson, American Institute of Physics, 1999, pp. 48–58.
12. Surko, C., Gilbert, S., and Greaves, R., “Progress in Creating Low-energy Positron Plasmas and Beams”, in *Nonneutral Plasma Physics III* (AIP Conference Proceedings 498), edited by J. J. Bollinger, R. L. Spencer, and R. C. Davidson, American Institute of Physics, 1999, pp. 3–9.
13. Fine, K., “The ATHENA Antihydrogen Experiment”, in *Nonneutral Plasma Physics III* (AIP Conference Proceedings 498), edited by J. J. Bollinger, R. L. Spencer, and R. C. Davidson, American Institute of Physics, 1999, pp. 40–47.
14. Rutherford, P., and Frieman, E., *Physics of Fluids*, **11**, 569–585 (1968).
15. Taylor, J., and Hastie, R., *Plasma Physics*, **10**, 479–494 (1968).
16. Lee, W., *Physics of Fluids*, **26**, 556–562 (1983).
17. White, R. B., *Theory of Tokamak Plasmas*, North-Holland Physics, Elsevier Science Publishers B.V., P.O. Box 103, 1000 AC Amsterdam, The Netherlands, 1989, see p.66.
18. Littlejohn, R., *Physics of Fluids*, **24**, 1730 (1981).
19. Davidson, R. C., *Physics of Nonneutral Plasmas*, Addison-Wesley Publishing Company, 350 Bridge Parkway, Suite 209, Redwood City, CA 94065, 1990, see equation (5.13.8) on page 271.
20. O'Neil, T., *Physics of Fluids*, **26**, 2128–2135 (1983).
21. Dubin, D. H., and O'Neil, T., *Physical Review Letters*, **78**, 3868–3871 (1997), see equation (8).

Design And Test Of A Beam Line For Extraction Of Slow Antiprotons From A Multi- Ring Electrode Ion Trap

K. Yoshiki Franzen^{1,2}, H. Higaki², T. Ichioka², M. Hori³, Z. Wang², N. Kuroda², S. Yoneda², H. A. Torii², K. Komaki² and Y. Yamazaki^{1,2}

¹Atomic Physics Laboratory, RIKEN, Wako 351-01, Japan

²Institute of Physics, University of Tokyo, Komaba 3-8-1, Meguro-ku, Tokyo, Japan

³CERN, CH-1211 Geneva 23, Switzerland

Abstract. A new monoenergetic slow antiproton beam facility has recently been installed at the CERN Antiproton Decelerator (AD). The system is designed to deliver pulsed or continuous antiproton beams in the 10-1000 eV energy region which is suitable for various interesting atomic and molecular spectroscopic and collision studies. The antiprotons obtained from the AD are slowed down to around 100 keV by passing the Radio Frequency Quadrupole Decelerator (RFQD) and then captured in a multi-ring electrode ion trap. After electron cooling down to a few eV, the antiprotons will be extracted out from the trap into a collision chamber via a differential pumping system. In this paper, we present recent results in which the antiproton capture and cooling phases of this scheme have been successfully demonstrated. Furthermore, the design and tests of the extraction and differential pumping system are presented.

INTRODUCTION

A new monoenergetic slow antiproton beam facility has recently been installed at the CERN Antiproton Decelerator (AD) [1]. The system is designed to deliver pulsed or continuous antiproton beams in the 10-1000 eV energy region which is suitable for several interesting atomic and molecular spectroscopic and collision studies. Such a slow antiproton beam will be produced in several steps [2,3]. The antiprotons are initially provided by the CERN Antiproton Decelerator (AD) ring at 5.3 MeV/u and slowed down to around 100 keV when passing through a Radio Frequency Quadrupole Decelerator (RFQD). The beam is further slowed down to around 10 keV by passing a degrader foil. The particles are then trapped inside a multi-ring electrode trap. In the trap the confined antiprotons form a non-neutral two-component plasma together with previously trapped and synchrotron radiation cooled electrons. This configuration eventually causes electron cooling of the antiprotons down to a kinetic energy of the order of 1 eV. The cooled antiprotons are then to be extracted and transported to an experimental chamber where the beam intersects with an atomic or molecular gas target beam. However, since it is unavoidable to have a relatively high background pressure in the collision chamber ($\sim 10^{-6}$ Torr) and the required pressure inside the trap must be very low ($< 10^{-11}$ Torr), it is necessary to

utilize a transport beam line equipped with a differential pumping system between the two regions. One of the difficulties with extraction of charged particles starting inside a solenoidal magnetic field is that the unguided trajectories tend to follow the field lines, which are strongly diverging at the ends of the magnet. Furthermore, focusing of the beam even outside the magnetic field is in general limited which is a direct consequence of the conservation of total angular momentum. In addition, the finite dimension of the plasma source must be considered in any realistic extraction scheme.

EXPERIMENT

The ion trap consists of a set of ring electrodes positioned coaxially inside the bore tube of an Oxford 5 T superconducting solenoid magnet. See Fig. 1. The details of the design of the electrodes and the cabling system have been previously reported [2-5]. The size of the magnet coil is approximately 1.8 m in length and 22 cm in inner diameter. The pressure measured outside the bore tube has typically been around 2×10^{-10} Torr. However, since the temperature of the bore tube can be lowered to around 10 K or even lower during measurements it is expected that the pressure in the trap region is at least one order lower than this value. A $200 \mu\text{g}/\text{cm}^2$ carbon degrader foil is positioned 60 cm upstream of the magnet center which is used to degrade the antiproton beam received from the AD via the RFQ decelerator. Electrons are injected by a Spindt-type electron emitter [6] from down stream of the magnet coil, a few cm off the magnet axis and guided by the converging magnetic field into the trap region. A set of Cherenkov counters and plastic scintillator track detectors were positioned outside the magnet in order to monitor the time of arrivals and positions of charged pions emitted after antiproton annihilations [7].

The design of the extraction beam line was based on detailed Monte-Carlo simulations using a commercial software by Field Precision, which works well within a PC environment. By defining the geometries of the solenoid coil and the electrostatic

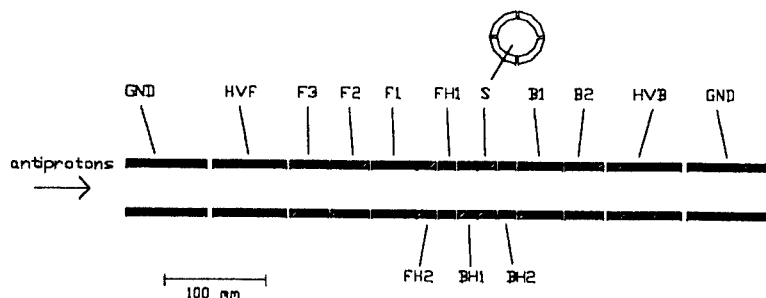


FIGURE 1. Schematic cross section of the ASACUSA trap electrodes. The electrode named S is segmented into four pieces.

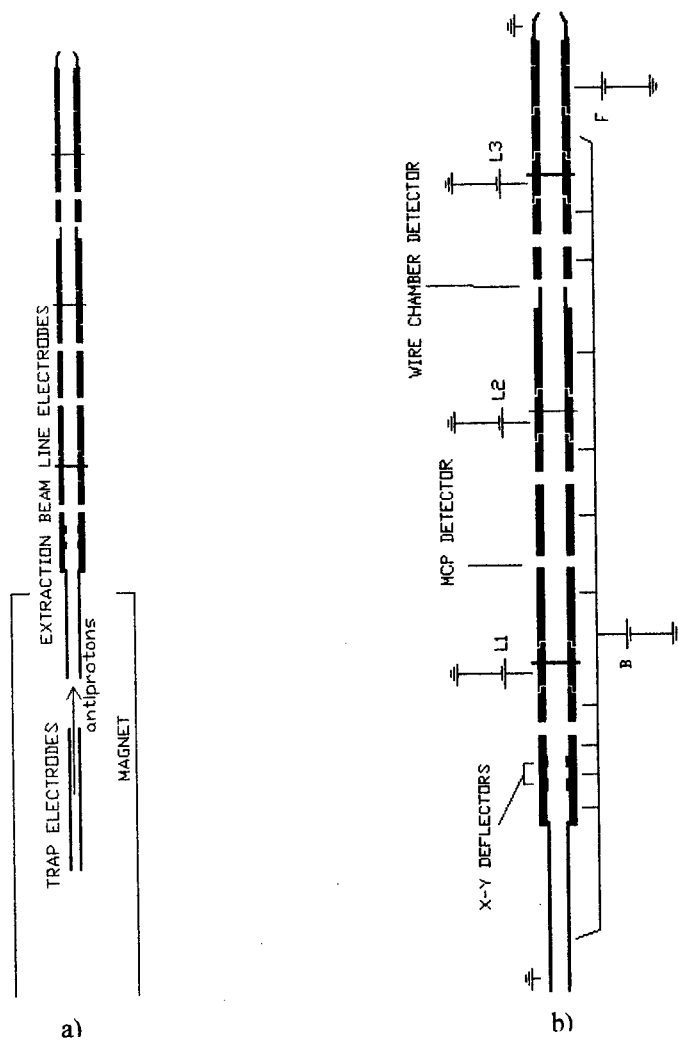


FIGURE 2. Schematic cross sections of a) the ASACUSA trap and extraction beam line electrodes and b) the extraction beam line electrodes. The beam travels from down to up in the figure. See the text for further information.

lenses and also by defining the current density and respective voltages, dense matrices representing both the static magnetic and electric fields were obtained. The initial conditions of a large number of antiprotons representing the plasma source were defined by assuming an antiproton plasma in the trap of a cylindrical shape with 2 mm in diameter and of homogenous density. Furthermore, it was assumed that the antiprotons have energies of 1 eV in the perpendicular direction relative to the magnetic field. The trajectories of the antiprotons extracted from the trap region were then calculated and the focal properties of the beam in the target chamber were estimated at several extraction energies. An optimized configuration could be found for maximum transport and focusing at the beam intersection point in the experimental chamber. See Table 1. The effective values of the diameters are given by $4x_{rms}$ where x_{rms} is given by the root-mean-square of one transversal coordinate at the focal point for all the studied trajectories. The effective values of the divergence angles are given by $2x'_{rms}$ where x'_{rms} is given by the root-mean-square of the slopes relative to the beam line axis at the focal point for the same trajectories [8]. Minimization of these values, each representing an envelope of the respective beam parameter, while keeping a 100% transmission efficiency of the system were the main criteria of the design. In addition all the practical requirements on vacuum, high voltage electrostatic lenses, materials etc. were taken into account. A schematic overview of the resulting design can be observed in Fig. 2.

After capture and cooling, the antiprotons are extracted from the trap by raising the potentials of electrodes F2, F1, FH2, FH1, BH1, S, BH2 and B1 up to the potential of electrode B2, which is kept lower than the potential of electrode F3 (see Fig. 1). The electrodes HVF and HVB are at this stage kept at ground potential. The antiprotons then enter the beam line electrode system, which penetrates into the homogenous part of the solenoidal magnetic field as illustrated in Fig. 2a. After passing a grounded electrode the antiprotons reach the electrodes with a potential B, which accelerates or decelerates the antiprotons to a kinetic energy of few hundreds eV inside the beam line, see Fig. 2b. Around this position they also pass a double set of electrostatic x-y deflectors, which provides a mean to align the trajectories against the beam line axis. The beam then reaches electrodes and an aperture, which are kept at a potential L1 as can be seen in Fig. 2b. Here a cylindrically symmetric accelerating electric field forces the beam to pass the aperture, which is high voltage floatable and of adjustable size. The typical maximum kinetic energy of the beam around the aperture is a few keV. Exiting the aperture the beam is decelerated down to a few hundreds eV. This deceleration provides further focusing which at correctly applied potentials makes the antiprotons leave the lens system again as a parallel beam. With an aperture size of 4 mm in diameter it is estimated that the pressure downstream of the aperture can be kept around 100 times as high as the pressure upstream. The

TABLE 1. Antiproton beam focus parameters versus extraction energy.

Extraction energy (eV)	Effective beam diameter (mm)	Effective divergence angle (deg)
10	6	± 18
100	5	± 6.5
250	4	± 4.9

minimum measured background pressure after baking in the downstream region is in the 10^{-10} Torr region, which is obtained by a 1000 l/s turbo molecular pump. The functions of the lens systems kept at the potentials L2 and L3 in Fig. 2b are exactly the same as for the one just described. Down stream of the aperture kept at the potential L2 a 400 l/s turbo molecular pump gives a background pressure in the 10^{-9} Torr range while turbo molecular pumps installed in an experimental chamber will provide the pumping downstream of the aperture at potential L3. The three apertures set at sizes around 4 mm in diameter thus provide the required differential pumping efficiency. The beam is finally focused into the experimental chamber by passing the electrode at potential F and finally a grounded electrode as illustrated in Fig. 2b. The focal point of the beam is 25 mm downstream from the end of the last electrode, which is at ground potential. To eliminate any electric stray fields at this point it is possible to attach a mesh to the downstream surface of this electrode. To optimize the extraction and transportation of the beam there are two detectors installed along the beam line which functions are to monitor the beam profile. The first one, which is marked MCP DETECTOR in Fig. 2b, is a microchannel plate system equipped with a delay line anode. This will give information on both the arrival timing and the position of each detected antiproton. The downstream detector of the beam line, marked WIRE CHAMBER DETECTOR in Fig. 2b, gives the possibility to measure the beam profile during pulsed extraction while providing a high transmission.

RESULTS

Before starting experiments with antiprotons it was shown that we could trap and compress electrons, H^- and positive ion plasmas using the described trap system. During these experiments we also performed non-neutral plasma diagnosis by utilizing a tank circuit. These results are described in detail elsewhere [4]. During our first four weeks of AD beam time in June 2001 the following results were acquired.

Fig 3a exhibits the signal from a Cherenkov counter detector positioned close to the end of the magnet closest to the RFQD. At this end a gate valve is mounted which in this case was closed, thus blocking the beam. The time scale is relative to a given start signal which is correlated to the arrival of antiprotons kicked out from the AD. As can be observed, pulses arrived and annihilated against the gate valve at 1.25 μ s and at 1.75 μ s, each corresponding to incoming antiprotons of 5 MeV and 85 keV energies respectively. The pulse with the lower energy corresponds to antiprotons decelerated by the RFQ Decelerator. By observing the corresponding signal from a Cherenkov counter positioned close to the gate valve mounted at the opposite end of the magnet and with the other gate valve opened an additional broader feature was found at around 3-5 μ s, see Fig. 3b. This indicates that the antiprotons had undergone further deceleration due to passage through the carbon degrader foil when entering the magnet. The energy corresponding to the position of this peak is 20 keV and lower. By applying a -10 kV potential to the trap electrode HVB as seen in Fig.1, it was observed that the low energy tail of the degraded energy peak was reduced. This is

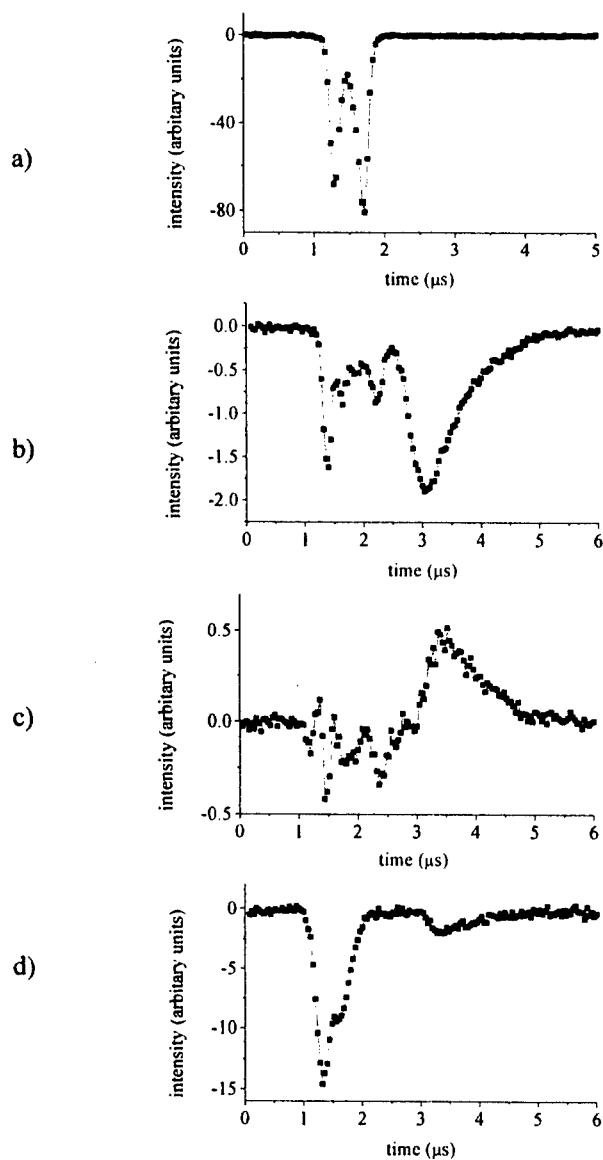


FIGURE 3. Signals acquired with a Cherenkov counter a) positioned upstream of the trap with the upstream gate valve closed, b) positioned downstream of the trap with the upstream gate valve opened, c) positioned downstream of the trap showing the difference between with and without -10 kV applied to electrode HVB and d) positioned upstream of the trap with the upstream gate valve opened and with -10 kV applied to electrode HVB. See the text for further information.

illustrated in Fig. 3c, which is a spectrum showing the signal difference obtained with the high voltage on and off. The peak with a maximum at $3.5 \mu\text{s}$ is thus explained by reflection of low energy antiprotons towards the entrance end of the magnet. This was confirmed by again observing the signal from the upstream Cherenkov counter, which showed an additional low energy peak when high voltage was applied (see Fig. 3d).

The next step was to confirm confinement of antiprotons. For this purpose the plastic scintillator detectors were positioned in parallel to the magnet axis. By applying the -10 kV potentials to the electrode HVF (see Fig. 1) of the trap before the reflected antiprotons could escape as in Fig. 3d they could be trapped. After 1 s they were released by removing the high voltage potentials, which quickly resulted in annihilation as can be seen in Fig. 4a. A rough estimate of the number of captured antiprotons is given by counting the number of pulses within the peak around 1 s and by taking the solid angle of the detector and the multiplicity of the charged pions emitted after annihilation into account. This gives a number around 300000

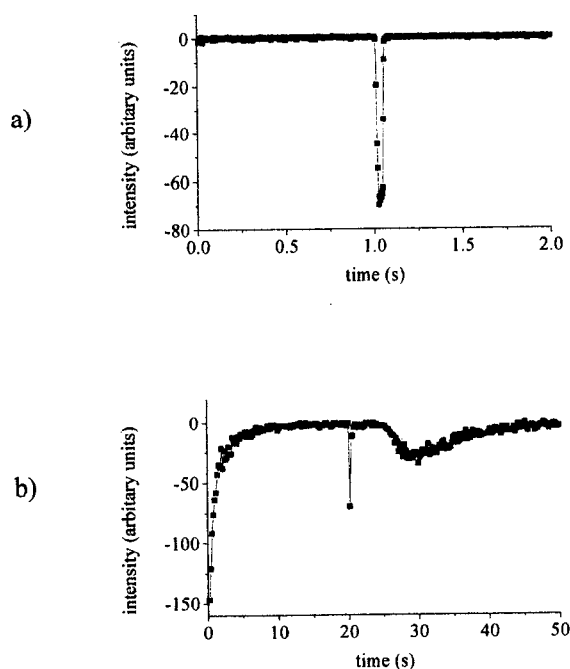


FIGURE 4. Signals acquired with a plastic scintillator detector positioned parallel to the trap magnet. The panels show a) antiprotons annihilating after 1 s trapping time and b) electron cooled antiprotons confined in a well of 100 V depth after the -10 kV high voltages applied to the end electrodes of the trap have been turned off after 20 s trapping time.

antiprotons captured from one shot. Furthermore, it was also shown that we could cool down the captured antiprotons to less than 100 eV and probably much less. This is exhibited in Fig. 4b, which again shows the signal acquired with the plastic scintillator detector. However, 50 s before the antiprotons were captured, 60 eV electrons were injected and confined within the trap region. Previous experiments had shown that the number of trapped electrons during identical conditions was of the order of 10^8 . At the high magnetic field utilized in these series of measurements (3.3 T) the electrons quickly lose their kinetic energy due to synchrotron radiation. The -10 kV high voltage potentials applied to the end electrodes of the trap was turned off at 20 s after the antiproton injection which can be seen in Fig. 4b as a narrow peak. However, a well of depth 100 V was kept on until 50 s after the injection. It can be clearly seen in the figure how the annihilation continues up to this time, which shows that there are still antiprotons inside the trap region after the high voltage has been turned off.

Our next goal during the allocated AD beam time in October 2001 will include extraction studies of the slow antiprotons. Here we briefly report on experiments in which the above-described system was used to extract slow positive ions from the trap to the focal point. By ionizing the residual gas inside the trap region with the electron beam, positive ions were created and trapped. These ions were extracted from the trap by using the same procedure as previously described for antiproton extraction but with the opposite sign of the applied potentials. For instance, the potential applied to the

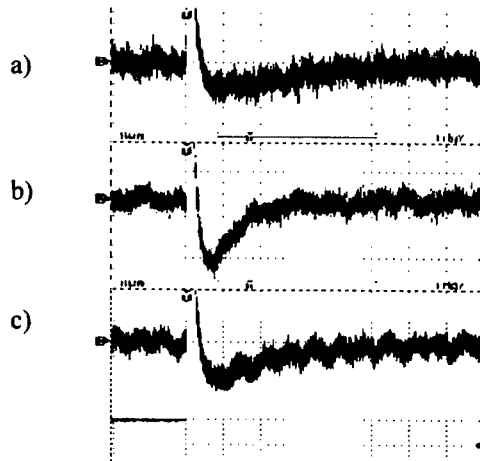


FIGURE 5. The raw signal obtained from the second aperture via a charge amplifier with potential $L1$ set to a) -500 V, b) -3410 V, and c) -4500 V. The changing trap well potential was used as a trigger pulse. The vertical scale is 500 mV/div and the horizontal scale is 10 ms/div. The gain of the charge amplifier is 164 mV per 10^6 charged particles.

trap electrode B2 was in one case set to 500 V. The ions then entered the extraction beam line electrodes with kinetic energies around 500 eV and were decelerated down to around 250 eV by setting B in Fig. 2b to a potential 250 V. The positive ions reaching the aperture of the lens L2 (Fig. 2b), which in this case served as a Faraday cup, were monitored with a charge amplifier while varying the potential L1. As can be observed in Fig. 5 there is certainly a dependence on the applied potential L1 and the maximum throughput was obtained at $L1 = -3410$ V, which is the value predicted by the calculations. By utilizing the second and third lens systems (marked by L2 and L3 in Fig. 2b) the extracted ions were transported to the focal point of the beam line where the current of positive ions reaching the surface of a MCP detector was measured. A rough estimate gives that 10^5 positive ions per extraction reached the focal point at 250, 100 and 10 eV extraction energies with the apertures set at 6 mm in diameter.

In addition slow extraction tests monitoring the beam profile after the first aperture with the MCP detector system (see Fig. 2b) equipped with a delay line anode were performed. Figure 6 shows some examples of these results acquired during similar conditions except for different L1 voltages (see Fig. 2b). The ions were extracted at 250 eV. According to the discussed calculations the transmittance of the beam should at this extraction energy be at maximum for $L1 = -3640$ V. This seems to be confirmed by the experiment since the measurements with $L1 = -3000$ V (Fig. 6a) and $L1 = -4000$ V (Fig. 6c) both exhibit a weaker signal compared with the case of a correctly applied potential (Fig. 6b). During these tests, the positive ions were extracted very slowly from the trap, even during periods up to several tens of seconds. It was observed that the current and the beam profile remained almost constant during the extraction. A similar detector is presently being prepared in order to monitor the antiproton beam profile measured at the focal point of the beam line.

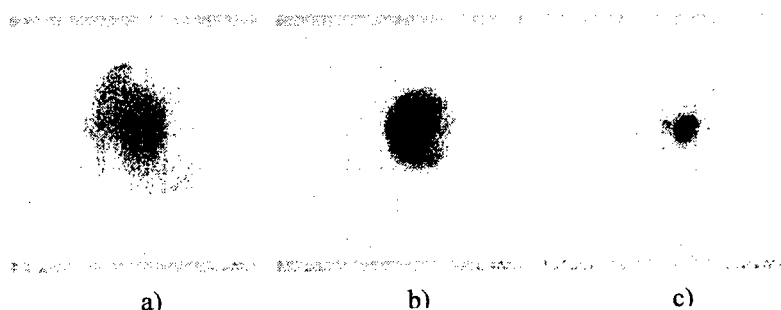


FIGURE 6. The beam profile as measured by a position sensitive MCP detector during slow extraction of positive ions from the trap via an aperture of 4 mm in diameter. The applied potentials L1 were a) -3000 V, b) -3640 V (optimized according to calculations) and c) -4000 V.

CONCLUSIONS

The most important technical features of the slow antiproton extraction beam line were described. Recent results of the antiproton capture and cooling phases were presented. Furthermore, preliminary test results of the extraction beam line using positive ions were presented showing the possibility to extract charged particles as a slow beam from the trap via a three-stage differential pumping system. The system is now ready to be tested and optimized for the delivery of a slow antiproton beam at CERN.

ACKNOWLEDGMENTS

We are most grateful to the Antiproton Decelerator (AD) staff at CERN for providing us with the antiproton beam.

Postdoctoral Fellowships from the Japanese Society for the Promotion of Science (JSPS) and the Science and Technology Agency (STA) financially supported four of the authors (K.Y.F., H.H., M.H. and Z.W.) during these experiments.

REFERENCES

1. Baird S. et al., "Design study of the antiproton decelerator", in *Ad. Technical Report*, edited by Maury S., CERN/PS 96-43 (AR), CERN, 1996
2. Yamazaki Y., *NIM B* **154** 174-184 (1999)
3. Yamazaki Y., "Antiprotons and the ASACUSA project", in *Non-Neutral Plasma Physics III*, edited by Bollinger J. J. et al., AIP Conference Proceedings 498, New York, 1999, pp. 48-58
4. Ichioka T., Higaki H., Hori M., Oshima N., Kuroki K., Mohri A., Komaki K. and Yamazaki Y., "Multi-ring trap as a reservoir of cooled antiprotons", in *Non-Neutral Plasma Physics III*, edited by Bollinger J. J. et al., AIP Conference Proceedings 498, New York, 1999, pp. 59-64
5. Ichioka T., Ph.D. thesis, University of Tokyo, 2001
6. Spindt C. A. et al., *IEEE Trans. On Elec. Dev.* **38** 2355-2363 (1991)
7. Leo W. R., *Techniques for Nuclear and Particle Physics Experiments*, Springer-Verlag, Berlin, 1994, pp. 36-37 and pp. 157-213
8. Reiser M., *Theory and Design of Charged Particle Beams*, John Wiley & Sons, New York, 1994, pp. 59

Spectroscopy of Rydberg Atoms in Non-Neutral Cold Plasmas

D. Feldbaum, N. V. Morrow, S. K. Dutta, G. Raithel

*Department of Physics, University of Michigan
Ann Arbor, MI 48109-1120*

Abstract. The electric field in mm-sized one-component non-neutral plasmas is measured using the Stark effect of Rydberg atoms embedded in them. The plasmas are clouds of cold Rb^+ -ions, which are produced by UV photoionization of laser-cooled Rb atoms in a magneto-optic trap. The dependence of the electric field on the number of ions and the Coulomb explosion of the ion clouds have been studied.

INTRODUCTION

Highly excited Rydberg atoms [1] are very sensitive to static and AC electric and magnetic fields, and can be used for the spectroscopic detection and compensation of such fields. Rydberg atoms have been used to detect microwave and FIR radiation [2], to measure and to compensate weak static electric fields [3], and to study QED level shifts and cavity-QED effects involving only few microwave photons [4]. The spectroscopy of Rydberg atoms has been employed to diagnose electric fields in DC and high-frequency discharge plasmas [5]. In this report, we use Rydberg atom spectroscopy to determine the electric field in millimeter-sized, strongly coupled plasmas that since recently can be generated by the laser excitation of laser-cooled clouds of atoms [6]. The field-measurement method described in this report will have future applications in the characterization of these plasmas and the study of their evolution.

EXPERIMENT

Our experiment has recently been described in Ref. [7]. In a two-step optical excitation, laser-cooled rubidium atoms confined in a volume of order 1mm^3 are first excited from the ground state $5S_{1/2}$ to the $5P_{3/2}$ state using a 780nm diode laser pulse of a few μs duration. A short UV laser pulse ($\lambda_{\text{UV}} = 355\text{nm}$, duration $< 10\text{ns}$, pulse energy up to 10mJ) fired during the diode laser pulse partially ionizes the $5P_{3/2}$ -atoms, which have an ionization wavelength of $\lambda_{\text{ion}} = 479.1\text{nm}$. The resultant photoelectrons have 0.9eV initial kinetic energy and mostly escape on a time scale of a few ns, leaving behind a cloud of slow Rb^+ -ions. At a variable delay time after the UV pulse

and while the 780nm-laser is still on, the remaining $5P_{3/2}$ -atoms that are embedded in the ion plasma are excited by a blue dye laser pulse ($\lambda \approx 480\text{nm}$, duration $< 10\text{ns}$, bandwidth $\approx 10\text{GHz}$). The blue pulse excites bound Rydberg states, the Stark effect of which we use to measure the electric fields of the non-neutral Rb^+ -plasma.

The Rydberg atoms are detected as follows. The ion plasma represents an electron trap with a depth U_0 given by the ion number, the cloud size and the profile of the charge distribution [6]. In most of our experiments $U_0 < 0.9\text{eV}$, in which case no or only few UV-generated photoelectrons are retained in the electron trap. The blue laser pulse, which is introduced shortly after the UV pulse and mostly excites bound Rydberg atoms, contains a small portion of ASE (amplified spontaneous emission) with $\lambda < \lambda_{\text{ion}}$. This above-threshold ASE directly photoionizes of order 10^3 $5P_{3/2}$ -atoms, producing electrons with about 10meV energy. These electrons are trapped in the ion plasma. Thermal ionization of a small percentage of the bound Rydberg atoms excited by the blue pulse may add some more trapped electrons [7]. Within a few μs , l -changing collisions between the trapped electrons and the Rydberg atoms efficiently promote the latter into long-lived high- l states. During the Coulomb expansion of the ion plasma, the depth U_0 of the plasma electron trap approaches zero. During that time, the electrons trapped in the plasma are gradually released, producing a plasma decay signal in our microchannel-plate (MCP) electron detector, which is located about 10cm from the atomic cloud. The high- l Rydberg atoms, which are not affected by the plasma expansion, thermally ionize with a probability of order 50% on a time scale of order 10ms [7]. This time scale exceeds the plasma decay time by a factor of about 10^4 . The delayed thermal electrons originating in the high- l Rydberg atoms are counted by the MCP detector in a gate that starts well after the plasma decay, yielding a noise-free signal of the Rydberg atom excitation. The Rydberg excitation spectra used to determine the plasma electric field are obtained by recording the delayed electron counts as a function of the wavelength of the blue laser.

Fig.1 shows a typical experimental Rydberg excitation spectrum of atoms in an electric-field-bearing plasma. Moving through the spectrum displayed in the upper panel of Fig.1 from right to left, we observe that the electric field first manifests itself in the appearance of p -lines and of triangular-shaped “ h -features”, both caused by electric-field-induced state mixing. Each triangular h -feature reflects one manifold of hydrogenic states with the same principal quantum number n , which - due to the linear Stark effect - fan out over an energy range $3n^2E$ (atomic units) [1]. As n increases, the h -features progressively expand and acquire more and more overall oscillator strength. Eventually, they fill in all spectral regions of originally zero oscillator strength between the discrete non-hydrogenic s -, p - and d -lines. The lower three panels of Fig.1 highlight the fact that there are three types of such spectral gaps, which we label hs -, mid - and pd -gaps. The gaps become filled in exactly in that order, at quite well defined critical wavelengths. Those wavelengths can be readily converted into critical effective quantum numbers n_{hs} , n_{mid} , and n_{pd} . The n_i are robust indicators for the electric field, because they are solely determined by the

general spreading behavior of the quasi-continuous *h*-features. No absolute line strength or line-strength ratio needs to be determined. Near the ionization threshold, the electric field leads to a termination of the Rydberg series at a low value of *n* (45 in Fig. 1) and to continuum lowering.

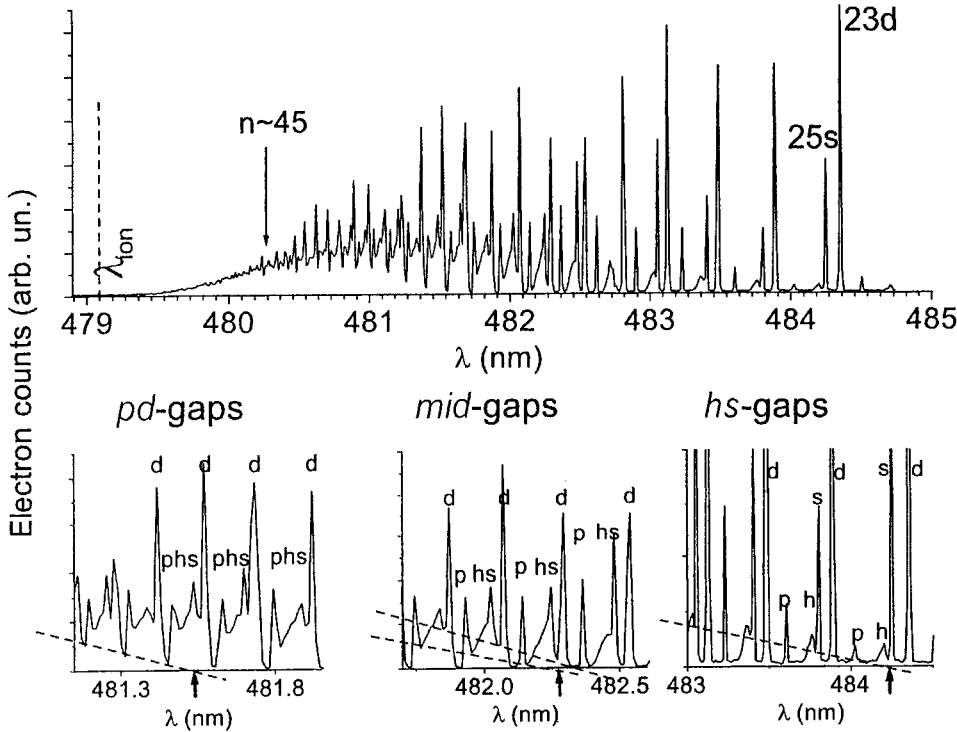


FIGURE 1 Experimental Rydberg excitation spectrum of ^{87}Rb $5P_{3/2}$ -atoms embedded in a laser-generated ion plasma. There exist three types of spectral gaps with low oscillator strength, which we denote *hs*-, *mid*- and *pd*-gaps. Due to the Stark effect, the spectral gaps become filled in at certain critical wavelengths that depend on the strength of the plasma electric field. The detail plots in the lower row show how we determine the critical wavelengths.

The origin of the closing of the spectral gaps becomes evident by a consideration of the Stark map of rubidium. Fig.2 shows that the *hs*-gap below the hydrogenic levels with principal quantum number *n* disappears when the energy shift $-3n^2E/2$ of the most red-shifted hydrogenic state equals the splitting $0.13n^{-3}$ between the unshifted hydrogenic energy $-1/(2n^2)$ and the energy of next-lower *s*-state, $-1/[2(n+0.13)^2]$. There, the numerical value 0.13 is the non-integer part of the *s*-quantum defect of Rb. The gaps between the states $(n+3)s$ and $(n+1)d$ and between the hydrogenic states $(n-1)$ and the states $(n+2)p$ close at practically identical electric fields; we label those gaps *mid*-gaps. Finally, the *pd*-gaps disappear when neighboring hydrogenic manifolds meet, *i.e.* when $3n^2E = n^{-3}$. Thus, the knowledge of the quantum defects is

sufficient to find approximate relations between electric-field strength and the above introduced critical quantum numbers n_{hs} , n_{mid} , and n_{pd} .

The electric field in our approximately Gaussian ion clouds follows a probability distribution, which we have calculated and found to be strongly dominated by a peak around a most probable electric field E_{max} . Using a large set of isotropic excitation spectra of Rydberg atoms in fixed electric fields, and employing the electric-field probability distributions of Gaussian ion clouds as weighting functions, we have calculated model spectra of Rydberg atoms embedded in Gaussian ion clouds. The model spectra, which qualitatively appear identical to the experimental spectrum in Fig.1, have been used to establish the following relationships between the most probable electric field E_{max} and the values of n_{hs} , n_{mid} , and n_{pd} :

$$\begin{aligned} E_{max} &= 0.050 n_{hs}^{-5} \\ E_{max} &= 0.145 n_{mid}^{-5} \\ E_{max} &= 0.260 n_{pd}^{-5} \end{aligned} \quad (1)$$

(field in atomic units).

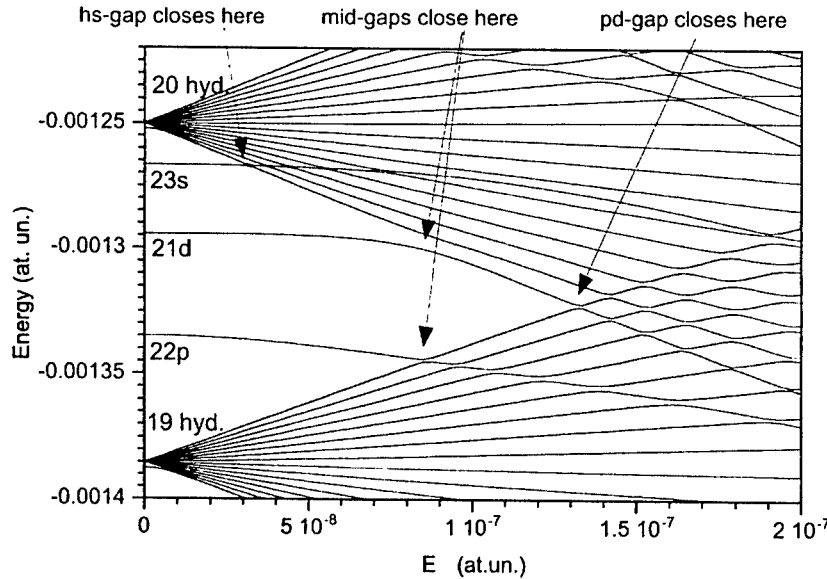


FIGURE 2 Stark map of Rb for magnetic quantum number $m=0$ in the vicinity of the $n=19$ and $n=20$ hydrogenic manifolds.

We have used Eqs.1 to experimentally determine the values of E_{max} in ion clouds with diameters of ~ 1 mm and various ion numbers. The delay time between the UV-pulses used to produce the ions and the blue pulses that excite Rydberg atoms embedded in the ion clouds is 23ns, which is long enough for the UV-generated photoelectrons to

leave, but short enough that no significant Coulomb expansion takes place. The spectra obtained in a few such experiments are displayed in Fig.3, where a typical profile of the ion cloud at the time of its creation is also shown. The critical wavelengths λ_{hs} , λ_{mid} , and λ_{pd} , indicated by arrows in the right panel of Fig.3, have been determined as shown in Fig.1. Using the ionization wavelength of rubidium, $\lambda_{ion}=479.1\text{nm}$, the corresponding critical quantum numbers n_{hs} , n_{mid} , and n_{pd} are obtained from

$$\left(\frac{1}{\lambda_{ion}} - \frac{1}{\lambda_i} \right) = \frac{0.010974\text{nm}^{-1}}{n_i^2}, \quad (2)$$

where $i=hs, mid$ or pd . Then, using Eqs.1, for each spectrum up to three spectroscopic measurements of E_{max} are obtained. The relative uncertainty of each single electric-field value is $\sim 30\%$. Within that uncertainty, the different electric-field values obtained for the individual spectra agree well. The electric-field values quoted in Fig.3 are the averages over all field values obtained for the respective spectra.

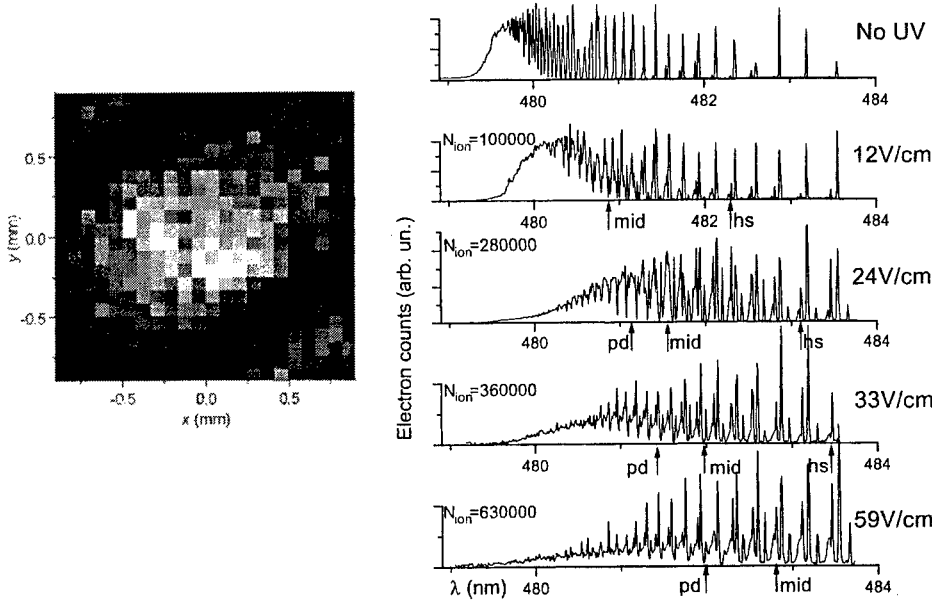


FIGURE 3

Left: Area density distribution of a typical ion cloud. The image is obtained by taking the difference between the atomic area density before and after the UV pulse. The atomic density distributions are measured by absorptive atom cloud imaging. The gray scale of the image ranges from 0 (black) to $4.5 \times 10^7 \text{ cm}^{-2}$ (white).

Right: Excitation spectra of ^{87}Rb $5P_{3/2}$ -atoms embedded in mm-sized photo-excited plasmas that contain the indicated approximate numbers of Rb^+ -ions, N_{ion} . The most probable electric fields E_{max} , shown on the right, are determined spectroscopically and carry an uncertainty of about 20%.

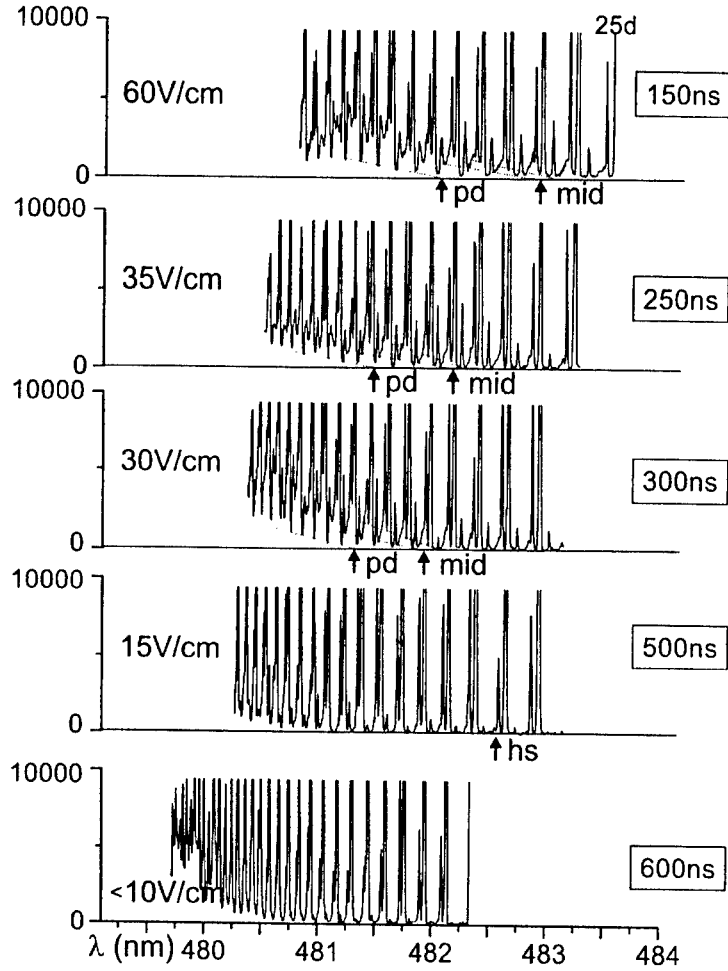


FIGURE 4 Excitation spectra of ^{87}Rb $5P_{3/2}$ -atoms embedded in mm-sized photo-excited plasmas for the indicated delay times between the UV and the blue laser pulse. The most probable plasma electric fields E_{max} , shown on the left, are determined from the spectra and carry an uncertainty of about 20%.

Since we can vary the delay time between the UV and the blue pulse over a range of about $10\mu\text{s}$ with a precision of 10ns, the presented method of electric-field measurement is time-sensitive. Further, since the Rydberg excitation is a two-step resonant process, we can, in principle, measure the electric field vector with high spatial resolution by using crossed focused laser beams with adjustable polarizations. Temporally and spatially resolved measurements of the electric field will be an excellent tool to study the electric-field distribution, the plasma microfields (which may reveal ion ordering), and the dynamics of the plasma expansion. As a first step in that direction, we have varied the delay time between the UV and the blue pulse. A typical result, shown in Fig.4, demonstrates that the most probable electric field E_{max}

decays over a time of order 500ns, which shows that the Coulomb explosion of the plasma cloud takes about 500ns.

ACKNOWLEDGMENTS

We acknowledge support by the NSF (Grant PHY-9875553) and partial support by the Chemical Sciences, Geosciences and Biosciences Division of the Office of Basic Energy Sciences, Office of Science, U.S. Department of Energy. Support has also been provided by the Optical Physics Interdisciplinary Laboratory (OPIL) and the FOCUS Physics Frontier Center at the University of Michigan. We further thank Prof. P. Bucksbaum for generous loaning of equipment, and B. K. Teo for assistance with the experiment.

REFERENCES

1. Gallagher, T. F., *Rydberg Atoms*, Cambridge University Press, Cambridge 1994.
2. Ducas, T. W., Spencer, W. P., Vaidyanathan, A. G., Hamilton, W. H., Kleppner, D., *App. Phys. Lett.* **35**, 382 (1979), Figger, H., Straubinger, R., Walther, H., Leuchs, G., *Opt. Comm.* **33**, 37 (1980), Gross, M., Goy, P., Fabre, C., Haroche, S., Raimond, J. M., *Phys. Rev. Lett.* **43**, 343 (1979).
3. Neukammer, J., Rinneberg, H., Vietzke, K., Koenig, A., Hieronymus, H., Kohl, M., Grabka, H.-J., Wunner, G., *Phys. Rev. Lett.* **59**, 2947 (1987).
4. *Cavity Quantum Electrodynamics*, edited by P. R. Berman, Academic Press, Inc., San Diego 1994.
5. Ganguly, B. N., *J. Appl. Phys.* **6**, 571 (1986), Shoemaker, J. R., *et al.*, *Appl. Phys. Lett.* **52**, 2019 (1988), Hebner, G. A., *et al.*, *J. Appl. Phys.* **76**, 4036 (1994).
6. Killian, T. C., *et al.*, *Phys. Rev. Lett.* **83**, 4776 (1999).
7. Dutta, S. K., Feldbaum, D., Walz-Flannigan, A., Guest, J. R., Raithel, G., *Phys. Rev Lett.* **86**, 3993 (2001).

Ultracold Neutral Plasmas

T. C. Killian*, M. J. Lim†, S. Kulin† and S. L. Rolston†

*Rice University, Department of Physics and Astronomy, Houston, TX 77005

†National Institute of Standards and Technology, Gaithersburg, MD 20899-8424

Abstract. By photoionizing a sample of laser-cooled xenon atoms, we create ultracold neutral plasmas with initial temperatures of 1-1000 K and densities as high as 10^{10} cm^{-3} . The plasma is formed by the trapping of electrons by the residual positive charge that is left after some electrons initially leave the sample. We excite plasma oscillations with applied radio frequency fields and use this to monitor the expansion of the unconfined plasma. We have observed significant recombination of the plasma into Rydberg atoms (up to 20 %). At these low temperatures, the only traditional form of recombination that could be significant is three-body recombination (TBR), but we see a number of trends in direct contradiction to what one would expect from classical TBR theory.

Recent experiments conducted at the National Institute of Standards and Technology in Gaithersburg have opened a new regime of ultracold neutral plasmas with temperatures as low as a 1 K. Studies of the methods and conditions for forming the plasma[1], excitation and detection of plasma oscillations[2], dynamics of the plasma expansion[2], and collisional recombination into Rydberg atomic states[3] have demonstrated that ultracold neutral plasmas provide a powerful and flexible environment in which to test our fundamental understanding of plasmas physics.

The recipe for an ultracold neutral plasma starts with laser-cooled and trapped neutral atoms[4]. In a table-top apparatus, with a proper configuration of laser beams and magnetic fields, a few million atoms are laser cooled to approximately $10 \mu\text{K}$. The peak density is about $2 \times 10^{10} \text{ cm}^{-3}$ and the spatial distribution of the cloud is Gaussian with an rms radius $\sigma \approx 200 \mu\text{m}$. Many different elements can be laser cooled, and ultracold plasma experiments at NIST were performed with metastable xenon. More information on laser cooling and trapping of metastable xenon can be found in [5].

To produce the plasma, atoms are photoionized barely above threshold with a narrow-bandwidth pulsed laser. The kinetic energy of the original neutral atoms is negligible, so the energetics of the plasma is entirely determined by the photoionization process. Because of the small electron-ion mass ratio, the electrons have an initial kinetic energy (E_e) approximately equal to the difference between the photon energy and the ionization potential. E_e/k_B can be as low as the bandwidth of the ionizing laser, which is $\sim 100 \text{ mK}$ with standard pulsed dye lasers, but most studies so far have dealt with E_e/k_B between 1 and 1000 K. The initial kinetic energy for the ions is in the mK range.

Immediately after photoionization, the charge distribution is everywhere neutral. Due to the kinetic energy of the electrons, the electron cloud expands, but on this time scale the ions are essentially immobile. The resulting local charge imbalance creates an internal electric field that produces a Coulomb potential energy well for electrons. If the well never becomes deeper than E_e , all the electrons escape. If enough atoms are

photoionized, however, only an outer shell of electrons escapes, and the well becomes deep enough to trap the rest. After the untrapped fraction has escaped, the cloud as a whole is no longer strictly neutral. Simulations show that electrons escape most easily from the edges of the spatial distribution, however, and the center of the cloud is well described as a neutral plasma.

The number of atoms ionized (N_i), and thus the density of the plasma (n), is controlled by varying the energy of the photoionizing laser pulse. Lower E_e and higher N_i lead to a greater fraction of the initially created electrons being trapped. For the coldest and densest conditions, over 90% of the electrons are confined.

For a given E_e there is a threshold number of positive ions required for trapping electrons. This threshold was demonstrated and studied in [1]. Theoretically and experimentally, it can be shown that trapping occurs when the Debye screening length, $\lambda_D = \sqrt{\epsilon_0 k_B T_e / e^2 n}$, becomes less than the size of the sample σ . Here, ϵ_0 is the electric permittivity of vacuum, k_B is the Boltzmann constant, and e is the elementary charge. The electron temperature, T_e , is approximately equal to E_e / k_B [6]. An ionized gas is normally not considered a plasma unless the Debye length is smaller than the size of the system [7], so the threshold for electron trapping is also the threshold for the formation of a plasma. In our experiment, the Debye length can be as low as 500 nm, while the size of the sample is $\sigma \approx 200 \mu\text{m}$. The condition $\lambda_D < \sigma$ for creating a plasma is thus easily fulfilled. Electron trapping can also be interpreted as a form of ambipolar diffusion.

Figure 1a shows electron signals from an ultracold neutral plasma created by photoionization at time $t = 0$. A small DC field (about 1 mV/cm) directs free electrons to a single channel electron multiplier for detection. The first peak at about 1 μs represents electrons that leave the sample and create the charge imbalance and Coulomb potential well. On a longer time scale, the plasma expands and the depth of the Coulomb well decreases, allowing the remaining electrons to leave the trap. This produces the broad peak at $\sim 25 \mu\text{s}$. Colder and denser plasmas survive for as long as 300 μs before all the electrons escape.

It is possible to perform experiments on the system during the expansion. In [2], plasma oscillations were excited during this time interval by applying a radio frequency (rf) electric field to the plasma. The oscillations were used to map the plasma density distribution and reveal the particle dynamics and energy flow during the expansion of the ionized gas.

In the absence of a magnetic field, the frequency of plasma oscillations is given by $f_e = (1/2\pi) \sqrt{e^2 n_e / \epsilon_0 m_e}$ [8], where n_e is the electron density and m_e is the electron mass. This expression is valid in a homogeneous medium and for excitations localized in regions of constant density in a spherically symmetric plasma. Discussions during the conference highlighted the need for a detailed analysis of the mode structure of plasma oscillations in this system, but we have so far assumed that we excite localized modes during our experiment.

Plasma oscillations with frequencies from 1 to 250 MHz have been observed, corresponding to resonant electron densities, n_r , between $1 \times 10^4 \text{ cm}^{-3}$ and $8 \times 10^8 \text{ cm}^{-3}$. There are small corrections to the expression for f_e due to finite temperature [9] and strong coupling [10, 11]. These were neglected in the analysis of [2], but if these effects could be observed and measured, they would provide a great deal of information on the

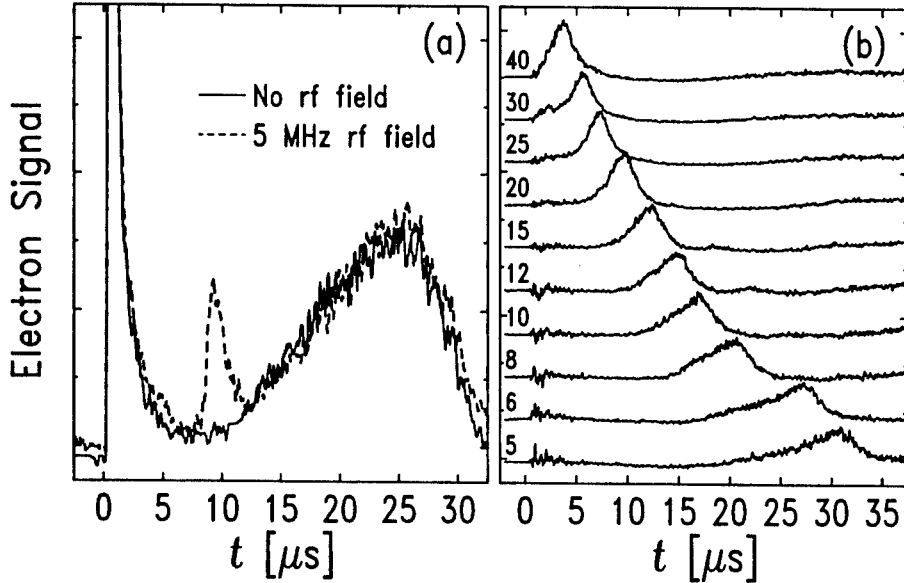


FIGURE 1. Electron signals from ultracold plasmas created by photoionization at $t = 0$. (a) 3×10^4 atoms are photoionized and $E_e/k_B = 540$ K. If an rf field is applied during the expansion, resonant excitation of plasma oscillations produces an extra peak on the electron signal. (b) 8×10^4 atoms are photoionized and $E_e/k_B = 26$ K. For each trace, the rf frequency in MHz is indicated, and the nonresonant response has been subtracted. The signals have been offset for clarity. The resonant response arrives later for lower frequency, reflecting expansion of the plasma. For 40 MHz, $n_r = 2.0 \times 10^7 \text{ cm}^{-3}$, and for 5 MHz, $n_r = 3.1 \times 10^5 \text{ cm}^{-3}$.

dynamics of ultracold neutral plasmas and perhaps on the physics of two-component strongly coupled systems.

The applied rf field efficiently excites plasma oscillations and pumps energy into the electron gas when the frequency is resonant with the average density in the plasma (\bar{n}). Collisions redistribute this energy and heat the electrons. This increases the evaporation rate of electrons out of the Coulomb well, which produces the plasma oscillation response on the electron signal (Fig. 1a). The resonant response arrives later for lower frequency (Fig. 1b) as expected because \bar{n} decreases in time. With some analysis, such data implies that after a few μs the plasma expands with a constant velocity. A hydrodynamic model developed in [2] shows that the pressure of the electron gas drives the expansion, and the expansion velocity is a sensitive probe of the electron thermal energy at early times.

Recombination into Rydberg atoms in an ultracold neutral plasma was studied in [3]. At temperatures ranging from 1-1000 K, and densities from 10^5 - 10^{10} cm^{-3} , up to 20% of the initially free charges recombine on a timescale of $100 \mu s$. Figure 2 is an electron signal from an ultracold neutral plasma that shows the formation of Rydberg atoms. The plasma is formed as described above. After the plasma has expanded so that the ions no longer form a Coulomb well and all free electrons have escaped, the electric field is increased to 120 V/cm in $\sim 100 \mu s$. This field can ionize Rydberg atoms bound by

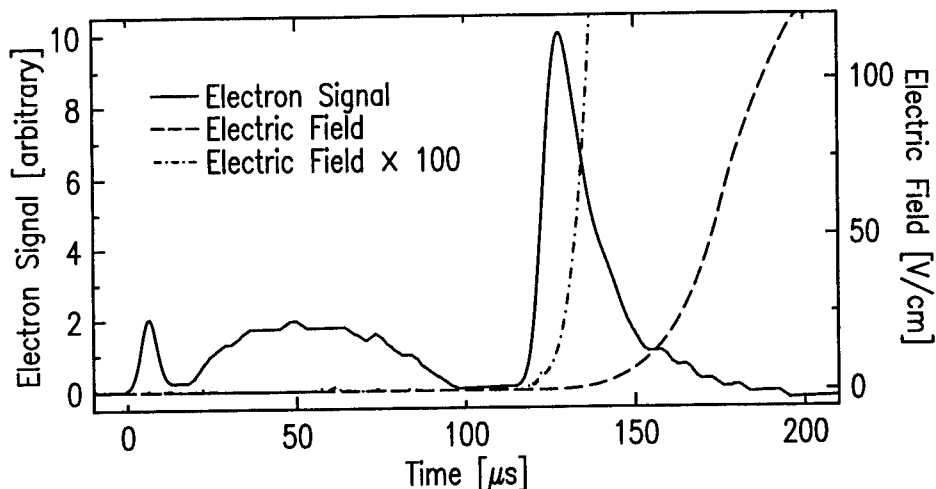


FIGURE 2. Electron signal from a plasma created by photoionizing 10^5 atoms at $t = 0$, with $E_e/k_B = 206$ K. The first and second features represent free electrons escaping from the plasma. The third feature arises from ionization of Rydberg atoms. A 5 mV/cm field is present before the large field ramp commences at about $120 \mu\text{s}$, and the collection and detection efficiency for the first and second features is approximately 10% of the efficiency for electrons from Rydberg atoms.

as much as 70 K, corresponding to a principle quantum number of about $p = 47$. The number of Rydberg atoms formed is inferred from the number of electrons reaching the detector, and the distribution of Rydberg atoms as a function of p is constructed from the fields at which the atoms ionize.

Figure 3 shows typical Rydberg atom data. As N_i increases, or E_e decreases, a greater fraction of charges recombine and the Rydberg atom distribution shifts toward more deeply bound levels. The integral of each curve yields the total number of Rydberg atoms formed. The expected rates for radiative recombination or dielectronic recombination are many orders of magnitude too low to account for the observed Rydberg atom formation. We turn to three-body recombination (TBR), which is expected to dominate at ultracold temperatures.

Models of population distributions in equilibrium plasmas take into account TBR, collisional ionization, and collisional and radiative population redistribution. They predict a density-independent maximum in the Rydberg atom distribution at levels bound by a few $k_B T$ [12]. This contradicts the trend observed in this experiment toward more deeply bound levels as N_i increases or E_e decreases (Fig. 3).

Another surprising result was found by measuring Rydberg atom distributions at various times after photoionization. Most of the Rydberg atoms form $20 - 100 \mu\text{s}$ after photoionization. By this time the plasma density has decreased three to four orders of magnitude below its initial peak value. A naive application of standard TBR theory implies that to maintain such a high recombination rate during this expansion, the temperature would have to drop below 1 mK. Evaporative cooling due to the escape of electrons from the edge of the plasma, and adiabatic cooling due to the expansion of the

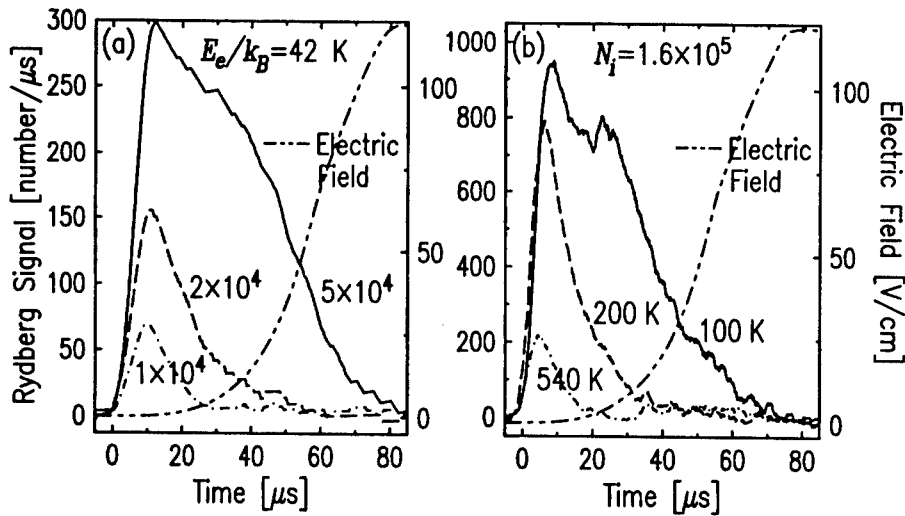


FIGURE 3. Rydberg ionization signals for various plasma conditions approximately 100 μs after photoionization. The time origin is the start of the electric field ramp. (a) Constant $E_e/k_B = 42$ K. N_i is indicated near each curve. (b) Constant $N_i = 1.6 \times 10^5$. E_e/k_B is indicated near each curve.

system could produce such extreme cooling. This is an exciting possibility. At such a low temperature the system would have an electron Coulomb coupling parameter $\Gamma_e \approx 300$. Single-component systems with such strong coupling behave as solids and minimize their potential energy by forming Wigner crystals [13]. If the cooling is less extreme, perhaps recombination in expanding ultracold plasmas proceeds through a qualitatively different mechanism than TBR. Liquid-like spatial correlations between particles should develop in the plasma as it cools to $\Gamma_e \approx 1$. Through a many-body process, spatially correlated ions and electrons could freeze out during plasma expansion, resulting in Rydberg atoms. A detailed model of the thermodynamics of the expanding plasma, or an experimental probe of the temperature of the electrons is needed to explore these possibilities.

These studies have demonstrated the fascinating behavior of ultracold neutral plasmas. The work on recombination clearly shows that much more needs to be done in order to understand this system, and also that improved diagnostics of temperature and density would be of great value. This is especially important for studying spatial correlations and looking for strong coupling in the two-component system. O'Neil at this conference and others [14] have found in simulations that electrons in ultracold neutral plasmas initially heat to $\Gamma_e \lesssim 1$ within a few plasma oscillation periods. Murillo [15] found that ions reach equilibrium in a liquid state. Currently, simulations are difficult to carry out for the longer time scales of the plasma expansion.

REFERENCES

1. T. C. Killian, S. Kulin, S. D. Bergeson, L. A. Orozco, C. Orzel, and S. L. Rolston, *Phys. Rev. Lett.* **83**, 4776 (1999).
2. S. Kulin, T. C. Killian, S. D. Bergeson, and S. L. Rolston, *Phys. Rev. Lett.* **85**, 318 (2000).
3. T. C. Killian, M. Lim, S. Kulin, S. D. Bergeson, and S. L. Rolston, submitted *Phys. Rev. Lett.*
4. H. J. Metcalf and P. van der Straten, *Laser Cooling and Trapping*, (Springer, New York, 1999).
5. M. Walhout, H. J. L. Megens, A. Witte, and S. L. Rolston, *Phys. Rev. A* **48**, R879 (1993).
6. As discussed later in the paper, theoretical results indicate that when the system's initial density and kinetic energy correspond to the region of strong coupling for a single component system in thermal equilibrium, the charged particles heat rapidly as potential energy associated with disorder is converted into kinetic energy.
7. F. F. Chen, *Introduction to Plasma Physics*, (Plenum Press, New York, 1974).
8. L. Tonks and I. Langmuir, *Phys. Rev.* **33**, 195 (1929).
9. D. Bohm and E. P. Gross, *Phys. Rev.* **75**, 1851 (1949).
10. Charged particles in a plasma are strongly coupled when their thermal energy is less than the Coulomb interaction energy between nearest neighbors. The situation is characterized quantitatively by the Coulomb coupling parameter, $\Gamma_x = (Z_x^2 e^2 / 4\pi\epsilon_0 a_x) / k_B T_x$, where Z_x is the charge of species x , $a_x = (4\pi n_x / 3)^{-1/3}$ is the Wigner-Seitz radius for density n_x , and T_x is the temperature. In a one-component strongly coupled plasma, $\Gamma > 1$ for only one species. In a two-component strongly coupled system, $\Gamma > 1$ for positive and negative charges. For the highest density and lowest temperature ultracold neutral plasmas produced, both electrons and ions are initially strongly coupled.
11. G. Kalman, K. I. Golden, and M. Minella, in *Strongly Coupled Plasma Physics*, edited by H. M. Van Horn, and S. Ichimaru, (University of Rochester Press, Rochester, 1993), p. 323.
12. J. Stevefelt, J. Boulmer, and J-F. Delpech, *Phys. Rev. A* **12**, 1246 (1975).
13. For a review see *Invited and Tutorial Papers from the 40th Annual Meeting of the Division of Plasma Physics of the APS*, Special Issue of *Phys. Plasmas* **6** (1999).
14. A. N. Tkachev and S. I. Yavlenko, *Quantum Electronics* **30**, 1077 (2000).
15. M. S. Murillo, *Phys. Rev. Lett.* **87**, 115003-1 (2001).

Numerical Simulation of Ultracold Plasmas

Stanislav G. Kuzmin and Thomas M. O'Neil

Physics Department, University of California at San Diego, La Jolla CA 92093-0319 USA

Abstract.

In recent experiments, ultracold neutral plasmas were produced by photoionizing small clouds of laser-cooled atoms. It has been suggested that the low initial temperature of these novel plasmas leads directly to strong correlation and order. In contrast, we argue that rapid intrinsic heating raises the electron temperature to the point where strong correlation cannot develop. The argument is corroborated by a molecular dynamics simulation of the early time plasma evolution.

In these proceedings, Killian *et al.* describe an interesting new type of plasma: small, ultracold, neutral, plasma clouds. The plasmas are produced by rapidly photoionizing small laser cooled clouds of neutral atoms [1, 2, 3]. The energy (or frequency) of the ionizing photons is adjusted to barely exceed the ionization energy of the atoms.

These novel plasmas present interesting challenges to theory. For example, it has been suggested that the low initial temperature leads to strong correlation and order [1]. In contrast, we argue that rapid intrinsic heating raises the electron temperature to the point where strong correlation cannot develop.

The basic idea is easy to understand physically. For a plasma in thermal equilibrium, the strength of correlation is determined by the coupling parameter $\Gamma = e^2/akT$, where a is the Wigner-Seitz radius (i.e., $4\pi a^3 n/3 = 1$). For the maximum density and lowest electron temperature reported in the experiments [i.e., $n \simeq 2 \times 10^9 \text{ cm}^{-3}$ and $T_e \simeq 0.1 \text{ K}$], the electron coupling parameter has the value $\Gamma_e \simeq 30$, and the ion coupling parameter is much larger. Thus, one might expect the low temperatures to lead to strong correlation.

However, the plasma is not created in a state of thermal equilibrium. Before photoionization, the neutral atoms are uncorrelated, so immediately after photoionization ion-ion and electron-electron correlations are negligible. There may be some electron-ion correlation that remains as an artifact of the ionization process, but this is not a thermal equilibrium correlation. For example, there is no long range order.

Thermal equilibrium correlations can develop only through the action of Coulomb interactions as the plasma evolves. However, as the correlations begin to develop, the correlation energy is released to the electron plasma as heat, and this limits the strength of correlation reached. To reach a correlation strength corresponding to $\Gamma_e \simeq 1$, each electron picks up thermal energy $kT_e \simeq e^2/a$. At this point the coupling parameter has the value

$$\Gamma_e = e^2/akT_e \simeq (e^2/a)/(e^2/a) = 1,$$

so further development of correlation ceases. Even if the initial electron temperature were zero, corresponding formally to infinite Γ_e , strong correlation would not develop.

Heating associated with the liberation of correlation energy also was considered by Murillo [4]. However, he treats the electrons only as a dielectric fluid that Debye shields the interaction between the ions. His analysis focuses on the liberation of correlation energy for a system of Debye shielded ions. Unfortunately, this approach misses the electron heating that dominates the early stages of evolution.

Another way to understand the electron heating is to note that electrons are born in a spatially varying potential, and immediately begin to move downhill. A typical electron picks up kinetic energy e^2/a while moving an interparticle spacing, a . The time scale for this initial heating is approximately $a/\sqrt{e^2/am_e} \sim \omega_p^{-1}$, where ω_p is the plasma frequency.

This heating is the beginning of the collisional process by which the plasma approaches a state of thermal equilibrium. For the low temperatures of these plasmas the thermal equilibrium state is a recombined neutral gas. The collisional cascade of electrons to deeper and deeper binding in the Coulomb wells of ions is called three-body recombination [5]. In this process, the recombination energy is carried off by a second electron (rather than a photon) and enters the plasma as heat. For these plasmas, three-body recombination is very rapid—much faster than radiative recombination. Although three-body recombination is not the focus of this paper, our simulation must include this physics since the heating is a byproduct of the recombination. The initial recombination is into weakly bound (high n Rydberg states), so a classical molecular dynamics simulation captures the essential physics.

The simulation is challenging because the time scale for an electron bound in one of these Rydberg states is much shorter than the time scale for a typical electron. In plasma simulations of this kind some authors have used two time scales: one for particles with near neighbors and another for the remaining particles [6]. Another variant is to use piecewise analytic solutions for Kepler orbits. We prefer a treatment that doesn't make special assumptions about particles with near neighbors, but seamlessly encompasses the continuum of time scales required.

Fortunately, such a treatment was developed previously in computational studies of binary star formation in globular clusters. The binary stars are the analogue of the high n Rydberg atoms, and the cluster is the analogue of the plasma cloud. We have adapted a code developed originally by Aarseth [7] for the study of binary star formation.

The code is a molecular dynamics simulation in the sense that the force on a given particle from each of the other particles is calculated directly. Time integration is effected with a predictor-corrector scheme using a fourth-order polynomial fit to the orbit. The crucial feature is that the time step for each particle is adjusted independently depending on such factors as the rate of change of the acceleration. Thus, a bound electron can have a much shorter time step than a typical electron without slowing down the whole simulation. To keep all of the particles moving in near synchrony, the code advances next the time step for the particle that is furthest behind in absolute time. To evaluate the force on this particle, the other particle positions are extrapolated back in time to exact synchrony using the polynomial fit to the orbits.

By using properly scaled length and time, the number of parameters that define a simulation is reduced to a minimum. Here length is scaled by the Wigner-Seitz radius a and time by the inverse of the plasma frequency ω_p^{-1} . With these scalings, the equations

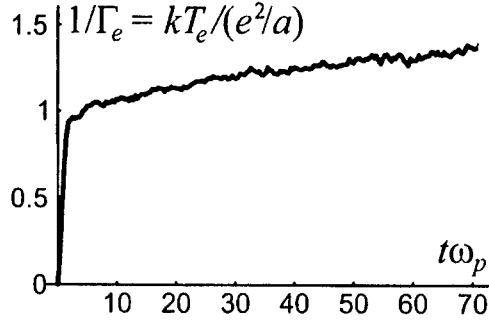


FIGURE 1. Scaled temperature versus scaled time.

of motion and initial conditions are specified by four parameters: the mass ratio m_i/m_e , the number of electrons (which is equal to the number of ions) N , the initial value of the coupling parameter Γ_e , and a rounding parameter ϵ for the Coulomb potential.

To avoid singularities, the Coulomb potential is rounded to the form

$$1/\sqrt{|\mathbf{r}_1 - \mathbf{r}_2|^2/a^2 + \epsilon^2}$$

where $\epsilon \ll 1$. For this simulation ϵ is chosen to have the value $1/31$, and this value is small enough that the rounded potential is a good approximation to the Coulomb potential for the vast majority of particles. For a few deeply bound pairs, the approximation is marginal [e.g., $1/\epsilon = 31$ and $\max[E_{\text{binding}}/(e^2/a)] \simeq 25$], but these deeply bound pairs are not the focus of this investigation.

To give correlations the maximum opportunity to develop, the initial electron temperature and the initial ion temperature are taken to be zero, corresponding to $\Gamma_e(t=0) = \infty$ and $\Gamma_i(t=0) = \infty$.

The mass ratio is chosen to have the value $m_i/m_e = 100$. This relatively low value insures that the ions have time to participate in the correlation dynamics during the course of the simulation. The electron-electron correlation function relaxes to a steady-state form in a few scaled time units, and the ion-ion correlation function in a time that is longer by $\sqrt{m_i/m_e} = 10$. The simulation runs for $t_{\text{max}}\omega_p = 70.9$ scaled time units and energy is conserved to an accuracy of 0.1%.

So that the correlation function takes the simple form $G(\mathbf{r}_1, \mathbf{r}_2) = G(|\mathbf{r}_1 - \mathbf{r}_2|)$, we arrange the initial and boundary conditions to insure uniform plasma density. Specifically, 4096 electrons and 4096 ions are distributed randomly inside a spherical volume bounded by a reflecting wall. The correlation measurements are made well away from the wall. In scaled units, the radius of the sphere is determined by the number of electrons, $(r_s/a)^3 = N$.

The initial density profiles for the experimentally produced plasma clouds were Gaussian [1, 2, 3]. One should think of the uniform density spherical plasmas as a small central section of a larger Gaussian cloud.

Figure 1 shows a plot of the scaled temperature [i.e., $1/\Gamma_e(t) = kT_e(t)/(e^2/a)$] versus the scaled time $t\omega_p$. To obtain this plot, histograms of electron kinetic energies are

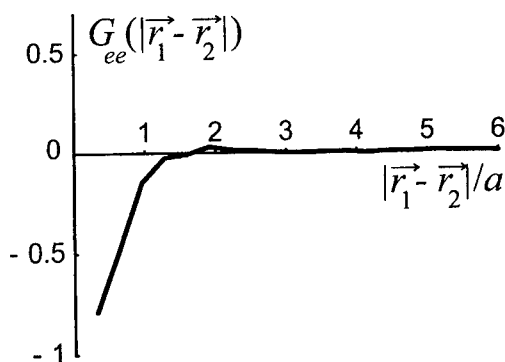


FIGURE 2. Electron-electron correlation function, averaged from $t\omega_p = 3.5$ to $t\omega_p = 7.1$.

made (excluding tightly bound electrons) and matched to Maxwellians. Rapid heating to $\Gamma_e \simeq 1$ is clearly visible. The longer-term slower heating is associated with three-body recombination.

Figure 2 shows the electron-electron correlation function averaged over the time interval $t\omega_p = 3.5$ to 7.1 . The correlation function starts out flat, corresponding to randomly distributed electrons, but quickly relaxes to the form shown in Fig. 2 and retains this form. The only change with increasing time is in the width of the region near $|\mathbf{r}_1 - \mathbf{r}_2| = 0$ where $G_{ee} \simeq -1$. This value for G_{ee} reflects the fact that it is energetically unfavorable for two electrons to be at the same location, and the width of the region is of order $|\mathbf{r}_1 - \mathbf{r}_2| \simeq e^2/kT_e$. In measurements of G_{ee} at later times the width is observed to decrease as the plasma temperature slowly increases.

For comparison, Fig. 3 shows the correlation function for a one component plasma in thermal equilibrium at correlation strengths $\Gamma = 1, 10, 20$, and 40 [8]. As expected, the correlation curve in Fig. 2 corresponds in shape to the $\Gamma = 1$ curve in Fig. 3. The curves in Fig. 3 for $\Gamma = 10, 20$, and 40 exhibit oscillations indicating the presence of local order, that is, of a local lattice. The lack of these oscillations in Fig. 2 shows that such order is missing in the electron distribution for the ultracold plasma.

Figure 4 shows the ion-ion correlation function averaged over the time interval $t\omega_p = 67.4$ to 70.9 . Again the correlation function starts out flat and relaxes to the form shown, although the relaxation time is longer than for the electrons. The absence of oscillations shows that local order is missing.

Figure 5 shows the electron-ion correlation function averaged over the time interval $t\omega_p = 3.5$ to 7.1 . In this case, G_{ei} is positive near $|\mathbf{r}_1 - \mathbf{r}_2| = 0$, since it is energetically favorable for an electron to be near an ion. However, this positive electron-ion correlation is not an indication of the local order characteristic of strong correlation; rather it reflects the beginning of recombination.

For this simulation, we see that intrinsic rapid heating prevents the development of strong correlation (order) even though the initial electron and ion temperatures are zero [i.e., $\Gamma_e(0) = \Gamma_i(0) = \infty$]. However, one might worry that the result is a consequence of the low mass ratio or of the reflecting wall boundary conditions. After all, electron

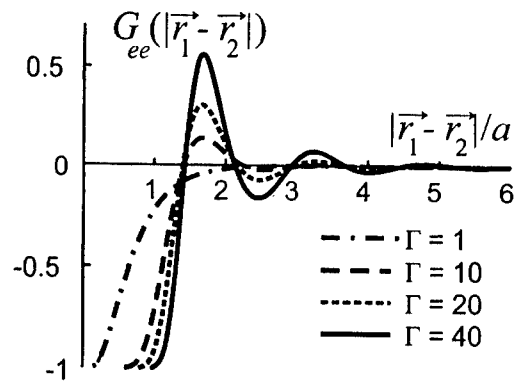


FIGURE 3. Correlation function for one component plasma.

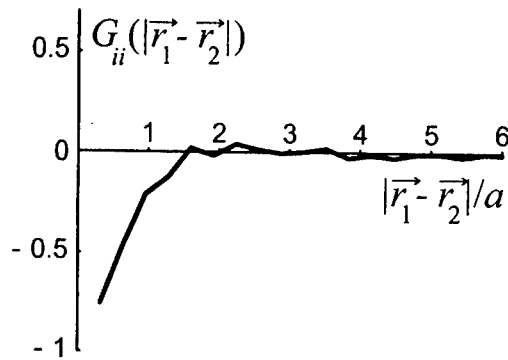


FIGURE 4. Ion-ion correlation function averaged over the time interval $t\omega_p = 67.4$ to $t\omega_p = 70.9$.

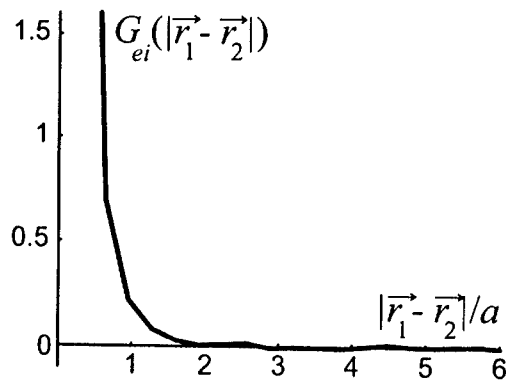


FIGURE 5. Electron-ion correlation function averaged over the time interval $t\omega_p = 3.5$ to 7.1 .

evaporation from an unbounded cloud is a cooling mechanism. Consequently, we carried out an extensive simulation for 4096 electrons and 4096 ions in an unbounded cloud with a Gaussian initial density distribution and a realistic mass ratio (for Xe ions). Again, we observed the rapid initial heating to $\Gamma_e \simeq 1$ followed by slower heating due to three-body recombination. The evaporative cooling could not compete with the heating.

One important caveat is that the simulations follow only the early time evolution of the plasma. Later, the plasma undergoes expansion, and this can be a strong cooling mechanism that reduces the temperature. Our studies imply only that the initial low temperatures do not directly lead to strong correlation and order during early times.

Finally, we note that the experiments themselves provide some evidence against early strong correlation. The plasma expansion is driven by the electron pressure, but the effective pressure becomes negative for a strongly correlated plasma [9]. If there were no intrinsic heating and the cloud were strongly correlated, the pressure would be negative and the cloud would not expand.

ACKNOWLEDGMENTS

The authors thank Professor J. Kuti for suggesting the Aarseth molecular dynamics simulation. This work was completed with the support of National Science Foundation grant PHY-9876999.

REFERENCES

1. T.C. Killian, S. Kulin, S.D. Bergeson, L.A. Orozco, C. Orzel, and S.L. Rolston, Phys. Rev. Lett. **83**, 4776 (1999).
2. S. Kulin, T.C. Killian, S.D. Bergeson, and S.L. Rolston, Phys. Rev. Lett. **85**, 318 (2000).
3. T.C. Killian, M. Lim, S. Kulin, S.D. Bergeson, and S.L. Rolston, Phys. Rev. Lett. **86**, 3759 (2001).
4. M.S. Murillo, Phys. Rev. Lett. **87** 11503 (2001).
5. P. Mansbach and J. Keck, Phys. Rev. **181**, 275 (1969).
6. G. Zwicknagel, D. Klakow, P.G. Reinhard, and C. Toepffer, Contrib. Plasma Phys. **33**, 395 (1993).
7. S.J. Aarseth, "Direct methods for N-Body simulations," in *Multiple Time Scales*, edited by J.U. Brackbill and B.I. Cohen, Academic Press, Publisher, New York, 1985, p. 377.
8. D.H.E. Dubin, private communication.
9. D.H.E. Dubin and T.M. O'Neil, Rev. Mod. Phys. **71**, 87 (1999).

SECTION 2

STRONGLY COUPLED PLASMAS, HIGHLY CHARGED IONS, AND DUSTY PLASMAS

Experimental Dynamics of Stressed, Strongly Correlated Magnetized Plasmas

T. B. Mitchell*, J. J. Bollinger[†], W. M. Itano[†] and D. H. E. Dubin**

^{*}Department of Physics and Astronomy, University of Delaware, Newark, DE 19716

[†]Time and Frequency Division, National Institute of Standards and Technology, Boulder, CO 80305

^{**}Department of Physics, University of California at San Diego, La Jolla, CA 92093

Abstract. We study the control of the rotation of a laser-cooled ion crystal in a Penning trap by a rotating electric field perturbation. We show that application of a small torque produces sudden angular jumps or ‘slips’ of the crystal orientation spaced by intervals when the crystal is phase-locked or ‘stuck’ relative to the rotating perturbation. The distribution of angular slips is described by a power law, where the power-law exponent depends on the applied torque. We believe this system is driven by a constant force and that small perturbations or thermal effects trigger the slips.

Non-neutral plasmas confined in Penning-Malmberg traps are used in a variety of experiments including plasma physics, Coulomb crystal studies, precision spectroscopy, antimatter research, and storage of highly charged ions [1]. Recently there has been a great deal of interest in using a rotating electric field perturbation to control the global $\mathbf{E} \times \mathbf{B}$ rotation of these plasmas [2, 3, 4]. For crystallized ion plasmas, phased-locked control of the plasma rotation has been demonstrated [4], which has important implications for atomic clocks [5] and for quantum computation with trapped ions [6].

In this manuscript we study the limits to phase-locked control due to the application of a small torque produced by the radiation pressure of a weak laser beam. We observe sudden angular jumps or ‘slips’ of the crystal orientation spaced by intervals when the crystal orientation is phase-locked or ‘stuck’ relative to the rotating perturbation. Stick-slip behavior similar to that observed here is found in many different and diverse systems: for example, in studies of friction between two surfaces [7, 8], in experiments on avalanches and slips in granular systems [9, 10, 11], and as the underlying process in spring-block models of earthquakes [12, 13]. Many of these systems, including the study presented here, exhibit a power-law distribution of the slip amplitudes, indicative of an underlying critical point [14, 15].

Our work uses the Penning-Malmberg trap at NIST to store $\sim 20,000$ $^9\text{Be}^+$ ions. The ions interact by unscreened Coulomb repulsion and are Doppler laser-cooled [16] to millikelvin temperatures, where they become strongly coupled. The degree of coupling is quantified by the Coulomb coupling parameter,

$$\Gamma \equiv \frac{1}{4\pi\epsilon_0} \frac{e^2}{a_{\text{ws}} k_B T}, \quad (1)$$

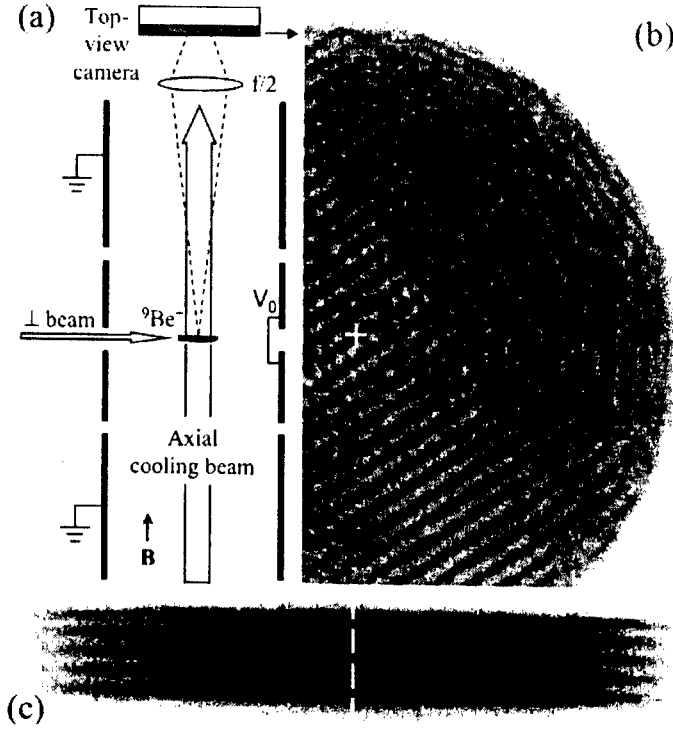


FIGURE 1. (a) Schematic of the cylindrical Penning trap and the top-view imaging system. The side-view imaging system is not shown. (b) Strobed top-view image of a 5 axial plane $^9\text{Be}^+$ ion crystal with a bcc structure, similar to those used in this study. (c) Side-view image (unstrobed) of the same ion crystal. The diameter ($2r_{\text{Be}}$) of the $^9\text{Be}^+$ ions is $495 \mu\text{m}$. Ions of greater mass are located at $r > r_{\text{Be}}$ but do not fluoresce in the laser beam. The rotation axes are indicated.

which is the ratio of the Coulomb potential energy of neighboring ions to the kinetic energy per ion. Here, ϵ_0 is the permittivity of the vacuum, e is the charge of an ion, k_B is Boltzmann's constant, T is the temperature, and a_{WS} is the Wigner-Seitz radius, defined by $4\pi(a_{\text{WS}})^3/3 = 1/n_0$, where n_0 is the ion number density. With coupling parameters greater than $\Gamma \simeq 1$ the ions are strongly coupled [17], and when $\Gamma \geq 172$ they form a Coulomb crystal (a classical Wigner crystal) [18, 19]. Structurally similar Coulomb crystals are believed to exist in dense astrophysical matter, such as the interior of white dwarfs and the outer crust of neutron stars [20]. Interestingly, observations of power-law statistics of soft γ -ray (SGR) events have recently been interpreted as evidence that the Coulomb crystal comprising the outer crust of a magnetized neutron star can undergo very large-scale slips ('starquakes') [21, 22]. The measured power law exponents of the neutron starquakes lie within the range of exponents we measure here (see Fig. 3).

Figure 1(a) shows the experimental setup [4, 19]. We create $^9\text{Be}^+$ ions by ionizing ^9Be atoms in a separate trap (not shown) and then transferring the ions to the main trap for experimentation [23]. The $^9\text{Be}^+$ ions were confined radially by a uniform magnetic

field $B=4.465$ T (cyclotron frequency $\Omega_c/2\pi = 7.608$ MHz) in the \hat{z} direction and axially by a potential difference of $V_0 = -500$ V applied between the center and end electrodes of the trap. Near the trap center the trap potential is quadratic and given by $m\omega_z^2(z^2 - r^2/2)/(2e)$, where the axial frequency $\omega_z/2\pi = 565$ kHz for ${}^9\text{Be}^+$. Here r and z denote the cylindrical radius and axial coordinates. Due to the axial magnetic field and the radial components of the ion space charge and trap electric fields, the ion crystal rotates at a frequency ω_r about the trap symmetry axis \hat{z} .

In our work the plasma has had sufficient time to evolve to a thermal equilibrium state where its rotation and density is uniform across the cloud [24]. For 20,000 trapped ions with $\omega_r/2\pi = 22.8$ kHz (typical of this work), the ion plasma has a density of 7.1×10^7 cm^{-3} and a lenticular shape with a radial diameter $2r_0 \approx 1$ mm and an aspect ratio $\alpha = z_0/r_0 \approx 0.05$. Here, $2z_0$ denotes the axial extent of the plasma at $r = 0$. In addition to ${}^9\text{Be}^+$ ions, ions of greater mass ('heavy ions') such as BeH^+ and BeOH^+ are created by reactions with ${}^9\text{Be}^+$ ions and background neutral molecules. For the work discussed here, typically 20 % to 50 % of the plasma consisted of heavy impurity ions. These ions are sympathetically cooled to temperatures similar to the ${}^9\text{Be}^+$ ions and, due to the rotation, centrifugally separate to larger radii, where they crystallize [25, 26].

To control ω_r , we applied an electric field perturbation rotating about the \hat{z} axis at frequency ω_{rp} [4]. The rotating perturbation applies a torque on the radial boundary of the plasma (on the non-fluorescing, heavy ions) by creating a small-amplitude traveling wave. The torque due to this wave is then transferred to the plasma interior through the strong inter-particle Coulomb forces, which act to bring the plasma to the same rotation frequency as ω_{rp} [24]. We observe similar stick-slip motion with both dipole and quadrupole rotating fields. However, most measurements, including those we report here, were taken with a dipole rotating field.

The radial binding force of the trap is due to the Lorentz force produced by the plasma's rotation through the magnetic field. Therefore changing ω_r changes the radial binding force of the trap and provides a sensitive way to adjust the overall shape and structural phase of the plasma. In this work, the frequency of the rotating perturbation ω_{rp} was kept near $2\pi \times 22.8$ kHz and slightly adjusted to produce a disk-shaped plasma consisting of 5 axial planes with a bcc-like crystal structure in the plasma center [19]. Because $\omega_r \ll \Omega_c$, the ion motion in a direction perpendicular to the magnetic field is determined principally by $\mathbf{E} \times \mathbf{B}$ guiding center dynamics [27].

The main cooling-laser beam ($\lambda = 313$ nm) was directed along the z axis and tuned 10 to 20 MHz lower in frequency than a hyperfine-Zeeman component of the $2s\ ^2S_{1/2} \rightarrow 2p\ ^2P_{3/2}$ resonance with a natural linewidth of 19 MHz. This beam's power was ~ 50 μW and the beam was focused to a ~ 0.5 mm waist at the ion crystal. A second cooling beam (\perp beam in Fig. 1(a)), derived from the same laser, was directed perpendicularly to \hat{z} and had a ~ 70 μm waist and ~ 1 μW power. Both the perpendicular and parallel cooling lasers were required to form a well defined crystal in the disk-shaped plasmas discussed here. Although we did not measure the ion temperature, the theoretical cooling limit is 0.5 mK, and an experimental upper bound of $T < 10$ mK has been measured in previous experiments [23]; for a density of $n_0 = 7.1 \times 10^7$ cm^{-3} , these limits give a range of $112 < \Gamma < 2230$. An indirect estimate of the ions' coupling parameter, based on observations of when the bcc(110) structural phase was exclusively favored, is $\Gamma \sim 600$

[28].

The \perp beam is normally directed through the radial center ($r = 0$) of the crystal in order to minimize its applied torque while providing a low Doppler-cooling temperature [16]. In this experiment, we offset the \perp -beam position slightly (5 to 30 μm) from the plasma center to produce a torque on the $^9\text{Be}^+$ ions in the same direction as the plasma rotation. The resultant torque from the \perp beam was larger than any other ambient torque due to, for example, resonances between modes and asymmetries in the trap construction [29] or background gas drag [30].

A series of lenses formed side- and top-view images of the ion fluorescence, with viewing directions perpendicular and parallel to the magnetic field respectively, on either a gateable charge-coupled device (CCD) camera, or on an imaging photomultiplier tube. The resolution of the optical systems was $\sim 4 \mu\text{m}$, while typical interparticle spacings were $\sim 15 \mu\text{m}$. By detecting the ion fluorescence synchronously with the rotating perturbation drive, images of the individual ions that make up the Coulomb crystals were obtained. Figure 1(b) shows a strobed, top-view CCD camera image of a 5-axial plane crystal in the bcc structural phase, accumulated over 40 s. The ion positions are well localized in the plasma center; however, at larger radii they are blurred.

To investigate the blurring we used an imaging photomultiplier tube in the top-view position to record the positions and detection times of the fluorescence photons. Data sets consisted of 125 ms intervals of data recorded each second over long periods of time (up to 5000 s). Images similar to those in Fig. 1(b) were created for each 125 ms interval by constructing 2D histograms of the ion fluorescence in the frame of the rotating perturbation. The orientation θ_{cry} of the central crystallized region in the rotating frame was determined (modulo π due to the bcc crystal bilateral symmetry) with an uncertainty of $\sim 0.002\pi$ radians [31].

In Fig. 2 we plot $\theta_{\text{cry}}(t)$ for two data sets that differ mainly in the amount of \perp -beam torque. Over long time scales the \perp -beam torque produces a slightly faster rotation (a rotational ‘creep’) of the $^9\text{Be}^+$ crystal relative to the rotating perturbation. For example, in data set 2 $\Delta\omega \equiv \omega_r - \omega_{rp} \approx 2\pi \times 8 \text{ mHz}$. Over shorter time scales, as shown in the inset of Fig. 2, much of this crystal rotation takes place with sudden jumps in θ_{cry} , ‘slips’, whose time scale is too fast to be captured by the top-view diagnostic. Intermittent behavior is a common feature in the plastic deformation (creep) of many materials (see [32] for references). Let $\Delta\theta_{\text{cry}}$ denote the angular displacement between two successive measurements of θ_{cry} . The statistics of $\Delta\theta_{\text{cry}}$ consists of a normal distribution (from measurement error) centered about zero with a width of $\sim 0.002\pi$, and infrequent larger slips. Due to the known sign of the \perp -beam torque and the π ambiguity mentioned above, we choose $\Delta\theta_{\text{cry}}$ to lie in the range $[0, \pi)$. To separate statistically significant slips from measurement error we further require $0.007\pi \leq \Delta\theta_{\text{cry}} \leq 0.97\pi$. We find that statistically significant slips account for greater than 90 % of the measured change in θ_{cry} .

The \perp -beam torque is applied to all the $^9\text{Be}^+$ ions in the radial interior of the crystal. The rotating perturbation, however, applies its torque on the outer radial boundary of the heavy ions. We therefore believe the stress due to the competition between these torques is greatest in the region of the heavy ions and anticipate that the slips of Fig. 2 are due to ion motion between the radial boundary of the $^9\text{Be}^+$ ions, r_{Be} , and the overall radial boundary of the plasma, r_0 . This is supported by the top-view images and by simulation

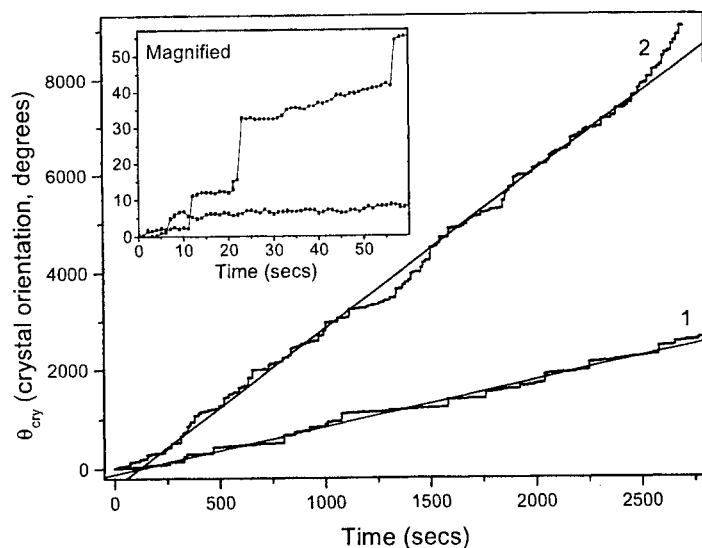


FIGURE 2. Crystal orientation θ_{cry} in the frame of the rotating perturbation for two data sets with different \perp -beam torques. The torque is greater in data set 2. The lines are from a linear regression fit. The inset shows a magnified plot of the first 60 s of data.

work discussed below, which show most slips occurring as approximate rigid rotations of the ${}^9\text{Be}^+$ ions. Because the simulation slips occur at a radius slightly greater than r_{Be} , and r_{Be} varied from data set to data set, we characterize a slip amplitude A_{slip} by the linear distance $\Delta\theta_{cry}r_{Be}$.

Figure 3 shows the distribution $f(A_{slip})$ of slips for the two data sets shown in Fig. 2. Because we can not distinguish between slips with amplitude A_{slip} or $A_{slip} + n\pi r_{Be}$, where n is an integer, we fitted to the function $f_{slip} \propto \sum_{n=0}^{n_{cut}} (A_{slip} + n\pi r_{Be})^{-\gamma}$ to determine the agreement of the data with a power law distribution. Here n_{cut} is a cutoff that could depend on the system size, creep rate, or other factors. We obtain a good fit for any n_{cut} but find that χ^2 goes through a weak minimum at $n_{cut}=6$, and therefore use that value in the following analysis. This results in measured γ s slightly larger ($<10\%$ and within the uncertainty of the fit) than those resulting from $n_{cut}=1$. In the insert of Fig. 3 we plot the measured power-law exponent γ as a function of the creep rate $\Delta\omega \cdot r_{Be}$ for 10 data sets with the same rotating perturbation strength but different \perp -beam torques. We find that γ decreases as the creep rate, a measure of the applied \perp -beam torque, increases. Decreases in the stick-slip exponent with increased drive have been observed in some experimental systems [8, 33, 34], but not in all [32].

Inspection of Fig. 2 shows that the waiting periods (the time intervals between successive slips) are typically many seconds. An analysis of the waiting periods shows a peaked distribution with median waiting periods ranging from 4 s for the highest \perp -beam torques to 12 s for the lowest \perp -beam torques. In Fig. 4 we plot the frequency of slips versus waiting time for a data set with moderate torque. The frequency was normalized as before by dividing the number of slips n_{slip} by the binwidth and the duration

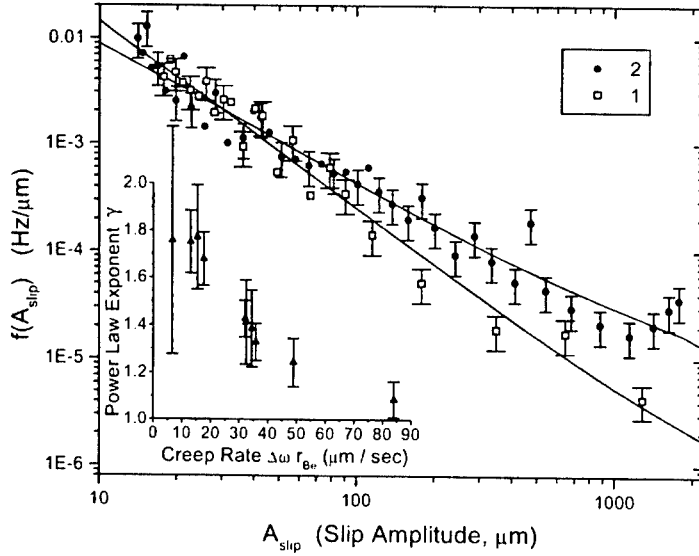


FIGURE 3. Distribution $f(A_{slip})$, where $f(A_{slip})dA_{slip}$ is the frequency of slips between A_{slip} and $A_{slip} + dA_{slip}$, for the two data sets shown in Fig. 2. The lines are fits to a power law with a cutoff as described in the text. The insert shows the measured power-law exponent γ versus applied torque, as parameterized by the creep rate, for all of the data sets.

of the data set (4882 s).

Earthquakes are another phenomena that exhibit power-law frequency versus amplitude behavior and peaked waiting time distributions. Although there has been no consensus on which is the ‘correct’ distribution, it has been suggested that the waiting-time distributions of earthquakes can be described by lognormal [35], Weibull [36] or Gaussian [37] statistics. In Fig. 4 we also plot 3-parameter fits of the data to these distributions. The Weibull distribution, often used to model the time until failure of brittle materials, is

$$\rho(t) = A_0 \frac{m t^{m-1} e^{-(t/t_0)^m}}{t_0^m}, \quad 0 < t < \infty, \quad m > 0, \quad (2)$$

and has a median waiting time value of $t_{med} = (\log 2)^{1/m} t_0$. A Weibull model for failure can be derived theoretically as a form of an extreme-value distribution, governing the time to failure of the ‘weakest link’ of many competing processes [38]. When the shape parameter $m = 1$, the Weibull distribution reduces to the exponential distribution $\rho(t) = A_0 e^{-(t/t_0)}$. The exponential distribution is produced by a system with a constant failure rate and thus no dependence on the state of the system (i.e., it is ‘memoryless’). Distributions where $m \neq 1$ result when the outcome of a trial depends in part on how long the trial has been conducted.

As seen in Fig. 4, the fit to a Weibull distribution results in a significantly smaller χ^2 (chi squared per degree of freedom), and this is true for the other data sets as well. If we sum up the χ^2 of fits for all of the 10 data sets, the Gaussian and lognormal

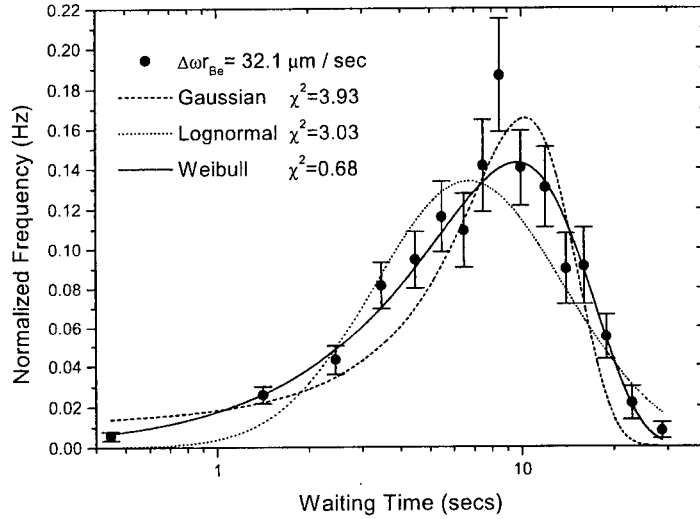


FIGURE 4. Distribution of waiting times between slips for a data set with a moderate torque.

fits have statistically the same value (18.5 and 21.1), but the Weibull fit produces $\sum \chi^2 = 10.8$. The average and standard deviation of the shape parameter m is 1.96 ± 0.35 , perhaps indicating that the ion crystal has a ‘memory.’ For large m , $p(t)$ approaches a delta function. Ward and Goes [36] have used $\nu = 1/m$ to parameterize the degree of aperiodicity, and found in their earthquake simulation data that as they increased the magnitudes of the quakes considered, both t_{med} and m increases. We also find these trends in our ion-crystal data.

Previous workers in the analysis of SGR ‘starquake’ statistics have looked for correlations between waiting times and the amplitude of the γ -ray burst. In order to investigate this with our data, we sorted a total of 918 slips from 4 data sets with similar torque by increasing slip amplitude, and then into groups of ~ 150 slips. We next fitted the time intervals of each of these groups to a Weibull distribution. We did this both for the time interval until the next slip of any amplitude (Δt^+) and for the interval from the previous slip (Δt^-). The results are plotted in Fig. 5, and show evidence for increasing t_{med} for Δt^- , and much less or no correlation for Δt^+ . This is at variance with results from SGRs, where either no correlation has been seen [21, 39, 40], or an anticorrelation seen for Δt^+ [41].

Most experiments exhibiting stick-slip behavior are performed with ‘constant-velocity driving’ where the force is applied through an effective elastic coupling [8, 9, 10]. The driving force of the system is something like $F(t) = K(Vt - x(t))$ where ‘ x ’ is the ‘position’ of an element in the system (for example, the position of a bead or slider block in a chain), K is the effective spring constant that couples the applied force to each element in the system, and V is the constant average velocity that is imposed on the system. Stick-slip motion occurs for small V and K , and a critical point exists in the limit $V \rightarrow 0$ and $K \rightarrow 0$ [15, 33]. If the system gets stuck, it will eventually slip again

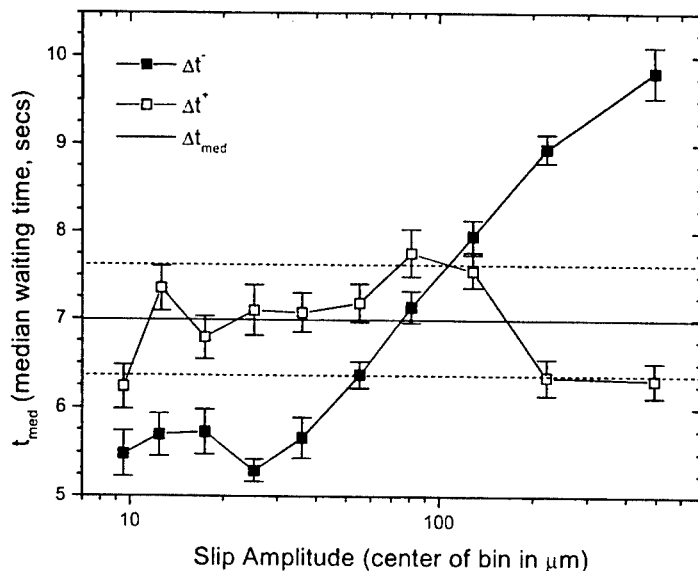


FIGURE 5. Measured t_{med} versus slip amplitude. The lines indicate the mean value and standard deviation measured for random slip amplitudes.

because the driving force increases linearly until slip occurs.

However, our experiment is performed under conditions more similar to ‘constant-force driving’ since the \perp -beam radiation-pressure force is constant in time and applied directly to the ${}^9\text{Be}^+$ ions. In constant-force driving the system undergoes a depinning transition at a critical force F_c and moves with constant average velocity proportional to $(F - F_c)^\beta$ for $F > F_c$ and critical exponent β [33]. If a constant-force system gets stuck for a long period of time, then this indicates $F < F_c$ and the system should permanently stick.

In fact the observed waiting times (Fig. 4) are long compared to any known dynamical time scales due to internal modes of the system. Why doesn’t the system permanently stick? One possibility is that the slips could be excited by an external perturbation. By deliberately modulating the amplitude of the cooling and torquing lasers we have established that the amplitude noise present in these beams is not high enough to trigger slips. Another source of perturbations is the neutral atoms of the $\sim 10^{-8}$ Pa vacuum background. We have measured that the relative abundance of ${}^9\text{Be}^+$ ions to heavy impurity ions decreases with an e-folding time of ~ 10 hours, due to collisions with background neutrals. With a cloud of 20,000 ions, this gives a median time between collisions of ~ 1.25 s. However, the relationship between these collisions and slips, if any, is unclear. For example, if all slips were caused simply by collisions, the waiting time distribution for slips would be exponential, in contrast to what is observed.

We have performed molecular-dynamics simulations with 1000 ions (40 % ${}^9\text{Be}^+$, 60 % heavy ions) with the goal of better understanding the dynamics and origin of the slips. About four months of computation time has been required to simulate the

equivalent of ~ 1.2 s of experimental time. The simulations have produced three events which can be interpreted as slips. In these events, a rearrangement of a small number of heavy ions in the vicinity of a lattice defect produces a sudden change in the orientation of the crystal. Once started, the slip eventually stops because the driving force of the \perp -beam is not sufficient to sustain continuous motion. Because it appears that the rearrangement of a few ions can trigger a slip, thermal fluctuations of the ions may be responsible for starting the slips in both experiment and simulation. However, the simulations also show the presence of a torsion mode of large amplitude and low frequency (~ 10 Hz) that produces a time-dependent stress which may also play a role in triggering slips. This mode was not observed in the experimental data, possibly because of damping from laser cooling.

In summary, we have observed creep and stick-slip motion in the rotational control of laser-cooled ion crystals in a Penning trap. We believe this system is constant-force driven and may be an experimental example of a subcritical state [15] where the slips are triggered by thermal fluctuations or by other as yet unidentified perturbations such as collisions with neutral background atoms. The trapped-ion crystal system discussed here possesses most of the features of a self-organized critical state [14, 15]. Therefore further investigations of the stick-slip behavior over a wider range of control parameters (\perp -beam torque, temperature, rotating perturbation strength, background pressure) could be useful for understanding the applicability of the this concept to real physical systems. Finally, minimizing the occurrence of the slips is important for some applications [5, 6]. This can be done by minimizing the \perp -beam torque, either through active control of the \perp -beam position or by appropriate tailoring of the \perp -beam profile [42]. Increasing the strength of the rotating electric field perturbation should also decrease the frequency of slips due to small ion rearrangements. Two data sets taken with half the rotating perturbation strength of the data sets analyzed here showed an increase in the number of slips and rotational creep of the ion crystal.

ACKNOWLEDGMENTS

This research was supported by the Office of Naval Research and the National Science Foundation (Dubin). We thank S. Zapperi, R. L. Kautz, J. M. Kriesel, J. P. Schiffer, and D. J. Wineland for useful comments, and B. M. Jelenković and X.-P. Huang for technical assistance.

REFERENCES

1. Anderegg, F., Schweikhard, L., and Driscoll, C. F., editors, *Non-Neutral Plasma Physics IV*, AIP, New York, 2001.
2. Greaves, R. G., and Surko, C. M., *Phys. Rev. Lett.*, **85**, 1883–1886 (2000).
3. Hollmann, E. M., Anderegg, F., and Driscoll, C. F., *Phys. Plasmas*, **7**, 2776–2789 (2000).
4. Huang, X.-P., Bollinger, J. J., Mitchell, T. B., and Itano, W. M., *Phys. Plasmas*, **5**, 1656–1663 (1998).
5. Tan, J. N., Bollinger, J. J., and Wineland, D. J., *IEEE Trans. Instrum. Meas.*, **44**, 144–147 (1995).
6. Cirac, J. I., and Zoller, P., *Phys. Rev. Lett.*, **74**, 4091–4094 (1995).
7. Demirel, A. L., and Granick, S., *Phys. Rev. Lett.*, **77**, 4330–4333 (1996).

8. Ciliberto, S., and Laroche, C., *J. Phys. I France*, **4**, 223–235 (1994).
9. Nasuno, S., Kudrolli, A., and Gollub, J. P., *Phys. Rev. Lett.*, **79**, 949–952 (1997).
10. Albert, I., Tegzes, P., Kahnig, B., Albert, R., Sample, J. G., Pfeifer, M., Barabási, A.-L., Vicsek, T., and Schiffer, P., *Phys. Rev. Lett.*, **84**, 5122–5125 (2000).
11. Frette, V., Christensen, K., Malthe-Sørenssen, A., Feder, J., Jøssang, T., and Meakin, P., *Nature*, **379**, 49–52 (1996).
12. Olami, Z., Feder, H. J. S., and Christensen, K., *Phys. Rev. Lett.*, **68**, 1244–1247 (1992).
13. Burridge, R., and Knopoff, L., *Bull. Seismol. Soc. Am.*, **57**, 341–371 (1967).
14. Bak, P., Tang, C., and Wiesenfeld, K., *Phys. Rev. Lett.*, **59**, 381–384 (1987).
15. Vespignani, A., and Zapperi, S., *Phys. Rev. E*, **57**, 6345–6362 (1998).
16. Itano, W. M., Brewer, L. R., Larson, D. J., and Wineland, D. J., *Phys. Rev. A*, **38**, 5698–5706 (1988).
17. Ichimaru, S., Iyetomi, H., and Tanaka, S., *Phys. Rep.*, **149**, 91–205 (1987).
18. Itano, W. M., Bollinger, J. J., Tan, J. N., Jelenković, B., Huang, X.-P., and Wineland, D. J., *Science*, **279**, 686–689 (1998).
19. Mitchell, T. B., Bollinger, J. J., Dubin, D. H. E., Huang, X.-P., Itano, W. M., and Baughman, R. H., *Science*, **282**, 1290–1293 (1998).
20. Van Horn, H. M., *Science*, **252**, 384–389 (1991).
21. Cheng, B., Epstein, R. I., Guyer, R. A., and Young, A. C., *Nature*, **382**, 518–520 (1996).
22. Göğüş, E., Woods, P. M., Kouveliotou, C., van Paradus, J., Briggs, M. S., Duncan, R. C., and Thompson, C., *Astrophys. J.*, **532**, L121–L124 (2000).
23. Brewer, L. R., Prestage, J. D., Bollinger, J. J., Itano, W. M., Larson, D. J., and Wineland, D. J., *Phys. Rev. A*, **38**, 859–873 (1988).
24. Dubin, D. H. E., and O’Neil, T. M., *Rev. Mod. Phys.*, **71**, 87–172 (1999).
25. O’Neil, T. M., *Phys. Fluids*, **24**, 1447–1451 (1981).
26. Larson, D. J., Berquist, J. C., Bollinger, J. J., Itano, W. M., and Wineland, D. J., *Phys. Rev. Lett.*, **57**, 70–73 (1986).
27. Dubin, D. H. E., and O’Neil, T. M., *Phys. Rev. Lett.*, **60**, 511–514 (1988).
28. Mitchell, T. B., Bollinger, J. J., Huang, X.-P., Itano, W. M., and Dubin, D. H. E., *Phys. Plasmas*, **6**, 1751–1758 (1999).
29. Mitchell, T. B., Bollinger, J. J., Huang, X.-P., and Itano, W. M., “Crystalline Order in Strongly Coupled Plasmas”, in *Trapped Charged Particles and Fundamental Physics*, edited by D. H. E. Dubin and D. Schneider, AIP, New York, 1999, pp. 309–318.
30. Wineland, D. J., Bollinger, J. J., Itano, W. M., and Prestage, J. D., *J. Opt. Soc. Am. B*, **2**, 1721–1729 (1985).
31. The crystal images occasionally showed defect lines that moved slowly across the crystal and prevented a definitive measurement of θ_{cry} . This occurred more frequently with larger torque. In this case shorter time series separated by intervals when θ_{cry} could not be unambiguously determined were appended to each other without introducing discontinuities in θ_{cry} at the junctures.
32. Miguel, M.-C., Vespignani, A., Zapperi, S., Weiss, J., and Grasso, J.-R., *Nature*, **410**, 667–671 (2001).
33. Lacombe, F., Zapperi, S., and Hermann, H. J., *Phys. Rev. B*, **63**, 104104 (2001).
34. Zapperi, S., Cizeau, P., Durin, G., and Stanley, H. E., *Phys. Rev. B*, **58**, 6353–6366 (1998).
35. Nishenko, S. P., and Buland, R., *Bull. Seismol. Soc. Am.*, **77**, 1382 (1987).
36. Ward, S. N., and Goes, S. D. B., *Geophys. Res. Lett.*, **20**, 2131–2134 (1993).
37. Pepke, S. L., Carlson, J. M., and Shaw, B. E., *J. Geophys. Res.*, **99**, 6769–6788 (1994).
38. Weibull, W., *J. Appl. Mech.*, **9**, 293–297 (1951).
39. Laros, J. G., Fenimore, E. E., Klebesadel, R. W., Atteia, J.-L., Boer, M., Hurley, K., Neil, M., Vedrenne, G., Kane, S. R., Kouveliotou, C., Cline, T. L., Dennis, B. R., Desai, U. D., Orwig, L. E., Kuznetsov, A. V., Sunyaev, R. A., and Terekhov, O. V., *Astrophys. J.*, **320**, L111–L115 (1987).
40. Vidale, J. E., Ellsworth, W. L., Cole, A., and Marone, C., *Nature*, **368**, 624–626 (1994).
41. Göğüş, E., Woods, P. M., Kouveliotou, C., van Paradus, J., Briggs, M. S., Duncan, R. C., and Thompson, C., *Astrophys. J.*, **526**, L93–L96 (1999).
42. The \perp -beam torque can be reduced with a beam that has a large waist and frequency dispersion across the waist that matches the ion Doppler shifts due to the plasma rotation.

Laser-Induced Wakes in Ion Crystals[†]

J.M. Kriesel¹, J.J. Bollinger¹, T.B. Mitchell², L.B. King³ and
D.H.E. Dubin⁴

¹*Time & Frequency Division, National Institute of Standards & Technology, Boulder, CO 80305*

²*Department of Physics & Astronomy, University of Delaware, Newark, DE 19716*

³*Dept. of Mech. Eng., Michigan Technological University, Houghton, MI 49931*

⁴*Physics Department, University of California, San Diego, CA 92093*

Abstract. Wakes in a Coulomb crystal are produced by “pushing” with radiation pressure on a rotating spheroidal cloud of laser-cooled ${}^9\text{Be}^+$ ions. The wakes are stationary in the lab frame and are caused by the interference of “drum-head” type oscillations. Velocity images of these wakes are obtained directly through the dependence of the ion fluorescence on Doppler shifts, and new analytical calculations accurately reproduce these experimental wake images. The technique demonstrates a way to excite and study modes, that were not accessible with previous techniques.

[†] *Work of the U.S. Government; not subject to U.S. copyright.*

INTRODUCTION

Mode studies [1–3] provide an excellent way to diagnose, control, and probe cold ion clouds. Previously at NIST-Boulder, electric fields (due to either applied voltages or trap imperfections) acting on the entire cloud were used to excite modes of relatively long wavelength on the order of the cloud’s size [2,3]. In this article, we present results on a novel way to locally excite a spectrum of waves with relatively short wavelength by “pushing” with radiation pressure on a crystallized ion cloud. In the experiments shown here, the waves interfere “downstream” from the push to produce a wake pattern that is stationary in the lab frame, analogous to the wake behind a ship moving in deep water [4]. The technique offers a way to locally probe and diagnose ion clouds and demonstrates a method for studying waves that were not accessible with previous techniques. In addition, wakes in Coulomb crystals are also of current theoretical interest [5,6], primarily due to recent experiments in two-dimensional (2D) Dusty Plasma crystals [7,8].

EXPERIMENTAL SETUP

A schematic of the experimental setup [9] is shown in Fig. 1(a). We use a cylindrical Penning-Malmberg trap to confine $N_{\text{tot}} = 15\,000$ to $45\,000$ ${}^9\text{Be}^+$ ions

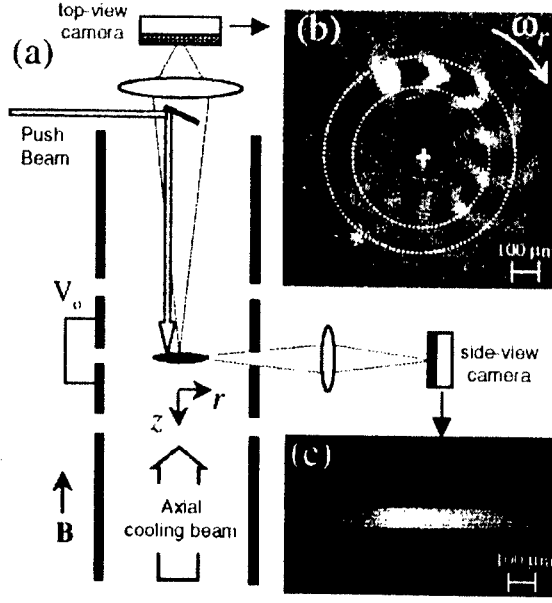


FIGURE 1. (a) Schematic of the cylindrical Penning-Malmberg trap and imaging diagnostics. (b) Top-view image of the differential fluorescence $\Delta I(r, \theta)$ for an $\alpha = 0.042$ Be^+ ion crystal. The annular region defined by the dotted circles is analyzed to obtain dispersion relationship data. (c) Side view image of an $\alpha = 0.042$ crystal.

at a density of $n \sim 2 \times 10^8 \text{ cm}^{-3}$ with an axial magnetic field of $B = 4.465 \text{ T}$ (giving a cyclotron frequency of $\Omega_c/2\pi = 7.6 \text{ MHz}$) and an electrostatic potential of $V_o = -1000 \text{ V}$ (giving an axial frequency of $\omega_z/2\pi = 800 \text{ kHz}$). The radial extent of our clouds varies from $R_o = 0.3$ to 2 mm , which is much smaller than the radius of the trap walls $R_w = 2.0 \text{ cm}$. The ion clouds are spheroidal in shape (i.e. an ellipse of revolution) described by an aspect ratio $\alpha \equiv Z_o/R_o$, where $2Z_o$ is the axial extent of the cloud. The aspect ratio is directly related to the rotation frequency ω_r , which we control with a dipole “rotating-wall” perturbation [10].

Thus, we are able to experimentally set the cloud shape α by using the rotating wall to set ω_r . Here, $\omega_r/2\pi$ ranges from 42.5 kHz to 128 kHz with a respective range in aspect ratio from $\alpha = 0.005$ (corresponding to a 2D single plane) to $\alpha = 1.0$ (corresponding to a 3D spherical-shaped cloud). For the images in Fig. 1, $\alpha = 0.042$ with $\omega_r/2\pi = 45 \text{ kHz}$, and in both images the cloud extended slightly beyond the aperture limit of the cameras.

The ions are laser-cooled to temperatures $T \lesssim 5 \text{ mK}$ (giving coupling parameters of $\Gamma \gtrsim 200$) using a tunable laser set slightly to the red of a strong atomic transition in $^9\text{Be}^+$ ions [9]. The fluorescence due to the axial cooling beam (shown in Fig. 1 pointing in the $-\hat{z}$ direction) provides our primary diagnostic. The resolution of the optical systems is $\sim 4 \mu\text{m}$, whereas, the inter-particle spacing is $\sim 10 \mu\text{m}$. Unlike

previous mode studies [3], we do not strobe the camera; instead, we simply collect the fluorescence continuously for 30 s to 120 s to generate an image.

The relative intensity of the fluorescence is highly sensitive to an ion's axial velocity since the cooling laser is tuned to a relatively steep part of the transition curve. Ions that are moving towards the axial cooling beam ($v_z > 0$) are Doppler-shifted closer to the resonance peak, hence they scatter more photons and fluoresce more strongly; conversely, those moving away from the beam ($v_z < 0$) are Doppler-shifted further from resonance and fluoresce less strongly. For random thermal motion the effects average out. However, for coherent ion motion the changes in fluorescence enable the identification and measurement of axial oscillations using this so-called "Doppler velocimetry" diagnostic [3].

For the present experiments we excite waves in our ion crystals by pushing on them with laser radiation. The "push beam" is derived from the same near-resonant laser used for cooling; however, it has a relatively narrow waist ($\sim 50 \mu\text{m}$) and is offset from the rotation axis (center of the cloud) by $R_{pb} = 155 \mu\text{m}$ to $450 \mu\text{m}$.

EXPERIMENTAL RESULTS

Fig. 1(b) shows an example of Doppler velocimetry for a laser-induced wake. Here we show the change in fluorescence $\Delta I(r, \theta) \equiv I(r, \theta) - I_o(r, \theta)$, where we subtract off a "background" top-view image $I_o(r, \theta)$ taken without the push beam from a top-view image $I(r, \theta)$ taken with the push beam. The large white spot is due to the push beam located at a distance $R_{pb} \approx 320 \mu\text{m}$, but the alternating dark and light arcs are variations in fluorescence intensity due to coherent ion motion [11]. We estimate [12] that in this case the peak change in fluorescence corresponds to a change in velocity by $\Delta v_z \sim \pm 1 \text{ m/s}$. We further estimate [13] that this Δv_z corresponds to a displacement of $\Delta z \sim \pm 0.3 \mu\text{m}$, which is much less than the inter-particle spacing. In other words, we are able to detect oscillations of very small amplitude due to the extreme sensitivity available with our Doppler velocimetry diagnostic.

These laser-induced wakes are analogous to wakes behind a ship moving in deep water [4]. Due to the radiation pressure, ions receive a downward "kick" as they rotate through the push beam, similar to the kick that water experiences as it passes under a moving ship. In both situations, the push excites a large spectrum of waves traveling in all possible directions at speeds described by a dispersion relationship. The observed wakes are stationary in the frame of the source and are due to the constructive interference of waves that satisfy the stationary phase condition [4]. Along the direction of motion, this condition is satisfied by transverse waves with a phase velocity ω/k that matches the relative velocity v of the source. For our rotating ion crystals, the motion is along a circle of radius R_{rp} with $v = \omega_r R_{rp}$.

We obtain dispersion relationship data $\omega(k)$ by assuming that the mode pattern in an annular region directly behind the push is due primarily to transverse waves; we fit a damped [14] sinusoid to the average change in intensity in this region to

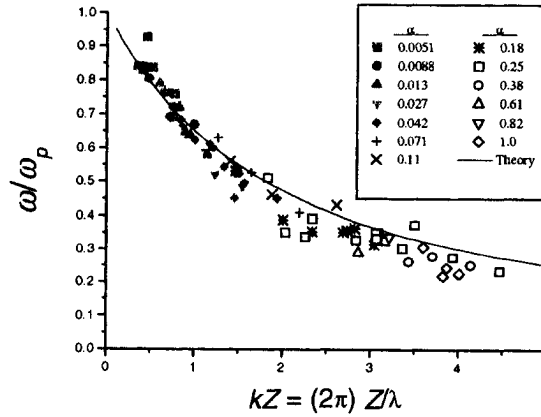


FIGURE 2. Measured dispersion relationship for clouds of various aspect ratios compared to a theoretical dispersion relationship for drum-head oscillations on an infinite planar slab of thickness $2Z$.

obtain $k = 2\pi/\lambda$; and use the relationship $\omega/k = \omega_r R_{pb}$ to obtain ω . For example, for the annular region defined by the dotted circles in Fig. 1(b), the distance between peaks gives $\lambda \approx 185 \mu\text{m}$, which in turn gives $\omega/2\pi \approx 490 \text{ kHz}$ using the calculated velocity $\omega_r R_{pb} \approx 90 \text{ m/s}$.

Dispersion relationship data obtained in this manner is shown in Fig. 2, where the different symbols correspond to different aspect ratios. Here the wave frequency is scaled by the plasma frequency $\omega_p = [2\omega_r(\Omega_c - \omega_r)]^{1/2}$, and the wavenumber is multiplied by half the cloud thickness Z at the radial position of the push beam. For a single aspect ratio, different wake patterns are generated by changing R_{pb} , which effectively changes the relative velocity of the push beam.

THEORY

To obtain a theoretical dispersion curve with which to compare to the data we consider fluid-like, drum-head oscillations in an infinite planar slab of thickness $2Z$. Using an analysis similar to that in References [2] and [5], we obtain

$$\tan\left[\frac{kZ}{\sqrt{\omega_p^2/\omega^2 - 1}}\right] = \sqrt{\omega_p^2/\omega^2 - 1}. \quad (1)$$

For a given value of kZ this equation has an infinite number of solutions; however, we consider only the lowest-order mode, for which our diagnostic is most sensitive (for higher-order modes axial variations in fluorescence will tend to average out in our top-view images). The dispersion relationship for these modes is plotted as the

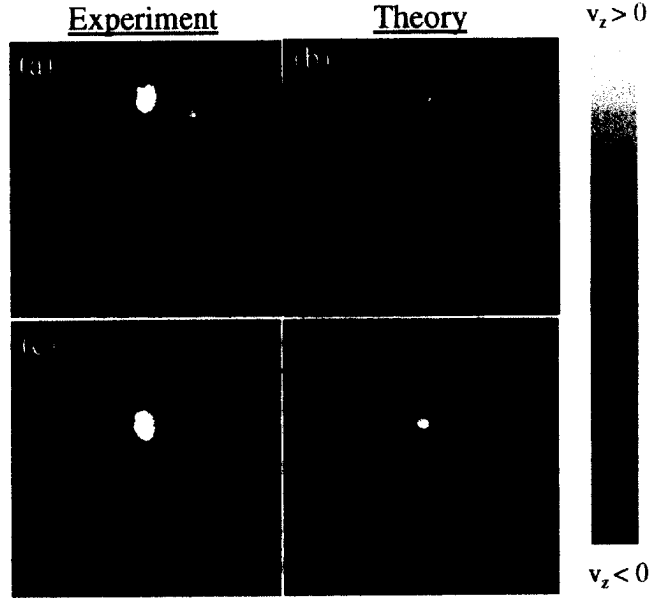


FIGURE 3. Experimental images of wakes for clouds with (a) $\alpha = 0.042$ and (c) $\alpha = 0.25$ shown alongside corresponding theoretical wakes (b) and (d) for the respective experimental parameters. The color scale corresponds to variations in velocity due to coherent motion of the ions.

solid curve in Fig. 2. This theory curve agrees very well with the data, particularly for disk-like clouds with low aspect ratio.

We are also able to theoretically predict the experimental wake patterns as shown by the comparison in Fig. 3. Here, the experimental image in Fig. 3(a) is the same as that shown in Fig. 1(b) for an $\alpha = 0.042$ cloud, and the one in Fig. 3(c) is for a somewhat thicker cloud with $\alpha = 0.25$ and $\omega_r/2\pi = 60$ kHz. For the theoretical calculations (b) and (d), we take into account the finite spot size and sum over the excited waves in a rotating slab. These calculations are able to capture the main features of the experimental images very well. The patterns are dominated by arc-shaped transverse wakes; however, lateral wakes also add additional structure.

We do not observe Mach cones in our ion crystals, even under high velocity conditions ($v > 10^4$ m/s). This is because the Mach condition is satisfied only if the disturbance moves faster than *all* of the excited waves. According to the dispersion relationship shown in Eq. 1 and Fig. 2, there is no theoretical limit to the speed of the waves that we consider here, i.e. $\omega/k \rightarrow \infty$ as $k \rightarrow 0$. Mach cones are also not observed in the case of gravity waves in water for the same reason; however, they do occur for sound waves in air and in dusty plasma crystals [7,8] due to the finite limit on the speed of sound in these systems.

SUMMARY AND DISCUSSION

In summary, we use radiation pressure to generate stationary wakes in a rotating Coulomb crystal of Be^+ ions. These wakes are theoretically well understood as resulting from the interference of drum-head oscillations. The experiments demonstrate a novel method of exciting waves in spheroidal ion crystals with potentially important applications. For example, by using the dispersion relationship, the method can be turned into a top-view diagnostic for the cloud parameters (i.e. ω_r , N_{tot} , α , etc.). Also, with a setup slightly different from that presented here, it may be possible to study (as yet unobserved) $\mathbf{E} \times \mathbf{B}$ shear modes by modulating the power of a perpendicular push beam. Since these modes occur only in solid-like plasmas, such experiments would provide a new tool with which to study the correlations in a strongly coupled plasma. In addition, these studies should also be useful in efforts to gain precise control over the rotational motion of the ions, which will be necessary for planned experiments on quantum information processing using ion crystals confined in a Penning trap.

This research is supported by the Office of Naval Research and the National Science Foundation (Dubin). We gratefully acknowledge useful comments on this manuscript by Dr. Wayne Itano and Dr. Brana Jelenković.

REFERENCES

1. D.H.E. Dubin, Phys. Rev. Lett. **66**, 2076 (1991).
2. J.J. Bollinger, D.J. Heinzen, F.L. Moore, W.M. Itano, D.J. Wineland, and D.H.E. Dubin, Phys. Rev. A **48**, 525 (1993).
3. T.B. Mitchell, J.J. Bollinger, X.-P. Huang, and W.M. Itano, Optics Exp. **2**, 314 (1998).
4. Lord Kelvin (Sir W. Thomson), Proc. Royal Soc. of London **42**, 80 (1887).
5. D.H.E. Dubin, Phys. Plasmas **7**, 3895 (2000).
6. X. Wang, A. Bhattacharjee, and S. Hu, Phys. Rev. Lett. **86**, 2569 (2001).
7. See article "Waves in a 2D Dusty Plasma Crystal" by J. Goree *et. al.* in these same proceedings.
8. D. Samsonov, J. Goree, Z.W. Ma, A. Bhattacharjee, H.M. Thomas, and G.E. Morfill, Phys. Rev. Lett. **83**, 3649 (1999).
9. For more detail see article "Experimental Dynamics of Stressed, Strongly Correlated Magnetized Plasmas" by T.B. Mitchell, *et. al.* in these same proceedings.
10. X.-P. Huang, J.J. Bollinger, T.B. Mitchell, and W.M. Itano, Phys. Rev. Lett. **80**, 73 (1998).
11. The thin concentric dark and light circles are an artifact of the crystal structure.
12. For this estimate we assumed that Doppler broadening was negligible and used the slope of the transition curve at a detuning of 10 MHz.
13. For this estimate we used $\Delta z = \Delta v_z / \omega$ with $\omega = (2\pi) 490$ kHz.
14. In these experiments the waves are damped primarily by the axial cooling beam.

Specific Heat and Latent Heat in Finite and Infinite One-Component Plasmas

J. P. Schiffer

Argonne National Laboratory, Argonne, IL 60439 and University of Chicago, Chicago, IL 60637

Abstract. The phase transition from liquid to ordered state has been explored in Molecular Dynamics simulations of confined one-component plasma clouds (as in ion traps). The latent heat and specific heat have been extracted and compared with Coulombic matter. The transition temperature is found to be lower for finite systems than for infinite matter, and the difference depends on the number of confined particles.

A one-component plasma (OCP) is known to have a transition from a liquid to a solid phase at a temperature corresponding to $\Gamma \approx 170$ -180 [1], where $\Gamma \equiv (q^2/a_{WS})/kT$, and a_{WS} is the Wigner-Seitz radius of the volume occupied by one ion. The behavior of the latent heat is discussed in the literature, (though the one plot of specific heat that has been published [2] omits the peak in the specific heat for the transition).

The configuration of finite, confined plasmas (fewer than 100,000 ions) shows a different type of ordering from that in infinite matter at low temperatures: concentric, equidistant shells with 2-dimensional ordering within the shells, instead of a bcc structure [3]. The question of how sharp these transitions are in the finite systems, and where they occur, has not previously been explored.

Molecular Dynamics simulations were carried out, first for a system of 10,000 ions confined in a static, isotropic harmonic well, with a confining force of $F = -Kr$. The system was cooled gradually to a temperature that corresponds to $\Gamma \approx 30,000$. The outer two shells for this system are shown in Fig. 1 together with the shell structure.

The potential energy of the system was extracted after equilibrium had been established. The potential energy is given by

$$U = 1/2K \sum_i r_i^2 + \sum_{i,j>i} q^2/r_{ij} \quad (1)$$

where r_i is the radial distance from the origin and r_{ij} is the distance between two ions and q is the charge of the ions.

Then, temperature increases were applied by two different methods. In one, the temperature was simply increased by scaling up the velocities, and the system was allowed to equilibrate for some 40 plasma periods (with about 120 time steps in the

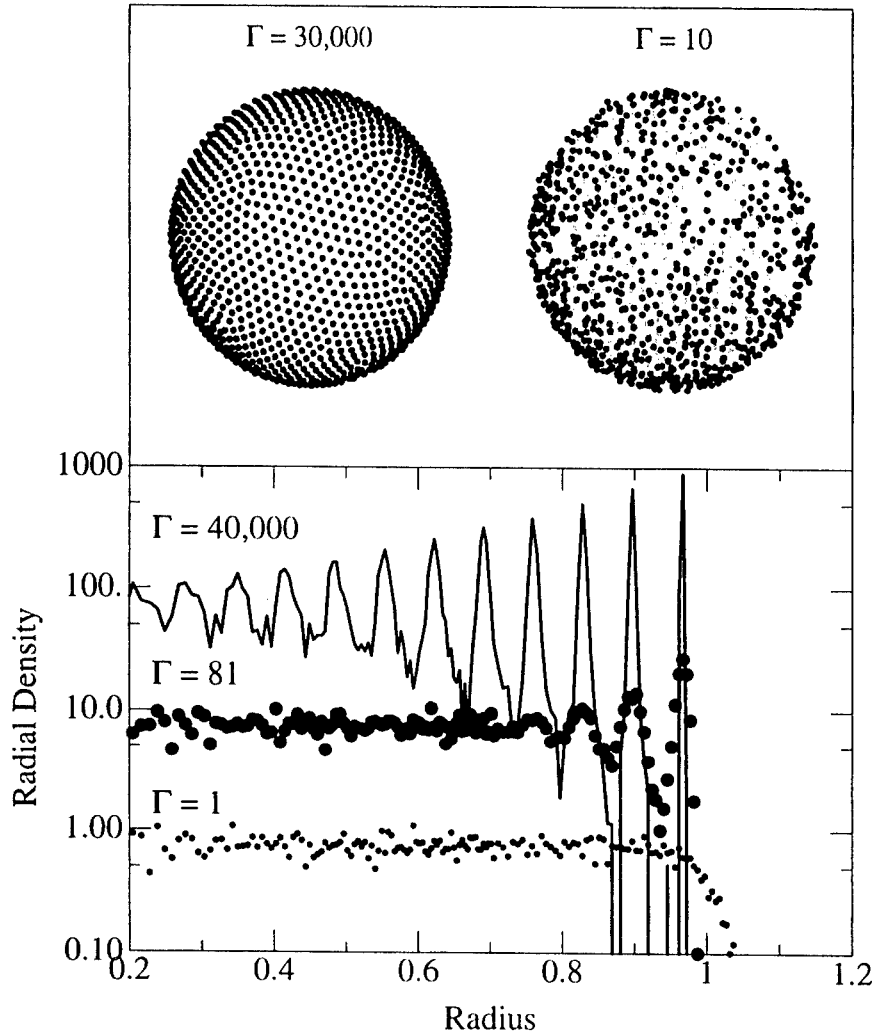


FIGURE 1. The upper part of the figure shows the outer layers of 10,000 ions. On the left is a very cold system with the outer shell shown in black, and the second shell in grey. On the right is a system in the liquid regime with no structure, with the selection of particles in the same radial regions. The lower part of the figure shows the radial density for three values of the temperature. The solid curve is a frozen, well-ordered system, the large points are in a region where the temperature is somewhat above the melting point and the small points are in the liquid regime.

simulation per plasma period). Then the following ~ 100 plasma periods were used to establish the new partition between kinetic energy (temperature) and potential energy. Alternatively, the temperature was increased in steps by assigning a random velocity to each particle picked from a Boltzmann distribution with the appropriate mean temperature, and then allowing the system to settle. This latter method seemed to allow the use of somewhat shorter time periods to establish a new equilibrium. The

two procedures gave very similar results. These times for equilibration and for establishing the averages were arrived at after some experimentation — a shorter time gave non-reproducible results. Attempts were also made at similar calculations in which the systems was cooled, rather than heated. Just as in laboratory experiments to determine the melting or freezing temperatures of materials, only the melting process seemed to give consistently reproducible results.

The results are shown in Fig. 2. At low temperatures, since the particles are oscillating about their equilibrium positions, the energy increments are distributed equally between kinetic and total energies. At a temperature, corresponding roughly to the above mentioned melting point in the infinite OCP, there is a step in potential energy, corresponding to the latent heat of melting. These data are displayed in a slightly different form in Fig. 3 where the upper part of the figure shows the potential energy divided by the kinetic energy for both the 10,000 ion simulation and the infinite OCP, the latter from [4]. The lower part of the figure shows the specific heat, taken as the increments in temperature divided by the corresponding increments in total energy. There appears to be a small difference in the transition energy, the point where the specific heat has its maximum value, in that the peak in the 10,000 ion system occurs at $\sim 20\%$ lower temperature: $\Gamma \approx 210$, instead of 173.

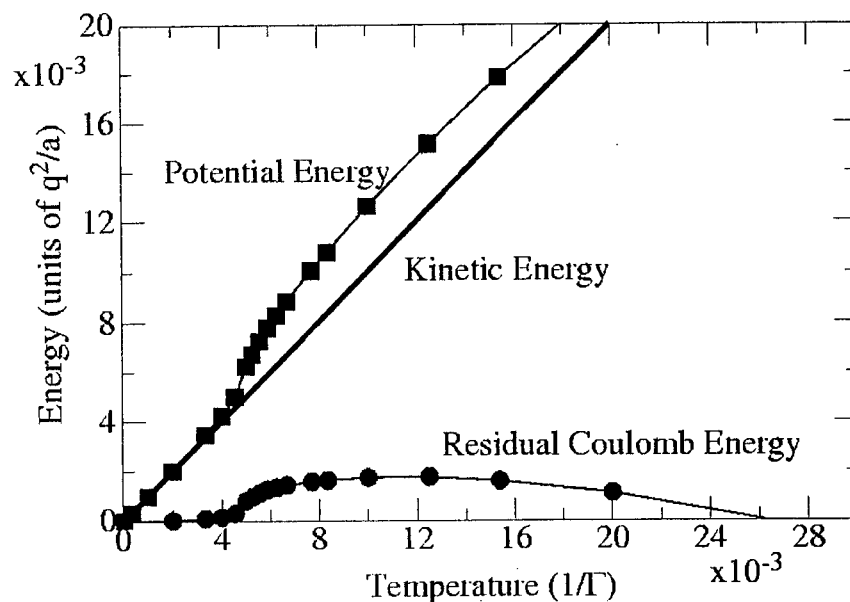


FIGURE 2. The potential energy in a 10,000 ion system is plotted as squares against the kinetic energy, in the same units of q^2/a_{WS} . At low temperature, the zero in potential energy is chosen arbitrarily as the value at $T = 0$. For $T < 0.005$ the particles oscillate about their equilibrium positions and the total energy is divided equally between the kinetic and potential energies. The deviation in the potential energy at $T \approx 0.005$ corresponds to the transition from an ordered to a disordered structure. At the bottom, the difference between the potential and kinetic energies is plotted.

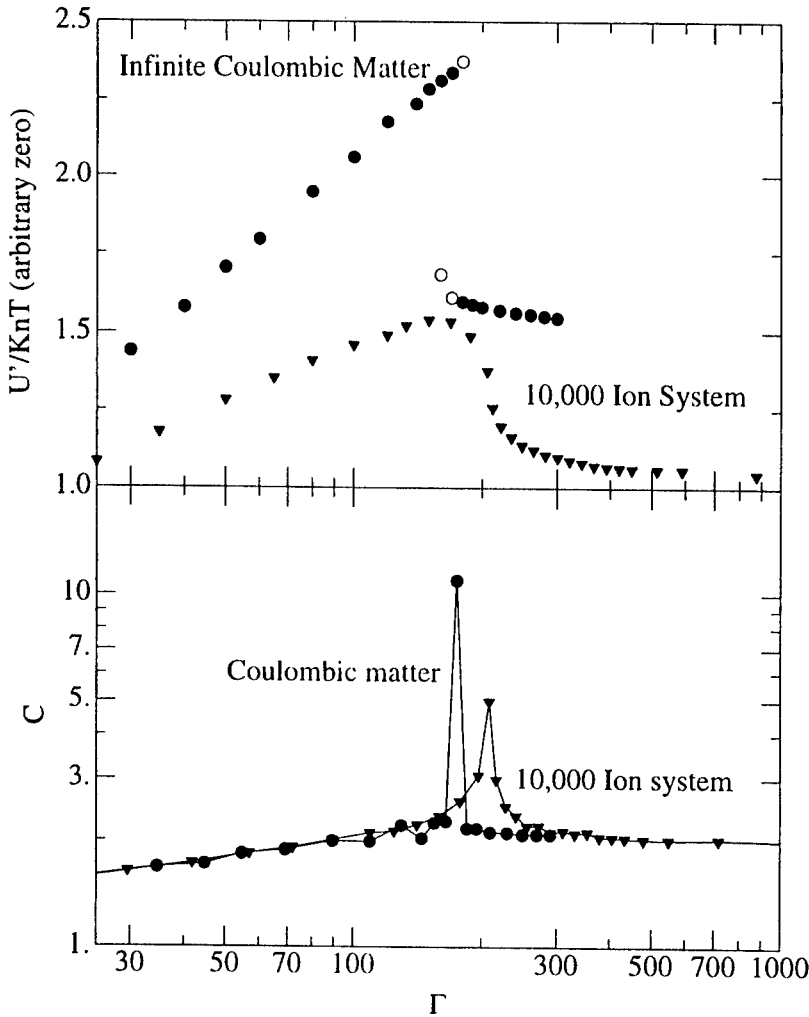


FIGURE 3. The upper part of the figure shows the total energy, U' , divided by the temperature for infinite Coulombic matter [4] as circular dots, compared to the simulations for 10,000 ions as triangles. The origins on the vertical scale are displaced. On the right (low-temperature) part of the curve the ratio is constant for both, as expected. The lower part of the figure shows the specific heat C derived from the same sets of data.

Next, the different measures of ordering were investigated:

- the width of the shells,
- the related maxima in the radial densities for each shell,
- the heights of the maxima in the 2-dimensional correlation function $g(r)$ within the shells,
- the heights of the maxima in the 3-dimensional $g(r)$ over the entire volume of the cloud.

All of these showed the maximum rate of change near the transition temperature in the specific heat, and at a temperature lower than the transition temperature for the infinite OCP. This consistency is not surprising, since the ordering is the source of the latent heat. An example is shown in Fig. 4.

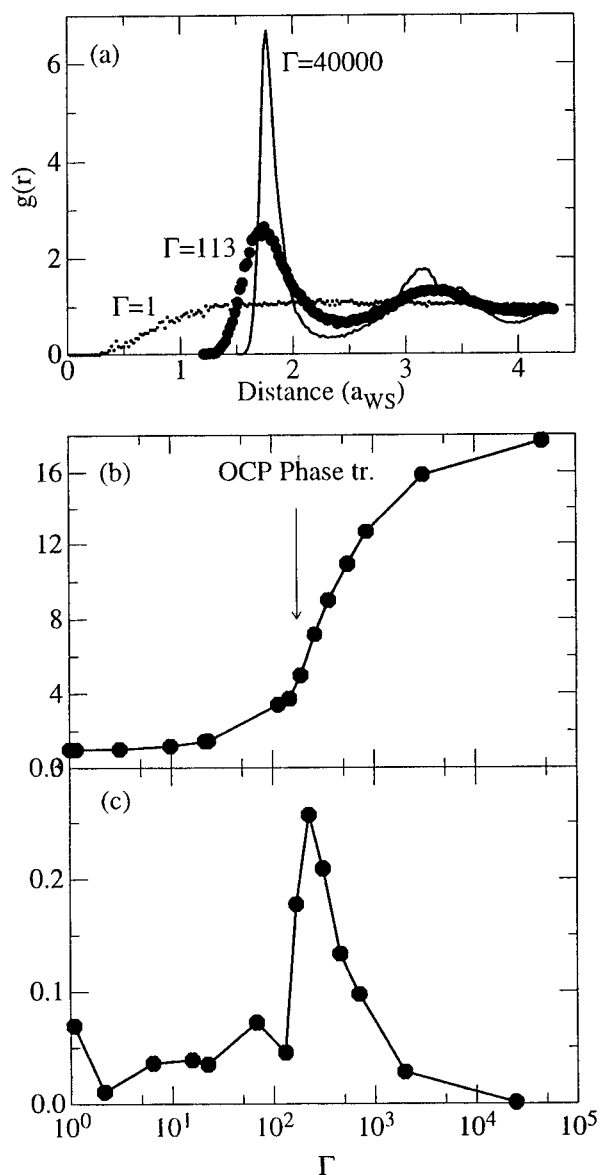


FIGURE 4. In (a) the 3-dimensional correlation function $g(r)$ is plotted for three values of Γ , in (b) the ratio of the maximum in $g(r)$ to the following minimum is shown, also as a function of Γ , while in (c) the derivative of this ratio is plotted.

In order to investigate the question of whether the lowering of the transition temperature is real or not, similar calculations were carried out for 1000 and 100 ions. These are displayed in Fig. 5. It is clear that the peaks in specific heat are broader and weaker in the smaller systems. For both 1000 and 100 ions the calculations were repeated several times in order to ascertain that the effects were reproducible. As is shown in the lower part of Fig. 5, there indeed appears to be a systematic trend in the transition temperature becoming lower for the smaller clusters.

Such a trend appears to have a simple explanation, in that ions on the surface do not see nearest neighbors on the outside, and thus their mobility is not constrained in the same way as for ions in the interior. Such effects are known to occur in atomic and molecular clusters (for instance for gold atoms [5]), but there the interactions are short range. One might expect, that with ionic clusters where the interaction is purely through the long-range Coulomb force, the effect might have a different character. The lower part of Fig. 5 shows that the transition temperature, as a function of the fraction of ions that are in the surface layer, seems to obey a simple dependence.

For real ion traps, the geometry considered here is close to that in Penning traps, where for the rotating cloud the effects of rotation at low temperature may be transformed away by the choice of the coordinate frame. The above simulations may therefore be expected to be directly tested there. The question of the transition temperatures in ions confined in rf-traps (Paul traps, and other configurations) is not necessarily so clear. The fact that the imposed rf motion does not cause appreciable heating of a cold plasma has been shown [6] but no further studies have been made. Therefore, a simulation was carried out for 1000 ions in rf confinement as described in [6]. In these systems a quasi-temperature is defined, that includes only motion that is aperiodic in the rf field: only motion that corresponds to displacements in complete rf periods are considered. The kinetic energy in the rf motion can be orders of magnitude higher. For calculations of specific heat, the potential energy of the system also needs to be known, and this clearly oscillates during the rf motion. Two methods were tried:

- a) averaging the *potential energy* over complete rf cycles, or
- b) averaging the *coordinates* of each ion and computing the potential energy corresponding to these average coordinates.

The two methods gave essentially identical results. One might have expected that because the method of confinement involves a continuous driven oscillation of all particles, plasmas confined in such a field might perhaps be more fragile and melt more easily (at lower temperatures) than those confined in static field. However, the specific heat from the simulations in the rf field peaked at a value of Γ that was consistent with the static calculations and no such effect was observed.

The values of specific heat much above the transition temperature could not be extracted from the rf-confined system because, as was shown in [6], at these temperatures there is increasing self-heating, "rf heating", from the coupling of the rf motion into the random heat of the plasma and to obtain meaningful results for these higher temperatures will require further study. However, it is clear that the rf motion does not appear to make systems confined in such an environment any more fragile with respect to melting than those confined in static fields.

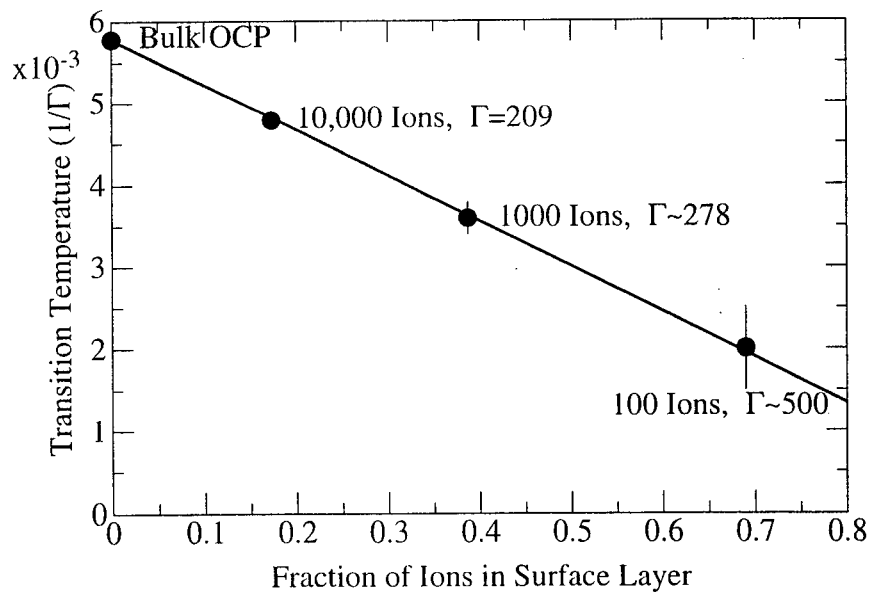
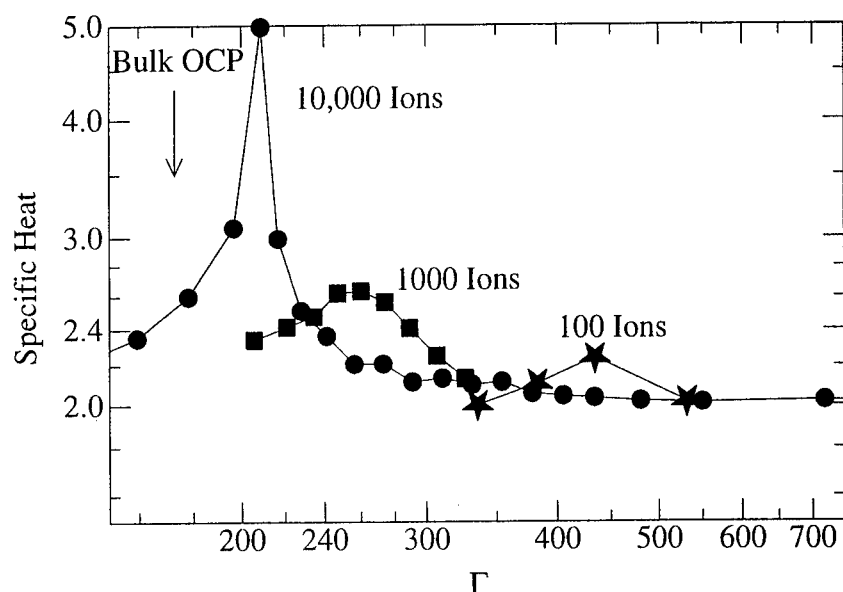


FIGURE 5. The upper part of the figure shows specific heats from simulations of 10,000, 1000 and 100 ions (circles, squares, and stars). The lower part of the figure shows the transitions temperatures (temperatures at which there is a peak in the specific heat) as a function of the number of ions in the surface layer for these systems. The line corresponds to $T = T_{OCP} \times (1 - 0.96 \times \text{fraction})$.

ACKNOWLEDGMENTS

This research was supported by the U.S. Department of Energy, Nuclear Physics Division, under Contract W-31-109-ENG-38, and the author would like to thank J. Jellinek for advice in connection with atomic clusters.

REFERENCES

1. Brush, S. G., Salin, H. L., and Teller, E., *J. Chem. Physics* **45**, 2102 (1966); Pollock, E. L. and Hansen, J. P., *Phys. Rev A* **8**, 3110, (1973); Slattery, W. L., Dooley, G. D., and DeWitt, H. E., *Phys. Rev A* **21**, 2087 (1980).
2. Rahman, A. and Schiffer, J., *Phys. Rev. Lett.* **57**, 1133 (1986); Dubin, D. H. E. and O'Neil, T. M. *Phys. Rev. Lett.* **60**, 511 (1988).
3. Dubin, D. H. E. and O'Neil, T. M., *Rev. Mod. Phys.* **71**, 87 (1999).
4. Farouki, R. T. and Hamaguchi, S., *Phys. Rev. E* **47**, 4330 (1993).
5. Buffat, Ph. and Borel, J. P., *Phys. Rev. A* **13**, 2287 (1976).
6. Schiffer, J. P., Drewsen, M., Hangst, J. S., and Hornekaer, L., *Proc. Natl. Acad. Sci.* **97**, 10697 (2000).

Ion Coulomb Crystals and Some Applications

Michael Drewsen,

Liv Hornekær, Niels Kjærgaard, Kristian Mølhave, Anne-Marie
Thommesen, Zelinda Videsen, Anders Mortensen, and Frank Jensen

*Institute of Physics and Astronomy, University of Aarhus,
Ny Munkegade, Building 520, DK-8000, Aarhus C, Denmark
E-mail: drewsen@ifa.au.dk*

Abstract. In this contribution, we present some of our recent results involving ion Coulomb crystals in linear Paul traps. A few results regarding single component crystals are discussed, but the main focus is on properties of two-component crystals and their applications in the fields of cold molecular physics and quantum optics.

SINGLE-COMPONENT ION COULOMB CRYSTALS

When trapped ions are cooled below a certain critical temperature (typically about ten milli-Kelvin) they form spatially ordered structures sometimes referred to as ion Coulomb-crystals. Such crystals of various sizes containing single atomic ion species have now for more than ten years been investigated in various types of traps (See, e.g., Ref. [1-6] and references therein). As examples, in Fig. 1 CCD-images of an ion Coulomb crystals for five different trap potentials are shown.

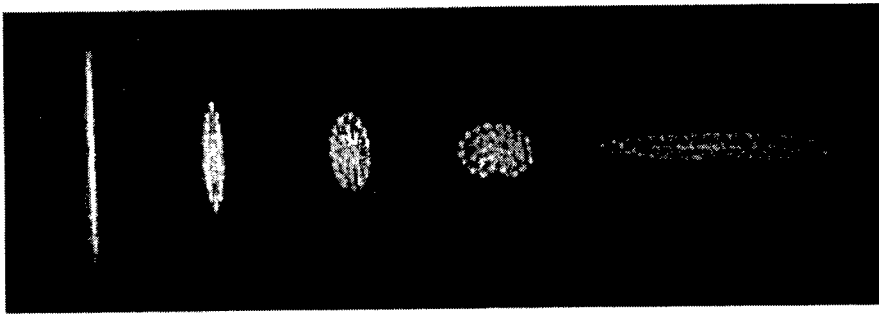


FIGURE 1. CCD-images of an ion Coulomb crystal of about $100\ ^{24}\text{Mg}^+$ ions for five different trapping potentials. The crystals are rotational symmetric around a left-right axis in the figure. The first image corresponds to a nearly pancake-like structure while the last one is cigar-like shaped.

The detailed structures of such crystals have now in a number of experiments been shown to be in good agreement with theoretical predictions [1-6], and the shape of the outer boundary of these cold crystals has been shown to be very similar to that of a cold, homogeneously charged liquid for a large variety of trapping parameters, as seen in Fig. 2 (See also Ref. [7]). Only in extreme limits where the ion Coulomb crystals become one-dimensional string-like or two-dimensional pancake-like, deviations from the liquid model appears. The latter is clearly seen in Fig. 2, when the aspect ratio of the crystal gets above 20.

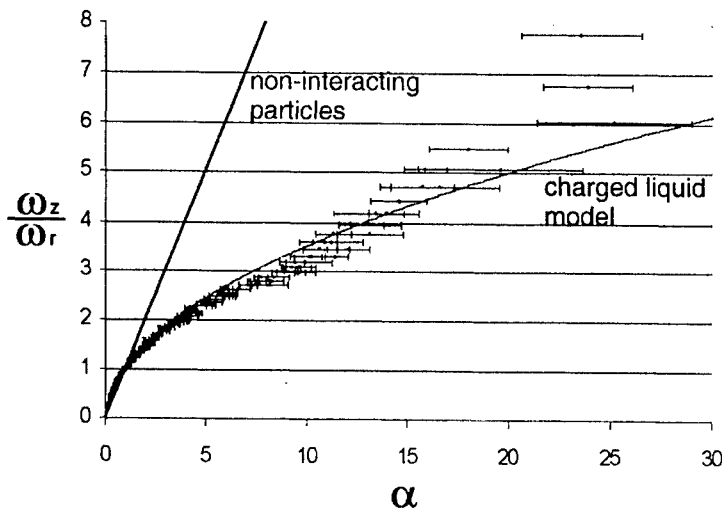


FIGURE 2. Measured radial to axial aspect ratio α of the crystal shown in Fig. 1 for corresponding calculated ratio of the axial to radial trap oscillation frequencies, ω_z/ω_r . The two graphs shows the expected relation between these two quantities in a non-interacting particle and a cold charged liquid model.

So far, only in Penning traps it has been possible to create large enough ion Coulomb crystals that structures associated with infinite two- and three-dimensional crystals (e.g., hexagonal and bcc-structures) have been observed [3,4]. Recently, we have conducted several experiments with large pure ion plasmas created by resonantly enhanced photo-ionization [8] in order to observe similar structures in a linear Paul trap. For the largest ion plasma ($\sim 15,000$ ions) that can be viewed by the CCD-camera system, we observe no central structures, but only few shell structures at the outer plasma boundary as reproduced in Fig. 3. RF-field induced heating might be one reason for the lack central structures. However, since molecular dynamics simulations with up to 10^5 ions (see contribution by H. Totsuji, *et al.* in this proceeding) also seems to fail to reproduce central structures when starting from an initial random distribution, the reason might be more subtle.

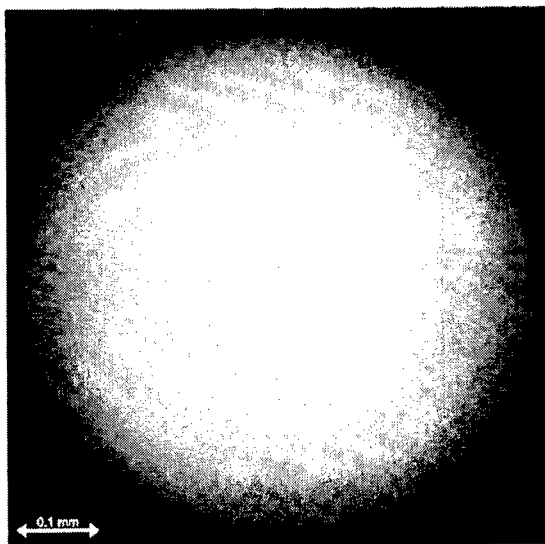


FIGURE 3. Cold ion plasma consisting of $\sim 15,000$ $^{40}\text{Ca}^+$ ions. If fully crystallize, the plasma should consist of about 22 shells, but only a few shells at the outer boundary is observed.

As reported by N. Kjærgaard *et al.* elsewhere in the present proceeding, our group has also recently investigated Coulomb crystals in a pulse-excited Paul trap.

MULTI-COMPONENT CRYSTALS

Though crystals containing few impurity ions have been observed since the first experiments, so far not much attention has been paid to experimental studies and applications of ion Coulomb-crystals of multi-species. Recently, we have, however, studied some properties of two-component crystals (bicrystals) in linear Paul traps.

Structures of Two-Species Coulomb Crystals

If more than one ion species is present at the same time in the trap, new more complex orderings appear. In our group we have recently investigated the structures of ion Coulomb crystals containing both laser-cooled $^{24}\text{Mg}^+$ and $^{40}\text{Ca}^+$ ions [7]. Examples of pictures of such bicrystals are shown in Fig. 4. The reason for the obvious radial separation of the two ion species is that for singly-charged ions the oscillation frequency along the static field axis of the trap is independent of the ion mass, while in the radial plane the oscillation frequency increases with decreasing mass of the ions. Hence, in the radial plane it is energetically most favorable for the ions to segregate with $^{24}\text{Mg}^+$ ions closest to the trap axis. The cylindrical structures of the $^{24}\text{Mg}^+$ ions in these crystals are found to be surprisingly identical to those expected for an infinitely long crystal that is radial confined by a harmonic potential [7]. This similarity is perhaps most obviously seen in Fig. 5, where one observes a string of 47 $^{24}\text{Mg}^+$ ions,

which are equidistantly spaced. Even for crystals with an equal amount of the two ion species, the shape of the outer boundary of the $^{40}\text{Ca}^+$ part of the crystal is only slightly influenced by the presence of the $^{24}\text{Mg}^+$ [7].

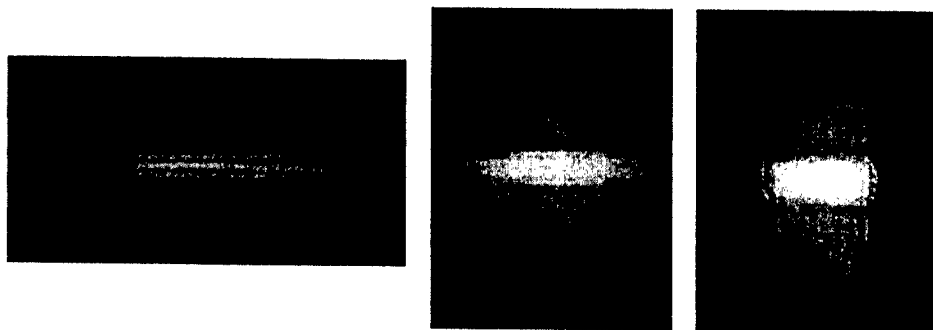


FIGURE 4. CCD-images of a bicrystal composed of ~ 3000 $^{40}\text{Ca}^+$ and ~ 300 $^{24}\text{Mg}^+$ ions for three different trapping potentials. The dark gray and the light gray color code correspond to fluorescence from Ca^+ and Mg^+ ions, respectively.

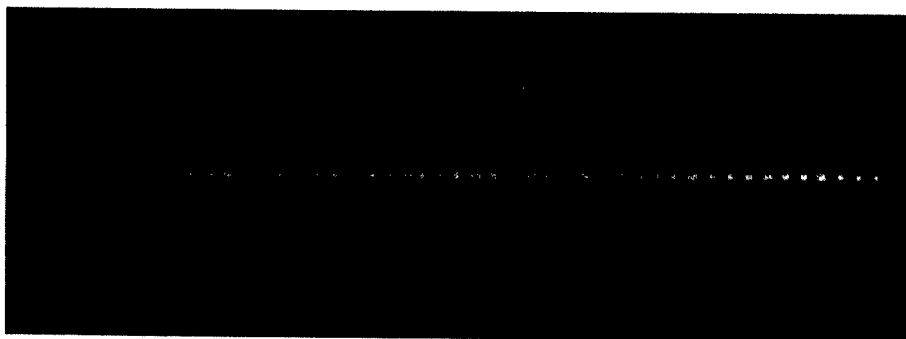


FIGURE 5. CCD-image of a bicrystal composed of ~ 1300 $^{40}\text{Ca}^+$ and 47 $^{24}\text{Mg}^+$ ions (Color code as in Fig. 4). Note that the $^{24}\text{Mg}^+$ ions are arranged in an equidistant string structure.

We have also initiated investigations of bicrystal structures with other ion species. One interesting example is the case where two ion species with the same charge to mass ratio are present in a linear Paul trap. The result of a molecular dynamics simulation of such a (spherical) bicrystal containing 150 $^{40}\text{Ca}^+$ and 150 $^{80}\text{A}^{2+}$ ions (here ^{80}A just means any element or molecule with mass 80) is shown in Fig. 6. Surprisingly, as is immediately observed, the two ion species mixes in common shells. The radius R of these bicrystals (and hence the shell separation) follows a very simple law:

$$R = (3/(4\pi)(N_{\text{Ca}}/n_{\text{Ca}} + N_{\text{A}}/n_{\text{A}}))^{1/3}, \quad (1)$$

where N_{Ca} and N_{A} are the numbers of the two ion species, and n_{Ca} and n_{A} the densities in the case where only the single species is present in the trap.

This law, which essential states that the two species fully mixes, is graphically presented in Fig. 7 together with data obtained from simulations.

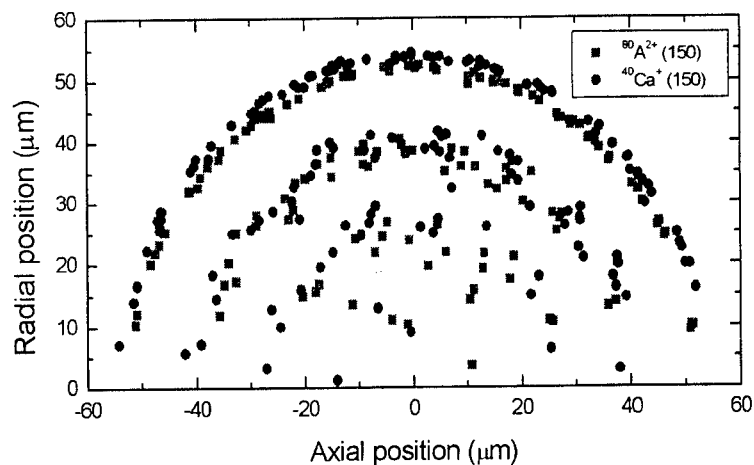


FIGURE 6. Results from molecular dynamics simulation of a bicrystal containing 150 $^{40}\text{Ca}^+$ and 150 $^{80}\text{A}^{2+}$ ions in a linear Paul trap. Note how the two ion species mixes in common shells.

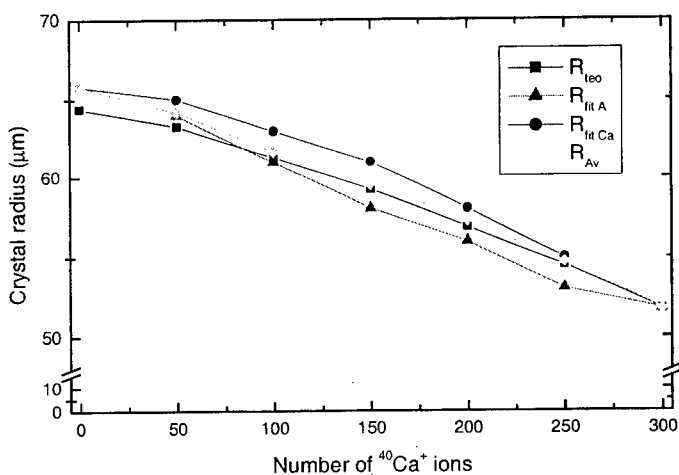


FIGURE 7. Radius of spherical bicrystals consisting of $^{40}\text{Ca}^+$ and $^{80}\text{A}^{2+}$ ions in a linear Paul trap for various contents of $^{40}\text{Ca}^+$ ions. The total number of ions is always 300. Notation: R_{teo} - radius found from Eq.(1), $R_{\text{fit A}}$ - radius obtained from fit to position of $^{80}\text{A}^{2+}$ ions in the outer shell, $R_{\text{fit Ca}}$ - radius obtained from fit to position of $^{40}\text{Ca}^+$ ions in the outer shell, and R_{Av} - a weighted average of $R_{\text{fit A}}$ and $R_{\text{fit Ca}}$.

Sympathetic Cooling

One application of bicrystals is to laser cool only one ion species and let the other species be sympathetically cooled through the Coulomb interaction with the directly cooled ions [9-11]. Since the Coulomb interaction is long ranging, one can very effectively achieve sympathetic cooling at time scales of seconds, which is much shorter than the typical storage time (up to hours) of the ions in the trap. An example of the result of sympathetic cooling is shown in Fig. 8. This figure shows the observed fluorescence from laser cooled $^{40}\text{Ca}^+$ ions (~2000 ions) cooling O_2^+ molecular ions (~500 ions), formed by electron bombardment of a gas of O_2 molecules let into the trap vacuum chamber. Since the O_2^+ ions are lighter than the $^{40}\text{Ca}^+$ ions, when cooled they form cylindrical structures equivalent to the Mg^+ ions in Fig. 4, and, indeed, a hollow (non-fluorescing) cylindrical structure is present in Fig. 8. It is generally not easy to obtain a value of the exact temperature of the sympathetically cooled ions, but from pictures like that in Fig. 8, where crystal structures of the laser-cooled $^{40}\text{Ca}^+$ ions are clearly observed, we can from simulations of such two-component ion plasmas conclude that the temperature cannot be above some tens of milliKelvins. A more direct temperature measurement has been possible with crystals as the ones shown in Fig. 4. By observing the fluorescence from $^{24}\text{Mg}^+$ ions as function of the detuning of a weakly exciting laser an upper temperature can be established from the broadening of the line profile. In Fig. 9, such a profile is presented together with a Voigt-profile fit, which corresponds to a temperature of 45 mK.

Since direct laser cooling can only be applied to a very limited number of singly-charged atomic ions, sympathetic cooling highly expands the possibilities of detailed investigation and manipulation of other ion species including molecular ions, as shown in Fig. 8, and multi-charged ions [12]. The spatial segregation of the ions with different masses makes it, furthermore, possible to, e.g., make a laser beam only interacting with the ion species of interest. For instance, sympathetically cooled ions on a central string in larger bicrystals (see Fig. 5) will be an ideal target for high-resolution spectroscopy and can probably be applied in metrology related research.

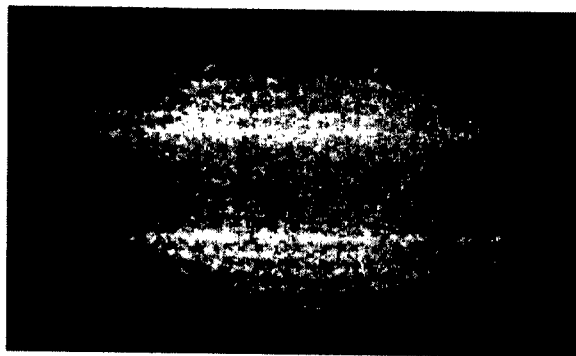


FIGURE 8. A bicrystal containing O_2^+ and $^{40}\text{Ca}^+$ ions. Since the O_2^+ ions are lighter than the Ca^+ ions, they form a cylindrical structure equivalent to the Mg^+ ions in Fig. 4. This shows up in the picture as a hollow (non-fluorescing) cylindrical structure.

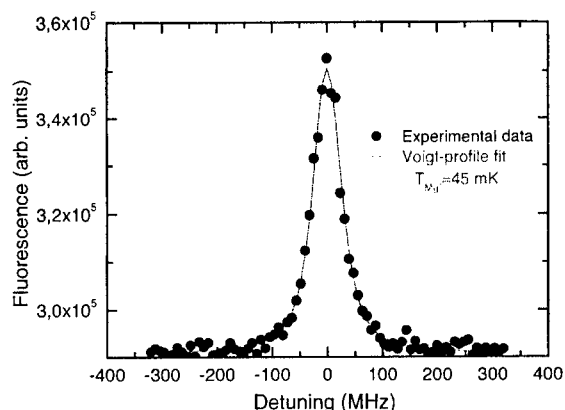


FIGURE 9. Fluorescence from $^{24}\text{Mg}^+$ ions as function of the detuning of a weakly exciting laser. The full circles are the obtained data points, while the full line represents a Voigt-profile fit, which corresponds to a temperature of 45 mK

COLD MOLECULAR PHYSICS

In the previous section it was shown that molecular ions produced by electron ionization could be trapped and cooled sympathetically to very low translational temperatures. With such a translational cold and spatially localized molecular ion target one can investigate various possibilities of cooling the molecular ion's internal degrees of freedom, i.e., rovibrational motions. From simple theoretical considerations [13], it is not believed that the Coulomb interaction will efficiently cool these degrees of freedom. Due to the multi-level structures of molecules, standard laser cooling will not apply either. However, since the trapping time can be of the order of minutes or more, we plan to investigate various new cooling schemes, which might bring the molecular ions into specific internal states. If this will be achieved, such cold state-specific molecular ions can be an interesting playground for performing, e.g., various coherent-controlled molecular dynamics experiments.

Ion Coulomb crystals are furthermore interesting targets for reaction experiments. So far, we have studied a few reactions between laser-cooled ions in Coulomb crystals and neutral molecules. For larger crystals of Mg^+ ions we have, e.g., studied photochemical reactions with H_2 and D_2 gasses [11]. Monitoring the change in the fluorescence rate from the remaining Mg^+ ions as a function of reaction time, reaction rates were determined. Furthermore, the reaction product ions could be deduced to be MgH^+ or MgD^+ in a non-destructive way by monitoring their radial position with respect to two Mg^+ isotopes in the Coulomb crystal as illustrated in Fig. 10. By only applying resonant light to the $^{24}\text{Mg}^+$ ions, isotope specific reactions could be obtained.

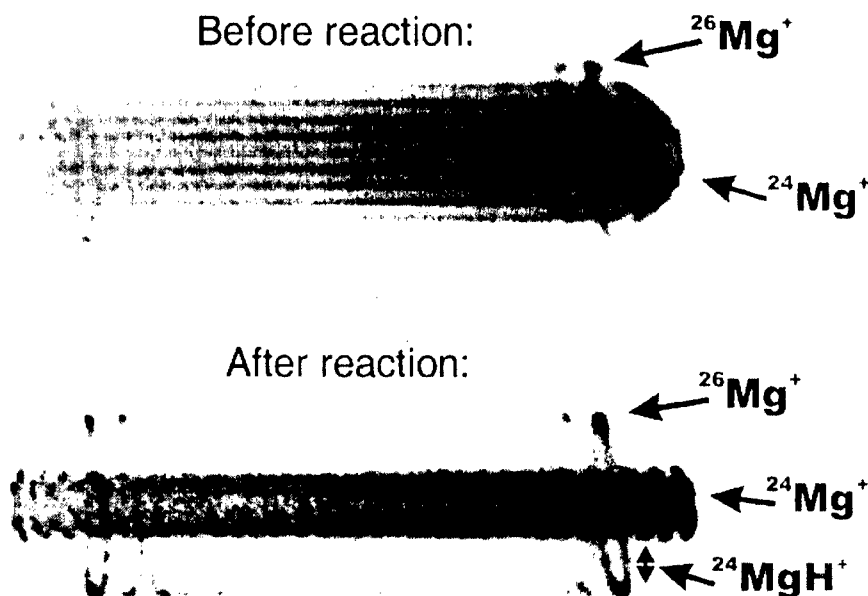


FIGURE 10. CCD-images of the fluorescence from $^{24}\text{Mg}^+$ and $^{26}\text{Mg}^+$ ions before and after the reaction of $^{24}\text{Mg}^+$ ions with a H_2 gas. The product ions $^{24}\text{MgH}^+$ appear as a non-fluorescent cylindrical region between the two magnesium isotopes.

We have very recently initiated experiments with the aim of studying reaction processes on the single molecule level. This can be achieved by, e.g., initially having a string of laser-cooled Ca^+ ions, which can individually be monitored by a CCD-camera as shown in Fig. 11a. By introducing a thermal O_2 gas at a very low pressure (typically $<10^{-9}$ torr) into the trap region, one can observe how the individual Ca^+ ions disappear by time and leave non-fluorescing ions in the string, which from additional experiments are known to be CaO^+ ions (see Fig. 11b). Monitoring the fluorescence integrated over the whole string of ions as a function of time, one observes significant discrete changes in the fluorescence level, revealing the fundamental discrete nature of the reactions. Whether such "digital" information on the reaction processes will give fundamental new insight into chemical reactions is still unclear, but the technique could certainly be used in studies of extremely low rate reactions, due to the long storage time of the cold ions. Since the product ions can typically be trapped and cooled, multi-step reactions can furthermore be studied. An example of the product of a two-step reaction is shown in Fig. 11c. Here the ion string of Fig. 11b has been subjected to a CO gas, which in reaction with CaO^+ leads to reappearance of fluorescing Ca^+ ions and CO_2 . A few dark spaces (ions) are still present in Fig. 11c due to unknown impurity reactions.

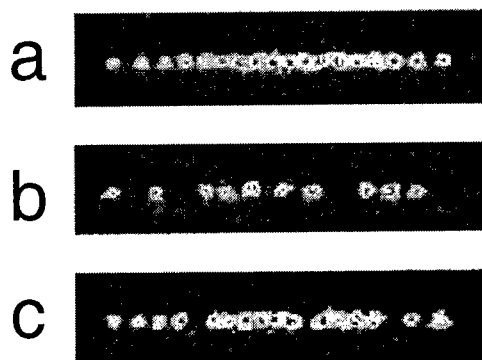


FIGURE 11. a) A string of 18 laser-cooled Ca^+ ions. b) The same string as in figure a), but after reactions with thermal O_2 molecules, which lead to the production of non-fluorescing CaO^+ ions. c). The string of ions in Fig. b) after reactions with CO molecules. Reactions between CaO^+ ions and CO molecules lead to reappearance of fluorescing Ca^+ ions and CO_2 . A few dark spaces (ions) are still present due to unknown impurity reactions.

QUANTUM MEMORY FOR LIGHT

In order to make future quantum information networks operational, one will need to store quantum information temporarily. Since quantum information most likely will be transferred in the form of light, naturally, one seeks to find appropriate quantum memory devices for quantum states of light.

Recently, two independent experiments have demonstrated that a pulse of coherent light can be temporarily stored as a collective excitation of a cold atomic ensemble [14,15]. The idea behind these experiments suggests that not only coherent light pulses, but also light with non-classical characters can be stored. Both experiments relied on a very large reduction of the group velocity of the light pulse as well as on the atomic medium being optically thick in the absence of a control laser beam. It has, however, been shown that these requirements can be relaxed if the atomic ensemble is placed within a high-finesse optical cavity [16], where the light pulse, due to multiple reflections, will pass the atoms several times. In short, the proposal is based on dynamical impedance matching of the light pulse of interest to an optical cavity with absorption in the form of a stimulated rapid adiabatic transfer process in the atomic media. The absorption rate of the light carrying the quantum information is controlled via a strong classical laser pulse. By the adiabatic transfer process, the initial quantum information of the light pulse is transferred into collective coherent excitation of the atomic ensemble. By a time reversal of the classical light pulse the initial quantum state of light will be regenerated as an output from the cavity.

In our view, the atomic sample in the optical cavity could advantageously be a Coulomb crystal of a few thousand ions. Ions in such crystals may have storage life times of tens of minutes, and have internal state coherence times of the order of a second or more. Using bi-crystals as the ones shown in Fig. 4 and Fig. 8, one species

can be used as the storage medium, while the other can be directly laser cooled and sympathetically cool the “memory” ions.

In such experiments we plan to use $^{40}\text{Ca}^+$ ions as “memory” ions since they have suitable electronic transitions for the quantum storage of light in the near infrared where non-classical light sources are available. The $^{40}\text{Ca}^+$ ions will be cooled sympathetically by $^{44}\text{Ca}^+$ ions, which we plan to load in appropriate amounts using isotope-selective resonant two-photon ionization of an atomic beam [8].

ACKNOWLEDGMENTS

The presented work has been possible due to financial support from the Danish National Research Foundation, the Danish Research Council, and the Carlsberg Foundation.

REFERENCES

1. Birkel, G., Kassner, S., and Walther, H., *Nature* **357**, 310 (1992).
2. Drewsen, M., *et al.*, *Phys. Rev. Lett.* **81**, 2878 (1998).
3. Itano, W. M., *et al.*, *Science* **279**, 686 (1998).
4. Mitchell, T. B., *et al.*, *Science* **282**, 1290 (1999).
5. Block, M., Drakoudis, A., Leutner, H., Siebert, P., and Werth, G., *J. Phys. B.* **33**, L375 (2000).
6. Schätz, T., Schramm, U., and Habs, D., *Nature* **412**, 717 (2001).
7. Hornekær, L., *et al.*, *Phys. Rev. Lett.* **86**, 1994 (2001).
8. Kjærgaard, N., *et al.*, *Appl. Phys. B* **71**, 207 (2000).
9. Larson, D. J., *et al.*, *Phys. Rev. Lett.* **57**, 70 (1986).
10. Bowe, P., *et al.*, *Phys. Rev. Lett.* **82**, 2071 (1999).
11. Mølhave, K. and Drewsen, M., *Phys. Rev. A* **62**, 011401(R) (2000).
12. Gruber, L., *et al.*, *Phys. Rev. Lett.* **86**, 636 (2001).
13. Mølmer, K., private communication.
14. Liu, C., *et al.*, *Nature* **409**, 490 (2001).
15. Phillips, D. F., *et al.*, *Phys. Rev. Lett.* **86**, 783 (2001).
16. Lukin, M. D., Yelin, S. F., and Fleischhauer, M., *Phys. Rev. Lett.* **84**, 4232 (2000).

Coulomb Crystals in a Pulse-Excited Linear Paul Trap

N. Kjærgaard, K. Mølhave, and M. Drewsen

Institute of Physics and Astronomy, Aarhus University, DK-8000 Aarhus C, Denmark

Abstract. We present results from recent experiments with laser cooled $^{24}\text{Mg}^+$ ions captured in a pulse-excited linear Paul trap. As discussed in [1–3], the radial/transverse dynamics of charged particles in an electric quadrupole trap with a pulsed voltage excitation is analogous to that of particles travelling through the alternating gradient (AG) magnetic quadrupole lattice of a storage ring or transport channel. Hence, the pulse-excited Paul quadrupole trap may be used to emulate non-neutral beam propagation. In a series of experiments, we have investigated the stability of stationary Coulomb crystals. The results comply with current theory of crystalline plasmas and beams. We observe, however, that the plasma may stay crystalline beyond the expected stability region in a hitherto unseen configuration consistent with a string of rotating discs.

INTRODUCTION

When a charged particle travels through a magnetic quadrupole it experiences a focusing force in one dimension and a defocusing force in the perpendicular dimension. However, by combining two quadrupoles with opposite polarities into a doublet a net focusing effect can be obtained in both dimensions as illustrated in Fig. 1. Alternating gradient (AG) magnetic quadrupole focusing was proposed by Courant, Livingston, and Snyder [4] in the early 1950's¹ and despite its simplicity, this concept revolutionized accelerator design [6] and is today widely used in storage rings to achieve transverse confinement of particles along the design orbit. The resulting transverse dynamics can be emulated in the stationary frame of an electric quadrupole trap [1–3] and in recent experiments we have exploited this analogy to investigate the stability of laser cooled $^{24}\text{Mg}^+$ Coulomb crystals produced and imaged as described in [7].

THE PULSE-EXCITED LINEAR PAUL TRAP

The linear Paul trap employed in the experiments consists of four cylindrical electrodes, as shown in Fig. 2(a), with a radius of $R = 4.0$ mm; the radius of the inscribed inter-electrode space is $r_0 = 3.5$ mm. To operate the trap in a pulsed mode, the periodic rf voltage $\phi_\tau(t)$ shown in Fig. 2(b) is applied to the rods. The pulsed waveform is characterized by an amplitude V_{rf} , a period T , and a pulse duration τT . As indicated

¹ The idea had been suggested earlier by Christofilos [5] but was unpublished.

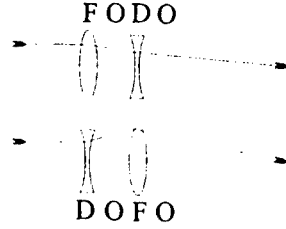


FIGURE 1. Principle of AG focusing. A focusing-defocusing or defocusing-focusing lens pair gives rise to net focusing. For equally strong lenses the inter-lens distance should be less than twice the magnitude of the lens focal length. The combination 'Focusing (F)-Drift (O~"zero")-Defocusing (D)-Drift (O~"zero")' is commonly referred to as a *FODO cell*.

in Fig. 2(a), the pulses are applied alternately ($\frac{\pi}{2}$ / $\frac{\pi}{2}$) to the two pairs of diagonally opposite quadrupole rods with a phase delay of $T/2$. The resulting voltage difference between adjacent rods then varies as shown in Fig. 2(c). The time-dependent electric potential near the axis approximates a perfect quadrupole

$$\Psi_p(x, y, t) = \frac{\phi_\tau(t) - \phi_\tau(t - T/2)}{2} \frac{x^2 - y^2}{r_0^2}, \quad (1)$$

and gives rise to pseudo-harmonic radial confinement. The corresponding radial oscillation frequency ω_p can be calculated from the one period transfer matrix [3, 8]. In Eq. (1), the time elapsed between subsequent focusing and defocusing pulses is $T/2$ and all pulses have the same duration and amplitude. For an energetic ion beam in a magnetic AG storage ring, this corresponds to propagation through a regular so-called

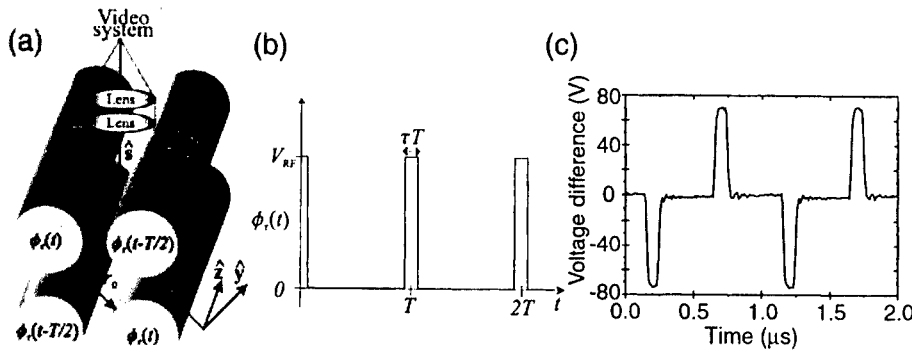


FIGURE 2. (a) The linear Paul trap. Time-varying voltages $\phi_\tau(t)$ and $\phi_\tau(t - T/2)$ are applied to adjacent rods as shown. To obtain axial confinement of ions, each electrode is sectioned into three and an additional dc voltage U_{dc} is applied to the eight end-pieces with respect to the center-pieces. (b) The pulsed, time-varying waveform $\phi_\tau(t)$. (c) Example of the measured time-varying voltage differences between adjacent quadrupole rods when the dual channel amplifier applies voltage pulses alternately to the two pairs of diagonally opposite quadrupole rods; $\omega_{RF} = 2\pi \times 1$ MHz and pulse duration 100 ns (i.e., $\tau = 0.1$).

FODO-lattice². The parameters can, however, be varied quite arbitrarily with respect to duration and delay and still give rise to radial confinement. The pulses are produced by a dual-channel pulse amplifier with inputs from two pulse generators triggered at the desired repetition frequency by a function generator. Each channel of the pulse amplifier is rated to a pulse amplitude of 200 V at $\omega_{RF} = 2\pi \times 1$ MHz with a minimum pulse duration < 100 ns. An axial confinement force is achieved by sectioning each of the quadrupole rods into three as shown in Fig. 2(a) and applying an additional dc voltage U_{dc} to the eight end-pieces. This gives rise to a static, approximately harmonic potential $\Psi_s(x, y, z) = \eta z_0^{-2} U_{dc} [z^2 - (x^2 + y^2)/2]$, where η is a geometric factor. In the current experiments, $z_0 = 5.4$ mm corresponding to $\eta = 0.248$ and the harmonic approximation is valid up to a few millimeters from the trap center. The single particle axial oscillation frequency is $\omega_z = \sqrt{-a/2}\omega_{rf}$, where $a = -4\eta e U_{dc}/m z_0^2 \omega_{rf}^2$. We note that the axially confining force arising from the static potential Ψ_s is accompanied by a radial, defocusing force. Denoting the radial distance to the trap axis by ρ the radial component of this force is $F_{s,\rho} = m(\omega_z^2/2)\rho$.

Cold Plasma in a Harmonic Trap

The linear Paul trap can be described as a harmonic trap with an effective potential of the form (using cylindrical coordinates)

$$\Phi(\mathbf{r}) = \frac{m\omega_z^2}{2e} (z^2 + \beta\rho^2), \quad (2)$$

where

$$\beta = \frac{\omega_p^2 - \frac{1}{2}\omega_z^2 - \omega_\phi^2}{\omega_z^2}. \quad (3)$$

Here, ω_ϕ accounts for a possible angular rotation frequency of the trapped plasma about the z -axis and this defocusing term usually equals zero for a linear Paul trap. We note that the meaning of β is nothing but the (resulting) radial to axial confinement force ratio.

Neglecting variations on an inter-particle scale, the density of a low temperature plasma (cold fluid) in a harmonic trap is constant and given by

$$n_0 = \frac{\epsilon_0}{e} \nabla^2 \Phi = \frac{2\epsilon_0 m \omega_z^2}{e^2} \left(\beta + \frac{1}{2} \right) = \frac{2\epsilon_0 m}{e^2} (\omega_p^2 - \omega_\phi^2), \quad (4)$$

independent of ω_z . Furthermore, the shape of the cold plasma can be shown to be a spheroid [9] and is hence uniquely described through the length of the envelope semi-axes Z (along the trap axis) and R (in radial direction). The spheroid aspect ratio $\alpha = Z/R$ and the β -parameter in Eq. (3) is related [9] as shown in Fig. 3(b).

² The current setup is restricted to emulate the quadrupole focusing/defocusing forces of a storage ring. For more involved experiments on crystalline beam emulation, one could look into the possibilities of implementing shear from bending by perturbing the crystals sideways with a suitable, periodic, transverse electric force.

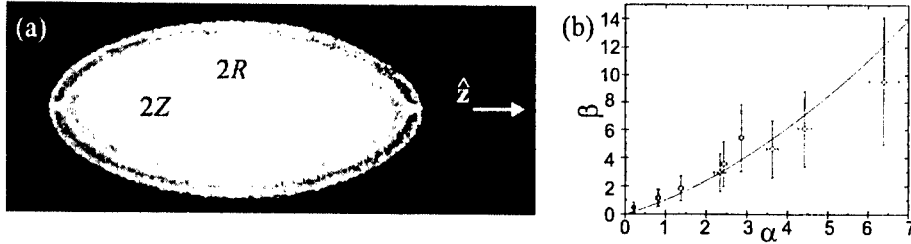


FIGURE 3. (a) Example of a Coulomb crystal with a shape and density described well by cold fluid theory with $\omega_p = 0$. The ions are arranged in closed spheroidal shells. (b) The relation between α and β as given by cold fluid theory (line). β for a string-of-discs state crystal (o) calculated from experimental parameters using Eq. (3) with $\omega_p = 0.31 \times \omega_{rf}$.

The shape of (non-rotating) Coulomb crystals in a linear Paul trap has previously been shown to be described well by cold fluid theory [10]. Figure 3(a) shows an image of such a crystal in the pulse-excited trap.

Bulk plasma oscillations in the cold fluid occur at the plasma frequency $\omega_p = \sqrt{e^2 n_0 / \epsilon_0 m}$ which also equals the maximum bulk mode frequency in the case of a crystal [11]. From Eq. (4) we get $\omega_p^2 = 2(\beta + 1)\omega_z^2 = 2(\omega_p^2 - \omega_0^2)$. To avoid a 1:2 (parametric resonance) relationship between frequency of a bulk mode and the rf driving field we have the criterion $2\omega_p < \omega_{rf}$. This is equivalent to the tune condition for a crystalline ion beam as predicted by theory [12].

RESULTS FROM EXPERIMENTS

In a recent series of experiments, we investigated the stability properties of laser cooled $^{24}\text{Mg}^+$ Coulomb crystals when approaching the $2\omega_p = \omega_{rf}$ resonance condition [13]. In this contribution, we shall only briefly summarize and discuss some of the results from this work. Notably, it was found that trapped crystals (initially in stable, closed shell configuration comparable to the one shown in Fig. 3) become unstable and blow up to a gaseous cloud state when the plasma frequency is increased to hit the parametric resonance. The plasma frequency was increased by increasing ω_p through the rf waveform amplitude V_{rf} , while all other parameters were kept constant. The observed stability limit was in excellent agreement with the one predicted by theory and seemed quite insensitive to the axial confinement and the number of particles (~ 50 – 1000). Surprisingly, the plasma was, however, observed to settle into a different and hitherto unobserved ordered structure when ω_p was increased slightly above the value of instability (see Fig. 4). This final state has lower density and different spheroidal envelope than the initial closed shell structure observed just before hitting the point of instability, and appears as an axially ordered string of discs. By averaging over more frames we have, furthermore, seen indications of radial ordering within the discs (see Fig. 5).

As mentioned above, the initial closed shell structure shown in Fig. 4 is described well by cold fluid theory with the plasma in a non-rotating state. This cannot be the

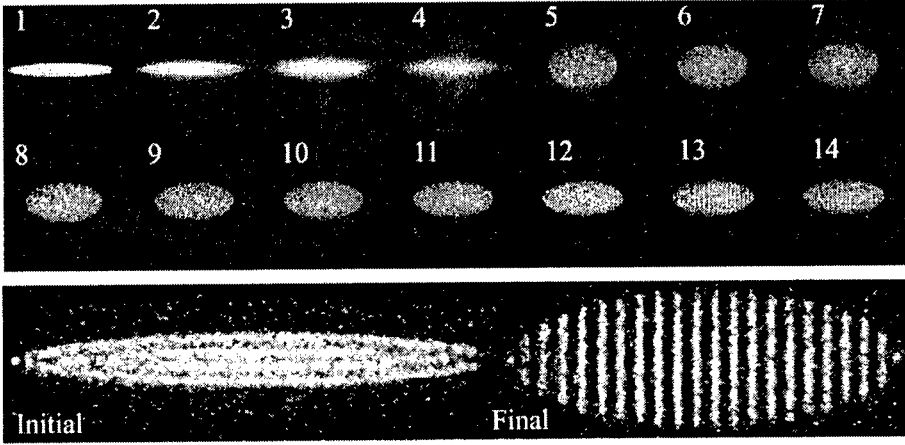


FIGURE 4. Upper part: Frame sequence (1-12) showing the closed shell→string-of-discs structural transition for about 370 ions when passing the parametric resonance $2\omega_p = \omega_{rf}$; the sequence was acquired with 5 frames/s and the trap was operated at $\omega_{rf} = 2\pi \times 700$ kHz with $\tau = 0.14$. Lower part: Close-up images of the initial and final state for the structural transition.

case for the final state as we only increase V_{rf} slightly to induce the structural transition so that ω_p enters with approximately the same amount in the expressions for density and shape. Moreover, if one, anyway, considers a slight increase in ω_p , this implies an increase both in density and aspect ratio, in contrast to the observations of the final state. However, the observed quantities might be explained from the cold fluid equations by assuming the plasma to be in a rotating state with $\omega_\phi \neq 0$ [see, e.g., Eq. (4)]. This conjecture is supported by measurements performed on the string-of-discs state where ω_z was varied and the corresponding aspect ratio was recorded [13]. By assuming the plasma to be rotating at the frequency $\omega_\phi = 0.31 \times \omega_{rf}$, we obtain the expected relation between β and α as given by cold fluid theory [see Fig. 3(b)]. Otherwise (i.e., putting $\omega_\phi = 0$), β calculated from Eq. (3) would be an order of magnitude off. A mechanism leading to rotation and which, furthermore, yields the assumed frequency is not clear at present.

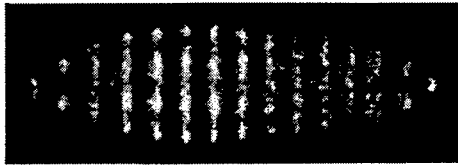


FIGURE 5. String-of-discs structure showing radial ordering. The image was obtained by averaging over 5 frames (=1 s).

CONCLUSION AND DISCUSSION

In conclusion, we have investigated the stability of Coulomb crystals in a pulse-excited linear Paul trap having the same transverse dynamics as a storage ring with AG magnetic confinement. The observations agree well with current theory on crystalline plasmas and beams. Notably, it seems that the criterion $2\omega_p < \omega_{rf}$ should be taken very seriously. However, at the stability limit we observed crystals to survive by rearranging in axially ordered structures. The observation was shown to be consistent with a string of rotating discs. We recently learned about some early work by Blümel *et al.* [14] where similar “layered structures” were found in connection with molecular dynamics simulations of up to 500 laser cooled ions in a conventional Paul trap. Why these simulations give rise to layered structures instead of ending up in a closed shell structure as found in equivalent work (see, e.g., [15] and references therein) is not clear at present. The possible and likely connection to our work will a subject of future studies.

ACKNOWLEDGMENTS

This work was supported by the Danish National Research Foundation through Aarhus Center of Atomic Physics, the Danish Research Council, and the Carlsberg Foundation. N.K. gratefully thanks the organizing committee of the 2001 Workshop on Non-Neutral Plasmas for financial support.

REFERENCES

1. Okamoto, H., and Tanaka, H., *Nucl. Instrum. Methods A*, **437**, 178 (1999).
2. Davidson, R. C., Qin, H., and Shvets, G., *Phys. Plasmas*, **7**, 1020 (2000).
3. Kjærgaard, N., and Drewsen, M., *Phys. Plasmas*, **8**, 1371 (2001).
4. Courant, E. D., Livingston, M. S., and Snyder, H. S., *Phys. Rev.*, **88**, 1190 (1952).
5. Christofilos, N. C., U. S. patent no. 2.736,799, filed March 10, 1950, issued February 28, 1956.
6. Bryant, P. J., in *Proceedings of the CERN Accelerator School: Fifth General Accelerator Physics Course*, edited by S. Turner, CERN 94-01, Geneva, 1994, vol. 1, p. 1.
7. Kjærgaard, N., *et al.*, *Appl. Phys. B*, **71**, 207 (2000).
8. Courant, E. D., and Snyder, H. S., *Ann. Phys.*, **3**, 1–48 (1958).
9. Dubin, D. H. E., *Phys. Rev. E*, **53**, 5268 (1996).
10. Drewsen, M. *et al.*, these Proceedings.
11. Dubin, D. H. E., and Schiffer, J. P., *Phys. Rev. E*, **53**, 5249 (1996).
12. Wei, J., Okamoto, H., and Sessler, A. M., *Phys. Rev. Lett.*, **80**, 2606 (1998).
13. Kjærgaard, N., Mølhave, K., and Drewsen, M., *Phys. Rev. Lett.* (2001), submitted.
14. Blümel, R., *et al.*, in *Proceedings of the 5th International Symposium on Quantum Optics*, Springer, 1989.
15. Schiffer, J. P., *et al.*, *Proc. Natl. Acad. Sci. U.S.A.*, **97**, 10697 (2000).

Trapped Highly Charged Ion Plasmas

E. Takács¹ and J. D. Gillaspy²

National Institute of Standards and Technology, Gaithersburg, MD 20899

Abstract. Electron Beam Ion Trap (EBIT) devices and their special features are reviewed with attention to applications in highly charged ion plasma research. EBIT properties are presented based on information extracted from a variety of experiments reported in the literature. Topics discussed include typical parameters (Debye length, Wigner-Seitz radius, Coulomb coupling parameter, density, temperature, etc.), magnetic trapping mode, ion cloud shape, rotation, and evaporative cooling. We conclude that the quantitative understanding of highly charged ion plasmas inside an EBIT requires improved modeling and advanced diagnostic techniques.

INTRODUCTION

Heavy ions with dozens of electrons removed, so-called highly charged ions, have a wide range of potential applications. Imagine an atomic system that is stripped to its core, with only a few electrons remaining at most. The electronic binding energy that must be overcome to further ionize such a system can be over a thousand times higher than that in ordinary ions or atoms. Even more striking, the potential energy liberated when such a highly charged ion re-neutralizes itself can be nearly a million times larger than that of a conventional ion.

Because many atomic properties scale with high powers of the nuclear charge, ions along an isoelectronic sequence (ions with different nuclear charges, but the same number of electrons) quickly enter exotic regimes where conventional intuition fails. Forbidden electronic transitions can become stronger than those allowed by electric dipole selection rules, and energy levels can become strongly affected by the structure of the vacuum [1,2].

The enormous amount of free potential energy and ultra-compact size that highly charged ions possess is as unique as their exotic atomic structure. When such ions approach surfaces, their strong electrostatic pull on bulk electrons can be felt many atomic diameters away. As a result, highly charged ions are very effective in modifying or breaking chemical bonds and crystal structures on the nanometer length scale [3].

The natural curiosity to study such exotic ions in the extreme strong field limit was one of the driving forces to build a device, such as an Electron Beam Ion Trap (EBIT), that can be accommodated in a small laboratory. The first EBIT was put into operation at the Lawrence Livermore National Laboratory [4,5] almost fifteen years ago. Shortly after this, the National Institute of Standards and Technology (NIST) became the

¹ Also at Massachusetts Institute of Technology, Cambridge, MA 02139 and University of Debrecen, Debrecen, Bem tér 18, Hungary, H-4026, E-mail: endre.takacs@nist.gov ² E-mail: john.gillaspy@nist.gov

second place in the world to have a working EBIT [6,7], followed by new constructions in several other laboratories [8-12].

EBITs are not the only machines that can create ions in high charge states, but certainly they are one of the most versatile, offering great control over the experimental conditions in which highly charged ions are produced. The success of the EBIT is proven by the numerous widely-cited experiments that have been carried out by since its inception [4,5,13-18].

Although the device is still in the process of rapid evolution, the fact that current small-scale EBITs can already produce millions of highly charged ions per second suggests that applications that take advantage of the unusual properties of very highly charged ions should be pursued. Some of the basic scientific studies which will underlie applications of such exotic ions are being carried out by the highly charged ion community, while more immediate applications are being pursued by industrial entrepreneurs [19] (and references contained in [2]).

As EBIT devices may one day be capable of producing much larger numbers of highly charged ions, it is interesting to survey the capabilities and properties of the present machines to help further the development of possible future designs. The basic mechanisms of ion production and operation of the EBIT is theoretically understood; the evolution of the charge states and the dynamical ionization and recombination balance between the neighboring charges can qualitatively be accounted for with model calculations [20-23]. However, there are indications in several experiments that a quantitative understanding remains to be developed.

Detailed understanding of EBIT properties is hampered by the fact that only a limited number of experiments have been performed that specifically target the properties of the highly charged plasma inside an EBIT. There is, however, a large database of indirect information contained in other types of measurements. In the present paper, we will attempt to put these pieces of information together in a coherent manner to provide a general experimental overview of the detailed operation and features of an EBIT. We will also point out some discrepancies that have accumulated in the fifteen years of experience with the device that might point to a better understanding of its operation and that could possibly even be exploited in future applications. We hope that with this summary we will stimulate people from the broader scientific community to contribute to a cross-disciplinary attack on some of the problems, and in particular to put forward advanced diagnostic and modeling ideas that will ultimately help to realize new applications for highly charged ions.

HIGHLY CHARGED ION BEAMS AND CLOUDS

Most of the applications that take advantage of highly charged ions require large numbers ions in the form of high quality clouds or beams. EBITs, in this sense, already qualify as one of the best devices to study. The source region is rather simple and well controllable, and is qualitatively similar to the precision controlled traps that the non-neutral plasma community uses. Understanding the basic properties of these traps can serve as a foundation for designing new, innovative highly charged ion devices. However, as in atomic structure, it might well be that conventional plasma

properties have to be rethought in the highly charged ion regime, in which case existing EBITs could be used as test-beds for these ideas.

Some members of the conventional non-neutral plasma community have argued that highly charged ions could offer some attractive possibilities for the study of strongly coupled systems at relatively high temperatures [24]. Some of the advantages of using highly charged ions in quantum information schemes have also been discussed [25]. One of the first steps towards these goals was the experimental realization of a highly charged ion crystal in a precision trap that was filled with ions from an EBIT [26,27]. Some of the cooling schemes applicable to highly charged ions have already been put into operation in an EBIT [28-30].

Another interesting possibility is related to the quest for crystalline ion beams with high center-of-mass energies (>1 MeV, but with small relative energy <1 eV). These beams would provide the unprecedented quality and brightness sought in many applications [31-33]. The idea of creating crystalline ion beams in storage rings was proposed more than fifteen years ago [34]. Despite some promising results [35,36], the experimental realization in high-energy devices appears to be still lacking [32].

An alternative approach to the crystalline ion beam problem [37] was recently experimentally realized [32] in a small-scale storage ring. The idea is to first create a crystalline ion cloud at rest using methods and tools that are applied in strongly coupled ion cloud studies, and then to accelerate it to high energies without destroying the ordered structure. The experiment, which used singly charged ions and laser cooling to create the ion crystals at rest, was able to demonstrate acceleration to about 1 eV energy [32]. It is believed that scaled-up versions of this scheme can be used as high-energy storage rings.

Direct laser cooling of highly charged ions is problematic because of the scarcity of visible transitions. It has recently been demonstrated, however, that sympathetic laser cooling can be equally effective [38]. This alternative cooling technique has also been shown to be very effective for highly charged ions [26,27]. In addition, there may be other, non-laser based cooling schemes that have yet to be fully developed [45,46].

One of the major differences between Penning traps and EBITs is the presence of a monoenergetic, high-energy, high-density electron beam at the center of the trap. Some groups, however, have modified their Penning traps to include an electron beam [39-42]. These works are not motivated by the desire to create highly charged ions, but rather to create better confinement conditions and more dense plasmas for applications such as alternative nuclear fusion devices. The dense electron beam creates a steep spatial ion density gradient that helps to locally overcome the density limitations posed by the Brillouin limit [39,40]. Similar gradients have been observed in recent EBIT experiments [43,44]. Furthermore, typical ion densities found in EBITs (see below) are already above the Brillouin limit.

The possibility of creating high ion cloud densities and high brilliance beams using present EBITs without auxiliary laser cooling may not be that far-fetched. Recent model calculations [45,46] suggest that evaporative cooling could be significantly enhanced under certain conditions, and thus even the strongly correlated regime might be achievable this way.

ELECTRON BEAM ION TRAPS

The basic operational principle and the details of the EBIT components can be found in several recent reviews [47,48]. These papers give a design and modeling point of view of the operation of the present-day EBITs. In the present work, we would like to review a few experiments that determined some of the important operating parameters of the machine. In some cases these results were not even the main goal of the particular experiment, but rather a byproduct. Since these experiments were done with different machines, using different types of ions, and different experimental techniques, their direct comparison might not be justified in all cases. However, a semi-comprehensive review of the data might help to shed some light on the capabilities of EBITs and to give a general feel for the operating parameter ranges.

Operation

The creation of highly charged ions in an EBIT is based on the interactions of ions with a high density electron beam of about 1 keV to 30 keV energy. The electron beam is produced by a commercial electron gun and is highly compressed by a pair of superconducting magnets producing homogenous field of about 3 T in the center of the machine. Neutral atoms or singly charged ions are injected into a three element Penning trap and then are stripped of most of their bound electrons during consecutive interactions with the electron beam. The average ionization stage in equilibrium can be selected by properly choosing the energy of the electron beam. Radially the ions are confined by both the electric field of the electron beam and the high magnetic field. The effect of the magnetic field dominates only for large distances from the electron beam. Once the ions of the desired charge state are produced, the electron beam can be used for exciting electronic transitions for spectroscopic studies, or it can be turned off completely, leaving the axial confinement solely to the magnetic field [49,50]. Details of the modeling of ion creation [47] and the trapping dynamics [48] are described elsewhere. The NIST EBIT is also equipped with a highly efficient ion extraction and transport system, with a built-in charge-to-mass ratio separator. This system can be used for diagnostic purposes to infer charge state distributions inside the trap, or as a facility for ion-surface and ion-gas collision experiments.

In the following paragraph we summarize the typical plasma parameters of EBIT ion clouds. The measurements that provided the input for these determinations will be presented in later sections.

Typical plasma parameters

Plasma conditions created in EBITs are similar to those of the solar corona. Electron densities are around 10^{12} cm^{-3} and electron energies are approximately equal to (or above) those found in 10 million Kelvin temperature plasmas. One distinctive difference is that in the EBIT the electron energy is monoenergetic, with a width of only about 16 eV [70] to 70 eV [71]. A typical relative energy spread, $\Delta E/E$, is under

1 %. The narrow energy spread is the key to creating a charge state distribution that only includes a few ionization stages. In the case of ions with closed shell electronic configurations, close to 100 % charge state purity can be achieved [77]. In a more typical case, there would be a distribution of charge states present. The charge-to-mass spectrum of extracted ions [72,73] can be used to monitor the degree of charge state purity.

Typical measured densities of particular charge states in multi-component EBIT ion clouds range from $5 \times 10^8 \text{ cm}^{-3}$ to $1 \times 10^{10} \text{ cm}^{-3}$ [7,61]. Local ion densities can be higher than these values because of the steep gradient in the space charge potential of the electron beam. Typical measured ion temperatures are between 70 eV [65] and 700 eV [66, 64], increasing as the ion charge increases.

The Debye length for typical ion densities (n) and temperatures (T) inside an EBIT,

$$\lambda_D = \sqrt{\frac{\epsilon_0 k T}{n q^2}} \quad (1)$$

is around 20 μm to 60 μm . This value is relatively small mainly because of the high charge (q) of the ions. The size of the ion cloud is 2 to 20 times this value.

The average distance between ions of a particular charge state is given by the Wigner-Seitz radius,

$$a = \sqrt[3]{\frac{3}{4\pi n}} \quad (2)$$

about 3 μm to 8 μm . These Debye lengths and Wigner-Seitz radii are similar to those for typical singly charged ion plasmas, but other parameters that scale with the ion charge can be very different. One such parameter that scales quadratically with ion charge is the average potential energy between neighboring ions:

$$V_a = \frac{q^2}{4\pi\epsilon_0 a} \quad (3)$$

For ions of high charge-states this can be 3 or 4 orders of magnitude higher than for singly charged systems. It can be more than 1 eV in absolute value. This leads to another strongly scaling quantity, the Coulomb coupling parameter:

$$\Gamma = \frac{q^2}{4\pi\epsilon_0 a k T} \quad (4)$$

Because of the high ion charge, even at temperatures close to 1 million Kelvin Γ is more than 0.01. If the cloud could be cooled to room temperature, Γ would be around 50, which is well into the range where liquid phase behavior is predicted [60].

EXPERIMENTAL CHARACTERIZATION OF EBITs

Although there have been over 300 EBIT publications since the first one in 1988, relatively few experiments have been performed to date that determine the parameters described in the previous section. In the following subsections, we discuss these few experiments, and point to corresponding theoretical work.

Electron beam

The spatial distribution of the electron beam has been measured using a variant of an x-ray pinhole camera [5, 74, 75], and using Thomson scattering [76]. The x-ray imaging experiments rely on the fact that excited state lifetimes in highly charged ions are so short that x-rays are emitted essentially instantaneously at the location that they interact with the electron beam. A map of the x-ray emission from the ions, therefore, reflects the electron beam density distribution directly. The measurements are in rough agreement with predictions based on Herrmann theory [51], although there have been some discrepancies on the order of 20 %. Generally, it has been assumed that the electron beam spatial distribution is Gaussian, with a radius r_{II} containing 80 % of the electron beam given by,

$$r_{II} = \frac{r_B}{\sqrt{2}} \sqrt{1 + \sqrt{1 + 4\left(\frac{8mkT_c r_c^2}{e^2 B^2 r_B^4} + \frac{B_c^2 r_c^4}{B^2 r_B^4}\right)}} \quad (5)$$

where B_c is the magnetic field in the electron gun cathode region; T_c is the temperature of the cathode; r_c is the radius of the cathode; B is the magnetic field at the central drift tube; m is the rest mass of the electron; k is the Boltzmann constant; r_B is the Brillouin radius:

$$r_B = \sqrt{\frac{I_c \sqrt{E_c}}{4.74 \cdot 10^5 \cdot \pi B^2}} \quad (6)$$

determined by the electron current, I_c , and the electron energy, E_c .

In order to understand the presence of the parameter B_c in the above expression, it is useful to consider some further details of the EBIT design. The electrons are emitted from a heated cathode in a Pierce-type electron gun configuration [4,5,48] located in the fringing field region of the main trap magnet. The electrons are accelerated towards a positively biased drift tube region (the trap center) by a series of guiding electrodes. It has typically been assumed that the maximum current density is achieved by minimizing the radius in expression (5), implying that the field at the cathode should be zero. In this case, however, the trap magnet acts as a magnetic mirror, and a significant number of electrons will be reflected back away from the trap. We have shown that theoretically the optimum field is actually a few tenths of a mT (a few gauss) [52]. The control of the magnetic field is aided by a steel plate placed above

the electron gun, and a coil built into a sealed chamber that surrounds the electron gun [5,52]. The magnitudes of the various EBIT parameters ($r_c \sim 1.5$ mm, $T_c \sim 1000$ K, for example) allow one to simplify expression (5) considerably to,

$$r_H \approx \left(\frac{8mkT_c r_c^2}{e^2 B^2} \right)^{1/4} \quad (7)$$

On its way towards the drift tubes, the electron beam is compressed by the increasing magnetic field. Model calculations show that the 3 T magnetic field in the trap region is homogenous over the 3 cm long ion trap region to better than 0.05 % [44].

Magnetic trapping

The early EBIT papers stated that the ions were trapped in the radial direction by the electrostatic field provided by the electron beam (see, for example [5]). The magnetic field was presented as a technical detail needed to adiabatically compress the electron beam to high densities at the trap center. From the onset of our work [7,50], however, we have taken a somewhat different view, which emphasizes the direct effect of the magnetic field on the ion confinement. With this point of view, we first reported an experiment that demonstrated that an EBIT can be used to measure some properties of highly charged ions (excited state lifetimes, for example) more efficiently when the electron beam is turned off [50]. This work was stimulated by some related work on ion cloud diagnostics at Livermore [53-57]. Both the atomic lifetime measurements and the cloud diagnostic studies showed that after an initial expansion, the ion cloud stabilized after the electron beam was turned off. Only trap losses like cross-field diffusion and charge exchange with the background gas then lead to a decrease of the ion signal. Similar issues have been studied more thoroughly outside of the EBIT community e.g. [24, 60]. We suggest that using an EBIT to produce highly charged ions, and then switching to the “magnetic trapping mode” of operation might be particularly interesting for many advanced plasma studies.

Ion cloud shape

It is only recently that an image of the measured ion cloud shape has been reported [2]. Most of the experiments have simply used the EBIT as a light source or as an ion source for atomic physics or ion-surface studies, with relatively little effort allocated to study the macroscopic properties of the ion cloud itself. Ironically, much of the work that *has* been published rests on assumptions about the spatial distribution of the ions in the cloud.

The first systematic study of the ion cloud shape was published recently [43]. This work used a CCD camera and an optical lens system. Data was collapsed along the axis of the electron beam to produce a 1-dimensional cross sectional image with improved signal-to-noise ratio. Complimentary data, taken under rather different EBIT

operating conditions, have been reported in the PhD thesis of M. Tarbutt [44]. Both of these works were predated by some spatial information that was obtained by Serpa *et al.* [50] in connection with the measurement of excited-state atomic lifetimes. In this work, the entire spectrometer table was mounted on sliding rails and was moved perpendicular to the EBIT observation direction by piezoelectric translators, allowing the transverse distribution of light at the entrance slit of the spectrometer to be mapped out. Some earlier unpublished work using CCD imaging was briefly described in a Livermore annual report [58].

The lack of any work in imaging the ion cloud immediately after the first EBIT came online can be partly understood by realizing that it was quite a few years before the first visible-light spectroscopy was done on an EBIT [18]. The reason for this is that the scaling laws cause most of the transition energies to shift into the x-ray energy range as the ion charge is increased. There are a few unusual transitions, however, that stay in the visible range, because of a fortuitous energy-level crossing. One of these transitions has been predicted [59] and found [18] in the Ti-like isoelectronic sequence. There are also transitions that during their rapid scaling to shorter wavelengths from the infrared or microwave range, pass through the visible range at a particular charge state or narrow range of charge states. Notable examples of the latter are visible hyperfine transitions in high Z elements.

Another requirement for cloud imaging is that the line should have a lifetime that is long compared to the time it takes the ion to complete several cycles of its motion (the cyclotron frequency varies from $1.2 \times 10^7 \text{ s}^{-1}$ to $1.3 \times 10^8 \text{ s}^{-1}$ for ions ranging from U^{10+} to Ar^{18+}). This condition is necessary, because electron impact excitation can only take place inside the electron beam. As mentioned above, if the emitting transition has a short lifetime (like in most of the x-ray lines), the image only reflects the product of the electron and ion densities, not the full ion cloud shape.

The cloud imaging experiments of Porto *et al.* [43] used Ar^{13+} , Xe^{31+} , and Xe^{32+} ions and the experiments of Tarbutt [44] used Ar^{10+} ions for the measurements. Both experiments concluded that the ion cloud has a density distribution that sharply peaks in the center of the EBIT. Porto *et al.* assumed thermal equilibrium for the ion cloud to model the shape of the measured distribution in the self-consistent field of the electron beam and the ion clouds. The fits suggest that the ions may indeed be close to thermal equilibrium. The temperatures obtained from the fits fall within expected values [43]. At lower trapping voltages, the experimentally obtained widths became wider than what is expected for even the maximum possible temperatures, which was interpreted as a signature that the ion cloud is non-thermal.

Ion cloud rotation

The possible collective rotation of the ion cloud has not been taken into account in any of the previous work with EBITs. Clouds of highly charged ions in thermal equilibrium in a pure magnetic field with densities close to the Brillouin limit should rotate collectively at half the cyclotron angular frequency [60]. How this situation is modified by the presence of the electron beam has yet to be studied in detail.

Ion number and density

The ion densities can be measured by detecting x-rays originating from processes with well-known cross sections, assuming the electron density is known. One of these is the so-called radiative recombination, which can be calculated to better than few percent accuracy [13]. This method was used by Gillaspay *et al.* [7] and by Margolis *et al.* [61] to determine the number Ba^{46+} ions in the trap (3.1×10^5) or, with fewer assumptions, the ion density ($1.0 \times 10^8 \text{ cm}^{-3} - 1.1 \times 10^9 \text{ cm}^{-3}$). Margolis *et al.* [61] also measured densities of $1.3 \times 10^{10} \text{ cm}^{-3}$ and $0.7 \times 10^{10} \text{ cm}^{-3}$ for Ar^{16+} and Ar^{17+} ions respectively using the same method.

A different technique was used by Schweikard *et al.* [54] to determine the number of ions inside the EBIT. In [54] electrical probes were inserted into the EBIT to detect ion cyclotron resonance (ICR) signals induced by the ions. From the induced currents, the number of ions is inferred to be 10^5 to 10^6 for high charge state Kr ions (Kr^{34+} , Kr^{35+} , and Kr^{36+}). Using these numbers and assuming approximately 10^{-3} cm^3 for the volume of the ion cloud, we infer $10^8 \text{ cm}^{-3} - 10^9 \text{ cm}^{-3}$ for the average ion densities, in reasonable agreement with the results of the x-ray method.

It should be noted that the estimated densities using the ICR method are averages over the entire ion cloud, whereas the x-ray method samples only the region where the electron beam overlaps with the ion cloud. Because of the density gradient, the x-ray method should yield higher values than the average density. A better determination of the local ion densities could be performed by combining either of these methods with imaging techniques.

Charge state distribution

The evolution of the charge state distribution when the electron beam is on is determined by a set of coupled differential equations including source and loss terms for each charge state [20]. Once equilibrium is reached, recombination with electrons to produce lower charge states and re-ionization keep a balance between the neighboring charge states. Model calculations can account for the qualitative behavior of the time dependence, however discrepancies have been reported in several cases [62,63]. One of the critical issues that comes up in many experiments is the overlap factor between the electron beam and the ion cloud [20,63]. The modeling of this parameter relies on the knowledge of the properties of the ion cloud. As it has been shown in the imaging experiments [43,44], this can be very complicated, especially if non-thermal clouds are present. Further understanding calls for advanced modeling of the highly charged ion cloud.

Ion temperatures

A routine procedure in spectroscopy to determine ion temperatures is the measurement of the Doppler broadening of spectral lines. This method assumes that the emitting ions are in thermal equilibrium, a condition that might not be satisfied in some cases as suggested by the direct imaging results. Collective ion cloud rotation

could also cause spectral line broadenings, which might explain why the experiments have not indicated very low temperatures, even in cases where the axial potential barrier was very small. Nevertheless, the broadening of a relatively narrow spectral line, measured by high-resolution instruments, gives a general idea about the temperature ranges that highly charged ions are subjected to in EBITs.

The NIST EBIT group [7,64] used a Fabry-Perot spectrometer to measure the width of a visible magnetic dipole transition in Ba^{34+} . The experimental results indicated an ion temperature between 500 eV and 1000 eV. These values are much less than what the depth of the potential trap would allow, which for such a high charge-state amounted to about 17 keV (the reason for this reduced temperature is given in the next section). Similar conclusions were drawn from the x-ray line-width measurements of Beiersdorfer *et al.* [65,66] using Ti^{20+} ions. In these cases, the measured widths indicated equilibrium temperatures of 70 eV - 700 eV. Although the temperatures showed a dependence on the axial trap depth, the measured values were generally smaller than the possible temperatures Ti^{20+} ions were allowed to take, similarly to the observation of the NIST group using Ba^{34+} ions. Neither of the measurements took into account the possible collective rotation of the ion cloud, so the actual ion temperatures could have been even lower than those inferred from the measurements.

Evaporative cooling

The interaction of the ions with the dense and energetic electron beam continuously pumps energy into the cloud via inelastic collisions at a rate of a few keV/s [20]. At this rate of heating, most of the ions would quickly boil out of the trap. However, evaporative cooling of the higher charge state ions by elastic collisions with lower charge state ions that preferentially escape the trap strongly modifies this situation. Evaporative cooling of heavy ions can be even more efficient using lighter ions purposely injected into the trap. These lighter ions can be rapidly stripped bare, after which their charge state evolution is truncated.

Evaporative cooling of highly charged gold (Au^{69+} , Au^{68+} , Au^{67+} , etc.) by low charge state Ti ions (maximum Ti^{22+}) was successfully demonstrated by Schneider *et al.* [67]. Using this method, trapping times of several hours have been observed, demonstrating the presence of a strong cooling mechanism. Model calculations of the effect [69] predicted that highly charged heavy ions can be trapped for indefinitely in this way.

Conventional evaporative cooling in an EBIT [67-69], as described above, differs from evaporative cooling in neutral atom traps in that there is no time-dependence of the trap potentials. This cooling is not lossy because it depends on collisions with lower charge state ions that "see" a different trap depth. There have been two recent model investigations [45,46], which propose improved evaporative cooling schemes for an EBIT using time-dependent potentials. Because of the long-range nature of the strong Coulomb interaction, evaporative cooling works very differently in the case of highly charged, compared to the neutral atom case. At low temperatures, instead of getting weaker, the evaporative cooling mechanism can be accelerated, leading to very low achievable temperatures.

REFERENCES

- [1] I. Martinson, *Reports of Progress in Physics* **52** (1989) 157.
- [2] J.D. Gillaspay, *Journal of Physics B: Atomic, Molecular and Optical Physics* **34** (2001) R93.
- [3] R. Minniti, L.P. Ratliff, J.D. Gillaspay, *Physica Scripta* **T92** (2001) 22.
- [4] M.A. Levine, R.E. Marrs, J.R. Henderson, D.A. Knapp, and M.B. Schneider, *Physica Scripta* **T22** (1988) 157
- [5] M.A. Levine, R.E. Marrs, J.N. Bardsley, P. Beiersdorfer, C.L. Bennett, M.H. Chen, T. Cowan, D. Dietrich, J.R. Henderson, D.A. Knapp, A. Osterheld, B.M. Penetrante, M.B. Schneider, and J.H. Scofield, *Nuclear Instruments and Methods in Physics Research B* **43** (1989) 431.
- [6] J.D. Gillaspay, J.R. Roberts, C.M. Brown, and U. Feldman, *Proceedings of the VIth International Conference on the Physics of Highly Charged Ions*, eds. P. Richard, M. Stockli, and C.D. Lin, (AIP press, New York, 1993), *AIP Conference Proceedings* **274** (1993) 682.
- [7] J.D. Gillaspay, Y. Aglitskiy, E.W. Bell, C.M. Brown, C.T. Chantler, R.D. Deslattes, U. Feldman, L.T. Hudson, J.M. Laming, E.S. Meyer, C.A. Morgan, A.I. Pikin, J.R. Roberts, L.P. Ratliff, F.G. Serpa, J. Sugar and E. Takács, *Physica Scripta* **T59** (1995) 392.
- [8] J.D. Silver, A.J. Varney, H.S. Margolis, P.E.G. Baird, I.P. Grant, P.D. Groves, W.A. Hallett, A.T. Handford, P.J. Hirst, A.R. Holmes, D.J.H. Howie, R.A. Hunt, K.A. Nobbs, M. Roberts, W. Studholme, J.S. Wark, M.T. Williams, M.A. Levine, D.D. Dietrich, W.G. Graham, I.D. Williams, R. Oncil, and S.J. Rose, *Review of Scientific Instruments* **65** (1994) 1072.
- [9] C. Biedermann, A. Forster, G. Fussmann, and R. Radtke, *Physica Scripta* **T73** (1997) 360.
- [10] F.J. Currell, J. Asada, K. Ishii, A. Minoh, K. Motohashi, N. Nakamura, K. Nishizawa, S. Ohtani, K. Okazaki, M. Sakurai, H. Shiraishi, S. Tsurubuchi, and H. Watanabe, *Journal of the Physical Society of Japan* **65** (1996) 3186.
- [11] T. Werner, G. Zschornack, F. Grossmann, V.P. Ovsyannikov, and F. Ullmann, *Nuclear Instruments and Methods in Physics Research B* **178** (2001) 260.
- [12] J.R.C. Lopez-Urrutia, B. Bapat, I. Draganic, A. Werdich, and J. Ullrich, *Physica Scripta* **T92** (2001) 110.
- [13] R.E. Marrs, M.A. Levine, D.A. Knapp, and J.R. Henderson, *Physical Review Letters* **60** (1988) 1715.
- [14] P. Beiersdorfer, S. Vongoleer, M. Bitter, E. Hinnov, R. Bell, S. Bernabei, J. Felt, K.W. Hill, R. Hulse, J. Stevens, S. Suckewer, J. Timberlake, A. Wouters, M.H. Chen, J.H. Scofield, D.D. Dietrich, M. Gerassimenko, E. Silver, R.S. Walling, and P.L. Hagelstein, *Physical Review A* **37** (1988) 4153.
- [15] J.R. Henderson, P. Beiersdorfer, C.L. Bennett, S. Chantrenne, D.A. Knapp, R.E. Marrs, M.B. Schneider, K.L. Wong, G.A. Doschek, J.F. Seely, C.M. Brown, R.E. LaVilla, J. Dubau, and M.A. Levine, *Physical Review Letters* **65** (1990) 705.
- [16] D. Schneider, D. Dewitt, M.W. Clark, R. Schuch, C.L. Cocke, R. Schneider, K.J. Reed, M.H. Chen, R.E. Marrs, M. Levine, and R. Fortner, *Physical Review A* **42** (1990) 3889
- [17] R.E. Marrs, S.R. Elliott, and D.A. Knapp, *Physical Review Letters* **72** (1994) 4082
- [18] C.A. Morgan, F.G. Serpa, E. Takács, E.S. Meyer, J.D. Gillaspay, J. Sugar, J.R. Roberts, C.M. Brown and U. Feldman, *Physical Review Letters* **74** (1995) 1716.
- [19] G. Borsoni, N. Bechu, M. Gros-Jean, M.L. Korwin-Pawłowski, R. Laffitte, V. Le Roux, L. Vallier, N. Rochat, and C. Wyon, *Microelectronics Reliability* **41** (2001) 1063.
- [20] B. M. Penetrante, J. N. Bardsley, D. DeWitt, M. Clark, and D. Schneider, *Physical Review A* **43** (1991) 4861.
- [21] B. M. Penetrante, D. Schneider, R. E. Marrs, and J. N. Bardsley, *Review of Scientific Instruments* **63** (1992) 2806
- [22] H.S. Margolis, *D.Phil. Thesis, Oxford University*, 1994.
- [23] I.V. Kalagin, D. Küchler, V.P. Ovsyannikov, and G. Zschornack, *Plasma Sources in Science and Technology* **7** (1998) 441.
- [24] X.P. Huang, J. J. Bollinger, W.M. Itano, J.N. Tan, B. Jelenkovic, T.B. Mitchell, and D.J. Wineland, *Hyperfine Interactions* **115** (1998) 41.
- [25] D.J. Wineland, C. Monroe, W.M. Itano, D. Leibfried, B.E. King, and D.M. Meekhof, *Journal of Research of the National Institute of Standards and Technology* **103** (1998) 259.
- [26] L. Gruber, J.P. Holder, J. Steiger, B.R. Beck, H.E. DeWitt, J. Glassman, J.W. McDonald, D.A. Church, and D. Schneider, *Physical Review Letters* **86** (2001) 636.
- [27] J.P. Holder, L. Gruber, H.E. DeWitt, B.R. Beck, D.A. Church, and D. Schneider, *Physica Scripta* **T92** (2001) 158.
- [28] B. M. Penetrante, J. N. Bardsley, M. A. Levine, D. A. Knapp and R. E. Marrs, *Physical Review A* **43** (1991) 4873.
- [29] B. M. Penetrante, M. A. Levine, and J. N. Bardsley, *Proceedings of the International Symposium on Electron Beam Ion Sources and their Applications*, ed. A. Herschovitch (AIP press, New York, 1989), *AIP Conference Proceedings* **188** (1989) 145.
- [30] R. E. Marrs, *Review of Scientific Instruments* **67** (1996) 941.

- [31] T. Schatz, U. Schramm, and D. Habs, *Hyperfine Interactions* **115** (1998) 29.
- [32] T. Schatz, U. Schramm, and D. Habs, *Nature* **412** (2001) 717.
- [33] J. Beebe-Wang, N. Elander, and R. Schuch, *Physica Scripta* **57** (1998) 36.
- [34] J. P. Schiffer and P. Kienle, *Zeitschrift für Physik A, Atoms and Nuclei* **321** (1985) 181.
- [35] M. Steck, K. Beckert, H. Eickhoff, B. Franzke, F. Nolden, H. Reich, B. Schlitt, and T. Winkler, *Physical Review Letters* **77** (2001) 3803.
- [36] R.W. Hasse, *Physical Review Letters* **83** (2001) 3430.
- [37] R. Blumel and P.E. Smaldino, *Physics Letters A* **260** (1999) 495.
- [38] P. Bowe, L. Horneaker, C. Brodersen, M. Drewsen, J. S. Hangst, and J. P. Schiffer, *Physical Review Letters* **82** (1999) 2071.
- [39] D.C. Barnes, R.A. Nebel, and L. Turner, *Physics of Fluids B* **5** (1993) 3651.
- [40] G. Zhuang, W. Liu, C. Yu, J. Zheng, C. Fu, J. Xie, K. Zhao, B. Bai, X. Liang, S. Zhao, and J. Chi, *Physics of Plasmas* **7** (2000) 3912.
- [41] R.G. Greaves, M.D. Tinkle, and C.M. Surko, *Physical Review Letters* **74** (1995) 90.
- [42] M. H. Holzschneider, *Physica Scripta* **T59** (1995) 69.
- [43] J.V. Porto, I. Kink, and J.D. Gillaspay, *Review of Scientific Instruments* **71** (2000) 3050.
- [44] M.R. Tarbutt, *D.Phil. Thesis, Oxford University*, 2000.
- [45] R.E. Marrs, *Nuclear Instruments and Methods in Physics Research B* **149** (1999) 182.
- [46] T. Kinugawa, F.J. Currell, and S. Ohtani, *Journal of Physical Society of Japan* **68** (1999) 3763.
- [47] F.J. Currell, *Trapping Highly Charged Ions: Fundamentals and Applications* ed. J.D. Gillaspay (New York: Nova Science), 2001.
- [48] G. Fussmann, C. Biedermann, and R. Radtke, *Advanced Technologies Based on Wave and Beam Generated Plasmas* eds. H. Schluter and A. Shivarova (Kluwer Academic Publishers), 1999, 429.
- [49] L. Schweikhard, P. Beiersdorfer, G. V. Brown, J. R. Crespo Lopez-Urrutia, S. B. Utter, and K. Widmann, *Nuclear Instruments and Methods in Physics Research B* **142** (1998) 245.
- [50] F.G. Serpa, C.A. Morgan, E.S. Meyer, J.D. Gillaspay, E. Trabert, D.A. Church, and E. Takács, *Physical Review A* **55** (1997) 4196.
- [51] G.J. Hermann, *Journal of Applied Physics* **29** (1958) 127.
- [52] E. Takács, E. S. Meyer, J. D. Gillaspay, J. R. Roberts, C. T. Chantler, L. T. Hudson, R. D. Deslattes, C. M. Brown, J. M. Laming, J. Dubau, and M. K. Inal, *Physical Review A* **54** (1996) 1342.
- [53] P. Beiersdorfer, B. Beck, S. Elliott, and L. Schweikhard, *Rapid Communications in Mass Spectrometry* **8** (1994) 141.
- [54] L. Schweikhard, J. Ziegler, P. Beiersdorfer, B. Beck, St. Becker, and S. Elliott, *Review of Scientific Instruments* **66** (1995) 448.
- [55] P. Beiersdorfer, St. Becker, B. Beck, S. Elliott, K. Widmann, and L. Schweikhard, *Nuclear Instruments and Methods in Physics Research B* **98** (1995) 558.
- [56] P. Beiersdorfer, B. Beck, St. Becker, and L. Schweikhard, *International Journal of Mass Spectrometry and Ion Process* **157/158** (1996) 149.
- [57] P. Beiersdorfer, L. Schweikhard, J. Crespo Lopez-Urrutia, and K. Widmann, *Review of Scientific Instruments* **67** (1996) 3818.
- [58] Electron Beam Ion Trap, *Annual Report 1994, Lawrence Livermore National Laboratory*, ed. D. Schneider, UCRL-ID-121572, 1995.
- [59] U. Feldman, P. Indelicato, and J. Sugar, *Journal of the Optical Society of America B* **8** (1991) 3.
- [60] T.M. O'Neil, *Physica Scripta* **T59** (1995) 341.
- [61] H. S. Margolis, A. J. Varney, R. A. Jarjis, and J. D. Silver, *Nuclear Instruments and Methods in Physics Research B* **98** (1995) 562.
- [62] N.J. Peacock, R. Barnsley, M.G. O'Mullane, M.R. Tarbutt, D. Crosby, J.D. Silver, and J.A. Rainnie, *Review of Scientific Instruments* **72** (2001) 1250.
- [63] E. Takács, Z. Berényi, Cs. Szabó, J.D. Gillaspay, and A.G. Calamai, *to be published*, 2001.
- [64] H. Adler, E.S. Meyer, F.G. Serpa, E. Takács, J.D. Gillaspay, C.M. Brown, and U. Feldman, *Nuclear Instruments and Methods in Physics Research B* **98** (1995) 581.
- [65] P. Beiersdorfer, V. Decaux, and K. Widmann, *Nuclear Instruments and Methods in Physics Research B* **98** (1995) 566.
- [66] P. Beiersdorfer, V. Decaux, S. R. Elliott, and K. Widmann, *Review of Scientific Instruments* **66** (1995) 303.
- [67] M.B. Schneider, M.A. Levine, C.L. Bennett, J.R. Henderson, D.A. Knapp, and R.E. Marrs, *Proceedings of the International Symposium on Electron Beam Ion Sources and their Applications*, ed. A. Herschovitch (AIP press, New York, 1989), AIP Conference Proceedings **188** (1989) 158.
- [68] B. M. Penetrante, J. N. Bardsley, M.A. Levine, D.A. Knapp, and R.E. Marrs, *Physical Review A* **43** (1991) 4873.

- [69] D. Schneider, M.W. Clark, B.M. Penetrante, J. McDonald, D. DeWitt and J. N. Bardsley, *Physical Review A* **44** (1991) 3119.
- [70] D. DeWitt, D. Schneider, M.H. Chen, M.W. Clark, J.W. McDonald, and M.B. Schneider, *Physical Review Letters* **68** (1992) 1694.
- [71] R.E. Marrs, M.A. Levine, D.A. Knapp, and J.R. Henderson, *Electronic and Atomic Collisions*, eds. H.B. Gilbody, W.R. Newell, F.H. Read, and A.C.H. Smith (Elsevier Science Publishers B.V.), 1988.
- [72] A.I. Pikin, C.A. Morgan, E.W. Bell, L.P. Ratliff, D.A. Church, and J.D. Gillaspay, *Review of Scientific Instruments* **67** (1996) 2528.
- [73] L.P. Ratliff, E.W. Bell, D.C. Parks, A.I. Pikin, and J.D. Gillaspay, *Review of Scientific Instruments* **68** (1997) 1998.
- [74] D.A. Knapp, R.E. Marrs, S.R. Elliott, E.W. Magee, and R. Zasadinski, *Nuclear Instruments and Methods in Physics Research A* **334** (1993) 305.
- [75] S.B. Utter, P. Beiersdorfer, J.R.C. Lopez-Urrutia, and K. Widmann, *Nuclear Instruments and Methods in Physics Research A* **428** (1993) 276.
- [76] H. Kuramoto, I. Yamada, H. Watanabe, M. Sawasaki, C. Yamada, and S. Ohtani, *Physica Scripta* **T92** (2001) 351.
- [77] S. Chantrenne, P. Beiersdorfer, R. Cauble, and M.B. Schneider, *Physical Review Letters* **69** (1992) 265.

Cold Highly Charged Ions In A Penning Trap: Experiment and Simulation

J. P. Holder⁺, L. Gruber^{*,§}, D. A. Church⁺ and D. Schneider^{*}

⁺Physics Department, Texas A&M University, College Station TX 77843-4242

^{*}Lawrence Livermore National Laboratory (LLNL), Livermore, CA 94550

[§] Present Address: Spectra Physics Laser, Inc. 1305 Terra Bella Ave., Mountain View, CA 94043

Abstract. Using the LLNL EBIT/RETRAP system non-neutral plasmas of highly charged ions were produced and cooled to temperatures around one Kelvin. These strongly coupled plasmas can model white dwarf astrophysical plasmas in the laboratory. These systems may also have potential application to quantum computation. The experimental results from the last operations of the trap at Livermore are discussed. Molecular dynamics simulation results are discussed as a guide to past and future experiments. The status and future plans for RETRAP at LBNL's 88 inch Cyclotron are discussed.

INTRODUCTION

Strongly coupled plasmas are characterized by the ratio of the Coulomb interaction between particles with charge q to the thermal energy of the particles ($k_B T$) being greater than one. This Coulomb coupling parameter:

$$\Gamma = \frac{q^2}{4\pi\epsilon_0 a_0 k_B T} \quad (1)$$

with the Wigner-Seitz radius

$$a_0 = \left(\frac{3}{4\pi n} \right)^{\frac{1}{3}} \quad (2)$$

Where n is the number density of the charged particles. If Γ exceeds ~ 172 (for infinite one component plasma) the plasma crystallizes and is referred to as a "Coulomb crystal" or for finite crystals at higher Γ s "Coulomb cluster"[1]. White Dwarf stars contain plasmas with fully stripped ions and degenerate electrons that can be treated as strongly coupled non-neutral plasmas. Crystallization and other thermodynamic properties (chemical layering, etc.) effect the luminosity function, which is used for astrophysical chronometry[2,3].

Cold, confined and relatively numerous highly charged ions are of interest for precision fundamental spectroscopic measurements[4]. These transitions, coupled with the charge scaling of motions in a trap, provide an additional "parameter space" for the investigation of trap based quantum coherence and computation experiments. To study mixed strongly coupled non-neutral plasmas and to prepare for precision

fine-structure and hyperfine-structure laser spectroscopy on ground term transitions of highly-charged ions, a source of highly charged ions (EBIT) and a cryogenic Penning trap for capturing and cooling these highly charged ions (RETRAP) have been developed at Lawrence Livermore National Lab [5,6,7].

EXPERIMENT

The scheme used in the experiment to cool highly charged ions to the lowest realizable temperature via sympathetic cooling with laser cooled ions. Be^+ ions are used for both their low mass to charge ratio ($m/q=9$) and the reasonable cooling laser transition (reachable with commercial available internally doubled ring dye laser). Be^+ ions were produced in a metal vapor vacuum arc (MeVVA) source. The Be^+ ions were analyzed by a 90 degree bending magnet (to eliminate other charge states and species produced in the MEVVA) and focused through a series of ion optics into a tube at a potential near the MEVVA extraction potential of approximately 7.5 keV. A high voltage switch lowers the potential of the tube to near ground, "de-accelerating" the Be^+ ions, so they can then relatively slowly pass into a hyperbolic trap where an auxiliary "capture" electrode is pulsed to confine the ions. These ($\sim 10^5$) ions were initially cooled to near room temperature by tuning (via trap ring-endcap voltage) their axial oscillation frequency into resonance with a cryogenic parallel tuned circuit. The heating of the parallel circuit by currents induced by fluctuations in the centroid of the confined ion motion, together with ion-ion collisional coupling, initially cools the ions at an exponential rate with a time constant of several minutes.

Eventually, the cooling is dominated by a transverse laser beam de-tuned several GHz below the cycling resonance transition near 313 nm [8]. With decreased de-tuning of the cooling laser, the ions then rapidly cooled to below 1 K, as evidenced by a decrease in light scattering, and confirmed by probing the Be ions with a weak second laser tuned through a nearby non-cycling transition. Using slightly altered trap potentials more Be^+ ions can be 'stacked' into the trap, with a cooling rate enhanced by the presence of previously cooled Beryllium ions.

Then beam pulse of Xe^{44+} ions from the EBIT (analyzed by a similar magnet, passing through ion optics and a bender now with potentials applied) is then similarly captured into the Penning ion trap previously filled with cold Be^+ ions. Electrode switching and collisions with the xenon ions initially heat the Be^+ ions. This heating is associated with an increase in fluorescence rate. This laser scattering quickly re-cools the Be^+ ions, which cools the ~ 400 caught Xe ions. The mixed ion cloud cools, different charge-to-mass ratio ions separate with the cold highly charged Xe ions in the center of the trap and the Be^+ ions in an annulus that we image using scattered 313 nm light. A more detailed account of the procedure and results can be found in ref. [7]. Laser induced fluorescence from a magnetic dipole transition in the ground term of a suitable highly-charged ion can be potentially used to image the highly charged species in the trap[4].

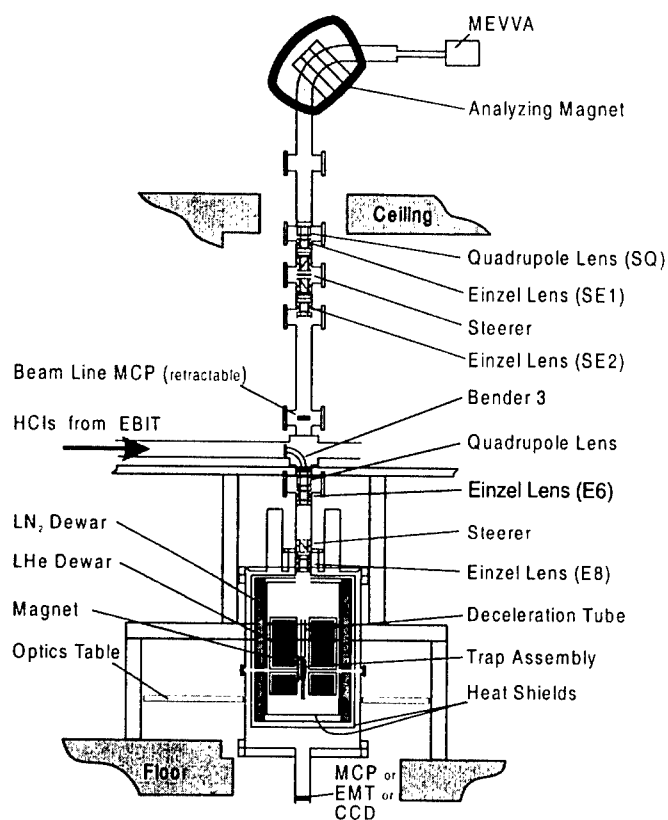


FIGURE 1. Setup to inject MeVVA ions into trap at LLNL. Magnet is used to separate charge states produced by MeVVA.

The shape of Be^+ fluorescent image can be used to determine the plasma parameters such as density and rotation rate. An ion species of interest can be excited by cyclotron resonance excitation (in the present trap configuration the frequencies associated with ω_+ , the modified cyclotron frequency is excited) resulting in heat transfer to the Be^+ ions and, typically, an increase in scatter of cooling laser light by the hotter Be^+ ions. Both the frequency and time response of this heating signal are of interest.

A preliminary study of cooling laser detuning (cooling power) with various radio frequency excitations (heating) of an ion cloud resulting from a $\text{Be}^+ - \text{Xe}^{34+}$ capture shows interesting features (see figure 3). These signals may possibly indicate crystallization, some other configuration/coupling change between species or some systematic effect that is not understood. The laser tuning was monitored (using the fundamental of the doubled laser) against an I_2 absorption cell for stability in frequency and amplitude. Similar signals have been assigned for small numbers of

ions in a Paul trap[9]. Unfortunately, pump laser failure and other considerations prevented further studies. We wish to pursue similar studies at the new location of the experiment.

The trap contents, when warmer, can be examined with the tuned circuit used for electronic cooling as described above. The trap contents can also be destructively probed by releasing the ions into various charged particle detectors.

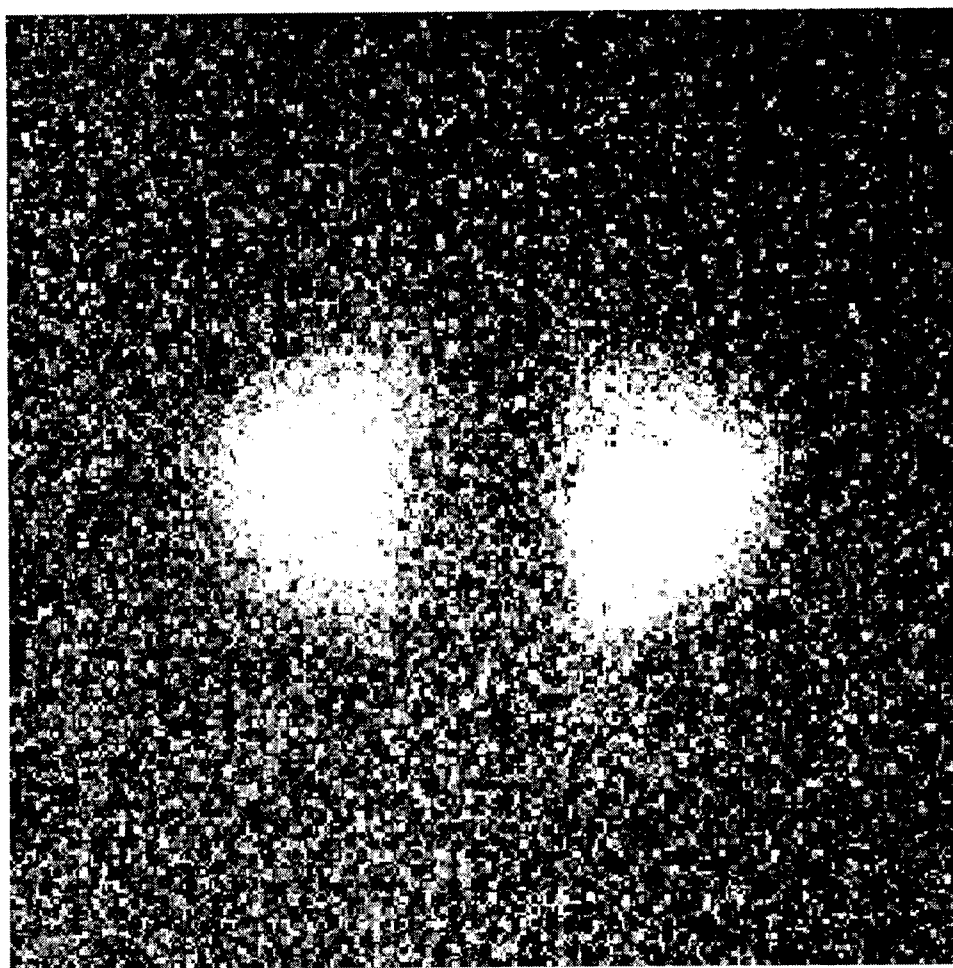


FIGURE 2. Image of Be^+ ion cloud containing Xe^{34+} and daughter charge exchange ions. B field is roughly vertical. With the cooling laser detuning and simulations it is estimated that the Xe ion temperature is approximately 1K. The image has been analyzed to give an Be^+ ion density $2.16 \cdot 10^{14} \text{ m}^{-3}$ and a Xe^{34+} density of $6.4 \cdot 10^{12} \text{ m}^{-3}$. This corresponds to a Γ value of about 577.

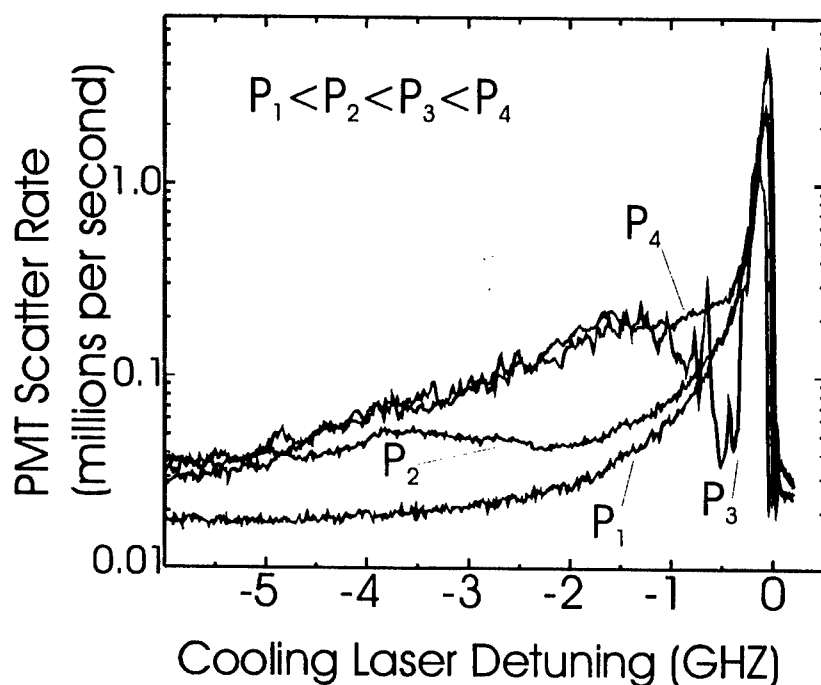


FIGURE 3. Cooling laser tuning curves. Main perpendicular cooling laser is used. P_1 is base curve with no extra radio frequency heating applied. From other experiments the plasma temperature is about 1 Kelvin when the the detuning for the P_1 curve is 200 MHz. The other curves have small amounts of radio frequency power applied near the Be^+ cyclotron frequency. The trap contains Be^+ , Xe^{34+} and charge exchange daughter products. Plasma conditions are similar to that of Figure 2. The same ion cloud is used for all curves.

SIMULATION

A molecular dynamics code originally developed by E. L. Pollock, and used by H. DeWitt et al. to model strongly coupled plasmas [10] has been modified to run on personal computers. It was modified to exclusively calculate the interaction of two ion species confined in a Penning trap. Simple heating or cooling of each individual species was provided.

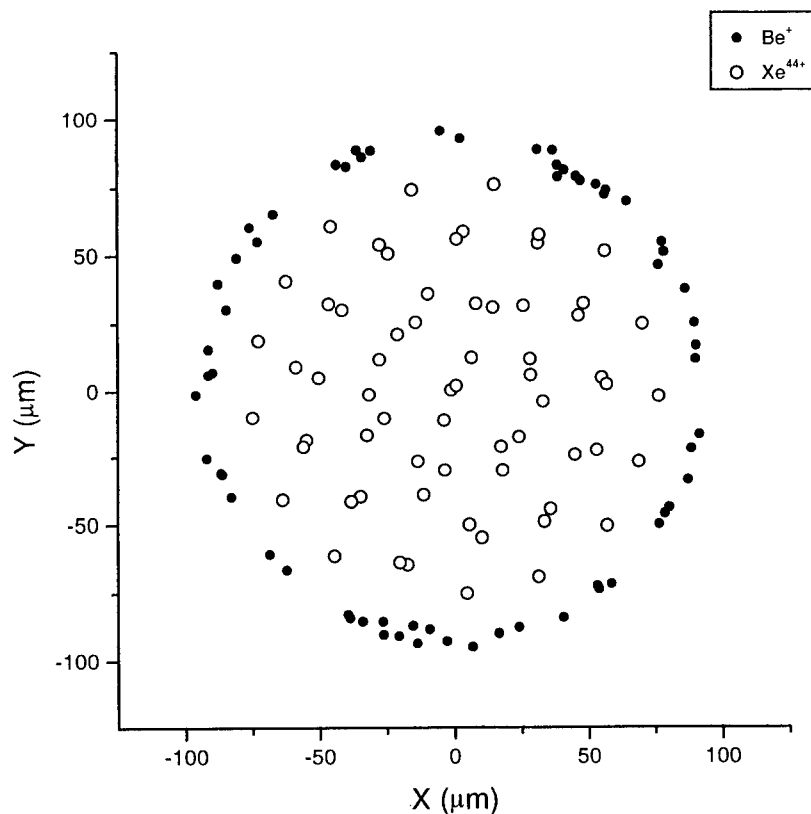


FIGURE 4. A “snapshot” x-y projection of the cloud of 64 Be^+ and 64 Xe^{44+} ions used for heating rate calculations. This projection is for 0.5 Kelvin axial cooling of the Be^+ ions and 1000 Kelvin/(particle • second) axial heating of the Xe^{44+} ions. The trap parameter is $q = -2.0$ corresponding to about 540 Volts applied to our trap. The rotation frequency of the cloud is approximately 865 kHz.

Simulations of the motion of 5 to 64 multiply charged ions (experimental ~100-500) and 64 to 200 Be^+ (experimental $\sim 10^5$) ions were performed using fields, potentials, ion masses, and ion charges correspond to those used in the experimental work. Initially, the ions were arranged in a body-centered cubic lattice, with random assignment of initial locations of each species. The center of mass was placed at the trap center to simplify calculation. The ions were assigned pseudo-random initial velocities corresponding to an initial temperature, with the net linear momentum of the ensemble set to zero. The initial ion density, aspect ratio of the lattice, and ion rotation velocity were assigned.

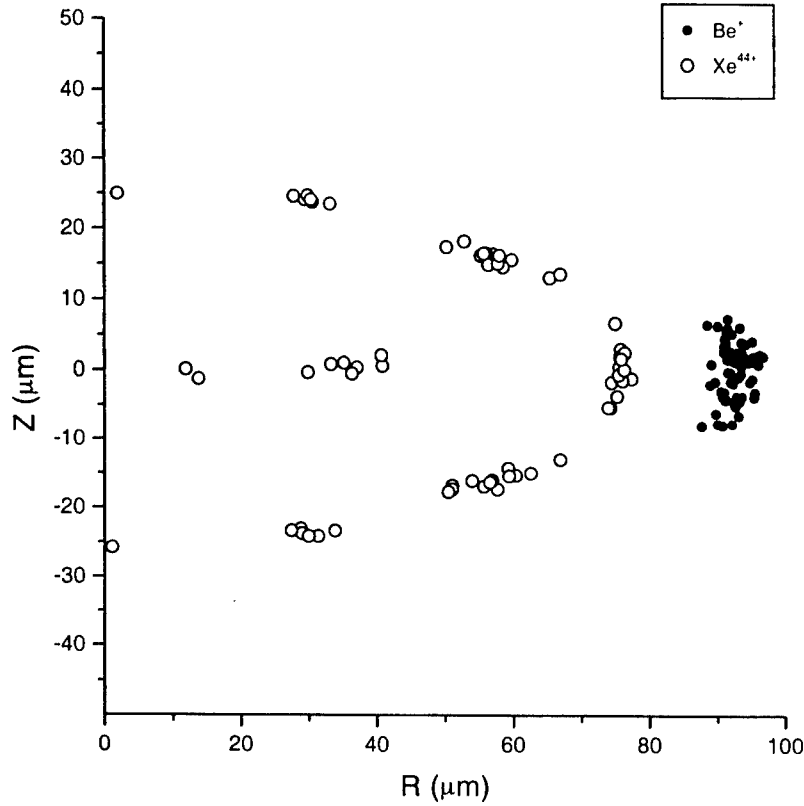


FIGURE 5. A "snapshot" cylindrical R-z projection of the ion cloud described in Figure 4.

The electrostatic force between each pair of particles was calculated using Coulomb's Law between point charges. The electrostatic trap potential was modeled as an ideal hyperbolic potential, with the voltage applied between ring and end caps of a trap of specified size characterized by a single parameter q_{trap} . For the 9.34 mm scale length trap, $q_{\text{trap}} = -2$ corresponds to about 540 V. This approximates the voltage at which the axial oscillation of a Be^+ ion is resonant with the 2.5 MHz tuned circuit. The value $q_{\text{trap}} = -0.039$ corresponds to a shallow axial well, used experimentally for lower ion plasma rotation frequencies, resulting in greater interaction stability between the laser beam and the plasma. Dynamic features associated with ion confinement measurements, such as r.f. excitations, thermal bath coupling to tuned circuits, and image charges, were not modeled.

The equation of motion of the ions was integrated in the lab frame using the Verlet method [11], based on the Störmer formula $\mathbf{r}_i(t + \tau) = 2\mathbf{r}_i(t) - \mathbf{r}_i(t - \tau) + \tau^2 \mathbf{a}_i(t) + O(\tau^4)$. Here \mathbf{a}_i is the acceleration of ion i due to the electric and magnetic forces of the trap,

as well as the Coulomb forces. Since the trap symmetry axis is aligned with the uniform magnetic field B , this equation is simplest to apply in the z coordinate. For the x and y radial coordinate, the time-centered velocity $\mathbf{v}_i(t) = (\mathbf{r}_i(t + \tau) - \mathbf{r}_i(t - \tau))/2\tau + O(\tau^3)$ was used to evaluate the Lorentz force in the Stoermer formula and to get implicit expressions for $x(t + \tau)$ and $y(t + \tau)$ in terms of present acceleration, x and y position, and a single past time step of stored past x and y positions. A more sophisticated approach is described in the work of Spreiter and Walter, which we hope to incorporate in future simulations[12]. The parameter τ was chosen to be a fraction of the period of the initial plasma oscillation, so that it is also small enough to follow the largest cyclotron frequency of the simulation. It was found that small values of τ ($\sim 30 - 300$ ps compared to ~ 150 ns Be^+ cyclotron period) resulted in a stable simulation start.

The mean squared axial velocity component (proportional to axial temperature T_z of each species) is averaged for every other step. Every 1000 steps, an estimate of the rigid body rotation frequency was made, and in that reference frame, the mean squared radial velocity for each species (proportional to T_r) was calculated and recorded, along with the fixed frame kinetic energies and potential energies of the ions. When simulating cooling, if the running average axial temperature of an ion species exceeds the specified temperature by 3 %, the former z -axis positions of the species being “cooled” (proportional to axial velocity in a harmonic well) were re-scaled using a Taylor series expansion to approach the desired temperature. The other ion species could also be “heated” axially by a similar scaling, allowing a fixed amount of kinetic energy to be added on average to each ion. The temperature of the heated species can approach a steady state with the cooled species. Typically, the target temperature is lowered in steps as the system approaches quasi-steady state.

Major results of the simulation include observation of the onset of properties of a highly magnetized non-neutral plasma [13,14]. The multiply charged ions, with higher cyclotron frequencies, exhibited this effect at higher temperatures than the Be^+ ions, (ranging from 40 K to 2 K for Xe^{44+}) depending on density (or equivalently cloud rotation frequency), as the “radial cyclotron temperature” decoupled at an exponential rate from the “axial temperature”.

For example, a simulation of 64 Be^+ ions and 64 Xe^{44+} ion in a $q_{\text{trap}} = -2.0$ well and with a cold rigid body rotation frequency of 865 kHz, this temperature was about 0.5 Kelvin. A snapshot of this simulation is shown in Figures 4 and 5. The ions are separated, as discussed below. However, the radial and axial motions remain coupled through the ion cloud rotation. The Be^+ ions were not significantly magnetized for simulated temperatures > 1 Kelvin.

Typically, the multiply charged ions and Be^+ ions centrifugally separate, as Figures 3 and 4 show. This centrifugal separation occurs when the plasma rotates as a rigid body. The “pseudopotentials” associated with the plasma rotation for each species then differ, because of the different mass-to-charge ratios, causing the ions with higher mass to charge ratio (in this case Be^+) to move radially outward and separate from the HCLs. The separation temperature was found to depend on the trap parameter q_{trap} and rotation frequency (bounds of which depend on q_{trap}) as expected, although the current code (no spacial averaging / small numbers of particles) and mode of

simulation (step down of set temperature) does not track the separation in detail. Simultaneously ordering of the HCIs can be seen, first as shells, then, at lower temperatures, rings of ions are apparent. The shell surfaces then have the characteristic triangular structure of 2D Coulomb systems [14,15].

Additional work involves the study of the effect of heating sources on the multiply charged ion temperatures given an experimentally measurable Be^+ temperature. From simulated motion and atomic data, spectroscopic lineshapes can be calculated and parameters for future experiments estimated. For example, Ca^{14+} has been caught and electronically cooled in our trap. Unfortunately, Be^+ laser cooling was not functioning at that time due to laser failure. Calculations are proceeding to model this system to optimize our procedure for a future experimental opportunity.

THE MOVE

The Retrap facility has been moved to the Lawrence Berkeley National Laboratory. The trap is now sited on the roof of a target cave at the LBL 88" cyclotron[16]. The system is now undergoing preliminary testing with a MeVVA ion source. Several electron cyclotron resonance (ECR) ion sources will be available to continue work with highly charged ions. The laser capabilities needed for cooling and spectroscopy is to be reestablished in the near future. The cyclotron and associated ion source technology will allow the trapping and study of rare isotopes. The effect of charge state, for example, on various nuclear decay mechanisms can be studied.

ACKNOWLEDGMENTS

This work was performed under the auspices of the U.S. Department of Energy by the University of California Lawrence Livermore National Laboratory under Contract No. W-7405-ENG-48. Support of Texas A&M authors through NSF grant PHY-9876899 and State of Texas ARP #010366-0018-1997.

Thanks to Dr. G. Zwicknagel for pointing out the work of Spreiter and Walter.

REFERENCES

1. O'Neil, T.M., *Physics Today* **52**, 24-30 (1999).
2. Chabrier, G., "Review on white dwarf cooling theory" in *11th European Workshop on White Dwarfs*, edited by S. -E. Solheim and E.G. Meistas , ASP Conference Series 169, San Francisco: Astronomy Society of the Pacific, 1999, p. 369.
3. www.whitedwarf.org
4. Church, D. A. *et al*, "RETRAP: An Ion Trap for Laser Spectroscopy of Highly-Charged Ions" in *Trapped Charged Particles and Fundamental Physics*, edited by D.H.E. Dubin and D. Schneider, AIP Conference Proceedings 457, New York: American Institute of Physics, 1999, pp. 235-241.
5. Schneider,D, *et al.*, *Rev. Sci. Instrum.* **65**, 3472 (1994).
6. Gruber, L., *Cooling of Highly Charged Ions in a Penning Trap*, UCRL-LR-138667, Lawrence Livermore National Laboratory, 2000.
7. Gruber, L. *et al*, *PRL* **86**, 636-639 (2001).
8. Brewer,L.R. *et al.*, *Phys. Rev A* **57**, 859 (1988).
9. Blumel, R. *et al*, *Nature* **334**, 309-13 (1988).
10. DeWitt, H.E *et al*, "Monte Carlo Simulation of the OCP Freezing Transition" in *Strongly Coupled Plasma*, edited by H. M. Van Horn and S. Ichimaru, Rochester: University of Rochester Press, 1993, p. 425.
11. Verlet, L., *Phys. Rev* **159**, 98 (1967).
12. Spreiter, Q., and Walter, M., *J. Comput. Phys.* **152**, 102-119 (1999).
13. Peurrung, A. J. *et al*, *Int. J. Mass Spectrom. Ion Processes* **157/158**, 39 (1996).
14. Dubin, D.H.E. and O'Neil,T.M., *RMP* **71**, 87 (1999).
15. Hasse. R.W. and Schiffer, J.P., *Ann. of Phys.* **203**, 419 (1990).
16. <http://www-nsd.lbl.gov/nsd/user88/>

EBIT in the Magnetic Trapping Mode: Mass Spectrometry, Atomic Lifetime Measurements, and Charge Transfer Reactions of Highly Charged Atomic Ions

Lutz Schweikhard*, Peter Beiersdorfer§, Elmar Träbert£

* *Inst. f. Physik, Johannes-Gutenberg-Universität D-55099 Mainz, Germany*
present address: Inst. f. Physik, Ernst-Moritz-Arndt-Universität, D-17487 Greifswald, Germany

§ *Lawrence Livermore National Laboratory, Livermore, CA 94550, USA*

£ *Ruhr-Universität Bochum, Germany, and IPNAS, Université de Liège, Belgium*

Abstract. Although it may sound like a contradiction in terms, the electron beam ion trap (EBIT) works as an ion trap even when the electron beam is switched off. We present various experiments that exploit the „magnetic trapping mode“ for investigations of ion confinement, charge exchange processes, atomic lifetime and ion mass measurements.

INTRODUCTION

Since its introduction, the electron beam ion trap (EBIT) [1] has played a significant role in the field of atomic x-ray spectroscopy. Similar to the electron beam ion source (EBIS), production and storage of highly charged atoms are effected by the use of an intense electron beam (typically of the order of a hundred milliamperes) of high energy (a few to a few hundred kiloelectronvolts) which is compressed by a strong magnetic field (several Teslas). The electron density in the beam is in the 10^{12} cm^{-3} range thus exceeding the rest gas density of typically 10^6 cm^{-3} . In contrast to the conventional EBIS configuration, the magnetic field is provided by a set of Helmholtz coils which allows x-ray and optical windows for radial line-of-sight access to the center of the trap. The pioneering work at Livermore has been followed by several research groups all over the world.

Conventionally the x-ray production is closely related to the interaction of the stored ions with the electron beam, e.g. by electron impact excitation, by radiative or dielectronic recombination. Thus, it is not obvious what could be gained from

switching off the electron beam once the highly charged ions are created. Since the middle of the nineties, however, a series of such experiments has been performed that aimed at a mass analysis of the trapped ion ensemble [2-4]. To this end, the two electron beam ion traps at Livermore, SuperEBIT and EBIT-II, were operated in a Penning-trap-like „magnetic trapping mode“ (MTM), in contrast to the „electron trapping mode“ (ETM) during ion production [5,6]. In the new mode, the drift tube voltages provide an axial electric trapping potential that complements the Lorentz force for radial ion confinement.

When the electron beam is switched off, the plasma changes within a fraction of a millisecond from being electron-dominated to ion-dominated. The space charge compensation provided for the ion cloud then ends as well as the attractive potential. Consequently, the ion cloud expands somewhat, as was recently quantified by the NIST EBIT group [7]. Distant ion-ion collisions redistribute the angular momenta with respect to the trap axis. Work at LLNL found this process to be irreversible: when the electron beam is switched on again, even as soon as after 1 ms, the ion cloud does not shrink back to its old size, but a new (electron beam-dominated) cloud is being built up from neutral atoms and low-charge ions along the axis, i.e. inside of the old ion cloud. The actual transition between the two steady-state conditions may become the subject of future ion-cloud dynamics studies.

MASS SPECTROMETRY

For a mass spectrometric (MS) analysis of the ion ensemble, the ions' cyclotron motion is excited by radio frequency signals on electrodes, which are inserted through the observation slots of the inner drift tube. Similarly, the image charges of the revolving ions are picked up and Fourier-analyzed to determine the mass-over-charge ratios of the stored ions. These Fourier transform - ion cyclotron resonance (FT-ICR) measurements [3,4] have included the determination of the number of ions as well as the ion storage time. The coherence time of the ICR-induced collective ion motion was found to be of the order of 1 to 2 ms, allowing a charge-to-mass resolution of about 5×10^{-5} . The validity of the method was checked by comparing the relative abundance of different charge states as found by FT-ICR and by x-ray techniques [8,9]. Similarly, the relative abundance of different isotopes was measured and compared to known ratios. In addition, the radial extent of the ion cloud was inferred.

Future progress will require to overcome a number of technical obstacles: For one, broadband excitation is not as easily accomplished as in conventional FT-ICR MS, since the range of cyclotron frequencies that have to be addressed is much wider for highly charged atomic ions. A typical FT spectrum obtained following broadband excitation is shown in Fig. 1. The signals from isotopically pure heliumlike through bare krypton ions are observed between 18 and 20 MHz. (Note that signals from light ions, such as bare nitrogen or oxygen, are missing, which illustrates the

displacement of low-Z ions by higher-Z ions in the ETM.) The figure illustrates another technical obstacle, i.e., a relatively large noise pickup in spite of the use of the shortest leads possible (by direct radial arrangement out of the trap). The noise level changes throughout the day and cannot easily be subtracted. Frequency shifts are expected due to relativistic effects at those higher cyclotron frequencies [10, 11]. These combine with the radial inhomogeneity of the magnetic field. The main obstacle, however, is the typical EBIT drift-tube construction where only small excitation and detection electrodes can be inserted (and only one for each function) in contrast to the much larger excitation and detection electrodes (i.e. differential electrode pairs) in use in conventional FT-ICR. We plan to redesign the trap's middle drift tube into four segments. Each segment pair will be used for either excitation or detection. Note that similarly the Tokyo EBIT has recently been equipped with a middle drift tube with six segments.

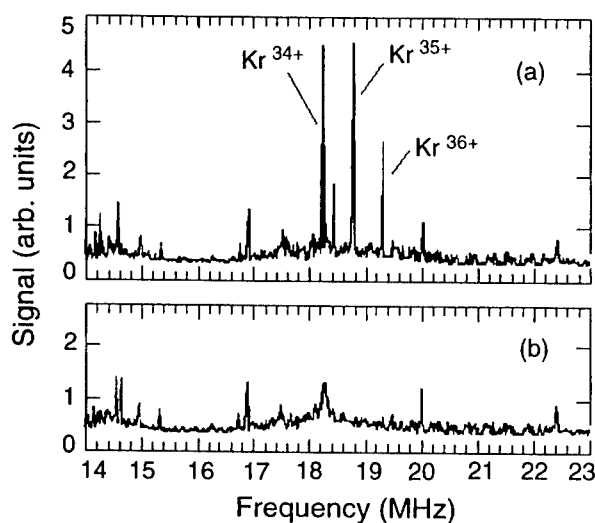


FIGURE 1. FT-ICR spectrum of krypton ions as produced in the electron mode by a 130-mA, 80-keV electron beam: (a) following broadband excitation by sweeping from 23 MHz down to 17 MHz within 100 μ s. (b) noise spectrum in the absence of excitation.

The FT-ICR studies laid the foundation for further investigations and uses of the magnetic mode. For example, why not have a look at the x-ray and optical signals, just as in the ETM? There are two sources of excited states available in the MTM as described in the following sections: (a) Excited metastable levels that have been populated in the electron mode just before the electron beam is switched off. (b) Electron transfer reactions from neutral atoms or molecules during the MTM.

ATOMIC LIFETIME MEASUREMENTS

Most atomic levels of highly charged ions have lifetimes in the picosecond range and are thus best studied by beam-foil spectroscopy. However, there is a class of levels that is far too long-lived for this traditional technique, but is of interest for the diagnostics of astrophysical and laboratory plasmas: the fine structure levels of the ground configurations of highly ionized atoms and similar levels in low-lying configurations that – for reasons of parity – cannot decay by the emission of electric dipole (E1) radiation. These levels are easily excited even in thermal plasmas, but their emission by higher-multipole order radiation can be observed only if they are not collisionally quenched, that is in environments of such low particle density as in the solar corona, tokamak discharges, or ion traps operating under ultra-high vacuum conditions.

The same electron beam of EBIT that produces highly charged ions is available for collisional excitation and de-excitation. When these processes suddenly end, one can follow the signal on a given spectral line with time and thus obtain the lifetime of the upper level. The Livermore EBIT group has pioneered such lifetime measurements, first by a modulation of the electron beam energy around the excitation threshold of the level of interest, e.g. the $1s2s\ ^3S_1$ level in He-like Ne^{8+} ions, and recently by switching the beam off completely [12,13]. Some of the subsequent work on the same level in He-like ions of N through Mg, covering level lifetimes from some 30 μs to several milliseconds, provides the most stringent test (better than 0.5%) on the exceedingly accurate theoretical predictions.

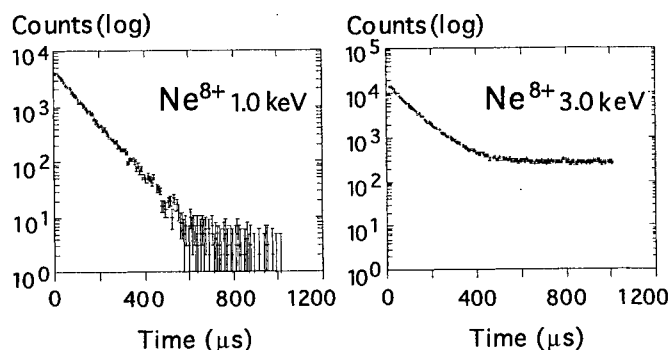


FIGURE 2. X-ray observation of the M1 decay of the lowest triplet level in He-like Ne ions [14]. Left: Excitation just above threshold, right: Excitation energy sufficient to also produce H-like and bare Ne ions. The curve tail results from CX (recombination).

In addition to these x-ray observations, a second realm of atomic lifetime determinations are the electric-dipole „forbidden“ M1 and E2 transitions that occur

in the visible spectrum and that are responsible for the long-time mysterious corona lines in the spectrum of the sun. Lifetimes in the range up to 15 ms have been measured for electronic states of Ar [15], K and Kr ions. Because of the poorer signal-to-noise ratio of detectors for visible light (in contrast to x-ray detectors), these measurements have reached a routine accuracy of „only“ 2% - which however is sufficient to exceed the intrinsic accuracy of the current theoretical predictions of in-shell M1/E2 transition rates by an order of magnitude.

Note that for any lifetime measurement a good characterization of the MTM is essential. In particular, the ion storage time and ion cloud dynamics need to be well known, lest the ions drift out of the solid angle subtended by the photon counters, reducing the apparent radiative lifetimes. For millisecond lifetimes, the correction for the finite ion confinement time has to be established, e.g., by employing charge exchange rate measurements, as is discussed in the next section.

ELECTRON TRANSFER REACTIONS

After the electron beam has been switched off, any delayed emission from the decay of *short-lived* levels signifies level population by charge exchange (CX) processes. With spectrally resolved photons, the individual ionic charge state reached after CX can be determined, and CX can be mapped for a number of charge states simultaneously. A typical spectrum illustrating the CX-induced K-shell emission in the magnetic trapping mode is shown in Fig. 3.

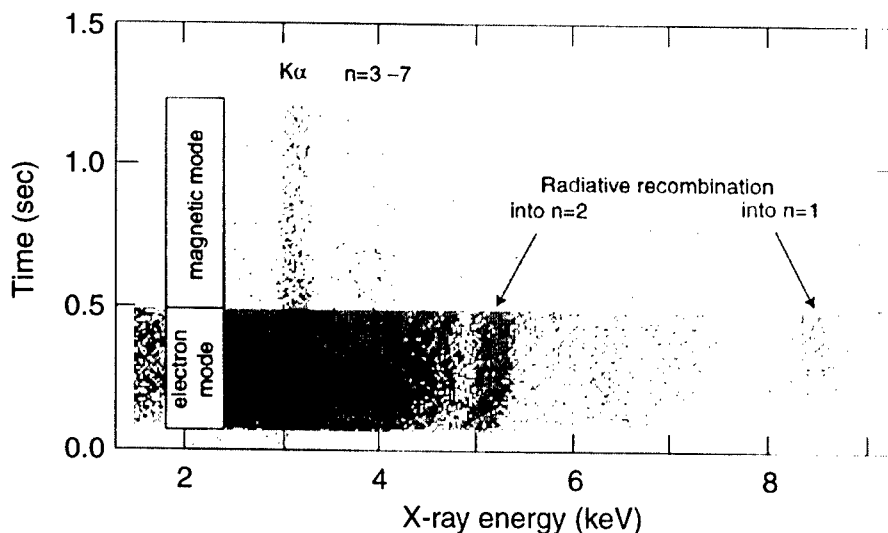


FIGURE 3. Argon K-shell x-ray emission observed in ETM and MTM (from ref. 16).

While CX measurements are interesting with respect to atomic [16] and space physics [17], and gas pulses may be applied to the trap volume for that purpose deliberately [8], they also provide information on the magnetic trapping mode. In recent EBIT-II experiments, rather similar effective confinement time constants (storage times of order 300 ms) were found by direct x-ray observation of He-like Kr ions and in the decay curve tails (cascades) of optical measurements on Kr ions with partly filled 3p and 3d shells, indicating that under the vacuum conditions in EBIT-II the confinement time in the MTM depends only weakly on the ion charge. For SuperEBIT, with its better vacuum, ion storage times of more than 20 s were measured. This showed that CX is the dominant loss process in the MTM. Other loss processes, such as radial diffusion or scattering into the axial loss cone, are much slower.

In addition, the ion storage time was found to depend on the trap potential that confines the ions in the axial direction. High potentials reduced the ion confinement time. We attribute this to the fact that the ions attain a higher temperature during the electron mode when confined in a deeper well [5], which in turn results in an increased likelihood for CX due to the higher ion velocity.

CONCLUSION AND OUTLOOK

The deployment of the MTM of EBIT has only just begun. Three major directions of study have been identified: Mass spectrometry, lifetime determinations and charge exchange measurements. Future extensions may include precision MS of known ions (as compared to mass analysis of unknown ensembles), coincidence measurements of decay cascades after CX, or the determination of the charge state of the previously neutral atoms after the reaction by MS, either by FT-ICR of the ions in the trap or after ejection and (time-of-flight or magnetic-sector) MS. So far the CX partners have been neutral atoms of noble gases. An obvious extension is the use of more and more complex reaction partners: small molecules, larger molecules, atomic and molecular clusters. Finally, it may be worth noting that by switching from the electron to the magnetic trapping mode, the highly charged ions are essentially "transferred" (in time) from their source to a Penning trap without the need of two (spatially) separated devices and a transfer line. Thus, in principle any EBIT/re-trap type of experiment may be reconsidered with the magnetic trapping mode as an alternative.

ACKNOWLEDGMENTS

The work at the University of California Lawrence Livermore National Laboratory was performed under the auspices of the Department of Energy under Contract No. W-7405-Eng-48 and supported in part by the Chemical Sciences, Geosciences and Biosciences Division of the Office of Basic Energy Sciences, Office of Science, U.S. Department of Energy. LS thanks the DAAD for travel support, ET acknowledges support by DFG (Germany) and FNRS (Belgium). We thank Daniel Thorn for his help in preparing the figures.

REFERENCES

1. Levine, M.A., Marrs, R.E., et al., *Physica Scripta T* **22**, 157-163 (1988).
2. Beiersdorfer, P., Beck, B., et al., *Rapid Commun. Mass Spectrom.* **8**, 141-143 (1994).
3. Schweikhard, L., Ziegler, J., et al., *Rev. Sci. Instrum.* **66**, 448-450 (1995).
4. Beiersdorfer, P., Becker, St., et al., *Nucl. Instr. Meth. B* **98**, 558-561 (1995).
5. Beiersdorfer, P., Schweikhard, L., et al., *Rev. Sci. Instrum.* **67**, 3818-3826 (1996).
6. Beiersdorfer, P., Beck, B., et al., *Int. J. Mass Spectrom. Ion Proc.* **157/158**, 149-161 (1996).
7. Porto, J.V., Kink, I., and Gillaspay, J.D., *Rev. Sci. Instrum.* **71**, 3050-3058 (2000).
8. Schweikhard, L., Beiersdorfer, P., et al., *Nucl. Instrum. Meth. B* **142**, 245-252 (1998).
9. Beiersdorfer, P., Schweikhard, L., et al., *Physica Scripta T* **80A**, 121-123 (1999).
10. Schweikhard, L., Alber, G.M., and Marshall, A.G., *Physica Scripta* **46**, 598 - 602 (1992).
11. Guan, S., Gorshkov, M.V., al., *Phys. Rev. A* **47**, 2730-2737 (1993).
12. Crespo López-Urrutia, J.R., Beiersdorfer, P., et al., *Phys. Rev. A* **57**, 238-241 (1998).
13. Träbert, E., Beiersdorfer, P., et al., *Phys. Rev. A* **60**, 2034 - 2038 (1999).
14. Träbert, E., Beiersdorfer, P., and Utter, S. B., *Physica Scripta T* **80**, 450 - 452 (1999).
15. Träbert, E., Beiersdorfer, P., et al., *Astrophys. J.* **541**, 506-511 (2000).
16. Beiersdorfer, P., Olsen, R., et al., *Phys. Rev. Lett.* **85**, 5090-5093 (2000).
17. Beiersdorfer, P., Lisse, C.M., et al., *Astrophys. J. Lett.* **549**, L147-L150 (2001).

Structure and Madelung Energy of Coulomb Clusters

Hiroo Totsuji, Tokunari Kishimoto, Chieko Totsuji and Kenji Tsuruta

*Graduate School of Natural Science and Technology and Faculty of Engineering,
Okayama University, Tsushimanaka 3-1-1, Okayama 700-8530, Japan*

Abstract. The ground state of the system of charged particles of one species confined by the three-dimensional, isotropic, and parabolic potential is investigated by molecular dynamics simulations. It is shown that, with the increase of the system size or the number of particles in the system N , the ground state changes from the shell-structured system to the finite bcc lattice with reconstructed surface. The critical value of the transition is estimated to be between $N = 10^4$ and $N = 2 \times 10^4$. The nucleation of the bcc lattice in the shell-structured cluster of 2×10^4 ions is observed.

INTRODUCTION

The systems of charges of one species confined in the external field provide us with a stage where various properties of strongly coupled plasmas manifest themselves in a simple and clear way. This system can be realized in the Penning-Malmberg [1] and Paul traps [2, 3] and direct experimental observations of these properties have been an excitement in recent years.

The ground state of these finite systems is strongly influenced by the geometry of confinement. When the external potential is the spherically symmetric parabola and the number of charges in the system is small, the structures such as icosahedron or spherical shells give the ground state. When the system has sufficiently large number of particles, it is expected that the ground state contains the bcc lattice as its main part: The ground state of the (infinite) one-component plasma is the bcc structure.

In experiments, the bcc lattice at the central part has been observed for large cloud of charges of the size more than 10^5 [4, 5]. The transition of the ground state from the shell structure to the bcc lattice has been expected to occur at the system size of 2×10^5 or larger [6]. It seems, however, that numerical simulations of larger systems may give more precise information related to this transition. The purpose of this paper is to compare the cohesive energy, sometimes called the Madelung energy, of these structures and show that the transition occurs between $N = 10^4$ and $N = 2 \times 10^4$ by molecular dynamics simulations of large clusters.

PARAMETERS AND MADELUNG ENERGY

Let us here fix some notations for these clusters of charges. The Hamiltonian of our system H is given by $H = K + U$, where K is the kinetic energy

$$K = \sum_{i=1}^N \frac{1}{2} m \left(\frac{d\mathbf{r}_i}{dt} \right)^2, \quad (1)$$

and U , the potential energy

$$U = \sum_{i>j}^N \frac{q^2}{|\mathbf{r}_i - \mathbf{r}_j|} + \sum_{i=1}^N \frac{1}{2} k r_i^2. \quad (2)$$

We define the Wigner-Seitz radius a_{WS} by

$$a_{WS} = \left(\frac{q^2}{k} \right)^{1/3} \quad (3)$$

and rewrite K and U into the form

$$K = m \left(\frac{a_{WS}}{t_0} \right)^2 \sum_{i=1}^N \frac{1}{2} \left(\frac{d\mathbf{r}'_i}{dt'} \right)^2 \quad (4)$$

$$U = \left(\frac{q^2}{a_{WS}} \right) \left(\sum_{i>j}^N \frac{1}{|\mathbf{r}'_i - \mathbf{r}'_j|} + \sum_{i=1}^N \frac{1}{2} (r'_i)^2 \right). \quad (5)$$

Here the coordinates of particles are normalized by a_{WS} and the time is normalized by t_0 .

In the fluid approximation where charges are regarded as continuum, the ground state is the uniform distribution up to the radius R

$$R = \left(\frac{Nq^2}{k} \right)^{1/3} = N^{1/3} a_{WS} \quad (6)$$

with the density

$$n = \frac{3}{4\pi} \frac{k}{q^2}. \quad (7)$$

We note that a_{WS} defined by (3) is the average mean distance or the ion-sphere radius in this approximation;

$$\frac{4\pi}{3} n a_{WS}^3 = 1. \quad (8)$$

The potential energy of the ground state in the fluid limit U_{homo} is given by

$$U_{homo} = \frac{3}{5} N^2 \frac{q^2}{R} + \frac{3}{10} N k R^2 = \frac{9}{10} N^{5/3} \frac{q^2}{a_{WS}}. \quad (9)$$

For given distribution of particles, we define the Madelung energy U_M by

$$U_M = U - U_{homo}. \quad (10)$$

At zero temperature, the behavior of the system is determined only by U . Therefore (5) indicates that our system is characterized by only one parameter, the system size N . At finite temperatures, we define the parameter Γ which represents the strength of the Coulomb coupling by

$$\Gamma = \frac{q^2}{k_B T a_{WS}}. \quad (11)$$

The static properties of the system at finite temperatures are characterized by the parameter Γ and the system size N .

In the fluid approximation, the radius of uniform distribution oscillates with the frequency

$$\omega_p = \left(\frac{3k}{m} \right)^{1/2} = \left(\frac{3q^2}{ma_{WS}^3} \right)^{1/2} = \left(\frac{4\pi q^2 n}{m} \right)^{1/2}. \quad (12)$$

This frequency characterizes the macroscopic evolution of our system. One of characteristic time scales of the microscopic evolution may be the time to move the mean distance by thermal velocity $a_{WS}/(k_B T/m)^{1/2}$ which is related to ω_p as

$$\omega_p \frac{a_{WS}}{(k_B T/m)^{1/2}} = (3\Gamma)^{1/2}. \quad (13)$$

NUMERICAL METHOD

Scaling with system size

We perform the molecular dynamics simulations. In this case, most of the computational time is consumed in the computation of the force on each particle and, with the naive method, the computational time increases rapidly in proportion to N^2 in our system where particles interact via the long-ranged Coulomb potential. We therefore adopt the fast multipole method [7] which enables one to perform molecular dynamics simulations of long-range force systems with the $O(N)$ -scaling under controlled accuracy.

In the fast multipole method, the system is divided recursively into small cells and the interaction between particles belonging to well-separated cells is computed based on the multipole expansion and Taylor expansion. The number of smallest cells is 8^{level} and the level is adjusted so that the smallest cell has about 8 particles on the average [7]. For the system size of $N = 10^5$, we adopt the following parameters for the fast multipole method: the level of 5, multipole expansion up to 2^6 -th order, the Taylor expansion up to 6th order, the well-separatedness of 2 (in the highest level, direct computation is applied for nearest and next-nearest neighbor cells). In the course of molecular dynamics simulation, the accuracy of the Madelung energy is kept at least for the first 4 digits and the direct computation is performed for final relaxed states. The parameters for smaller systems are also determined to give the accuracy at least of the same order.

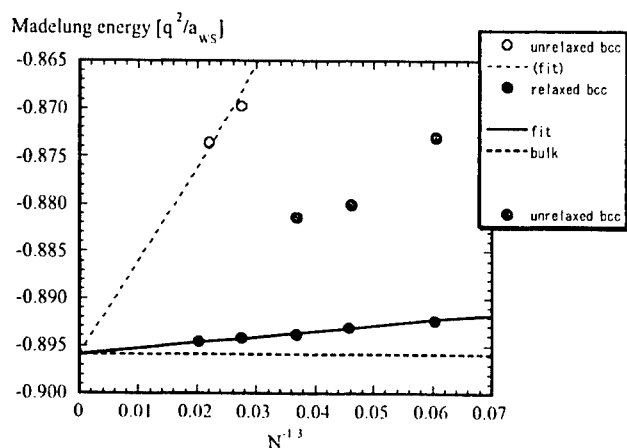


FIGURE 1. Madelung energy vs. system size for spherical bcc matter. Solid circles are the values with relaxed surface and solid line is the interpolation. Open and gray circles are examples of values without relaxation.

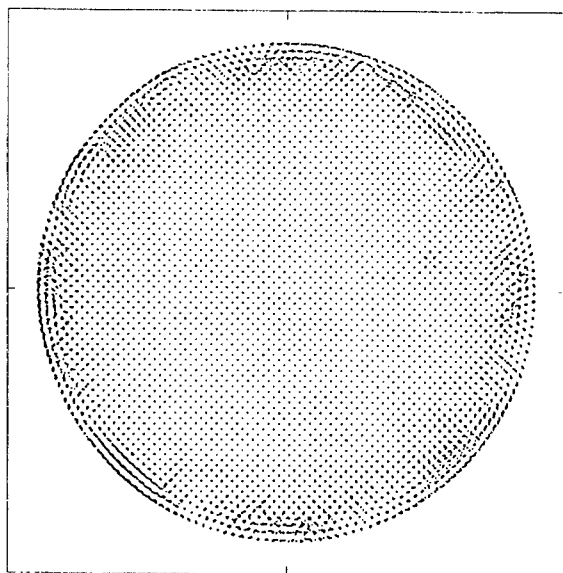


FIGURE 2. Particle distribution near the equatorial plane in spherical bcc matter with relaxed surface for $N = 120,032$. Positions of particles in the domain $|z| < 2.7a_{ws}$ are projected.

The temperature is controlled by the Nosé-Hoover method. In order to keep the homogeneity of the temperature, we attach multiple thermostats each controlling the kinetic energy of about 5000 particles.

Initial conditions

For the system of the size N , the radius of particle distribution in the fluid-limit ground state is determined as (6). The initial positions for the shell structure is given by the uniform random distribution of particles within this sphere. The velocities are given by the random distribution corresponding to the temperature specified by the value of Γ . After annealing with Γ values between 100 and 150 for sufficiently many steps in measures of the time scales (12) and (13), we slowly decrease the temperature.

Another set of initial conditions is the spherical cutout of the three-dimensional lattice and the random distribution of velocities. In this case, the value of Γ is kept just above the melting point (low temperature side) of the infinite lattice for a sufficiently long time to allow the system to relax before slowly increased.

MADELUNG ENERGY OF RELAXED SPHERICAL BCC MATTER

The spherical cutout of the bcc lattice has rather high surface energy as is shown in Fig. 1. When we anneal this system keeping the temperature near but below the melting point, we obtain the spherical bcc matter with reconstructed surface. The Madelung energy of the spherical bcc matter with reconstructed surface is also shown in Fig. 1 for the system sizes $N = 4544, 10,464, 20,288, 48,928, \text{ and } 120,032$. We observe that the relaxation near the surface largely reduces the Madelung energy [8]. This is not expected from the high values of the Madelung energy of unrelaxed spherical bcc matter. An example of the structure is shown in Figs. 2 and 3. We observe that the relaxation has occurred within a few layers at the surface.

In the limit of very large values of N , the Madelung energy may have the form

$$\frac{U_M}{Nq^2/a_{WS}} = E_\infty + \frac{E_s}{N^{1/3}}, \quad (14)$$

where the second term expresses the effect of the surface. When fitted to this form with $E_\infty = -0.895929$ (the Madelung energy of an infinite bcc solid), as shown in Fig. 1 by the solid line, we have $E_s = 0.0605$.

MADELUNG ENERGY OF SHELL-STRUCTURED SPHERICAL CLUSTERS

Starting from the random distribution in the sphere of radius R given by (6), we first anneal the system at the temperature above the melting temperature of bulk one-component

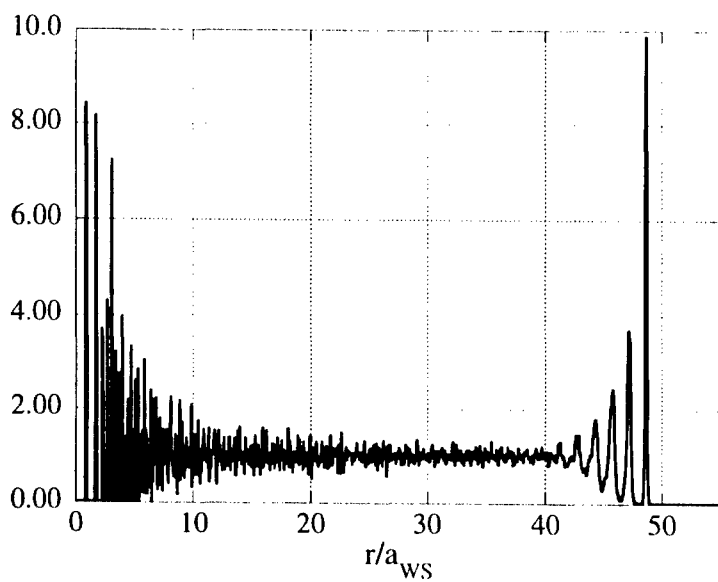


FIGURE 3. Radial distribution of particles in spherical bcc matter with relaxed surface for $N = 120,032$.

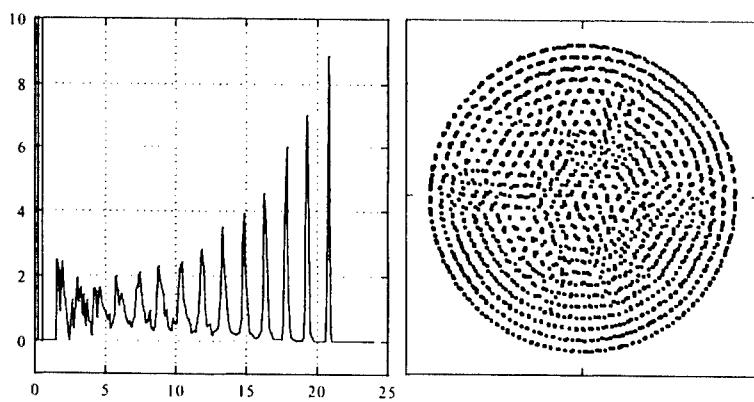


FIGURE 4. Particle distribution in shell-structured spherical cluster with $N = 10,000$ (left). Positions of particles near the equatorial plane with $|z| < 1.2a_{ws}$ are projected (right).

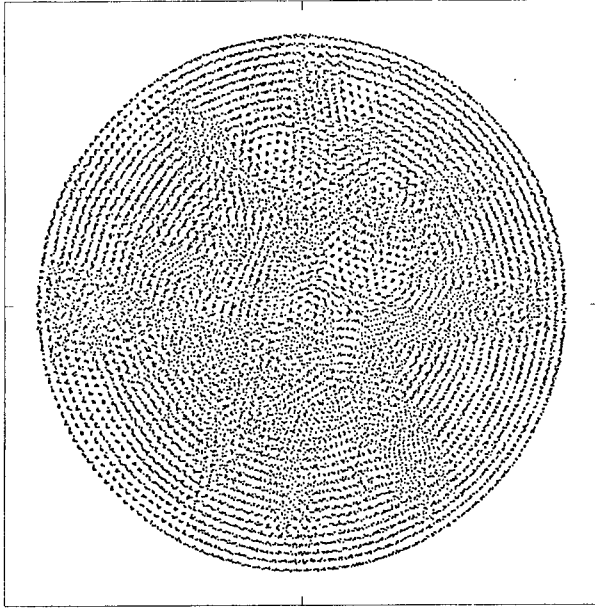


FIGURE 5. Particle distribution in shell-structured spherical cluster with $N = 100,000$.

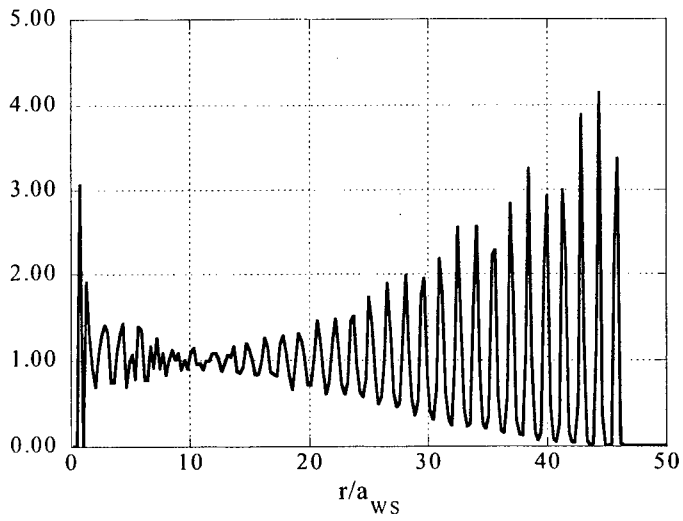


FIGURE 6. Projected positions of particles in the domain $|z| < 2.6a_{WS}$ for $N = 100,000$.

plasma. The typical value of Γ is around 100. We then slowly decrease the temperature of the system. The results are shown in Figs. 4, 5, and 6.

The values of the Madelung energy of the shell-structured spherical system of the size $N = 5 \times 10^3$, 10^4 , 20288, and 10^5 are shown in Fig. 7. These values of the Madelung energy can be interpolated by the formula

$$\frac{U_M}{Nq^2/a_{WS}} = -0.8940 + 0.0219N^{-1/3}. \quad (15)$$

The largest simulated system in reports was $N = 2 \times 10^4$ [9].

TRANSITION OF THE GROUND STATE

The Madelung energies of the shell-structured clusters and of finite bcc matters with relaxed surface are compared in Fig. 7. We observe that, when the system size exceeds the critical value N_c , the ground state changes from the shell-structured cluster to the finite bcc lattice with relaxed surface. The critical system sized is given by the crossing of these Madelung energies and, in Fig. 7, is estimated to be around 10^4 . We here note that these Madelung energy, especially of shell structures, could become lower by annealing the system repeatedly. The crossing, however, does not seem to be larger than 2×10^4 . Taking into account this possibility, we here conclude that

$$10^4 < N_c < 2 \times 10^4. \quad (16)$$

NUCLEATION OF BCC LATTICE

The shell-structured cluster is still is a local minimum of the Madelung energy in the domain where $N > N_c$ and the bcc lattice with relaxed surface is the global minimum. Therefore it is not strange that the shell-structured cluster does not evolve to the bcc lattice with relaxed surface in simulations. One may, however, expect that there is a chance for the bcc lattice develops in the clusters of larger sizes. We here show one of such examples.

The distribution of particles near the equatorial plane of the cluster of $N = 20,288$ is shown in the left panel of Fig. 8. We observe that there exist a part where we have the structure with the straight planes rather than a curved plane in accordance with the surface. The structure factor for the particles in this domain is shown in the right panel of Fig. 8. We clearly see that the Bragg spots forms the fcc structure in the wave-number space. We have confirmed that the spacing between Bragg spots agree with those of the bcc lattice with the average density of this cluster. This domain thus forms the bcc lattice nucleated from the shell-structured cluster.

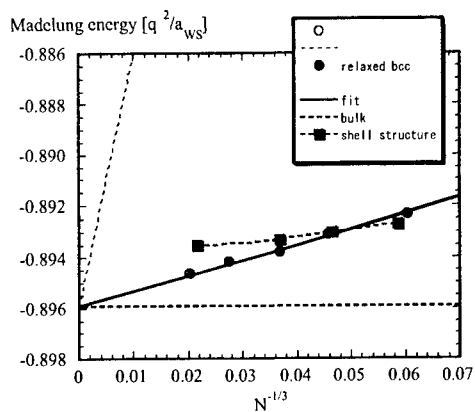


FIGURE 7. Madelung energy of spherical coulomb system vs. $N^{-1/3}$. Filled circles are relaxed spherical bcc matter and squares are shell structured systems.

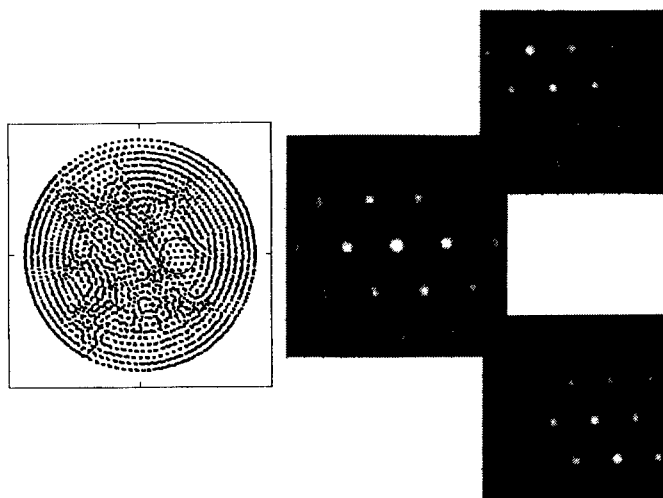


FIGURE 8. Bragg pattern from the central part (circled) of the shell-structured cluster of $N = 20,288$. Shown are consecutive three planes in reciprocal space where spots form the fcc lattice corresponding to bcc structure in real space.

CONCLUSIONS

It is shown that the ground state of the spherical coulomb clusters changes from shell-structured clusters to the finite bcc lattice with relaxed surface at the system size between 10^4 and 2×10^4 . In the shell-structured cluster of 2×10^4 , the nucleation of the bcc lattice is observed.

ACKNOWLEDGMENTS

This work has been partly supported by the Grants-in-Aid for Scientific Researches of the Ministry of Education, Culture, Sports, Science, and Technology of Japan, Nos. 08458109 and 11480110.

REFERENCES

1. Gilbert, S. L., Bollinger, J. J., and Wineland, D. J., Phys. Rev. Lett. **60**, 2022 (1988).
2. Birkel, G., Kassner, S., and Walther, H., Nature (London) **357**, 310 (1992).
3. Drewsen, M., Brodersen, C., Hornekær, L. J., Hangst, S., and Schiffer, J. P., Phys. Rev. Lett. **81**, 2878 (1998).
4. Itano, W. M., Bollinger, J. J., Tan, J. N., Jelenković, B., Huang, X. -P., and Wineland, D. J., Science **279**, 686 (1998).
5. Bollinger, J. J., Mitchell, T. B., Huang, X. -P., Itano, W. M., Tan, J. N., Jelenković, B., and Wineland, D. J., Phys. Plasmas, **7**, 7 (2000).
6. Dubin, D. H. E., and O'Neil, T. M., Rev. Mod. Phys. **71**, 87 (1999).
7. Greengard, L., and Rokhlin, V., J. Comput. Phys. **73**, 325 (1987).
8. Kishimoto, T., Totsuji, C., Tsuruta, K., and Totsuji, H., Physics Letters A **281**, 256 (2001).
9. Schiffer, J. P., *Non-Neutral Plasma Physics II*, edited by J. Fajans and D. H. E. Dubin, AIP Conference Proceedings 331, New York, 1995, p. 191.

Formation and Structural Transitions of 3D Coulomb Crystals in Dusty Plasmas

Yasuaki Hayashi

*Department of Electronics and Information Science, Kyoto Institute of Technology
Matsugasaki, Sakyo-ku, Kyoto, Japan*

Abstract. 3D Coulomb crystals were formed in dusty plasmas using smaller fine particles growing in a methane/argon plasma. The structures were confirmed to be bct, fcc and hcp. The process of the structural transition from bct to fcc was analyzed and it was found that the transition occurred by the slip of crystal planes of bct(110), which are parallel to the fcc(111) planes. The direction of the slip was bct[110] and fcc[211]. This process of transition between the two crystal structures and the relations in crystal planes and axes agree with the martensitic transformation.

INTRODUCTION

The crystal ordering of charged fine particles in plasmas by the Coulomb or shielded Coulomb force is an attractive physical phenomenon. It was theoretically predicted in 1986 [1] and experimentally discovered in 1994 by three groups independently [2-4]. The lattice sizes are usually more than $100\ \mu\text{m}$ and the arrangement of fine particles in a plasma can be observed even by the naked eye.

In dusty plasmas, i. e., plasma containing dust fine particles, larger monodisperse fine particles form the two-dimensional Coulomb crystal, a simple-hexagonal one. The formation is probably due to the effect of positively charged ion flow on fine particles sinking in a sheath region [5-7]. However, we found that three-dimensional Coulomb crystals can be formed by smaller fine particles, less than about $2\ \mu\text{m}$ in diameter [8-10]. By the accurate size control of growing fine particles in plasmas, finely ordered three-dimensional (3D) Coulomb crystals were formed [11,12]. The three-dimensional structures, which were observed by the use of laser-light scattering and two CCD video cameras at the same time, were mainly body-centered tetragonal (bct) and face-centered cubic (fcc). The bct (110) and fcc(111) planes were parallel to an electrode. bct forms a part of face-centered orthorhombic (fco).

In this paper, the growth mechanism of monodisperse spherical fine particles, the formation of 3D Coulomb crystals, and the analyses of structural transition between two 3D crystals are described.

GROWTH OF MONODISPERSE FINE PARTICLES

Carbon fine particles were grown in a plasma of methane diluted in argon by coating the seeds of ultra-fine particles of graphite. The coated carbon material was found to be the hydrogenated amorphous carbon by its refractive index with the use of the in-situ measurement method of Mie-scattering ellipsometry [13,14].

The distribution function of ultra-fine particles is generally log-normal as

$$N(d) = \frac{1}{\sqrt{2\pi} d \ln \sigma} \exp \left\{ -\frac{[\ln d - \ln d_m]^2}{2 [\ln \sigma]^2} \right\}, \quad (1)$$

where d , d_m and σ represent particle size, the geometric mean size and the geometric standard deviation, respectively. If fine particles grow by coagulation, the type of distribution function does not change, although the geometric mean size and the standard deviation change [15]. However, when they grow by coating, a size distribution approaches the monodisperse one with growth as indicated by the following equation:

$$N(d) = \frac{1}{\sqrt{2\pi} \pi (d - d_c) \ln \sigma} \exp \left\{ -\frac{[\ln(d - d_c) - \ln d_m]^2}{2 [\ln \sigma]^2} \right\}, \quad (2)$$

where d_c means the thickness of coated material on the seeds of ultra-fine particles.

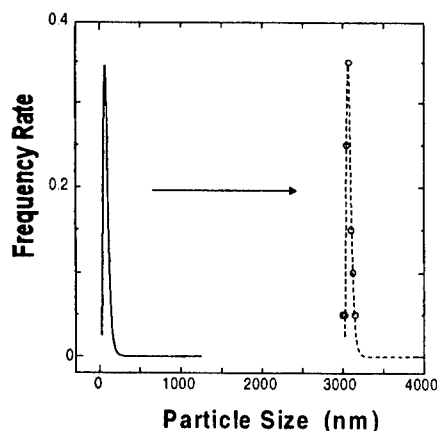


FIGURE 1. Size distribution of 20 grown fine particles (open circles). Solid line shows a log-normal distribution for $d_m=75\text{nm}$ and $\sigma=1.5$, and dotted line shows a distribution obtained by the shift of the log-normal distribution by 3000nm on the size axis.

Figure 1 shows a size distribution of 20 grown fine particles determined with the use of a scanning electron microscope (SEM). The dotted line in the figure shows a distribution indicated by eq.(2) for $d_m=75\text{nm}$, $\sigma=1.5$, and $d_c=3000\text{nm}$, which is obtained by the shift of a log-normal distribution of $d_m=75\text{nm}$ and $\sigma=1.5$. A SEM image of two grown carbon fine particles is shown in Fig.2 [16]. They indicate spherical shapes and uniform size. These results certify that monodisperse fine particles can be grown in the plasma.

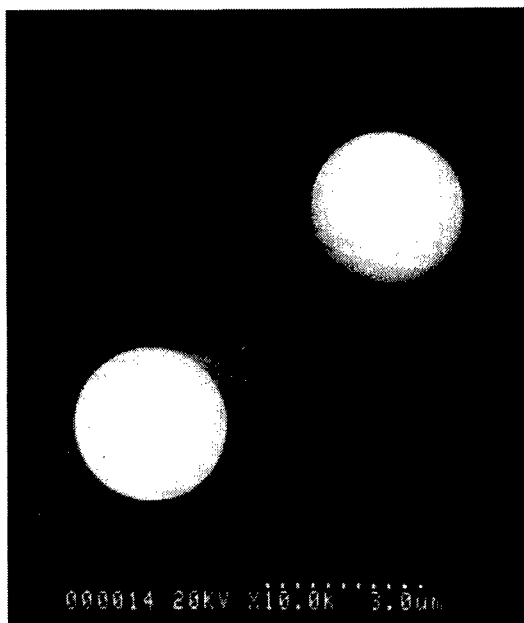


FIGURE 2. SEM image of grown carbon fine particles.

FORMATION OF 3D COULOMB CRYSTALS

In order to form three-dimensional Coulomb crystals and to analyze the structure, the size of growing fine particles was monitored and controlled using the Mie-scattering ellipsometry and two CCD video cameras, which were placed to acquire the top and side views of Coulomb crystal. An argon-ion-laser (wavelength:488 nm) and a diode-laser (690 nm) were used for the observation of particle arrangement by light scattering. Since the light intensity of the former laser is several-times higher than that of the latter, particle arrangements in a top view were indicated by the scattered light of argon-ion-laser. However, those in a side view were shown by that of a diode laser because an optical filter was put in front of the CCD.

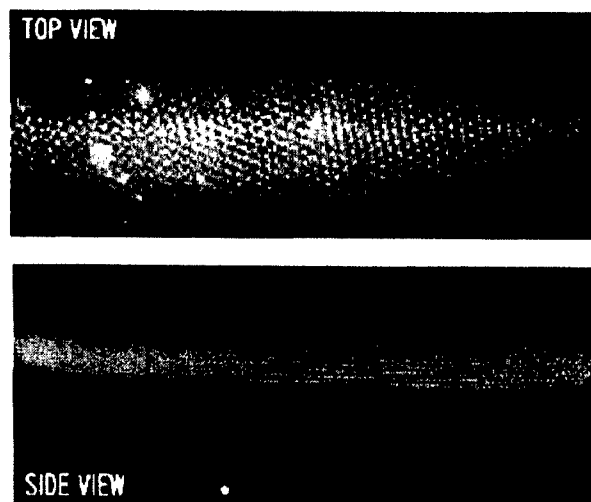


FIGURE 3. Top and side views of particle arrangement. Particle arrangements in the top view show those in the lowest few layers in the side view, and particle arrangements in the side view show those in the few vertical layers shown in the top view.

Figure 3 shows a top and a side views. Particle arrangements in the top view show those in the lowest few layers in the side view, and particle arrangements in the side view show those in the few vertical layers shown in the top view.

In fig.4, the time evolutions of the top and bottom positions of fine particle group are shown. As the bottom position almost did not change, the height of laser light needed not to be arranged during the observation.

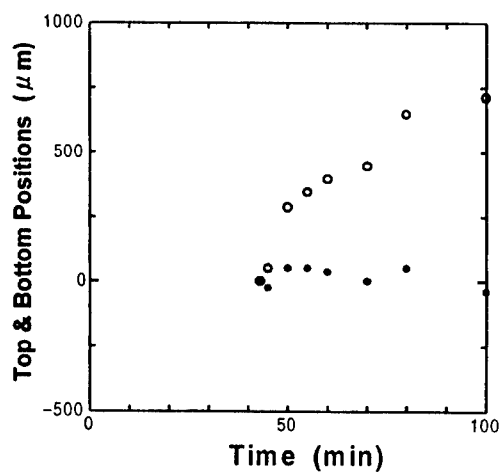


FIGURE 4. Time evolutions of top (open circles) and bottom (closed circles) positions of fine particle group.

Three-dimensional Coulomb crystals were formed by the control of the particle size around $2\text{ }\mu\text{m}$ in this experiment. A typical top-view image showing 3D Coulomb crystals is shown in Fig.5 [12]. In the image, regular triangle structures are observed in the middle and a square is found in the upper region. Since brighter spots indicate the fine particles in a lower layer, overlapping states of the lowest three layers can be known, i. e., fcc-like, hcp(hexagonal close-packed)-like and bcc(body-centered cubic)-like structures are seen in the right-middle, left-middle and upper regions, respectively. The distance between two horizontal layers were determined from the side-view image taken at the same time for the top-view. The ratio of the distance between the lowest two horizontal layers to the length of the triangle side was $0.82 : 1$ for the fcc-like structure. In comparison, the ratio for fcc is $\sqrt{2/3} : 1 = 0.816 : 1$. Furthermore, the ratio of the longer side length of the rectangle, to the shorter side length, to the distance between the lowest layer and the third lowest layer was $1.50 : 1 : 1.49$ for the bcc-like structure. Again in comparison, the ration for bcc is $\sqrt{2} : 1 : \sqrt{2} = 1.411 : 1 : 1.411$. Since the error of the values is less than 5 %, the former structure can be regarded as fcc with (111) planes parallel to an electrode and the latter regarded as bct (body-centered tetragonal) with (110) planes parallel to it. The hcp-like structure can be also regarded as hcp because the ratio of the distance between the lowest two horizontal layers to the length of a triangle side is equal to that of fcc.

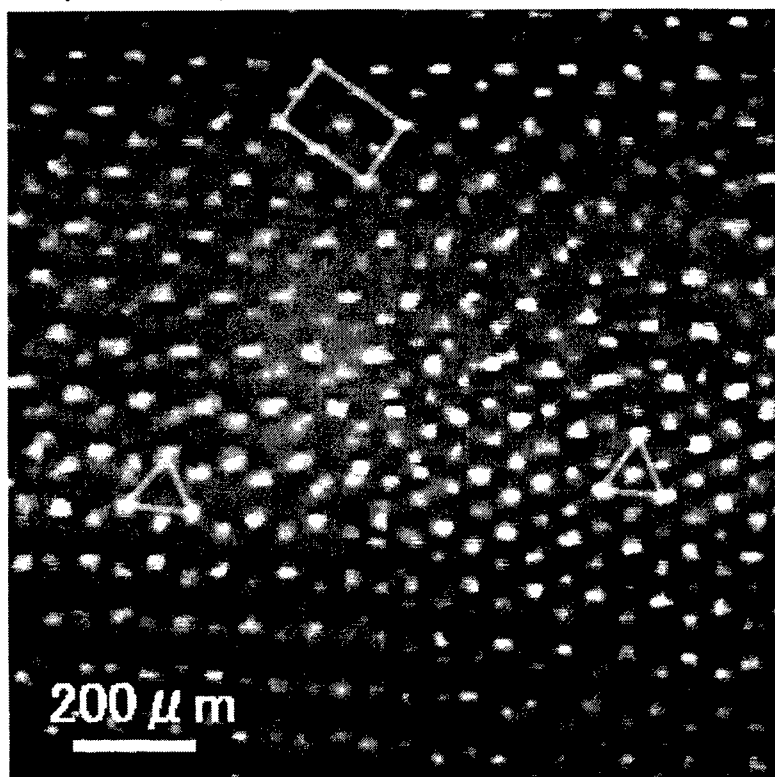


FIGURE 5. Top view of 3D Coulomb crystals.

STRUCTURAL TRANSITION BETWEEN TWO 3D COULOMB CRYSTALS

Structural transitions between bcc-like and fcc-like Coulomb crystals were distinguishably observed several times in the top view video images for 20 min. Figure 6 shows the top and the side views of the particle arrangements in the process of transition from bcc-like to fcc-like structure [12]. In the side views, it is recognized that the slip of the crystal planes occurred during the transition. Corresponding to the change of the side views, the gradual separation of the pairs of particles, which are in the lowest layer and the third lowest layer, is observed in the top views. Fine particles forming a bcc-like structure, which is equivalent to a fcc structure, pile up in alternate horizontal layers in the top view. Hence, the separation is observed alternately in the two directions of crystal axes.

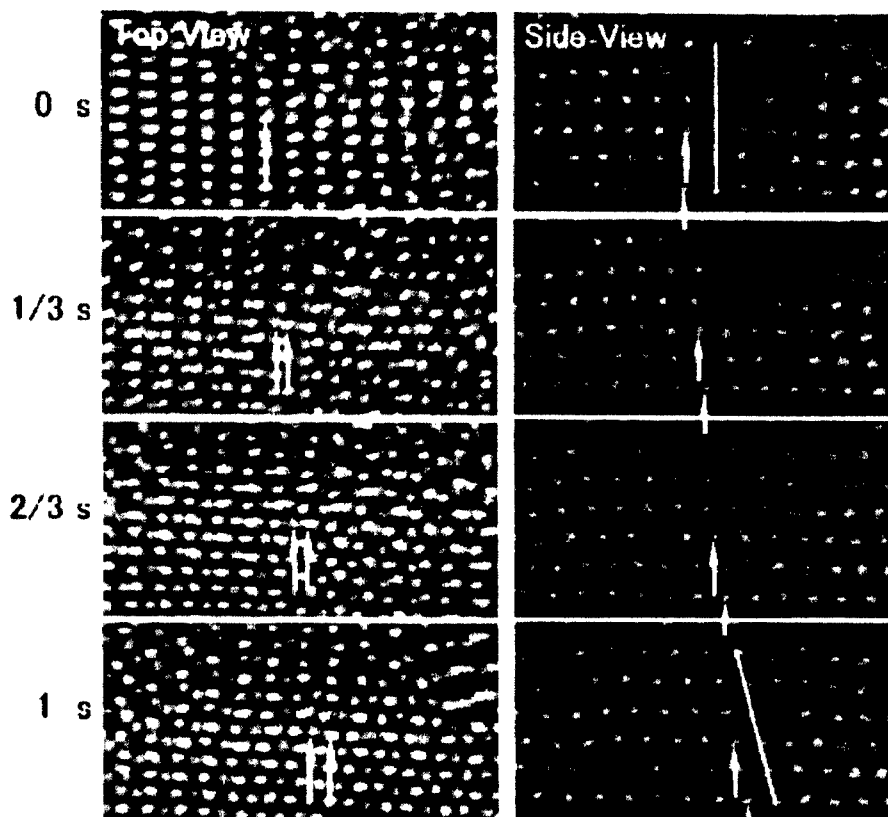


FIGURE 6. Top and side views of particle arrangements in process of transition from bcc-like to fcc-like structure in one second.

An explanatory drawing of the transition is shown in Fig.7. The direction of the slip is a $fcc[100]$ direction, which is equivalent to a $bcc[110]$ or $bct[110]$ direction for a special relation among the lattice satisfied.

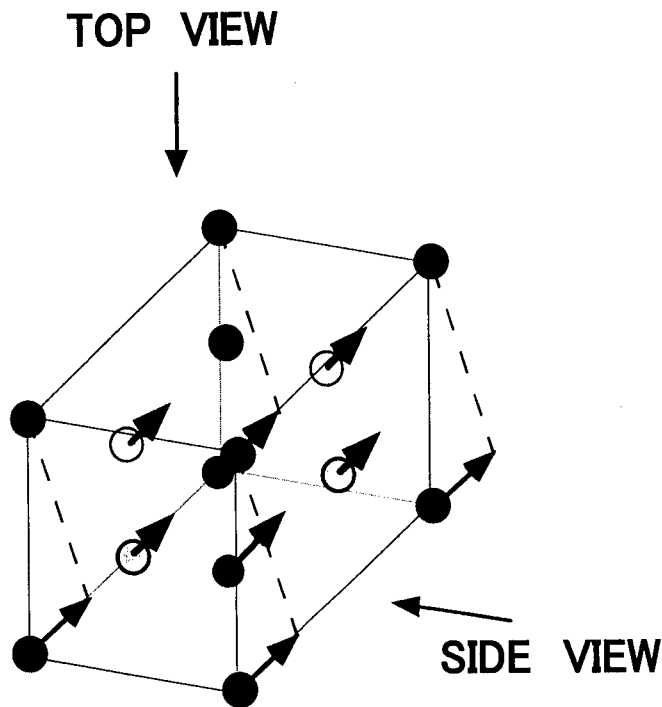


FIGURE 7. Explanatory drawing of transition between two 3D Coulomb crystals.

Figure 8 shows the change of particle arrangements of 49 particles in the lowest two layers in one second, corresponding to 0 sec and 1 sec images in the top views in Fig.6. It is seen in the figure at 1 s that each particle in the second lowest layer is at the center of three particles forming a regular triangle in the lowest layer as is seen in Fig.5. Similarly, the structural change of Coulomb crystals between bct and fcc can be explained by the slip of crystal planes, $bct(110)$ and $fcc(111)$. The direction of slip is $bct[110]$ and $fcc[211]$. This process of the transition between the two crystal structures and the relations of the crystal planes and the axes agree with the martensitic transformation of Nishiyama's scheme [17], which is observed when iron changes the structures between the austenite (fcc) and the martensite (bct or bcc) phases in the processes of hardening and tempering.

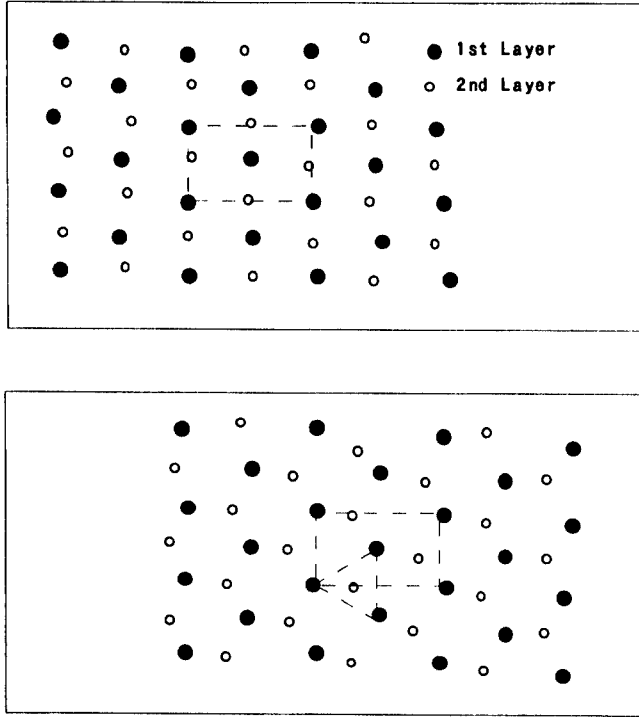


FIGURE 8. Change of particle arrangements of 49 particles in the lowest two layers in one second, corresponding to 0 s and 1 s images in the top views in Fig.6.

In order to understand the structural transition from Coulomb energy distribution, two non-dimensional parameters are defined. One is the ratio of one lattice constant to another in the plane of a slip, b/a , and the other is the ratio of slip distance to a lattice constant, $h/(b/2)$, as indicated in the upper figure of Fig.9. In the lower figure, Coulomb energy distribution per particle in units of $Q^2 / (4 \pi \epsilon_0 r_a)$, where Q and r_a are the charge of fine particles and the Wigner-Seitz radius, respectively, is shown as functions of b/a and $h/(b/2)$ for $r_a/r_D=3$, where r_D is the Debye-length. Since the energy is calculated using the inter-layer distance between horizontal planes being constant for the value of fcc, the point of minimum energy is seen at fcc but not at bcc in the figure.

The coordinates of each particle position indicated in Fig.8 were determined with the use of the Scion Image [18]. And the average values of the two non-dimensional parameters were calculated to be $b/a=1.664$ and $h/(b/2)=0.115$ at 0 sec and $b/a=1.709$ and $h/(b/2)=0.308$ at 1 sec. It is shown by the comparison of the result with Fig.9 that the change of particle arrangement is on the way to a fcc structure from a bct structure. The stability of the fcc structure was supported by the further analytical result of the transition: the value of $h/(b/2)$ did not exceed 0.34 [19].

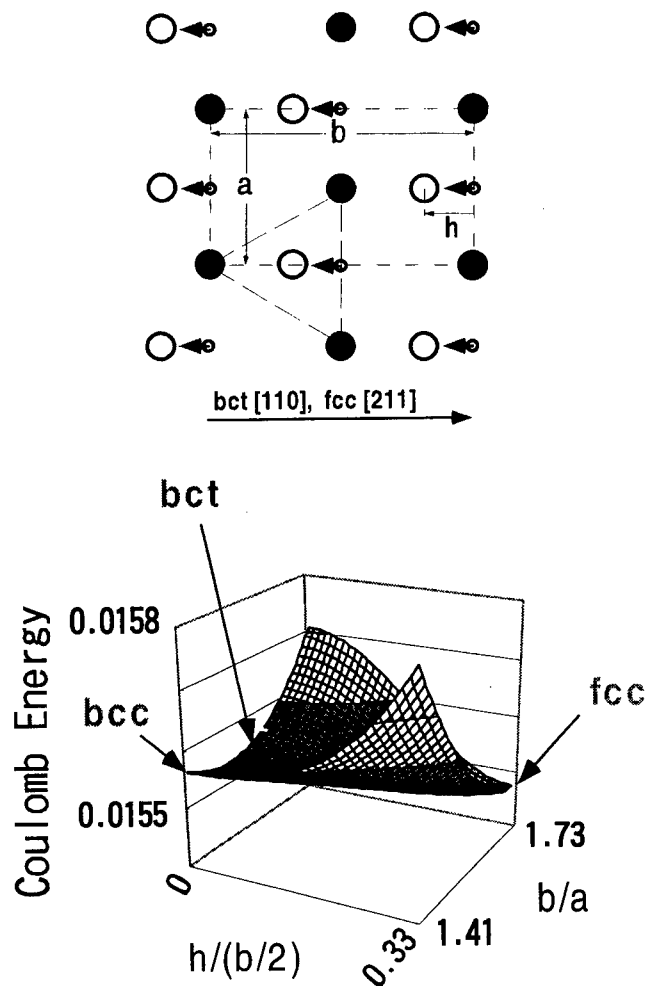


FIGURE 9. Coulomb energy distribution per particle in units of $Q^2 / (4 \pi \epsilon_0 r_s)$, where Q and r_s are the charge of fine particles and the Wigner-Seitz radius, respectively.

CONCLUSION

3D Coulomb crystals were formed in dusty plasmas using smaller fine particles growing in a methane/argon plasma. The structures were confirmed to be bct, fcc and hcp. The process of the structural transition from bct to fcc was analyzed and it was found that the transition occurred by the slip of crystal planes of bct(110), which are parallel to the fcc(111) planes. The direction of the slip was bct[110] and fcc[211]. This process of transition between the two crystal structures and the relations in crystal planes and axes agree with the martensitic transformation of Nishiyama's scheme. In conclusion, dusty plasma Coulomb crystals can be good models for real atomic crystals.

REFERENCES

1. Ikezi, H., *Phys. Fluids*, **29**, 1764-1766 (1986).
2. Hayashi, Y., and Tachibana, K., *Japan. J. Appl. Phys.* **33**, L804-L806 (1994).
3. Chu, J. H., and Lin, I., *Phys. Rev. Lett.* **72**, 4009-4012 (1994).
4. Thomas, H., Morfill, G. E., Demmel, V., Goree, J., Feuerbacher, B., and Mohlmann, D., *Phys. Rev. Lett.* **73**, 652-655 (1994).
5. Melandso, F., and Goree, J., *Phys. Rev. E*, **52**, 5312-5326 (1995).
6. Melzer, A., Schweigert, V. A., Schweigert, I. V., Homann, A., Peteres., S., and Piel, A., *Phys. Rev. E*, **54**, R46-R49 (1996).
7. Takahashi, K., Ohishi, T., Shimomai, K., Hayashi, Y., and Nishino, S., *Phys. Rev. E*, **58**, 7805-7811 (1998).
8. Hayashi, Y., and Tachibana, K., *J. Vac. Sci. Technol. A*, **14**, 506-510 (1996).
9. Hayashi, Y., Takahashi, K., and Tachibana, K., *Advanced in Dusty Plasmas*, Singapore: World Scientific, 1997, pp.153-162.
10. Hayashi, Y., and Takahashi, K., *Japan. J. Appl. Phys.* **36**, 4976-4979 (1997).
11. Hayashi, Y., *Phys. Rev. Lett.* **83**, 4764-4767 (1999).
12. Hayashi, Y., *Phys. Scripta*, **T89**, 112-116 (2001).
13. Hayashi, Y., and Tachibana, K., *Japan. J. Appl. Phys.* **33**, L476-L478 (1994).
14. Hayashi, Y., and Tachibana, K., *Japan. J. Appl. Phys.* **33**, 4208-4211 (1994).
15. Yoshida, T., Okuyama, K., Kousaka, Y., and Kida, Y., *J. Chem. Eng. Japan*, **8**, 317-322 (1975).
16. Hayashi, Y., and Tachibana, K., *Oyo Buturi* [in Japanese], **64**, 565-569 (1995).
17. Nishiyama, Z., *Sci. Rep. Tohoku Univ.* **23**, 637- (1934).
18. <http://www.scioncorp.com>
19. Hayashi, Y., in preparation for publication.

Dusty Plasmas under Microgravity

Hiroo Totsuji, Chieko Totsuji, Tokunari Kishimoto and Kenji Tsuruta

*Graduate School of Natural Science and Technology and Faculty of Engineering,
Okayama University, Tsushimaoka 3-1-1, Okayama 700-8530, Japan*

Abstract. The structures of Yukawa systems spherically confined under the condition of microgravity are analyzed by molecular dynamics simulations. It is shown that the system is separated into the outer and the inner parts and well-developed shells appear in the outer part at low temperatures. In the case of Yukawa mixtures, there occurs the separation of species according to the magnitude of charges.

INTRODUCTION

Dusty plasmas have provided us with an important example of nonneutral plasmas. One of main differences from other nonneutral plasmas composed of ions or electrons is that dust particles have large masses and the effect of gravity plays a key role in determining their behavior.

Recently, some experiments under the condition of the microgravity have been performed [1]. In this case, the gravity can be mostly neglected and we may observe various new aspects of dusty plasmas which have been hidden by the effect of gravity in experiments on earth. We may also expect the investigation of dusty plasmas under microgravity might lead to some new method to synthesize and process useful materials. The purpose of this paper is to extend our theoretical and numerical analyses on the structures of dusty plasmas under the gravity[2][3] and analyze dusty plasmas under microgravity.

We assume that the particles interact via the isotropic repulsive Yukawa potential

$$\frac{q^2}{r} \exp(-\kappa r), \quad (1)$$

where q is the charge and $1/\kappa$ is the screening length. It is known that the ion flow in the sheath or other effects may induce anisotropy into the interaction. Here we show interesting features of the system without those effects, expecting that they remain so when the anisotropy is taken into account as a perturbation.

In the case of uniform one-component Yukawa system, we have two parameters, the density n and the temperature T , which we characterize by two dimensionless parameters

$$\Gamma = \frac{q^2}{k_B T a} \quad \text{and} \quad \xi = \kappa a, \quad (2)$$

where a is the mean distance defined by $a = (3/4\pi n)^{1/3}$.

In the case of mixtures with species $i = 1, 2, \dots$, we have the densities n_i , the charges q_i , the masses m_i , and the total number density n_{tot} as parameters: $n_{tot} = \sum_i n_i$. We here consider the case of binary mixtures and denote the species by $i = 1, 2$. We define the parameter Γ_1 (denoted as Γ in figures) by

$$\Gamma_1 = \frac{q_1^2}{k_B T a}, \quad (3)$$

where the mean distance a is defined for the total density n_{tot} as $a = (3/4\pi n_{tot})^{1/3}$. In thermal equilibrium, static properties are characterized by the following four parameters

$$\Gamma_1, \quad \xi, \quad \frac{q_2}{q_1}, \quad \frac{n_2}{n_1}. \quad (4)$$

EXTERNAL CONFINING POTENTIAL

We consider Yukawa systems in the environment of very small gravity and assume that Yukawa particles are spherically confined by an external potential. As the source of the external potential, we assume that the sheath with the uniform space charge

$$en_{sh} \quad (r > r_0) \quad (5)$$

surrounds the domain of electrically neutral plasma of radius r_0 . We denote the electrostatic potential due to the charges in the sheath by $\phi_{ext}(r)$. The external potential for Yukawa particles with the charge $-q$ is given by $-q\phi$ or

$$-q\phi_{ext}(r) = 0 \quad (r < r_0) \quad (6)$$

and

$$-q\phi_{ext}(r) = \frac{q(4\pi en_{sh}r_0^3)/3}{r_0} \left[\frac{1}{2} \left(\frac{r}{r_0} \right)^2 + \frac{r_0}{r} - \frac{3}{2} \right] \quad (r > r_0). \quad (7)$$

NUMERICAL METHOD

In order to have as many particles as possible in the system, we here adopt the molecular dynamics with the $O(N)$ scaling [5, 6]. The typical system size in our simulations is $N = 10^4$. The temperature is controlled by the Nosé-Hoover method. For mixtures, we assume the same mass for all species. In the classical case, the static properties do not depend on particles masses, though the relaxation time in general, especially for the energy, increases with the mass ratio. In this paper, we are interested in only static properties after relaxation.

RESULTS AND DISCUSSION

One-Component Yukawa System

Some examples of the results of simulations with 10^4 particles are shown in Figs. 1, 2, and 3, where the radial distributions and the position of shells are shown. The results are summarized as follows. (1) The system is separated into the outer and the inner parts. (2) In the outer part, a thin shell is formed at the surface of the system. The distribution of particles on this shell is a two-dimensional lattice with defects. Inside of the outermost shell, there appears a series of shells as in the case of one-component plasma confined by parabolic potential. The average density is higher than the inner part. (3) The shells become higher and sharper with the decrease of the temperature for fixed values of ξ . At fixed temperature, they become higher and sharper with the decrease of ξ or the increase of the coefficient of confining potential. (4) In the inner part, the average density is low and the shell structure is not clear.

Yukawa Mixtures

The results for the mixture of Yukawa particles where the total number is 10^4 and $n_2/n_1 = 1$, $q_2/q_1 = 10$, and $q_2/q_1 = 5$ are shown in Figs. 4, 5 and 6. One of the most remarkable phenomena may be the separation of particles with different values of charges. This tendency becomes strong with the increase of the screening length and the decrease of the temperature. As for the relative position of shells of each species, we are still trying to give simple interpretations.

Analysis of Structures at Low Temperatures in Fluid Limit

Here we present a theoretical analysis on the structure of one-component Yukawa particles at low temperatures based on the variational approach which is successful for the two-dimensional case [7]. In what follows we adopt the fluid approximation and express the density of particles by $\rho(\mathbf{r})$. The total number of particles N is related to $\rho(\mathbf{r})$ by

$$\int d\mathbf{r} \rho(\mathbf{r}) = N. \quad (8)$$

The interaction is expressed as

$$U_{int} = \frac{q^2}{2} \iint d\mathbf{r} d\mathbf{r}' \frac{\exp(-\kappa|\mathbf{r} - \mathbf{r}'|)}{|\mathbf{r} - \mathbf{r}'|} \rho(\mathbf{r}) \rho(\mathbf{r}') \quad (9)$$

and the external potential is given by

$$U_{ext} = (-q) \int d\mathbf{r} \phi_{ext}(\mathbf{r}) \rho(\mathbf{r}). \quad (10)$$

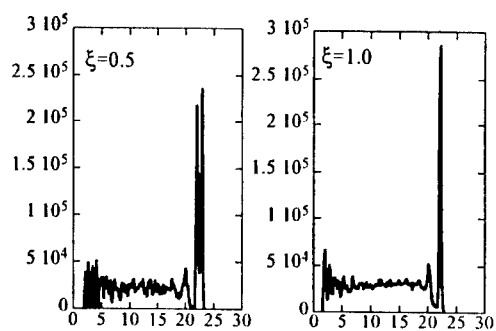


FIGURE 1. Distribution vs. radial distance measured in a in spherically confined Yukawa system under microgravity: Effect of screening length for $\Gamma = 50$.

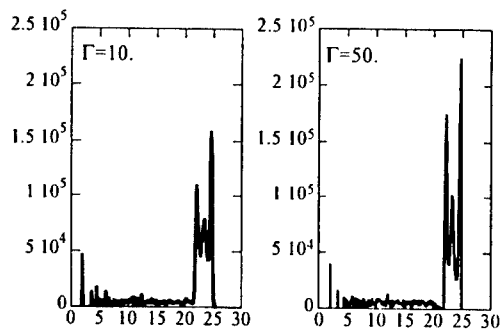


FIGURE 2. The same as Fig. 1: Effect of temperature for $\xi = 0.1$.

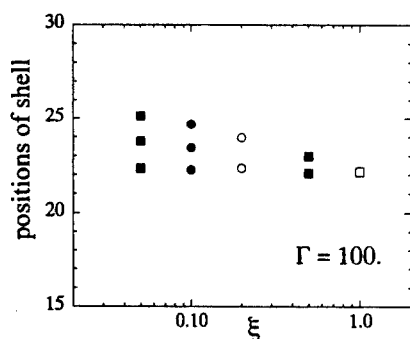


FIGURE 3. Position of shells measured in a vs. ξ .

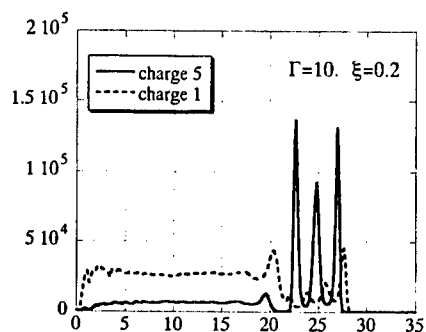


FIGURE 4. Distribution vs. radial distance measured in a in Yukawa mixture with charge ratio 5 ($\Gamma = \Gamma_1$).

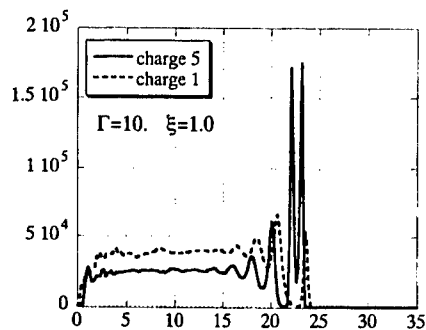


FIGURE 5. The same as Fig. 4 for $\xi = 1.0$.

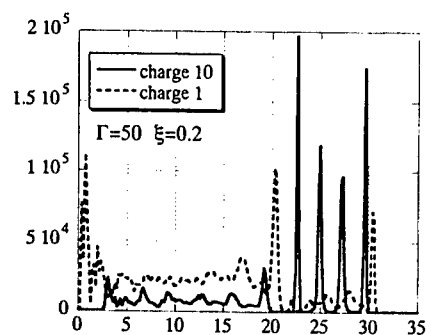


FIGURE 6. The same as Fig. 4 for charge ratio 10.

Let us find $\rho(\mathbf{r})$ which minimizes the value of $U_{int} + U_{ext}$ under the condition (8). The variation with respect to $\rho(\mathbf{r})$ leads to

$$\int d\mathbf{r} \left[(-q)\phi_{ext}(\mathbf{r}) + q^2 \int d\mathbf{r}' \rho(\mathbf{r}') \frac{\exp(-\kappa|\mathbf{r} - \mathbf{r}'|)}{|\mathbf{r} - \mathbf{r}'|} \right] \delta\rho(\mathbf{r}) = 0 \quad (11)$$

and

$$\int d\mathbf{r} \delta\rho(\mathbf{r}) = 0. \quad (12)$$

Denoting the Lagrange's multiplier by μ , we have

$$(-q)\phi_{ext}(\mathbf{r}) + q^2 \int d\mathbf{r}' \rho(\mathbf{r}') \frac{\exp(-\kappa|\mathbf{r} - \mathbf{r}'|)}{|\mathbf{r} - \mathbf{r}'|} = \mu \quad (13)$$

and the value of μ is determined by (8).

When we denote the source charge density of the external potential by $e\rho_{ext}(r)$ as

$$\Delta\phi_{ext}(\mathbf{r}) = -4\pi e\rho_{ext}(\mathbf{r}), \quad (14)$$

we have from (13)

$$\rho(\mathbf{r}) = \frac{\kappa^2}{4\pi q} \phi_{ext}(\mathbf{r}) + \frac{e}{q} \rho_{ext}(\mathbf{r}) + \frac{\kappa^2}{4\pi q^2} \mu. \quad (15)$$

When the external charge density is given by (5), we have

$$\rho(r) = \frac{\kappa^2}{4\pi q^2} \mu \quad (r < r_0) \quad (16)$$

and

$$\rho(r) = \frac{\kappa^2}{4\pi q^2} \mu + \frac{e}{q} n_{sh} \left(1 - \frac{1}{3} (\kappa r_0)^2 \left[\frac{1}{2} \left(\frac{r}{r_0} \right)^2 + \frac{r_0}{r} - \frac{3}{2} \right] \right) \quad (r > r_0). \quad (17)$$

We observe that the density is low in the central part $r < r_0$ and increases stepwise by $(e/q)n_{sh}$ at $r = r_0$, separating the inner and outer parts of the system. This tendency is in agreement with the behavior of the results of simulation when the layering structure in the outer part is averaged: The latter seems to appear when the effect of discreteness or the correlation is taken into account.

When we denote the maximum radius of distribution by r_m , the condition (8) gives

$$\begin{aligned} \frac{N}{(4\pi r_0^3/3)} &= \frac{e}{q} n_{sh} \left[\left(\frac{r_m}{r_0} \right)^3 - 1 \right] \\ &- \frac{e}{q} n_{sh} (\kappa r_0)^2 \left[\frac{1}{10} \left(\frac{r_m}{r_0} \right)^5 - \frac{1}{2} \left(\frac{r_m}{r_0} \right)^3 + \frac{1}{2} \left(\frac{r_m}{r_0} \right)^2 - \frac{1}{10} \right] + \frac{\kappa^2}{4\pi q^2} \left(\frac{r_m}{r_0} \right)^3 \mu. \end{aligned} \quad (18)$$

This relation and the condition $\rho(r_m) = 0$ determine the parameters μ and r_m .

Discussion

The average distribution may be understood within the consideration in the fluid limit and, since the repulsion between particles increases with the charge, we may naturally have the separation of charges in the case of mixtures. The formation of structures beyond the average distribution is related to the correlation between particles [2, 3].

It has been shown that particles distributed in the inner part may serve as the source of the force in the radial direction which plays the role of the gravity in the formation of layered structures [4]. The shells on the periphery in the one-component case thus correspond to the one-dimensional layers under the gravity. The structures in the case of mixtures seem to need more elaborate analysis.

CONCLUSIONS

In this paper, we have analyzed the behavior of particles interacting via the repulsive isotropic Yukawa potential when the effect of gravity is neglected. In the confined Yukawa system of one species, the layered (shell) structure is formed from outer boundary of the system. This structure becomes clear and sharp with the decrease of the temperature or the increase of the screening length. Within each layer, particles are organized into two-dimensional lattice with defects.

When we have two kinds of Yukawa particles in our confined system, we have a separation according to the relative magnitude of charges: The species with larger charge tends to distribute on the periphery. There is also the tendency to form layered structures. Both becomes significant when the temperature is low and the screening length is large.

ACKNOWLEDGMENTS

This work has been partly supported by the Grants-in-Aid for Scientific Researches from the Ministry of Education, Culture, Sports, Science, and Technology of Japan Nos. 08458109 and 11480110.

REFERENCES

1. For example, G. E. Morfill *et al.*, Phys. Rev. Lett. **83**, 1598(1999).
2. H. Totsuji, T. Kishimoto, and C. Totsuji, Phys. Rev. Lett. **78**, 3113(1997).
3. H. Totsuji, T. Kishimoto, C. Totsuji, and T. Sasabe, Phys. Rev. E **58**, 7831(1998).
4. H. Totsuji, T. Kishimoto, C. Totsuji, and K. Tsuruta, Physica Scripta **T89**, 117(2001).
5. For example, S. Pfalzner and P. Gibbon, *Many-Body Tree Method in Physics*, Cambridge University Press, Cambridge, 1996;
6. L. Greengard and V. Rokhlin, J. Comp. Phys., **73**, 325(1987).
7. H. Totsuji, C. Totsuji, and K. Tsuruta, to appear in Phys. Rev. E.

SECTION 3

CHARGED PARTICLE BEAMS AND FREE-ELECTRON LASERS

Kinetic Effects in High Gain Free-Electron Lasers

B. Hafizi^{a,1} and C.W. Roberson^b

^a Plasma Physics Division, Naval Research Laboratory, Washington, DC 20375

^b Physical Sciences Division, Office of Naval Research, Arlington, VA 22217

Abstract. A formalism based on the Vlasov-Maxwell system has been developed that provides a fully kinetic description of a free-electron laser (FEL) operating in the high gain regime. The analysis allows for guiding of the optical beam through the gain process and guiding of the electron beam by the weak focusing provided by realistic wiggler gradients. Thus, betatron oscillations and emittance are naturally included. Additionally, intrinsic energy spread as well as energy spread due to space charge effects is included. The analysis predicts a novel electron beam equilibrium flow in which the effect of wiggler gradients tends to cancel that due to space charge, leading to a flow with reduced axial velocity spread. Since the FEL mechanism is sensitive to the axial velocity spread on the beam, this special flow appears to be useful in enhancing FEL gain. This and other issues related to FEL operation are discussed in this paper. It is shown that the scaled thermal velocity $S = v_{th} / (v_b - v_{ph})$ is a useful measure of beam quality in the context of FELs. Here, v_{th} is the thermal velocity on the beam, v_b is the beam velocity and v_{ph} is the phase velocity of the ponderomotive wave. The scaled thermal velocity depends on beam emittance, energy spread and electron density and is a useful indicator of beam quality since it provides a measure of the thermal spread as observed in the phase velocity frame. Analogies between the high gain FEL and plasma two-stream instability are discussed.

INTRODUCTION

After the first experiments in the late seventies demonstrating lasing in the infrared the free-electron laser (FEL) became the alternate concept to all coherent radiation sources from microwaves to X-rays [1]. This was motivated by the FEL's tunability, wavelength accessibility and potential for high power operation. After 20 years, the focus of FEL research for scientific applications has shifted to UV and X-ray wavelengths where coherent sources are rare or nonexistent. The accelerator and beam quality requirements are similar to a linear collider. The lack of mirrors in the hard X-ray regime has focused the effort to single pass high gain FEL operation. Figure 1 is a sketch of such an FEL. The lower panel in Fig. 1 shows the exponential gain and nonlinear saturation of this collective instability by trapping of the beam

¹ Icarus Research, Inc., PO Box 30780, Bethesda, MD 20824-0780

particles in the potential wells of the space charge waves. Similar exponential growth and nonlinear trapping of the beam particles has been observed in a two-stream instability [2]. The form of the dispersion relation for the high gain FEL and the two-stream instability is similar. The two-stream instability in the cold beam limit is a hydrodynamic, or fluid, instability. The exponential growth is due to coupling of positive and negative energy modes on the beam by the plasma. In the kinetic, or warm

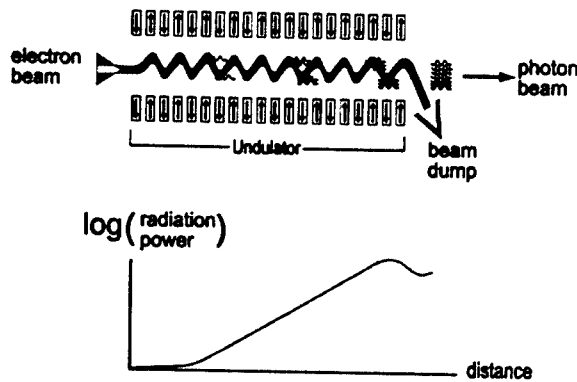


FIGURE 1. Upper panel: FEL amplifier configuration. Lower panel: Growth of radiation in SASE regime. (tesla.desy.de)

beam limit, the real part of the plasma dispersion relation remains unchanged by the beam, and the growth is by inverse Landau damping. O'Neil and Malmberg [3] have examined this change in topology of the dispersion from the fluid to the kinetic limit. They found that when the scaled thermal velocity $S = (v_{th} / v_b)(2n_0 / n_b)^{1/3}$ is small compared to unity the instability is in the fluid limit. When S is approximately equal to or greater than unity, the instability is in the kinetic limit. Here, v_{th} is the thermal velocity on the beam, v_b is the beam velocity, n_0 is the plasma and n_b is the beam density. More generally this can be written as $S \equiv v_{th} / (v_b - v_{ph})$, which we adopt as the FEL beam quality [4]. The specifics of FEL physics are contained in v_{ph} , the phase velocity of the ponderomotive wave. For the two-stream instability these two definitions of S are equivalent. In addition to the usual contributions to the effective thermal velocity from the beam emittance and energy spread, this includes the FEL physics through v_{ph} . Conceptually S may be viewed as a measure of how the thermal spread on the beam as viewed from the ponderomotive/space charge wave frame of reference.

KINETIC ANALYSIS

The electron beam couples with the beat wave arising from the radiation field and the wiggler field. The beat wave is also referred to as the ponderomotive wave.

The radiation field can be due to either small amplitude injected beam ('seed') radiation or spontaneous emission. The absence of a source at X-ray wavelengths, for example, means that FEL amplifiers in this regime run in the self amplified spontaneous emission (SASE) mode; Fig. 1. In SASE the growth of the radiation at first is essentially linear (the 'lethargy' regime) as a rough phase relationship is established with the electrons. Then the growth becomes exponential and is accompanied by strong modulation of the electron beam on the optical scale. Growth in the exponential regime leads to extraction of energy from the electron beam, which is slowed down and eventually trapped in the ponderomotive buckets. In complete analogy with two-stream instability, in the saturated regime trapped particle oscillations lead to characteristic oscillations in the optical field intensity.

The resonance condition in the FEL interaction is expressible as

$$\omega - (k + k_w)v_z = 0, \quad (1)$$

where v_z is the axial electron velocity, ω and k are the frequency and wavenumber of the radiation field, $k_w = 2\pi/\lambda_w$ is the wiggler wavenumber and λ_w is the wiggler period. It follows from Eq. (1) that the beat (ponderomotive) wave phase velocity is

$$\beta_{ph} \equiv \frac{v_{ph}}{c} = \frac{\omega}{k + k_w}. \quad (2)$$

Two regimes of electron beam interaction with the beat wave can be distinguished, as indicated in Fig. 2. The sketches in the top row correspond to

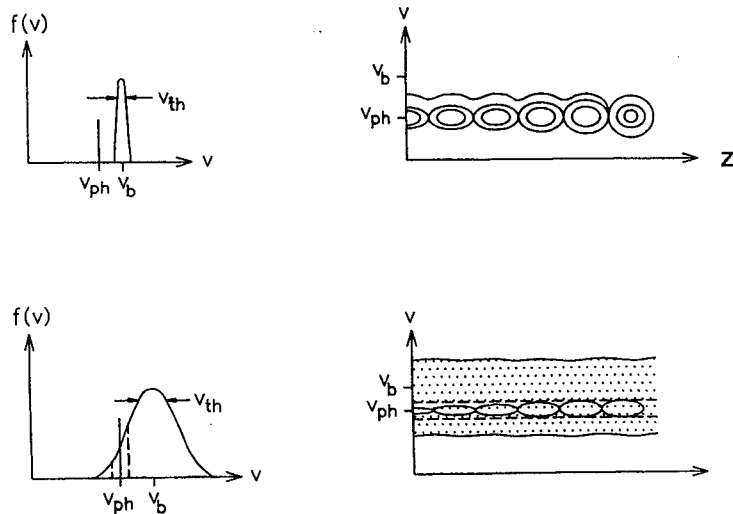


FIGURE 2. Velocity distribution function & longitudinal phase space. Upper panel: Cold beam regime. Lower panel: Warm beam regime.

interaction in the cold beam regime wherein the phase velocity lies outside of the electron distribution function. In phase space the electrons interact with and lose energy as the ponderomotive buckets grow with propagation distance, eventually becoming trapped in the buckets. In contrast, in the warm beam regime, the lower pair of plots in Fig. 2, only a fraction of the electrons participate in the interaction. Clearly, for high efficiency operation the cold beam regime is preferable as it permits a larger extraction from the electron beam.

Kinetic analysis of the FEL is based on the Vlasov-Maxwell system of equations. The equilibrium is constructed from the constants of motion and the perturbed distribution function is obtained by integration over unperturbed orbits [4]. Fundamentally, the electron equilibrium orbits consist of two oscillatory contributions. The fine scale motion is the wiggler motion, while betatron oscillations take place over a much longer scale, as shown in Fig. 3. The wiggler motion is due to the alternating polarity of the magnets comprising the wiggler and can be averaged over. Betatron oscillations arise since in a realizable wiggler the magnetic field is larger near the pole faces. An electron that approaches the pole face experiences an increasing field that deflects it back towards the axis. The initial transverse phase space of the electron beam (i.e., emittance) determines the range of betatron orbits in the wiggler. Writing the axial electron velocity (normalized to c) as

$$\beta_z = \beta_{z0} + \delta\beta_z, \quad (3a)$$

where

$$\beta_{z0} = 1 - \frac{1 + a_w^2/2}{2\gamma_0^2} \quad (3b)$$

is common to all electrons, the deviation in the axial velocity is expressible as

$$\delta\beta_z = \frac{1 + a_w^2/2}{\gamma_0^2} \frac{\delta\gamma}{\gamma_0} - \frac{1}{2} k_{\beta 0}^2 y_\beta^2 + \frac{k_{p0}^2}{2\beta_{z0}\gamma_{z0}\gamma_0^{1/2}} y_\beta^2. \quad (3c)$$

Here, $k_{p0} = (4\pi n_0 |e|^2 / mc^2)^{1/2}$ and $k_{\beta 0} = a_w k_w / 2^{1/2} \gamma_0 \beta_{z0}$ are the plasma and betatron wavenumbers, respectively, n_0 is the density, y_β is the betatron oscillation amplitude and $a_w = |e| A_w / mc^2$ is the normalized wiggler amplitude, with A_w defined below. [4]. The first term in Eq. (3c) is due to intrinsic energy spread on the beam from the accelerator. The second term is due to betatron oscillations and the last term arises from space charge effects.

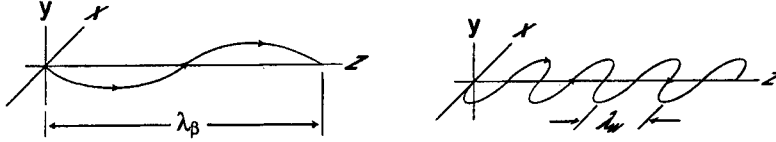


FIGURE 3. Left: Betatron oscillations in vertical plane. Right: Wiggle motion in horizontal plane.

A physical process that affects FEL operation significantly is related to diffraction of the radiation beam. A 2- or 3-D theory is necessary to take account of diffraction. Typically a laser beam is brighter in the center than at the edges and tends to spread in the transverse direction. Electron beams also have a similar profile and tend to spread laterally due to emittance. The combined effect of these is that the growth rate of the instability is higher in the central portion. This leads to the phenomenon of gain guiding—leading to the impression that the laser beam is guided, whereas in fact the diffractive loss is constantly compensated by higher growth near the center of the beam.

The wiggler vector potential is given by,

$$\mathbf{A}_w = A_w \cosh(k_w y) \sin(k_w z) \mathbf{e}_x$$

while the vector potential of the radiation field has the form

$$\mathbf{A}_s = \frac{1}{2} A_s(y, z) \exp[i(kz - \omega t)] \mathbf{e}_x + c.c.$$

The equilibrium electron beam distribution function is constructed from the constants of motion and has the form,

$$F(E, P_x, J) = \frac{I_b / (\beta_{z0} I_0)}{2\pi m c r_e \varepsilon_N} \frac{\exp[-(E - E_0)^2 / (\sigma_y m c^2)^2]}{\sqrt{\pi} \sigma_y m c^2} \\ \times \delta(P_x) \exp(-k_{\beta 0} J / m c \varepsilon_N k_\beta)$$

where $J = \iint dy dp_y / 2\pi$ is the area of transverse phase space, ε_N is the normalized emittance and σ_y is the energy spread.

EXAMPLES

To illustrate the effects of beam quality on FEL operation and, in particular, the utility of the scaled thermal velocity in identifying the regime of operation, three examples will be discussed in the following.

In the first example, the scaled growth rate $\text{Im } \mu/D$ and S are plotted as a function of scaled emittance $k_s \epsilon$ in Fig. 4. Observe that the growth rate decreases with emittance, as expected. Over the same range of emittance, S starts out from very small values and passes through unity for $k_s \epsilon \approx 1/3$ and then increases rapidly thereafter indicating transition into the warm beam regime.

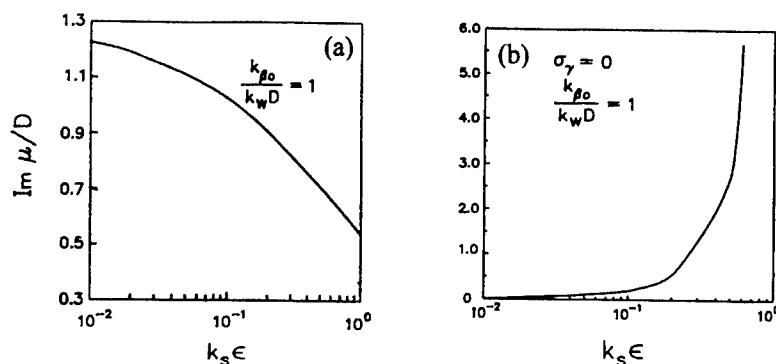


FIGURE 4. (a): Scaled growth rate versus scaled emittance. (b): Scaled thermal velocity versus scaled emittance.

The next example is useful since it can be related to a problem of current interest. Namely, the growth rate of FELs in the X-ray regime can be very small if GeV class electron beams are utilized. Physically this is due to the fact that at high energies electrons are very stiff with very small quiver motion. To compensate for this the electron beam current can be increased to enhance the growth rate. There are several techniques for increasing electron beam current, using RF beams, chicanes, etc. to rotate electron bunches in longitudinal phase space, as indicated in Fig. 5.

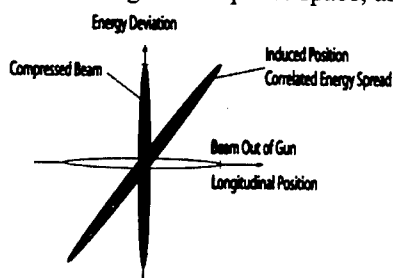


FIGURE 5. Bunch rotation & compression in longitudinal phase space.

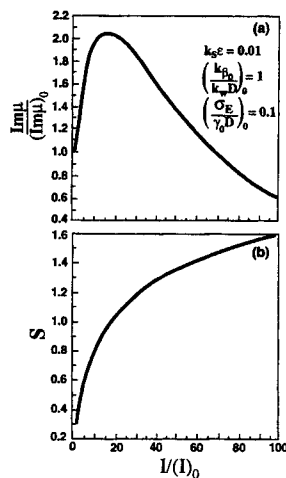


FIGURE 6. (a) Growth rate ratio & (b) scaled thermal velocity versus compression ratio

By rotating the electron bunch the length of the bunch is reduced and thus the current goes up. But by Liouville's theorem the axial momentum spread has to increase. Since the latter tends to spoil the FEL resonance it is not *a priori* obvious if longitudinal beam compression is useful. To study this Fig. 6 shows a plot of the growth rate of the compressed beam $\text{Im} \mu$ normalized to that for an uncompressed beam $(\text{Im} \mu)_0$ as a function of the compression ratio. The compression ratio is the same as the ratio of current in the compressed beam to that in the uncompressed beam $I/(I)_0$. Figure 6 shows that for relatively small compression the growth rate is in fact increased. Eventually, however, the increased spread in axial momentum dominates and the growth rate no longer increases. Not surprisingly, the optimal compression is seen to correspond to $S \approx 1$.

As a final example it is interesting to consider a compact (e.g. bench top) FEL. The lasing wavelength in an FEL is given by

$$\lambda = \frac{1 + a_w^2/2}{2\gamma_0^2} \lambda_w. \quad (4)$$

Planned X-ray free electron laser experiments at SLAC and DESY employ wigglers with cm-scale periods and GeV electron beams to generate radiation at X-ray wavelengths. As can be seen from Eq. (4) one may also obtain lasing in the X-ray regime by using μm -scale wiggler periods along with modest energy (10's of MeV) electron beams. Such fine-scale wigglers are readily available in the form of T³ lasers. The electromagnetic field of a laser beam can induce wiggler motion of electrons just as well as the magnetic field of a conventional wiggler. The only difference between a magnetostatic wiggler and an electromagnetic wiggler is that in the latter case the factor-of-2 in the denominator of Eq. (4) is to be replaced by 4. At

low voltages, however, space charge can become an issue. Fortunately there appears to be a solution to this that at first sight is rather surprising. It turns out that there can be an equilibrium flow of a finite-emittance electron beam in a wiggler wherein space charge forces, wiggler focusing and emittance are balanced. For this matched beam the spread in axial velocity due to wiggler gradients and space charge [the last two terms in Eq. (3c)] tend to cancel.



FIGURE 7. Electron beam transverse profile versus propagation distance. Electron gun is to the left. Upper panel: Betatron oscillation in absence of space charge. Lower panel: Nearly matched electron beam with self-field parameter = 0.85.

Figure 7 shows an example where space charge effects are included (lower panel) and excluded (upper panel). The self-field parameter is defined by $SFP = [(k_p / k_{\beta 0}) / (\gamma_{z0} \gamma_0^{1/2} \beta_{z0})]^2$. With no space charge the beam undergoes betatron oscillations. With an appropriate amount of charge in the bunch the beam is nearly matched and $\delta\beta_z$ is reduced [5], beam quality is improved and transition to the warm beam regime takes place for much larger emittance, as indicated in Fig. 8.

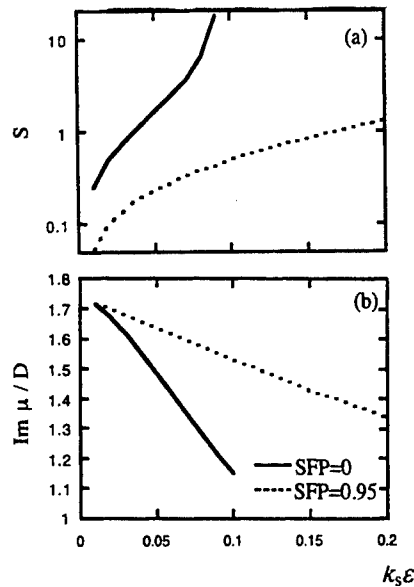


FIGURE 8. (a) Scaled thermal velocity & (b) growth rate versus scaled emittance. Dashed curves correspond to no space charge. Solid curves include space charge effects with SFP = 0.95.

In summary it is shown that the scaled thermal used in Ref. 3, when written in the more general form $S \equiv v_{th} / (v_b - v_{ph})$, makes an excellent definition of electron beam quality for FELs. For example, using this definition it is possible to determine if beam compression will increase or decrease the growth rate. When S is plotted as a function of emittance one can readily ascertain if the FEL is in the kinetic regime, with substantially reduced growth rate. Finally, it is shown that there is an unusual mode of operation when space charge effects are important and yet beam quality is improved.

REFERENCES

1. Roberson, C.W., and Sprangle, P., *A Review of Free Electron Lasers*, Phys. Fluids B **1**, 3-42 (1989).
2. Gentle, K.W., and Roberson, C.W., *Observations of Beam-Plasma Instability*, Phys. Fluids **14**, 2780-2782 (1971).
3. O'Neil, T.M., and Malmberg, J.H., *Transition of Dispersion Roots from Beam-Type to Landau-Type Solutions*, Phys. Fluids **11**, 1754-1760 (1968).
4. Hafizi, B., and Roberson, C.W., *Role of Beam Quality in Free-Electron Lasers*, Phys. Plasmas **3**, 2156-2162 (1996).
5. Gordon, D.F., *et al.*, these proceedings.

Self-Compensation for the Axial Velocity Spread in a Wiggler Field

D.F. Gordon*, B. Hafizi[†], C.W. Roberson** and P. Sprangle*

*Naval Research Laboratory, Washington, D.C. 20375, USA

[†]Icarus Research, Inc., P.O. Box 30780, Bethesda, Maryland 20824-0780, USA

**Physical Sciences Division, Office of Naval Research, Arlington, VA 22217, USA

Abstract. In order to obtain optimal performance from a free electron laser (FEL), the axial velocity spread on the electron beam must be small as it propagates through the wiggler field. Treated separately, both the wiggler-induced betatron motions and the self-induced space charge forces tend to increase the axial velocity spread and degrade the performance of the FEL. However, it has been shown analytically [B. Hafizi and C.W. Roberson, *Phys. Plasmas* **3**, 2156 (1996)] that when both effects are treated self-consistently an equilibrium exists wherein the space charge forces exactly compensate for the betatron motion. This leads to the surprising result that for a continuous beam, increasing the beam current can improve the beam quality.

INTRODUCTION

The quality of the electron beam used in a free electron laser (FEL) can be quantified in terms of the scaled thermal velocity, S , given by [1]

$$S = \frac{v_{th,z}}{v_b - v_{ph}}$$

where v_b is the average velocity of the beam, $v_{th,z}$ is the root-mean-square (rms) spread in the axial velocity, and v_{ph} is the phase velocity of the fastest growing ponderomotive wave. When the axial velocity spread is large enough so that $S \gg 1$, the FEL operates in a kinetic regime where the cold beam approximation is invalid. This generally results in a drastic reduction in the efficiency of the FEL since only a fraction of the electrons contribute to the growth of the radiation.

The axial velocity spread on the beam is initially determined by the beam emittance and energy spread. As the beam propagates, both the wiggler fields and the beam's own self-fields cause the axial velocity spread to evolve. When the beam current is low, the self-fields can be neglected, and the axial velocity spread only evolves because of the betatron oscillations caused by the wiggler field. This leads to an axial velocity spread in the form of a shear $\nabla_{\perp} v_z$. Here, v_z is the axial velocity of the electron fluid and ∇_{\perp} is the transverse gradient. When the self-fields are included, they oppose the betatron oscillations and reduce the shear. Indeed, in the case of a continuous beam, an equilibrium can be found such that forces due to the self-fields exactly cancel the forces due to the focusing fields of the wiggler [1]. In this paper, we perform numerical

calculations illustrating this equilibrium. The case of a pulsed beam will be considered in a future paper.

NUMERICAL MODEL

We study the electron beam flow in a FEL by numerically following the orbits of a large number of particles under the influence of a prescribed wiggler field and a dynamically computed self-field.

The particles are initially loaded into a Gaussian weighted hyper-ellipsoid in six dimensional phase space. They are advanced in time using the standard Boris pusher [2].

The self field model is derived from a method used in the Los Alamos code Trace3D. First, an ellipsoid is fitted to the particle positions via

$$\sigma_\alpha^2 = \frac{1}{N} \sum_i (\alpha_i - C_\alpha)^2$$

where N is the number of particles, i is the particle index, α is one of the three spatial coordinates, and C_α are the coordinates of the beam centroid. The force exerted on a particle by the self fields is then approximated by

$$F_x = 5^{-3/2} \frac{q}{4\pi\epsilon_0} \frac{3Q}{\gamma^2} \beta \frac{1-f}{\sigma_x(\sigma_x + \sigma_y)\sigma_z} x \quad (1)$$

$$F_y = 5^{-3/2} \frac{q}{4\pi\epsilon_0} \frac{3Q}{\gamma^2} \beta \frac{1-f}{\sigma_y(\sigma_x + \sigma_y)\sigma_z} y \quad (2)$$

$$F_z = 5^{-3/2} \frac{q}{4\pi\epsilon_0} \frac{3Q}{\gamma^2} \beta \frac{f}{\sigma_x\sigma_y\sigma_z} z \quad (3)$$

where ϵ_0 is the permittivity of free space, q is the charge of the particle, Q is the total charge in the beam, γ is the relativistic factor of the beam, and f is the "space charge form factor" which was tabulated by Lapostolle using data obtained numerically. In this paper, $\sigma_z \rightarrow \infty$ which leads to $f \rightarrow 0$. The factor of $5^{-3/2}$ converts the dimensions of the Gaussian weighted ellipsoid into the dimensions of the equivalent uniform weighted ellipsoid.

The wiggler field is modeled according to the formula given in Ref. [3] for parabolic pole pieces:

$$B = B_0 \left[\sinh(2^{-1/2}k_w x) \sinh(2^{-1/2}k_w y) \cos(k_w z) \hat{x} \right. \\ \left. + \cosh(2^{-1/2}k_w x) \cosh(2^{-1/2}k_w y) \cos(k_w z) \hat{y} \right. \\ \left. - 2^{-1/2} \cosh(2^{-1/2}k_w x) \sinh(2^{-1/2}k_w y) \sin(k_w z) \hat{z} \right]$$

Here, k_w is the wiggler wavenumber and $\hat{x}, \hat{y}, \hat{z}$ are the unit vectors. The electron beam propagates in the z -direction, with the wigggle motion in the x - z plane. The parabolic pole pieces provide equal focusing in both transverse directions.

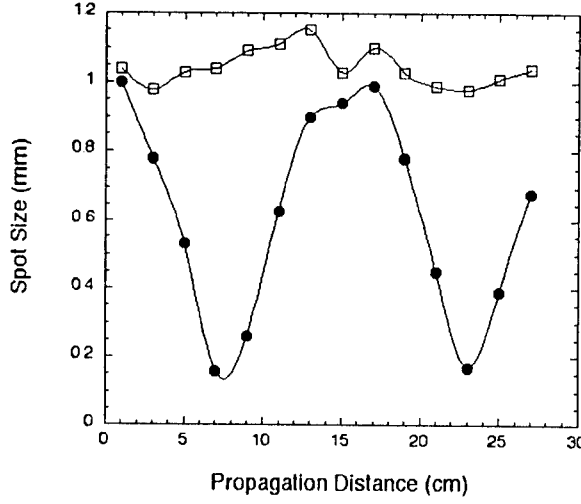


FIGURE 1. Variation of spot size with propagation distance for a beam with and without space charge. Solid circles represent data from a calculation with $J = 0$, open squares represent data from a calculation with $J = 8 \text{ kA/cm}^2$. As expected, self fields extend the betatron wavelength.

SELF COMPENSATION

In the case of a continuous beam, the effect of self fields is to modify the betatron wavenumber according to [1]

$$k_\beta = k_{\beta 0} (1 - \text{SFP})^{1/2} \quad (4)$$

where

$$\text{SFP} = \left(\frac{k_p/k_{\beta 0}}{\gamma_{z0}\beta_{z0}\gamma_0^{1/2}} \right)^2$$

Here, $k_p^2 = 4\pi n e^2 / mc^2$, n is the electron density, e is the electronic charge, $k_{\beta 0} = a_w k_w / \sqrt{2} \gamma_0 \beta_{z0}$ is the betatron wavenumber due to the wiggler field only, $a_w = e B_0 / k_w m c^2$ is the peak normalized vector potential of the wiggler field, β_{z0} is the axial velocity of the beam normalized to c , and $\gamma_0 = (1 - \beta_{z0}^2)^{-1/2}$. Although this formula was derived for flat pole pieces, it remains valid for parabolic pole pieces as well. Note that if the self field parameter (SFP) is unity, the betatron wavenumber vanishes and the beam is in equilibrium.

In the case of finite emittance, the matched beam condition becomes

$$\epsilon_n = \gamma_0 \beta_{z0} k_\beta \sigma_r^2$$

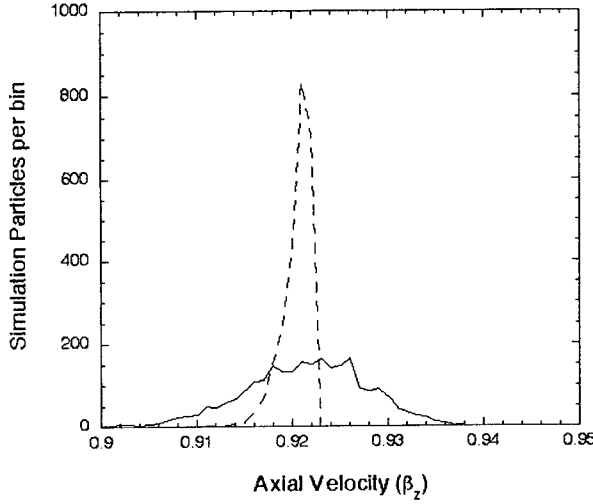


FIGURE 2. Axial velocity distribution for a continuous beam 10 cm into the wiggler field. The solid line is the data for $J = 0$, the dashed line is the data for $J = 8 \text{ kA/cm}^2$

where ϵ_n is the normalized emittance (in units of length · radians), and σ_r is the radius of a uniform density continuous beam. For a finite spot size, equilibrium occurs for $k_\beta > 0$. However, for emittances typical of a high quality photo-injector [4, 5], the beam is nearly in equilibrium for $k_\beta = 0$.

We now consider numerical calculations of the electron orbits in a wiggler field with $B_0 = 3 \text{ kG}$ and $\lambda_w = 2\pi/k_w = 5 \text{ cm}$. The beam had initial dimensions of $\sigma_x = \sigma_y = 1 \text{ mm}$, and initial emittance of zero. Fig. 1 shows measurements of σ_y at several z positions. The solid circles correspond to the case where the current density, J , vanishes. In this case the beam undergoes betatron oscillations at the expected frequency. The open squares correspond to the case where $J = 8 \text{ kA/cm}^2$ which gives $\text{SFP} = 0.8$. In this case the spot size is nearly constant. According to Eq. (4), the best equilibrium should occur for $\text{SFP} = 1$. In the numerical calculation, however, $\text{SFP} = 1$ led to a larger deviation in spot size than $\text{SFP} = 0.8$. The discrepancy may be related to the conversion between Gaussian and uniform beams.

Fig. 2 illustrates the effect of space charge on the axial velocity distribution. The solid curve corresponds to the case where $J = 0$ while the dashed curve corresponds to the case where $J = 8 \text{ kA/cm}^2$. The distribution is significantly narrower in the case of the high current beam. This is a result of the fact that in the presence of strong self-fields forward momentum is not lost to betatron motions.

CONCLUSIONS

Numerical calculations support the assertion that self-fields can improve the quality of an electron beam for FEL applications. By opposing the focusing forces of the wiggler field, self-fields can increase the betatron wavelength and reduce the spread in axial velocity. This reduces S and improves the performance of the FEL.

ACKNOWLEDGMENTS

This work was supported by the Office of Naval Research. D.F.G. is supported by the National Research Council.

REFERENCES

1. Hafizi, B., and Roberson, C. W., *Phys. Plasmas*, **3**, 2156–2162 (1996).
2. Boris, J. P., *Proc. Fourth Conf. Num. Sim. Plasmas* (1970).
3. Scharlemann, E. T., *J. Appl. Phys.*, **58**, 2154–2161 (1985).
4. Ben-Zvi, I., et al., *Nucl. Instrum. Methods Phys. Res. A*, **318**, 208–211 (1992).
5. O'Shea, P., et al., *Phys. Rev. Lett.*, **71**, 3661–3664 (1993).

An Experiment to Transfer Angular Momentum from a Helical Low Energy Proton Beam to a Trapped Electron Plasma

D. S. Todd, R. E. Pollock

*Indiana University Department of Physics and Cyclotron Facility (IUCF)
Milo B. Sampson Lane, Bloomington IN 47408-1398*

Abstract. As part of a continuing program of beam-plasma interaction studies, a low energy (2-10 keV) proton beam will be injected on a helical trajectory into a trapped electron plasma in a 1.6 T cryogenic solenoid. The proton source is a conventional duoplasmatron, but operated well below its design extraction energy. Beam tests over the desired energy range have established a mode with submillimeter beam focus and currents of a few μA . The beam will be transported into the high field, displaced, and then inflected by a sudden impulse onto an offset helical trajectory of low pitch. The electron plasma trapping potential will provide a fine pitch control and will serve as an analyzer of the residual longitudinal momentum (helix pitch). Previous experiments in this laboratory employing proton beams of high energy (50-300 MeV) in a storage ring have shown that an electron plasma absorbs angular momentum and energy from the proton beam - for example exhibiting expansion through beam misalignment which breaks the trap azimuthal symmetry. The expectation is that a lower energy beam, traversing the plasma at velocity well below that of a typical wave mode, may be more effective in torque transfer. A possibility may exist for significant plasma compression with judiciously chosen settings of the helix position offset relative to the plasma surface. Progress in design and implementation of the low energy injection scheme will be presented.

INTRODUCTION

In the past few years, a proton beam in the Cooler storage ring at the Indiana University Cyclotron Facility (IUCF) has been used for first tests of the response of an electron plasma to a passing fast beam. Initial experiments indicated an energy transfer from beam to plasma which was substantially larger than predicted from single particle collision rates, and which exhibited variation from one beam exposure to the next — indicative of some significant uncontrolled parameter. A non-destructive monitor of plasma radius was then developed [1] so that transfer of energy and angular momentum could both be observed. With this new capability it was found that the beam torque on the plasma was unexpectedly sensitive to beam translations and rotations with respect to the trap symmetry axis. In particular, the beam angle was identified as the uncontrolled parameter in the early studies. A description of this work is being prepared for publication elsewhere.

The beam in the storage ring is fast and rigid, so that particle velocity ($v/c > 50\%$) is much larger than plasma wave or thermal velocities ($v/c < 2\%$). The beam is thus unlikely to participate in the dynamics through two-stream instabilities. We suspect that

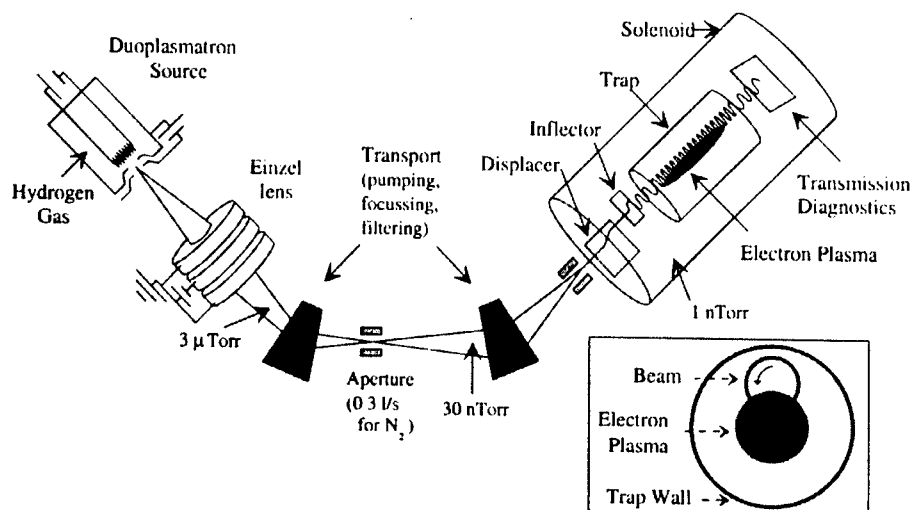


FIGURE 1. Beam-plasma layout in the laboratory. Inset gives an end view of the "corkscrew" beam interacting with the electron plasma.

the plasma density perturbation (the plasma attempting to screen out the beam collective field) is being dragged through the rotating plasma by the immovable beam and the resulting viscous drag is responsible for the observed torque.

The experiment whose preparation is described in the present report is an attempt to probe the beam-plasma interaction in the opposite beam velocity limit. Using ion source technology we can prepare a beam of protons in a much lower velocity range ($0.2\% < v/c < 0.5\%$). We have designed transport elements to carry this beam into the high field trap solenoid, to produce controlled displacements, and to convert longitudinal into transverse momentum so the beam path is a helix of variable pitch. By analogy to electron cooling, the angular momentum of the beam helical motion may be transferrable to the plasma. The proton helix rotates at the cyclotron frequency while the electron plasma counterrotates at the rotation frequency of drift motion in its self electric field (see inset Figure 1).

SOURCE AND TRANSPORT

A hydrogen-fed duoplasmatron ion source will produce a beam whose principle charged components are protons, H_2^+ , and H_3^+ [2]. By operating the source far below its intended extraction voltage, we have produced beams with kinetic energies as low as 1 keV. Downstream sector magnets allow for the isolation of any of the three ion species, and by employing an einzel lens, proton beams have been focused to sub-millimeter diameter.

The duoplasmatron source has a turbine pumping the chamber adjacent to the extraction aperture. This region maintains a pressure of about $3 \mu\text{Torr}$, with the source H_2 gas flow somewhat below the value giving maximum ion current. As the electron plasma

tolerates a background pressure of about 3 nTorr, a drop in pressure along the transfer beam line of order 10^3 is needed.

We take advantage of the small beam waist after the first bend to insert a conductance-limiting aperture of 8 mm diameter and 100 mm length where the transition from elastomer seals to bakeable all-metal construction is taking place. The 75 l/s ion pump at the second bend is expected to bring the pressure in this region to the 10^{-8} Torr range.

The final beam waist is located within the displacer in the trap chamber so the last conductance limiter must have a bigger aperture and will reduce the pressure by only about one order of magnitude. If necessary, a second turbopump, normally used for roughing, can be attached to the first magnet chamber after the lens aperture to obtain a further reduction. A schematic layout is given in Figure 1.

DISPLACER AND INFLECTOR

When the beam enters the solenoid it is converging and traveling along the axis of trap. An electrostatic mirror placed on the axis of the trap would convert some of the beam's momentum from parallel to perpendicular to the trap axis, but the range of possible helix radii and guiding center locations would be severely limited, therefore inducing helical motion will be done in two steps. First, an electrostatic displacer radially shifts the beam off-axis, then an electrostatic inflector gives the offset beam a transverse kick to induce cyclotron motion about a magnetic field line.

For displacement, employment of drift motion within the high B field adjacent to the trap is ruled out by space constraints. Because a low-energy beam of finite diameter is spread by the momentum-position correlation (dispersion) imposed as the beam enters the E field element, an E field magnitude $E_0 < 0.1$ MV/m must be used giving a device length > 0.2 m.

The displacer is instead located in the throat of the solenoid. The first bend pair occurs in a weak B field and the second bend pair in a moderate B field so the beam exits along a field line (Figure 2). By employing (x, y) pairs, the cyclotron motion can be compensated over a range of beam energies and trap B field strengths. Compensation fails if bends in either plane are separated by an integer multiple of half-gyrowavelengths. In practice this means that the last deflector element lies at $B/B_0 < 10\%$. The steel jacket of the solenoid produces a rapid falloff of B (half-length about 0.05 m) in the displacer region which is essential to the selected design.

The four E field values of the displacer plates are to be adjusted so coherent cyclotron motion is minimized. In this way the tuning of the displacer and of the following inflector is largely decoupled.

The inflector is designed to accept a beam of charged particles moving along a B field line in a strong uniform field and to convert most of the momentum from parallel to perpendicular to the trap axis. Note that the adiabatic invariant responsible for mirroring must be broken to do so. A localized electric field impulse will serve provided the time duration is short compared to the cyclotron angular period ($\frac{qB}{m} * dt < 1$).

A planar electrostatic mirror with small gap, tilted at 45° , will give a 90° deflection in the low B limit. The mirror potential qV must exceed half the beam ki-

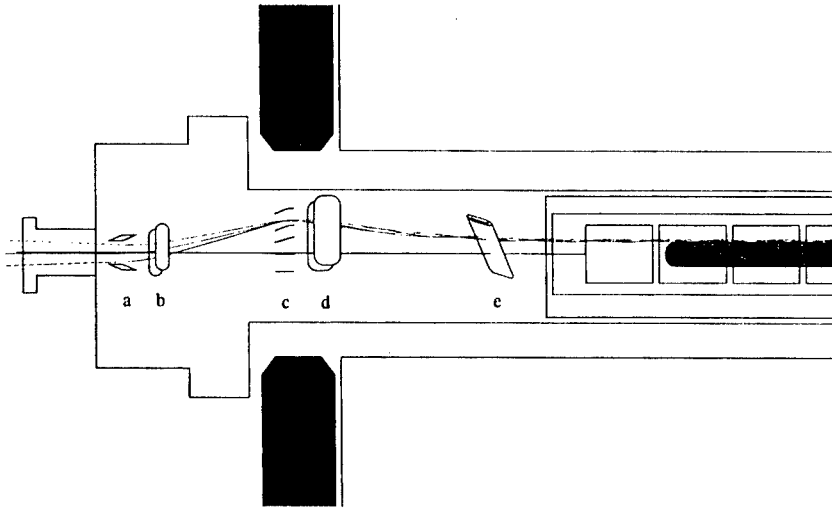


FIGURE 2. Side view of a numerical simulation of the beam being displaced by the four electrostatic elements (a-d) that make up the displacer. The inflector's position is shown (e) for reference.

netic energy T , which limits the concept to beam energies of a few keV. The uniform longitudinal deceleration $a_z = \frac{qE_z}{m}$ reduces the incident speed $v_{z0} \simeq v = (\frac{2T}{m})^{\frac{1}{2}}$ to zero in time $dt = v/a_z < \frac{m}{qB}$ or rearranging $a_z * \frac{m}{q} = E_z > v * B$ so the force inside the gap is mainly electric. For protons with $\frac{v}{c} = 0.5\%$ ($T = 11.7$ keV) and $B = 1.6$ T, this means $E = \sqrt{2}E_z > 2.4$ MV/m. Note the resulting constraint on gap g since $V = g * E > \frac{T}{2q}$, with $E_z = \sqrt{2}E > (\frac{1}{8})^{\frac{1}{2}} (\frac{T}{gq})$. If we choose the minimum E_z then $g > (\frac{1}{8})^{\frac{1}{2}} (\frac{T}{qV}) = (\frac{1}{8})^{\frac{1}{2}} (\frac{mv}{2qB}) = (\frac{1}{32})^{\frac{1}{2}} R$ where $R = \frac{mv}{qB}$ is the radius of the cyclotron orbit after inflection ($R = 9.8$ mm, $g > 1.75$ mm for the speed chosen above). Tracking simulations show that $dt < (\frac{\pi}{2}) * (\frac{m}{qB})$ is tolerable so that we choose $g = 2.5$ mm and $E < 2$ MV/m for the inflector mirror.

After leaving the mirror, the cyclotron motion about a fixed guiding center would lead to a second mirror encounter and to the beam returning along the incident direction. The mirror angle must therefore be reduced, and the mirror must have an edge so the helical path wraps around the edge with sufficient pitch to clear the backside. By tilting the mirror about a second axis normal to the field and to the first axis, the encounter may be delayed until a full cyclotron period giving a minimum pitch $= 2g$. The proper choice of the two direction cosines which specify the double tilt gives a similar minimum pitch over the design range $5 < R < 10$ mm. Figure 3 shows tracking through a planar mirror with semicircular ends to illustrate this point. The view is down the gap. The E field is generated from a 2D relaxation. Note the spread in pitch caused by field non-uniformity in the end region at the lower rigidity. Periodic focussing by the regularly spaced grid wires contributes to the spread in helix pitch, but is omitted here for clarity.

The longitudinal velocity at 1.6 T and 5 mm pitch is $v/c = 0.04\%$ with a stopping potential of 75 eV. This potential is in the range of the electron trap end potential so it

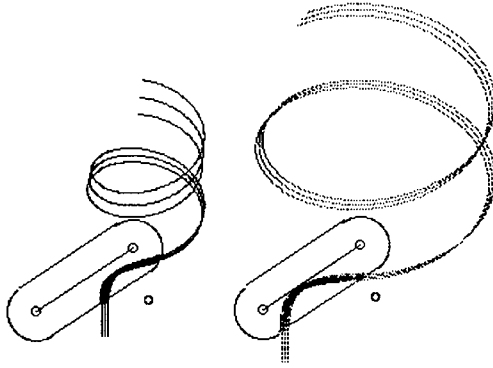


FIGURE 3. Doubly-tilted inflector imparts helical motion to beam entering from below along $B=1.3T$ field. Proton beams of 2keV with $E=0.6kV/mm$ (left), and 8keV with $E=1.6kV/mm$ (right), give helix radii of 5 and 10 mm respectively. Note that entering the non-uniform field of the semi-cylindrical end (in order to obtain clearance at the lower energy) results in an increased spread in helix pitch. The starting rays are separated in x by $\pm 0.3mm$. The auxiliary steering wire on the lower right is unbiased in these examples.

is possible to further reduce the longitudinal velocity as the proton helix enters the trap. This reduction is discussed in the following section.

BEAM-PLASMA INTERACTION

The electron plasma is confined axially by an inverted potential well which is formed by keeping the end rings of the trap at ground potential and floating the center of the trap near 200 V. A positive charge entering the trap will be slowed parallel to the axis by the plasma trapping well. For a beam on a helical trajectory this slowing occurs and causes a decrease in pitch or complete reflection of the beam. The decreased pitch is advantageous since the beam rotates more and interacts longer with the plasma before leaving the trap. The fact that the plasma potential reduces the well potential near the axis means that beam particles nearer the axis of the trap will not be slowed as much as ones near the wall of the trap as is seen in the numerical simulations of Figure 4. In the figure, the beam can be seen to rotate about the trap axis as it travels the length of the plasma. The presence of the plasma's radial electric field introduces an $\mathbf{E} \times \mathbf{B}$ drift about the trap center that would not be present were the plasma not there. Note that, though the electric field is weaker for the beam outside the plasma than for a beam on the edge of the plasma, the reduction of the former's helix pitch gives it more interaction time for the drift to take place and gives both beams a similar precession angle while passing the plasma. Though the precession of the beam helix will complicate post-interaction beam diagnostics, it will have little effect on the torquing mechanism.

Adjusting the beam helix position and radius will allow for the application of different torques. A compressional torque is expected when the helix straddles the plasma surface, whereas an expansion torque should be seen when the beam and plasma are coaxial.

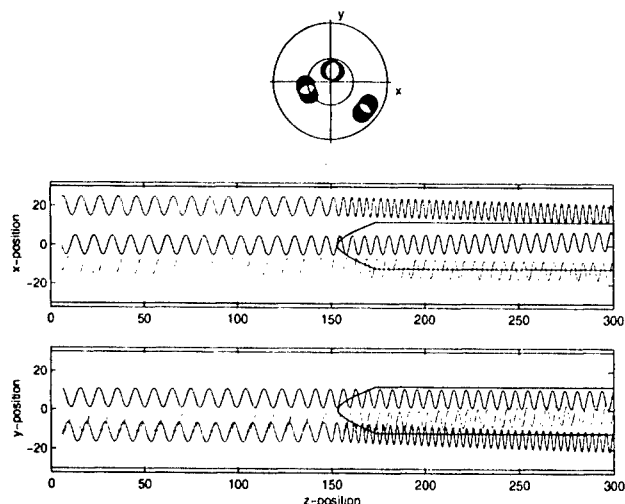


FIGURE 4. Numerical simulation of protons on helical trajectories fired at an electron plasma trapped in a negative potential energy well. The well is created by a cylinder of radius 30 being grounded except for $z \geq 150$ where the cylinder potential is positive.

STATUS

The electron plasma portion of the setup was placed in service last year. The proton source was commissioned at the start of 2001, and designs of transport, displacer and inflector elements have been developed based on measured beam properties. We are presently waiting for UHV welded vacuum components to emerge from our shop. The tests of proton beam properties in the empty solenoid should then be followed by the first slow beam-plasma studies later this year.

ACKNOWLEDGMENTS

This work has been supported in part by the U.S. Department of Energy under grant DE FG0297 ER 54433 A002, and by the U.S. National Science Foundation under grant NSF PHY 96 02872.

REFERENCES

1. Pollock, R. E., Ellsworth, J., Muterspaugh, M. W., and Todd, D. S., "Proton Beam-Electron Plasma Interactions", in *Non-Neutral Plasma Physics III*, edited by J. J. Bollinger, R. L. Spencer, and R. C. Davidson, AIP Conference Proceedings 498, New York, 1999, pp. 336–337.
2. Moak, C. D., Banta, H. E., Thurston, J. N., Johnson, J. W., and King, R. F., *The Review of Scientific Instruments*, **30**, 694–699 (1959).

Intrabeam Scattering and Halo Formation in Intense Ion Beams

N. Uhlmann* and G. Zwicknagel*

**Institut für Theoretische Physik, Universität Erlangen-Nürnberg,
Staudtstr. 7, D - 91058 Erlangen, Germany*

Abstract. An essential problem for the operation of high current linacs is the control of beam losses due to halo formation. Here we concentrate on an interplay between intrabeam scattering (IBS) and the incidence of particles which are driven to high amplitudes by resonances with the nonlinear space charge fields of a mismatched beam. For these studies, we developed a particle-core-molecular-dynamics (PCMD) method which suitably joins the time evolution in framework of the envelope equations and a calculation of IBS between pseudo-particles with a renormalized charge. With this technique we investigated continuous KV-beams in a FODO channel. Our first results strongly suggest, that IBS in fact supports the halo formation in a mismatched beam.

INTRODUCTION

One of the most critical aspects for a successful operation of a high current linac is the control of beam losses, since only a very small fraction of particles can be tolerated to collide with the accelerator structures. Such beam losses are associated with the formation of a halo of particles significantly outside the beam core. Substantial theoretical effort is presently addressed to the understanding of halo formation, e.g. to the stability of collective excitation modes which has been studied in the framework of the nonlinear Vlasov-Maxwell equations by both analytical and numerical approaches [1, 2, 3, 4]. Also the resonances between nonlinear space charge forces outside the core of a mismatched beam and the betatron oscillations have been identified as a source for a halo. This has been studied mainly by a frequency map analysis of the single particle motion in framework of a particle core (PC) model [3]. Hard collisions between the beam particles, which are neither included in the Vlasov-Maxwell equation nor the particle core approach, could also scatter particles into a halo. But for the typical beam parameters of high power linacs, it is very unlikely that this intrabeam scattering (IBS) is sufficiently effective to directly drive a beam halo [5]. IBS may, however, play a non-negligible role in amplifying the other mechanisms. We here focus on an interplay between intrabeam scattering (IBS) and the incidence of particles which are pushed to high amplitudes by nonlinear resonances driven by the space charge fields of a mismatched beam. As a fully microscopic numerical treatment including all mutual Coulomb interactions of the beam particles, and thus all space charge phenomena *and* IBS, considerably exceeds the capacity even of modern computers, we developed an alternative method. These so-called particle-core-molecular-dynamics (PCMD) simulations suitably join the time evolution of the beam core in framework of the envelope equations with a microscopic calculation of the Coulomb interactions between pseudo-particles with a renormalized charge.

THE PARTICLE-CORE-MOLECULAR-DYNAMICS METHOD

The equations of motion for the position \mathbf{r}_α and the velocity \mathbf{v}_α of a particle with mass m and charge q in an accelerator structure or a storage ring can be written in a local center of mass frame of the beam as

$$\frac{d\mathbf{r}_\alpha}{dt} = \mathbf{v}_\alpha, \quad \frac{d\mathbf{v}_\alpha}{dt} = \mathbf{K}(\mathbf{r}_\alpha, t) - \frac{1}{m} \nabla \Phi(\mathbf{r}_\alpha, t). \quad (1)$$

Here \mathbf{K} denotes all the forces on the particle due to the beam manipulating elements of the structure and Φ represents the potential generated by all the other charged particles in the beam. In case of an ideal FODO-channel extending along the z -direction, the external forces are linear and $\mathbf{K}(\mathbf{r}, t) = (K_1(t)x, K_2(t)y, 0)$, where the $K_i(t)$ only depend on time t or likewise on the position s along the channel. In general a numerical treatment of Eq. (1) is unavoidable. The most complete approach are molecular dynamics (MD) simulations which take completely into account all the mutual Coulomb interactions between the beam particles and thus include IBS without any approximation. They have been applied successfully for low current beams and studies of e.g. beam crystallization and related issues [6, 7, 8, 9, 10]. Because the numerical effort scales like N^2 the computational effort is, however, prohibitive for high current beams which require at least $N \sim 10^7$.

If one is, on the other hand, interested e.g. in the motion of a few particles in the nonlinear space charge fields outside the beam core, one can assume a given space charge field due to the large number of core particles with regular motion and neglect the charges of the actual test-particles. This approach becomes easily applicable for the Kapchinsky-Vladimirsky (KV) distribution, where a fairly simple self-consistent solution exists. The continuous KV-beam has the uniform charge density $\rho(s) = \lambda_z \Theta(1 - x^2/a^2(s) - y^2/b^2(s)) / \pi a(s)b(s)$ with envelopes $a(s)$ and $b(s)$ which vary with the position in the FODO channel $s = \gamma\beta ct$ according to

$$\frac{d^2 a}{ds^2} + K_x(s)a - \frac{\xi}{a+b} - \frac{\epsilon_x^2}{a^3} = 0 \quad \text{and} \quad x \leftrightarrow y, a \leftrightarrow b. \quad (2)$$

In Eq. (2) the constants ϵ_i are the emittances, $\xi = (qI)/(\pi\epsilon_0 mc^3 \gamma^3 \beta^3)$ is the space charge parameter for a beam current I , $\lambda_z = I/c\gamma\beta$ is the line density and β, γ are the relativistic factors. Here the potential $\Phi(\mathbf{r}, t)$ generated by the space charge of the beam can be obtained analytically from the known $\rho(t)$ via the Poisson equation. Combining now the time evolution of the core, given by a numerical solution of Eq. (2), and the particle motion, Eq. (1), establishes the particle core (PC) model, see e.g. [3]. As we are mainly interested in the influence of IBS on the small fraction of beam particles which may form a halo, we separate the collective selfconsistent space charge field from the individual particle-particle collisions. The basic idea is now to use the PC model for a KV-beam of density n and charge density qn as a starting point and to superimpose a MD treatment for a relatively small number (\sim some hundred) N_t of test-particles in a small slice moving with the beam. Applying periodic boundary conditions along the beam extension, i.e. in z -direction, the test-particles then constitute an additional beam of density $n_t \ll n$ which is subject to the external forces \mathbf{K} , the space charge

fields generated by the underlying KV-beam and the direct Coulomb collisions between the test-particles. But in the test-particle beam IBS is strongly reduced as compared to the real beam with the much higher density n . Because no length scale exists for the Coulomb interaction, we compensate the smaller test-particle density by increasing the test-particle charge to a renormalized value q_t . The N_t test-particles with mass m and charge q_t are now propagated according to Eq. (1) feeling the same external forces as the physical beam particles and the potential

$$\Phi(\mathbf{r}_\alpha, t) = \sum_{\beta \neq \alpha}^{N_t} \frac{q_t^2}{4\pi\epsilon_0 |\mathbf{r}_\alpha - \mathbf{r}_\beta|} + \int \frac{d^3r'}{4\pi\epsilon_0 |\mathbf{r}_\alpha - \mathbf{r}'|} \frac{a_0 b_0}{\gamma a b} \Theta \left(1 - \frac{x'^2}{a^2} - \frac{y'^2}{b^2} \right), \quad (3)$$

with $n = I/q\beta c\pi a_0 b_0$, $a_0 = a(s=0)$, $b_0 = b(s=0)$ and the step function $\Theta(z)$. Here the test-particles directly interact as charges q_t but couple with the original charge q to the space charge field of the underlying real beam. To avoid double counting, the space charge field ($\propto q^2 n$) of the core beam is corrected by the test-particle contribution ($\propto q_t^2 n_t$). This combination of MD simulations and the PC model, the particle-core-molecular-dynamics (PCMD) method, allows to study IBS also for intensive beams on a qualitative and, at least, semi-quantitative level, with a moderate computational effort. The crucial point is the appropriate choice of the test-particle charge q_t . Taking $q_t = 0$ we retrieve a pure PC description with a completely two dimensional dynamics in the transversal plane. It turns into a three dimensional, pure MD simulation of the test-particle beam if $q_t^2 n_t$ approaches $q^2 n$ and the space charge term completely vanishes. But then we deal with a dilute beam of high charges with a much lower current $I_t = I(q_t n_t / qn)$. The disappearance of the space charge term $\propto (q^2 n - q_t^2 n_t)$ defines, for a given density n_t , a critical, upper limit q_c for the test-particle charge by $q_c = q(n/n_t)^{1/2}$. Meaningful applications of the PCMD description are restricted to values $q_t \ll q_c$, where the model is expected to reproduce the basic effects of interparticle correlations and IBS.

The coupling within a real beam of density n and temperature T is described by the plasma parameter $\Gamma = (q^2/4\pi\epsilon_0 k_B T)(4\pi n/3)^{1/3}$, which can be interpreted as the ratio between the potential energy of a pair of particles at their mean distance and the mean thermal energy. For a large plasma parameter intrabeam scattering (IBS) leads to a secular growth of emittance [6]. But here, we consider beams of protons, $q = e$, with a large temperature, so that the plasma parameter is small, with typical values around $\Gamma \sim 10^{-5}$. It is, however, a key quantity to characterize the beam properties, and the test-particle beam in the PCMD description should have a similar plasma parameter Γ_t as the real beam, where $\Gamma_t/\Gamma = (q_t/q)^2 (n_t/n)^{1/3} = (q_t/q_c)^2 (q_c/q)^{4/3}$ with $q_c = q(n/n_t)^{1/2}$. An analogous argument concerns the scattering rate $\nu = n\langle v \rangle \sigma(\langle v \rangle)$ for beam particles with an averaged relative velocity $\langle v \rangle$ and a scattering cross section $\sigma(\langle v \rangle)$. It can be estimated by taking the Coulomb cross section $\sigma \sim (q^2/4\pi\epsilon_0 m \langle v \rangle^2)^2$. This yields $\nu \propto nq^4$ and a ratio of the scattering rates in the test-particle beam and the real beam $\nu_t/\nu = (q_t/q)^4 n_t/n = (q_t/q_c)^4 (q_c/q)^2$. For the envisaged high current proton beams, test-particle numbers $N_t \sim 1000$ and typical settings in the PCMD simulations, we have $n_t \sim 10^{-5} n$ and $q_c \sim 10^2 q$. Hence, a test-particle charge $q_t \sim 10 q \sim 0.1 q_c$ can be chosen which allows a matching of the physical relevant parameters, i.e. $\Gamma_t \approx \Gamma$ and $\nu_t \approx \nu$, while being fairly below the critical value q_c where the model breaks down.

PCMD SIMULATIONS OF A BEAM IN A FODO CHANNEL

With the outlined PCMD scheme we studied a continuous beam of 100 MeV protons in a FODO channel of 500 periods of 1 m and with a beam current $I=0.8$ A, which may represent the peak current in the bunch for a linac with a beam current in the mA range. The geometry of the nominal FODO cell was taken from Ref. [3]. The external focusing is $K_x = -K_y = 12 \text{ m}^{-2}$, the emittances are $\epsilon_x = \epsilon_y = 10^{-6} \text{ m}$ and the space charge parameter is $\xi = (eI)/(\pi\epsilon_0 mc^3 \gamma^3 \beta^3) = 9.6 \times 10^{-7}$. With these settings a matched solution of the envelope equations Eq. (2) is constructed numerically and yields $a_0 = 1.43 \times 10^{-3} \text{ m}$, $b_0 = 8.54 \times 10^{-4} \text{ m}$, $da/ds(0) = 0$ and $db/ds(0) = 0$ at $s = 0$ ($t = 0$). With these initial conditions, the envelopes $a(s), b(s)$ are propagated according to Eq. (2) throughout the structure and thereby define the time dependent core field contribution in expression (3). For the KV-distribution the corresponding beam density is $n = 1.0 \times 10^{10} \text{ cm}^{-3}$ and the plasma parameter is $\Gamma \approx 1.4 \times 10^{-5}$ when averaging over the temperatures $T_x(s)$ and $T_y(s)$ which are in the range $2.9 \times 10^5 \dots 8.4 \times 10^5 \text{ K}$ and are connected to the envelopes via $k_B T_x/m = \epsilon_x^2 (\gamma \beta c)^2 / 4a^2$ and $k_B T_y/m = \epsilon_y^2 (\gamma \beta c)^2 / 4b^2$. The initial conditions $\{\mathbf{r}_\alpha(0), \mathbf{v}_\alpha(0)\}$ of $N_t = 800$ test-particles are generated according to a KV-distribution in the transversal degrees of freedom $f(x, y, v_x, v_y) \propto \delta(1 - x^2/a^2 - y^2/b^2 - mv_x^2/4k_B T_x - mv_y^2/4k_B T_y)$ and homogeneously in z -direction. The density of the test-particle beam is $n_t = 7.3 \times 10^4 \text{ cm}^{-3}$ and $q_c = 3.7 \times 10^2 q$. The simultaneous propagation of the N_t test-particles, given by Eqs. (1) and (3), is treated within a usual MD scheme by standard numerical algorithms with a time step which guarantees a sufficient temporal resolution as required for both the rapid changes of the external focusing and close Coulomb collisions between the test-charges. In z -direction periodically continued slices of the beam are considered, while no boundaries exist in the radial direction. To study a mismatched beam, a 20% larger a_0 than for the matched solution is chosen and taken as input for the envelope propagation (2) with the same space charge parameter and emittances. Since the current is kept at $I = 0.8 \text{ A}$, the beam density n and the test-particle density n_t are lower for the mismatched beam, but the ratio n_t/n and thus q_c are the same as for the matched beam.

In our first studies, we concentrate on the qualitative effects of IBS on the halo formation and are mainly interested in density profiles $\rho(\kappa, t)$ and particle numbers $N(\kappa, t)$ which are sampled by counting and normalizing the number of events in a given interval of the normalized transversal position $\kappa = (x_\alpha^2/a(t)^2 + y_\alpha^2/b(t)^2)^{1/2}$. Usually also some time average over a couple of time steps is performed.

Unfortunately, there is no clear cut definition of a halo. The sharp edges of a KV-beam provide, however, at least a explicit distinction between particles inside and outside the core. This is already anticipated in the normalized distance κ , where values $\kappa \leq 1$ indicate particles inside the core, regardless of its actual shape as given by $a(t)$ and $b(t)$. Fig. 1 presents PCMD-simulation results of the particle density $\rho(\kappa, \tau)$ as a function of κ for various q_t and different positions τ in the FODO channel, and for a matched and a mismatched beam. Clearly visible are the following general trends of the density at $\kappa > 1$: it increases with q_t , that is, the strength of the Coulomb collisions, i.e. IBS, and the number of passed structures, and, compared to the matched beam, substantial larger $\rho(\kappa > 1)$ are observed for the mismatched beam. These effects are specifically

pronounced at the largest shown $q_t = 50$, where IBS is presumably unrealistic high. The more realistic scenario, with $\Gamma_t \approx \Gamma$ and $v_t \approx v$ is close to $q_t = 10$. Here, only moderate effects show up. The difference between matched and mismatched beam is, however, as well highly significant. The relative number $N_\kappa(\tau)/N_t$ of (test-) particles within a certain interval of $\kappa > 1$ (not plotted) shows the same trends as $\rho(\kappa, \tau)$. Here for realistic IBS rates, corresponding to $q_t = 10 \dots 20$ a fraction of $\approx 10^{-4}$ of the beam particles are

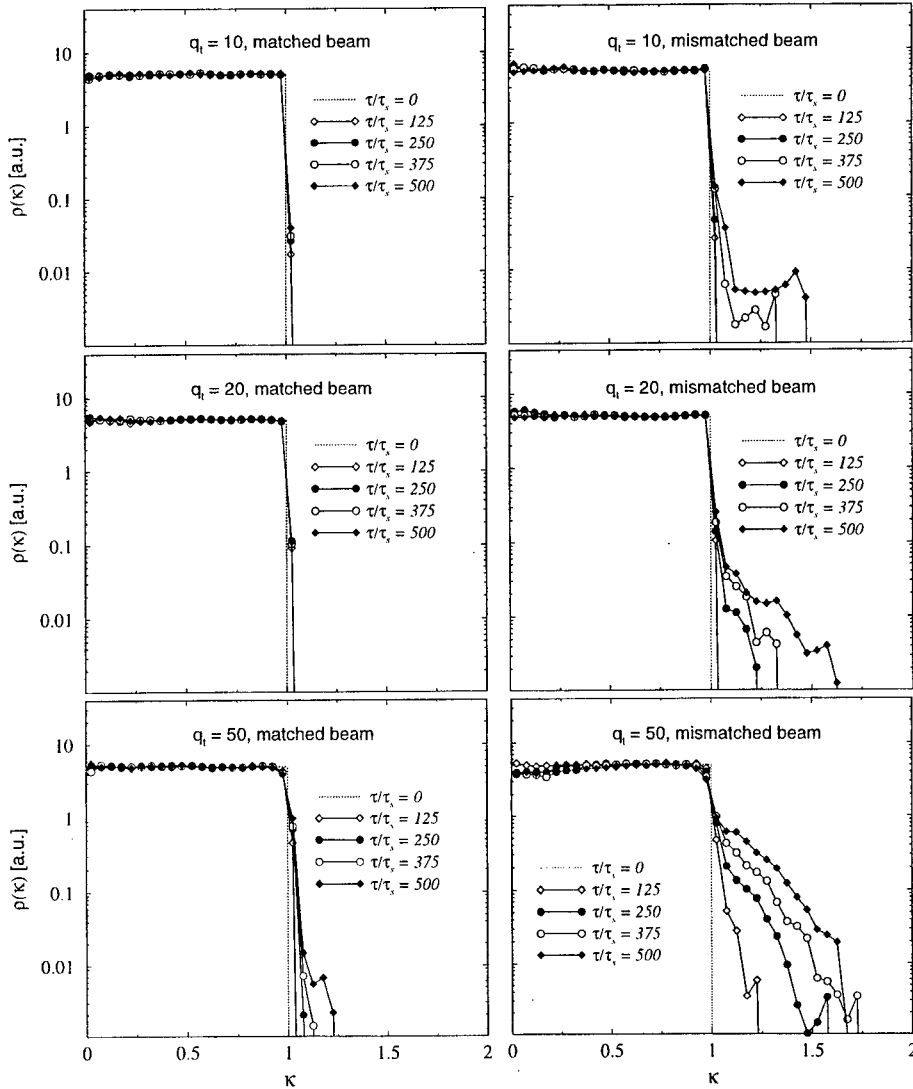


FIGURE 1. PCMD results for the test-particle density ρ as a function of the dimensionless distance $\kappa = (x_a^2/a(t)^2 + y_a^2/b(t)^2)^{1/2}$ for various test-particle charges q_t and different positions τ in the FODO channel in units of the length τ_s of one elementary structure. The matched KV-beams are shown on the left, the mismatched one on the right.

around $\kappa = 1.5$ at the end of the channel ($\tau \gtrsim 400 \tau_r$). But we remark the problem of statistics for these PCMD-runs with $N_t = 800$ particles and the related strong fluctuations of the extracted quantities. When performing more independent simulation runs and/or using larger particle numbers we expect a comparable fraction of particles at even larger κ .

In summary, first results obtained with the PCMD-model for a KV-beam in a FODO channel demonstrate that even rather small IBS rates significantly enhances the number of particles outside the beam core in a mismatched high current beam. In the matched beam, yet much higher IBS, produces only a small number of particles slightly above the surface of the core. This strongly supports the existence of a scenario whereby already a small amount of IBS is sufficient to transport a non-negligible fraction of particles in the region of nonlinear space charge forces outside the beam core within the typical time scale of beam acceleration in a linac. In the case of a mismatched beam, resonances between these nonlinear space charge forces and the betatron oscillations push the particles away from the core to higher amplitudes. This mechanism has been already identified in a pure PC-picture [3] when studying particles which have been explicitly put in the nonlinear region outside the core. Including IBS the population of this region is provided by the hard collisions which thus serve as a trigger for the elevation of particles by the space charge force resonances. This supplies a strong evidence that IBS serves as an indirect source for the halo formation in a mismatched beam. To verify if this has real significance for the beam losses in a high current linac, subsequent and supplementary more quantitative investigations are needed.

ACKNOWLEDGMENTS

We gratefully acknowledge valuable and stimulating discussions with M. Comunian and A. Pisent and the kind hospitality of the 'Laboratori Nazionali di Legnaro' during a one month stay. This work has been supported by a grant from the European Commission in framework of the TMR/Large Scale Facility program, under Contract N. ERBFMGECT 980110.

REFERENCES

1. J.Struckmeier, J.Klabunde and M.Reiser, Part. Accel. **15** (1984) 47.
2. R.C.Davidson, H.Qin and P.J.Channel, Phys.Rev. ST Accel.Beams **2** (1999) 074401.
3. A.Bazzani, M.Comunian and A.Pisent, Part.Accel. **63** (1999) 79.
4. E.Sonnendrucker, A.Friedman, J.J.Barnard, D.P.Grote and S.M.Lund, Nucl.Instr. and Meth. **A464** (2001) 470.
5. R.L.Gluckstern and A.V.Fedotov, Phys.Rev.ST Accel.Beams **2** (1999) 054201.
6. M.Seurer, P.-G.Reinhard and C.Toepffer, Nucl.Instr. and Meth. **A351** (1994) 286.
7. C. Toepffer, M. Seurer and Q. Spreiter Fusion Engineering and Design, **32 - 33** (1996) 175.
8. M. Seurer und C. Toepffer, Hyp.Int. **108** (1997) 333.
9. M. Seurer, C. Toepffer, V. Variale, A. Pisent, L. Tecchio and A. Burov, Nucl.Instr.Meth. in Phys.Res. **A395** (1997) 275.
10. M. Seurer, P.-G. Reinhard, C. Toepffer, Nucl.Instr.Meth. in Phys.Res. A **415** (1998) 503.

Crystalline Ion Beams in the RF Quadrupole Storage Ring PALLAS

U. Schramm, T. Schätz, and D. Habs

Ludwig-Maximilians-Universität München, Sektion Physik, D-85748 Garching, Germany

Abstract.

We report on the crystallization of laser cooled Mg^+ ion beams circulating in the table-top rf quadrupole storage ring PALLAS at a velocity of 2800 m/s (beam energy 1 eV). A sudden collapse of the transverse beam size and the low velocity spread clearly indicate the phase transition to a one-dimensional linear string of ions. This crystalline beam shows exceptional stability, surviving for more than 3000 revolutions without cooling. Close to the phase transition, the spatial beam profile of non-crystalline beams was found to exhibit an unexpected two component Gaussian distribution. Although its origin is not yet fully understood, we can exploit this effect for the identification of two- and three-dimensional crystalline beams.

INTRODUCTION - THE QUEST FOR CRYSTALLINE BEAMS

Threading ions like pearls on a string in high-energy storage rings by freezing out the inter-particle motion [1, 2, 3, 4, 5] opens opportunities far beyond the means of standard accelerator physics [6, 7]. The usual heating due to collisions of particles within the beam almost completely vanishes, giving rise to a state of unprecedented brilliance and exceptional stability. To reach this ultimate goal, beam cooling techniques were improved continuously. With electron cooling, very dilute beams of highly charged ions were observed to exhibit liquid-like order [8, 9] with unique applications in mass spectrometry [10]. With refined laser cooling methods [11, 12], an ambiguous reduction of intra-beam heating [13] was reported for $^9\text{Be}^+$ ion beams. Space-charge limited densities were reached for laser cooled $^{24}\text{Mg}^+$ ion beams [14], but no clear evidence for beam crystallization has been found in high-energy storage rings so far.

This fact stands in contrast to the routine generation of elongated ion crystals at rest in ring [15] and linear traps [16, 17]. As an illustration and as a reference, in fig. 1 we present images of ion crystals at rest [6, 18], gained with our storage ring PALLAS (Paul Laser coolIng Acceleration System), described below. Ions appear ordered since their mutual Coulomb-repulsion overcomes their mean kinetic energy. The overall Coulomb-repulsion is compensated by an external parabolic trapping potential $\Psi(r, z)$. A strong asymmetry in the radial and longitudinal confinement [18] leads to the prolate shape of the crystals. The formation of the crystalline structure is well understood [3, 15, 17, 19, 20]. The Coulomb-crystal evolves from a linear string of ions over a zig-zag band to three-dimensional helices when the dimensionless linear ion density $\lambda = (N/z) \cdot a$ [19], N denoting the number of particles and a the Wigner-Seitz radius, increases. This can be achieved either by adding more ions, or by reducing the radial confinement.

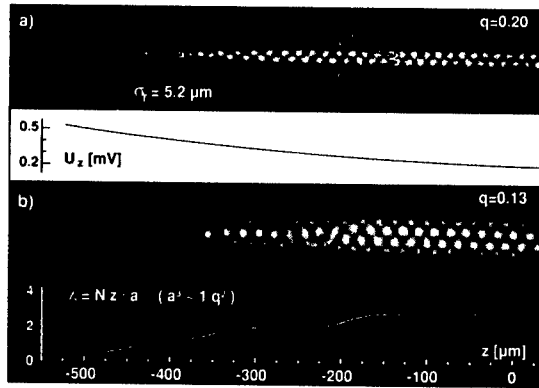


FIGURE 1. Fluorescence images of ion crystals at rest in PALLAS. In addition to the radial confinement in the rf quadrupole, the ions are confined longitudinally in a comparably weak static potential U_z . The Coulomb-crystal becomes more complex when the linear ion density λ increases with lowered confining potential from a) to b) or when it increases step-wise along the axis z , as illustrated in b). (Reprinted from [6] with permission from Macmillan Magazines, Ltd.)

In high-energy storage rings, gaseous (emittance dominated) ion beams are heated by intra-beam scattering. In combination with the varying focusing and bending elements, this mechanism couples part of the beam energy into the random ion motion. Cooling now increases the phase space density of the beam, and further amplifies the scattering rate [21, 22]. For a given cooling rate, this vicious circle could only be overcome by increasing the number of focusing sections in the storage ring [23, 24] to achieve a more continuous focusing, or by choosing a sufficiently low ion density [13]. Once having attained the ordered state with sufficient cooling, this heating mechanism should vanish and the beam should collapse to the crystalline state. Additionally, the maintenance of a crystalline beam is expected to impose severe restrictions to the storage ring lattice [23, 25, 20]. The excitation of oscillatory modes of an ion crystal passing through the periodic bending and focusing sections has to be carefully avoided. Numerical simulations yield that to maintain a beam crystal (and, more fundamental, to prevent envelope instabilities of space charge dominated beams [26, 27]), the number of repeating focusing sections P (the periodicity of the ring) has to be larger than $2\sqrt{2} \cdot Q$, the storage ring tune Q being the number of radial oscillations per revolution [28]. This criterion coincides with the validity criterion for treating (time dependent) strong focusing in the (time-averaging) smooth approximation [29]. Also, the beam has to withstand shear in the bending sections which implies that large crystalline beams must orbit with constant angular velocity.

THE RF QUADRUPOLE STORAGE RING PALLAS

To bridge this gap and to experimentally elucidate the conditions necessary for attaining and maintaining crystalline beams in high-energy rings, we constructed the low-energy

rf quadrupole storage ring PALLAS. Sketched in fig. 2, it can be considered as a ring-shaped quadrupole ion guide [15, 29, 30, 18, 6]. The bending radius of the ring amounts to $C/2\pi = 57.5$ mm at an aperture of the quadrupole structure of $r_0 = 2.5$ mm. For radial confinement and bending of the ion beam, a typical rf voltage $U_{rf} = 350$ V at a frequency $\Omega = 2\pi \cdot 6.3$ MHz is applied between the quadrupole ring electrodes. The resulting harmonic pseudo-potential $\Psi(r) = qU_{rf}/8 \cdot (r/r_0)^2$ is characterized by the stability parameter $q = 2eU_{rf}/m\Omega^2 r_0^2 \approx 0.28$, where e and m stand for the charge and mass of the $^{24}\text{Mg}^+$ ion [31]. The corresponding single-particle secular frequency amounts to $\omega_{sec} = q\Omega/\sqrt{8} = 2\pi \cdot 625$ kHz. This transverse oscillation in the confining pseudo-potential is equivalent to the betatron oscillation [28] of particles in a synchrotron with its alternating focusing and de-focusing magnets. In the quadrupole ring, these discrete but periodic structures are represented by the alternating phase of the rf voltage. The focusing conditions of a beam of velocity $v \approx 2800$ m/s are described by the number of oscillations per round-trip $Q = \omega_{sec}/2\pi \cdot C/v \approx 80$ and the periodicity of the lattice $P = \Omega/2\pi \cdot C/v \approx 800$. Evidently, the postulated maintenance conditions for crystalline beams are fulfilled ($P = \sqrt{8}/q \cdot Q$). However, the tune and the periodicity can be varied independently to investigate their influence on the stability of crystalline beams.

PALLAS is surrounded by sixteen segmented drift tubes, which can either be used to transport and position ions along the orbit [18] or to manipulate the velocity distribution of stored ion beams [6, 7]. Their voltage penetration at the closed orbit amounts to 0.5 % [30]. Care has been taken to keep potential distortions at the orbit below 100 meV and to provide perfect grounding of the drift tubes to enable circulating ion beams at low velocities. The ions are Doppler-cooled on the closed $3s^2S_{1/2} - 3p^2P_{3/2}$ transition. Two frequency doubled dye lasers provide the required wavelength of 280 nm at an intensity close to saturation. The resonance fluorescence is recorded either with a fast photomultiplier (PM) or imaged with an intensified CCD camera.

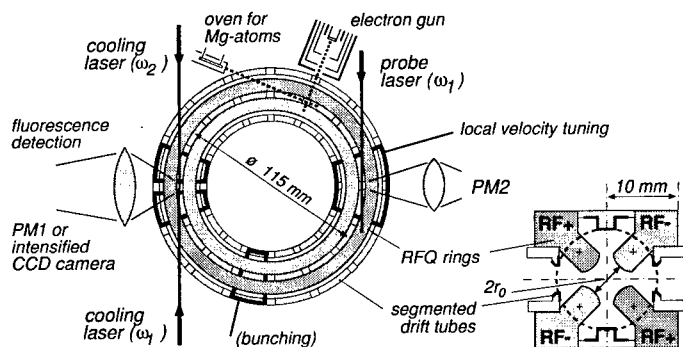


FIGURE 2. Axial and radial cut through the rf quadrupole storage ring PALLAS. The circumference of the orbit enclosed by the ring-shaped quadrupole electrodes amounts to $C = 361$ mm. Sixteen segmented drift tubes are distributed around the ring and can be powered individually. The accented tubes are used to localize ions in the laser cooling section, to locally shift the velocity distribution for monitoring purposes, or to bunch an ion beam. To load the ring, a weak beam of ^{24}Mg -atoms is ionized inside the trapping volume by a focused electron beam and simultaneously laser-cooled to zero velocity.

1D CRYSTALLINE ION BEAMS (STRINGS)

Ions are accelerated by the light pressure of the continuously tuned co-propagating laser beam (force: $+F_1$). The force profiles are sketched in fig. 3a). The final beam velocity is defined to $v = 2800$ m/s by the counter-propagating and thus decelerating laser ($-F_2$), held at fixed frequency. The longitudinal velocity spread of the beam is reduced by the dispersive character of the combined laser force (optical molasses). The typical behaviour of a cold ion beam is shown in fig. 3a). The fluorescence rate increases, as the detuning of the co-propagating laser is decreased. Then, as it approaches the resonance, the forces start to compensate and the rate drops off again. An increase of the confining potential drastically changes the behaviour, as demonstrated in fig. 3b). Here (grey curve), at first the fluorescence follows the previous curve, then decreases abruptly, and subsequently rises to a sharp peak whose width is dominated by the saturation broadened line-width of the transition. This signature of an abrupt decrease, marked by the arrow, has been previously observed in ion traps [32, 33] and indicates the phase transition to the crystalline state. After a slight reduction of the confining potential, the phase transition cannot be resolved any more (black curve). This suggests that the ions are confined sufficiently strong to form a string but do not experience unnecessary rf heating, which is responsible for the visibility of the above phase transition [6].

For the calibration of the typical fluorescence yield per ion in a crystalline beam, the absolute number of ions in an ion crystals at rest was counted. These ions were accelerated and the corresponding fluorescence rate was measured. A typical peak rate of 3 kHz per ion (in a 1 mm window) subject to the scanning co-propagating laser (as in fig. 3b and fig. 6a) was determined. The absolute fluorescence rate of a non-crystalline beam amounts to about 30% of the crystalline.

The phase transition is furthermore pinpointed by the sudden decrease of the transverse beam size shown in fig. 4. The transition is induced by increasing the radial fo-

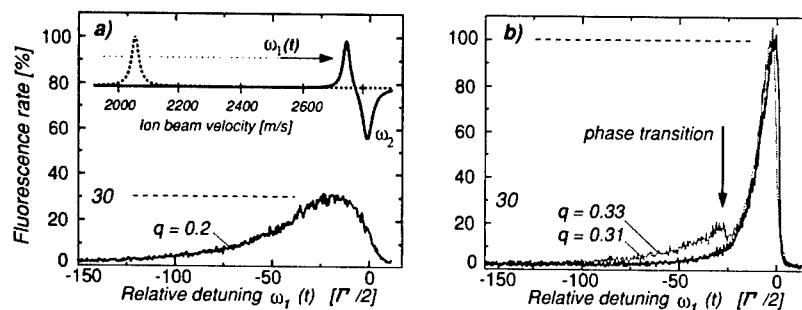


FIGURE 3. Fluorescence rate of the ion beam as a function of the frequency detuning of the co-propagating laser (in terms of half the natural transition line width $\Gamma = 2\pi \cdot 42.7$ MHz). This accelerating laser is slowly tuned (within 4s) towards the resonance with the counter-propagating, decelerating laser at fixed frequency, which defines the nominal velocity. Fig. a) shows the relative signal of a non-crystalline beam, where in fig. b), the marked discontinuity is characteristic of the phase transition to the crystalline beam. The crystalline beam contained 18,000 Mg^+ ions, as deduced from the absolute fluorescence rate. (Reprinted from [6] with permission from Macmillan Magazines, Ltd.)

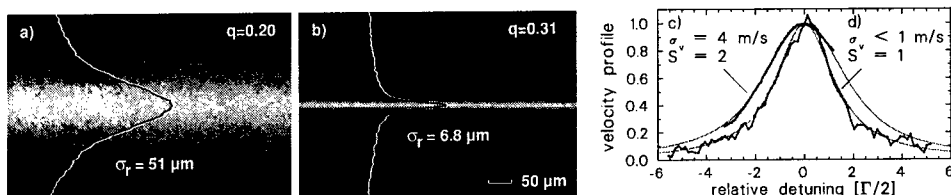


FIGURE 4. Transverse beam profiles before a) and after b) the phase transition, which is induced by increasing the confining potential. For a probe of the longitudinal velocity distribution, the local ion velocity is varied periodically (tube voltage amplitude $\approx 60 \text{ mV}$, frequency $= 1 \text{ Hz}$) inside the pair of drift tubes opposite to the cooling section and thus tuned over the resonance with the fixed frequency probe laser. The corresponding fluorescence rate is recorded. Voigt-profiles (grey lines) are used to disentangle the Doppler-contribution σ_v for the two measurements from the saturation (S) broadened width of the $3s^2S_{1/2} - 3p^2P_{3/2}$ transition. (Reprinted from [6] with permission from Macmillan Magazines, Ltd.)

cusing strength. Since only the longitudinal ion motion is directly laser cooled, this procedure is necessary to enhance the coupling between the ions and thus the cooling of the transverse ion motion. The spatial profile of the crystalline beam coincides with that of a string of ions at rest (fig. 1a) which is, however, close to the spatial resolution of the imaging system. The number of particles in the string (18,000) denotes a mean inter-particle distance $d \approx 20 \mu\text{m}$ and thus a linear density $\lambda = 0.4$ which is consistent with the assumption of the formation of a linear string [19]. The beam radius σ_r corresponds to an initial transverse temperature of $T_{\perp} = 30 \text{ K}$ for the non-crystalline and to a resolution limited value of $T_{\perp} < 0.4 \text{ K}$ for the crystalline beam.

The longitudinal velocity spread of the beam was probed opposite to the cooling section (see fig. 2). Since the probe laser beam was derived from the cooling beam, it could not be frequency tuned. For the detection of a velocity dependent fluorescence signal, the ions were velocity shifted (3% of the beam velocity over a path length of 20 mm) while entering and leaving the pair of drift tubes accented in fig. 2. For a slow (1 Hz) periodic variation of the resulting local ion velocity inside the tube, the fluorescence rate was recorded. To assure that the crystalline structure was not affected, the shape of the beam profile was monitored. The resulting line profiles in fig. 4c) and d) reveal a width of the velocity distribution of 4 m/s ($T_{\parallel} = 50 \text{ mK}$) for the cold but non-crystalline beam and less than 1 m/s ($T_{\parallel} < 3 \text{ mK}$) for the crystalline beam, close to the Doppler-limit of 1 mK .

Usually, the inter-ion coupling strength is described by the plasma parameter $\Gamma_p = (e^2/4\pi\epsilon_0 d) \cdot (1/kT)$, the ratio of the mutual potential energy of ions to their mean thermal energy kT . In the longitudinal degree of freedom, Γ_p amounts to 250 for the circulating ion string. It even exceeds the theoretical threshold of 180 which is required for the formation of three-dimensional ion crystals [34, 20]. The independent measurement of the transverse temperature of the crystal reveals a value of $\Gamma_p > 2$. This value consistently points towards strong coupling, where both components have to be identical, since, for ion beams, a collapse of the beam heating due to intra-beam scattering is expected for $\Gamma_p > 0.5$ [21, 22]. In summary, the full phase space density has

been determined to increase by a factor of at least 10^4 and, assuming $T_{\perp} = T_{\parallel}$, beyond 10^6 in the above phase transition [6].

Moreover, already the weakly confined non-crystalline beam (fig. 4a and c) appears to show some Coulomb-order [7]. Its longitudinal temperature leads to a plasma parameter $\Gamma_p > 3$ with the assumption that the typical inter-ion distance is of the order of the radial beam extension $d \sim 2 \cdot \sigma_r$. Under this anisotropic condition ($T_{\parallel} \ll T_{\perp}$), the ions perform more than ten betatron oscillations during one binary collision [9]. Therefore, the particles can be regarded as smeared out in the transverse direction by their fast oscillation, but localized in the longitudinal to within the mean particle separation of $\bar{d} \approx 20 \mu\text{m}$. They behave like transverse discs which cannot overtake each other, and Coulomb-order over several neighbouring discs should occur. One expects a partial decoupling of the longitudinal and transverse motion [35], responsible for the inefficient indirect cooling of the transverse motion in the weak confining potential.

STABILITY OF ION CRYSTALS AND CRYSTALLINE BEAMS

One of the outstanding properties of ion crystals is their elasticity which leads to a strong suppression of the coupling of the periodic rf motion into random thermal motion [36]. Under continuous laser-cooling, circulating ion strings were observed to survive for many hours without any significant ion loss. For the qualitative study of the heating rates, both cooling lasers were simultaneously blocked for a given period of time. The lasers were unblocked and the fluorescence rate was measured [6, 7]. For the ion crystal at rest (a helix as depicted in fig. 1b), the fluorescence rate immediately reappears at its full strength for blocking periods of up to 90 s, as shown in fig. 5a)-c). This indicates the persistence of the crystalline state. In contrast, after a blocking time of

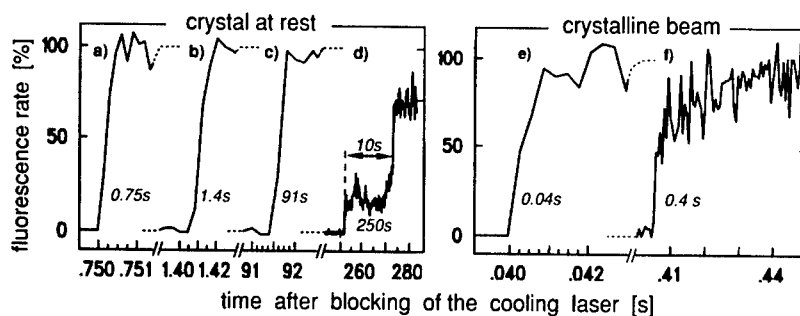


FIGURE 5. Fluorescence signal of the ion crystal at rest and the crystalline beam after blocking and unblocking the cooling lasers. The crystal at rest a)-d) survives blocking periods of the order of seconds to minutes, where for a) the time resolution of $250 \mu\text{s}$ excludes the possibility of melting and subsequent re-crystallization within the rise-time of the fluorescence signal. For the blocking period of 250 s the crystal melts d) and re-crystallizes after 10 s of cooling on a time-scale of seconds. The crystalline beam e)-f) shows an instantaneous recovery after 40 ms e). After blocking the cooling for 400 ms f), the count rate jumps back to 50 % of the initial level and fully recovers within a time scale of 10 ms. (Reprinted from [6] with permission from Macmillan Magazines, Ltd.)

250 s (fig. 5d), the fluorescence reappears to a level of only 25 % which is characteristic for the gaseous cloud (compare fig. 3a and b). After the melting of the crystal, the ions are heated due to Coulomb-scattering in the presence of the rf field. Ions are lost out of the velocity range defined by the relative detuning of the two cooling lasers. This results in a strong reduction of the cooling rate, as reflected in the comparably long time span of 10 s needed for the re-crystallization. The survival time of $6 \cdot 10^8$ rf periods reasonably coincides with recent simulations [36] of ion crystal stability in time-varying potentials. A similar procedure for the crystalline ion beam also results in an immediate restoration of the fluorescence signal after 40 ms of blocking the lasers (fig. 5e). After a period of 400 ms (fig. 5f) the signal reappears at a level of 50 %, a signal rate that reflects the survival of a less dense crystalline beam. Subsequently, the signal fully recovers on a ms time scale. We therefore propose the formation of a two phase regime, in which a string of decreased ion number survives. From the fast recovery time and the fact that the beam is only cooled on a fraction of 1 % of the orbit, it seems unlikely that ions are dominantly heated in longitudinal direction. Probably, a fraction of the beam either forms a cold halo or starts to show the disc-like behaviour, discussed above.

2D-3D CRYSTALLINE BEAMS (ZIG-ZAGS AND HELICES)

The attainment of crystalline beams of higher linear density ($\lambda > 0.7$) than the strings discussed so far is of general interest concerning the feasibility of increased luminosity at high-energy rings. In particular, the question of shear and the consequence of cooling to constant angular velocity becomes important as well as the increased coupling of the beam to the time-varying confining potential [23, 25, 4, 5, 20]. However, the unambiguous identification of 2D and 3D crystalline beams becomes more difficult.

In fig. 6a)-b), we present images of a crystalline beam right at the threshold of the transition from the 1D string to the 2D zig-zag configuration. A slight decrease of the confining potential ($q = 0.22 \rightarrow 0.20$) corresponds to an increase in the linear density of $\lambda = 0.70 \rightarrow 0.77$ and therefore to the evolution of a zig-zag beam [19]. In fig. 6c) the latter profile b) is enlarged. Its absolute shape can be reproduced by the sum of two profiles of the corresponding linear string (fig. 6a), divided in amplitude by a factor of two and displaced vertically by $\pm 6 \mu\text{m}$. Furthermore, we observed (fig. 6d) a similar discontinuity in the fluorescence signal when the laser is tuned as in the case of the string (fig. 3b), which supports the interpretation of the beam profile. The orientation of the zig-zag beam is always vertical to circumvent shear [7]. Compared to the profile of 2D crystals at rest (fig. 1a), the contrast of the beam profile is markedly reduced, which still could be a problem of the comparably low overall count-rate.

For the description of the measured profiles of the crystalline and of the non-crystalline beams (see fig. 4 and 6) close to the phase transition, a double Gaussian distribution with the width σ^c and σ^h and the amplitude I^c and I^h of a core and a halo component has to be applied. In fig. 7, the amplitude ratio I^h/I^c as well as the width of the halo σ^h are shown as a function of the width σ^c of the central core. For the non-crystalline beams (open symbols), where the width is a measure of the temperature, σ^c and σ^h are normalized to $U_{rf} = 350 \text{ V}$ ($q = 0.28$) according to $kT \propto \Psi(\sigma) \propto (U_{rf} \cdot \sigma)^2$.

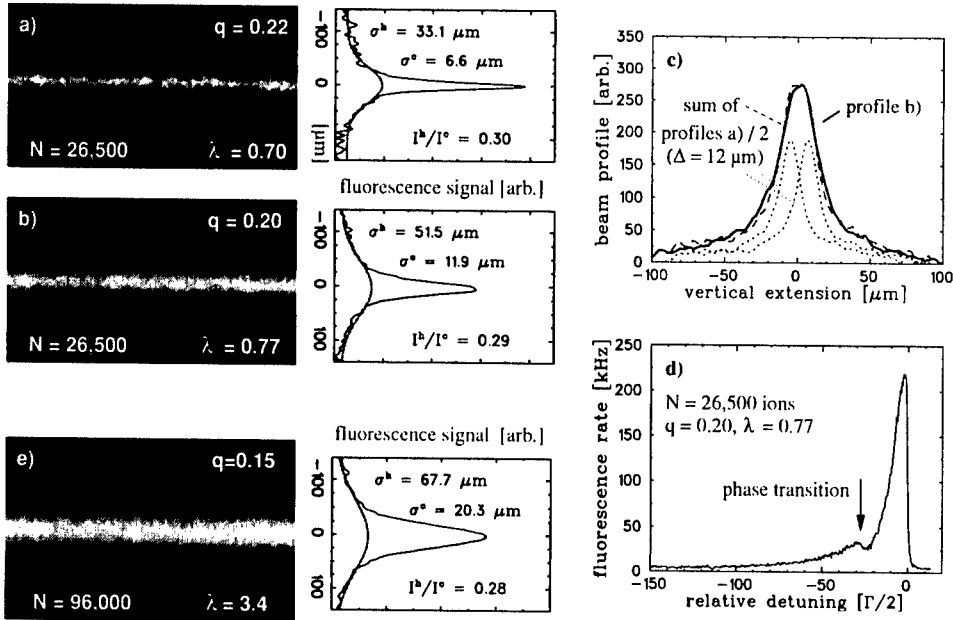


FIGURE 6. Vertical beam profiles of the same beam for two slightly different confining potentials a)-b), which demonstrate the transition from the string to the zig-zag. In c), the shape of this zig-zag beam is analyzed, where in d), its fluorescence rate is depicted as a function of the (dynamic) laser detuning. The profile e) belongs to a 3D crystalline beam, presumably a helix with a string in the center.

For the transition to the 1D crystalline beam around $\sigma^e \approx 10 \mu\text{m}$, we find a significant reduction of the amplitude ratio of the halo to the core component I^h/I^e . This separation is even more pronounced in the original data (some non-crystalline data points were recorded at low rf voltages of about $U_{rf} \approx 150 - 250 \text{ V}$ and thus plotted at radii σ^e , normalized to lower values). The remaining halo contribution is observed to coincide for all crystalline ion strings in flight and at rest, recorded in PALLAS and taken from ref. [15]. The coincidence suggests that this contribution might be due to scattering of light in the optical imaging system or at least due to a process not attributed to the crystalline beam. Furthermore, the amplitude ratio remains nearly constant for the zig-zag beam (marked with the left arrow) although the width of its core component has naturally increased. This fact is valid also for larger crystals at rest, where the width of the core can be described by a Woods-Saxon profile. This set of reference data allows the distinction of 1D and 2D crystalline beams from non-crystalline beams although the reason for the significant halo component observed in the transverse profiles of the non-crystalline beams remains unclear at the moment.

The beam profile, presented in fig. 6e), belongs to a beam of 96,000 ions. Already from the comparably small width in relation to the high particle number, one can roughly estimate the beam to be crystalline (compare fig. 4a). The ratio I^h/I^e (marked with the right arrow in fig. 7) clearly corresponds to that of a crystalline structure. The linear

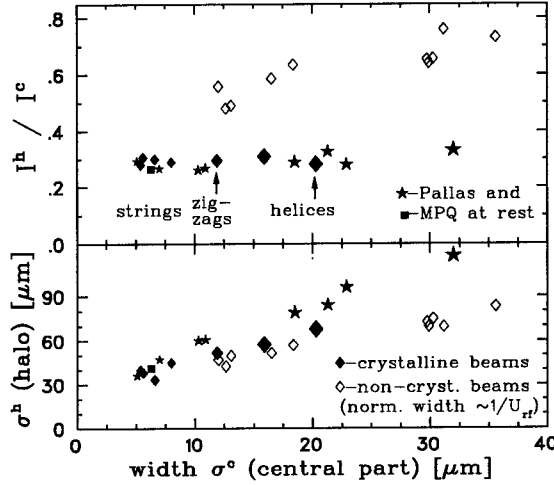


FIGURE 7. For coasting beams as well as for a variety of ion crystals at rest, the behaviour of the beam profile, described by a two component Gaussian distribution, is shown as a function of the width σ^c of the central component. For the non-crystalline beams (open symbols), σ^c and σ^h are normalized to $U_{rf} = 350$ V. The marked points correspond to the beam profiles presented in the previous figure.

density of $\lambda = 3.4$ corresponds to a helix encircling a string [19]. Though cooled to constant linear velocity, this large crystalline beam withstands bending shear. According to [23], for the high betatron tune of $Q \approx 40 > \lambda$, the Coulomb force within the crystal is strong enough to arrange constant angular velocity.

Concerning the formation of the two component profiles which were observed to be characteristic for the non-crystalline beams in PALLAS, we can only speculate at present [7]. The linear relation of σ^h and σ^c suggests some correlation between both components. Since the scaling is independent of the longitudinal cooling strength and of the focusing potential, a radius dependent heating rate seems to be less probable. The width σ of a beam is related to its transverse temperature $kT_{\perp} \propto m\omega_{sec}^2 \sigma^2$. Thus, one could imagine the co-existence of individual (halo) ions and short string fragments (core) of different collective mass at the same temperature T_{\perp} to describe the two components. Both phases could simultaneously exist at different orbital positions in the storage ring, since cooling is restricted to only a fraction of the circumference. In ion trap experiments [32], bi-stability is well established. Also transverse oscillations of short crystalline strings were observed [18]. However, the effect has to be further explored.

SUMMARY AND OUTLOOK

The realization of circulating ion strings [6] and of first vertical zig-zag and helical structures in PALLAS allows to experimentally investigate many questions concerning the formation of crystalline beams in high-energy rings, known up to now only from simulations [4, 5, 20]. The focusing conditions, the linear ion density, and the beam

velocity can be independently varied, the latter presently between 10^3 and 10^4 m/s. In the near future, we plan to implement optical Schottky-diagnosis to study noise spectra of cold and crystalline beams, which carry further information about collective effects. Furthermore, bunching of an ion beam was studied and will be reported elsewhere [7].

ACKNOWLEDGEMENTS

This work has been supported by the DFG (HA1101/8) and the MLL. We acknowledge fruitful discussions with P. Kienle and H. Walther and technical support by R. Neugart.

REFERENCES

1. Parkhomchuk, V., "Review of Electron Cooling Investigation at the Novosibirsk INP", in [5], pp. 409-420 and Pestrikov, D.V., "Schottky Spectra and Crystalline Beams", in *ibid.*, pp. 275-294.
2. Schiffer, J.P., Kienle, P., *Z. Phys. A* **321**, 181 (1985).
3. Rahman, A., Schiffer, J.P., *Phys. Rev. Lett.* **57**, 1133-1136 (1986).
4. Hasse, R.W., Hofmann, I., Liesen, D., (eds.), *Crystalline Ion Beams*, GSI report, GSI-89-10, (1989).
5. Maletic, D.M., Ruggiero, A.G., (eds.), *Crystalline Beams*, World Scientific, Singapore, 1996.
6. Schätz, T., Schramm, U., Habs, D., *Nature* (London), in press (16/8/2001).
7. Schramm, U., Schätz, T., Habs, D., submitted to *Phys. Rev. Lett.* (2001).
8. Steck, M., et al., *Phys. Rev. Lett.* **77**, 3803-3806 (1996).
9. Hasse, R.W., *Phys. Rev. Lett.* **83**, 3430-3433 (1999) and these proceedings.
10. Radon, T., et al., *Nucl. Phys. A* **677**, 75-99 (2000).
11. Lauer, I., et al., *Phys. Rev. Lett.* **81**, 2052-2055 (1998).
12. Eisenbarth, U., et al., *Nucl. Instr. and Meth. A* **441**, 209-218 (2000).
13. Eisenbarth, U., et al., *Hyp. Int.* **127**, 223-235 (2000) and these proceedings.
14. Madsen, N., et al., *Phys. Rev. Lett.* **83**, 4301-4304 (1999).
15. Birkel, G., Kassner, S., Walther, H., *Nature* **357**, 310-313 (1992).
16. Raizen, M.G., et al., *Phys. Rev. A* **45**, 6493-6501 (1992).
17. Drewsen, M., et al., *Phys. Rev. Lett.* **81**, 2878-2881 (1998) and these proceedings.
18. Schramm, U., Schätz, T., Habs, D., "Laser-cooling of Ions and Ion Acceleration in PALLAS", in *Appl. of Acc. in Research and Industry*, ed. J.L. Duggan, AIP Conf. Proc. **576**, in press (2001).
19. Hasse, R.W., Schiffer, J.P., *Annals of Phys.* **203**, 419-448 (1990).
20. Habs, D., Grimm, R., *Ann. Rev. Nucl. Part. Sci.* **45**, 391-428 (1995).
21. Seurer, M., Spreiter, Q., Toepffer, C., "IBS in Dense and Cold Beams", in [5], pp. 311-328.
22. Wei, J., et al., "Diverse Topics in Crystalline Beams", in [5], pp. 229-252.
23. Schiffer, J.P., "The Physics of Crystalline Ion Beams", in [5], pp. 217-228.
24. Spreiter, Q., Seurer, M., Toepffer, C., *Nucl. Instr. Meth. A* **364**, 239-242 (1995).
25. Wei, J., Okamoto, H., Sessler, A.M., *Phys. Rev. Lett.* **80**, 2606-2609 (1998).
26. Riabko, A., et al., *Phys. Rev. E* **51**, 3529-3546 (1995).
27. Kjaergaard, N., Drewsen, M., *Phys. of Plasmas* **8**, 1371-1375 (2001).
28. Bryant, P.J., Johnson, K., *Circular Accelerators and Storage Rings*, Cambridge Univ. Press, 1993.
29. Schätz, T., et al., "Towards crystalline ion beams - the PALLAS ring trap", in *Trapped Charged Particles and Fund. Phys.*, eds. D. Dubin, D. Schneider, AIP Conf. Proc. **457**, 1999, pp. 269-273.
30. Schätz, T., Schramm, U., Habs, D., *Hyp. Int.* **115**, 29-36 (1998).
31. P.K. Gosh, *Ion Traps*, Clarendon Press, Oxford (1995).
32. Diedrich, F., et al., *Phys. Rev. Lett.* **59**, 2931-2934 (1987).
33. Blümel, R., et al., *Nature* **334**, 309-313 (1988).
34. Dubin, D.H.E., *Phys. Rev. A* **42**, 4972-4982 (1990).
35. Hasse, R.W., *Phys. Rev. A* **46**, 5189 (1992).
36. Schiffer, J.P., et al., *Proc. Natl. Acad. Sci. USA* **97**, 10697-10700 (2000)

Multiple Coulomb Ordered Strings of Ions in a Storage Ring

Rainer W. Hasse

GSI Darmstadt, D-64291 Darmstadt, Germany

Abstract. We explain that the anomalous frequency shifts of very close masses measured in the high precision mass measurement experiments in the ESR storage ring result from the locking of Coulomb interacting strings of ions. Here two concentric strings which run horizontally close to each other for many revolutions are captured into a single string if their thermal clouds overlap. They give up their identity and lock into an average frequency.

Last conference [1], see also ref. [2], we reported on theoretical analyses of experiments with low density highly charged ions cooled to ultralow momentum spread in a storage ring. It was shown that the ions here run on strings not being able pass each other any more. In this contribution we extend this work and conclude that in recent high precision mass measurements under similar conditions two (or more) adjacent strings have been created which are so closely situated that they loose their identity and form a common string, cf. also ref. [3].

In a recent paper, Radon *et al.* [4] reported on high precision mass measurements with Schottky mass spectrometry of many new isotopes in the region $57 \leq Z \leq 84$ with a high resolving power of 3.3×10^5 . This value is not only limited by the stability of the bending and focussing magnets but also by the effect of anomalous frequency shifts discussed below. In this experiment fully stripped isotopes were produced by fragmentation of a $^{209}\text{Bi}^{67+}$ beam at 930 MeV/u, separated in the fragment separator, and stored and cooled in the storage ring ESR. The electron cooler cooled down the remaining few thousand isotopes to a longitudinal velocity spread as low as $\delta v/v = 7 \times 10^{-7}$, where $v = \beta c = 0.685c$ is the beam velocity. The corresponding momentum spread was $\delta p/p = \gamma^2 \delta v/v = 1.3 \times 10^{-6}$, where $\gamma = 1.37$ is the relativistic factor.

For fixed magnetic rigidity $B\rho$ around 7 Tm each species of the beam has its own frequency $f_i = v/C_i$, where C_i is the length of its trajectory close to the circumference of the ESR, $C=108.4$ m. Neighboring masses Δm by their slightly different trajectories due to different rigidities, thus have different frequencies

$$\frac{\Delta f}{f} = -\alpha_p \frac{\Delta(m/q)}{(m/q)} \pm \left(1 - \frac{\gamma^2}{\gamma_t^2}\right) \frac{\delta v}{v}. \quad (1)$$

Here q is the charge and $\gamma_t = 2.67$ is the transition energy which is connected to the slip factor $\eta = \gamma^{-2} - \gamma_t^{-2} = 0.39$ and to the momentum compaction factor

$$\alpha_p = \frac{1}{\gamma_t^2} = \int_0^C \frac{D(z)}{r(z)} \frac{dz}{C} = 0.14, \quad (2)$$

where $D(z)$ is the dispersion function and $r(z)$ is the local radius of the central orbit. Note that without the effect of dispersion from the bending magnets, $\alpha_p = 0$, the average length of the trajectories and, hence, all frequencies would be the same.

The measurements were done at the 16th harmonic of the revolution frequency 1.9 MHz, hence $f=30.4$ MHz and the noise frequency from the last term of eq. (1) is about 15 Hz. At present, experiments are under way [5] at the transition energy, $\gamma = \gamma_t$, in which these noise effects are eliminated although no cooling is needed. Each spectrum obtained was averaged up to ten thousand times and the masses were identified and determined with sophisticated analysis on the basis of eq. (1).

In the results typical deviations were found from the measured frequencies of known isotopes as compared to the known calibration values. As shown in Fig. 1, if there are at least two masses so close to each other that their difference in frequencies is smaller than about 80...90 Hz, on the average the lower (higher) one is shifted characteristically to a higher (lower) value. According to eq. (1) this anomalous effect limits the mass resolution to about $20 \mu u$ and such masses then have to be discarded from the results. They are the major reason for the systematic errors. The authors believe that *due to a high number of ions circulating with close distances next to each other in the ESR, Coulomb interactions may lead to collective coupled motion.*

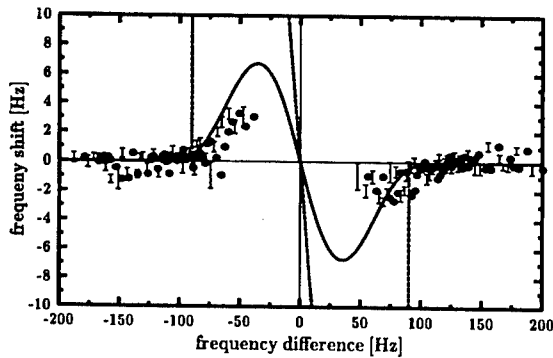


FIGURE 1. Average anomalous frequency shifts of neighboring isotopes vs. difference between their measured frequencies. Each point is the average of about 100 data (after ref. [4]). The result of the model calculation included (full line) and the sawtooth curve (dashed line, only partly in the frame) which would result without folding are discussed below.

In what follows we explain and make a model for the origin of these anomalous frequency shifts on the basis of the anticipation that the ions run on correlated trajectories. The situation here is similar to the one of the machine experiments on the anomalous jump to very low momentum spreads in the ESR [6] and in the SIS [7]. There it has been shown [2] that under the experimental conditions intra-beam scattering is completely suppressed and that the ions cannot pass each other any more and, thus, run on strings.

With the parameters give above and a mean tune of $Q = 2.3$ the Wigner-Seitz radius is $a_{WS} = (3q^2/2m\omega_\beta^2)^{1/3} = 14 \mu m$, where the betatron frequency $\omega_\beta = Q\omega_{rev}$ is the Q -fold of the revolution frequency. The Wigner-Seitz radius roughly is the closest distance which ions can attain in infinite Coulomb matter at zero temperature. With

2000 (5000) ions in the ring the particles have an average distance in the beam direction of $d = 5(2)$ cm and a linear density of $\lambda = a_{ws}/d = 0.00025$ (0.0007), which is well within the region of stable strings, $\lambda < 0.7$ [8]. The average Coulomb energy between two particles at distance d is $e_C = q^2\gamma/d = 0.19$ (0.47) meV. With the methods of ref. [2] we derive a longitudinal kinetic energy $T_{\text{long}} = m(c\beta \delta v/v)^2/(8 \ln 2) = 3$ meV and take the same transverse kinetic energy as in [6], $T_{\text{trans}} = 1.5$ eV. The *FWHM* transverse thermal diameter of the projection of the ion cloud onto the transverse plane calculated in the harmonic oscillator potential generated by the betatron frequency $\omega_\beta = 2\pi Q\beta c/C$ becomes $2\delta x = 4d\sqrt{\lambda^3 T_{\text{trans}}/3e_C} = 46 \mu\text{m}$ [9]. An estimate for the transverse emittance from $\epsilon_{\text{trans}} = (\delta x)^2/\beta_{\text{trans}}$ with $\beta_{\text{trans}} \approx 15$ m [6] being the average transverse beta function in the free sections yields the extremely low value $4 \times 10^{-5} \pi$ mm mrad. All these parameters are of the same order of magnitude as in the experiments of ref. [6]. Consequently, in the present experiment the ions have to run on strings as well.

Nuclides with different masses but with the same velocity run on different trajectories which are horizontally displaced so that, apart from fluctuations from noise, $v = Cf$ remains constant, thus

$$\frac{\Delta C}{C} = -\frac{\Delta f}{f}. \quad (3)$$

This difference in length of trajectory transforms into the horizontal displacement $-\Delta x = (C/2\pi)\Delta f/f = 17 \text{ m} \times \Delta f/f$ which attains the value 43...48 μm for the experimental value of Fig. 1 of the onset of the anomalous frequency shifts at $\Delta f = 80\text{...}90$ Hz. In addition, the dispersion by the bending magnets also causes a horizontal displacement

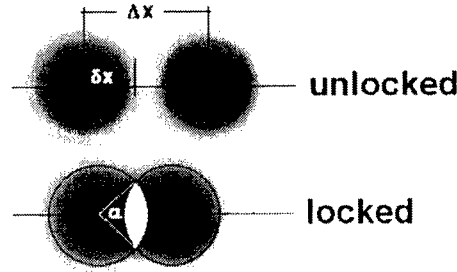


FIGURE 2. Schematic drawing of the projection of the ion clouds onto the transverse plane in the unlocked and locked cases.

due to the remaining thermal fluctuations. With the dispersion function of the ESR, the average dispersion is about $\bar{D} \approx 2.4$ m. Hence the maximum thermal displacement $\bar{D}\delta v/v \approx 1.7 \mu\text{m}$ should be small as compared to the displacement of eq. (3). An additional displacement from the centrifugal force can be neglected since this effect would be smaller by a factor of $\Delta x/C \approx 4 \times 10^{-7}$.

This fact leads to the model of Fig. 2, namely that if the displacement is larger than the thermal diameter, the two (or more) strings run on well separated trajectories yielding two (or more) distinct peaks in the Schottky spectrum which lie at the correct positions. However, in the opposite case when the clouds overlap, the strings lose their identity and lock partially or fully into the same frequency, thus smaller frequencies apparently become larger and vice versa.

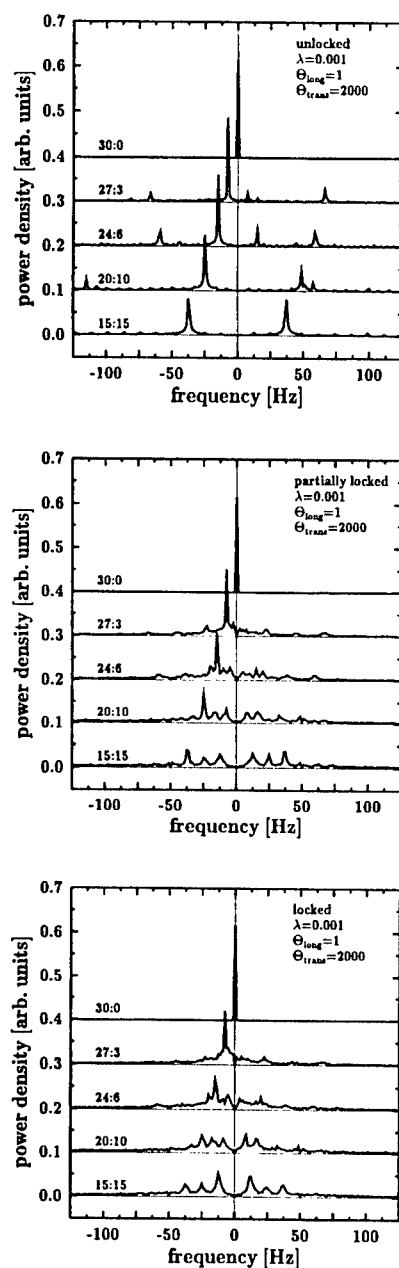


FIGURE 3. Theoretical averaged Fourier spectra around the third harmonic from Molecular Dynamics calculations with 30 particles in a repeating boundary box distributed over two strings with the occupation numbers written at the bases. Unlocked, partially locked and locked means that the displacements of the strings are larger, in between and smaller than the thermal diameter. Θ_{long} and Θ_{trans} are the longitudinal and transverse kinetic energies in units of the Coulomb interaction energy of two particles at distance d and λ is the linear density.

Assuming that this locking is not *ad hoc* but by virtue of the averaging procedure over the experimental data that there is a smooth transition with a probability proportional to the overlap region of the clouds, $P = [\alpha - \sin(\alpha)]/\pi$, where α is the opening angle of Fig. 2, and folding this probability together with the experimental resolution of 15 Hz into the sawtooth curve $-f\Theta(|90 \text{ Hz}| - f)$ of shifts (the dashed lines in Fig. 1), where Θ is the Heaviside function, yields the result of Fig. 1. The dashed sawtooth line would result if the strings were always captured if their thermal radii start to overlap. Note that apart from the uncertainty coming from the assumed capture probability this model has no free parameters and that the result agrees nicely with the experiment.

In order to substantiate this we performed classical 3D Molecular Dynamics calculations with the methods of refs. [8],[9] in the geometry of an infinite straight cylinder. Here 30 particles are distributed in a disk over two strings with different occupation. Their initial positions and velocities are distributed randomly according to their available longitudinal and transverse kinetic energies (the number of particles in the simulation is limited by the computer memory for the fast Fourier transform). The small disk of the cylinder has repeating boundary conditions, thus summing up all Coulomb interactions by Ewald summation, see ref. [8]. The effect of different masses or frequencies in this straight geometry is transformed to different velocities of the strings according to eq. 1, i.e. a relative velocity in the rest frame which corresponds to a frequency difference of 75 Hz. No cooling mechanism is incorporated. All positions over 5000 betatron oscillations in a lattice with solenoidal focusing with the mean tune of the ESR are then Fourier transformed and each spectrum has been averaged over 11 runs with different random initial conditions to yield Fig. 3. Here the occupation numbers of the strings are written at the bases and the relative temperatures with respect to the average Coulomb interaction energy between two ions are indicated in the key.

The upper frame treats the unlocked case where the distance between the strings is much larger than the thermal diameter. Here the difference of 75 Hz between the frequencies of the two central peaks in the lower curve with equal occupation corresponds to the relative velocity between the strings. Although the strengths of the peaks vary with the occupation their distance remains constant. In the bottom frame, the locked case, the particles have lost their identity resulting in a broad random distribution. The partially locked case is intermediate.

There is indication that the effect of locking or capture is not restricted to the existence of ultra-cold chains. As pointed out in ref. [10], during the preparation of the precision mass experiments similar anomalous frequency shifts have been observed in an experiment with a bare $^{197}\text{Au}^{79+}$ beam at 295 MeV/u. Its isotopes $^{196,195,194}\text{Au}^{79+}$ and other strongly populated fragments had velocity spreads of about $\delta v/v = 10^{-5}$ and thermal widths of about 4 mm. By scraping the primary beam down to a width of 600 μm and under steady electron cooling the velocity spread decreased by one order of magnitude. Nearby fragment nuclides with slightly larger masses then acquired anomalous negative frequency shifts of the order of a few Hertz, see Fig. 4. This effect remained if the primary beam was further scraped to a width of 50 μm .

Evidently, the low intensity fragment isotopes (with negative shifts and error bars) and masses slightly larger than the mass of the primary beam (with nearly zero shifts and no error bars) have been absorbed into the cloud of the primary beam itself, thereby reducing their frequencies slightly. Unfortunately, there are no isotopes with masses

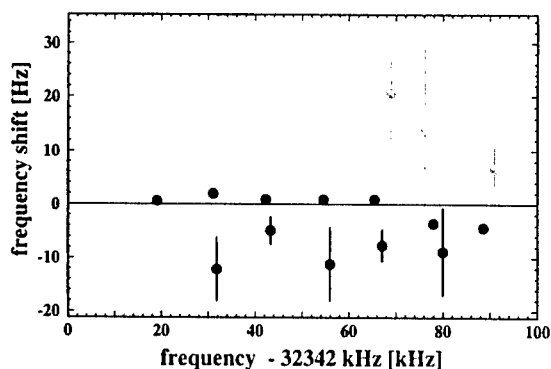


FIGURE 4. Measured anomalous frequency shifts in a relatively warm beam. The dots with nearly zero shifts belong to isotopes of the primary beam, others are nearby fragment nuclides. The gray dots are questionable by the lack of intensity (after ref.[10])

slightly less than the primary beam masses with sufficient population. Hence in Fig. 4 the gray dots should be discarded because the signals came from very few ions only.

In summary, we have shown that with the high precision mass measurements in the ESR very cold multiple strings of ions have been produced which either run parallel to each other or lock into a single string if their displacement becomes very small.

The Windows simulation program RODS (Representation Of Dynamical Strings) is available on the web page www-aix.gsi.de/~hasse/hasse.html. The author likes to thank Z. Patyk for pointing out this problem and H. Geissel, K.E.G. Löbner, T. Radon and B. Schlitt for valuable discussions on the experiments.

REFERENCES

1. R.W. Hasse, *Proc. 1999 Workshop on Nonneutral Plasma Physics, Princeton, NJ. August 1-5*, AIP Conf. Proc. **198**, 329 (1999)
2. R.W. Hasse, *Phys. Rev. Lett.* **83**, 3430 (1999)
3. R.W. Hasse, *Phys. Rev. Lett.* **86**, 3028 (2001)
4. T. Radon, H. Geissel, G. Münzenberg, G. Franzke, Th. Kerscher, F. Nolden, Yu.N. Novikov, Z. Patyk, C. Scheidenberger, F. Attallah, K. Beckert, T. Beha, F. Bosch, H. Eickhoff, M. Falch, Y. Fujita, M. Hausmann, F. Herfurth, H. Irnich, H.C. Jung, O. Klepper, C. Kozhuharov, Yu.A. Litvinov, K.E.G. Löbner, F. Nickel, H. Reich, W. Schwab, B. Schlitt, M. Steck, K. Sümmerer, T. Winkler, and H. Wollnik, *Nucl. Phys. A* **677**, 75 (2000)
5. M. Hausmann, F. Attallah, K. Beckert, F. Bosch, A. Dolinskiy, H. Eickhoff, M. Falch, B. Franczak, H. Geissel, Th. Kerscher, O. Klepper, H.-J. Kluge, C. Kozhuharov, K.E.G. Löbner, G. Münzenberg, F. Nolden, Yu.N. Novikov, T. Radon, H. Schatz, C. Scheidenberger, J. Stadlmann, M. Steck, T. Winkler, and H. Wollnik, *Nucl. Inst. Meth. in Pys. Res. A* **446**, 569 (2000)
6. M. Steck, K. Beckert, H. Eickhoff, B. Franzke, F. Nolden, H. Reich, B. Schlitt and T. Winkler, *Phys. Rev. Lett.* **77**, 3803 (1996)
7. R.W. Hasse, M. Steck, *Proc. 7th Europ. Part. Acc. Conf.*, 26-30 June 2000, Vienna (2000) p. 274
8. R.W. Hasse, and J.P. Schiffer, *Ann. Phys. (NY)* **203**, 419 (1990)
9. R.W. Hasse, *Phys. Rev. A* **46**, 5189 (1992)
10. B. Schlitt, *PhD. thesis Univ. Heidelberg*, GSI report DISS. 97-01, GSI Darmstadt (1997)

SECTION 4

COLLECTIVE MODES

Thermal Excitation of Trivelpiece-Gould Modes in a Pure Electron Plasma

Francois Anderegg*, Nobuyasu Shiga*, James R. Danielson*, Daniel H.E. Dubin*, C. Fred Driscoll* and Roy W. Gould†

*Dept. of Physics and Institute for Pure and Applied Physical Sciences, UCSD, La Jolla CA USA
92093-0319

†California Institute of Technology, Mail Stop 128-95, Pasadena CA 91103

Abstract. Thermally excited plasma modes are observed in trapped, near-thermal-equilibrium pure electron plasmas over a temperature range of $0.05 < T < 5$ eV. The measured thermal emission spectra together with a separate measurement of the wave absorption coefficient uniquely determines the temperature. Alternately, kinetic theory including the antenna geometry and the measured mode damping (i.e. spectral width) gives the plasma impedance, obviating the reflection measurement. This non-destructive temperature diagnostic agrees well with standard diagnostics, and may be useful for expensive species such as anti-matter.

Even in a stable plasma there are a finite level of fluctuating electric field and plasma waves. The plasma waves are “normal modes” [1] of the system, and represent degrees of freedom which are excited in thermal equilibrium. Plasma waves are emitted by particles as they move about in the plasma, and they are absorbed (e.g. Landau-damped) by the plasma. The balance between emission and absorption leads to a thermal level of field fluctuation. Thermally excited modes can be a diagnostic tool for non-neutral plasmas as shown by Gould for cyclotron waves [2]. Similarly, center of mass modes are commonly used in the “single particle regime” with a highly tuned resonant circuit [3].

We describe measurements of spontaneous thermal excitation of Trivelpiece-Gould (TG) modes. The thermal radiation observed comes from collective plasma modes. The spectrum of these modes shows several well-separated peaks at the frequency of TG modes. The radiation we describe comes from one of these peaks, typically from the lowest longitudinal and radial mode number of an azimuthally symmetric mode.

Here, the spectrum of thermally-excited T-G modes is measured in near-thermal-equilibrium pure electron plasmas over a temperature range of $0.05 < kT < 5$ eV, using a room-temperature receiver. The received spectrum for each mode is nominally a Lorentzian at frequency f_0 with width γ , superimposed on a background noise level; non-Lorentzian spectra also occur, when the receiver noise and impedance is non-negligible. By Nyquist's theorem, these fluctuations represent thermal noise generated by the real part of the plasma impedance Z_p [4]. The area of the received spectral peak is proportional to kT , but it also depends on the antenna coupling as represented by Z_p . This impedance can be measured directly by a separate wave reflection/absorption measurement, or it can be calculated from a kinetic theory of random test particles. Overall, the technique allows a rapid non-destructive diagnostic of the plasma temperature with

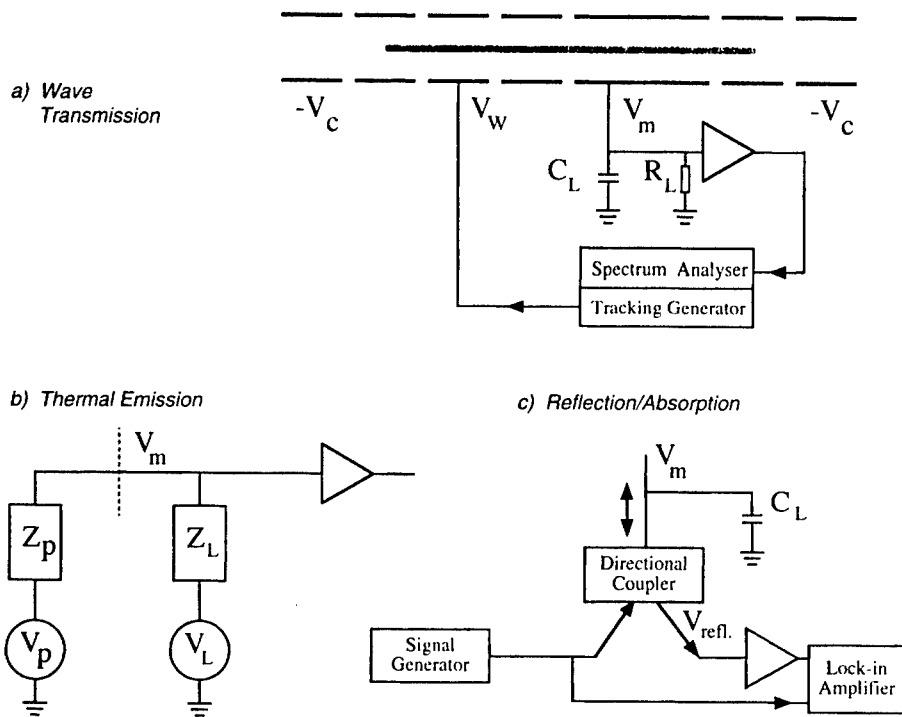


FIGURE 1. Schematic diagram of the cylindrical Penning-Malmberg trap with (a) the wave transmission/reception electronics; (b) the thermal emission equivalent circuit; and (c) the reflection/absorption electronics.

$\pm 25\%$ accuracy.

Fluctuation measurements were obtained from pure electron plasmas combined in two similar Penning-Malmberg traps, "EV" and "IV" [5], differing mainly in plasma diameter and magnetic field strength. The EV trap consists of a series of hollow conducting cylinders of radius $r_w = 3.8$ cm contained in ultra-high vacuum at $P \approx 10^{-10}$ Torr with a uniform axial magnetic field of $B = 375$ G. Electrons are injected from a hot tungsten filament, and contained axially by voltages $V_c \approx -200$ V on end electrodes. Typical plasmas have $N \approx 10^9$ electrons in a column length $L_p \approx 24$ cm, with a plasma radius $r_p \approx 1.7$ cm and a central density $n_0 \approx 10^7$ cm $^{-3}$. For IV, the parameters are $B = 30$ kG, $r_p = 0.2$ cm, $r_w = 2.86$ cm, and $L_p = 41$ cm.

The plasma density profile $n(r)$ and the thermal energy T are obtained by dumping the plasma axially and measuring the total charge passing through a hole in a scanning collimator plate. Both measurements require shot-to-shot reproducibility of the injected plasma, and we typically obtain variability $\delta n/n \leq 1\%$. The EV plasmas expand radially towards the wall with a characteristic "mobility" time of $\tau_m \approx 100$ sec, so the electrons are repetitively injected and dumped. On IV, a "rotating wall" perturbation at $f \sim$

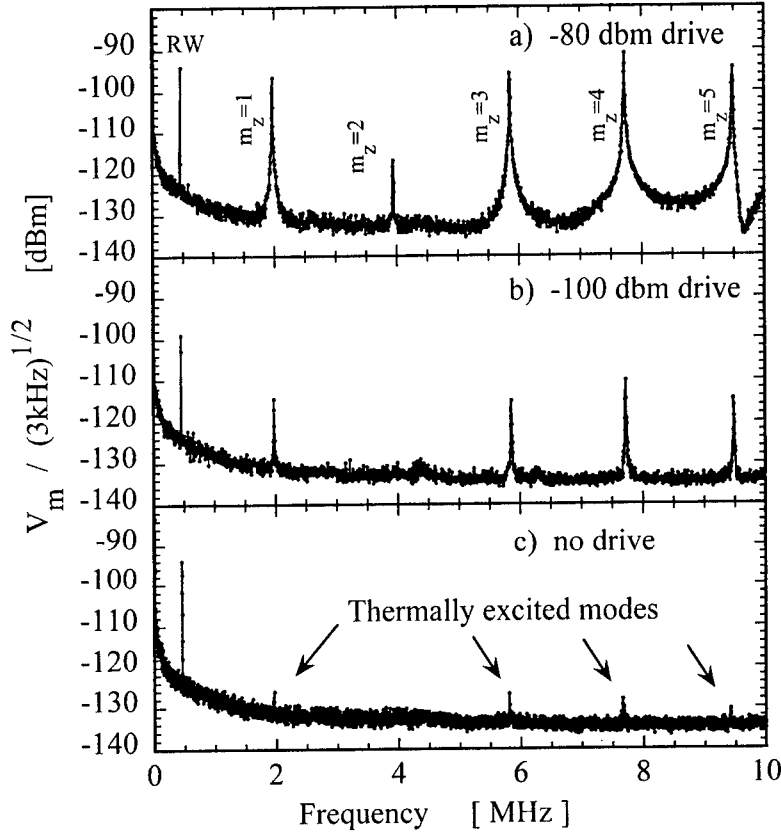


FIGURE 2. a) Spectrum of $m_\theta = 0$, $m_z = 1, 2, \dots, 5$ Trivelpiece-Gould modes for 3 drive amplitudes including no drive, i.e. thermally excited.

0.5 MHz is used to obtain steady-state confinement of the electron column [6].

The parallel temperature T_{\parallel} of the electrons can be measured by slowly lowering the confinement voltage and measuring the escaping charge [7, 8]. On EV, the electrons equilibrate to $T \lesssim 1$ eV soon after injection, whereas the electrons in IV cool to $T \approx 0.05$ eV due to cyclotron radiation. To control the temperature, we apply auxiliary “wiggle” heating by modulating one electrode voltage at a frequency $f = 0.8 - 1.0$ MHz. The amplitude and duration of the heating is adjusted to obtain temperatures up to $T \lesssim 5$ eV; higher temperatures cause background gas ionization and a slow increase in N .

We perform plasma wave *transmission* experiments by applying an RF voltage of amplitude V_w to a (360°) wall electrode at one end of the column (Fig. 1a). V_w induces density perturbations δn in the column which in turn induce the measured voltages V_m on a (360°) receiving electrode with finite load impedance. The load impedance is

$R_L = 750 \Omega$ (IV) or 50Ω (EV) in parallel with $C_L \simeq 440$ pF (IV) and $C_L = 165$ pF (EV).

Figures 2a and 2b show the spectrum of standing $m_\theta = 0$ Trivelpiece-Gould modes [9] excited with excitations of $V_w = -80$ dBm ($22 \mu\text{V}$) and -100 dBm ($2.2 \mu\text{V}$) at frequencies $f = 0.01 - 10$ MHz. These standing waves are plasma oscillations with wavenumber $k_z = \pi m_z / L_p$. Here $\omega_p \equiv (2\pi) 28 \text{ MHz } (n/10^7 \text{ cm}^{-3})^{1/2}$ is the plasma frequency, modified by the finite trap radius, at frequencies

$$f \approx \frac{\omega_p}{2\pi} r_p m_z \frac{\pi}{L_p} \left[\frac{1}{2} \ln r_w / r_p \right]^{1/2} \left[1 + \frac{3}{2} \left(\frac{\bar{v}}{v_\phi} \right)^2 \right]. \quad (1)$$

The axial mode number is $m_z = 1, 2, \dots, 5$, and thermal corrections depend on the ratio of $\bar{v} \equiv (kT/m)^{1/2}$ to the wave phase velocity v_ϕ . In this paper, we focus only on the lowest radial mode $m_r = 1$.

The peak amplitudes are proportional to V_w , as expected for a linear system; the lesser sensitivity for $m_z = 2$ is due to the placement z_c and length ($L_c = 11.7$ cm) of the detection cylinder. The peak amplitudes for the continuous sinusoidal modes are independent of the bandwidth (BW = 3 kHz) of the spectrum analyzer; whereas the spectral amplitude of the inter-mode noise decreases as $(\text{BW})^{-1/2}$ as expected. At $V_w = -100$ dBm, the mode fluctuations have amplitude $\delta n/n \sim 10^{-5}$. The peak labelled RW is the rotating wall drive; the measurements presented here have also been obtained with the drive off.

Small peaks representing thermally excited modes are still visible in Fig. 2c when the transmitter electrode is grounded ($V_w = 0$). These peaks have amplitudes of $-124 \text{ dBm}/\sqrt{3 \text{ kHz}}$, representing voltage fluctuations on the electrode with spectral intensity $V_m \approx 2.6 nV/\sqrt{\text{Hz}}$.

Figure 3 shows received spectra of the thermally excited $m_z = 1$ mode for 4 similar plasmas of different temperature. The mode frequency f_0 increases with temperature, as expected from Eq. (1). The width of the spectral peak represents mode damping, and this width increases substantially as Landau damping becomes significant for $T \gtrsim 0.5$ eV. We will see below that the integral $\int \frac{V^2}{\text{BW}} df$ corrected for the load impedance will correspond to the thermal energy $\frac{1}{2} kT$.

Figure 1b shows a circuit modeling the reception of thermal noise from the plasma. The thermally excited fluctuating plasma voltage V_p flows through a plasma impedance Z_p , then through a load impedance Z_L with its inevitable noise V_L . Near a mode at frequency $\omega_0 = 2\pi f_0$, the plasma admittance Z_p^{-1} is given by a simple pole, as

$$Z_p^{-1} = \frac{R_p^{-1} \gamma_p}{i(\omega - \omega_0) + \gamma_p}. \quad (2)$$

As will be seen below, the plasma resistance R_p depends on γ_p and on the geometric coupling between the plasma and the receiving electrode. The measured load resistance R_L and capacitance C_L give

$$Z_L^{-1} \equiv R_L^{-1} + i\omega C_L \quad (3)$$

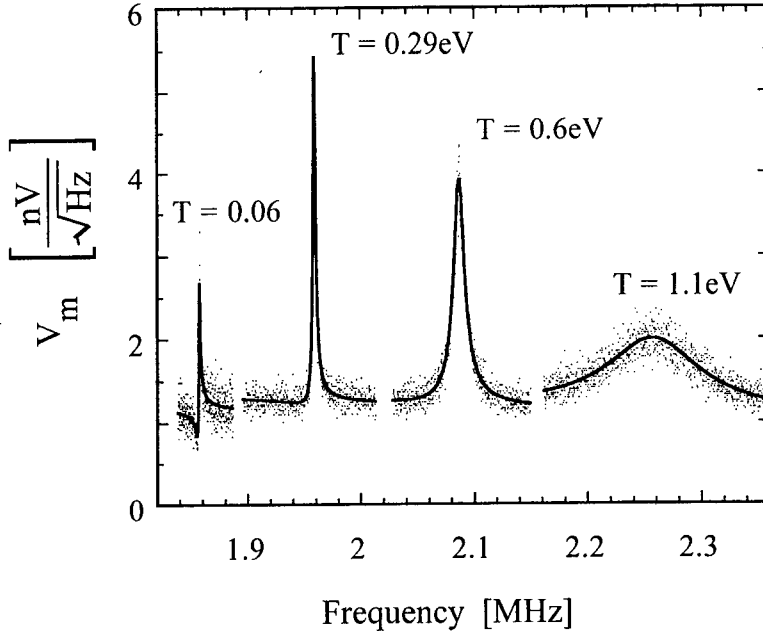


FIGURE 3. Spectra of the thermally excited $m_0 = 0$, $m_z = 1$, mode for different plasma temperature; the solid lines are fits to Eq. (4).

which is essentially constant over the mode resonance; this simple Z_L differs from the resonant-circuit loads commonly used in harmonic traps with a small number of particles [3].

Nyquist's theorem says that the spectral density of the square of the noise voltage is proportional to the kT times real part of the impedance, for both the plasma and the load noise sources [4]. A voltage-divider fraction $Z_L/(Z_p + Z_L)$ of the plasma voltage V_p will be measured on the electrode as V_m , together with an analogous fraction of the (uncorrelated) load noise, giving

$$\frac{V_m^2(f)}{df} = 4kT Z_p^{\text{Re}} \left(\frac{Z_L}{Z_p + Z_L} \right)^2 + 4kT_L Z_L^{\text{Re}} \left(\frac{Z_p}{Z_p + Z_L} \right)^2, \quad (4)$$

where $Z^{\text{Re}} \equiv \text{Re}\{Z\}$ and $Z^{\text{Im}} \equiv \text{Im}\{Z\}$. Using Eqs. (2) and (3), Eq. (4) can be explicitly written as

$$\frac{V_m^2(f)}{df} = 4kT_L Z_L^{\text{Re}} + 4 \frac{kT}{R_p} |Z_L|^2 \left(1 + \frac{Z_L^{\text{Re}}}{R_p} \right)^{-2} \left[\frac{\alpha \gamma_{\text{tot}}^2 - \beta \gamma_{\text{tot}} (\omega - \omega_0)}{\gamma_{\text{tot}}^2 + (\omega - \omega_0')^2} \right], \quad (5)$$

where

$$\begin{aligned}\gamma_{\text{tot}} &= \left(1 + \frac{Z_L^{\text{Re}}}{R_p}\right) \gamma_p \\ \omega'_0 &= \omega_0 - \frac{Z_L^{\text{Im}}}{R_p} \gamma_p \\ \alpha &= 1 - \frac{T_L}{T} \left\{ \frac{Z_L^{\text{Re}}}{R_p} - 2 \frac{(Z_L^{\text{Re}})^2}{|Z_L|^2} \right\} \\ \beta &= 2 \frac{T_L}{T} \left(1 + \frac{Z_L^{\text{Re}}}{R_p}\right) \frac{Z_L^{\text{Re}} Z_L^{\text{Im}}}{|Z_L|^2}.\end{aligned}$$

For relatively high plasma temperature, one can assume $\beta = 0$, and Eq. (5) describes a simple Lorentzian resonance superimposed on a uniform noise background. The spectrum is then characterized by 4 parameters: 3 characterize the resonance, as frequency $\omega_0/2\pi$, width γ_{tot} , and amplitude kT/R_p ; and the 4th parameter of the load temperature T_L sets the background level. Best-fit values of kT/R_p obtained for the 4 spectra of Fig. 3, together with the separately measured plasma temperature T , then imply values of $R_p = 81, 160, 850$ and 7800Ω .

In contrast, both T and R_p are uniquely determined by the emission spectrum alone for regimes where the load-generated noise "filtered" by the plasma resonance becomes significant, as in the $T = 0.06$ eV case of Fig. 3. Here, the spectrum is not a simple Lorentzian, and a fifth parameter, R_p/Z_L^{Re} , is required for a complete fit to Eq. (5). The plasma impedance is effectively filtering the noise generated by Z_L^{Re} creating a "dip" in the trace at ω_0 . The imaginary part of Z_L creates a small shift $\omega_0 - \omega'_0$ of the plasma peak relative to the noise "dip." For the narrow peak of $T = 0.06$ eV, the frequency shift is comparable to the width of the plasma mode. Under these conditions, the noise generated by Z_L^{Re} is effectively performing the reflection measurement described below. A 5-parameter fit to this spectrum gives $T = 0.03$ eV and $R_p = 81 \Omega$, consistent with the 4-parameter fit and separately measured temperature.

For most of our data, we have near-Lorentzian V_m spectra; and to use them as a temperature diagnostic, R_p must be obtained independently. This plasma resistance R_p (and full impedance Z_p) can be obtained either from a reflection/absorption measurement, as shown in Fig. 1c; or from a first-principles kinetic analysis of the plasma fluctuations [1] including the trap/antenna geometry, as discussed below.

The direct reflection/absorption measurement of Z_p uses a directional coupler and lock-in detector to determine the reflection coefficient $\tilde{r}(f)$ for a weak wave at frequency f incident on the receiving antenna and plasma. This (complex) reflection coefficient is defined as the voltage fraction (and phase) which is reflected by the plasma-loaded antenna compared to that reflected by an open circuit without antenna or plasma, i.e.

$$\tilde{r} \equiv V_{\text{ref}}(\text{plasma})/V_{\text{ref}}(\text{open}). \quad (6)$$

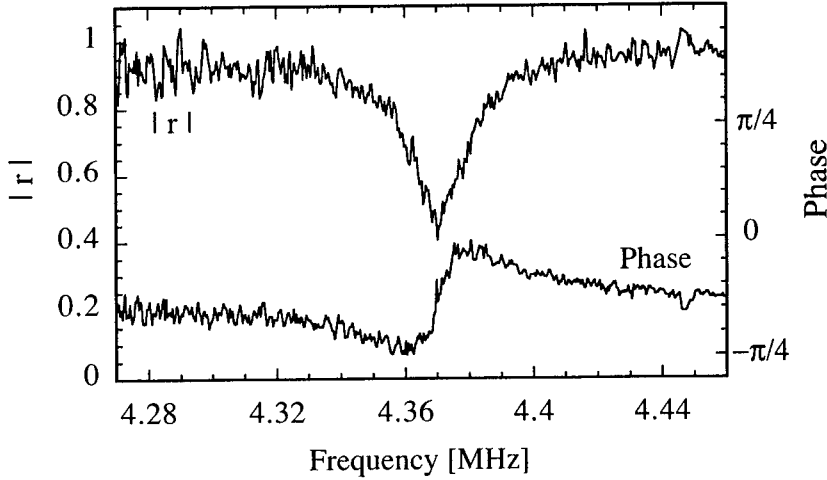


FIGURE 4. Measured magnitude and phase of the reflection coefficient \tilde{r} .

This reflection coefficient depends on the impedance Z_{tot} connected to the directional coupler compared to the impedance $Z_0 = 50 \Omega$ of the coupler itself, as [4]

$$Z_{\text{tot}} = Z_0 \frac{(1 + \tilde{r})}{(1 - \tilde{r})}. \quad (7)$$

Here, $Z_{\text{tot}}^{-1} = Z_p^{-1} + i\omega C_L$ is the total impedance of the plasma-loaded antenna, given by the plasma impedance Z_p in parallel with the capacitance C_L of the electrode and connecting cable.

Figure 4 shows the measured amplitude and phase of the reflected wave as the frequency is scanned across the $m_z = 1$ mode. (The data is from EV, where the frequencies are about $2 \times$ higher than on IV.) Away from the mode, the entire signal is reflected. On resonance, about 60% of the incident wave is absorbed by the plasma, and 40% is reflected. A fit to the data gives the parameters of Z_{tot} as $f_0 = 4.37$ MHz, $\gamma/\omega = 2.4 \times 10^{-3}$, $R_p = 153 \Omega$, and $C_L = 155$ pF. In essence, the depth of the absorption dip indicates how close R_p is to the 50Ω of the directional coupler.

Alternately, a kinetic analysis reproduces the Nyquist theorem and gives R_p in terms of geometry and the mode damping γ_p . Integrating in frequency over the $m_\theta = 0$, $m_z = 1$, $m_r = 1$ mode gives a mean-square radial electric field on the wall of

$$\delta E_r^2 = kT \frac{8}{r_w^2 L_p} \cos^2\left(\frac{\pi z}{L_p}\right) \mathcal{J}(x) \left(\frac{R_p}{R_p + Z_L^{\text{Re}}} \right) \frac{1}{4\pi\epsilon_0}, \quad (8)$$

with $\mathcal{J}(x) \equiv [J_0^2(x) + J_1^2(x)]/(\partial D/\partial x)^2$, $D(x) \equiv xJ_1(x)\ln(r_w/r_p) - J_0(x)$, and $x = (\omega_p^2/\omega_0^2 - 1)^{1/2}\pi r_p/L_p$. Here, J_0 and J_1 are Bessel functions of the first kind, and for simplicity we have kept only lowest-order terms in r_w/L_p . Note that δE_r represents the radial component of the electric field at the wall, not the total wave electric

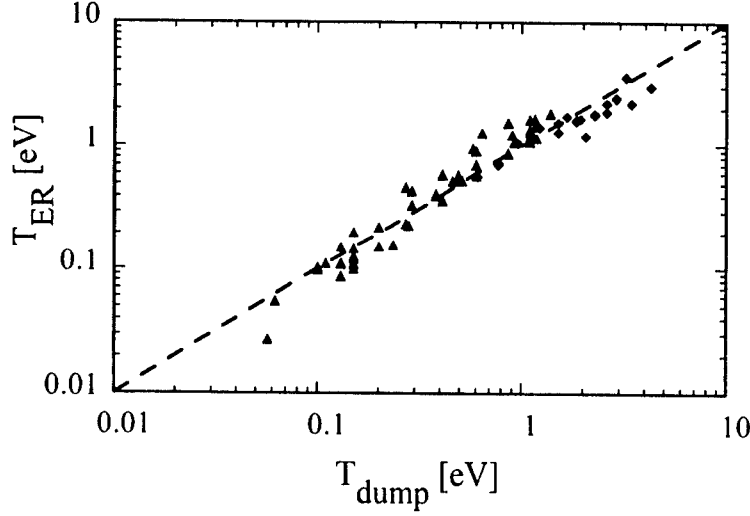


FIGURE 5. Plasma temperature measured by emission/reflection technique, compared to the standard dump temperature measurement. The triangles are from the IV apparatus and the diamonds are from the EV apparatus.

field. This δE_r induces the measured fluctuating charge δQ on a cylindrical electrode of length L_c located at z_c , given by

$$\delta Q^2 = 2kT \left(\frac{R_p}{R_p + Z_L^{\text{Re}}} \right) \mathcal{G} (4\pi\epsilon_0) \quad (9)$$

with

$$\mathcal{G} \equiv L_p \frac{\mathcal{I}(x)}{\pi^2} \left[\sin \left(\frac{\pi(z_c + L_c)}{L_p} \right) - \sin \left(\frac{\pi z_c}{L_p} \right) \right]^2.$$

From the circuit perspective of Fig. 1b, $\omega_0^2 \delta Q^2$ represents the mode-integrated mean-square current, so $\omega_0^2 \delta Q^2 = \int df (V_p^2 / df) (Z_p + Z_L)^{-2} = 2kT \gamma_p / (R_p + Z_L^{\text{Re}})$ using Eqs. (2) and (3). Thus, we obtain

$$\gamma_{\text{tot}} \equiv \gamma_p + \gamma_L = (R_p + Z_L^{\text{Re}}) \omega_0^2 \mathcal{G} (4\pi\epsilon_0). \quad (10)$$

That is, the kinetic analysis gives mode-integrated fluctuating currents proportional to kT , and identifies the total mode damping as proportional to the sum of the resistances R_p and Z_L^{Re} in the plasma and the load, scaled by the geometric factors \mathcal{G} and ω_0 .

For typical EV parameters of $r_p = 1.66$ cm, $r_w = 3.8$ cm, $L_p = 23.5$ cm, $z_c = 0$, $L_c = 5.8$ cm, $n = 8.45 \times 10^6$ cm⁻³, and $\omega_p^2 / \omega_0^2 = 41.3$, we obtain $x = 1.41$, $D = 0.072$, $\mathcal{G} = 1$ cm/2.02 and $\gamma_{\text{tot}} / \omega_0 = (R_p + Z_L^{\text{Re}}) / 7.2 \times 10^4 \Omega$.

It is important to note that Z_L^{Re} contributes to the mode damping on an equal footing with R_p . For example, an external load resistance of $Z_L^{\text{Re}} = 72 \Omega$ induces a baseline

mode damping of $\gamma_L/\omega_0 = 10^{-3}$. Thus, even small receiver resistance can contribute significantly to mode damping.

Figure 5 displays the inferred plasma temperature T_{ER} , obtained from the emission spectra and reflection/absorption measurements, versus the plasma temperature T_{dump} measured by dumping the plasma. The plasma temperature was controlled by adding "wiggle heating" at one end of the column, and data was taken for plasmas with a range of "geometric" parameters (n, r_p, L_p) on both EV (diamond symbols) and IV (triangle symbols). The values of T_{ER} were obtained from 4-parameter fits to the emission spectra, together with a separately obtained value of R_p .

Conceptually, determining R_p amounts to determining the plasma/antenna geometry factor G of Eq. (10). Moreover, G does not depend significantly on plasma temperature, so one determination of G suffices for all plasmas with the same geometric parameters.

On EV, we measured R_p from the reflection/absorption technique over a plasma temperature range of $0.5 < T < 5\text{eV}$. This gave $30 < R_p < 2000\Omega$, implying "internal" plasma dampings of $5 \times 10^{-4} < \gamma_p/\omega_0 < 0.02$. Over this temperature range, we verified that the observed γ_{tot} is proportional to the total resistance, with a best-fit value giving $G = 1\text{ cm}/2.26$. This is in close agreement with the algebraic formula for G .

On IV, the value of R_p was determined from a single 5-parameter fit to the non-Lorentzian " $T = 0.06$ " spectrum of Fig. 3, giving $G = 1\text{ cm}/5.3$. A direct calculation of G using the "measured" $r_p = 0.2\text{ cm}$ gives $G = 1\text{ cm}/3.45$; but this discrepancy is within the uncertainty in the determination of small plasma radius r_p on IV.

It should be emphasized that steady-state plasmas often exhibit spectral peaks which are 10 to 100 times larger than thermal, because the mode is being externally driven. For example, noise on the ostensibly steady confinement voltages V_c or ambient RF signals may stimulate particular plasma modes without proportionately increasing the plasma temperature. Similarly, particular modes in a warm plasma can be damped (i.e. cooled) with an external feedback circuit, decreasing the peak mode amplitude by $25\times$, without substantially cooling the plasma. That is, the plasma modes are relatively weakly coupled to the theorist's thermal bath [10]. Since each mode has only kT of energy compared to the $10^9 kT$ in the entire plasma, it is rather easy for particular experimental manipulations to overwhelm the mode energy; so this thermometer is rather fragile.

ACKNOWLEDGMENTS

This work is supported by Office of Naval Research Grant No. N00014-96-1-0239 and National Science Foundation Grant PHY-9876999. We thank Dr. R.E. Pollock for suggesting this work and demonstrating that thermally excited TG modes can be observed; and Dr. T.M. O'Neil for many fruitful discussions.

REFERENCES

1. N. Krall and A.W. Trivelpiece, *Principles of Plasma Physics* (McGraw-Hill, 1973), Ch. 11.
2. R.W. Gould, *Phys. Plasmas* **2**, 2151 (1995).
3. D.J. Wineland and H.G. Dehmelt, *J. Appl. Phys.* **46**, 919 (1975).

4. R.W. Gould, "Thermal Excitation of Modes in a Non-Neutral Plasma," in this proceedings.
5. F. Anderegg, X.-P. Huang, E. Sarid, and C.F. Driscoll, Rev. Sci. Instrum. **68**, 2367 (1997).
6. F. Anderegg, E.M. Hollmann, and C.F. Driscoll, Phys. Rev. Lett. **81**, 4875 (1998); E.M. Hollmann, F. Anderegg, and C.F. Driscoll, Phys. Plasmas **7**, 2776 (2000).
7. D.L. Eggleston, C.F. Driscoll, B.R. Beck, A.W. Hyatt, and J.H. Malmberg, Phys. Fluids B **4**, 2432 (1992).
8. B.R. Beck, J. Fajans, and J.H. Malmberg, Phys. Plasmas **3**, 1250 (1996).
9. S.A. Prasad and T.M. O'Neil, Phys. Fluids **26**, 665 (1983); A.W. Trivelpiece and R.W. Gould, J. Appl. Phys. **30**, 1784 (1959).
10. C.F. Driscoll, J.H. Malmberg and K.S. Fine, Phys. Rev. Lett. **60**, 1290 (1988); T.M. O'Neil and D.H.E. Dubin, Phys. Plasmas **5**, 2163 (1998).

Thermal Excitation of Modes in a Non-neutral Plasma

Roy W. Gould

California Institute of Technology, Pasadena, CA 91125

Abstract. We examine theoretically the thermal fluctuations in a non-neutral plasma, as observed on a segmented electrode surrounding the plasma, using the Nyquist theorem. The fluctuation spectrum is peaked at frequencies which correspond to modes of the plasma. Measurement of these fluctuations and of the input admittance of the plasma in the vicinity of one of the mode resonances can be used to give a completely experimental, and non-destructive, measurement of the plasma temperature. Since some of the modes are negative energy modes and exhibit negative absorption due to the plasma rotation, a direct application of the Nyquist theorems will not give correct results for the non-axisymmetric modes. This problem is circumvented by first calculating the fluctuations in a frame rotating with the plasma and transforming to the laboratory frame. This results in a modification of Nyquist's theorem. Measurement issues are discussed.

INTRODUCTION

Recent experimental measurements[1] of the fluctuations in a cylindrical pure electron plasma show that the fluctuation spectrum is peaked at frequencies of the Trivelpiece-Gould modes[2] and that they are thermal in origin. Measurements are made by observing the frequency spectrum of the fluctuating signal on a "patch" electrode which is part of the conducting cylinder which surrounds the plasma. We show the situation schematically in Figure 1. We show the field lines of a few

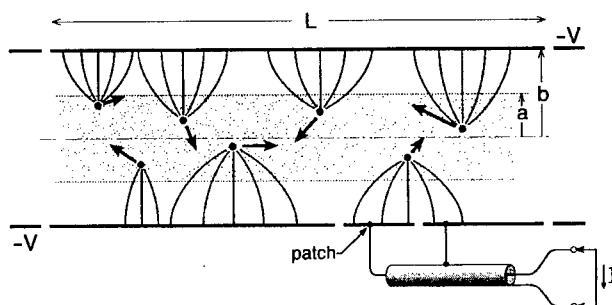


FIGURE 1. Charged particles in a cylindrical conducting cylinder. Field lines to the wall are indicated and arrows indicate the particle velocity. Fluctuations of the charge on patch result in a current $I(\omega)$ in the external circuit.

selected particles. They terminate on charges which reside on the conducting wall at $r = b$. As the particles move, these wall charges change so that there are fluctuating charges and currents induced on the wall. We show a small patch used to measure the fluctuations. We want to find the fluctuating charge on the patch or, alternatively, the fluctuating (displacement) current which flows to the patch.

There are various methods by which fluctuations can be calculated. In *thermal equilibrium*, the principle of detailed balance says that emission and absorption must be balanced, so that one can obtain the emission from a knowledge of the absorption and the temperature. Nyquist's Theorem[3] is a well-known application to electrical circuits which relates thermal fluctuations to the dissipative part of the admittance or impedance functions of an electrical circuit. This theorem was later generalized to Hamiltonian systems by Callen and Welton[4] and applied to a wide class of dynamical systems. It is called the generalized Nyquist theorem, or the fluctuation-dissipation theorem. These methods require a knowledge of the input admittance of the patch. In plasmas, fluctuating quantities can also be calculated from two-particle distribution functions, or using Rostoker's dressed test particle approach[5]. The latter approach is not limited to systems in thermodynamic equilibrium (although they must be stable) but is harder to apply except in the most simple situations (e.g. spatially uniform plasmas).

This paper is divided into two parts: a discussion of the application of Nyquist's theorem to the axisymmetric ($m = 0$) modes, then a discussion of the non-axisymmetric ($m \neq 0$) modes, some of which are negative energy modes to which Nyquist theorem cannot be applied directly. Instead, we calculate the fluctuations in the rotating frame using Nyquist's theorem, where all modes are positive energy modes. We then transform this result to the laboratory frame. This leads to a modification of the Nyquist result, essentially an *extension* of Nyquist's theorem to rotating systems.

NYQUIST'S THEOREM

Nyquist's theorem relates the mean-square fluctuations to the real part of the admittance of electric circuit, $Y(\omega) = I(\omega)/V(\omega)$. As seen from the coaxial connector in Figure 1, we can view the plasma as an electric circuit which has an admittance, $Y_p(\omega)$, which describes the linear response of the plasma. We have previously discussed[6] the properties of $Y_p(\omega)$ in connection with the transfer of angular momentum and energy to a plasma through the excitation of non-axisymmetric Trivelpiece-Gould modes. This function has simple poles at each of the mode frequencies. $Y_p(\omega)$ is also a quantity which can be measured experimentally. It reflects the properties of the plasma and we shall assume that it is at the temperature of the plasma, T_p . Accordingly, we have the equivalent electrical circuit of Figure 2,

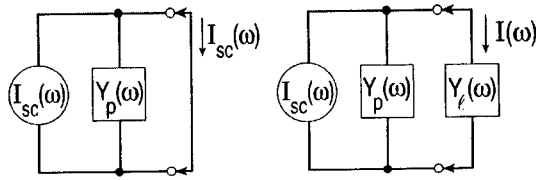


FIGURE 2. (a) Norton Equivalent Circuit with a short circuit,
(b) Norton Equivalent Circuit with a load admittance, Y_l

in which the effect of the thermal fluctuations of the circuit are represented by a current generator with mean square current $|I_{sc}^2(\omega)|$ in frequency range $d\omega$

$$|I_{sc}^2(\omega)| = \frac{2}{\pi} \kappa T_p \operatorname{Re}\{Y_p(\omega)\} d\omega \quad (1)$$

in parallel with $Y_p(\omega)$, as illustrated in Figure 2.

Near one of the mode frequencies where the plasma can be resonantly excited, $Y_p(\omega)$ has a simple pole at the mode frequency so that

$$Y_p(\omega) \simeq \frac{R_{res}}{-i(\omega - \omega_{res}) + \gamma_{res}}, \quad (2)$$

where ω_{res} and γ_{res} are the frequency and line width of the mode[6]. R_{res} is the residue at the pole and depends upon the sector position and dimensions, as discussed later in the paper. Note that the admittance is *real* and equal to R_{res}/γ_{res} at line center. Furthermore, $|I_{sc}^2(\omega)|$ has a Lorentzian lineshape.

The basic idea is to measure both the fluctuation spectrum, e.g. the mean-square current flowing in the load admittance, and the input admittance and then to use Eq. 1 to determine the plasma temperature. A very important point here is that the external load affects the measurement and must be properly taken into account in interpreting the measurements. Note that the current flowing through the load, $I(\omega)$, is generally less than the short-circuit current $I_{sc}(\omega)$ by the factor $Y_l(\omega)/[Y_l(\omega) + Y_p(\omega)]$ and the voltage across the load is $V(\omega) = I(\omega)/Y_l(\omega)$. The external load will, in general, introduce additional mode damping and make an additive contribution to γ_{res} , thus increasing the linewidth. Since the load is not, in general, at the same temperature as the plasma it may also cool the mode slightly. The mode is thermally excited by the particles at T_p but also cooled by an external load at a lower temperature, T_l . The mode temperature is determined by a competition between these processes. Furthermore, if not all parts of the system are at temperature T_p , then the measured temperature will be a weighted average temperature, weighted according to the dissipation of the various parts. Thus the copper electrodes, which have very little dissipation, will not affect the measured temperature significantly. If there are radial temperature gradient (electrons equilibrate along field lines very quickly but not necessarily across field lines) we expect observed temperature to be an average

temperature, weighted according to where the dissipation occurs. Since the $m = 0$ and $m = 2$ mode fields have different radial dependences, one might be able to determine whether a radial temperature gradient exists from measurements using two different modes.

NON-AXISYMMETRIC MODES AND NEGATIVE ABSORPTION

In thermal equilibrium emission is related to absorption, and fluctuations to dissipation. The axisymmetric modes are all positive energy modes and the Nyquist theorem works fine. However some of the non-axisymmetric modes are negative energy modes, i.e. their excitation *releases* energy from the plasma and they exhibit negative dissipation. Recall that the $m = 1$ diocotron mode can be destabilized by attaching a resistor to the patch[7], and that the damping of the $m = 2$ diocotron mode is *reduced* by attaching a resistor to the patch[8]. It is the modes whose azimuthal phase velocity are less than the rotation angular velocity, $0 < \omega/m < \omega_{rot}$, which we shall refer to as the slow modes, which are negative energy modes. Their excitation releases some of the energy of rotation. The real part of the patch input admittance associated with modes in this frequency range is negative. Nyquist's theorem (and the fluctuation-dissipation theorem) can not be applied to such a situation. Yet we expect the plasma to be in thermal equilibrium if these modes are not destabilized.

The reason for this paradox is the nature of the equilibrium. In making the case for thermal equilibrium, it is generally assumed that the walls are smooth, the system is axisymmetric, and angular momentum and energy are constants of the motion[9]. The equilibrium which results is very special, the plasma is rotating as a whole and has angular momentum. For some purposes, including the discussion of thermal fluctuations, it is more appropriate to view the plasma in the rotating frame, in which the plasma appears stationary. In this frame the plasma has no negative energy modes. We expect that the dynamics will be the same in either frame, except for the coordinate transformation. The effect of transforming to the rotating frame introduces a uniform rigid neutralizing background charge. This situation is frequently referred to as the one-component-plasma (OCP).

We can apply the Nyquist theorem (or fluctuation-dissipation theorem) in the rotating (primed) frame, i.e. to the OCP. For this purpose we will not consider a patch electrode, but will instead express the potentials and electric field at the wall ($r = b$) in terms of their Fourier components (with $k = n\pi/L$),

$$\begin{aligned}\phi' &= \sum_{k,m} \phi'_{km} e^{ikz + im\theta' - i\omega' t} \\ E'_r &= \sum_{k,m} E'_{rkm} e^{ikz + im\theta' - i\omega' t}.\end{aligned}$$

We calculate the fluctuations of the various Fourier components in the rotating frame and then transform that result to the laboratory (unprimed) frame. The

frequencies of the fluctuations will be Doppler shifted: $\omega' = \omega - m\omega_r$ or $\omega = \omega' + m\omega_r$, where ω_r is the rotational angular velocity. The mode frequencies ω_{mnp} are also Doppler shifted by the rotation so that $\omega_{mnp} = \omega'_{mnp} + m\omega_r$.

We imagine that a small potential (one Fourier component) is applied at $r = b$ and that this produces a corresponding Fourier component of the radial electric field at $r = b$ which is proportional to the applied potential. We define the linear response function, or susceptibility $\chi'_{km}(\omega')$, of the plasma[6] as the ratio of the radial electric field produced to the potential which causes it, i.e.

$$E'_{rkm} = -\chi'_{km}(\omega') \frac{\phi'_{km}}{b}. \quad (3)$$

To apply Nyquist theorem, we need a *current* to go along with the potential. For this purpose we define a displacement current at the wall $I'_{km} = -i\omega'\epsilon_o S E'_{rkm}$. The complex power delivered to the plasma is

$$P = \frac{1}{2} \int_S i\omega' \epsilon_o E'_r \phi'^* dS = \frac{1}{2} i\omega' \epsilon_o S \sum_{k'm'} E'_{rkm} \phi'^*_{km} = \frac{1}{2} \sum_{km} I'_{km} \phi'^*_{km},$$

where $S = 2\pi bL$ is the total area of the cylinder, I'_{km} is the current, and * denotes the complex conjugate. Because E'_{rkm} is proportional to ϕ'_{km} , I'_{km} is also proportional to ϕ'_{km} . Thus

$$I'_{km} = \left[\frac{-i\omega'\epsilon_o S}{b} \chi'_{km} \right] \phi'_{km} = Y'_{km} \phi'_{km}. \quad (4)$$

Y'_{km} is the admittance of *one* Fourier component which we shall use in Nyquist's theorem to determine the fluctuation in electric field at the wall, and the corresponding fluctuating current and wall surface charge density in frequency range $d\omega'$ are:

$$|I_{km}(\omega')|^2 = \frac{2}{\pi} \kappa T \operatorname{Re}\{Y'_{km}(\omega')\} d\omega',$$

$$|\sigma_{km}(\omega')|^2 = \frac{1}{\omega'^2 S^2} |I_{km}(\omega')|^2 = \frac{2}{\pi} \kappa T \frac{\epsilon_o}{Sb} \operatorname{Im}\left\{\frac{\chi'_{km}(\omega')}{\omega'}\right\} d\omega'.$$

$\operatorname{Im}\left\{\frac{\chi'_{km}(\omega')}{\omega'}\right\}$ is always positive because the system is in equilibrium in the rotating frame and therefore stable. The fluctuations are the same in both frames, except for Doppler shift of frequencies $\omega' = \omega - m\omega_r$. The linear response function is the same in both frames except for Doppler shift of frequencies, i.e. $\chi_{km}(\omega) = \chi'_{km}(\omega')$. Finally, the fluctuating wall charge in the laboratory frame is

$$|\sigma_{km}(\omega)|^2 = \frac{2}{\pi} kT \frac{\epsilon_o}{Sb} \operatorname{Im}\left\{\frac{\chi_{km}(\omega - m\omega_r)}{\omega - m\omega_r}\right\} d\omega. \quad (5)$$

From the Fourier components of the fluctuating charge we can calculate the fluctuating patch current when it is short-circuited

$$I_{sc} = -i\omega \int_{S_p} \sigma dS = -i\omega S_p \sum_{km} F_{km} \sigma_{km} ,$$

where S_p is the patch area and F_{km} is a patch shape factor (≤ 1). The mean square fluctuating current, $|I_{sc}(\omega)|^2$, is therefore

$$|I_{sc}(\omega)|^2 = \frac{2}{\pi} \kappa T \frac{\omega \epsilon_0 S_p^2}{S_b} \sum_{km} |F_{km}|^2 \text{Im} \left\{ \frac{\omega}{\omega - m\omega_r} \chi'_{km}(\omega - m\omega_r) \right\} d\omega . \quad (6)$$

Direct calculation of the patch admittance in the lab frame gives

$$Y_p(\omega) = \frac{\omega \epsilon_0 S_p^2}{S_b} \sum_{km} |F_{km}|^2 \text{Im} \{ \chi_{km}(\omega) \} . \quad (7)$$

Patch fluctuations are no longer simply related to patch admittance. However, Equation (6) is much simpler when only one azimuthal wave number contributes significantly to the admittance (for example, near the resonance of a mode). In this case

$$|I_{sc}(\omega)|^2 = \frac{2}{\pi} \kappa T \text{Re} \left\{ \frac{\omega}{\omega - m\omega_r} Y_p(\omega) \right\} d\omega . \quad (8)$$

Thus even when $\text{Re}\{Y_p(\omega)\} < 0$ (for potentially unstable modes) we can obtain the fluctuation level in thermal equilibrium. This result is very similar to the Nyquist result, the difference being that the factor $\frac{\omega}{\omega - m\omega_r}$ appears. This factor is negative whenever $\text{Re}\{Y_p(\omega)\}$ is negative, so that the product is always positive. Notice however that this factor is important even for the positive energy non-axisymmetric modes (when both factors are positive). It reflects the effect of rotation on the *magnitude* of the fluctuation spectrum.

DISCUSSION

To determine the plasma temperature, measure the fluctuating voltage $|V^2(\omega)|$ across the load admittance *near one of the mode resonances* with a load $Y_l(\omega)$ connected to the patch. Also measure the input admittance of the plasma $Y_p(\omega)$ at very low signal level so as not to drive the plasma mode into the nonlinear regime. This measurement can be done by measuring the complex reflection coefficient of the plasma with a 50Ω directional coupler, converting the measured reflection coefficient, $r(\omega)$, to the complex admittance using¹ $Y(\omega)/Y_o = [1 - r(\omega)]/[1 + r(\omega)]$, then using the expression

$$|V^2(\omega)| \approx 4kT_p \text{Re} \left\{ \frac{\omega}{\omega - m\omega_r} Y_p(\omega) \right\} d\omega / |Y_l(\omega + Y_p(\omega))|^2 \quad (9)$$

1. The loci of both $Y(\omega)$ and $r(\omega)$ versus ω are circles in the complex plane. This property can be useful in fitting experimental data.

to obtain the plasma temperature T_p . This assumes that one mode dominates the fluctuation spectrum and the plasma admittance. For the $m = 0$ modes the new factor $\frac{\omega}{\omega - m\omega_r}$ is unity, but for *all* non-axisymmetric modes this factor must be taken into account.

In making measurements it is important that the load admittance not destabilize any of the negative energy modes. An axisymmetric patch does not couple to the negative energy modes so this is not an issue. However if the patch is not axisymmetric, the real part of the load admittance should be very small at the frequencies which might lead to destabilization of any negative energy modes. There must be no, or very little, growth of these modes prior to or during a measurement. This can be accomplished with a capacitive load, which will only cause a small frequency shift of the mode.

CONCLUSIONS

The thermal equilibrium of a non-neutral plasma is an exceptional kind of equilibrium. It has angular momentum and energy due to its rotation and it is not in thermal equilibrium with the outside world. However, it is in thermal equilibrium in a rotating frame when there are no non-axisymmetric perturbations so that the system has constant angular momentum. A patch electrode which produces only axisymmetric fields does not break the angular momentum constraint and does not destroy the equilibrium. Such a patch electrode can be used to weakly excite the axisymmetric modes of the plasma and to measure the thermal fluctuations of these modes without destroying the thermal equilibrium of the plasma. This makes possible a non-destructive, purely experimental, measurement of the plasma temperature using the Nyquist theory of fluctuations associated with these modes in thermal equilibrium.

On the other hand, the slow non-axisymmetric modes have negative energy and exhibit negative resistance and negative absorption. Nyquist's theorem of fluctuations can not be applied directly to these modes because the real part of their input admittance is negative. However, we have shown here that it is still possible to relate the fluctuations associated with non-axisymmetric modes to the real part of the input admittance, even when the latter is negative! In doing so, we have derived a *modified Nyquist theorem for rotating equilibria*. In this new result there appears an additional factor

$$\omega/(\omega - m\omega_r),$$

which is negative for the negative energy slow modes for which the real part of the patch impedance is negative. For the axisymmetric modes, this new factor is unity and we recover the usual Nyquist result.

We obtained this result by calculating the fluctuations in the frame rotating with the plasma, where the plasma is in thermal equilibrium and then transforming the result to the laboratory frame. In the rotating frame all modes are stable and none are

negative energy modes. Although the results of this paper were derived for cylindrical plasmas, it is clear they apply as well to spheroidal plasmas[10].

Finally, it should be possible to observe the fluctuations associated with non-axisymmetric modes, and to use them to determine the plasma temperature. However, in dealing with non-axisymmetric patches and modes, it is important that the load admittance connected to the patch not have a significant real part, else a negative energy mode may be destabilized and slowly grow. This can be achieved by using a capacitive load, whose effect is to shift the mode frequency very slightly.

ACKNOWLEDGEMENT

The author is grateful to F. Anderegg for communicating the experimental results and to members of the U.C.S.D group for stimulating discussions.

REFERENCES

- [1] F. Anderegg, N. Shiga, J. R. Danielson, C. F. Driscoll, D. E. Dubin, and R. W. Gould, "Thermal Excitation of Trivelpiece-Gould Modes in a Pure Electron Plasma" in *Non-Neutral Plasma Physics IV* (these proceedings), edited by F. Anderegg, L. Schweikhard, and C. F. Driscoll.
- [2] A. W. Trivelpiece and R. W. Gould, *J. Appl. Phys.* **30**, 1784 (1959), S. A. Prasad and T. M. O'Neil, *Phys. Fluids* **22**, 278 (1979).
- [3] H. Nyquist, *Phys. Rev.* **32**, 110 (1928).
- [4] H. B. Callen and T. A. Welton, *Phys. Rev.* **83**, 34 (1951).
- [5] N. Rostoker, *Nuclear Fusion*, **1**, 101 (1961).
- [6] R. W. Gould, "Wave Angular Momentum in Non-neutral Plasmas", *Non-Neutral Plasma Physics III*, Am. Inst. Phys. p 170 (1999).
- [7] W. D. White, J. H. Malmberg and C. F. Driscoll, *Phys. Rev. Lett.* **49**, 1822 (1982).
- [8] N. S. Pillai and R. W. Gould, *Phys. Rev. Lett.* **73**, 2849 (1994).
- [9] T. M. O'Neil and D. H. E. Dubin, *Phys. Plasmas* **5**, 2163 (1998).
- [10] D. H. E. Dubin, *Phys. Rev. Lett.* **66**, 2076 (1991).

Using the Plasma Noise Spectrum to Measure the Parallel Temperature in a Nonneutral Plasma

M. Takeshi Nakata, Grant W. Hart, Bryan G. Peterson

*Department of Physics and Astronomy
Brigham Young University
Provo, UT 84602 USA*

Abstract. A simple, non-destructive diagnostic for the temperature of a non-neutral plasma is desirable as plasma lifetimes increase and the confined species become more exotic. If the confinement system includes an isolated wall sector, the motion of the charges beneath that sector will result in a noise signal that can be directly related to the velocity distribution of the confined particles. Care must be taken to differentiate the resulting plasma signal from the instrumental noise spectrum and the strong signals from plasma oscillation modes. The theoretical basis of the relationship between the noise spectrum and the temperature as well as experimental results are presented.

INTRODUCTION

A simple, non-destructive parallel temperature diagnostic is desirable as plasma lifetimes increase and the confined species become more exotic. Thus, we have developed a way to use the plasma noise spectrum from a isolated wall sector to measure the parallel temperature of the plasma.



FIGURE 1. Schematic of our Malmberg-Penning Trap with ring numbers

To measure the plasma noise spectrum of a plasma, we use an isolated wall sector commonly found in a Malmberg-Penning Trap. Fig. 1 illustrates how our Malmberg-Penning Trap is configured. In this trap, Rings 1 and 9 are used to confine our electron plasma. This trap operates in the normal fill-prepare-experiment-dump cycle.

Typical parameters for this trap are the electron density $n \sim 10^7 \text{ cm}^{-3}$, confining potential of $\phi_c \sim -150 \text{ V}$, an axial magnetic field of $B_z \sim 700 \text{ G}$, an electron thermal energy of $kT \sim 1 \text{ eV}$, and an average axial transit time of about $\sim 1.5 \mu\text{s}$. [1]

Our noise spectrum diagnostic basically consists of a wall sector in this trap, a charge sensitive pre-amp, and a spectrum analyzer.

NOISE SPECTRUM THEORY

The basis of this diagnostic is that the motion of the charges beneath the wall sector induces a noise signal that is directly related to the velocity distribution of the confined particles.

To better understand this signal, we developed a simulation to study the plasma noise spectrum. This simulation calculates the induced charge on a wall sector by the particles using the solution for a cylindrical green function. We also assumed in our simulation that these particles were not interacting with each other and that we had hard walls as the confining potentials.

To better understand this signal, we began by looking at what one electron does under a wall sector. As an electron passes underneath the wall sector, it induces a charge in that sector, as a function of time. This signal is measured as a pulse in our detector.

The amplitude of the pulse is related to the charge that is induced on the wall sector by the electron. This amplitude does not change with velocity.

In contrast, the width of this pulse is a function of velocity of the electron under the wall sector. As the velocity of the electron under the sector increases, the width of the pulse decreases.

By Fourier transforming this signal, we find that the frequency spectrum is also a function of velocity of the electron. As the velocity of the electron increases, it lowers the transit time of the electron under the wall sector, which translates to higher frequencies in the corresponding spectrum.

For a collection of electrons in our plasma, the relevant velocity is the thermal velocity of the electrons, which is related to the temperature of the plasma in the direction parallel to the confining magnetic field.

$$v_{th} = \sqrt{\frac{2k_B T}{m_e}} \propto l_{ring} f$$

Thus, the frequency is proportional to the square root of the parallel temperature $\sqrt{T_{||}}$.

Fig. 2 illustrates how the plasma noise spectrum varies with the temperature. As temperature increases, the width of the spectrum correspondingly increases. This also shows how our most temperature sensitive region is between 1 to 3 MHz when we use ring 5 as a detector.

The amplitude of this spectrum is also influenced by both the parallel temperature and number of particles in the plasma. As the parallel temperature increases, the amplitude at $f = 0$ Hz goes as $\sim T^{-1/4}$. As the number of particles increases, the amplitude increases as \sqrt{N} .

The \sqrt{N} scaling demonstrates how each electron contributes in an incoherent manner to the induced charge. In consequence, while the time domain signal is incoherent, the frequency domain signal adds up as \sqrt{N} .

This signal is just the shot noise of the plasma current passing beneath the wall sector. It is the fluctuations on top of the overall charge signal in the time domain. Thus, by examining the frequency spectrum of this signal, one can determine the parallel velocity distribution and therefore the parallel temperature of the electron plasma. Typical times

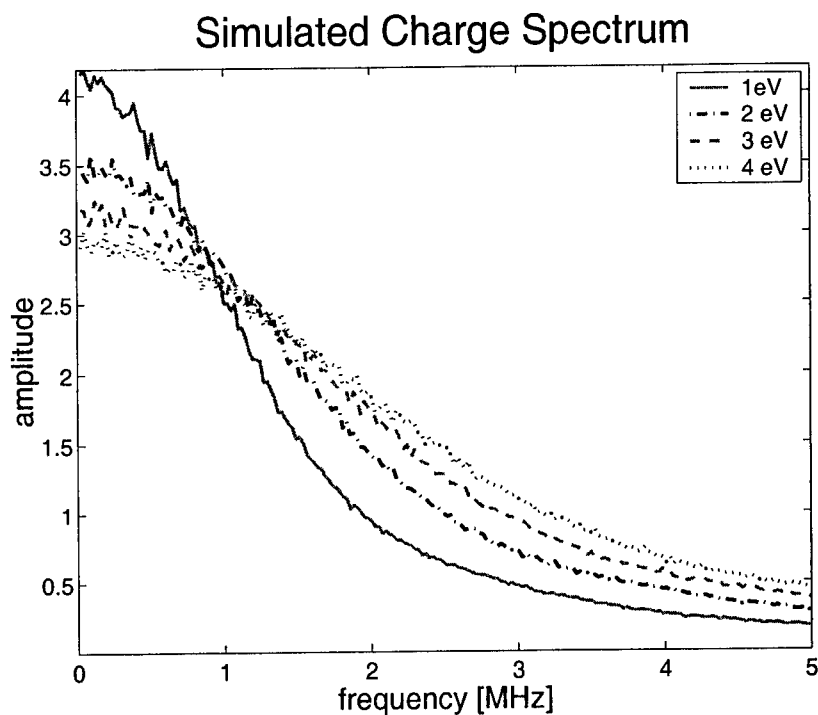


FIGURE 2. Simulated Spectrum for a plasma passing through 20cm ring. Amplitudes has been normalized.

for an electron in a 1 eV plasma under a ring of 20 cm is $\sim 0.5\mu\text{s}$ which implies a typical frequency of ~ 2 MHz.

NOISE TEMPERATURE DIAGNOSTIC

Acquisition of the Spectrum

In our experiment, we used an isolated wall sector on this trap to measure the noise spectrum of the plasma. We used the center wall sector on our trap (Ring 5 in Fig. 1) because it is insensitive to the $n_z = 1$ normal mode which usually is found in our temperature sensitive range of 1 to 3 MHz for our plasma parameters.

This signal is first amplified by an Amp Tek A250 charge sensitive amplifier. This amplifier is AC coupled and configured to produce a signal proportional to the charge on the wall sector. We are careful not to saturate this amplifier by using an optically coupled JFET transistor to ground the input when the plasma is filled and dumped.

Since our plasma noise spectrum is a broad spectrum and is small compared to other electromagnetic oscillations found in the environment, a swept spectrum analyzer was

chosen to be used in the acquisition of our noise spectrum. To obtain the plasma noise spectrum, we acquire both the spectrum with plasma and the spectrum without plasma under the wall sector and subtract the two.

The spectrum analyzer is limited by its sweep time. Our plasma evolves during the sweep time of about 20 ms. To get better time resolution we set our spectrum analyzer to zero span to acquire our noise spectrum. At this setting, the spectrum analyzer looks at one frequency and records the amplitude as a function of time. In effect, this gives us the best frequency resolution possible for a given amount of sweeping time.

However, one of the drawbacks to this method is that we need to take a new shot (plasma) for each frequency. We also average 5 traces to account for shot-to-shot variability. In consequence of using this method, our acquisition of the spectrum becomes a long process and not a short process as we had hoped for.

Postprocessing

Using this method, we can obtain how the plasma noise spectrum evolves with time. Thus, our data set is of time, frequency, and amplitude. Of course in postprocessing this data, we take one spectrum for one time.

Our first step in this postprocessing is to subtract the spectrum with plasma from the spectrum without plasma. Next, we take into account the frequency response of the charge sensitive amplifier by normalizing our spectrum from the measured frequency response.

Finally, we fit our data to our simulated spectrum. To do this, we first eliminate frequency bands which have the mode frequencies and then use a nonlinear least squares algorithm to fit to the simulation. In this algorithm, the amplitude and the width of the simulated spectrum is used as adjustable parameters to fit to the data spectrum.

In the end, we use the standard evaporation method [2] by slowly dumping (~ 1 ms) the plasma to find how the temperature of the plasma changes with time for comparison to the noise temperature technique.

RESULTS

Fig. 3 illustrates some typical data from our spectrum analyzer. This data was taken with the peaks of the mode frequencies truncated. This figure demonstrates that there is a plasma noise spectrum that is similar to our simulation. The 'x' data points is the spectrum that was used to fit to our simulated curve, the solid dark gray line. We eliminated the shaded frequencies band from the raw spectrum, the dash line curve to obtain this spectrum.

In Fig. 4, both fitting parameters are plotted as a function of time. These parameters are the amplitude² and temperature of the spectrum.

The amplitude² plot shows how fitting amplitude A is proportional to square-root of number of particles \sqrt{N} as we expected from our simulation. The normalized number of

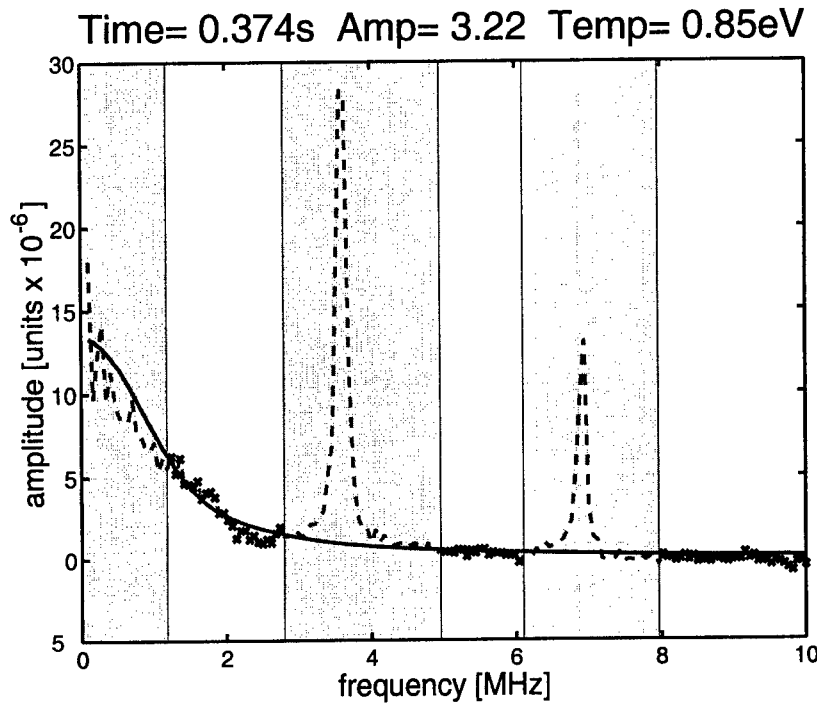


FIGURE 3. 5 Oct 2000, #1 - Relative Amplitude vs. Frequency

particles is normalized in the following way:

$$A^2 \times \frac{\langle \bar{N} \rangle}{\langle \bar{A}^2 \rangle}$$

where A is the fitting amplitude and N is the number of particles. The number of particles N is calculated from by integrating radial density profiles.

The temperature plot illustrates that the noise spectrum method does generally follow the evaporation method until later times past 0.40 s. After 0.40 s, the evaporation method deviates from the noise spectrum method. This illustrates how the evaporation method is sensitive the central temperature of the plasma and the noise spectrum is sensitive to the radially averaged temperature of the plasma. After 0.40 s, plasma expansion heats the outer regions of the plasma.

Another thing to notice from these plots is the fact that both of these parameters correlate to each other. As the amplitude² is farther away from the normalized number of particles N like around 0.28 s, the noise diagnostic method is farther away from the evaporation method.

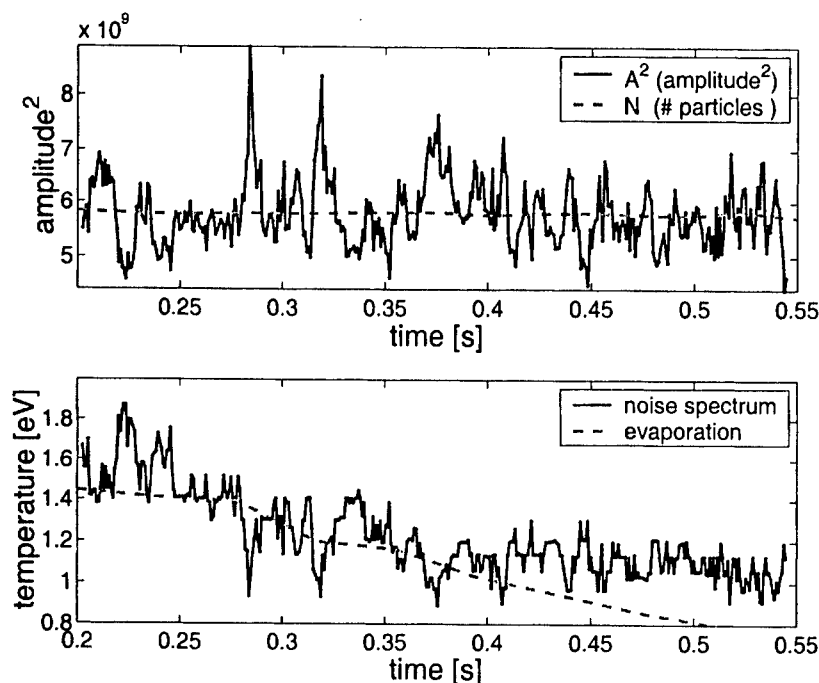


FIGURE 4. 5 Oct 2000, #1 - Fitting Parameters

CONCLUSION

In conclusion, we found out that the plasma noise spectrum can be used as a temperature diagnostic as long as we have a good signal to noise ratio and are clear from plasma modes in the 1 to 3 MHz range. We find that this method is not as practical as we had hope for because plasma modes usually dominate in that range where our sensitivity to temperature is most significant. It also takes some time to obtain this measurement. However, we did find that we can get the radially averaged temperature of a nonneutral plasma by the using plasma noise spectrum.

REFERENCES

1. G. W. Hart, *Phys. Fluids B* 3, 2987 (1991).
2. D. L. Eggleston, *Phys. Fluids B* 4, 3432 (1992).

Trapped Particle Asymmetry Modes in Non-Neutral Plasmas

Andrey A. Kabantsev, C. Fred Driscoll, Terry J. Hilsabeck,
Thomas M. O'Neil, and Jonathan H. Yu

Physics Department, University of California at San Diego, La Jolla CA 92093-0319 USA

Abstract.

Novel trapped particle asymmetry modes propagate on cylindrical electron columns when axial variations in the wall voltage cause particle trapping. These modes consist of $\mathbf{E} \times \mathbf{B}$ drifts of edge-trapped particles, partially shielded by axial flows of interior untrapped particles. A simple theory model agrees well with the observed frequencies and eigenfunctions; but the strong mode damping is as yet unexplained. These modes may be important in coupling trap asymmetries to particle motions and low frequency $\mathbf{E} \times \mathbf{B}$ drift modes.

INTRODUCTION

Single species plasmas confined in cylindrical traps with static electric and magnetic fields are utilized in research ranging from basic plasma and fluid dynamics to spectroscopic frequency standards to anti-matter containment [1]. The plasma confinement times can be hours or days, generally limited by azimuthal asymmetries in the trapping fields which couple angular momentum into the rotating plasma [2]. This coupling can be enhanced by mode resonances [3], and plasma modes occur on frequency scales ranging from the (high) cyclotron frequency Ω_c , to the plasma frequency ω_p , to the (low) $\mathbf{E} \times \mathbf{B}$ drift frequency ω_E . However, the well-studied "diocotron" drift modes have axial wavenumber $k_z \simeq 0$, and so do not readily couple the plasma electrostatic energy into particle kinetic energy.

Here, we describe novel "trapped particle asymmetry" modes which propagate azimuthally at low $\mathbf{E} \times \mathbf{B}$ drift frequencies, but which have $k_z \neq 0$ and thus couple to particle kinetics. These modes exist when axial variations in the wall potential cause the equilibrium plasma to have axially trapped particles. Experimentally, we generate the trapped particles by applying a "squeeze" voltage to a central cylindrical electrode; but smaller trapping potentials are caused by wall irregularities, and are probably endemic to these traps.

These asymmetry modes can have azimuthal mode number $m = 1, 2, \dots$, but we focus on $m = 1$ here. Dynamically, the modes are an $\mathbf{E} \times \mathbf{B}$ drift motion of the edge-trapped particles, with axial flows of interior untrapped particles giving partial Debye shielding. A simple theory model with these characteristics shows close correspondence with the measured frequencies and radial eigenfunctions of the modes. The modes are observed to be strongly damped, but this damping is not yet understood. These modes are particularly simple cylindrical analogues to the trapped drift modes which can contribute

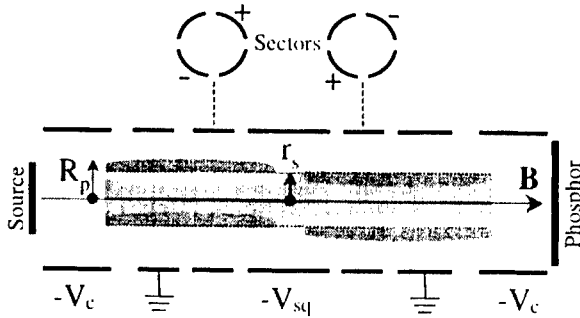


FIGURE 1. Schematic of the cylindrical trap with "squeezed" electron column and applied sector voltages.

to anomalous plasma transport in tokamak-like and toroidal multipole configurations of neutral plasmas [4, 5].

EXPERIMENTAL SETUP

The cylindrical confinement geometry and a schematic of the mode are shown in Fig. 1. A nominally cylindrical column of electrons from a hot tungsten source is confined radially by a uniform magnetic field $B = 4$ kG and confined axially by negative voltages $-V_c = -100$ V on end cylinders. Typical electron columns have a central density $n_0 \approx 1.5 \times 10^7 \text{ cm}^{-3}$ over a length $L_p \approx 50$ cm, with a column radius of $R_p \approx 1.2$ cm inside a wall radius $R_w = 3.5$ cm. The z -averaged electron density $n(r, \theta, t)$ can be (destructively) measured at any time by dumping the electrons axially onto a phosphor screen imaged by a CCD camera [6].

The individual electrons have a thermal energy $T \approx 1$ eV, giving an axial bounce frequency $f_b \equiv \bar{v}/2L_p \approx 0.5$ MHz and a Debye shielding length $\lambda_D \equiv (T/4\pi e^2 n)^{1/2} \approx 0.2$ cm. The unneutralized electron charge results in a central potential $\phi_0 \approx -30$ V, and the radial electric field causes the column to $\mathbf{E} \times \mathbf{B}$ drift rotate at a rate $f_E(r) \equiv cE(r)/2\pi rB \lesssim 50$ kHz. Figure 2 shows typical radial profiles of density and rotation for a θ -symmetric column.

When a negative "squeeze" voltage $-V_{sq}$ is applied to a central cylinder, electrons are excluded from the column periphery under the squeeze ring, and those electrons located at radii at $r > r_s$ are trapped axially in one end or the other. For small V_{sq} , a fraction $\epsilon_{tr} \approx V_{sq}/\phi_0$ of all the electrons are trapped axially.

Linear $\mathbf{E} \times \mathbf{B}$ drift modes with azimuthal mode numbers $m = 1, 2, \dots$ propagate on this trapped particle equilibrium. The ubiquitous $m = 1$ center-of-mass "diocotron" mode is essentially uniform in z (i.e. $k_z \approx 0$), and is nominally unaffected by small V_{sq} . In contrast, the $m = 1$ "trapped particle asymmetry" mode described here has odd parity in z : the perturbations are essentially uniform within each end, but of *opposite sign* on either side of the squeeze, as shown schematically in Fig. 1. Moreover, the perturbations

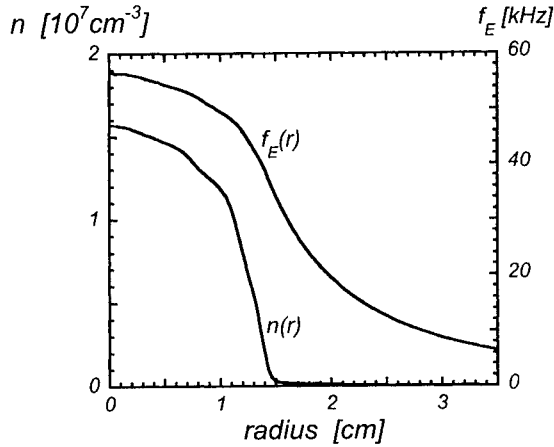


FIGURE 2. Radial profiles of density $n(r)$, and $\mathbf{E} \times \mathbf{B}$ rotation frequency $f_E(r)$.

in the trapped particles at $r > r_s$ are partially “shielded” by perturbations of opposite sign in the untrapped particles at $r < r_s$; and these untrapped particles slosh from end to end in response to the $\mathbf{E} \times \mathbf{B}$ drift evolution of the trapped particles.

Experimentally, these odd- z -parity $m = 1$ asymmetry modes can be excited with + and – voltages applied to opposing wall sectors, with the voltages oppositely phased at the two ends. Any single wall sector can be used as a receiver, or sectors can be used in combination to verify or utilize the θ - and z -symmetries of the modes.

EXPERIMENTAL RESULTS

Figure 3 shows the measured frequencies f_a and f_d as the applied squeeze voltage V_{sq} is varied. The asymmetry mode frequency f_a is at or near the edge rotation frequency $f_E(R_p)$ for $V_{sq} \ll \phi_0$. As V_{sq} is increased, the trapping separatrix r_s moves inward, and f_a decreases. For $V_{sq} \gtrsim \phi_0$, the column is cut in half, and the asymmetry mode becomes degenerate with the diocotron mode. With all particles trapped, the asymmetry mode is equivalent to two separate diocotron modes, 180° out of phase. The diocotron frequency f_d increases slightly with V_{sq} , because the effective line density of the column increases as particles are excluded from the squeeze ring. Both f_a and f_d scale as $f \propto B^{-1}$, as expected for $\mathbf{E} \times \mathbf{B}$ drift modes.

Figure 4 shows that the asymmetry mode damping rate γ_a also depends on V_{sq} , decreasing roughly as $\gamma_a \propto (1 - V_{sq}/\phi_0)$ in the regime $V_{sq} \gtrsim \phi_0/10$ where γ_a can be readily measured. Comparing Figs. 3 and 4, we can see that $\gamma_a/f_a \lesssim 1/20$, so the mode is strongly damped except at $V_{sq} \gtrsim \phi_0$. However, we observe essentially no magnetic field dependence to the damping [at fixed V_{sq}/ϕ_0] in the range of $0.39 \text{ kG} \leq B \leq 10 \text{ kG}$, i.e. $\gamma_a \propto B^0$. (A weak dependence on B arises experimentally because the equilibrium plasma potential ϕ_0 depends weakly on B .) Thus, $\gamma_a/f_a \propto B^1$ and the mode is relatively

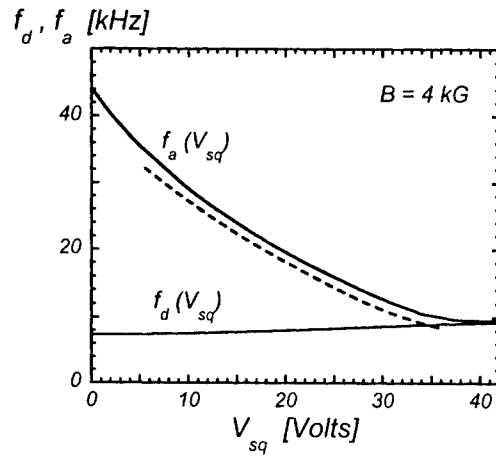


FIGURE 3. Measured frequencies f_a and f_d vs squeeze voltage V_{sq} ; f_a calculated from the kinetic model (dashed).

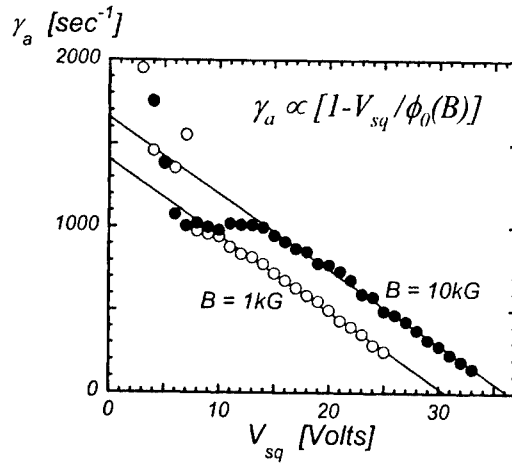


FIGURE 4. Measured decay rate γ_a of the asymmetry mode vs squeeze voltage V_{sq} at two extreme values of the magnetic field. Plasma potential ϕ_0 is less at low magnetic field due to enhanced radial transport of the particles.

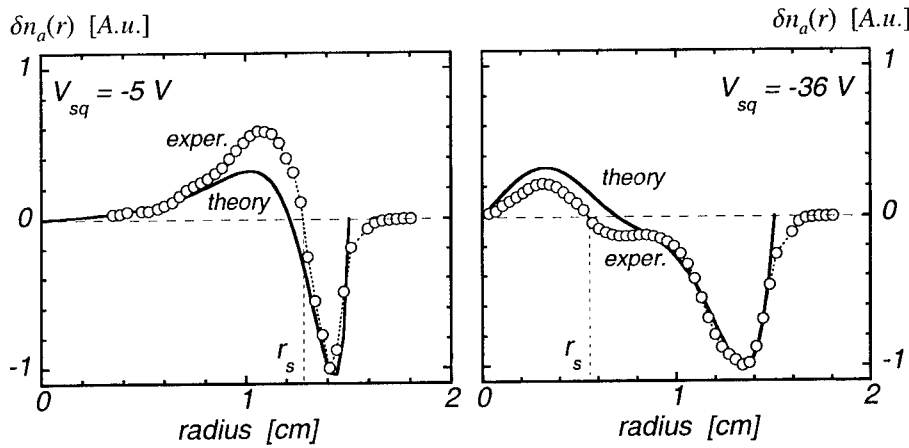


FIGURE 5. Measured (circles) and calculated from the kinetic model (solid) asymmetry mode eigenfunctions $\delta n_a(r)$ for $V_{sq} = -5V$ (left) and $V_{sq} = -36V$ (right).

less strongly damped at lower magnetic fields.

As yet, the cause of this damping is not understood, but experimental signatures (like $\gamma_a \propto r_s^1 B^0$) suggest diffusive mixing between the trapped and untrapped populations. Also, for $V_{sq} < \phi_0/10$, there are suggestions that spatial Landau damping (scaling as B^{-1}) may occur, but this damping depends critically on the density profile near R_p .

The density eigenfunctions $\delta n_a(r)$ of the asymmetry mode can be obtained from a time sequence of measurements of the density $n_h(r, \theta, t)$ z -averaged over only *half* the plasma. To dump only half the column, V_{sq} is increased to $-100V$ immediately before lowering V_c to dump the plasma onto the phosphor screen. The $m = 1$ perturbations in $n_h(r, \theta, t)$ are then fit to a sum of 2 modes (asymmetry and diocotron), as

$$\int d\theta n_h(r, \theta, t) e^{-im\theta} = \sum_{j=a,d} \delta n_j(r) e^{i2\pi f_j t - \gamma_j t}.$$

The residual to this fit is small, and the eigenfunctions are obtained with little ambiguity. The real parts of the asymmetry mode eigenfunction δn_a (scaled arbitrarily) obtained for $V_{sq} = -5V$ and $V_{sq} = -36V$ are shown in Fig. 5; with proper choice of θ -origin, the imaginary part of δn_a is essentially zero.

The mode shows a negative perturbation at $r > r_s$ and a positive perturbation for $r < r_s$; and the signs of these perturbations reverse for $z \rightarrow -z$ and for $\theta \rightarrow \theta + \pi$. The observed position of the zero-crossing at r_s varies with V_{sq} , consistent with the “waistline” radius obtained from (r, z) Poisson solutions for the equilibrium with the measured charge and applied wall potentials.

THEORETICAL MODELS

Fluid theory and kinetic theory models further support the interpretation of the asymmetry mode as trapped $\mathbf{E} \times \mathbf{B}$ drifting edge particles which are Debye-shielded by sloshing interior particles. In these models, the applied squeeze voltage is presumed to create a (zero-length) barrier for particles at $r > r_s$, creating two outer regions with axial lengths L_1 and L_2 . In contrast, interior particles with $r < r_s$ move freely over length $L_1 + L_2$.

Because the axial bounce frequency is large compared to the $\mathbf{E} \times \mathbf{B}$ rotation frequency and the mode frequency, the bounce-average density perturbation in any one of the three regions, $\bar{\delta n}$, is related to the bounce-average potential perturbation in that region, $\bar{\delta \phi}$, through

$$\bar{\delta n}(r) = \frac{c}{2\pi B r} \frac{\partial n_0}{\partial r} \frac{m \bar{\delta \phi}(r)}{m f_E(r) - f}. \quad (1)$$

Within any of the regions, rapid axial streaming yields the adiabatic response

$$\delta n(r, z) = \bar{\delta n}(r) + \frac{e n_0}{T} [\delta \phi(r, z) - \bar{\delta \phi}(r)]. \quad (2)$$

This type of response gives rise to Debye shielding, making $\delta \phi(r, z)$ and $\delta n(r, z)$ nearly z -independent except near the plasma ends and the squeeze region. Thus, we approximate $\delta n(r, z) \approx \delta n_j(r)$ and $\delta \phi(r, z) \approx \delta \phi_j(r)$, with $j = 1, 2$ representing the left and right sides relative to the barrier. Poisson's equation for the two sides is then

$$\begin{aligned} & \frac{1}{r} \frac{\partial}{\partial r} r \left(\frac{\partial}{\partial r} \delta \phi_j \right) - \frac{m^2}{r^2} \delta \phi_j \\ &= \begin{cases} \frac{2ec}{Br} \frac{\partial n_0}{\partial r} \frac{m \delta \phi_j}{m f_E - f} & , r > r_s \\ \frac{2ec}{Br} \frac{\partial n_0}{\partial r} \frac{m \delta \phi_b}{m f_E - f} + \frac{4\pi e^2 n}{T} (\delta \phi_j - \delta \phi_b) & , r < r_s \end{cases} \end{aligned} \quad (3)$$

Here, $\delta \phi_b \equiv (L_1 \delta \phi_1 + L_2 \delta \phi_2)/(L_1 + L_2)$ is the potential averaged over both sides, and the boundary condition is $\delta \phi_j(R_w) = 0$.

Fortunately, the even and odd axial symmetries of the diocotron and asymmetry modes decouple the equations. For $\delta \phi_1(r) = \delta \phi_2(r) = \delta \phi_b(r)$, both equations reduce to the usual equation for a diocotron mode. For $L_1 \delta \phi_1(r) = -L_2 \delta \phi_2(r)$, giving $\delta \phi_b(r) = 0$, we obtain an eigenvalue equation for the asymmetry mode potentials.

For a uniform density profile of density n_0 and radius R_p , the eigenfrequency $f \equiv f_a$ is

$$\frac{f_a}{f_E(0)} = m - \frac{(R_w^{2m} - R_p^{2m})(I_{m-1} R_p^{2m} - I_{m+1} r_s^{2m})}{R_p^{2m}(I_{m-1} R_w^{2m} - I_{m+1} r_s^{2m})}. \quad (4)$$

Here, $I_{m\pm 1} \equiv I_{m\pm 1}(r_s/\lambda_D)$ are modified Bessel functions of the first kind. In the limit of $\lambda_D \rightarrow 0$, the interior region acts like a conductor, and the exponentially large $I_{m\pm 1}$ may be replaced by 1 in Eq. (4). The boundary r_s is determined by radial integration of Poisson's equation with density n_0 out to radius r_s giving $\phi(R_w) = -V_{sq}$. Figure 6

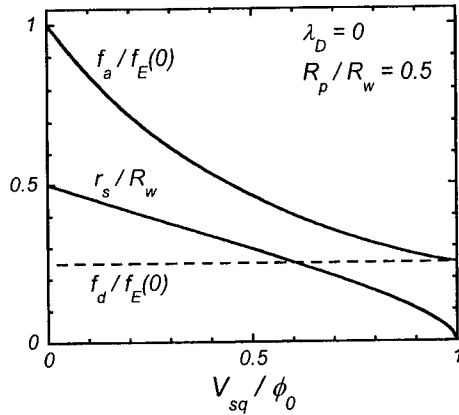


FIGURE 6. Separatrix radius r_s vs V_{sq}/ϕ_0 for uniform density model, giving f_a from Eq. (4) and constant f_d .

shows r_s , f_a , and f_d versus V_{sq} for this uniform density model with $R_p = 0.5R_w$ and $m = 1$. There is an obvious general correspondence between this coarse estimate and the experiment (Fig. 3).

A kinetic analysis allowing for trapped and untrapped particles co-existing at each radius gives a more realistic approximation to the experiments. The squeeze causes a potential barrier of strength $\Delta\phi(r)$, giving a trapped particle density $n_t(r) = n(r)\text{erf}[(e\Delta\phi/T)^{1/2}]$ and an untrapped density $n_u = n - n_t$. The equilibrium Poisson solutions show that $\Delta\phi$ is essentially zero for small radii and that it rises sharply near r_s to a value much larger than T . Thus, the kinetic treatment essentially smoothes the discrete transition model over a radial scale of a few λ_D .

The frequency f_a versus V_{sq} predicted by this kinetic theory using the measured $n(r)$ and the calculated $\Delta\phi(r)$ is given by the dashed curve in Fig. 3, showing close agreement with the measured frequencies. The 10% discrepancy may reflect the non-zero length of the barrier and consequent increase in trapped particle densities.

Similarly, the eigenfunctions $\delta n_a(r)$ obtained from the kinetic analysis show general correspondence with experiments (Fig. 5). The discrepancy for $r \gtrsim 1.5$ cm may be an artifact of the profile truncation applied theoretically.

MAGNETIC TILT, MODE COUPLING AND TRANSPORT

Although the asymmetry modes can propagate in a trap with perfect θ -symmetry, our larger interest is in traps with (inevitable) θ -asymmetries. These asymmetries commonly arise from construction imperfections in the trap walls (especially in the sectorized cylinders) or in the magnet. The asymmetries can have arbitrary θ - and z -dependence, but it

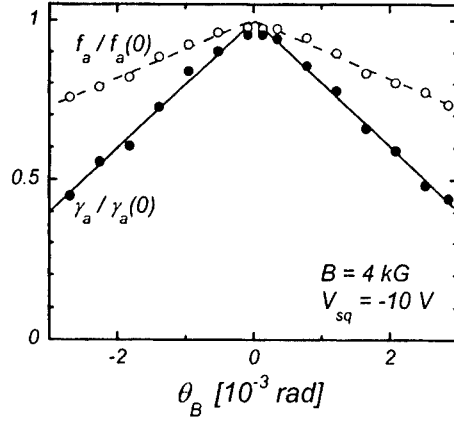


FIGURE 7. Measured frequency f_a and decay rate γ_a vs magnetic tilt θ_B , normalized to values at $\theta_B = 0$.

is common to refer to their dominant m and k_z components. One of the more prevalent asymmetries is a $m = 1$, $k_z = \pi/L_p$ “tilt” of the magnetic field with respect to the trap axis, characterized by an angle $\theta_B \equiv B_\perp/B_z$.

The qualitative behavior of the asymmetry mode remains unchanged even with moderately large magnetic tilt. Figure 7 shows f_a decreasing linearly by 30% and γ_a decreasing by 60% at fixed $V_{sq} = -10$ V as the magnetic tilt is increased to $\theta_B = \pm 3 \times 10^{-3}$ radian. These quantitative changes are mainly due to a decrease in the plasma potential ϕ_0 (caused by tilt-induced particle transport). Consequently, the ratio V_{sq}/ϕ_0 increases and the effective trapping barrier is enhanced. This will produce a decrease in the mode frequency and decay rate according to the trends depicted in Figs. 3 and 4.

Trapped particles may be an inherent part of Penning-Malmberg traps for a variety of reasons. Some intentional manipulations, such as “squeeze damping” of the diocotron mode [7, 8] obviously create equilibria as described here. The wide variety of “nested traps” being built for overlapping confinement of positrons and anti-protons [9, 10] have populations of trapped and untrapped particles. Most subtly, z -variations in the effective wall voltage can arise from small unintentional construction anomalies. For example, a variation in wall radius among cylinders gives an effective potential $V_{sq} \approx \phi_0 \Delta R_w/R_w$; this gives a trapped fraction $\epsilon_{tr} \approx \Delta R_w/R_w$, so $\epsilon_{tr} \gtrsim 10^{-3}$ is probably common to all devices.

The existence of trapped particle asymmetry modes substantially alters the theory perspective on particle transport due to θ -asymmetries in the trap construction. Resonant particle transport theories [3] utilize integration along unperturbed orbits, which is invalid with the bulk trapped particle populations described here, or even with microscopic trapping [11]. Similarly, 2D bounce-averaged invariants suggest that particles are confined to equipotential surfaces, and a k_z variation is required for radial particle transport; however, all previously-known modes with $k_z \neq 0$ have frequencies near ω_p as opposed to f_d .

Experimentally, there are strong indications that the asymmetry mode contributes to

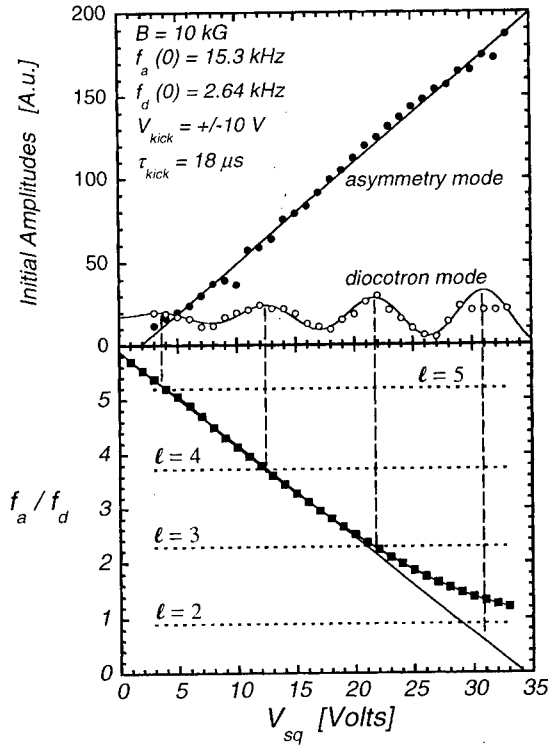


FIGURE 8. (a) “Excitability” of the asymmetry (closed circles) and diocotron (open circles) modes vs squeeze voltage V_{sq} . (b) Measured ratio f_a/f_d (squares) vs squeeze voltage V_{sq} . The horizontal dashed lines show the resonance [Eq. (6)] of sloshing particles. The vertical dashed line indicates an obvious correspondence of these resonances to the maxima in the diocotron mode amplitude.

asymmetry-induced transport by coupling between the static $m \neq 0$ $k_z \neq 0$ asymmetry and the $k_z \approx 0$ diocotron modes. When the external asymmetry is a magnetic tilt ($\theta_B \neq 0$), the diocotron mode has axially sloshing particles [12] at low frequency $f_d \ll f_b$, which can be thought of as a slow change in the equilibrium. A simple picture of what occurs with a misaligned plasma column is that the particles tend to accumulate wherever they can be closer along the magnetic field lines to their image charge in the wall, since that is a region of lower energy. Consequently, a small amount of the density ($\delta n \propto \theta_B$) sloshes axially from one end to the other as the diocotron mode causes the plasma column to orbit around the magnetic axis of the trap. This axial motion can then couple to the axially sloshing interior particles in the asymmetry mode. The coupling leads to the diocotron mode damping through excitation of the strongly damped asymmetry modes, and consequently to bulk radial transport of the particles.

The characteristics of this coupling are presently being investigated. Figure 8(a) shows the “excitability” of the asymmetry and diocotron modes as functions of the applied squeeze voltage. “Excitability” is simply the initial amplitude of the mode excited from

the wall sectors by a fixed $m = 1$ kick with odd parity in z (Fig. 1). The small excitation of the diocotron mode at $V_{sq} \approx 0$ occurs only because the sectors at $\pm z$ have slightly different coupling to the plasma. As squeeze voltage is increased, the asymmetry mode "excitability" increases linearly, in accord with the change of the trapped particle fraction ϵ_{tr} . In contrast, the excitation of the diocotron mode shows increasing oscillations about the $V_{sq} \approx 0$ level [Fig. 6(a)].

The maxima in these oscillations may be due to resonance in the axial velocities of sloshing particles shared by the two modes. Thus, we could expect that in resonance

$$\frac{f_E - f_a}{2\pi k_a} = \frac{f_E - \ell f_d}{2\pi k_d}, \quad (5)$$

where k_a and k_d are effective axial wave vectors ($k_a > k_d$) for the sloshing particles in corresponding modes, and $\ell = 2, 3, \dots$ is the order of the resonance. Figure 8(b) shows the measured ratio f_a/f_d as a function of the squeeze voltage. Comparing Figs. 8(a,b), we see that the maxima in the diocotron mode amplitude corresponds to the particular ratios of these mode frequencies, obtained directly from Eq. (5) using a quite reasonable ratio of the wave vectors $k_a/k_d \approx 1.45$ as the single adjustable parameter

$$\frac{f_a}{f_d} = \ell \frac{k_a}{k_d} + \frac{f_E}{f_d} \left(1 - \frac{k_a}{k_d} \right). \quad (6)$$

This result may provide a clue as to why the diocotron mode has shown a squeeze dependent damping [7, 8]. Of course, the underlying assumptions and simplifications of the observed coupling remain to be examined. Nevertheless, our results allow us to speculate that the asymmetry modes are important in coupling trap asymmetries to particle motions and low frequency $\mathbf{E} \times \mathbf{B}$ drift modes.

ACKNOWLEDGMENTS

This work was supported by Office of Naval Research grant N00014-96-1-0239 and National Science Foundation grant PHY-9876999.

REFERENCES

1. J.J. Bollinger, R.L. Spencer, and R.C. Davidson (editors), *Non-Neutral Plasma Physics III*, American Institute of Physics Conf. Proc. 498 (New York: American Institute of Physics, 1999).
2. J.M. Kriesel and C.F. Driscoll, Phys. Rev. Lett. **85**, 2510 (2000).
3. D.L. Eggleston and T.M. O'Neil, Phys. Plasmas **6**, 2699 (1999).
4. A.J. Redd, *et al.*, Phys. Plasmas **6**, 1162 (1999).
5. M. Nadeem, *et al.*, Plasma Phys. Control. Fusion **37**, 1169 (1995).
6. K.S. Fine, W.G. Flynn, A.C. Cass, and C.F. Driscoll, Phys. Rev. Lett. **75**, 3277 (1995).
7. B.P. Cluggish, Ph.D. thesis, Univ. of California at San Diego (1995).
8. K.S. Fine, Ph.D. thesis, Univ. of California at San Diego (1989).
9. M. Charlton, *et al.*, Phys. Rep. **214** (2), 67 (1994).
10. D. Hall and G. Gabrielse, Phys. Rev. Lett. **77**, 1962 (1996).
11. D.H.E. Dubin, Phys. Rev. Lett. **79**, 2678 (1997).
12. G.W. Hart, Phys. Fluids B **3**, 2987 (1991).

Simulations of the Instability of the $m = 1$ Self-Shielding Diocotron Mode in Finite-Length Nonneutral Plasmas

Grant W. Mason and Ross L. Spencer

Department of Physics and Astronomy, Brigham Young University, Provo, Utah 84602

Abstract. The “self-shielding” $m = 1$ diocotron mode in Malmberg-Penning traps has been known for over a decade to be unstable for finite length nonneutral plasmas with hollow density profiles. Early theoretical efforts were unsuccessful in accounting for the exponential growth and/or the magnitude of the growth rate. Recent theoretical work has sought to resolve the discrepancy either as a consequence of the shape of the plasma ends or as a kinetic effect resulting from a modified distribution function as a consequence of the protocol used to form the hollow profiles in experiments. We have investigated both of these finite length mechanisms in selected test cases using a three-dimensional particle-in-cell code that allows realistic treatment of shape and kinetic effects. We find that a persistent discrepancy of a factor of 2-3 remains between simulation and experimental values of the growth rate.

INTRODUCTION

Nonneutral plasmas, typically ions or electrons, can be confined for long periods of time in a cylindrical Malmberg-Penning trap similar to that shown in Fig. 1. A stiff axial magnetic field confines the particles radially, and charged rings at the ends of the otherwise grounded cylinder provide electrostatic longitudinal confinement. Diocotron modes are azimuthal drift waves in the cylindrical plasma that vary spatially as $\exp(im\theta)$. The theory of diocotron modes in nonneutral plasmas has its origins in seminal papers by Levy [1], Briggs, Daugherty and Levy [2], and the comprehensive treatment of nonneutral plasmas by Davidson [3].

The azimuthal mode of interest here occurs for hollow density profiles where the azimuthal flow of the plasma exhibits shear to create a rotation frequency profile $\omega_0(r)$ that rises with increasing radius from the center, peaks, then decreases to the wall. The resulting $m = 1$ mode (“self-shielded”) has a frequency near the peak of the frequency profile.

In the infinite length approximation, this mode is predicted not to be exponentially unstable for all radial density profiles of the plasma column. In contrast, when the plasma column is of finite length, the self-shielding $m = 1$ mode has been experimentally shown to be exponentially unstable for hollow density profiles [4, 5, 6].

Several theoretical attempts have been made to understand the origin of the instability [7, 8, 9, 10], but have failed to account for the exponential character of the stability and/or the size of the growth rate. In particular, Smith [8] has drawn attention to finite length effects and Finn *et al.* [11] have drawn attention to the importance of the shape

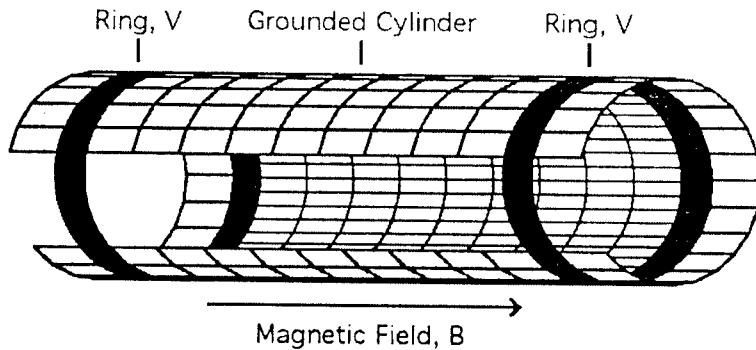


FIGURE 1. A Malmberg-Penning Trap. The axial magnetic field B confines charged particles radially and voltages V on the rings confine the nonneutral plasma longitudinally in the cavity space between the rings.

of the ends of the plasma based on an analogy to vortex stretching from topography variations in shallow fluid dynamics for geophysical flows. The theory of Finn, *et al.* when adapted to vortex dynamics in nonneutral plasmas, demonstrates that the radial variation of the equilibrium plasma length causes compression of the plasma parallel to the magnetic field while conserving the line integrated density. Their theory predicts the observed exponential growth of the instability, but predicts a growth rate that is still somewhat more than a factor of two less than a test case taken by Finn *et al.* [11] from data of Driscoll [5].

Coppa *et al.* [12] have refined the theory of Finn *et al.* but the refinements prove relatively small when applied to the test case of Finn *et al.*

Hilsabeck and O'Neil [13] develop a Zero Debye Length Reduced Description, but also fail to predict large enough growth rates based on end shape and length alone. However, they also observe that experimental procedures to produce plasmas with hollow profiles involve lowering the confining ring potentials and dumping preferentially the particles in the tail of the original Maxwellian velocity distribution, thus effectively truncating the velocity distribution near the center of the plasma. For certain distributions of axial energies, the instability can be substantially affected.

Here we report the results of three-dimensional particle-in-cell simulations that attempt to account for the remaining quantitative disagreement.

THEORY

We first consider electrons confined in cylindrical geometry by an axial magnetic field and an electrostatic potential. The equations describing the motion are isomorphic to those of two-dimensional fluid flow [1, 2] in the limit that the length of the plasma is much greater than its radius. In the case of the nonneutral plasma, the particles are considered to bounce longitudinally while drifting azimuthally. The bounce frequency is

taken to be much larger than the azimuthal $\mathbf{E} \times \mathbf{B}$ drift, so that the longitudinal dynamics is effectively separated from the bounce-averaged azimuthal drift. The fundamental equations of the Drift-Poisson Model then become (in the infinite length approximation),

$$\frac{\partial \rho}{\partial t} + \nabla \cdot (\rho \mathbf{u}) = 0 \quad \mathbf{u} = -\frac{\nabla \phi \times \hat{\mathbf{z}}}{B} \quad \nabla^2 \phi = -\frac{\rho}{\epsilon_0}. \quad (1)$$

The equations can be linearized assuming

$$\rho = \rho_0 + \rho_1 e^{i(m\theta - \omega t)} \quad \phi = \phi_0 + \phi_1 e^{i(m\theta - \omega t)} \quad \mathbf{u} = \mathbf{u}_0 + \mathbf{u}_1 e^{i(m\theta - \omega t)}, \quad (2)$$

leading to the diocotron mode equation,

$$(\omega - m\omega_0(r)) \left[\frac{1}{r} \frac{d}{dr} \left(r \frac{d}{dr} \phi_1 \right) - \frac{m^2 \phi_1}{r^2} \right] - \frac{mq}{\epsilon_0 B r} n'_0(r) \phi_1 = 0. \quad (3)$$

In the infinite length approximation, the self-shielding mode has frequency $\omega = \omega_0(r_{\max})$ for which,

$$\phi_1 = r(\omega - \omega_0(r)), \quad r \leq r_{\max} \quad (4)$$

$$\phi_1 = 0, \quad r > r_{\max}, \quad (5)$$

where $\omega_0(r)$ is the equilibrium rotation frequency profile and r_{\max} is the radius at which the profile peaks. The eigenfrequency is real and the mode is neutrally stable in this infinite length approximation.

Finn *et al.* identify two instability mechanisms when finite length plasma columns are considered. The first occurs when the shape of the end of the plasma is such that there is a radial variation of the equilibrium plasma length. In this case during motion there can be a compression of the plasma by the confining potential that conserves the line integrated density parallel to the magnetic field. The second mechanism is a perturbation of the plasma length when particles interact with the confining potential at the ends. Finn *et al.* demonstrate that both mechanisms give instability with comparable growth rates. The mode equation becomes [11],

$$\begin{aligned} (\omega - m\omega_0(r)) \left[\frac{1}{r} \frac{d}{dr} \left(r \frac{d}{dr} \phi_1 \right) - \frac{m^2 \phi_1}{r^2} \right] - m \frac{n'_0}{r} \phi_1 = \\ + \frac{mq}{\epsilon_0 B} \frac{n_0}{r} \frac{L'_0(r)}{L_0(r)} \phi_1 + \frac{q}{\epsilon_0} (\omega - m\omega_0(r)) n_0 \frac{\Lambda[\phi]}{L_0} \phi_1, \end{aligned} \quad (6)$$

where $L_0(r)$ and $L'_0(r)$ are respectively the equilibrium radial profile of the plasma length and its radial derivative. The functional $\Lambda[\phi]$ is the first order correction to the plasma length caused by perturbations in the potential [11]. To make the analysis tractable, Finn *et al.* approximate the equilibrium length of the plasma by a quadratic function. However, perturbations in the plasma length (Λ) were implemented ignoring curvature of the ends as a simple approximation.

The work of Hilsabeck and O'Neil and of Coppa *et al.* include refinements to the theory and implementation of Finn *et al.* Both accept an arbitrary plasma shape, use realistic axial boundary conditions, and incorporate perturbations in the plasma length self-consistently using a Green's function. Solutions are by numerical methods. Both efforts find similar growth rates for the self-shielded mode that are several times smaller than the comparable test case taken from experiment. Calculated real frequencies of the mode are slightly smaller than the maximum of the rotation profile in contrast to experimental values that may be 25% lower than the maximum of the profile [13].

Hilsabeck and O'Neil conclude that quantitative agreement with the measured growth rates and frequencies requires the inclusion of a kinetic effect which arises from the experimental method used to load the hollow density profiles. The experimental protocol is assumed to truncate the high-velocity tails of the longitudinal velocity distribution in a radially dependent way. This can be important because the fast particles penetrate into a region in the ends of the plasma where their $\omega_0(r)$ is reduced compared to slower particles that do penetrate so deeply. If the longitudinal velocity distributions have radial dependence, the dynamics of the mode can be altered.

SIMULATIONS

In this paper we take a numerical approach by doing particle-in-cell simulations. The method has the advantage of incorporating realistic boundary and end conditions in detail while also providing diagnostic information about the plasmas that are otherwise unknown in the experiments or in the methods of Finn *et al.* and of Hilsabeck and O'Neil. We perform numerical experiments with the intent of helping to understand whether plasma shape and/or kinetic effects are adequate to predict experimentally measured growth rates for the unstable $m = 1$ diocotron mode in finite-length plasmas.

Azimuthally symmetric equilibria are computed separately using a two-dimensional $(r - z)$ Successive Over-Relaxation (SOR) code [14]. Two-dimensional density and electric potential arrays are passed from the equilibrium code to the simulation code and interpolated onto a three-dimensional Cartesian grid. The three-dimensional density is then represented by particles-in-cells (PIC). The azimuthal symmetry of the distribution of particles is broken by small density perturbations or initial displacements of each particle chosen to seed a particular azimuthal mode using the infinite-length theory for the mode shapes.

In the present work, the plasma is typically represented by about 10^6 computational "particles" that, in turn, each represent several thousand plasma electrons. The computation is done in three-dimensional Cartesian geometry into which is embedded the confining cylinder. The grid used was $65 \times 65 \times 129$ for plasmas that were typically 0.30 m in length with a Debye length of ≥ 0.003 m. Short-legged differential operators for the Laplacian operator are used at the cylindrical boundary so that the cylindrical shape is treated realistically. Likewise, boundary conditions are implemented realistically, with a grounded cylinder sandwiched between confinement rings at each end held at sufficient potential to confine the plasma. Beyond the rings (longitudinally) and away from the plasma on each end is a short buffer zone of grounded cylinder at the end of

which periodic boundary conditions ($\partial\phi/\partial z = 0$) are maintained to complete the boundary conditions for the computation region.

Poisson's equation is solved by distributing density to the computational grid and using a three-dimensional multigrid algorithm to solve Poisson's Equation. Particles are moved in the (x, y) -plane assuming $\mathbf{E} \times \mathbf{B}$ drift motion and using a predictor-corrector algorithm. In the longitudinal z -direction we use Newton's Second Law and a leap-frog algorithm. Densities are distributed to the grid, fields are computed from Poisson's Equation, particles are moved in response to the fields, and new densities are computed to begin the cycle anew.

RESULTS

We have considered two "families" of equilibria. The first is based on a test case used by Finn *et al.* [11]. The electron plasma had a radius $r_p = 0.02$ m, confined within a cylinder of radius $r_w = 0.038$ m. The magnetic field was 375 G and the confining ring potentials were -50 V. The central cylinder had a length of 0.32 m. The rings had a width of 0.03 m and in this case the length of the buffer zone was zero.

The radial density profile of the plasma in the Finn theory was given by the parametrization,

$$n_0(r) = n_0(0)[1 - (r/r_p)^2]^2[1 + (\mu + 2)(r/r_p)^2] \quad (7)$$

for $r \leq r_p$ and zero elsewhere. The radial profile of the length of the plasma was parametrized by Finn *et al.* as

$$L_0(r) = L_0(0)[1 - \kappa(r/r_w)^2], \quad (8)$$

where r_w is the radius of the cylinder. The hollowness of the profile was controlled by the parameter μ and the curvature of the ends was described by the parameter κ . In the test case computed by Finn *et al.*, μ was chosen to be 3, resulting in a ratio $n_{max}/n_0 = 1.28$. and a value for κ of 0.25.

We prepared a simulation using the same radial density profile, plasma radius, cylinder radius, confining ring potentials and magnetic field as the Finn *et al.* test case. We chose a plasma temperature of 1.2 eV and a plasma length of 0.30 m. Under these conditions the value of kappa was approximately 0.3 and the value of n_{max} was 6.28×10^{12} particles per cubic meter corresponding to $\omega_0(max) = 1.44 \times 10^6 \text{ sec}^{-1}$. Plasma length profiles for the series of simulations based on the Finn *et al.* test case are shown in Fig. 2. Observe that the vertical scale is truncated. The radial variation of L_0 is relatively small compared to the overall length of the plasma. The profiles in Fig. 2 do not appear to be strictly parabolic, so our value of kappa (0.3) is only a rough approximation to the Finn value of 0.25.

At each time step of the simulation a longitudinally line-integrated density function was formed and then Fourier analyzed to find the amplitude and phase of the $m = 1$ mode. The phase signal as a function of time was used to measure the real frequency of the mode and an exponential function was fitted to the amplitude signal (as a function of time) to obtain the growth rate. The amplitude signal rises with an apparent exponential

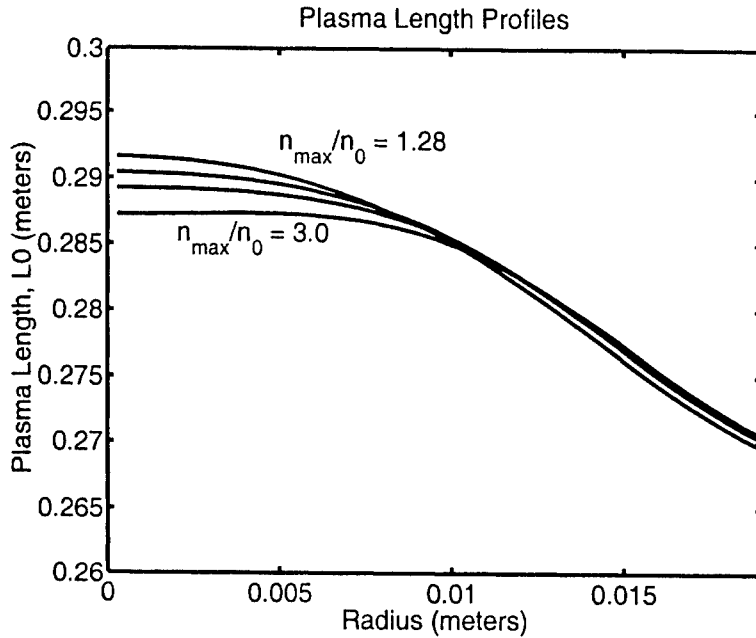


FIGURE 2. Radial length profiles for the plasmas identified with asterisks in Fig. 4. A parabolic fit ($L(x) = L_0(1 - \kappa(r/r_w)^2)$) to the uppermost curve yields roughly a value $\kappa \approx 0.3$. As n_{max}/n_0 increases, the profiles are less and less parabolic.

growth, but the signal wobbles slightly with time relative to the exponential. We have indicated with error bars an estimate of the uncertainty that this gave to the growth rate measurements. Figure 3 shows a typical amplitude signal with a corresponding exponential growth for comparison as well as the corresponding phase signal.

The results of the simulations are shown in Fig. 4. The ratio of growth rate to real mode frequency is about 0.007 compared to the Finn *et al.* result of 0.009, the Coppa *et al.* result of 0.008, and the experimental value of 0.025. Our real frequency was $1.40 \times 10^6 \text{ sec}^{-1}$ which is consistent with the expectation of a real frequency near the maximum of the radial rotation profile of our equilibrium ($1.44 \times 10^6 \text{ sec}^{-1}$). In each case in Fig. 4, the simulation gives a real frequency of the mode to within 1-3% of the maximum of the rotation profile $\omega_0(\text{max})$.

We completed the first "family" of simulations by maintaining the value of $n_0(\text{max})$ and deepening the profile using the Finn *et al.* radial density parameterization with $\mu = 5.66, 8.19, 15.07$. The corresponding ratios n_{max}/n_0 are 1.64, 2.00, 3.00. These growth rates are also shown in Fig. 4 as the points marked with the asterisk (*) symbol. The point at $n_{max}/n_0(0) = 2$ is coincident with the prediction of our drift-kinetic code.

The second family of simulations was done to address the possibility suggested by Hilsabeck and O'Neil that the persistent discrepancy between experiment and theory may be a kinetic effect when particles of differing energies penetrate the confining potential at the ends to differing degrees. This effect may be enhanced because, experimen-

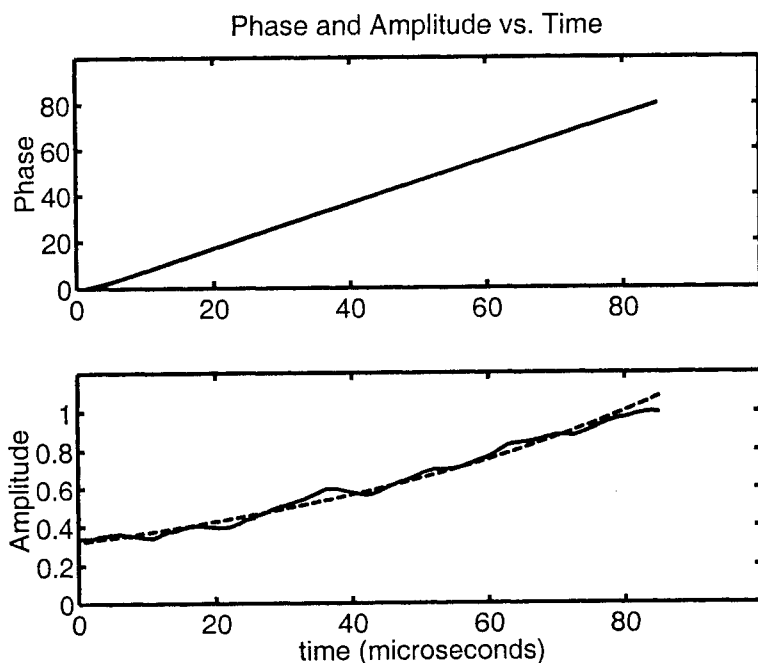


FIGURE 3. (Upper) The phase signal in radians from which the real frequency ω_r of the mode is determined. The phase signal from the simulation is remarkably linear. (Lower) An exponential growth curve compared to the amplitude signal for the $m = 1$ mode from the particle-in-cell simulations. Error flags on the simulation results plotted in Fig. 4 are estimates of the uncertainty in growth rate determinations based on figures like this one.

tally, the hollow profiles are created from a non-hollow profile by temporarily lowering the end potentials. This procedure allows more particles to escape near $r = 0$ than at larger radii, but also depletes the Maxwellian distribution of velocities in a radially dependent way. The nonmaxwellian distributions created in this way will depend heavily on the protocol used to create the plasmas and experimental velocity distribution data are not available for a specific test case.

For purposes of simulation, we began with a flat-topped density profile. We again used a magnetic field of 375 G and a temperature of 1.2 eV. However, the radius of the cylinder was 0.05 m and the plasma length about 0.35 m. The central density plateau was 5×10^{12} per cubic meter. The confining ring potentials were -200 V. The central cylinder had a length of 0.44 m, rings a width of 0.03 m, and a buffer zone length of 0.05 m.

The equilibrium was calculated and loaded into the simulation code as before. However, when the code began, the ring voltages (boundary conditions) were reduced linearly over a 1 μsec period of time to some fraction of the original confining value chosen to reduce the potential near $r = 0$ to a value close to the central potential of the plasma. The rings were then held down at this destination potential for 4 μsec , then linearly raised

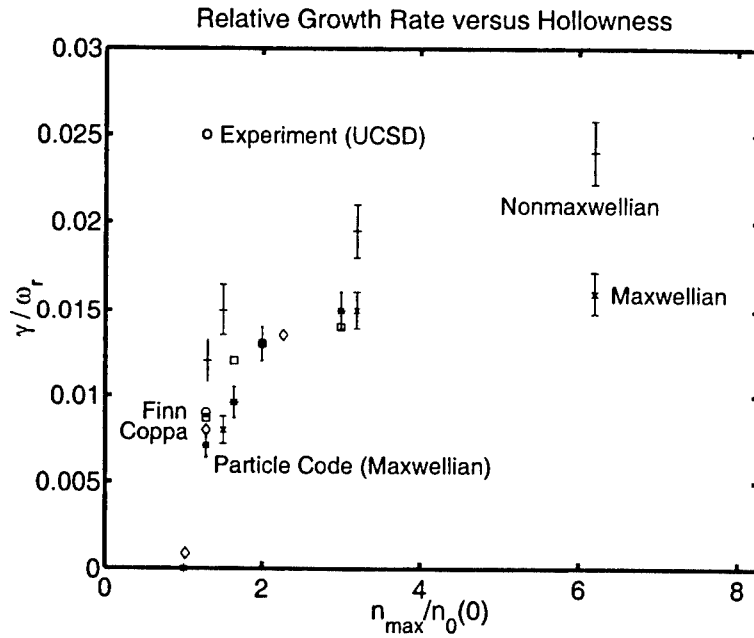


FIGURE 4. Comparisons of calculated growth rates to the theory of Finn *et al.* and an experimental test case (open circles). Asterisks (*) mark simulation points based on a test case of Finn *et al.* taken from experiment (UCSD). Hyphens (-) mark simulation points obtained by depleting the tails of the longitudinal velocity distributions. Corresponding Maxwellian cases are marked by "x" for comparison. Also included for comparison are predictions from our drift-kinetic code calculation (open boxes) and results of the "complete model" of Coppa *et al.* marked with diamonds.

again to the original value over a final microsecond. The resulting density profile was hollow and not unlike the profiles obtained from the Finn *et al.* formula. The degree of hollowness ($n_{max}/n_0(0)$) was controlled by the fraction applied to the -200 V ring potentials when the confining potentials were lowered. Since the potential remained down for several bounce times, virtually all particles with longitudinal velocities below a certain critical value were removed. The velocity distributions resulting from this protocol had a radial dependence and since equilibration times were much longer than the time of our simulation, the resulting velocity distributions as a function of radius were and remained "nonmaxwellian" through the course of the simulation. The hollowed density profiles created in this way are shown in Fig. 5. Figure 6 shows the corresponding root-mean-square velocity profiles.

Three plasmas were created using the protocol described above with $n_{max}/n_0 = 1.5, 3.2, 6.2$. The corresponding density profiles are shown in Fig. 5. The growth rates are shown in Fig. 4 marked with the hyphen (-) symbol. The 6.2 point is labelled as "nonmaxwellian." For comparison, we took the radial density profiles from these three nonmaxwellian simulations and created distributions differing only in that the longitudinal velocity distributions were Maxwellian at all radii (with temperature 1.2

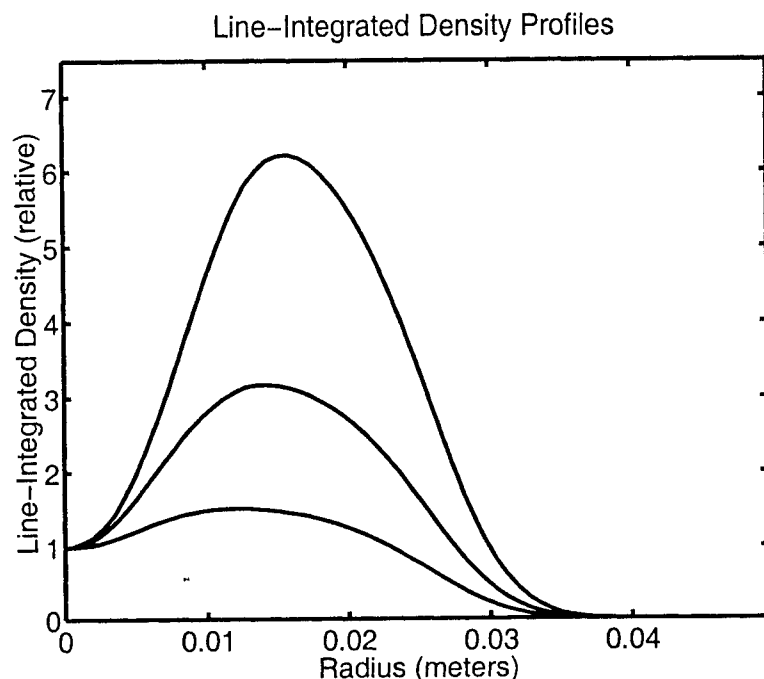


FIGURE 5. Simulated hollow line-integrated density profiles obtained by temporarily lowering the potentials on the confinement rings according to the protocol described in the text. Absolute line integrated densities at $r = 0$ are 1.10×10^{12} (bottom), 5.12×10^{11} (middle), and 2.52×10^{11} (top) particles per square meter.

eV). These are shown in Fig. 4 marked with the "x" symbol. The nonmaxwellian growth rates are enhanced over their Maxwellian counterparts by factors of 1.9, 1.3, and 1.5 for n_{max}/n_0 equal to 1.5, 3.2, and 6.2 respectively.

As an approximate check of the results of our simulations and to provide an additional comparison to results by Finn *et al.* and Coppa *et al.*, we have used a separate linear drift-kinetic eigenvalue code to compute growth rates. The code, which was originally written for the infinitely-long plasma approximation, was easily modified to include the L'_0/L_0 term on the right-hand-side of Eq. 6 but not the Λ term. The eigenvalue code uses equilibria calculated separately by the same SOR code used to calculate equilibria for the simulations using density profiles from Eq. 7. See Fig. 4.

This independent calculation reproduces the Finn *et al.* growth rate almost exactly at $n_{max}/n_0 = 1.28$, coincides exactly with the simulation point at $n_{max}/n_0 = 1.64$, and meshes smoothly with the results of Coppa *et al.* using their "complete model." The results of our eigenvalue code are shown as open squares in Fig. 4. The results of Coppa *et al.* are shown as open diamonds.

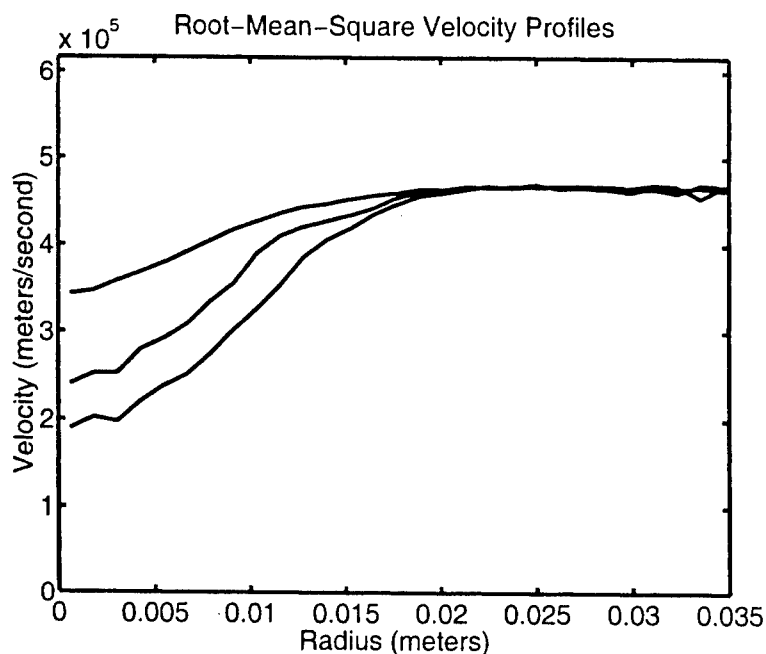


FIGURE 6. Radial root-mean-square velocity (v_z) profiles for the simulated plasmas of Fig. 5. The corresponding velocity distributions at each radius are identified as "nonmaxwellian" in Fig. 4.

CONCLUSIONS

We have used particle-in-cell simulations to compute growth rates for the hollow, finite-length $m = 1$ self-shielded diocotron mode. We have investigated test cases where the persistent discrepancy between theory and experiment may be a consequence of the shape of the ends of the plasma or kinetic effects arising from a nonmaxwellian velocity distributions introduced in the experimental preparation of the plasmas. In none of the test families were we able to achieve growth rates as large as the experimental value. Real frequencies computed in the simulations for the self-shielding mode were typically within about 3% of the maxima of the respective rotation profiles. Thus, we agree with the conclusion of Hilsabeck and O'Neil that the end shape effects we considered are alone insufficient to remove the discrepancy with experiment.

We have also simulated a nonmaxwellian longitudinal velocity distribution effect suggested by Hilsabeck and O'Neil. The effect increases growth rates by 30-90% compared to Maxwellian control cases. Nevertheless, the simulation is still a factor of 2.0 too low to remove the discrepancy with experiment at $n_{max}/n_0(0) = 1.28$. However, the two methods which we used to create the nonmaxwellian distributions may not correspond to the actual experimental protocols, leaving some room yet for further study.

ACKNOWLEDGEMENTS

We gratefully acknowledge helpful discussions with J. M. Finn, D. del Castillo-Negrete, T. M. O'Neil, D. H. E. Dubin, T. J. Hilsabeck, and A. A. Kabantsev. S. N. Rasband provided helpful results from a recently-developed cold-fluid code against which we compared test runs from the PIC code described in this paper. We also gratefully acknowledge the use of facilities of the Brigham Young University Supercomputing Center.

REFERENCES

1. R. H. Levy, Phys. Fluids **8**, 1288 (1965); **11**, 920 (1968).
2. R. J. Briggs, J. D. Daugherty, and R. H. Levy, Phys. Fluids **13**, 421 (1970).
3. R. C. Davidson, *Theory of Nonneutral Plasmas* (Benjamin, Reading, MA, 1974).
4. C. F. Driscoll and K. S. Fine, Phys. Fluids B **2**, 1359 (1990).
5. C. F. Driscoll, Phys. Rev. Lett. **64**, 645 (1990).
6. A. Kabantsev and C. Driscoll, in *Non-Neutral Plasmas III*, edited by J. Bollinger, R. Spencer, and R. Davidson (American Institute of Physics, New York, 1999), pp. 208-213.
7. R. A. Smith and M. N. Rosenbluth, Phys. Rev. Lett. **64**, 649 (1990).
8. R. A. Smith, Phys. Fluids B **4**, 287 (1992).
9. S. N. Rasband, R. L. Spencer, and R. R. Vanfleet, Phys. Fluids B **5**, 669 (1993).
10. S. N. Rasband, Phys. Plasmas **3**, 94 (1996).
11. J. M. Finn, D. del Castillo-Negrete, and D. C. Barnes, Phys. Plasmas **6**, 3744 (1999).
12. G. G. M. Coppa, A. D'Angola, G. L. Delzanno, and G. Lapenta, Phys. Plasmas **8**, 1133 (2001).
13. T. J. Hilsabeck and T. M. O'Neil, Phys. Plasmas **8**, 407 (2001).
14. R. L. Spencer, S. N. Rasband, and R. R. Vanfleet, Phys. Fluids B, **5**, 1738 (1993).

Large Amplitude $m = 1$ Diocotron Mode Measurements in the Electron Diffusion Gauge Experiment ¹

Thomas G. Jenkins, Kyle A. Morrison, Ronald C. Davidson, and
Stephen F. Paul

Plasma Physics Laboratory, Princeton University, Princeton, NJ 08543

Abstract. Smaller-diameter pure electron plasmas are generated in the Electron Diffusion Gauge (EDG) using a thoriated tungsten filament wound into a spiral shape with an outer diameter which is $1/4$ of the trap wall diameter. The $m = 1$ diocotron mode is excited in the plasma by means of the resistive-wall instability, using a resistor-relay circuit which allows the mode to be induced at various initial amplitudes. The dynamics of this mode may be predicted using linear theory when the amplitude is small. However, it has been observed [e.g., Fine *et al.*, Phys. Rev. Lett. **63**, 2232 (1989)] [1] that at larger amplitudes the frequency of this mode (relative to the small-amplitude frequency) exhibits a quadratic dependence on the mode amplitude. In this paper, the frequency shift and nonlinear dynamics of the $m = 1$ diocotron mode in the EDG device are investigated.

In this paper theoretical and experimental results relating to the nonlinear dynamics of the $m = 1$ diocotron mode in the standard Malmberg-Penning trap configuration are discussed. The experimental apparatus is first briefly described. The linear, infinite-length theory of this mode is then summarized for reference purposes, together with a qualitative summary of the effects of finite plasma length on the mode dynamics. The resistive-wall instability is then discussed as a means of exciting the desired modes in the experiment. It is shown that the observed growth rate of this instability is consistent with theoretical predictions and past experiments. Additionally, it is shown that the instability provides a means to excite the $m = 1$ mode to amplitudes large enough that a change in scaling of the mode frequency shift with amplitude is observed.

EXPERIMENTAL APPARATUS

The Electron Diffusion Gauge (EDG) was constructed to study the interaction of a pure electron plasma with background neutral gases [2]. It follows the standard Malmberg-Penning trap configuration, consisting of a cylindrical conducting shell subdivided axially into rings. The EDG has six rings of radius $R_w = 2.54$ cm; the rings vary from two to four inches in axial length, and one of them is azimuthally subdivided into two half-cylinders. A pure electron plasma is confined axially within the cylinder configuration

¹ Research supported by the Office of Naval Research.

by applying a large negative potential (typically ≈ -147 V) between two nonadjacent rings. Radial confinement is provided by a magnetic field ($B = 300 - 600$ G) aligned with the cylinder axis, and the plasma is created by thermionic emission of electrons from a thoriated tungsten filament. Typical plasmas in EDG have central number density $n_0 \approx 10^7$ /cm³, axial line density $N_L \approx 3 \times 10^7$ /cm, length $L_p \approx 15$ cm, temperature $T = 1 - 2$ eV, and column radius $R_p = 0.64 - 1.27$ cm.

LINEAR THEORY OF DIOCOTRON MODES

Using cylindrical coordinates, and assuming a system of infinite extent parallel to the magnetic field $B\hat{z}$, consider a single-species plasma within a conducting cylindrical shell of radius R_w . The linear theory of diocotron modes is developed by making the assumption that the motion perpendicular to the magnetic field corresponds to an $\mathbf{E} \times \mathbf{B}$ drift, where \mathbf{E} is the electric field created by the plasma. Treating the plasma as an incompressible fluid, and using the continuity and Poisson equations, gives the closed system of equations

$$\mathbf{u} = \frac{-\nabla\Phi \times \hat{z}}{B}, \quad \frac{\partial n}{\partial t} + \mathbf{u} \cdot \nabla n = 0, \quad \nabla^2\Phi = -\frac{qn}{\epsilon_0}, \quad (1)$$

for the three physical quantities \mathbf{u} , n , and Φ , which are, respectively, the fluid velocity, particle number density, and electric potential. In Eq. (1) ϵ_0 is the permittivity of free space, and q is the charge of the confined particles including the sign.

Assuming that the temporal and angular dependence of the linearized quantities varies as $\exp i(m\theta - \omega t)$, the above equations are linearized to give the eigenvalue equation [3, 4] for a plasma of infinite length

$$[\omega - m\omega_0(r)] \left[\frac{1}{r} \frac{\partial}{\partial r} \left(r \frac{\partial \Phi_1}{\partial r} \right) - m^2 \frac{\Phi_1}{r^2} \right] = \frac{qm\Phi_1}{\epsilon_0 r B} \frac{\partial n_0}{\partial r}. \quad (2)$$

where $\omega_0(r) \equiv (rB)^{-1} \partial \Phi_0 / \partial r$. For $m = 1$ (assumed for the remainder of this paper), Eq. (2) admits simple solutions for the perturbed potential eigenfunction and eigenfrequency [5] of the form

$$\Phi_1 \propto r[\omega - \omega_0(r)], \quad \omega = \frac{|q|}{2\pi\epsilon_0} \frac{N_L}{R_w^2 B} \equiv \omega_\infty. \quad (3)$$

The mode frequency is obtained by using Gauss' Law in conjunction with the boundary condition imposed by the conducting cylinder, namely, that $\Phi_1(R_w) = 0$. The quantity N_L is the axial line density (the number density per unit axial length) of the plasma.

Physically, the $m = 1$ mode may be described as a combination of two rotational motions. The first is the equilibrium motion, i.e., the azimuthal $\mathbf{E} \times \mathbf{B}$ rotation of the plasma column around its own axis. The second is the perturbed motion, wherein the entire plasma column is displaced slightly from the z -axis, and precesses around the axis at frequency ω_∞ .

An early theoretical treatment [6] of the effects of finite plasma length predicts that the mode frequency ω should be shifted slightly upward, by a quantity which depends on the

ratio of the plasma radius R_p to the trap wall radius R_w . More recent work [7] modifies this hypothesis to include the dependence of the shift on the plasma temperature T and axial number density N_L . For typical EDG operating parameters, both theories predict a frequency shift of 10 – 20%, which is consistent with observations [8].

THE RESISTIVE-WALL INSTABILITY

It can be shown that the $m = 1$ diocotron mode is a negative-energy mode, which grows in amplitude as energy in the plasma is dissipated. This result can be obtained from a simple image charge calculation, modeling the plasma as a line charge with linear charge density $\lambda = qN_L$. The line charge is inside and parallel to the axis of a conducting cylinder of radius R_w , but displaced from the cylinder axis by a distance D . The equivalent image problem replaces the conducting cylinder by another line charge with charge density $-\lambda$, displaced from the original cylinder axis by a distance R_w^2/D along the ray from this axis to the original charge λ .

When $D \ll R_w$, consistent with linear theory, the electric field of the image charge causes a radial force per unit length on the plasma. Integration yields the energy per unit length when the plasma is displaced from the axis, i.e.,

$$\frac{F}{l} \approx \frac{q^2 N_L^2 D}{2\pi\epsilon_0 R_w^2} \Rightarrow \frac{W}{l} \approx -\frac{q^2 N_L^2 D^2}{4\pi\epsilon_0 R_w^2}. \quad (4)$$

The relevant physics in the expression for the energy W is contained in the negative sign and the dependence of the mode energy on D^2 . Displacing the plasma from the cylinder axis in the presence of dissipation excites the mode.

The plasma's motion induces image currents in the trap walls, which are ordinarily grounded (except for the confining end potentials). Consequently, dissipation (and thus an instability) may be introduced in the system by connecting a resistor R between a section of the trap wall and ground. Assuming that such a section has axial length L_s , and spans the azimuthal angle $\Delta\theta$, White *et al.* [9] have calculated the growth rate of the mode (which is proportional to the real part of the impedance between the trap section and ground) as

$$\gamma = \frac{4\epsilon_0}{\pi} \frac{L_s^2}{L_p} \omega^2 \sin^2\left(\frac{\Delta\theta}{2}\right) \left[\frac{R}{1 + \omega^2 R^2 C^2} \right]. \quad (5)$$

where C is the inherent capacitance of this section of the trap relative to the rest of the system, L_p is the plasma length, and ω is the mode frequency.

In EDG, a section of the trap wall of length $L_s = 5.08$ cm and azimuthal span $\Delta\theta = \pi$ is used to resistively grow the $m = 1$ diocotron mode, keeping the magnetic field and plasma line density constant in order to maintain a constant mode frequency $\omega/2\pi \approx 39.6$ kHz (left graph) and 38.0 kHz (right graph). In each case the plasma length is $L_p \approx 15$ cm and the wall capacitance $C \approx 200$ nF. The data, shown in Figure 1, agrees very well with the theoretical growth rate calculation except at high resistances. One explanation for this effect could be that a stray path to ground with a large, but finite

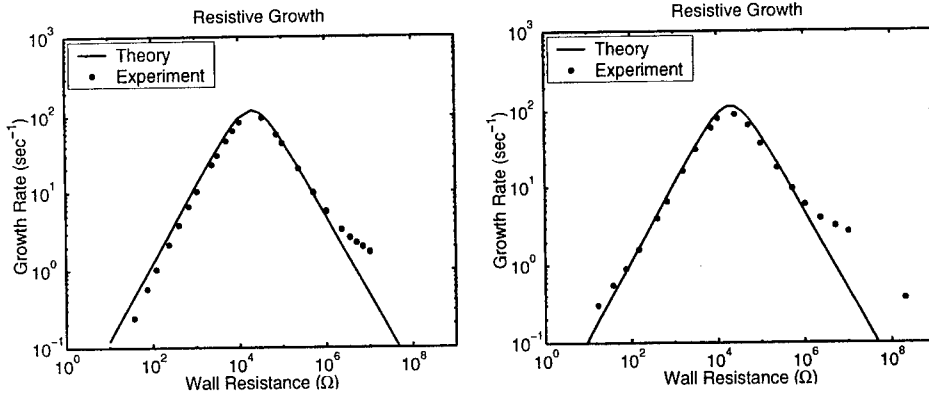


FIGURE 1. Measurements of the growth rate of the resistive-wall instability as a function of wall resistance, plotted together with the theoretical prediction of Eq. (5) (solid line). The data on the right was previously measured in EDG by Chao *et al.* [10].

resistance R_s exists between the wall sector and ground. Such a path would modify the impedance Z of this sector, such that

$$\text{Re}(Z) \propto \left[\frac{R}{1 + \omega^2 R^2 C^2} \right] \Rightarrow \text{Re}(Z) \propto \left[\frac{R(1 + R/R_s)}{(1 + R/R_s)^2 + \omega^2 R^2 C^2} \right]. \quad (6)$$

This results in a negligible change in the shape of the theoretical curve for $R_s \gg R$, but has a significant effect for $R_s \sim R$. The original growth rate, for $R \gg 1/\omega C$, decreases as $1/R$, but the asymptotic behavior of the new growth rate in the same regime is independent of R , i.e., it is simply a constant multiplying R_s . Choosing $R_s = 3.86 \text{ M}\Omega$ gives the best fit (in the least-squares sense) to the recent data, as shown in Figure 2. However, further investigation on this point is needed, particularly at very large resistances.

MODE GROWTH TO NONLINEAR AMPLITUDES

Using the resistive-wall instability as a means of exciting the $m = 1$ mode to large amplitudes, the nonlinear effects resulting from large amplitudes can be studied. The nonlinear problem of the dependence of the mode dynamics on mode amplitude was first treated theoretically by Prasad and Malmberg [11], who used a perturbation theory approach to show that for small displacements, the frequency of this mode should shift such that $(\omega - \omega_\infty)/\omega_\infty \propto (D/R_w)^2$, where D is the mode amplitude (displacement of the plasma column from the z -axis). This result was also obtained using a different model by Fine [12], and was experimentally investigated by Fine *et al.* [1], who give the empirical formula

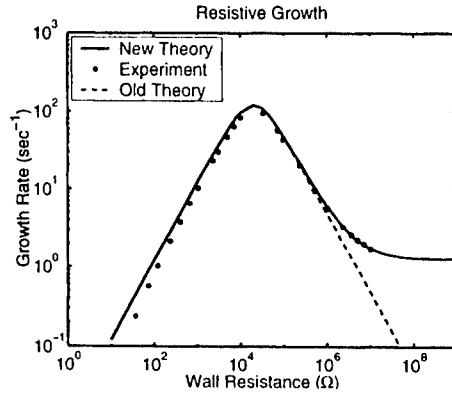


FIGURE 2. Measurements of the growth rate of the resistive-wall instability as a function of wall resistance, plotted together with the theoretical prediction of Eq. (5) (solid line) and the modified prediction of Eq. (6) (dashed line).

$$\frac{\omega - \omega_\infty}{\omega_\infty} = \left[1 - 7.3 \left(\frac{R_p}{R_w} \right)^6 \right] \left(\frac{D}{R_w} \right)^2 \quad (7)$$

for the scaling of the frequency shift as a function of mode amplitude.

Experiments aimed at verifying these results in EDG were performed by Chao [13], and the results of these experiments are shown in Figure 3. However, the radii of the plasmas used in these experiments were approximately equal to the filament radius $R_f = R_w/2 = 1.27$ cm, and as a result, the range of off-axis displacements in which

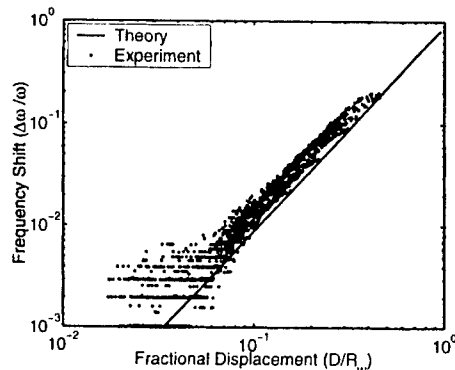


FIGURE 3. Data obtained by Chao [13] measuring the frequency shift $(\omega - \omega_\infty)/\omega_\infty$ as a function of relative displacement (D/R_w) , together with the prediction of Fine *et al.* [1] (solid line). The scatter at low frequency shifts is due to nonideal measurement apparatus.

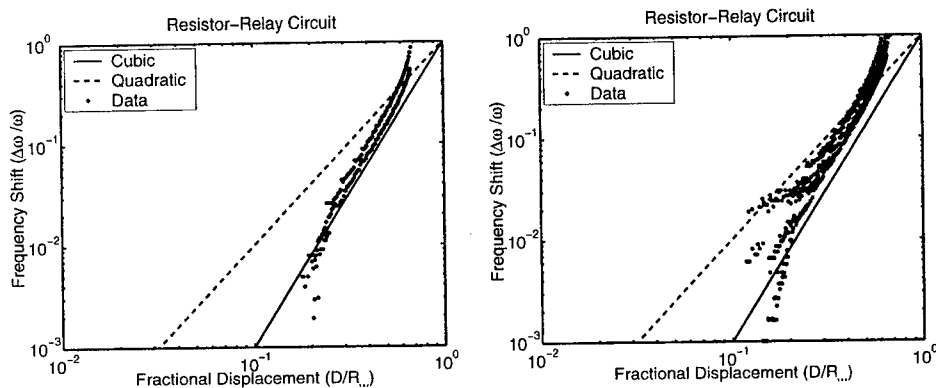


FIGURE 4. Measurements of the mode frequency shift as a function of relative mode displacement (D/R_w) for large relative displacements. Modes were excited using the relay circuit, with a resistance of 2.1 – 4.1 k Ω applied to the sectored trap wall for 0.2 seconds. Cubic (solid line) and quadratic (dashed line) dependences are plotted for reference. It is only the slope of these lines that is physically meaningful.

experiments could be performed was limited by eventual contact of the plasma with the trap wall. To test the scaling at large amplitudes, a smaller filament of radius $R_f = R_w/4 = 0.64$ cm was installed in EDG, and the resulting smaller-radius plasmas were excited by the resistive-wall instability to large relative amplitudes. Resistances were placed between the wall sector and ground for approximately 0.2 seconds, after which the wall sector was shorted to ground by a relay circuit. Modes of varying initial amplitude were obtained by changing the wall resistance, and measurements of the plasma displacement and frequency were subsequently taken as the mode damped.

In the present experiments, we find a persistent discrepancy between our data and the observation of Fine *et al.* [1] that the frequency shift scales quadratically in the relative mode amplitude. The data, shown in Figure 4, indicates that the dependence of this shift on amplitude is cubic for displacements on the order of the plasma diameter ($D/R_w \approx 0.3 - 0.5$). For larger displacements, the shift is proportional to successively higher powers of the displacement (limited by contact of the plasma with the trap wall). The behavior at high relative displacements may be consistent with the work of Fine *et al.*, who show that the frequency shift is an effect caused by distortion of the cylindrical shape of the plasma (due to interaction with the image charge distribution in the cylinder walls). Since the relative amplitudes in the experiments of Fine *et al.* were small ($D/R_w \leq 0.25$), this distortion was simply characterized by the quadrupole moment of the plasma. For larger relative displacements, however, the distortion is probably more complicated (thus requiring higher-order multipole moments for an accurate description). At low relative displacements, it is not clear why the scaling appears to be cubic rather than quadratic. Trap asymmetries may have caused the plasma to expand radially as the experiment progressed, which may have resulted in slight charge loss to the wall. The plasma's subsequent relaxation to a new quasi-equilibrium as the mode damped may have introduced physical effects which have not been considered previously.

CONCLUSION

In this paper, we have reviewed the linear theory of the $m = 1$ diocotron mode and the effects of finite plasma length on this theory. In addition, it has been shown that the $m = 1$ mode can be excited to large amplitudes by the resistive-wall instability, and that the growth rate of this instability agrees well with theoretical predictions. Finally, the nonlinear frequency shift of this mode at large amplitudes has been measured, and a cubic scaling of the frequency shift at large amplitudes (as opposed to the quadratic scaling observed at lower amplitudes) has been observed.

REFERENCES

1. Fine, K. S., Driscoll, C. F., and Malmberg, J. H., Phys. Rev. Lett. **63**, 2232 (1989).
2. Chao, E. H., Davidson, R. C., and Paul, S. F., J. Vac. Sci. Technol. A **17**, 2050 (1999).
3. Levy, R. H., Phys. Fluids **8**, 1288 (1965).
4. Davidson, R. C., *Physics of Nonneutral Plasmas*, Addison Wesley, Redwood City, CA, 1990, Ch. 6.
5. Levy, R. H., Phys. Fluids **11**, 920 (1968).
6. Prasad, S. A., and O'Neil, T. M., Phys. Fluids **26**, 665 (1983).
7. Fine, K. S., and Driscoll, C. F., Phys. Plasmas **5**, 601 (1998).
8. Chao, E. H., Paul, S. F., and Davidson, R. C., J. Vac. Sci. Technol. A **17**, 2034 (1999).
9. White, W. D., Malmberg, J. H., and Driscoll, C. F., Phys. Rev. Lett. **49**, 1822 (1982).
10. Chao, E. H., Davidson, R. C., Paul, S. F., and Morrison, K. A., Phys. Plasmas **7**, 831 (2000).
11. Prasad, S. A., and Malmberg, J. H., Phys. Fluids **29**, 2196 (1986).
12. Fine, K. S., Phys. Fluids B **4**, 3981 (1992).
13. Chao, E. H., Ph.D. Thesis, Princeton University, 1999.

$m = 1$ Diocotron Mode Damping in the Electron Diffusion Gauge (EDG) Experiment

Stephen F. Paul, Kyle A. Morrison, Ronald C. Davidson, Thomas G. Jenkins

Plasma Physics Laboratory, Princeton University, Princeton, New Jersey 08543, USA

Abstract. The evolution of the amplitude of the $m = 1$ diocotron mode is used to measure the background neutral pressure in the Electron Diffusion Gauge (EDG), a Malmberg-Penning trap. Below 5×10^{-8} Torr, the dependence on pressure scales as $P^{1/4}$, and is sensitive to pressure changes as small as $\Delta P = 5 \times 10^{-11}$ Torr. Previous studies on the EDG showed that the diocotron mode is more strongly damped at higher neutral pressures. Both the diocotron mode damping rate and the plasma expansion rate depend similarly on experimental parameters, i.e., conditions which favor expansion also favor suppression of the diocotron mode. The sensitivity of the mode evolution is examined as a function of the resistive growth driving conditions, which are controlled by the amount of wall resistance connected to the trap.

Nonneutral plasmas confined in Malmberg-Penning traps have been used to investigate important fundamental plasma phenomena [1, 2, 3]. For the Electron Diffusion Gauge (EDG) device at Princeton, the research program has emphasized examining the effects of collisions between the confined pure electron plasma and the background neutral gas as a means for determining the neutral gas pressure over a wide range. In recent theoretical work [4, 5], the expansion rate of a pure electron plasma was related to the rate of collisions between the electrons and the neutrals. The expansion rate has also been measured experimentally [6, 7], but these diagnostic techniques require repeated formation and termination of the plasma to determine the expansion rate. This approach is time-consuming and requires excellent reproducibility of the plasma conditions. At high pressures, the expansion rate is observed to scale classically [8], however the scatter in the data and the presence of asymmetry-induced expansion has limited the detection of neutral pressure in the EDG to $P > 10^{-8}$ Torr.

An alternative, non-destructive approach that does not require the determination of the entire density profile is the measurement of the growth and/or decay of the $m = 1$ diocotron mode. While the term "diocotron mode" was first used to describe instabilities in hollow nonneutral electron columns which have a shear in the angular flow velocity [9], in this paper it refers to low-frequency, electrostatic oscillations with azimuthal mode number $m = 1$. For small-amplitude perturbations, the physical interpretation of the mode is a plasma column, displaced from the central axis of the trap, that precesses at the diocotron mode frequency about the trap axis, defined as the center of symmetry of the cylinders that surround the plasma. The mode amplitude, A , is the distance from the center of the plasma column to the trap axis, and the growth/damping rate is defined as $(1/A) \times dA/dt$. As is typical in Malmberg-Penning traps, a uniform axial magnetic

field provides the radial confinement, and applied electric potentials on end cylinders provide axial confinement.

The co-linear, cylindrical copper trap electrodes have a wall radius of $R_w = 2.54$ cm, and the applied end potentials are typically -145V. The magnetic field is generated by a solenoid with an axial current profile adjusted so that the amplitude variation in the trap region is less than 0.2% of the total field, which may be varied from 300 to 600 G. The trap assembly is enclosed in an aluminum vacuum chamber and is pumped with a turbomolecular pump and a cryogenic pump to as low as 5×10^{-11} Torr. Helium gas is bled into the chamber with a precision metering valve and the fill pressure is measured with Bayard-Alpert ionization gauges located on either side of the trap. Details concerning the electron source and the method of trap operation have been described elsewhere [6].

The trapped electron plasma has an initial density in the range $8 \times 10^6 \text{ cm}^{-3} < n < 3 \times 10^7 \text{ cm}^{-3}$, temperature T of about 1-2 eV, radius $R_p \simeq 1.2$ cm, and length $L_p \simeq 15$ cm. For these parameters, the Debye length ($\lambda_D = (T/4\pi ne^2)^{1/2}$) is smaller than the diameter of the plasma ($R_p \simeq 6\lambda_D$) and $\omega_{pe}^2/\omega_{ce}^2 < 0.01$, where $\omega_{pe} = (4\pi ne^2/m_e)^{1/2}$ is the electron plasma frequency and $\omega_{ce} = eB/m_e c$ is the electron cyclotron frequency. In thermal equilibrium, the $\mathbf{E} \times \mathbf{B}$ rotation frequency typically ranges from 10 kHz to 100 kHz. In a recent modification, the electron emitting filament was replaced one half as large. While the resulting plasma has half the initial radius of the previous plasmas, the line density, electric field, and diocotron frequency are approximately the same as before.

In the EDG experiment, one of the copper cylinders that surrounds the plasma is divided into two half-cylinders, so the mode amplitude is measured as an oscillating voltage induced by image charges on the half-cylinders by the precessing column [10]. Any odd-numbered diocotron mode ($m = 1, 3, \dots$) can be detected by adding a complex sensing impedance in series between either "half cylinder" and ground, but only the $m = 1$ mode has been investigated in these experiments.

CONTROLLING THE RESISTIVE GROWTH OF THE $m = 1$ DIOCOTRON MODE

In the absence of wall resistance or collisions with background neutrals, the $m = 1$ mode in an infinitely long plasma is predicted to be marginally stable regardless of the profile shape. However, given the finite sensing impedance that must be applied to record the diocotron mode amplitude, some amount of resistance must be present. Physically, a resistive wall dissipates the electrical potential energy of the plasma column, causing it to move nearer to the wall, i.e., the mode amplitude grows. For a plasma with a monotonically decreasing radial density profile, resistive-wall destabilization was predicted and experimentally verified by White [11].

In the EDG, resistively-driven growth has been reduced considerably in comparison with previous studies [12] by employing a larger reactive (non-dissipating) admittance.

The admittance is defined as $Y = 1/R + i\omega C$, and the dissipated power is

$$\langle P \rangle = \frac{I^2}{2} \text{Re} \{1/Y\} = \frac{I^2}{2} \cdot \frac{R}{1 + (\omega RC)^2}, \quad (1)$$

where I is the current, C is the capacitance, and ω is the $m = 1$ mode frequency. For $(\omega RC)^2 \gg 1$, the dissipated power can be reduced by increasing R and C subject only to a minimum signal level, which is proportional to $1/\omega C$, and the signal offset due to bias currents in the amplifier, which is proportional to R .

To increase the growth rate above this minimum, the wall resistance can be increased simply by connecting the opposite cylinder through a series resistor to ground. For small series resistors, R_s , i.e., $(\omega R_s C)^2 \ll 1$, the growth rate of the resistive-wall instability increases linearly with R_s [12]. This value is determined empirically by choosing a resistor small enough to avoid forcing the plasma column into the trap wall, yet large enough to observe a reasonable signal.

PRESSURE SENSITIVITY OF THE $m = 1$ DIOCOTRON MODE

As mentioned in the introduction, collisions with neutral particles apply a torque to the plasma, causing it to expand and lose potential energy. Because the diocotron mode amplitude grows at the expense of the plasma's energy, the mode may be stimulated by collisions. A calculation assuming that the expansion of the plasma is sufficiently slow that the radial density profile can be regarded as stationary on the time scale of the instability has predicted a growth rate that scales linearly with neutral pressure [13, 14]. In previous experiments on the EDG device, however, increased background gas pressure resulted in substantial, non-exponential *damping* of the diocotron mode and the mode duration *decreased* with pressure (scaling as $P^{-1/2}$ in the range from 10^{-9} to 10^{-7} Torr [7]). The assumption of a stationary density profile [13, 14] is likely invalid because the plasma expands on a time scale comparable to the predicted growth time of the instability, however the physical mechanism of the pressure-induced damping is still unexplained.

In the present series of experiments, diocotron mode sensitivity at even lower pressures was investigated under several experimental conditions, including reducing the plasma diameter by employing both 1" and 1/2" diameter filaments. All data were taken in a magnetic field of 600 Gauss and the line density was approximately $2 - 3 \times 10^7 \text{ cm}^{-1}$. Six neutral helium pressure scans are shown in Fig. 1, one with a neutral pressure as low as 5×10^{-11} Torr. In all cases, the damping rate is strongly sensitive to helium pressures greater than 5×10^{-8} Torr. For three of the scans, the sensitivity at lower pressures was too slight to discern, and for two of the scans, the damping rates increased with pressure approximately as $P^{1/4}$. The discrepancy between the pressure scaling in this experiment and the experiment cited in the previous paragraph [7] is that the present results include the correction for the ion gauge's sensitivity to helium, and the previous data were plotted versus gauge pressure.

The differences in the behavior of the growth rate at low neutral pressure appears to depend mainly on two quantities:

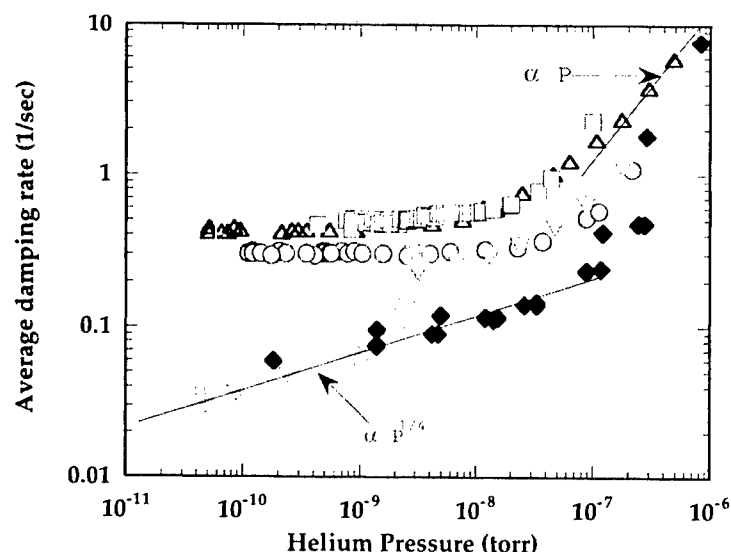


FIGURE 1. Plot of average damping rate of the diocotron mode versus neutral pressure, corrected for the ion gauge's sensitivity to helium in the gas mixture. The open circles are from the 1/2" diameter filament and the other data are from the 1" diameter filament.

1. The initial diocotron mode amplitude, which is controlled by momentarily connecting a cylinder through a series $1k\Omega$ resistor to ground *via* a time-adjustable relay.

2. The net diocotron mode growth rate, which is controlled by balancing the resistive growth against the inherent damping. This mode growth was driven throughout the discharge by connecting one 200 pF trap half-cylinder to ground through a 25Ω resistor. This corresponds to a resistively-driven growth rate of $0.2 - 0.3 \text{ sec}^{-1}$.

For the open squares and triangles in Fig. 1, the mode was resistively grown for about 0.2 seconds and then allowed to damp without further forcing. In this case, the initial amplitude was about 2-3 mm, which is about 10% of the wall radius. Operating in this manner has the advantage of a very nearly exponential decay, i.e., the decay rate is nearly constant and data windowing is not necessary. At pressures above 5×10^{-8} Torr, the damping rate scaled linearly with pressure, but below that, the damping rate was 0.4 sec^{-1} regardless of the pressure. This was repeated with a smaller filament with the expectation that the smaller plasma radius would delay charge loss and other interactions with the trap wall. But, as shown by the open circles, the low-pressure sensitivity was even weaker.

Surmising that the damping due to neutral pressure was being masked by resistively forcing the plasma too far off-axis, scans were performed with smaller initial diocotron mode amplitude. In addition to the reduction in amplitude, the mode *damping rate* was also observed to decrease (by a factor of four at low pressure), as represented by the closed diamonds in Fig. 1. Pressure sensitivity was observed, with the decay rate, γ ,

scaling as $P^{1/4}$ down to about 10^{-9} Torr but the decay was not exponential.

Previous observations [7] revealed that maximum sensitivity to changes in neutral pressure are realized when the net diocotron damping rate is minimized, i.e., the mode is made to last as long as possible. In the scan depicted by both the closed and open inverted triangles in Fig. 1, small values of wall resistance (connected throughout the discharge) were added to drive the mode in order to reduce the net decay rate. This is in contrast to the strong resistive destabilization that was employed only at the very beginning of the discharge. At pressures below 3×10^{-9} Torr (closed inverted triangles), the mode damped initially as before, but then began to grow, as shown in Fig. 2. After 10-20 seconds, the mode peaked and decayed again, but not exponentially. The value of the static resistance was chosen to maximize the mode amplitude but still prevent the plasma from striking the wall and losing charge. The recorded damping rate was the negative of the average growth rate calculated from the time of peak amplitude to the time corresponding to half of the peak amplitude. These modes lasted more than 50 seconds and the decay rate scaled as $P^{1/4}$ (depicted by the closed inverted triangles) down to 5×10^{-11} Torr, the base pressure of the EDG.

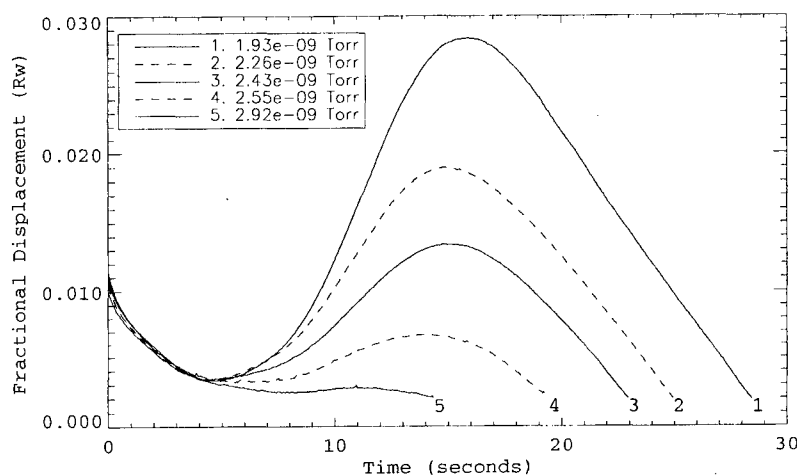


FIGURE 2. Evolution of the mode amplitude in the region of highest sensitivity to pressure. Whereas the pressure varies by about 50%, the damping rate varies by a factor of three. In all the scans at low pressure, the exponential decay (seen here during the first four seconds) is not sensitive to pressure.

For pressures above 3×10^{-9} Torr, the mode did not grow. As shown by the open inverted triangles in Fig. 1, the pure exponential decay was insensitive to pressure in a manner similar to the scan with the strongly forced initial amplitude. The abrupt transition from mode growth to mode damping between 2 and 3×10^{-9} Torr is remarkable because the mode behavior is very sensitive to pressure (approximately P^3). Mode evolutions in this region are shown in Fig. 2. Though unexplained at present, a very sensitive measurement of neutral pressure might be achieved if this behavior can be extended to lower pressure.

Overall, the pressure sensitivity of the diocotron mode damping is very reminiscent of that observed with plasma expansion:

1. At high pressures, the sensitivity to pressure appears to scale linearly with neutral pressure.
2. At low pressures both expansion and mode damping are much less pressure sensitive. Unlike expansion, the mode damping exhibits a weak dependence on pressure.
3. The transition in the pressure sensitivity is at 4×10^{-8} Torr.
4. The faster than linear dependence of mode damping on diocotron mode frequency [12] is similar to the $B^{-3/2}$ dependence of the asymmetry-induced plasma expansion on magnetic field [6].

Qualitatively, at higher pressure, the mode appears to be strongly damped when the plasma expands rapidly due to electron-neutral collisions. At lower pressure it appears to be mildly damped when the plasma is expanding slowly due to asymmetries. There is evidence that damping rate is affected by the plasma expansion but the determination that the expanding plasma is causing mode decay requires further experiments. The mode behavior appears to be determined by a balance between the growth driven by the resistive instability and the damping mechanisms, some of which are observed to be pressure dependent - either directly or coupled through the column expansion. There is likely more than one source of mode damping because of the variability in nature of the damping. When the mode amplitude is grown with a high wall resistance and then allowed to decay on its own, the damping is exponential. The rate of exponential decay is seen to be less with smaller initial amplitude. When the net damping rate is reduced by adding a modest wall resistance, the decay is not exponential. The non-exponential damping is very sensitive to neutral pressure in a narrow pressure range.

This research was supported by the Office of Naval Research.

REFERENCES

1. Fajans, J., and Dubin, D. H., editors, *Nonneutral Plasma Physics II*, vol. 331, American Institute of Physics, 1994, and references therein.
2. Davidson, R. C., *Physics of Nonneutral Plasmas*, Addison-Wesley, Reading, MA, 1990, and references therein.
3. Bollinger, J. J., Spencer, R. L., and Davidson, R. C., editors, *Nonneutral Plasma Physics III*, vol. 498, American Institute of Physics, 1999, and references therein.
4. Davidson, R. C., and Moore, D. A., *Phys. Plasmas*, **3**, 218 (1996).
5. Davidson, R. C., and Chao, E. H., *Phys. Plasmas*, **3**, 2615 (1996).
6. Chao, E. H., Davidson, R. C., and Paul, S. F., *J. Vac. Sci. Technol. A*, **17**, 2050 (1999).
7. Chao, E. H., Davidson, R. C., Paul, S. F., and Morrison, K. A., *Phys. Plasmas*, **7**, 831 (2000).
8. Morrison, K. A., Davidson, R. C., Paul, S. F., Belli, E. A., and Chao, E. H., *Phys. Plasmas*, **8**, 3506 (2001).
9. Buneman, O., Levy, R., and Linson, L., *J. Appl. Phys.*, **37**, 3203 (1966).
10. Kapetanakis, C. A., and Trivelpiece, A. W., *J. Appl. Phys.*, **42**, 4841 (1971).
11. White, W. D., Malmberg, J. H., and Driscoll, C. F., *Phys. Rev. Lett.*, **49**, 1822 (1982).
12. Chao, E. H., Paul, S. F., and Davidson, R. C., *J. Vac. Sci. Technol. A*, **17**, 2034 (1999).
13. Davidson, R. C., and Chao, E. H., *Phys. Lett. A*, **219**, 95 (1996).
14. Davidson, R. C., and Chao, E. H., *Phys. Plasmas*, **3**, 3279 (1996).

Magnetic Shear Stabilization of Diocotron Instability

S. Kondoh, T. Tatsuno, and Z. Yoshida

*Graduate School of Frontier Sciences, University of Tokyo,
7-3-1 Hongo, Bunkyo-ku, Tokyo 113-0033, Japan*

Abstract. The diocotron instability in a magnetized non-neutral plasma is a close cousin of the Kelvin-Helmholtz instability. A sheared magnetic field brings about coupling between the diocotron modes and the Langmuir waves that propagate along the magnetic field. Motion of electrons parallel to the magnetic field cancels the electric charge produced by the diocotron modes, resulting in stabilization of the diocotron instability.

I INTRODUCTION

Recently a variety of new concepts on non-neutral plasma confinement has been proposed [1-3], which significantly differ from the conventional Penning/Malmberg trap [4]. The Prototype Ring Trap (Proto-RT) experiment [1,5] is aimed at pure magnetic confinement of a toroidal non-neutral plasma that is not in a rigid-rotating thermal equilibrium state. In such a system, the plasma flow is generally sheared, and the diocotron instability [6] can be destabilized. Application of magnetic shear is expected to be most effective to stabilize the electrostatic modes. However, exact stability analysis has not been completed, except for the special case of an electron beam with a relativistic speed [7].

The physical mechanism of the diocotron instability is explained as follows [8] (see Fig. 1): When a non-neutral slab plasma has a finite thickness, a perturbation on one of the two plasma surfaces produces surface charges. The resulting perturbed electric field yields an $\mathbf{E} \times \mathbf{B}$ flow in the plasma, and the opposite surface is also perturbed. The motion of the opposite surface brings about a reciprocal perturbation, and the waves on the two surfaces couple with each other. Under certain conditions, this coupling yields a positive feedback, and the diocotron instability occurs.

When a non-neutral plasma is confined in a uniform magnetic field, the diocotron modes propagating in the perpendicular direction to the magnetic field are independent of any modes that propagate in the parallel direction. However, if the magnetic field has a shear (see Fig. 2), the wave vector may

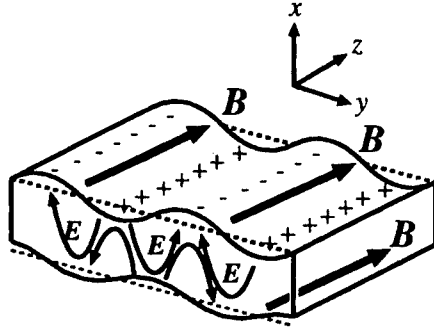


FIGURE 1. Physical picture of diocotron modes in a uniform magnetic field. Perturbation on one of the two plasma surfaces produces the surface charge and causes the electrostatic field perturbation. This perturbed electric field shakes the body of the plasma itself through $E \times B$ drift, and the other surface is also perturbed. The perturbation on the latter surface in turn shakes the former one in the same way. Thus, the waves on the two surfaces couple with each other. Under certain conditions, the diocotron modes can be unstable.

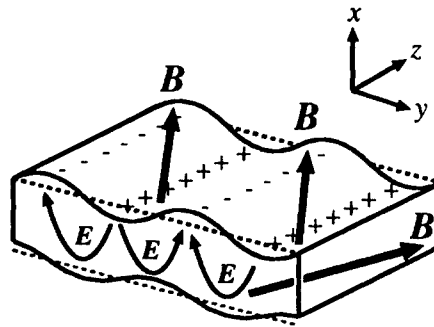


FIGURE 2. Physical picture of stabilizing effect of a sheared magnetic field on diocotron modes. The wave vector almost always has a local parallel component, and the diocotron modes cannot be independent of the parallel modes, such as the Langmuir wave or the plasma oscillation. Therefore, a coupling between them is caused. In a cold non-neutral plasma, the surface charge perturbation produced by the diocotron modes is canceled by the parallel motion of charged particles. Thus, the diocotron instability is stabilized by the sheared magnetic field.

have a local parallel component $k_{\parallel}(x)$, and the diocotron modes interact with the parallel modes, such as the Langmuir wave or the plasma oscillation. In a cold non-neutral plasma, the surface charge perturbation produced by the diocotron modes is short-circuited by the parallel motion of charged particles, if the diocotron frequency ω_D is much smaller than the plasma frequency ω_p , i.e., when a low density plasma embedded in a strong magnetic field. Therefore, we expect that the diocotron instability is stabilized in a sheared magnetic field.

In this paper, we consider a slab plasma with a flat-top density profile

and show the stabilizing effect of magnetic shear analytically. The diocotron instability is formally equivalent to the Kelvin-Helmholtz instabilities in fluids and plasmas [9]. The magnetic shear stabilization of these instabilities is of the common interest and has a variety of applications (see Sec. IV).

II EIGENEQUATION FOR DIOCOTRON MODES IN A SHEARED MAGNETIC FIELD

A Slab plasma model in a sheared magnetic field

We consider a slab electron plasma embedded in a sheared magnetic field (see Fig. 2). The plasma has a finite thickness 2Δ in the x -direction. We assume that all equilibrium quantities are functions of only x . We consider a sheared magnetic field such as

$$\mathbf{B} = (0, B_y(x), B_z), \quad (1)$$

where B_z is a constant. Since a non-neutral plasma has a self-electric field, there is a stationary flow that is approximately equivalent to the $\mathbf{E} \times \mathbf{B}$ drift for low densities.

The governing equations are

$$\frac{\partial n}{\partial t} + \mathbf{v} \cdot \nabla n + n \nabla \cdot \mathbf{v} = 0, \quad (2)$$

$$\frac{\partial \mathbf{v}}{\partial t} + (\mathbf{v} \cdot \nabla) \mathbf{v} = -\frac{1}{s^2} (\mathbf{E} + \mathbf{v} \times \mathbf{B}), \quad (3)$$

$$\nabla^2 \phi = -n, \quad (4)$$

where n is normalized by the typical electron density $n_0(0)$, t by the inverse of the diocotron frequency $\omega_D^{-1} = \epsilon_0 B_z / e n_0(0)$ (ϵ_0 is the vacuum dielectric constant and e is the elementary electric charge), the spatial coordinates x, y, z by the half thickness of the slab plasma Δ , \mathbf{v} by the mean flow velocity at the plasma surface $|\mathbf{v}_0(1)|$, \mathbf{B} by the axial magnetic field B_z , \mathbf{E} by the mean electric field at the plasma surface $|\mathbf{E}(1)|$, $s \equiv \omega_p / \omega_c = \omega_D / \omega_p$ is a dimensionless parameter, and $\mathbf{E} = -\nabla \phi$. Since we consider a low-density plasma in a strong axial magnetic field, we may assume $s \ll 1$. In this limit, we can replace Eq. (3) with

$$\mathbf{v}_\perp = \frac{-\nabla \phi \times \mathbf{B}(x)}{B(x)^2}, \quad (5)$$

$$\frac{\partial v_\parallel}{\partial t} + (\mathbf{v} \cdot \nabla) v_\parallel = \frac{1}{s^2} \nabla_\parallel \phi, \quad (6)$$

where $B(x) = \sqrt{B_y(x)^2 + B_z^2}$. Linearizing Eqs. (2), (5), and (6), we finally obtain [10]

$$\left(\frac{d^2\phi_1}{dx^2} - k^2\phi_1\right) + \frac{1}{\omega - k_\perp v_{\perp 0}} \frac{d}{dx} \left(\frac{k_\perp n_0}{B}\right) \phi_1 + \frac{n_0 k_\parallel^2}{s^2(\omega - k_\perp v_{\perp 0})^2} \phi_1 = 0, \quad (7)$$

where we have Fourier-transformed all perturbed variables $\Psi(x, y, z, t)$ as

$$\Psi(x, y, z, t) = \Psi_0(x) + \Psi_1(x) \exp[i(\omega t - k_y y - k_z z)]. \quad (8)$$

III STABILIZING EFFECT DUE TO PARALLEL MOTION

A Non-resonant frequency regime

First, we show that the diocotron modes are stabilized ($\omega_i = 0$) for wave numbers without resonance between the phase velocity and the plasma flow, that is, $\omega_r - k_\perp v_{\perp 0} \neq 0$ for all x . Multiplying Eq. (7) by ϕ^* and integrating it over $(-\infty, \infty)$, we obtain from the imaginary part

$$\omega_i \int_{-\infty}^{\infty} \left[\frac{1}{|\omega - k_\perp v_{\perp 0}|} \frac{d}{dx} \left(\frac{k_\perp n_0}{B}\right) + \frac{2n_0 k_\parallel^2 (\omega_r - k_\perp v_{\perp 0})}{s^2 |\omega - k_\perp v_{\perp 0}|^4} \right] |\phi_1|^2 dx = 0. \quad (9)$$

Here we used the boundary condition

$$\phi_1(\pm\infty) = 0. \quad (10)$$

Since $s^2 \ll 1$ and $\omega_r - k_\perp v_{\perp 0} \neq 0$ at any point in the plasma region, we obtain $\omega_i = 0$, which means stability. This mathematical treatment is same as the standard Rayleigh's analysis [11].

B Dispersion relation with resonances

If the plasma has a resonant point, the analysis in Sec. III A does not apply to check whether the eigenvalues ω for Eq. (7) are real or not. In this case, we need to solve Eq. (7) directly. The eigenfunction determined by Eq. (7) is oscillatory, because the sign of the last term, which we assumed to be very large ($s \ll 1$), is positive. If ω is not real, the real and imaginary parts of the eigenfunction have a relative phase angle of about $\pi/2$. When we consider a density profile with a sharp boundary, we have to connect both the real and imaginary parts of the eigenfunction at the plasma surfaces using the same boundary condition. If both of them have a different phase angle, this process fails, which implies that ω must be real.

The essential characteristic of this eigenvalue problem is well understood by the following simplified model. First, we neglect the second term $k^2\phi_1$ in the bracket of the first term of Eq. (7) in the plasma region $(-1, 1)$, since it is much smaller than the last term when $n_0 \simeq 1$. We also assume that $k_\perp n_0/B$ jumps at $x = \pm 1$ and its variation is negligible anywhere else, i.e.

$$\frac{d}{dx} \left(\frac{k_\perp n_0}{B} \right) = f(x) [\delta(x+1) - \delta(x-1)], \quad (11)$$

where $f(x)$ is a given finite function. Furthermore, we assume

$$\frac{n_0(x)k_\parallel(x)^2}{s^2} \equiv a^2 = \text{const.} \gg 1, \quad (12)$$

$$k_\perp(x)v_{\perp 0}(x) = x. \quad (13)$$

Under these assumptions, we can solve Eq. (7) analytically, and the dispersion relation is given by [10]

$$\begin{aligned} & \left[(a + k\omega_i)^2 - k^2\omega_r^2 + \left(k + \frac{1}{2}\right)^2 + f(-1)f(1) - \left(k + \frac{1}{2}\right)(f(-1) + f(1)) \right. \\ & \quad \left. + k\omega_r(f(-1) - f(1)) + i(a + k\omega_i)(f(-1) - f(1) - 2k\omega_r) \right] (\omega + 1)^{2ai} \\ & = \left[(a - k\omega_i)^2 - k^2\omega_r^2 + \left(k + \frac{1}{2}\right)^2 + f(-1)f(1) - \left(k + \frac{1}{2}\right)(f(-1) + f(1)) \right. \\ & \quad \left. + k\omega_r(f(-1) - f(1)) - i(a - k\omega_i)(f(-1) - f(1) - 2k\omega_r) \right] (\omega - 1)^{2ai}, \quad (14) \end{aligned}$$

where $\omega = \omega_r + i\omega_i$. We can show that ω is real for Eq. (15). where $\omega_r = \text{Re } \omega$ and $\omega_i = \text{Im } \omega$. Taking the absolute number of Eq. (15) gives

$$\frac{|A_1|}{|A_2|} = \exp \left[a \arg \left(\frac{\omega + 1}{\omega - 1} \right) \right], \quad (15)$$

where

$$\begin{aligned} A_1 &= (a + k\omega_i)^2 - k^2\omega_r^2 + \left(k + \frac{1}{2}\right)^2 + f(-1)f(1) - \left(k + \frac{1}{2}\right)(f(-1) + f(1)) \\ & \quad + k\omega_r(f(-1) - f(1)) + i(a + k\omega_i)(f(-1) - f(1) - 2k\omega_r), \quad (16) \end{aligned}$$

$$\begin{aligned} A_2 &= (a - k\omega_i)^2 - k^2\omega_r^2 + \left(k + \frac{1}{2}\right)^2 + f(-1)f(1) - \left(k + \frac{1}{2}\right)(f(-1) + f(1)) \\ & \quad + k\omega_r(f(-1) - f(1)) - i(a - k\omega_i)(f(-1) - f(1) - 2k\omega_r). \quad (17) \end{aligned}$$

If $\omega_i > 0$, the left-hand side of Eq. (16) is greater than unity, while the right-hand side is less than unity. Therefore, $\omega_i > 0$ cannot be satisfied. If $\omega_i < 0$, the left-hand side of Eq. (16) is less than unity, while the right-hand side is greater than unity. Therefore, $\omega_i < 0$ cannot be satisfied. Thus $\omega_i = 0$, which means stability. If $\omega_i \neq 0$, the eigenfunctions of the three regions ϕ_I , ϕ_{II} , and ϕ_{III} cannot be connected properly at $x = \pm 1$.

IV SUMMARY

We have shown that the magnetic shear has a strong stabilizing effect on the diocotron instability. The fluid motion parallel to the magnetic field short-circuits the charge perturbation of the diocotron modes. The scaling parameter is $s \equiv \omega_D/\omega_p$. Since the time scale of the parallel motion is $\sim \omega_p^{-1}$, the condition $s \ll 1$ enables the parallel motion of the plasma to cancel the perturbed charge sufficiently. Typical non-neutral plasmas in laboratories satisfy this condition.

Mathematically the last term of the eigenequation (7) prohibits non-real eigenvalues, because the last term makes the eigenfunction oscillatory. If $\omega \notin \mathcal{R}$, the relative phase angle between the real and imaginary parts of the eigenfunction is about $\pi/2$. This phase angle disables both the real and imaginary parts of the eigenfunction to be connected properly at the plasma surfaces.

We note that our analysis is based on a modal approach which, however, may not be complete for non-Hermitian systems [12–14]. There remains a possibility of secular algebraic behavior, although we have shown that there are no exponentially unstable modes. This problem will be discussed elsewhere.

REFERENCES

1. Z. Yoshida, Y. Ogawa, J. Morikawa, *et al.*, *Non-Neutral Plasma Physics III*, AIP Conference Proceedings 498 (American Institute of Physics, Princeton, 1999) p.397.
2. S. Robertson and B. Walch, *Phys. Plasmas* **7**, 2340 (2000).
3. K. Avinash, *Phys. Plasmas* **1**, 3731 (1994).
4. J. H. Malmberg and J. S. deGrassie, *Phys. Rev. Lett.* **35**, 577 (1975).
5. S. Kondoh and Z. Yoshida, *Nucl. Instrum. Meth. Phys. Res. A* **382**, 561 (1996).
6. R. C. Davidson, *Physics of Nonneutral Plasmas* (Addison-Wesley, California, 1990).
7. E. Ott and J. M. Wersinger, *Phys. Fluids* **23**, 324 (1980).
8. W. Knauer, *J. Appl. Phys.* **37**, 602 (1966).
9. C. F. Driscoll and K. S. Fine, *Phys. Fluids B* **2**, 1359 (1990).
10. S. Kondoh, T. Tatsuno, and Z. Yoshida, *Phys. Plasmas* **8**, 2635 (2001).
11. S. Chandrasekhar, *Hydrodynamic and Hydromagnetic Stability* (Clarendon Press, Oxford, 1961).
12. L. N. Trefethen, A. E. Trefethen, S. C. Reddy, and T. A. Driscoll, *Science* **261**, 578 (1993).
13. G. D. Chagelishvili, A. D. Rogava, and I. N. Segal, *Phys. Rev. E* **50**, R4283 (1994).
14. S. M. Mahajan and A. D. Rogava, *Astrophys. J.* **518**, 814 (1999).

$l = 1$ Diocotron Instability of Single Charged Plasmas in a Cylindrical Penning Trap with Central Conductor

M. Romé*, A. V. Arefiev[†], I. A. Kotelnikov** and R. Pozzoli*

*I.N.F.M. and Dipartimento di Fisica, Università degli Studi di Milano, Italy

[†]Physics Department, University of Texas at Austin, TX, U.S.A.

**Budker Institute of Nuclear Physics and Physics Department, Novosibirsk State University, Russian Federation

Abstract. The linear stability analysis of the $l = 1$ diocotron perturbations in a single charged plasma confined in a cylindrical Penning trap is critically revisited. Particular attention is devoted to the instability due to the presence of stationary points in the radial profile of the azimuthal rotation frequency. The asymptotic analysis of Smith and Rosenbluth [1] for the case of a single-bounded plasma column (algebraic instability proportional to $t^{1/2}$) is extended to the case of a cylindrical Penning trap with an additional coaxial inner conductor, and it is shown that the algebraic instability found in the case of a single-bounded plasma column becomes exponential at longer times. The relevant linear growth rate is computed by a suitable inverse Laplace transform (contour integral in the complex plane). The analytical results are compared with the numerical solution of the linearized two-dimensional drift Poisson equations.

INTRODUCTION

The linear stability analysis of the $l = 1$ diocotron perturbations in a low density single charged plasma, radially bounded by two cylindrical conductors held at fixed potential, is critically reviewed. Using a model with a radial step density profile, Levy [2] showed that the plasma is neutrally stable when it is in contact with one or both conductors, or if the charge on the inner conductor is large enough. If the central conductor is absent, the $l = 1$ diocotron mode is neutrally stable, while lower $l \geq 2$ modes may be unstable. The effect of a central conductor on the stability of an hollow plasma column has been also studied experimentally [3].

Particular attention is devoted here to the instability due to the presence of one or several stationary points in the radial profile of the azimuthal rotation frequency of the plasma. The asymptotic analysis of Smith and Rosenbluth [1] for the case of a single-bounded plasma column (instability proportional to $t^{1/2}$) is extended to include algebraic instabilities growing as t^α , with $1/2 < \alpha \leq 1$. The asymptotic analysis is generalized to the case of a trap with a coaxial cylindrical inner conductor, and it is shown that the algebraic instability found in the previous case becomes exponential at longer times: the relevant linear growth rate are computed. Finite length and finite Larmor radius effects are neglected.

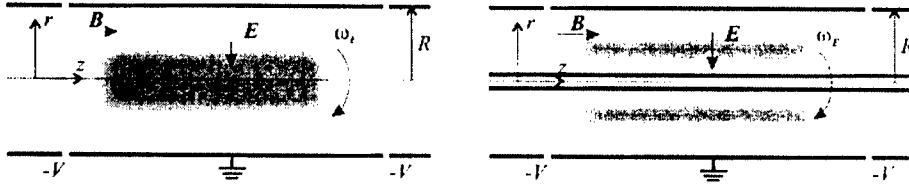


FIGURE 1. Scheme of a cylindrical Penning trap. **Left:** without central conductor; **Right:** with central conductor.

BASIC EQUATIONS

In the model, a one component plasma is assumed to be contained within two infinitely long cylindrical conducting walls, of radii a and R , respectively. The external conductor is grounded (see Fig. 1). The case where the central conductor is absent is treated simply by setting $a = 0$. The system is immersed in a static and uniform magnetic field $\vec{B} = B\hat{z}$, directed along the axis of the trap. In the model considered here, the evolution of the system is described by the two-dimensional drift Poisson equations [4], written in polar coordinates (r, θ) ,

$$\frac{\partial n}{\partial t} + (\nabla\phi \times \nabla n) \cdot \hat{z} = 0, \quad \nabla^2 \phi = n. \quad (1)$$

Adimensional quantities are used. The density, n , is normalized over an arbitrary reference density, \hat{n} ; the lengths over the radius of the outer conductor, $\hat{r} = R$ (an explicit notation for R is kept in the following); the frequencies over $\hat{\omega} = 4\pi e^2 \hat{n} / m\omega_c$, where $\omega_c = -eB/mc$ (e and m being the charge and the mass of the particles, respectively, and c the velocity of light in vacuo); the potential, ϕ , over $\hat{\phi} = 4\pi e \hat{n} \hat{r}^2$; and the electric charge per unit length on the central conductor, Q , over $\hat{Q} = \pi e \hat{n} \hat{r}^2$.

Linearizing Eqs. (1) for perturbations $\delta\phi = \phi_l(r, t)e^{il\theta}$ and $\delta n = n_l(r, t)e^{il\theta}$ with a given azimuthal number l , yields the following second-order differential equation for the potential amplitude ϕ_l (see, e.g., Ref. [4]):

$$\left[\frac{\partial}{\partial t} + il\omega_E(r) \right] \left[\frac{1}{r} \frac{\partial}{\partial r} r \frac{\partial}{\partial r} - \frac{l^2}{r^2} \right] \phi_l - \frac{il}{r} n'_0(r) \phi_l = 0; \quad (2)$$

$$\omega_E(r) = \frac{1}{r^2} \int_a^r n_0(r) r dr + \frac{Q}{2r^2},$$

where $n_0(r)$ and $\omega_E(r)$ are the unperturbed density and the unperturbed azimuthal frequency of the plasma, respectively, and a prime denotes the radial derivative. Eq. (2) has to be supplemented with the boundary conditions $|\phi_l(0)| < +\infty$, $\phi_l(R) = 0$ in the case without central conductor, and $\phi_l(a) = 0$, $\phi_l(R) = 0$ in the case with central conductor, respectively.

In the following, the analysis is restricted to the case $l = 1$. The Laplace transforms for the perturbed potential and density can be written in this case as

$$\phi_p(r) = r[p + i\omega_E(r)] \int_r^R \frac{h(x) - \bar{h}(p)}{x^3[p + i\omega_E(x)]^2} dx; \quad (3a)$$

$$n_p(r) = \frac{n_1(r, 0)}{p + i\omega_E(r)} - i n_0'(r) \int_r^R \frac{h(x) - \bar{h}(p)}{x^3[p + i\omega_E(x)]^2} dx, \quad (3b)$$

where

$$h(r) = \int_a^r x^2 n_1(x, 0) dx; \quad \bar{h}(p) = \int_a^R \frac{h(x) dx}{x^3[p + i\omega_E(x)]^2} \bigg/ \int_a^R \frac{dx}{x^3[p + i\omega_E(x)]^2}. \quad (4)$$

The inversion of the Laplace transforms, e.g., $\phi_1(r, t) = \int_{Br} \frac{dp}{2\pi i} \phi_p(r) e^{pt}$, involves an integration in the complex plane along a Bromwich contour, Br , which goes to the right of all the transform's singular points and branch cuts.

TRAP WITHOUT CENTRAL CONDUCTOR

The inverse Laplace transformation can be performed in a closed form if $a = 0$, recovering the result of Ref. [1]:

$$\phi_1(r, t) = r \int_r^R [h(x)/x^3] [1 + i\omega_E(r)t - i\omega_E(x)t] e^{-i\omega_E(x)t} dx; \quad (5a)$$

$$n_1(r, t) = n_1(r, 0) e^{-i\omega_E(r)t} - i t n_0'(r) \int_r^R [h(x)/x^3] e^{-i\omega_E(x)t} dx. \quad (5b)$$

It is readily seen that an unstable perturbation can not grow faster than t , as the integrals in Eqs. (5) are decreasing functions of time. An asymptotically non-decaying solution can originate from the density jumps, from the two ends of the interval of integration in Eqs. (5), or from the stationary points inside the same interval.

If $n(r)$ is non-monotonic, $\omega_E(r)$ may also be non-monotonic with its extrema being the points of stationary phase for the integrand functions in Eqs. (5). If $r = r_0$ is a nondegenerate stationary point for ω_E ($\omega_E'(r_0) = 0$, $\omega_E''(r_0) \neq 0$), then

$$\phi_1 \approx \frac{i\sqrt{2\pi} r h(r_0)}{\sqrt{|\omega_E''(r_0)|} r_0^3} [\omega_E(r) - \omega_E(r_0)] H(r_0 - r) \sqrt{t} \exp \left[-i\omega_E(r_0)t - \frac{i\pi}{4} \text{sign}(\omega_E'') \right], \quad (6)$$

where $H(x)$ is the Heaviside's step function. The perturbation grows in this case proportionally to \sqrt{t} [1] (SR-instability).

In the presence of an inflection point, r_* , of the ω_E profile, different situations may occur, according to the value of $\omega_E'(r_*)/\omega_E''(r_*)$. If $\omega_E'(r_*)/\omega_E''(r_*) < 0$, $\omega_E(r)$ has two extrema at $r_{\pm} = r_* \pm \sqrt{-2\omega_E'/\omega_E''}$. At large times, $t \gg |\Gamma|^{-1}$, with $\Gamma \equiv \sqrt{8\omega_E'^3/9\omega_E''}$,

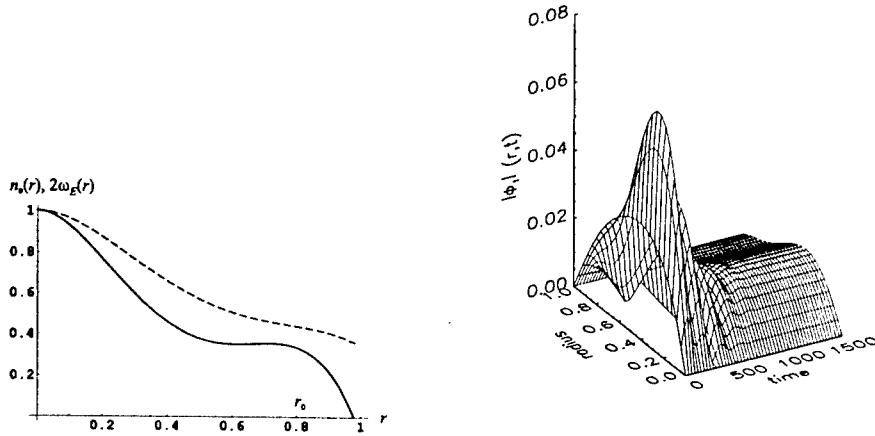


FIGURE 2. Left: Smooth n_0 profile (solid line) and corresponding ω_E profile (dashed line), which give rise to exponentially damping initial perturbations. Right: Amplitude of the perturbed potential, $|\phi_1|(r,t)$, vs. r and t .

these extrema contribute separately to ϕ_1 , and the initial perturbation grows as \sqrt{t} . If $\omega'_E(r_*) = 0$, these points merge at $r = r_*$, and the perturbation grows proportionally to $t^{2/3}$:

$$\phi_1 \approx \frac{i2^{1/3}\Gamma(1/3)rh(r_*)}{3^{1/6}|\omega_E'''|^{1/3}r_*^3} [\omega_E(r) - \omega_E(r_*)] H(r_* - r) t^{2/3} e^{-i\omega_E t}. \quad (7)$$

Finally, if $\omega'_E(r_*)/\omega_E'''(r_*) > 0$, the extremum points move into the complex plane, while ϕ_1 grows algebraically according to Eq. (7) in the initial time evolution, $t \ll |\Gamma|^{-1}$, and then decays exponentially at late times (this situation is illustrated in Fig. 2):

$$\phi_1 \approx \frac{i\sqrt{2\pi}rh(r_*)}{(2\omega'_E\omega_E''')^{1/4}r_*^3} [\omega_E(r) - \omega_E(r_*)] H(r_* - r) \sqrt{t} \exp[-i\omega_E t - \Gamma t]. \quad (8)$$

The frequency of the “saturated” mode is $\omega_E(R)$ (Levy’s mode). In general, if the ω_E profile presents a stationary point, r_* , of order m ($\omega_E^{(j)}(r_*) = 0$ for $j < m$, and $\omega_E^{(m)}(r_*) \neq 0$), the following asymptotic behavior of the perturbed potential is obtained:

$$\phi_1 \approx \frac{2}{m} \left| \frac{m!}{\omega_E^{(m)}(r_*)} \right|^{1/m} \Gamma\left(\frac{1}{m}\right) t^{1-1/m} i r \frac{h(r_*)}{r_*^3} [\omega_E(r) - \omega_E(r_*)] H(r_* - r) e^{-i\omega_E(r_*)t} \times \left\{ \cos\left(\frac{\pi}{2m}\right) + i \left[\frac{(-1)^{m-1} - 1}{2} \right] \text{sign}(\omega_E^{(m)}(r_*)) \sin\left(\frac{\pi}{2m}\right) \right\}. \quad (9)$$

For $m = 2$, this formula reduces to Eq. (6), and for $m = 3$ to Eq. (7).

Finally, a linear growth of the amplitude of an initial perturbation is found if an interval exists where $\omega_E(r)$ is constant, and if this interval does not contain the whole plasma column. This situation can be realized by means of a two-column plasma, where the densities of the internal ($0 \leq r \leq b_0$) and external ($a_1 \leq r \leq b_1$) columns are related by $n_0(b_0)b_0^2 = n_0(a_1)a_1^2$. In this case:

$$\phi_1 \approx it r [\omega_E(r) - \omega_E(a_1)] H(a_1 - r) e^{-i\omega_E(a_1)t} \int_{a_1}^{b_1} [h(x)/x^3] dx. \quad (10)$$

TRAP WITH CENTRAL CONDUCTOR

The SR-instability comes from the neighborhood of a nondegenerate stationary point r_0 of ω_E . This instability can be interpreted as the contribution of the branching point $p = -i\omega_E(r_0)$ in the complex p -plane. When a central conductor is present in the trap, it results

$$\bar{h}(p) \simeq \frac{\mathcal{J}(p + i\omega_E(r_0))/r_0^3}{\mathcal{J}(p + i\omega_E(r_0))/r_0^3 + \beta(p)} h(r_0); \quad (11)$$

$$\mathcal{J}(\sigma) = \frac{\pi e^{-i\pi \text{sign}[\omega_E''(r_0)]/4}}{\sqrt{|2\omega_E''(r_0)|} \sigma^{3/2}}, \quad \beta(p) = \frac{1}{2a^2[p + i\Delta\omega_E][p + i\omega_E(a)]},$$

where $\Delta\omega_E = n_0(a)/2$ and $\omega_E(a) = Q/2a^2$, respectively. The function $\mathcal{J}(\sigma)$ is two-valued since it contains the rational power $3/2$ of $\sigma = p + i\omega_E(r_0)$. The "physical sheet" of the Riemann surface, $\arg[\sigma] \in (-\pi, \pi)$, corresponds to the complex σ -plane with the branch cut $\sigma \in (-\infty, 0]$. The effect of the central conductor turns out to be negligible at small times, $t \ll T \approx |\omega_E''|^{1/3} \omega_E^{-4/3} r_0^2 a^{-4/3}$, while at larger times, $t \gg T$, the algebraic SR-instability disappears. The inverse Laplace transform can be performed (asymptotically for $t \rightarrow \infty$), by means of a suitable deformation of the inversion (Bromwich) contour inside the "physical sheet". In particular, an exponential instability is found if $[\omega_E(r_0) - \Delta\omega_E][\omega_E(r_0) - \omega_E(a)] > 0$, with a growth rate (in the limit $a \rightarrow 0$)

$$\gamma = \frac{3^{1/2} \pi^{2/3} a^{4/3}}{2^{2/3} r_0^2 |\omega_E''|^{1/3}} [\omega_E(r_0) - \omega_E(a)]^{2/3} [\omega_E(r_0) - \Delta\omega_E]^{2/3}. \quad (12)$$

Typical results of the analysis and the numerical simulations of Eqs. (2) in the case with central conductor are shown in Figs. 3-4.

CONCLUSIONS

The existence of $l = 1$ diocotron instabilities in a charged plasma confined in a cylindrical Penning trap, growing with time faster than the SR-instability ($\propto t^\alpha$, with $1/2 < \alpha \leq 1$), has been pointed out. In addition, it has been shown that the presence of an inner conductor (even very thin and uncharged) can transform the algebraic instability into an exponential one at late times. A criterion for the occurrence of the exponential instability

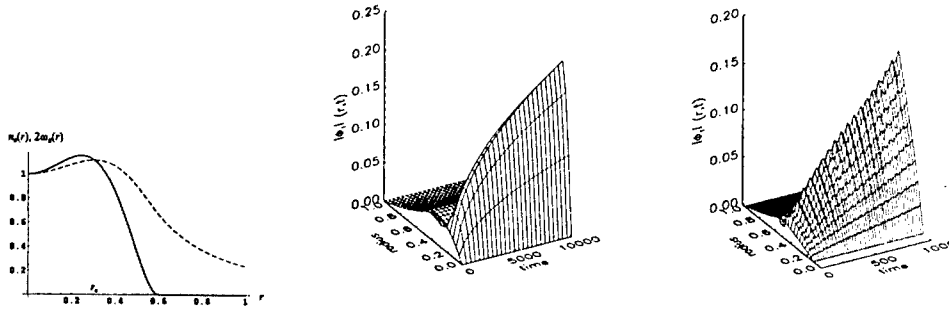


FIGURE 3. Left: $n_0(r)$ (solid line) and $\omega_E(r)$ (dashed line) profiles, which determine a SR algebraic instability [1]: $n_0 = [1 + (r/r_p)^2/\Delta] [1 - (r/r_p)^2]^2$ for $r < r_p$, $n_0 = 0$ for $r > r_p$, with $\Delta = 0.25$, $r_p = 0.6$. Center: Amplitude of the perturbed potential, $|\phi_1|(r,t)$, vs. r and t . Right: Amplitude of the perturbed potential, $|\phi_1|(r,t)$, vs. r and t , for the density profile truncated at the radius $a = 0.05$ of the central conductor. Q corresponds to the total charge of the particles lying within $r = 0.05$ in the previous case.

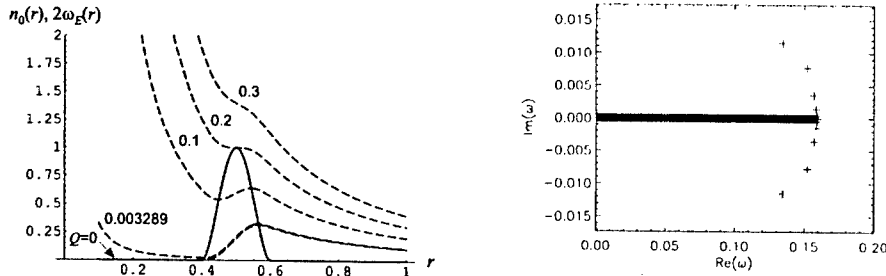


FIGURE 4. Left: Generalized parabolic density profile (solid line) used in the computations: $n_0 = [1 - (r - r_c)^2/r_p^2]^2$ for $|r - r_c| < r_p$ and $n_c = 0$ otherwise (with $r_c = 0.5$ and $r_p = 0.1$) and ω_E profiles (dotted lines), plotted for $a = 0.1$ and different values of Q . Right: Example of frequency spectrum, for $Q = 0$ and $a = 0.2, 0.1, 0.05, 0.025$, and 0.001 . The continuum spectrum lies on the $\text{Re}[\omega]$ axis from 0 to $\omega_E(r_0)$. For a given a , there are two complex conjugate discrete frequencies, which converge to $\omega_E(r_0)$ as $a \rightarrow 0$. Stable solutions ($\text{Im}[\omega] < 0$) do not belong to the “physical” sheet of the Riemann surface.

and the growth rate have been computed analytically in the limit of thin inner conductor. This work has been supported by the Italian Ministry of Education and Scientific Research.

REFERENCES

1. R. A. Smith and M. N. Rosenbluth, Phys. Rev. Lett. **64**, 649 (1990).
2. R. H. Levy, Phys. Fluids **8**, 1288 (1965).
3. G. Rosenthal, G. Dimonte, and A. Y. Wong, Phys. Fluids **30**, 3257 (1987).
4. R. C. Davidson, *Physics of Nonneutral Plasmas*, (Addison Wesley, Redwood City, California, 1990).

Rigorous Fluid Model for 3D Analysis of the Diocotron Instability

G.G.M. Coppa*, A. D'Angola*, G.L. Delzanno* and G. Lapenta†

*Istituto Nazionale di Fisica per la Materia (INFN) and Dipartimento di Energetica, Politecnico di Torino, Corso Duca degli Abruzzi 24, 10129 Torino, Italy

†Istituto Nazionale di Fisica per la Materia (INFN) and Theoretical Division, Los Alamos National Laboratory, Los Alamos, NM 87545, USA

Abstract. A refinement to the theory published by Finn *et al.* is presented here. Compression effects are taken into account by a rigorous definition of the plasma length and by modifying the expression of the velocity field. The perturbation of the plasma length is calculated exactly by a suitable Green function. Growth rates and real frequencies of the unstable $m_0 = 1$ mode are compared with the experimental values, showing a good agreement when compression effects are strong (i.e., for short traps).

INTRODUCTION

The $m_0 = 1$ diocotron instability is one of the open problems in non-neutral plasma theory. According to the classical theory, the $m_0 = 1$ diocotron spectrum does not present discrete unstable modes (regardless of the equilibrium density profile) [1], while the continuum spectrum can only produce an algebraic growth proportional to $t^{1/2}$ [2]. On the contrary, experiments show that the linear growth of the mode is exponential [3, 4].

Finn *et al.* [5] provided a justification of the $m_0 = 1$ diocotron instability in terms of compression of the plasma column due to the confining potential along the axial direction of the trap. However, the theory by Finn *et al.* neglects the finite electron temperature and the effects of the perturbation of the plasma length in the axial direction are treated in a simplified manner. These two issues are treated rigorously in a recent work by the Authors [6].

In particular, the new model differs from the one in Ref. [5] for three main aspects:

1. a rigorous definition of the length of the plasma column is used;
2. an effective electrostatic potential is introduced, in order to calculate the $\mathbf{E} \times \mathbf{B}$ drift on a string of variable axial density (finite temperature effects are included);
3. the perturbation of the plasma length, induced by density variations, is calculated in terms of a suitable Green function.

In the present work the theory presented in Ref. [6] is reviewed and comparisons with experimental data provided by Kabantsev and Driscoll [4] are presented.

THE PHYSICAL MODEL

A Penning trap confining an electron plasma is considered in the following. The central electrode, which extends between $z = -L_c/2$ and $z = L_c/2$, is grounded, while the end electrodes (each having length L_s) are at a negative potential, $-V$. The radius of the trap is indicated by R_w and the gap between the central and the end electrodes is L_g .

The main difference of the present model with respect to the classical one is regarding electrons as string of variable length and, consequently, of variable density (while in the classical approach they are considered as strings of uniform density). Since the plasma length changes radially (due to the confining potential), the columns are compressed or rarefied as they move radially. This phenomenon is known as compression effect.

The model can be deduced starting from the following two hypotheses:

1. Due to the presence of an axial magnetic field, in the characteristic time scale of the diocotron instability the Maxwell-Boltzmann distribution is reached only along the z direction [7] and the particle density is

$$n(r, \theta, z, t) = n_c(r, \theta, t) \exp \left[\frac{\phi(r, \theta, z, t) - \phi_c(r, \theta, t)}{\Theta} \right] \quad (1)$$

where $\Theta = kT/e$ is the electron temperature expressed in Volts, while $n_c(r, \theta, t)$ and $\phi_c(r, \theta, t)$ are respectively the electron density and the electrostatic potential in the central region of the trap, i.e., for $|z| < L_c/2$.

2. Electrons move in the transverse plane due to the $\mathbf{E} \times \mathbf{B}$ drift velocity:

$$\mathbf{v}_\perp(r, \theta, z, t) = \frac{1}{B_0} \mathbf{E}_\perp(r, \theta, z, t) \times \hat{\mathbf{e}}_z. \quad (2)$$

The continuity equation

Instead of $n_c(r, \theta, t)$, experiments yield the line integrated density, $\sigma(r, \theta, t)$, given by

$$\sigma(r, \theta, t) = \int_{-\infty}^{+\infty} n(r, \theta, z, t) dz = n_c(r, \theta, t) \mathcal{L}(r, \theta, t), \quad (3)$$

where the effective length of the plasma column, $\mathcal{L}(r, \theta, t)$, has been defined as

$$\mathcal{L}(r, \theta, t) = \int_{-\infty}^{+\infty} \exp \left[\frac{\phi(r, \theta, z, t) - \phi_c(r, \theta, t)}{\Theta} \right] dz. \quad (4)$$

Averaging the continuity equation for $n(r, \theta, z, t)$ over z , one obtains a new continuity equation for the line integrated density

$$\frac{\partial \sigma}{\partial t} + \nabla_\perp \cdot (\mathbf{V}_\perp \sigma) = 0 \quad (5)$$

with the velocity given by a suitable z -averaged $\mathbf{E} \times \mathbf{B}$ drift.

The z -averaged $\mathbf{E} \times \mathbf{B}$ drift

The present theory differs from the one by Finn *et al.* [5] in the evaluation of \mathbf{V}_\perp . In fact, the velocity is here calculated in terms of the $\mathbf{E} \times \mathbf{B}$ drift estimated on a whole string (a similar assumption has been employed by Fine and Driscoll [8]) and it is given by

$$\mathbf{V}_\perp = \frac{1}{B_0} \frac{\int n \mathbf{E}_\perp dz}{\int n dz} \times \hat{\mathbf{e}}_z = \frac{1}{B_0} \hat{\mathbf{e}}_z \times \frac{\int \exp\left(\frac{\phi}{\Theta}\right) \nabla_\perp \phi dz}{\int \exp\left(\frac{\phi}{\Theta}\right) dz}. \quad (6)$$

Equation (6) can be rewritten as

$$\mathbf{V}_\perp = \frac{1}{B_0} \hat{\mathbf{e}}_z \times \nabla_\perp \phi_{\text{eff}}, \quad (7)$$

where the effective potential, $\phi_{\text{eff}}(r, \theta, t)$, is defined as

$$\phi_{\text{eff}} = \phi_c + \Theta \log \frac{\mathcal{L}}{\mathcal{L}_{r=0}}. \quad (8)$$

The model

The model is completed by the Poisson equation for ϕ . The set of equations can be written in a more compact way by defining the quantity $\Psi(r, \theta, z, t) = \phi(r, \theta, z, t) - \phi_c(r, \theta, t)$, which represents the correction to the potential in a trap of finite length, with respect to the one in a trap of infinite length. Finally, the following system of equations is to be solved:

$$\left\{ \begin{array}{l} \frac{\partial \sigma}{\partial t} = -\mathbf{V}_\perp \cdot \nabla_\perp \sigma \\ \mathbf{V}_\perp = \frac{1}{B_0} \hat{\mathbf{e}}_z \times \nabla_\perp \phi_{\text{eff}} \\ \mathcal{L} = \int \exp\left(\frac{\Psi}{\Theta}\right) dz \\ \nabla^2 \Psi = \frac{e}{\epsilon_0} \frac{\sigma}{\mathcal{L}} \left[\exp\left(\frac{\Psi}{\Theta}\right) - 1 \right] \\ \nabla_\perp^2 \phi_c = \frac{e}{\epsilon_0} \frac{\sigma}{\mathcal{L}} \\ \phi_{\text{eff}} = \phi_c + \Theta \log \frac{\mathcal{L}}{\mathcal{L}_{r=0}} \end{array} \right. \quad (9)$$

TABLE 1. Confining potential and geometrical parameters of the experiments performed by Kabantsev and Driscoll [4].

	V [V]	L_r [cm]	L_g [cm]	L_s [cm]
A	36	34.6	0.175	6.8
B	80	20.7	0.175	13.8
C	100	7	0.175	6.8

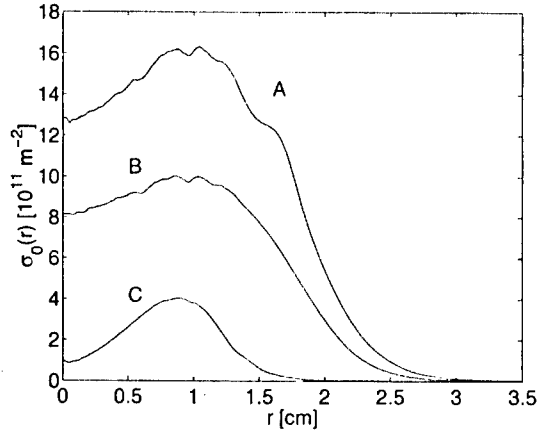


FIGURE 1. Experimental line integrated density from experiments by Kabantsev and Driscoll [4].

A modified Rayleigh criterion for linear stability and the conservation of canonical angular momentum and of the energy of the system can be deduced from system (9) [6]. The criterion proves that when $\sigma_0(r)$ is a monotonic function, the system is linearly stable.

COMPARISON WITH EXPERIMENTAL RESULTS

Growth rates calculated with the present theory have been compared with those resulting from recent experiments performed by Kabantsev and Driscoll [4]. For each experiment the electron temperature is approximately 1 V and the axial magnetic field is $B_0 = 0.4$ T. Three different cases (labelled A – B – C) have been considered. Table 1 summarizes the confining voltage and the geometrical parameters of the trap for these cases.

For each case, the initial z -integrated density, $\sigma_0(r)$, is reported in Fig. 1. From such measured density distributions, the corresponding profiles for $n_c(r)$ and $\mathcal{L}(r)$ have been calculated, by solving Eqs. (9) iteratively for the initial equilibrium. The results of the calculations are presented in Figs. 2 and 3. Growth rates of the instability, γ , and real frequencies, f , for the $m_0 = 1$ mode have been evaluated by linearizing system (9). Table 2 summarizes the results.

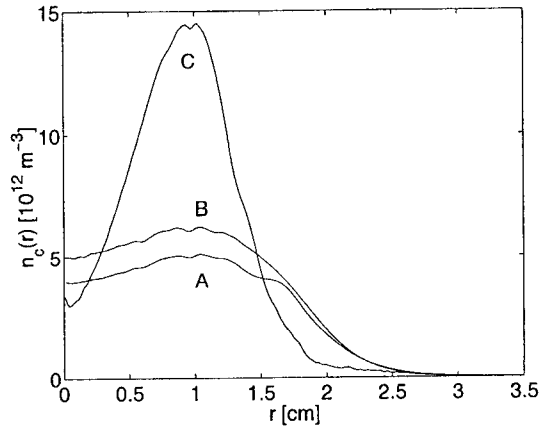


FIGURE 2. Equilibrium density profile calculated from experimental σ_0 .

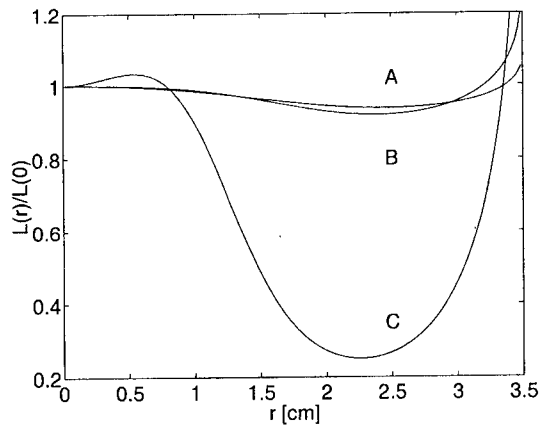


FIGURE 3. Equilibrium length profile calculated from experimental σ_0 .

A few considerations are in order. It can be noticed that in a short trap (case C) compression effects are very strong and the equilibrium length profile varies considerably with r . On the contrary, for longer traps (cases A and B) the equilibrium length profile has a small variation with respect to its value for $r = 0$ (10% inside the plasma radius). When compression effects are small (i.e., for long traps), the growth rates calculated with the present theory are not comparable with the corresponding experimental values. Viceversa, when compression effects are strong (i.e., for short traps) the agreement between theory and experiment is remarkable. When compression effects are small, the disagreement between theory and experiment is probably to be explained in terms of kinetic effects, as pointed out in Refs. [9] and [10].

TABLE 2. Real frequency and growth rate (in kHz) for the unstable $m_0 = 1$ mode

	experiment			theory		
	f	γ	γ/f	f	γ	γ/f
A	17.9	6.0	0.34	17.0	0.99	0.058
B	23.2	5.6	0.24	21.0	0.93	0.044
C	42.7	10.6	0.25	36.1	8.5	0.24

ACKNOWLEDGMENTS

The authors gratefully thank Andrey Kabantsev and Fred Driscoll for providing experimental data used in the present work. The authors are also grateful to John Finn and Diego del Castillo-Negrete for stimulating discussions about the linear theory of the $m_0 = 1$ mode and to Thomas O'Neil, Daniel Dubin, David Schecter and Terry Hilsabeck for their useful suggestions.

Work performed with a partial support by the Italian National Group for Mathematical Physics (GNFM-INDAM, research project: "Kinetic Theory and Fluid Models for Non-Neutral Plasmas") and by the USA Department of Energy under contract W-7405-ENG-36.

REFERENCES

1. Davidson, R. C., *An Introduction to the Physics of Nonneutral Plasmas*, Addison-Wesley, Redwood City, 1990.
2. Smith, R. A., and Rosenbluth, M. N., *Phys. Rev. Lett.* **64**, 649-652 (1990).
3. Driscoll, C. F. and Fine, K. S., *Phys. Fluids B* **2**, 1359-1366 (1990).
4. Kabantsev, A. A., and Driscoll, C. F., "End Shape Effects on the $m_0 = 1$ Diocotron Instability in Hollow Electron Columns" in *1999 Workshop on Nonneutral Plasmas*, edited by J. J. Bollinger, R. L. Spencer, R. C. Davidson, AIP Conference Proceedings 498, New York, 1999, pp. 208-213.
5. Finn, J. M., del-Castillo-Negrete, D., and Barnes, D. C., *Phys. Plasmas* **6**, 3744-3758 (1999); Finn, J. M., del-Castillo-Negrete, D., and Barnes, D. C., *Phys. Rev. Lett.* **84**, 2401-2404 (2000).
6. Coppa, G. G. M., D'Angola, A., Delzanno, G. L., and Lapenta, G., *Phys. Plasmas* **8**, 1133-1141 (2001).
7. Dubin, D. H. E., and O'Neil, T. M., *Phys. Plasmas* **5**, 1305-1314 (1998).
8. Fine, K. S., and Driscoll, C. F., *Phys. Plasmas* **5**, 601-607 (1998).
9. Hilsabeck, T. J., and O'Neil, T. M., *Phys. Plasmas* **8**, 407-422 (2001).
10. Coppa, G. G. M., and Ricci, P., "Non-Collisional Kinetic Model for Non-Neutral Plasmas in a Penning Trap: General Properties and Stationary Solutions", these proceedings.

Diocotron Spectrum with Compression Effects

G. L. Delzanno*, V. I. Pariev[†], G. Lapenta** and J. M. Finn[‡]

**Istituto Nazionale di Fisica per la Materia (INFN) and Dipartimento di Energetica, Politecnico di Torino, Corso Duca degli Abruzzi 24, 10129 Torino, Italy*

[†]*Theoretical Division, Los Alamos National Laboratory, Los Alamos, NM 87545, USA and Lebedev Physical Institute, Leninsky Prospect 53, Moscow B-333, 117924, Russia*

***Istituto Nazionale di Fisica per la Materia (INFN) and Theoretical Division, Los Alamos National Laboratory, Los Alamos, NM 87545, USA*

[‡]*Theoretical Division, Los Alamos National Laboratory, Los Alamos, NM 87545, USA*

Abstract. The diocotron spectrum for a simplified model of Malmberg-Penning traps that includes compression effects due to end curvature is investigated herein. Performing an initial value treatment, we find that there is a class of length profiles for which the linearized eigenvalue equation of the model can be integrated in quadratures (integrable case). In this case, there is only algebraic growth when the effective angular frequency has a maximum (hollow profile) or a minimum, and the model is mathematically equivalent to the zero curvature (2D Euler) case. Furthermore, we study profiles that are slightly different from the integrable one (the difference being characterized by a small parameter, ϵ), finding that the frequency of the unstable $l = 1$ mode scales as $\epsilon^{2/3}$. Analytical calculations and numerical simulations are found in remarkable agreement.

INTRODUCTION

The analogy between the 2D Euler equations for an incompressible and inviscid fluid and the classical equations for the evolution of a non-neutral plasma (2D drift-Poisson model) in a Penning trap is well known [1]. According to the linear theory, the 2D drift-Poisson model has demonstrated to be satisfactory only for (exponentially unstable) perturbations with azimuthal mode number $l > 1$. On the other hand, it can be proved theoretically that perturbations with mode number $l = 1$ are always stable, regardless of the initial equilibrium density profile [1]. Experiments, however, show that the linear growth of the $l = 1$ mode is exponential [2].

New fluid-dynamics models have been developed for a non-neutral plasma, trying to solve the problem of the $l = 1$ diocotron instability [3, 4]. These works show that a possible explanation of the instability comes from the finite curvature of the ends of the plasma column due to the confining voltage (i.e. compression effects).

The present study investigates the modification of the low-frequency branch of the diocotron spectrum when these compression and finite electron temperature effects are taken into account.

PHYSICAL MODEL

We focus our attention on a simplified version of the model developed by some of the authors in Ref. [4]. In normalized units, the model is the following:

$$\begin{cases} \frac{\partial \sigma}{\partial t} = -\mathbf{V}_\perp \cdot \nabla_\perp \sigma \\ \mathbf{V}_\perp = \hat{\mathbf{e}}_z \times \nabla_\perp \phi_{\text{eff}} \\ \nabla_\perp^2 \phi = \frac{\sigma}{L_0} \\ \phi_{\text{eff}} = \phi + \alpha \log \frac{L_0}{L_0, r=0} \end{cases} \quad (1)$$

For a detailed derivation of this model we refer to Refs. [4, 5, 6]. Compression effects are retained in the terms depending on the normalized temperature α (assumed to be uniform) and on the normalized effective plasma length $L_0(r)$. The relation between physical and dimensionless quantities can be found in Ref. [5]. The effective plasma length is assumed fixed in time and this makes the model 2D.

The motivation of this study is that this approximated model is still able to capture the features of the $l = 1$ diocotron instability (as shown in Ref. [4]) but, since it is 2D, it is possible to perform analytical calculations to match numerical simulations. Our goal is to get some insights on the effects of both temperature and length profile on the diocotron spectrum that will help us in the study of the complete model of Ref. [4].

ALGEBRAIC INSTABILITY IN INTEGRABLE CASE

First, we perform an analysis similar to the one by Smith and Rosenbluth [7]. Applying the Laplace transformation to the linearized time-evolution equation that can be deduced from model (1), one obtains:

$$(\omega - l\Omega) \left[\frac{1}{r} \frac{d}{dr} \left(r \frac{d\delta\phi_\omega}{dr} \right) - \frac{l^2}{r^2} \delta\phi_\omega \right] + \frac{l}{r} \frac{\sigma'_0}{L_0} \delta\phi_\omega = i \frac{\delta\sigma(r, 0)}{L_0} \quad (2)$$

where the prime means derivative with respect to r and $\delta\phi_\omega$ and $\delta\sigma(r, 0)$ are respectively the Laplace transformed perturbation of the potential and the initial perturbation of the line integrated charge density. A new effective angular frequency has been defined

$$\Omega(r) = \omega_E(r) + \frac{\alpha L'_0(r)}{r L_0(r)} \quad (3)$$

where $\omega_E(r) = \phi'_{c0}(r)/r$ is the $\mathbf{E} \times \mathbf{B}$ equilibrium angular frequency in the central plane of the trap. In the limit of $L_0 = \text{const}$, Eq. (2) reduces to the classical Euler case.

After some algebra, it can be shown that under a certain condition Eq. (2) can be integrated in quadratures, i.e. $\delta\phi_\omega(r) = r[\omega - \Omega(r)]$ is a solution of the problem for $l = 1$. We refer to this case as the integrable case. The condition is that the following equation be satisfied:

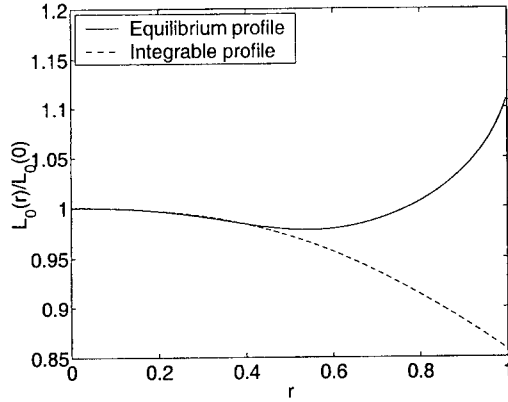


FIGURE 1. Effective length profiles.

$$\chi'' + \frac{\chi'}{r} - \frac{\chi}{r^2} = \frac{\sigma_0 \chi}{\mathcal{L}_0 \alpha}, \quad (4)$$

where $\chi = \mathcal{L}_0'/\mathcal{L}_0$. In this case, provided that the effective angular frequency has a stationary point, the system is algebraically unstable and the mode perturbation grows asymptotically proportionally to \sqrt{t} (as for the classical 2D Euler case [7]). This result has been confirmed numerically.

Given the equilibrium initial parameters, Eq. (4) can be used to obtain the integrable length profile and in general this profile will be different from the one that comes from the equilibrium solution for a given configuration of the Penning trap. In order to make these two profiles as close as possible inside the plasma radius (which is the most important region, as pointed out in Ref. [3]) we use the boundary conditions $\chi(0) = 0$ and $\chi'(0) = \mathcal{L}_{0,eq}''(0)/\mathcal{L}_{0,eq}(0)$. Note however that one could in principle choose the geometry of the trap (which determines the equilibrium profile) to match the integrable length profile $\mathcal{L}_{0,integ}(r)$.

Figure 1 shows the length profiles. The equilibrium length profile is calculated for the same geometrical and physical parameters of Ref. [4], with the choice of confining voltage $V = 50$ V and temperature $\Theta = 7.5$ V. Accordingly, we choose the normalized temperature $\alpha = 0.42$ and the normalized equilibrium density profile [3, 4]:

$$n_0(r) = \frac{\sigma_0}{\mathcal{L}_0} = \begin{cases} n_0(0) \left[1 - \left(\frac{r}{r_p} \right)^2 \right]^2 \left[1 + (\mu + 2) \left(\frac{r}{r_p} \right)^2 \right], & r \leq r_p \\ 0, & r > r_p, \end{cases} \quad (5)$$

with $n_0(0) = 6.2$, $\mu = 3$ and $r_p = 0.59$.

INITIAL VALUE TREATMENT

In Eq. (2), the Laplace transformation of the perturbation of the potential is defined as $\delta\phi_\omega(r) = \int_0^{+\infty} e^{i\omega t} \delta\phi(r, t) dt$, while the inverse Laplace transformation is given by $\delta\phi(r, t) = \int_{-\infty+i\eta}^{+\infty+i\eta} \delta\phi_\omega(r) e^{-i\omega t} \frac{d\omega}{2\pi}$ where η is a large enough real positive number, such that all irregular points of the function $\delta\phi_\omega$ are located below the line $\text{Im } \omega = \eta$ in the complex plane of ω .

We introduce the function $\psi(r, \omega) = r\delta\phi_\omega(r)$ and solve the second order equation for ψ induced by Eq. (2). Unlike $\delta\phi_\omega$, the solutions for ψ are bounded at $r \rightarrow 0$, which is necessary for Eq. (6) below.

We perform our analysis in the vicinity of the stationary point r_s ($\omega_s = \Omega(r_s)$), by using the method of matched asymptotic expansions for $\psi(r, \omega)$. For simplicity, the initial perturbation is chosen to be localized, $\delta\sigma(r, 0) = \sigma_i \delta(r - r_i)$, as it is done in Ref. [8]. This method gives the following result

$$\delta\phi(r, t) = -\frac{ir_s\sigma_i}{3r\mathcal{L}_0(r_i)} \int_C \frac{e^{-i\omega t}}{\omega - \Omega(r_i)} \times \left(\psi_r(r, \omega)\psi_s(R_w, \omega) - \frac{3\pi}{2} i \left(\frac{\Omega''|_{r_s}}{2\Delta} \right)^{3/2} \psi_r(R_w, \omega)\psi_r(r, \omega) - \psi_r(R_w, \omega)\psi_s(r, \omega) \right) \times \frac{\psi_r(r_i, \omega)\psi_s(0, \omega) - \psi_s(r_i, \omega)\psi_r(0, \omega)}{\psi_r(0, \omega) \left(-\frac{3\pi}{2} i \left(\frac{\Omega''|_{r_s}}{2\Delta} \right)^{3/2} \psi_r(R_w, \omega) + \psi_s(R_w, \omega) \right) - \psi_s(0, \omega)\psi_r(R_w, \omega)} \frac{d\omega}{2\pi}. \quad (6)$$

Here the contour C goes around the vertical branch cut attached to the point $\omega = \omega_s$ in the complex plane of ω . $\psi_r(r, \omega)$ and $\psi_s(r, \omega)$ are two linear independent solutions of the homogeneous part of the Laplace transformed equation such that $\psi_r \sim O((r - r_s)^2)$ and $\psi_s \sim O(1/(r - r_s))$ in the vicinity of r_s . We have also introduced $\Delta = \omega - \omega_s$ and $\Omega''|_{r_s} = \frac{d^2\Omega}{dr^2} \Big|_{r=r_s}$.

Two merging singular points are present when r approaches r_s and the contour of integration in the complex plane of r should always go between these two points [9].

We expand in power of Δ the integrand of Eq. (6) and perform the integral. Each term of the expansion contributes as $\int_C \Delta^\nu e^{-i\omega t} \frac{d\omega}{2\pi} \propto t^{-\nu-1} e^{-i\omega_s t}$. The algebraic instability ($\nu < -1$) is only possible if the term proportional to $\Delta^{-3/2}$ in the denominator of expression (6) vanishes, i.e. if $\psi_r(0, \omega) = 0$ or $\psi_r(R_w, \omega) = 0$. In the integrable case $\psi_r = r^2(\Omega(r) - \omega_s)$ and, therefore, $\psi_r(0, \omega) = 0$. Thus, in the integrable case, the leading term of the expansion has $\nu = -3/2$ (from the numerator of Eq. (6)) and the calculation of the contour integral leads to growth $\propto \sqrt{t}$. Exact calculations of the contour integral (6) recover the asymptotic formula obtained by the stationary phase method in Ref. [7].

When the length profile deviates only a little from the integrable profile (we refer to this case as non-integrable case), $\mathcal{L}_0 = (1 - \epsilon)\mathcal{L}_{0,\text{integ}} + \epsilon\mathcal{L}_{0,\text{eq}}$, where ϵ is a small parameter, the perturbation to the solutions of Eq. (2) are $\propto \epsilon$. In particular, $\delta\psi_r \propto \epsilon$ and $\psi_r(0, \omega) \propto \epsilon$. Since $\psi_r(0, \omega) \neq 0$, algebraic growth does not occur in the non-integrable

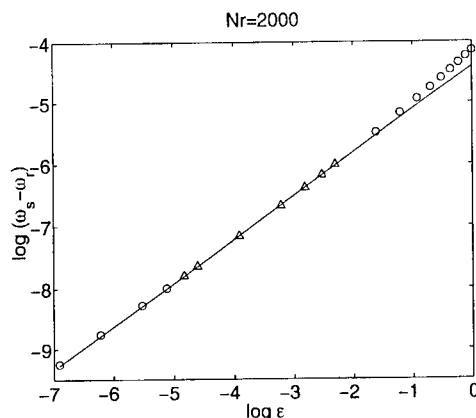


FIGURE 2. Frequency shift of the unstable $l = 1$ mode, log-log scale.

case (continuum modes near the endpoint $\omega = \omega_s$ phase mix according to $t^{-1/2}$ in this case). The zeroes of the denominator in Eq. (6) determine the discrete eigenfrequencies. One can see that for small ϵ the eigenfrequencies exist with $\Delta \propto \epsilon^{2/3}$ (as predicted by Smith in Ref. [10] for an ad-hoc model and seen in Ref. [3]). These eigenfrequencies are located close to the edge of the continuum ω_s .

Numerical simulations have been done to compare with analytical predictions. Specifically, Fig. 2 shows the frequency shift of the real frequency (ω_r) of the unstable $l = 1$ mode with respect to the edge of the continuum, for ϵ between 0 and 1. We perform the best fit with the least squares method only for the points marked with triangles, since for very small ϵ there is a loss of accuracy and for large ϵ the perturbation theory fails. We find $\omega_s - \omega_r \propto \epsilon^{0.70}$, in good agreement with the result $\omega_s - \omega_r \propto \epsilon^{2/3}$ obtained from Eq. (6).

Figure 3 shows the growth rate (γ) of the unstable $l = 1$ mode as a function of ϵ . Remarkably, we find $\gamma \propto \epsilon^{0.65}$, in excellent agreement with $\gamma \propto \epsilon^{2/3}$. One can also notice that the integrable case is a very specific case and as soon as one moves a little bit from this profile, an exponential growth is found.

Furthermore, another discrete mode appears at the lower edge of the continuum (in the integrable case this mode is the stable diocotron mode). As predicted analytically and confirmed numerically, its real frequency shift (with respect to the lower edge of the continuum) scales proportionally to ϵ .

REFERENCES

1. Davidson, R. C., *An Introduction to the Physics of Nonneutral Plasmas*, Addison-Wesley, Redwood City, 1990.
2. Driscoll, C. F., and Fine, K. S., *Phys. Fluids B* **2**, 1359-1366 (1990).
3. Finn, J. M., del-Castillo-Negrete, D., and Barnes, D. C., *Phys. Plasmas* **6**, 3744-3758 (1999); Finn, J. M., del-Castillo-Negrete, D., and Barnes, D. C., *Phys. Rev. Lett.* **84**, 2401-2404 (2000).

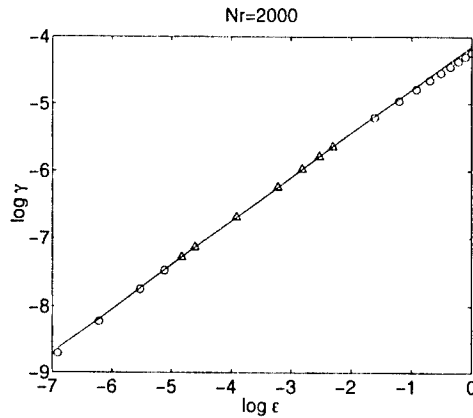


FIGURE 3. Growth rate of the unstable $l = 1$ mode, log-log scale.

4. Coppa, G. G. M., D'Angola, A., Delzanno, G. L., and Lapenta, G., *Phys. Plasmas* **8**, 1133-1141 (2001).
5. Lapenta, G., Delzanno, G. L., and Finn, J. M., "Non-linear PIC Simulation in a Penning Trap", these proceedings.
6. Coppa, G. G. M., D'Angola, A., Delzanno, G. L., and Lapenta, G., "Rigorous Fluid Model for 3D Analysis of the Diocotron Instability", these proceedings.
7. Smith, R. A., and Rosenbluth, M. N., *Phys. Rev. Lett.* **64**, 649-652 (1990).
8. Case, K. M., *Phys. Fluids* **3**, 143-148 (1960).
9. Istomin, Ya. N., and Pariev, V. I., *Mon. Not. Roy. Astron. Soc.* **281**, 1-26 (1996).
10. Smith, R. A., *Phys. Fluids B* **4**, 287-289 (1992).

Modes in a Nonneutral Plasma Column of Finite Length

S. Neil Rasband and Ross L. Spencer

Department of Physics and Astronomy, Brigham Young University, Provo, Utah 84602

Abstract. A Galerkin, finite-element, nonuniform mesh computation of the mode equation for waves in a non-neutral plasma of finite length in a Cold-Fluid model gives an accurate calculation of the mode eigenfrequencies and eigenfunctions. We report on studies of the following: (1) finite-length Trivelpiece-Gould modes with flat-top and realistic density profiles, (2) finite-length diocotron modes with flat density profiles. We compare with the frequency equation of Fine and Driscoll [Phys Plasmas **5**, 601 (1998)].

INTRODUCTION

The familiar Cold-Fluid drift model for the nonneutral plasma gives inside the plasma the mode equation for the perturbed potential [1].

$$\frac{1}{r} \frac{\partial}{\partial r} \left(r \frac{\partial \Phi^{(1)}}{\partial r} \right) - \frac{m^2}{r^2} \Phi^{(1)} + \left(\left(1 - \frac{\omega_p^2(r)}{(\omega - m\omega_0)^2} \right) \frac{\partial^2 \Phi^{(1)}}{\partial z^2} \right) + \frac{m \frac{\partial \omega_p^2(r)}{\partial r}}{\Omega r (\omega - m\omega_0)} \Phi^{(1)} = 0 \quad (1)$$

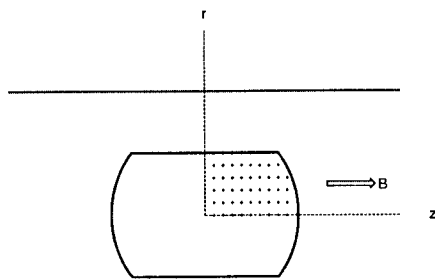


FIGURE 1. Region of Computation

The computation region is illustrated in Figure 1 with $0 \leq r \leq r_{\text{wall}}$ and $0 \leq z \leq z_{\text{wall}}$, where the plasma in this region is confined to the region with the crosses.

Equation (1) can be written in the form

$$\nabla \cdot (\epsilon \cdot \nabla \Phi^{(1)}) = 0,$$

where

$$\epsilon = \begin{bmatrix} 1 & \frac{i}{\Omega} \int \frac{\frac{\partial \omega_p^2(r)}{\partial r}}{(\omega - m\omega_0(r))} dr & 0 \\ \frac{-i}{\Omega} \int \frac{\frac{\partial \omega_p^2(r)}{\partial r}}{(\omega - m\omega_0(r))} dr & 1 & 0 \\ 0 & 0 & 1 - \frac{\omega_p^2(r)}{(\omega - m\omega_0(r))^2} \end{bmatrix} \quad (2)$$

and

$$\Omega = \frac{qB}{mc}, \quad \omega_0 = \frac{q}{m\Omega r} \frac{\partial \Phi_0}{\partial r}.$$

Construct a decomposition of the region of interest into triangular elements, where the plasma boundary is approximated by edges of the triangles. Figure 2 shows an example with $r_{\text{wall}} = 3.81\text{cm}$ and $z_{\text{wall}} = 30\text{cm}$.

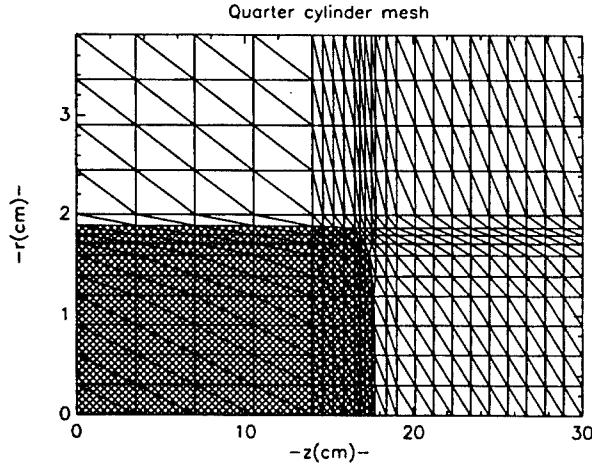


FIGURE 2. A triangulation of a plasma equilibrium. The region occupied by the plasma is shaded. Note that the scales for the vertical and horizontal axes are not the same.

Each triangle has 6 nodes (3 mid-points for the sides and 3 vertices) and on each node I a parabolic function:

$$\Psi_I(x, y) = \beta_1 + \beta_2 x + \beta_3 y + \beta_4 x^2 + \beta_5 xy + \beta_6 y^2.$$

This function is defined so that it has value 1 at the I th node and 0 at all other nodes in the triangle. Then approximate $\Phi^{(1)}$ as a sum over nodes:

$$\Phi^{(1)}(x, y) = \sum_I C_I \Psi_I(x, y).$$

Boundary nodes have the C_I determined from boundary conditions on $\Phi^{(1)}(x, y)$.

The Galerkin integration of Eq.(1) multiplied by the approximating functions Ψ_J proceeds numerically by doing one triangular element at a time. If the element is outside the plasma, then $\epsilon = 1$, otherwise it is as given in Eq.(2). This gives a matrix equation for the C_I .

$$\sum_I A_{JI} C_I = 0$$

with nonzero values of C_I only for certain values (eigenvalues) of ω . In practice we set

$$\sum_I A_{JI} C_I = 1, \quad \text{for each } J \quad (3)$$

and look for ω such that $\max(C_I) \rightarrow \infty$ or so that $1/\max(C_I) \rightarrow 0$.

TRIVELPIECE-GOULD (M=0) MODES

As a first example we present the results for a flat-top density profile with the plasma edge at $r_{\text{plasma}} = 1.89\text{cm}$, $z_{\text{plasma}} = 17.71\text{cm}$. The triangulation for this equilibrium is shown in Figure 2. The aspect ratio $\alpha = 9.37$ and $r_{\text{plasma}}/r_{\text{wall}} = 0.496$. For the modes that can be compared with the results in Table II of Jennings, Spencer, and Hansen [2] the agreement is excellent.

Figure 3 shows a scan in frequency for even modes in z with some of the prominent modes indicated.

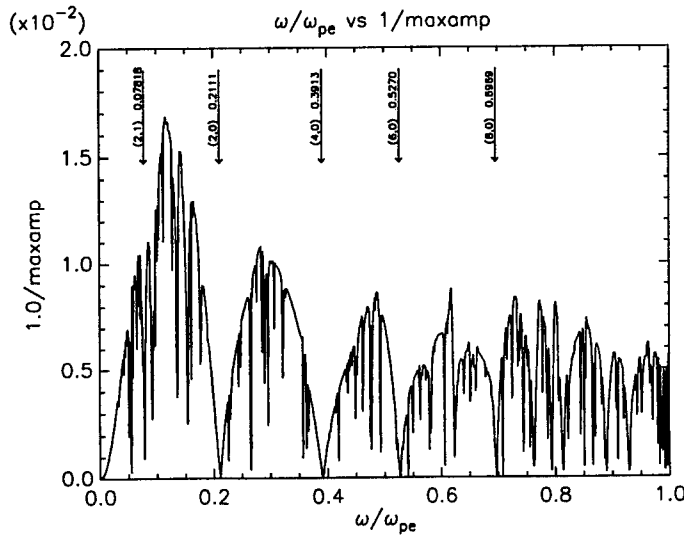


FIGURE 3. Scan of $1/\max(C_I)$ as described following Equation (3) for even modes.

A similar scan in frequency for the same equilibrium but odd modes gives frequencies $\omega/\omega_{pe} = 0.1079, 0.3060, 0.4630, 0.5766$ for the modes (1,0), (3,0), (5,0), and (7,0), respectively. Figure 4 shows the perturbed potential eigenfunctions for some of these modes.

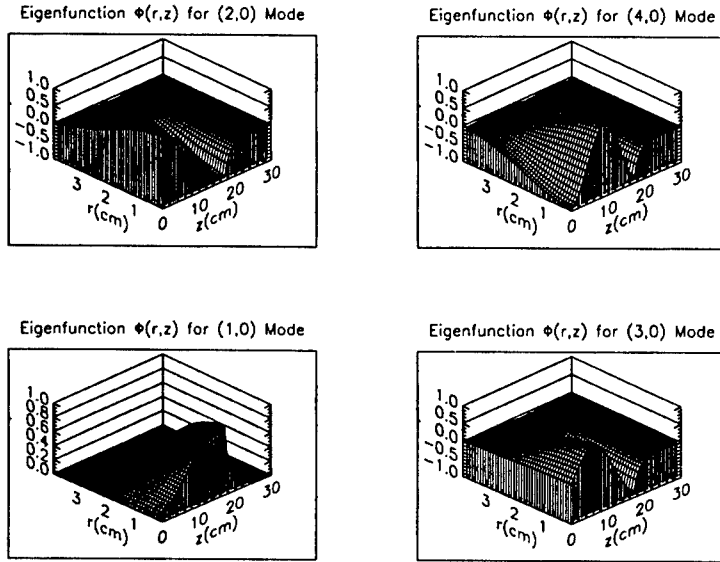


FIGURE 4. Perturbed potential eigenfunctions for selected modes

Lastly, for $m=0$ modes we consider briefly the effect of a radial dependence in the density profile. We compute equilibria [3] whose midplane density is

$$n(r)/n_0 = (1 - \sqrt{(1.5/\nu)(r/r_{\text{wall}})^2}) \exp(-(r/r_l)^\nu).$$

We choose $r_l = r_{\text{wall}}/2$ and compare two choices for ν , $\nu = 5.0, 40.0$, corresponding to a more-or-less average monotonic profile and a flat profile, respectively. Figure 5 shows the profiles with the corresponding (2,0) mode frequencies. The changes in the mode frequencies for such changes in density profiles are on the order of 10%.

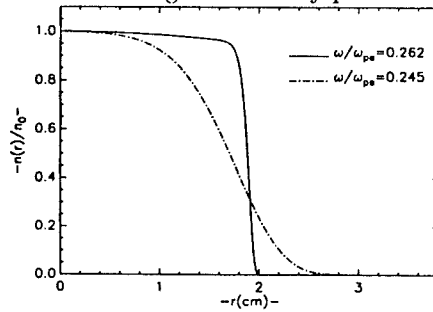


FIGURE 5. Density profiles and frequencies for (2,0) modes.

THE DIOCOTRON (M=1) MODE

We examined the finite-length diocotron mode frequency for a number of differing equilibria with varying plasma radii. All equilibria have flat-top density profiles and are computed in a Malmberg trap with radius $r_{\text{wall}} = 3.81\text{cm}$, half-length $z_{\text{wall}} = 30.0\text{cm}$ and magnetic field 375 G. Figure 6 shows the shift in frequency from the infinite length result as a function of the plasma radius. This figure also compares these results to those obtained with the formula of Equation (24) in Fine and Driscoll [4].

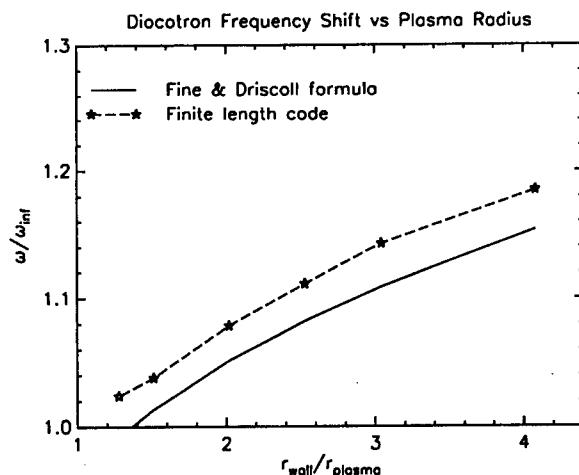


FIGURE 6. Diocotron frequency shift as a function of plasma radius.

For the case of $r_{\text{wall}}/r_{\text{plasma}} = 2.0$ Figure 7 shows the shape of the perturbed plasma potential in the quarter cylinder computation region. For a fixed z value less than the plasma half-length it is evident that inside the plasma the perturbed potential dependence on r is almost linear. A detailed examination of these eigenfunctions shows that inside the plasma their dependence on r is like $r + ar^3 + \dots$ and in z like $1 + bz^2 + \dots$ with a and b small for long plasmas. This is consistent with solutions inside the plasma that go like a modified Bessel function I_1 in r and $\cosh(kz)$ in z , with k very small corresponding to a wavelength much longer than the length of the confining cylinder [1].

This curvature in r is readily seen for a pancake-like equilibrium. In Figure 8 we show the edge curve for a pancake-like equilibrium with $r_{\text{plasma}} = 2.524\text{cm}$ and $z_{\text{plasma}} = 0.138\text{cm}$ for an aspect ratio of $\alpha = 0.055$. This Figure also includes a plot of the scaled perturbed potential as a function of r for a fixed value of z where the curvature is readily apparent. The $m=1$ diocotron mode for this equilibrium has a frequency of $\omega/\omega_{pe} = 0.00902$.

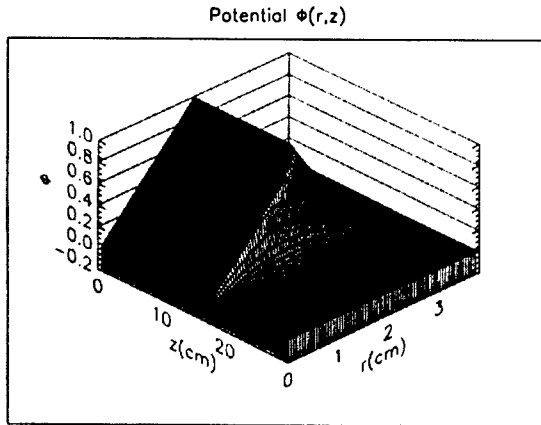


FIGURE 7. Perturbed Potential in the quarter cylinder for a $m=1$ diocotron mode

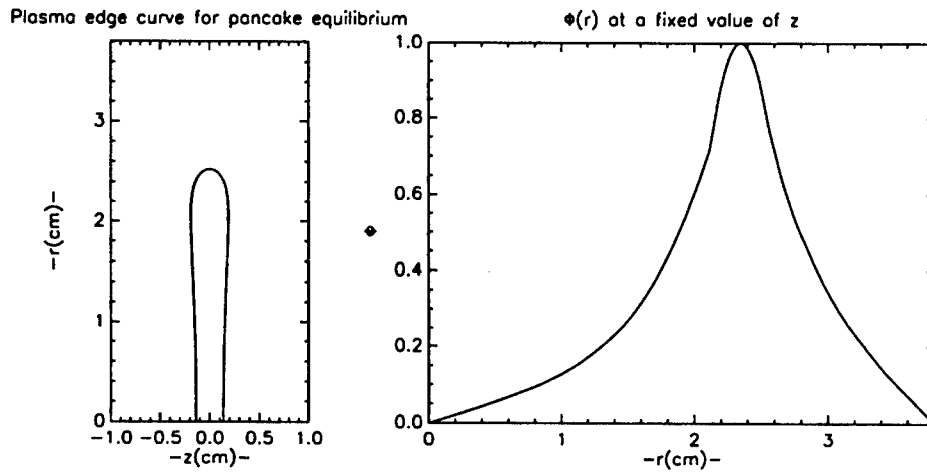


FIGURE 8. Pancake-like plasma edge and perturbed potential as a function of r for a fixed value of $z = 0.05\text{cm}$

REFERENCES

1. Prasad, S. A. and O'Neil, T. M., *Phys. Fluids*, **26**, 665 (1983).
2. Jennings, J. K., Spencer, R. L., and Hansen, K. C., *Phys. Plasmas*, **2**, 2630 (1995).
3. Spencer, R. L., Rasband, S. N., and Vanfleet, R. R., *Phys. Fluids B*, **5**, 4267 (1993).
4. Fine, K. S. and Driscoll, C. F., *Phys. Plasmas*, **5**, 601 (1998).

Interacting Solitons in a Nonneutral Plasma

Grant W. Hart and Bryan G. Peterson

*Department of Physics and Astronomy
Brigham Young University
Provo, Utah 84602*

Abstract. We have been continuing our study of solitons and nonlinear interactions in a pure electron plasma. The solitons are grown from large amplitude normal-mode oscillations. When grown in this way, it is convenient to divide the resulting wave into two parts: localized soliton-like structures and global normal-mode-like waves. These two parts interact weakly with each other and cause various interesting effects. When we launch two solitons by using the $n_z = 2$ mode, the normal mode part quickly converts to an $n_z = 1$ mode and causes one of the solitons to disappear. Later, when only one soliton exists, the $n_z = 1$ mode is locked to it. Because the soliton speed is faster than the linear wave speed, this increases the frequency of the normal-mode part of the system. It appears that when the soliton amplitude drops below some critical value, the two parts of the system decouple and propagate separately.

INTRODUCTION

We have been studying electrostatic Trivelpiece-Gould modes in a nonneutral plasma confined in a Malmberg-Penning trap[1]. Our plasma is 60 cm long and about 2 cm in radius. The plasma temperature is about 1 eV[2]. We have previously reported work showing that at large amplitude these waves have some of the properties of solitons[3], but that work was limited by the fact that signals from only two of the wall sectors could be recorded on a single shot. We synchronized the signals from different rings by recording a common ring on all of the shots. This limited our ability to evaluate events that were not reproducible from shot to shot. In this study we were able to record all of the wall signals on a single shot basis and therefore study the interesting events that were not reproducible between shots.

GROWTH OF SOLITONS FROM NORMAL MODES

A soliton is a wave in a dispersive medium that is large enough that nonlinear steepening effects just balance the dispersive spreading, causing it to propagate unchanged. Solitons occur in many physical situations[4].

The cold fluid equations for a plasma in a cylinder can be manipulated, making some assumptions, into the form of the first integral of the Korteweg-deVries equation[5]. This means that these solitons should have the properties of the well known solutions of that equation.

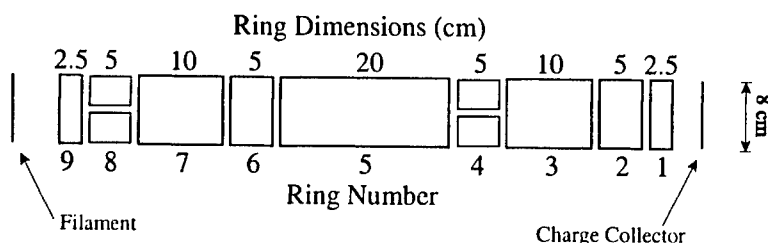


FIGURE 1. Characteristics of the wall rings in our trap.

Solitons in a nonneutral plasma have been created in two ways. One is to put a large potential step on a confining ring[6, 7]. This requires a relatively large voltage (tens to hundreds of volts.) Another way is to create them from normal modes[5]. With this second method, which is the one used in this paper, the confining potentials of the plasma are oscillated at a frequency slightly (about 30 kHz) above the normal mode frequency of the plasma (about 4.22 MHz). This has the effect of repeatedly hitting the pulses at just the right time with a small voltage, building them up to large pulses.

The number of solitons created from a given normal mode is initially equal to n_z (the mode number of the standing wave, which is equal to the number of half-wavelengths in the plasma.) In numerical simulations the pulses have the characteristic sech^2 shape of KdV solitons[5]. The fact that the driving frequency has to be above the normal mode frequency is an indication that the solitons are traveling faster than the linear wave speed of the plasma. If they traveled at the linear wave speed, they should travel one wavelength in one period and have a frequency equal to the normal mode frequency.

EXPERIMENTAL SETUP

These signals are detected by the image charge induced in the wall sections of our Malmberg-Penning trap. Figure 1 shows the lengths, positions and identification numbers of the rings in our trap. We usually recorded data on rings 3, 5, 6 and 7. With low amplitude oscillation, we just get normal mode oscillations. The characteristics of normal mode oscillations are that the signals are sinusoidal in time with a fixed 0 or 180 degree phase difference between them. The relative amplitudes are also fixed by the identity of the mode and the geometry of the wall sections. With a larger amplitude drive, you see the negative bump of the soliton as it passes underneath each ring. These characteristics are illustrated in Fig. 2. Part (A) shows a normal mode oscillation, while part (B) of the figure shows two counterpropagating solitons. The presence of two solitons can be inferred from the fact that the bumps on rings 3 and 7 are in phase and that ring 5 shows a bump which is roughly twice as big as on the other rings, since both solitons are under it at the same time. Part (C) shows a later time when one of the solitons has disappeared, as will be discussed later. Note that the time scale on part (C) is twice as long as on the other plots. In this plot the signal on ring 5 is closer in size to that on rings 3 and 7. The sequencing of the peaks through the rings can clearly be followed in this plot.

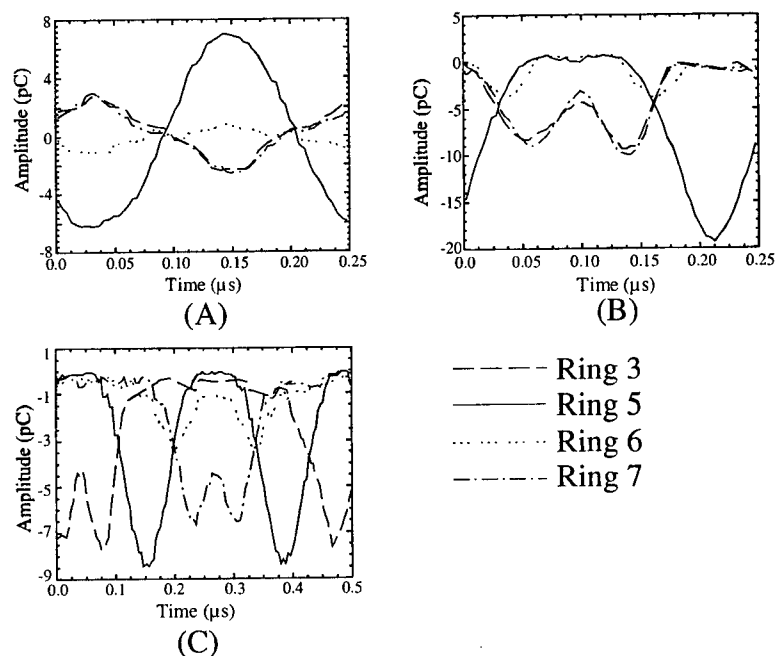


FIGURE 2. Signals for normal modes and solitons. Part (B) shows the signals recorded for a small amplitude oscillations with all of the characteristics of a normal mode oscillation. Part (B) shows the signals when two counterpropagating solitons are present in the system. Part (C) shows the signals when one soliton is present in the system.

EXPERIMENTAL RESULTS

Figure 3 shows the signal recorded on ring 5 as a function of time. The time interval when the system goes from two solitons to one is shown in the first shaded area. The characteristic decrease in amplitude on this ring by a factor of two can clearly be seen. The second shaded region shows the time interval when the second soliton disappears and the signal becomes indistinguishable from a normal mode signal. It appears that both of these events occur because of interactions between the normal modes and the propagating solitons.

In order to describe the signals that we see in all of our rings, it is necessary to break the signal into two parts: a global, sinusoidal in space and time, normal mode part and one or two localized soliton parts. We can calculate and measure the sensitivity of each ring to the two lowest normal modes.

We use a nonlinear least-squares fitting algorithm to fit our four ring signals to these normal mode and soliton parts. Figure 4 shows a typical fit of ring 6 data to two solitons and two normal modes. The normal mode part comes from all four rings together and the soliton parts are derived from just this ring's signal. Note that we describe the signals on these rings as superpositions of these different parts. This is not completely accurate since the solitons are nonlinear waves, but it seems that the interactions are small enough

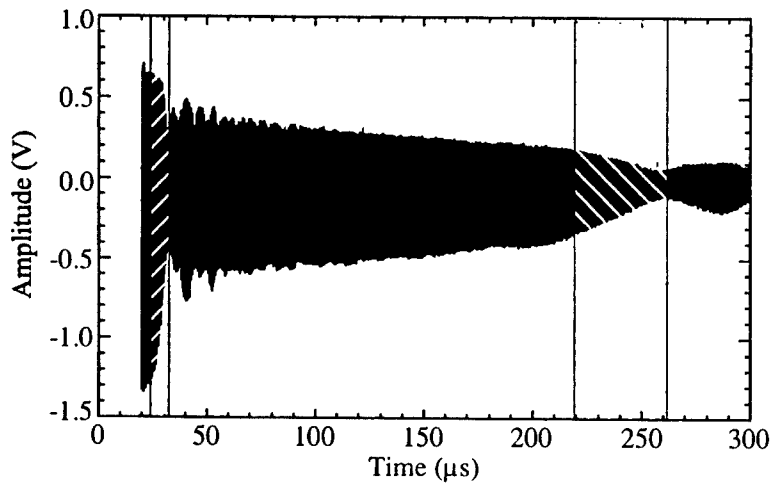


FIGURE 3. Signal recorded on ring 5 as a function of time. The first shaded region shows the time interval when one of the solitons is disappearing. The second shaded region shows the time when the second soliton also goes away.

that this works fairly well, except possibly when the two solitons pass through each other.

The first interaction between the normal modes and the solitons occurs when one of the solitons disappears. The initial state of the plasma is with two equal solitons and a moderate amount of the $n_z = 2$ normal mode. Shortly into the shot this mode undergoes mode conversion from $n_z = 2$ to $n_z = 1$. It appears to be the interaction with this $n_z = 1$ mode that causes one soliton to disappear. As can be seen in figure 4, one of the solitons hits the end of the plasma (at the time of the dip between the two peaks) while the $n_z = 1$ mode is rising, while the other hits while it is falling. One shrinks while the other grows. Figure 5 shows the signal on ring 3 as one soliton slows down and widens as its amplitude decreases. This disappearance takes place over a period of 10 to 20 bounce periods of the soliton.

After one of the solitons disappears, the remaining soliton and the normal mode lock into a fixed phase relationship that persists for hundreds of bounces. Interestingly, the frequency of the normal mode is raised by this interaction with the soliton. The width and frequency of the soliton do not change significantly during this time. At some time later, which depends on the specific shot, the remaining soliton also disappears fairly rapidly, although much slower than the disappearance of the first. It appears to occur on a timescale of 50-60 bounce periods. As shown in figure 6, the characteristics of this disappearance are that normal mode frequency drops to its unperturbed value and the soliton rapidly slows down and widens until its width is essentially a half wavelength of the normal mode. At that point it appears to become part of the normal mode. The soliton and the normal mode also dephase from each other somewhat during this time period, as if they have become decoupled. It is unclear exactly what is the trigger for this series of events. The soliton amplitude is slowly decreasing as it bounces. It appears

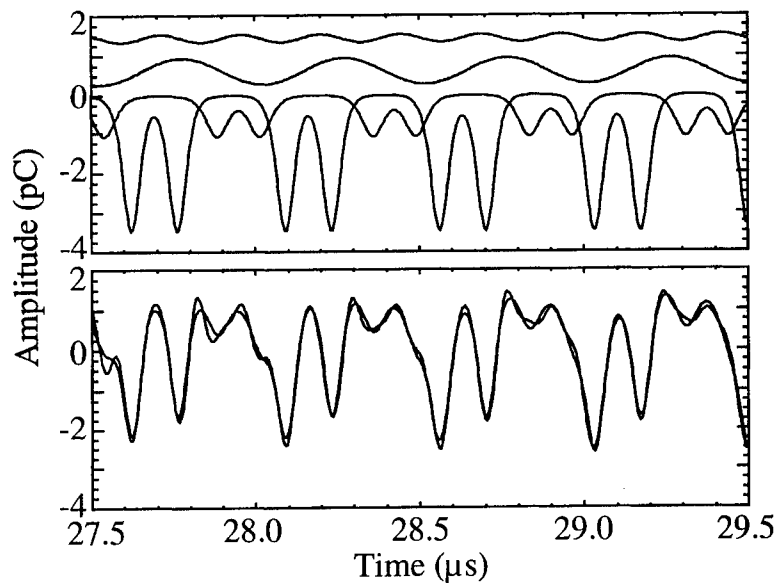


FIGURE 4. Least squares fit of ring 6 data to two solitons and two normal modes. The bottom trace shows both the data and the fit. The top trace shows the different components of the fit. The normal mode signals have been offset vertically for clarity.

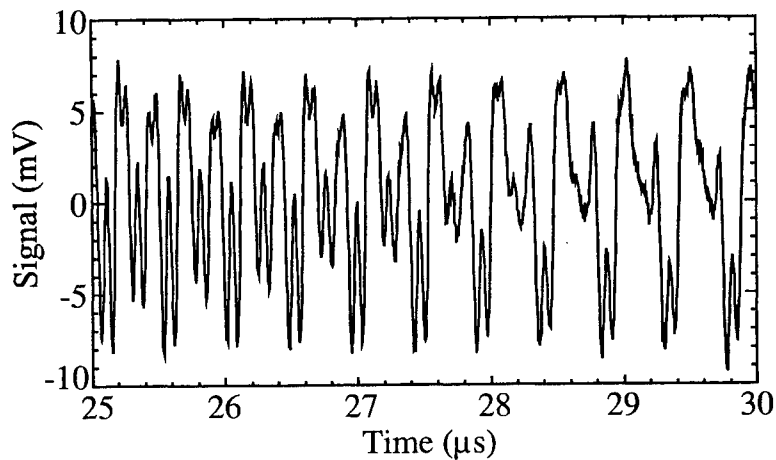


FIGURE 5. When the $n_z = 1$ mode grows, one of the solitons decreases in amplitude and velocity and disappears from the system.

that there is a minimum soliton amplitude necessary to force the coupling between the soliton and the normal mode. There are some indications that this minimum amplitude depends on the frequency shift between the coupled system and the unperturbed normal

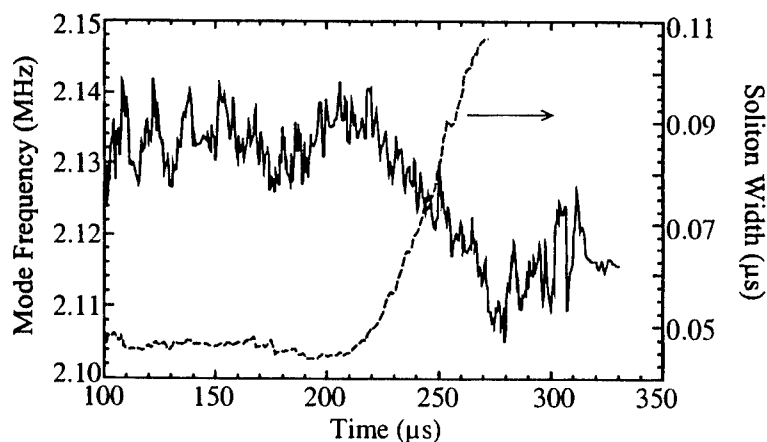


FIGURE 6. When the soliton amplitude gets small enough, the normal mode decouples from the soliton and its frequency drops to its natural frequency. During the same period the width of the soliton increases until it is about one half wavelength of the normal mode.

mode. We do not yet have enough data to verify this.

CONCLUSIONS

When solitons are grown from normal modes in a nonneutral plasma, some of the normal mode character persists underneath the solitons. Interactions between these normal modes and the solitons appear to cause the disappearance of one of the solitons at early times and of the other at much later times, although the mechanisms of the two disappearances appear to be different.

REFERENCES

1. deGrassie, J. S. and Malmberg, J. H., *Phys. Rev. Lett.* **39**, 1077 (1972).
2. Hart, G. W. *Phys. Fluids B*, **3**, 2987 (1991).
3. Hart, G. W., Spencer, R. L. and Peterson, B. G., *Non-Neutral Plasma Physics III*, AIP conf. Proc. 498, edited by J. Bollinger, R. Spencer and R. Davidson (AIP, New York, 1999) p. 182.
4. Ikezi, H., Barrett, P. J., White, R. B., and Wong, A. Y., *Phys. Fluids* **14**, 1997 (1971) and references contained therein.
5. Hansen, K. C., "The Linear and Nonlinear Stages of the Electrostatic Modes of a Warm, Nonneutral Plasma", Master's Thesis, Brigham Young University (1995).
6. Moody, J. D., and Driscoll, C. F., *Phys. Plasmas*, **2** 4482 (1995).
7. Neu, S. C. and Morales, G. J., *Phys. Plasmas*, **2** 3033 (1995).

Experimental Observation of Fluid Echoes in a Non-Neutral Plasma

Jonathan H. Yu and C. Fred Driscoll

*Dept. of Physics and Institute for Pure and Applied Physical Sciences,
University of California at San Diego, La Jolla CA 92093-0319 USA*

Abstract. Experimental observation of a nonlinear fluid echo is presented which demonstrates the reversible nature of spatial Landau damping, and that non-neutral plasmas behave as nearly ideal 2D fluids. These experiments are performed on UCSD's CamV Penning-Malmberg trap with magnetized electron plasmas. An initial $m_i = 2$ diocotron wave is excited, and the received wall signal damps away in about 5 wave periods. The density perturbation filaments are observed to wrap up as the wave is spatially Landau damped. An $m_i = 4$ "tickler" wave is then excited, and this wave also Landau damps. The echo consists of a spontaneous appearance of a third $m_e = 2$ wave after the responses to the first two waves have inviscidly damped away. The appearance time of the echo agrees with theory, and data suggests the echo is destroyed at least partly due to saturation.

Longitudinal plasma wave echoes have been previously observed in a neutral plasma [1], and here we present observation of diocotron wave echoes in a pure electron plasma. Diocotron waves vary as $\delta n(r, \theta) = \tilde{\delta n}(r) \exp[i(m\theta - \omega t)]$, with essentially no z -variation. These waves can be considered low frequency $\mathbf{E} \times \mathbf{B}$ drift modes representing surface waves or bulk shape distortions of the electron column. The diocotron mode damping seen here is a result of spatial Landau damping [2]. The echo's existence depends on the reversibility of the phase mixing process, and thus demonstrates the reversible nature of spatial Landau damping.

Theory predicts that echoes occur in ideal (incompressible and inviscid) 2D fluids [3], and the echo has been studied numerically in 2D fluid shear flows [4]. In the 2D $\mathbf{E} \times \mathbf{B}$ drift approximation, the dynamics of electrons in a pure electron plasma are isomorphic to that of an ideal 2D fluid. The density, drift velocity, and electrostatic potential of the electron plasma correspond to the vorticity, velocity, and streamfunction of the 2D ideal fluid, respectively [5]. Detecting the echo in a non-neutral plasma is striking, since one might think that non-ideal effects would destroy phase information in the density distribution.

The diocotron waves and echoes are excited and received using wall sectors of a cylindrical Penning-Malmberg trap. Fig. 1 is an oscilloscope trace of the signal received from opposite 60° wall sectors. This detection scheme gives a maximum response to $m = 2$ perturbations.

An initial $m_i = 2$ wave is excited by applying $V_i = 5 - 30V$ to two opposite 60° wall sectors (different from the detection sectors) for about one half of an $m = 2$ period. The first pulse of Fig. 1 is the signal received as the initial wave of amplitude A_i decays in about five oscillations due to spatial Landau damping. A second $m_i = 4$ "tickler" wave is then excited a time τ after the initial wave is excited. The tickler wave is excited by

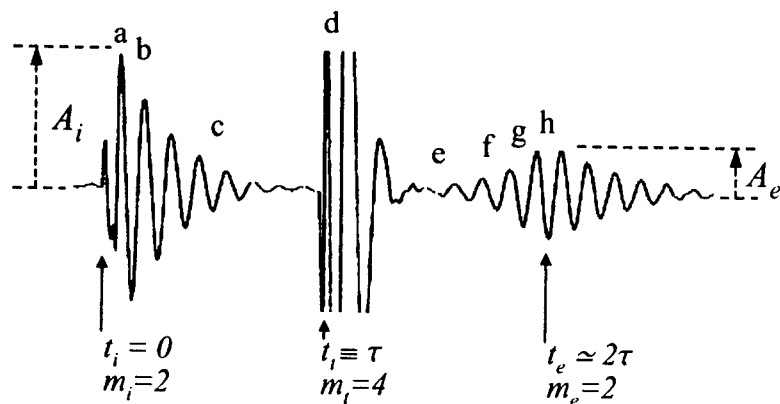


FIGURE 1. The signal received from two opposite sectors of a wall cylinder shows the initial, tickler, and echo waves.

applying a square pulse of $V_t = 1 - 40V$, for about one half of an $m_t = 4$ period, to four 30° sectors each separated by 90° . The second pulse of Fig. 1 shows the time at which the $m_t = 4$ tickler wave is excited. This signal is not actually the $m = 4$ plasma oscillation, but rather a direct coupling of the tickler excitation to the wall detector. The third wave packet of Fig. 1 is the received echo, and the peak echo response occurs at a time $t_e \approx 2\tau$. The peak echo amplitude is denoted A_e .

We have also imaged the spatial evolution of the electron density during wave damping and echo generation. At a chosen time in the evolution, the plasma is dumped onto a phosphor screen and recorded by a CCD camera. The perturbation images shown in Fig. 2 are created by subtracting a θ -symmetric density image from the density image of the perturbed plasma, giving $\delta n(r, \theta, t)$. These images directly represent phase space evolution, since angular momentum is proportional to r^2 in our magnetized electron plasma. Thus, the filamentary images illustrate the theory concepts of phase mixing (and un-mixing).

The first three images of Fig. 2 show the initial $m_i = 2$ wave forming spiral filaments as the perturbation evolves in the sheared background. The images in Fig. 2 correspond to the times labelled by the letters in Fig. 1. The $m_t = 4$ wave is excited in Fig. 2d, and the thin filaments are the remnants of the initial wave. The tickler wave nonlinearly interacts with these remnants, producing an $m_e = 2$ echo response which peaks in Fig. 2h.

Theory gives an expression for the time of the echo appearance, and this expression agrees with experiments. In the resonance layer where $\omega_E(r) = \omega/m$, the initial perturbation can be written as $\tilde{\delta}n_i(r)\exp[im_i(\theta - \omega_E(r)t)]$. Likewise, the tickler perturbation varies as $\tilde{\delta}n_t(r)\exp[im_t(\theta - \omega_E(r)(t - \tau))]$, but also modulates the initial wave. This cre-

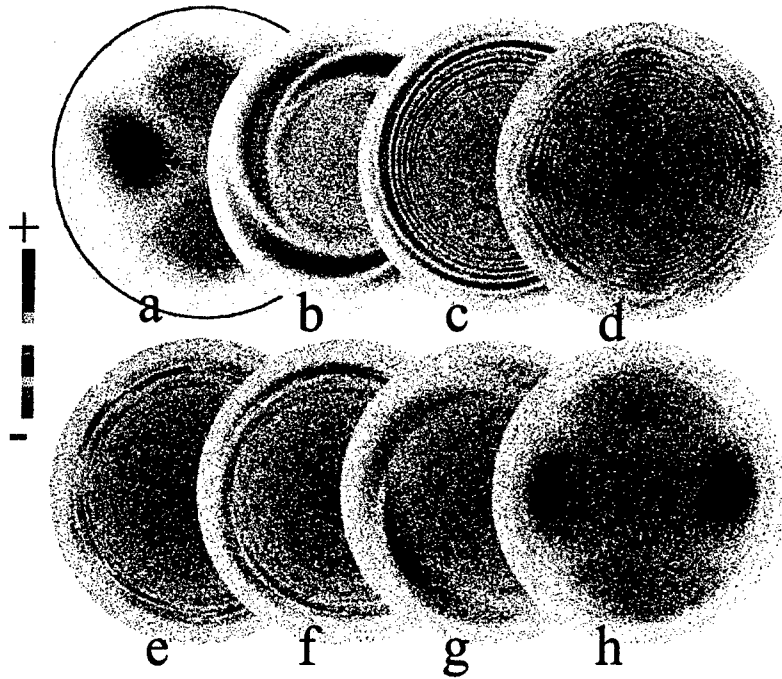


FIGURE 2. Density perturbation images at the eight successive times marked in Fig. 1. Figs. a, d, and h show the initial, tickler, and echo waves at maximal amplitude. Figs. a - c show the spiral density filamentation and wind-up of strong spatial Landau damping. Figs. f - h show the "unwinding" which creates the echo.

ates a second order perturbation varying as

$$\delta n_e(r, \theta, t) = \tilde{\delta} n_i(r) \tilde{\delta} n_t(r) \exp[i(m_t - m_i)\theta + im_t \omega_E(r)\tau - i(m_t - m_i)\omega_E(r)t]. \quad (1)$$

The time of the peak echo response occurs when a radial integral over the perturbation in Equation (1) does not phase mix to zero, and this occurs when the phase has no radial dependence [6]. Equating the ω_E terms of Equation (1) to zero yields the time of the peak echo response

$$t_e = \tau m_t / (m_t - m_i). \quad (2)$$

At this time the echo perturbation in Equation (1) has a θ dependence of $m_e = m_t - m_i$. This mode number expression agrees with the observed $m_e = 2$ structure of the echo.

We find that the predicted time for the echo response, given by Equation (2), fits the data. Fig. 3 shows the measured time of the echo response t_e , versus the time of the

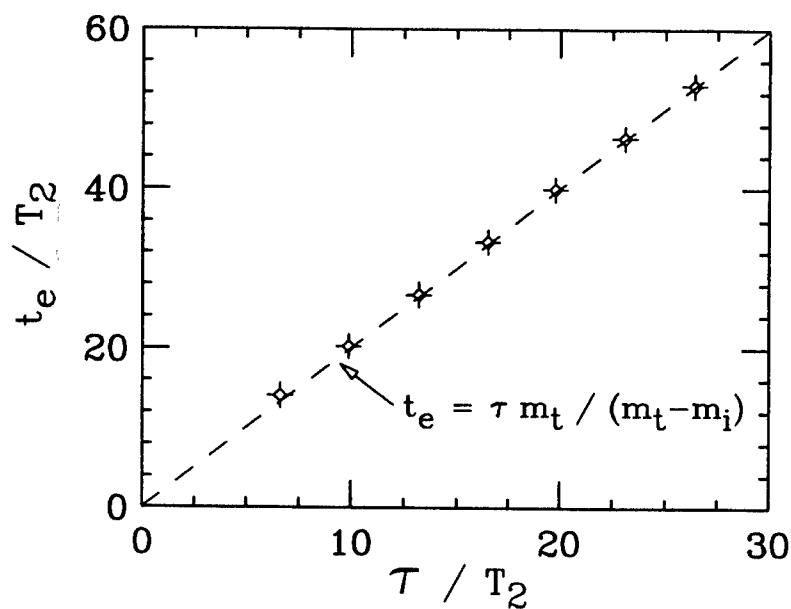


FIGURE 3. Measured time t_e of the peak echo response versus tickler delay time τ .

tickler launch τ , both scaled by $m = 2$ wave periods T_2 . The theoretical line $t_e = 2\tau$ is shown as a dashed line.

The initial and tickler waves do not have symmetric roles in their interaction leading to the echo. Fig. 4 shows the echo amplitude A_e , measured at $t = t_e$, versus τ , for four different (V_i, V_t) combinations. A_e increases approximately linearly for small τ , and then peaks and decreases at larger τ . τ_{max} is defined as the tickler launch time which results in the maximum measured echo amplitude. We find τ_{max} does not depend on A_i (see dashed curves of Fig. 4). However, the solid curves of Fig. 4 show that τ_{max} does depend on A_t . In addition, the three curves with $V_i = 15V$ give nearly the same A_e at τ_{max} .

The observed asymmetry in initial and tickler wave roles is consistent with the theory idea of saturation destroying the echo at large τ . A ballistic theory for the echo amplitude yields $A_e(t = t_e) \propto A_i J_1(\beta A_t \tau)$, where J_1 is a Bessel function of the first kind, and β is a function of m_i and m_t [6]. A_t is the maximum tickler wave amplitude and is assumed to be proportional to the applied V_t . The initial wave amplitude A_i determines the echo amplitude A_e at τ_{max} , while the tickler wave amplitude A_t determines τ_{max} itself. These theory results agree with the curves in Fig. 4, indicating that saturation is at least partly responsible for the decrease of A_e at large τ .

Theory of echo saturation yields as many as 300 $m = 2$ wave periods in τ_{max} , while experiments give no more than about 50 $m = 2$ wave periods. The discrepancy between theory and experiment at small tickler wave amplitudes suggests that non-ideal effects

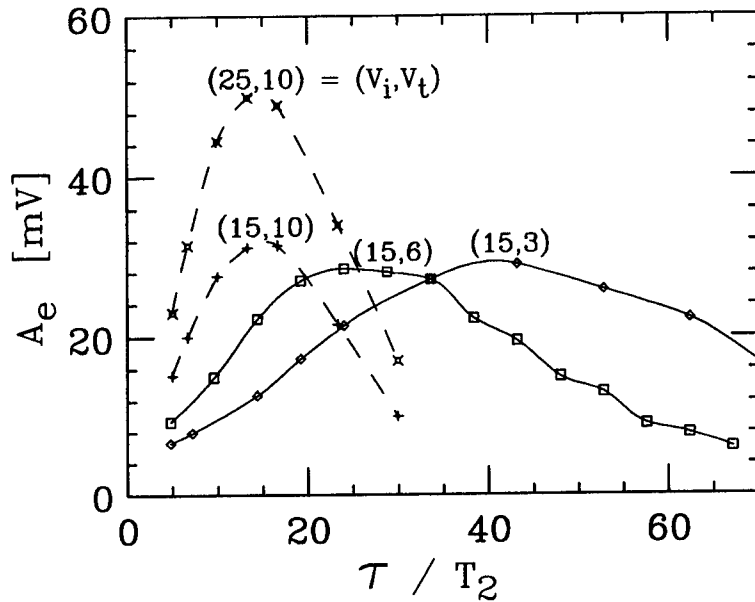


FIGURE 4. Measured amplitude A_e of the echo at $t = t_e$ versus τ . The numbers in parenthesis are the initial and tickler external excitations in volts. The decrease in echo amplitude at large τ is due at least partly to saturation.

may destroy the echo. One non-ideal effect is the magnetron drifts resulting from the end confinement fields, which cause θ -smearing [7] and which would presumably kill the echo. In addition to θ -smearing, viscosity can also wreak havoc on the ideal 2D fluid isomorphism. As the density perturbation filaments wind up, the radial spacing between filaments decreases and the filaments become thinner. After sufficient spiral wind-up the radial gradients would approach a magnitude for which viscosity is appreciable, and phase information would be destroyed. The influence of these non-ideal effects on the echo will be pursued in future work.

ACKNOWLEDGMENTS

This work was supported by Office of Naval Research grant N00014-96-1-0239 and National Science Foundation grant PHY-9876999.

REFERENCES

1. J. H. Malmberg, C. B. Wharton, R. W. Gould and T. M. O'Neil, *Phys. of Fluids* **11**, 6 (1968); D. R. Baker, N. R. Ahern, and A. Y. Wong, *Phys. Rev. Lett.* **20**, 7 (1968).
2. R. J. Briggs, J. D. Daugherty, and R. H. Levy, *Phys. Fluids* **13**, 421 (1970).
3. R. W. Gould, *Phys. Plasmas* **2**, 6 (1994).
4. J. Vanneste, P. J. Morrison, T. Warn, *Phys. Fluids* **10**, 1398 (1998); D. A. Bachman, Ph.D. dissertation, California Institute of Technology (1997).
5. C. F. Driscoll and K. S. Fine, *Phys. Fluids B* **2**, 1359 (1990).
6. T. M. O'Neil and R. W. Gould, *Phys. of Fluids* **11**, 1 (1968).
7. A. J. Peurrung and J. Fajans, *Phys. Fluids B* **5**, 12 (1993).

Landau Damping of Electron Plasma Waves in the Linear and Trapping Regimes

James R. Danielson, Francois Anderegg, Nobuyasu Shiga, Kevin Rigg,
and C. Fred Driscoll

*Dept. of Physics and Institute for Pure and Applied Physical Sciences,
University of California at San Diego, La Jolla CA 92093-0319 USA*

Abstract.

Linear Landau damping and nonlinear wave-particle trapping oscillations are observed with $m_0 = 0$ standing plasma waves (Trivelpiece-Gould modes) in a trapped pure electron plasma. The measured linear damping rate ($10^{-3} \lesssim \gamma/\omega \lesssim 10^{-1}$) agrees quantitatively with Landau damping theory for moderate plasma temperatures ($1 < T < 3$ eV), and exceedingly low wave amplitudes ($\delta n/n < 10^{-6}$). At larger amplitudes, the wave initially damps at the Landau rate, then develops trapping oscillations at frequency ω_{tr} , causing the effective damping rate to decrease with amplitude as first predicted by O'Neil in 1965. For comparison, the measured damping rate is observed to decrease dramatically when the resonant particles are eliminated by truncating the nominally Maxwellian velocity distribution.

INTRODUCTION

The first experiments demonstrating linear Landau damping [1] were reported over 30 years ago by measuring the spatial damping length (k_i) of Trivelpiece-Gould (T-G) waves in an open-ended neutral plasma column [2, 3]. T-G waves are longitudinal electrostatic plasma oscillations (Langmuir waves), modified by the cylindrical boundary [4]. Landau damping occurs when resonant electrons absorb energy from the wave; these electrons have axial velocity $v_z = v_{ph}$, where v_{ph} is the wave phase velocity. Nonlinear trapping oscillations were also measured in these plasmas [5, 6]. These oscillations in the wave amplitude occur when the resonant electrons become trapped and oscillate in the wave potential. Other nonlinear effects such as plasma wave echoes [7] and sideband frequency generation [8] were also observed. Even with this long history, the nonlinear regime of Landau damping and the long time behavior of Landau damped waves continues to be a subject of investigation [9, 10].

Pure electron plasmas exhibit the same plasma wave-particle resonance phenomena, since the neutral plasma ions do not participate in the dynamics [12]. Trivelpiece-Gould waves are also found in non-neutral plasmas contained in cylindrical Penning-Malmberg traps. For example, the torque from the "rotating wall" perturbations used for steady state confinement of electron [13] and positron plasmas [14] has been shown to be due to the excitation of asymmetric ($m_0 = 1$ or 2) T-G modes. Further, the spectrum of thermally-excited $m_0 = 0$ T-G modes has been measured in an electron plasma near thermal equilibrium [15].

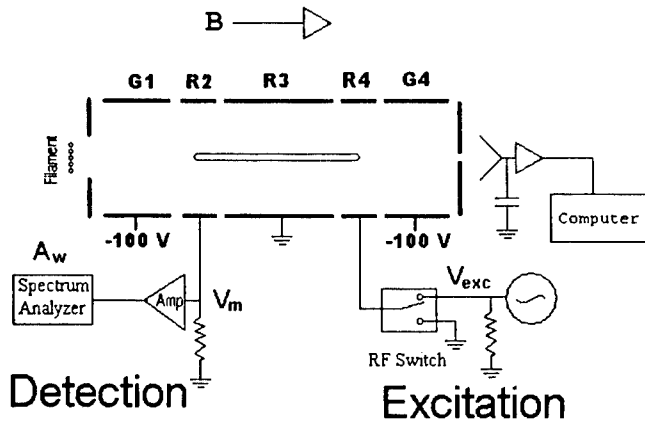


FIGURE 1. Schematic of EV Penning-Malmberg trap.

In this letter, we describe measurements of linear and nonlinear damping of standing $m_0 = 0$ T-G waves in a pure electron plasma. The dispersion relation for these long wavelength modes is dominated by the finite radial size, with phase velocity approximately independent of mode frequency; and this frequency regime has not been previously studied. In the small amplitude regime, the measured temporal damping rates ($\omega_i \equiv -\gamma$) show quantitative agreement with the predictions of linear Landau damping. Experiments also show that larger amplitude waves exhibit trapping oscillations; and that these oscillations decrease the wave damping, as first predicted by O'Neil [16]. When the resonant particles are eliminated experimentally by truncating the nominally Maxwellian velocity distribution, the measured damping rates decrease dramatically [3].

APPARATUS

Two different Penning-Malmberg electron traps were used, both represented schematically by Fig. 1. The two principle differences between the traps are magnetic field strength and typical plasma radius. The IV machine has a superconducting solenoid, giving an axial field of 30 kGauss; whereas the EV machine has a water-cooled solenoid with an axial field of 380 Gauss. In both traps, electrons from a tungsten filament are confined in a series of conducting cylinders in a ultrahigh vacuum with background pressure $P < 10^{-10}$ Torr.

The IV machine has a wall radius of $R_w = 2.86$ cm, with a plasma radius of $R_p \approx 0.2$ cm and plasma length $L_p \approx 41$ cm (aspect ratio $L_p/R_p \approx 200$). The EV machine has $R_w = 3.51$ cm, with $R_p \approx 1.0$ cm and $L_p \approx 24$ cm (aspect ratio ≈ 24).

The traps are operated in an inject-hold-dump cycle. Both machines trap approximately 10^9 electrons total; with a central density $n_0 \approx 10^7 \text{ cm}^{-3}$ for EV, and $n_0 \approx 2 \times 10^8 \text{ cm}^{-3}$ for IV. The electron source for IV is in the fringing magnetic field, so the electrons are compressed to a smaller radius and correspondingly a higher density. The plasma density is measured by dumping the plasma through a movable hole onto a

Faraday cup.

The EV machine uses a magnetic “beach analyzer” for measurement of the perpendicular plasma temperature [17]. The parallel temperature is measured on IV and EV by slowly ramping the dump gate voltage while measuring the collected charge as a function of confinement voltage. The escaping charge is fit to the exponential tail of a Maxwellian to give an estimate that is accurate to about 10% for temperatures $T \gtrsim 0.2$ eV [18]. The relatively rapid perp-to-parallel thermal equilibration rate [19, 17] ($v_{\perp\parallel} \approx 10^3 \text{ sec}^{-1}$ for IV and $v_{\perp\parallel} \approx 10^2 \text{ sec}^{-1}$ for EV) allows these experiments to be described by a single temperature [$T_{\perp} = T_{\parallel} = T(r)$]. Furthermore, the radial temperature variations are small enough to be ignored here.

The T-G modes are excited by a short burst (10 cycles) at the wave resonant frequency (ω_0) applied to cylinder R4. The resulting wave density fluctuations induce image charges on cylinder R2, and these are detected using either a low-noise current amplifier or a low-noise 50-ohm RF amplifier. The received signal is filtered and fed into a RF spectrum analyzer tuned to the resonant frequency with a bandwidth of 300 kHz. A separate signal generator is usually attached to cylinder R3 to provide controlled heating of the plasma [20]. The heating frequency is set close to the thermal bounce frequency ($\bar{f}_b = \bar{v}/2L_p$), which is less than $1/3 \omega_0$, assuring no coupling to the T-G mode.

For these experiments we launch the $m_z = 1$, $m_r = 1$ T-G mode, also known as the “sloshing” mode. This is the lowest order longitudinal oscillation of the plasma column, and has the nodes of the axial electric field (E_z) at the ends. This means that the wavelength λ is approximately twice L_p , with wavenumber $k_z = 2\pi/\lambda \approx \pi/L_p$. Numerical simulations have shown that the finite length of the plasma column acts to slightly increase the effective wavelength [21], thus making the effective wavenumber k_z^{eff} slightly smaller than π/L_p . Numerical solutions of the drift-kinetic equations for an infinite-length column with $n(r)$ and $T(r)$ determine a wavenumber k_z^{∞} which gives the observed mode frequency ω . We presume that the finite-length column has $k_z^{\text{eff}} = k_z^{\infty}$, and calculate the wave velocity as $v_{\text{ph}} = \omega/k_z^{\text{eff}}$.

THEORY

Landau was the first to describe the resonant interaction of electrostatic waves with particles traveling at the wave phase velocity, v_{ph} [1]. Depending on the slope of the particle velocity distribution at v_{ph} , this resonant interaction can cause either wave damping or wave growth. For Langmuir waves in an infinite homogeneous plasma with a Maxwellian velocity distribution, Landau calculated a damping γ_{LD} given by

$$\frac{\gamma_{\text{LD}}}{\omega} \approx \sqrt{\frac{\pi}{8}} \left(\frac{v_{\text{ph}}}{\bar{v}} \right)^3 \exp \left[-\frac{1}{2} \left(\frac{v_{\text{ph}}}{\bar{v}} \right)^2 \right], \quad (1)$$

with $v_{\text{ph}} = \omega/k_z^{\text{eff}}$ and $\bar{v} \equiv \sqrt{T/m}$. This equation comes from an approximate expansion of the Zeta function to lowest order in the parameter \bar{v}/v_{ph} [22]. In the early experiments by Malmberg *et al.* [2], a similar expression for k_i/k_r was tested by varying the wave phase velocity and measuring the corresponding spatial damping length k_i using a

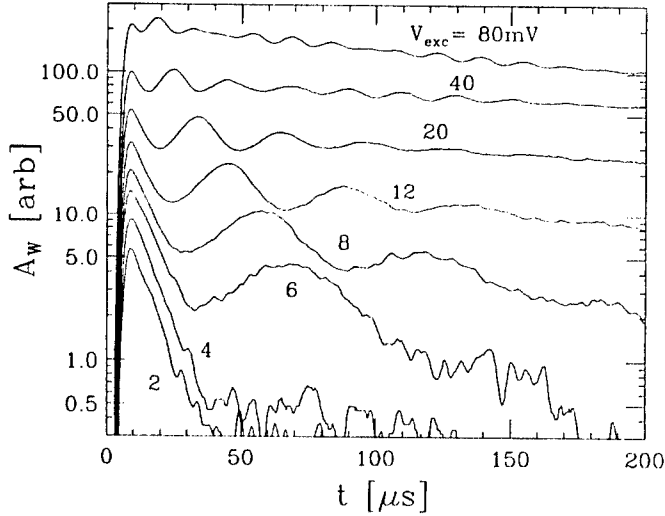


FIGURE 2. Decay of received amplitude versus time for various excitation amplitudes (V_{exc}). The waves were excited by a 10 cycle burst at 3.2 MHz ($\bar{v}^2/v_{ph}^2 = .08$).

plasma at a fixed temperature. For our experiments, the mode frequency is approximately

$$\omega \approx \left(\frac{k_z^{eff}}{k_{\perp}} \right) \omega_p \left[1 + \frac{3}{2} \left(\frac{\bar{v}}{v_{ph}} \right)^2 \right], \quad (2)$$

where $1/k_{\perp} \approx R_p \sqrt{\frac{1}{2} \ln(R_w/R_p)}$ and $\omega_p = \sqrt{4\pi n e^2/m}$, so the phase velocity is relatively insensitive to any change in frequency. In order to vary the damping rate we heat the plasma. This changes \bar{v} at roughly constant v_{ph} , enabling a comparison to Eq. (1). The slight temperature dependence of the phase velocity is accounted for in the estimates of \bar{v}/v_{ph} .

RESULTS

Figure 2 shows a logarithmic plot of the received wave amplitude versus time for different excitation amplitudes (V_{exc}). Three observations can be made: First, the peak of the received wave amplitude A_w depends linearly on the amplitude V_{exc} of the drive, as expected for linear waves. Second, for low amplitudes ($V_{exc} < 4$ mV), the wave damps exponentially, at a rate independent of amplitude; this is the regime of linear Landau damping. Third, as V_{exc} is increased above 8 mV, we observe the appearance of nonlinear temporal oscillations that inhibit the damping of the wave. At larger amplitudes ($V_{exc} \gtrsim 20$ mV), we observe that after the fast initial damping the wave exhibits oscillations with very little average amplitude decay.

From the data in Figure 2, we define three quantities for comparison to theory. First, the initial damping of the wave is defined to be γ_{lin} . Second, the (slower) average decay

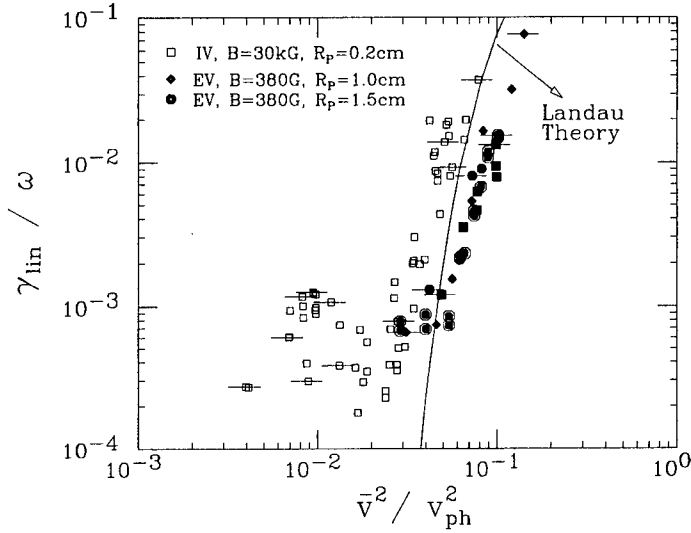


FIGURE 3. Measured linear damping rate compared to prediction of Landau.

rate of the wave over $200 \mu\text{s}$ is defined to be γ_{avg} . Third, we define a trapping frequency ω_{tr} by measuring the time Δt between the peak of the excitation and the peak of the first oscillation, with $\omega_{\text{tr}} \equiv 2\pi/\Delta t$.

Data sets similar to Figure 2 were taken over a range of plasma temperatures, thereby varying the value of \bar{v}/v_{ph} . Figure 3 is a plot of the initial damping γ_{lin} versus $\bar{v}^2/v_{\text{ph}}^2$, along with the Landau prediction from Eq. (1). For high temperatures, the data agrees with the linear theory of Landau over 2 decades in damping, an apparent 50% uncertainty in $\bar{v}^2/v_{\text{ph}}^2$. At lower temperatures, where Landau damping is expected to be small, we observe a damping "floor" of $10^{-3} - 10^{-4}$ which is likely caused by resistive dissipation in the measurement circuit [15].

The nonlinear effects are summarized in Figure 4, where the normalized average damping rate $\gamma_{\text{avg}}/\gamma_{\text{lin}}$ and the normalized trapping frequency $\omega_{\text{tr}}/\gamma_{\text{lin}}$ are plotted versus wave excitation amplitude V_{exc} . Also plotted is a dashed line showing the expected scaling of $\omega_{\text{tr}} \propto V_{\text{exc}}^{1/2}$. The trapping frequency shows good agreement with the expected scaling at high amplitudes, but shows a small systematic deviation at the lowest excitation amplitudes. This deviation is expected because for wave amplitudes such that $\omega_{\text{tr}}/\gamma_{\text{lin}} \sim 1$ there is significant damping before the first trapped particles can execute a complete trapping oscillation, leading to an effective trapping field that is slightly smaller than initially. This effect has been seen in numerical self-consistent calculations of the damping rate as a function of time [23] and in experiments by Franklin [24].

The average damping rate γ_{avg} is seen in Figure 4 to drop by more than an order of magnitude from the Landau rate as ω_{tr} becomes larger than γ_{lin} . This drop is expected, since trapped particles cause a periodic re-growth of the wave. However, theory predicts the wave damping should eventually become zero, in the absence of other decay

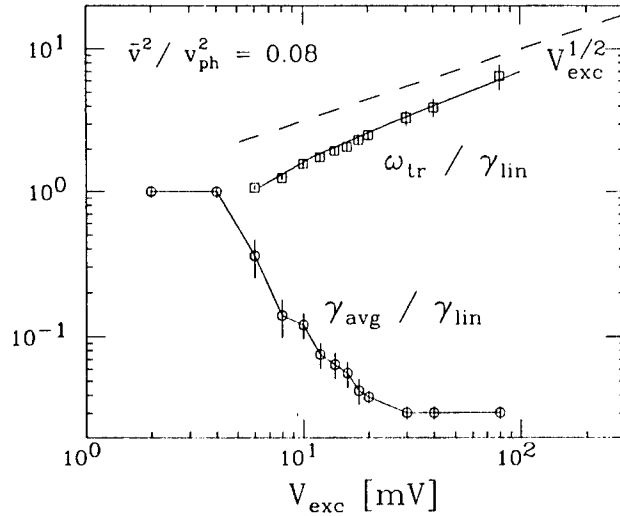


FIGURE 4. Normalized trapping frequency and normalized average decay rate versus excitation voltage. The dashed curve shows the expected scaling of trapping frequency with amplitude.

mechanisms. The experiments always measure some amount of residual damping. This residual damping, also seen clearly at low temperatures in Fig. 3, has been identified as due to resistive elements in the excitation and detection circuits [15]. In Figure 4, the small damping rate ($\gamma_{\text{avg}}/\gamma_{\text{lin}} \approx .03$) at large amplitudes corresponds to an effective real part of the external impedance of about 5Ω [15].

We have verified that γ_{lin} is due to resonant particles at v_{ph} by experimentally truncating the particle velocity distribution. When the confinement gate is ramped down, the highest energy particles are the first to escape. To measure damping on a truncated distribution, the plasma is first prepared by ejecting the high energy particles, then the wave is excited and the damping rate measured. It was observed that if the electrons with $v_z \gtrsim v_{\text{ph}}$ were ejected over most of the plasma radius, then the fast initial damping does not occur; the wave only damps at the residual resistive-damping rate. This qualitatively shows the sensitivity of the damping rate on the details of the tail of the velocity distribution, as would be expected for Landau damping.

CONCLUSIONS

At very small wave amplitudes, linear Landau damping is observed over the range $10^{-3} < \gamma_{\text{lin}}/\omega < 10^{-1}$. There appears to be some systematic shift between the two different apparatuses used. This is most likely due to the different geometry, namely the plasma aspect ratio (R_p/L_p), and the closeness of the plasma to the wall (R_p/R_w). For instance, the overlap of the mode potential and the plasma density shows substantial radial dependence. These profile effects could easily lead to errors in the estimated phase velocity and thus lead to a systematic error in applying the theory.

From the measured received wall voltage we can calculate the magnitude of E_z for the launched T-G mode. This value for E_z gives an expected trapping frequency ($\omega_{tr} \equiv \sqrt{ek_z E_z/m}$) that differs from the measured value by a factor of 3. However, uncertainties in the detector calibration and theoretical predictions have made it difficult to make an absolute comparison.

Unlike the early experiments [5, 6], the spectrum of T-G modes is discrete at these long wavelengths. This means we do not expect to have any sideband instability develop, and experimentally none have been observed. This unique characteristic should allow future experiments to contribute to the debate over the long time behavior of Landau damped waves [9, 25, 26].

ACKNOWLEDGMENTS

We gratefully acknowledge helpful advice on the theory from Profs. D.H.E. Dubin and T.M. O'Neil. This work was supported by Office of Naval Research grant N00014-96-1-0239 and National Science Foundation grant PHY-9876999. We also thank Mr. Fidel Zamora for excellent technical support.

REFERENCES

1. L. D. Landau, J. Phys. USSR **10**, 45 (1946).
2. J. H. Malmberg and C. B. Wharton, Phys. Rev. Lett. **6**, 184 (1964).
3. J. H. Malmberg, C. B. Wharton, and W. E. Drummond, "Landau Damping of Electron Plasma Waves," in *Proc. of Conf. on Plasma Physics and Controlled Nuclear Fusion Research*, IAEA, Vienna, Austria, 1966, p. 485.
4. A. W. Trivelpiece and R. W. Gould, J. Appl. Phys. **30**, 1784 (1959).
5. J. H. Malmberg and C. B. Wharton, Phys. Rev. Lett. **19**, 775 (1967).
6. R. N. Franklin, S. M. Hamberger, G. Lampis, and G. J. Smith, Proc. R. Soc. Lond. A. **347**, 1 (1975).
7. J. H. Malmberg, C. B. Wharton, R. W. Gould, and T. M. O'Neil, Phys. Rev. Lett. **20**, 95 (1968).
8. C. B. Wharton and J. H. Malmberg, Phys. Fluids **11**, 1761 (1968).
9. G. Brodin, Phys. Rev. Lett. **78**, 1263 (1997).
10. M. B. Isichenko, Phys. Rev. Lett. **78**, 2369 (1997).
11. P. J. Barrett, H. G. Jones, and R. N. Franklin, Plasma Physics **10**, 911 (1968).
12. L. M. Linson, Phys. Fluids **14**, 805 (1971).
13. E. M. Hollmann, F. Anderegg and C. F. Driscoll, Phys. Plasmas **7**, 2776 (2000).
14. R. G. Greaves and C. M. Surko, Phys. Plasmas **8**, 1879 (2001).
15. F. Anderegg, N. Shiga, *et al.*, in this Proceedings.
16. T. O. O'Neil, Phys. Fluids **8**, 2255 (1969).
17. A. W. Hyatt, C. F. Driscoll, and J. H. Malmberg, Phys. Rev. Lett. **59**, 2975 (1987).
18. D. L. Eggleston, C. F. Driscoll, B. R. Beck, A. W. Hyatt, and J. H. Malmberg, Phys. Fluids B **4**, 3432 (1992).
19. B. R. Beck, J. Fajans, and J. H. Malmberg, Phys. Rev. Lett. **68**, 317 (1992).
20. B. P. Cluggish, J. R. Danielson and C. F. Driscoll, Phys. Rev. Lett. **81**, 353 (1998).
21. J. K. Jennings, R. L. Spencer, and K. C. Hansen, Phys. Plasmas **2**, 2630 (1995).
22. C. J. McKinstrie, R. E. Giacone, and E. A. Startsev, Phys. Plasmas **6**, 463 (1999).
23. R. Sugihara and T. Kamimura, Journ. Phys. Soc. Japan **33**, 206 (1972).
24. R. N. Franklin, S. M. Hamberger, and G. J. Smith, Phys. Rev. Lett. **29**, 914 (1972).
25. V. E. Zakharov and V. I. Karpman, Sov. Phys. JETP **16**, 351 (1963).
26. Y. Midzuno and R. Sugihara, Journ. Phys. Soc. Japan **43**, 2068 (1977).

Collective Motional Resonances and Instabilities of an Electron Cloud Stored in a Penning Trap

D. BISWAS¹, P. PAASCHE¹, T. VALENZUELA¹, C. ANGELESCU¹,
S. ANANTHAMURTHY², G. WERTH¹

¹*Johannes Gutenberg University, Institut fuer Physik, D-55099 Mainz, Germany*

²*Bangalore University, Department of Physics, 560056, Bangalore, India*

Abstract. We have experimentally investigated the behaviour of an electron cloud confined in a Penning trap at weak superimposed magnetic fields. Exciting the motional frequencies of the electrons by an external drive field we found the axial mode split into two components which were identified as center-of-mass and individual electron oscillations. When the trapping potential was varied, rapid electron loss appeared at numerous values of the applied voltage. They are determined by the relation $n_z\omega_z + n_m\omega_m = \omega_c$. ω_z , ω_m , ω_c are the axial, magnetron, and cyclotron frequency of the trapped electrons, respectively. The reason for this loss is attributed to higher order contributions to the ideal quadrupole trapping potential.

Introduction

The behaviour of an electron cloud confined in Penning traps has been extensively investigated experimentally [1] and theoretically [2] in the general context of the characterization of non-neutral plasmas. In particular the mode structure of the motional oscillations serves to derive properties of the plasma such as density, rotation frequency or shape. The experiments that investigate these properties were performed under conditions, where the temperature of the plasma was low (4K) and the confinement took place far away from the stability limit of the Penning trap. This limit occurs when $\omega_c^2 = 2\omega_z^2$, $\omega_c = (e/m)B$ being the free electron cyclotron frequency and $\omega_z = (2eV/md^2)^{1/2}$ the axial oscillation frequency, in a trap of characteristic dimension d . B is the magnetic field strength and V , the voltage applied to the trap. In our experiment we confine electrons at weak magnetic fields, approaching the limit of stability. Furthermore the electron temperature is high in the absence of cooling mechanisms.

Experiment

We used a trap with hyperbolic electrodes of characteristic dimension $d = 2$ cm. The magnetic field along the z -axis was produced by two Helmholtz coils of 27 cm mean diameter, driven by currents up to 25 A producing a field up to 0.01 T. The trap has been used previously in laser spectroscopic experiments and had holes of several mm diameter drilled into the ring electrode. These holes together with possible misalignments, caused higher order contributions to the trapping potential, which in the ideal case is a quadrupole potential.

The trap was loaded with electrons from a tungsten filament placed several cm below one endcap electrode in pulses of several ms length. After a preset time which could be varied between 10 ms and virtually infinity, detection took place by a tuned circuit consisting of an inductance and the trap electrodes as capacitance. The circuit was weakly excited at its resonance frequency ω_0 (10 MHz). When the positive trap voltage, applied to the ring electrode, is ramped down, the electrons axial oscillation frequency ω_z changes. At a certain voltage ω_z coincides with ω_0 . Then the electrons absorb energy from the circuit, which consequently is damped. The r.f. amplitude across the circuit is rectified and the corresponding signal is proportional to the stored electron number. The total number is estimated from observed space charge shifts to about 10^5 . The method of detecting the stored electron cloud is in principle nondestructive. During the detection process, however, the electrons gain energy from the tank circuit. In addition they are ejected from the trap as consequence of higher order components in the trapping potential as shown below. This results in a total storage time of only a few second. Therefore we decided to ramp the trapping voltage down to negative voltages. This ensures elimination of all electrons from the trap and each creation-detection cycle starts with a completely empty trap.

Axial oscillation

When we apply an additional r.f. field to one of the electrodes or to the electron gun using it as antenna and sweep the frequency of this field, the electrons become excited whenever it coincides with one of the motional modes. Some of the electrons leave the trap and the motional resonances appear as minima in the detection signal. Fig. 1 shows such a spectrum which contains the fundamental oscillation frequencies ω_m (magnetron), ω_z (axial), and ω_c' (perturbed cyclotron) as well as some linear combinations or multiple of these frequencies. The number of observed combinations depends on the amplitude of the applied r.f. field. A high resolution scan of ω_z or $2\omega_z$ shows, that these frequencies have two components: A broad asymmetric minimum accompanied on the high frequency side by a narrow more symmetric minimum (Fig.2). Changing the stored ion number shows that the position of the broad minimum is shifted to higher frequency with decreasing electron number while the sharp

minimum does not change its position. When extrapolating both frequencies to vanishing electron number they coincide (Fig. 3). From this we conclude that the broad minimum corresponds to the excitation of the individual electrons in the cloud which experience the space charge of the surrounding cloud, while the sharp minimum is the center-of-mass mode of the whole ion cloud, which, of course, is independent of space charge. This observation is similar to the behavior of a molecular ion cloud stored in a Paul trap [3]. Similarly the appearance of the coherent oscillation of the ion cloud can be explained as a parametric instability of the axial motion under the influence of the additional drive field. As outlined in [3] the excitation of the coherent mode requires a minimum threshold excitation amplitude when the ion motion is damped. As main damping mechanism we consider collisions of the ion cloud with rest gas molecules, although our background pressure is of the order of 10^{-9} mbar. This assumption is justified by the fact that the threshold amplitude in our experiments is about 0.2 V whereas in the corresponding experiment on molecular ions it was of the order of 10 V. This change in order of magnitude reflects the difference in collisional cross section of electrons or molecular ions with background molecules.

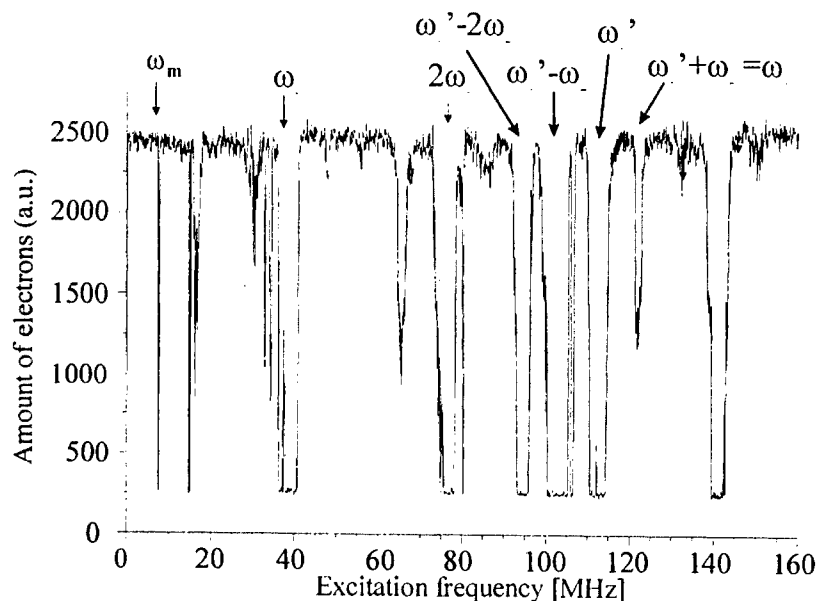


FIGURE 1. Motional spectra of a stored electron cloud in a Penning trap for different amplitudes of a r.f. drive field. Some of the identified resonances are labeled, the others are axial and magnetron sidebands to these frequencies.

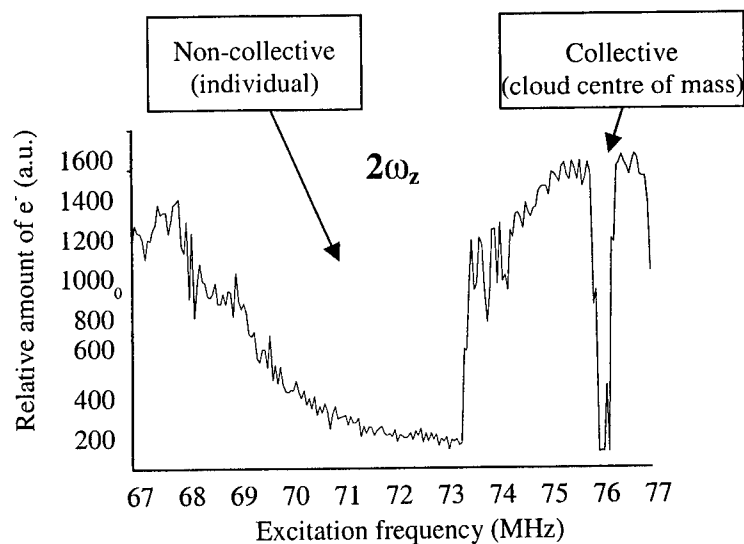


FIGURE 2. High resolution scan of the frequency $2\omega_z$ showing the collective (individual) and non-collective (center-of-mass) components of this mode

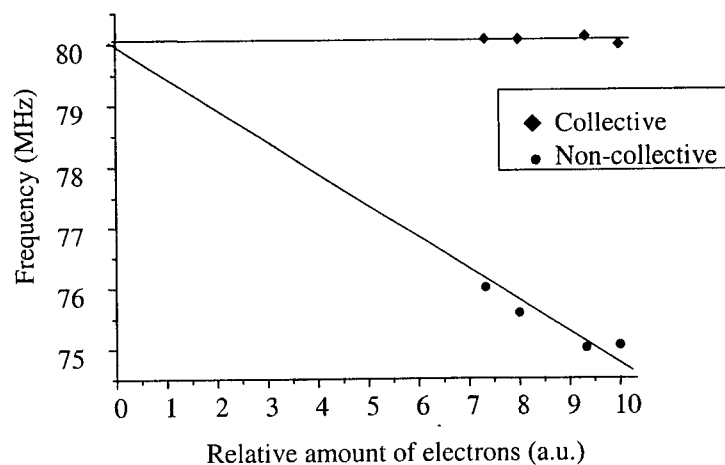


FIGURE 3. Space charge shift of the collective and non-collective resonances. Both frequencies coincide at vanishing electron number

Instabilities In Electron Confinement

When we varied the trapping potential we observed that it was impossible to detect stored electrons at values which are within less than about half of the maximum voltage allowed for stable confinement. This voltage follows from the stability

criterion for Penning traps $\omega_c^2 = 2\omega_z^2$: $V_{max} = (e/4m)d^2B^2$. Also at distinct lower values of V minima in the detected ion number were observed. The strength of these minima as well as their number increases with the storage time. When the storage time exceeds several seconds, storage of electrons is virtually impossible. Fig. 4 illustrates the observation for a given strength of the magnetic field.

When we plot our observations for different magnetic fields, keeping the storage time constant and calibrating the trapping voltage in percentages of V_{max} we find that the instabilities occur at the same positions. These positions are given by a simple relation between the motional frequencies of the electrons:

$$n_z\omega_c + n_m\omega_m = \omega_c \quad (1)$$

n_z, n_m are integers.

This relation can be understood in analogy to similar observations in a Paul trap [4,5]: When the trap potential contains multipole components in addition to the ideal quadrupole part it can be described by a series expansion:

$$\Phi(r, \theta, \varphi) = V \sum_{n=0}^{\infty} C_{2n} (r/d)^{2n} P_{2n}(\cos\theta), \quad (2)$$

where P_{2n} are the Legendre polynomials and C_{2n} are constants. It has been shown for Paul traps [6] that for a potential with nonvanishing coefficients C_{2n} the ion motion becomes unstable for operating conditions which fulfill the relation

$$n_r\omega_r + n_z\omega_z = \Omega \quad (3)$$

where ω_r and ω_z are the radial and axial oscillation frequencies of the ion motion and Ω the driving frequency of the trapping potential. When we consider an electron orbiting in a constant magnetic field of a Penning trap with the cyclotron frequency ω_c the constant inhomogeneous electric trapping field acts as a time varying electric field in the rest frame of the electron. Thus the cyclotron frequency replaces the driving frequency in eqn. (3). The axial frequency remains unchanged and the radial frequency is replaced by the magnetron frequency yielding eqn. (1). Fig. 4 shows that the observed instabilities can be well assigned to those operating points as predicted by eqn. (1).

Conclusions

We have observed the simultaneous appearance of individual (non-collective) and center-of-mass (collective) resonances in the excitation of the axial oscillation of a stored electron cloud in a Penning trap. At operating point determined by a simple relation between the axial, magnetron and cyclotron oscillation frequencies of the electrons, the confinement becomes unstable. This is attributed to the existence of higher order components in the electric potential of the trap.

Acknowledgements

Our experiments were supported by the Deutsche Forschungsgemeinschaft. S.A. acknowledges support from the DST-DAAD Indo-German exchange Program

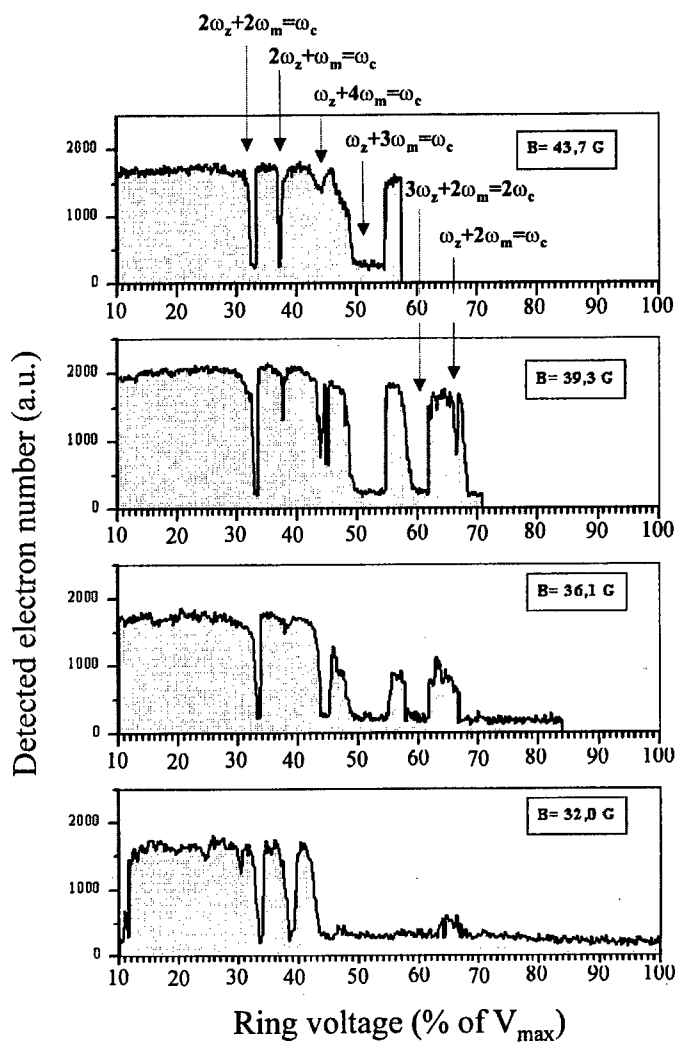


FIGURE 4. Observed instabilities of electron confinement and assignment to predictions following eqn (1)

References

1. Weimer, C.S., Bollinger, J.J., Moore, F.L., and Wineland, D.J., *Phys. Rev. A* **49**, 3842-3852 (1994)
2. Dubin, D.H., *Phys. Rev. Lett.* **66**, 2076-2079 (1991)
3. Alheit, R. et al., *Phys. Rev. A* **56**, 4023-4031 (1997)
4. Alheit, R., Henning, C., Morgenstern, R., Vedel, F. and Werth, G., *Appl. Phys. B* **61**, 277-283 (1995)
5. Alheit, R., Kleindam, S., Vedel, F., Vedel, M., and Werth, G., *Int. J. Mass Spectr. Ion Proc.* **154**, 155-169 (1996)
6. Wang, Y., Franzen, J., and Wanczek, K.P., *Int. J. Mass Spectr. Ion Proc.* **124**, 125-144 (1993)

SECTION 5
TRANSPORT

Amplitude Scaling of Asymmetry-Induced Transport

D.L. Eggleston and B. Carrillo

Occidental College, Physics Department, Los Angeles, CA 90041

Abstract. Our initial experiments on asymmetry-induced transport in non-neutral plasmas found the radial particle flux at small radii to be proportional to ϕ_a^2 , where ϕ_a is the applied asymmetry amplitude. Other researchers, however, using the global expansion rate as a measure of the transport, have observed a ϕ_a^1 scaling when the rigidity (the ratio of the axial bounce frequency to the azimuthal rotation frequency) is in the range one to ten. In an effort to resolve this discrepancy, we have extended our measurements to different radii and asymmetry frequencies. Although the results to date are generally in agreement with those previously reported (ϕ_a^2 scaling at low asymmetry amplitudes falling off to a weaker scaling at higher amplitudes), we have observed some cases where the low amplitude scaling is closer to ϕ_a^1 . Both the ϕ_a^2 and ϕ_a^1 cases, however, have rigidities less than ten. Instead, we find that the ϕ_a^1 cases are characterized by an induced flux that is comparable in magnitude but opposite in sign to the background flux. This suggests that the mixing of applied and background asymmetries plays an important role in determining the amplitude scaling of this transport.

INTRODUCTION

Malmberg-Penning traps are now being used in a variety of experiments. Understanding the properties of these traps is thus of considerable practical as well as fundamental interest. It has long been known that confinement in Malmberg-Penning traps is limited by the presence of asymmetric electric and magnetic fields. Early confinement studies found that at low neutral pressures the confinement time was much less than expected from transport due to electron-neutral collisions [1]. It was suggested that this anomalous transport was due to the presence of electric or magnetic fields that break the cylindrical symmetry of the trap. The presence of such asymmetries would produce a radial component to the $E \times B$ drift that would lead to particle loss to the walls of the trap. This suggestion led to a number of experiments [2-8] employing *applied* asymmetries in order to study the transport in a controlled manner. Most of the experiments have used electric asymmetries since these are easily applied and manipulated using the sector wall portions of the confinement region of the trap.

A basic issue of asymmetry-induced transport is the scaling of the transport with asymmetry amplitude. Current theory [9] predicts two transport regimes depending on the amplitude of the asymmetry in the plasma ϕ . For smaller amplitudes (the plateau regime), the radial flux is proportional to the square of the asymmetry potential ϕ^2 . For larger amplitudes (the banana regime), the flux scales like the square root of the asymmetry potential $\phi^{1/2}$.

Experiments on amplitude scaling have used a variety of measures to characterize the transport and have applied the asymmetries in different ways. Notte and Fajans [3] applied a switched DC voltage to a 50 degree wall patch in the central part of the confinement region. Following earlier work, they measured the time τ_m for the central density to decrease by one-half and found that this confinement time scaled like ϕ_a^{-m} with $1.7 < m < 2.1$. This scaling roughly agrees with plateau-regime scaling, although the voltages used in this experiment (up to 40 volts) would seem to be much too high to satisfy the plateau regime requirement.

More recently, Kriesel and Driscoll [6-8] have employed switched DC voltages applied at the end of the plasma column to study this transport over a wide range of parameters. For most of these experiments they used the rate of change of the mean-square-radius $\Delta\nu$ (with the background rate subtracted off) to characterize the transport. They found two transport regimes determined by the experimental value of the rigidity, which is the ratio of the axial bounce frequency to the azimuthal rotation frequency. When the rigidity was between one and ten, the expansion rate $\Delta\nu$ scaled like ϕ_a^1 , whereas higher values of rigidity gave a ϕ_a^2 scaling.

Our earlier studies [5] in a modified trap (described below) found that the time rate of change of the plasma density dn/dt (measured at one radius) scaled like $\phi_a^{2.1}$ for small asymmetry amplitude and like $\phi_a^{1.3}$ for larger amplitudes. The radial flux Γ was found to have a similar scaling. The rigidity for these measurements was small (approximately 0.2), and our ϕ_a^2 scaling thus seemed to contradict the result of Kriesel and Driscoll. The expansion rate $\Delta\nu$, however, is related to a radial integral [7] of the particle flux Γ , so the contradiction could not be established by measurements of Γ at a single radius. We have thus expanded our range of measurements to resolve this issue. Although the results are generally in agreement with those previously reported, we have observed some cases where the low amplitude scaling is closer to ϕ_a^1 . Both the ϕ_a^2 and ϕ_a^1 cases, however, have rigidities less than ten. Instead, we find that the ϕ_a^1 cases are characterized by an induced flux that is comparable in magnitude but opposite in sign to the background flux.

EXPERIMENTAL RESULTS

Our experiments are performed in the modified Malmberg-Penning trap shown in Figure 1. The usual plasma column is replaced by a biased wire running along the axis of the trap. Electrons injected into this device have the same dynamical motions as those in a normal non-neutral plasma (i.e. axial bounce and azimuthal drift motions), but collective contributions to the asymmetry potential are largely

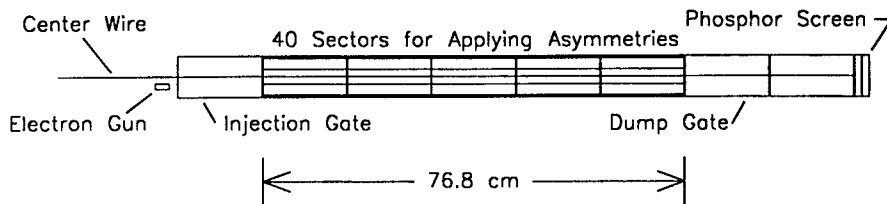


FIGURE 1. Schematic of the Occidental Trap. The plasma is replaced by a biased wire that maintains the basic dynamical motions of the injected electrons. Forty wall sectors allow for the application of asymmetries consisting of essentially one Fourier mode.

eliminated since the lower density (10^5 cm^{-3}) and higher temperature (4 eV) of the electrons give a Debye length larger than the trap radius. The asymmetry potential within the confinement region is thus essentially the vacuum potential and we need not be concerned with plasma modifications of the asymmetry potential. Despite these changes in the plasma parameters, the confinement time scaling with no applied asymmetries [10] shows the same $(L/B)^2$ dependence found in higher density experiments [11,12], thus supporting the notion that the asymmetry-induced transport is a single particle effect.

For the current experiments, forty wall sectors are employed to produce the applied asymmetry. By judiciously selecting the voltage applied to each sector we can produce an asymmetry consisting of essentially a single Fourier mode, thus eliminating the sum over modes in the transport theory [9] and making for a simpler comparison between theory and experiment. We use AC voltages at a variable frequency f since this gives us an additional experimental parameter that can be varied independently of other quantities. Electrons injected into the trap are quickly dispersed into an annular distribution [13]. At the end of an experimental cycle the electrons are dumped onto a phosphor screen and the resulting image is digitized with a cooled CCD camera. A radial cut through this image gives the axially-integrated density profile $n(r, t)$ of the electrons. For this study it is then useful to numerically integrate the density profile to obtain the quantity $g(r, t)$:

$$g(r, t) = -\frac{1}{r} \int_0^r r dr \cdot n(r, t)$$

The time derivative of $g(r, t)$ then gives the radial particle flux $\Gamma(r, t) = dg/dt$.

Figure 2 shows a typical set of data. The quantity $g(r, t)$ is plotted vs time for various asymmetry amplitudes. A line is then fit to the initial slope of these curves to obtain the radial flux. Note that, at the higher amplitudes and later times, the slope changes as the initial plasma is modified by the transport. Plotting the data in this way allows us to note and avoid these saturated cases. Also note that the flux is not zero for zero applied asymmetry, i.e. there is a nonzero background flux Γ_0 . Finally, note that because we have an annular plasma both positive and negative fluxes are observed.

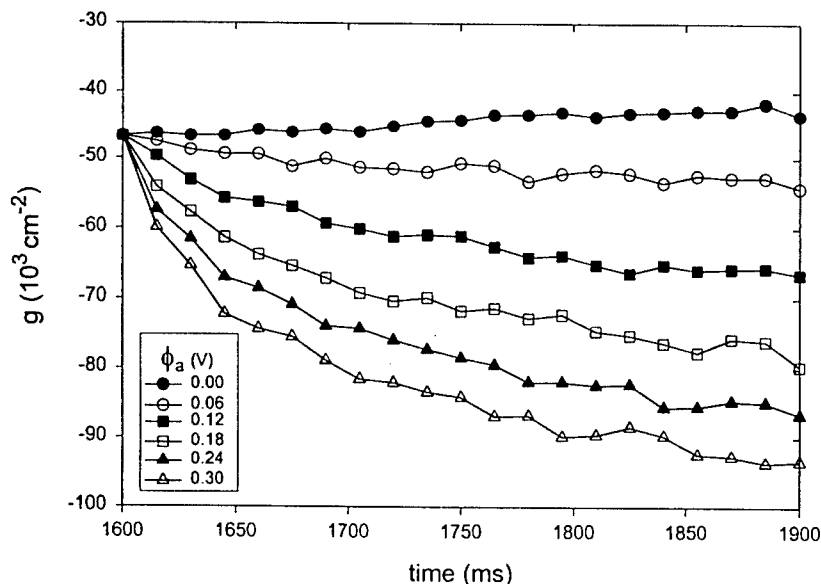


FIGURE 2. A typical data set showing the computed quantity $g(r, t)$ versus time with asymmetry amplitude as a parameter. The slope of these curves gives the radial flux $\Gamma = dg/dt$.

Figure 3 shows the magnitude of the net flux $\Delta\Gamma = |\Gamma_{induced} - \Gamma_0|$ vs asymmetry amplitude with radial position as a parameter. The experimental conditions are similar to those of reference [5], figure 3 (center wire bias = -80V, $B = 365G$, $f = 1MHz$). The log-log plot allows us to determine the scaling exponent m , where $\Delta\Gamma \propto \phi_a^m$. Typical error bars are shown, and lines of slope one and two are drawn for comparison to the data. The results are similar to those reported in reference [5]: the net flux scales like ϕ_a^2 for low amplitude asymmetries, in agreement with plateau-regime theory. At higher amplitudes, the scaling exponent falls off to a smaller value in the range 0.5 to 1.4. This may indicate a transition to banana-regime scaling, but the data is not sufficient to support this conclusion. Note that there is no dramatic dependence of m on radius, so if we were to calculate the expansion rate $\Delta\nu$ as in reference [8] the low amplitude scaling would still be ϕ_a^2 .

Further exploration of our parameter space has found some cases showing scaling closer to ϕ_a^1 and some of these cases are shown in Figure 4. For these parameters (as above except $f = 0.35MHz$), the ϕ_a^1 cases occur at smaller radii while ϕ_a^2 cases occur at larger radii, so, again, a calculation of expansion rate would not yield a ϕ_a^1 scaling.

Under what conditions do we obtain fluxes with a ϕ_a^1 scaling? In Figure 5 we plot the scaling exponent m versus the rigidity for the cases we have considered. Note that all these cases have rigidity less than ten (the borderline value for the Kriesel/Driscoll regimes), and, more importantly, that the same value of rigidity

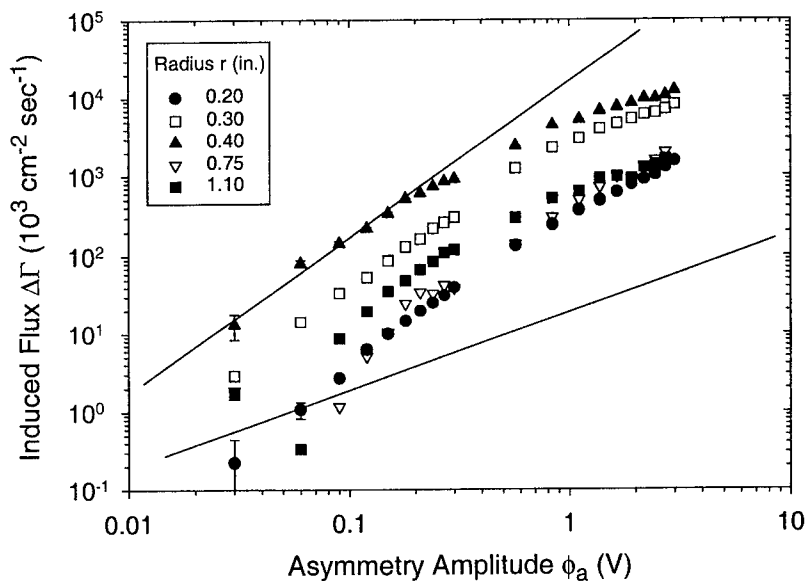


FIGURE 3. Log-log plot of the net asymmetry-induced flux $\Delta\Gamma$ vs. the applied asymmetry amplitude at the wall ϕ_a . The asymmetry frequency f is 1MHz. Lines of slope one and two are shown for comparison. For the cases shown the low amplitude scaling is close to ϕ_a^2 .

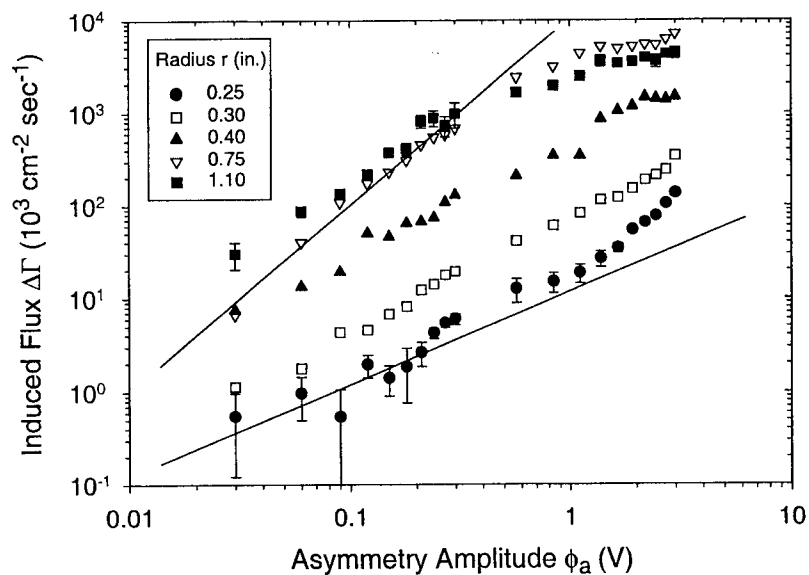


FIGURE 4. Log-log plot of $\Delta\Gamma$ vs. ϕ_a for $f = 0.35\text{MHz}$. For the lower radii the scaling exponent is close to one.

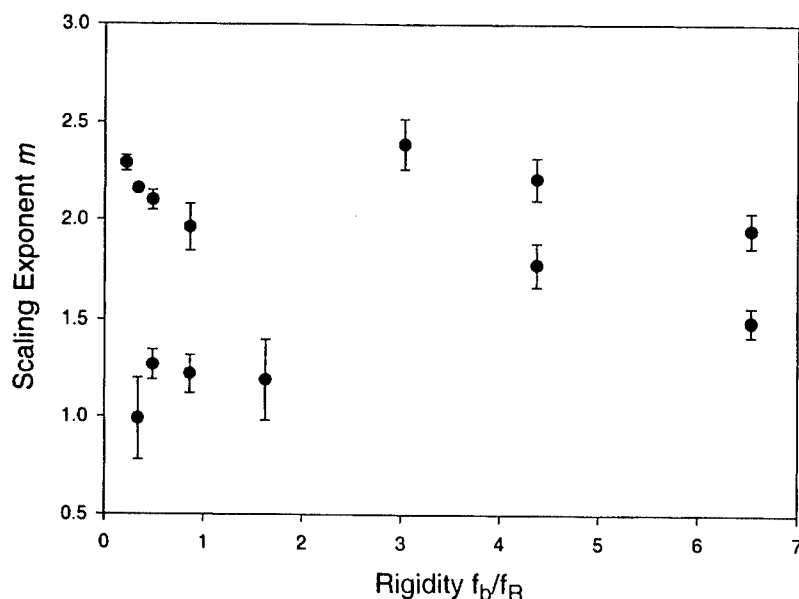


FIGURE 5. Scaling exponent m vs. rigidity. No correlation is observed with this parameter.

gives both $m \approx 1$ and $m \approx 2$ cases. Thus, in our experiment the scaling exponent is not correlated with rigidity.

We have tried to find correlation with other parameters as well. Since our experiments use a nonzero asymmetry frequency f , it might make sense that the rigidity should be modified from f_b/f_R to $f_b/(f - f_R)$ since presumably this ratio measures rigidity relative to the asymmetry. A plot of the data, however, shows no correlation of the scaling exponent with this modified rigidity either. Other quantities that fail to correlate with m include $f - f_R$, $(f - f_R)/f_R$, Γ_0 , and $\Gamma_{induced}$.

A re-examination of the original data for the $m = 1$ cases shows typical g vs t plots like the one shown in Figure 6. For these cases, the background flux is comparable in magnitude to the induced flux. Following this clue, we have plotted in Figure 7 the scaling exponent vs the ratio of the background flux to the induced flux at a typical asymmetry value of 0.3V. The correlation here is good, with $m = 2$ cases corresponding to smaller values of $\Gamma_0/\Gamma_{0.3V}$ and the $m = 1$ cases corresponding to larger negative values.

DISCUSSION

The fact that our $m = 1$ cases occur when the background flux is comparable in magnitude to the induced flux suggests a simple mixing of applied and background asymmetries. Suppose that the true flux scaling is $\Gamma \propto \phi_a^2$ and that when both

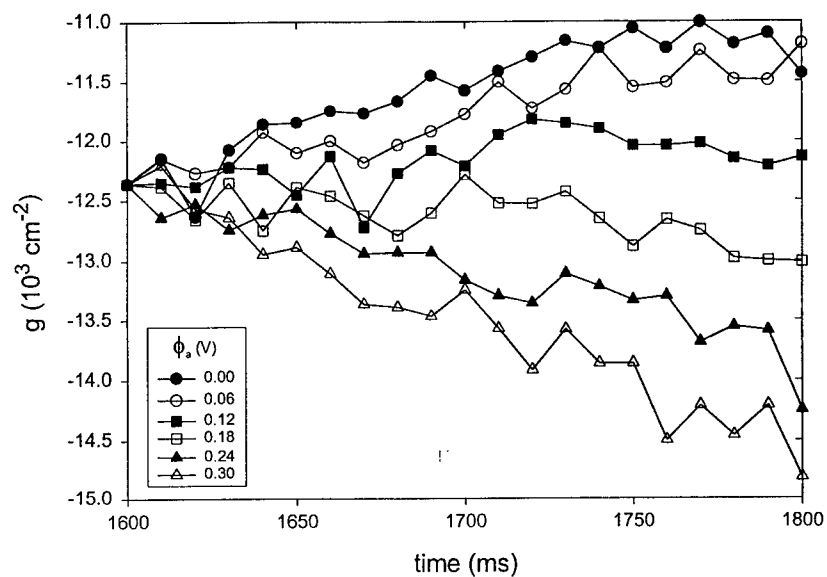


FIGURE 6. Typical g vs. t data for cases yielding a scaling exponent near one.

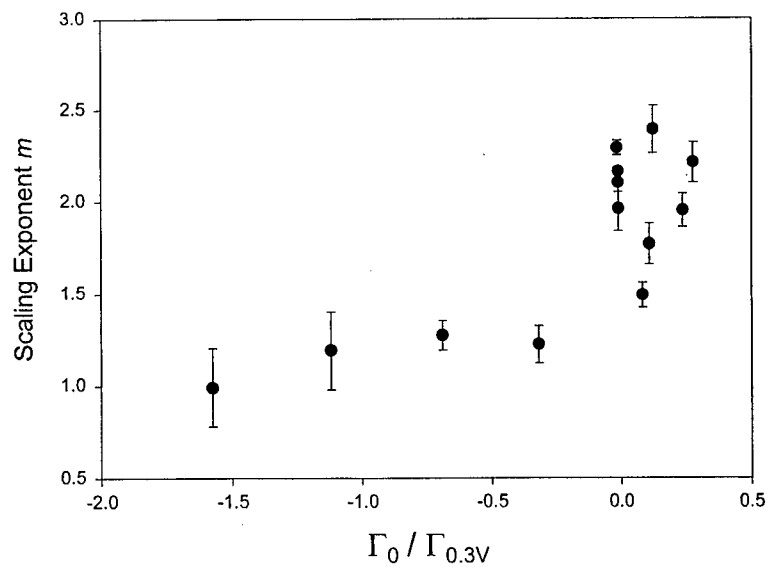


FIGURE 7. The scaling exponent shows a correlation with the ratio of the background flux Γ_0 to a typical induced flux $\Gamma_{0.3V}$

a background asymmetry ϕ_0 and an applied asymmetry ϕ_a are present they add directly. The total asymmetry squared is then $\phi_a^2 + 2\phi_a\phi_0 + \phi_0^2$ and if $\phi_a \ll \phi_0$, we obtain $\Gamma - \Gamma_0 \propto \phi_a$. Such a model, however, is not consistent with the details of the experimental data or with the theory. At least one experimental case where the flux scales like ϕ_a^1 occurs in the middle of our plasma with ϕ_a^2 cases at smaller and larger radii. The above model would then require a background asymmetry that is peaked in the middle of the plasma and it is hard to imagine how such an asymmetry could be produced. This direct addition model is also inconsistent with the theory, which says the flux is given by a sum of terms, one for each Fourier mode produced by the asymmetries. In our case, the background asymmetry is static (i.e. zero frequency) while the applied asymmetry has a nonzero frequency. These will necessarily give different Fourier modes that should not add directly. It would seem that the explanation for our observed correlation must be at a deeper level than simple addition of asymmetry potentials.

It is interesting to ask whether the Kriesel/Driscoll results can be explained in terms of our findings. From the data in reference [7], it appears that the ϕ_a^1 scaling does occur for cases where the induced transport is comparable to the background transport. The ϕ_a^2 cases are harder to judge because the background was so small it was declared to be zero. Although this would fit into our scheme (i.e. $\Gamma_0/\Gamma_{\text{induced}}$ would be zero), a more careful measurement would be required to settle this question.

It has been suggested [14] that the ϕ_a^1 scaling is due to the large size of the asymmetries employed in some experiments. In these cases the small-perturbation assumption of the quasi-linear theory is violated. If the applied asymmetry is large enough ($e\phi \gg kT$), particles will be excluded from (or pulled into) the vicinity of the biased wall sector. The perturbation of the distribution function δf would thus be large and saturated (i.e. no longer dependent on the perturbed potential in the plasma $\delta\phi$). Since the transport goes like the product $\delta f \delta\phi$ the dependence would be linear in the asymmetry amplitude. While this model might explain some experimental results (for example, the fall-off of our scaling exponent with asymmetry amplitude), it does not seem consistent with the bulk of the data, either in our experiments or those of others. For example, when we observe ϕ_a^1 scaling, it is observed even at very low asymmetry amplitudes. In contrast, Notte and Fajans observed ϕ_a^2 scaling even at extremely high asymmetry potentials. It is also not understood why this model should depend on rigidity, so it cannot explain the two scaling regimes observed by Kriesel and Driscoll.

CONCLUSION

We find that in most cases the asymmetry-induced transport in our experiment produces a net radial flux that scales like the square of the applied asymmetry amplitude for small asymmetries and falls off to a weaker dependence ($m = 0.5 - 1.4$) for larger amplitudes. We have found some cases that give a low-amplitude

scaling exponent closer to one, and these cases occur when the induced flux is comparable in magnitude but opposite in sign to the background flux. We do not yet understand the reason for this correlation.

ACKNOWLEDGMENTS

This work was supported by U.S. Department of Energy grant DE-FG03-98ER54457. Summer stipend for B.C. was provided by NSF-CAMP.

REFERENCES

1. J. H. Malmberg and C. F. Driscoll, *Phys. Rev. Lett.* **44**, 654 (1980).
2. D. L. Eggleston, T. M. O'Neil, and J. H. Malmberg, *Phys. Rev. Lett.* **53**, 982 (1984).
3. J. Notte and J. Fajans, *Phys. Plasmas* **1**, 1123 (1994).
4. X.-P. Huang *et al.*, *Phys. Rev. Lett.* **78**, 875 (1997).
5. D.L. Eggleston, in *Non-Neutral Plasma Physics III*, edited by John J. Bollinger *et al.*, AIP Conference Proceedings 498, 1999, pp. 241-249.
6. Jason M. Kriesel and C. Fred Driscoll, *op. cit.*, pp. 256-265.
7. J. M. Kriesel, Ph.D. thesis, University of California San Diego, 1999.
8. J. M. Kriesel and C. F. Driscoll, *Phys. Rev. Lett.* **85**, 2510 (2000).
9. D. L. Eggleston and T. M. O'Neil, *Phys. Plasmas* **6**, 2699 (1999).
10. D. L. Eggleston, *Phys. Plasmas* **4**, 1196 (1997).
11. C. F. Driscoll and J. H. Malmberg, *Phys. Rev. Lett.* **50**, 167 (1983).
12. C. F. Driscoll, K. S. Fine, and J. H. Malmberg, *Phys. Fluids* **29**, 2015 (1986).
13. D. L. Eggleston, *Phys. Plasmas* **1**, 3850 (1994).
14. T. M. O'Neil, private conversation, 2001.

Quadrupole Induced Resonant Particle Transport in a Pure Electron Plasma

E. P. Gilson* and J. Fajans†

*Plasma Physics Laboratory, Princeton University, Princeton, New Jersey, 08543

†Department of Physics, University of California, Berkeley, California, 94720

Abstract. We performed experiments that explore the effects of a quadrupole magnetic field on a pure electron plasma confined in a Malmberg-Penning trap. This work is important both as an example of resonant particle transport and for antihydrogen (\bar{H}). The \bar{H} experiments plan to use magnetic quadrupole neutral atom traps to confine \bar{H} atoms created in double-well positron/antiproton Malmberg-Penning traps. Our results show that a quadrupole field of only 0.020 G/cm can cause significant transport when applied to a 1 cm radius plasma confined by an axial field of 100 G. Our model describes the shape of the plasma and shows that resonant electrons follow trajectories that take them on large radial excursions, leading to enhanced transport. If the electrons are off resonance, then diffusion will not be greatly enhanced. The measured diffusion scales like the square of the quadrupole field strength, inversely like the square of the axial magnetic field and, below resonance, like the square of the $\mathbf{E} \times \mathbf{B}$ rotation frequency. The location of the resonance in parameter space scales accordingly as we vary the length and temperature of the plasma. However, the temperature used in fitting the data differs from the independently measured temperature by a factor of four, suggesting that our description of the effect as purely diffusive is not correct.

INTRODUCTION

Antihydrogen (\bar{H}) experiments at CERN by the ATHENA [1] and ATRAP [2] collaborations need to trap antihydrogen, antiprotons and electrons in the same place. However, neutral atom traps with magnetic field gradients may not be compatible with Malmberg-Penning traps because magnetic field gradients break the cylindrical symmetry of Malmberg-Penning traps, degrading their confinement properties. This asymmetry induced transport may prevent the use of Malmberg-Penning traps in \bar{H} experiments. Beyond its immediate importance to \bar{H} research, this phenomenon is also of interest in the general plasma community. It is relevant both in the study of resonant particle transport in Malmberg-Penning traps [3, 4, 5, 6, 7, 8] and in tandem mirror machines [9, 10, 11, 12, 13].

We have applied an axially invariant, transverse, quadrupole magnetic field to a pure electron plasma confined in a Malmberg-Penning trap and observed its effects on the shape of the plasma and on transport. We find that the shape of the plasma follows the surface of a magnetic flux tube if the bulk rotation of the plasma is slow compared to the axial bounce time of the electrons. The plasma shape is cylindrical if the bulk rotation of the plasma is fast compared to the axial bounce time. Measurements of the radial transport show a strong resonant behavior that is not in complete agreement with our model of the effect, but is consistent with many of the predicted scalings. We expect that

this transport will make it difficult to confine antiprotons and positrons long enough to create \bar{H} atoms.

EXPERIMENT

We apply a transverse, axially invariant, quadrupole magnetic field to a Malmberg-Penning trap using two different sets of coils. We can apply a transverse quadrupole field at any angle, θ_0 , by adjusting the relative current in each coil. The total magnetic field is then

$$\mathbf{B} = B_z \hat{z} + \beta_1 (x\hat{x} - y\hat{y}) + \beta_2 (y\hat{x} + x\hat{y}), \quad (1)$$

where $\beta = \sqrt{\beta_1^2 + \beta_2^2}$ is the strength of the quadrupole field in G/cm and $\tan(2\theta_0) = \beta_1/\beta_2$. In our experiment, the axial field ranges from 40 – 1500 G, while $\beta \leq 1.0$ G/cm for the coils we constructed. Even though these quadrupole fields are weak compared to B_z at a typical plasma radius of 1 cm, we find that they produce strong transport. Figure 1 shows that a flux tube that is circular at $z = 0$ is elliptical at either end, but with the ellipses rotated by 90° with respect to one another.

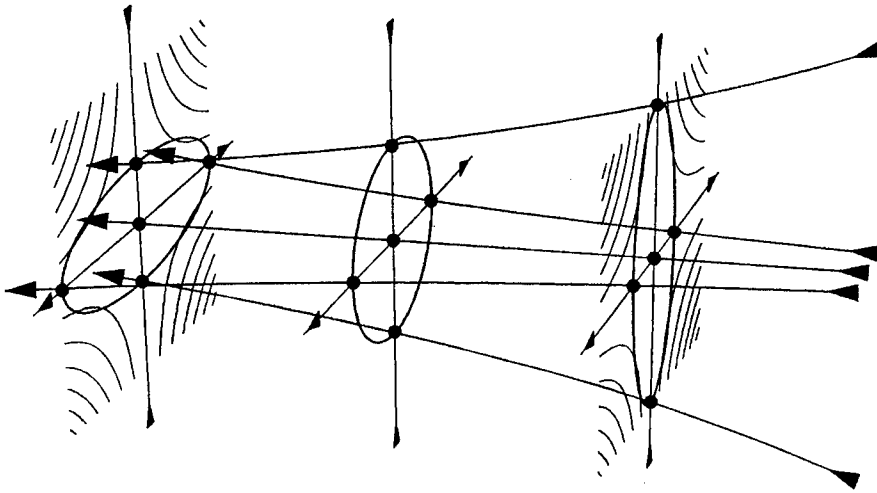


FIGURE 1. The lines with arrows show the field lines produced by adding a small, transverse, quadrupole field with $\theta_0 = 0$ to a strong axial field. A flux tube that is circular at $z = 0$ is elliptical as you move away from $z = 0$. The transverse cross sections show the field lines for the transverse quadrupole field alone.

The quadrupole field has four-fold symmetry and so there exists a resonance condition,

$$\omega_b = \frac{N\pi}{2}, \quad (2)$$

for which an electron rotates about the trap axis by $N\pi/2$ radians as it travels across the length of the trap. The rotation frequency about the trap axis is given by the $\mathbf{E} \times \mathbf{B}$ frequency, ω , and the bounce time is given by $t_b = L/v_z$. We show below that the $N = 1$

resonance is the most important resonance and so we say that if $\omega t_b \gg \pi/2$, the electron is above resonance and if $\omega t_b \ll \pi/2$, the electron is below resonance.

We measure the effects of the quadrupole field using both the wall of the trap and a phosphor coated glass substrate. We use the trap wall to detect the image charge on a confinement gate that is divided into four azimuthal sectors of 90° extent. This allows us to measure the quadrupole moment of the plasma at the axial location of the gate. The phosphor collects the dumped plasma, producing an image whose brightness is proportional to the z -integrated plasma density, $n(r, \theta)$. We extract radial transport quantities from these plasma images.

PLASMA SHAPE

The quadrupole field changes the trajectories of the electrons and thus changes the shape of the plasma. With transport present, the plasma's density and shape change with time. If the characteristic transport time is greater than the other time scales in the system, then we can imagine that the plasma exists in a quasi-equilibrium state at any instant in time. It is the shape of the quasi-equilibrium plasma that we are interested in.

Measures of the plasma's shape are the ellipticity, ϵ , and the orientation angle, θ_p . The ellipticity is the RMS length of the plasma cross section divided by the RMS width, and θ_p is the angle that the major axis of the ellipse makes with the x axis. We can measure ϵ and θ_p either directly from the plasma images or from the signal induced on the wall of the trap as measured by the four-sectored gate. The signal that we use to measure the quadrupole moment is the combination $(V_1 + V_3) - (V_2 + V_4) \propto \epsilon - 1$, where V_i are the voltages induced on the wall sectors.

We expect that when $\overline{\omega t_b} \ll 1$ (where the overbar denotes some suitable average value for the plasma as a whole), the electrons largely follow the field lines in Figure 1. The plasma has the shape of a magnetic flux tube. We expect that when $\overline{\omega t_b} \gg 1$, the radial oscillations average out and the plasma is cylindrical. The data in Figure 2, derived from plasma images, show that the plasma changes from elliptical at small $\overline{\omega t_b}$ (large B_z) to cylindrical at large $\overline{\omega t_b}$ (small B_z). At large B_z , $\theta_p \approx \theta_o = -45^\circ$ and gradually changes to $\theta_o + 90^\circ$ at small B_z . This rotation away from θ_o at low B_z is likely due to the effects of the radial component of the imaging field we use. At lower B_z , the imaging field creates a larger $\mathbf{E} \times \mathbf{B}$ rotation. Lastly, we see that by scaling out a factor of β , the data for various β/B_z coincide. Thus, $\epsilon - 1$ at a given B_z is proportional to β .

Using the wall sectors, we explore the z dependence of the below-resonance ($\overline{\omega t_b} \ll 1$) plasma shape. We measure ϵ at the end of several plasmas with different lengths at fixed β and we find that $\epsilon - 1$ at the end of the plasma is proportional to L . We measure ϵ at the middle, left end, and right end of a plasma and the data in Figure 3 demonstrate that $\epsilon - 1$ is equal and opposite at $\pm z_o$ and is 0 at $z = 0$. Further, $\epsilon - 1$ is also proportional to β . Unfortunately, it is not possible to verify the axial invariance of the above-resonance ($\overline{\omega t_b} \gg 1$) plasma in our experiment because we cannot simultaneously move the four-sectored gate around and be in the above-resonance regime.

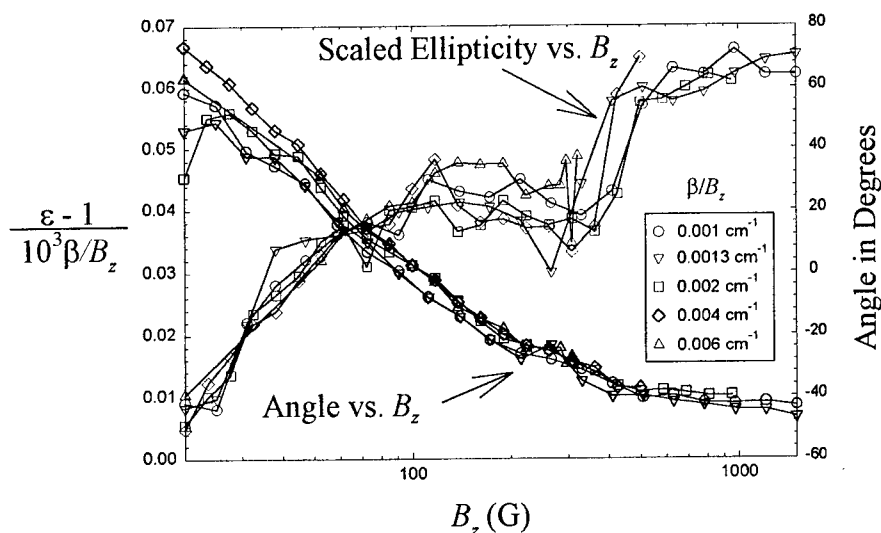


FIGURE 2. Varying B_z changes ω and thus $\overline{\omega t_b}$. $\epsilon(B_z) - 1$ approaches zero at low B_z (large ωt_b) and is proportional to β . $\theta_p \approx \theta_o = -45^\circ$ at large B_z and the change in $\theta_p(B_z)$ is likely due to imaging fields.

TRANSPORT

We envision the effect of the quadrupole field to be a diffusion process. The quadrupole field causes electrons to have trajectories with radial excursions. The smallest collisions, however, can knock electrons from one trajectory to another. We study transport using a simplified model in which we can find the electron trajectories analytically. We estimate the step size, λ , from these trajectories, postulate a collision frequency, ν , and form a diffusion coefficient, $D = \lambda^2 \nu f$, where f is the fraction of electrons participating in the diffusion.

We can guess what the trajectories look like by considering several examples. Figure 4 shows that a resonant electron ($\omega t_b = \pi/2$) that starts at 45° below the x axis is on field lines with radial components directed radially outwards as it bounces back and forth across the trap. This resonant electron moves to a larger radial position than it started at. For $N > 1$, N odd, there are the higher order resonances with smaller radial excursions. For N even, the radial displacements cancel. For other initial angles and other values of ωt_b , the trajectories may move inwards or oscillate radially.

If the guiding center of an electron follows a magnetic field line, then

$$\frac{dr}{dt} = \frac{\beta r v_z \cos[2\theta(t)]}{B_z}. \quad (3)$$

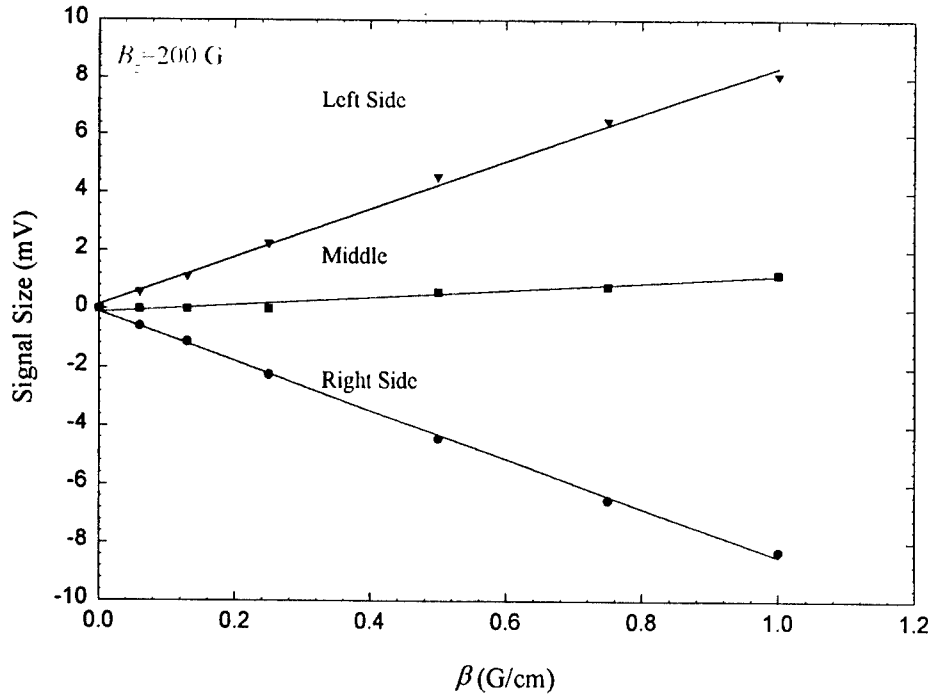


FIGURE 3. Placing the pickup gate at different axial positions ($z = 0, \pm 10.3$ cm) allows us to measure the relative ellipticity at the left, middle, and right of the plasma. We see that the signal in the center of the plasma vanishes, while the signal is equal and opposite at the ends of the plasma. The signal is proportional to β .

Because frequent collisions will disturb the electrons before they can go very far, we estimate the step size to be $\lambda = r(v^{-1}) - r_0$.

$$\lambda \approx r_0 \left(\frac{4\omega L\beta}{B_z N^2 \pi^2 v} \right), \quad (4)$$

where we have assumed that $\theta(t) = \omega t - \pi/4$ and that we can replace v_z with $2\omega L/N\pi$ by virtue of the resonance condition in Eq. (2).

Since electrons that are not exactly resonant also contribute to the transport, we must calculate the width of the resonance. For a given v_z , there is a resonant rotation frequency ω_R and we define the width of the resonance, $\Delta\omega$, through the relationship, $\omega = \omega_R + \Delta\omega$. To determine $\Delta\omega$, we note that the solution of Eq. (3) depends on $\Delta\omega$ through its dependence on $\theta(t) = \omega t + \theta_0 = (\omega_R + \Delta\omega)t + \theta_0$. Since the solution to Eq. (3) is an oscillatory function, we choose $\Delta\omega$ so that $t = v^{-1}$ corresponds to the first maximum of $r(t)$. This is equivalent to requiring that the extra angle of rotation, $\Delta\phi = \Delta\omega/v$, before a collision should be no greater than $\pi/4$.

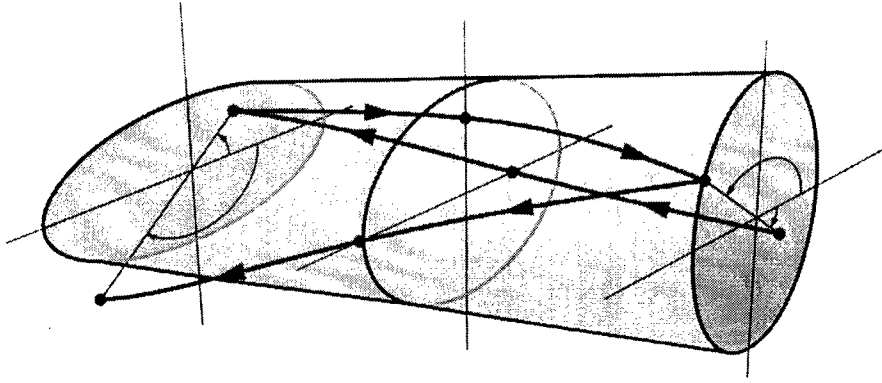


FIGURE 4. An electron that begins 45° below the x axis and rotates by 90° as it travels the length of the trap is resonant and moves ever outwards.

We construct the diffusion coefficient by writing $f = \sqrt{m/2\pi kT} \exp(-v_z^2/2v_{th}^2) \Delta v_z$, where $v_{th} = \sqrt{kT/m}$. Since the resonant electron has $\omega = (N\pi/2)(v_z/L)$, we can write $\Delta\omega/\omega = \Delta v_z/v_z$, or $\Delta v_z = Lv/2N$. Putting this all together gives

$$D_N = r_o^2 \frac{8\omega^2 L^3 \beta^2}{B_z^2 N^5 \pi^4} \sqrt{\frac{m}{2\pi kT}} \exp\left(-\frac{\omega^2}{2\omega_{th}^2}\right), \quad (5)$$

where $\omega_{th} \equiv N\pi v_{th}/2L$. Summing over odd N gives the total diffusion. However, the factor of N^{-5} implies that the diffusion is dominated by the $N = 1$ resonance.

We may describe the resonant behavior of $D_N(\omega)$ qualitatively. Above resonance, the plasma is rotating relatively quickly, and so for an electron to be resonant it must have a relatively large v_z . But the Maxwellian distribution ensures that there are few electrons moving very fast and so the diffusion is suppressed. Below resonance, there are plenty of resonant electrons in the thermal distribution, but now the step size is small and again, diffusion is suppressed.

The scaling of D with β^2 and the cancellation of the collision frequency, ν , are typical of diffusion in the so-called "plateau" regime. $D_N(\omega)$ has a maximum, D_{max} , at $\omega_{res} = \sqrt{2}\omega_{th}$. Therefore, D_{max} scales like $\omega^2 \exp(-\omega^2/2\omega_{th}^2)|_{\omega_{res}} \approx \omega_{th}^2$. This makes the overall L scaling of $D_{max} L^3 \omega_{th}^2 \propto L$, and the overall kT scaling $\omega_{th}^2/\sqrt{kT} \propto \sqrt{kT}$.

When $\omega \ll \omega_{th}$ (below resonance), the exponential term is close to unity and can be ignored. In this regime, $D \propto (\beta r_o \omega/B_z)^2 L^3$. Since $\omega \propto 1/B_z$, D scales like L^3/B_z^4 , in contrast to the usual L^2/B_z^2 that is attributed to resonant particle transport [4]. But, if β/B_z is constant, as would be the case if the quadrupole field perturbation came from asymmetries in the solenoidal magnet, the scaling is L^3/B_z^2 .

To measure D from $n(r, t)$, we manipulate the diffusion equation to give,

$$D = \frac{dN/dt}{2\pi r_o dn/dr|_{r=r_o}}, \quad (6)$$

where $N(t) = \int_0^{r_o} n(r,t) 2\pi r dr$. We measure the slope dn/dr from a single image with $n(r) = \frac{1}{2\pi} \int_0^{2\pi} n(r,\theta) d\theta$. The θ -averaging is acceptable because the quadrupole fields used for transport measurements are small enough that the plasma shape is cylindrical, even for the below-resonance plasmas. We image plasmas held for different times to measure the time dependence of $n(r,t)$. We choose a radius, r_o , calculate $N(t)$ and compute dN/dt . The choice of t is arbitrary since we do not expect transport to have an explicit time dependence and we choose t by some auxiliary condition, for example to have $\omega(r_o)$ be constant across a data set.

We measure $D(\beta_1, \beta_2)$ for many ω , B_z , L , and kT . Figure 5 shows a typical plot of D versus the transverse quadrupole field. We find that the minimum diffusion does not occur at zero perturbation. This is evidence that we are correcting for naturally occurring field errors by applying a quadrupole field. The surfaces $D(\beta_1, \beta_2)$ allow us to verify the β^2 scaling predicted by the model. We find that, over parameters available to us ranging from $\omega = 8.0 \times 10^5 \text{ rad s}^{-1}$ to $3.0 \times 10^6 \text{ rad s}^{-1}$, D scales like β^2 .

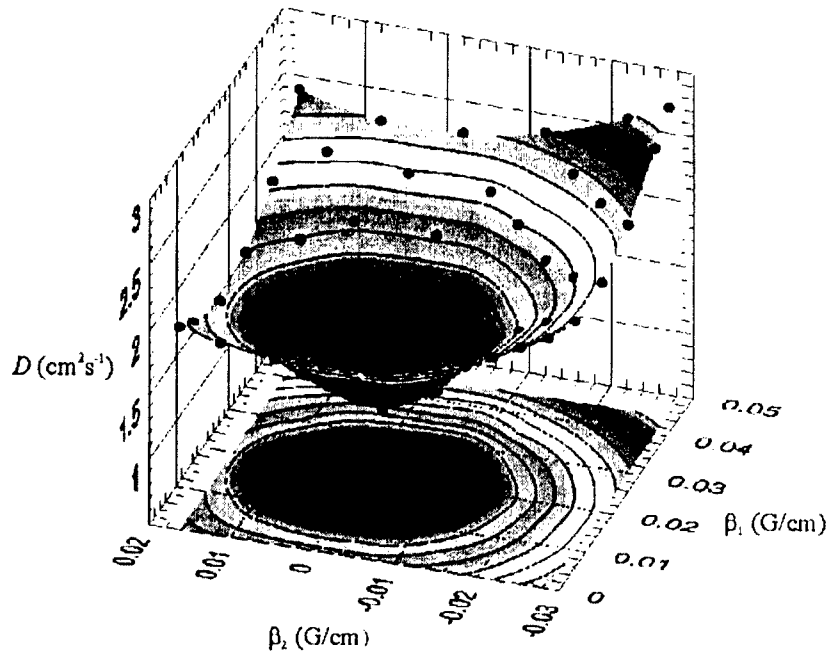


FIGURE 5. Diffusion from the application of a quadrupole field. This data is taken at $B_z = 100 \text{ G}$, $r_o = 0.95 \text{ cm}$, and $\omega = 2.0 \times 10^6 \text{ rad s}^{-1}$. We choose values of β_1 and β_2 in a checkerboard pattern and the data (solid dots) show that there is an optimal quadrupole field and that diffusion increases away from this optimal value.

We investigate the ω dependence of the phenomenon by measuring the average D at a distance of $\beta = 0.020 \text{ G/cm}$ from the minimum of the $D(\beta_1, \beta_2)$ surface. This averaging over θ_o dominates statistical uncertainty in D of approximately 7%. Figure 6 shows $DB_z^2(\omega)$ for several B_z , $L = 28 \text{ cm}$, $r_o = 0.95 \text{ cm}$, and $kT = 1.6 \text{ eV}$. The data show that the quadrupole field enhances diffusion resonantly in ω . As ω increases from 10^5 rad s^{-1} ,

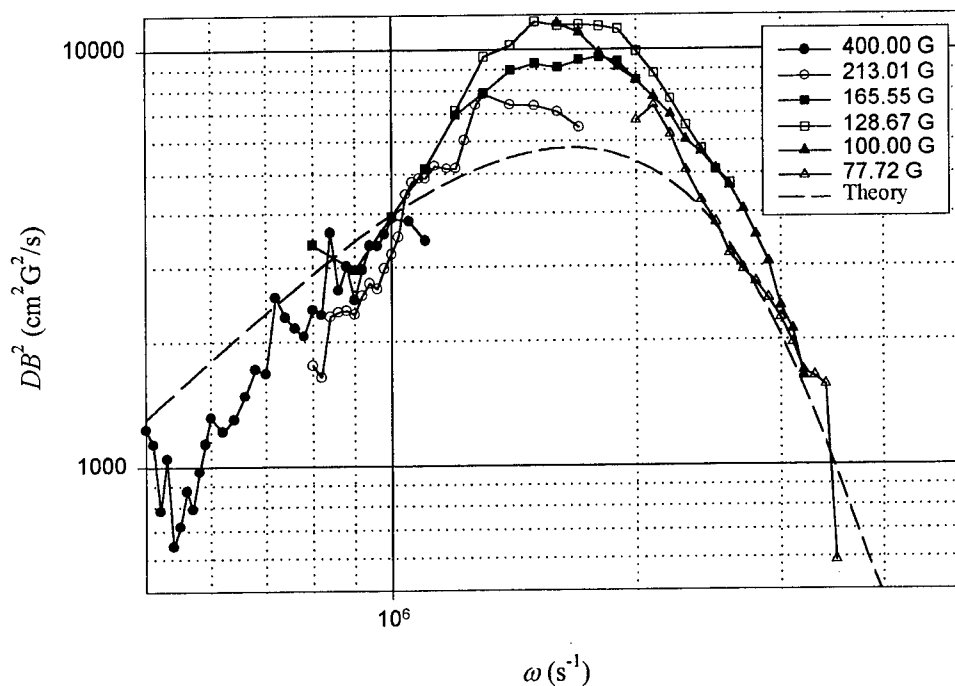


FIGURE 6. DB_z^2 shows a strong resonance in ω . There is an explicit B_z^{-2} dependence and for small ω the diffusion scales like ω^2 . The theory fit agrees best with the data if we use a multiplicative factor of 0.3 and an artificially low temperature of 0.34 eV. The independently measured temperature is 1.6 eV.

the diffusion grows. But above $\omega \approx 2 \times 10^6 \text{ rad s}^{-1}$ the diffusion decreases again. We observe that there is an explicit B_z^{-2} scaling, since the data for various B_z in Figure 6 overlap. Our formula for D scales like ω^2 at small ω and a least squares fit to the data with $\omega < 1.3 \times 10^6 \text{ rad s}^{-1}$ gives an exponent of 2.05 ± 0.09 .

To be a bounce resonant effect, the peak in ω should shift as we vary L and kT . We repeat the measurements of D as a function of ω as in Figure 6 for plasmas with smaller L . Figure 7 shows that the peak moves to larger ω as L decreases, although the exact dependence on L is difficult to obtain from these data. We find that D_{max} decreases as L decreases. To test the temperature dependence, we heated the plasma for 1 ms by applying a noise signal to the wall of the trap after injecting the plasma. Although the resonance moves to larger ω , we observe that D_{max} decreases as kT increases. Our model predicts that D_{max} should increase as kT increases.

Figure 6 includes a curve representing our model with terms up to $N = 10$. The theory curve shows moderate agreement with the data if we use an overall multiplicative factor of about 0.3, and set kT to be 0.34 eV. A multiplicative factor of order unity might be expected given the rough nature of our calculation. However, independent measurements of kT give $kT = 1.6 \text{ eV}$ and this discrepancy is more serious and remains unexplained.

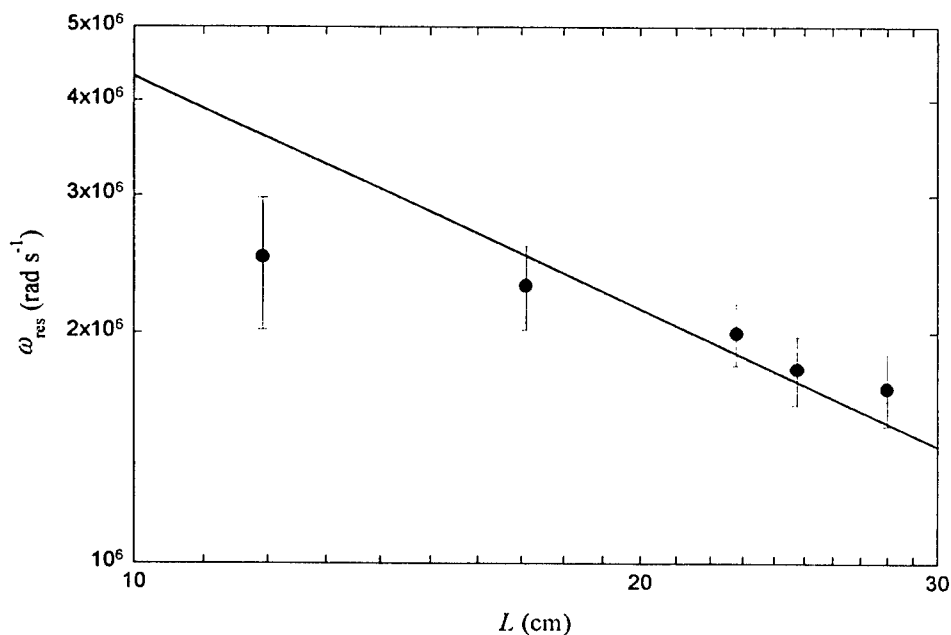


FIGURE 7. The value of ω_{res} decreases as L increases. Excluding the shortest plasma, the data are marginally consistent with a line with slope -1 (solid line).

We find that it is difficult to test the radial dependence of the diffusion. Clean measurements are possible only in a small neighborhood near $r \approx 1$ cm. This trouble comes from the noise in the measurements of dn/dr at extreme radii and the measurements of dN/dt at large radii. At large and small radii, $dn/dr \approx 0$ and is therefore susceptible to statistical and numerical noise. At large radii, $dN/dt \approx 0$. In either case, $D \approx (dN/dt)/(dn/dr)$ is poorly behaved.

CONCLUSIONS

We have applied an axially invariant, transverse quadrupole field to a pure electron plasma confined in a Malmberg-Penning trap and observed the effects the quadrupole field has on the shape of the plasma and on transport within the plasma. The quadrupole field distorts the parallel magnetic field lines into flux tubes with elliptical cross sections. Whether the $\mathbf{E} \times \mathbf{B}$ rotation is faster or slower than the bounce time determines the properties of both the plasma shape and the amount of transport.

If the plasma rotates quickly, we observe the plasma to smear out into a cylinder. If the plasma rotates slowly, we observe that the plasma has the shape of a flux tube, circular in the center and elliptical on each end but with the ellipses rotated by 90° with respect to

one another. The ellipticity is proportional to both the quadrupole field and to the length of the plasma.

The transport created in the plasma by the quadrupole field exhibits a strong resonance in ω . We observe diffusion coefficients of order $1 \text{ cm}^2/\text{s}$ at resonance for a perturbation of only 0.020 G/cm . This is a weak field compared to those necessary for the confinement of antihydrogen. The field is comparable to what one expects as possible natural quadrupole errors in Malmberg-Penning traps.

By changing the length and temperature of the plasma and observing that the resonant frequency changes accordingly, we have demonstrated that the transport is a bounce resonant effect. The β , ω , B_z and L scalings are consistent with our simple model of the effect, while the kT scaling of our model does not agree with the data. The r dependence proves difficult to test. This disagreement between our model and our experimental observations suggest that perhaps nonresonant particles make a significant contribution to the transport, or perhaps that the transport is not purely diffusive. A model that directly predicts the radial particle flux may better describe our experimental results.

A quadrupole field greatly enhances radial transport in a Malmberg-Penning trap when the plasma is in resonance with the field. Therefore, the ATHENA and ATRAP collaborations will have difficulty using quadrupole fields in conjunction with Malmberg-Penning traps to form antihydrogen. Typical experimental parameters will be $B_z = 2 \text{ T}$, $n = 10^8 \text{ cm}^{-3}$ and $T = 4 \text{ K}$ [14]. We estimate that $\omega t_b \approx 0.6$, placing them near the resonance. Even if operating off resonance, the magnitude of the quadrupole field will be strong enough to severely limit confinement times.

ACKNOWLEDGMENTS

This work was supported by the Office of Naval Research and by the Los Alamos National Laboratory.

REFERENCES

1. Holzscheiter, M. H., et al., *Hyperfine Interactions*, **109**, 1997 (1997).
2. Gabrielse, G., and S.L. Rolston, L. H., *Phys. Lett. A*, **129**, 38 (1988).
3. Keinigs, R., *Phys. Fluids*, **24**, 1447 (1981).
4. Driscoll, C. F., and Malmberg, J. H., *Phys. Rev. Lett.*, **50**, 167 (1983).
5. Keinigs, R., *Phys. Fluids*, **27**, 206 (1984).
6. Malmberg, J. H., Driscoll, C. F., Beck, B., Eggleston, D. L., Fajans, J., Fine, K., Huang, X. P., and Hyatt, A. W., "Experiments with pure electron plasmas", in *Nonneutral Plasma Physics*, edited by C. Roberson and C. Driscoll, American Institute of Physics, New York, 1988, vol. AIP 175, p. 28.
7. Eggleston, D. L., and O'Neil, T. M., *Phys. Plasmas*, **6**, 2699 (1999).
8. Kriesel, J., and Driscoll, C., *Phys. Rev. Lett.*, **85**, 2510 (2000).
9. Ryutov, D., and Stupakov, G., *Sov. J. Plasma Phys.*, **4**, 278 (1978).
10. Ryutov, D., and Stupakov, G., *Sov. Phys. Dokl.*, **23**, 412 (1978).
11. Cohen, R., *Nuclear Fusion*, **19**, 1579 (1979).
12. Cohen, R., Nevins, W., and Stupakov, G., *Nuclear Fusion*, **23**, 611 (1982).
13. Chirikov, B., *Sov. J. Plasma Phys.*, **5**, 492 (1979).
14. Gabrielse, G. (1999), private communication.

Shear Reduction of 2D Point Vortex Diffusion

Daniel H. E. Dubin and C. Fred Driscoll

Physics Department, University of California at San Diego, La Jolla CA 92093-0319 USA

Abstract.

Theory and simulations establish the effects of shear on the collisional diffusion of a 2D point vortex gas. For finite shear, the diffusion is considerably smaller than previous zero-shear theories predict, scaling inversely with the shear. Surprisingly, changing the sign of the applied shear changes the diffusion by an order of magnitude.

INTRODUCTION

The collisional diffusion of point vortices in 2 dimensions is a classic problem in non-equilibrium statistical physics, with relevance to turbulence and transport in Euler fluids and neutral plasmas, rotating superfluid helium, the behavior of Type-II superconductors, and dislocations in solids. Here, we analyze the effects of an overall shear in the fluid flow on the diffusion of the point vortices, finding that the diffusion is strongly reduced.

Early work on diffusion of 2D point vortices focused on the case of a quiescent, homogeneous shear-free gas [1, 2]. When the vortices are distributed randomly, representing high-temperature thermal fluctuations, Taylor and McNamara showed that the diffusion coefficient (for diffusion in 1 direction) has the following simple form:

$$D^{TM} = \frac{1}{8\pi} \sqrt{\sum_{\alpha} \frac{N_{\alpha} \gamma_{\alpha}^2}{\pi}} \quad (1)$$

where N_{α} is the number of point vortices of type α , each with circulation γ_{α} . The diffusion coefficient is not an intensive quantity because the diffusion process is dominated by large "Dawson-Okuda vortices" whose size is of order the system size [2]. However, for finite temperature, these authors all suggested that Debye shielding limits the maximal vortex size to approximately the Debye length λ_D .

Here, we show that in the presence of applied shear, the Dawson-Okuda vortices are disrupted and the diffusive transport is greatly reduced [3, 4] compared to Eq. (1). This result may be relevant to current experiments and theories in fusion plasmas, which also observe reduced transport in the presence of shear [5]. In such plasmas, the fluctuations are unstable and turbulent; and so the transport is difficult to determine theoretically. However, in a stable gas of point vortices, statistical theory determines the transport explicitly. Our theory may therefore be considered as a simple paradigm for the shear-reduction of transport seen in more complex turbulent systems.

The theory also applies directly to experiments on pure ion plasmas or pure electron plasmas confined in cylindrical columns by a uniform magnetic field $B\hat{z}$ [6, 7]. In some parameter regimes, the individual particles act as z -averaged "rods" of charge that $\mathbf{E} \times \mathbf{B}$ drift in (r, θ) due to the electric fields of all the other rods. Under such conditions, these $\mathbf{E} \times \mathbf{B}$ drifts are the main cause of collisional diffusion, dominating over the classical diffusion [8] caused by velocity-scattering collisions. Using laser "tagging" techniques, ion experiments have directly measured the test-particle diffusion, and show quantitative correspondence with the present theory [9]. Electron experiments in the 2D regime have established that the bulk viscosity is strongly enhanced as the shear is reduced [10], but the theory of this (closely related) transport coefficient is not yet complete.

The $\mathbf{E} \times \mathbf{B}$ dynamics of a collection of charged rods is isomorphic to a gas of point vortices [11]: each rod, with charge $\bar{q} \equiv q/L_p$ per unit length, is equivalent to a point vortex with circulation

$$\gamma \equiv -\bar{q} (4\pi c/B). \quad (2)$$

Furthermore, such plasmas rotate with a rotation frequency $\omega(r) = v_\theta(r)/r$ that may have substantial radial shear, depending on the particle density $n(r)$. We characterize the shear by a local shear rate

$$S(r) \equiv r d\omega/dr. \quad (3)$$

For comparison to electron columns of length L_p , we take $\bar{q} = -e/L_p$ and $B > 0$, giving $\gamma > 0$ and $\omega > 0$. For comparison to ion experiments, the sense of rotation remains positive if one takes $\bar{q} = +e/L_p$ and $B < 0$, giving $\gamma > 0$ and $\omega > 0$. We also note that the 2D areal density $n[\text{cm}^{-2}]$ considered here is related to the 3D density $n^{3D}[\text{cm}^{-3}]$ as $n = L_p n^{3D}$.

THEORY

In order to evaluate the diffusion in such a sheared plasma/point vortex gas, we consider N identical vortices confined to a cylindrical patch of radius R , with *uniform* 2D areal density

$$n = N/\pi R^2, \quad (4)$$

giving an average interparticle spacing $a \equiv (\pi n)^{-1/2}$. To this vortex patch an *external* sheared rotation $\omega(r)$ is applied, with uniform shear rate S .

In physical systems, the rotation $\omega(r)$ would follow from $n(r)$ through Poisson's equation. For this system a dimensionless measure of the shear rate can be defined as

$$s = 2S/n\gamma, \quad (5)$$

which is the shear rate compared to local vorticity density. For a uniform patch, one sees that $n\gamma = 2\omega$, but for non-uniform $n(r)$ the local vorticity density $n\gamma$ is distinct from the local rotation rate ω .

In this analysis, we focus on the case of moderate to strong dimensionless shear, i.e. $|s| > 1$, although comparison to experiments suggests that the results are valid for

$|s| < 1$. We derive the results of our statistical theory for self diffusion, and compare these results to molecular dynamics and vortex-in-cell simulations. For comparison to ion experiments, see the paper by Anderegg *et al.* in this Proceedings [9]. We find that the simulations agree with our theory provided that s is negative (i.e. negative shear, the usual circumstance in a stable pure electron plasma).

Surprisingly, however, when $s > 0$, the transport observed in the simulations is roughly an order of magnitude smaller than our theory predicts. We will discuss a qualitative explanation of the vortex trapping effects which cause the differences in diffusion, but at present no precise theory exists. We note that our point vortices (with $\gamma > 0$) are *prograde* for $s > 0$, and *retrograde* for the experimentally relevant case of $s < 0$. Similar trapping effects cause macroscopic prograde vortices to move up (or down) a background vorticity gradient at a rate substantially less than would a retrograde vortex [12]. The connection between the microscopic diffusion and macroscopic gradient-driven dynamics becomes more apparent when the present diffusion theory is generalized to two species: when one species represents macroscopic vortices with large circulation, a non-diffusive (indeed anti-diffusive) gradient-driven velocity is obtained [13].

The theory analyzes the collisions of vortices moving with a background sheared flow, as shown schematically in Fig. 1. We first describe theory for the diffusion that applies to the negative shear regime $s \lesssim -1$. In this case, two separate collisional processes are responsible for radial diffusion: small impact parameter collisions between vortices, described by a Boltzmann formalism, and large impact parameter collisions, described by a quasilinear formalism.

In Fig. 1a, the shaded region shows the range of possible streamlines (in the center-of-mass frame) for small impact parameter collisions. For example, vortex 1 may flow up and to the right and then back down because of a collision with vortex 2, which correspondingly flows down, to the left, and back up. These binary collisions cause a net radial displacement of each vortex, and a sequence of uncorrelated collisions gives diffusion. The unshaded region shows possible large impact parameter collisions, where the vortices merely move slightly in and back out while streaming past each other. In this case, simultaneous interaction with other distant vortices is required for radial displacement and diffusion.

For these collisions, small and large impact parameters mean initial radial displacements between vortices that are smaller or larger than a distance $2l$, where the "trapping distance" l is defined as

$$l \equiv \sqrt{-\gamma/4\pi S} = a/\sqrt{-2s}. \quad (6)$$

Note that for $s > 0$, the trapping distance is undefined, since the trapping extends to infinity in this simple model; and this will be seen to have a profound effect on the diffusion.

The streamlines show the trajectories of 2 identical vortices in the shear flow, at radial positions r_1 and r_2 . For simplicity, we take $|r_1 - r_2| \ll r_1$, and introduce local cartesian coordinates in a moving frame with an origin initially at $\mathbf{R}(0) = [\mathbf{r}_1(0) + \mathbf{r}_2(0)]/2$, and moving with the local fluid rotation velocity $\omega(R(0))$. The x axis of this frame corresponds to the radial direction, and the y axis corresponds to the direction of local

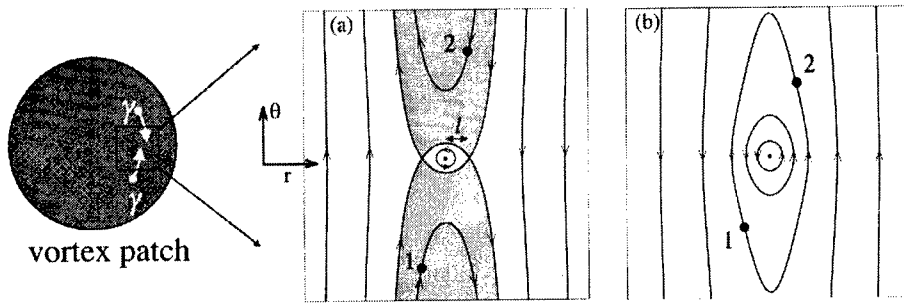


FIGURE 1. Collisional interaction of 2 point vortices, showing streamlines in the rotating frame for the interaction region for (a) $s < 0$, giving retrograde vortices; and (b) $s > 0$, giving prograde vortices.

flow (the θ -direction). In this coordinate frame, the vortices have positions $\Delta \mathbf{r} \equiv \mathbf{r} - \mathbf{R}$, where $\Delta \mathbf{r}_1 \equiv (x_1, y_1)$, and $\Delta \mathbf{r}_2 \equiv (x_2, y_2)$.

The 2-vortex interaction is described by the stream function

$$\psi(\Delta \mathbf{r}_1, \Delta \mathbf{r}_2) = \frac{S}{2}(x_1^2 + x_2^2) + \frac{\gamma}{4\pi} \ln[(x_1 - x_2)^2 + (y_1 - y_2)^2]. \quad (7)$$

Here the term proportional to the shear rate S is the stream function due to the shear flow, and the logarithmic term describes the vortex interaction. The motion of vortex 1 then follows from the Hamiltonian equations

$$\frac{dx_1}{dt} = -\frac{\partial \psi}{\partial y_1}, \quad \frac{dy_1}{dt} = \frac{\partial \psi}{\partial x_1}, \quad (8)$$

and similarly for vortex 2. Under this dynamics, ψ is a conserved quantity, and it is straightforward to show that $\Delta \mathbf{r}_1 + \Delta \mathbf{r}_2$ is also conserved, taking the value

$$\Delta \mathbf{r}_1 + \Delta \mathbf{r}_2 = 0. \quad (9)$$

Applying Eq. (9) to Eq. (7), ψ can be written as a function of the position of vortex 1 alone:

$$\psi(x_1, y_1) = S[x_1^2 - l^2 \ln[4(x_1^2 + y_1^2)]], \quad (10)$$

where the trapping distance l is given by Eq. (6). Contours of constant ψ are displayed in Fig. 1, with the origin $(x_1, y_1) = 0$ at the center of the figure.

For $s < 0$, vortices are retrograde (rotating against the shear), and they follow one of the symmetric pairs of trajectories shown in Fig. 1a. The vortex pairs always have reflection symmetry through the center of the figure, moving in opposite directions in this frame of reference. The separatrix in Fig. 1(a) has stagnation points at $x = \pm l, y = 0$, and using Eq. (10) this implies that the separatrix $x_s(y)$ is determined by

$$\begin{aligned} x_s^2 &= l^2(1 + \ln[(x_s^2 + y^2)/l^2]) \\ &\approx l^2(1 + \ln[y^2/l^2]), \end{aligned} \quad (11)$$

where the second line is correct for $y \gg l$.

Binary Boltzmann Collisions

Vortices that begin in the shaded region inside the separatrix take a radial step due to their interaction. For inter-particle spacing greater than the trapping length, i.e. $a > l$ and $|s| > 1$, an uncorrelated sequence of these small impact parameter collisions will occur, causing radial diffusion of the vortices.

This diffusion can be estimated as $v\Delta r^2$, where the radial step Δr is of order l , and the collision rate $v \sim n|S|l^2$ is the number of vortices per unit time carried by the shear flow into the shaded trapping region of a given vortex (Fig. 1a). This results in a diffusion coefficient $v\Delta r^2 \sim n|S|l^4 \sim \gamma/|s|$.

A rigorous Boltzmann calculation of the radial diffusion due to these small impact parameter collisions agrees with this estimate. To determine the diffusion coefficient D^B , we integrate over random steps due to a flux Γ_y of vortices carried by the shear flow:

$$\Gamma_y = n|S\rho|, \quad (12)$$

where n is the areal density (in cm^{-2}) and $\rho = x_2 - x_1$ is the x -displacement (impact parameter) between the vortices when the vortices are well-separated in y (i.e. before the collision begins, but after the previous collision with some other vortex has ended). Let us call this y -displacement y_0 . Then Fig. 1(a) shows that if $|\rho| \leq 2x_s(y_0)$, the two vortices will take a step in the x -direction of magnitude $|\rho|$ as they exchange x -positions in the collision.

The Boltzmann diffusion coefficient is therefore

$$D^B = \frac{1}{2} \int_{-2x_s(y_0)}^{2x_s(y_0)} d\rho \rho^2 \Gamma_y. \quad (13)$$

Using our previous expression for Γ_y , the integral can be performed yielding $D^B = 4n|S|x_s^4(y_0)$. Finally, Eq. (11) implies that $x_s(y_0)$ depends only logarithmically on y_0 , so an estimate for y_0 is sufficient. Therefore, for y_0 we use the mean y displacement between collision events (the mean free path), $y_0 \simeq 1/(4ln)$. Then the Boltzmann diffusion coefficient becomes

$$D^B = \frac{\gamma}{2\pi^2|s|} \ln^2 \left(\frac{e\pi^2 s^2}{4} \right), \quad (14)$$

where we have employed Eqs. (5), (6) and (11). The logarithm increases D_B over our previous estimate of $\gamma/|s|$ because the shaded region in Fig. 1(a) diverges logarithmically with increasing $|y|$, increasing both the size of the radial step Δr and the collision rate v .

Multiple Distant Collisions

However, the Boltzmann result for self-diffusion given by Eq. (14) neglects diffusion from large impact parameters. In the Boltzmann description, two vortices with a large

impact parameter (outside the shaded region) stream by one another and suffer no net change in radial position. Actually, large impact parameter collisions are not isolated events; many are occurring simultaneously, leading to random motion in the fluctuations.

An estimate of the diffusion from these distant collisions is easily obtained. For these collisions the step size is now smaller than before, because interacting vortices are farther apart. If the impact parameter between vortices is ρ , the radial step Δr is of order $\Delta t \gamma / \rho$, where Δt is the time over which the interaction takes place. For particles streaming along unperturbed circular orbits, $\Delta t \sim 1/|S|$, which implies a small step $\Delta r \sim l^2 / \rho$. There are many of these interactions per unit time; the collision rate is $\nu \sim n|S|\rho^2$, leading to a diffusion coefficient $\nu \Delta r^2 \sim n|S|l^4 \sim \gamma/|s|$, which is the same order as Eq. (14).

This diffusion from multiple distant collisions can be obtained more quantitatively from a quasilinear calculation [3] based on the Kubo formula

$$D^K = \int_0^\infty dt \langle \delta v_r(t) \delta v_r(0) \rangle. \quad (15)$$

Here $\delta v_r(t)$ is the radial velocity fluctuation of a test vortex at position (r, θ) due to $p = 1, \dots, N$ other vortices at positions (r_p, θ_p) , and $\langle \rangle$ denotes an ensemble average over a random distribution of the vortices within the vortex patch.

The velocity fluctuation is determined by a superposition of N flow fields [14],

$$\delta v_r(t) = -\frac{\gamma}{4\pi r} \sum_{p=1}^N \frac{\partial}{\partial \theta} \ln |\mathbf{r} - \mathbf{r}_p|^2, \quad (16)$$

easily written in terms of Fourier modes:

$$\delta v_r(t) = \frac{\gamma}{4\pi r} \sum_{p=1}^N \sum_{\substack{m=-\infty \\ m \neq 0}}^{\infty} \frac{im}{|m|} e^{im(\theta - \theta_p)} (r_{<}/r_{>})^{|m|}, \quad (17)$$

where $r_{<(>)}$ is the lesser (greater) of r and r_p . The time integral in the Kubo formula can then be done using integration along unperturbed orbits, assuming that each vortex merely rotates about the center of the vortex patch, i.e. $r_p = \text{const}$, $\theta_p(t) = \omega(r_p)t + \theta_{p0}$. The ensemble average can also be easily calculated using standard techniques for random distributions, converting $\langle \sum_p \sum_{\bar{p}} \rangle$ to $\sum_{\bar{p}} \delta_{p\bar{p}} \int r_p dr_p d\theta_{p0} n(r_p)$.

The result, after performing the θ_{p0} and t integrals, is

$$D^K = \frac{\gamma^2}{(4\pi r)^2} \sum_{\substack{m=-\infty \\ m \neq 0}}^{\infty} 2\pi^2 \int_0^\infty r_p dr_p n(r_p) \delta(m[\omega(r) - \omega(r_p)]) \left(\frac{r_{<}}{r_{>}} \right)^{2m}. \quad (18)$$

The δ -function, arising from the time integral over unperturbed orbits, implies that resonant interactions are the most important to the transport process. If we then assume that $\omega(r)$ is monotonic in r so that only $r = r_p$ contributes, the radial integral yields

$$D^K = \frac{n\gamma^2}{8r|\partial\omega/\partial r|} \sum_{\substack{m=-\infty \\ m \neq 0}}^{\infty} \frac{1}{|m|}. \quad (19)$$

Collision Logarithms

The divergent sum occurs because nearby vortices following unperturbed orbits take a long time to separate and therefore take a large radial step. However, the sum can be cut off by noting that there is a minimum separation d for which unperturbed orbits are a good approximation. Adding the cutoff to Eq. (19) implies

$$D^K = \frac{\gamma}{2|s|} \ln[r/d], \quad (20)$$

where we have used Eq. (5).

One possible estimate for d is the trapping distance l , since vortices separated by l do not follow unperturbed orbits. Another possibility is that vortices diffuse apart before they are carried away by the shear, and so cannot be treated with unperturbed orbit theory. For vortices separated in r by a distance δ , the time to shear apart a distance of order δ is given by $1/|S|$, and the time to diffusively separate by a distance δ is $\delta^2/4D^K$. Setting the two times equal gives the diffusion-limited minimum separation $\delta = [4D^K/|S|]^{1/2}$.

Accordingly, in Eq. (20) we take the maximum of our two estimates:

$$d = \text{Max}(\delta, l). \quad (21)$$

Note that Eqs. (5), (6) and (20) imply that $\delta/l = \sqrt{(8\pi/|s|) \ln[r/d]}$, so the shear required to make $\delta < l$ is rather large. In our simulations it will turn out that $\delta > l$, so we use $d = \delta$ in Eq. (20).

Finally, the total diffusion coefficient is the sum of the Boltzmann and Kubo diffusion from small and large impact parameter collisions:

$$D = D^B + D^K. \quad (22)$$

Of course, Eq. (22) is correct only when the shear is large enough so that $D < D^{TM}$, where D^{TM} is the zero-shear result given by Eq. (1). However, comparing Eqs. (1) and (22), we see that only a small shear, $s \sim O(1/N^{1/2})$, is required to meet this inequality. When $|s| \approx 1$, Boltzmann collisions no longer occur since $a < l$, so $D^B = 0$; but Eq. (20) for D^K still holds. This implies that Eq. (22) is valid when $D^K \lesssim D^{TM}$, or $|s| \gtrsim \ln[r/d] \sqrt{16\pi^3/N}$. In other words, small shears wipe out the large-scale Dawson-Okuda vortices responsible for the diffusion predicted by Eq. (1).

SIMULATIONS

We have tested this theory using numerical simulations of N identical point vortices, initially placed randomly inside a circular patch, with an applied uniform external shear rate S . We find that Eq. (22) works well for $s \lesssim -1$, but overestimates the diffusion for $s \gtrsim 1$.

As a check of the numerics, we employ two separate simulation techniques, a 2D molecular dynamics (MD) method for point vortices, and a 2D particle in cell (PIC)

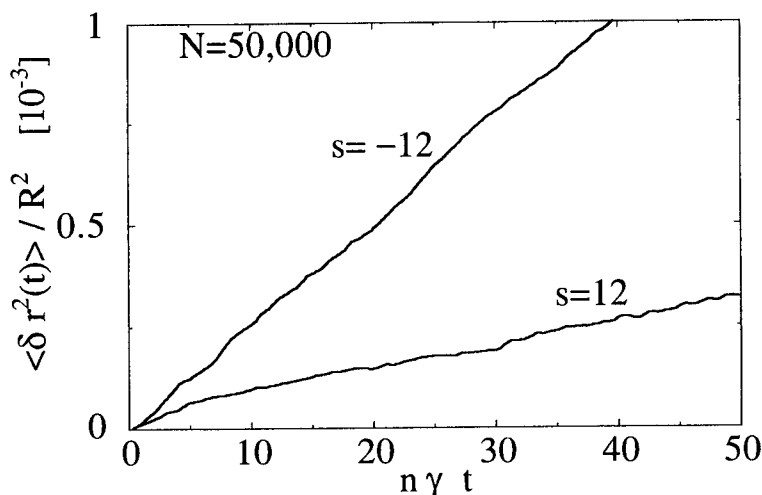


FIGURE 2. Mean square change in radial position of vortices vs. time, $\langle \delta r^2(t) \rangle$, for $N = 50,000$. Two shear rates are shown, $s = 12$ and $s = -12$.

simulation. The MD simulation is a standard N^2 code using the 4th order Runge-Kutta method. The PIC simulation has been described previously [12]. In the PIC simulation the diffusion coefficient is an increasing function of the number of grid points, but for sufficiently fine grid the diffusion is independent of the number of grid points to within our measurement error of about 30%. We use up to a 2048×2048 square grid in the largest PIC simulations. In both the PIC and MD codes, time steps are chosen to conserve energy at the 0.1% level or better over the course of the simulation, and angular momentum (mean square radius of the cylindrical patch) is typically conserved even more accurately. Also, the timestep was varied by factors of two in both codes, with no observable change in the diffusion.

In order to measure the diffusion coefficient, we chose as test particles all vortices in the band of radii from $0.43R$ to $0.57R$. For these vortices we followed the mean square change in radial position, $\langle \delta r^2(t) \rangle$, where for vortex i , $\delta r_i(t) = r_i(t) - r_i(0)$. (We also verified that $\langle \delta r(t) \rangle = 0$.)

Two examples with $N = 50,000$ are shown in Fig. 2, for the cases $s = \pm 12$. Here, the unexpectedly low diffusion for $s > 0$ is apparent. The diffusion coefficient is found from the equation $\langle \delta r^2(t) \rangle = 2Dt$. More precisely, we fit a straight line to the segment of the curve that has nearly constant slope, and we take D as half the slope of that line.

RESULTS

Figures 3, 4, and 5 summarize our results for the self-diffusion coefficient. Figure 3 displays the diffusion coefficient as a function of the particle number N for four different values of the shear parameter, $s = 0, -1.2, -12$, and $+12$. The first case corresponds to

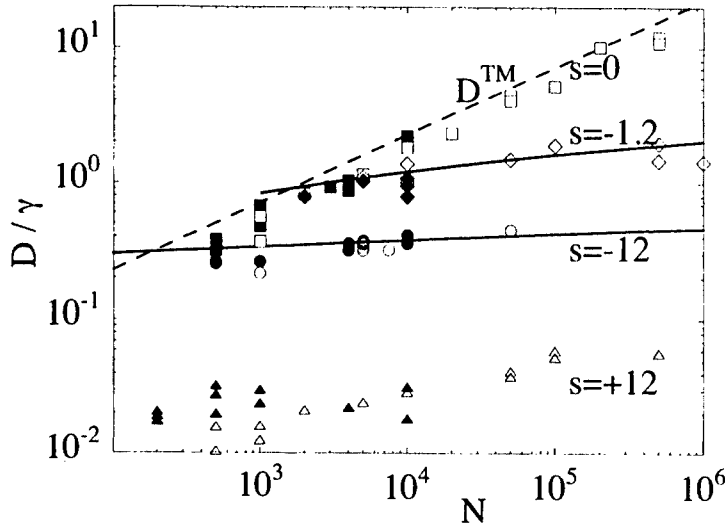


FIGURE 3. Self-diffusion coefficient vs. particle number N , for shear rates $s = 0, -1.2, -12$ and 12 . Solid points are from MD simulations, open points are from PIC simulations. The dashed line is Eq. (1). The solid lines are Eq. (22), evaluated at $s = -1.2$ and $s = -12$.

a shear free plasma, and can be seen to match the expected Taylor-McNamara scaling, Eq. (1), shown by the dashed line. The cases $s = -1.2$ and -12 correspond to moderate and strong negative shear. The measured diffusion matches Eq. (22) quite well. However, for $s = +12$ the diffusion is an order of magnitude smaller.

For perspective, we note that both the Taylor-McNamara diffusion and the collisional diffusion follow from the discreteness of the vorticity. If we let the discreteness go to zero by letting $N \rightarrow \infty$ at fixed total circulation, then the diffusion will *decrease* as N increases. This is shown in Fig. 4, where the diffusion is scaled as $D/N\gamma$; this scaling can also be written $D/(4\pi cQ/B)$, where $Q = Nq$ is the total charge in the 2D system. From the perspective of Fig. 4, the shear-free diffusion $D^{\text{TM}}/N\gamma$ decreases as $N^{-1/2}$, since the fluctuation-induced Taylor-McNamara vortices are weaker by $N^{1/2}$. On the other hand, for finite scaled shear s , the scaled diffusion $D/N\gamma$ decreases as N^{-1} since the collisionality is proportional to the discreteness.

In Fig. 5, the diffusion coefficient is shown as a function of shear for fixed particle number $N = 10^4$. The scaling with s matches Eq. (22) when $s < 0$. At large s , we obtain $D \propto 1/|s|$, although both Boltzmann and Kubo logarithms also introduce dependence on shear, which at low shear can be quite strong. Generally at low to moderate shear, the Kubo result dominates, but at low N or large shear the Boltzmann result dominates.

However, for $s > 0$ the vortices are prograde, and the simulations do not match Eq. (22): the measured diffusion is up to an order of magnitude less than the theory, depending on the shear rate. It is not surprising that the Boltzmann diffusion theory fails to work for this case; the Boltzmann picture of nearby particles reflecting off one

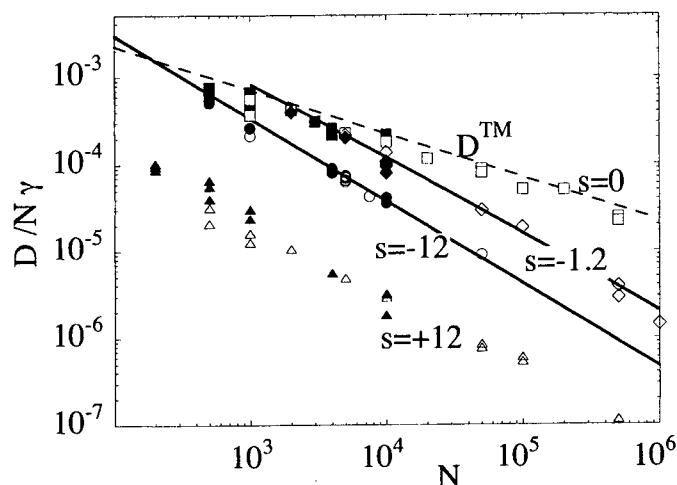


FIGURE 4. Same as Figure 3, except that the diffusion rates are scaled by the total circulation $N\gamma$. This figure shows that dividing a system with fixed circulation $N\gamma$ into more particles N (i.e. taking the "plasma limit") results in decreased collisional diffusion.

another is no longer correct. Two isolated vortices orbit around one another rather than suffer reflections, as shown in Fig. 1b. As a result, the measured $\langle \delta r^2(t) \rangle$ has a large slope at early times as vortices begin to rotate around one another, but then relaxes to a smaller slope as vortices return to their initial radii (see Fig. 2).

Figure 5 shows that even if one neglects Boltzmann diffusion, Kubo diffusion by itself also overestimates the $s > 0$ simulation results. We believe that fluctuations now consist of several self-trapped vortices following elliptical orbits similar to the streamlines of Fig. 1b. Vortices return to their initial radii several times, and net transport occurs only through the break-up of these fluctuations through interaction with other similar fluctuations. The Kubo theory fails because the unperturbed orbit approximation fails for such fluctuations. A proper transport theory must go beyond the unperturbed orbit approximation in this case; such a theory will be the subject of future work.

DISCUSSION

This purely 2-dimensional theory needs further development with regard to Debye shielding, multiple species, and trapping effects in collisions of prograde vortices. Moreover, comparison to real 3-dimensional systems requires consideration of end effects (perturbations to the 2D velocity due to end confinement fields) and an understanding of the transition from 3D collisional dynamics to 2D bounce-averaged dynamics.

Considerations of Debye shielding by both Taylor and McNamara [1] and Dawson and Okuda [2] lead to the conclusion that thermal fluctuations will cause eddies with a maximal size of about λ_D . The more difficult problem of evaluating the dynamics of shielding during 2D point vortex collisions in a sheared plasma has yet to be solved. Preliminary analysis suggests that the shear disrupts the shielding, and a nonshielded

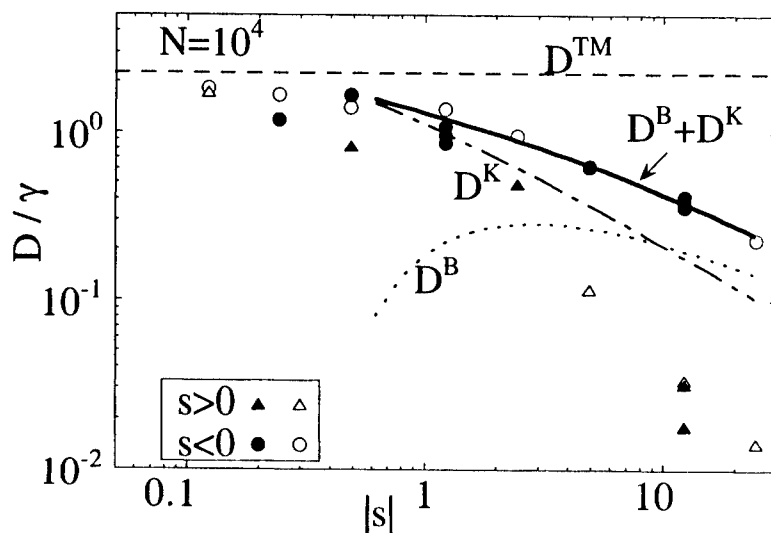


FIGURE 5. Self-diffusion coefficient vs. the shear rate s , for $N = 10,000$. Solid points are from MD simulations, open points are from PIC simulations. The dashed line is Eq. (1), and the solid line is Eq. (22). The dot-dashed line and the dotted line are the separate Kubo and Boltzmann contributions to the diffusion, Eqs. (20) and (14) respectively.

interaction may be a reasonable approximation. However, more work remains before this question can be answered definitively.

Extension of the present diffusion theory to multiple species is straightforward and is presently being developed [13]. Preliminary results show that there is a dissipative rearrangement of the vorticity of each species, and that species with higher circulation tend to concentrate in regions of higher total vorticity. This counter-intuitive, seemingly non-diffusive concentration effect is consistent with analyses [12] and experiments [15] which demonstrate that macroscopic vortices move *up* a background vorticity gradient. This effect is also consistent with the fundamental idea of an inverse cascade in 2D turbulence, whereby energy flows to large scales through the process of vortex merger [16].

Developing a consistent analysis of the trapping effects which occur with prograde vortices may represent the hardest of these 2D theory problems. In prograde shear, two like-sign point-vortices may be bound in compound "atoms" for arbitrarily long times; at present no theory can describe the effects of these bound states on diffusion. Similar bound states occur when one has both positive and negative vortices, as in neutral plasmas; then the problems include non-conservation of particle number and momentum, as well as infinite negative energies.

Perturbed 2D vortex velocities due to 3D end effects have been considered with regard to collisional viscosity [17, 18], and are presently being incorporated into diffusion theory [13]. Here, several effects may be important. The plasma (and charged rod) length L_p may vary with radial position. Moreover, the axial energy of the bounding particle

may affect the length of the bounce-averaged rod, and may also affect the $(r - \theta)$ motion of the rod. The lack of agreement between theory and experiments on 2D viscosity suggests that these effects are not yet adequately understood.

Finally, we note that experiments and theory are now developing the connections between 3-dimensional and 2-dimensional collisions in the presence of shear. Here, the controlling parameter seems to be the number of axial bounces which a particle makes before being sheared apart from neighboring particles, defined as $N_b \equiv (\bar{v}/2L_p)/r\omega'_E \equiv f_b/S$. The particle kinetic velocity \bar{v} does not appear in present theory of 2D $\mathbf{E} \times \mathbf{B}$ drift collisions of charged rods, but it does appear in the analogous 3D theory of "long-range" or " $\mathbf{E} \times \mathbf{B}$ drift" collisions between charged particles. Indeed, theory and experiments [9] show that diffusion in the 2D regime is enhanced over diffusion in the 3D regime by the factor N_b , specifically $D^{3D}/D^{2D} = 0.47N_b$. Moreover, experiments on viscosity in the 2D regime [10] show essentially the same enhancement.

Thus, from the 2D perspective of this paper, one would say that vortex diffusion is reduced by shear, because the shear separates distant vortices before the collision can be completed. From the 3D perspective, one would say that diffusion is enhanced when the shear is sufficiently small that particles can have multiple correlated collisions as they bounce axially. Expanding this perspective to include end effects for both viscosity and diffusion remains the challenge for future theory and experiments.

ACKNOWLEDGMENTS

This work was completed with the support of National Science Foundation grant PHY-9876999 and Office of Naval Research grant N00014-96-1-0239.

REFERENCES

1. J.B. Taylor and B. McNamara, *Phys. Fluids* **14**, 1492 (1971).
2. J.M. Dawson, H. Okuda and R.N. Carlile, *Phys. Rev. Lett.* **27**, 491 (1971); H. Okuda and J.M. Dawson, *Phys. Fluids* **16**, 408 (1973).
3. D.H.E. Dubin and D.Z. Jin, "2D Collisional Diffusion of Rods in a Magnetized Plasma with Finite $\mathbf{E} \times \mathbf{B}$ Shear," in *Non-Neutral Plasma Physics III*, AIP Conf. Proceedings 498 (American Institute of Physics, New York, 1999), p. 233.
4. D.H.E. Dubin and D.-Z. Jin, "Collisional Diffusion in a 2-dimensional Point Vortex Gas," *Phys. Lett. A* **284**, 112 (2001).
5. K.H. Burrell, *Phys. Plasmas* **4**, 1499 (1997); P.W. Terry, *Rev. Mod. Phys.* **72**, 109 (2000); H. Biglari *et al.*, *Phys. Fluids B* **2**, 1 (1990).
6. F. Anderegg *et al.*, "Test Particle Transport due to Long Range Interactions," *Phys. Rev. Lett.* **78**, 2128 (1997).
7. D.H.E. Dubin, "Test Particle Diffusion and the Failure of Integration along Unperturbed Orbits," *Phys. Rev. Lett.* **79**, 2678 (1997).
8. C.L. Longmire and M.N. Rosenbluth, *Phys. Rev.* **103**, 507 (1956).
9. F. Anderegg, C.F. Driscoll and D.H.E. Dubin, "Shear-Limited Test Particle Diffusion in 2-Dimensional Plasmas," this proceedings.
10. J.M. Kriesel and C.F. Driscoll, "Measurements of Viscosity in Pure-Electron Plasmas," *Phys. Rev. Lett.* **87**, 135003-1 (2001).
11. R.H. Levy, *Phys. Fluids* **8**, 1288 (1965); **11**, 920 (1968).

12. D.A. Schecter and D.H.E. Dubin, "Vortex motion driven by a background vorticity gradient," *Phys. Rev. Lett.* **83**, 2191 (1999); D.A. Schecter and D.H.E. Dubin, "Theory and Simulations of 2D Vortex Motion Driven by a Background Vorticity Gradient," *Phys. Fluids* **13**, 1704 (2001).
13. D.H.E. Dubin, to be published.
14. P.G. Saffman, *Vortex Dynamics* (Cambridge Univ. Press, 1992), p. 116.
15. A. Kabantsev, C.F. Driscoll, D.H.E. Dubin, and D.A. Schecter, "Experiments and Theory on 2D Electron Vortex Dynamics in Sheared Flows," *Proc. 11th Intl. Toki Conf. on Potential and Structure in Plasmas*, Nagoya, to appear (2001).
16. P.J. Kundu, *Fluid Mechanics* (Academic Press, San Diego, 1990).
17. D.H.E. Dubin and T.M. O'Neil, "Two-Dimensional Bounce-Averaged Collisional Particle Transport in a Single-Species Non-Neutral Plasma," *Phys. Plasmas* **5**, 1305 (1998).
18. D.H.E. Dubin, "Collisional Transport in Nonneutral Plasmas," *Phys. Plasma* **5**, 1688 (1998).

Shear-Limited Test Particle Diffusion in 2-Dimensional Plasmas

Francois Anderegg, C. Fred Driscoll, and Daniel H. E. Dubin

*Dept. of Physics and Institute for Pure and Applied Physical Sciences,
University of California at San Diego, La Jolla CA 92093-0319 USA*

Abstract.

Measurements of test-particle diffusion in pure ion plasmas show 2D enhancements over the 3D rates, limited by shear in the plasma rotation $\omega_E(r)$. The diffusion is due to "long-range" ion-ion collisions in the quiescent, steady-state Mg^+ plasma. For short plasma length L_p and low shear $S \equiv r \partial\omega_E/\partial r$, thermal ions bounce axially many times before shear separates them in θ , so the ions move in (r, θ) as bounce averaged "rods" of charge (i.e. 2D point vortices). Experimentally, we vary the number of bounces over the range $0.2 \leq N_b \leq 10,000$. For long plasmas with $N_b \leq 1$, we observe diffusion in quantitative agreement with the 3D theory of long-range $\mathbf{E} \times \mathbf{B}$ drift collisions. For shorter plasmas or lower shear, with $N_b > 1$, we measure diffusion rates enhanced by up to $100\times$. For exceedingly small shear, i.e. $N_b \geq 1000$, we observe diffusion rates consistent with the Taylor-McNamara estimates for a shear-free thermal plasma. Overall, the data shows fair agreement with Dubin's new theory of 2D diffusion in shear, which predicts an enhancement of $D^{2D}/D^{3D} \approx N_b$ up to the Taylor-McNamara limit.

In turbulent fusion plasmas, experiments [1] have observed reduced transport in the presence of sheared flow, but the transport is difficult to calculate theoretically [2]. Here we report measurements of test particle diffusion in a quiescent magnesium ion plasma for direct comparison to a new theory of collisional diffusion in a 2D point-vortex gas with background shear. The ions are kept in steady state with a rotating wall [3] drive superimposed on the confining potential at one end. We observe that for short plasmas (2D) the diffusion rate is up to 100 times larger than for long plasmas (3D). This can be easily understood if we introduce N_b , the number of bounces that a particle makes, in the rotating frame, before being sheared apart (in the θ direction) from a neighboring particle.

We find that N_b controls the 2D transport enhancement over the 3D case. Stated differently, if N_b is large, neighboring particles interact for longer periods of time, leading to more transport. For large N_b the ions can be described as bounce averaged "rods" of charge (which theorists refer to as "2D point vortices"). In the absence of shear, the transport is limited by the Taylor-McNamara paradigm [4], where thermal fluctuations excite large scale, but short lived, convective cells. In the presence of shear, new quantitative theoretical work [5] predicts that the diffusion coefficient is inversely proportional to the shear.

In our experiment, the transport is controlled by the bounce averaged shear, i.e. the average shear that a particle experiences averaged over one bounce along a magnetic field line of the trap. To experimentally determine the $\mathbf{E} \times \mathbf{B}$ shear, we use a laser induced

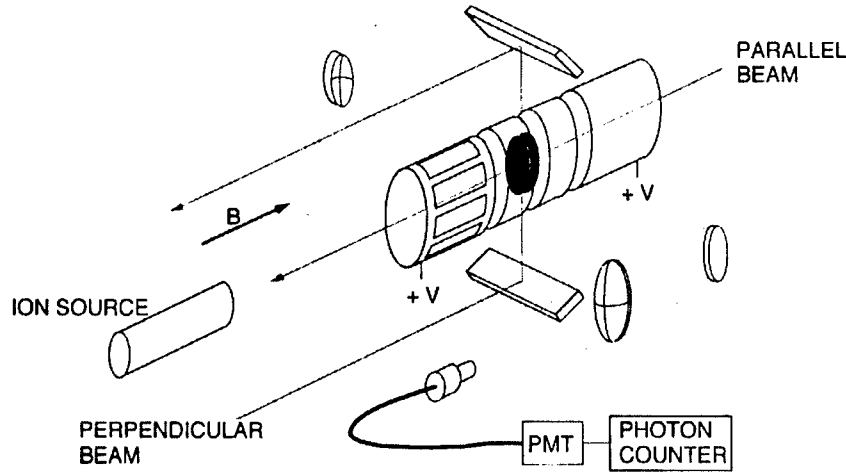


FIGURE 1. Schematic diagram of the cylindrical trap.

fluorescence (LIF) diagnostic, giving the density $n(r)$, the temperature $T(r)$ and the fluid rotation velocity $v_{\text{tot}}(r)$ in the θ direction using a perpendicular laser beam as shown in Fig. 1. All the LIF measurements are made in the central plane ($z = 0$) of the plasma. For the present work, we have about 10^8 magnesium ions, with a plasma length $L_p \simeq 1$ cm, and a plasma radius $r_p \simeq 2$ cm; the temperature is controlled from 0.1 eV to 4 eV; and the magnetic field is $B = 3$ Tesla. More details about the apparatus and diagnostic can be found in Ref. [6].

The density, temperature and rotation profiles are shown in Fig. 2 for a plasma with small shear (a) and for a plasma with large shear (b). We fit the rotation profile v_{tot} to a smooth third order polynomial. We numerically solve Poisson's equation using the smooth fit to v_{tot} and $T(r)$ with the wall potentials as boundary conditions; and obtain $n(r, z)$ and $\phi(r, z)$. From this solution, one obtains the shear rate $S(r, z) = r d\omega_E(r, z)/dr$ and the bounce averaged dimensionless shear rate [5]

$$\langle s(r) \rangle_z = \left\langle \frac{S(r, z)}{2\pi n(r, z) ce/B} \right\rangle_z.$$

The dimensionless shear rate $s(r)$ represents, for the case of a "top hat" profile, the shear rate divided by the local rotation rate. Figure 2 also shows $\langle s \rangle_z$; the squares represent the bounce average shear, the solid line a simple estimate of $s(r, z = 0)$ directly from $v_E(r) = v_{\text{tot}}(r) - v_{\text{dia}}(r)$ where the diamagnetic drift is calculated from the measured $n(r)$ and $T(r)$. In the case of Fig. 2(a) which has a very small shear for small radius, $\langle s(r) \rangle_z \simeq s(r, z = 0)$ for $r < 1$ cm.

The electronic spin orientation of the ground state of Mg^+ is used to "tag" the test particles. The flux of test particles Γ_t is obtained from the measured test particle density n_t as

$$\Gamma_t(r, t) = -\frac{1}{r} \int_0^r dx x \frac{\partial}{\partial t} n_t(x, t) + \int_0^r dx x \frac{2n_t(x, t) - n(x)}{\tau_s(x)};$$

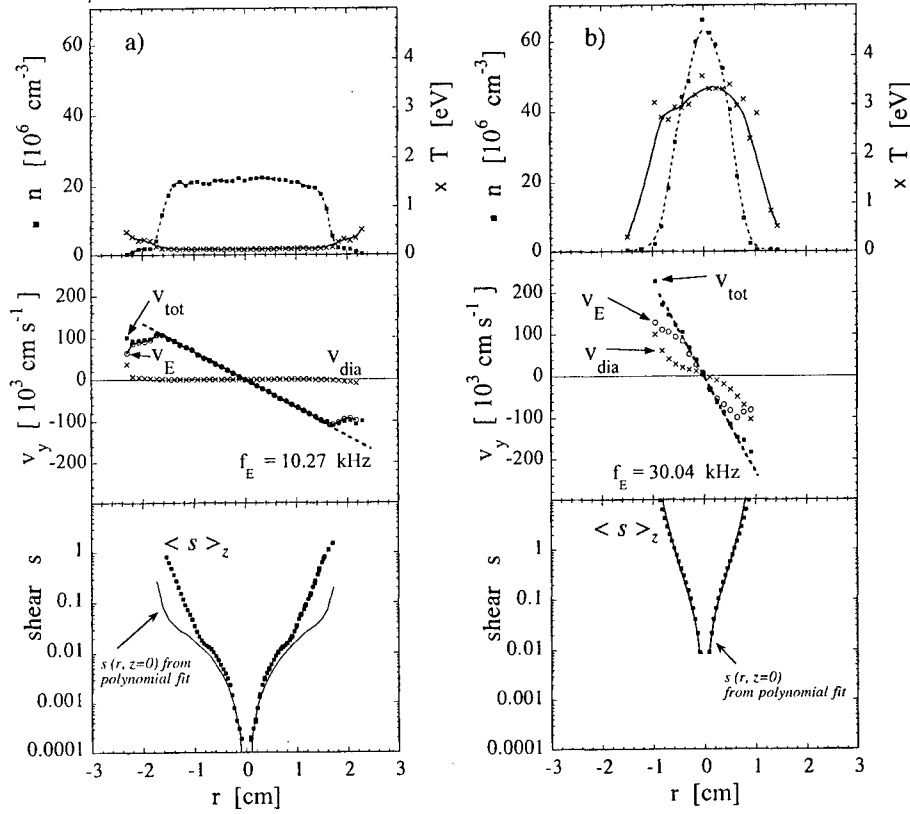


FIGURE 2. Profiles of density n , temperature T , velocity v , and dimensionless shear s . (a) Small shear case; (b) large shear case.

the second term corrects for the weak spontaneous spin flip at a measured rate τ_s^{-1} . We verify that the flux of test particles is proportional to the gradient of the concentration of test particles, i.e.

$$\Gamma_t(r, t) = -D(r)n(r)\frac{\partial}{\partial r}\left(\frac{n_t(r, t)}{n(r)}\right)$$

and obtain the local diffusion coefficient $D(r)$.

Figure 3 shows preliminary measurement of the diffusion coefficient normalized to the plasma length L_p and magnetic field B as a function of the dimensionless bounce-averaged shear $\langle s \rangle_z$. For $\langle s \rangle_z \gtrsim 0.1$ the measured diffusion coefficient agrees quantitatively with the 3D diffusion coefficient previously measured in long plasmas [7]; here, D^{3D} is calculated with values of n and T appropriate to the high-shear data points. As the shear decreases, the diffusion coefficient increases roughly proportional to s . For

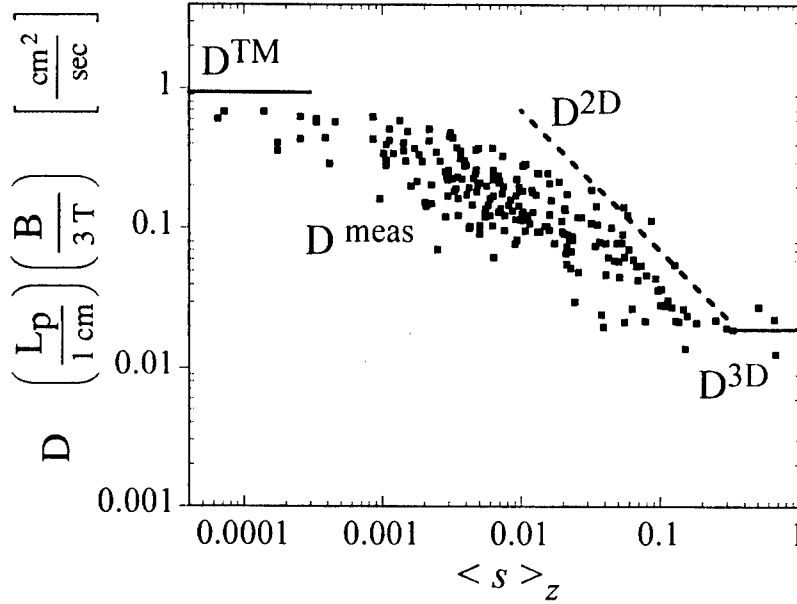


FIGURE 3. Diffusion coefficient normalized to plasma length L_p and magnetic field B versus the dimensionless bounce average shear.

$\langle s \rangle_z \leq 5 \times 10^{-3}$ the diffusion coefficient approaches a limit within a factor of two of the Taylor-McNamara shear-free theory. Here, D^{TM} is calculated from the number of particles N in the low-shear plasmas.

Recent theoretical work has investigated diffusion processes in the presence of shear for a collection of 2D point vortices [5]. Overall, the data shows fair agreement with the present theory, but proper consideration of the end shape and Debye shielding of the fluctuations will have to be included. To summarize the theories, we have the 3D long range collisional diffusion [8]:

$$D^{3D} = 2\alpha\sqrt{\pi}n\bar{v}b^2r_c^2\ln(\bar{v}/\Delta v_{\min})\ln(\lambda_D/r_c) \propto B^{-2}nT^{1/2},$$

where $\alpha = 3$ represents the multiple effective collisions due to “velocity caging.” This is in quantitative agreement with the experiments [7] in long plasmas (i.e. $N_b \leq 1$). Here $b \equiv e^2/T$ is the classical distance of closest approach, and the minimum relative velocity for these collisions is $\Delta v_{\min} \approx (n\bar{v}^3b^2\sqrt{r_c\lambda_D})^{1/3}$.

The 2D shear-limited diffusion [5] is

$$D^{2D} = \frac{1}{2\langle s \rangle_z} \left(\frac{e}{L_p} \frac{4\pi c}{B} \right) \ln\left(\frac{r}{d}\right) \propto B^{-1}\langle s \rangle_z^{-1}L_p^{-1},$$

where $d \equiv (4D^{2D}/|S|)^{1/2}$ is the (diffusion-limited) minimum impact parameter for these collisions. In the limit of zero shear, Taylor and McNamara calculated [4] a diffusion

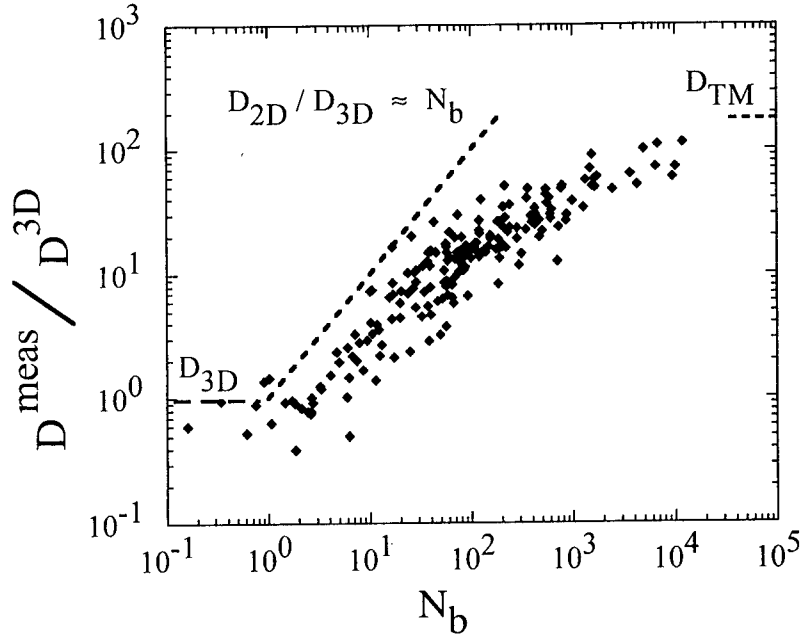


FIGURE 4. The diffusion coefficient normalized by the 3D long range $\mathbf{E} \times \mathbf{B}$ drift collision case increases with N_b .

(neglecting considerations of Debye shielding) of

$$D^{\text{TM}} = \frac{ce}{2\pi^{1/2} B L_p} \frac{\sqrt{N}}{L_p} \propto B^{-1} N^{1/2} L_p^{-1}.$$

These theories scale differently with all plasma parameters. However the enhancement ratio D^{2D}/D^{3D} depends only on the number of bounces a particle makes in the rotating frame before being sheared apart, given by

$$N_b \equiv \frac{f_b}{r\omega'_E} = \frac{\bar{v}}{2L_p r\omega'_E}.$$

Figure 4 shows the measured diffusion coefficient normalized to D^{3D} . The solid line is the theory prediction at $B = 3$ T for $D^{2D}/D^{3D} \approx N_b$. One can see that the diffusion increases as particles interact for longer periods, i.e. for large N_b . For $N_b \leq 2$ the diffusion is correctly described by 3D long-range collisions; in contrast for $N_b \gtrsim 5000$ the diffusion approaches the Taylor-McNamara limit. For $1 < N_b < 100$, the predicted D^{2D}/D^{3D} is in fair agreement with the experiments, being generally about $3 \times$ larger

than observed. Further theory and experiments may elucidate the effects of the end confinement fields and the effects of Debye shielding.

ACKNOWLEDGMENTS

This work was supported by Office of Naval Research grant N00014-96-1-0239 and National Science Foundation grant PHY-9876999. We also thank Mr. Fidel Zamora for excellent technical support.

REFERENCES

1. Burrell, K. H., *Phys. Plasmas* **4**, 1499 (1997).
2. Terry, P. W., *Rev. Mod. Phys.* **72**, 109 (2000); Biglari, H. *et al.*, *Phys. Fluids B* **2**, 1 (1990).
3. Huang, X.-P., Anderegg, F., Hollmann, E. M., O'Neil, T. M., and Driscoll, C. F., *Phys. Rev. Lett.* **78**, 875 (1997); Anderegg, F., Hollmann, E. H., and Driscoll, C. F., *Phys. Rev. Lett.* **81**, 4875 (1998); Hollmann, E. M., Anderegg, F., and Driscoll, C. F., *Phys. Plasmas* **7**, 2776 (2000).
4. Taylor, J. B. and McNamara, B., *Phys. Fluids* **14**, 1492 (1971).
5. Dubin, D. H. E., *Phys. Lett. A* **284**, 112 (2001). See also D.H.E. Dubin and C.F. Driscoll in this Proceedings.
6. Anderegg, F., Huang, X.-P., Sarid, E., and Driscoll, C. F., *Rev. Sci. Instrum.* **68**, 2367 (1997).
7. Anderegg, F., Huang, X.-P., Driscoll, C. F., Hollmann, E. M., O'Neil, T. M., and Dubin, D. H. E., *Phys. Rev. Lett.* **78**, 2128 (1997).
8. Dubin, D. H. E., *Phys. Rev. Lett.* **79**, 678 (1997).

Classical Collisional Diffusion in the Annular Penning Trap

Qudsia Quraishi,* Scott Robertson,* and Bob Walch[†]

**Department of Physics, University of Colorado, Boulder, Colorado 80309-0390*

[†]*Department of Physics, University of Northern Colorado, Greeley, Colorado 80639*

Abstract. Transport of particles and energy by cross-field diffusion has been studied in the annular Penning trap in which a nonneutral plasma of electrons is contained between concentric cylinders. At densities sufficiently low ($<10^5 \text{ cm}^{-3}$) to suppress mobility transport arising from the space charge electric field, the dominant source of transport is diffusion from collisions of electrons with added helium gas. The particle diffusivity, when corrected for asymmetry transport, is observed to scale linearly with collision frequency and inversely with the square of the axial magnetic field. Measurements of the electron energy distribution as a function of time show an initial mean energy of 0.3 eV which decreases with time as a result of diffusion cooling.

INTRODUCTION

The classical diffusivity coefficient of electrons perpendicular to a magnetic field can be written as $D_{\perp} = v_c r_L^2$, where v_c is the frequency of electron collisions with another species and r_L is the thermal Larmor radius. There is limited experimental data that supports this equation. In charge neutral plasmas, cross-field diffusion of electrons and ions occurs at the ambipolar rate. Electrostatic turbulence driven by currents or density gradients often causes additional transport that masks the classical transport. Current driven turbulence is absent in the Q-machine and in afterglows and in these plasmas demonstration of proper scaling of ambipolar diffusion with magnetic field and with collision frequency has been possible.^{1,2} In the Malmberg-Penning trap, transport of electrons has been measured arising from collisions with a background gas.^{3,4} In this trap, the space charge electric field of the electrons usually results in transport by mobility being greater than that by diffusion. In this work, we examine diffusion of electrons in an annular version of the Malmberg-Penning trap⁵ in which electrons are confined between concentric cylinders at ground potential. The electrons are confined radially by an axial magnetic field and axially by negative potentials applied to grids at the ends. At sufficiently low density, the mobility transport from the space charge electric field is much smaller than the diffusive transport. We demonstrate for a wide range of magnetic fields and collision frequencies that the measured diffusivity, when

corrected for additional transport from trap asymmetry, has the expected classical scaling with collision frequency and magnetic field. The data also show that the mean electron energy falls with time as a consequence of diffusion cooling.

Theoretical treatments of transport beginning with the fluid equations in cylindrical geometry give a radial particle flux

$$\Gamma = -D_{\perp} \frac{dn}{dr} + n \mu_{\perp} E_r, \quad (1)$$

where,

$$D_{\perp} = v_e m T / q^2 B_z^2 = v_e r_L^2, \quad (2)$$

is the perpendicular diffusion coefficient,

$$\mu_{\perp} = m v_e / q B_z^2, \quad (3)$$

is the perpendicular mobility coefficient, n is the electron density, m is the electron mass, v_e is the electron-neutral collision frequency, T is the electron temperature in energy units, r is the radial cylindrical coordinate, q is the negative electron charge, E_r is the radial electric field, and B_z is the axial magnetic field. For collisions of electrons with neutral gas, the collision frequency does not vary spatially and the diffusion equation has the same form as the equation for heat conduction. For concentric cylinders of radii r_o and $2r_o$ and for a constant diffusivity, the e-folding time for the lowest order mode⁶ is $\tau_D = 0.1025 r_o^2 / D_{\perp}$. This decay time is very nearly that for parallel planes of separation r_o , which is $(r_o/\pi)^2 / D_{\perp}$. The temperature dependent diffusivity D_{\perp} decreases with time as a consequence of the diffusion cooling, thus the exponential dependence of the decay time is an approximation.

For measurement of diffusion alone, electric fields must be kept sufficiently small for transport by mobility to be much less than that by diffusion. With the concentric cylinders kept at ground potential, a residual electric field arises from the space charge of the electrons. The ratio of the mobility flux to the diffusive flux can be found approximately by modeling the cylinders as parallel plates. In this case, the lowest order solution to the diffusion equation has a density which varies with distance as $n_o \sin(\pi x/L)$ where x is the coordinate, L is the plate separation, and n_o is the central density. This gives, from Poisson's equation, a sinusoidal potential distribution with a peak value $\phi_o = n_o q L^2 / \epsilon_o \pi^2$ and a cosinusoidal electric field with amplitude $E_o = n_o |q| L / \epsilon_o \pi$. The ratio of the mobility flux at the boundary Γ_m to the diffusive flux at the boundary Γ_D is approximately

$$\frac{\Gamma_m}{\Gamma_D} = \frac{n_o \mu_{\perp} E_o}{D_{\perp} \frac{dn}{dx}} = \left(\frac{L}{\pi \lambda_D} \right)^2, \quad (4)$$

where λ_D is the Debye length. The mobility flux at the wall is overestimated by $n_o \mu_L E_o$ because the density at the wall is zero rather than n_o . Thus we can ensure that the diffusive flux is dominant by reducing the density such that $\lambda_D > L/\pi$. For concentric cylinders of separation r_o , the plate separation L is replaced by r_o . A similar inequality applies to transport in the usual Malmberg-Penning trap.⁴

THE APPARATUS

The annular Penning trap used for this study has larger dimensions and a greater magnetic field than the trap described previously.⁵ The new trap, Fig. 1, is designed to have the maximum plasma volume that will fit inside a preexisting vacuum chamber and water-cooled coil set. There are eight pancake-like coils with a bore of 30 cm which are spaced to create a field which varies $< 1\%$ within the trapping volume. The vacuum is created by a 20-cm diffusion pump and the base pressure is $\sim 10^{-7}$ Torr. The pressure of helium is set by a precision leak valve and is measured by an ionization gauge tube located 1.2 m above the experiment. The gauge is calibrated for N_2 and the reading is divided by 0.2 to correct for the differing response to He.

The trapping volume is between concentric cylinders of electropolished stainless steel 61 cm in length. The inner cylinder has an outer radius of $r_o = 38.1$ mm and the outer cylinder has an inner radius of 74.2 mm giving an aspect ratio of 1.95 and a trapping volume of 7.7 liters. Adjacent to the ends of the cylinders are annular grids with 85% transparency that are held at -24 V to confine the electrons. Experiments consist of repeated fill, hold, and dump cycles controlled by a computer interface. Data are acquired at intervals of 10 or 20 μ s, which is much shorter than the experimental time scales of 10–300 ms.

The trap is filled with secondary electrons from helium that are created within the trap by a stream of primary electrons from a filament at one end. The filament is oriented radially and spans the distance from the inner cylinder to the outer cylinder. The filament is biased to -140 V for a few milliseconds to load the trap. The background gas is helium because low energy collisions of electrons with helium are elastic and the collision cross section for momentum transfer varies slowly with energy.^{7,8} The energies of the confined electrons are usually below 1 eV and the cross section rises about 20% between 0 eV and 1 eV. The electron-neutral collision frequency is $\nu_c = n_{He} \sigma(v) v$, where v is the electron velocity, $\sigma(v)$ is the collision cross section, and n_{He} is the helium density, and is shown as a function of electron energy in Fig. 2a. The relationship between the filling density, helium pressure and the current of primaries was investigated in the smaller trap.⁹

The electron density profile is measured by removing one grid potential to dump the confined charge onto a set of five concentric annular rings. A grounded grid adjacent to the annuli reduces electrostatic pickup from the switched grid. Active integrators measure the collected charge. The charge is corrected for the absorption by the two meshes and the density is calculated by assuming that it is uniform along the length of the cylinders.

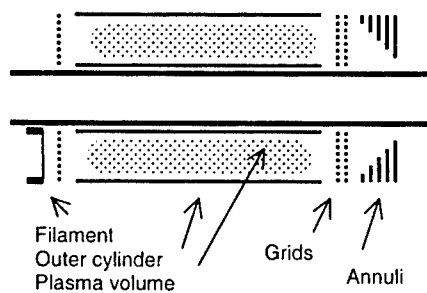
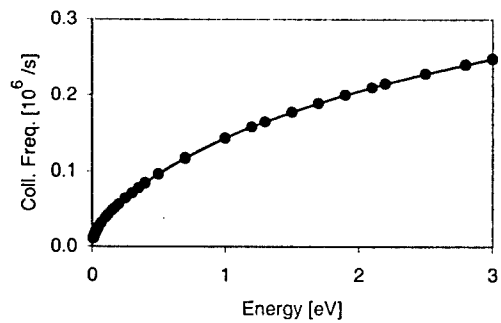
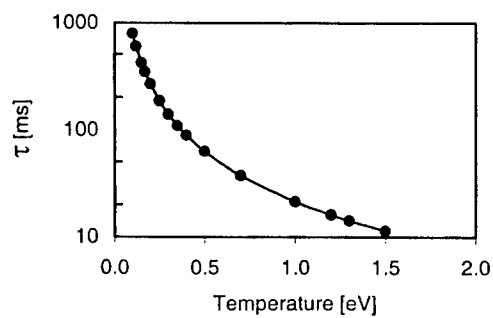


FIGURE 1. Schematic diagram of the annular Penning trap (not to scale).



A)



B)

FIGURE 2. (A) The collision frequency from the tabulated cross sections in reference [7] as a function of energy at a helium pressure of 1 mTorr. (B) The calculated diffusive decay constant τ_D from Eq. (2) as a function of temperature for $B_z = 35$ mT and a pressure of 1 mTorr.

The electron temperature is determined by lowering the potential barrier so that electrons are dumped onto the annuli in a time of order one millisecond. The current collected at an annulus at each instant is determined by the number of electrons just able to cross the falling potential barrier and is thus proportional to the distribution function.¹⁰ The confining voltage V is switched from -24 V to -5 V and then is ramped linearly through zero at a rate of 1 V/ms. With finite electron density, there is a negative space charge potential with a peak value ϕ_o midway between the cylinders. Electrons with kinetic energy at the midplane greater than $q(V-\phi_o)$ are those able to pass the barrier. Electrons have a large number of collisions (~ 400 at 0.1 eV) during the sweeping of the analyzer voltage, thus the losses from the trap include all the particles with total kinetic energy greater than $q(V-\phi_o)$. This principle of operation is different from that of an analyzer in a collisionless plasma for which the detected particles are those with parallel energy greater than $q(V-\phi_o)$. At the low densities used in these experiments, $\phi_o < 0.1$ V.

EXPERIMENTS

Experiments are performed using repeated fill, hold and dump cycles shown in Fig. 3. The overlapping traces are from the charge integrator connected to the middle annulus. The axial field is 35 mT and the pressure is 0.5 mTorr. The trap is filled by biasing the filament negatively for 6 ms. During this interval, primary electrons strike the annulus and create the charge pedestal seen at early times. The confined electrons are dumped onto the annulus after a 20 ms holding period that is increased in increments of 7 ms. The filament heating is adjusted so that at the first dump time the charge collected is approximately 18 pC, which corresponds to an initial density of 7×10^4 cm⁻³. This gives a plasma frequency of 1.5×10^7 s⁻¹, which is very much less than the cyclotron frequency of 6×10^9 s⁻¹.

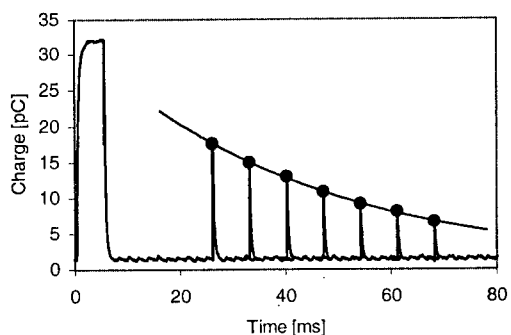


FIGURE 3. Oscilloscope showing operation of the experiment. The signals show the charge dumped on the middle annulus for seven fill, hold and dump cycles. The curve passing through the peaks is a fitted exponential function determined by the least-squares method. For these data, $B_z = 35$ mT and the pressure is 0.5 mTorr.

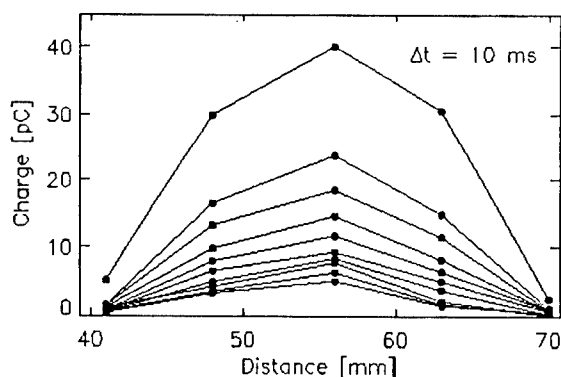


FIGURE 4. A plot of the radial distribution of density as a function of time. These data are for an axial field of 35 mT and a pressure of 0.5 mTorr. The interval between profile measurements is 10 ms.

The effect of mobility transport arising from the space charge electric field was quantified by taking additional data with initial charges of 36 and 54 pC. The e-folding times were observed to fall 10% with each 18 pC increase. Thus the measured e-folding times with 18 pC of initial charge are approximately 10% lower than the value obtained by extrapolating the data to zero charge.

Density profiles are obtained as a function of time by recording the charge dumped onto each of the five annuli at successively later times. A typical set of density profiles is shown in Fig. 4 for the same conditions as in Fig. 3. The profile is peaked in the center and decays self-similarly indicating that the lowest order mode of the diffusion equation is dominant.

The distribution function measured by lowering the grid potential is shown in Fig. 5 for standard conditions, 35 mT and 0.5 mTorr, and for hold times of 9, 10, 12, and 16 ms. These data were taken with 9 pC of initial charge for which $\phi_0 < 0.05$ V and thus the data are not corrected for the effect of space charge potential. The nonzero values for $f(E)$ at negative energies are due to the finite response time of the electronics. The point at which the signal has fallen to half its peak value after the zero is passed, -0.05 V, is therefore an approximate measure of the resolution of the energy analyzer. The mean energy calculated from the measured distribution function is 0.3 eV at the first dump time. The initial mean energy varies weakly with magnetic field and filling pressure. The mean energy, when used as the temperature, gives a Debye length of 15 mm and a thermal Larmor radius of 0.04 mm at 35 mT. The inequality to make the mobility transport small, $\lambda_D > r_0 / \pi = 12$ mm, indicated by Eq. (4), is barely satisfied. However, comparisons of data with different filling densities show that the additional transport from mobility is indeed small thus indicating that the inequality is too stringent.

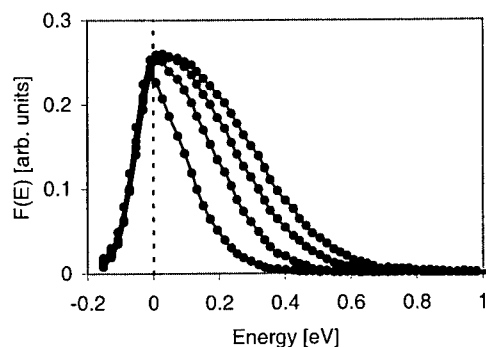


FIGURE 5. The distribution function $f(E)$ at the middle annulus for hold times of 9, 10, 12, and 16 ms, an axial field of 35 mT and a pressure of 0.5 mTorr. The distribution becomes narrower with time.

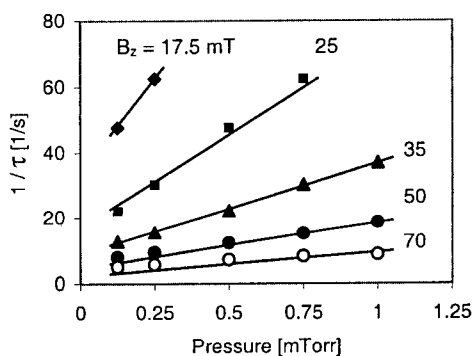


FIGURE 6. Dependence of the fitted decay constant upon the pressure of helium at magnetic fields of 17.5, 25, 35, 50, and 70 mT.

The dependence of the decay constant ($1/\tau_D$) upon the pressure of helium is shown in Fig. 6 for five values of magnetic field and five values of pressure. A linear dependence upon pressure is expected from the linear dependence of diffusivity upon collision frequency. Linear regressions made to the data do not extrapolate to zero diffusivity at zero pressure indicating an additional mechanism for loss. Experiments in the Malmberg-Penning trap have shown the existence of transport arising from trap asymmetries^{11,12,13} which becomes evident at low pressure. The asymmetries may have their origin in the construction of the trap, misalignment of the trap with the magnetic field, or from electric fields arising from contact potentials. There is a range of parameters in the Malmberg-Penning trap for which the asymmetry transport scales inversely with the square of B_z . In Fig. 6, the solid line at 35 mT is a

linear regression to the data. The lines at other magnetic fields are this regression scaled inversely with the square of B_z . These lines are good fits to the data and indicate that both the collisional transport and asymmetry transport have approximately the same inverse-square scaling with magnetic field. The accessible region of parameter space is limited to $B_z < 70$ mT by the magnetic field power supply and to pressures of ≤ 1 mTorr by the vacuum gauge. Data are also limited to decay times longer than 10 ms as a result of time constants associated with the diagnostic system. This prevents acquisition of data with both the highest pressures and lowest magnetic fields.

The four data points in Fig. 6 at the highest two fields and lowest two pressures lie slightly above the scaled regression. The longest confinement times cause the temperature to fall more slowly which increases the decay constant. This data could be scaled in a way that removes the temperature dependence. However, this region of parameter space is dominated by asymmetry transport and the temperature dependence of this transport in the annular trap has not been established.

The initial temperature value of 0.30 eV gives a calculated e-folding time of 140 ms (Fig. 2b) at a pressure of 1 mTorr and a magnetic field of 35 mT. The corresponding decay constant is 7 s^{-1} . The fitted decay constant at these conditions from Fig. 6 is 38 s^{-1} . The data at low pressure indicates that 8 s^{-1} of this is due to asymmetry transport. Thus that part of the decay constant from collisions is 30 s^{-1} , which is approximately a factor of 3.7 greater than that calculated from the collision cross section. It is inappropriate, however, to expect close agreement between the fitted e-folding times and τ_D from the fluid approach with constant D_\perp because $f(E)$ is not Maxwellian and the falling mean electron energy results in a time dependence which is not exponential.

SUMMARY AND CONCLUSION

An annular Penning trap confining a nonneutral low density plasma of electrons has been used to measure the diffusive cross-field transport from collisions of the electrons with helium gas. The measured decay times are reduced by about 10% by the additional transport from mobility driven by the space charge electric field. There is also transport from asymmetry that is found by extrapolation of the data to zero helium density. This contribution to transport is then subtracted from the data to obtain that part of the decay constant due to collisions. The corrected decay constants scale classically, i.e., linearly with the helium density and as the square of the magnetic field. The falling electron temperature results in a time dependent diffusivity. Precise comparisons between measured and calculated decay times will require numerical solutions to the equations for both particle and thermal transport.

ACKNOWLEDGMENTS

The authors acknowledge the assistance of John Klein and Matt Triplett in the development of the apparatus and diagnostic tools.

REFERENCES

- ¹ N. D'Angelo and N. Rynn, *Phys. Fluids* **4**, 1303 (1961).
- ² A. I. Anisimov, N. I. Vinogradov, V. E. Golant, and B. P. Konstantinov, *Sov. Phys. – Tech. Phys.* **7**, 884 (1963).
- ³ J. S. DeGrassie and J. H. Malmberg, *Phys. Fluids* **23**, 63 (1980).
- ⁴ M. H. Douglas and T. M. O'Neil, *Phys. Fluids* **21**, 920 (1978).
- ⁵ S. Robertson and B. Walch, *Rev. Sci. Instrum.* **70**, 2993 (1999).
- ⁶ H. S. Carslaw and J. C. Jaeger, *Conduction of Heat in Solids* (Oxford University Press, London, 1959), second edition, Chapter 7.10.
- ⁷ R. W. Crompton, M. T. Elford, and R. L. Jory, *Aust. J. Phys.* **20**, 369 (1967).
- ⁸ R. W. Crompton, M. T. Elford, and A. G. Robertson, *Aust. J. Phys.* **23**, 667 (1970).
- ⁹ B. Walch and S. Robertson, *Phys. Plasmas* **7**, 2340 (2000).
- ¹⁰ D. L. Eggleston, C. F. Driscoll, B. R. Beck, A. W. Hyatt, and J. H. Malmberg, *Phys. Fluids* **B4**, 3432 (1992).
- ¹¹ C. F. Driscoll and J. H. Malmberg, *Phys. Rev. Lett.* **50**, 167 (1983).
- ¹² D. L. Eggleston, *Phys. Plasmas* **4**, 1196 (1997).
- ¹³ J. M. Kriesel and C. F. Driscoll, *Phys. Rev. Lett.* **85**, 2510 (2000).

Investigation of the Expansion Rate Scaling of Plasmas in the Electron Diffusion Gauge Experiment ¹

Kyle A. Morrison, Ronald C. Davidson, Stephen F. Paul, Thomas G. Jenkins

Plasma Physics Laboratory, Princeton University, Princeton, NJ 08543

Abstract. The expansion of the Electron Diffusion Gauge (EDG) pure electron plasma due to collisions with background neutral gas atoms is characterized by the pressure and magnetic field scaling of the profile expansion rate $(d/dr)\langle r^2 \rangle$. Data obtained at higher background gas pressures[1] than previously studied[2] is presented. The measured expansion rate in the higher pressure regime is found to be in good agreement with the classical estimate of the expansion rate[3].

INTRODUCTION

Pure electron plasmas are trapped in the Electron Diffusion Gauge (EDG) device[2, 4, 5, 6], a cylindrically symmetric Malmberg-Penning trap[7] with wall radius $R_w = 2.54$ cm. Previously reported experimental results[2, 6] from the EDG device indicated that the expansion rate of the plasmas is about a factor of four faster than that predicted theoretically. The predicted expansion rate[3] is derived using a fluid treatment of the plasma, and assumes that the (elastic) electron-neutral collision frequency is not a function of time beyond its dependence on the plasma temperature. In this paper, further measurements[1] performed at higher helium background pressures ($P_{He} = 1 \times 10^{-7}$ Torr to 2×10^{-5} Torr) are reported that support the theoretical prediction[3].

Malmberg-Penning traps have a uniform magnetic field parallel to the common axis of several identical cylindrical electrodes, the outer two of which are electrically biased [2, 4, 5, 6, 7]. The EDG device is equipped with a collimating plate and Faraday cup to allow measurements of the plasma's density profile: the particles along an axial chord aligned with the small hole in the collimating plate (the "total" density diagnostic) pass through to the Faraday cup, which measures the amount of charge along that chord (the "local" density diagnostic). By forming several (well-reproduced) plasmas in succession, a series of line-integrated, radial profiles is obtained and used to follow the expansion of the plasma. To determine the plasma behavior at different gas pressures, helium gas is fed into the chamber at different, controlled rates to produce the desired background neutral pressure[2, 4, 5, 6].

¹ Note: Portions of this paper are reprinted from Ref.[1].

EXPANSION RATE MEASUREMENTS

The expansion rate of the plasma in the EDG device is determined as previously described [2, 4, 5, 6]: the mean-square radius of the plasma is computed numerically according to the expression

$$\langle r^2 \rangle = \frac{\int_0^{R_w} dr 2\pi r^2 Q(r)}{\int_0^{R_w} dr 2\pi r Q(r)}, \quad (1)$$

where

$$Q(r) = -\frac{e}{A_h} \int dz \int_{A_h} dr' d\theta n(r', \theta, z). \quad (2)$$

Here, A_h is the area of the collimating hole, and $n(r', \theta, z)$ is the number density of the plasma electrons. The quantity $Q(r)$ corresponds to the axially-integrated profile measured with the local density diagnostic, and is an average over the area of the local density diagnostic's collimating hole (radius = 1/16 in.). The plasma expansion rate may be estimated by fitting a plot of mean-square plasma radius versus time with a curve, and taking the slope of that curve to be the instantaneous expansion rate. In contrast, earlier experiments[8, 9] obtained qualitatively similar scaling results to those presented here with comparable Malmberg-Penning traps by measuring the decay of the plasmas' central density, i.e., both the time it takes for the central density to reach one-half of its initial value, τ_m , and the time rate of change of the inverse central density, $(d/dt)[1/n(r=0, t)]$. For the EDG experiment, however, we have determined the expansion rate from the measured density profiles using a linear fit to the early part of the mean-square radius evolution data.

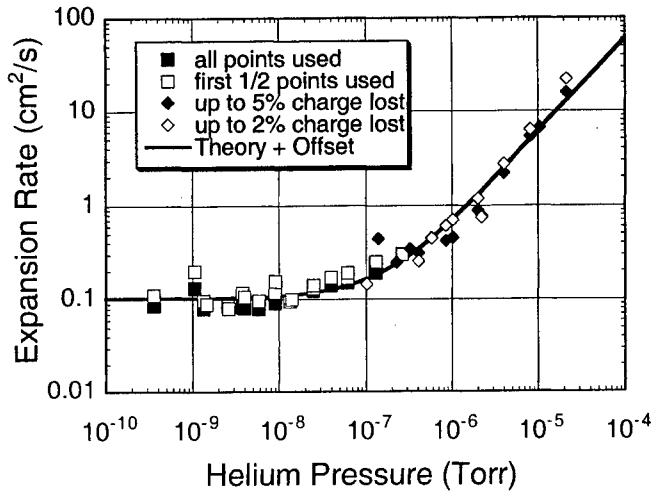


FIGURE 1. The measured plasma expansion rates $(d\langle r^2 \rangle/dt)$ at a magnetic field of $B = 610$ Gauss are plotted[1] versus background neutral helium pressure. The squares denote the previous data[2], the diamonds denote the new data[1], and the solid curve is a combination of the theoretical prediction in Eq. (3) plus a constant offset. The plasma line density is $N_L = 3.41 \times 10^7$ electrons/cm.

Figure 1 shows the composite result of the experimental measurements at a $B = 610$ G magnetic field. The data ranging from 3×10^{-10} Torr to 2×10^{-7} Torr, represented by squares, are the data from the previous studies[2, 4, 5, 6]. Each set of mean-square radius data at a particular pressure is represented twice on this plot. Open squares denote the expansion rate determined using only the first half of the mean-square radius evolution data during a four-second time evolution. Closed squares denote the expansion rate determined by using the entire mean-square radius time evolution. Open diamonds denote expansion rates computed using only mean-square radius data taken before 2% of the total plasma charge has been lost, and closed diamonds denote expansion rates computed with the data taken before 5% of the plasma has been lost.

The solid curve in the plot in Fig. 1 is the expansion rate predicted theoretically[3], with an added offset to account for the effects of trap asymmetries[8, 10, 11] at low pressures. The expansion rate in the linear region has previously been calculated[3] to be

$$\frac{d}{dt} \langle r^2 \rangle = \frac{2N_L e^2 v_{en}(T)}{m_e \omega_{ce}^2} \left(1 + \frac{2T}{N_L e^2} \right), \quad (3)$$

where $\omega_{ce} = eB/m_e c$ is the electron cyclotron frequency, $v_{en}(T) = n_n \sigma_{en} v_{Th}$ is the electron-neutral collision frequency, T is the plasma temperature (in ergs), and N_L is the line density of the plasma column. The theoretical curve plotted in Fig. 1 assumes $T = 2$ eV and $N_L = 3.41 \times 10^7$ electrons/cm, and the offset used is $0.1 \text{ cm}^2/\text{sec}$. At pressures exceeding 10^{-7} Torr, the data in Fig. 1 is consistent with the linearly-varying theoretical prediction in Eq. (3). The fit to the data obtained for the previous study[2] resulted in a calculated expansion rate that is factor of four greater than the unadjusted theoretical curve because the data used did not extend to a high enough pressure to produce purely electron-neutral collision-dominated expansion. Note that the theoretical curve plotted in Fig. 1 is not a fit, but an absolute prediction of the fluid theory[3].

In using Eq. (3), however, there is a caveat: at pressures above $P = 10^{-7}$ Torr, the electron-neutral collision frequency in the EDG device is greater than the electron-electron collision frequency [12], and the assumption of uniform temperature across the cross section of the plasma is not necessarily valid. This assumption is used to derive the equation for the expansion rate in Eq. (3), which nonetheless agrees with the measured data. This is interpreted to mean that any effects of a non-uniform plasma temperature on the expansion rate are negligibly small for the EDG device in this parameter range.

Figure 2 shows the results of higher-pressure expansion measurements taken at a $B = 300$ G magnetic field. The squares denote expansion rates computed using the measurements taken before 2% of the plasma has been lost, and the diamonds denote expansion rates computed before 5% of the plasma has been lost. The data used for the expansion rates denoted by triangles is restricted to the profiles in the expansion where low relative error in the computation of $\langle r^2 \rangle$ was obtained. This approximate criterion often results in fewer mean-square radius measurements being used in the computation of the expansion rates than for the 2% case, but in all cases fewer measurements than the number used for the 5% case.

The 300 G data in Fig. 2 also agree with a linear dependence of the expansion rate on background gas pressure. Of the theoretical curves shown, the curve that best describes the linear portion of the data in Fig. 2 is the one that assumes a temperature

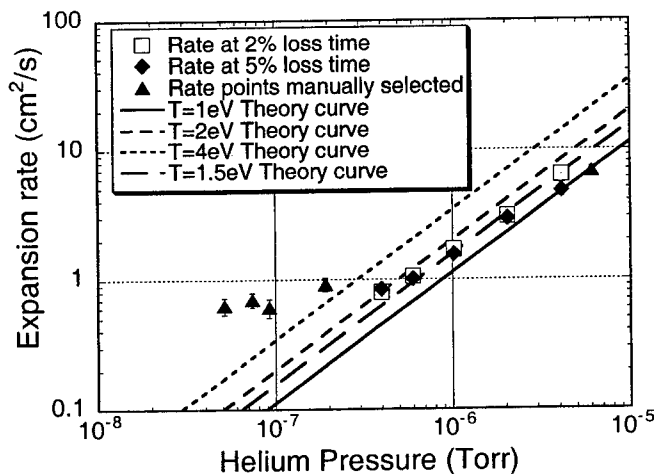


FIGURE 2. The measured plasma expansion rates ($d\langle r^2 \rangle / dt$) at a magnetic field of $B = 300$ Gauss are plotted[1] versus background neutral helium pressure. Theoretical curves for plasma temperatures of $T = 1, 1.5, 2$, and 4 eV are included for comparison. The plasma line density is $N_L = 2.85 \times 10^7$ electrons/cm.

of $T = 1.5$ eV. Plasma temperatures inferred for profiles measured at different times can have different values, however, making it difficult to describe the behavior of the expansion rate with a single theoretical curve.

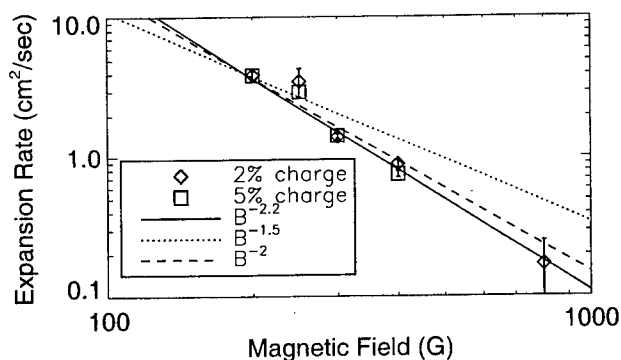


FIGURE 3. The measured plasma expansion rates ($d\langle r^2 \rangle / dt$) are plotted[1] versus magnetic field strength B . The points are best fit by a curve proportional to $B^{-2.19}$. Curves for the lower-pressure scaling[2] of $B^{-1.5}$ and the theoretical scaling B^{-2} are also included.

Expansion rate data has also been taken at $P = 10^{-6}$ Torr at several different values of magnetic field, and the results are presented in Fig. 3. These results indicate that the expansion rate scales as $B^{-2.190 \pm 0.015}$ in the EDG device when electron-neutral collisions dominate the expansion (at higher pressures). The previous (lower-pressure) measurements in the EDG device, in the regime where asymmetry-induced expansion

dominates, produced a scaling of $B^{-1.5 \pm 0.1}$, which is also at variance with the $(L/B)^2$ scaling for that regime reported previously by Driscoll, *et. al*[13, 14]. The measured scaling at higher pressure in the EDG device is in reasonable agreement with the theoretical scaling (B^{-2}) in Eq. (3).

The estimation of the instantaneous expansion rate is complicated by the fact that the temperature changes during the course of the plasma's evolution. In the EDG device, the temperature at a given point in time is routinely inferred by fitting density profile data with the predicted quasi-equilibrium density profile[3]

$$n(r,t) = \hat{n}(t) \exp \left\{ \frac{e\phi(r,t) - e\hat{\phi}(t)}{T} - \frac{r^2}{\langle r^2 \rangle(t)} \left(1 + \frac{N_L e^2}{2T} \right) \right\}, \quad (4)$$

where $\hat{n}(t)$ is the central density as a function of time, $\phi(r,t)$ is the electrostatic potential (the solution of Poisson's equation), and $\hat{\phi}(t)$ is the on-axis electrostatic potential. A Poisson solver routine[15] is used obtain a density profile consistent with both the Boltzmann distribution along the field lines and Poisson's equation. It is important to note that the same fluid theory[3] used to predict the the expansion rate in Eq. (3) is used to predict the quasi-equilibrium density profile in Eq. (4), so the inferred temperatures are imperfect indicators of the actual temperature at pressures above $P = 10^{-7}$ Torr.

Figure 4 shows the temperature evolution at 300 G for background gas pressures of 1×10^{-7} Torr and 1×10^{-6} Torr. In these plots, the black circles are the temperatures determined from the Poisson solver routine, the diamonds are the temperatures determined from fitting the line-integrated profile data directly, and the squares circumscribe points where the inferred Debye length is less than one-fifth of the plasma diameter. The solid curves correspond to the theoretical prediction[16] given the initial conditions, assuming global energy conservation, elastic electron-neutral collisions, and a uniform temperature across the plasma cross-section.

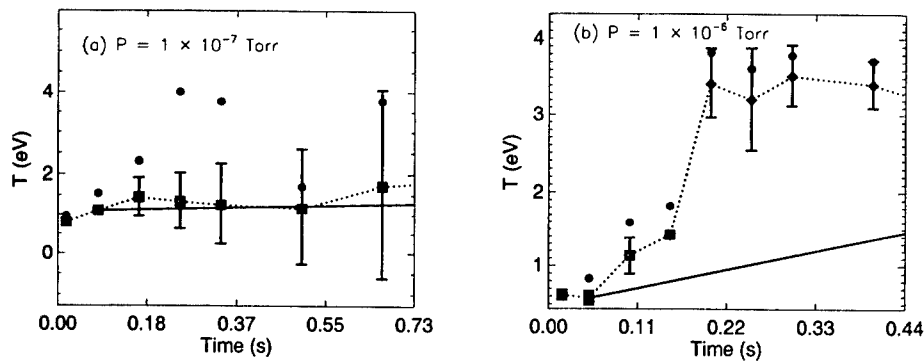


FIGURE 4. These plots display the inferred plasma temperature evolution for the $B = 300$ G data at pressures of 1×10^{-7} Torr and 1×10^{-6} Torr, respectively. The solid line is the theoretical prediction[16]. The dots are obtained from the Poisson solver routine, and the diamonds are obtained from fitting the line-integrated data.

The 10^{-7} Torr data are typical of what was previously measured at lower pressures[2, 4, 5, 6]. The inferred temperatures for the 10^{-6} Torr data after the plasma has lost 2% of the total charge, however, are greater than that predicted theoretically. The reason for the sizeable increase in the inferred temperature in Fig. 4(b) is not understood presently. The plasma is slowly and continuously losing charge throughout the measured density evolution, so wall interactions may be disturbing the evolution of the plasma and forcing it out of the expanding quasi-equilibrium assumed for the temperature inference procedure. It may not be valid to use profile measurements to infer the plasma's temperature under these conditions.

The plasma expansion rate is in good agreement with theoretical predictions[3] at pressures above $\sim 3 \times 10^{-7}$ Torr in the EDG device. The magnetic field scaling of the expansion rate at higher pressures and low rigidity is measured to be proportional to $B^{-2.2}$, in reasonable agreement with the theoretical scaling (B^{-2}) in Eq. (3). Anomalous high temperatures at 1×10^{-6} Torr and 300 G suggest that the plasma may leave its quasi-equilibrium state after the plasma is in good contact with the trap wall.

ACKNOWLEDGMENTS

This research was supported by the Office of Naval Research.

REFERENCES

1. K. A. Morrison, R. C. Davidson, S. F. Paul, E. A. Belli, and E. H. Chao, *Phys. Plasmas* **8**, 3506 (2001).
2. E. H. Chao, R. C. Davidson, S. F. Paul, and K. A. Morrison, *Phys. Plasmas* **7**, 831 (2000).
3. R. C. Davidson and D. A. Moore, *Phys. Plasmas* **3**, 218 (1996).
4. E. H. Chao, S. F. Paul and R. C. Davidson, *J. Vac. Sci. Technol.* **17**, 2034 (1999).
5. E. H. Chao, R. C. Davidson and S. F. Paul, *J. Vac. Sci. Technol. A* **17**, 2050 (1999).
6. E. H. Chao, R. C. Davidson, S. F. Paul, and K. A. Morrison, *Proceedings of the 1999 Workshop on Nonneutral Plasmas* (Princeton University, 1999); American Institute of Physics Conference Proceedings, No. 498, edited by J. Bollinger, R. C. Davidson, and R. Spencer (American Institute of Physics, Melville, NY, 1999), p. 278.
7. J. S. deGrassie and J. H. Malmberg, *Phys. Rev. Lett.* **39**, 1077 (1977).
8. J. H. Malmberg and C. F. Driscoll, *Phys. Rev. Lett.* **44**, 654 (1980).
9. J. S. deGrassie and J. H. Malmberg, *Phys. Fluids* **23**, 63 (1980).
10. J. M. Kriesel and C. F. Driscoll, *Phys. Rev. Lett.* **85**, 2510 (2000).
11. J. Notte and J. Fajans, *Phys. Plasmas* **1**, 1123 (1994).
12. E. H. Chao, Ph.D. Thesis, Princeton University (1999).
13. C. F. Driscoll and J. H. Malmberg, *Phys. Rev. Lett.* **50**, 167 (1983).
14. C. F. Driscoll, K. S. Fine and J. H. Malmberg, *Phys. Fluids* **29**, 2015 (1986).
15. E. H. Chao, R. C. Davidson, S. F. Paul, and K. S. Fine, *Proceedings of the 1999 Workshop on Nonneutral Plasmas* (Princeton University, 1999); American Institute of Physics Conference Proceedings, No. 498, edited by J. Bollinger, R. C. Davidson, and R. Spencer (American Institute of Physics, Melville, NY, 1999), p. 461.
16. R. C. Davidson and E. H. Chao, *Phys. Plasmas* **3**, 2615 (1996).

Decay of the Diocotron Rotation and Transport in a New Low-Density Asymmetry-Dominated Regime

Eli Sarid,^{*} Erik Gilson and Joel Fajans

*Physics Department, University of California, Berkeley
Berkeley, CA 94720-7300*

^{}Permanent address: NRCN, P.O. 9001, Beer Sheva 84190, Israel*

Abstract. The decay of the diocotron rotation was studied in a new regime in which trap asymmetries dominate. The decay does not conserve angular momentum, and is strongest for small, low-density columns. For such columns decay of the diocotron mode within few diocotron periods was observed, orders of magnitude faster than the rotational pumping prediction. However, transition to decay dominated by rotational pumping was observed for larger and denser columns. The new regime is characterized by “magnetron-like” rotation in the trap, dominated by the end confinement fields. The asymmetry-dominated transport was also studied, and found to depend linearly on the line density (and not the density) over nearly 4 orders of magnitude.

INTRODUCTION

The $l=1$ diocotron mode of non-neutral plasmas in Malmberg-Penning traps have been studied for more than 20 years [1]. Usually it has been observed to be a long-lived mode, with 10^4 - 10^5 rotations as a typical damping time. Several years ago, the damping was studied and understood within the “rotational damping” paradigm [2,3]. In this work we describe a new regime of damping and transport for which most of the predictions of “rotational pumping” theory do not hold. This regime is characterized by very fast damping of the diocotron mode, with no conservation of angular momentum. The damping is especially strong for small, low-density columns, and the damping time can be as short as few rotations around the trap axis. There is a solid experimental basis to associate this damping with asymmetries of the end confinement fields, probably due to misalignment of the end confining cylinders with the central cylinder.

However, the appearance of this new regime is not a characteristic of a particular machine. Rather, it is the properties of the trapped electron column that determine whether the diocotron mode is damped due to the rotational pumping mechanism or due to the new asymmetry-dominated mechanism. With the photo-cathode machine, where the new regime was first explored, we were able to retrieve a typical “rotational pumping” behavior for columns that were big and dense enough. And with a second

trap, we similarly found the properties of the new regime when we studied sufficiently small and rarified plasma columns.

In this paper we report on the characteristics of the new regime and contrast them with the behavior typical of rotational pumping. Transport in this asymmetry-dominated regime is also discussed. Using different-size columns, we found that the mobility time t_m depends linearly on the line density (and not the density) over nearly 4 orders of magnitude.

While there is a solid experimental data basis for characterizing the new regime as a magnetron-like, asymmetry-dominated, low-density regime, more work needs to be done theoretically to study the mechanism by which these asymmetries cause the fast damping of the diocotron mode.

EXPERIMENTAL SYSTEM

Most of the experiments presented here were done with the photo-cathode machine of UC Berkeley[4]. The trap consists of just three cylinders, of radius $R_w=20$ mm. The two end confinement cylinders (the "inject" cylinder and the "dump" cylinder) are 8 cm long. The "central" cylinder where the electrons are trapped is 20 cm long. There are no sectors to drive, damp or even listen to the diocotron mode.

The photo cathode machine allows great flexibility in choosing the initial distribution of the electrons. Here this flexibility was used to control two parameters: the size of the column and its initial displacement from the trap axis. Control of the column density is obtained by changing the illumination level of the photo cathode (changing the voltage driving the halogen light source) and by changing the bias level of the photo cathode with respect to the grounded central cylinder. Either the illumination level or the photo cathode bias level can limit the density of the electron columns: the former by determining the number of available electrons emitted from the photo cathode, the latter due to space charge effects. When space charge effects dominate, the bias of the photo cathode is approximately equal to the potential at the center of the resulting electron column. We will refer to this potential as the "plasma potential" or V_p .

The experiments described here were performed with electron columns with initial radius R_p of 1, 2 or 4.5 mm. These will be referred to, according with their diameters, as 2, 4 or 9 mm columns. These radii are small compared with the wall radius R_w . The small radius, combined with low density, is what distinguishes the experiments described here from previous studies of the diocotron damping. The electron densities in our experiments were 10^6 - 4×10^7 cm⁻³.

A 3T-superconducting magnet produces the axial magnetic field required for the trap. Unless noted otherwise, all the photo-cathode machine experiments described below were performed at 3T field.

The diagnostics of the trapped electrons is obtained by dumping them on a phosphor screen, and imaging the screen with a 1024×1024 CCD nitrogen-cooled camera. Almost all of the data analyzed in this work was obtained using these images.

Gradually damping the electrons and measuring the current to the phosphor screen enabled a crude measurement of the electron temperature. A typical temperature of our trapped electrons was 0.5 eV. With plasma potentials of typically less than 2 V (unless otherwise noted), confinement voltages of 20 V were enough to well-confine the electron columns.

To verify that the observations of a new damping regime are “universal” and not particular to a specific machine, we also performed experiments with a second machine. Here a spiral filament produces the electrons and the magnetic field, produced by a water-cooled coil, is limited to 1500 G. Some control on the size and density of the electron columns in this machine is possible by using different bias voltages for the filament. By such technique we observed the diocotron damping for columns with radii of 3 to 11 mm ($R_w=19.05$ mm), and densities of 10^6 - 4×10^7 cm $^{-3}$.

CHARACTERISTICS OF THE NEW REGIME

Fast damping of the diocotron mode was observed for small and low-density electron columns. Figure 1 shows the trajectory of the center-of-mass of such a column with an initial radius of 1 mm, and initial maximum density of 1.2×10^6 cm $^{-3}$. The initial displacement from the center was 2.5 mm ($0.125 R_w$). The decay of the diocotron mode was exponential, with a time constant of 204 ms (about 4 diocotron periods). Figure 1(b) shows that while the decay is very close to being an exponential one, some oscillations with the periodicity of the diocotron mode can be observed.

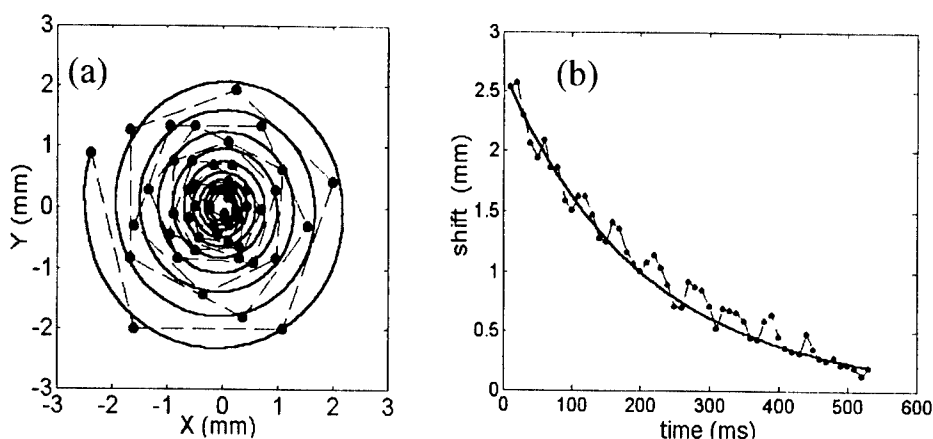


FIGURE 1. a) The trajectory of the center-of-mass of a small and low density electron column. b) The distance from the center as function of time. The solid line is a best-fit to an exponential decay.

The damping time τ_d of the diocotron mode was found to depend on both the density and the size of the electron columns. Here we shall define τ_d as the time it takes for the displacement from the center to decrease to half its initial value. Figure 2 shows the damping time τ_d for 2 and 4 mm columns. The same data is presented as function of four different parameters characterizing the columns: density (Fig. 2a), line density (Fig. 2b), diocotron period (Fig. 2c) and plasma potential (Fig. 2d). It can be seen that for both the 2 mm and the 4 mm columns, τ_d increases linearly with density, line density and plasma potential. However, density is an inadequate parameter to predict τ_d : higher density 2 mm columns can have smaller τ_d than lower density 4 mm columns. Line density (Fig. 2b) is a better predictor, but the best predictors for τ_d are the diocotron period or the plasma potential. 2 mm and the 4 mm columns having similar diocotron periods or similar plasma potentials have also very similar τ_d .

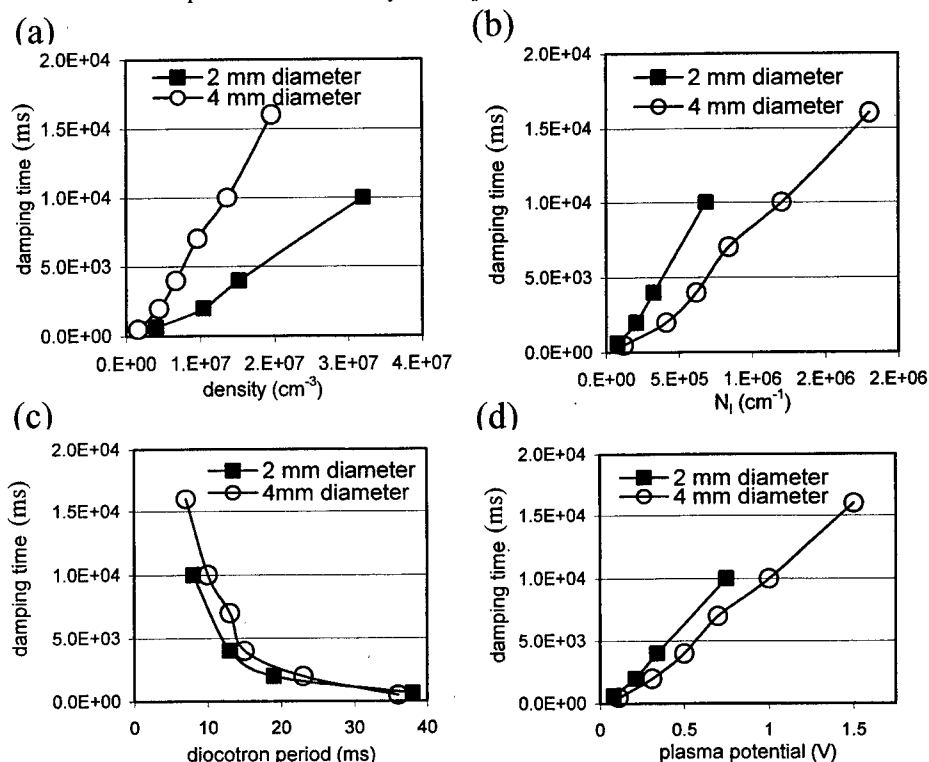


FIGURE 2. Diocotron damping time for columns with initial diameter of 2 and 4 mm. The same data is presented as function of four different parameters characterizing the columns: density, line density, diocotron period and plasma potential.

The dependence on size and density (or on plasma potential) shown in Fig. 2 is very different from the dependence that was found in previous experiments [2] that

could be explained by the rotational pumping theory [3]. The damping rate in the new regime decreases for larger and denser columns, while in the rotational pumping regime, it increases strongly for larger columns, and is approximately independent of the density.

We found that we could obtain diocotron damping following closely the predictions of rotational pumping theory when we started with larger and denser electron columns than those of Fig. 2. Figure 3 presents the results of experiments with 9 mm columns, together with the previously discussed results for the 2 and the 4 mm columns. Since plasma potential proved to be a useful parameter for determining the damping rate for the smaller columns, we continue to use it as the parameter to characterize the columns.

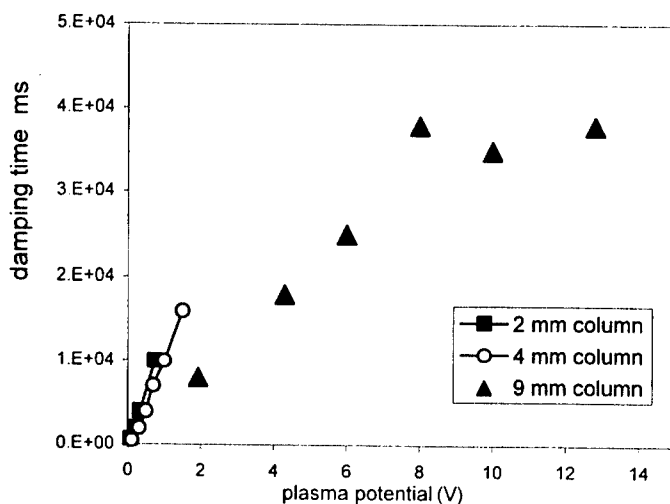


FIGURE 3. Comparison of the diocotron damping time vs. the plasma potential for columns with initial diameter of 2, 4 and 9 mm.

The data for the 9 mm columns in Fig. 3 show the transition between two different regimes: for low density 9 mm columns, with V_p well below 10 V, the damping time increases linearly with plasma potential. For the denser 9 mm columns, however, the damping becomes independent of plasma potential. The damping time of nearly 40 s for the higher density 9 mm columns is in accordance with rotational pumping theory predictions[3]. All the data in Fig. 3 were taken with confinement voltages V_c of 20 V, except for the 2 rightmost points for which a ratio of 0.4 was kept between the plasma potential and the V_c , leading to the use of V_c of 25 and 30 V, respectively (similar transition is observed for constant ratio $V_p/V_c=0.4$ for all the 9 mm points, but we chose to present the $V_c=20$ V data for lower V_p to enable comparison with data for the smaller columns).

The data suggests that the two regimes are dominated by two different and independent mechanisms for the damping of the diocotron rotation. The diocotron mode of the 2 and the 4 mm columns damp almost exclusively by a new mechanism. For large and dense columns this new mechanism becomes weak, while the larger size makes the rotational pumping mechanism strong. The damping for low-density 9 mm columns is lower than the extrapolation of the data for the small columns, showing the combined effects of the two decay mechanisms.

COMPARISON OF THE NEW REGIME AND ROTATIONAL PUMPING

There are important aspects in which the behavior of the new regime is different from that of rotational pumping. The most important one is the lack of conservation of angular momentum in the new regime. Figure 4 follows the evolution in time of the total number of electrons, the displacement from the axis D , the root mean square radius of the electrons with respect to the column center $\langle r^2 \rangle^{1/2}$, and the total angular momentum $D^2 + \langle r^2 \rangle$ for two sets of experiments. On the right side is the evolution characterizing a dense 9 mm column, showing behavior typical of rotational pumping: as the displacement goes down, the column expands so that the total angular momentum remains constant (or even slightly increases). The data on the left side is for a 4 mm column. While the total number of electrons is still conserved, the total angular momentum is definitely not: the expansion is small and is not sufficient to compensate for the decrease of displacement from the center.

Grouping together the data for many sets of experiments, it can be seen that fast damping rate of the diocotron mode is associated with significant loss of angular momentum. Figure 5a shows the ratio of the final and initial angular momentum as function of the number of rotations it took the mode to damp (the "final" angular momentum is for columns that reached the center). Loss of angular momentum was less than half of the initial value for columns for which damping took at least thousands of rotations. When faster damping was observed (hundreds of rotations or less), most of the initial angular momentum was lost.

For the experiments where fast, non-angular-momentum-conserving decay was observed, most of the motion of the columns around the center of the trap was caused by the radial fields near the confining electrodes (a "magnetron" effect). This is to be contrasted by the motion of columns for which slow, angular-momentum conserving decay of the diocotron mode was observed. For the latter, it is the interaction with the image charges that is responsible for the drift motion in the trap. Figure 5b demonstrates this by showing the ratio of the observed diocotron period to that calculated for infinitely-long columns having the same line density distribution as that of the actual columns. The data are presented as function of the same parameter that was used in Figure 5a: the number of rotations it took the diocotron mode to damp. The figure looks very much like Fig 5a: when the decay is fast, end effects are important and angular momentum is not conserved. When the decay is slow, end effect are negligible and angular momentum is conserved.

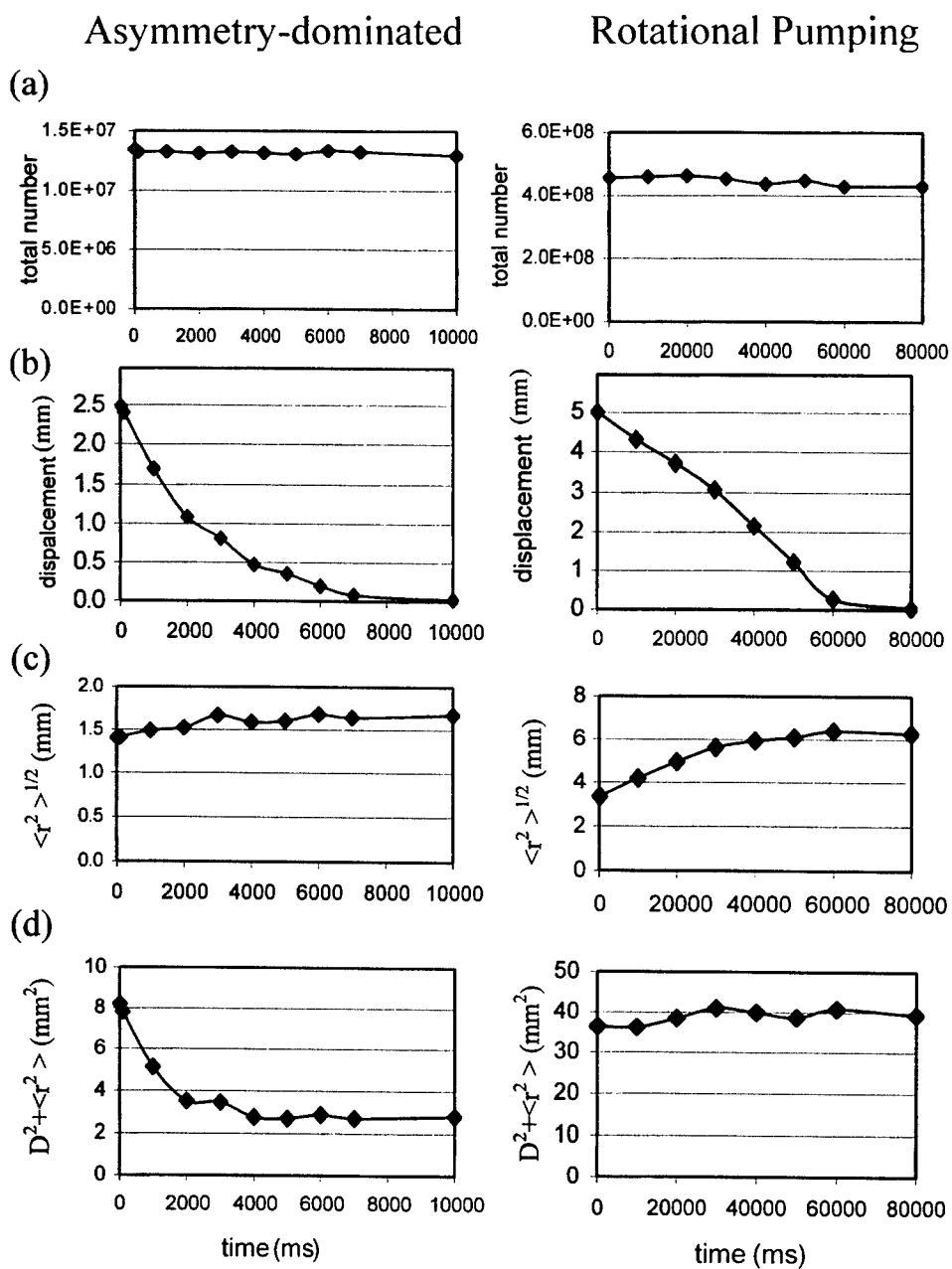


FIGURE 4. Comparison of asymmetry-dominated diocotron decay (left) with a decay dominated by rotational pumping (right). The new regime is characterized by non-conservation of angular momentum (Figure 4d, see text).

The transition between the two regimes is accompanied by one more phenomenon: observed shifts of the position of the “center” around which the columns drift, and on which they finally settle[5]. This shift is significant: up to 1.5 mm ($0.075 R_w$). Most of this shift coincides with the transition region shown in Fig. 5. Thus it coincides with the transition to higher significance of the end confinement fields and to non-conservation of angular momentum. It can be understood if one assumes that the end confinement rings are misaligned with the center ring. We verified that the shift is more sensitive to changed in the end fields near the “inject” ring, where presumably the misalignment is larger.

Putting all the pieces of the puzzle together, we can now characterize the new regime of fast diocotron damping. It is dominated by asymmetries in the end confinement fields that lead to non-conservation of angular momentum.

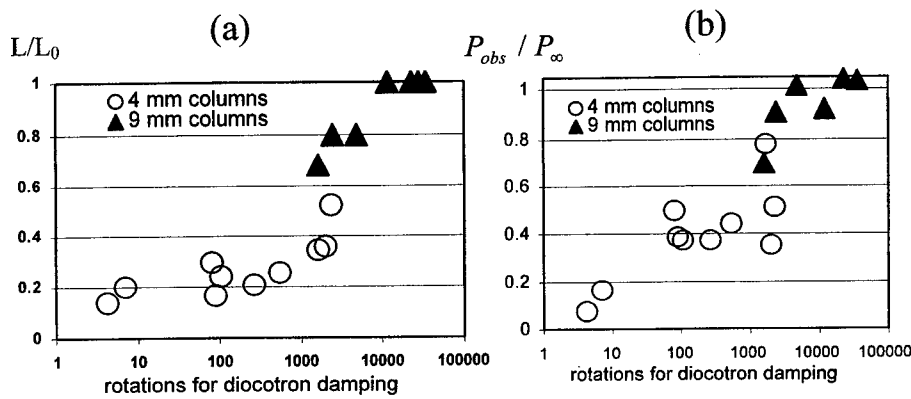


FIGURE 5. (a) level of non-conservation of angular momentum. (b) observed diocotron period relative to the period for an infinitely long column- both vs. the number of rotations for damping of the diocotron mode.

ASYMMETRY-DOMINATED TRANSPORT

The expansion rate observed for off-axis columns is much larger in our experiments than that of on-axis columns, and it increases for larger initial displacements. This holds for both the rotational pumping regime and the asymmetry regime. However, the expansion rate was more substantial in the rotational pumping regime. In that regime it was large enough to compensate for the damping of the diocotron mode in terms of the conservation of angular momentum. In the asymmetry regime this was not the case, as we have seen. For columns starting close to the axis ($\sim 0.1 R_w$), there was little expansion before the columns settled on-axis, and most of the angular momentum associated with the initial displacement was lost.

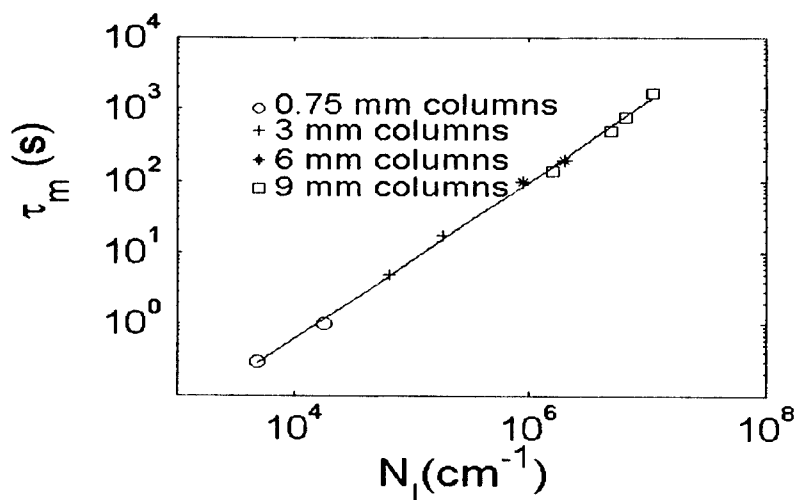


FIGURE 6. τ_m as function of line density. The solid line is a power-law best fit, with slope of 1.1.

Transport for on-axis columns was studied for columns of different size: starting with tiny, 0.75 mm diameter columns, up to the 9 mm columns that were already discussed. It was found that the mobility time τ_m depends nearly linearly on the line density, as shown in Fig. 6 (recently, it was found that τ_m for “rigid” columns depend linearly on density, but only same-size columns were compared [6] in that study).

ADDITIONAL EXPERIMENTAL CHECKS

The ‘universality’ of the new regime was demonstrated in additional experiments performed with a conventional, spiral filament, low magnetic field machine. Changing the size and density of the resulting plasma was done by manipulating the bias voltage of the filament, and an initial displacement was actively introduced using sector patches available in that machine. Although we could not obtain by that means extremely small columns comparable to those studied in the photo cathode machine, we were able to demonstrate that the new regime can be observed in that machine as well. For the smaller and lower-density columns we observed shortening of the decay time (to hundreds of rotations), we saw shifts of the center characterizing the motion of the column in the trap, and also non-conservation of angular momentum. The latter, however, was less clear than in the photo cathode machine because of changes in the measured total number of electrons.

With both machines we checked the effect of the magnetic field on the decay rate. We found, in both, that increasing the field increases the damping time for the smaller, lower-density columns. In the photo-cathode machine, the decay time increased from 150 ms at 5 kG to 650 ms at 30 kG, somewhat weaker than a linear one. For both

machines, the decay rate was found to be weakly sensitive to the steering angle of the magnetic field. That was the case even for tilts of several mrad that caused shifts of the "center" which were larger than that observed when using columns with different plasma potentials (the latter are presumably associated with electric errors).

Finally, in both machines we found that increasing the background gas pressure by 2 to 3 orders of magnitude did not cause significant changes in the decay rate of the diocotron mode.

DISCUSSION

In this work we reported on the finding of a new regime of diocotron-mode decay. Starting with small electron columns displaced from the center of the trap, we studied the rate in which this displacement decays and the column reaches the center of the trap. We found that for small and rarified electron columns this decay is very fast, down to few rotation periods around the center of the trap.

The new regime was found to differ from the known "rotational pumping" regime in almost every aspect. We understand our data on the decay of the diocotron mode as the result of two different decay mechanisms, acting independently of each other. Rotational pumping depends on the length changes that occur during the rotation of the column around its own axis, and is therefore very sensitive to the size of the column. For small columns it becomes weaker. On the other hand, the new regime is insensitive to the size of the column (for fixed plasma potential). Thus it will dominate for small columns, especially if their plasma potential is low also due to low density (rotational pumping decay is independent of density in the regime studied here).

Several phenomena were observed to occur in the transition region between the "rotational pumping" regime and the new regime: increased importance of the end confining fields, shifts in the center around which the columns rotate and finally settle, and non conservation of angular momentum. All these implicate that asymmetries in the end confining fields are responsible for the new regime. The shifts of the center can be understood as being due to misalignment of the end confining rings with respect to the central ring. "Strong" (large and dense) columns rotate around the center of the central rings, because they move primarily due to the effect of the image charges induced on the walls of this ring. On the other hand, "weak" (small and low-density) columns move mainly under the influence of the end fields (magnetron-like motion) and thus are sensitive to the position of the end confinement rings. Table 1 summarizes the differences between the rotational pumping regime and the new, asymmetry-dominated, regime.

The mechanism by which asymmetries in the end fields cause increased damping of the diocotron mode should be further studied. It seems almost to defy the second

law of thermodynamics: one expects non-conservation of angular momentum to increase $\sum r^2$, rather than to decrease it. Violation of the second law does not occur, however, since the displacement from the axis is coupled to a very low rotation frequency, compared with the rotation around the column axis. We think that length changes connected with the motion in the non-symmetric trap are responsible for the observed decay of the diocotron mode. This will be the topic of future work.

TABLE 1. Comparison Between Rotational Pumping and the New Asymmetry Regime		
	Rotational Pumping	New Asymmetry Regime
Conservation of Angular Momentum	yes	no
Prime Mover in Trap	Image charges	End Confinement Fields
Reason for diocotron damping	Length changes (self-rotation)+collisions	Trap asymmetries (asymmetries in the confinement fields)
Damping rate is high for	Large columns	Small low-density columns
Dependence on column radius	Stronger than quadratic	Weak (for fixed plasma potential)
Dependence on plasma potential	Weak (for fixed radius)	linear
B dependence	Weak	$\leq 1/B$

ACKNOWLEDGMENTS

We want to thank Jonathan Wurtele and Vladimir Gorgadze for their work on the theoretical understanding of the observed phenomena. We also thank Tom O'Neil for useful discussions. The research was supported by ONR and NSF.

REFERENCES

1. DeGrassie, J.S. and Malmberg, J.H., *Phys. Fluids* **23**, 63-81 (1980).
2. Cluggish, B. and C.F. Driscoll, *Phys. Rev. Lett.* **74**, 4213-4216 (1995).
3. Crooks, S.M and O'Neil, T.M., *Phys. Plasmas* **2**, 355-364 (1995).
4. Durkin, D. and Fajans, J., *Phys. Fluids* **12**, 289-293 (2000).
5. Dr. Dan Durkin also observed shifts in the rotation centers.
6. Kriesel, J.M. and Driscoll, C.F., *Phys. Rev. Lett.* **85**, 2510-2513 (2000).

Breaking the Azimuthal Symmetry- Jumping off-axis or Staying Away from the Axis?

Eli Sarid,¹ Catalin Teodorescu², Phil Marcus³ and Joel Fajans

Physics Department, University of California, Berkeley, Berkeley, CA 94720-7300

¹*Permanent address: NRCN, P.O. 9001, Beer Sheva 84190, Israel*

²*West Virginia University, P.O. 6315, Morgantown, WV 26506-6315*

³*Mechanical Engineering, University of California, Berkeley, CA 94720*

Abstract. We performed experiments with electrons in a Malmberg-Penning trap, as well as 2D fluid simulations, and found conditions that lead to off-axis equilibrium states. We found that unstable initial distributions whose average distance from the axis is larger than about half the wall radius end up in off-axis states. These states consist of a small strong vortex and a large diffuse background, each having about half of the initial charge. We present a simple model showing that for small initial distributions, on-axis solutions maximize the background radius and thus the entropy. For extended initial distributions, no on-axis solutions are available and staying off-axis is necessary for the conservation of angular momentum.

GOING OFF-AXIS

Several theoretical studies discussed the possibility of off-axis equilibrium states of a cylindrically bounded guiding-center plasma [1-3]. Those solutions were obtained in the frame of statistical theories, based on the assumption of ergodicity, constrained by conservation laws. Those studies were not followed by experimental verification. We demonstrate that such off-axis solution can indeed be obtained, but under different conditions than those implied by previous studies. We also give a simple model, examining a limited phase space, that explains the behavior we observed, and emphasize the importance of the conservation of angular momentum as the reason for “going off-axis”.

Here we show that sufficiently extended, unstable initial distributions of electrons in a Malmberg-Penning trap can end up in off-axis states. We corroborate our experiments with 2D fluid simulations showing the same behavior. The transition between initial distributions that lead to on-axis and off-axis solutions is quite sharp: the average distance of the electrons from the trap axis needs to be about half the wall radius, r_w , for off-axis solutions to be obtained. The exact geometry of the initial distribution is not crucial: we obtained the same behavior whether we started with rings, bars (elongated rectangles) or tri-bars (three rectangles merging in the center of the trap). All the initial distributions had on-axis center-of-mass, and led to off-axis solutions when they were sufficiently extended.

The electron experiments were performed with the photo-cathode machine [4]. With this machine, various initial distributions of electrons could be easily obtained. The time evolution is studied with repeated experiments, damping the electrons on a phosphor screen after varying hold times.

Figure 1 shows an example for a typical time evolution, starting with a large ring of electrons. The ring breaks due to diocotron instability into discrete "vortices". After a short period of mixing and merging these vortices end up in a single strong vortex, and an extended "background". In the case of Fig. 1, this background reached the trap wall and has also a "hole" in it. The smaller coherent vortex, with density comparable to the initial one, is shifted off-axis. So is, although to a lesser degree, the center of mass of the total distribution of the electrons. All this happens on a short time scale (30 ms) over which it can be assumed that 2D fluid-like physics is sufficient to understand the phenomena. Over a much longer time scale (hundreds of ms) the center of mass slowly approaches the axis of the trap.

Figure 2 shows an example for a time evolution, with a smaller ring of electrons as the initial distribution. Qualitatively, the evolution is similar to that of the larger distribution: the ring breaks into discrete "vortices", the vortices merge and eventually end up in a single strong vortex with an extended "background". Here, however, the smaller coherent vortex is on-axis. The background is more uniform than in Fig. 1 and does not reach the wall (for even smaller rings, we find backgrounds with smaller radius in the final state).

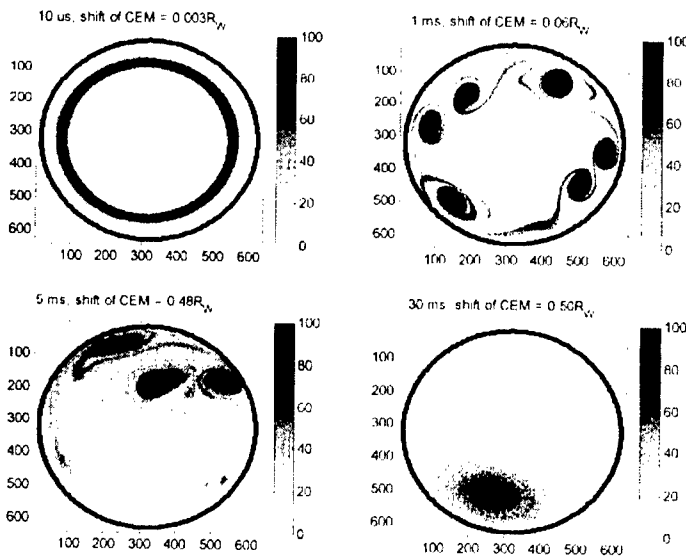


FIGURE 1. Going off-axis: with a large ring of electrons as the initial condition.

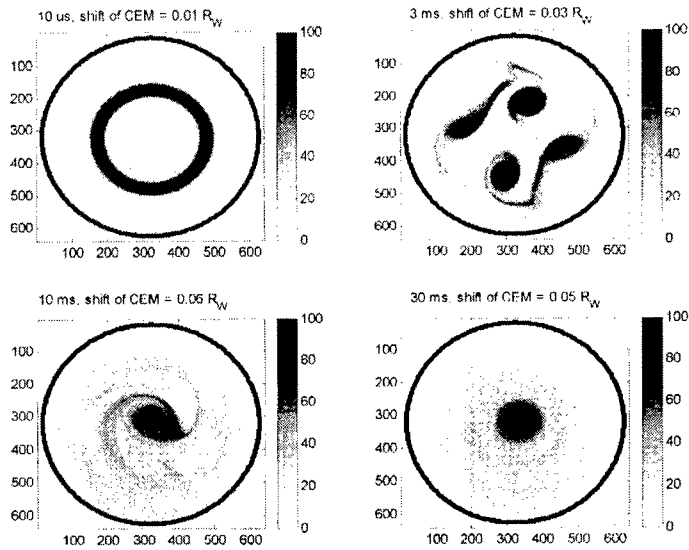


FIGURE 2. Staying on-axis: with a small ring of electrons as the initial condition.

There is a relatively sharp transition between the initial conditions that lead to on-axis solutions and those that lead to off-axis ones. Figure 3 shows the shift of the strong coherent vortex as function of the average initial radius of the ring. It can be seen that for rings whose average initial radius was smaller than about half the wall radius, on-axis vortices result. For larger rings, off-axis states appear, with a steep increase of the shift as function of the initial radius.

To verify our assumption that the observed phenomenon can be understood within the frame of 2D fluid dynamics, we ran a simulation solving the Euler equation using a spectral code. Indeed, the same transition from on-axis to off-axis states was observed in the simulation. The simulation was useful also in verifying that going off-axis happens with strict conservation of charge and angular momentum.

The experiments using bars and the tri-bars as the initial distributions yielded similarly sharp transitions between the conditions that lead to on-axis solutions and those that lead to off-axis states. In the case of the bars and the tri-bars, the initial distribution naturally broke to two or three vortices, respectively. After the merging of these vortices, an on-axis strong vortex resulted in the case of the smaller shapes, an off-axis one in the case of the more extended initial distributions. In terms of the average distance of the electrons from the axis, the transition occurred in a somewhat smaller average distance ($\geq 0.4 r_w$) than in the rings experiments.

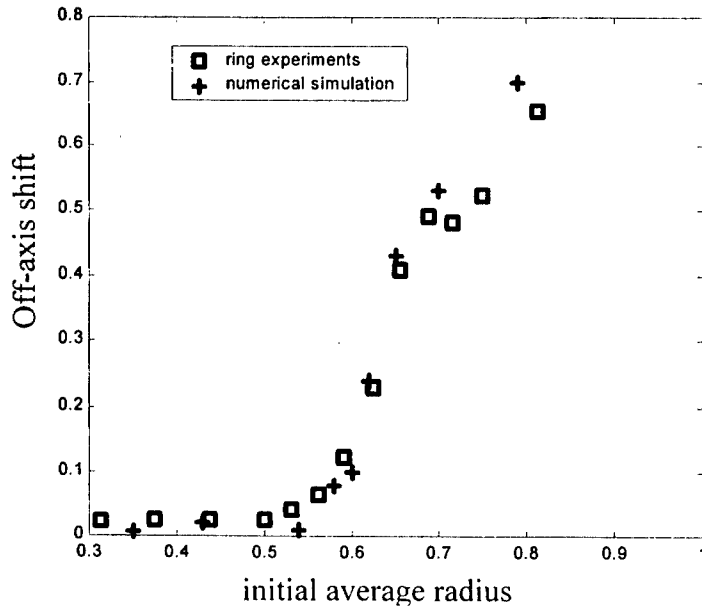


FIGURE 3. Off-axis shift of the coherent “disk” in the final state, as function of the initial average radius of the rings. Both the initial radius and the off-axis shift are normalized for $r_w=1$. There is a very good agreement between the results of the electron experiments and the 2D fluid simulation code.

A SIMPLE MODEL

We found that useful insights can be gained by looking at a very simple model, characterizing the final state with a minimum set of parameters, while restricting these states to those that roughly correspond to those observed in both experiments and simulations. A restricted phase space available to the final states is obtained under the assumption of conservation of total charge, energy and angular momentum.

We shall limit the discussion that follows to the case of a uniform density ring as the initial distribution of charge. The final states that we shall check consist of a high-density small disk and a large diffuse background. Both disk and background are assumed to be circular and of uniform density. The background is centered on the trap axis, while the small disk has a shift D from the axis (D might be zero). The background has radius of r_b (which might be as large as the wall radius, but can also be smaller).

In what follows we shall take two more assumptions, which will limit the number of parameters needed to describe the background to just two: D and r_b . They are:

- 1) The dynamics of the instability, the merging and the mixing, lead to a sizable, approximately constant, fraction of the initial charge to be eventually found in the diffuse background.

- 2) The density of the small “coherent” disk is close to the (uniform) density of the initial ring.

To make these assumptions concrete, we shall assign specific values to the fraction of the initial charge that goes to the final state background, and to the density of the final coherent disk. We choose to look at final states in which half of the initial charge is in the coherent disk and half in the background, with the density of the small disk being 0.7 that of the initial density. The two specific values we choose are based on the results of both the experiments and the simulations, but they are not crucial to the emerging physical picture. With these assumptions, only D and r_b remain as free parameters that characterize the final states. While the actual final states are richer in content than this simple model (see for example the hole in the background in Fig. 1), we find that this model is sufficient to illuminate the physical mechanism behind the going “off-axis”.

Figure 4 shows the families of solutions obtained for various values of r_b , from $r_b=0.6$ up to the cases where the background fills the trap up to the wall radius, $r_b=1$. For each value of the initial average radius of the ring, there is a continuum of possible solutions conserving charge, energy and angular momentum. These solutions have smaller shifts D of the small coherent objects for larger values of the background radius r_b . For average initial radius smaller than about half the wall radius, $D=0$ (on-axis) solutions are available with $r_b<1$. However, no such solutions exist for larger average initial radii. Such large rings have high angular momentum, and, in the frame of our model, conservation of angular momentum is not possible for on-axis states even if the background extends to the wall. The “missing” angular momentum results in the shift of the coherent disk from the axis of the trap.

Among the available solutions for each initial average radius, the system chooses the one with maximum r_b . Maximizing the radius of the background is equivalent in the frame of our model to a requirement of maximum entropy or minimum enstrophy (in the frame of our model, we cannot not distinguish between these two requirements, as they yield the same solutions). With this principle, we can see how Figure 4 predicts the behavior observed in the experiments and in the simulations: up to about half the wall radius, maximizing the radius of the background leads to on-axis solutions. These solutions have larger background for larger initial average radius. The transition to off-axis shifts occurs when the background needs to extend to the wall to satisfy conservation of angular momentum. For larger rings, conservation of angular momentum is possible only for off-axis solutions. The observed shift D grows quickly, and the $r_b=1$ curve is very similar to the shifts observed in Figure 3 for rings whose average radius is larger than half the wall radius.

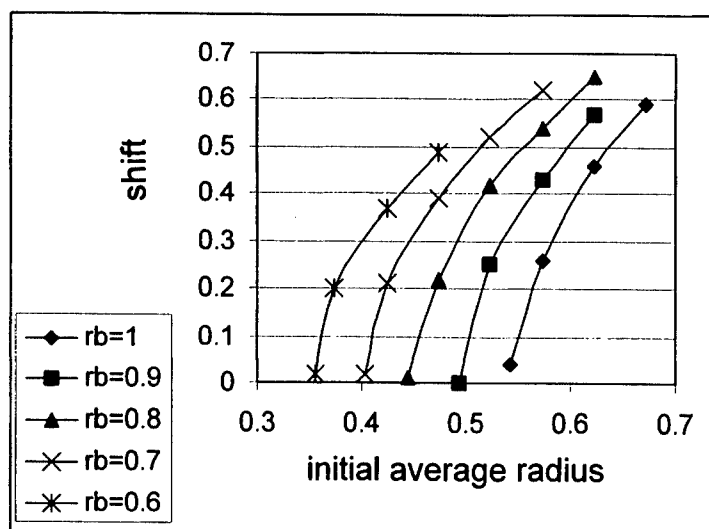


Figure 4. Solutions of the simple model for the final states, satisfying conservation of charge, energy and angular momentum, for various background radii.

DISCUSSION

In our model we discussed only the initial and final states, and we considered the states available under the constraints of conservation of charge, angular momentum and energy. In these we followed the attitude of previous studies [1-3]. Unlike those studies, however, we further restricted the final states considered to those that consist of both a strong coherent vortex and a diffuse background, each having half the charge. The exact fraction of the initial charge found in the background is not crucial. We verified that modified assumptions, putting a third or two thirds of the charge in the background, lead to the same transition between on-axis and off-axis solutions. Only the position of the transition point shifts somewhat as we vary our assumptions.

More can be said about the dynamics that leads to the production of the final states we considered. The evolution of the intermediate stages, after the initial unstable distribution breaks, has some resemblance to the behavior of a system of point vortices [5]. Studying the case of point vortices distributed on a ring, we found the even for Havelock unstable configurations, the center of mass stays on-axis if the vortices are distributed on a small enough ring. For vortices distributed over a circle with a radius larger than about half the wall radius, the center of mass goes off-axis. But such considerations are limited, because they do not consider the mixing and merging that lead to the extended background, carrying a sizable (about half) of the initial charge. Maximizing the extent of this background leads to on-axis states available only up to a certain initial radius.

In summary, we studied the production of off-axis equilibrium states, and for the first time presented both experiments and simulations in which they result. With a simple model, we showed that going off-axis could be understood as necessary to conserve angular momentum in a restricted family of solutions available to the system when the initial angular momentum is large. These solutions maximize the radius of the background, thereby maximizing entropy or minimizing enstrophy. Emphasizing the role of angular momentum threshold is in contrast to previous studies [1-3] that suggested that the transition occurs for distributions that have high energy for a given value of angular momentum.

ACKNOWLEDGMENTS

We thank Leah Zimmerman for performing some of the first experiments showing that large rings go “off-axis”. The help of Ashraf Youssef who wrote the 2D fluid simulation code is greatly appreciated. The research was supported by NSF and ONR.

REFERENCES

1. Smith, R.A., *Phys. Rev. Lett.* **63**, 1479-1482 (1989).
2. Smith, R.A., and O’Neil, T.A., *Phys. Fluids B* **2**, 2961-2975 (1990).
3. Chen, P. and Cross, M.C., *Phys. Rev. E* **54**, 6356-6363 (1996).
4. Durkin, D. and Fajans, J., *Phys. Fluids* **12**, 289-293 (2000).
5. Durkin, D. (private communication).

SECTION 6

2D FLUID DYNAMICS

Two-Dimensional Vortex Dynamics With Background Vorticity

David A. Schecter

Advanced Study Program

National Center for Atmospheric Research,¹ P.O. Box 3000, Boulder, CO 80307

Abstract. Magnetized electron plasmas have been used to study the dynamics of two-dimensional vortices in a cloud of background vorticity. Experiments have shown that background vorticity can calm chaotic vortex motion, and cool a system of intense vortices into a crystal equilibrium. Further experiments have shown that weak vortices tend to migrate to extrema in the background vorticity distribution. The electron plasma experiments have motivated new theories on two-dimensional vortex dynamics with background vorticity. The experiments and related theories are summarized.

Energetic, roughly two-dimensional (2D) vortices abound in nature [1]. Examples are oceanic eddies, tropical cyclones, and the Jovian hurricanes. Remarkably, magnetized electron plasmas are excellent systems for studying high Reynolds-number 2D vortex dynamics experimentally [2]. Recent electron plasma experiments have shed light on how 2D vortices interact with the environmental flow, i.e., with background vorticity. This article reviews the experiments, and related theories.

ELECTRON PLASMA EXPERIMENTS

Figure 1 is a schematic diagram of the experimental device [2]. A long column of electrons is confined in a hollow cylindrical conductor. The electrons are trapped axially by negative dc voltages on two end-cylinders, and radially by a uniform axial magnetic field $B\hat{z}$. The apparatus is equipped to destructively measure the z -averaged electron density $n(r, \theta, t)$. By raising the voltage of one end-cylinder (right), the electrons are released onto a phosphor screen. The resulting density image is recorded with a CCD camera. The evolution of n is observed by a sequence of experiments, in which the the initial conditions are the same, but the release-times vary.

Under proper conditions [2], the electron density n is governed approximately by a set of two-dimensional fluid equations, known as 2D drift-Poisson flow:

¹⁾ The National Center for Atmospheric Research is supported by the National Science Foundation.

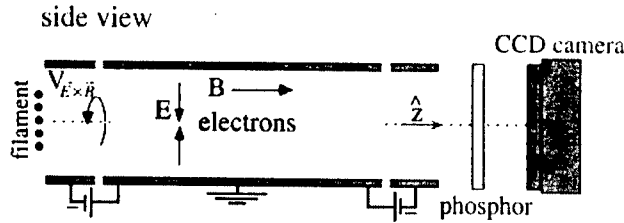


FIGURE 1. Confinement device (Penning-Malmberg trap) and imaging diagnostic, used to study 2D vortex dynamics with an electron plasma.

$$\frac{\partial n}{\partial t} + \vec{v} \cdot \nabla n = 0, \quad \vec{v} = -\nabla \frac{c}{B} \phi \times \hat{z}, \quad \nabla^2 \phi = 4\pi e n. \quad (1)$$

Here, $\vec{v}(r, \theta, t)$ is the $\vec{E} \times \vec{B}$ drift velocity field, and $\phi(r, \theta, t)$ is a 2D electrostatic potential. The boundary condition on the electrostatic potential is $\phi = 0$ at the wall of the confinement cylinder.

Defining the streamfunction, $\psi(r, \theta, t) \equiv c\phi/B$, and the vorticity, $\zeta(r, \theta, t) \equiv \hat{z} \cdot \nabla \times \vec{v}$, we may recast 2D drift-Poisson flow as follows:

$$\frac{\partial \zeta}{\partial t} + \vec{v} \cdot \nabla \zeta = 0, \quad \vec{v} = -\nabla \psi \times \hat{z}, \quad \nabla^2 \psi = \zeta. \quad (2)$$

By amazing coincidence, Eqs. (2) are the 2D Euler equations, which also govern two-dimensional flows in uniform-density inviscid incompressible fluids.

Comparing (2) to (1), we see that the vorticity ζ is proportional to the electron density n by the relation $\zeta = 4\pi e c B^{-1} n$. So, in the electron plasma experiments, *measuring electron density is equivalent to measuring vorticity*.

CHAOS TO CRYSTAL

Figure 2(a) shows the evolution of electron density (vorticity) in an experiment performed at the University of California, San Diego [3]. Initially, the density is distributed in a spiral, resembling a hot tungsten filament that is used to create the electrons. Subsequently, the density evolves into a system of N clumps (dark spots) immersed in a diffuse background plasma. Each density clump corresponds to an intense vortex, spinning counter-clockwise, and the diffuse background plasma corresponds to a low level of background vorticity.

To appreciate the influence of background vorticity on the vortex motion, let us first consider the vortex dynamics without background vorticity. In the absence of background vorticity, the vortex dynamics is Hamiltonian. Ignoring minor wall effects, the Hamiltonian is given by [4]

$$H = -\frac{1}{4\pi} \sum_{i < j} \Gamma_i \Gamma_j \ln [(x_i - x_j)^2 + (y_i - y_j)^2], \quad (3)$$

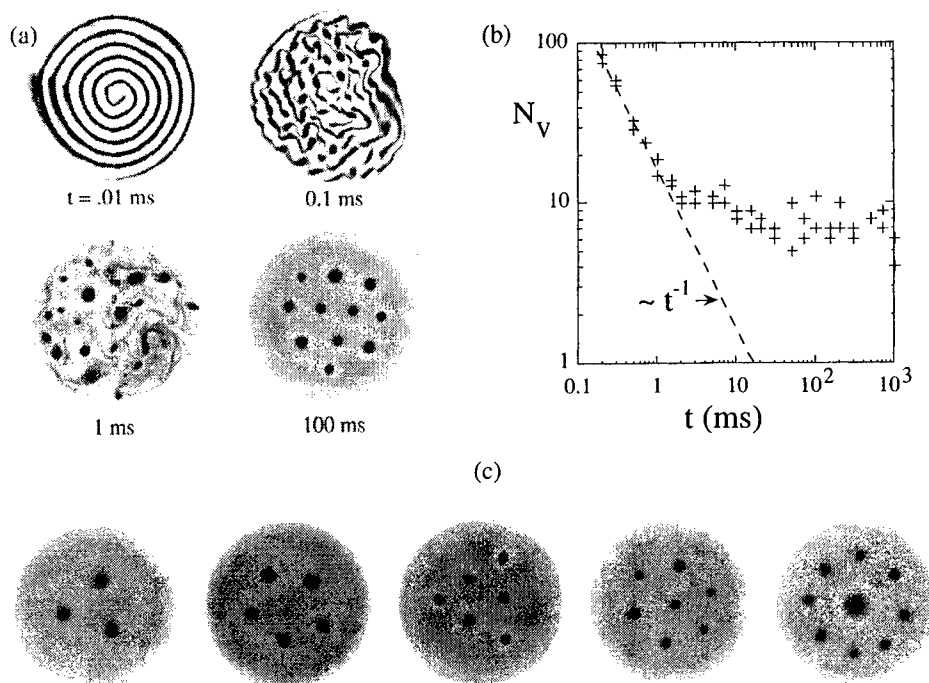


FIGURE 2. Spontaneous formation of a vortex crystal in an initially turbulent electron plasma [3]. (a) Time evolution of z -averaged electron density (vorticity). Darker shades indicate higher density. (b) Number of vortices versus time. (c) Selection of vortex crystals obtained from initial conditions similar to that in (a).

where Γ_i is the circulation (area integral of vorticity) of the i^{th} vortex, (x_i, y_i) is the position of the i^{th} vortex in a Cartesian coordinate system, and $i, j = 1, 2, \dots, N$. The canonically conjugate coordinates are $(q_i, p_i) \equiv (\sqrt{\Gamma_i} x_i, \sqrt{\Gamma_i} y_i)$, and the dynamics is given by Hamilton's equations: $\dot{q}_i = \partial_{p_i} H$, $\dot{p}_i = -\partial_{q_i} H$.

Because the vortex dynamics is Hamiltonian (without background vorticity), it is generally chaotic. During this chaotic motion, two vortices occasionally become close enough to merge. Numerical simulations of 2D Hamiltonian vortex dynamics, punctuated by occasional mergers, show that the number of vortices N_v decays as a power law in time, $t^{-\xi}$, where ξ is a positive constant of order unity [5]. Figure 2(b) compares the expected power-law decay to an electron plasma experiment. The scatter in the data is due to the destructive imaging technique. Initially, N_v exhibits the expected power-law decay; however, when $t \simeq 10$ ms, mergers cease.

The arrest of vortex mergers is due to the formation of a "vortex crystal" equilibrium [Fig 2(a), 100ms; Fig. 2(c)]. A vortex crystal is an array of intense vortices that rotates rigidly in a diffuse background. Jin and Dubin proposed that vortex crystals form due to the ergodic mixing of background vorticity by the intense vor-

tices [6]. Using a version of Lynden-Bell statistics [7], they showed that a vortex crystal equilibrium is the most probable state that can result from such mixing, for a given energy, angular momentum and total circulation of the flow. These maximum entropy states are compared to the experiments in Ref. [6]: they accurately predict the arrangement of vortices, and details of the background vorticity distribution.² Since the electron plasma experiments, the formation of vortex crystals has been observed in various numerical simulations of 2D Euler flow [8,9].

MOTION TO THE EXTREMA

The spontaneous formation of vortex crystals in 2D turbulence demonstrates the importance of background vorticity in spectacular fashion. Of course, other effects of background vorticity have been recognized for decades. For example, it is well-known that vortices move toward extrema of the background vorticity distribution. The details of this process have been studied rigorously in dynamical meteorology [12], for the main purpose of understanding hurricane trajectories.³ However, a new theory was required to explain the vortex motion in electron plasmas [13].

Unlike terrestrial hurricanes, vortices in electron plasmas are typically exposed to intense background shear. In this sense, electron vortices are more like Jovian hurricanes, which are contained in strongly sheared zonal jets [10], or mesovortices within hurricanes [9,11]. Intense background shear creates a disparity in the rates at which vortices of opposite sign migrate to extrema of background vorticity. Furthermore, sufficiently large shear will arrest the migration. These results are discussed below.

Figure 3(a) is a numerical simulation that illustrates vortex motion through axisymmetric background vorticity, similar to what might exist in an electron plasma. At $t = 0$, a clump (black dot) and a hole (white dot) are placed at the same radius r_v . The clump is a positive vortex, spinning counter-clockwise, whereas the hole is a negative vortex, spinning clockwise. In time, both vortices redistribute the local background vorticity. In response, the clump moves radially inward, to the peak of background vorticity, whereas the hole moves radially outward, toward a minimum of background vorticity.

The opposite motion of clumps and holes is easily understood. Suppose that there is only one vortex of circulation Γ_v , and that the vortex is point-like. The vorticity distribution is a sum of the background contribution (b) and the vortex contribution (v); i.e., $\zeta = \zeta_b + \Gamma_v \delta(\vec{r} - \vec{r}_v)$. It is well-known that the 2D Euler equations, with rotationally symmetric boundary conditions, conserve the canonical angular momentum,

²⁾ The final number of vortices and their individual vorticity profiles are not predicted. They are taken from the observed vortex crystals and fixed in computing the maximum entropy states.

³⁾ The background vorticity affecting hurricane motion includes planetary vorticity, as well as the vorticity associated with the environmental wind.

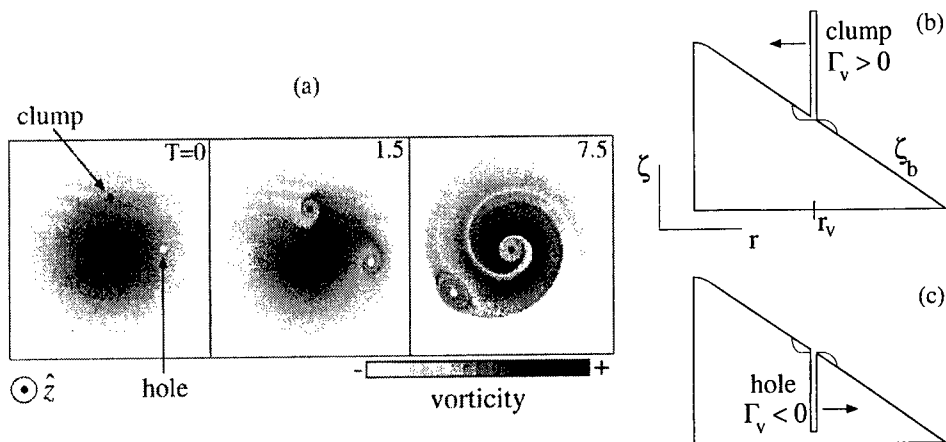


FIGURE 3. Vortex motion in an axisymmetric background vorticity distribution. (a) Numerical simulation. $T \equiv t \times |S[r_v(0)]|$. (b,c) The redistribution of local background vorticity by a vortex increases $\langle r^2 \rangle_b$. By conservation of P_θ , clumps and holes must react oppositely.

$$P_\theta \equiv \int d^2\vec{r} \zeta r^2 = \Gamma_b \langle r^2 \rangle_b + \Gamma_v r_v^2. \quad (4)$$

Here, $\Gamma_b > 0$ is the total circulation of the background flow, and $\langle r^2 \rangle_b$ is the ζ_b -weighted spatial average of r^2 . As illustrated in Figs. 3(b) and 3(c), the redistribution of background vorticity by the vortex tends to create a local plateau in the θ -average of ζ_b . This increases $\langle r^2 \rangle_b$. To conserve P_θ , a clump ($\Gamma_v > 0$) must decrease r_v and move up the background vorticity gradient, whereas a hole ($\Gamma_v < 0$) must increase r_v and move down the gradient.

Let us now consider the vortex-background interaction in greater detail. The Euler equation for the evolution of vorticity can be written as two separate equations. The first equation is for the vortex motion,

$$\frac{d}{dt} \vec{r}_v = \vec{v}_b(r_v, \theta_v, t). \quad (5)$$

Here, \vec{v}_b is the background velocity field; that is, $\vec{v}_b = -\nabla\psi_b \times \hat{z}$, where $\nabla^2\psi_b = \zeta_b$. Since the background vorticity is initially axisymmetric, i.e., $\zeta_b(\vec{r}, t=0) = \bar{\zeta}_b(r)$, the background velocity is initially circular, i.e., $\vec{v}_b(\vec{r}, t=0) = \bar{v}_b(r)\hat{\theta}$. The second equation is for the advection of background vorticity,

$$\frac{\partial}{\partial t} \zeta_b + (\vec{v}_b + \vec{v}_v) \cdot \nabla \zeta_b = 0, \quad (6)$$

where $\vec{v}_v = \hat{z} \times \Gamma_v (2\pi)^{-1} \nabla \ln(|\vec{r} - \vec{r}_v|)$ plus a small correction due to the wall. The vortex trajectory is obtained by integrating Eqs. (5) and (6) simultaneously.

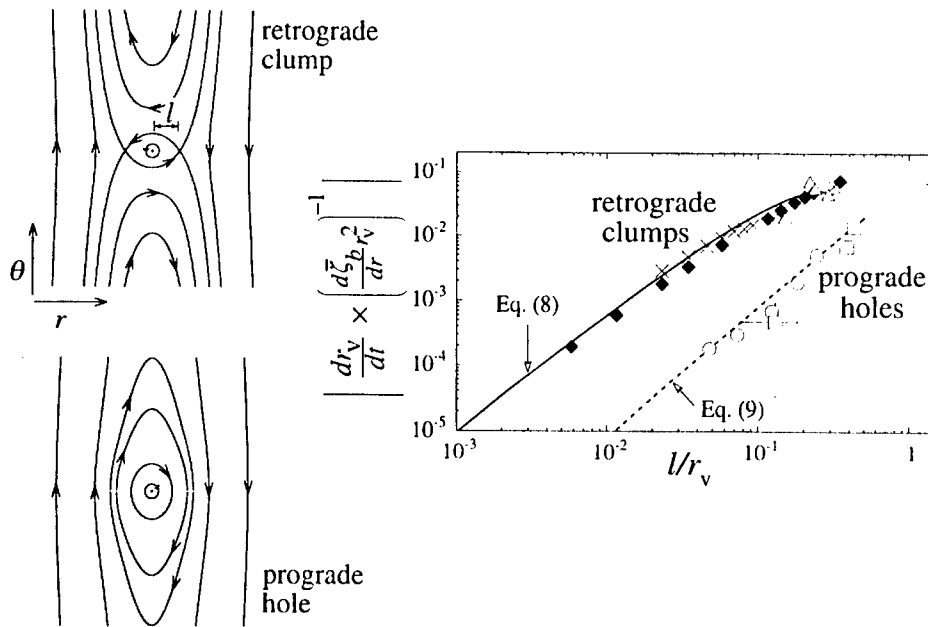


FIGURE 4. (Left) Stream lines about a retrograde clump and a prograde hole. (Right) The radial speeds of retrograde clumps and prograde holes of various strengths (l/r_v) in axisymmetric background vorticity. Retrograde clumps: the \times s and diamonds are numerical simulations, the triangles are electron plasma experiments, and Eq. (8) is computed with $c = 0.43$. Prograde holes: the circles are numerical simulations, and the squares are electron plasma experiments.

Neglecting changes to ζ_b [Eq. (6)], a single vortex merely orbits the center of background vorticity, with angular frequency $d\theta_v/dt = r_v^{-1}\bar{v}_b(r_v)$. However, as explained previously, the background vorticity perturbation causes the vortex to drift radially. The radial velocity, dr_v/dt , is sensitive to whether the vortex is retrograde or prograde. A vortex is retrograde if it rotates against the local background shear, whereas a vortex is prograde if it rotates with the local background shear. Precisely, let $S(r)$ denote the local shear-rate, $r d(\bar{v}_b r^{-1})/dr$. Then, $\Gamma_v/S(r_v) < 0$ for a retrograde vortex, whereas $\Gamma_v/S(r_v) > 0$ for a prograde vortex. Here, we consider examples in which the background vorticity decreases monotonically with r , so that $S(r)$ is negative. Therefore, in these examples, clumps are retrograde and holes are prograde.

The stream lines about a retrograde clump and a prograde hole are shown in Fig. 4 (left). There are two stagnation points at radial distances $\pm l$ from the center of the retrograde vortex, where

$$l \equiv \sqrt{\left| \frac{\Gamma_v}{2\pi S(r_v)} \right|}. \quad (7)$$

In contrast, there are no stagnation points in the vicinity of a prograde vortex.

Schecter and Dubin [13] derived analytical expressions for the radial velocities of retrograde and prograde vortices, for the regime in which $l/r_v \ll 1$. This regime corresponds to a weak vortex in strong background shear. For a retrograde vortex,

$$\frac{d}{dt}r_v = \pm \frac{\pi}{2} \frac{d\bar{\zeta}_b}{dr}(r_v) l^2 \ln(c r_v/l), \quad (8)$$

where $+/-$ is for clumps/holes, and c is a constant of order unity that depends on the particular form of $\bar{\zeta}_b(r)$. For a prograde vortex,

$$\frac{d}{dt}r_v = \pm \frac{1}{4\pi} \frac{d\bar{\zeta}_b}{dr}(r_v) l^2. \quad (9)$$

In both cases, the radial speed increases with the local background vorticity gradient, and decreases as the local shear-rate intensifies. Note that the prefactor $(1/4\pi)$ in Eq. (9) is much less than the prefactor $(\pi/2)$ in Eq. (8). Moreover, the logarithmic factor does not appear in Eq. (9). Thus, as l/r_v approaches zero, a prograde vortex will move orders of magnitude slower than a retrograde vortex of equal strength.

The plot in Fig. 4 shows the radial vortex velocity (dr_v/dt) as a function of vortex strength (l/r_v) for a set of numerical simulations, and for several electron plasma experiments. In each case, a single vortex moved through a background vorticity resembling that in Fig. 3(a).⁴ The simulations are described in Ref. [13], and the experiments are described in Refs. [14,15]. The data compares favorably to the analytical predictions of Schecter and Dubin. Recently, Kiwamoto and collaborators used a magnetized electron plasma to examine the motion of retrograde clumps more extensively [16]. Their data also agrees with Eq. (8).

The data in Fig. 4 are for cases in which $\varepsilon(r) \equiv \frac{d}{dr} \left(\frac{\bar{v}_b}{r} \right) / \frac{d\bar{\zeta}_b}{dr} \ll 1$ at the radial position r_v of the vortex. However, if $\varepsilon(r_v)$ surpasses a critical value, Eqs. (8) and (9) become invalid, and the radial velocity of the vortex drops abruptly to zero. For prograde vortices, Schecter and Dubin estimated that the critical value of $\varepsilon(r_v)$ is unity. For retrograde vortices, Schecter and Dubin estimated that the critical value of $\varepsilon(r_v)$ is of order $\sqrt{8\pi^2 \ln(r_v/l)}$. Both estimates are consistent with numerical simulations [13].

DANCING WITH THE DIOCOTRON MODES

The theoretical work of Schecter and Dubin [13] neglects the interaction of the vortex with the global modes of the background vorticity, i.e., the diocotron modes. While usually valid (Fig. 4), such neglect is unjustified if the orbital frequency of a vortex resonates with a neutral, or weakly damped diocotron mode. In such a case,

⁴) There is one exception: the datum with error bars was obtained from an electron plasma experiment in which there were two prograde holes [15].

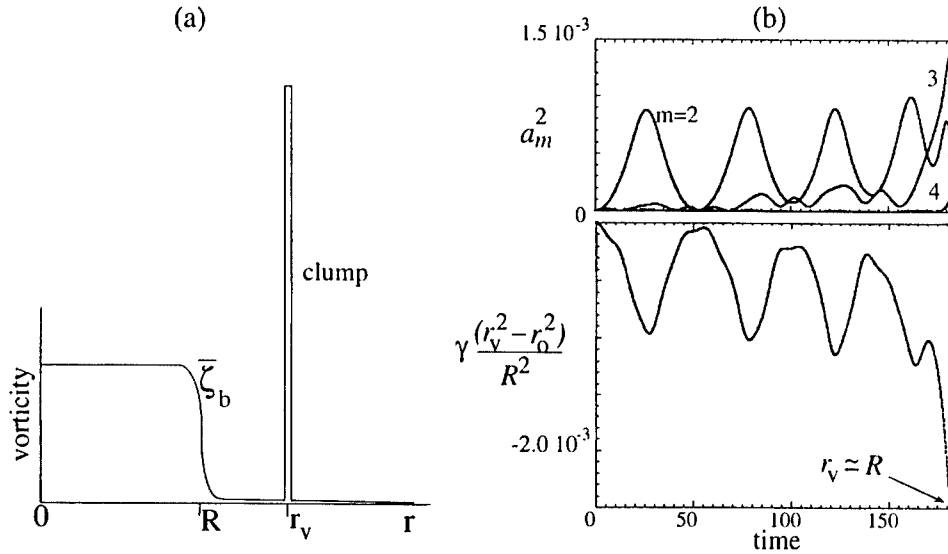


FIGURE 5. Example in which the radial motion of a clump is controlled by diocotron modes, as opposed to a local background vorticity perturbation. (a) Initial vorticity distribution. (b) Diocotron mode amplitudes and radial position of the clump versus time, in units of $2\pi R^2/\Gamma_b$. A sequence of resonances causes the clump to merge with the core of the background vorticity [17].

there can be significant radial motion even if $\frac{d\bar{\zeta}_b}{dr}(r_v)$ is zero, or if $\varepsilon(r_v)$ is above its critical value. The following example illustrates this point.

Consider the initial vorticity distribution in Fig. 5(a). The background vorticity $\bar{\zeta}_b(r)$ consists of a uniform core ($r < R$), and an outer skirt ($r > R$), where the vortex resides. By assumption, the vorticity in the outer skirt is negligible, so that $\Gamma_b \simeq \pi R^2 \bar{\zeta}_b(0)$. In addition, $d\bar{\zeta}_b/dr \simeq -\bar{\zeta}_b(0)\delta(r - R)$.

The background vorticity perturbation will be concentrated at the core radius R . Expanding this perturbation in a Fourier series yields

$$\zeta_b \simeq \bar{\zeta}_b(r) + \frac{\Gamma_b}{\pi R} \delta(r - R) \sum_{m=1}^{\infty} a_m(t) \cos[m\theta - \varphi_m(t)], \quad (10)$$

where $\Gamma_b/\pi R$ is a convenient normalization factor. The Fourier components are the “diocotron modes” of the background vorticity. Exciting a diocotron mode corresponds to displacing ($m = 1$) or deforming ($m \geq 2$) the core. In the following, it will be assumed that the vortex is weak and that the mode amplitudes are small; i.e., $\gamma \equiv \Gamma_v/\Gamma_b \ll 1$, and $a_m \ll 1$. Changes to the axisymmetric component of background vorticity are of order a_m^2 , and are neglected in Eq. (10).

The vortex-mode dynamics may be put in Hamiltonian form [17]. The canonically conjugate variables for the m^{th} mode are $(q_m, p_m) \equiv (-\varphi_m, a_m^2/m)$, and the

canonically conjugate variables for the vortex are $(q_v, p_v) \equiv (-\sqrt{\gamma} \theta_v, \sqrt{\gamma} r_v^2/R^2)$. The equations of motion are Hamilton's equations: $(\dot{q}_m, \dot{p}_m) = (\partial_{p_m} H, -\partial_{q_m} H)$, and $(\dot{q}_v, \dot{p}_v) = (\partial_{p_v} H, -\partial_{q_v} H)$, where (ignoring wall effects)

$$H = -\frac{\Gamma_b}{2\pi R^2} \times \left\{ \gamma \ln(p_v) + \sum_{m=1}^{\infty} (m-1) p_m - 2\gamma \sum_{m=1}^{\infty} \gamma^{\frac{m}{4}} \sqrt{\frac{p_m}{m p_v^m}} \cos \left[\frac{m}{\sqrt{\gamma}} q_v - q_m \right] \right\}. \quad (11)$$

The first term in braces accounts for the advection of the vortex in the unperturbed circular flow. The middle term accounts for the free propagation of diocotron modes, in the absence of the vortex. The final term couples the vortex motion to the modes. The Hamiltonian in Eq. (11) neglects mode-mode interaction terms, which are of order a_m^2 .

Of course, the vortex-mode interaction conserves canonical angular momentum. Minus the constant unperturbed background contribution, the (dimensionless) canonical angular momentum can be written as follows:

$$\tilde{P}_\theta = \sum_{m=1}^{\infty} a_m^2 + \gamma \frac{r_v^2}{R^2}. \quad (12)$$

Suppose that a clump ($\gamma > 0$) excites a mode. Then, $\sum a_m^2$ increases. To conserve \tilde{P}_θ , r_v must decrease. In contrast, if a hole ($\gamma < 0$) excites a mode, r_v must increase to conserve \tilde{P}_θ .

Figure 5(b) illustrates the vortex-mode dynamics governed by the Hamiltonian in Eq. (11). At $t = 0$, a clump ($\gamma = .0025$) is placed at $r_v = r_o = 1.418R$, and the mode amplitudes are all zero. The clump principally orbits the center of the background with angular velocity $d\theta_v/dt \simeq \bar{v}_b(r_v)/r_v = \Gamma_b/2\pi r_v^2$. At $r_v = 1.418R$, this angular velocity equals the natural phase velocity of the $m = 2$ diocotron mode. Consequently, the clump resonantly excites the $m = 2$ mode. By conservation of \tilde{P}_θ , this resonance causes the clump to move radially inward. As the clump approaches the core, $d\theta_v/dt$ increases. This causes resonances with higher order diocotron modes: first the $m = 3$, then the $m = 4$, etc. The sequence of resonances incrementally pulls the clump into the core.

Lansky, O'Neil and Schechter [17] derived a condition for which the clump will merge with the core. For the case in which the initial clump position is $r_o = 1.418R$, γ must be greater than about 0.002. Otherwise, the initial oscillations of r_v [Fig. 5(b)] will not bring the clump close enough to the core to resonantly excite higher order modes. Electron plasma experiments have yet to verify this merger condition.

However, Durkin and Fajans [18] have used a magnetized electron plasma to examine the interaction of diocotron modes with a clump that is already inside the core ($r_v < R$). In this case, there are no vortex-mode resonances. Nevertheless, the clump can weakly excite the diocotron modes. This creates a wave along the

edge of the core. Eventually, the wave breaks. The wave-breaking process alters the background vorticity profile, and can generate one or more vorticity holes. The measured wave-breaking time is proportional to $\gamma^{-1} \ln(\gamma^{-1})$, provided that $r_v \lesssim 0.7R$. This result agrees with a recent theory by Jin and Dubin [19].

Clearly, background vorticity enriches 2D vortex dynamics. Background vorticity can cause the spontaneous formation of vortex crystals (Fig. 2), and can spatially separate vortices of opposite sign (Fig. 3). Recent work in non-neutral plasma physics has shed some light on 2D vortex dynamics with background vorticity, but surely more surprises await.

ACKNOWLEDGMENTS: The author thanks Prof. C.F. Driscoll and Dr. A. Kabantsev for providing experimental data. The author also thanks Prof. D.H.E. Dubin, Prof. T.M. O'Neil, Dr. I.M. Lanski and Dr. D.Z. Jin for their contributions to the theory presented. This research was supported in part by the National Science Foundation (PHY-9876999) and the Office of Naval Research (N00014-96-1-0239).

REFERENCES

1. D.G. Dritschel and B. Legras, *Phys. Today* **46**, 44 (1993).
2. C.F. Driscoll and K.S. Fine, *Phys. Fluids B* **2**, 1359 (1990).
3. K.S. Fine, A.C. Cass, W.G. Flynn and C.F. Driscoll, *Phys. Rev. Lett.* **75**, 3277 (1995).
4. G.K. Batchelor, *An Introduction to Fluid Dynamics*, Cambridge Univ. Press (1967).
5. G.F. Carnevale, J.C. McWilliams, Y. Pomeau, J.B. Weiss and W.R. Wang, *Phys. Rev. Lett.* **66**, 2735 (1991).
6. D.Z. Jin and D.H.E. Dubin, *Phys. Rev. Lett.* **80**, 4434 (1998).
7. D. Lynden-Bell, *Mon. Not. R. Astron. Soc.* **136**, 101 (1967).
8. D.A. Schecter, D.H.E. Dubin, K.S. Fine and C.F. Driscoll, *Phys. Fluids* **11**, 905 (1999); D.Z. Jin and D.H.E. Dubin, *Phys. Rev. Lett.* **84**, 1443 (2000).
9. J.P. Kossin and W.H. Schubert, *J. Atmos. Sci.* **58**, 2196 (2001).
10. R. Beebe, *Chaos* **4**, 113 (1994).
11. M.T. Montgomery, V.A. Vladimirov and P.V. Denissenko, *J. Fluid Mech.*, submitted.
12. G.F. Carnevale, R.C. Kloosterziel and G.J.F. Van Heist, *J. Fluid Mech.* **233**, 119 (1991); R.K. Smith and W. Ulrich, *Q.J.R. Meteorol. Soc.* **119**, 207 (1993); R.T. Williams and J. C.-L. Chan, *J. Atmos. Sci.* **51**, 1065 (1994); More in Ref. [13].
13. D.A. Schecter and D.H.E. Dubin, *Phys. Rev. Lett.* **83**, 2191 (1999); D.A. Schecter and D.H.E. Dubin, *Phys. Fluids* **13**, 1704 (2001).
14. A. Kabantsev, C.F. Driscoll, D.H.E. Dubin and D.A. Schecter, to appear in 11th Intl. Toki Conf. on Potential and Structure in Plasmas (Nagoya, Dec. 2000);
15. X.P. Huang, K.S. Fine and C.F. Driscoll, *Phys. Rev. Lett.* **74**, 4424 (1995).
16. Y. Kiwamoto, K. Ito, A. Sanpei and A. Mohri, *Phys. Rev. Lett.* **85**, 3173 (2000).
17. I.M. Lansky, T.M. O'Neil and D.A. Schecter, *Phys. Rev. Lett.* **79**, 1479 (1997).
18. D. Durkin and J. Fajans, *Phys. Rev. Lett.* **85**, 4052 (2000).
19. D.Z. Jin and D.H.E. Dubin, *Phys. Fluids* **13**, 677 (2001).

Continuously Injected Plasma Columns

Tom Pasquini, Joel Fajans

Department of Physics, University of California, Berkeley, CA, 94720

Abstract. Electron plasma columns continuously injected into a Malmberg-Penning trap display a rich evolution. Electrons emitted from an illuminated photocathode are trapped in the electrostatic well formed by the negatively biased photocathode and the trap end cylinder. Initially, the injections form cylinders of uniform density. As the density increases, the columns hollow in an attempt to match the potential profile of the equipotential cathode. The hollow columns are subject to the diocotron instability, and as the evolution becomes increasingly turbulent, the columns slowly expand to the trap wall. We present preliminary results and analysis of the trapping mechanism and the 2D dynamics of a continuously injected system.

INTRODUCTION

Malmberg-Penning traps consist of a series of collimated conducting cylinders, or gates, aligned along a strong magnetic field. Electron plasmas are confined in these traps by appropriately biasing the trap cylinders to form an axial electrostatic well. Radial confinement is provided by a strong magnetic field. Electrons are injected into the trap by momentarily grounding an “inject” gate near the cathode, and allowing electrons from the negatively biased cathode to enter the trap (Fig. 1). The plasma can be imaged by briefly grounding the “dump” gate. The image formed on the phosphor screen is recorded by a CCD camera. Typically, electrons are injected into a trap for only a short time; here we study this injection process and examine the columns formed by long-term injection. For these studies we used the Berkeley Photocathode trap [1], in which electrons are created by photoemission. The trap is otherwise similar to most other Malmberg-Penning traps, and employs a magnetic field of 3T.

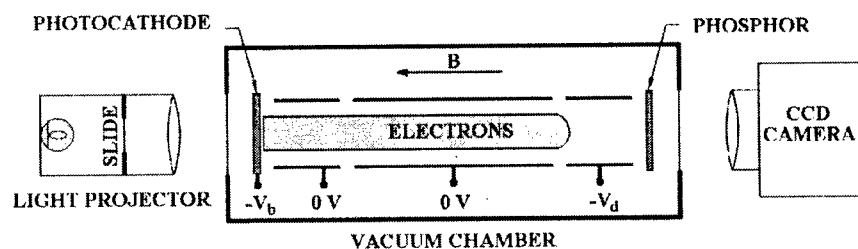


FIGURE 1. Schematic of the experimental apparatus during injection phase. The inject gate is on the left, and the dump gate on the right.

INJECT TIME DEPENDENT TRAPPING

Initially, electrons ejected from the cathode enter the trapping region, reflect off the dump gate, and are reabsorbed by the cathode. The electron density depends on the cathode current and the bounce time of an average electron. Calculations based on an average axial energy of 5eV and the measured electron emission current of $10\mu\text{A}$ ¹ from the photocathode give an electron density of $3\times 10^6\text{e}/\text{cm}^3$. Thus, there are approximately 2×10^7 electrons circulating in the 10cm long, 0.5 cm radius column. These electrons are trapped when the inject gate is biased negatively. Measurements (Fig. 2) find roughly similar numbers. However, as shown in the figure, the number of trapped electrons increases with time. At $100\mu\text{s}$ the number of trapped electrons is an order of magnitude greater than the number trapped initially.

Trapping Mechanism

Since the negatively biased photocathode forms a potential barrier, it can trap low energy electrons. Unperturbed electrons emitted from the photocathode have sufficient energy to traverse the trap and be reabsorbed by the photocathode. If, however, an electron loses axial energy within the trapping region (Fig. 3), it may not be able to return to the photocathode. This energy loss could result from a collision with a neutral gas atom, another electron, or from an electrostatic instability.

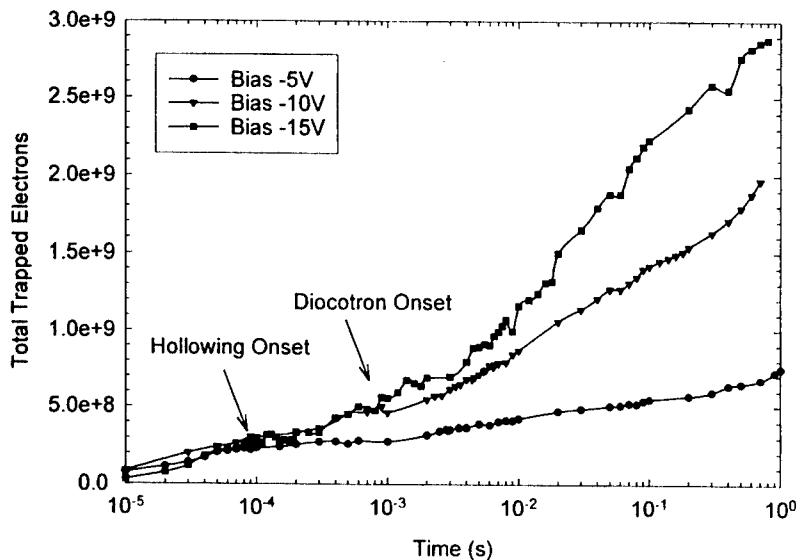


FIGURE 2. The total number of trapped electrons as a function of time for three values of the photocathode bias. The arrows indicate the approximate location of the onset of the column hollowing and diocotron stages of column evolution.

¹ Initially, the cathode operates in the emission limited regime.

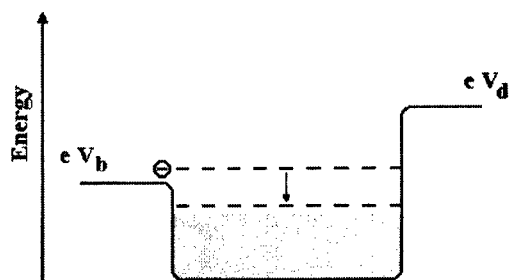


FIGURE 3. An electron may become trapped between the photocathode (V_b) and the dump gate (V_d) if it suffers an energy loss within the trapping region.

Residual gas collisions do not explain the observed trapping rates [2]. The residual gas in the trap is likely Cesium (Cs) at a chamber pressure of $<10^{-8}$ Torr ($n_{Cs}=3\times10^{14}\text{m}^{-3}$). Thus, using the Cs cross-section $\sigma = 5\times10^{-18}\text{m}^2$, the trapping rate is $2\times10^4\text{e}^-/\mu\text{s}$, two orders of magnitude smaller than the experimental trapping rate. Additionally, no change in the trapping rate is seen when the chamber pressure is raised to 10^{-6} Torr by turning the chamber pump off for several minutes.

Electron-electron collisions are also insufficient to explain the observed trapping rate. Assuming that an electron must scatter by 10° to become trapped and that the electron density is $1\times10^7\text{cm}^{-3}$, the calculated trapping rate is $1\times10^3\text{e}^-/\mu\text{s}$, three orders lower than the observed trapping rate. Note that only large angle scattering events are relevant, as multiple small angle collisions do not have time to operate in one transit.

EVOLUTION OF CONTINUOUSLY INJECTED PLASMAS

As the total charge increases, the system progresses through four stages [2]. In the first stage, the density of the column rises from approximately $10^6\text{e}^-/\text{cm}^3$ to approximately $10^7\text{e}^-/\text{cm}^3$ within the first $100\mu\text{s}$ of injection. The column profile changes from peaked at the center to flat-topped over this same time (Fig. 4a,b). For longer injection times, the column begins to hollow out as the space charge inhibits further injection into the center of the column. The central density decreases slightly while the density of the outer edge increases by a factor of three. By approximately 1ms , the column profile has become very sharp at the edge (Fig. 4c). The resulting column potential matches the cathode potential, in agreement with predictions by Driscoll and Malmberg [3]. The hollow ring configuration is unstable and undergoes a diocotron instability lasting approximately 10ms (Fig. 4d,e,f). In the final stage (beyond 100ms), the circumference of the original column emits streams of electrons that become wrapped into strong vortices orbiting in a diffuse background (Fig. 4g). The hollow column expands to several times its original size, eventually coming into contact with trap wall.

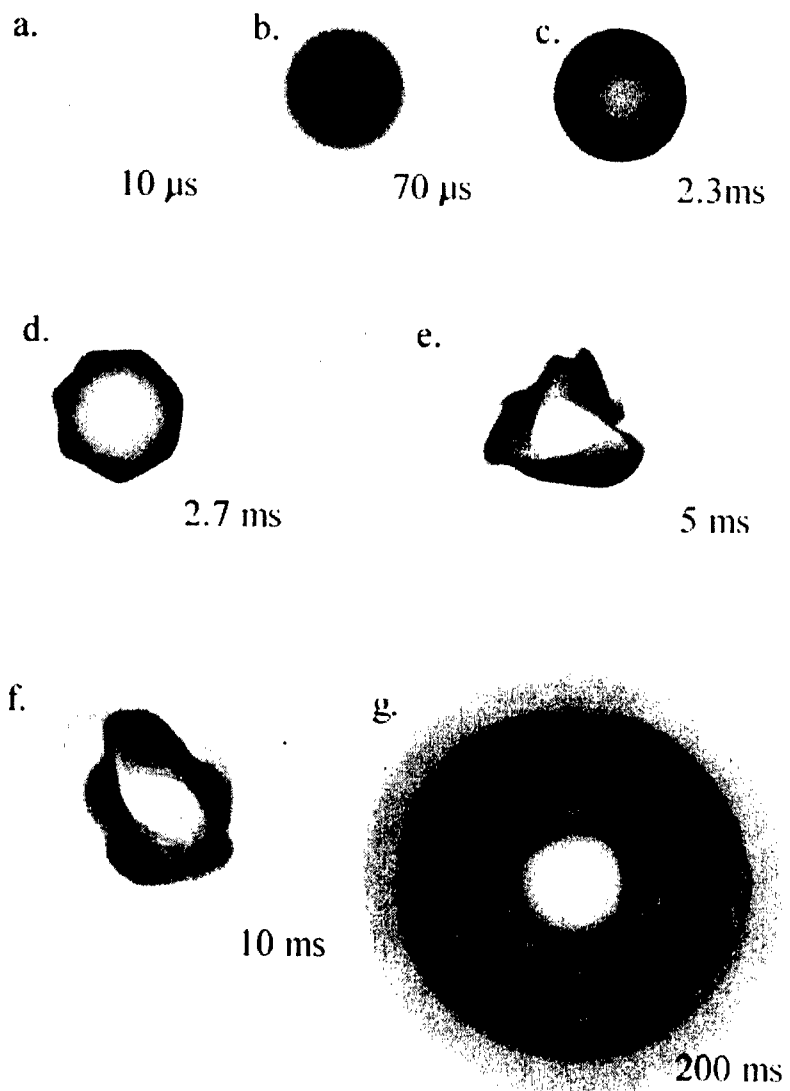
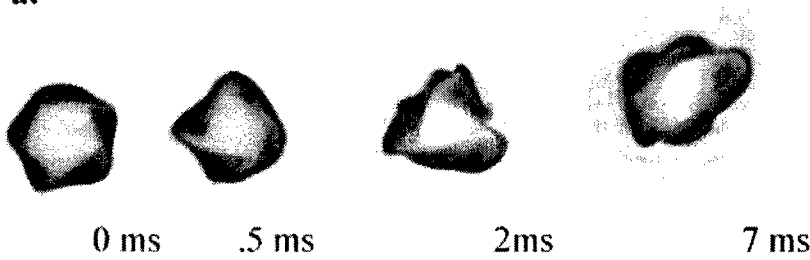


FIGURE 4. The evolution of a continuously injected plasma column demonstrating the four stages described in the text. The gray scales for the first 3 images (a,b,c) are the same to emphasize density differences as the column evolves to its hollow state. The edge of image (c) is highly saturated, masking the sharp profile along the circumference. The remaining images have been individually scaled for contrast. Color images may be found at <http://socrates.berkeley.edu/~fajans/>.

a.



b.

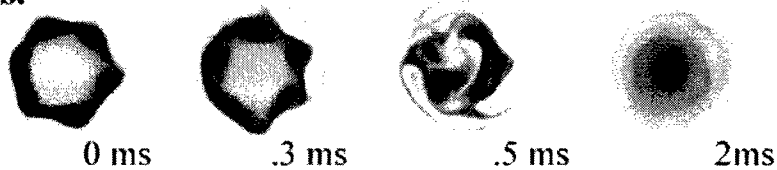


FIGURE 5. The progression of the diocotron instability a) in the presence of electron injection and b) without injection. Times shown are the time after the onset of the instability.

While the initial hollowing of continuously injected plasma columns is well understood, the evolution beyond the onset of the diocotron instability has not been studied previously. The diocotron instability itself changes in the presence of a background injection of electrons. The side-by-side progression sequences in Figure 5 show that the diocotron instability proceeds more slowly. This may be due to newly injected electrons smearing the diocotron density structures, thereby decreasing the self-consistent fields that drive the instability. The progression of the instability also expands the column significantly with the background electron injection. Normally, angular momentum conservation inhibits the expansion of the electron column. When electrons are continuously injected however, the new electrons change the angular momentum and the column can expand.

The final state of the system is a central ring surrounded by several strong vortices. Filaments often join the vortices and the central ring, and all these structures are immersed in a diffuse background (Fig. 6). New electrons enter the system primarily on the central ring. We postulate that this state results as follows: As shown in Figure 6a, the strong vortices deform the central ring. These deformations become filamented and extend radially away from the central ring, eventually winding around themselves. The small-scale structures in the resulting spirals smear out (Fig. 6b), and the spirals turn into vortices. Interactions with other vortices stretch, and eventually break the filaments connecting the vortices to the central ring. Newly formed vortices

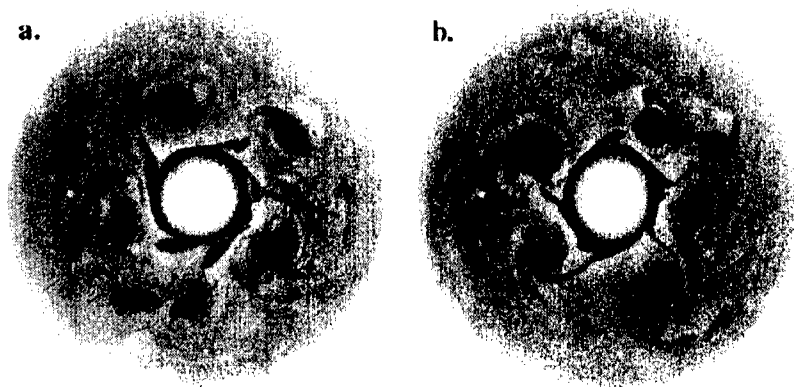


FIGURE 6. The long-term evolution of a continuously injected plasma column. The circumference of the original column is continuously supplied with electrons from the photocathode. Figure a) shows the early stages of filamentation (A) perturbation and (B) extension. Figure b) shows the later stages (C) capture and (D) spiraling. Images are representative of development at 200ms.

interact turbulently with the other vortices. Eventually viscosity destroys the vortex, and the vortex smears into the background. Before the vortex dissipates, it may come close enough to the central ring to cause a deformation, reinvigorating the cycle.

CONCLUSIONS

As shown by this work, the injection of plasma columns by a photocathode shows several well-defined stages of development. The theory for this development is not fully formed at this time, nor is the trapping mechanism understood. In the future, we hope to explore the trapping mechanism and its effect on electron temperature, density and 2D dynamics.

ACKNOWLEDGMENTS

Dr. Dan Durkin observed many of the phenomena recorded here and developed the trap itself. We thank Prof. Philip Marcus for discussions of 2D dynamics. This work is supported by NSF and ONR.

REFERENCES

1. D. Durkin and J. Fajans, *Rev Sci. Instrum.*, **70**:4539, 1999.
2. D. Durkin, Ph.D. Thesis, University of California. Berkeley, 1998.
3. C.F. Driscoll and J.H. Malmberg, *Phys. Fluids*, **19**:760, 1976.
4. A.J. Peurrung and J. Fajans, *Phys. Fluids A*, **5**:493, 1993.

Experimental and Numerical Study of Asymmetric Vortex Merger in a Pure Electron Plasma

M. Amoretti*, D. Durkin[†], J. Fajans[†], R. Pozzoli* and M. Romé*

*I.N.F.M. (U.d.R. Milano Università) and Dipartimento di Fisica, Università degli Studi di Milano,
Via Celoria 16, 20133 Milano, Italy

[†]Department of Physics, University of California at Berkeley, Berkeley, California 94720-7300

Abstract. The merging of an intense localized vortex with an extended vortex is investigated by means of an experimental analysis performed on a Malmberg-Penning trap with photocathode, and numerical simulations with a two-dimensional (2D) particle in cell (PIC) code. The study is restricted to highly nonlinear conditions, where the perturbative approach does not hold. A very good agreement between experimental results and simulations is obtained. It is found that the localized vortex is firstly wrapped around by the extended vortex, then moves towards the center of the system, eventually approaching an almost stationary state of rotation characterized by the formation of vorticity holes. During the whole evolution the extended vortex gains energy from the field surrounding the vortices, while the energy of the localized vortex remains constant.

INTRODUCTION

Under suitable conditions, the dynamics perpendicular to the imposed magnetic field of a pure electron plasma confined in a Malmberg-Penning trap is equivalent to that of a 2D incompressible, inviscid fluid [1], where the vorticity ζ is proportional to the 2D electron density n . This fact allows to investigate on such a system nonlinear processes occurring in 2D inviscid flows; in particular vortex merger and filamentation, which play a dominant role in the evolution of turbulence [2].

We consider here the process of interaction between an extended vortex and one very localized vortex (almost pointlike) under conditions, which have now become experimentally accessible, where the existing perturbative analysis [3] does not apply. The experimental investigation of this process is performed on a Malmberg-Penning trap (see Fig. 1) with photocathode [4], which allows to produce well-defined and well-localized vortices of almost uniform vorticity. The interpretation of the process is based on the Hamiltonian character of the motion, and numerical simulations with the 2D (in real space) PIC code XOOPIC [5].

Numerical investigations of the interaction of two isolated vortices of uniform vorticity, were reported, e.g., in Refs. [6, 7, 8]. In Ref. [6], in particular, it was pointed out the possibility of a merger by "entrainment" of the larger-vorticity region within the smaller-vorticity region. In Ref. [8], all possible regimes of interaction were investigated, but assuming identical vorticity for the two vortices. These works were all based on contour dynamics simulations. In Ref. [7], based on the use of a low-order Hamiltonian moment

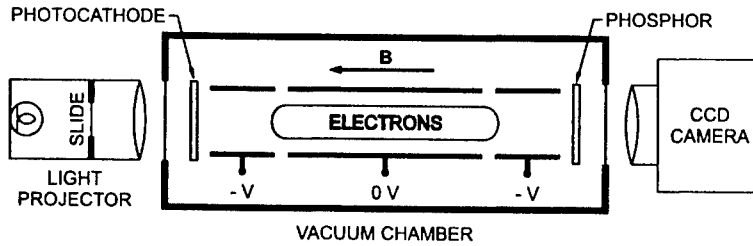


FIGURE 1. The Malmberg-Penning Trap with the photocathode [4]. The desired initial 2D electron distribution is created by projecting the appropriate light image onto a cesium antimonide photocathode and grounding the left cylinder; electrons are emitted only where there is light, and they stream along the magnetic field lines into the central confinement region, preserving their distribution.

model and a pseudospectral algorithm, it was pointed out how the interaction between two unequal vortices, of different size and vorticity, could cause one of the two vortices to dominate. In the language of Ref. [7], the case studied here corresponds to the smaller vortex being *victor*.

The dynamics of the system is described by the divergence-free velocity field $\mathbf{u}(x, y, t) = \mathbf{e}_z \times \nabla \psi(x, y, t)$, where the evolution of the stream function ψ is determined by the conservation of the vorticity $\zeta \equiv \mathbf{e}_z \cdot \nabla \times \mathbf{u}$,

$$\partial \zeta / \partial t + [\zeta, \psi] = 0, \quad (1)$$

where $[a, b] \equiv \partial a / \partial y \cdot \partial b / \partial x - \partial a / \partial x \cdot \partial b / \partial y$ is the Poisson bracket, the coordinates y, x are conjugate variables with respect to the Hamiltonian ψ , and

$$\nabla^2 \psi = \zeta. \quad (2)$$

The functions ψ and ζ are related to the electric potential ϕ and electron density n by the relations $\phi = (B/c)\psi$ and $n = (B/4\pi ec)\zeta$, respectively, where B is the magnetic field strength and the other notations are standard. The evolution of the system is determined by appropriate initial and boundary conditions for ψ . In particular, the free-slip boundary condition $\psi = 0$ on the circular wall corresponds to the condition $\phi = 0$ for the electrostatic potential.

We refer to two initially circular vortices with uniform vorticities $\zeta_e \ll \zeta_p$, and initial radii $a_e \gg a_p$ (the indices e, p denote the extended and the pointlike vortex, respectively). The experimentally investigated range of parameters in general corresponds to conditions, in which the initial field ψ exhibits a separatrix, with its X-point located outside the two vortices. Reference parameters can be taken $\Gamma_p/\Gamma_e \approx 10^{-1}$, with the initial distance d between the centers of the two vortices in the range $1 + \Gamma_p/\Gamma_e < d/a_e < 2$, with $\Gamma_{e,p} = \pi \zeta_{e,p} a_{e,p}^2$ the circulation of the two vortices. A discussion of the characteristics of the merging process when the above parameters are varied is reported in Ref. [9].

In the cases under consideration the analysis which can be carried on, following Refs. [3, 10, 11], has a very narrow domain of validity since the shape of the extended vortex is soon highly distorted from its initial condition, the merging being very fast and lasting few rotation periods.

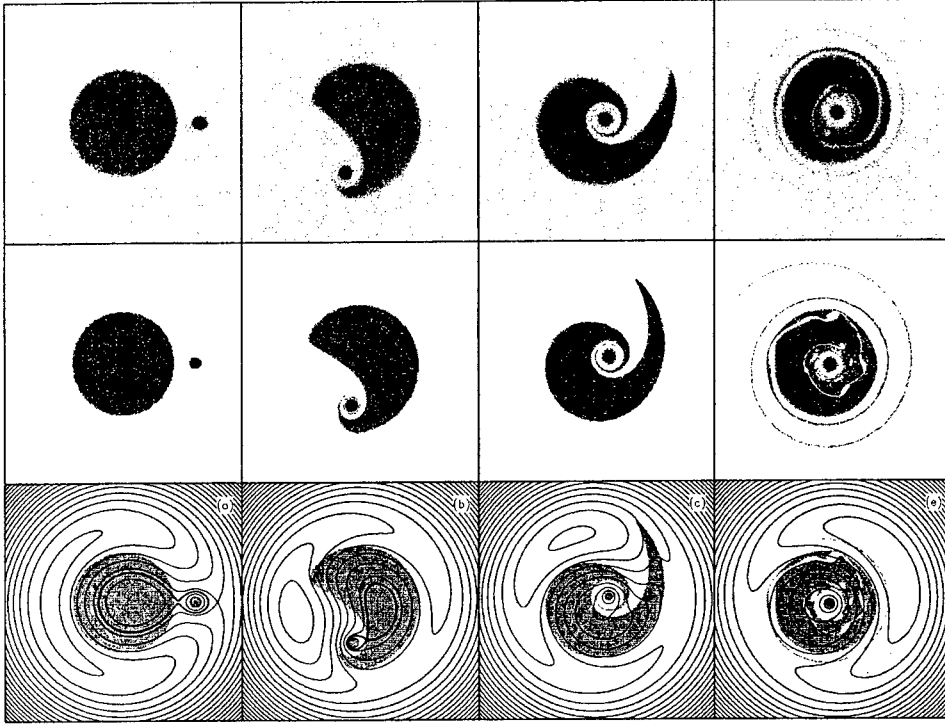


FIGURE 2. Time evolution of the interaction of a point vortex with an extended vortex. First row: density (experimental results). Second row: density (PIC simulation). Third row: contour plot of the corotating potential $\bar{\Psi}$ (PIC simulation): the thick line represents the separatrix crossing the extended vortex. The lengths are normalized over R_w . From left to right, the data refer to $t = 0.0, 0.5, 1.0$, and 4.0 , respectively, with the time measured in units of the period of rotation of the extended vortex, $4\pi/\zeta_e$.

Fig. 2 in the first row shows the experimentally detected images (the intensity is proportional to the axially integrated electron density) at different times of the evolution: from the initial condition to the final almost stationary state. The corresponding plots obtained by PIC simulations are shown in the second row of the same figure. The number N of macroparticles used in the simulations is $\leq 10^5$ with a 256×256 square grid. The parameters of the simulation are the same as in the experimental situation. The stability of the results with respect to variations of N and grid size has been verified.

The agreement between experimental data and simulation shows that the behavior of the system is indeed 2D Eulerian, even in this highly nonlinear regime; this confirms the potentiality of Malmberg-Penning traps for fluid dynamics experiments.

To describe the evolution of the system, we focus on the behavior of the stream function in a reference frame which rotates with the angular velocity, ω , of the localized vortex, $\bar{\Psi} = \psi - \omega(x^2 + y^2)/2$. The initial condition of the system appears far from the equilibrium, which is characterized by a vorticity field depending on the space variables only through $\bar{\Psi}$. In the case under consideration, we chose a value of ω corresponding

to the angular velocity of the localized vortex, $\omega \simeq \Gamma_e/(2\pi d^2)$. For high enough values of the ratio Γ_p/Γ_e (verifying the conditions mentioned above), a separatrix of the $\bar{\psi}$ field exists, with an hyperbolic point located between the centers of the two vortices, as shown in the first plot in the third row of Fig. 2. Moreover, such separatrix crosses the extended vortex so that a finite part of it lies outside the separatrix: this part gives rise to the wrapping process.

The region enclosed by the separatrix around the localized vortex can be crossed by few fluid particles only, and forms a zero vorticity region which surrounds the localized vortex during the whole evolution of the system. This has been remarked also in the analysis of the motion of a localized vortex in a space dependent vorticity background [10]. The presence of the mentioned hyperbolic point determines the shape of the extended vortex during the initial phase of wrapping, as shown in the second plot, a key role being due to the different behavior of fluid particles in the neighborhood of that point. As wrapping develops, the related shift of the center of vorticity of the extended vortex feeds the process and leads to the coalescence of the hyperbolic point with the elliptic point associated to the extended vortex. Then, $\bar{\psi}$ exhibits a single maximum in the region of interest, as shown in the last two plots.

The second phase of the motion is characterized by formation and stretching of filaments, and effective reconnection of the vorticity field with the related formation and stirring of holes, which occurs due to the Kelvin-Helmholtz instability arising in the spiral channel of zero vorticity inside the extended (constant vorticity) vortex [7]. During this process the $\bar{\psi}$ field does not show significant large scale evolution. The constraint of vorticity conservation does not allow the system to reach a state where ζ is a function of $\bar{\psi}$ only.

Finally, we consider the behavior of the energy flows during the merger. The energy density is given by $\varepsilon(x, y, t) = \frac{1}{2}|\nabla\psi|^2$. This is initially concentrated near the boundaries of the two vortices, and it has a local minimum in the region around the above mentioned X-point. The total energy of the system, E , is a constant of motion and reads

$$E = \frac{1}{2} \int_S |\nabla\psi|^2 dS = \sum_i E_i, \quad (3)$$

where the integration is over the whole space within the circular boundary, and the energies E_i , with $i = e, p, b$, have been introduced, representing the energy associated to the extended vortex, the localized vortex, and the region surrounding the two vortices (background), respectively. The behavior of the energy amount in the two vortices and in the background is shown in Fig. 3, where the time evolution of the E_i 's is shown. During the whole process the energy of the pointlike vortex approximately does not change, while the energy of the extended vortex increases (almost linearly), at the expense of the energy of the background.

ACKNOWLEDGMENTS

This work was partially supported by the Office of Naval Research, and by the Italian Ministry of Education and Scientific Research.

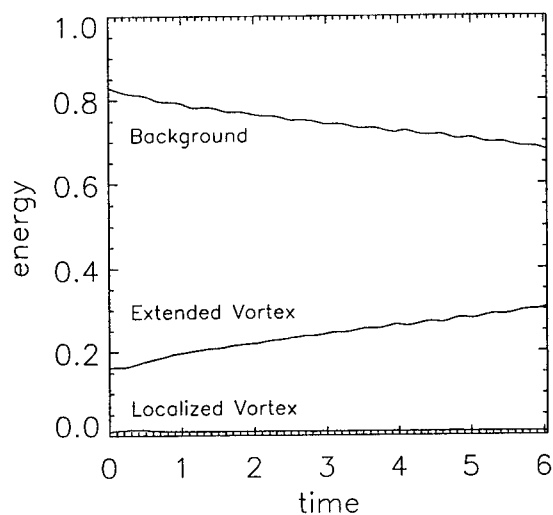


FIGURE 3. Time evolution of the total fluid energy of the two vortices and the background (PIC simulation). The data are the same as in Fig. 2.

REFERENCES

1. R. H. Levy, *Phys. Fluids* **8**, 1288 (1965).
2. J. C. McWilliams, *J. Fluid Mech.* **219**, 361 (1990).
3. I. M. Lansky, T. M. O'Neil, and D. A. Schecter, *Phys. Rev. Lett.* **70**, 1479 (1997).
4. D. Durkin and J. Fajans, *Rev. Sci. Instrum.* **70**, 4539 (1999).
5. J. P. Varboncoeur, A. B. Langdon, and N. T. Gladd, *Comp. Phys. Comm.* **87**, 199 (1995).
6. E. A. Overman and N. J. Zabusky, *Phys. Fluids* **25**, 1297 (1982).
7. M. V. Melander, N. J. Zabusky, and J. C. McWilliams, *Phys. Fluids* **30**, 2610 (1987).
8. D. G. Dritschel and D. W. Waugh, *Phys. Fluids A* **4**, 1737 (1992).
9. M. Amoretti, D. Durkin, J. Fajans, R. Pozzoli, and M. Romé, *Phys. Plasmas* **8**, 3865 (2001).
10. D. A. Schecter and D. H. E. Dubin, *Phys. Rev. Lett.* **83**, 2191 (1999).
11. D. Z. Jin, Ph.D. thesis, University of California, San Diego, 1999.

INTERACTION OF ELECTRON VORTICES UNDER THE INFLUENCE OF BACKGROUND VORTICITY DISTRIBUTION

Y. Kiwamoto, K. Ito, A. Sanpei, Y. Soga, T. Yuyama and T. Michishita

*Department of Fundamental Sciences, Faculty of Integrated Human Studies, Kyoto University
Kyoto 606-8501, Japan*

Abstract. We report experimental studies on vortex dynamics carried out recently in Kyoto University by using electron plasmas that are trapped in the Malmberg configuration with variety of initial configurations. This report includes (1) relaxation of many-clump dynamic states to "crystallization", (2) single clump dynamics in a background vorticity distribution, (3) two-clump interaction in a low-level background vorticity distribution, and (4) accelerated "crystallization" of three clumps in a background vorticity distribution. Details are provided in companion papers reported in this workshop.

INTRODUCTION

A set of equations that describe 2-dimensional (2D) motion of guiding centers of electrons transverse to the externally applied homogeneous magnetic field $\mathbf{B}_0 = B_0 \hat{z}$ are isomorphic to those of the 2D Euler fluid of non-charged particles [1,2]. The simple relation $\zeta = en/\epsilon_0 B_0 = \omega_p^2/\omega_c$ between the electron density n and the vorticity $\zeta(x, y) = \zeta \hat{z} = \nabla \times \mathbf{v}(x, y)$ substantially eases the diagnostics of the flow distribution with $\mathbf{v} = \mathbf{E} \times \mathbf{B}_0/B_0^2 = \hat{z} \times \nabla \phi/B_0$ in the electron plasma. Here ω_p and ω_c are the local plasma and cyclotron frequency, respectively. Since the stream function ψ , defined by $\mathbf{v} = \hat{z} \times \nabla \psi$, is related to potential distribution simply by $\phi = B_0 \psi$, the electrostatic analysis is directly applicable to the flow dynamics [2-4].

The potential distribution $\phi(x, y)$ is obtained numerically from $n(x, y)$ that is determined experimentally by means of the 2D luminosity distribution $I(x, y)$ on charge-coupled-device (CCD) camera images [3,4]. This diagnostic includes dumping all electrons along the magnetic field lines to a surface coated with 20nm-thick-Aluminum that also serves to electronically determine the total charge of electrons $-eN$ [5]. The linear relationship has been demonstrated between $I(x, y)$ and the line-integrated electron density distribution $n(x, y)L = \int dz n(x, y, z)$ in a wide dynamic range of 1 : 3000 with a high sensitivity of 1 count per 10 electrons [4]. In this experiment the potential

distribution of the trap is modified from the Penning-equilibrium configuration [6] to the Malmberg-trap configuration so as to minimize the variation of the axial length [7]. The typical length is $L = 235$ mm over the cross section.

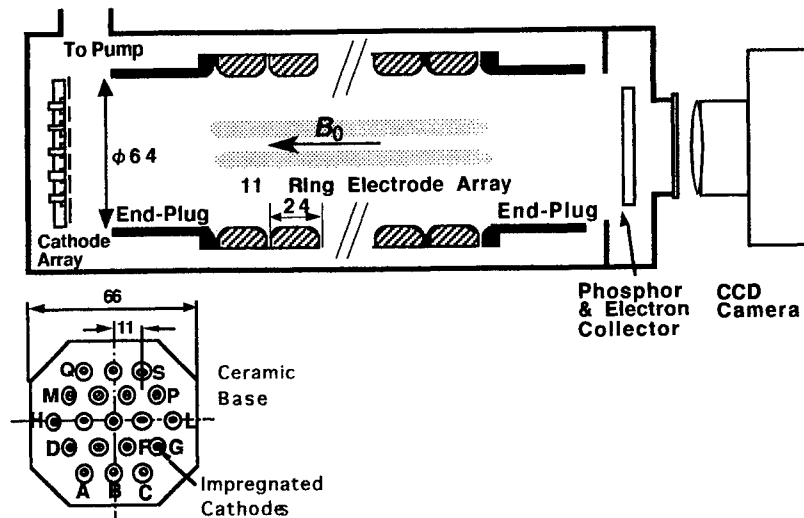


FIGURE 1. Schematic configuration of the experiment.

In the experimental setup as shown in Fig. 1 we use an array of 19 small electron emitters each of which can be operated independently to generate strings of electrons. Electrons in each string rotate around the string axis to form a vortex string with the initial diameter of < 1 mm. The strings advect each other in a conducting cylindrical wall at 32 mm from the machine axis. In addition to various configurations of electron strings (point vortices or clumps in 2D space), we can generate different shapes and levels of continuous vorticity distribution by combining repeated injection, mixing and relaxation of the strings and partially dumping electrons in the equilibrated distribution [5].

EXPERIMENTAL RESULTS

Relaxation of Many Vortex Strings to Crystal Structures

The most striking among the observations on vortex dynamics must be the formation of crystal states of vortices starting from spiral vorticity distribution that breaks apart into nearly a hundred of vortex strings [8]. Instead of relying on the instability process to generate the vortex strings we examine the dynamics by specifying the number of the strings as well as the position and circulation of each string. Even with highly reproducible initial distributions of the present experiment, the 19 vortices at maximum

go into random states of motion and repeat punctuated merging as well. During periods between intermittent merging, a decreasing number of vortex strings form regular arrays of “crystal” as illustrated in Fig. 2.

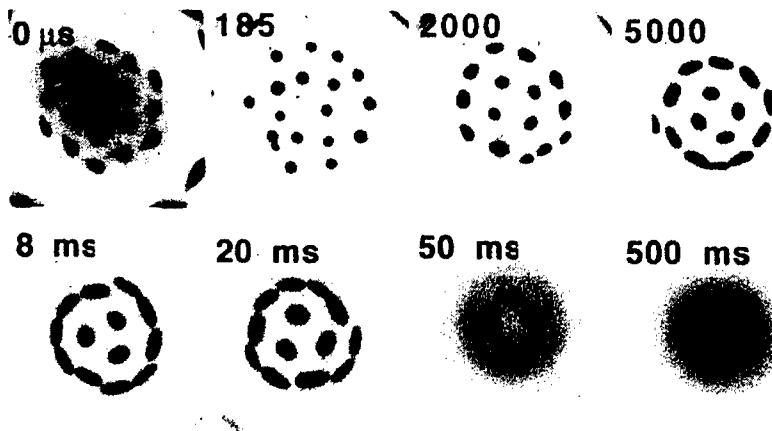


FIGURE 2. Time evolution of vorticity distribution starting from 19 clumps in vacuum.

In the process of the relaxation relatively weak strings are broken into thin sheets (filamented), and get folded into a stronger clump coming nearby. A noticeable process involved here is that some fraction of the sheets remains unabsorbed and forms a rugged background vorticity distribution. The self-generated background vortices significantly affect the process of interactions among remaining clumps. In this paper we focus on the role of the background vortices in the 2D dynamics of clumps that form various shapes of meta-equilibrium distribution as displayed in Fig. 3 in the relaxation process.

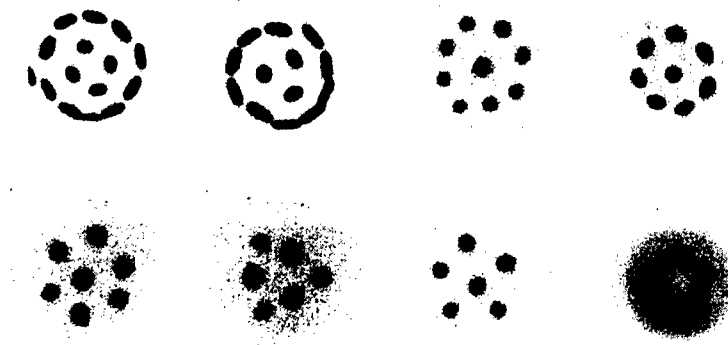


FIGURE 3. Meta-equilibrium vorticity distributions observed in the relaxation process. From [9,10].

Single Clump Dynamics in a Background Vortex

As a basic elementary process we examine the dynamics of a single vortex string in interaction with a background vortex with broad distribution. This configuration is also among well-discussed processes in planetary atmosphere, and qualitative behavior has been examined experimentally with normal fluids [11]. Quantitative examination became available only after Schecter and Dubin proposed a theoretical model based on the linearized equation of motion of the Euler fluid [12].

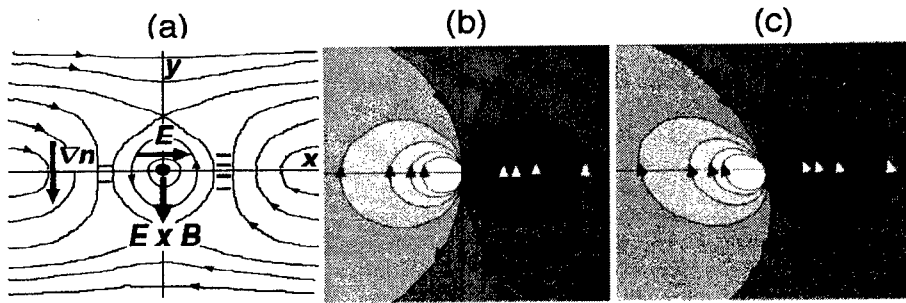


FIGURE 4. Perturbed vorticity distribution of the background in the slab model without shear (b) and with shear (c). The corresponding plasma distribution is shown in (a). From [5].

The velocity field of a clump, which is advected in the background vortex, locally modifies the latter's vorticity distribution ζ_b if $\partial\zeta_b/\partial r \neq 0$. In the rest frame of the clump, the higher (lower) vorticity of the background is moved to the lower (higher) region of ζ_b , and the perturbation $\delta\zeta_b$ forms a dipole structure aligned with the direction of the clump's motion as shown in Figs. 4 (b) and (c). In Fig. 4 ζ_b increases downward while the clump moves to the left in the lab. frame. The solid curves in (b) and (c) stand for the contours of $\delta\zeta_b$ as determined in the theoretical model with arrows indicating the direction of the advection. The dipole distribution of $\delta\zeta_b$ generates a transverse velocity field at the center to drive the clump downward in the direction of increasing ζ_b .

The experimentally determined vorticity distribution is plotted in Fig. 5 as a function of time in μs . The upper panel shows the total vorticity distribution $\zeta = \zeta_v + \zeta_b$. The clump's distribution ζ_v initially set at the periphery of the background vortex moves into the center of the background. The time required for this merging is within a couple of orbital rotation time. The perturbation $\Delta\zeta = \zeta - \zeta_{b0}$ is determined by subtracting the initial background distribution ζ_{b0} from each distribution in the upper panel and displayed in the lower panel. We can observe negative (positive) $\Delta\zeta$ in front of

(behind) the clump in qualitative agreement with Figs. 4 (b)-(c) [5, 9, 10].

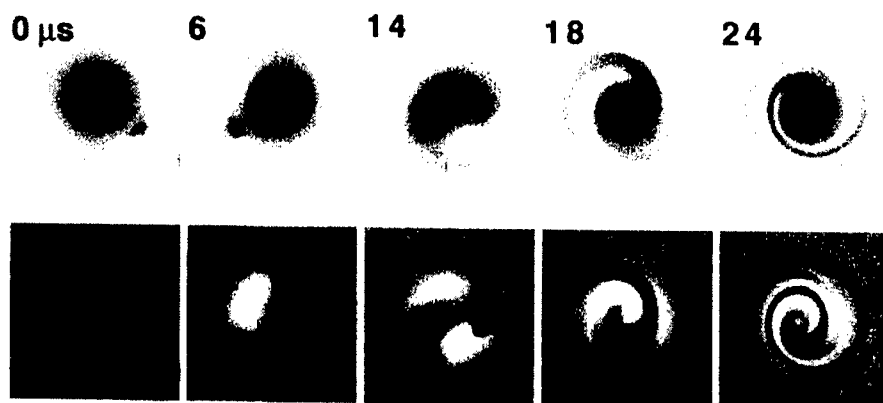


FIGURE 5. A clump climbs up the vorticity gradient of the background. The upper panels show the total vorticity while the lower panels present the increment $\Delta\zeta$ of the vorticity from the initial distribution. Darkness represents the height of the vorticity. The white in the lower panels indicates negative $\Delta\zeta$. From [9,10].

In the experiment, though the circulation Γ_v of clumps is less than a few percent of Γ_b of the background, the modification of the background distribution is substantially large and the perturbation does not remain local. If we decrease Γ_v , the clump is stretched into a filament by the shear in the background before it reaches the center. The radial distance r_v of the clump from the center of the vorticity distribution is plotted as a function of time in Fig. 6 for different values of $\Gamma_v \propto N_v/10^6 = (1.6\Delta, 4.4\Box, 8.7\circ, 17\bullet)$ starting from the same radial location in the fixed profile of the background vorticity distribution. The clump begins its free motion at 15 μ s on disconnection from the electron source.

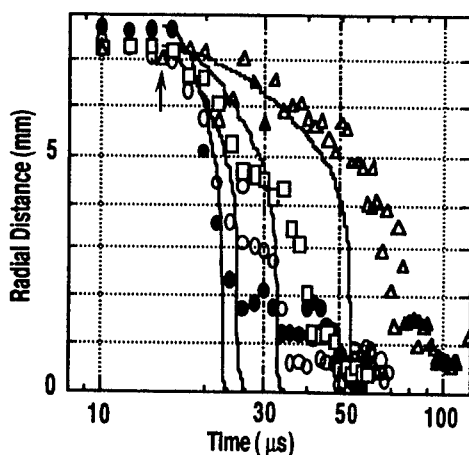


FIGURE 6. Radial distance of clumps with different circulations. From [5].

The solid curves stand for the radial distance as calculated from the Schecter's equation of motion by using the full experimental parameters of the initial distribution. Here we put the logarithmic factor $\ln(cr_v/\ell)$ in the equation to be 1. In the experiment the half-width $\ell = (\Gamma_v/2\pi A)^{1/2}$ of the separatrix reaches the radial distance r_v as the clump moves inward, and the logarithmic factor becomes zero indicating the breakdown of the slab-geometry approximation. If we do not drop the logarithmic factor and let the geometric coefficient $c=1.5$, the calculated r_v does not decrease below 1mm (for small Γ_v) or 2mm (for large Γ_v). This cutoff distance of r_v qualitatively agrees with the radius where the orbit deviates from the initial path as observed in Fig. 6.

Avoiding the problems associated with the logarithmic factor, we examine the radial velocity of the clump along the initial trajectory of its motion. We compare the time required for the clump to travel from 10% to 90% point of the initial radial distance. The experimental value τ_{Exp} is evaluated by smoothly extrapolating the initial orbit below 3 mm. The corresponding theoretical value τ_{Model} is evaluated from the orbit calculated in the same manner as in Fig. 6. We have confirmed a clear scaling $\tau_{\text{Exp}} \approx 2\tau_{\text{Model}}$ for a wide range of experimental parameters [5]. This observation indicates the validity of the model equation as well as the necessity for more rigorous theoretical treatment in the range $cr_v/\ell \leq 1$. It should be noted also that the 2D field distribution $\phi(x, y)$, calculated numerically from the observed density distribution, predicts the $E \times B$ drift velocity of the clump that is consistent with the observed trajectories of the clumps for the whole radial range [13].

Two Clump Interaction in a Background Vortex

As an elementary process in the interaction among clumps, we examine trajectories of two clumps immersed in different levels of vorticity of the background. Example frames of the vorticity distribution are shown in Fig. 7. In contrast to the dynamics in vacuum, the two vortices approach in a time of a couple of rotations either to merge into one or to form a binary vortices. The binaries revolve stably at a distance of less than two vortex diameters at which they should get merged in vacuum [14].

Preliminary experiments carried out before the NNP workshop in 1999 have revealed that the time τ_{Merge} required for the merging or forming the binary state scales as $\propto \Gamma_b^{-k}$ with the exponent of $k=0.8-1$ [15]. Assuming then unknown profile of the background as gaussian, the characteristic time scale of τ_{Merge} was approximated to τ_{Model} [16]. However, detailed experimental analyses carried out later with improved diagnostic technique have not led to a conclusion that τ_{Merge} show the same

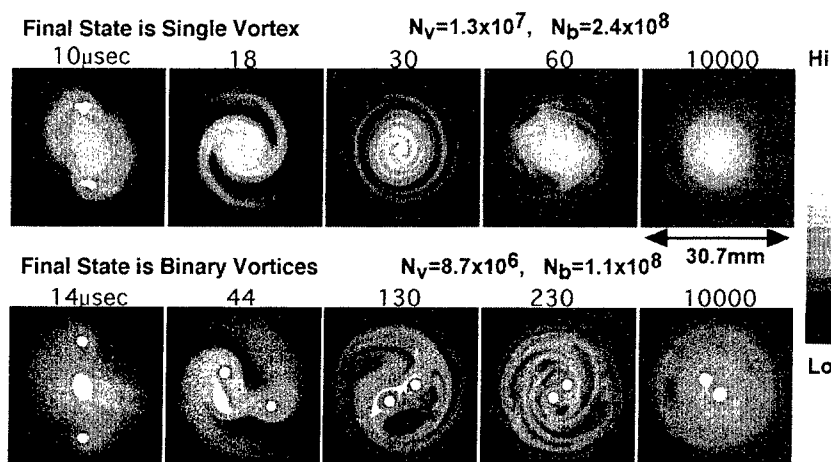


FIGURE 7. Time evolution of vortex dynamics including two clumps and background vortex.

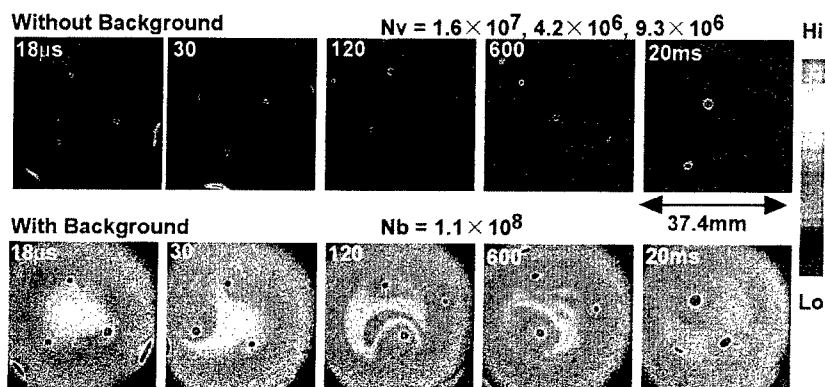


FIGURE 8. Three clumps of different strength are crystallized in the presence of a low-level background vorticity distribution.

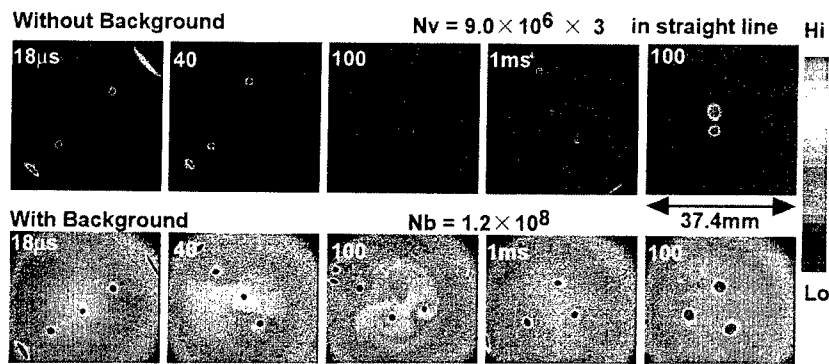


FIGURE 9. Three clumps in straight line are crystallized in the presence of a low-level background vorticity distribution.

parameter dependence as τ_{Model} .

Recent observations indicate that three vortices, two clumps plus a background vortex, almost equally take part in the evolution of the whole vortex dynamics. When the gradient of the background vorticity is large enough, the clumps quickly move up the hill of the background vorticity to merge around the background's peak. This is the case where the Schecter-Dubin model is the dominant process. When the background gradient is not large enough, however, the clumps modify the background locally first to form structures that surround them. The fine structures dressed by the clumps exert strong influence on the interaction between the clumps as well as between each clump and the remaining part of the background vortex. In these processes various shapes of areas with depleted vorticity (patched holes accompanying the clumps and ring holes surrounding them) are generated [3,9,10,17]. The difference in the initial conditions, separating the fates of the vortex dynamics is quite subtle.

Crystallization of Three Clumps in a Background Vortex

At least three clumps may be required to test crystallization of discrete vortices in the simplest form. When three clumps are placed at the vertices of a regular triangle in vacuum, they keep the relative location unchanged in a rigidly rotating frame only if the initial distribution is highly symmetric. If the symmetry is broken in terms of the relative positions or by the imbalance of the circulations, the clumps continue unsettled motion until non-ideal processes set in or one of them moves out to touch the wall.

As in the case of two clump dynamics, the presence of a low level background vortex changes the dynamical state drastically. Figure 8 shows how the initial distribution of symmetrically placed clumps with uneven circulations $\Gamma_v \propto N_v/10^6 = (16, 9.3, 4.2)$ evolves in vacuum (upper panels) and in the presence of the background vortex with $\Gamma_b \propto N_b/10^8 = 1.1$ (lower panels). The clumps start free motion at $t = 18\mu\text{s}$ as indicated at the upper left corner. It is clearly observed that the symmetric layout of the clumps is lost in a couple of rotation times in vacuum. The center of mass (CM) of the three-clump system also rotates indefinitely. When a background vortex is added, the clumps are forced to remain at azimuthally symmetric positions and the radial excursion of the CM decreases substantially.

The differences from the vacuum dynamics are associated with modifications of the background distribution. The average height of the background distribution is lower than those of the clumps by a factor of 14-60, and the background distribution is locally modified around each clump as soon as the free motion sets in. The extent of the modification differs for different strengths of clumps as evidently observed in the lower panels at $t = 20\text{-}600\mu\text{s}$. The radial extent of the modified distribution is larger for the stronger clump. Typical states of meta-equilibrium are associated with a ring hole

around the clumps as observed in the lower panel at $t = 20\text{ms}$.

The triangular distribution in meta-equilibrium states of three clumps is realized even from initial states far from the final configurations. Figure 9 shows that the clumps initially placed in a straight line also form a robust triangular configuration after experiencing interactions with the background vortex. The background vorticity distribution restricts excursion of the clumps within a limited area and let the clumps settle at triangular vertices and finally prevent them from merging. The responsible dynamics of the background vortex for this crystallization appears to be the deformation of its distribution agitated in the relatively strong field of each clump. The net field of each clump tends to get equalized, but not fully, by the shielding dress of the modified distribution of the background vortex.

DISCUSSION AND CONCLUSIONS

In this paper we have examined the role of the background vorticity distribution that exerts a decisive influence on the 2D dynamics of clumps. The vorticity gradient in the background tend to advect the clumps to climb the slope. But in most actual situations the reaction from the clumps is so substantial that various shapes and scales of structures are generated in the background distribution. Such structures in turn remarkably modify the interaction among clumps so that they find relative positions which lasts for as long a period as exceeding 100 rotations. These stable states of meta-equilibrium are responsible for the formation of vortex crystals.

Ring holes are generated around the clumps with different sizes corresponding to the circulations of the clumps (see Fig. 8). Coulomb shielding by the holes is requested in the statistical model of the crystallization[18]. Our observations indicates that the amount of the negative circulations of the ring holes do not exceed 20 % of the clumps and usually remain below a few percent. [17]

The time required for three clumps to form a meta-equilibrium triangle decreases as the height of the background vorticity increases. Observations indicates that there is no threshold for the accelerated crystallization in the background level that separates from the dynamic states in the vacuum. We have confirmed such continuous transitions by decreasing the height of the background vorticity well below 0.05% of the clumps' local vorticity [19]. The tendency of saturation has also been observed that the crystallization time does not decrease to less than a couple of rotation times as the background level increases above 1% of the clumps'.

Our experimental investigations indicate that fates of the dynamics of interacting clumps are sensitively influenced through the interaction with a low level distribution of the vortex that surrounds them. However, we have not reached a satisfactory explanation in terms of existing statistical models. From experimental point of view the deformations of the holes appear to be essential for meta-equilibration of the clumps'.

configuration, namely the apparently static state is supported by fine-scale dynamics.

We tend to understand the phenomena as follows: In the meta-equilibrium states of the clumps, the background vortex has rugged distribution with fine structures and remains in a dynamic state, continuously adjusting its spatial profile with incompressible fine-scale flows along intricate paths. When the background dynamics becomes unable to sustain the force balance among the clumps, merging between clumps occurs in a short period to form another meta-equilibrium distribution with reduced number of clumps. The crystallized distributions as shown in Fig. 2 manifest such states punctuated by the intermittent merging.

ACKNOWLEDGMENTS

The authors thank Prof. A. Mohri for stimulating discussion. This work was supported by a Grant-in-Aid from the Ministry of Education, Science, Sports and Culture and partly by the collaborative research program of National Institute for Fusion Science.

REFERENCES

1. Levy, R. H., Phys. Fluids **11**, 920 (1968).
2. Fine, K. S., Driscoll, C. D., Malmberg, J. H., and Mitchell, T. B., Phys. Rev. Lett. **67**, 588 (1991).
3. Huang, X. -P., Fine, K. S., and Driscoll, C. F., Phys. Rev. Lett. **74**, 4424 (1995).
4. Ito, K., Kiwamoto, Y., Sanpei, A., Jpn. J. Appl. Phys. **40**, 2558 (2001).
5. Kiwamoto, Y., Ito, K., Sanpei, A., Mohri, Phys. Rev. Lett. **85**, 3173 (2000).
6. Higaki, H. and Mohri, A., Jpn. J. Appl. Phys. **36**, 5300 (1997).
7. Finn, J. M., del Castillo-Negrete, D., and Banes, D. C., Phys. Plasmas **6**, 3744 (1999).
8. Fine, K. S., Cass, A. C., Flynn, W. G., Driscoll, C. F., Phys. Rev. Lett. **75**, 3277 (1995).
9. Kiwamoto, Y., *BUTSURI* (Bull. Phys. Soc. Jpn.) **56**, 253 (2001).
10. Kiwamoto, Y., J. Plasma Fusion Research **77**, 338 (2001).
11. Nezlin, M. V., and Snezhkin, E. N., *Rossby Vortices, Spiral Structures, Solitons*, Springer-Verlag, Berlin Heidelberg, 1993.
12. Schecter, D. A., and Dubin, H. E., Phys. Rev. Lett. **83**, 2191 (1999).
13. Ito, K., Kiwamoto, Y., Sanpei, A., to be published; also partly reported in this workshop.
14. Mitchell, T. B., Driscoll, C. D., and Fine, K. S., Phys. Rev. Lett. **71**, 1371 (1993).
15. Kiwamoto, Y., Mohri, A., Ito, K., Sanpei, A., and Yuyama, T., *Non-neutral Plasma Physics III* ed. by J. Bollinger, R. L. Spencer, R. C. Davidson, AIP Conf. Proc. **498**, 1999, pp.99-105.
16. Kiwamoto, Y., Ito, K., Sanpei, A., Mohri, A., Yuyama, T., Michishita, T., J. Phys. Soc. Jpn. (Lett.) **68**, 3766 (1999).
17. Sanpei, A., Kiwamoto, Y., Ito, K., J. Phys. Soc. Jpn. (Lett.) **70**, No.10 (2001).
18. Jin, D. Z. and Dubin, D. H. E., Phys. Rev. Lett. **80**, 4434 (1998).
19. Sanpei, A., Kiwamoto, Y., Ito, K., Soga, Y., to be published; also partly reported in this workshop.

Electron Vortex Dynamics and Two-Dimensional Field Analysis

K. Ito*, A. Sanpei* and Y. Kiwamoto†

*Graduate School of Human and Environmental Studies, Kyoto University, Sakyo-ku, Kyoto
606-8501, Japan

†Department of Fundamental Science, Integrated Human Studies, Kyoto University,
Kyoto 606-8501, Japan

Abstract. In recent paper [K. Ito, *et al.*, Jpn. J. Appl. Phys. **40**, 2558 (2001)], we present a fast and sufficiently accurate procedure to construct the potential and the electric field distribution from the observed electron density distribution in two-dimensional plane. Using this procedure, we obtain quantitative agreement between the observed velocity of the clump motion and the calculated velocity of that determined by the field analysis. In addition, the strong deformation of the clump is observed when that moves in the shear of the background vortex.

INTRODUCTION

The dynamics of a nonneutral electron plasma that is strongly magnetized and homogeneous along the magnetic field is equivalent with the two-dimensional (2D) Euler fluid [1, 2]. The correspondence between the electron density $n(x, y)$ and the vorticity $\zeta(x, y)$ and that between the electric potential $\phi(x, y)$ and the stream function $\psi(x, y)$ eases the diagnostics and analyses of the electron vortex motion compared with those for neutral fluid vortices. The 2D structures of the density (vorticity) distribution is determined experimentally in terms of the luminosity distribution of electrons collected on a phosphor screen that serves also as a collector of the total charge to determine the total number of electrons [3, 4].

From the observed 2D density distribution, we determine the electrostatic potential and electric field distribution in the 2D plane by employing Fourier-Bessel series expansion of the observed density distribution for fast numerical processing [4]. The potential distribution $\phi(x, y)$ conforms to the stream function $\psi(x, y)$ in terms of fluid dynamics, so that many aspect of fluid dynamics can be presented in the language of electromagnetism. This fast numerical analysis is essential for detailed and extensive studies of vortex dynamics or turbulence.

We have experimentally observed radial oscillations in the trajectory of a clump of a vorticity moving up the slope of the background vorticity distribution [3]. This oscillation is not expected from the linear theory [5], and we were led to the interpretation that the main mechanism responsible for the oscillations is the azimuthal electric field associated with the differential rotation of the perturbed density distribution in the background behind the clump [3].

Using this field analysis, we have obtained quantitative agreement between the observed speed of the oscillation and the calculated speed determined by the field analysis. It also demonstrates the influence of structures in the background vortex on the dynamics of coherent vortices [6, 7, 8, 9]. On the other hand, it is observed that the clump is stretched in the background vortex shear along the stream function. There is a possibility that it also influences the vortex motion.

The experiment is carried out with the Malmberg trap. The details of the experimental configuration have been reported in refs. 3 and 4.

DERIVATION OF POTENTIAL FIELD FROM OBSERVED DENSITY DISTRIBUTION^[4]

In the Malmberg trap configuration, the magnetic field \mathbf{B}_0 is homogeneous and the axial distribution of the vacuum-field potential ϕ^v is flat in the trap region. Therefore, we can safely approximate that the chord-averaged density $n(x, y) = n_l(x, y)/L$ represents the actual density distribution of the electrons. Here, L is the axial length of the trap region expected from ϕ^v . Because L is much larger than the transverse dimension of the electron density distribution, we can introduce a 2D analysis for determining the potential distribution in the main part of the trapped region by neglecting the effects from the ends [4].

The potential distribution generated by the electrons is given in a 2D form $\phi(r, \theta)$ that satisfies the Poisson's equation.

$$\left(\frac{1}{r} \frac{\partial}{\partial r} r \frac{\partial}{\partial r} + \frac{1}{r^2} \frac{\partial^2}{\partial \theta^2} \right) \phi(r, \theta) = \frac{e}{\epsilon_0} n(r, \theta). \quad (1)$$

The contribution of the conducting wall surrounding the plasma enters as a boundary condition $\phi(R, \theta) = 0$ at the wall of a radius R .

First, we Fourier-expand Poisson's equation in the azimuthal angle θ to obtain a set of ordinary differential equations in the radial coordinate r . $\phi_m^{c,s}(r)$ and $n_m^{c,s}(r)$ are the m th Fourier component of the potential and the density, respectively. The density part $n_m^{c,s}(r)$ are calculated from the observed CCD images. We further expand $n_m^{c,s}(r)$ in a series of Bessel functions $J_m(z)$ to determine the associated terms of the potential that is obtained as,

$$\begin{aligned} \phi(r, \theta) = & \frac{e}{2\epsilon_0} \sum_{n=1}^{\infty} \beta_{0n}^c J_0\left(\frac{\chi_{0n}}{R} r\right) \\ & + \frac{e}{\epsilon_0} \sum_{m=1}^{\infty} \left\{ \cos m\theta \sum_{n=1}^{\infty} \beta_{mn}^c J_m\left(\frac{\chi_{mn}}{R} r\right) + \sin m\theta \sum_{n=1}^{\infty} \beta_{mn}^s J_m\left(\frac{\chi_{mn}}{R} r\right) \right\}, \quad (2) \end{aligned}$$

where $J_m(\chi_{mn}) = 0$ with $n = 1, 2, 3, \dots$, and

$$\beta_{mn}^{c,s} = - \frac{2}{\{\chi_{mn} J_{m+1}(\chi_{mn})\}^2} \int_0^R dr r J_m\left(\frac{\chi_{mn}}{R} r\right) n_m^{c,s}(r).$$

Here the upper limit of the azimuthal mode number m_{max} and the radial mode number n_{max} are taken as $m_{max} = 100$ and $n_{max} = 100$. The calculation of the potential requires about 1 min. on a personal computer. Once the potential distribution $\phi(r, \theta)$ is constructed, the electric field can be determined from $\phi(r, \theta)$.

Similarly, we can also reconstruct the density profile if we remove the constant e/π and replace the coefficients $\beta_{mn}^{c,s}$ with $\alpha_{mn}^{c,s} = -(\chi_{mn}/R)^2 \beta_{mn}^{c,s}$ in eq. (2). The discrepancy Δ_e between the original density profile n_o and the reconstructed profile n_{FB} may be defined as

$$\Delta_e = \frac{\sqrt{\sum (n_{FB} - n_o)^2}}{\sum n_o} \quad (3)$$

by summing all the pixels. In most cases, Δ_e is found to be less than 1%.

DYNAMICS OF A CLUMP IN THE BACKGROUND VORTEX

In this section, we show an experimentally observed dynamics of a clump in a background vorticity distribution. In our experiments, generally, the radius of the clump is very small compared with that of the background vortex, and the circulation Γ_c of clump is less than a few percent of Γ_b . The circulation Γ is proportional to the electron number N . However, the vorticity of the clump ζ_c is ten times as high as that of the background vortex ζ_b . Accordingly, we can assume the clump as the strong point vortex in our experiments.

Figures 1 show typical time evolution of the 2D vorticity distribution. Here, the electron number of the clump and background vortex is $N_c = 1.2 \times 10^7$ and $N_b = 1.9 \times 10^8$, respectively. The upper panels are total vorticity distribution $\zeta(x, y, t)$ observed

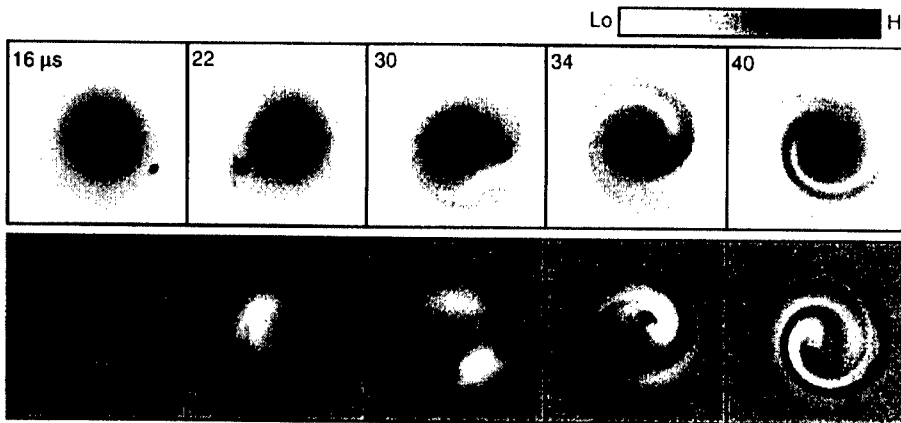


FIGURE 1. Time evolution of 2D vorticity distribution. The upper panels show the total vorticity distribution observed with CCD camera. The lower panels show the perturbed part of the background vortex from the initial background vortex distribution.

with CCD camera. It is observed that the clump climbs up the background vorticity gradient as it rotates creating a spiral streak behind it.

The lower panels show the perturbed part of the background vortex distribution $\delta\zeta_b(x, y, t)$ which is determined by subtracting the initial background distribution $\zeta_b(x, y, 0)$ from each distribution $\zeta(x, y, t)$ in the upper panels. It is observed that the negative (positive) perturbation in front (behind) of the clump. It is considered that this deformation of the background vortex generates the radial electric field, and the $\mathbf{E} \times \mathbf{B}$ drift caused by this field drive the radial motion of the clump.

ANALYSIS OF THE CLUMP DYNAMICS

Figure 2(a) shows the radial distance r_c of a clump from the center of the background vorticity against the time with different circulation of clumps ($N_c = (2.4 - 6.3) \times 10^6$) when the background vorticity profile is fixed ($N_b = 1.9 \times 10^8$). The clump begins its free motion at $15 \mu\text{s}$ on disconnection from the electron source. Solid lines represents radial distance calculated from the Schecter's theoretical model [5] using the full experimental parameters of the initial distribution. The experimentally observed orbit of the clump is in almost agreement with the orbit obtained from the theoretical model. In the experiment, however, we can observe the oscillation of the orbit of the clump motion. We consider that the oscillation of the orbit is driven by the azimuthal electric field caused by the strong deformation of the background vortex [3].

Figure 2(b) shows the radial velocity of the clump motion in the case indicated by open triangles in Fig. 2(a). The open triangles represent the radial velocity calculated from the observed radial distance of the clump. The closed triangles indicate the radial velocity driven by $\mathbf{E} \times \mathbf{B}$ drift when the electric field acting on the clump is calculated with the field analysis. The solid line represents the radial velocity calculated from the

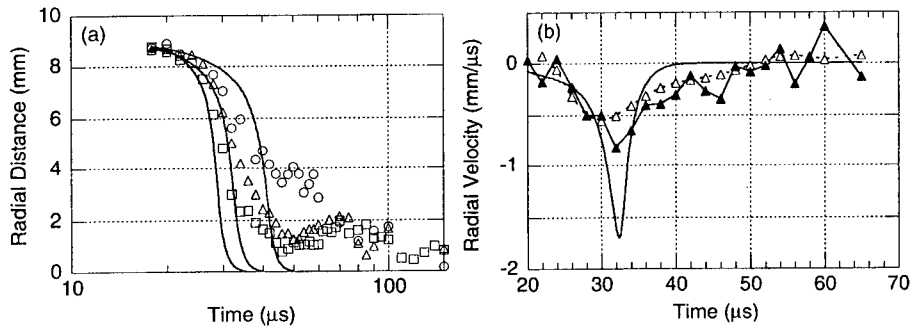


FIGURE 2. (a) The symbols are indicate the observed radial distance r_c of the clump from the center of the background vortex for different $N_c/10^6 = 2.4(\bigcirc), 4.1(\triangle), 6.3(\square)$. Solid lines represents the radial distance calculated from the Schecter's theoretical model. (b) Radial velocity of the point vortex in the case of $N_c = 4.1 \times 10^6$ in Fig. 2(a). Open triangles represent the directly observed velocity from observed vorticity distribution and closed triangles indicate the velocity calculated with the field analysis method. Solid line shows the velocity expected from the theoretical model.

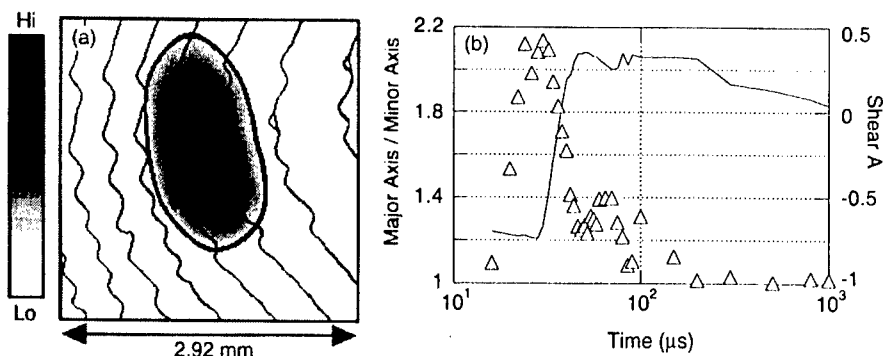


FIGURE 3. (a) Typical image of a clump stretched with the shear of the background vortex at $t = 30 \mu\text{s}$. Thin lines represent the stream function. Thick line indicates the $1/e$ contour of the vorticity. (b) Open triangles represent the ratio of the major axis to minor axis. The solid line indicates the shear of the background vortex.

theoretical model.

The radial velocity calculated with the field analysis is in good agreement with the observed velocity. It is noticed that the reverse of the radial velocity is reproduced from the field analysis. Therefore, we actually confirm the reverse of the radial velocity driven by the $\mathbf{E} \times \mathbf{B}$ drift by the field analysis. It indicates that this fast numerical analysis is essential for detailed and extensive studies of vortex dynamics.

It is observed that the maximum velocities calculated from the experimental data are slow compared with the theoretical value. We also consider that it originates in a strong deformation of the background vortex and that of the clump mentioned below.

We examine the influence which the background vortex exerts on the clump. Figure 3(a) shows the typical vorticity distribution around the clump in the background vortex. Thin lines represent the stream function and thick line indicates the $1/e$ contour of the clump vorticity. It is observed that the clump is stretched along the stream function.

Figure 3(b) plots the ratio a of the major axis to minor axis of the clump (Δ) and the rotation shear $A = -r d\Omega_b/dr$ of the background vortex (solid line) as a functions of the time. Here, $\Omega_b(r)$ is the angular frequency of rotation of the background vortex. The clump is round ($a \approx 1$), immediately after the free motion of clump starts. After that, the clump is stretched swiftly along the stream function. The clump is stretched most ($a \approx 2.2$) at $t = 30 \mu\text{s}$ when the shear A of the background vortex is strongest and the radial velocity of the clump is fastest as shown in Figs. 3(b) and 2(b). When the clump approaches the center of the background vortex, the shear A of the background vortex becomes weak and the clump rounds again. It is confirmed that a clump is stretched with a shear of a background vortex.

In a numerical simulation of neutral fluid, it has been considered that the deformation of the vortex is very important to the merging between vortices [10]. We have reported that the merging between the clumps is accelerated in the background vortex. On the other hand, we have observed that two clumps continue to revolve around each other with a fixed distance though they approach in close distance in the background vor-

tex [7]. We consider that the clump dynamics and the interaction between these in the background vortex are controlled by not only the transformation of the background vortex but also the clump deformation caused by the interaction between the clump and the background vortex.

CONCLUSIONS

We have developed a fast procedure to numerically construct the 2D field distribution from the observed image data directly related to the electron density distribution. We have examined the dynamics of the clump in the background vorticity distribution using this field analysis. As a result, we have obtained the quantitative agreement between the observed velocity of the clump motion and the calculated velocity determined by the field analysis. It includes the oscillation of the clump orbit. It is considered that this method is useful for extensive studies of vortex dynamics or turbulence.

We also examine the deformation of the clump. It is observed that the clump which has the strong vorticity is stretched in the background shear. We have considered that the clump deformation caused by the background vortex shear plays a role as important as the background vortex deformation in the dynamics of a clump and interaction between these in the background vortex.

ACKNOWLEDGMENTS

The authors thank Prof. A. Mohri for stimulating discussion. This work was supported by a Grant-in-Aid from the Ministry of Education, Science, Sports and Culture and by the collaborative research program of National Institute for Fusion Science.

REFERENCES

1. Levy, R. H., Phys. Fluids **11**, 920 (1968).
2. Fine, K. S., Driscoll, C. F., Phys. Rev. Lett. **74**, 4424 (1995).
3. Kiwamoto, Y., Ito, K., Sanpei, A., and A., Mohri, A., Phys. Rev. Lett. **85**, 3173 (2000).
4. Ito, K., Kiwamoto, Y., and Sanpei, A., Jpn. J. Appl. Phys. **40**, 2558 (2001).
5. Schecter, D. A., and Dubin, D. H. E., Phys. Rev. Lett. **83**, 2191 (1999).
6. Jin, D. Z. and Dubin, D. H. E., Phys. Rev. Lett. **80**, 4434 (1998).
7. Kiwamoto, Y., Ito, K., Sanpei, A., Mohri, A., Yuyama, T., and Michishita, T., J. Phys. Soc. Jpn. (Letter) **68**, 3766 (1999).
8. Sanpei, A., Kiwamoto, Y., and Ito, K., J. Phys. Soc. Jpn. (Lett.) **70**, No.10(2001).
9. Kiwamoto, Y., Ito, K., Sanpei, A., et al. reported in this workshop.
10. Melander, M.V., Zabusky, N.J. and McWilliams, J.C., J. Fluid Mech. **195**, 303 (1988).

Characteristics and Generation Mechanism of Holes in an Extended Electron Vortex

Akio Sanpei¹, Kiyokazu Ito¹, Yukihiro Soga² and Yasuhito Kiwamoto^{1,2}

¹Graduate School of Human and Environmental Studies, Kyoto University, Sakyo-ku, Kyoto 606-8501

²Faculty of Integrated Human Studies, Kyoto University Sakyo-ku, Kyoto 606-8501

Abstract. In nonneutral plasma, depleted regions (holes) in the vorticity often play a controlling role in the evolution of two-dimensional turbulence. We report experimental investigations of the generation process of ring holes (three-dimensionally annular depletion) surrounding a strongly-peaked clump of vorticity (point vortex) immersed in the background of a spatially extended vorticity distribution, and determine the empirical scaling for the generation time of the ring holes. Moreover, we report geometrical features of the ring hole, and report that ring holes play an important role for crystallization.

INTRODUCTION

Regions of excessive (depleted) density in the 2D plane are called clumps (holes) in the vorticity distribution. In nonneutral plasma, only density depressions (holes) can partially shield coulomb force because there are no counter-charge particles. In the early stage of our experimental studies of point vortex dynamics carried out in the presence of various shapes and different levels of a background vorticity distribution [1,2,3], we have observed the appearance of patched holes or ring holes. Such ring hole configurations have been introduced in a theoretical model for explaining crystallization of clumps in the framework of statistical mechanics [4]. According to this model, the ring hole acts to be as a barrier against local entropy transport. Huang *et al.*, have experimentally examined the formation and dynamics of patched holes [5]. Schecter and Dubin theoretically analyzed the motion of a point hole in a background vortex [6]. It was pointed out that the holes have controlling effects on the speed of the evolution of turbulence because of their slow motion relative to clumps. Here we examine the time scale of generation and geometry of ring hole. And we report geometrical features of the ring hole. Finally, we discuss the effect of the ring hole for crystallization. The experimental data obtained using electron plasma confined in a Malmberg trap. The details of the configuration and diagnostics have been reported elsewhere [1,2,3,7].

OBSERVED PROCESS OF HOLE FORMATION

First, we suggest the experimental result of generation process of ring hole. Figure 1 shows the snapshots of the dynamics of a clump injected at $t=10 \mu\text{sec}$ in a low-density region of the background vortex. The vorticity strength is proportional to the darkness, and the black dot represents the clump. The peak value $\zeta_{v,0}$ of the vorticity $\zeta_v(x,y)$ of the clump is about 180 times higher than that of the local background vorticity $\zeta_b(x,y)$, and its circulation $\Gamma_v(x,y) = \iint dx dy \zeta_v(x,y)$ is about 18% of the background circulation $\Gamma_b(x,y) = \iint dx dy \zeta_b(x,y)$. The clump generates a rotational flow around its center, which has a direction same as that generated by the background vortex ($t=20 \mu\text{sec}$). The interacting flows make the clump climb along the gradient $\partial\zeta_b(r)/\partial r$ of the background vortex, and consequently spiral streak of the vorticity perturbation is generated [3]. A part of the low vorticity area is dragged by the clump into the higher vorticity area of the background to generate a spiral streak winding around its center ($t=70 \mu\text{sec}$). The differential flow around the clump tightens the fold of the spiral streak ($t=120 \mu\text{sec}$). Two points along the spiral streak reconnect ($t=180 \mu\text{sec}$), and the depleted-vorticity region involved in the background forms a ring that surrounds the clump ($t=5 \text{ msec}$). Once generated, the ring hole has a long lifetime comparable to that of the clump ($t=500 \text{ msec}$).

Now we attempt to make a quantity analysis of the generation of ring hole in terms of stream field. The vortex dynamics is strongly affected by the presence of the shear in a rotational background flow [3]. We examine the shear flow including the contribution of the clump by applying a field analysis to the observed data [8]. The potential distribution $\phi(x,y)$ is determined numerically from the experimentally determined density $n(x,y) \propto \zeta(x,y)$ of electrons [8]. Figure 2 shows the vorticity distribution and the equipotential surfaces that conform to the streamlines in the rest frame of the clump.

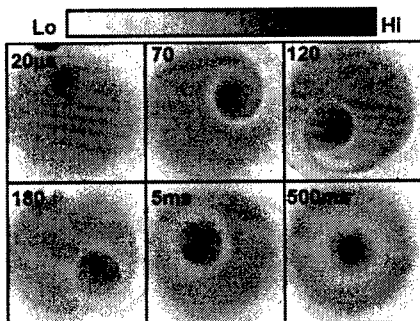


Figure 1. Snapshots of the vorticity distribution generating a ring hole around a clump interacting with the background vortex.

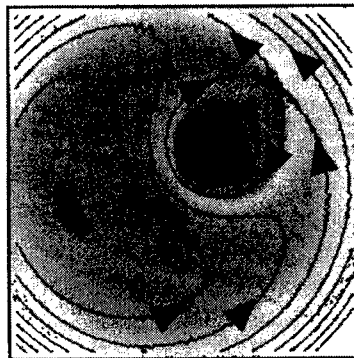


Figure 2. Vorticity distribution and the streamlines at $t=70 \mu\text{sec}$ in the stationary frame of the clump.

We can observe a set of closed lines around the clump and a stagnation point that distinguishes the background flow in the outer region. A part of the low vorticity area in the vicinity of the stagnation point is dragged into the higher vorticity region of the background vortex. It is also observed that the spiral streak extends along the separatrix.

We note that the starting point of the spiral streak is not at the edge of the distribution of the background vortex but it is close to the outer stagnation point lying well inside the background vortex. Our current understanding is that the density accumulates near the stagnation point and produces the electric field across the initial separatrix to drive electrons from the low-density area inward along the separatrix. The relative location of the streak of depletion in the vorticity distribution with respect to the contours of streamlines supports this interpretation. After the streak travels along the separatrix to form a full circle around the clump, there occurs a moment of reconnection to complete the topology of the ring hole.

EMPIRICAL SCALING OF RECONNECTION TIME

We have observed the formation process of the ring hole, by injecting a clump in the periphery of the background vorticity distribution that has various profiles as illustrated in Fig. 3(a). The arrow indicates the radial position of the injection. We define a reconnection time T_R as the time that has elapsed from the injection of the clump to the completion of ring-shaped depletion circulating around it. The reconnection time intricately depends on Γ_v and the local condition imposed by the distribution $\zeta_b(r)$ of the background vortex. After several trials of data analysis, we have reached a satisfactory expression for the entire data as described below.

Figure 3(b) plots the observed T_R against the circulation Γ_v of the clump for four different distributions of the background vortex. We have found empirically that a power law holds between T_R and Γ_v and that the power depends on $\beta = |\zeta_b \partial \zeta_b(r)/\partial r|$ at the initial location of the clump. The fitting lines for the data set in Fig. 3(b) provide an empirical relation, $T_R \propto (\Gamma_0/\Gamma_v)^{(\beta_0/\beta)^2}$, where the fitting parameters are $\Gamma_0 = 15 \text{ m}^2\text{sec}^{-1}$, and $\beta_0 = 8.9 \times 10^9 \text{ m}^{-1}\text{sec}^{-2}$. The coefficient of the empirical scaling is determined by plotting the observed values of $T_R (\Gamma_0/\Gamma_v)^{-(\beta_0/\beta)^2}$ against β .

The final relation reads as,

$$T_{R-CAL} = b \left(\frac{\beta_0}{\beta} \right)^{1/2} \left(\frac{\Gamma_0}{\Gamma_v} \right)^{(\beta_0/\beta)^2} \quad (1)$$

where $b = 5.2 \times 10^2 \text{ } \mu\text{sec}$. Figure 4 plots the observed values of the reconnection time T_{R-EXP} against the associated values T_{R-CAL} obtained from the empirical relation given by eq.(1).

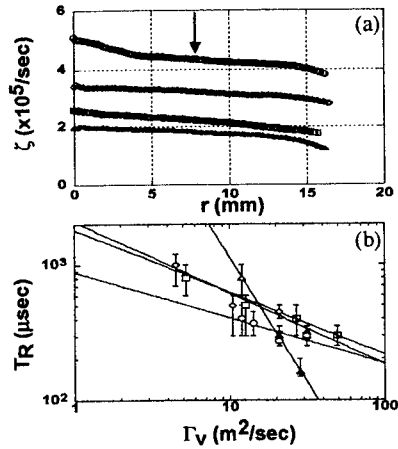


Figure 3.(a) Radial profiles of the background vortex. (b) Reconnection time is plotted against Γ_v . Each symbol corresponds to different profiles.

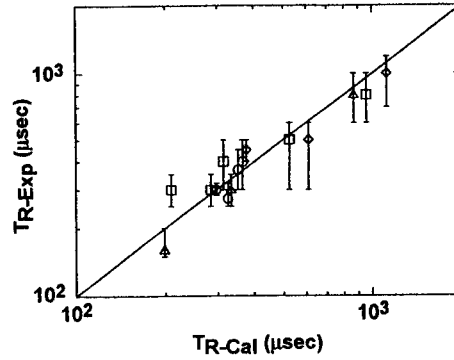


Figure 4.Observed reconnection time is plotted against the prediction of the empirical scaling (1). It reproduces a wide class of the observed data satisfactorily.

It demonstrates that eq.(1) reproduces a wide class of the observed data satisfactorily. We don't have a clear physical meaning of this empirical formula, but we guess reconnection time have some dependence on rotational shear $A = -r d\Omega_b(r) / dr$, what may have more physical meaning to reconnection time than local parameter β . Here, $\Omega_b(r)$ is the angular frequency of rotation of the background vortex. We have examined our experimental data with shear and obtained similar empirical relation to eq.(1) using local parameter β . We observe that new empirical relation can also reproduce the observed data within a reasonable width of scatter that is slightly larger than that from eq.(1). Detail discussion about these empirical relations has been reported elsewhere [9].

GEOMETRY OF RING HOLE

Now we report about the size of the ring holes. The radius R_{HO} of the outer edge of the ring hole depends on Γ_v and profile $\zeta_b(r)$ of the background vorticity. As Γ_v increases, R_{HO} increases to the order of the radius of the stagnation zone $l = (\Gamma_v / 2\pi |A|)^{1/2}$ calculated by field analysis [8].

And the maximum depth in $\zeta_H(x,y)$ of the ring hole decrement from the unperturbed level of the background vorticity $\zeta_b(r)$ also depends on Γ_v and $\zeta_b(r)$. Our observations indicate that the maximum ζ_H is less than 20% of the local $\zeta_b(r)$, and less than 1% of the peak vorticity ζ_{v0} of the clump. We should note that ζ_H is much smaller than the decrement in the open spiral streak generated in the wake of a clump that can reach almost 50-100% of ζ_b [3].

Let us examine shielding effects that the ring hole may have by defining the circulation of the hole as $\Gamma_H = \int dx dy \zeta_H(x,y)$. Figure 5 plots Γ_H against Γ_v , and we can observe a positive correlation between Γ_H and Γ_v . For all this state of our understanding, the experimental data in Fig.5 clearly indicate that Γ_H lies from 5% to 20% of Γ_v .

This experimental evidence might raise a question as to the fully-shielded vortex model in Ref. [4] and to a naive assumption of $\Gamma_H = \Gamma_v$ introduced in Ref. [10].

Here let us note that the vortex-merging is not driven directly along the force between symmetric vortices but that merging requires transverse field associated with asymmetric deformations in the distribution of the vortices. The drive for merging is weak so that it may be modified by some redistribution in the hole vorticity $\zeta_b(x,y)$ even if $\Gamma_H \ll \Gamma_v$.

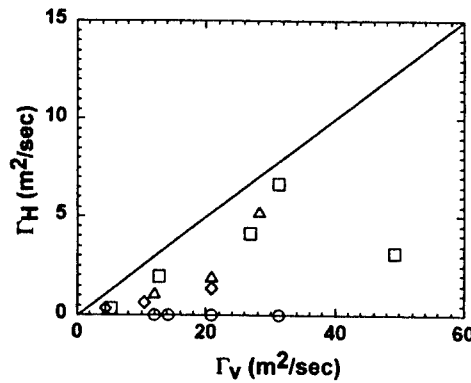


Figure 5. Figure plots Γ_H against Γ_v .
 Γ_H / Γ_v Does not Exceed 1/4.

RING HOLES IN LATTICE CONFIGURATION

We now discuss the appearance of ring holes surrounding multiple clumps immersed in the background vorticity distribution. To simplify, we consider the evolution of three clumps required to test crystallization of discrete vortices. Figure 6 illustrates the dynamics of three clumps with uneven circulations ($\Gamma_v \propto N_v / 10^6 = 16, 9.3, 4.2$) placed at the vertices of a regular triangle in background vortex ($\Gamma_v \propto N_v / 10^8 = 1.1$). Evolution time is indicated at the upper left corner (clumps start free motion at $t = 18 \mu\text{sec}$). If clumps are in the absence of background vorticity distribution, they move chaotically due to mutual advection, and do not reach stable configuration. In the long run, they sometimes merge, or one of them goes away from the range of vision. On the contrary, clumps, immersed in a background vorticity, evolve into symmetric triangular array surrounded by ring holes. In the first process of dynamics, clumps move chaotically due to the interaction between the clumps and the background, and give rise to the fine structures in background vorticity. Deformation of background vorticity distribution is larger for the stronger clump. In the process of development, fine structures in background vorticity vanish and three clumps are arrested into a stable pattern. And we can observe ring holes surrounding clumps with different size corresponding to the circulation of the clumps.

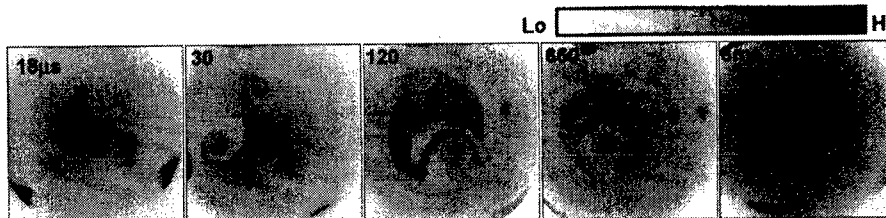


Figure 6. Snapshots of the crystallization of three clumps with different circulation immersed in lower background vorticity distribution.

This experimental result suggests that background vortex helps to generate symmetric lattice of multiple clumps with deformation of its distribution. The configuration of ring hole partially shield the interaction among clumps so that they find best positions that lead to the final stable state of equilibrium.

SUMMARY

In summary, we have experimentally studied the generation process of a ring hole around a clump that is placed in different initial distributions of the background vortex. The location of the hole generation is related to the separatrix produced in the shear flow of the background vortex. The time scale of the hole generation is empirically obtained; the scaling is related to the local gradient of the background vorticity. It is reported also that ring holes play an important role for crystallization of clumps, even though Γ_H lies from 5% to 20% of Γ_v .

ACKNOWLEDGEMENTS

The authors thank Professor A. Mohri for stimulating discussion. This work was supported by a Grant-in-Aid from the Ministry of Education, Culture, Sports, Science and Technology and by the collaborative research program of the National Institute for Fusion Science.

REFERENCES

1. Kiwamoto, Y., Mohri, A., Ito, K., Sanpei, A., and Yuyama, T., Non-neutral Plasma Physics III ed. by J. Bollinger, R. L. Spencer, R. C. Davidson, AIP Conf. Proc. 498, 1999, pp.99-105.
2. Kiwamoto, Y., Ito, K., Sanpei, A., Mohri, A., Yuyama, T., Michishita, T., J. Phys. Soc. Jpn. (Lett.) 68, 3766 (1999).
3. Kiwamoto, Y., Ito, K., Sanpei, A., Mohri, Phys. Rev. Lett. 85, 3173 (2000).
4. Jin, D. Z. and Dubin, D. H. E., Phys. Rev. Lett. 80, 4434 (1998).
5. Huang, X. -P., Fine, K. S., and Driscoll, C. F., Phys. Rev. Lett. 74, 4424 (1995).
6. Schecter, D. A., and Dubin, H. E., Phys. Rev. Lett. 83, 2191 (1999).
7. Kiwamoto, Y., Ito, K., Sanpei, A., *et al.* reported in this workshop.
8. Ito, K., Kiwamoto, Y., Sanpei, A., Jpn. J. Appl. Phys. 40, 2558 (2001).
9. Sanpei, A., Kiwamoto, Y., Ito, K., J. Phys. Soc. Jpn. (Lett.) 70, No.10 (2001).
10. Durkin, D. and Fajan, J., Phys. Rev. Lett. 85, 4052 (2000).

Nonlinear PIC Simulation in a Penning Trap

G. Lapenta*, G. L. Delzanno[†] and J. M. Finn**

**Istituto Nazionale per la Fisica della Materia (INFN) and Theoretical Division, Los Alamos National Laboratory, Los Alamos, NM 87545, USA*

[†]Istituto Nazionale di Fisica per la Materia (INFN) and Dipartimento di Energetica, Politecnico di Torino, Corso Duca degli Abruzzi 24, 10129 Torino, Italy

***Theoretical Division, Los Alamos National Laboratory, Los Alamos, NM 87545, USA*

Abstract. We study the nonlinear dynamics of a Penning trap plasma, including the effect of the finite length and end curvature of the plasma column. A new cylindrical PIC code, called KANDINSKY, has been implemented by using a new interpolation scheme. The principal idea is to calculate the volume of each cell from a particle volume, in the same manner as it is done for the cell charge. With this new method, the density is conserved along streamlines and artificial sources of compressibility are avoided. The code has been validated with a reference Eulerian fluid code. We compare the dynamics of three different models: a model with compression effects, the standard Euler model and a geophysical fluid dynamics model. The results of our investigation prove that Penning traps can really be used to simulate geophysical fluids.

INTRODUCTION

Malmberg-Penning traps are often characterized as a tool to simulate, in a plasma, the 2D dynamics described by the Euler equations. However, it is well known that the classical 2D drift-Poisson model (mathematically equivalent to the 2D Euler model [1]) is unable to capture the features of the $k = 1$ diocotron instability. In this approximation, there are no unstable modes [2] and the continuum spectrum can give only algebraic growth [3]; instead, experiments show an exponential growth of the mode [4].

Recently, the research has focused on trying to resolve this contradiction between theory and experiments. Finn *et al.* [5] were the first to explain the instability in terms of effects due to the finite length and end curvature of the plasma column (compression effects) and later Coppa *et al.* [6] improved this fluid model by modifying the expression for the velocity field, by including temperature effects and by using the exact Green's function for the plasma length. Hilsabeck and O'Neil [7] pointed out that kinetic effects might also be important in the $k = 1$ diocotron instability.

Interestingly, when compression effects are taken into account, the classical analogy between the 2D drift-Poisson model and the Euler model for an incompressible and inviscid fluid breaks down. Instead, a new analogy between non-neutral plasmas and geophysical fluid dynamics (GFD) arises [5, 8], in which the plasma length plays the role of the inverse of the fluid depth. This analogy is very important from the point of view of performing geophysical experiments in Penning traps.

In the present contribution, we focus on a simplified version of the model presented in Ref. [6], obtained by neglecting the temporal variation of the plasma length. As shown in Ref. [6], this model is still $k = 1$ unstable. The model is compared with the Euler model and with the γ -plane approximation of the geophysical fluid dynamics.

We present simulations of the nonlinear dynamics obtained with the cylindrical PIC Code KANDINSKY, showing that GFD can be actually simulated in Penning traps.

PHYSICAL MODEL

A cylindrical Malmberg-Penning trap confining an electron plasma is considered in the following. The trap consists of three electrodes. The central cylinder, which extends between $z = -L_c/2$ and $z = L_c/2$, is grounded, while the two cylindrical end caps are at a negative potential, $-V$. An uniform magnetic field provides radial confinement, while the potential difference between the central electrode and the end caps provides axial confinement.

In typical experiments, the electron cyclotron radius is much smaller than the typical size of the device, allowing the guiding center approximation. Furthermore, the dependence of the plasma properties along the axial direction can be simplified considerably thanks to the rapid bouncing motion between the end caps. However, a correct description of the diocotron instability, especially for the $k = 1$ mode, requires one to include the effect of finite length of the plasma in the axial direction and end curvature.

Following the approach in Refs. [5, 6], the particles are described by strings of variable length, which change their axial length and, consequently, their density, if they move radially due to the $\mathbf{E} \times \mathbf{B}$ drift. The effective axial length is calculated self-consistently by solving the Poisson equation in the trap and assuming thermodynamic equilibrium along the axial direction [9]. In normalized units, the model consists of the following system of equations [6]:

$$\left\{ \begin{array}{l} \frac{\partial \sigma}{\partial t} = -\mathbf{V}_\perp \cdot \nabla_\perp \sigma \\ \mathbf{V}_\perp = \hat{\mathbf{e}}_z \times \nabla_\perp \phi_{\text{eff}} \\ \mathcal{L} = \int \exp\left(\frac{\Psi}{\alpha}\right) dz \\ \nabla^2 \Psi = \frac{\sigma}{\mathcal{L}} \left[\exp\left(\frac{\Psi}{\alpha}\right) - 1 \right] \\ \nabla_\perp^2 \phi_c = \frac{\sigma}{\mathcal{L}} \\ \phi_{\text{eff}} = \phi_c + \alpha \log \frac{\mathcal{L}}{\mathcal{L}_{r=0}} \end{array} \right. \quad (1)$$

where $\sigma(r, \theta, t) = \frac{eR_w}{\epsilon_0 \hat{\phi}_{c0}(0)} \hat{\sigma}$ is the density integrated along axial direction, $\mathbf{V}_\perp(r, \theta, t) = \frac{B_0 R_w}{\hat{\phi}_{c0}(0)} \hat{\mathbf{V}}_\perp$ is the plasma velocity in the plane (r, θ) , $\mathcal{L}(r, \theta, t) = \frac{\hat{\mathcal{L}}}{R_w}$ is the effective length of the plasma, $\Psi(r, \theta, z, t) = \frac{\hat{\phi}(r, \theta, z, t) - \hat{\phi}_c(r, \theta, t)}{\hat{\phi}_{c0}(0)}$ is the correction to the potential in a trap of finite length with respect to the value in a trap of infinite length, $\phi_{\text{eff}}(r, \theta, t)$ is the effective potential, $\alpha = \frac{\Theta}{\hat{\phi}_{c0}(0)}$ is the electron temperature, $t = \frac{\hat{\phi}_{c0}(0)}{B_0 R_w^2} \hat{t}$ is the time and R_w is the wall radius. Hatted quantities are physical and have dimensions; the corresponding normalized quantities share the same symbol but are not hatted. Subscripts c and 0 label, respectively, quantities evaluated in the central plane and unperturbed quantities. For further details on the model and its derivation we refer to Refs. [6] and [10].

The model can be regarded as quasi-2D since only the potential in the trap depends on the axial coordinate and can be reduced to a fully 2D model by neglecting the time variation of the effective plasma length (in this case one does not need to solve the 3D Poisson equation). In this approximation the new model becomes:

$$\begin{cases} \frac{\partial}{\partial t}(n_c \mathcal{L}_0) = -\mathbf{V}_\perp \cdot \nabla_\perp (n_c \mathcal{L}_0) \\ \mathbf{V}_\perp = \hat{\mathbf{e}}_z \times \nabla_\perp \phi_{\text{eff}} \\ \nabla_\perp^2 \phi_c = n_c \\ \phi_{\text{eff}} = \phi_c + \alpha \log \frac{\mathcal{L}_0}{\mathcal{L}_{0,r=0}} \end{cases} \quad (2)$$

where we used the fact that $\sigma = n_c \mathcal{L}_0$ and $\mathcal{L}_0(r)$ is obtained from the initial equilibrium solution.

Compression effects due to the finite length of the plasma are included in the first and second equation of system (2). In the limit of $\alpha = 0$ and $\mathcal{L}_0/\mathcal{L}_{0,r=0} = 1 - sr^2$ the model described by Eqs. (2) reduces to the model proposed by Finn *et al.* (Eq. (38), Ref. [5]a).

In the following we will focus our attention on model (2), since it is simplified but still able to capture the features of the $k = 1$ diocotron instability (as shown in Ref. [6]). The spectrum of eigenvalues of model (2) is investigated in Ref. [11].

Our aim is to compare the dynamics of model (2) with the standard Euler model:

$$\begin{cases} \frac{\partial n_c}{\partial t} = -\mathbf{V}_\perp \cdot \nabla_\perp n_c \\ \mathbf{V}_\perp = \hat{\mathbf{e}}_z \times \nabla_\perp \phi_c \\ \nabla_\perp^2 \phi_c = n_c \end{cases} \quad (3)$$

and with the geophysical fluid dynamics (GFD) model [12]:

$$\begin{cases} \frac{\partial}{\partial t} \left(\frac{\xi + 2\Omega}{h} \right) = -\mathbf{V}_\perp \cdot \nabla_\perp \left(\frac{\xi + 2\Omega}{h} \right) \\ \mathbf{V}_\perp = \hat{\mathbf{e}}_z \times \nabla_\perp \Psi \\ \nabla_\perp^2 \Psi = \xi \end{cases} \quad (4)$$

where ξ is the vorticity, Ω is the rotation frequency, h is the height of the free surface of the fluid relative to the bottom topography, Ψ is the streamfunction and $(\xi + 2\Omega)/h$ is the potential vorticity. Model (4) is obtained from the shallow-water equations in the limit of small Rossby number, namely in the quasi-geostrophic approximation. As pointed out in Ref. [5], with $\Omega = 0$ the effective length of the plasma \mathcal{L}_0 plays in model (2) the same role played by $1/h$ in GFD. It is this analogy which leads to the possibility of simulating experimentally geophysical fluid dynamics in a Penning trap.

In all the models, a quantity is advected by the velocity field: the density (vorticity) n_c for Euler, the line integrated density $n_c \mathcal{L}_0$ for model (2) and the potential vorticity for GFD. All these models have the same equation for the velocity field, but only for the Euler case is the velocity field directly calculated from the quantity which is advected. In model (2) the velocity field is calculated from the solution of the Poisson equation plus an extra term which retains curvature and thermal effects, while in GFD the velocity field is determined by the vorticity ξ .

PIC CODE

The PIC code KANDINSKY has been developed based on a standard cylindrical PIC code previously developed [13] by the authors in collaboration with Gianni Coppa

and Antonio D'Angola at the Politecnico di Torino. A cylindrical PIC code has many advantages: very low viscosity; boundary conditions can be imposed exactly; the Fast Fourier Transform (FFT) can be used to solve the Poisson equation resulting in an improvement of the speed of the code. Nevertheless, it is well known that cylindrical PIC codes can potentially suffer from a number of problems. Of particular importance to the present study are the noise that typically arises in the center of the system, the non-conservation of enstrophy, and the growth of the maximum value of the density during simulations (inconsistent with incompressible flows). In the following subsections we will show how to improve the cylindrical PIC scheme and to solve the problem.

The problem

In order to understand the origin of the problems that affect cylindrical PIC codes, we will start with a simple exercise. Consider the 1D uniform cartesian grid of Fig. 1a and consider one particle of unit charge located at positions A, B or C. It is possible to calculate the density of each cell with the volume-weighted (Cloud-In-Cell) interpolation scheme, which is the most common scheme adopted in PIC codes. When the particle is in position A, it contributes only to the first cell and the density is $\rho_1 = 1/\Delta x$ (Δx is the grid spacing); when the particle is in position B, it is spread equally on the two cells and $\rho_1 = \rho_2 = 1/(2\Delta x)$; when the particle is in position C, it contributes only to the second cell and $\rho_2 = 1/\Delta x$. During the motion of the particle from A to C, the density at the particle position fluctuates between $1/(2\Delta x)$ and $1/\Delta x$ but on average it is conserved over long Lagrangian trajectories. Furthermore, this fluctuation is reduced when summed over the number of particles per cell, and this source of noise is manageable.

We now repeat the same exercise for the uniform cylindrical grid of Fig. 1b. In general a particle would contribute to two cells in θ and two cells in r direction, since the grid is 2D. In this specific example, we place A, B and C at the same azimuthal angle $\Delta\theta/2$, so there is only contribution to one cell in θ and the problem can be considered 1D. When the particle is in position A, it contributes only to the first cell and $\rho_1 = 2/(\Delta r^2 \Delta\theta)$ (Δr and $\Delta\theta$ are, respectively, the grid spacing in r and θ directions); when the particle is in position B, its charge is spread equally between the two cells but the different volume of the two cells leads to different densities, $\rho_1 = 1/(\Delta r^2 \Delta\theta)$ and $\rho_2 = 1/(3\Delta r^2 \Delta\theta)$. When the particle is in position C, it contributes only to the second cell and $\rho_2 = 2/(3\Delta r^2 \Delta\theta)$. Again during the motion from A to C the density is transferred from the first cell to the second, but in this case the total density of the particle does not remain constant, even on average. In particular, the density decreases as the particle moves away from the center of the system and this means that the CIC interpolation scheme, applied to a cylindrical grid with uniform spacings Δr and $\Delta\theta$, intrinsically violate the incompressibility condition. This effect is partially compensated for on average because more particles are in the cell of volume $r\Delta r\Delta\theta$ for large r .

This simple exercise points out that, when dealing with non-uniform cell volumes, standard interpolation schemes produce fictitious compressibility.

We emphasize that this problem affects not only the cylindrical geometry but it occurs whenever a grid of non-uniform volume is used.

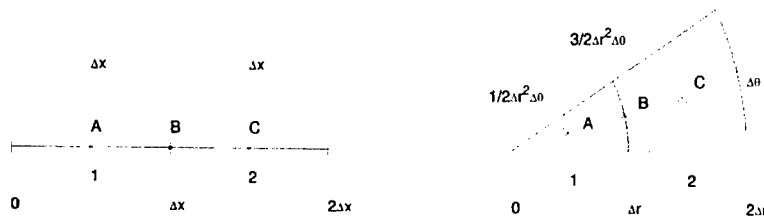


FIGURE 1. a) Uniform cartesian grid (left); b) Uniform cylindrical grid (right).

The solution

According to [14], we define natural coordinates, $\vec{\omega} = (\zeta, \eta)$ by mapping each cell of the physical grid onto a unit square cell in the space of natural coordinates. Therefore, in the space of natural coordinates the grid is uniform and cartesian. We define a shape function $s(\vec{\omega} - \vec{\omega}_p)$ in order to interpolate from the particles to the grid and vice-versa, normalized to $\int \int s d\zeta d\eta = 1$ in the space of natural coordinates. Then, the shape function in the physical space is $S(\mathbf{x}(\vec{\omega}) - \mathbf{x}_p(\vec{\omega}_p)) = s(\vec{\omega} - \vec{\omega}_p)$. When the grid and the particles move with the fluid velocity and the interpolation scheme is consistent with the choice of the grid, it can be shown that the natural coordinates are constants of the motion [14]; in other words, $s(\vec{\omega} - \vec{\omega}_p)$ is constant during the Lagrangian phase in the space of natural coordinates.

In order to solve the problem that we described in the previous paragraph, we introduce the volume associated with each particle, V_p , in the same manner as it is done for the particle charge q_p , and to calculate the volume of each cell we use the same interpolation scheme adopted for the charge:

$$V(\vec{\omega}) = \sum_p V_p w(\vec{\omega} - \vec{\omega}_p), \quad (5)$$

where w is the assignment function associated with the shape function s [15]. Then the density is given by:

$$\rho(\vec{\omega}) = \frac{\sum_p q_p w(\vec{\omega} - \vec{\omega}_p)}{\sum_p V_p w(\vec{\omega} - \vec{\omega}_p)}. \quad (6)$$

This definition gives conservation of ρ along the Lagrangian trajectories of each particle, since q_p and V_p are constant (determined at the beginning of each simulation) and each particle is advected with constant w in the space of natural coordinates.

PIC summary

The KANDINSKY code consists of four parts: the loading of particles, the interpolation scheme, the Poisson solver and the particle mover. The implementation of each

part of the code has been realized taking into account the characteristics of the physical system to be simulated.

- **Loading particles**

In order to provide a precise, noiseless representation of the initial electron density distribution, computational particles are allowed to have different charge. This can be obtained by using the Mass Matrix formulation [16], according to which the particle properties are calculated at the beginning of each simulation.

- **Interpolation particle-grid**

The density on the grid is calculated from the particles through the new interpolation scheme defined in Eq. (6). The classic Cloud-In-Cell (CIC) method [15] is used for the interpolation functions. Slightly different expressions are used when a particle approaches the center or the boundary of the domain.

- **Poisson solver**

The Poisson equation can be solved with an efficient algorithm based upon the Fast Fourier Transform in θ , assuming a piecewise constant density distribution in r [13]. A set of decoupled differential equations is obtained for the Fourier components $\tilde{\phi}_k(r)$:

$$\frac{1}{r} \frac{d}{dr} \left(r \frac{d\tilde{\phi}_k}{dr} \right) + \frac{1}{r^2} \left(\frac{\sin \frac{\Delta\theta}{2}}{\frac{\Delta\theta}{2}} \right)^2 \tilde{\phi}_k = \tilde{n}_k(r). \quad (7)$$

Eqs. (7) are solved using a finite difference scheme. Then the velocity field can be calculated by using the central difference discretization.

- **Interpolation grid-particle**

Given the velocity field on the grid, the velocity on each particle can be calculated using the same CIC interpolation scheme:

$$\mathbf{v}_p = \sum_c \mathbf{v}_c w(\vec{\omega}_c - \vec{\omega}_p). \quad (8)$$

- **Particle mover**

Particles are moved solving the equations of motion $d\mathbf{r}_p/dt = \mathbf{v}_p$ discretized with the fourth-order Runge-Kutta method.

Figures 2 and 3 compare two simulations that only differ in using (6) (in the following we will refer to this code as an Advanced PIC code or KANDINSKY code) or the usual $\rho = \sum_p q_p w/(r\Delta r\Delta\theta)$ (Standard PIC code) for interpolating the density on the grid. This run has been done for an initial hollow density profile with a $k = 2$ perturbation. It can be noticed that very early some differences arise, in particular the Standard PIC code develops some high density vortices (the maximum value of the density almost doubles from the first to the last picture of Fig. 2) while this does not happen for the Advanced PIC code (the maximum of the density remains constant). In the Standard PIC code, we add an artificial compressibility to the system which is manifested by the localized vortices with increasing density.

Furthermore, in the Standard PIC code enstrophy grows because of the contribution of high density vortices, while we would expect enstrophy to be constant (as it is theoretically for the Euler model) or to decrease slowly (because the density develops smaller

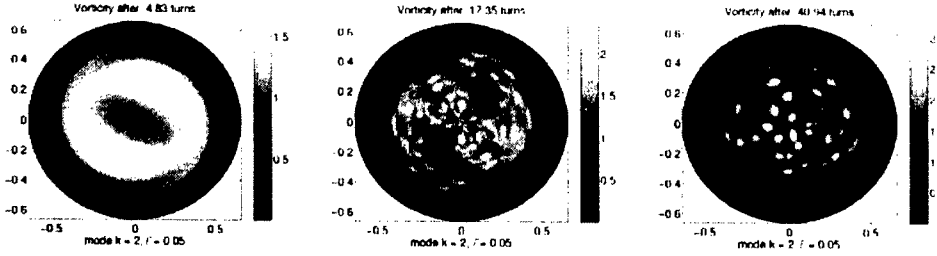


FIGURE 2. Standard PIC Code for a $k = 2$ instability in a hollow profile.

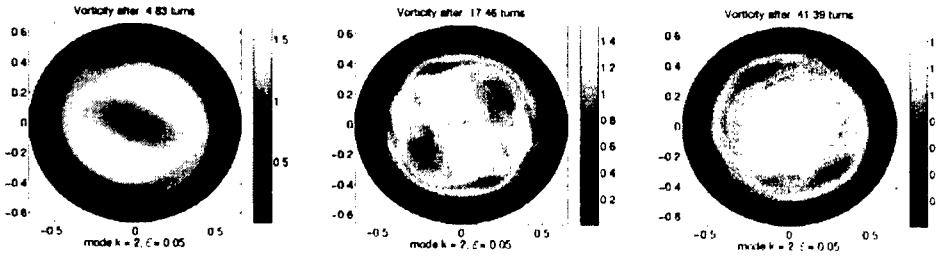


FIGURE 3. KANDINSKY Code for a $k = 2$ instability in a hollow profile.

and smaller length scales and at some point it is dissipated by numerical viscosity). Indeed, for the Advanced PIC code, enstrophy is a slowly decreasing function of time.

VALIDATION TESTS

In this section we use the Euler model, which can be obtained from system (2) by taking $\mathcal{L}_0(r) = \text{const}$, in order to compare our results with analytical results and with a reference Eulerian fluid code. In all of our simulations we use an initial equilibrium density profile of the form

$$n_{c0}(r) = \begin{cases} n_0(0) \left[1 - \left(\frac{r}{r_p} \right)^2 \right]^2 \left[1 + (\mu + 2) \left(\frac{r}{r_p} \right)^2 \right] & 0 \leq r \leq r_p \\ 0 & r > r_p, \end{cases} \quad (9)$$

which depends on three parameters: $n_0(0)$, r_p and μ . The last one is particularly important: for $\mu > 0$ the profile is hollow (possible diocotron instability) where for $\mu < 0$ the profile is monotonic (always stable). The simulations below are done with $\mu = 10$, $r_p = 0.59$ and $n_0(0)$ is specified to give $\int_0^{R_w} n_{c0}(r) 2\pi r dr = 1$. The normalized temperature α is chosen equal to 0. According to [6] the equilibrium profile of σ is obtained by $\sigma_0 = n_{c0} \mathcal{L}_0$. The initial charge density is perturbed by modifying the particle charge as $q'_p = q_p [1 + \epsilon \cos(k\theta)]$, where k is the mode number and ϵ is the perturbation amplitude. The system is discretized with a $N_r \times N_\theta$ grid and using N_p particles. In the cases below

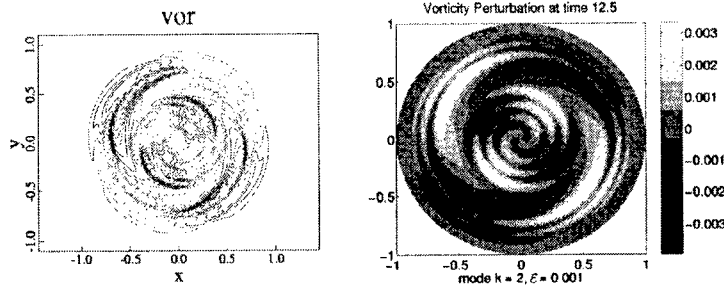


FIGURE 4. Vorticity (density) perturbation from a) Eulerian Fluid Code: linear phase (left); b) KANDINSKY Code: linear phase (right).

we use $N_r = 150$, $N_\theta = 128$, $N_p = 558208$, the average number of particles per cell is 49 and the time step is $dt = 0.1$.

• Test of accuracy

Three important conserved quantities are canonical angular momentum, proportional to $P = \int \int r^2 n_c r dr d\theta$, electrostatic energy, proportional to $H = \int \int n_c \phi_c r dr d\theta$, and enstrophy, proportional to $Z = \int \int n_c^2 r dr d\theta$. (There are additional invariants $\int \int f(n_c) r dr d\theta$, with f any function.)

The first two quantities are conserved well by the code (in a run with $k = 2$, $\epsilon = 0.01$ and $t_{max} = 600$, not shown): $\delta P/P = 0.6\%$ and $\delta H/H = 0.3\%$. The enstrophy is weakly conserved due to filamentation, but still the code preserved it well: $\delta Z/Z = 5\%$.

• Comparison with a Reference Eulerian Fluid Code

The code has been compared with a reference Eulerian fluid code in both the linear and nonlinear phase. Figs. 4a and 4b show the evolution of the perturbation of the density at $t = 12.5$. The initial perturbation has been chosen very small ($\epsilon = 0.001$) in order to remain in the linear phase. The agreement between the two codes is remarkable and one can notice that the fluid code has more numerical viscosity than the PIC code.

Figs. 5a and 5b show the evolution of the density after a large initial perturbation ($\epsilon = 0.25$). The two codes agree very well, even in this nonlinear case. It should be noticed that the Eulerian code cannot follow with enough accuracy the region with steep gradients outside the core region.

SIMULATIONS

In this section, we analyse the dynamics of models (2), (3) and (4). We compare different runs with $k = 1$ and $\epsilon = 0.001$. Model (2) can simulate GFD by using a suitable equilibrium length profile, as it will be explained in the following. The shallow-water equation for the potential vorticity can be simplified assuming small topography variations or small variations of the Coriolis parameter. In the last case, $(\xi + 2\Omega)/h$ can be approximated as $\xi + \beta r - \gamma r^2$. For $\gamma = 0$ we have the β -plane approximation, while for $\beta = 0$ we have the γ -plane approximation [12]. The analogy between non-neutral plasmas and GFD is established using the linear theory, where $\beta - 2\gamma r$ can be identified with $n_{c0}(r)\mathcal{L}'_0(r)/\mathcal{L}_0(r)$ [5, 8]. Moreover, due to the fact that $\mathcal{L}'_0(0) = 0$, it follows that

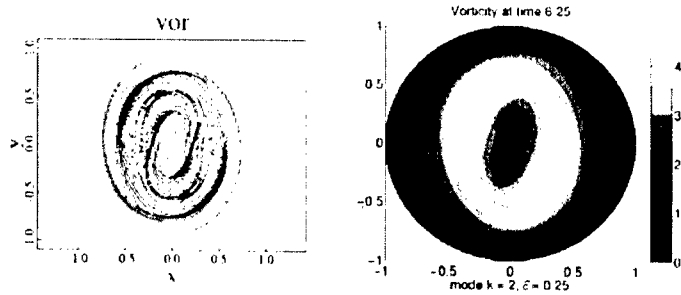


FIGURE 5. Vorticity (density) from a) Eulerian Fluid Code: nonlinear phase (left); b) KANDINSKY Code: nonlinear phase (right).

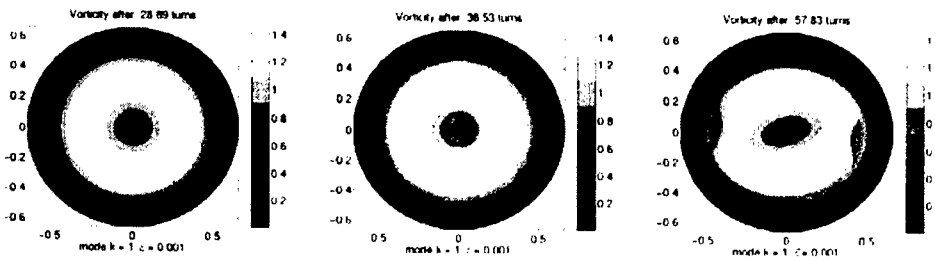


FIGURE 6. Evolution of the density n_r according to the Euler model.

$\beta = 0$ and thus we are in the limit of the γ -plane approximation. Therefore, in order to simulate the γ -plane approximation of GFD, we use model (2) with $\alpha = 0$ and the length profile obtained by solving

$$n_{c0}(r) \frac{\mathcal{L}'_0(r)}{\mathcal{L}_0(r)} = -2\gamma r, \quad (10)$$

with the initial density profile given by (9) and $\gamma = sn_0(0)$ (this is the value of γ obtained from (10) assuming a parabolic profile $\mathcal{L}_0 = 1 - sr^2$, a constant density profile $n_{c0} = n_0(0)$ and in the limit of small radius, as shown in Ref. [8]). Model (4) is then also simulated in the limit of γ -plane approximation, using the same $\gamma = sn_0(0)$. In all the simulations below we use the curvature $s = 0.5$.

Figure 6 shows the evolution of the density for the Euler model after an initial $k = 1$ perturbation. The model does not develop any $k = 1$ instability and a slowly growing $k = 2$ mode eventually dominates. Figure 7 shows the density at the same times according to model (2). This model exhibits a strong $k = 1$ diocotron instability which dominates the $k = 2$ mode seen in Fig. 6. The low-density core region is pushed off-axis and the high-density region fills the center of the trap. At later times (not shown), the low-density region is redistributed by filamentation or in big vortices. The same picture can be drawn from Fig. 8, which shows the vorticity (density) evolution of the GFD model. The density develops the same features in Figs. 7 and 8 with small differences at later times due to nonlinearities.

Clearly, the comparison of Figs. 6, 7 and 8 proves that a Penning trap can simulate GFD and particularly its peculiar features not present in the classic Euler model.

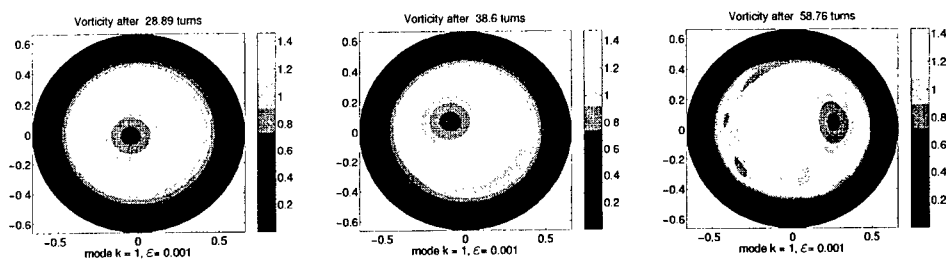


FIGURE 7. Evolution of the density n_c according to model (2).

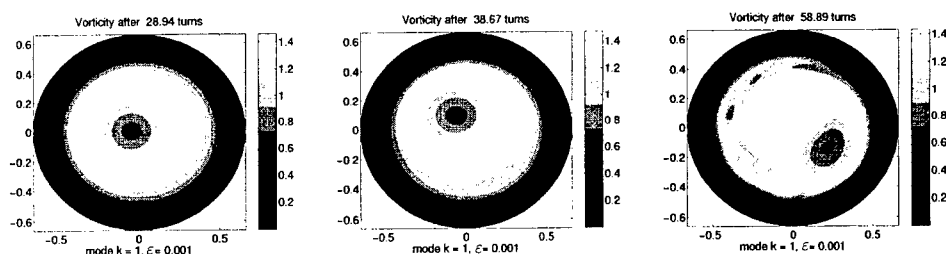


FIGURE 8. Evolution of the vorticity ξ according to the GFD model.

REFERENCES

1. Briggs, R. J., Daugherty, J. D., and Levy, R. H., *Phys. Fluids* **13**, 421-432 (1970).
2. Davidson, R. C., *An Introduction to the Physics of Nonneutral Plasmas*, Addison-Wesley, Redwood City, 1990.
3. Smith, R. A., and Rosenbluth, M. N., *Phys. Rev. Lett.* **64**, 649-652 (1990).
4. Driscoll, C. F., and Fine, K. S., *Phys. Fluids B* **2**, 1359-1366 (1990).
5. Finn, J. M., del-Castillo-Negrete, D., and Barnes, D. C., *Phys. Plasmas* **6**, 3744-3758 (1999); Finn, J. M., del-Castillo-Negrete, D., and Barnes, D. C., *Phys. Rev. Lett.* **84**, 2401-2404 (2000).
6. Coppa, G. G. M., D'Angola, A., Delzanno, G. L., and Lapenta, G., *Phys. Plasmas* **8**, 1133-1141 (2001).
7. Hilsabeck, T. J., and O'Neil, T. M., *Phys. Plasmas* **8**, 407-422 (2001).
8. del-Castillo-Negrete, D., Finn, J. M., and Barnes, D. C., "The modified drift-Poisson model: analogies with geophysical flows and Rossby waves", in *1999 Workshop on Nonneutral Plasmas*, edited by J. J. Bollinger, R. L. Spencer, R. C. Davidson, AIP Conference Proceedings 498, New York, 1999, pp. 147-152.
9. Dubin, D. H. E., and O'Neil, T. M., *Phys. Plasmas* **5**, 1305-1314 (1998).
10. Coppa, G. G. M., D'Angola, A., Delzanno, G. L., and Lapenta, G., "Rigorous Fluid Model for 3D Analysis of the Diocotron Instability", these proceedings.
11. Delzanno, G. L., Pariev, V. I., Lapenta, G., and Finn, J. M., "Diocotron Spectrum with Compression Effects", these proceedings.
12. Salmon, R., *Lectures on Geophysical Fluid Dynamics*, Oxford University Press, New York, 1998.
13. Coppa, G. G. M., D'Angola, A., and Lapenta, G., "Simulation of the Evolution of the Diocotron Instability", in *1999 Workshop on Nonneutral Plasmas*, edited by J. J. Bollinger, R. L. Spencer, R. C. Davidson, AIP Conference Proceedings 498, New York, 1999, pp. 129-134.
14. Brackbill, J. U., and Ruppel, H. M., *Jour. of Comp. Phys.* **65**, 314-343 (1986).
15. Hockney, R. W., and Eastwood, J. W., *Computer simulation using particles*, Adam Hilger, Bristol, 1988.
16. Burgess, D., Sulsky, D., and Brackbill, J. U., *Jour. of Comp. Phys.* **103**, 1-15 (1992).

SECTION 7

GENERAL THEORY

Energy Loss of Ions by Collisions with Magnetized Electrons

G. Zwicknagel* and C. Toepffer*

**Institut für Theoretische Physik, Universität Erlangen-Nürnberg,
Staudtstr. 7, D - 91058 Erlangen, Germany*

Abstract. The interaction of ions with electrons in the presence of an external magnetic field is a basic process for the description of the transport properties of a magnetized plasma, as e.g. the energy loss of ions to the superimposed electron beam in the electron cooler of a storage ring. But a comprehensive description of binary collisions of ions and electrons in the presence an external magnetic field has still to be established. Here, we recently achieved some progress by calculating the energy transfer in binary ion-electron collisions both by fully numerical classical-trajectory-Monte-Carlo (CTMC) simulations and by perturbation theory. These two techniques and some first results are presented and discussed, in particular the strong dependencies of the energy loss on the direction of the ion motion with respect to the magnetic field and on the anisotropy of the velocity distribution of the electrons.

INTRODUCTION

One fundamental process for the description of the transport properties of a magnetized plasma is the interaction of ions and electrons in the presence of an external magnetic field. Prominent examples are the resulting cooling of ions by a surrounding electron plasma in a trap or by the energy loss of the ions to the superimposed electron beam in the electron cooler of a storage ring. Although electron cooling in a storage ring is a well established method, a lot of observations are not yet satisfactorily explained and understood. Here, an improvement of the theoretical understanding has to start with the energy loss of a highly charged heavy ion in a magnetized anisotropic electron plasma, which is the fundamental process in the electron cooler. Whereas the energy loss of ions in unmagnetized electron plasmas has already been studied extensively [1], a qualified and comprehensive description of the interaction of ions with magnetized electrons is still an open problem and a rather formidable task. The presence of a magnetic field considerably complicates the description of the energy loss mainly because of the loss of symmetries as compared to the case of an isotropic nonmagnetized electron plasma.

At weak coupling between the ion and the magnetized electrons a linear response description of the energy loss is applicable, where the energy loss is given in a closed form in terms of the dielectric function, see e.g. [1, 2]. The appropriate dielectric function which describes the response of an ideal plasma of magnetized electrons with an anisotropic velocity distribution can be derived analytically and is given in most textbooks on plasma physics, e.g. in [3]. Its rather complex structure implies, however, a very intricate numerical evaluation of the final expression for the energy loss. Such a

numerical analysis is in progress [4] and an important subject for an advanced understanding of the stopping power at these conditions.

Also the description of the energy loss as a result of subsequent binary ion-electron collisions is strongly complicated by the presence of a magnetic field as compared to the nonmagnetic case where the energy transfer in a collision is a function only of the relative velocity. With magnetic field, additional dependencies show up and the ion-electron motion no more separates in a center-of-mass and relative part, in general. This makes even binary ion-electron collisions to a rather exhausting and challenging problem. Thus the energy loss is typically treated on an approximative level only. Starting with the expression for the energy loss by nonmagnetized ion-electron collisions, the influence of the magnetic field enters only through certain cutoffs which divide the possible impact parameters into several classes corresponding to slow and fast and/or nonmagnetized and magnetized collisions. For each of these cases a separate contribution to the energy loss with a specific Coulomb logarithm is formulated, see e.g. [5] for details. More accurate descriptions of the energy loss have to start with a detailed treatment of ion-electron collisions in a magnetic field. Here we discuss two different approaches for the determination of the energy transfer in this type of binary collisions; first a fully numerical classical-trajectory-Monte-Carlo (CTMC) scheme and, additionally, a perturbation treatment up to 2nd order in the ion-electron interaction.

ION-ELECTRON COLLISIONS IN A MAGNETIC FIELD

We consider the interaction between an ion (mass M , charge Ze , position \mathbf{R} , velocity $\mathbf{V} = \dot{\mathbf{R}}$) and an electron (m , $-e$, \mathbf{r}_e , $\mathbf{v}_e = \dot{\mathbf{r}}_e$) in a static, homogeneous magnetic field \mathbf{B} (and a vector potential $\mathbf{A} = c(\mathbf{B} \times \mathbf{r})/2$) in framework of classical mechanics. This is specified by the Lagrangian \mathcal{L}

$$\mathcal{L} = \frac{m}{2}v_e^2 + \frac{M}{2}V^2 - \frac{e}{2}(\mathbf{B} \times \mathbf{r}_e) \cdot \mathbf{v}_e + \frac{Ze}{2}(\mathbf{B} \times \mathbf{R}) \cdot \mathbf{V} - \Phi(|\mathbf{r}_e - \mathbf{R}|). \quad (1)$$

Because the two-body interaction $\Phi(\mathbf{r}_e, \mathbf{R}) = \Phi(|\mathbf{r}_e - \mathbf{R}|)$ depends only on the relative distance, we next perform a transformation to the cms ($\mathbf{R}_{cm}, \mathbf{V}_{cm}$) and relative the frame ($\mathbf{r}_r, \mathbf{v}_r$), defined through $\mathbf{R}_{cm} = (m\mathbf{r}_e + M\mathbf{R})/(m+M)$, $\mathbf{V}_{cm} = (m\mathbf{v}_e + M\mathbf{V})/(m+M)$, and $\mathbf{r}_r = \mathbf{r}_e - \mathbf{R}$, $\mathbf{v}_r = \mathbf{v}_e - \mathbf{V}$. In these coordinates, the Lagrangian (1) takes then the form

$$\begin{aligned} \mathcal{L} = & \frac{m+M}{2}V_{cm}^2 + \frac{\mu}{2}v_r^2 - \Phi(r_r) + \frac{(Ze-e)}{2}(\mathbf{B} \times \mathbf{R}_{cm}) \cdot \mathbf{V}_{cm} \\ & + \frac{\mu^2}{2}\left(\frac{Ze}{M^2} - \frac{e}{m^2}\right)(\mathbf{B} \times \mathbf{r}_r) \cdot \mathbf{v}_r - \frac{\mu}{2}\left(\frac{Ze}{M} + \frac{e}{m}\right)\{(\mathbf{B} \times \mathbf{R}_{cm}) \cdot \mathbf{v}_r + (\mathbf{B} \times \mathbf{r}_r) \cdot \mathbf{V}_{cm}\}, \end{aligned} \quad (2)$$

where μ is the reduced mass $\mu^{-1} = M^{-1} + m^{-1}$. The resulting equations of motions in the cms and relative frame are:

$$\begin{aligned}\frac{d}{dt}(m+M)\mathbf{V}_{cm} &= (Ze-e)(\mathbf{V}_{cm} \times \mathbf{B}) - \mu\left(\frac{Ze}{M} + \frac{e}{m}\right)(\mathbf{v}_r \times \mathbf{B}) \\ \frac{d}{dt}\mu\mathbf{v}_r &= \mu^2\left(\frac{Ze}{M^2} - \frac{e}{m^2}\right)(\mathbf{v}_r \times \mathbf{B}) - \mu\left(\frac{Ze}{M} + \frac{e}{m}\right)(\mathbf{V}_{cm} \times \mathbf{B}) - \nabla\Phi(r_r)\end{aligned}\quad (3)$$

Expressions (2) and (3) already offer very useful insight in the complications which here appear compared to the case without a magnetic field. In the nonmagnetic case only the first terms of the Lagrangian (2) are present and the motion separates in a cm- and a relative part in the usual way. But with magnetic field the cms motion is coupled to the relative motion, as given by the last term of \mathcal{L} (2) and the corresponding terms in Eqs.(3), and the cm-velocity \mathbf{V}_{cm} is not conserved. While the total energy E , that is, the Hamiltonian $\mathcal{H} = (m+M)V_{cm}^2/2 + \mu v_r^2/2 + \Phi(r_r) = E = E_{cm} + E_r$, is a constant of motion ($d\mathcal{H}/dt = 0$), the cm-energy $E_{cm} = (m+M)V_{cm}^2/2$ and the relative energy $E_r = \mu v_r^2/2 + \Phi(r_r)$ are not conserved separately and the problem cannot be reduced to three relevant degrees of freedom, in general. This is, however, possible for electron-electron collisions, which are of great interest as well when discussing transport properties of a magnetized plasma. Setting formally $Z = -1, M = m, \mu = m/2$, the prefactor of the coupling term in Eq. (2) cancels and the Lagrangian takes the form $\mathcal{L}_{ee} = \mathcal{L}_{cm}(\mathbf{V}_{cm}, \mathbf{R}_{cm}) + \mathcal{L}_r(\mathbf{v}_r, \mathbf{r}_r)$. This possible reduction to a much simpler system makes a very important difference between ion-electron collisions and electron-electron collisions in a magnetic field.

As $M \gg m, \mu \rightarrow m$ and for cases where the cyclotron period of the ion is large compared to the collision time, we may also consider a simpler problem by calculating the energy transfer in an ion-electron collision under the assumption that the ion velocity is constant up to terms $O(m/M)$, i.e. $\mathbf{V} = \text{const} + O(m/M)$. Neglecting terms of $O(m/M)$, the cm-velocity $\mathbf{V}_{cm} = \mathbf{V} + O(m/M)$ remains constant as well, whereas the time evolution of the cm-energy

$$\frac{dE_{cm}}{dt} = \mathbf{V}_{cm} \cdot \frac{d}{dt}(m+M)\mathbf{V}_{cm} = -e \mathbf{V} \cdot (\mathbf{v}_r \times \mathbf{B}) + O\left(\frac{m}{M}\right) \quad (4)$$

is still coupled to the relative motion, which is now determined by

$$\frac{d}{dt}m\mathbf{v}_r = -\nabla\Phi(r_r) - e(\mathbf{v}_r \times \mathbf{B}) - e(\mathbf{V} \times \mathbf{B}) + O\left(\frac{m}{M}\right). \quad (5)$$

There exists, up to terms $O(m/M)$, the conserved quantity

$$K = \frac{m}{2}v_r^2 + \Phi(r_r) + e(\mathbf{V} \times \mathbf{B}) \cdot \mathbf{r}_r \quad (6)$$

which replaces the total energy as a constant of motion in the limit $M \gg m$. The magnetic term in K is here associated with the non-conservation of E_{cm} , Eq. (4).

ENERGY TRANSFER AND ENERGY LOSS

To calculate the energy loss of an ion in a magnetized electron plasma we have first to determine the energy transfer to the ion $\Delta E_M = M(V'^2 - V^2)/2$ from the velocities $\mathbf{v}'_r, \mathbf{V}'_{cm}$ after a binary ion-electron collision with given initial velocities $\mathbf{v}_r, \mathbf{V}_{cm}$ (and positions $\mathbf{r}_r, \mathbf{R}_{cm}$), where $\mathbf{V} = \mathbf{V}_{cm} - \mu/M\mathbf{v}_r$ and $\mathbf{V}' = \mathbf{V}_{cm}' - \mu/M\mathbf{v}'_r$. In the limit $M \gg m$, the energy change $dE_M/dt = M\mathbf{V} \cdot d\mathbf{V}/dt$ during the collision is in leading order given by $dE_M/dt = M\mathbf{V}_{cm} \cdot d\mathbf{V}_{cm}/dt + m\mathbf{V} \cdot d\mathbf{v}_r/dt$. This results, using Eqs. (4) - (6), in an energy transfer

$$\Delta E_M = e(\mathbf{V} \times \mathbf{B}) \cdot (\mathbf{r}'_r - \mathbf{r}_r) - m\mathbf{V} \cdot (\mathbf{v}'_r - \mathbf{v}_r) = -\frac{m}{2}(v_r'^2 - v_r^2) - m\mathbf{V} \cdot (\mathbf{v}'_r - \mathbf{v}_r). \quad (7)$$

The required final velocity \mathbf{v}'_r is now calculated both within a fully numerical approach and by perturbation theory.

The fully numerical evaluation of the energy loss is based on a classical-trajectory-Monte-Carlo (CTMC) like treatment. Here the relevant equations of motion, see Eq. (5),

$$m \frac{d\mathbf{v}_r}{dt} = -\nabla \left[-\frac{Ze^2}{4\pi\epsilon_0 r} \exp\left(-\frac{r}{\lambda}\right) \right] - e(\mathbf{v}_r \times \mathbf{B}) - e(\mathbf{V} \times \mathbf{B}), \quad \frac{d\mathbf{r}_r}{dt} = \mathbf{v}_r, \quad (8)$$

are integrated numerically for a given set of initial conditions using a modified Velocity-Verlet algorithm which has been specifically designed for particle propagations in a (strong) magnetic field. It is described in detail in Ref. [6]. The ion-electron interaction Φ is modeled by a Yukawa type screened Coulomb interaction with a screening length λ , which here represents an additional external parameter. The numerical integration starts, for cases with $r_c < \lambda$, at an ion-electron distance r_r of several λ and stops when r_r exceeds this distance again after the collision. If the cyclotron radius r_c of the electron exceeds λ , this distance is enlarged by r_c . To achieve the required accuracy the constant of motion K (6) is monitored and the actual time-step is adapted continuously. The resulting relative deviations of K are of the order of $10^{-6} \dots 10^{-5}$. The initial conditions are, besides the fixed, constant ion velocity \mathbf{V} , the relative velocity \mathbf{v}_r , a phase ϕ of the helical motion of the electron in the magnetic field and the position \mathbf{r}_r . This initial position is related to an impact parameter \mathbf{b} which lies in a plane perpendicular to the initial velocity of the guiding center in the relative frame $\mathbf{g}_r(t=0) = -V_x \mathbf{e}_x + \mathbf{v}_r \cdot \mathbf{e}_z$, where we assumed $\mathbf{B} = B\mathbf{e}_z$ and $\mathbf{V} = V_x \mathbf{e}_x + V_z \mathbf{e}_z$. See also Ref. [7] for more details. From the changes of the relative velocity, $\mathbf{v}_r \rightarrow \mathbf{v}'_r$, for a specific trajectory we then obtain the energy transfer $\Delta E_M(\mathbf{v}_r, \mathbf{V}, \mathbf{b}, \phi)$ as a function of the initial values $\mathbf{v}_r, \mathbf{V}, \mathbf{b}, \phi$. As the next step, an averaging over the phases ϕ and the impact parameters \mathbf{b} is performed by a Monte-Carlo sampling which results in the quantity

$$\langle \Delta E_M(\mathbf{v}_r, \mathbf{V}) \rangle = \int d^2b \int_0^{2\pi} \frac{d\phi}{2\pi} \Delta E_M(\mathbf{v}_r, \mathbf{V}, \mathbf{b}, \phi). \quad (9)$$

The actual number of computed trajectories needed for $\langle \Delta E_M \rangle$ is adjusted by monitoring the convergence of the averaging procedure. Typically, around 10^5 trajectories are required for one set of parameters $\mathbf{v}_r, \mathbf{V}, B$. To finally obtain the energy loss, i.e. the energy

change of the ion per unit path length, the averaged energy transfer $\langle \Delta E_M \rangle$ is multiplied with the flux density of electrons $n|\mathbf{g}_r|$, which is directed parallel to the normal vector of the area element d^2b , and integrated over the electron distribution, that is,

$$\frac{dE}{ds} = \frac{1}{V} \frac{dE}{dt} = \frac{n}{V} \int d^3v_e f(\mathbf{v}_e) |\mathbf{g}_r| \int d^2b \int_0^{2\pi} \frac{d\phi}{2\pi} \Delta E_M(\mathbf{v}_r, \mathbf{V}, b, \phi) \quad (10)$$

The energy loss dE/ds (10) basically represents the energy change per time dE/dt as an average over the number of collisions per time and the energy transfer per collision.

In the second approach the velocity transfer $\Delta \mathbf{v}_r = \mathbf{v}'_r - \mathbf{v}_r$ is calculated in a 2nd-order perturbation treatment of the relative motion

$$m \frac{d\mathbf{v}_r}{dt} = -\nabla \left[-\frac{Ze^2}{4\pi\epsilon_0 r_r} \right] - e(\mathbf{v}_r \times \mathbf{B}) - e(\mathbf{V} \times \mathbf{B}), \quad \frac{d\mathbf{r}_r}{dt} = \mathbf{v}_r, \quad (11)$$

using the bare Coulomb interaction $\Phi = -Ze^2/4\pi\epsilon_0 r_r$. The approximate solution starts with the analytically given trajectory $\mathbf{r}_0(t)$, $\mathbf{v}_0(t) = \dot{\mathbf{r}}_0(t)$ for the unperturbed electron motion, i.e. $\Phi = 0$ and

$$m \frac{d\mathbf{v}_0}{dt} + e(\mathbf{v}_0 \times \mathbf{B}) = -e(\mathbf{V} \times \mathbf{B}).$$

Using the trajectory $\mathbf{r}_0(t)$ for calculating the force between ion and electron, a 1st-order correction $\mathbf{r}_1, \mathbf{v}_1$ with

$$m \frac{d\mathbf{v}_1}{dt} + e(\mathbf{v}_1 \times \mathbf{B}) = -\nabla \Phi(r)|_{\mathbf{r}=\mathbf{r}_0}, \quad \frac{d\mathbf{r}_1}{dt} = \mathbf{v}_1$$

provides the velocity transfer $\delta \mathbf{v} = \mathbf{v}'_1 - \mathbf{v}_1$ which is $O(Z)$. In the next step a $O(Z^2)$ velocity transfer $\delta^{(2)} \mathbf{v} = \mathbf{v}'_2 - \mathbf{v}_2$ is obtained from a 2nd-order correction to the unperturbed motion by taking into account the additional force due the 1st-order displacement of the trajectory \mathbf{r}_1 . Here

$$m \frac{d\mathbf{v}_2}{dt} + e(\mathbf{v}_2 \times \mathbf{B}) = -[\nabla \Phi(r)|_{\mathbf{r}=\mathbf{r}_0-\mathbf{r}_1} - \nabla \Phi(r)|_{\mathbf{r}=\mathbf{r}_0}],$$

where the parenthesized force term is expanded up to contributions linear in \mathbf{r}_1 .

Three regimes for the velocity transfer can be distinguished:

- (i) The Coulomb field is dominant when the cyclotron radius r_c of the electrons is larger than the distance of closest approach b_0 . Then, for an initial velocity \mathbf{v}_r ,

$$\delta \mathbf{v} = -\frac{Ze^2}{4\pi\epsilon_0 m} \frac{2}{v_r b_0^2} \mathbf{b}_0 \quad \delta^{(2)} \mathbf{v} = -\left(\frac{Ze^2}{4\pi\epsilon_0 m} \right)^2 \frac{2}{v_r^4 b_0^2} \mathbf{v}_r \quad (12)$$

- (ii) For the case of a large magnetic field with $r_c < b_0$ the transversal motion of the electron is quenched and there remains only the relative motion with respect to the guiding center, $\mathbf{g}_r = -V_x \mathbf{e}_x + \mathbf{v}_r \cdot \mathbf{e}_z$.

- (a) If the pitch δ is larger than b_0 the helix is stretched and there apply the same expressions (12) with $\mathbf{v}_r \rightarrow \mathbf{g}_r$.
- (b) Most interesting is the case of tight helices, where $\delta \ll b_0$. Here remains only a velocity transfer parallel to the magnetic field $\mathbf{B} = B\mathbf{e}_z$,

$$\delta\mathbf{v} = \frac{Ze^2}{4\pi\epsilon_0 m} \frac{2V_x \cos(\psi)}{g_r^2 b_0} \mathbf{e}_z \quad \delta^{(2)}\mathbf{v} = - \left(\frac{Ze^2}{4\pi\epsilon_0 m} \right)^2 \frac{2V_x^2 \mathbf{g}_r \cdot \mathbf{e}_z}{g_r^6 b_0^2} \mathbf{e}_z \quad (13)$$

provided that the ion has a velocity component V_x perpendicular to the magnetic field.

The energy loss of the ion is now obtained by integrating the energy transfer ΔE_M (7) first over an area element $\hat{\mathbf{v}}_r b_0 db_0 d\psi$ parallel to the relative current density $n\mathbf{v}_r$ and then over the velocity distribution $f(\mathbf{v}_e)$, i.e.

$$\frac{dE}{ds} = \frac{1}{V} \frac{dE}{dt} = \frac{n}{V} \int d^3v_e f(\mathbf{v}_e) \mathbf{v}_r \cdot \hat{\mathbf{v}}_r 2\pi \int_{b_{min}}^{b_{max}} db_0 b_0 \langle \Delta E_M \rangle_\psi. \quad (14)$$

In the ψ -averaged energy transfer $\langle \Delta E_M \rangle_\psi$ all terms $O(Z)$ vanish because of symmetry and up to $O(Z^2)$ we have

$$\langle \Delta E_M \rangle_\psi = -m\mathbf{V} \cdot \langle \delta^{(2)}\mathbf{v} \rangle_\psi - \frac{m}{2} (-2\mathbf{v}_r \cdot \langle \delta^{(2)}\mathbf{v} \rangle_\psi + \langle (\delta\mathbf{v})^2 \rangle_\psi). \quad (15)$$

The b_0 integration exceeds from $b_{min} = Ze^2/4\pi\epsilon_0 m v_r^2$ to the screening length $b_{max} = \lambda$. Hard collisions are taken into account by regularizing the emerging b_0 -integrals according to $\int_{b_{min}} db_0/b_0 \rightarrow \int_0 db_0/b_0/(b_0^2 + b_{min}^2)$. This procedure yields the exact result for the bare Coulomb case.

RESULTS

A comprehensive analysis of the energy loss of ion-electron collisions in a magnetic field is still in progress. For our current calculations we have been mainly interested in the specific situation in the electron cooler at the TSR storage ring at Heidelberg [8] and thus concentrated on the corresponding parameters, that is, an ion charge state $Z = 6$, an electron density $n = 8 \times 10^6 \text{ cm}^{-3}$, magnetic field strengths around $B = 0.01 \text{ T}$ and an anisotropic velocity distribution $f(\mathbf{v}_e)$ of the electrons. It is modeled as a product of two Maxwell distributions for the parallel and the transversal degrees of freedom (with respect to \mathbf{B}), i.e.

$$f(\mathbf{v}_e) = f(v_\perp, v_\parallel) = \frac{m}{2\pi k_B T_\perp} \left(\frac{m}{2\pi k_B T_\parallel} \right)^{1/2} \exp\left(-\frac{mv_\perp^2}{2k_B T_\perp}\right) \exp\left(-\frac{mv_\parallel^2}{2k_B T_\parallel}\right) \quad (16)$$

with temperatures $k_B T_\perp = 11.5 \text{ meV}$, $k_B T_\parallel = 0.1 \text{ meV}$, an anisotropy $T_\perp/T_\parallel = 115$ and respective thermal velocities $v_{th,\perp} = (k_B T_\perp/m)^{1/2} = 4.5 \times 10^4 \text{ m/s}$, $v_{th,\parallel} = (k_B T_\parallel/m)^{1/2} =$

4.2×10^3 m/s, i.e. $v_{th,\perp}/v_{th,\parallel} = 10.7$ and screening lengths $\lambda_{D,\perp} = (\epsilon_0 k_B T_{\perp} / e^2 n)^{1/2} = 2.8 \times 10^{-4}$ m, $\lambda_{D,\parallel} = (\epsilon_0 k_B T_{\parallel} / e^2 n)^{1/2} = 2.6 \times 10^{-5}$ m. Some examples for the energy loss dE/ds as obtained from the CTMC procedure, Eqs. (8)-(10), and the 2nd-order perturbation treatment, Eqs. (11)-(15), are shown in Figs. 1 and 2 as function of the ion velocity V in units of $v_{th,\parallel}$; in Fig. 1 for a magnetic field $B = 10$ mT and different directions $\alpha = 0^\circ, 30^\circ, 60^\circ$ and 90° of the ion motion, and in Fig. 2 for $\alpha = 0^\circ, 60^\circ$ and various $B = 2.5$ mT, 10 mT and 40 mT, where $\cos(\alpha) = \mathbf{B} \cdot \mathbf{V} / BV$. These results are compared with the energy loss of an ion in an anisotropic electron plasma without magnetic field ($B = 0$), where the equations of motion (8) can be solved analytically and the

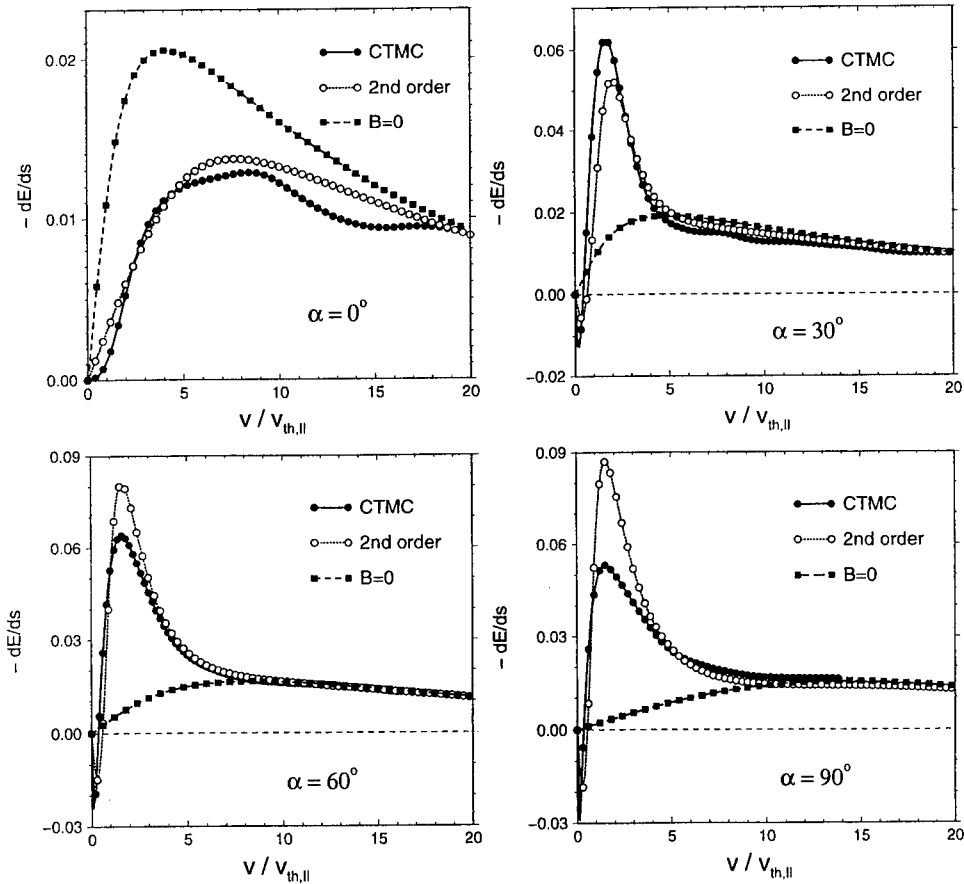


FIGURE 1. Energy loss dE/ds scaled in units of $4\pi n(Ze^2/4\pi\epsilon_0)^2/mv_{th,\parallel}^2$ as function of the ion velocity V in units of $v_{th,\parallel} = 4.2 \times 10^3$ m/s and for different directions of the ion motion $\alpha = 0^\circ, 30^\circ, 60^\circ$ and 90° . Results for $B = 10$ mT as obtained from the CTMC method and the 2nd-order perturbation treatment are compared with the respective energy loss without magnetic field ($B = 0$) [1]. In all cases, the used screening length is $\lambda = 1 \times 10^{-4}$ m and $T_{\perp}/T_{\parallel} = 115$.

energy loss (10) is thus given in closed form [1]. In all cases dE/ds is scaled in units of $4\pi n(Ze^2/4\pi\epsilon_0)^2/mv_{th,\parallel}^2$ which equals 0.75 eV/cm for the given parameters.

For an ion motion along the magnetic field, i.e. $\alpha = 0^\circ$, a significant suppression of the energy loss compared to the nonmagnetized case occurs, which increases with increasing magnetic field. This feature has also been found in a perturbative treatment of the equivalent case of an ion at rest [9] and for the closely related equilibration of the transversal and longitudinal temperatures in a magnetized electron plasma by electron-electron collisions [10]. In all these case the cm-energy E_{cm} is conserved and a complete separation in cms and relative motion is possible, in contrast to the case

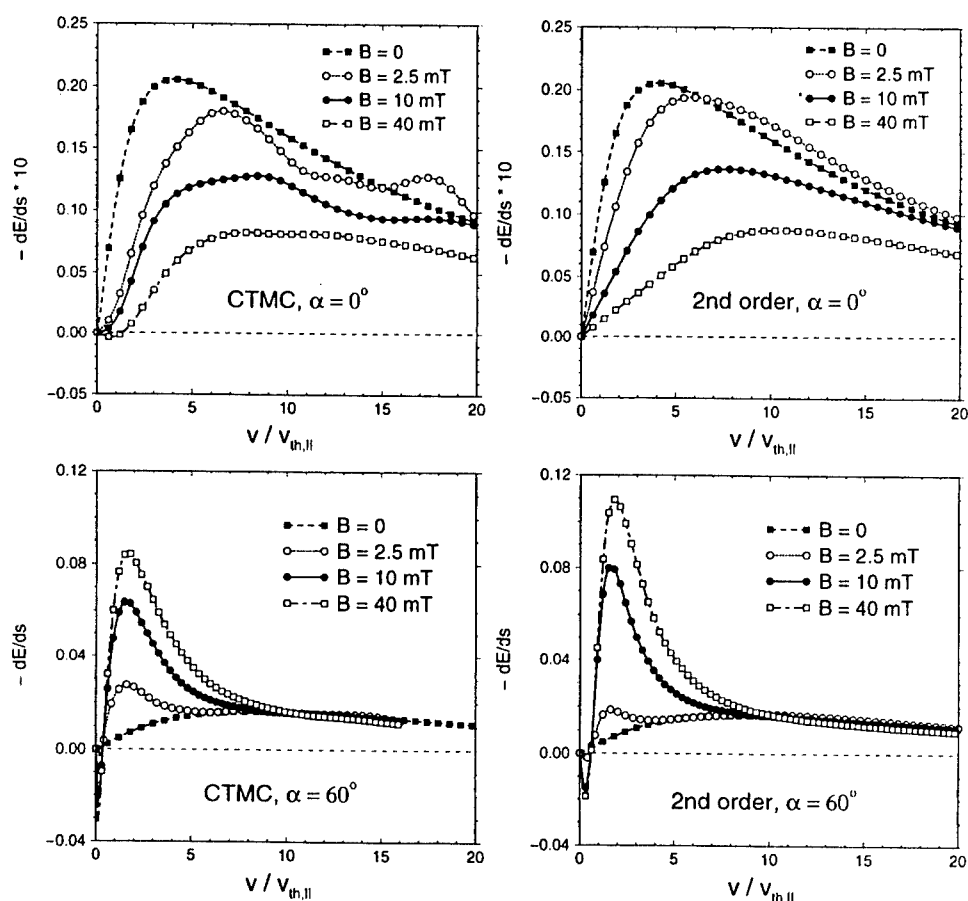


FIGURE 2. Energy loss dE/ds scaled in units of $4\pi n(Ze^2/4\pi\epsilon_0)^2/mv_{th,\parallel}^2$ as function of the ion velocity V in units of $v_{th,\parallel} = 4.2 \times 10^3$ m/s. Shown are results of the CTMC method (left) and the 2nd-order perturbation treatment (right) for different magnetic field strength $B = 2.5$ mT, 10 mT and 40 mT and the two directions $\alpha = 0^\circ$ (top) and 60° (bottom) together with the analytically obtained dE/ds for $B = 0$. The screening length is again $\lambda = 1 \times 10^{-4}$ m and $T_\perp/T_\parallel = 115$.

with a transversal component of the ion motion, that is, $\alpha \neq 0^\circ$. Here the presence of a magnetic field causes a strong enhancement of the energy loss at low ion velocities which increases with B . For even lower velocities $V < v_{th,\parallel}$ and $\alpha \neq 0^\circ$ we observe negative values of the energy loss which correspond to an energy gain and thus an acceleration of the ion. Both features, the strong enhancement and the negative values, are related to the nonequilibrium situation of a highly anisotropic velocity distribution. This can be concluded from calculations of the energy loss for a much lower anisotropy of $T_\perp/T_\parallel = 4$, as presented in Fig. 3. Here almost no negative values of the energy loss appear and only rather small enhancements can be found at large angles α and very low velocities. In general a reduction of the energy loss compared to the nonmagnetized case

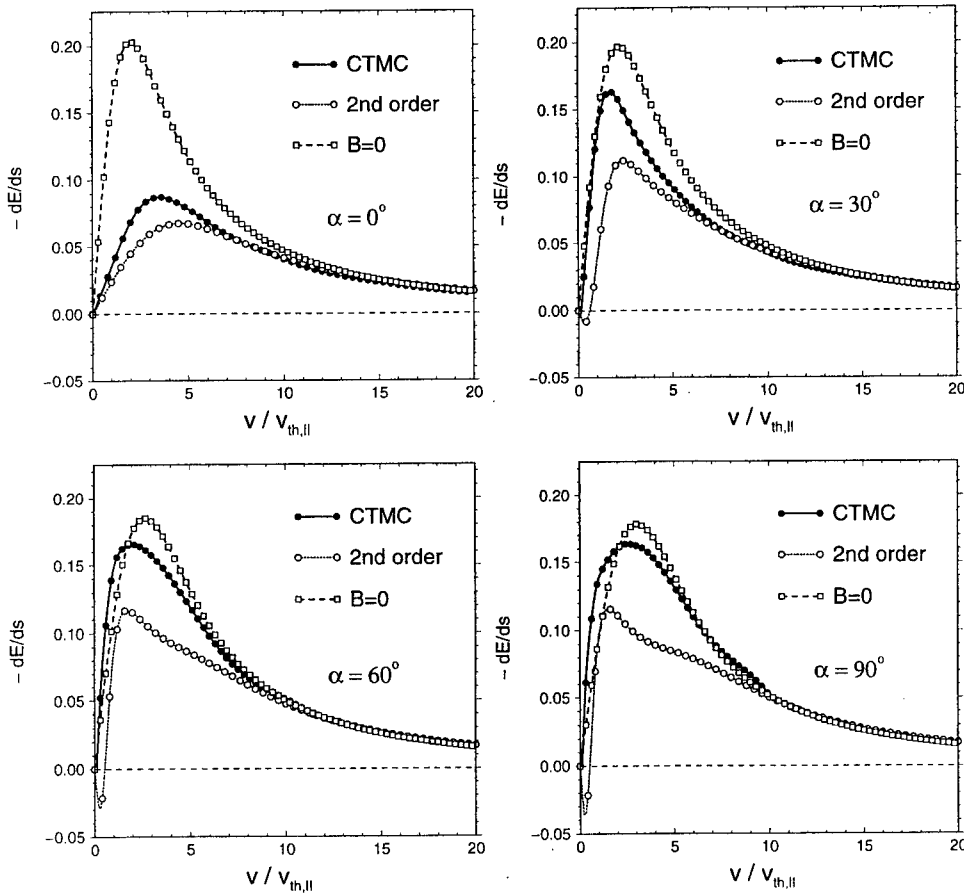


FIGURE 3. Energy loss dE/ds scaled in units of $4\pi n(Ze^2/4\pi\epsilon_0)^2/mv_{th,\parallel}^2$ as function of the ion velocity V in units of $v_{th,\parallel} = 1.2 \times 10^4$ m/s and for different directions of the ion motion $\alpha = 0^\circ, 30^\circ, 60^\circ$ and 90° . Results for $B = 50$ mT as obtained from the CTMC method and the 2nd-order perturbation treatment are compared with the energy loss for $B = 0$ [1]. The used screening length is $\lambda = 2.5 \times 10^{-5}$ m and $T_\perp/T_\parallel = 4$.

is observed, which is strongest at $\alpha = 0^\circ$ but only very weak at $\alpha = 90^\circ$. Compared to the CTMC results, the 2nd-order perturbation treatment here predicts a much stronger reduction of dE/ds and much bigger negative values. It reproduces, however, very well the essential general features of the energy loss by magnetized ion-electron collisions as found by the CTMC method, in particular, in the previous case of the highly anisotropic electron distribution.

OBSERVATIONS AND CONCLUSIONS

The presented results for the energy loss by ion-electron collisions in a magnetic field, as obtained from both a fully numerical investigation and a 2nd-order perturbation treatment, give an impression of the characteristic and important effects. One essential observation is the strong directional dependence with respect to \mathbf{B} , i.e. on α , in particular for a highly anisotropic electron distribution with $T_\perp/T_\parallel \gg 1$. This situation is characterized by a strong reduction of dE/ds with increasing B for $\alpha = 0$, a substantial enhancement of dE/ds with increasing B for $\alpha \neq 0$, and an energy gain of the ion at $v \lesssim v_{th,\parallel}$, at variance with the case of vanishing anisotropy, $T_\perp/T_\parallel \sim 1$. There we found an overall reduction of dE/ds which increases with B and decreases with α . But in all cases, the magnetic field significantly affects the energy loss only at low ion velocities V . These features and the results of the CTMC calculations are generally well reproduced by the outlined 2nd-order perturbation treatment. In a further step, after an additional averaging over the distribution of the ion velocities, the obtained results will be compared to the experimentally measured cooling forces [8]. This work is in progress.

REFERENCES

1. G. Zwicknagel, C. Toepffer and P.-G. Reinhard, Phys.Rep. **309** (1999) 117.
2. H. B. Nersisyan, M. Walter, G. Zwicknagel, Phys.Rev.E **61** (2000) 7022.
3. S. Ichimaru, *Basic Principles of Plasma Physics*, Benjamin Reading, Massachusetts 1973.
4. M. Walter, private communications, 2001.
5. I.N. Meshkov, Phys. Part. Nucl. **25** (1994) 631.
6. Q. Spreiter and M. Walter, J.Comput.Phys. **152** (1999) 102.
7. G. Zwicknagel, in *Non-neutral Plasma Physics III*, eds. J.J. Bollinger, R.L. Spencer and R.C. Davidson, AIP Conference Proceedings **498**, 1999, p. 469.
8. M. Beutelspacher, PhD Thesis, Universität Heidelberg, 2000.
9. D.K. Geller and J.C. Weisheit, Phys.Plasmas **4** (1997) 4258.
10. M.E. Glinsky, T.M. O'Neil, M.N. Rosenbluth, K. Tsuruta and S. Ichimaru, Phys.Fluids B **4** (1992) 1156.

Floquet Theory of the Quantum Dynamic Kingdon Trap

R. Blümel

Department of Physics, Wesleyan University, Middletown, CT 06459-0155

Abstract. The dynamic Kingdon trap is an excellent device for the investigation of chaos and quantum chaos, both theoretically and experimentally. Since it may be interpreted as an electrodynamical version of a Penning-Malmberg trap, it is also suited for the study of strongly coupled periodically or aperiodically driven nonneutral plasmas. Floquet theory provides a natural framework for the quantum mechanics of the periodically driven dynamic Kingdon trap.

The dynamic Kingdon trap is an electrodynamical trap for the storage of charged particles [1]. It resembles an electrodynamical version of a Penning-Malmberg trap [2] and can be used to study nonlinear effects in forced nonneutral plasmas such as rf heating or phase transitions [1]. It can also be used to study classical and quantum chaos [3,4] in oscillating fields. Even a single charged particle stored in a dynamic Kingdon trap may experience a transition to chaos [1,5]. This makes the dynamic Kingdon trap an ideal system, both experimentally and theoretically, for studying quantum chaos effects.

In its simplest form the dynamic Kingdon trap consists of a straight wire surrounded by a conducting cylinder [1]. A superposition of an ac and a dc voltage is applied between the wire and the cylinder such that the dc voltage attracts a charged particle placed between wire and cylinder into the direction of the wire. The voltages induce surface charges on the wire of magnitudes σ_{ac} and σ_{dc} , respectively. The main strength of the dynamic Kingdon trap is that it is capable of storing charged particles at zero angular momentum. We will exclusively focus on this case from now on. In addition we will assume that the particle has zero momentum parallel to the wire. Introducing the radial coordinate r of the charged particle and the unit vector \hat{r} in the radial direction, the force acting on a trapped charged particle of charge Z is given by

$$\vec{F}(\vec{r}, t) = \frac{Z}{2\pi\epsilon_0 r} [\sigma_{dc} + \sigma_{ac} \cos(\Omega t)] \hat{r}, \quad (1)$$

where Ω is the angular frequency of the applied ac voltage. Choosing

$$l = \left| \frac{2Z\sigma_{dc}}{\pi\epsilon_0 m\Omega} \right|^{1/2} \quad (2)$$

as the unit of length (m is the mass of the trapped particle), and $2/\Omega$ as the unit of time, we define $\rho = r/l$ as the dimensionless radial coordinate and $\tau = \Omega t/2$ as the dimensionless time. Written in these dimensionless quantities, and defining the control parameter $\eta = \sigma_{ac}/(2\sigma_{dc})$, Newton's equation $m\ddot{\vec{r}} = \vec{F}(\vec{r}, t)$ yields the Kingdon equation [1,6]

$$\frac{d^2\rho}{d\tau^2} + [1 - 2\eta \cos(2\tau)] \frac{1}{\rho} = 0 \quad (3)$$

as the classical equation of motion of the charged particle. Phase-space portraits [3] of (3) reveal the presence of a dominant trapping island surrounded by a chaotic sea [1].

The force \vec{F} acting on a charged particle in the dynamic Kingdon trap can be derived from the potential

$$V(r, t) = \left| \frac{Z\sigma_{dc}}{2\pi\epsilon_0} \right| \ln\left(\frac{r}{l}\right) [1 - 2\eta \cos(\Omega t)] \quad (4)$$

via $\vec{F} = -\vec{\nabla}V = -\hat{r}\partial V/\partial r$. We use this potential in the time-dependent Schrödinger equation for a single particle in the dynamic Kingdon trap:

$$i\hbar \frac{\partial \psi(\vec{r}, t)}{\partial t} = -\frac{\hbar^2}{2m} \Delta \psi(\vec{r}, t) + V(r, t) \psi(\vec{r}, t). \quad (5)$$

Because of the cylindrical symmetry of the trap and our assumption of zero angular momentum and zero momentum along the wire we have $\psi(\vec{r}, t) = \beta(r, t)$. Switching to dimensionless variables and defining $\varphi(\rho, \tau) = \rho^{1/2} \beta(\rho, \tau)$ we obtain the one-dimensional radial Schrödinger equation

$$i\alpha \frac{\partial \varphi(\rho, \tau)}{\partial \tau} = -\frac{\alpha^2}{2} \left[\frac{\partial^2 \varphi(\rho, \tau)}{\partial \rho^2} + \frac{1}{4\rho^2} \varphi(\rho, \tau) \right] + [1 - 2\eta \cos(2\tau)] \ln(\rho) \varphi(\rho, \tau), \quad (6)$$

where we defined the effective dimensionless Planck constant α , given by

$$\alpha = \left| \frac{\hbar\Omega\pi\epsilon_0}{Z\sigma_{dc}} \right|. \quad (7)$$

Technically (6) is a linear partial differential equation with time-periodic coefficients. In this case Floquet's theory [7] applies. It states that solutions of (6) exist which are of the form

$$\phi_\mu(\rho, \tau) = \exp(-i\mu\tau) \Phi_\mu(\rho, \tau), \quad (8)$$

where μ , in general a complex number, is the Floquet exponent and $\Phi_\mu(\rho, \tau)$ is a π -periodic function. These solutions of (6) are of prime importance to us, since we are interested in the long-time behavior of trapped quantum solutions. In this case it is convenient to study the wave function of the trapped particle at times that correspond to integer multiples of π . Given a starting state $|\varphi_0\rangle = |\varphi(\rho, \tau = 0)\rangle$, the quantum states of the trapped particle at times $\tau_m = m\pi$ are given by

$$|\varphi(\tau_m)\rangle \equiv |\varphi_m\rangle = \hat{U}^m |\varphi_0\rangle, \quad m = 0, 1, 2, \dots, \quad (9)$$

where \hat{U} is the one-cycle propagator, i.e. the time evolution operator of the system from $\tau = 0$ to $\tau = \pi$. Applying (9) to the Floquet solutions (8) for one cycle ($m = 1$) we have immediately

$$\hat{U} |\phi_\mu(\rho, \tau = 0)\rangle = |\phi_\mu(\rho, \tau = \pi)\rangle = \exp(-i\mu\pi) |\phi_\mu(\rho, \tau = 0)\rangle. \quad (10)$$

This equation shows that in addition to their mathematical significance, the Floquet solutions (8) at $\tau = \tau_m$ have a very direct physical meaning: they are the eigenfunctions of the one-cycle propagator \hat{U} . Floquet solutions of time-periodic quantum systems were studied in detail in the quantum literature. Among the first were Shirley [8] and Zeldovich [9]. The Floquet exponent μ is also known as the quasienergy, and the wave functions $\Phi_\mu(\rho, \tau)$ are known as the quasienergy wave functions [9].

Since according to (10) the Floquet states reproduce themselves up to a phase factor after propagation with \hat{U} , the Floquet states are non-spreading wave packets. Therefore, for periodically driven systems such as the dynamic Kingdon trap, the Floquet states are the closest analogues of the stationary states of a time-independent quantum system.

Computing the Floquet states of the dynamic Kingdon trap shows that they come basically in two varieties: (i) narrow states located inside of the trapping island, and (ii) broad states characterized by a large overlap with the chaotic sea. For sufficiently small α the states localized within the trapping island resemble harmonic oscillator states forming a systematic sequence of states characterized by an increasing number of zeros within the trapping island. This sequence is finite since at some point these Floquet states become so wide that they "spill out" of the trapping island and leak out into the chaotic sea. Even the "broad states" of the chaotic sea may harbor some surprises. It is possible that these states are not entirely delocalized over the chaotic sea, but show Anderson localization phenomena [10] akin to similar effects observed in the kicked rotor [11] and the hydrogen atom in a strong microwave field [12]. Computing the Wigner transforms

$$f_\mu(\rho, p) = \frac{1}{2\pi\alpha} \int \phi_\mu(\rho + s/2) \phi_\mu^*(\rho - s/2) e^{-ips/\alpha} ds \quad (11)$$

of the Floquet states localized inside of the trapping island shows that these states are not only localized inside of the island as far as their space coordinates are concerned, but are entirely localized inside of the island in phase space.

Of all of the quantum dynamical traps the dynamic Kingdon trap is perhaps the most interesting one from a nonlinear dynamics point of view. Loaded with only a single charged particle the trap shows a mixed phase space that possesses all of the classic phase-space morphology, including regular islands and a chaotic sea. Experimentally accessible quantum chaotic systems are rare. Due to its simplicity the dynamic Kingdon trap has a realistic chance of joining the currently small family of quantum chaos experiments. Among these the dynamic Kingdon trap is perhaps closest in spirit to the hydrogen atom in a strong microwave field [12,13]. Both systems are driven by external ac fields, and both systems show a mixed phase space. While it is known that the hydrogen atom in a strong microwave field possesses a true ionization continuum with unnormalizable quantum states, the nature of the quasienergy spectrum of the dynamic Kingdon trap is not currently known. Because of its simple, but nevertheless representative phase-space structure, the dynamic Kingdon trap has much to offer for theoretical and experimental quantum chaos research. Since the dynamic Kingdon trap resembles an electrodynamical version of a Penning-Malmberg trap [2] and since it is possible to store many charged particles simultaneously in a dynamic Kingdon trap [1], the dynamic Kingdon trap is also an excellent device for studying strongly forced nonneutral plasmas.

The author gratefully acknowledges financial support by NSF grants PHY-9900730 and PHY-9984075.

REFERENCES

1. Blümel, R., *Phys. Rev. A* **51**, R30-R33 (1995); *Appl. Phys. B* **60**, 119-122 (1995); *Physica Scripta T* **59**, 126-130 (1995); 369-379 (1995).
2. Driscoll, C.F., and Fine, K.S., *Phys. Fluids B* **2**, 1359-1366 (1990).
3. Lichtenberg, A.J., and Lieberman, M.A., *Regular and Stochastic Motion*, Springer, New York, 1983.
4. Gutzwiller, M.C., *Chaos in Classical and Quantum Mechanics*, Springer, New York, 1990.
5. Peik, E., and Fletcher, J., *J. Appl. Phys.* **82**, 5283-5286 (1997).
6. Linz, S.J. *Phys. Rev. A* **52**, 4282-4284 (1995).
7. Ince, E.L., *Ordinary Differential Equations*, Dover, New York, 1956.
8. Shirley, J.H., *Phys. Rev.* **138**, B979-B987 (1965).
9. Zel'dovich, Ya.B., *Sov. Phys. JETP* **24**, 1006-1009 (1967).
10. Anderson, P.W., *Phys. Rev.* **109**, 1492-1505 (1958).
11. Fishman, S., Grempel, D.R., and Prange, R.E., *Phys. Rev. Lett.* **49**, 509-512 (1982).
12. Casati, G., Chirikov, B.V., Guarneri, I., and Shepelyansky, D.L., *Phys. Rep.* **154**, 77-123 (1987).
13. Koch, P.M., and van Leeuwen, K.A.H., *Phys. Rep.* **255**, 289-403 (1995).

Kinetic Description of a Degenerate, Rotating, Non-neutral Electron Plasma in External Magnetic Fields in the Framework of the Thomas-Fermi-Dirac Theory

V. G. Molinari, F. Rocchi and M. Sumini (*)

*INFN-BO and Laboratorio di Montecuccolino,
Dipartimento di Ingegneria Energetica, Nucleare e del Controllo Ambientale,
University of Bologna, Italy*
vincenzo.molinari@mail.ing.unibo.it marco.sumini@mail.ing.unibo.it
federico.rocchi@mail.ing.unibo.it

Abstract. Aim of this work is to extend the results obtained in a previous study on the magnetic confinement and stability of a quantum degenerate non-neutral fermion plasma. This extension consists in the inclusion in the previously set up model of the effects of the exchange forces, and generalises the Thomas-Fermi (TF) approach used in the referenced work towards a Thomas-Fermi-Dirac (TFD) statistical description. The TF model has not only been used extensively and with success in these years to study atomic, nuclear and molecular properties, or to evaluate features of matter in extreme conditions such as low temperatures and/or high densities typical of astrophysics and inertial confinement fusion experiments, but also to found hydrodynamic theories for the diffusion and stability of fermion plasmas, one component non-neutral degenerate fluids, plasmas etc. In this paper an equation for density profiles in cylindrical symmetry is found, from the semiclassical kinetic theory of quantum gases, which takes into account the effects of temperature, average velocity, external magnetic field and quantum exchange. Numerical solutions of this equation for the case of complete quantum degeneracy are given and comparisons with the previous results are carried out.

INTRODUCTION

A many-body charged particle system in which there is not overall charge neutrality can have, as has been shown since the early '70s, collective oscillations and excitations as well as shielding and screening effects [1]; this many-body collection of charged particles is therefore termed a non-neutral plasma (NNP). In certain physical situations the NNP is in such conditions that also global effects of quantum nature are present and observable [2,3,4]. These conditions, which append the adjective "degenerate" to an NNP, are realized when the average distance between neighboring particles is of the order of the dimension of the quantum wave field of the particles themselves [5] (de Broglie length); this in turn depends on the number density and temperature of the plasma itself: the lower the temperature and the higher the density, the higher quantum effects are and more and more degenerate the NNP is. Shielding is

highly affected by quantum effects and the screening of the potentials, with its influence on the spatial dependence of density, is a main subject of this paper. In this work, in fact, the results of a previous study [6] on the magnetic confinement and stability of a quantum degenerate fermion NNP in the presence of external forces are extended by including the role of exchange potentials on the particles; the extension consists then in taking the description from a Thomas-Fermi level to a Thomas-Fermi-Dirac one. Density profiles in cylindrical coordinates and symmetry will be computed for a completely degenerate electron NNP. Semiclassical kinetic theory of gases, i.e. the Boltzmann-Uehling-Uhlenbeck (BUU) equation, and quantum statistics in the form of the Fermi statistics are the starting point for this analysis.

THE MODEL

For the case of an electron gas the BUU equation for the electron distribution function f can be written [4,6] as

$$\frac{\partial f}{\partial t} + \mathbf{v} \cdot \frac{\partial f}{\partial \mathbf{r}} + \frac{\mathbf{F}}{m} \cdot \frac{\partial f}{\partial \mathbf{v}} = \int (f' f_1 (1 - \gamma f) (1 - \gamma f_1) - f f_1 (1 - \gamma f') (1 - \gamma f'_1)) g \sigma(g, \chi) d\Omega d\mathbf{v}_1 \quad (1)$$

where $\gamma = \frac{h^3}{2m^3}$. Since a stationary solution with density vanishing at infinity is expected, the form of f is known to be a local Fermi distribution [7], for which the collision term of eq. (1) is vanishing; it is more convenient then to make use of the H theorem and consequently write the equation in the structure adequate for the logarithm of the distribution function [7]; if a finite average velocity \mathbf{v}_0 must also be taken into account, then eq. (1) reduces to:

$$(\mathbf{v}_0 + \mathbf{c}) \cdot \frac{\partial \ln f}{\partial \mathbf{r}} + \left(\frac{\mathbf{F}}{m} - \left(\mathbf{v}_0 \cdot \frac{\partial}{\partial \mathbf{r}} \right) \mathbf{v}_0 \right) \cdot \frac{\partial \ln f}{\partial \mathbf{c}} - \frac{\partial \ln f}{\partial \mathbf{c}} \cdot \mathbf{c} : \frac{\partial \mathbf{v}_0}{\partial \mathbf{r}} = 0 \quad (2)$$

where \mathbf{c} is the peculiar velocity. Introducing, the local Fermi distribution function

$$f_F(\mathbf{r}, \mathbf{c}) = \frac{\gamma^{-1}}{A(\mathbf{r}) e^{\frac{mc^2}{2kT(\mathbf{r})}} + 1} = \frac{\gamma^{-1}}{e^{\frac{\frac{1}{2}mc^2 - \mu(\mathbf{r})}{kT(\mathbf{r})}} + 1} \quad (3)$$

into eq. (2) the following equation is obtained:

$$\frac{e^{\frac{mc^2}{2kT}}}{e^{\frac{mc^2}{2kT}} + 1} \left[(\mathbf{v}_0 + \mathbf{c}) \cdot \left(\frac{\partial A}{\partial \mathbf{r}} - A \frac{mc^2}{2kT^2} \frac{\partial T}{\partial \mathbf{r}} \right) + \left(\frac{\mathbf{F}}{m} - \left(\mathbf{v}_0 \cdot \frac{\partial}{\partial \mathbf{r}} \right) \mathbf{v}_0 \right) \cdot \mathbf{c} \frac{mA}{kT} - \frac{mA}{kT} \mathbf{c} \mathbf{c} : \frac{\partial \mathbf{v}_0}{\partial \mathbf{r}} \right] = 0 \quad (4)$$

If eq. (4) is to be satisfied then all the coefficients of successive powers of the peculiar velocity between square brackets must identically vanish; hence:

$$\frac{mA}{kT} \mathbf{c} \cdot \frac{\partial \mathbf{v}_0}{\partial \mathbf{r}} = 0, \quad \mathbf{v}_0 \cdot \frac{\partial A}{\partial \mathbf{r}} = 0 \Rightarrow \mathbf{v}_0 \perp \frac{\partial A}{\partial \mathbf{r}} \quad (5a,b)$$

$$A \frac{mc^2}{2kT^2} \mathbf{c} \cdot \frac{\partial T}{\partial \mathbf{r}} = 0 \Rightarrow \frac{\partial T}{\partial \mathbf{r}} = 0, \quad \frac{\partial A}{\partial \mathbf{r}} + \frac{A}{kT} \left(\mathbf{F} - m \left(\mathbf{v}_0 \cdot \frac{\partial}{\partial \mathbf{r}} \right) \mathbf{v}_0 \right) = 0 \quad (5c,d)$$

These equations are as general as eq. (4) but are indeed extremely useful; in particular eq. (5c) states that the temperature must be constant and eq. (5d) establishes an equilibrium relation between the various external and internal forces acting over the gas. It also provides a relation between the chemical potential μ and all other forces.

We consider now an electron gas, in condition of cylindrical symmetry with respect to \mathbf{z} axis, described through cylindrical coordinates $\mathbf{r} = [r, \vartheta, z]$. The external force is given by a constant and uniform magnetic field along the symmetry axis, $\mathbf{B} = B\mathbf{z}$; the remaining internal force is given by the self-consistent Vlasov electric field. Under these conditions all the quantities in eq. (5d) will depend at most on r alone. This allows a simple form of \mathbf{v}_0 to be found through eq. (5a); taking into account that to have stable equilibrium no radial velocity must be present, we have that $\mathbf{v}_0 = v_{0z}\mathbf{z} + \boldsymbol{\omega} \times \mathbf{r}$, where $\boldsymbol{\omega} = \omega\mathbf{z}$ is a constant vector, directed along the symmetry axis, representing an angular velocity for the gas. Now, inserting this expression and the Lorentz force into eq. (5d), only a scalar equilibrium equation that connects the gradient of the chemical potential, the Lorentz force and the centrifugal force remains:

$$kT \frac{d}{dr} (\ln A) - e(E_r + \omega r B) + m_e \omega^2 r = 0 \quad (6)$$

Expressing the electric field as $E_r = -\frac{dV}{dr}$, with as b.c. $\lim_{r \rightarrow 0} V(r) = 0$, we get:

$$\mu(r, T) = \mu(0, T) + eV(r) + \frac{1}{2} m_e \omega (\omega - \omega_c) r^2 \quad (7)$$

where $\mu(0, T)$ is the chemical potential for an uniform and homogeneous electron gas [4,5,8,9,10], i.e. the value of the chemical potential when no forces are present, and

$\omega_c = \frac{eB}{m_e}$ is the cyclotron frequency, representative of the external magnetic field. The

electric potential exchange effects, of purely quantum nature, are taken into account, in the simplest way, through the Dirac and Slater formalism [8,9,10,11,12], by adding to eq. (7) a suitable term proportional to the cubic root of the local particle density (local density approximation, LDA), as happens in the usual Thomas-Fermi-Dirac, TFD, theory of atoms. This means that it is assumed here an equal number of upward- and downward- oriented spins. In this way the repulsive effects between electrons of parallel spins, generating the s.c. "Fermi hole" or "exchange hole" around a generic test particle, are considered; however, attractive effects due to other kinds of correlations (f.i. attraction between antiparallel spins) are not included. Of the many relativistic or non-relativistic LDA models [13] the non-relativistic Dirac-Slater, DS, one has been chosen because of its simplicity, both from a mathematical point of view

and from the physical one. The fact that it is not a relativistic potential is coherent with the other assumptions of the present model. In addition, as it happens with other exchange potentials, the DS one can easily be related to variational forms and inserted in the larger theoretical frame of density functional methods. In fact the DS potential can be derived from the following density functional:

$$E_X^{(D)}[n] = -C_X \int n^{4/3}(\mathbf{r}) d\mathbf{r} \quad (8)$$

where, in SI units, $C_X = \frac{3}{4} \frac{e^2}{4\pi\epsilon_0} \left(\frac{3}{8\pi} \right)^{1/3}$. So, the DS exchange potential is simply:

$$W_X^{(D)} = -\frac{e^2}{4\pi\epsilon_0} \left(\frac{3n(\mathbf{r})}{8\pi} \right)^{1/3}. \quad (9)$$

It must be observed here that the rhs of eq. (9) cannot be added directly to eq. (7), as is usually done in the TFD method; in fact, in the present model, eq. (7) is naturally linked to the condition, different from the usual TFD one and deriving from the above stated b.c. for $V(r)$, that for $r \rightarrow 0^+$ the fermions must possess the characteristics of an uniform and homogeneous gas; because $n(0) \neq 0$ then a very important normalizing term must also be added, so that eq. (7) finally becomes:

$$\mu(r, T) = \mu(0, T) + eV(r) + \frac{1}{2} m\omega(\omega - \omega_c) r^2 - \frac{e^2}{4\pi\epsilon_0} \left(\frac{3n(r)}{8\pi} \right)^{1/3} + \frac{e^2}{4\pi\epsilon_0} \left(\frac{3n(0)}{8\pi} \right)^{1/3} \quad (10)$$

Inserting eq. (10) into the Fermi distribution function and integrating over all the velocity space via Sommerfeld's Lemma at first order, one gets the following relation, generalized to take into account finite temperature and average velocity:

$$n(r) = \frac{8\pi}{3h^3} \left[2m_c \left(eV(r) + \frac{1}{2} m_c \omega(\omega - \omega_c) r^2 + \mu_0 - \frac{e^2}{4\pi\epsilon_0} \left(\frac{3(n(r) - n(0))}{8\pi} \right)^{1/3} \right) \right]^{3/2} \cdot \left[1 + \frac{(\pi kT)^2}{8} \left(eV(r) + \frac{1}{2} m_c \omega(\omega - \omega_c) r^2 + \mu_0 - \frac{e^2}{4\pi\epsilon_0} \left(\frac{3(n(r) - n(0))}{8\pi} \right)^{1/3} \right)^{-2} \right] \quad (11)$$

where $\mu_0 = \mu(0, 0) \equiv E_F$ is the s.c. Fermi energy.

For the case of complete degeneracy ($T=0$) one gets from eq. (11):

$$an^{2/3} + br^2 + c + dn^{1/3} - dn_0^{1/3} = eV \quad (12)$$

where $n(0) \equiv n_0$, $a = \frac{1}{2m} \left(\frac{3\hbar^3}{8\pi} \right)^{2/3} > 0$, $b = -\frac{1}{2} m\omega(\omega - \omega_c)$, $c = -\mu_0 < 0$,

$d = \frac{e^2}{4\pi\epsilon_0} \left(\frac{3}{8\pi} \right)^{1/3} > 0$. For $r \rightarrow 0^+$ eq. (12) tends to $an_0^{2/3} + c = 0$ which is the usual expression for an uniform and homogeneous electron gas. Also, for $d \rightarrow 0^+$ eq. (12) gives the simple TF equation in absence of exchange forces. Requiring now the self-consistency of electron density and electric potential, imposing that eq. (12) satisfy Poisson's equation, a non-linear equation for only the electron density remains:

$$n'' - \frac{1}{3n} (n')^2 + \frac{n'}{r} = \frac{n^{2/3}}{(2/3 an^{1/3} + 1/3 d)} (gn - 4b) \quad (13)$$

where $g = \frac{e^2}{\epsilon_0} > 0$, with particle number normalization and cylindrical symmetry b.c.:

$$\lim_{r \rightarrow 0^+} n(r) = n(0) = n_0, \quad \lim_{r \rightarrow 0^+} \frac{dn}{dr} = 0. \quad (14)$$

ANALYTICAL RESULTS

A solution vanishing at infinity for eq. (13) is obtainable if and only if [6] its rhs near the origin is negative; this means that to have confinement it must be $gn_0 < 4b$, *independently* of the value of d . This important result shows that exchange effects don't alter at all the s.c. confinement region [6], hence they don't alter the value of the confining necessary magnetic field too, for the considered gas at the given angular velocity. Exchange effects do indeed alter the confinement radius for the gas, in the direction of extending it above that of the purely TF model, as is to be expected, as stated above, because of the presence of "Fermi holes".

NUMERICAL RESULTS, COMPARISONS AND DISCUSSION

Eq. (13) has been solved numerically. Figure 1 compares, at the same number of confined particles per unit length, magnetic field and angular velocity, in doubly-logarithmic scale, the TF and TFD density profiles. The role of the repulsive exchange holes is distributed between the two effects of lowering the density at the origin of the TFD solution and of increasing its confinement radius.

CONCLUSIONS

The quantum exchange effects between parallel-spinned electrons have been included in a semiclassical model of a one-component, non-neutral, degenerate,

fermion plasma. The plasma rotates around its symmetry axis in a cylindrical configuration and is magnetically confined. In this way the model has been extended

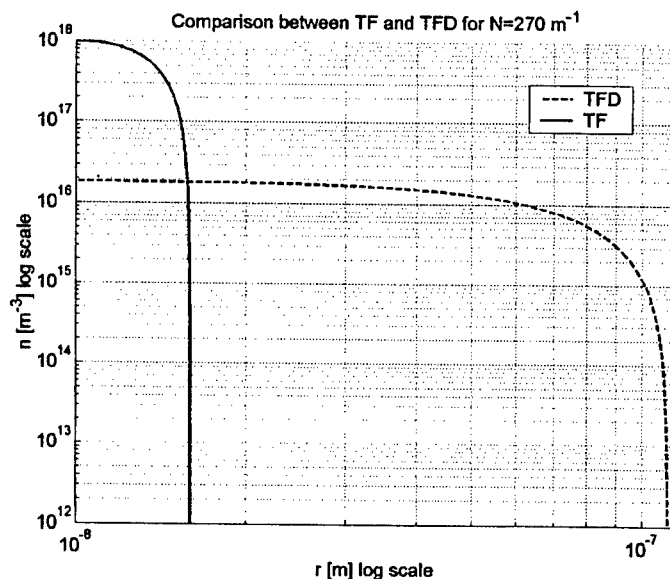


FIGURE 1. Comparison between TF and TFD models for $N=270 \text{ m}^{-1}$, $\omega = 4.2\text{E}+6 \text{ Hz}$ and $\omega_c = 8.0\text{E}+14 \text{ Hz}$.

through a local density approximation from a TF description level to a TFD one, as it happens f.i. for the electronic theory of atoms. The usual expression of the exchange potential has been modified for the special needs of the model. The equation for the density profile of the plasma has been solved numerically. It is seen that the s.c. confinement region is not altered by the exchange effects, even if the confinement radius becomes larger because of the repulsive effects of the “Fermi holes”.

REFERENCES

1. Davidson, R. C., *Theory of Nonneutral Plasmas*, W. A. Benjamin Inc., Reading, Massachusetts, 1974.
2. Cowan, R. D. and Ashkin, J., *Phys. Rev.* **105**, 1 (1957), 144-157.
3. Rozsnyai, B. F., *Phys. Rev. A* **5**, 3 (1972), 1137-1149.
4. Lihoff, R. L., *Kinetic Theory: Classical, Quantum and Relativistic Descriptions*, 2nd ed., J. Wiley & Sons, N. Y. 1998.
5. Pathria, R. K., *Statistical Mechanics*, 2nd ed., Butterworth&Heinemann, Oxford 1996.
6. V. G. Molinari, M. Sumini and F. Rocchi, *EPJ-D* **12**, 211-217 (2000).
7. Chapman, S., and Cowling, T. G., *The Mathematical Theory of Non-uniform Gases*, CUP, Cambridge 1961.
8. Lundquist, S., and March, N. H., (eds.), *Theory of the Inhomogeneous Electron Gas*, N.Y. and London 1983.
9. March, N. H., *Self-Consistent Fields in Atoms*, Pergamon, Oxford 1975.
10. Parr, R. G., and Yang, W., *Density-Functional Theory of Atoms and Molecules*, OUP, Oxford 1989.
11. Slater, J. C., *Quantum Theory of Matter*, 2nd ed., McGraw-Hill Book Company, New York 1968.
12. Slater, J. C., *Quantum Theory of Atomic Structure*, 2 vols., McGraw-Hill Book Company, New York 1960.
13. Liu, S., and Parr, R. G., *Journal of Molecular Structure (Teechem)*, **501-502**, 29-34 (2000).

Analytic Potentials for Realistic Electrodes

S. E. Barlow, A.E. Taylor and K. Swanson

*W.R. Wiley Environmental Molecular Sciences Lab
Pacific Northwest National Laboratory
P.O. Box 999 (K8-88)
Richland, WA 99352*

Abstract. We show how Laplace's equation can be accurately solved when the boundary conditions are not amenable to direct analytic treatment. This problem arises for nearly all real electrodes. Our approach systematically combines numerical relaxation techniques with analytic expansions to produce a provably unique solution.

INTRODUCTION

Many problems in physics and engineering begin with a solution to Laplace's equation:

$$\nabla^2 \Phi(\mathbf{r}) = 0 \quad (1)$$

where $\Phi(\mathbf{r})$ is a potential in some volume of space determined by the boundary conditions. Analytic solutions to this partial differential equation are limited to geometries that precisely match an orthogonal coordinate system. For example, eq. (1) can be readily solved for the rectangular or cylindrical box by the method of separation of variables. Although this method is very powerful, by itself it suffers from at least two shortcomings. First, the solutions take the form of infinite sums over special functions and are rather difficult to interpret physically. And second, the rigorous requirements of the boundaries are almost never met in practise. For instance, in electrostatic problems, gaps between electrodes are required to maintain potential differences, further in real instruments it is often necessary to put holes in the electrodes to provide access to the internal volume. Sometimes it is desirable to shape boundary electrodes that do not even approximately match those of an orthogonal coordinate system, e.g., the hyperbolic ion trap. Finally, the analytical techniques cannot readily account for construction errors that inevitably arise in real devices.

Equation (1) may also be solved numerically. In recent years, computer codes have been developed to tackle some of the short comings listed above. In these codes, the boundary conditions are mapped onto a grid. The potential is then found by a series of "relaxation" calculations. The most widely used of these codes is the SIMION[1], but others are available. These codes produce a "potential array" for

the volume of interest. Like the analytical approaches mentioned above, numerical solutions tend to provide little direct insight into the physics of interest.

A powerful technique for providing insight into the physical consequences of a potential is the "multipole-pole" expansion. The multipole expansion of a potential may be formally accomplished by writing the solutions to eq. (1) in spherical coordinates and then changing to the desired coordinate system—generally cylindrical polar (r, θ, z) or cartesian (x, y, z) coordinates. For example in cylindrical-polar coordinates, with cylindrical symmetry the solution of eq. (1) is

$$\Phi(r, z) = V \sum_{n=0}^{\infty} \frac{C_n}{r_0^n} \Phi_n(r, z) \quad (2)$$

where V is some potential value; r_0 is a distance or size scaling factor; the C_n are the constants to be determined from the boundary conditions; and $\Phi_n(r, z)$ are the various "orders" of the solution to eq. (1). Since many electrostatic problems have cylindrical symmetry, and the treatment is simpler (two instead of three dimensions) all further discussions here will be limited to this case. The multipole expansion is particularly useful because the behavior of a system is normally governed by the lowest order terms that are present in the potential. The trick is to find a way to reliably and accurately evaluate the C_n 's. In the following section, we outline the steps that allow us to evaluate these constants from numerical calculations. (Much more detail is provided in our paper, scheduled for publication in 2001.[2])

EVALUATION OF MULTIPOLE COEFFICIENTS FROM NUMERICAL RELAXATION CALCULATIONS

Computation of the C_n 's proceeds in four steps. First, the boundary value problems is set-up using some sort of numerical relaxation calculation. Second, we extract from the relaxation calculation the potential over a "virtual Gaussian surface." In the third step, this virtual surface is used to evaluate the coefficients in the sums of the formal solution of eq. (1). Finally, the formal solution is expanded term by term in a Taylor series to evaluate the C_n 's.

Setting up the Problem

In general the problem is set up by defining the symmetries, boundary shapes and grid size through the GUI of the relaxation code, e.g. SIMION. Care must be taken to insure that the grid is sufficiently fine to resolve the details of the problem adequately. SIMION uses a uniform cartesian grid, which simplifies the next step, but the cost is some loss of precision. While we have no requirement for a uniform mesh (grid) we do need to have the potential specified on cylindrical surfaces

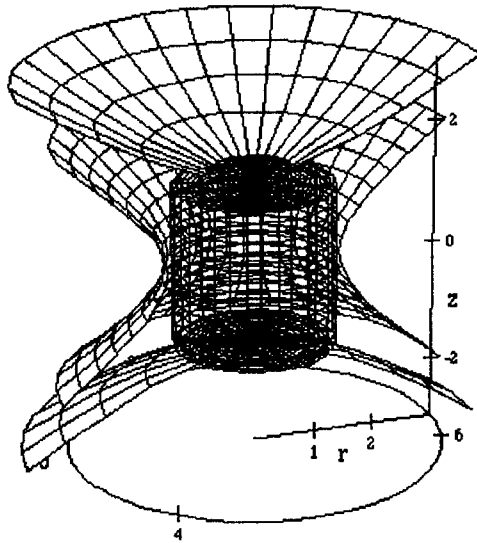


FIGURE 1. Schematic of hyperbolic trap electrodes and inscribed cylinder.

$(r = a, z)$ and $(r, z = z_{\text{bottom or top}})$ where a is the radius and $z_{\text{bottom or top}}$ are the end of our “virtual Gaussian” surface.

Extracting the “Virtual Gaussian Surface”

As a practical matter, the bulk of the real work is done when the relaxation calculation has been performed. However, we are left with an array of numbers—the potential array—that may have 10^6 or more elements. What we must do next is to define our inscribed cylindrical surface such that it is as large as possible, but does not include any conductors. The cylinder’s axis of symmetry needs to coincide with the symmetry axis of the problem. We also need to define a $z = 0$ plane and “top” and “bottom” planes. This cylinder’s dimensions must be chosen to exactly match a line of grid points. With the cylinder so defined, we can then select those points in the potential array that fall on the cylinder’s surface. The SIMION code does not give direct access to the potential array file. We have written a small program that allows us to extract those portions of this file that we need for the calculations of the next section. This program and some documentation is available on the world wide web.[3]

The Analytic Potential

The solution of eq. (1) in a cylindrically symmetric domain that includes the axis of symmetry is

$$\Phi(r, \theta, z) = \sum_{s=0}^{\infty} \left\{ \alpha_{1,s} \cos \left[\frac{(2s+1)\pi(2z-z_t-z_b)}{2(z_t-z_b)} \right] I_0 \left[\frac{(2s+1)\pi r}{2(z_t-z_b)} \right] + \alpha_{2,s} \sin \left[\frac{2s\pi(2z-z_t-z_b)}{2(z_t-z_b)} \right] I_0 \left[\frac{4s\pi r}{2(z_t-z_b)} \right] \right\} + \sum_{s=1}^{\infty} \left\{ \alpha_{3,s} \sinh \left[\frac{(z-z_t)j_s}{c} \right] J_0 \left[\frac{j_s r}{c} \right] - \alpha_{4,s} \sinh \left[\frac{(z-z_b)j_s}{c} \right] J_0 \left[\frac{j_s r}{c} \right] \right\} \quad (3)$$

Here, $J_0(x)$ is the Bessel function of the first kind of order 0; and $I_0(x)$ is the modified Bessel function of order zero. The symbol j_s is the s^{th} zero of $J_0(x)$. If we designate the potential on the top of the cylinder as $V_t(r, z = z_t)$, that on the bottom as $V_b(r, z = z_b)$ and on the side as $V_r(r = c, z)$ we find for the α 's:

$$\alpha_{1,s} = \frac{2}{(z_t - z_b) I_0 \left[\frac{(2s+1)\pi c}{2(z_t-z_b)} \right]} \int_{z_b}^{z_t} V_r(z) \cos \left[\frac{(2s+1)\pi(2z-z_b-z_t)}{2(z_t-z_b)} \right] dz, \quad (4)$$

$$\alpha_{2,s} = \frac{2}{(z_t - z_b) I_0 \left[\frac{4s\pi c}{2(z_t-z_b)} \right]} \int_{z_b}^{z_t} V_r(z) \sin \left[\frac{2s\pi(2z-z_b-z_t)}{2(z_t-z_b)} \right] dz, \quad (5)$$

$$\alpha_{3,s} = \frac{2}{c^2 \sinh \left(\frac{(z_t-z_b)j_s}{c} \right) [J_1(j_s)]^2} \int_0^c V_b(r) J_0 \left(\frac{j_s r}{c} \right) r dr \quad (6)$$

and

$$\alpha_{4,s} = \frac{2}{c^2 \sinh \left(\frac{(z_t-z_b)j_s}{c} \right) [J_1(j_s)]^2} \int_0^c V_t(r) J_0 \left(\frac{j_s r}{c} \right) r dr. \quad (7)$$

where we use $V(r, z)$ found from the finite difference calculations as described below. The α 's tend to become rapidly small with s , so we find that only a few of these terms need to be explicitly evaluated unless we are interested in the solution very near a boundary. If the (x, y) plane at $z = 0$ is also a symmetry plane, the eqs (3) to (7) simplify because $\alpha_{2,s} = 0$ and $\alpha_{3,s} = -\alpha_{4,s}$.

The Multipole Expansion

Having found the α 's, the multipole expansion can be accomplished easily. We set $r = 0$ in eq.(3), since $J_0(0) = I_0(0) = 1$, we are left with trigonometric and hyperbolic trig functions whose power law expansions in z are readily found. Since each power of z is linearly independent, we merely collect like terms and add them up. By eq.(2), the sums for some power of z , say n is simply C_n/r_0^n .

The values we find for C_n are correct to within the accuracy of our initial relaxation calculation. They are also complete and unique, with respect to our choice of $z = 0$. Sometimes the choice of the origin will not be immediately obvious,

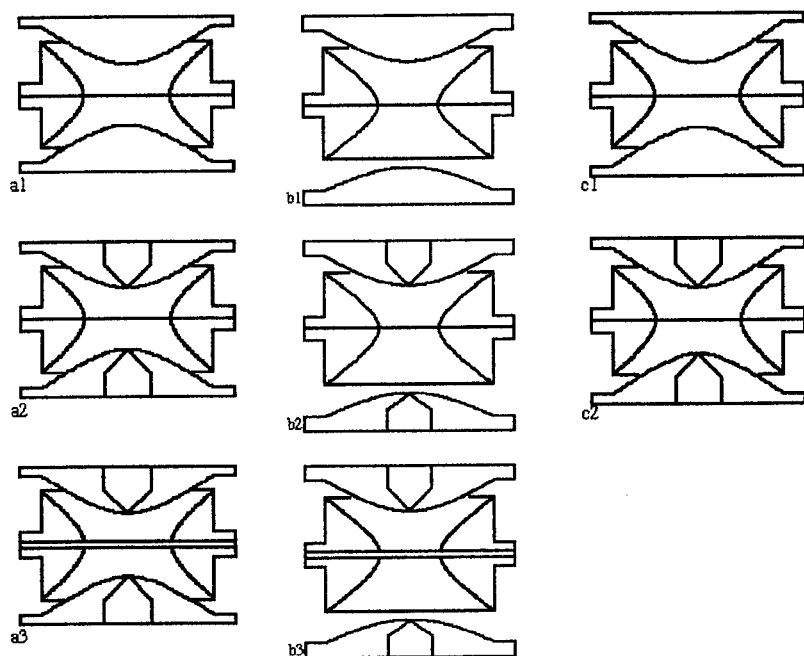


FIGURE 2. Sketches of various electrodes for which calculations were performed, see text and tables.

techniques for finding the point are discussed by Barlow et al.,[2] but lie outside the scope of this summary.

TABLE 1. Calculated even order C 's for nine variants of hyperbolic electrode structures

Trap Type	Fig. 2.	C_0	C_2	C_4	C_6
"Ideal" Trap		0.5	-1	0	0
Truncated Trap	a1	0.5007	-0.9799	$1.23(10)^{-4}$	$1.07(10)^{-3}$
+ endcap holes	a2	0.5010	-0.9784	$4.52(10)^{-3}$	$1.26(10)^{-2}$
+ ring slot	a3	0.4838	-1.0044	$-2.72(10)^{-2}$	$5.77(10)^{-2}$
Stretched Trap	c1	0.5567	-0.8777	$-1.51(10)^{-2}$	$-6.40(10)^{-3}$
+ endcap holes	c2	0.5569	-0.8767	$-1.26(10)^{-2}$	$-1.02(10)^{-3}$
Asymmetric Trap	b1	0.5007	-0.9801	$-2.26(10)^{-4}$	$8.02(10)^{-4}$
+ endcap holes	b2	0.5009	-0.9792	$2.13(10)^{-3}$	$6.72(10)^{-3}$
+ ring slot	b3	0.4818	-0.9855	$-3.07(10)^{-2}$	$4.61(10)^{-2}$

TABLE 2. Calculated odd order C's for nine variants of the hyperbolic electrode structure. Numbers in parenthesis are nominally zero. The * denotes value that were set to zero.

Trap Type	Fig. 2.	C_1	C_3	C_5
"Ideal" Trap		0	0	0
Truncated Trap	a1	$-1.[10]^{-9}$	$3[10]^{-9}$	$3[10]^{-9}$
+ endcap holes	a2	$-9.[10]^{-10}$	$3[10]^{-9}$	$-2[10]^{-9}$
+ ring slot	a3	$-2[10]^{-9}$	$6[10]^{-9}$	$-5[10]^{-9}$
Stretched Trap	c1	$-1[10]^{-9}$	$3[10]^{-9}$	$-2[10]^{-9}$
+ endcap holes	c2	$-1[10]^{-9}$	$2[10]^{-9}$	$-1[10]^{-9}$
Asymmetric Trap	b1	0*	$-3.06(10)^{-4}$	$-3.30(10)^{-4}$
+ endcap holes	b2	0*	$-1.45(10)^{-3}$	$-3.81(10)^{-3}$
+ ring slot	b3	0*	$-5.18(10)^{-3}$	$-6.55(10)^{-3}$

DISCUSSION

Figure (2) illustrates eight variations of hyperbolic electrodes for which we have done calculations. In each case, the hyperbolae were truncated at $2.8r_0$ to closely match electrode structures that we possess in the laboratory. The trap geometries labeled a1,a2, and a3, are symmetric trap structures with the endcap spacing $2z_0 = 2\sqrt{2}r_0$, where we successively add end cap holes and a ring slot to the already truncated and flanged electrodes. The end cap holes were set at $0.075r_0$ and the ring slot at closely match actual trap electrode structures. The structures labeled b1, b2, and b3 are asymmetric trap structures[4], with similar endcap holes and ring slot. The two structures labeled c1 and c2 have electrode shapes that are identical to those of a1 and a2, but the endcap spacing has been increased by 10.8% as is standard commercial practice.

Table 1 summarizes the even order coefficients for each of these trap geometries, while Table 2 shows our evaluation of the odd order.

REFERENCES

1. D.A. Dahl, SIMION 3D, V6.0, INEEL, Idaho Falls, ID, 1995.
2. S.E. Barlow, A.E. Taylor and K. Swanson, Int. J. Mass Spectrom., **207**, pg. 19, 2001.
3. Potential Extraction program is available at:
<http://www.emsl.pnl.gov/docs/idl/software/SimionPAViewer.html>.
4. M.L. Alexander, S.E. Barlow and J. Follansbee, Proc. 46th ASMS Conf., pg. 1173 1998.
5. J. Franzen, R.H. Gabling, M. Schubert and Y. Wang, in: *Practical Aspects of Ion Trap Mass Spectrometry, Vol. 1*, R.E. March and J.F.J. Todd, eds., CRC Press, NY (1995) Ch. 3.

Image Charge Forces Inside Conducting Boundaries

Mark D. Tinkle* and S. E. Barlow†

*Dynamics Technology, Inc., 21311 Hawthorne Blvd., Suite 300 Torrance, CA 90503-5610

†W.R. Wiley Environmental Molecular Sciences Lab, Pacific Northwest National Laboratory P.O. Box 999 (K8-88) Richland, WA 99352

Abstract. Evaluation of the force on a charge particle due to the surface charge distributions it induces in nearby conductors is generally a challenging problem. We show these forces can be evaluated explicitly and fairly simply in a number of elementary, but important cases.

INTRODUCTION

The force on a charged particle due to the charges it induces on nearby conducting surfaces is a factor in many scientific measurements. The effects of these forces are particularly important for non-neutral plasmas. Until now, general techniques for quantifying image charge forces have not been available. An important advance was made in a recent paper by Fine and Driscoll [1] which addressed the lowest order solutions to this problem for infinite cylindrical geometry including finite charge length effects. Here, we generalize those results considerably.

IMAGE CHARGE PSEUDOPOTENTIAL

The measurable physical variable associated with induced surface charge is the force it produces on the point charge. We would like to express this force as the gradient of a function of the point charge's position. There is a subtlety involved in this potential function that is best illustrated by a simple example using the method of images.

Motivating example

If a point charge of strength q is at a position $(x, y, z) = (x_0, 0, 0)$, $(x_0 > 0)$ with a grounded conductor in the y - z plane, we know from the method of images[2] that the electrostatic potential for $x > 0$ can be expressed as the sum of the potentials from the point charge and a fictitious image charge of strength $-q$ located at $(x, y, z) = (-x_0, 0, 0)$:

$$\phi(x, y, z) = \frac{q}{4\pi\epsilon_0} \left(\frac{1}{\sqrt{[(x-x_0)^2 + y^2 + z^2]}} - \frac{1}{\sqrt{[(x+x_0)^2 + y^2 + z^2]}} \right) \quad (1)$$

for $x > 0$. This is the potential that determines the force on an infinitesimal point charge, which is to say a point charge whose own induced surface charges produce negligible forces. Can we use it to find the force on the charge q ? We must first drop the potential produced by the charge, since it cannot exert a force on itself. This leaves the potential of the image charge, which evaluated along the x axis is just

$$\Phi_I(x, 0, 0) = \frac{-q}{4\pi\epsilon_0} \frac{1}{x+x_0}, \quad (2)$$

for $x > 0$. Two courses of action present themselves for finding the x -component of the force: take $\partial\Phi_I/\partial x$ and evaluate at $x = x_0$, or evaluate Φ_I at $x = x_0$ and take $\partial/\partial x_0$ of the result. The results differ by a factor of two:

$$\left. \frac{\partial\Phi_I}{\partial x} \right|_{x=x_0} = \frac{q}{4\pi\epsilon_0} \frac{1}{4x_0^2}, \quad (3)$$

and

$$\frac{\partial[\Phi_I|_{x=x_0}]}{\partial x_0} = \frac{q}{4\pi\epsilon_0} \frac{1}{2x_0^2}. \quad (4)$$

The force can be found directly from Coulomb's Law using the image charge[2]:

$$\vec{F} = \frac{-q^2}{4\pi\epsilon_0} \frac{1}{4x_0^2} \hat{x}, \quad (5)$$

so at least in this case, we have a choice of formulae for the force in terms of the potential:

$$\vec{F}(x_0) = -q \left. \frac{\partial\Phi_I}{\partial x} \right|_{x=x_0} \hat{x} \quad (6)$$

or

$$\vec{F}(x_0) = \frac{-q}{2} \frac{\partial[\Phi_I|_{x=x_0}]}{\partial x_0} \hat{x}. \quad (7)$$

The first choice seems like the natural one, but it requires us to keep a function of two position coordinates (x and x_0). The second choice contains an unfamiliar factor of $1/2$, but the force is reconstructed from a simple function of one position coordinate (x_0). This is the useful form, which we will now derive more generally.

General derivation

Next we find a general expression for the force on a point charge q in the presence of both fixed charges and conductors at fixed potentials.

$$\vec{F} = -q\nabla\phi - \frac{1}{2}q\nabla\Phi, \quad (8)$$

where ϕ is the ordinary electrostatic potential due to the fixed charges and potentials, and Φ is the potential due to charges induced by the point charge, evaluated at the point charge coordinate.

From the definition of the electrostatic potential ϕ , the work required to bring a point charge q in to position \vec{x} from infinity (where $\phi = 0$) while holding the charges producing ϕ fixed in place is $W = q\phi(\vec{x})$. The force on the particle is the negative of the gradient with respect to its position coordinate of the *total system energy* under the circumstances considered. If the charges producing $\phi(\vec{x})$ are indeed fixed and there are no other energy terms involving the position of the point charge, then the force is $\vec{F} = -q\nabla\phi$. This is the familiar result for an infinitesimal test charge, but it is a special case. It is not the definition of ϕ .

When a charge moves toward a conducting surface, the induced surface charges must bunch together, against their mutual repulsion, to maintain an equipotential. This adds a term to the total electrostatic energy of the system that acts to reduce the attractive force felt by the point charge, by exactly a factor of two. This is easily derived from the well-known expression for the total electrostatic energy (excluding self-energy) of n discrete charges:

$$W = \frac{1}{2} \sum_{j=1}^n q_j \Phi_j, \quad (9)$$

where Φ_j is the potential at charge q_j due to all the other charges.[3] If $j = 1$ denotes the point charge, and the others are the charges induced on a grounded conductor, then Φ_j is zero for all $j \neq 1$ (the induced charges) regardless of the position of the point charge, and the total electrostatic energy is

$$W = \frac{1}{2} q \Phi, \quad (10)$$

where $\Phi = \Phi_1$ is the potential at the point charge due to the induced surface charges. The force on the point charge is thus

$$\vec{F} = -\frac{1}{2} q \nabla \Phi, \quad (11)$$

where the gradient is taken with respect to the position of the point charge. If the conductor is at some potential other than ground, then we must add the familiar term $-q\nabla\phi$ to this thereby recovering eq.(8).

We refer to $\Phi(\vec{x})$ as the image charge pseudopotential, to emphasize its differences from ordinary potentials. Unlike $\phi(\vec{x})$, $\Phi(\vec{x})$ is not simply a solution of Laplace's or Poisson's equation, because its source term (the induced charge distribution) is a complicated functional of \vec{x} , the point charge location. Further, $\Phi(\vec{x})$ is only meaningful at the particular location of the charge. As we describe below, $\Phi(\vec{x})$ is proportional to the nonsingular part of $G(\vec{x}, \vec{x}')$, evaluated at $\vec{x} = \vec{x}'$. Thus, $\Phi(\vec{x})$ may be extracted from a family of solutions to Laplace's equation, but is not itself a solution. Numerous methods, include the classic "Method of Images" for solving these problems are discussed in Tinkle and Barlow.[4]

RESULTS

Generic limiting form

As a smooth region of a conductor is approached closely, the pseudopotential approaches that of an infinite flat plate. From the method of images, $\Phi \rightarrow -q/4\pi\epsilon_0 2d$ as $d \rightarrow 0$, where d is the distance to the surface. Thus if ξ_0 is the distance to a conductor along the ξ axis of a rectilinear coordinate system and the surface is perpendicular to the ξ axis where they intersect,

$$\Phi \rightarrow -\frac{q}{4\pi\epsilon_0\xi_0} \frac{1}{2(1-\xi)}, \quad (12)$$

as $\bar{\xi} \equiv \xi/\xi_0 \rightarrow 1$. If the geometry is symmetric in ξ , we can account for the limiting behaviors at both walls with the form

$$\Phi \rightarrow -\frac{q}{4\pi\epsilon_0\xi_0} \frac{1}{1-\xi^2}, \quad (13)$$

as $|\bar{\xi}| \rightarrow 1$. The complete solution for Φ along the ξ axis will be the sum of this divergent term and a finite term. Expressed as a power series expansion about the origin, it will have the form

$$\Phi = -\frac{q}{4\pi\epsilon_0\xi_0} \sum_{n=0}^{\infty} C_n \bar{\xi}^n, \quad (14)$$

with $C_n = 0$ for odd n , due to symmetry. The divergent term by itself has $C_n = 1$ for all even n . The results we obtain for specific geometries can all be expressed in this form, with different values for the coefficients. Tinkle and Barlow[4] present solutions of this form for a number of important cases including the spherical shell, parallel plates and the rectangular box.

Cylindrical Shell

By way of example, we show here the results for a cylindrical box. The calculations are rather complex,[4] however, solutions of the form

$$\Phi(\bar{\rho}, \bar{z}) = -\frac{q}{4\pi\epsilon_0 z_0} \sum_{m=0}^{\infty} \sum_{n=0}^{\infty} C_{m,n}(\alpha) \bar{\rho}^{2m} \bar{z}^{2n}, \quad (15)$$

can be found. Here α is the ratio of the cylinder's length to diameter—the "aspect ratio." The limiting values listed in Table 1 are in line with our generic discussion above. These coefficient terms are shown plotted in Figure 1.

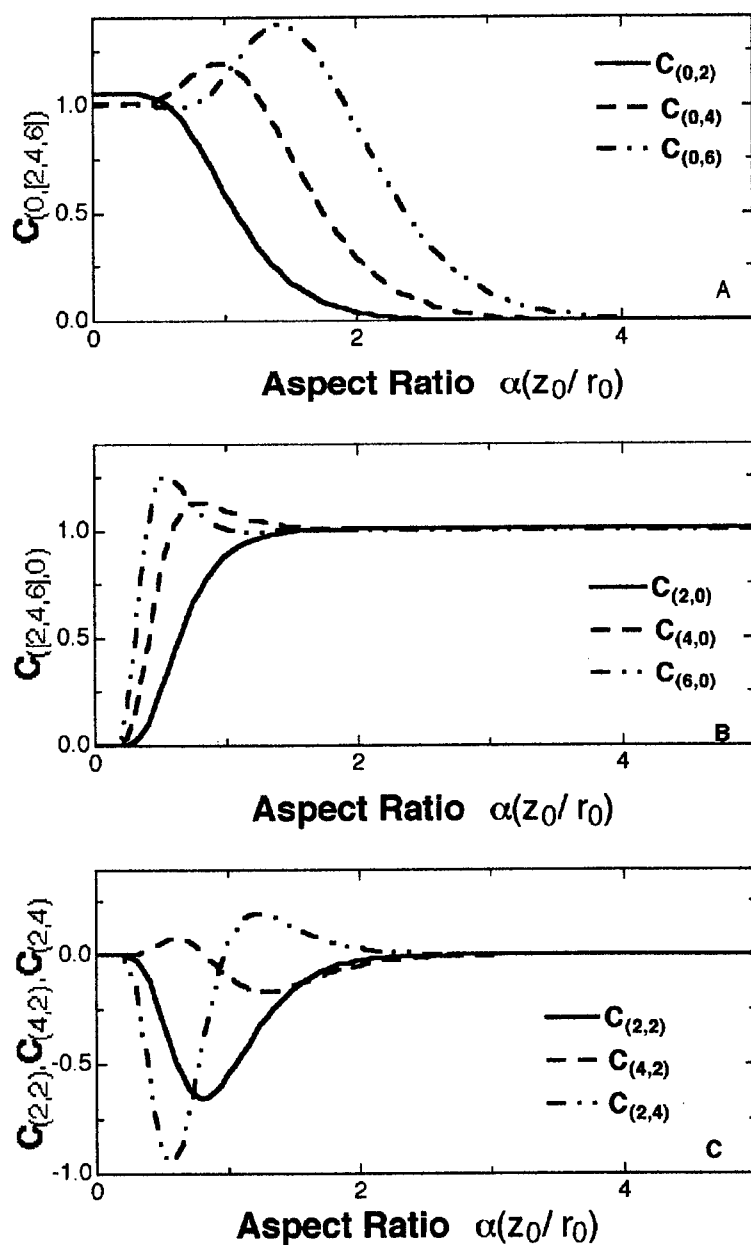


FIGURE 1. Plots of the the first six terms of the power series expansion of the image charge pseudopotential for a cylindrical box as functions of the aspect ratio. (A) The pure "axial" terms—powers of z only. (B) The pure "radial" terms—powers of r only. (C) The crossed "radial" and "axial" terms—powers of r and z .

TABLE 1. Asymptotic limits of image charge coefficients for cylindrical box, see text for explanation. *agrees with results of Fine and Driscoll [ref 1, eq(32)]

$C_{st,2s}$	$\alpha \rightarrow 0$ parallel plate	4 th Order Exp'l. Trap	$\alpha = 1$	$\alpha \rightarrow 0$ long tube
$C_{0,2}$	1.0518	0.7755	0.5880	0
$C_{0,4}$	1.0045	1.1669	1.1845	0
$C_{0,6}$	1.0005	1.0180	1.1246	0
$C_{2,0}$	0	0.7534	0.8792	1.0027*
$C_{4,0}$	0	1.1243	1.0884	1.0009
$C_{6,0}$	0	1.0572	1.0020	1.0003
$C_{2,2}$	0	-0.9157	-1.0309	0
$C_{4,2}$	0	-0.3470	-0.4359	0
$C_{2,4}$	0	0.1822	0.1884	0

ACKNOWLEDGMENTS

The research described here was performed at the W. R. Wiley Environmental Molecular Sciences Laboratory, sponsored by the Department of Energy's Office of Biological and Environmental Research and located at Pacific Northwest National Laboratory (PNNL). PNNL is operated by Battelle under Contract DE-AC06-76RLO 1830. This work was supported in part by the Office of Basic Energy Sciences, Chemical Sciences Division.

REFERENCES

1. K.S. Fine and C.F. Driscoll, *Phys. of Plasmas*, **5**, pg. 601, 1998.
2. J.D. Jackson, *Classical Electrodynamics*, 2nd ed., Wiley, NY, pg 54f, 1975.
3. W.R. Smythe, *Static and Dynamic Electricity*, 3rd ed., McGraw-Hill, NY, 1968, Ch 3, [esp. eq. 3.08 (2)]
4. M.D. Tinkle and S.E. Barlow, *J. Appl. Physics*, **90**, pg. 1612, 2001.

Non-Collisional Kinetic Model for Non-Neutral Plasmas in a Penning Trap: General Properties and Stationary Solutions

Gianni G.M. Coppa, Paolo Ricci

*Istituto Nazionale per la Fisica della Materia (INFN) and Dipartimento di Energetica,
Politecnico di Torino, Corso Duca degli Abruzzi 24 – 10129 Torino, Italy.
E-mail: ggmccoppa@polito.it, riccipaolo@libero.it*

Abstract. A non-collisional kinetic model for a non-neutral plasma in a Penning trap is presented. This model describes the evolution of the z -integrated distribution function of the particles, taking into account the three-dimensionality of the problem. The general properties of the model, in particular the conservation laws, are studied. The model is also related to the fluid model proposed by Finn *et al.* and refined by Coppa *et al.* Finally, numerical investigations are presented concerning the equilibrium solutions of the model.

INTRODUCTION

Usually, the dynamics of non-neutral plasmas confined in Penning-Malmberg traps is described by employing a two-dimensional drift-Poisson model, where charged particles are regarded as straight lines (strings) of uniform density, due to the very high value of the axial bouncing frequency. According to this model, the particles exhibit an $\mathbf{E} \times \mathbf{B}$ drift motion and the electric field is computed self-consistently from the charge density by using the Poisson equation.

This model predicts possible instabilities for the azimuthal modes $m_\theta > 1$. For the $m_\theta = 1$ mode, discrete modes are always stable for any density profiles [1], while the continuum spectrum can only produce an algebraic growth [2]. Nevertheless, experiments show that the mode growth is actually exponential: the contradiction between experimental results and the linear two-dimensional theory is a challenging problem in the theory of non-neutral plasmas.

The present work grounds on recent studies on the evolution of non-neutral plasmas in a Penning-Malmberg trap, pointing out the important role of kinetic effects and of the finite length of the device, in particular for the $m_\theta = 1$ diocotron instability [3-5]. In fact, when a particle approaches the border of the plasma, it feels a confining potential which, in general, depends upon both the radial and the axial coordinates. The radial component of the confining electric field causes an $\mathbf{E} \times \mathbf{B}$ drift in the azimuthal direction, affecting the rotation frequency. The drift depends upon the axial energy of the particles, which affects the penetration in the confining potential [6].

The aim of the present work is to develop a kinetic theory for non-neutral plasmas taking into account self-consistently all these effects. The kinetic model assumes that

the frequency are ordered as $\Omega_c \gg \Omega_b \gg \Omega_E$, being Ω_c the cyclotron frequency, Ω_b the bouncing frequency and Ω_E the $\mathbf{E} \times \mathbf{B}$ drift rotation, which is comparable to the frequency of the modes of interest. Within this assumption, the planar motion of the electrons is well described by the dynamics of their guiding centers, given by the $\mathbf{E} \times \mathbf{B}$ drift velocity, and the complete kinetic description of the plasma is then provided by the distribution function $f(r, \theta, z, \xi, t)$, where ξ is the axial energy of the particles. The description is completed by the self-consistent Poisson equation for the electrostatic potential $\phi(r, \theta, z, t)$.

In order to reduce the complexity of the problem, the dimensionality of the model is reduced by integrating along the axial direction. If the electrostatic potential "seen" by a string of electrons varies slowly in time, the ergodic distribution in the phase-space (z, v_z) can be assumed for the particles of the same energy and a kinetic equation for the z -integrated electron distribution, $F(r, \theta, \xi, t)$, can be deduced. The properties of such kinetic equation are the main subject of the present work.

DEDUCTION OF THE KINETIC EQUATION

The starting point in deducing the present model is the kinetic equation for the complete distribution function, $f(r, \theta, z, \xi, t)$,

$$\frac{\partial f}{\partial t} + \nabla_{\perp} \left(\frac{\mathbf{e}_z \times \nabla_{\perp} \phi}{B_0} f \right) + \frac{\partial}{\partial z} (v_z f) + \frac{\partial}{\partial \xi} \left(\frac{d\xi}{dt} f \right) = 0 \quad (1)$$

where the $\mathbf{E} \times \mathbf{B}$ drift approximation is used and the phase-space variable ξ is the axial energy of the particles

$$\xi = \frac{1}{2} m v_z^2 - e \phi(r, \theta, z, t) \quad (2)$$

while the time derivative of ξ is simply given by $d\xi/dt = -e \partial \phi / \partial t$.

The z -integrated distribution $F(r, \theta, \xi, t)$ is introduced by factorizing the distribution function as

$$f(r, \theta, \xi, z, t) = F(r, \theta, \xi, t) g(r, \theta, \xi, z, t) \quad (3)$$

The function g is defined assuming the particles of a given energy ξ to be distributed, in the phase-space (z, v_z), according to the ergodic distribution. Moreover, g is normalized in order that $\int g(r, \theta, \xi, z, t) dz = 1$. This leads to

$$g(r, \theta, \xi, z, t) = \frac{[e \phi(r, \theta, z, t) - \xi]^{-1/2}}{\int [e \phi(r, \theta, z, t) - \xi]^{-1/2} dz} \quad (4)$$

Within this assumption, the following equation for the function $F(r, \theta, \xi, t)$

$$\frac{\partial F}{\partial t} + \nabla_{\perp}(\mathbf{v}_D F) + \frac{\partial}{\partial \xi}(v_{\xi} F) = 0 \quad (5)$$

is obtained by integrating Eq. (1) along the axial direction and defining the bounce-averaged streaming velocities as

$$\mathbf{v}_D = \int \frac{\mathbf{e}_z \times \nabla_{\perp} \phi}{B_0} g dz \quad v_{\xi} = -e \int \frac{\partial \phi}{\partial t} g dz \quad (6)$$

The kinetic model is then completed by the self-consistent Poisson equation in the Penning trap

$$\nabla^2 \phi = \frac{e}{\epsilon_0} \int F(r, \theta, \xi, t) g(r, \theta, z, \xi, t) d\xi \quad (7)$$

Finally, it must be observed that the kinetic equation, obtained using the adiabatic invariant

$$I(\xi) = \frac{1}{2\pi} \int \sqrt{2m(\xi + e\phi)} dz \quad (8)$$

as phase-space variable instead of ξ is simpler, in principle; however, the inversion of Eq. (8), required in the solution of the Poisson equation, is a challenging numerical problem.

GENERAL PROPERTIES

The distribution function F can be related to physical quantities that can be measured experimentally. Denoting with $\sigma(r, \theta, t)$ the z -integrated plasma density (an experimentally-measurable quantity) and with $F_{\zeta}(r, \theta, \zeta, t)$ the normalized distribution of the kinetic energy of the particles, ζ , the distribution function F can be expressed as $F(r, \theta, \xi, t) = \sigma(r, \theta, t) F_{\zeta}(r, \theta, \zeta, t)$, with $\zeta = \xi + e\phi_m$, being ϕ_m the potential in the point where the kinetic energy of the particles is measured and $\int F_{\zeta}(\zeta, r, \theta, t) d\zeta = 1$.

The kinetic model presented here satisfies some conservation laws. The canonical angular momentum, \mathbf{L}_z , defined as

$$\mathbf{L}_z = -\frac{eB}{2} \int \int \int r^2 F(r, \theta, \xi, t) dr d\theta d\xi \quad (9)$$

and the angular momentum, l_z , proportional to the axial angular momentum of an incompressible fluid,

$$I_z = \int \mathbf{e}_z \cdot \mathbf{r} \times (\mathbf{E} \times \mathbf{B}) d\mathbf{r} \quad (10)$$

are both conserved.

As far as the energy is concerned, the total energy of the plasma, \mathbf{E}_{tot} , can be written as the sum of potential and kinetic energies, $\mathbf{E}_{\text{tot}} = \mathbf{E}_{\text{pot}} + \mathbf{E}_{\text{kin}}$, being

$$\begin{aligned} \mathbf{E}_{\text{pot}} &= -\frac{1}{2} \int \int e\phi F(r, \theta, \xi, t) g(r, \theta, z, \xi, t) d\mathbf{r} d\xi \\ \mathbf{E}_{\text{kin}} &= \frac{1}{2} \int \int m v_z^2(r, \theta, \xi, t) g(r, \theta, z, \xi, t) d\mathbf{r} d\xi \end{aligned} \quad (11)$$

The calculation of $d\mathbf{E}_{\text{tot}}/dt$ leads to the conclusion that the model conserves the total energy, as the variation of the energy of the plasma equals the power provided by the electrodes:

$$\frac{d\mathbf{E}_{\text{tot}}}{dt} = \frac{\epsilon_0}{2} \frac{d}{dt} \int \phi \nabla \phi \cdot \mathbf{n} dS \quad (12)$$

CONNECTION WITH A RECENTLY-PROPOSED FLUID MODEL

The present kinetic model can be related to the fluid model proposed by Finn *et al.* [5] and refined by Coppa *et al.* [4]. The main assumption of that model is that the Maxwell-Boltzmann distribution is reached along the axial direction, so that the particle density $n(r, \theta, z, t)$ can be expressed as

$$n(r, \theta, z, t) = N(r, \theta, t) \exp\left[\frac{e\phi(r, \theta, z, t)}{k_B T}\right] \quad (13)$$

where $N(r, \theta, t)$ is a function that does not depend upon z . Within this assumption, the continuity equation for the z -integrated density, $\sigma(r, \theta, t)$, is written as

$$\frac{\partial \sigma}{\partial t} + \nabla_{\perp} (\mathbf{V}_{\perp} \sigma) = 0 \quad (14)$$

where

$$\mathbf{V}_{\perp} = \frac{1}{B_0} \mathbf{e}_z \times \frac{\int \nabla_{\perp} \phi \exp[(e\phi)/(k_B T)] dz}{\int \exp[(e\phi)/(k_B T)] dz} \quad (15)$$

The fluid model can be deduced from the present kinetic model by integrating Eq. (5) with respect to ξ , assuming that the function $F(r, \theta, \xi, t)$ can be written as:

$$F(r, \theta, \xi, t) = F(r, \theta, t) \exp\left(-\frac{\xi}{k_B T}\right) \int \frac{dz}{\sqrt{e\phi + \xi}} \quad (16)$$

This assumption is equivalent to affirm that the electrons are distributed according to the canonical distribution; i.e. the electron density is proportional to $\delta(H - \xi) \exp[-\xi/(k_B T)]$.

NUMERICAL RESULTS

The electrostatic potentials, $\phi(r, z)$, corresponding to axially-symmetric distributions, $F(r, \xi)$, have been calculated by solving numerically the self-consistent Poisson equation [Eq. (7)]. The equation has been discretized in space (using a uniform grid) and energy. Then, suitable quadrature formulas have been used to evaluate the ξ and z -integrals. The Poisson equation has been solved by adding a term $\partial\phi/\partial t$ to the left hand-side and seeking the steady state solution of the diffusion-like equation so obtained.

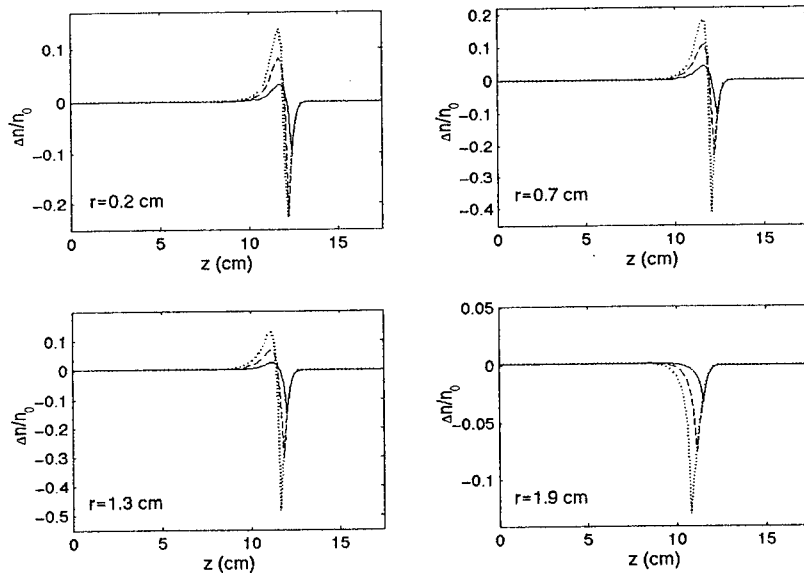


FIGURE 1. Plasma density difference, with respect to the Maxwellian distribution, for the Maxwellian distribution truncated at the energy $I = k_B T/2$ (dotted), $I = k_B T$ (dashed) and $I = 2k_B T$ (solid). The confining potential of the trap is $V = -50$ V, the central electrode length $L_c = 26$ cm, the end electrodes length $L_e = 4$ cm, the wall radius $R_w = 3.5$ cm, the plasma temperature $T = 1000$ K, the magnetic field $B_0 = 1$ T and, the parameters of the density profiles introduced by Finn [5] are: $n_0 = 5 \cdot 10^{12} \text{ m}^{-3}$, $\mu = 5$, $r_p = 2$ cm.

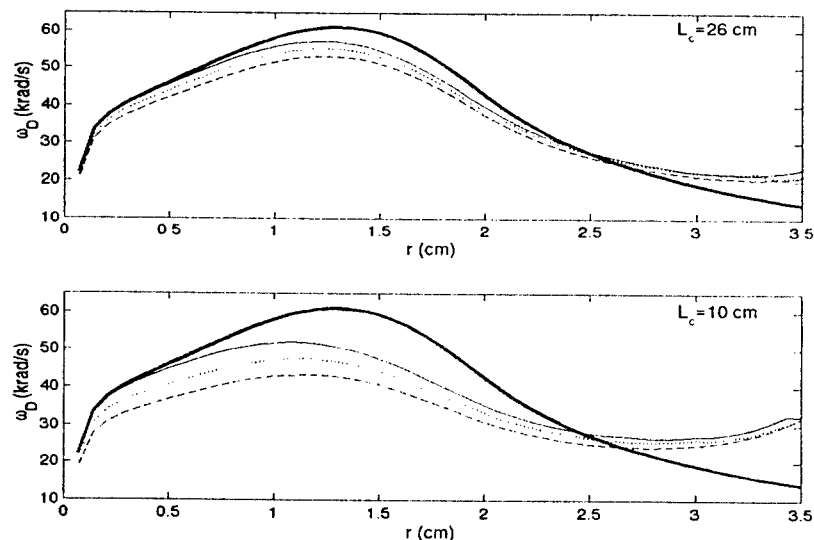


FIGURE 2. Bounce-averaged drift frequency for electrons with Maxwellian distribution at different axial energy: $\xi = 20.5$ eV (solid), $\xi = 23.3$ eV (dotted) and $\xi = 26$ eV (dashed) for two different values of L_c . The predictions of the 2-D theory are shown in thick solid line. The other trap parameters are the same as Fig.1.

The equilibrium solutions have been studied having fixed the plasma density at the center of the trap as the density profiles introduced by Finn *et al.* [5]. The velocity distributions have been chosen to be truncated Maxwellians, as suggested by Hilsabeck *et al.* [3].

Some numerical results are presented on Figs. 1-2. Figure 1 points out the effect of the velocity distribution on the plasma density by comparing different truncated Maxwellians. Figure 2 shows how the rotation drift frequency depends on the particle energy.

ACKNOWLEDGMENTS

Work performed with partial financial support by GNFM-INDAM (research project: "Kinetic Theory and Fluid Models for Non-Neutral Plasmas").

REFERENCES

1. Davidson, R.C., *An Introduction to the Physics of Non-Neutral Plasmas*, Addison-Wesley, Redwood City, 1990.
2. Smith, R.A., and Rosenbluth M.N., *Phys. Rev. Lett.* **64**, 649-652 (1990).
3. Hilsabeck, T.J., and O'Neil, T.M., *Phys. Plasmas* **8**, 407-422 (2001).
4. Coppa, G.G.M., d'Angola, A., Delzanno, G.L., and Lapenta, G., *Phys. Plasmas* **8**, 1133-1140 (2001).
5. Finn, J.M., del Castillo-Negrete, D., and Barnes, D.C., *Phys. Plasmas* **6**, 3744-3758 (1999).
6. Peurrung, A.J., and Fajans, J., *Phys. Fluids B* **2**, 693-699 (1990).

Forms and Oscillations Modes of Ion Cloud in the Linear RF-only Quadrupole Traps and in Ion Traps

A.A.Vedenov^{*}, E.N.Nikolaev[†]

^{*}*Russian Scientific Centre "Kurchatov Institute", Kurchatov pl.,1, Moscow 123182, Russia*

[†]*Institute for Energy Problems of Chemical Physics, Leninskij pr. 38, k.2 Moscow, 117829, Russia*

Abstract. Computer modelling of space configurations of ion clouds consisting of different m/z ions and dynamics of their motion in the presence of external (dipolar and quadrupolar) RF-field were analysed. Forms of ion clouds in ion traps were obtained by molecular modelling. It was shown that stratification of different m/z ions appears as a result of interaction of ion clouds with RF fields and with each other. For ions with high charge $q=30 e_{\text{electron}}$ and mass $m=30\,000 m_{\text{proton}}$ (electrosprayed protein ions in ion guides and ion traps) at ion densities $\sim 10^8 \text{ cm}^{-3}$ stratification takes place even at room temperatures. Coalescence of ion resonance frequencies for light and heavy equally charged ions in Paul ion trap was also demonstrated.

INTRODUCTION

Different types of ion electromagnetic traps (such as Paul ion trap, linear quadrupole radio-frequency trap, electrodynamic balance etc.) and quadrupole and multipole ion guides are currently in use in different modern mass spectrometers designed for analyses of molecular mixtures at high throughput conditions (proteomics) when ion densities and total ion numbers in traps and guides are high ($>10^6$) and ion-ion interaction is essential to properties of these devices even at room temperatures. In case of linear quadrupole it was found [1,2] that at high ion current in the mode of operation when ions are flying through a quadrupole and at high charge density in the accumulation mode (ions are accumulated in the quadrupole) large discrimination of ions with different mass to charge ratios (m/z) takes place. Besides, attempts of selective ejection by dipolar excitation of ions of particular m/z in the presence of high space charge revealed collective interaction of ion clouds of different m/z . Attempts were made to explain some aspects of this complex behaviour of such a system in two-dimensional zero temperature approximation [3,4]. The segregation of ions of different m/z occurs similar to segregation of immiscible liquids. Ions of smaller m/z are concentrated closer to the centre of the trap. In case, when supplementary external RF field (dipolar or quadrupolar) is applied to ion ensembles, a complex relative motion of ions with different m/z , interacting through Coulomb forces, takes place. In present work, we approximate an ion cloud by finite number of charges. Each charge interacts as a whole with a field of the trap, and also interacts through Coulomb forces with other charges. The interaction of an ionic cloud with residual gas is described as a

friction. The ordinary differential equations of ion motion are solved by Euler and fourth order Runge-Kutta methods.

MODEL

Two devices were modelled: Paul ion trap and linear quadrupole trap. An infinitely long wire quadrupole with an infinitely small wire diameter was used as a model for linear quadrupole trap analysis. To trap ions inside such a quadrupole we used two point charges of the same sign as trapped ions positioned on quadrupole axis at some distance from each other. This makes electric field three dimensional without axial and azimuthal symmetry. Analytical solution for the quadrupolar-dipolar field combination for this electrode geometry significantly simplifies digital analyses of ion behaviour. We suppose that characteristic ion cloud dimension is essentially less than the distance between electrodes. We used a quasi-potential approximation for description of electromagnetic forces in both traps. The value of quasi-potential (Kapitza-Dehmelt effective potential energy [5]) is proportional to the square of radial (and in case of Paul trap to both radial and z-displacement) ion displacement.

3-DIMENSIONAL STATIC CONFIGURATIONS

In the frame of this model we determined the forms of ion clouds for the mixture of different m/z ions at zero temperature. Force acting on i -th charge consists of the electric field force from all ion cloud charges q_k , each of which is positioned at the distance $R_{i,k}$ from charge i

$$E_{i,k} = \sum_k q_k R_{i,k} / |R_{i,k}|^3,$$

the force of the field from two end charges Q

$$E_{END} = \sum Q (R_i - z) / |R_i - z|^3$$

(here $z = \pm L$ are co-ordinates of end charges) and radial gradient of quasi-potential

$$U = -k (x^2 + y^2)/2.$$

Randomly chosen initial ion positions and velocities are relaxing to equilibrium positions. Effective friction of ions in a buffer gas was chosen so that relaxation time was some tens of a charge motion periods in quasi-potential well. We have found different ion cloud configurations with characteristic forms: disc, flattened ellipsoid, spherical ball, elongated ellipsoid, and thread. This sequence of configurations corresponds to growth of the ratio of transversal quasi-potential value to longitudinal one. The length X of linear chain of charged particles as function of ratio of particle charge q to trapping charge Q (placed at points $-L, +L$) can be represented approximately by the formula

$$4(Q/q)^{1/2} = (1-x^2)/x^{3/2},$$

$2X=2 \times L$ is equilibrium distance between two charges q placed on one line with trapping charges Q . The result of calculations coincides qualitatively with result of experiments [6,11].

STRATIFICATION IN AN ION TRAP

For both linear quadrupole and Paul traps pronounced radial stratification was demonstrated with lower m/z ions dominated near quadrupole axis and the trap centre, similar to what was observed experimentally in Penning trap [7,12] and in linear Paul trap [11]. For linear quadrupole separation of ions according to their m/z was also found in z -direction (along quadrupole axis). The stratification is the result of the balance of the Kapitza-Dehmelt effective potential force from the RF-field and the Coulomb force from the space charge. The dimensionless motion equations for n charges have a form

$$\begin{aligned} dz/dt &= v_z, \\ dv_z/dt &= -z + \Sigma z/r^3, \end{aligned} \quad (1)$$

(where summation is taken over all charges in trap) and analogous equations for x, y co-ordinates.

For Paul ion trap the units of time t_I , length l_I and velocity v_I are:

$$\begin{aligned} t_I &= 2 - M z_0^2 \Omega / (Vq), \\ z_I &= 2M z_0^4 \Omega^2 / V^2, \end{aligned}$$

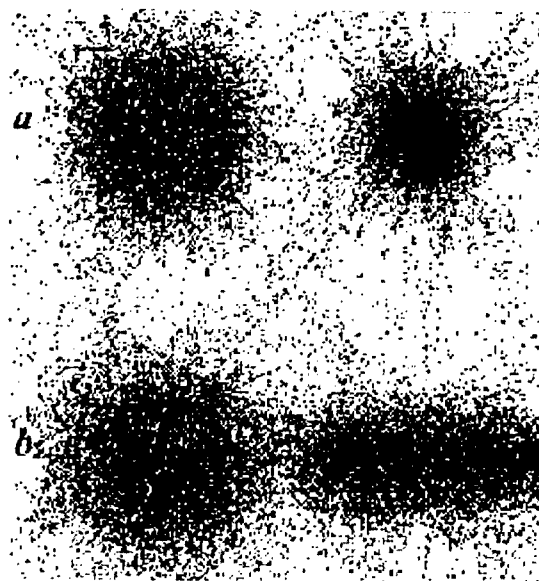


Fig.1. Ion cloud structure as averaged over dimensionless time interval from $t=0$ to $t=10000$. The beginning of separation at kinetic energy of ions corresponding to $\langle v_z^2 \rangle_{\text{average}} = 3$ (kinetic energy 300K). Clouds of higher and lower m/z are depicted separately with left cloud corresponding to high m/z and right to lower m/z . *a*- transverse view, *b*- longitudinal view.



Fig.2. Ion cloud structure as averaged over dimensionless time interval from $t=0$ to $t=10000$. Almost full separation at kinetic energy of ions corresponding to $\langle v_z^2 \rangle_{\text{average}} < 1$ (kinetic energy $< 100K$). Clouds of higher and lower m/z are depicted separately with left cloud corresponding to high m/z and right to lower m/z . *a*- transverse view, *b*- longitudinal view.

$v_l = z_l / t_l$, where M is ion mass, z_0 is the half of a distance between end cup electrodes in the ion trap, Ω is a frequency and V an amplitude of RF field. The average kinetic energy of ion longitudinal motion is $M v_l^2 / 2 \langle v_z^2 \rangle_{\text{average}}$. Visual inspection on computer monitor of ion cloud structures obtained as a result of equations (1) solution clearly shows separation of charges with different m/z at $\langle v_z^2 \rangle_{\text{average}} \leq 3$ (Fig.1). Then for $\Omega = 2\pi \cdot 0.5 \cdot 10^6$ Hz, $M = 3 \cdot 10^4$ Da, $q = 30$ elementary charges, $z_0 = 1$ cm, $V = 300$ V, we have $t_l = 1.410^5$ s, $z_l = 10^{-2}$ cm, $v_l = 0.7 \cdot 10^3$ cm/s and kinetic energy is $M v_l^2 / 2 \langle v_z^2 \rangle_{\text{average}} \approx 300^\circ \text{K}$.

For plasma density $\sim 10^8 \text{ cm}^{-3}$ the kinetic energy is of the order of averaged electrostatic energy per ion q^2/r (r is average distance between ions), so plasma coupling parameter $\Gamma = q^2/(rT) \approx 1$. The same criterion can be found in quite different way. There is a gap between inner droplet and outer envelope in the case of two component (two different m/z ions) system. These ensembles of ions could be considered as charged liquids [12]. The size of the gap has the order of magnitude of the inner droplet radius R . If amplitude of thermally excited surface waves of the droplet

$$x = (\bar{T}/4\pi\sigma)^{1/2} N^{1/2}$$

($N \approx n^{2/3} R^2$ is full number of surface oscillations) is less than the gap between clouds, $x < R$, then the liquids would be separated, in the opposite case they will be mixed.

We can suppose that

$$\sigma \approx n q^2,$$

$q = z \cdot e$, e is electron charge.

Then liquids would be separated, if

$$n q^2 R^2 > T N.$$

So the condition is nearly the same as

$$\Gamma = q^2/(4\pi a T) > 1,$$

Where $a = (3/(4\pi n))^{1/3}$ is Wigner-Seitz interparticle distance. It is possible that the separation can take place even at room temperatures, $n = 10^8 \text{ l/cm}^3$, $z = \sim 30$ as was described in [2]

COLLECTIVE OSCILLATIONS IN ION TRAP

Charged ion cloud oscillations - both longitudinal (z-oscillations) in ion traps [8-9] and transversal in a linear quadrupole traps [1-4] were investigated experimentally. The amplitude of the oscillations (parametric or forced) may be large - of the order of the trap dimensions. Peculiar feature of oscillations is that some characteristic ion frequencies, seen at small ion densities, disappear at higher ones. To model resonance dipolar excitation of ion motion in a Paul trap we applied excitation voltage to end caps of RF-only Paul trap. We have found a strong influence of the space charge value on the ion selection process. Computer modelling revealed strong correlation of ion motion of different m/z , which explains a coalescence of ion resonance peaks, observed experimentally [9] for isotopes of rare earth ions. We studied the coalescence of ion resonance frequencies for 3-D motion of 3 light and 9 heavy ($m_2/m_1=1.1$) equally charged ions in Paul ion trap. The light and heavy ion clouds are completely separated after relaxation period. The configuration is flat because longitudinal field in Paul trap is twice as large as the radial field. After relaxation an external periodical longitudinal force was applied and friction force was switched off. At small electrostatic ion interaction two resonances were observed with frequencies difference about 10%. As electrostatic interaction increased, this difference goes to zero.

CONCLUSION

Molecular modelling of multicomponent system of charged particles in a RF-traps have shown the possibility of different m/z ion cloud separation even at room temperature in case of multiply charged ions and high plasma densities. Criterion of separation obtained from the analyses of thermally excited surface waves of ion clouds coincides with $\Gamma=1$ criterion. Resonance peak coalescence correlate with stratification and takes place at nearly same Γ values.

ACKNOWLEDGEMENTS

Support from grants RFBR-99-03-33263, CRDF-RC1-2055 and INTAS-478 is greatly acknowledged.

REFERENCES

1. J.M. Campbell, B.A. Collings, D.J. Douglas, *Rapid Commun. Mass Spectrom.*, **12**, 1463-1474 (1998)
2. M.E. Belov, E.N. Nikolaev, G.A. Anderson, K.J. Auberry, R. Harkewicz, R.D. Smith. *J. Am. Soc. Mass Spectrom.*, **12**, 38-48 (2001)
3. Mikhail E. Belov; Eugene N. Nikolaev; Gordon A. Anderson; Harold R. Udseth; Mikhail V. Gorshkov; Tom Bailey; Richard D. Smith; *48 ASMS Meeting, Long Beach, CA, June 2000*

4. Aleksey Tolmachev; Richard Harkewicz; Christophe Masselon; Gordon Anderson; Sergey Rakov; Ljiljana Pasa-Tolic; Eugene Nikolaev; Mikhail Belov; Harold Udseth; Richard D. Smith; *48 ASMS Meeting, Long Beach, CA, June 2000*
5. L.D. Landau, E.M. Lifshitz. *Mechanics*. M., "Nauka", 1988, p. 123
6. P.T.H. Fisk, M.J. Sellars, M.A. Lawn, C. Coles, *Fifth Symp. Freq. Standards and Metrology*, ed. J.C. Bergquist, Woods Hole, MA, Oct. 1996 (World Scientific, Singapore, 1996), p. 27
7. Hidesuka Imajo et al. *Phys. Rev. A* **55**, 1276 (1997)
8. R. Albeit et al. *Phys. Rev. A* **56**, 4023 (1997); M.A.N. Ravzi et al. *Phys. Rev. A* **58**, R34 (1998)
9. K. Jungmann et al. *Phys. Rev. Lett.* **36**, 3451 (1987)
10. Vassily Hatzimanikatis, Leila H. Choe, and Kelvin H. Lee. *Biotechnol. Prog.* **15**, 312-318 (1999)
11. L. Horneker et al. *Phys. Rev. Lett.* **86**, 1994 (2001)
12. L. Gruber et al. *Phys. Rev. Lett.* **86**, 636 (2001)

Charge Sign Effect on the Coulomb Logarithm for a Two-Component (e.g., Antihydrogen) Plasma in a Penning Trap

J. R. Correa, Yongbin Chang, and C. A. Ordonez[†]

Department of Physics, University of North Texas, Denton, Texas 76203

Abstract. The magnitude of the center-of-mass scattering angle for a collision between two charges of the same sign is the same as the magnitude of the center-of-mass scattering angle for a collision between opposite single charges, everything else being equal. However, this equivalence only applies for a Coulomb interaction of infinite range. If the range of interaction between two charged particles is limited, as in a plasma, the center-of-mass scattering angle acquires a dependence on whether the two particles have the same or opposite charge signs. In the work presented, the effect that the two different charge sign combinations can have on the Coulomb logarithm is assessed by considering a cutoff Coulomb interaction potential. A substantial effect is predicted for neutral or partially neutralized plasmas in Penning traps.

INTRODUCTION

The Coulomb logarithm is a ubiquitous parameter in plasma physics. However, the commonly used expression for the Coulomb logarithm

$$\lambda = \ln \Lambda \quad (1)$$

is not accurate for small values of Λ where, for a representative binary collision, $\Lambda = 2b_{max}E_c/(kq_1q_2)$ [1]. Here b_{max} is the maximum impact parameter, E_c is the center-of-mass energy, q_1q_2 is the product of the charges, and k is the Coulomb constant [$k = 1/(4\pi\epsilon_0)$ in SI units or $k = 1$ in Gaussian units]. One reason Eq. (1) is not accurate for small values of Λ is that it is an approximation of a more general expression (see below). Another reason is that Eq. (1) considers collisions between two charged point particles using a pure Coulomb interaction potential. The actual range of interaction between two plasma particles is limited. As a result, the Coulomb logarithm should acquire a dependence on the sign of q_1q_2 . Here, a new expression for the Coulomb logarithm is derived by considering a cutoff Coulomb interaction potential that may be either attractive or repulsive. The present work extends the results presented in Ref. [1] to include the case of an attractive interaction potential. The new expression may be useful for describing

[†]) Electronic mail: cao@unt.edu

kinetic processes in two-component plasmas in nested Penning traps [2,3]. It should be noted that experiments aimed at merging positron and antiproton plasmas in nested Penning traps [4,5] may be able to observe the effect predicted by the theory presented here (or possibly be adversely affected by the effect). Also, the charge sign effect may affect a plasma's stopping power [6].

At this point, it is useful to define various scale lengths and use them to introduce criteria under which the present theory is intended to apply. First, consider two charged particles that experience a pure Coulomb collision. Initially, the charged particles are an infinite distance apart and moving towards each other. The closest possible approach between the particles occurs if they experience a head-on collision. The classical distance of closest approach for a head-on collision is $r_0(0) = kq_1q_2/E_c$, which applies for particles having the same charge sign. If the two particles are oppositely signed and are considered point particles, then $r_0(0) = 0$.

Now consider a one component plasma (OCP) [7] of infinite dimensions. The particles of the OCP are assumed to have a Maxwellian velocity distribution with uniform temperature T and density n . If a collision between two particles in the OCP is approximated as being a pure Coulomb collision, the average minimum distance of closest approach is approximately $r_{00} = kq^2/T$, where q is the charge of each particle and T is temperature in energy units. Another scale length associated with the OCP is the Wigner-Seitz radius, $r_a = [3/(4\pi n)]^{1/3}$, which is approximately the average distance between nearest neighbor particles of the OCP. A third scale length is the Debye length $\lambda_D = [T/(4\pi kq^2 n)]^{1/2} = \sqrt{r_a^3/(3r_{00})}$. The Debye length is the scale length over which the electric field of a charged plasma particle is not canceled (or "shielded") by an opposite electric field produced by the surrounding plasma. (When more than one plasma component is present, all plasma components associated with thermal speeds of the order of or larger than the speed of a particle being shielded contribute to that shielding.) A fourth scale length is the cyclotron radius. Assuming a uniform magnetic field of magnitude B and neglecting the effects of all other particles and fields, the average cyclotron radius of a particle in the OCP is approximately $r_c = \sqrt{mT}/(\ell|q|B)$. Here, m is the mass of a single particle and ℓ is a constant associated with the units used ($\ell = 1$ in SI units and $\ell = 1/c$ in Gaussian units with c as the speed of light).

The coupling parameter for the OCP is defined as $\Gamma = kq^2/(r_a T)$ [7]. The coupling parameter can also be written in terms of the scale lengths defined above: $\Gamma = r_{00}/r_a = (1/3)(r_a/\lambda_D)^2 = (1/3)^{1/3}(r_{00}/\lambda_D)^{2/3}$. The OCP is strongly coupled or strongly correlated if $\Gamma \gg 1$ and weakly coupled or weakly correlated if $\Gamma \ll 1$ [7]. For $\Gamma \geq 2$, the particle positions start to become correlated, and the plasma can exhibit liquid or crystal characteristics [7]. Finally, the OCP is strongly magnetized if $r_c \ll r_{00}$ or weakly magnetized if $r_c \gg r_{00}$ [8]. Below, we find that the transition between strong and weak magnetization occurs at $r_c \approx 0.1r_{00}$.

In Ref. [8], theoretical expressions for the anisotropic temperature relaxation rate are evaluated for both weakly and strongly magnetized nonneutral electron plasmas. The expressions are the same, except that for a strongly magnetized plasma the usual Coulomb logarithm is replaced by a different term. For weakly magnetized plasmas, the physics

associated with the collision dynamics is contained within the Coulomb logarithm. For strongly magnetized plasmas, the collision dynamics is modified by the magnetic field. In consideration of these things, we hypothesize that rates or time scales that are associated with velocity space scattering processes are describable by expressions that apply to both weakly and strongly magnetized plasmas, except for a term (the Coulomb logarithm) that changes (see also Ref. [2]). For strongly magnetized plasmas, we refer to the term as the Coulomb logarithm although it may not have a logarithmic dependence.

In the work presented here, two interacting plasma components are considered. The cyclotron radius for at least one of the plasma components is assumed to be smaller than the Debye shielding length associated with the presence of both plasma components. Also, each plasma component is weakly correlated and may be either weakly or strongly magnetized.

DERIVATION OF THE COULOMB LOGARITHM

The usual defining expression for the Coulomb logarithm is given by [1]

$$\lambda = \frac{1}{\rho_{\perp}^2} \int_0^{\infty} \sin^2 \left(\frac{\theta_c}{2} \right) b db, \quad (2)$$

where θ_c is the center-of-mass scattering angle for a collision between two plasma particles and $\rho_{\perp} = kq_1q_2/(2E_c)$. If we consider the classical center-of-mass scattering angle for a binary collision, then

$$\theta_c = \pi - 2b \int_{r_0}^{\infty} \frac{dr}{r^2} \left(1 - \frac{V(r)}{E_c} - \frac{b^2}{r^2} \right)^{-1/2}, \quad (3)$$

where $V(r)$ is the interaction potential and

$$0 = 1 - \frac{V(r_0)}{E_c} - \frac{b^2}{r_0^2} \quad (4)$$

identifies the point where \dot{r} equals zero, denoting a turning point (about which the trajectory is symmetric in the center-of-mass frame of reference). Thus, $r_0(b)$ is the classical distance of closest approach for a given impact parameter b . For a pure Coulomb collision, $V(r) = kq_1q_2/r$ and

$$\sin^2 \left(\frac{\theta_c}{2} \right) = \frac{1}{1 + b^2/\rho_{\perp}^2}. \quad (5)$$

Substituting Eq. (5) into Eq. (2), and introducing a maximum impact parameter b_{max} , yields

$$\lambda = \frac{1}{\rho_{\perp}^2} \int_0^{b_{max}} \frac{b}{1 + b^2/\rho_{\perp}^2} db = \ln \left(\sqrt{1 + \frac{b_{max}^2}{\rho_{\perp}^2}} \right) = \ln \left(\sqrt{1 + \Lambda^2} \right). \quad (6)$$

Equation (6) applies regardless of the sign of $\Lambda = 2b_{max}E_c/(kq_1q_2)$ and is symmetric for negative Λ with respect to positive Λ . Note that Eq. (1) is arrived at by taking the limit $\Lambda \gg 1$ and considering only positive values for q_1q_2 .

The Coulomb logarithm is now evaluated using a cutoff Coulomb interaction potential, everything else being the same. The cutoff Coulomb interaction potential has the form [1]

$$V(r) = kq_1q_2\left(\frac{1}{r} - \frac{1}{a}\right)\Theta\left(1 - \frac{r}{a}\right), \quad (7)$$

where Θ is the Heavyside step function and a is the cutoff length. If we introduce the variables $y = b/r$, $\Lambda_a = 2aE_c/(kq_1q_2)$, and $\beta = b/a$, the center-of-mass scattering angle is given by

$$\theta_c = \pi - 2 \int_0^\beta \frac{dy}{\sqrt{1-y^2}} - 2 \int_\beta^{y_0} \frac{dy}{\sqrt{1 + 2/\Lambda_a - 2y/\Lambda_a\beta - y^2}}, \quad (8)$$

where y_0 is found by solving

$$0 = 1 - \frac{2}{\Lambda_a\beta}(y_0 - \beta) - y_0^2. \quad (9)$$

Notice that Λ_a carries the information of the charge signs. Equation (9), for positive Λ_a , yields only one physically admissible solution for y_0 [1]. On the other hand, if Λ_a is allowed to be either negative or positive, multiple possible solutions are obtained. However, the ambiguity vanishes during the calculation of the center-of-mass scattering angle. Upon integration, the Coulomb logarithm for a cutoff Coulomb interaction potential is found to be

$$\lambda(\Lambda_a) = \frac{(1 + \Lambda_a)^2 \ln[(1 + \Lambda_a)^2]}{2(2 + \Lambda_a)^2} - \frac{\Lambda_a}{2(2 + \Lambda_a)}, \quad (10)$$

which applies for both attractive and repulsive interaction potentials.

EFFECT OF THE CHARGE SIGNS

Equation (10) is not symmetric for negative Λ_a with respect to positive Λ_a . This is shown in Fig. 1 where $\Lambda_a = \pm\Lambda$ is used. Unlike the case of the pure Coulomb interaction potential, the Coulomb logarithm for a cutoff Coulomb interaction potential depends on the sign of q_1q_2 .

A comparison between the present theory and numerical calculations [8] of the Coulomb logarithm for repulsive interactions within an OCP is presented in Fig. 2, where $\Lambda_a = \pm c_a\Lambda$ is used with a proportionality constant, c_a . (The reader is referred to Ref. [2] for more details on the type of comparison shown in Fig. 2.) Using $\Lambda_a = \pm c_a\Lambda$ amounts to setting $a = c_a b_{max}$, where b_{max} is set equal to the cyclotron radius. $c_a = 2$ is chosen

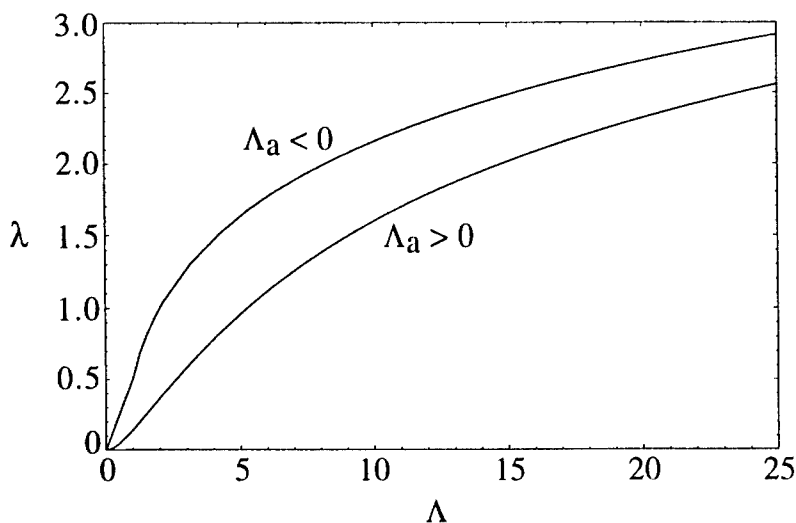


FIGURE 1. Equation (10) using $\Lambda_a = \pm\Lambda$.

because it yields the best fit (by eye) between Eq. (10) with $\Lambda_a > 0$ and the numerical calculations. (Thus, $a \approx 2r_c$.) Equation (10) with $\Lambda_a > 0$ is found to be within 10% of the numerical calculations for $\Lambda > 0.3$ ($\lambda > 0.06$). The transition from disagreement to good agreement between Eq. (10) with $\Lambda_a > 0$ and the numerical calculations may be considered to indicate that the transition from strong to weak magnetization occurs near $\Lambda = 0.3$ within an OCP. For the comparison using $\Lambda_a = -c_a\Lambda$, the prediction for an attractive interaction potential is compared with numerical calculations for a repulsive interaction potential. The result indicates that the charge sign effect is substantial over at least an order of magnitude of Λ values and should be observable in neutral or partially neutralized plasmas in Penning traps.

CONCLUSION

By considering a cutoff Coulomb interaction potential, a new expression for the Coulomb logarithm, Eq. (10), has been derived. The new expression for the Coulomb logarithm exhibits a dependence on whether the interaction potential is repulsive or attractive. For repulsive interactions, Eq. (10) was found to agree with numerical results for an OCP that is weakly magnetized (i.e., an OCP for which $r_c/r_{00} > 0.1$). For attractive interactions, the applicability of Eq. (10) is not expected to be restricted by the ratio r_c/r_{00} associated with each of two oppositely signed plasma components because the classical distance of closest approach can always be less than the smaller of the two cyclotron radii associated with the two components.

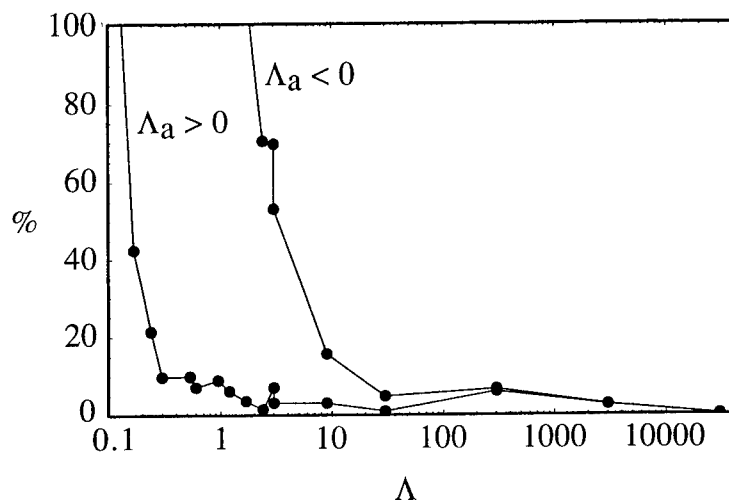


FIGURE 2. The percent difference between Eq. (10) using $\Lambda_a = \pm 2\Lambda$ and numerical calculations. The points are joined by lines to guide the eye.

ACKNOWLEDGMENTS

The authors would like to thank Dr. T. M. O'Neil for helpful comments. This material is based upon work supported by the National Science Foundation under Grant No. PHY-0099617

REFERENCES

1. C. A. Ordonez and M. I. Molina, *Phys. Plasmas* **1**, 2515 (1994).
2. Y. Chang and C. A. Ordonez, *Phys. Rev. E* **62**, 8564 (2000).
3. Y. Chang and C. A. Ordonez, "Two-Temperature Equilibration Rate for a Two-Component (e.g., Anti-hydrogen) Plasma in a Penning Trap," *2001 Workshop on Nonneutral Plasmas, San Diego, California, July, 2001*.
4. G. Gabrielse et al., *Phys. Lett. B* **507**, 1 (2001).
5. M. H. Holzschneider and M. Charlton, *Rep. Prog. Phys.* **62**, 1 (1999).
6. G. Zwicknagel, M. Walter, and C. Toepffer, "Energy Loss of Ions by Collisions With Magnetized Electrons," *2001 Workshop on Nonneutral Plasmas, San Diego, California, July, 2001*; G. Zwicknagel in *Non-Neutral Plasma Physics III*, edited by J. J. Bollinger, R. L. Spencer, and R. C. Davidson, AIP Conf. Proc. No. 498 (AIP, Melville, 1999), p. 469.
7. D. H. E. Dubin and T. M. O'Neil, *Rev. Mod. Phys.* **71**, 87 (1999).
8. M. E. Glinsky, T. M. O'Neil, M. N. Rosenbluth, K. Tsuruta, and S. Ichimaru, *Phys. Fluids B* **4**, 1156 (1992).

Two-Temperature Equilibration Rate for a Two-Component (e.g., Antihydrogen) Plasma in a Penning Trap

Yongbin Chang and C. A. Ordonez[†]

Department of Physics, University of North Texas, Denton, Texas 76203

Abstract. An expression for an equilibration time scale is developed that characterizes the rate for a group of test particles with a Maxwellian velocity distribution but different temperature from that of Maxwellian field particles to relax to the same temperature of the field particles. The expression, which can be used for any value of the Coulomb logarithm, is based on onefold integral expressions for Fokker-Planck velocity-space friction and diffusion coefficients presented elsewhere [Y. Chang and C. A. Ordonez, *Phys. Rev. E* **62**, 8564 (2000)]. A comparison with Spitzer's formula shows a noticeable difference when the Coulomb logarithm has values smaller than 10.

INTRODUCTION

An equilibration time scale is presented that characterizes the rate for a group of test particles with a Maxwellian velocity distribution but different temperature from that of Maxwellian field particles to relax to the same temperature of the field particles. Spitzer [1,2] formulated the equilibration time scale for a two-component plasma based on Chandrasekhar's formulas for the velocity space friction and diffusion coefficients [3,4]. Due to the approximations employed, Spitzer's formula for the equilibration time scale is limited to plasmas with large Coulomb logarithm values. The present theory is based on the binary collision model, but is not restricted in applicability by the value of the Coulomb logarithm. The reader is referred elsewhere [5,6] for more details regarding the applicability of the theory to plasmas confined in Penning traps. For example, the present theory can be used to predict the rate at which an antiproton plasma equilibrates with a low-temperature positron plasma, while both species are simultaneously confined by a nested Penning trap [7].

[†]) Electronic mail: cao@unt.edu

THE EQUILIBRATION TIME SCALE

Consider a single test particle moving in a plasma of Maxwellian field particles. The test particle will exchange its energy with the field particles due to collisions. In a single encounter of a test particle with a field particle, the exchange of energy, ΔE , is given by

$$\Delta E = \frac{1}{2}m (\Delta v^2 + 2v\Delta v_{\parallel}), \quad (1)$$

where m is the mass of the test particle, v is its speed, Δv is the magnitude of its velocity change due to the collision, and Δv_{\parallel} is the magnitude of its velocity change along its original direction. Averaging Eq. (1) over a Maxwellian velocity distribution for the field particles, the average time rate of change of the test particle energy is written as

$$\langle \Delta E \rangle = \frac{1}{2}m (\langle \Delta v^2 \rangle + 2v\langle \Delta v_{\parallel} \rangle). \quad (2)$$

In Eq. (2), $\langle \Delta v_{\parallel} \rangle$ and $\langle \Delta v^2 \rangle$ are the usual Fokker-Planck velocity-space friction and diffusion coefficients. Let us suppose that a group of test particles have a Maxwellian velocity distribution with temperature T , which is different from that of the field particles of temperature T_f . The equilibration time scale can be obtained simply by averaging Eq. (2) over a Maxwellian velocity distribution for the test particles. The rate of change of the test particle temperature is defined through the expression,

$$\frac{3}{2}nk \frac{dT}{dt} = \int \langle \Delta E \rangle f_M(v, T) dv, \quad (3)$$

where n is the density of the test particle species, k is Boltzmann's constant, and $f_M(v, T)$ is the Maxwellian velocity distribution with temperature T ,

$$f_M(v, T) = n \left(\frac{m}{2\pi kT} \right)^{3/2} \exp \left(-\frac{m}{2kT} v^2 \right). \quad (4)$$

Because the test particle velocity distribution is isotropic, the integral over solid angle can be carried out and Eq. (3) can be written as

$$\frac{dT}{dt} = \frac{8\pi}{3nk} \int_0^{\infty} \langle \Delta E \rangle f_M(v, T) v^2 dv. \quad (5)$$

Substituting Eq. (4) into Eq. (5) and carrying out a variable change, $u = v/v_{th}$ with the thermal velocity of a field particle defined as $v_{th} = \sqrt{2kT_f/m_f}$, a non-dimensional form of Eq. (5) can be written as

$$\frac{dT}{dt} = \frac{8\zeta^{3/2}}{3\sqrt{\pi}k} \int_0^{\infty} \langle \Delta E \rangle \exp(-\zeta u^2) u^2 du, \quad (6)$$

where $\zeta = T_f m / (T m_f)$ with m_f the mass of a field particle. The next step for the calculation of the equilibration time scale is to integrate Eq. (6). In order to integrate Eq. (6), one must substitute into Eq. (2) expressions for friction and diffusion coefficients.

SPITZER'S APPROACH TO THE EQUILIBRATION TIME SCALE

Spitzer employed Chandrasekhar's expressions for the friction and diffusion coefficients [2],

$$\langle \Delta v_{\parallel} \rangle = -\frac{4av_{th}\lambda G(u)}{\tau_0}, \quad (7)$$

and

$$\langle \Delta v^2 \rangle = \frac{2(av_{th})^2 \lambda \text{erf}(u)}{\tau_0 u}, \quad (8)$$

where $a = 2\mu/m$, the reduced mass is $\mu = mm_f/(m + m_f)$, λ is the Coulomb logarithm, the time scale for single particle interactions is $\tau_0 = (n_f v_{th} \pi r_0^2)^{-1}$, n_f is the density of the field particles, the interaction radius is defined as $r_0 = ZZ_f e^2 / (8\pi\epsilon_0 k (\mu T_f / m_f))$, Z and Z_f are the charge state of a test particle and field particle, e is the unit charge, ϵ_0 is the permittivity of free space, erf is the error function, and Chandrasekhar's function is defined as $G(u) = -\frac{1}{2} \frac{d}{du} (\text{erf}(u)/u)$. Substituting Eqs. (7) and (8) into Eq. (2), the integral in Eq. (6) can be carried out as

$$\frac{dT}{dt} = \frac{4m(av_{th})^2 \lambda \zeta^{1/2} (1 + \zeta - 2a^{-1})}{3\sqrt{\pi}\tau_0 k (1 + \zeta)^{3/2}}, \quad (9)$$

where the Coulomb logarithm has been approximated as being constant. Equation (9) can be rearranged into the standard form as

$$\frac{dT}{dt} = \frac{T_f - T}{\tau_{eq}^{\text{Spitzer}}}, \quad (10)$$

where $\tau_{eq}^{\text{Spitzer}}$ is the equilibration time scale obtained by Spitzer given by

$$\tau_{eq}^{\text{Spitzer}} = \frac{3mm_f}{8\sqrt{2}\pi n_f \lambda} \left(\frac{4\pi\epsilon_0}{ZZ_f e^2} \right)^2 \left(\frac{kT}{m} + \frac{kT_f}{m_f} \right)^{3/2}. \quad (11)$$

Spitzer's equilibration time scale applies when the Coulomb logarithm is large both because it was approximated as constant and because an approximation was employed in the process of obtaining Chandrasekhar's expressions for the friction and diffusion coefficients.

NEW APPROACH TO THE EQUILIBRATION TIME SCALE

Recently, a variable change technique [5,8-12] has been developed, which has been used for deriving the Fokker-Planck coefficients. Exact onefold integral expressions for Fokker-Planck velocity-space friction and diffusion coefficients have been obtained from

the new technique. These expressions make it possible to recalculate the equilibration time scale without placing a restriction on the value of the Coulomb logarithm. The expressions for the friction and diffusion coefficients are [5]

$$\langle \Delta v_{\parallel} \rangle = -\frac{av_{th}}{\tau_0 u^2} \int \left(\frac{\text{erf}(U) + \text{erf}(W)}{u_{\delta}} + \frac{\exp(-U^2) - \exp(-W^2)}{\sqrt{\pi} u_{\delta}^2} \right) du_{\delta} \quad (12)$$

and

$$\langle \Delta v^2 \rangle = \frac{(av_{th})^2}{\tau_0 u} \int \frac{\text{erf}(U) + \text{erf}(W)}{u_{\delta}} du_{\delta}, \quad (13)$$

where $U = u + u_{\delta}$, $W = u - u_{\delta}$, and $u_{\delta} = \Delta v / (av_{th})$ is the non-dimensional variable for velocity change. If we substitute Eqs. (12) and (13) into Eq. (2), Eq. (6) can be expressed as the following twofold integral:

$$\frac{dT}{dt} = \frac{4m(av_{th})^2 \zeta^{3/2}}{3\sqrt{\pi} \tau_0 k} \iint \left(\frac{\text{erf}(U) + \text{erf}(W)}{(2a^{-1} - 1)^{-1} u_{\delta}} - \frac{\exp(-U^2) - \exp(-W^2)}{2^{-1} \sqrt{\pi} a u_{\delta}^2} \right) \frac{u du du_{\delta}}{\exp(\zeta u^2)}. \quad (14)$$

The integral in Eq. (14) about u can be further reduced to

$$\frac{dT}{dt} = \frac{4m(av_{th})^2 \zeta^{1/2} (1 + \zeta - 2a^{-1})}{3\sqrt{\pi} \tau_0 k (1 + \zeta)^{3/2}} \int \exp\left(-\frac{\zeta u_{\delta}^2}{1 + \zeta}\right) u_{\delta}^{-1} du_{\delta}. \quad (15)$$

Let us rewrite Eq. (15) as

$$\frac{dT}{dt} = \frac{T_f - T}{\tau_{eq}^{new}}, \quad (16)$$

where the new equilibration time scale is obtained from Eq. (16) and Eq. (15) as

$$\tau_{eq}^{new} = \frac{3mm_f \tau}{16\mu^2} \left(\frac{1}{2} \int \exp(-x) x^{-1} dx \right)^{-1}. \quad (17)$$

Here, $\tau = (n_f v_{av} \pi r^2)^{-1}$, where the average relative speed between two different groups of Maxwellian particles is $v_{av} = \sqrt{8kT' / (\pi\mu)}$, and the interaction radius is defined as $r = ZZ_f e^2 / (8\pi\epsilon_0 kT')$. The non-dimensional interaction strength is defined as $x = H / (kT')$, in which the collision strength is defined as

$$H = \frac{\Delta p^2}{8\mu}, \quad (18)$$

where $\Delta p = m\Delta v$ is the magnitude of the momentum transfer for a collision event, and the reduced temperature is defined as

$$T' = \mu \left(\frac{T}{m} + \frac{T_f}{m_f} \right). \quad (19)$$

No approximations are used to arrive at Eq. (17). However the integral in Eq. (17) diverges due to the long range Coulomb interaction, and a cutoff must be imposed on the non-dimensional collision strength x . The minimum and maximum non-dimensional velocity change can be expressed in terms of the average relative speed and the Coulomb logarithm as [5]

$$u_{\delta, \min} = \frac{v_{av}}{v_{th}} e^{-\lambda} \quad (20)$$

$$u_{\delta, \max} = \frac{v_{av}}{v_{th}}. \quad (21)$$

For the two temperature system, the average relative speed is $v_{av} = 2((1 + \zeta)/(\pi\zeta))^{1/2} v_{th}$, and the integral limits for Eq. (17) become

$$x_{\min} = \frac{4}{\pi} e^{-2\lambda} \quad (22)$$

$$x_{\max} = \frac{4}{\pi}. \quad (23)$$

Substituting these into Eq. (17), we obtain the equilibration time scale

$$\tau_{eq}^{\text{new}} = \frac{3mm_f\tau}{8\mu^2\Gamma\left(0, \frac{4}{\pi}e^{-2\lambda}, \frac{4}{\pi}\right)} = \frac{3mm_f}{4\sqrt{2\pi}n_f\Gamma\left(0, \frac{4}{\pi}e^{-2\lambda}, \frac{4}{\pi}\right)} \left(\frac{4\pi\epsilon_0}{ZZ_f e^2}\right)^2 \left(\frac{kT}{m} + \frac{kT_f}{m_f}\right)^{3/2}, \quad (24)$$

where the zeroth-order incomplete gamma function $\Gamma(0, x_{\min}, x_{\max})$ is defined as

$$\Gamma(0, x_{\min}, x_{\max}) = \int_{x_{\min}}^{x_{\max}} e^{-x} x^{-1} dx. \quad (25)$$

The difference between Spitzer's approach and the present approach is characterized by the ratio

$$\frac{\tau_{eq}^{\text{Spitzer}}}{\tau_{eq}^{\text{new}}} = \frac{\Gamma\left(0, \frac{4}{\pi}e^{-2\lambda}, \frac{4}{\pi}\right)}{2\lambda}, \quad (26)$$

which is only a function of the Coulomb logarithm. With this, a comparison of Eq. (24) and Spitzer's result Eq. (11) is shown in Fig. 1. The new result Eq. (24) is generally larger than the traditional one. When the Coulomb logarithm is larger than 10, the difference is less than 5%. However, the difference can be substantial when the Coulomb logarithm is less than ten.

ACKNOWLEDGMENTS

This material is based upon work supported by the National Science Foundation under Grant No. PHY-0099617.

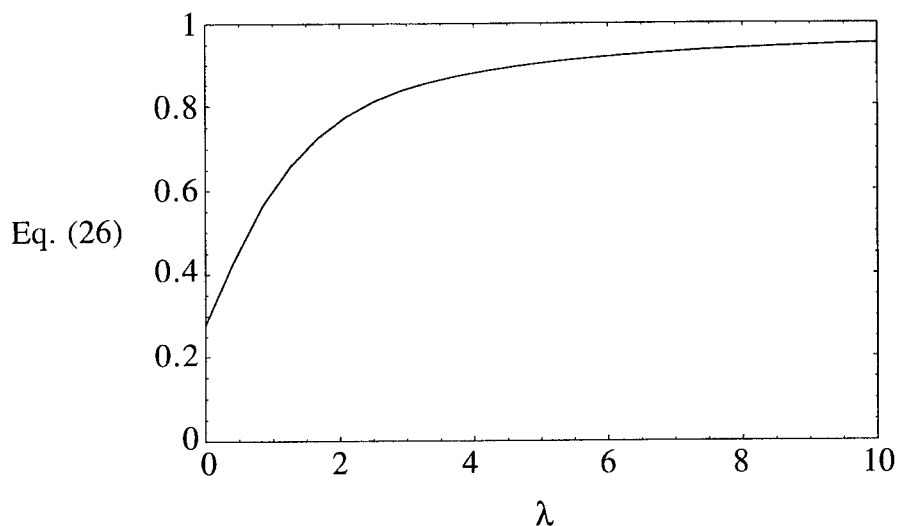


FIGURE 1. A plot of Eq. 26.

REFERENCES

1. L. Spitzer, Monthly Notices, Roy. Astron. Soc. (London) **100**, 396 (1940).
2. L. Spitzer, *Physics of Fully Ionized Gases* (Interscience, New York, 1962), Chap. 5.
3. S. Chandrasekhar, *Astrophys. J.* **97**, 255 (1943).
4. S. Chandrasekhar, *Principles of Stellar Dynamics* (University of Chicago Press, Chicago, 1994), Chapter 2 and Section 5.7.
5. Y. Chang and C. A. Ordonez, *Phys. Rev. E* **62**, 8564 (2000).
6. J. R. Correa, Y. Chang and C. A. Ordonez, "Charge Sign Effects on the Coulomb Logarithm for a Two-Component (e.g., Antihydrogen) Plasma in a Penning Trap," *2001 Workshop on Nonneutral Plasmas, San Diego, California, July, 2001*.
7. C. A. Ordonez, *Phys. Plasmas* **4**, 2313 (1997).
8. Y. Chang, *Phys. Fluids B* **4**, 313 (1992).
9. Y. Chang, Y. Huo, and G. Yu, *Phys. Fluids B* **4**, 3621 (1992).
10. Y. Chang, Y. P. Huo, and J. X. Liu, *Commun. Theor. Phys.* **20**, 359 (1993).
11. Y. Chang and D. Li, *Phys. Rev. E* **53**, 3999 (1996).
12. Y. Chang and C. A. Ordonez, *Phys. Plasmas* **6**, 2947 (1999).

Confinement Properties of Non-neutral and Neutral Plasmas in an Axially Symmetric System

Teruo Tamano and Isao Katanuma

University of Tsukuba, Tsukuba, Ibaraki 305-0045, Japan

Abstract. A general approach is established to examine confinement properties of both non-neutral and neutral axially symmetric plasmas. In this approach, problems are reduced to finding total minimum energy states under the conservation of total angular momentum and total number of particles. First, the well-known result of a non-neutral plasma in a cylindrical system is reproduced for checking the approach. Second, the approach is applied to analysis of confinement properties of tokamak plasmas with a transport barrier and it is shown that the tokamak with an internal transport barrier is in the minimum energy state.

INTRODUCTION

It is well known that a single species plasma in a Penning trap has a very long lifetime. This long confinement can be understood by the constancy of the total canonical angular momentum in a cylindrical system [1, 2]. The total canonical angular momentum is given by $P_\theta = \sum_j (m_j u_{\theta j} r_j + e_j A_{\theta j} r_j)$, where the first term is the kinetic term of the angular

momentum and the second term is the vector potential term of the angular momentum. In the case of a single species plasma, the vector potential term is much larger than the kinetic term. Then, the total angular momentum in a uniform magnetic field can be written as

$P_\theta = \frac{eB}{2} \sum_j r_j^2$. Accordingly, the location of the single species plasma particles is

constrained, and this is considered as the essence of the long confinement.

On the other hand, in a case of a neutral plasma, pairs of ions and electrons can escape together from the system without changing the vector potential term of the total angular momentum. This is considered to be the reason why the confinement of neutral plasmas is poor. However, the situation changes when the mechanical part of the total angular momentum dominates over the vector potential term. Then, the constancy of the total

canonical angular momentum places a constraint similar to that for the single species plasma.

In this paper, we establish an approach to examine confinement properties of both non-neutral and neutral plasmas under the constraint of conservation of the total angular momentum. First, the approach is applied to a cylindrical single species plasma in order to check its validity. Then, the approach is applied to a tokamak plasma with a transport barrier.

CYLINDRICAL SINGLE SPECIES PLASMA

In the case of a cylindrical single species plasma, the total angular momentum P_θ and the total number of particles N per unit length may be given by

$$P_\theta = 2\pi \int_0^a n(mu_\theta + eA_\theta)r^2 dr, \quad N = 2\pi \int_0^a nrdr. \quad (1)$$

The total energy U per unit length can also be conserved, where U is the sum of the total kinetic energy K and the total potential energy W , i.e., $U = K + W$. The total kinetic energy and the total potential energy can be written as

$$K = \pi \int_0^a nm u_\theta^2 r dr, \quad W = 2\pi \int_0^a \left(\frac{3}{2} nkT + \frac{1}{2} \epsilon_0 E^2 + \frac{B^2}{2\mu_0} \right) r dr. \quad (2)$$

The plasma equilibrium under the conservation of the total angular momentum and the total number of particles can be obtained by finding the state for the minimum total potential energy W . This problem is equivalent to finding the state for the maximum kinetic energy K when the total energy U is conserved.

The force balance equation is given by

$$E + u_\theta B = -\frac{1}{en} \frac{d(nkT)}{dr}, \quad (3)$$

where E is the radial component of the electric field. Eliminating u_θ from Eq. (2) and Eq. (3), one rewrites the total kinetic energy as

$$K = \pi \int_0^a nm \left(E + \frac{1}{en} \frac{d(nkT)}{dr} \right)^2 r dr. \quad (4)$$

Since the vector potential term of the total angular momentum for a single species plasma is much larger than the kinetic term, the total angular momentum in a uniform magnetic field is given by

$$P_\theta = \pi \int_0^a neBr^2 dr. \quad (5)$$

By use of the Poisson equation

$$n = \frac{\epsilon_0}{e} \frac{1}{r} \frac{d(rE)}{dr}, \quad (6)$$

Equation (5) becomes

$$P_\theta = \pi \epsilon_0 B \int_0^a r^2 \frac{d(rE)}{dr} dr. \quad (7)$$

Performing a partial integral of Eq. (7), one obtains

$$P_\theta = \pi \epsilon_0 B \left\{ E(a)a^2 - 2 \int_0^a Er^2 dr \right\}. \quad (8)$$

The total kinetic energy Eq. (4) can also be rewritten by use of Eq. (6) as

$$K = \frac{\pi \epsilon_0 m}{eB^2} \int_0^a \frac{d(rE)}{dr} \left(E + \frac{1}{en} \frac{d(nkT)}{dr} \right)^2 dr. \quad (9)$$

Performing a partial integral, one gets

$$K = \frac{\pi \epsilon_0 m}{eB^2} \left\{ \left[E a \left(E + \frac{1}{en} \frac{d(nkT)}{dr} \right) \right]_0^a - \int_0^a (rE) \frac{d}{dr} \left(E + \frac{1}{en} \frac{d(nkT)}{dr} \right)^2 dr \right\}. \quad (10)$$

Accordingly, the problem is reduced to finding the maximum value of Eq. (10) under the constraint of conservation of the total angular momentum given by Eq. (8). This variation problem is solved by using the Lagrangian undetermined multiplier method:

$$\delta(K - \lambda P_\theta) = 0, \quad (11)$$

where λ is an adjustable constant. Equation (11) leads to

$$\frac{d}{dr} \left\{ (rE) \frac{d}{dr} \left(E + \frac{1}{en} \frac{d(nkT)}{dr} \right)^2 - \lambda r^2 E \right\} = 0. \quad (12)$$

Integrating Eq. (12) and using the condition $u_\theta(0) = 0$, one obtains the following relation

$$E + \frac{1}{en} \frac{d(nkT)}{dr} = \pm \sqrt{\frac{\lambda}{2}} r. \quad (13)$$

Substituting Eq. (13) into Eq. (6), one gets

$$\frac{e}{\epsilon_0} n = \sqrt{2\lambda} - \frac{d}{dr} \frac{r}{en} \frac{d(nkT)}{dr}. \quad (14)$$

A good approximate solution for the plasma density is given by $n = n(0)(1 - e^{(r-a)/\lambda_D})$,

where the Debye length $\lambda_D = \sqrt{\epsilon_0 kT(0)/e^2 n(0)}$. This represents the well-known equilibrium with a density profile nearly constant up to the plasma radius a and sharply falling down to null within a few Debye length [1, 2].

TOROIDALLY SYMMETRIC TOKAMAK PLASMA

In the case of a neutral plasma in a toroidally symmetric system such as a tokamak, the total toroidal angular momentum P_ϕ is conserved. For flux surfaces having a concentric circular cross-section, one may write

$$P_\phi = 4\pi^2 R_0^2 \int_0^a n m u_\phi r dr, \quad N = 4\pi^2 R_0 \int_0^a n r dr. \quad (15)$$

where R_0 is the major radius of the axis and N is the total number of particles. The total energy U , the sum of the total kinetic energy K and the total potential energy W , may

also be conserved: $U = K + W$. The total kinetic energy averaged over flux surfaces may be written as $K = 4\pi^2 R_0 \int_0^a n m u^2 r dr$, where $u^2 = u_\phi^2 + u_\theta^2$. The total potential energy averaged over flux surfaces may be written as

$$W = 4\pi^2 R_0 \int_0^a \left\{ \frac{3}{2} n k (T_i + T_e) + \frac{1}{2} \epsilon_0 E^2 + \frac{B^2}{2\mu_0} \right\} r dr. \quad (16)$$

Thus, the maximum total kinetic energy corresponds to the minimum total potential energy. Therefore, the problem of finding the minimum potential energy state is reduced to find the maximum kinetic energy state under the constraint of the conserved total density and total angular momentum. This solution is again obtained by the Lagrangian undetermined multiplier method:

$$\delta(K - \lambda_1 N - \lambda_2 I'_\phi) = 0, \quad (17)$$

where λ_1 and λ_2 are constant. Equation (17) can be written in the form

$$(u^2 - \lambda_1 - \lambda_2 u_\phi) \frac{\partial n}{\partial u_\phi} + (2u_\phi - \lambda_2)n = 0. \quad (18)$$

The solution for Eq. (18) is given by

$$n = \frac{c}{u^2 - \lambda_1 - \lambda_2 u_\phi}. \quad (19)$$

COMPARISON OF THEORETICAL RESULTS WITH DIII-D DATA

The theoretical result is tested against actual tokamak experimental data. DIII-D plasmas with an internal transport barrier (ITB) are chosen as a test base. Density profiles of the DIII-D plasmas are computed from the measured toroidal angular (rotation) velocities based on Eq. (19). Figure 1 shows the measured density profile of QDB (Quiescent Double Barrier) mode DIII-D plasma as the solid curve [3] together with two examples of calculated theoretical density profiles (dashed and dotted curves). Either of them are a very good fit except for some mismatches near the edge.

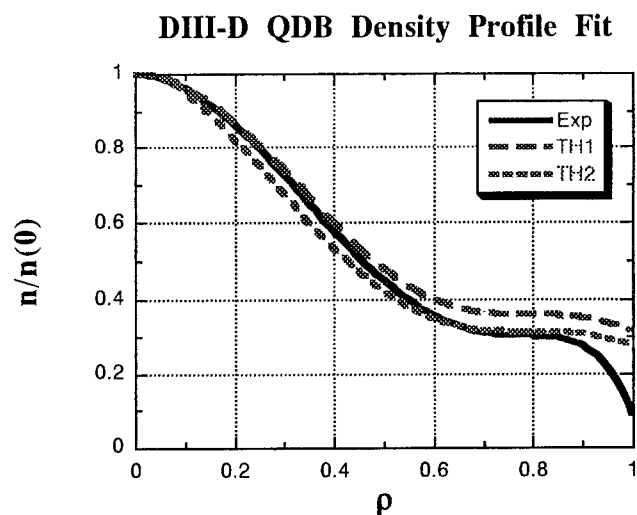


FIGURE 1. The normalized density profile of DIII-D QDB (shot number 106919 at 3 s) shown by the solid curve and two theoretical fits shown by dashed and dotted curves.

This indicates that the DIII-D plasma with an internal transport barrier is indeed a minimum (potential) energy state under the constraint of the conservation of total angular momentum.

CONCLUSION

An approach is established to examine equilibrium profiles for both non-neutral and neutral plasmas under the constraint of conservation of the total angular momentum. One important result obtained from this examination is that a tokamak plasma with an internal transport barrier is in a minimum energy state under the constraint of the conservation of total angular momentum.

REFERENCES

1. Malmberg, J.H., and O'Neil, T.M., Phys. Rev. Lett. **39**, 1333 (1977).
2. Dubin, D.H.E., and O'Neil, T.M., Rev. Mod. Phys. **71**(1), 20 (1999).
3. Burrell, K.H., *et al.*, Phys. Plasmas **8**, 2153 (2001).

SECTION 8
EXPERIMENTAL DEVICES AND
TECHNIQUES

Synchronization Effect in an Ion Trap Resonator

H. B. Pedersen, B. Amarant, O. Heber, M. L. Rappaport, and D. Zajfman

Department of Particle Physics, Weizmann Institute of Science, Rehovot, 76100,
Israel.

Abstract. Using a resonator-like electrostatic ion trap, we demonstrate that, under certain condition, it is possible to keep constant the width of a packet of ions oscillating between two mirrors. We show, using one dimensional calculations, that the effect is the result of Coulomb repulsion which, in a counter-intuitive way, keeps the ions together. Preliminary results of the exploitation of this phenomenon for high precision mass spectrometry are given.

I INTRODUCTION

The dynamics of a cloud of ions stored in an ion trap has been the subject of extensive studies for many years [1]. Using various techniques of cooling, such as laser cooling, it has been shown that transitions from “gas” to “liquid” and finally to “solid” phases can be observed. In this last case, ordering is achieved by the superposition of a strong external focusing force and the Coulomb repulsive force between the stored ions. In general, very low temperatures are needed in order to bring the system to an “organized” state, and usually the experiments can be performed with only a limited set of ions, such as Li^+ , Be^+ and Mg^+ .

During the last four years, our group (at the Weizmann Institute of Science) has developed and studied a new type of ion trap [2,3], in which fast (keV) ions are stored between two electrostatic mirrors, much like photons in an optical resonator. This ion trap has been used for the study of metastable negative ions [4,5], metastable states in atomic and molecular ions [6,7], and collision induced dissociation, using a beam extraction scheme [8]. In these studies, the trap was used as a “cooling” device, where the excited states produced by the ionization process in the ion source were allowed to decay. Recently [9], we have found that a certain type of ordering can be achieved in such a device with ions at high temperature (~ 1 eV). In this paper, we present a short overview of this new phenomenon which is related to the dynamics of small bunches of ions oscillating between the trap

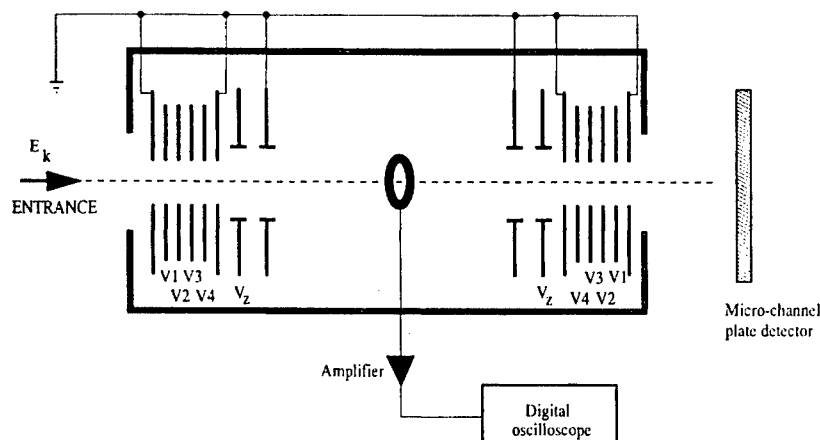


FIGURE 1. Schematic view of the ion beam trap. The bunch is injected through the left hand side of the trap. The central ring is the pick-up electrode. Note that the section between the innermost electrodes of the two mirrors is essentially field free.

mirrors. The effect, which manifests itself as a synchronization of the motion of the ions, leads to the interesting possibility of keeping the size of a packet of ions constant for a practically unlimited time, i.e., eliminating the debunching usually observed for ion bunches.

II EXPERIMENTAL SETUP

A schematic drawing of the electrostatic ion trap is shown in Fig. 1. The mechanical design of the ion trap and its operation have been described previously [2,3]. Briefly, the ion trap consists of two coaxial electrostatic mirrors each composed of a stack of eight cylindrical electrodes. The configuration of the trap is characterized by the potentials on five of these electrodes: V_1 , V_2 , V_3 , V_4 and V_z (see Fig. 1), the other three being grounded. Here we investigate a particular set of trap configurations, namely $\{V_1, V_2, V_3, V_4, V_z\} = \{V_1, 4.875 \text{ kV}, 3.25 \text{ kV}, 1.625 \text{ kV}, 4.06 \text{ kV}\}$, where $4.0 < V_1 < 6.0 \text{ kV}$. These configurations are characterized by a high value of V_z which causes the ions to be strongly focussed inside the mirror region [10].

Injection of an ion bunch into the trap is performed by keeping the electrodes on the entrance side of the trap at ground potential until the bunch enters the trap. The electrodes on the other side are kept at high potentials so that the ions are reflected back toward the entrance. Before the ion bunch returns to the entrance mirror, the potentials of its electrodes are rapidly ($\sim 100\text{-}200 \text{ ns}$) raised, thus confining the ions between the mirrors. At a residual pressure of $3 \times 10^{-10} \text{ Torr}$, a

typical lifetime of the ions in the trap is ~ 5 s. The trap stability criterion has been demonstrated [2,3,10] to be equivalent to the stability criterion of an optical resonator, namely

$$\frac{L}{4} < f < \infty, \quad (1)$$

where L is the effective distance between the mirrors and f is their focal lengths, assuming that the mirrors are symmetric.

Experiments were performed with ion beams of Ar^+ and Xe^+ , at an energy of 4.2 keV, produced in an electron impact ion source. The ions were mass analyzed using two consecutive magnets. The ion currents measured with the help of a Faraday cup located just after the trap were ~ 300 nA for Ar^+ , and ~ 100 nA for Xe^+ . Ion bunches of 0.2-100 μs were created with an electrostatic chopper.

The evolution of the ion bunch during storage was monitored with the help of a cylindrical pick-up electrode located at the center of the trap. The electrode length was 7 mm, and its diameter was 18 mm. The total capacitance of the pick-up electrode, connectors, and vacuum feedthrough was measured to be $C_p \sim 10$ pF. The pick-up electrode was connected to the gate of a Junction Field Effect Transistor (JFET) whose drain was fed to a charge sensitive amplifier. The amplified signal was recorded with a digital oscilloscope working at a sampling rate of 12.5 MHz, the area A under the signal being proportional to the number of ions N_i in a bunch.

The overall lifetime of the beam is obtained by measuring the rate of neutral particles leaking from the trap, using a microchannel plate (MCP) detector located after the trap. These neutral particles are formed in electron capture collisions between the stored ions and the atoms of the residual gas in the trap.

III RESULTS

A Diffusion

Figure 2(a) shows a typical signal as measured for Ar^+ , 200 μs after injection. The pulses are negative due to the polarity of the amplifier, and each pulse represents the passage of about 10^6 ions through the electrode. At this energy, and for this configuration, the oscillation time of the ions was measured to be ~ 3 μs (depending on V_1). The bunch duration, W (see Fig. 2(a)) was initially set to $W_0=170$ ns, which corresponds to a bunch width of 2.4 cm, which is longer than the length of the pick-up electrode. The development of this ion bunch at later time can be seen in Figs. 2(b-d), showing that debunching occurs on a time scale of ~ 500 μs . In the case shown here, the potential of the last electrode of the trap (see Fig. 1) was set to $V_1=5.5$ kV. The evolution of the ion bunch was quantified by fitting a Gaussian profile to each peak measured by the pick-up detector, plus a linear background.

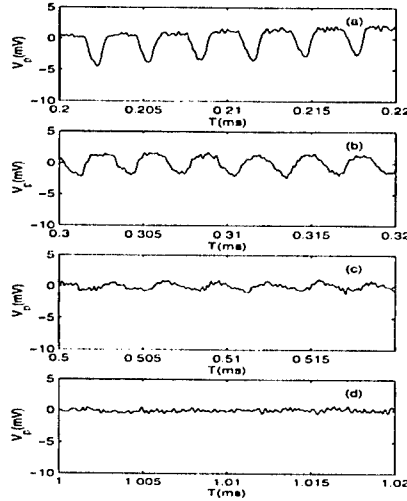


FIGURE 2. The signal observed with the pick-up electrode for an initially 170 ns wide bunch of Ar^+ at 4.2 keV for four different time intervals after injection: (a) 0.20-0.22 ms, (b) 0.30-0.32 ms, (c) 0.50-0.52 ms, (d) 1.0-1.02 ms.

The results of this fit are shown in Fig. 3 where the bunch width W_n is plotted as a function of the number of oscillations n (points). The initially confined bunch of ions is seen to broaden with a characteristic dependence on the number of oscillations. The lifetime of the ions stored in the trap was measured at the same time using the MCP detector and was found to be of the order of few seconds, i.e., much longer than the debunching time. Thus, under these conditions, the trap can be considered to be uniformly filled axially with ions after a storage time of ~ 1 ms. The diffusive behavior illustrated in Fig. 3 was typical for the evolution of bunches for a variety of potential configurations of the trap. In particular, with the configurations under investigation here, this behavior was seen for $V_1 \geq 4.9$ kV. It can be shown [10] that the bunch width evolves as

$$W_n = \sqrt{W_0^2 + n^2 \Delta T^2}, \quad (2)$$

where ΔT is the width of the distribution of oscillation times. This width is due to the initial velocity spread, the different trajectories existing in the trap, and the Coulomb repulsion. The line in Fig. 3 is Eq. 2 with $W_0=167$ ns and $\Delta T=5.9$ ns.

B Synchronization

Up to now, the behavior of the bunch was shown to follow the time dependence expected from simple arguments. In this part, we will show that a different behavior can be obtained for specific configurations of the trap. Figure 4 shows the evolution

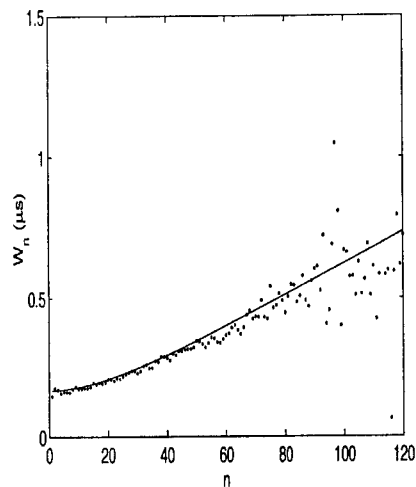


FIGURE 3. Measured bunch width as a function of oscillation number. The line is Eq. 2.

of an ion bunch injected into the trap with an initial width $W_0=130$ ns. In this specific case, the potential of the first electrode was set to $V_1=4.7$ kV. In contrast to the diffusive behavior seen in Fig. 2, the width of this ion bunch is conserved over the 90 ms shown in the figure.

More details on the evolution of the bunch can be seen in Figs. 5(a,b) where the bunch width and bunch area are shown as a function of the number of oscillations. After a rapid initial increase, the bunch width (Fig. 5(a)) stabilizes around 120 ns with some fluctuations for the first 5000 oscillations. For the whole time displayed here (and as long as could be measured), the bunch width is found to be constant, behavior very different from that shown in Fig. 3. The bunch area (Fig. 5(b)) shows both increases and decreases during the first 5000 oscillations, indicating that large amounts of ions are both collected and lost from the bunch during this time. Beyond 5000 oscillations, however, the number of ions in the bunch decreases exponentially with time, with a typical lifetime of 270 ms. Clearly, a very strong correlation between the ions is created in this situation, causing the bunch not to spread. This special behavior was observed when the potential of the first electrode was in the range $4.2 < V_1 < 4.9$ kV.

Additional information can be gained when even larger bunches are injected into the trap: In these cases, it was found that immediately after injection, the large bunch would fragment into several smaller bunches. Figure 6 shows the bunch width of the largest stored bunch. The width is seen to first rapidly decrease until it reaches a value of ~ 160 ns. Strong fluctuations are then observed, where the width increases and decreases during about 10^4 oscillations. At this point,

the bunch width stabilizes to a value of 160 ns and stays almost constant. This asymptotic bunch width was found to be a function of the electrode potential configuration (i.e., the value of V_1), and experiments performed with beams of Xe^+ at the same energy showed that the asymptotic bunch width, when measured in units of length, was identical to the values measured for Ar^+ . We have observed motion synchronization for times up to 330 ms (which corresponds to the maximum memory available for our digital oscilloscope) and since no changes in the width were observed on that time scale, one can safely assume that this width is constant for much longer time.

IV DISCUSSION

The origin of the special bunch evolution illustrated in Figs. 5 and 6 lies in the correlation of the ions due to their mutual interaction, which lead to synchronization of their motion [9]. In these cases, the ions in the bunch phase lock their motion due their *repulsive* Coulomb interaction, that effectively causes the bunch width to remain constant. That ions trapped in an electrostatic potential can synchronize their motion due to the *repulsive* Coulomb force between them may at first seem counter-intuitive. To illustrate that such synchronization can indeed occur we

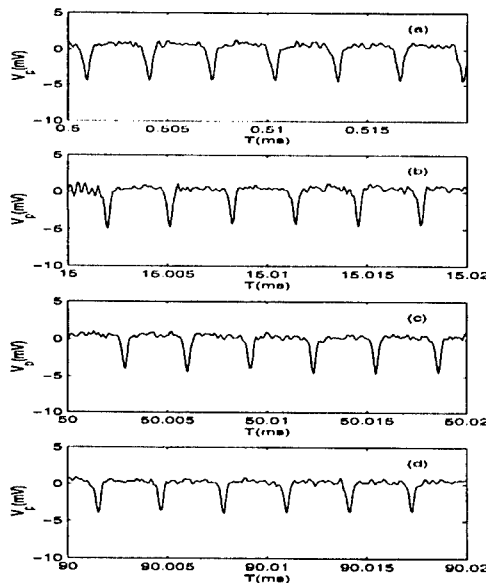


FIGURE 4. The signal observed with the pick-up electrode for an initially 170 ns wide bunch of Ar^+ at 4.2 keV stored with $V_1=4.7$ kV for four different time intervals after injection: (a) 0.5-0.52 ms, (b) 15-15.02 ms, (c) 50-50.02 ms, (d) 90.0-90.02 ms

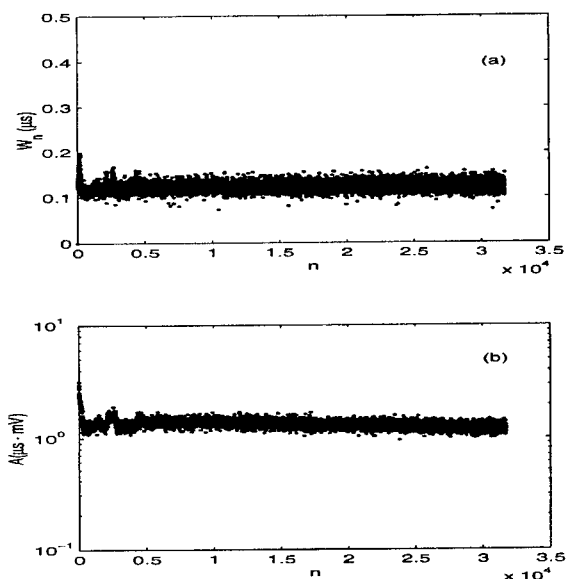


FIGURE 5. Evolution of a bunch of Ar^+ at 4.2 keV initially 170 ns wide, stored with $V_1=4.7$ kV. (a) The bunch width W_n and (b) the bunch area A .

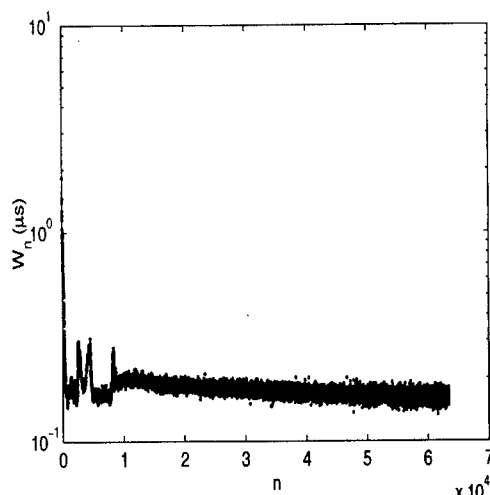


FIGURE 6. Bunch width as a function of the oscillation number for an initially wide bunch.

have numerically simulated the propagation of interacting ions in a flat-bottomed potential well bounded by walls of various slopes.

Clearly, such a model potential is a simplification of the situation existing in the experimental setup described above. However, it will be shown that even under these assumptions, the Coulomb repulsive force can lead to synchronization of the motion of the ions.

For a single ion moving in this potential, the period of oscillation (T) depends only on its energy (E): $T = T(E)$. Hence, for ions with a narrow spread in energy ΔE , the spread in oscillation time ΔT can be expressed as

$$\Delta T = \Delta E \cdot \frac{dT}{dE}. \quad (3)$$

In the simulation, thirty ions moving in the potential described above were followed. In order to allow ions to overtake each other in this one dimensional model, the ion-ion interaction is augmented with a minimum impact parameter ϵ and is given by:

$$F_{ij} = \frac{e^2}{4\pi\epsilon_0} \cdot \frac{1}{\Delta z_{ij}^2 + \epsilon^2} \quad (4)$$

The initial positions of the ions were chosen randomly according to a normal distribution of mean $\langle z \rangle = 0$ and width $\Delta z = 0.6$ mm, while the initial kinetic energies of the ions were selected from a distribution with mean $\langle E \rangle = 4200$ eV and $\Delta E = 0.6$ eV. Figure 7 shows the bunch width W_n as a function of the number of oscillations n with (dashed line) and without (solid line) interaction between the particles. Without the interaction, the bunch width increases as expected, with

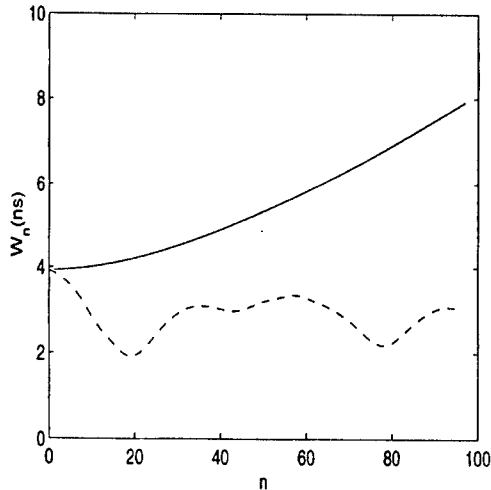


FIGURE 7. Calculated bunch width as a function of the oscillation number: Dashed line: with ion-ion interaction. Solid line: without ion-ion interaction.

a characteristic dependence which is close to the one shown in Fig. 3 and given in Eq. 2. However, when the interaction (Eq. 4) is turned on, the bunch width remains bound, which shows that the ion-ion interaction tends to synchronize the ion motion. It can be shown that the interaction between the ions occurs mainly at the turning points, where the ion density is the highest.

It is important to point out that such behavior is observed over a range of potential slopes, and is not due to a unique configuration known as time focusing, which is often used in Reflectron type electrostatic mirrors [11].

V MASS SPECTROMETRY

Since the trap is purely electrostatic, the oscillation time of an ion depends on its mass-to-charge ratio as

$$T = \frac{1}{f} \propto \sqrt{\frac{M}{q}} \quad (5)$$

where f is the oscillation frequency and M and q are the mass and charge, respectively. Hence, by measuring the oscillation time or frequency the mass-to-charge ratio can be determined. Since, as shown above, it is possible to keep the ions confined in a bunch for a very long time, it might be valuable to try to use such a system for high-precision mass spectrometry, much like the so called Fourier-transform mass spectrometry (FTMS). In the standard version of FTMS [12], the ions are trapped under the influence of magnetic and electric fields, and undergo cyclotron motion. In this case, high resolution is achieved because the ion motion is detected for many cycles, while the packet of ions does not lose its coherence. This is much like the situation we have reached in the present case, when the motion of ions is synchronized. However, if different masses are injected at the same time into the trap, would the "synchronization" effect be too strong, "capturing" all the ions (with different masses) in a single bunch?

To answer this question, we have performed a preliminary experiment in which two different isotopes of xenon ($^{131}\text{Xe}^+$ and $^{132}\text{Xe}^+$) with the same kinetic energy were injected at the same time into the ion trap. Figure 8 shows the fast Fourier transform (FFT) of the measured spectrum, after 200 ms of storage. The resolution is greatly improved over the non-synchronized cases (not shown) and the two isotopes are well separated, with a frequency difference which is in good agreement with the expected value. The resolution obtained in this case is $\Delta m/m = 2\Delta f/f = 6 \cdot 10^{-5}$, and this resolution improves with longer measurement times. More work needs to be done on this subject, but we have already observed additional effects such as frequency shifts for specific values of V_1 , indicating that the interaction between the bunches can be important as well.

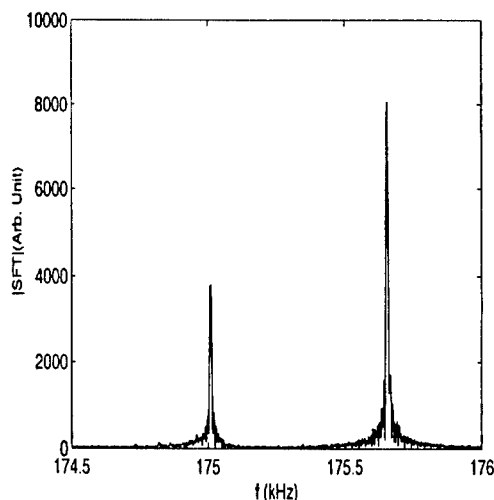


FIGURE 8. Fast Fourier transform of the pick-up signal for two isotopes of Xe^+ in the synchronized mode ($^{131}\text{Xe}^+$ is the right peak and $^{132}\text{Xe}^+$ is the left peak).

VI CONCLUSIONS

Using an electrostatic ion trap which allows for the trapping of fast ion beams, we have demonstrated that it is possible to keep the length of a bunch of ions constant, for a time which is much longer than expected. The effect shows up for specific values of the potential profile in the mirror regions. The asymptotic bunch width was found to be a characteristic of the ion trap geometry and the potential configuration. We have shown, using a simple one dimensional model, that such an effect is due to the Coulomb interaction between the ions. Preliminary results related to the use of such a system for high resolution mass spectrometry have also been obtained.

ACKNOWLEDGEMENT

This work was supported by the German Ministry of Education, Science, Research and Technology (BMBF) within the framework of the German-Israeli Project Cooperation in Future-Oriented Topics (DIP), by the Alhadeff Foundation and by the Minerva Foundation.

REFERENCES

1. For a review of ion traps see, e.g., Phys. Scr. **T59** (1995).

2. D. Zajfman, O. Heber, L. Vejby-Christensen, I. Ben-Itzhak, M. Rappaport, R. Fishman, and M. Dahan, *Phys. Rev. A* **55**, 1577 (1997).
3. M. Dahan, R. Fishman, O. Heber, M. Rappaport, N. Alstein, W. J. van der Zande, and D. Zajfman, *Rev. Sci. Instrum.* **69**, 76 (1998).
4. L. Knoll, K.G. Bhushan, N. Alstein, D.Zajfman, O.Heber and M.Rappaport, *Phys. Rev. A* **60**, 1710, (1999).
5. A. Wolf, K.G. Bhushan, I. Ben Itzhak, N. Alstein, D.Zajfman, O.Heber and M.Rappaport, *Phys. Rev. A* **59**, 267 (1999).
6. R. Wester, K.G. Bhushan, N. Alstein, D.Zajfman, O.Heber and M.Rappaport, *J. Chem. Phys.* **110**, 11830 (1999).
7. K. G. Bhushan, H. B. Pedersen, N. Alstein, O. Heber, M. L. Rappaport and D. Zajfman, *Phys. Rev. A.* **62**, 012504 (2000).
8. D. Strasser, K. G. Bhushan, H. B. Pedersen, R. Wester, O. Heber, A. Lafosse, M. L. Rappaport, N. Alstein and D. Zajfman, *Phys. Rev. A* **61**, 060705 (2000).
9. H. B. Pedersen, D. Strasser, S. Ring, O. Heber, M. L. Rappaport, Y. Rudich, I. Sagi, and D. Zajfman, *Phys. Rev. Lett.* **87**, 055001 (2001).
10. H. B. Pedersen, D. Strasser, O. Heber, M. L. Rappaport, and D. Zajfman, *Phys. Rev. A.*, submitted for publication
11. B. A. Mamyrin, V. L. Karataev, D. V. Shmikk, and V. A. Zagulin, *Sov. Phys. JETP*, **45**, 37 (1973).
12. A. G. Marshall and L. Schweikhard, *Int. J. Mass Spectrom. Ion Processes*, **118/119**, 37 (1992).

Paul Trap Simulator Experiment (PTSX) to Simulate Intense Beam Propagation Through a Periodic Focusing Quadrupole Field¹

Ronald C. Davidson, Philip C. Efthimion, Erik Gilson, Richard Majeski and Hong Qin

Plasma Physics Laboratory, Princeton University, Princeton, New Jersey 08543

Abstract. The Paul Trap Simulator Experiment (PTSX) is under construction at the Princeton Plasma Physics Laboratory to simulate intense beam propagation through a periodic quadrupole magnetic field. In the Paul trap configuration, a long nonneutral plasma column is confined axially by dc voltages on end cylinders at $z = +L$ and $z = -L$, and transverse confinement is provided by segmented cylindrical electrodes with applied oscillatory voltages $\pm V_0(t)$ over 90° segments. Because the transverse focusing force is similar in waveform to that produced by a discrete set of periodic quadrupole magnets in a frame moving with the beam, the Paul trap configuration offers the possibility of simulating intense beam propagation in a compact laboratory facility. The experimental layout is described, together with the planned experiments to study beam mismatch, envelope instabilities, halo particle production, and collective wave excitations.

PAUL TRAP CONFIGURATION

Periodic focusing accelerators and transport systems have a wide range of applications ranging from basic scientific research in high energy and nuclear physics, to applications such as spallation neutron sources, tritium production, heavy ion fusion, and nuclear waste transmutation, to mention a few examples [1-5]. Of particular interest, at the high beam currents and charge densities of practical interest, are the combined effects of the applied focusing field and the intense self fields produced by the beam space charge and current on determining detailed equilibrium, stability, and transport properties. The purpose of this paper is to describe the Paul Trap Simulator Experiment (PTSX) under construction at the Princeton Plasma Physics Laboratory that fully simulates the collective processes and nonlinear transverse dynamics of an intense charged particle beam propagating through a periodic quadrupole magnetic field configuration. The idea of using a single-species trap to model periodically-focused beam propagation has been discussed by Davidson, et al. [6], and by Okamoto and Tanaka [7], although the emphasis of their work is on solenoidal confinement [7], whereas the present paper focuses on periodic quadrupole confinement [1-6]. The equivalence of the Paul trap configuration to intense beam propagation through a periodic focusing quadrupole field is discussed in Ref. 6, and in Secs. 2 and 3 of this paper we describe the experimental configuration,

¹ Research supported by the Department of Energy and in part by the Office of Naval Research.

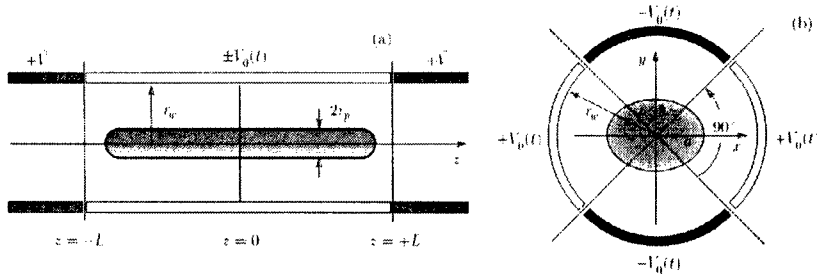


FIGURE 1. (a) Side view and (b) end view of Paul trap configuration.

and the planned experimental studies, respectively.

As illustrated in Fig. 1, to model an axially continuous charged particle beam (or a very long charge bunch), we consider a long one-component plasma column with length $2L$ and characteristic radius $r_p \ll L$, confined axially by applied dc voltage $\hat{V} = \text{const.}$ on end cylinders at $z = \pm L$. The particles making up the nonrelativistic nonneutral plasma in Fig. 1 have charge q and mass m . Transverse confinement of the particles in the $x-y$ plane is provided by segmented cylindrical electrodes (at radius r_w) which have applied oscillatory voltages $\pm V_0(t)$ with $V_0(t+T) = V_0(t)$ and $\int_0^T dt V_0(t) = 0$, where $T = \text{const.}$ is the period, and $f_0 = 1/T$ is the oscillation frequency. It is readily shown that the applied potential $\phi_a(x, y, t)$ near the axis ($r \ll r_w$) in Fig. 1 is given by [6]

$$q\phi_a(x, y, t) = \frac{1}{2} m \kappa_q(t) (x^2 - y^2), \quad (1)$$

where $\kappa_q(t)$ is defined by

$$\kappa_q(t) \equiv \frac{8qV_0(t)}{m\pi r_w^2}. \quad (2)$$

Note that $\kappa_q(t+T) = \kappa_q(t)$ and $\int_0^T dt \kappa_q(t) = 0$, and that $\kappa_q(t)$ has dimensions of $(\text{time})^{-2}$. Moreover, the leading-order correction to Eq. (1) is of order $(1/3)(r/r_w)^4$ [6].

The transverse Hamiltonian and the corresponding nonlinear Vlasov-Poisson equations, valid for the Paul trap configuration in Fig. 1, are identical in form to the corresponding equations describing the transverse dynamics of an intense nonneutral beam propagating through a periodic quadrupole magnetic field [6]. Because the transverse focusing force is similar in waveform to that produced by a discrete set of periodic quadrupole magnets in a frame moving with the beam, the Paul trap configuration offers the possibility of simulating intense beam propagation in a compact experimental facility. The Paul Trap Simulator Experiment (PTSX) is intended to simulate continuous beam propagation in a periodic focusing transport line.

PAUL TRAP SIMULATOR EXPERIMENT

The applied oscillatory voltage $V_0(t)$ typically results in a nonneutral plasma column that has a pulsating elliptical cross-section in the $x-y$ plane [6]. It is convenient to denote the on-axis ($r=0$) plasma density by \hat{n} and the corresponding plasma frequency by $\hat{\omega}_p \equiv (4\pi\hat{n}q^2/m)^{1/2}$. From Eq. (2), we denote the characteristic angular oscillation frequency $\hat{\omega}_q$ for the transverse motion of a single particle in the (maximum) focusing field by $\hat{\omega}_q \equiv |\hat{\kappa}_q|^{1/2} = [8q\hat{V}_0/\pi m r_w^2]^{1/2}$, where $\hat{V}_0 = |V_0(t)|_{max}$ is the maximum applied voltage. Transverse confinement [6] of the nonneutral plasma by the oscillatory voltage requires $\hat{\omega}_p/\sqrt{2} < \hat{\omega}_q$. On the other hand, to avoid the so-called envelope instability [3] associated with an overly strong focusing field, the oscillation frequency f_0 should be several times larger than $\hat{\omega}_q/2\pi$. Combining these inequalities gives $\hat{\omega}_p/\sqrt{2} < \hat{\omega}_q \ll 2\pi f_0$, or equivalently, for a singly-ionized pure ion plasma (ion mass number = A), such as barium or lithium,

$$1.49 \times 10^2 \left(\frac{\hat{n}}{A} \right)^{1/2} < 2.5 \times 10^5 \left(\frac{\hat{V}_0}{A r_w^2} \right)^{1/2} \ll f_0. \quad (3)$$

Here, \hat{n} , \hat{V}_0 , r_w , and f_0 are expressed in units of cm^{-3} , volts, cm, and s^{-1} , respectively. As illustrative parameters for a barium ion plasma, we take $\hat{V}_0 = 400V$ and $r_w = 10cm$. Equation (3) then gives the requirements that $\hat{n} < 1.1 \times 10^7 cm^{-3}$ and that f_0 exceed many tens of kHz.

An elevation view of the Paul Trap Simulator Experiment (PTSX) is illustrated in Fig. 2. The apparatus is approximately 3 m in overall length, and consists of a 10" O.D. electropolished stainless steel chamber with metal-sealed flanges to allow bakeout to 150° C. A centrally-located, six-way cross accommodates the laser-induced fluorescence (LIF) diagnostic. Both radial (through the six-way cross) and paraxial (through windows at the axial ends of the device) illumination of the ion population by the excitation laser are possible. The vacuum system consists of a 1,000 l/sec turbomolecular pump backed up by an oil-free roughing pump.

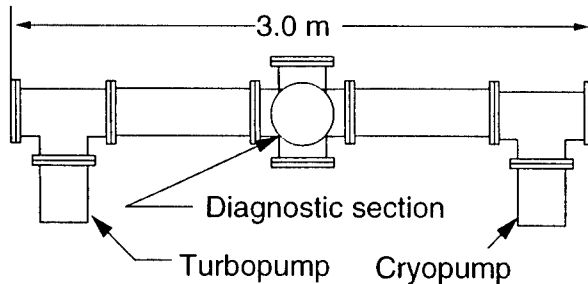


FIGURE 2. Elevation view of the Paul Trap Simulator Experiment.

The central confinement section of PTSX consists of four 200 cm long, azimuthally segmented stainless steel electrodes which produce the oscillatory quadrupole fields. The diameter of the confining electrode array is 20 cm. In the central section of the trap,

the gap between the electrodes is locally enlarged to allow passage of the laser beam for the laser-induced fluorescence diagnostic. A section of blackened high-transparency metallic mesh forms the electrodes in this section of the device, to allow imaging of the ion emission without disturbing the electric field configuration. An amplifier powers the electrodes in opposing pairs by means of a step-up transformer with two secondary windings. The amplifier is driven by a programmable waveform generator in order to permit adjustment of the waveform amplitude, pulse shape, and period in time.

Initial experiments in PTSX will utilize a barium-coated platinum or rhenium filament as an ion source, with rhenium being the favored material for good contact ionization efficiency. In this case, the spiral-wound filament is located at the midpoint of the segmented end-electrode section. In addition, a high-transparency grid is located in front of the filament, and a reflecting electrode is located behind the filament. This system is expected to be adequate for the simulation of low-intensity ion beams. If higher ion fluxes are required than can be supplied by the filament, then a barium-loaded rhenium plate will be substituted for the filament assembly.

EXPERIMENTAL RESEARCH PROGRAM

The PTSX experimental facility and associated diagnostic suite constitute a very flexible facility for simulating a wide range of nonlinear collective processes important in the propagation of intense charged particle beams over large distances. Most importantly, the flexible source geometry and ability to vary the voltage waveform $V_0(t)$, either dynamically or from experiment to experiment, permit detailed studies to be carried out over a wide range of density \hat{n} , average radius r_p , and choice of equivalent waveform for the quadrupole focusing field. Furthermore, the laser-induced fluorescence diagnostic capability will permit a detailed investigation of the evolution of the density profile, rms column radius, transverse emittance, and particle distribution function. An important dimensionless parameter s [6] that measures the beam intensity and the self-field intensity is defined by $s \equiv \hat{\omega}_p^2 / 2\hat{\omega}_q^2$. Here, $\hat{\omega}_p$ is the plasma frequency, and $\hat{\omega}_q$ is the effective transverse focusing frequency due to the applied quadrupole focusing field. In the moderate-intensity beams encountered in high energy and nuclear physics applications, the self-field parameter s typically satisfies $s \leq 0.2$, corresponding to emittance-dominated beams which are a few (or several) Debye lengths in diameter. On the other hand, for space-charge dominated beams of interest for heavy ion fusion, the self-field parameter s can approach unity, corresponding to very low transverse emittance, and near balance of the applied focusing force and the repulsive space-charge force. The PTSX facility has the capability to investigate collective nonlinear processes for values of the self-field parameter ranging from moderate self-field intensity to very high intensity.

The PTSX experimental program will focus on a variety of investigations of collective nonlinear processes of fundamental interest in the physics of intense charged particle beams. These studies will include the following areas of research.

(a) The effects of different waveforms for $V_0(t)$ will be determined, at fixed amplitude and frequency, on equivalent beam propagation through periodic quadrupole field geom-

etry. Waveforms ranging from sinusoidal to a (near) step-function lattice with variable fill factor will be used. Particularly important will be a determination of the conditions for quiescent (stable) matched-beam propagation over large (equivalent) distances.

(b) At fixed values of frequency $f_0 = 1/T$, if the focusing field amplitude is overly strong, with $\hat{\omega}_q T \geq \pi/2$, it is expected that the plasma column will be subject to the so-called envelope instability [3] in which the beam envelope and rms radius develop large-amplitude oscillations. This can lead to loss of equilibrium, beam mismatch, and ejection of so-called 'halo' particles from the core. Using a sinusoidal waveform for $V_0(t)$, experiments will be carried out intentionally exciting the envelope instability in order to determine its detailed nonlinear evolution and saturation, dependence on the intensity parameter s , and its effect on the production of halo particles.

(c) A critical problem in accelerator physics is the (unwanted) production of halo particles by beam mismatch induced, for example, by faulty magnet sets which have the incorrect field intensity, or are misaligned, etc. To test this effect in the PTSX facility, we will intentionally 'spoil' the voltage waveform $V_0(t)$ for short times (a few or several periods) in order to induce a mismatch.

(d) In related experiments, at fixed frequency $f_0 = 1/T$ and specified waveform (sinusoidal, say), we will adiabatically vary the amplitude of the oscillatory voltage pulse to simulate beam propagation through (long) transition regions where the focusing field amplitude is slowly varying (e.g., increasing slowly to compress the transverse dimension of the beam). Important will be a quantitative determination of how slow (i.e., over how many lattice periods) the transition has to be to assure quiescent (stable) beam propagation.

(e) One-component nonneutral plasmas and intense charged particle beams support a wide variety of collective oscillations that depend on the details of the distribution function, the focusing field strength, the self-field intensity parameter s , and geometric effects such as the proximity of the conducting wall. These oscillations typically involve various combinations of the frequencies $\hat{\omega}_q$, $\hat{\omega}_p$, and $(\hat{\omega}_q^2 - \hat{\omega}_p^2/2)^{1/2}$, modified by geometric effects (r_p/r_w). We will carry out a series of experiments on the PTSX that investigate detailed properties of collective excitations (either excited externally, or occurring naturally as the result of beam mismatch, imperfections in the voltage waveform, or as a consequence of an instability). In addition to testing and validating theoretical models of collective oscillations in intense charged particle beams, emphasis will be placed on identifying collective modes whose signature serves as a robust diagnostic for key properties of the beam, such as line density, transverse emittance, etc.

(f) Depending on the ion source used in the PTSX experiment, there is considerable flexibility to alter the input density profiles, ranging from normal (radially decreasing or uniform profiles), to slightly hollow, to hollow, to multiple beamlets (using 'masking' techniques). It is planned to investigate a variety of physics phenomena related to the input profiles from the ion source.

CONCLUSIONS

This paper has described the Paul Trap Simulator Experiment (PTSX), a flexible research facility to simulate intense beam propagation in periodic quadrupole field configurations. Experiments on PTSX will examine a wide range of collective processes important for intense beam propagation in alternating-gradient quadrupole field configurations.

REFERENCES

1. R. C. Davidson and H. Qin, *Physics of Intense Charged Particle Beams in High Energy Accelerators* (World Scientific, Singapore, 2001), and references therein.
2. A. W. Chao, *Physics of Collective Beam Instabilities in High Energy Accelerators* (John Wiley and Sons, Inc., New York, 1993).
3. M. Reiser, *Theory and Design of Charged Particle Beams* (John Wiley & Sons, Inc., New York, 1994).
4. See, for example, Proceedings of the 1999 Particle Accelerator Conference (IEEE Catalog Number 99CH36366), pp. 1–3778.
5. See, for example, Proceedings of the International Heavy Ion Fusion Symposium, Nuclear Instruments and Methods in Physics Research **A464**, pp. 1–674 (2001).
6. R. C. Davidson, H. Qin, and G. Shvets, *Phys. Plasmas* **7**, 1020 (2000).
7. H. Okamoto and H. Tanaka, *Nuclear Instruments and Methods in Physics Research* **A437**, 178 (1999).
8. W. Paul and H. Steinwedel, *Z. Naturforschung* **A8**, 448 (1953).
9. D. J. Wineland, W. M. Itano, and R. S. Vandyck, Jr., *Adv. Atom. Mol. Phys.* **19**, 135 (1983).

A Magnetic Trap For Simultaneous Confinement of Neutral Atoms and a Non-Neutral Plasma

Daniel H. E. Dubin

Physics Department, University of California at San Diego, La Jolla CA 92093-0319 USA

Abstract.

Three methods have been proposed for the simultaneous confinement of neutral atoms and a non-neutral plasma in close proximity [D.H.E. Dubin, *Phys. Plasmas* **8**, 4331 (2001)]. This note discusses one of these methods, in which particles are trapped in an axially-symmetric static magnetic field with a magnetic minimum in a ring around the axis of symmetry. Axial symmetry is required for confinement of the rotating non-neutral plasma, and the magnetic minimum traps the neutral atoms. This trap design may be useful for the production and confinement of cold antihydrogen.

INTRODUCTION

Over the past decade, minimum \mathbf{B} magnetic traps have developed into a standard technology for trapping neutral clouds of atoms [1]. These traps use magnetic fields with a local minimum in $|\mathbf{B}(\mathbf{r})|$ at a point where $|\mathbf{B}|$ remains nonzero.

In one standard trap design, the “Ioffe-Pritchard” trap [2], a pair of Helmholtz coils create a saddle point in $|\mathbf{B}|$ at the trap center. The saddle is transformed to a minimum by four Ioffe bars. The magnetic minimum creates a potential well for some atoms since atomic spins μ align either with or against the magnetic field. The magnetic dipole energy for spins aligned against the field is

$$E_M = -\mu \cdot \mathbf{B} = |\mu||\mathbf{B}|, \quad (1)$$

which is minimized at the trap center. The magnetic field does not vanish in the well; otherwise a spin could flip at the magnetic null (“Majorana flips” [3]) and the magnetic minimum would then expel the atoms rather than confine them.

The Ioffe-Pritchard trap is an excellent configuration for many purposes. However, the design is not cylindrically symmetric, and this is a problem for certain applications. One such application is the production and confinement of cold antihydrogen. Two experiments are currently underway to achieve this goal [4]. The experiments use Penning traps to trap two cold single species non-neutral plasmas consisting of anti-protons and positrons respectively, from which it is hoped that antihydrogen can be created by careful combination of the two species. The antihydrogen must then be confined in a neutral atom trap. A recent analysis [5] has shown that stable single-particle orbits exist for individual positrons and antiprotons trapped in the non-axisymmetric magnetic field produced by a Ioffe-Pritchard trap. However, if the trapped single-species plasmas are cold and of high density so as to maximize recombination rates when they are combined,

the large-scale static field asymmetries produced by the Ioffe bars will degrade plasma confinement, causing plasma heating and charged particle loss at levels that are probably unacceptable [6].

In recent work [7] three possible methods were put forward for trapping neutral atoms in close proximity to a cold, dense non-neutral plasma. One method relies on a novel cylindrically-symmetric magnetic configuration that can be used as a Penning trap to confine a non-neutral plasma, but also has a minimum in $|\mathbf{B}|$ so that it can simultaneously trap neutral atoms. The magnetic minimum is on a ring around the axis of symmetry of the trap. Potential well depths of order 1°K or more should be achievable with this trap design. It is important for the well to be as deep as possible, since the antihydrogen will be created at the plasma temperature of a few $^\circ\text{K}$, and will also have kinetic energy associated with the plasma rotation. In the next section we consider this trap design in more detail.

A second design, discussed in Ref. 1, uses a standard "time-averaged orbiting potential" (TOP) trap [8] to confine the neutral atoms. Like the Ioffe-Pritchard trap, this design imposes large-scale azimuthal magnetic asymmetries, but the asymmetries are made to rotate around the trap axis. This rotating magnetic field has two effects: first, the torque exerted on the plasma by the rotating field may act to spin up the plasma, possibly even keeping it confined indefinitely in much the same manner as electrostatic "rotating wall" asymmetries used in other experiments [9]. Second, the rotating field, in concert with a static cusp field, creates a time-averaged magnetic minimum at the trap center, with $|\mathbf{B}| \neq 0$ there. However, the effective depth of this potential minimum is probably limited to of order 0.1°K or less.

Reference 1 also considers a third design that, like the first design, uses static cylindrically-symmetric magnetic fields to confine both the plasma and the neutral atoms. Here the magnetic minimum is a null at the trap center. In order to keep neutral atoms away from this magnetic null, the neutral atom cloud is made to spin, creating a centrifugal potential that repels the cloud of neutrals from the trap center. The rate of rotation may be controlled with a small rotating magnetic field. The main static magnetic field contains sufficiently high multipole moments ($n = 4$ or higher) in order to overcome the centrifugal potential at large radius and trap the atoms in a ring. In this design, well depths of order 1°K or more could be obtained, depending on the rotation frequency of the neutral atoms and the strength of the magnetic field.

Although antihydrogen formation requires the recombination of positron and antiproton plasmas, the work presented here considers only the trapping of a single species plasma in conjunction with a neutral atom trap. There are several reasons for this: first, separate single species plasmas must be confined and cooled before recombination can be attempted. It would be easiest to do this nearby to the region where recombination and neutral atom trapping will occur, so it is important to consider the equilibrium of single species plasmas in the fields created by a neutral atom trap. Second, the recombination process itself is not yet understood: the partially-neutralized plasma may exhibit a host of instabilities, and issues regarding both the axial and radial confinement of such plasmas have not yet been resolved, although progress is being made [10, 11, 12]. By focussing on the trapping of a single species plasma in conjunction with neutral atoms, our work avoids these thorny issues.

However, our work could have some bearing on the recombination process: one

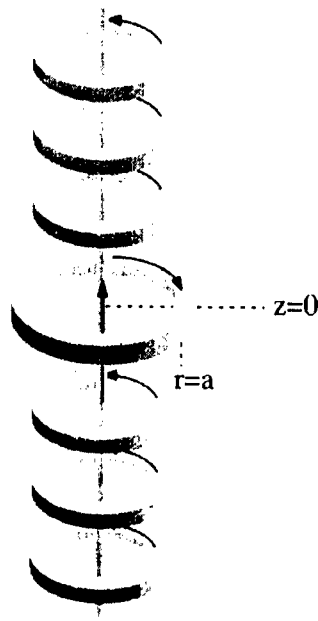


FIGURE 1. Magnetic coil configuration of a cylindrically-symmetric minimum- B Penning trap.

possible recombination technique would be to allow only a relatively small number of antiprotons at a time to enter into the positron region, so that the positron plasma remains nearly completely unneutralized. It might be hoped that a small density of antiprotons would have an insignificant effect on the positron stability, and that a description of the system as a single species plasma might then be relevant. In this scenario, one of the traps discussed in this paper could serve as the recombination section.

A CYLINDRICALLY-SYMMETRIC MINIMUM- B PENNING TRAP

Cylindrically-symmetric minimum- B equilibria have received considerable attention in the neutral plasma community due to their superior MHD stability properties [13]. The design considered here is similar to the "stuffed cusp," but with an added solenoidal magnetic field, which is required for non-neutral plasma confinement.

A schematic of the magnetic elements in the trap is shown in Fig. 1. The trap consists of a solenoidal magnetic field $B_0 \hat{z}$, which for simplicity is assumed to be uniform; an azimuthal magnetic field $B_\theta a \hat{\theta}/r$ created by a wire aligned along the axis of the solenoid, and the field from a current loop concentric with the solenoid whose current runs in the opposite direction to that of the solenoid. The latter field $\mathbf{B}_l(r, z)$ is most easily written

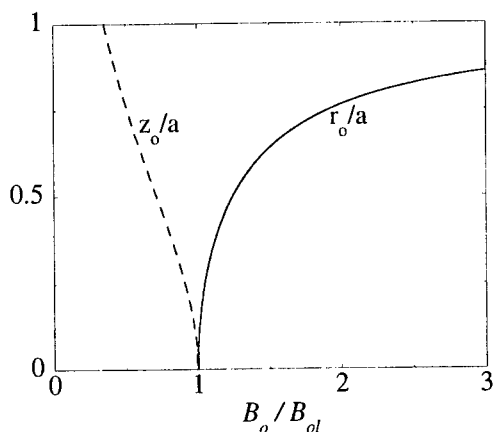


FIGURE 2. r and z location of the field null as the ratio of the solenoidal to loop field is varied. No B_θ field is applied.

in terms of the vector potential associated with the loop, assumed to have radius a :

$$\mathbf{B}_\ell(r, z) = -\frac{\partial A_{\theta_\ell}}{\partial z} \hat{r} + \frac{1}{r} \frac{\partial}{\partial r} (r A_{\theta_\ell}) \hat{z}, \quad (2)$$

where

$$A_{\theta_\ell}(r, z) = -\frac{2B_{0_\ell}a^2}{\pi\sqrt{a^2+r^2+z^2+2ar}} \left[\frac{(2-m)K(m) - 2E(m)}{m} \right], \quad (3)$$

$$m = \frac{4ar}{a^2+r^2+z^2+2ar}, \quad (4)$$

$K(m)$ and $E(m)$ are the complete elliptic functions [14], and $B_{0_\ell} = B_\ell(0, 0)$.

When $B_{0_\ell} < B_0$, the loop magnetic field cancels out the solenoidal field at a ring of radius r_0 in the plane of the loop (the $x-y$ plane). When $B_{0_\ell} > B_0$, the field is cancelled at points $\pm z_0$ along the z axis. The dependence of r_0 and z_0 on B_0/B_{0_ℓ} is shown in Fig. 2.

Without an applied azimuthal field B_θ , the ring at $r = r_0$ and $z = z_0$ is both a magnetic minimum and a magnetic null, which makes it unusable as an atom trap. With an azimuthal field, $|\mathbf{B}|$ no longer vanishes. Since the azimuthal field is monotonically decreasing with r , the location of the minimum is shifted outwards to a location $r_m > r_0$. For B_θ sufficiently large, the minimum disappears as it is pushed toward the loop.

Contours of constant $|\mathbf{B}|$ are shown in grayscale in Fig. 3 for the choices $B_0/B_{0_\ell} = 2.6$, giving $r_0 = 0.81a$; and $B_\theta/B_0 = 0.125$, giving $r_m = 0.83a$. For these parameters, contours of constant $|\mathbf{B}|$ with $|\mathbf{B}|/B_0 \lesssim 0.9$ do not intersect the walls of the apparatus.

For antihydrogen in the ground state, $|\mu| \simeq \hbar e/2m_e c$. According to Eq. (1), a solenoidal field of $B_0 = 2$ T therefore corresponds to a potential well of depth $(0.9 - 0.125/0.83)\mu B_0 = 1^\circ\text{K}$. Atoms with temperature less than this should collect around the minimum at $r = r_m$. A field $B_0 \gtrsim 8$ T increases the well depth above the

temperature of liquid helium, obviating the need to cool the trap walls with a dilution refrigerator.

We now turn to the non-neutral plasma confinement characteristics of this trap design. It is well-known that single-species plasmas can be confined in a thermal equilibrium state by static cylindrically symmetric fields [15]. The unneutralized charge cloud rotates about the trap axis with rotation frequency ω . For low plasma temperature such that the Debye length is small compared to the plasma size, the plasma density in thermal equilibrium is determined by the equation [15]

$$n(r, z) = \frac{m\omega}{2\pi e^2} (\Omega_{c_z}(r, z) - \omega), \quad (5)$$

where $\Omega_{c_z} = eB_z(r, z)/mc$ is the cyclotron frequency based only on the axial component of the total magnetic field. Here e is the charge and m the mass of the plasma particles. Note that the azimuthal field B_θ does not play a role in non-neutral plasma confinement.

Equation (5) follows from the fact that rotation through a magnetic field creates an effective potential well $\phi_B(r, z)$ for the particles, where

$$\phi_B(r, z) = \frac{e\omega r}{c} A_\theta(r, z) - \frac{m\omega^2 r^2}{2}. \quad (6)$$

The second term is the deconfining centrifugal potential and $A_\theta(r, z)$ is the θ -component of the magnetic vector potential, given by

$$A_\theta(r, z) = A_{\theta_l}(r, z) + \frac{1}{2} B_0 r^2, \quad (7)$$

where A_{θ_l} is the loop vector potential, given by Eq. (3). The potential ϕ_B can be thought of as due to a fictitious neutralizing background charge of density $n_B(r, z)$; that is, $\nabla^2 \phi_B(r, z) = 4\pi e^2 n_B(r, z)$. The equilibrium plasma density matches the density n_B out to a surface of revolution where the supply of plasma charge is exhausted. The shape of this surface is determined by the condition that it is an equipotential in the frame rotating with the plasma. Therefore to find the plasma shape, we solve the equation

$$\phi(r, z)|_S = \text{constant} \quad (8)$$

where S is the surface of the plasma, and ϕ is the total potential, including the self-consistent potential $\phi_P(r, z)$ from the plasma itself, and the potential $\phi_V(r, z)$ from voltages on surrounding electrodes:

$$\phi(r, z) = \phi_P(r, z) + \phi_V(r, z) + \phi_B(r, z). \quad (9)$$

Since our design has a central wire, required for the azimuthal field B_θ , a voltage V must be applied to the wire in order to repel plasma charges. This creates a hollow plasma. In Fig. 3 we assume the wire has radius $b = 0.05a$, and that there is a surrounding grounded cylindrical electrode at $r = a$. The plasma is assumed to be a long column. For large $|z|$ away from the loop, the magnetic field is nearly uniform, and the plasma forms a hollow column with uniform density $n_0 = (m\omega/2\pi e^2)(\Omega_0 - \omega)$, where $\Omega_0 = (eB_0/mc)$ is the

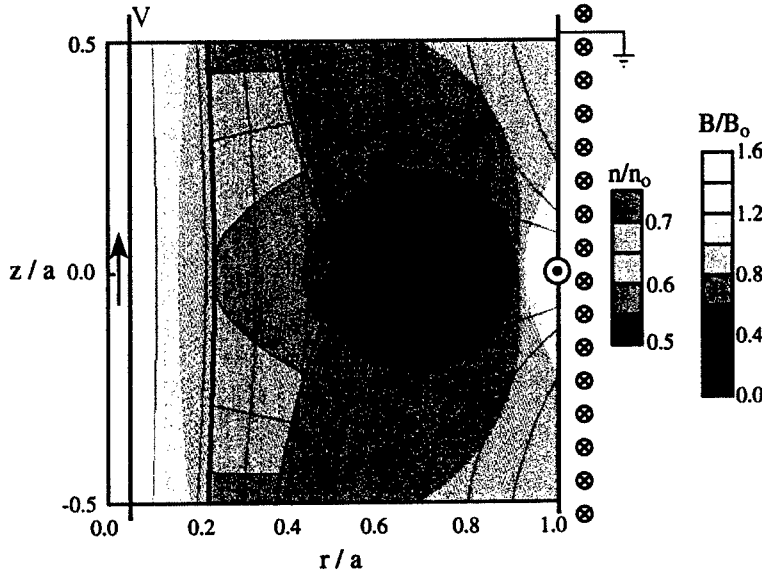


FIGURE 3. An example of plasma confinement in the cylindrically-symmetric minimum- B Penning trap. Plasma density is shown by colored contours, magnetic field intensity is shown by gray-scale contours. Green lines are magnetic flux surfaces. Arrows denote the location of current-carrying wires. Thick blue lines are electrodes. In this example, $B_0/B_{0i} = 2.6$, $B_\theta/B_0 = 0.125$, and $V = 0.38\pi en_0 a^2$.

cyclotron frequency associated with the solenoidal field only. The inner and outer radii of the hollow column, r_1 and r_2 , are related to the voltage V on the inner wire by the condition that $\phi(r_1, z) = \phi(r_2, z) = \text{constant}$:

$$V = \pi en_0 \left[r_2^2 - r_1^2 + 2r_1^2 \ln\left(\frac{r_1}{b}\right) - 2r_2^2 \ln\left(\frac{r_2}{a}\right) \right]. \quad (10)$$

In Fig. 3, we have chosen $r_1 = 0.2a$, $r_2 = 0.3a$, so that $V = 0.38\pi en_0 a^2$. We have also assumed that $\omega/\Omega_0 \ll 1$, so that we can neglect the centrifugal potential in ϕ_B [see Eq. (6)]. In this case we need not specify ω in determining the plasma equilibrium.

One can see from the figure that the plasma expands radially and decreases in density near $z = 0$, since the confining B_z field is weakest here. One can also see that the minimum B ring is well outside the plasma. This is hardly surprising, since B_z vanishes at $r_0 < r_m$, and the plasma must be confined in a region away from this point according to Eq. (5). In principle, it is possible to construct finite-length plasma equilibria that contain the minimum ring at r_m since B_z does not vanish at r_m , but rather at r_0 . However, the confinement potential $\phi(r, z)$ exhibits only a very weak minimum in this case.

Since the plasma rotates with frequency ω , neutral atoms created by recombination at radius r within this plasma will be created with a certain amount of angular momentum, $\ell_z = Mv_\theta r$, where M is the atomic mass and v_θ is the azimuthal velocity, which has an average value of ωr . This will create a tendency for the neutral atom cloud to spin. This rotation creates a deconfining centrifugal potential for the neutral atoms, which can be

expressed as an additional term in Eq. (1):

$$E_M = |\mu||\mathbf{B}| + \frac{1}{2} \frac{\ell_z^2}{Mr^2}. \quad (11)$$

So far we have assumed that this centrifugal term is negligible. However, this depends on the size of ℓ_z . In typical experiments, the rotation frequency $\omega/2\pi$ is on the order of several kHz. Taking the plasma radius to be $r_p \simeq 1$ cm, we may estimate angular momentum due to rotation as $\ell_z \sim M\omega r_p^2$. Then for an antihydrogen atom the centrifugal term is

$$0.5M\omega^2 r_p^4 / r^2 = 0.24^\circ\text{K} \left(\frac{\omega/2\pi}{1 \text{ kHz}} \right)^2 \left(\frac{r_p}{r} \right)^2 \left(\frac{r_p}{1 \text{ cm}} \right)^2.$$

One can see that a rotation frequency of 1 kHz and a plasma radius of 1 cm leads to a small centrifugal correction to E_M ; however, $\omega = 10$ kHz would cause a large change in the magnetic well, possibly leading to deconfinement, depending on the ratio of r_p/r at the location of minimum B . In order to trap large densities required for rapid recombination, a large magnetic field will therefore be required so that ω remains small.

Another potential difficulty with this design involves the central wire. Astute readers may already have noted that producing a tesla size field with a central wire (or wires) requires exceedingly high currents. Fortunately, the azimuthal field produced by the central wires need not be this large. Recall that the only purpose of the azimuthal field is to prevent Majorana flips by keeping $|\mathbf{B}|$ finite at the magnetic minimum. For cryogenic atoms, this can be accomplished with modest azimuthal fields, on the order of a few gauss. The argument is as follows. Majorana flips are prevented when the minimum spin precession frequency, $2\mu B_{\min}/\hbar$ (where $B_{\min} = B(r_m, z_m)$ is the minimum magnetic field strength), is much greater than the maximum rate of variation of the magnetic field as seen by an atom moving through the minimum, $(\bar{v} \nabla B/B)_{\max} \sim \bar{v} B_0 / a B_{\min}$, where \bar{v} is the thermal speed of the atoms. Comparing these two rates for antihydrogen yields

$$B_{\min} \gg 1.3 \text{ Gauss } (B_0/1 \text{ Tesla})^{1/2} (T/1^\circ\text{K})^{1/2} (a/1 \text{ cm})^{-1/2}. \quad (12)$$

Thus, a field of 10–100 Gauss at the magnetic minimum should be sufficient to prevent any Majorana flips from occurring, provided that the atoms are cold.

Finally, we note that it is possible to create a ring-minimum-B configuration that does not need a central wire: the “Furth-Andreoletti” trap [13]. This considerably simplifies the trap design, but unfortunately the depth of the magnetic minimum in such traps is exceedingly weak [16]. In Ref. 7 we discuss an axisymmetric trap design that also avoids the central wire, but has a well depth of order 1°K or more.

ACKNOWLEDGMENTS

The author gratefully acknowledges useful conversations with Dr. John Bollinger and Professors Travis Mitchell, Joel Fajans, and C. Fred Driscoll. This work was completed with the support of National Science Foundation grant PHY-9876999 and Office of Naval Research grant N00014-96-1-0239.

REFERENCES

1. See, for example, M.H. Anderson, J.R. Ensher, M.R. Mathews, *et al.*, *Science* **269**, 198 (1995); A. Griffin, D.W. Snoke and S. Tringari, *Bose-Einstein Condensation* (Cambridge U. Press, 1995); W. Ketterle, D.S. Durfee, and D.M. Stamper-Kern, "Making, Probing and Understanding Bose-Einstein Condensates," in *Bose-Einstein Condensation in Atomic Gasses*, edited by M. Ingusio, S. Stringari and C.E. Weiman (Ohmsha, Tokyo, 1999).
2. D.E. Pritchard, *Phys. Rev. Lett.* **51**, 1336 (1983); Y.V. Gott, M.S. Ioffe, and V.G. Tel'Kovskii, *Nuclear Fusion Suppl.* **3**, 1045 (1962).
3. E. Majorana, *Nuovo Cimento* **9**, 43 (1932).
4. G. Gabrielse, D.S. Hall, T. Roach, P. Yesley, A. Khabbaz, J. Estrada, C. Heimann, and H. Kalinowsky, *Phys. Lett. B* **455**, 311 (1999); M. Holtzscheiter and M. Charlton, *Rep. Prog. Phys.* **62**, 1 (1999).
5. T.M. Squires, P. Yesley and G. Gabrielse, *Phys. Rev. Lett.* **86**, 5266 (2001).
6. E. Gilson and J. Fajans, in *Non-Neutral Plasma Physics III*, American Institute of Physics Conference Proceedings **498**, edited by J. Bollinger, R. Spencer and R.C. Davidson (American Institute of Physics, New York, 1999), p. 250.
7. D.H.E. Dubin, *Phys. Plasmas* **8**, 4331 (2001).
8. W. Petrich, M.H. Anderson, J.R. Ensher and E.A. Cornell, *Phys. Rev. Lett.* **74**, 3352 (1995).
9. X.P. Huang, F. Anderegg, E.M. Hollmann, C.F. Driscoll, and T.M. O'Neil, *Phys. Rev. Lett.* **78**, 875 (1997); F. Anderegg, E.M. Hollmann, and C.F. Driscoll, *Phys. Rev. Lett.* **81**, 4875 (1998); X.P. Huang, J.J. Bollinger, T.B. Mitchell, W.M. Itano, and D.H.E. Dubin, *Phys. Plasmas* **5**, 1656 (1998).
10. D.D. Dolliver and C.A. Ordonez, in *Non-Neutral Plasma Physics III*, American Institute of Physics Conference Proceedings **498**, edited by J. Bollinger, R. Spencer and R. Davidson (American Institute of Physics, New York, 1999), p. 65.
11. C.A. Ordonez, *Phys. Plasmas* **4**, 2313 (1997).
12. D.S. Hall and G. Gabrielse, *Phys. Rev. Lett.* **77**, 1962 (1996).
13. V.V. Arsenin, *Fusion Technology* **35**, 3 (1999); R.F. Post, *Nuclear Fusion* **27**, 1579 (1987); H.P. Furth, *Phys. Rev. Lett.* **11**, 308 (1963).
14. M. Abramowitz and I. Stegun, *Handbook of Mathematical Functions* (U.S. Dept of Commerce, Washington, 1970), p. 590.
15. D.H.E. Dubin and T.M. O'Neil, *Rev. Mod. Phys.* **71**, 87 (1999).
16. Well depth depends on the precise field configuration. For the simple case of a multipole field of the form $B(r, z = 0) = B_0(r - 2Cr^3 - 3Dr^5)$ in the midplane, a well exists only for $C > 0$, $85/147 = 0.578... < D/C^2 < 3/5$ and the depth is of order $10^{-2}B_0$ or less. See R.F. Post, Ref. 9, for a more detailed discussion of Furth-Andreoletti traps.

Possible Antihydrogen Trapping Field and Nonneutral Plasma Density Limits

C. A. Ordonez[†] and D. D. Dolliver

Department of Physics, University of North Texas, Denton, Texas 76203

Abstract. Axisymmetric magnetic field configurations are being considered for trapping antihydrogen atoms that are recombined in Penning traps. As part of an effort to understand the nonneutral plasma confinement properties of axisymmetric configurations, which necessarily have radial field components, plasma confinement within a magnetic field that is purely radial is studied. Various density limits of nonneutral plasmas confined in radial magnetic fields are evaluated and compared to those of plasmas confined in axial magnetic fields.

ANTIHYDROGEN TRAPPING FIELD

A uniform magnetic field can be combined with the field of one or more axisymmetric current loops in order to produce axisymmetric magnetic well configurations. A combination of this type is being considered [1] for trapping antihydrogen atoms recombined in Penning traps such as those designed for obtaining overlap of positron and antiproton plasmas. Overlap of positron and antiproton plasmas may be achieved using either nested Penning traps [2] or by trapping one species in a virtual anode or cathode produced by the other in a magnetic well (this was hypothesized in Ref. [3]). An example configuration calculation for the field of a single current loop combined with a uniform field is shown in Fig. 1(a). The current loop consists of a current of -230 kA (negative according to the right hand rule) at a radius of 10 cm. The uniform field has a magnitude of 2 T and is directed parallel to the z axis. The field configuration illustrated in Fig. 1(a) produces a toroidal magnetic well having a well depth of about 0.5 T. In addition, the outer contour, which is nearly spherical, indicates the presence of an additional non-toroidal 1 T well depth. The electrode configuration in Fig. 1(b) would be for trapping a positron plasma that would form a virtual anode for trapping antiprotons. A disadvantage with the magnetic field configuration is that the field strength vanishes at the center of the toroidal magnetic well. Positron spin flips are possible in regions where the magnetic field strength vanishes [4]. Such Majorana transitions can result in loss of trapped antihydrogen atoms over a time scale determined by the collision rate. Too small a time scale would make it necessary for the magnetic well to have a non-zero minimum. It is possible to eliminate the zero field

[†]) Electronic mail: cao@unt.edu

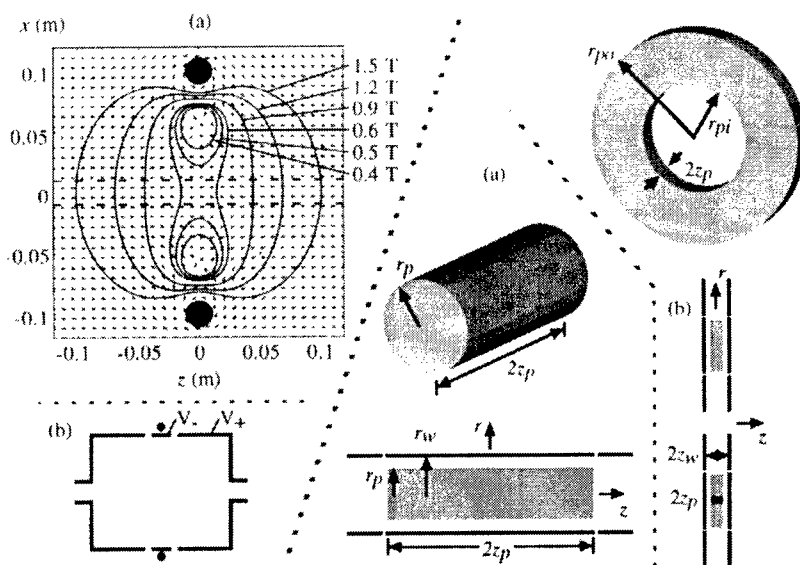


FIGURE 1. (Left) Axisymmetric magnetic field (a) and electrode (b) configurations. The magnetic field configuration is illustrated with a vector plot of the field superimposed on a contour plot of the field strength. The contours are for field strength values of 0.4, 0.5, 0.6, 0.9, 1.2, and 1.5 T. **FIGURE 2.** (Right) Illustration of two axisymmetric nonneutral plasma and electrode configurations. (a) A cylindrical plasma in a uniform axial magnetic field. (b) A washer-shaped annular plasma in radial magnetic field.

location by incorporating an axial current that produces a small azimuthal field outside of it. The axial current could be carried by a wire along the z axis or by a wire mesh, the location of which is illustrated by the dashed lines in Fig. 1(a). The mesh would have the shape of an axisymmetric tube that follows the local magnetic field lines and would have holes through which antihydrogen atoms could pass. To consider the possible use of a current carrying mesh, suppose overlapping positron and antiproton plasmas are confined radially inside the mesh by the axial magnetic field. If the overlap of positron and antiproton plasmas inside the mesh results in recombination, recombined antihydrogen atoms that pass through the mesh holes must lose energy to become trapped within the toroidal magnetic well. This may be possible if the antihydrogen atoms interact with antiprotons or positrons trapped in the magnetic field outside the mesh. Altogether, various possibilities exist for using axisymmetric configurations that produce a magnetic well. Such configurations necessarily include a magnetic field having a radial component.

NONNEUTRAL PLASMA DENSITY LIMITS

Various mechanisms that limit the density of nonneutral plasmas confined in radial and axial magnetic fields (see Fig. 2) are considered using the guiding center approximation

in this section (see also Ref. [5]). It is shown with example calculations that the density limits for a nonneutral plasma trapped in a radial magnetic field can be larger than the Brillouin limit. The Brillouin density limit is readily derived by considering a cylindrical single-species plasma centered along the z axis of a cylindrical coordinate system and aligned with a magnetic field. Such a configuration is illustrated in Fig. 2(a). Azimuthal symmetry is assumed, and only radial and axial coordinates (r, z) are referred to. Both the plasma density n and the magnetic field strength B are taken to be static and uniform. The plasma has a radius r_p , is confined within electrodes having an inner wall radius r_w , and is comprised of identical particles, each of charge state Z . The length $2z_p$ of the plasma is assumed to be much larger than the wall radius. Gauss' law provides a suitable approximation for the radial electric field strength at any axial position z that is far from the axial edges of the plasma, $z_p - |z| \gg r_w$. Hereafter, only axial positions z that are far from the axial edges of the cylindrical plasma are considered. The magnitude of the radial component of the electric field within the plasma is $E_r = Zenr/(2\epsilon_0)$, where e is the unit charge and ϵ_0 is the permittivity of free space. The forces on a particle in the plasma consist of a radially outward electric force $F_E = Z^2 e^2 nr/(2\epsilon_0)$, a radially outward centrifugal force $F_C = mv_\theta^2/r$, and a radially inward magnetic force $F_B = Zev_\theta B$. Here, m and v_θ are the particle mass and azimuthal drift speed. For radial confinement to occur, force balance requires $F_E = F_B - F_C$ or $n = \epsilon_0 B^2 (2\chi - \chi^2)/(2m)$ where $\chi = 2mv_\theta/(ZerB)$. The density is maximized when $\chi = 1$, which provides the Brillouin limit,

$$n_B = \frac{\epsilon_0 B^2}{2m}. \quad (1)$$

The Brillouin limit is illustrated by considering a xenon ion plasma in a 0.2 T magnetic field. The Brillouin limit for such a plasma is $8.1 \times 10^{11} \text{ m}^{-3}$.

Confinement in a radial field region is considered, as illustrated in Fig. 2(b). The configuration consists of a static, uniform-density, washer-shaped, single-species nonneutral plasma that is trapped in a radial magnetic field. Azimuthal symmetry is assumed, and the magnetic field in the region of trapped plasma is considered to have only a radial component. The axial plasma width $2z_p$ and the axial separation between electrodes $2z_w$ are both assumed to be much smaller than the radial plasma width $r_{po} - r_{pi}$, where r_{po} and r_{pi} are the outer plasma radius and inner plasma radius, respectively. Gauss' law in planar geometry provides a suitable approximation for the axial electric field strength at any radial position r that is far from the radial edges of the plasma, $r_{po} - r \gg z_w$ and $r - r_{pi} \gg z_w$. Hereafter, only radial positions r that are far from the radial edges of the washer-shaped plasma are considered, and the axial component of the electric field within the plasma is $E_z = Zenz/\epsilon_0$. The associated axially outward electric force on a particle must be balanced by an axially inward magnetic force, $F_B = Zev_\theta B$. Requiring $F_E = F_B$, the particle's azimuthal drift speed must be a linear function of z , $v_\theta = Zenz/(\epsilon_0 B)$. Hence, sheared rotation is a necessary characteristic of the plasma, and a technique (possibly a rotating field technique [6] or a magnetic field that increases with time) may need to be used to control axial plasma expansion.

The Brillouin density limit, Eq. (1), is not applicable to a plasma trapped in a radial magnetic field because a centrifugal force is absent from the axial force balance require-

ment. Instead, the applied radial electric field must provide a force that balances the centrifugal and magnetic gradient forces on plasma particles as well as the force resulting from the self-consistently produced self-electric field of the plasma. The centrifugal and magnetic gradient forces are first considered by evaluating the radial electric field strengths required to balance each. The radial electric field strength required to balance the centrifugal force is $E_C = F_C/(Ze) = mv_\theta^2/(Zer)$. The largest azimuthal drift speed $v_{\theta, \max}$ occurs at z_p , and axial force balance at z_p requires $v_{\theta, \max} = Zenz_p/(\epsilon_0 B)$. The radial electric field strength at z_p required to balance the centrifugal force is

$$E_C = \frac{Zemn^2 z_p^2}{\epsilon_0^2 r B^2}. \quad (2)$$

For example, for singly charged xenon ions confined at a density of $1.5 \times 10^{13} \text{ m}^{-3}$ in a 0.2 T magnetic field with $r = 25 \text{ cm}$ and $z_p = 0.5 \text{ cm}$, the electric field strength at z_p required for balancing the centrifugal force is calculated to be 250 V/m.

The radial electric field strength required to balance the magnetic gradient force is $E_M = F_M/(Ze)$. The magnetic gradient force on a plasma particle is $\mathbf{F}_M = -\mu \nabla B$ where μ is the magnetic moment associated with a cyclotron orbit [7]. For a magnetic field that has only a radial component in a cylindrical geometry, the condition $\nabla \cdot \mathbf{B} = 0$ requires $B = C/r$ where C is a constant. Hence, with $\nabla \rightarrow \hat{r} \partial/\partial r$, and approximating the magnetic moment as $\mu = T_\perp/B$ where T_\perp is the temperature (in energy units) associated with particle motion perpendicular to the magnetic field, $F_M = CT_\perp/(r^2 B)$. With $C = rB$,

$$E_M = \frac{T_\perp}{Zer}. \quad (3)$$

For example, for a plasma of singly charged particles having a temperature of 1 eV and $r = 25 \text{ cm}$, the electric field strength required for balancing the magnetic gradient force is calculated to be 4 V/m.

The self-electric field of the plasma is now considered, and the centrifugal and magnetic moment forces are ignored. An electric potential well along the magnetic field must be produced such that the plasma is confined radially. Integrating the axial electric field obtained using Gauss' law for a uniform density plasma, the difference in electric potential between the plasma midplane ($z = 0$) and the electrode wall surface is $V = Zenz_p(2z_w - z_p)/(2\epsilon_0)$. The electric potential difference V is approximately that produced by the space charge of the plasma, which tends to shield out the externally applied potential well. Hence, V can be considered an approximate minimum requirement for the magnitude of the externally applied radial well depth for confining the plasma in the limit of zero plasma temperature. [For a finite temperature plasma, V must be increased by an amount much larger than $T_\parallel/(Ze)$, where T_\parallel is the temperature associated with particle motion parallel to the magnetic field.] An associated "confinement voltage" density limit in a radial magnetic field is

$$n_{V,r} = \frac{2\epsilon_0 V}{Zez_p(2z_w - z_p)}. \quad (4)$$

For example, the density limit for a 1 cm wide cold nonneutral plasma of singly charged particles that extends axially to the electrodes, which are separated axially by 1 cm and produce a confinement voltage of 1000 V, is calculated to be $4.4 \times 10^{15} \text{ m}^{-3}$.

The approximate minimum confinement voltage needed for achieving confinement of a uniform cylindrical nonneutral plasma (in the zero temperature limit) along an axial magnetic field is similarly derived. Integrating the radial electric field obtained using Gauss' law, the difference in electric potential between the center of the plasma and the electrode wall inner surface is $V = Z e n r_p^2 [1 + 2 \ln(r_w/r_p)] / (4 \epsilon_0)$. The electric potential difference V is approximately that produced by the space charge of the plasma, and V can again be considered an approximate minimum requirement for the magnitude of the externally applied well depth. For a given value of V , the confinement voltage density limit for a cold nonneutral plasma in an axial magnetic field is

$$n_{V,a} = \frac{4 \epsilon_0 V}{Z e r_p^2 [1 + 2 \ln(r_w/r_p)]}. \quad (5)$$

For example, the density limit for a 1.41 cm diameter cold nonneutral plasma of singly charged particles that extends to the inner surface of the electrodes, which produce a confinement voltage of 1000 V, is calculated to be 4.4×10^{15} . The reason the same value is obtained as calculated for $n_{V,r}$ is that Eqs. (4) and (5) give the same value when the plasma extends to the wall and its width is increased by a factor of the $\sqrt{2}$ in Eq. (5).

The electric field produced by a nonneutral plasma is also associated with the possibility of electric breakdown at the inner surfaces of the surrounding electrode walls. Denoting the electric field strength at which breakdown occurs as E_w , Gauss' law can be used to write an associated "wall breakdown" density limit for a washer-shaped plasma in a radial magnetic field:

$$n_{E,r} = \frac{\epsilon_0 E_w}{Z e z_p}. \quad (6)$$

According to Ref. [8], field ionization, field desorption, and field evaporation processes at a tungsten anode surface begin to occur at significant rates for electric field strengths roughly between 10 and 50 V/nm. Choosing $E_w = 1 \text{ V/nm}$ and a plasma width of 1 cm for an example calculation, the resulting density limit is $1.1 \times 10^{19} \text{ m}^{-3}$ for $Z = 1$.

For a uniform cylindrical plasma within an axial magnetic field, Gauss' law can be used to write an associated wall breakdown density limit as

$$n_{E,a} = \frac{2 \epsilon_0 r_w E_w}{Z e r_p^2}. \quad (7)$$

For an example calculation, $E_w = 1 \text{ V/nm}$ is chosen along with a 2 cm diameter nonneutral plasma that extends radially to electrodes that have a 2 cm inner diameter. For singly charged particles, the associated wall breakdown density limit is the same as calculated for $n_{E,r}$, $1.1 \times 10^{19} \text{ m}^{-3}$, when the plasma extends to the wall and has twice the width.

The Brillouin density limit corresponds to an upper limit for radial force balance to be possible for a uniform cylindrical nonneutral plasma, provided the conditions for reaching

$\chi = 1$ are both possible and desirable. If not, a lower density limit occurs. For a given plasma radius, the density may be limited because the azimuthal drift speed may be limited. The largest drift speed $v_{\theta, \max}$ occurs at the radial plasma edge, and the effect results in what may be called the “drift speed” density limit in an axial magnetic field:

$$n_{d,a} = \frac{\epsilon_0 B^2 (2\chi_{\max} - \chi_{\max}^2)}{2m}; \quad \chi_{\max} = \frac{2mv_{\theta, \max}}{Ze r_p B} < 1. \quad (8)$$

It should be emphasized that Eq. (8) only applies when $\chi_{\max} < 1$. Various applications of the drift speed density limit are possible. For example, it is desirable for the speed of newly formed antihydrogen atoms to be sufficiently small for their trapping. If the anti-atoms are formed by antiproton collisions with positronium, the antiproton drift speed (as well as thermal speed) must be sufficiently small. As a second example, it may be desirable for the drift speed to be nonrelativistic for an electron plasma. An approximate density limit is obtained by setting $v_{\theta, \max}$ equal to the speed of light, provided $\chi_{\max} < 1$.

A drift speed density limit can also be applied to a nonneutral plasma in a radial field. Requiring force balance at z_p , the density limit in a radial magnetic field is

$$n_{d,r} = \frac{\epsilon_0 v_{\theta, \max} B}{Ze z_p}. \quad (9)$$

For example, consider singly charged xenon ions, and assume that it is desirable for the ion drift speed to be smaller than the thermal speed $\sqrt{T/m}$ (even though larger drift speeds are possible). The associated density limit for $T = 1$ eV ions within an axial width of 1 cm in a 0.2 T radial magnetic field is calculated to be $1.9 \times 10^{12} \text{ m}^{-3}$.

ACKNOWLEDGMENTS

This material is based upon work supported by the National Science Foundation under Grant No. PHY-0099617.

REFERENCES

1. See also: D. H. E. Dubin, “Three Designs for a Magnetic Trap that will Simultaneously Confine Neutral Atoms and a Non-Neutral Plasma,” *Phys. Plasmas* (to be published).
2. Y. Chang and C. A. Ordonez, *Phys. Rev. E* **62**, 8564 (2000); and references therein.
3. A. Mohri, T. Yuyama, Y. Kiwamoto, Y. Yamazawa and T. Michishita, *Jpn. J. Appl. Phys.* **37**, L1553 (1998).
4. M. H. Holzscheiter and M. Charlton, *Rep. Prog. Phys.* **62**, 1 (1999).
5. C. A. Ordonez in *Non-Neutral Plasma Physics III*, edited by J. J. Bollinger, R. L. Spencer and R. C. Davidson, American Institute of Physics **CP498**, 445 (1999).
6. E. M. Hollmann, F. Anderegg, and C. F. Driscoll, *Phys. Plasmas* **7**, 2776 (2000); and references therein.
7. G. Schmidt, *Physics of High Temperature Plasmas*, Second Edition (Academic Press, New York, 1979).
8. H. D. Beckey, *Principles of Field Ionization and Field Desorption Mass Spectrometry*, (Pergamon Press, New York, 1977).

Ion Trapping in the Virtual Cathode of the Penning Fusion eXperiment-Ions

M. M. Schauer, D. C. Barnes, K. R. Umstadter [*]

Los Alamos National Laboratory, Los Alamos, NM 87545, USA

Abstract. The goal of the Penning Fusion eXperiment-Ions (PFX-I) is the production of thermonuclear conditions in a Penning trap by means of spatial and/or temporal compression of a high temperature plasma. The present approach involves the confinement of positive ions in a virtual cathode produced by a nonthermal electron plasma held within a modified Penning trap. We report here on the first evidence of ions trapped in three dimensions in this manner. Experimental evidence of the maintenance of the non-Maxwellian electron energy distribution needed to produce the virtual cathode is presented.

We utilize the excellent confinement times achieved with Penning traps [1] for confining thermonuclear plasmas. For a practical value of reactivity, it is necessary to enhance the rms density beyond limitations imposed by the nonneutrality of the trapped plasmas. The density of a uniform, nonneutral plasma confined in a Penning trap is limited to the Brillouin limit [2] set by the balance between the repulsive force of the space charge of the plasma and the restoring force provided by its rotation in the external magnetic field.

However, focusing the orbits of the constituent particles can produce a nonuniform plasma with an enhanced density over some small volume. Indeed, enhanced densities, inferred to significantly exceed the Brillouin limit, have been demonstrated in a pure electron plasma [3, 4]. Focusing was achieved in these experiments by injecting low angular momentum electrons into trapping fields tuned so that the period of the motion in the radial plane is twice that of the motion along the trap axis. Hence, any orbit originating at the trap center was necessarily constrained to pass through the center again. In essence, a Penning trap operated in this manner can be thought of as an inertial electrostatic confinement (IEC) [5, 6] device where the vacuum fields of the trap replace the grids of a standard IEC machine. Since the grids constitute the chief source of particle and energy loss in most IEC experiments, this approach greatly improves confinement.

A limitation of this approach is that the axial and radial frequencies of motion depend differently on the charge-to-mass ratios of the constituent particles. Therefore, unlike IEC, this method only works for plasmas with a single charge-to-mass ratio, such as pure deuterium plasmas, and is not applicable to those systems offering the highest fusion cross sections, i.e. mixed deuterium and tritium plasmas.

One system that offers the possibility of focusing independent of the charge-to-mass ratio of the confined species is a spherically symmetric virtual cathode produced within a trapped electron plasma. Here, the potential providing ion confinement is produced by the space charge of the trapped electron cloud and is spherically symmetric, thereby ensuring that the confining force experienced by the ions is purely radial regardless of their charge-to-mass ratio. This configuration has the added advantage that, if the con-

fining potential is harmonic, i.e. produced by a uniform density electron cloud, in addition to being spherically symmetric, then implementation of such temporal compression schemes as the proposed periodically oscillating plasma sphere (POPS) is also possible. Theoretical work on POPS indicates the possibility of compression ratios as high as 1500:1, albeit in single species plasmas [7, 8].

Radial confinement of positively charged ions by the negative space charge of an electron beam has been routinely accomplished in the electron beam ion trap or EBIT apparatus, although radial trapping is also provided by the applied magnetic field [9, 10, 11]. In those experiments a high current electron beam makes a single pass through the experiment and provides confinement in the direction perpendicular to the beam axis. Electrodes held at positive, static voltage provide axial confinement. This EBIT technology is not directly applicable in the present situation, because the desired thermonuclear ion energy and reasonably high electron density requires very high electric fields be applied near the desired ion well volume. These high fields are incompatible with the separately powered electrodes used to produce the EBIT axial well. Additionally, the high electron energy and density imply very high total electron current, which is very difficult to produce in a single-pass electron device, such as EBIT.

An alternative technology, appropriate for the desired thermonuclear application is adopted here. A virtual cathode is formed within a single conductor by an electron beam which achieves high total current by a large recirculation fraction. That is, a very low source of electron current is reflected many times between two cathodes which provide axial electron confinement. Radial electron confinement is provided by an applied magnetic field of up to 2 T. An axial well results from the shape of the anode cavity through which this beam passes. Furthermore, this well may be shaped by producing an axial gradient of the guiding magnetic field, although this design feature has not been implemented in the results presented here.

In this letter we give a first report on confinement of positive ions in a virtual cathode produced by a recirculating electron beam held in the Penning fusion experiment-ions (PFX-I). Here, axial confinement of ions is provided exclusively by the space charge of the recirculating electrons, while radial confinement is provided by the beam space charge and a 2T applied magnetic field. These results represent a first step towards the ion focusing goal as the virtual cathode is produced by a recirculating electron beam, however no focusing of the orbits of either the trapped electrons or ions was attempted.

Unlike standard harmonic Penning traps, the PFX-I electrodes are not hyperboloids of revolution, although they do possess cylindrical symmetry. The upper endcap (UEC) consists of a metal cap that contains an independently biased BaO electron emitter. The lower endcap (LEC) is made of $\approx 50\%$ reflective grid formed from Molybdenum wire and can be held at constant voltage or discharged to ground externally through a 500 k Ω resistor ($\tau \sim 130\mu\text{s}$) to enable destructive measurement of the trapped particle inventory. The ring electrode has a 2 mm diameter hole passing through it with a diamond-shaped void machined into the midplane ($ID \approx 9\text{mm}$). Located below the trap are independently biased upper (UDT) and lower drift tubes (LDT) and a floating microchannel plate detector (MCP) which can be used together to detect and energy analyze particles ejected from the bottom of the trap when the LEC is discharged. Figure 1 is a schematic of the device.

To trap electrons both endcaps are held at negative potential, and the ring electrode is

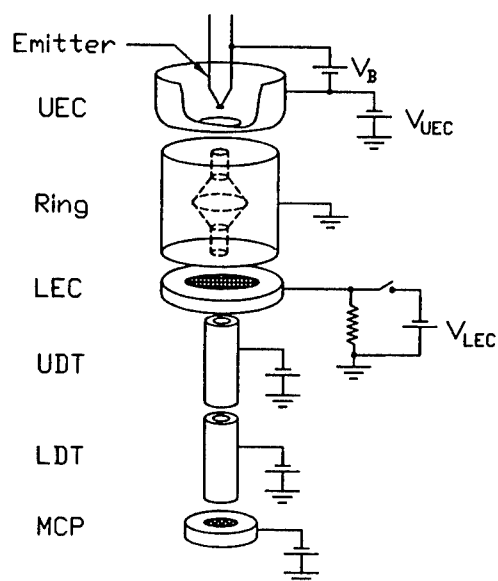


FIGURE 1. PFXI trap schematic. Figure is not to scale.

held at zero potential. The emitter is biased slightly positively ($V_B=0.5\text{V}$) with respect to the UEC, and electron emission is enabled by penetration from the trapping field. The LEC is biased 50V more negatively than the UEC ($V_{LEC}=-550\text{V}$ and $V_{UEC}=-500\text{V}$), so the electron beam is reflected back upon itself. With this emitter bias configuration, the depth of the axial well for electrons increases with increasing radial distance. Beam electrons drift outward radially into the deeper axial well due to field inhomogeneities and collisions with neutral background gas molecules, hence reflexing many times in the trap before being lost to the ring electrode.

The entire apparatus is housed inside a room temperature vacuum system with base pressure of approximately 2×10^{-6} Pa. Residual gas analyzer spectra show the background gas to be $\geq 97\%$ H_2 , and it is therefore assumed that any positive ions detected in the experiment are hydrogen ions. The vacuum system inserts into the warm bore of a superconducting magnet. The applied magnetic field was 2T for the measurements reported here.

The void in the midplane of the ring enables production of the virtual cathode when a nonthermal, i.e. beam-like, electron plasma is introduced into the trap. Neglecting end effects at the entrance and exit apertures, the potential within the grounded ring is uniform when no electron beam is present. Therefore, no confining fields exist. When a uniform density, electron beam is injected into the ring, the potential at the center of the void is now lower than within the entrance and exit channels. This can be seen by noting that the separation of an electron and its image charge is larger in the midplane of the ring than the corresponding separation in the entrance or exit channels. The resulting potential gradient provides axial confinement for positively charged particles.

It is important to note that production of a virtual cathode of significant strength

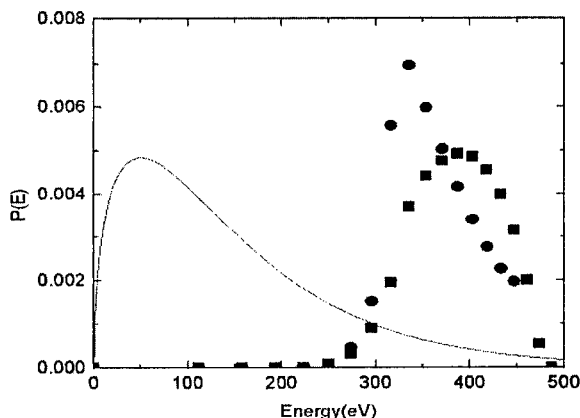


FIGURE 2. Energy spectra of the trapped electrons at 500 μ s (boxes) and 25 ms (circles). The solid line is a three-dimensional Maxwellian distribution with $kT=50$ eV for comparison purposes only.

requires an electron cloud with a nonthermal energy distribution [12, 13]. A plasma in thermal equilibrium will merely rearrange itself to cancel out any external electric fields yielding, at best, a field free region incapable of confining positive ions. Such a nonthermal distribution can be maintained in a Penning trap if the time for relaxation to thermal equilibrium is longer than the plasma confinement time.

We find this to be the case in PFX-I. By measuring the total electron inventory as a function of the delay between the termination of electron beam injection into the trap volume and the discharge of the LEC, we find the $1/e$ time for the plasma inventory to be approximately 30 ms. Although no direct measurement of the equilibration time has been made, we calculate an electron-electron collision time ranging from 45 ms to 80 ms for electron energies from 300 eV to 500 eV. This calculation assumes a constant density of $3.2 \times 10^9 \text{ cm}^{-3}$ based on the initial inventory, i.e. 500 μ s delay, of 5.8×10^8 electrons filling the entire trap volume from the LEC to the UEC.

Measurements of the electron energy distribution confirm the non-Maxwellian nature of the trapped electron plasma. Energy spectra were taken by measuring the electron inventory as a function of a negative bias voltage applied to the lower drift tube (LDT). All electrons with energy below this bias voltage were reflected and lost to the LEC grid rather than being counted by the MCP. A third order polynomial was then fitted to the data, and the derivative of this curve yielded the desired spectrum. Figure 2 shows typical spectra at 500 μ s and 25 ms. Although it is difficult to make definitive statements about the form of the electron energy distribution, it is clearly non-Maxwellian, and the electron plasma can be said to be far from thermal equilibrium, consistent with the measured confinement time and calculated collision time.

A self-consistent solution of the electrostatic problem for a strongly-magnetized electron beam with these observed parameters confirms that an electrostatic ion well of significant depth should be formed within the anode cavity. The electron density is $n_e = R(r)F(\phi)$, where r is the cylindrical radius and ϕ the electrostatic potential, and R and F functions determined by the radial and parallel energy distribution of electrons,

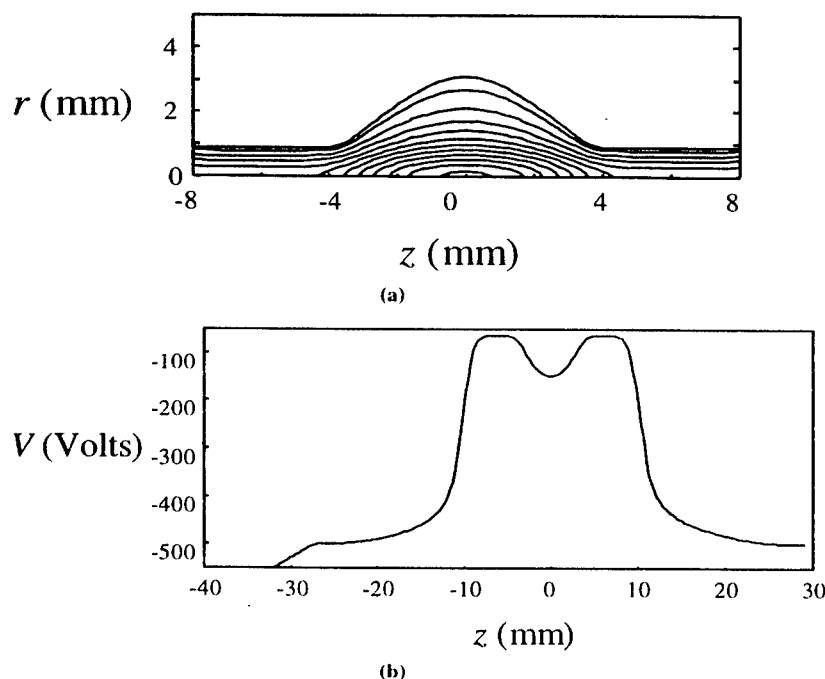


FIGURE 3. a) Theoretical contours of electrostatic potential in true perspective within the ring from the electrostatic solution. Dimensions are in mm. Central potential is -176V, while ion well depth is 100V. b) On-axis potential diagram of the trap from UEC to LEC.

respectively. To describe the PFX-I electron configuration, it is assumed that R is determined by a uniform source over $1/2$ the emitter tip radius and that the cross-B transport of electrons is independent of r . F is determined by assuming a uniform energy distribution of electrons between 300 eV and 500 eV.

A solution with the exact PFX-I electrostatic geometry has been found. Electron inventory is adjusted until the axial electric field near the UEC vanishes. This gives a value of 1.6×10^9 electrons, consistent with the observed inventory given the uncertainties in the absolute calibration of the electron collection efficiency and the approximations of the model used for the calculation. The electrostatic potential within the anode cavity is shown in Fig. 3(a). This electron-only solution gives an ion well of 20% of the applied voltage, or 100 V in the case under consideration.

Trapped ion space charge modifies this well depth prediction. Depending upon f_i , the ratio of the average ion density to the average electron density, this modification ranges from a small reduction of the well depth ($f_i \approx 0$) to nearly complete loss of the well ($f_i \approx 1$). Details of the ion source distribution and ion heating mechanisms determine f_i . Ultimately, one hopes to achieve $f_i \approx 0.1$ by tailoring the ion source and applying resonant ion heating.

Following confirmation of the non-Maxwellian nature of the electron distribution, the bias voltages applied to the LDT and MCP were set to negative 750V and negative

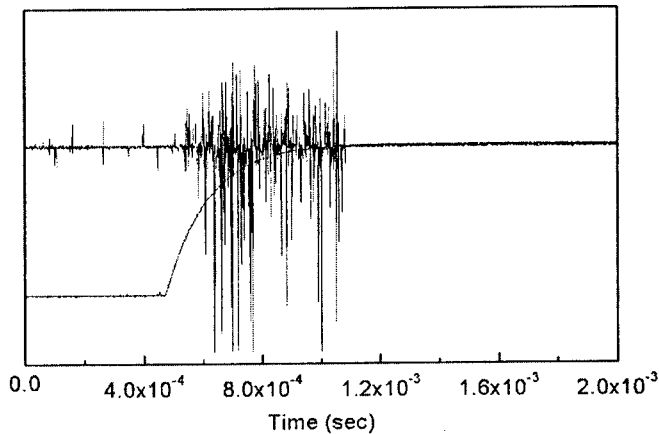


FIGURE 4. MCP output and LEC voltage (smooth curve) vs. time as the LEC is discharged with the system configured to reject negative particles from the MCP and the UDT at -10V.

800V, respectively, while the UDT was allowed to range from negative 100V to positive 100V. Since the electron beam energy was equal to the UEC voltage ($V_{UEC} = -500V$), in this configuration electrons released from the trap during discharge of the LEC were rejected from the MCP. Positive ions were either accelerated into the MCP for negative UDT voltages or rejected for positive UDT voltages. Figure 4 shows V_{LEC} and the MCP output as a function of time with the UDT at negative 10V. Typical rates of 5000 counts during the 750 μs counting window can be compared to a background counting rate of approximately 1 Hz.

The number of counts due to positive ions was found to decay as a function of time between cessation of electron injection into the trap and LEC discharge with the same time constant (~ 30 ms) as that found for the trapped electron lifetime decay. To ensure that the detected signal was not due to ion emission caused by electrons impinging on the grid during trap discharge, measurements of the positive signal appearing at the MCP were made while the full electron beam was allowed to strike the LEC grid. No enhancement above background was seen. Additionally, the trap was reconfigured to dump the electrons in the opposite direction, i.e. to the UEC rather than the LEC, while preserving the same accelerating potential for positive particles. The same positive particle signature was seen.

Finally, although the lifetime would be severely limited by loss to the 50% transmissive grid, it is possible that positive ions were trapped by the negative potential applied to the LEC relative to the positive ring and UDT. This possibility was discounted by discharging the UDT in the same manner that the LEC was discharged during regular operation. No enhancement of counts above background was seen. We therefore conclude that the positive particles arriving at the MCP during trap discharge are ions trapped in a virtual cathode provided by the electron space charge.

In order to determine the total number of trapped ions, one must know the detection efficiency at the MCP. An order of magnitude estimate can be obtained by measuring

the ion count rate on the MCP with the electron beam reflexing in the trap and with the MCP and both drift tubes biased to accelerate ions into the MCP. Comparing this measured rate with an expected rate calculated from the known neutral gas density, the energy and density of the beam electrons, and the ionization cross section for H_2 we find an efficiency on the order of 10^{-4} . This is presumably limited by losses to the LEC and LDT as well as by the detection efficiency of the MCP for ions. Losses to the LDT are exacerbated by its length (14 cm) and length-to-diameter ratio (30) compounded by its location in the fringe of the magnetic field at approximately half the central field value of 2T. Five-thousand ions collected at the MCP during the counting window then correspond to on the order of 10^7 total trapped ions with a density on the order of 10^9 cm^{-3} . Although this is only an order of magnitude estimate, one can compare this to the average electron density in the trap volume of $3 \times 10^9 \text{ cm}^{-3}$ indicating that f_i is on the order of 1.

Future work will concentrate on directly ascertaining the strength of the virtual cathode and increasing the ion well depth. Direct measurement of the ion well depth may be accomplished by measuring the Stark splitting of the optical lines of hydrogen [14] caused by the space charge of the electron plasma. Producing measurable splitting and increasing the overall strength of the cathode will, obviously, require greater electron density which in turn results from greater electron well depth. This necessitates raising the endcap voltages. We have conducted tests on some components of the present system to 75 kV in the presence of a 1 T magnetic field and have operated an electron beam in 1 T at 40 kV with a slightly modified geometry from the one used in the above reported measurements. We have also initiated investigations into different anode void shapes to study ion focusing.

We are grateful to M. H. Holzscheiter, L. Chacón, F. L. Ribe, L. S. Schrank for helpful conversations. This work was supported by the Office of Fusion Energy Sciences.

REFERENCES

- *. Present address: Archimedes Technology Group, 5405 Oberlin Drive, San Diego, CA 92117.
- 1. L. S. Brown and G. Gabrielse, *Rev. Mod. Phys.* **58**, 233 (1986).
- 2. L. Brillouin, *Phys. Rev.* **67**, 260 (1945).
- 3. T. B. Mitchell, M. M. Schauer, and D. Barnes, *Phys. Rev. Lett.* **78**, 58 (1997).
- 4. D. Barnes, T. Mitchell, and M. Schauer, *Phys. Plasmas* **4**, 1745 (1997).
- 5. W. Elmore, J. Tuck, and K. Watson, *Phys. Fluids* **2**, 239 (1959).
- 6. R. Hirsch, *J. Appl. Phys.* **38**, 4522 (1967).
- 7. R. Nebel and D. Barnes, *Fusion Tech.* **34**, 28 (1998).
- 8. D. Barnes and R. Nebel, *Phys. Plasmas* **5**, 2498 (1998).
- 9. M. Levine *et al.*, *Physica Scripta* **T22**, 157 (1988).
- 10. M. Levine *et al.*, *Nuc. Inst. Meth. Phys. Res.* **B43**, 431 (1989).
- 11. P. Beiersdorfer, L. Schweikhard, K. Widman, *EBIT Program Bi-Annual Report 1996-1997*, 104 (1998).
- 12. M. Schauer, K. Umstadter, and D. Barnes, *AIP Conf. Proc.* **498**, 425 (1999).
- 13. D. C. Barnes, M. M. Schauer, K. R. Umstadter, L. Chacon and G. Miley, *Physics of Plasmas* **7**, 1693 (2000).
- 14. H. Bethe and E. Salpeter, *Quantum Mechanics of One- and Two-electron Atoms* (Springer-Verlag, New York, 1957), p. 228.

Status of the Eltrap Project

M. Amoretti*, G. Bettega*, F. Cavaliere*, M. Cavenago[†], F. De Luca*,
R. Pozzoli* and M. Romé*

*I.N.F.M. (U.d.R. Milano Università) and Dipartimento di Fisica, Università degli Studi di Milano,
Via Celoria 16, 20133 Milano, Italy

[†]I.N.F.N. Laboratori Nazionali di Legnaro, via Romea 4, 35020 Legnaro, Italy

Abstract. The Malmberg-Penning trap Eltrap recently installed at the University of Milano, features a magnetic field with a high degree of uniformity in a relatively large plasma volume, and an enhanced light collection by the CCD camera. A modular electrode design allows several variations of the experimental configuration, suitable both for electron confinement and beam studies. The major electronic components of the apparatus are a waveform generator, which controls the inject-hold-dump cycle, and two personal computers, which control the data acquisition, the setting, and the timing of the experiments. Different electron sources have been proposed for the project, and studies for advanced source production are in progress.

INTRODUCTION

The Eltrap machine recently installed at the University of Milano is a Malmberg-Penning trap, with a magnetic field up to 0.2 T, and equipped with a CCD optical diagnostics. It is intended to be a small scale facility for electron plasma and beam dynamics experiments, and in particular for the study of collective effects, equilibrium states, and formation of coherent structures in these systems [1, 2, 3, 4, 5]. Its versatility should also allow different operational regimes [6].

The general scheme of Eltrap is shown in Fig. 1. Several characteristics are similar to those of the EV and CamV devices at UCSD [7, 8], its major limitation being the magnetic field strength. The machine can be also viewed as a scaled version (higher as linear dimensions, lower as for current and voltages) of several devices used in accelerator physics, as, e.g., Electron Beam Ion Sources or einzel lenses. In Eltrap, a magnetic field with a very high uniformity in a relatively large plasma volume has been designed and obtained (also by means of a careful placement of iron shims and the use of dipole correcting coils). The light collection is optimized by mounting the viewport on a reentrant flange, as shown in Fig. 1. The electronic control and acquisition systems are fully based on personal computers, and show some novelties concerning interfaces and pulse generation with respect to the solutions adopted in similar devices. Studies on different electron sources are in progress.

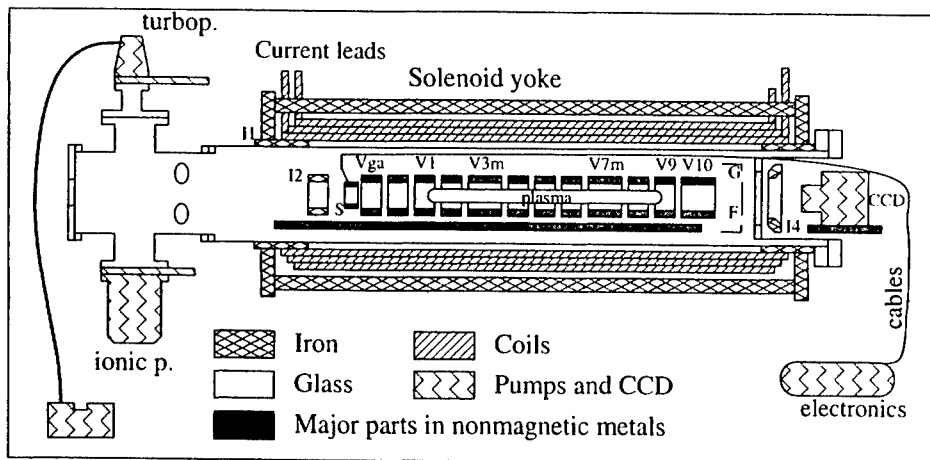


FIGURE 1. Scheme of the Eltrap machine.

DESIGN AND DESCRIPTION OF THE APPARATUS

The vacuum chamber of Eltrap is a 1.75 m long stainless steel tube with an outer diameter of 256 mm. The solenoid is 1.5 m long, with an inner diameter $D = 320$ mm. The gap between the vacuum tube and the magnet is available for the bakeout system, alignment purposes, and/or additional quadrupole windings.

The main requirement in the design of the magnet was to obtain a uniform field over a length $L \cong 1$ m, in the central region close to the axis. To this aim, a minimal coil length $L_1 = L + f_1 D$ is necessary (with $f_1 \cong 4/3$ for a stack of pancake coils). The practical need of wire connection requires that the end of the coil is tapered for a length $L_2 \cong 4$ cm. Since this can be detrimental to field uniformity, the coil has been made longer (length $L_3 = L + f_1 D + 2L_2$) and a 1 cm thick iron ring has been inserted inside each coil end (shims I1 and I3). Two additional truncated conical shims (I2 and I4) are used to further improve the field uniformity, since their presence concentrates the field lines towards the axis. Extensive numerical computations have been used to complete the magnet and shim design, giving a uniformity better than 10^{-3} within a distance of 0.5 m from the center of the magnet. In addition, the solenoid is enclosed in a soft iron cage made by two square end-plates and 12 axial bars: this simplifies the support system, and represents also a shield against the Earth's magnetic field. Both analytical estimates and numerical computations excluded the presence of a dodecapole field in the plasma over a 5×10^{-5} level.

The solenoid coil consists of three helical winding layers: this design has been chosen to avoid wire transposition in the coil central region. Each winding layers is trifilar. The nine conductors are water cooled in parallel and electrically connected in series. Four dipole correcting coils compensate errors in the main solenoid winding. The solenoid current is generated and controlled by a highly stabilized power supply ($dI/dt = 10^{-5}$ per hour, $V \leq 120$ V, $I \leq 600$ A).

The phosphor screen F is placed at a distance $\cong L_3/2 - D/2$ from the center of the magnet, inside the region of almost uniform magnetic field, in order to avoid image distortion effects. Placing the CCD camera close to phosphor screen is also beneficial, since the solid angle for light collection is $\Omega_1 = \pi d_l^2 / (4p^2)$, where p is the distance between F and the lens, and d_l is the diameter of the lens. To reduce p , a reentrant flange is used. This has also mechanical advantages: the shim I4 remains in air, and the phosphor screen can be sustained directly on the flange. This design allows $p \geq 100 \div 110$ mm and $\Omega_1 \leq 0.05$ sr. In order to get the desired magnification factor, $M = q/p > s_c/D = 0.28$, where $s_c = 25$ mm is the side of the CCD sensor, the distance q between the lens and the CCD sensor should be in the range [51, 76] mm. The operational ranges of the different parameters are: $q \in [64, 76]$ mm, $M \in [0.28, 0.52]$, $p \in [146, 230]$ mm, $\Omega_1 \in [0.029, 0.14]$ sr.

The phosphor coating (prepared by sedimentation of phosphor grains on a substrate made by BK-7 glass, sealed with an aluminum layer of 100 nm) of type P43 ($\text{Gd}_2\text{O}_2\text{S:Tb}$) has an emission spectrum from 360 nm to 680 nm, peaked at 545 nm and a decay time of 1 ms. The efficiency may reach 700-800 photons per electron (with an electrostatic potential on the phosphor screen $V_F = 15$ kV). The back-illuminated CCD camera is cooled to $190 \div 210$ K by a Peltier element and has 1024×1024 pixels (each pixel being a $24 \mu\text{m}$ side square with a full well capacity of 3.5×10^5 electrons). An IR filter reduces the background light from the electron source.

The confining electrodes (with inner diameter of 90 mm), are aligned and mounted on an aluminum bar, attached to the reentrant flange; this structure can be inserted in the vacuum chamber sliding on some screws fixed under the bar. The other end of the bar is supported by an insert in the opposite flange. The potentials on the electrodes are controlled using a 8-channels waveform generator (time resolution 100 ns, voltage range ± 100 V, slew rate $300 \text{ V}/\mu\text{s}$).

The control and acquisition system is based on two personal computers (see Fig. 2): the first (PC1) is dedicated to the acquisition of the data from the CCD camera, the second (PC2) controls the settings of power supply and waveform generator, the logging of analog signals (e.g., the residual gas pressure) and the synchronization of the experiment. PC2 is equipped with five acquisition cards; up to 40 digital I/O's, 4 timers, 16 analog differential ± 10 V inputs and 4 analog outputs are provided; 6 RS232C ports and a GPIB bus are also available. Several analog interfaces between the machine and the acquisition system were built, solving specific tasks as, e.g., slow ramps (rise time ≥ 1 ms), and total charge detection. Slow ramps (power supply of the source filament and the accelerating voltage on the phosphor screen) are directly controlled by the PC2 analog output. A ground isolator between PC and power supply, given by a 4N25 optocoupler and scaling resistors, is introduced. To measure the number of trapped electrons, the aluminum layer on the phosphor screen is connected to an high-impedance low noise amplifier. This amplifier is also designed to work in differential mode for future applications (detection of diocotron waves).

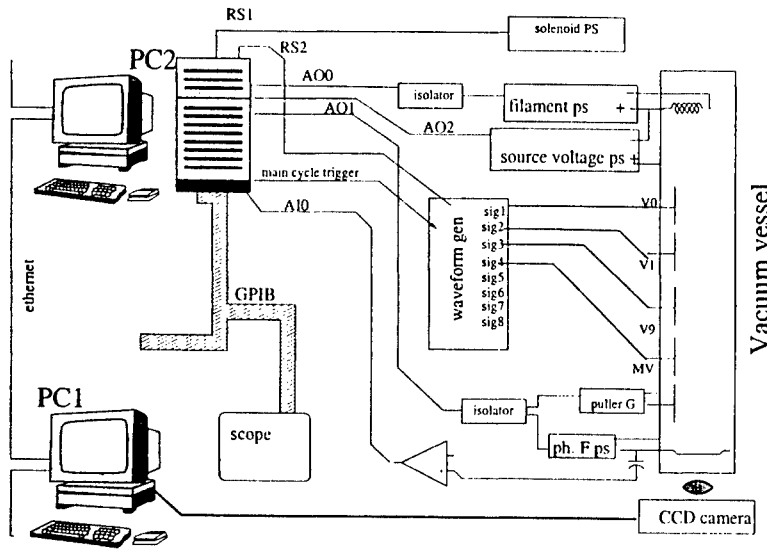


FIGURE 2. Scheme of the control and acquisition systems of the Eltrap machine.

ELECTRON SOURCES

The electron plasma is generated by a W/Th cathode arranged in a spiral shape [9], with diameter $D_f = 25$ mm. An extensive study of alternative sources (spiral carved disk of hot pressed W impregnated with Ba, and a W/Ce filament) has also been performed. The source is mounted inside a 44 mm long copper cup, which provides wire alignment and support and intercepts a fraction of the radiated heat; the wires are isolated by mullite tubes and connected to copper contacts, which are supported by macor isolators. The cup is attached to the electrode V_{ga} (see Fig. 1), thermally isolated from the bar by a macor spacer, so to distribute heat on a relatively large surface.

The generation of a relatively large plasma (diameter $2R_s \cong 60$ mm) with conventional filament sources proves difficult for the large amount of radiated heat P_m , which is related to the filament surface S_s , the filament current I_f and voltage V_f by

$$P_m = f_p \sigma S_s T_s^4 = \overline{I_f V_f} \quad (1)$$

where T_s is the working temperature, $f_p < 1$ is the relative emissivity (with geometrical corrections), σ is the Stefan-Boltzmann constant and the bar indicated time average. The emitted current I_s [10] is constrained by

$$I_s = f_i S_s A_r T_s^2 \exp[-\phi/(kT_s)] > \pi j_i R_s^2 \quad (2)$$

where $f_i \in [0.3, 1]$ is a numerical factor (determined by the geometry of the electrodes), ϕ is the work function of the material, $A_r = 120 \text{ A K}^{-2} \text{ cm}^{-2}$ is the Richardson constant and $j \cong 10 \text{ A m}^{-2}$ is a target value. To obtain this target value $\phi < 2.5 \text{ eV}$ is necessary;

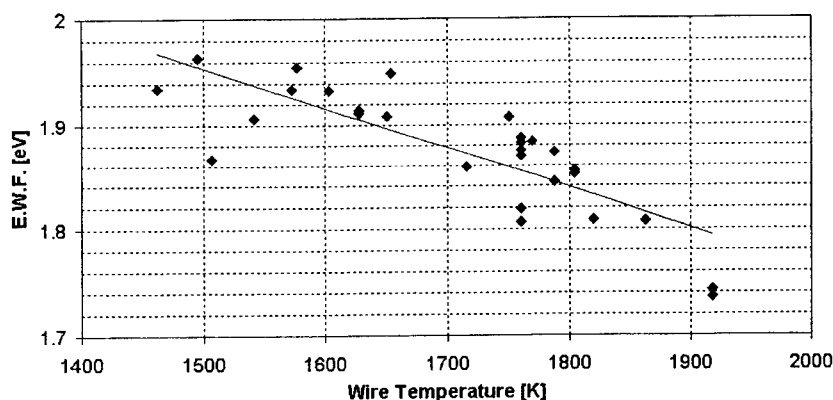


FIGURE 3. Test of a W/Ce spiral: thermionic emission work function. The solid line is the linear fit of the experimental data.

this is possible for hot pressed W with Ba impregnant ($\phi \cong 1.2 \pm 0.3$ eV), but the cost is quite high and machining can be troublesome.

Promising results of tests of a W/Ce source are reported in Fig. 3. A 1.5 turn spiral was prepared by carefully bending a 1 mm diameter W/Ce wire, with a total useful surface $S = 3.77$ cm². The emitted current I_s was measured as a function of the filament current I_f , in the range from 15 to 32 A (V_f ranged from 1 to 4.1 V). The temperature T was also measured by a pyrometer with a typical standard deviation error of ± 25 K; to reduce the error on T , the measured resistance of the filament R_f was scaled to $T = 1000$ K for every data point, using well-known tungsten resistivity data ($24.9 \mu\Omega$ cm at 1000 K and $56.7 \mu\Omega$ cm at 2000 K); a resistance $R_f(T = 1000 \text{ K}) = (0.059 \pm 0.002) \Omega$ is obtained. The wire temperature is then computed for each data point, so that ϕ may be obtained from Eq. (2) ($f_i = 1$ in our experiment).

PERSPECTIVES

The basic ELTRAP configuration uses five cylindrical electrodes (out of twelve electrodes) for the inject-hold-dump cycle, controlled by the waveform generator. The plan of the experiments concerns studies on the formation and evolution of long lived coherent structures in a confined electron plasma (parameter range: $B_0 = 200$ -2000 G, charge $Q = 10$ -600 nC, plasma length 20-80 cm). In the future the device will be also used to investigate the spatial disuniformities (transverse and axial) of an electron beam, due to collective effects. This is of interest for beam dynamics, being one of the most important causes of emittance growth in high brilliance beams (for FEL). To this aim, a moving phosphor equipped telescope will be possibly installed, for 3D analysis.

ACKNOWLEDGMENTS

The authors are grateful to F. C. Driscoll, J. Fajans, A. Cass and K. S. Fine for very valuable discussions and suggestions during the development of the ELTRAP project.

This work has been supported by the Italian Ministry of Education and Scientific Research, the National Institute for the Physics of Matter (I.N.F.M.) and the National Institute of Nuclear Physics (I.N.F.N.).

REFERENCES

1. D. H. E. Dubin and T. M. O'Neil, *Rev. Mod. Phys.* **71**, 87 (1999).
2. K. S. Fine, W. G. Flynn, A. C. Cass, and C. F. Driscoll, *Phys. Rev. Lett.* **75**, 3277 (1995).
3. D. Durkin and J. Fajans, *Phys. Rev. Lett.* **85**, 4052 (2000).
4. M. Romé, M. Brunetti, F. Califano, F. Pegoraro, and R. Pozzoli, *Phys. Plasmas* **7**, 2856 (2000).
5. M. Amoretti, D. Durkin, J. Fajans, R. Pozzoli, and M. Romé, *Phys. Plasmas* **8**, 3865 (2001).
6. R. Pozzoli and D. Ryutov, *Electromagnetic Waves and Electronic Systems* **3**, 12 (1998).
7. C. F. Driscoll, J. H. Malmberg, and K. S. Fine, *Phys. Rev. Lett.* **60**, 1290 (1988).
8. X. P. Huang, K. S. Fine, and C. F. Driscoll, *Phys. Rev. Lett.* **74**, 4424 (1995).
9. J. M. Kriesel and C. F. Driscoll, *Phys. Plasmas* **5**, 1265 (1998).
10. G. A. Haas, in *Methods of experimental physics*, vol. 4A, p. 1 (Academic Press, New York, 1967).

Bunching And Cooling Of Radioactive Ions With REXTRAP

F. Ames^{1,4}, D. Beck², G. Bollen³, O. Forstner⁴, D. Habs¹, G. Huber⁵,
K. Reisinger¹, P. Schmidt⁵

1) *Sektion Physik, LMU München, D-85748 Garching, Germany*

2) *GSI, Planckstr. 1, D-64291 Darmstadt, Germany*

3) *NSCL, Michigan State University, East Lansing, MI48824-1321, USA*

4) *ISOLDE-CERN, CH-1211 Geneva, Switzerland*

5) *Institut für Physik, J. Gutenberg-Universität, D-55099 Mainz, Germany*

Abstract. The properties of radioactive ion beams produced by the present on-line target ion source technology are often not suitable for direct post acceleration. For that purpose pulsed and cooled beams of higher charged ions are required. In the case of REX-ISOLDE, the post accelerator at the CERN-ISOLDE radioactive beam facility, a unique system for beam preparation is used. It consists of a gas-filled cylindrical Penning trap (REXTRAP) for bunching and cooling followed by an electron beam ion source for charge state breeding. The Penning trap has been successfully operated with an efficiency of up to 40% and a total number of up to 10^7 ions stored. Buffer-gas sideband cooling at the ions' cyclotron frequency is employed for centering of the ions in the trap. Space charge effects have been observed if more than 10^5 ions are stored. The main effects are frequency shifts for the centering frequency. They can not be explained by simple single ion trap theory, but can be reproduced in simulations.

INTRODUCTION

The aim of the REX-ISOLDE project [1] is to post-accelerate radioactive ions produced by the CERN ISOLDE facility up to an energy between 0.8 and 2.2 MeV/u. With this a new class of experiments studying nuclear structure physics, astrophysics and nuclear solid-state physics will become possible. Beams of radioactive ions are produced at ISOLDE by bombarding a target with high-energy protons, extracting and ionizing the reaction products and selecting the desired species by mass separation. The ions available have a typical energy of 60 keV, are singly charged and have a transversal beam emittance of about 35π mm mrad. Beam currents are ranging from a few ions per second up to several nA depending on the target ion source combination and the desired nuclide. Efficient post-acceleration requires highly charged ions and a pulsed beam with low emittance. Thus, beam preparation is necessary. For REX-ISOLDE a unique system has been chosen, which consists of a long cylindrical gas filled Penning trap for ion accumulation, bunching and cooling, and an electron beam ion source (EBIS) for charge state breeding. Final acceleration is done by a conventional heavy ion linac.

In a buffer buffer-gas filled Penning trap the reduction of the transversal phase space volume can be achieved by a sideband cooling technique using an excitation of the motion of stored ions at their cyclotron frequency. This has been theoretically studied and described in Ref. [2-4] and proven experimentally in [5]. The technique is well understood if only few ions are trapped, i.e. when no space charge effects have to be taken into account. Until now, no analytical model for describing the sideband cooling technique at the cyclotron frequency together with space charge effects is available but numerical simulations can be done [6].

THEORY

The theory of the motion of a particle inside a Penning trap has been described in many publications, see for example [4,7]. The potential inside a cylindrical electrode structure with appropriate symmetry and voltages applied can be approximated by

$$\Phi_r = \frac{m\omega_z^2}{2q} \left(z^2 - \frac{\rho^2}{2} \right) \quad (1)$$

where m and q are mass and charge of the trapped ion and ω_z its axial oscillation frequency. z and ρ are coordinates in a cylindrical coordinate system with origin at the trap's center. With a superimposed homogenous magnetic field B in z -direction the equation of motion leads to three eigen motions of particles in the trap: one oscillation in longitudinal (z) direction at the frequency ω_z and two circular motions in the perpendicular plane, the magnetron motion (ω_-) and the reduced cyclotron motion (ω_+), with

$$\omega_+ + \omega_- = \omega_c, \quad (2)$$

where $\omega_c = \frac{q}{m} B$ is the cyclotron frequency.

The influence of the buffer gas can be described as viscous force acting on the particle, which can be written as

$$\vec{F} = -\delta m \vec{v}. \quad (3)$$

δ can be taken from tabulated values for ion mobilities in gases [8]. Assuming this being only a small perturbation, the eigen frequencies will remain constant and only the amplitudes will undergo changes. In the case of the axial oscillation and the reduced cyclotron motion this leads to a reduction of the amplitude but for the magnetron motion the radius will increase. Thus, the particle motion becomes unstable.

An additional azimuthal quadrupolar electric field at the cyclotron frequency can be employed to couple the two radial motions. This leads to an exponential decrease of the amplitudes of both motions and results in a centering of the particles inside the trap. The corresponding time constants for the reduction of the radii are equal and for sufficient rf-amplitude they reach a minimum at

$$\alpha = -\frac{\delta}{2} . \quad (4)$$

For example, the damping constant for ^{133}Cs ions in Ar buffer gas at a pressure of 10^{-4} mbar is $\alpha = 150 \text{ s}^{-1}$. The final ion cloud size is determined by the collisions with the buffer gas and therefore by the temperature of the gas.

If a large number of particles are involved space charge will change the potential given in equation 1. But assuming an elliptically shaped charge distribution [9] the quadratic dependence of equation 1 will remain. Thus, the formalism for solving the equation of motion, especially equation 2, will remain valid.

EXPERIMENT AND RESULTS

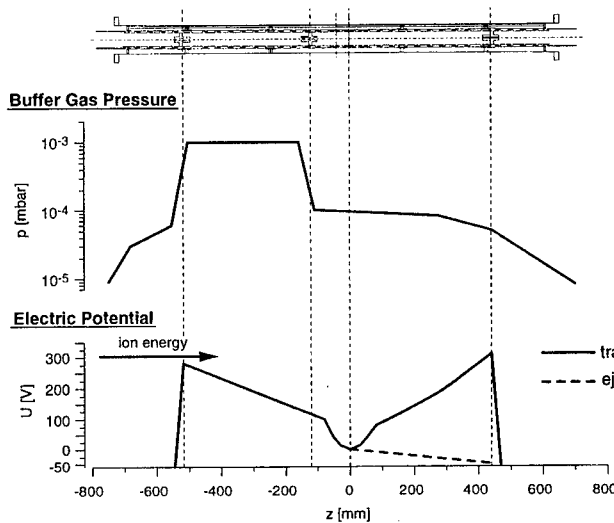


FIGURE 1. electrode structure, pressure and voltage distribution for REXTRAP.

The experimental set-up of REXTRAP is described in detail elsewhere [10]. In order to decelerate the ions in a first step the trap is placed on a high-voltage-platform near to 60 kV. Figure 1 shows the distribution of buffer gas pressure inside the trap as well as the potentials employed for accumulation and ejection of the ions. After passing the entrance potential hill of the trap the ions are finally stopped via collisions with the buffer gas atoms. They accumulate in the potential minimum at the trap center. A quadrupolar rf-field for the sideband cooling is applied to the fourfold segmented central trap electrode. After accumulation and cooling the potential hill at the trap exit is removed by switching down the potential at the corresponding electrodes, which releases the ions as a short bunch. The ions are accelerated again to ground potential, i.e. to 60 keV, and transported to the EBIS. For the sequence of accumulation and ejection a minimum cycle time of about 20 ms has been realized, which allow also short-lived isotopes to be handled.

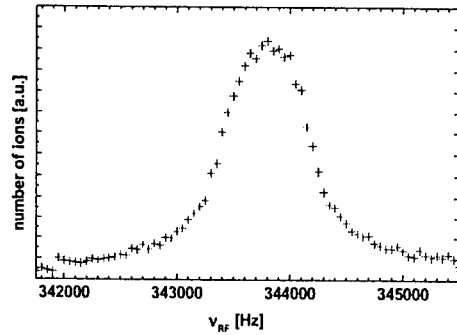


FIGURE 2. Number of ejected ^{133}Cs ions as a function of the applied radio frequency

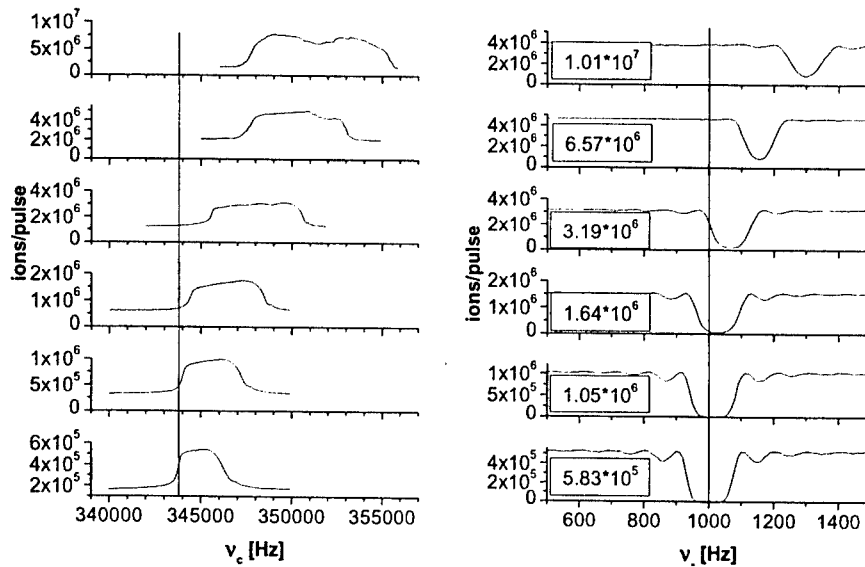


FIGURE 3. Number of ejected ions as a function of rf-frequencies for different number of stored ions. Left: signal as a function of the frequency of the quadrupolar rf-field for centering. Right: signal as function of the dipolar rf-field for driving the magnetron motion. The vertical lines represent the resonance frequencies for ion numbers below 10^5 .

Experiments have been performed with stable and radioactive ions ranging from ^7Li up to ^{181}Ta injected from a test ion source and from ISOLDE. As buffer gas the noble gases He, Ne and Ar have been used. A total efficiency of up to 40 % could be obtained. Since the exit diaphragm of the trap is smaller than the entrance one, successful cooling can be detected by an increase in the count rate of ejected ions. A typical cooling resonance for ^{133}Cs with a total numbers of less than 10^5 simultaneously stored ions is shown in figure 2. If the number of stored ions is increased a significant broadening of the resonance lines and a shift of the center can be observed. For ^{133}Cs this shift can be a few kHz, compared to the cyclotron frequency of about 345 kHz. The

effect can not be explained by the sum of the shifts of the magnetron or reduced cyclotron frequency.

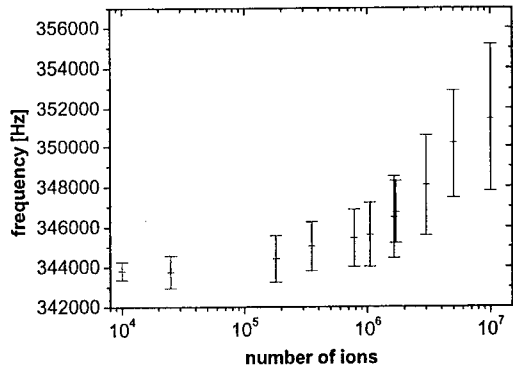


FIGURE 4 Centering frequency and width of centering resonances measured for ^{133}Cs ions

These two frequencies can be measured by applying an azimuthal dipole rf-field after cooling. In resonance this excitation increases the amplitude of the motion again and results in a loss of the ions. As an example figure 3 (right) shows the resonance lines for the excitation near the magnetron frequency. It can be seen, that the magnitude of the shift is much smaller than for the applied centering frequency. A similar result, with a small downshift, could be obtained for the reduced cyclotron frequency. In figure 4 a summary of all measured spectra for the cooling of ^{133}Cs is shown. In addition to the frequency shifts a decrease of the efficiency for ion ejection has been observed, indicating that even after centering the ion cloud's diameter becomes larger than the diameter of the exit diaphragm.

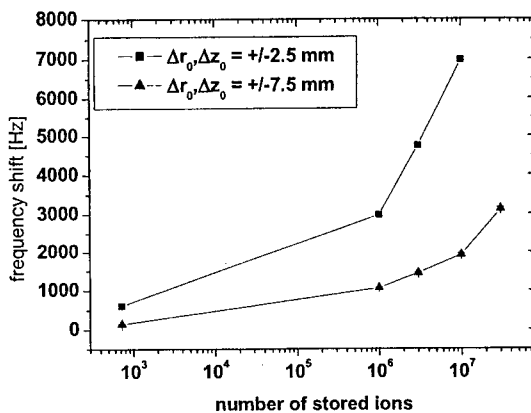


FIGURE 5 Calculated frequency shift for the centering of ^{133}Cs ions as a function of the number of stored ions for different initial ion cloud sizes according to simulations

To further understand this behavior simulations of the ion motion and the cooling process have been carried out, in which space charge effects have been taking into ac-

count. To simulate the Coulomb interaction between the ions their electrical charge was scaled in such a way that only about 2000 ions represent the charge of 10^7 ions. Figure 5 shows the optimum centering frequency obtained in such a way for two different initial cloud sizes as a function of the number of stored ions. A very similar behavior to that depicted in figure 4 can be observed. The final ion cloud sizes after 20 ms of sideband cooling according to the simulations could be determined to be about 5 mm in diameter and 10 mm in length for 10^7 stored ions.

SUMMARY

It has been demonstrated that a gas-filled Penning trap can be used for efficient accumulation and bunching of ions for ion beam preparation. For centering of the ions, i.e. a reduction of the transversal phase space, a sideband cooling technique at the cyclotron frequency has been used. Originally developed for the cooling of only a small number of ions this method has been extended to up to 10^7 stored ions. Space charge effects mainly cause an upward shift in the sideband cooling resonance. This behavior can not be understood easily by single ion theory, but it can be reproduced qualitatively by simulations. The strong dependence of the frequency on the initial size of the ion cloud indicates that the ion density is an important parameter.

For the accumulation and cooling of radioactive ions this is not a major drawback as in most cases only a small number of ions are delivered from the mass separator. However, in some cases isobaric contaminations can be higher. Here the adaptation of the applied frequency to the actual ion density can improve the cooling. First experiments could demonstrate an increase in the ion signal by a two-step increase in the frequency. To find an optimal excitation scheme for such cases further investigations will be done.

ACKNOWLEDGMENTS

This work has been funded by the German "Bundesministerium für Bildung und Forschung" under the contract number 06MZ9621 and the European Community network "EXOTRAP".

REFERENCES

1. D. Habs et al., *Hyperfine Interaction* **129** 43 (2000).
2. G. Bollen et al., *J. Appl. Phys.* **68** 4355 (1990).
3. G. Savard et al. *Phys Lett A* **158** 247 (1991).
4. M. König et al., *Int. J. Mass Spectrom. Ion Processes* **142** 95 (1995).
5. H. Raimbault-Hartmann et al., *Nucl. Instr. Meth.* **B126** 378 (1997).
6. D. Beck et al., *Hyperfine Interaction* **132** 469 (2001).
7. L.S. Brown, G. Gabrielse, *Rev. Mod. Phys.* **58** 233 (1986).
8. L.A. Viehland, E.A. Mason, *At. Dat. Nucl. Dat. Tab.* **60** 37 (1995) and references therein.
9. D.H.E. Dubin, T.M. O'Neil, *Rev. Mod. Phys.* **71** 87 (1999).
10. P. Schmidt et al. *Nucl. Instr. Meth.*, in press.

SHIPTRAP: A capture and storage facility on its way towards an RIB-facility

G. Marx*, J. Dilling*, H.-J. Kluge*, M. Mukherjee*, W. Quint*,
S. Rahaman*, D. Rodriguez*, G. Sikler*, M. Tarisien*, C. Weber* and the
SHIPTRAP Collaboration[†]

*GSI Darmstadt, Postfach 110552, D-64220 Darmstadt, Germany

†

Abstract. First off-line tests at the ion trap facility SHIPTRAP took place. The facility is being set up to deliver very clean and cooled beams of singly-charged recoil ions produced at the SHIP velocity filter at GSI, Darmstadt. SHIPTRAP consists of a gas cell for stopping and thermalizing high-energy recoil ions from SHIP, an rf ion guide for extraction of the ions from the gas cell, a linear rf trap for accumulation and bunching of the ions, and a Penning trap for isobaric purification. The physics programme of the SHIPTRAP facility comprises mass spectrometry, nuclear spectroscopy, laser spectroscopy and chemistry of transeinsteinium elements. The progress in testing the sub-systems separately and in combinations is reported.

INTRODUCTION

The interest in coupling ion traps to sources of radionuclides arises from the extremely small phase space in which ions reside in a trap, from the possible long storage time and from the extremely high purity that can be obtained. These are pre-requisites for high-accuracy experiments. The purification is very important since contaminants always plagued the investigation of exotic radioactive species. This separation not only allows for very sensitive and accurate experiments to be performed within the ion trap itself but also allows the collected radionuclides to be extracted from the trap and studied in a well-defined low-emittance ion beam. Together, these possibilities open a wide range of physics applications. SHIPTRAP will enable very sensitive and accurate experiments, performed within the ion trap itself or with an extracted beam. The half-lives of the most neutron-rich nuclides of the elements up to hassium ($Z = 108$) are longer than one second, which is also predicted by theory for a large number of ions in this region of the chart of nuclei. This is long enough to prepare the ions and to perform precision experiments. The ISOLTRAP experiment at ISOLDE/CERN [1], consisting of a rf trap for accumulation of the 60-keV ISOLDE ion beam, a first Penning trap for isobar separation and a second one for high-accuracy mass measurements of short-lived isotopes, has demonstrated the potential of the ion trap concept at ISOL (Isotope Separation On-Line) facilities. The present state of ion trap technology now makes it possible to couple a trap system to ion beams of higher energy (about 0.5 MeV/u) such as delivered by the velocity filter SHIP (separator for heavy-ion reaction products) at GSI. A similar project has been started at a recoil separator at Argonne (USA) while at INS (Tokyo)

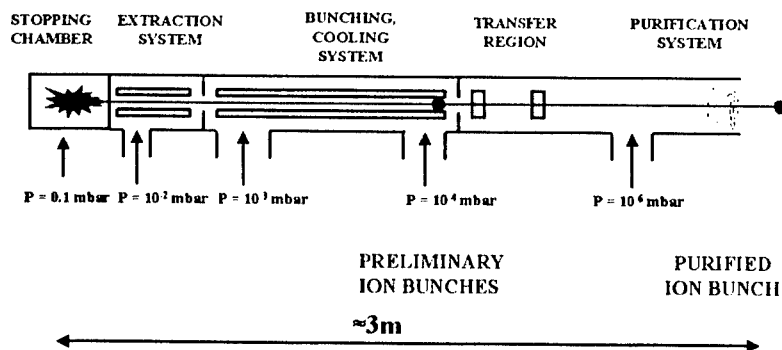


FIGURE 1. The overall SHIPTRAP configuration

a radiofrequency trap coupled to GARIS [2] has already been tested. The advantage of such facilities is that they enable the rich variety of physics experiments currently performed at ISOL facilities to be extended to isotopes for which target/ion source systems do not exist at ISOL facilities. The particular advantage that SHIPTRAP will have is the ability to extend these experiments to transuranic nuclides. Thus, SHIPTRAP will enable the application of refined ISOL techniques for the first time to nuclides with nuclear charge $Z > 92$, extending even to the superheavy elements of which many have a sufficiently long half-life for trap technology.

THE SHIPTRAP FACILITY

SHIP is a kinematic separator for reaction recoils from thin targets irradiated by beams from the heavy-ion linear accelerator UNILAC at GSI [3]. It is optimized for the separation of heavy elements produced by fusion of projectiles from $A = 40$ to 80 with heavy target nuclei such as lead or bismuth. The primary beam has an energy close to 5 MeV/u and time-averaged intensities of typically $2 \cdot 10^{12}$ - $5 \cdot 10^{12}$ ions/s.

The SHIPTRAP facility is setup at the exit of SHIP. It stops and thermalizes the produced recoil ions in a noble gas from which they are then extracted and collected in a trap. The system is outlined in Fig. 1. It consists of a stopping chamber containing the noble gas, an extraction system to bring the stopped ions into a vacuum region, a radiofrequency trapping system to collect the ions in this vacuum region and to cool them

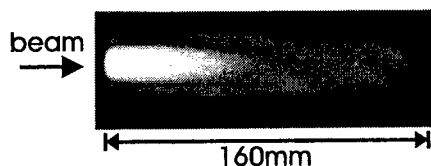


FIGURE 2. Stopping of Au^+ ions with an energy of 0.3 MeV in argon at 80 mbar. The light emitted in this process is recorded by a CCD-camera.

into well-defined bunches which are then extracted and injected into a Penning trap for isobaric purification. The Penning trap accumulates the ion bunches, filters out possible contaminants and further cools the collection to room temperature. This collection is then extracted on the demand of downstream experiments.

The noble gas in the stopping chamber, at pressures around one-tenth of an atmosphere, will thermalize recoil ions preferentially in the singly ionized state. An electric field, together with the gas flow, then guides the ions out of the chamber into the extraction system where they are separated from the gas. This system is a short quadrupole rod structure that confines the ions to its axis by an rf field while the noble gas is pumped away. An axial dc electric field applied to the segmented rods guides the ions along the axis towards the bunching system. The recent development for the SHIPTRAP stopping chamber and the extraction RFQ is described elsewhere [4]. In the ion bunching system, a 1m quadrupole rod structure immersed in a low-pressure buffer gas, the ions are trapped by a proper choice of longitudinal dc and transverse rf fields and cooled in collisions with the buffer gas. The RFQ-buncher has been set up and is currently being tested. The purification system into which these preliminary bunches are collected is based on a Penning trap similar to the one used for this purpose at the ISOLTRAP facility at ISOLDE. In such a system the contaminating isotopes are very effectively suppressed due to the high mass resolving power of the cooling process. Depending on the trapping time it can reach $M/\delta M(\text{FWHM}) = 10^5$.

The ion bunches delivered by this Penning trap system will have extremely low emittances, thermal energy spreads and pulse durations of typically less than a microsecond, although bunches of longer duration could be extracted if desired. With current ISOL beam technology these bunches could be delivered at any energy desired up to about 60 keV. In some cases it may be advantageous to use specifically those ions from SHIP that become neutral atoms in the stopping gas. These can then be re-ionized by a laser beam (resonance ionization spectroscopy, RIS) for delivery to the vacuum system. Such a scheme provides element selectivity, and for heavy elements isotopic selectivity as well, in the stopping chamber itself.

THE STOPPING CHAMBER AND THE EXTRACTION SYSTEM

A prototype gas cell was designed for tests at the Tandem Accelerator in Garching and at SHIP. At Garching, stopping of 0.3 MeV/u gold ions in a 80 mbar argon atmosphere was measured by detecting the light which is emitted during the electronic stopping

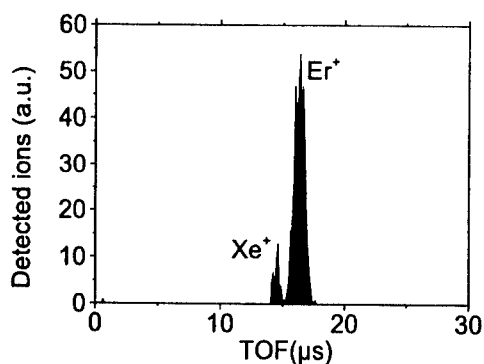


FIGURE 3. Test of stopping chamber: Erbium($^{166}\text{Er}^+$) and xenon ($^{132}\text{Xe}^+$) ions are laser ionized in the stopping chamber, accumulated in the RFQ buncher, extracted and detected by a multi-channel plate.

process with a CCD-camera (Fig.2). In the SHIPTRAP setup the beam of exotic nuclei produced and pre-separated at SHIP will enter the He-filled stopping chamber through a thin window [4]. In addition to the gas flow, static and RF fields guide the predominantly singly charged ions to the exit nozzle. The stopping gas is pumped off outside the extraction hole and the diverging beam is re-focused by the oscillating field of the following extraction RFQ. The prototype has been tested with ions internally produced by laser desorption (laser pulse width: 6 ns , repetition rate: 25 Hz) from an erbium filament inside the stopping chamber. The helium gas pressure in the stopping chamber was set to 20 mbar . The ions are guided into and accumulated in the RFQ buncher for 300 ms . The trapped and extracted ions are identified by time of flight (see Fig.3). No statement is possible for the efficiency of the transfer from the stopping chamber to the extraction system.

THE RFQ BUNCHER

The classical Quadrupole Mass Analyzer (QMA) is operated by applying on its rods a dc bias voltage U and a radio-frequency of amplitude V and frequency ω_{rf} . An ion with mass m and charge e , which enters the QMA performs an oscillation which is described by solution of the Mathieu equations. In this equation one defines a pair of dimensionless parameters a ($\frac{4eU}{m\omega_{rf}^2 r_0^2}$), proportional to the dc bias voltage U and q ($\frac{2eV}{m\omega_{rf}^2 r_0^2}$), proportional to the rf amplitude V . This pair of parameters characterizes the working point in a a, q -stability diagram. The motion of the ion is stable if the amplitude of the oscillation remains finite, and unstable if its amplitude rises exponentially. In our case the QMA was tested in rf-only mode, i.e. without a dc voltage U . Then the operating region lies on the q axis. For a certain rf voltage applied to the rods, all ions pass the filter for which q is less than the stability limit 0.908. The rods of the SHIPTRAP RFQ have

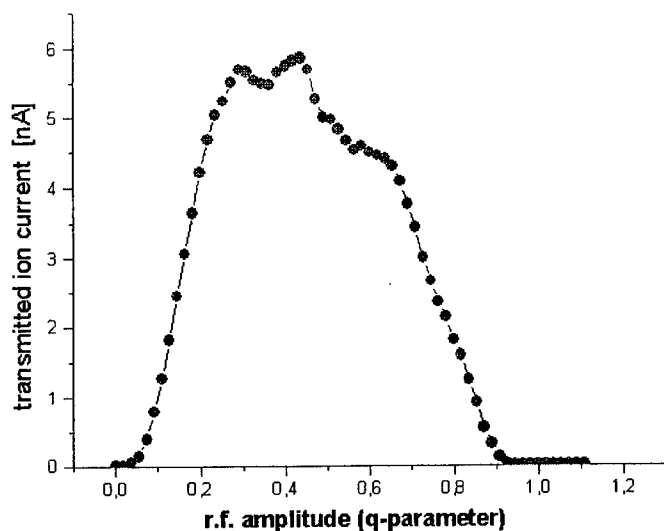


FIGURE 4. Transmission plot in rf-only mode for Ar^+ ions.

a diameter of 9 mm. The distance between two opposite rods is 7.86mm. In first tests in the rf-only mode with a calibrated ion source a transmission of about 93(5)% was achieved. Fig.4 shows a transmission plot for Ar^+ ions. The driving field frequency was set to $\nu_{rf} = 600\text{kHz}$. In simulations it was shown that the left edge of the transmission curve is affected by beam divergence, whereas the right edge is rather unaffected [6]. A lower transmission for low q values as beam divergence grows can be explained by the fact that ion entry angle grows; hence the probability of hitting the rods increases. The right edge is affected by beam width effects, becoming less abrupt as beam width grows. In simulations it was shown that this effect is more pronounced when the ion beam is not centered or annular. As a conclusion our transmission curves are indicating an off-axis ion source with low emittance.

The essential task of the RFQ buncher at SHIPTRAP is to accept the ions from the stopping chamber, to cool and to collect them. Therefore the RFQ buncher will be operated under buffer gas and it is necessary to investigate the influence of gas on the ion motion. The average effect of ion collisions with buffer gas molecules can be approximated by a frictional drag force. This is described by the Mathieu equation for the ion motion in free space but with an added velocity dependent term. Figure 5 shows three measured transmission curves at different pressures. One can see a tendency that the right edge of the stability diagram is shifted to higher q -values. Due to the damping of the ion motion one can apply higher quadrupole field strength until the ion motion becomes unstable. The information how much the stability region is increased under buffer gas operation is important since one tries to use the (limited) mass resolution of

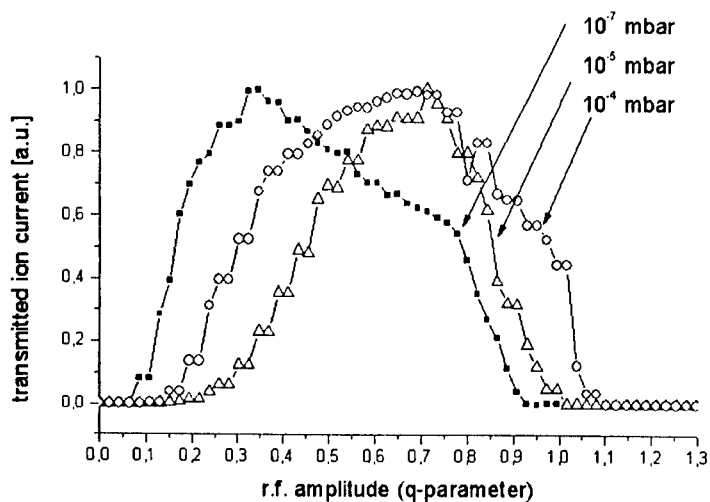


FIGURE 5. influence of buffer gas on the transmission curve

the RFQ in rf-only mode to suppress contamination of lighter ion species.

The qualitative overall effect of space charge on an ion beam in an RFQ rod structure, neglecting the size of an ion beam due to thermal motion of the ions, will push out the ions until those at the periphery of the beam experience an effective radial electric force from the confining field that balances the radial expansion force of the space charge. Assuming a uniform charge distribution along the beam axis, the space charge electric field at the edge of a beam of radius r is balanced by the effective trapping electric field. This results in a charge density $\rho_z = \frac{\pi \epsilon_0 m}{4 e} q^2 \omega_{rf} r^2$. For a typical set of operating conditions ($q=0.45$; $\omega_{rf}/2\pi=1\text{MHz}$; $r=2\text{mm}$; $m=100\text{amu}$) the linear charge density will be about 0.2nC/m . For the SHIPTRAP RFQ buncher of 1m length assuming a drift field to give the ions an axial velocity of 1000 m/s , the ion density along the device result in a maximum beam current of about 200 nA . Our tests have been done well below this space charge limit.

Trapping times of up to 30 s without significant ion loss have been achieved. Accumulation of ions with a dc-injection as well as a pulsed injection was demonstrated. The ions can be extracted in a pulsed mode in bunches with high phase space density and can be delivered to the high vacuum region.

THE PENNING TRAPS

A double trap system is installed within one magnet at SHIPTRAP. Both traps have cylindrical electrodes with an inner diameter of 30 mm . The purpose of the first trap is

to catch the ion bunch from the RFQ buncher and to purify the ion bunch. The second trap is for, e.g., mass measurements. The traps (distance between the centers of traps: 10 cm) are separated by a diaphragm.

Penning trap mass spectrometers at ISOLDE/CERN [1], Stockholm [7], and Argonne [8] use a time-of-flight method developed by Gräff et al. [9] to measure eigenfrequencies of trapped ions. The ions are ejected out of the trap and their time of flight to a detector is recorded. Typically this requires the detection of 100 - 1000 ions. Assuming a production rate in the order of 10^{-3} ions/s, e.g. for Sg ($Z = 106$), this would lead to a beam time of about 1 - 10 days. A non-destructive way to obtain eigenfrequencies of the ion motion is to monitor the image currents induced in the trap electrodes by the oscillating ions (Fig.6). Such a method is employed, e.g. at the University of Washington [10] and at MIT [11]. It allows the non-destructive identification of one single ion, and the required beam time for the mass measurement of a heavy element is much less than one day. In order to determine the detection sensitivity of such a device one has to estimate the image current which is given by

$$I_{ion} = \frac{1}{\sqrt{2}} \frac{r_{ion}}{D} \cdot q \cdot \omega_{ion}. \quad (1)$$

This signal can be detected via a tank circuit of quality factor Q . Taking into account the thermal noise of the circuit, the signal-to-noise ratio (S/N) is given by

$$\frac{S}{N} = \frac{\sqrt{\pi}}{2} \cdot \frac{r_{ion}}{D} \cdot q \cdot \sqrt{\frac{v}{\Delta v}} \sqrt{\frac{Q}{kT \cdot C}}, \quad (2)$$

where r_{ion} is the radius of the ion orbit in the trap, D characterizes the trap size, T is the temperature, and C the stray capacitance of the system. The signal-to-noise ratio can be optimized by a high quality factor Q , a low temperature T , and by minimizing the capacitance C . The setup at SHIPTRAP will consist of a cryogenic system with the trap environment at liquid nitrogen temperature and a superconducting tank circuit at 4 K. With an effective temperature of 30 K and an estimated Q of 1000 the power signal-to-noise ratio will be higher by a factor of 50 as compared to a room temperature setup.

THE SCIENTIFIC CASE FOR SHIPTRAP

Nuclear mass measurements of transuranium isotopes

A high-resolution Penning trap mass spectrometer coupled to the SHIPTRAP facility will allow for direct mass spectrometry of heavy actinide and transactinide isotopes, provided the background of unwanted ions can be sufficiently suppressed. In such measurements nuclear binding energies can be determined with high precision. Investigations of the heaviest elements at SHIP has led to the discovery of a shell-stabilized deformed region centered at $Z = 108$ and $N = 162$. This region of enhanced stability against fission interconnects the transuranium elements and the predicted superheavy shell located at

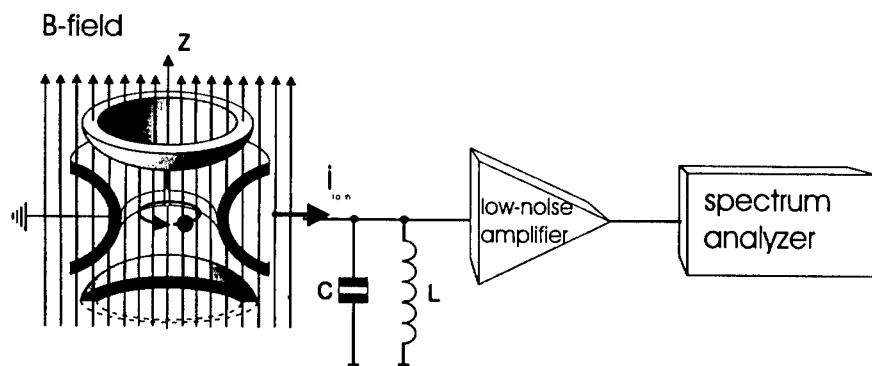


FIGURE 6. Principle of non-destructive FT-ICR technique. The image current of a single singly charged ion is picked up on a split electrode, amplified and analyzed.

$Z = 114$ and $N = 184$ [12]. For the most neutron-rich isotopes of the elements up to hassium ($Z = 108$) half-lives longer than 1 s were observed. These long half-lives open the possibility of high-accuracy mass measurements on heavy elements with ion traps [13].

Precision nuclear spectroscopy

SHIPTRAP will be an excellent facility for precision nuclear spectroscopy of short-lived nuclei. For such studies the bunches of radioactive ions will be delivered to a subsequent Penning trap. In this case, the Penning trap employed is a simple containment device, requiring as high a magnetic field as possible but with minimal requirements on magnetic field uniformity and electric field shape. Such a trap provides a radioactive "source" of a particular nuclear species that is completely free of the absorption and backscattering problems created by the backing material, problems that have plagued all previous high-precision nuclear spectroscopy on nuclear decays. Furthermore, because of the high magnetic field of such a trap, an array of beta, gamma and charged-particle detectors can be configured so that each detector presents a very clean spectrum of the activity it is meant to observe, suffering little background from the others. By including the observations of charged particles, studies can be made on β -delayed proton emission, β -decay and decay by cluster emission.

Nuclear fission studies

A careful study of nuclear fission gives a deeper insight into the influence of shell effects on nuclear dynamics. Fission-fragment mass distributions and total kinetic energies can vary significantly from one nucleus to another. For example, ^{256}Fm shows a double-humped mass distribution, similar to that for the lighter actinides, while ^{258}Fm

exhibits a narrow, symmetric mass distribution and exceptionally high total kinetic energies. This finding has been attributed to the influence of the double shell closure in ^{132}Sn on the fission process [14]. Another transition from asymmetric to symmetric fission has been observed around ^{226}Th . Knowledge of the systematics of the fission properties of nuclei leads to an improved understanding of nuclear-structure effects on nuclear dynamics. The experimental method which is best suited to study the fission properties of spontaneously fissioning nuclei which are only available in small numbers is to measure the energies of the two fission fragments in two opposite detectors.

Chemistry

One of the most fascinating studies of the heaviest actinides and the transactinides concerns the influence of increasingly strong relativistic effects on the valence-electron configuration of the atom and its consequences on chemical behaviour. The aim of such experiments is to compare the chemical properties with homologous elements. For example, the element $Z = 105$ (dubnium) is the chemical homologue to niobium ($Z = 41$) and tantalum ($Z = 73$) in group 5 of the Periodic Table. However, it is well known that relativistic effects gain an increasingly important role for the heaviest elements around $Z = 100$ and consequently the atomic and chemical properties of these elements may not behave as expected from periodicity. The valence electron configurations of these elements can be predicted by multi-configuration Hartree-Fock-Dirac calculations and other methods [15],[16]. At SHIPTRAP, reaction studies of trapped ions with small amounts of a reactive gas in an ion trap would allow kinetic studies by investigating the loss rate of an ionic species from the trap. In addition, this may give access to ion chemical studies of short-lived isotopes of the heaviest elements, which is mandatory for chemical studies in cases where all known isotopes of a given element are short-lived. Traps will also provide access to oxidation states which cannot be investigated with current chemical methods. It is expected that these investigations can be extended to short-lived transactinides with $Z > 106$ and $T_{1/2} < 100$ ms, which are out of reach to gas-chromatographic methods.

Optical spectroscopy of transeinsteinium elements

Laser spectroscopy is a very sensitive method for the investigation of atomic and nuclear properties of rare radioactive species [17]. Many experimental results have been obtained at ISOLDE (CERN) with the method of collinear laser spectroscopy. In special cases only about 100 ions/s are required for high-resolution hyperfine spectroscopy which yields information on the nuclear spin, the nuclear moments and the change of the nuclear charge radius as a function of the neutron number. For production rates of less than 100 ions/s the radiation detected resonance ionization spectroscopy (RADRIS) technique in a buffer gas cell is a powerful method. This method can be employed for the investigation of radioactive nuclides with half-lives as short as 1 ms and which are produced with rates of less than 10 ions/s, as demonstrated in spectroscopic investigations

of $^{240f}, ^{242f}$ Am fission isomers [18]. The combination of laser spectroscopy with SHIP-TRAP presents a unique possibility of investigating atomic, nuclear and ion chemical properties in the region of superheavy elements.

SUMMARY

The SHIPTRAP facility at GSI Darmstadt is designed to slow down heavy-ion projectiles from the velocity filter SHIP to thermal energies, to accumulate and cool them in an ion trap system and to deliver these ions as isobarically pure ion bunches with low emittance to experiments. After an intense simulating and construction phase all components are presently under test. SHIPTRAP will undergo a test beam time in winter 2001 and will start operation in Summer 2002. The experimental programme which is envisaged by the SHIPTRAP user community promises to give new insights into the nuclear, atomic and chemical properties of elements beyond uranium, the heaviest element available at usual ISOL facilities.

ACKNOWLEDGEMENT

We acknowledge financial support by the European Union (Network EXOTRAPs).

REFERENCES

1. G. Bollen et al., Nucl. Instr. and Meth. A 368 (1996) 675
2. S. Fujitaka et al., Nucl. Instrum. Methods B 126 (1997) 386.
3. G. Münzenberg et al., Nucl. Instrum. Methods 161 (1979) 65.
4. O. Engels et al., Hyp. Int. in print
5. G. Marx et al., The European Physical Journal D, Volume 4, Issue 3, 279-284
6. F. Muntean, Int. J. of Mass Spectrometry and Ion Processes 151 (1995) (197-206)
7. C. Carlberg et al., Phys. Rev. Lett. 83 (1999) 4506.
8. G. Savard et al., Nucl. Phys. A 654 (1999) 961c.
9. G. Gräff et al., Z. Phys. A 297 (1980) 35.
10. D. L. Farnham et al., Phys. Rev. Lett. 75 (1995) 3598.
11. M. P. Bradley et al., Phys. Rev. Lett. 83 (1999) 4510.
12. P. Möller et al., At. Data Nucl. Data Tables 59 (1995) 185.
13. J. Dilling et al., Hyp. Int. 127 (1999) 491
14. V.V. Pashkevich, Nuclear Phys. A 477 (1988) 1.
15. W.C. Martin and J. Sugar, Phys. Rev. A 53 (1996) 1911.
16. V. Pershina, Chem. Rev. 96 (1996) 1977.
17. E.W. Otten, in: Treatise on Heavy-Ion Science, Vol. 8, ed.D.A. Bromley (Plenum, New York, 1989) p. 517.
18. H. Backe et al., Phys. Rev. Lett. 80 (1998) 920.

Development of an RF ion guide for trapping energetic radioactive nuclear ions

M. Wada*, Y. Ishida*, T. Nakamura*, N. Oshima*, Y. Nakai*,
T.M. Kojima*, Y. Kanai*, H. Ohyama*, T. Kambara*, Y. Yamazaki*,
A. Yoshida*, T. Kubo*, Y. Matsuo*, Y. Fukuyama*, K. Okada†, K. Noda**,
S. Ohtani‡, H. Kawakami§ and I. Katayama§

*RIKEN, Hirosawa, Wako, Saitama 351-0198, Japan

†Department of Physics, Sophia University, Tokyo 102-8554, Japan

**National Institute for Radiological Science, Chiba 263-8555, Japan

‡Institute of Laser Science, University of Electro-Communications, Chofu 182-8585, Japan

§Institute of Particle and Nuclear Studies (IPNS), High Energy Accelerator Research Organization (KEK), Tsukuba 305-0801, Japan

Abstract. Although the projectile fragment separator (RIPS) at the RIKEN accelerator facility (RARF) provides wide variety of energetic radioactive beams, it is not adequate for low energy beam experiments such as precision spectroscopy of trapped ions. Aiming for an efficient deceleration and cooling of energetic radioactive ions, the development of an rf ion guide system which comprises a large He gas cell and an rf funnel structure in the cell is under progress.

A proof of the principle (pop) machine has been successfully tested on-line for collection of 70-MeV/u ^8Li ions. A compact gas cell of 70 cm in length and 10 cm in diameter with a He gas pressure of 30 Torr was placed after a variable wedge shaped energy degrader. The ions were stopped in the gas and were transported by a superposition of dc and rf electric field toward a small exit hole. The overall efficiency was 10^{-4} which can be separated into a gas stopping efficiency of 0.43 % and an ion-guide efficiency of 2.4 %. The former is limited by the volume of the cell and the pressure of the He gas. The latter is due to the present rf voltage limitation of 40 V. Both efficiency could be increased up to 10 % range by larger cell, higher pressure, and higher rf voltage, which would yield an expected overall efficiency of 1 %.

INTRODUCTION

At RIKEN a radioactive beam factory (RIBF) is under construction. The new facility consists of several stages of heavy ion cyclotron which provides 1-pμA, 350 MeV/u heavy ion beams, projectile fragment separators (Big RIPS) and storage rings (MUSES) [1]. The projectile fragment separator provides a wide variety of radioactive nuclear ions without any restrictions on chemical property or lifetime limit of the ions. The beam energy and quality is, however, not adequate for low-energy beam experiments, in particular for trapping experiments. Trapped unstable nuclear ions enable us to perform a variety of high precision experiments.

We will primarily apply this method to the precision spectroscopy of the hyperfine structure of various Be isotopes [2]. The hyperfine constant A shows a small but finite isotope dependence. The main part of this hyperfine anomaly stems from the finite distribution of the magnetism over the extended nucleus and is known as the Bohr-

Weisskopf effect [3]. The effect is empirically described by

$$A = A_{\text{point}}(1 + \epsilon_{\text{BW}}) \quad (1)$$

where A and A_{point} are the hyperfine constant for an extended and point-like nucleus, respectively, and ϵ_{BW} is the anomaly. Since A_{point} can not be obtained experimentally, we compare the ratio of A to the nuclear g_I -factor among the isotopes. The differential anomaly

$$^1\Delta^2 \equiv \frac{A^1/g_I^1}{A^2/g_I^2} - 1 \approx \epsilon_{\text{BW}}^1 - \epsilon_{\text{BW}}^2 \quad (2)$$

can then be evaluated.

We aim at the investigation of the neutron halo structure of the ^{11}Be nucleus through the measurements of the Bohr-Weisskopf effect which is sensitive to the radial distribution of the loosely bound valence neutron. A recent theoretical estimate supports the importance of the investigation of the Bohr-Weisskopf effect in connection with the nuclear structure of ^{11}Be [4]. We have been working towards the development of exact experimental techniques for this purpose [5, 6, 7].

In order to investigate the Bohr-Weisskopf effect of ^{11}Be , we must determine the hyperfine constant A and nuclear g -factor g_I for all the Be isotopes with an accuracy of at least 10^{-6} . A combined linear trap which consists of a superconducting Helmholtz magnet and a linear rf trap was constructed [8] for testing a laser microwave multiple resonance method. Figure 1 shows typical microwave resonance spectra for nuclear spin flip resonance and electron spin flip resonance. We could determine the hyperfine constant A and the nuclear g_I -factor in units of the atomic g_J -factor from the two sets of resonance frequencies using the Breit-Rabi formula. We obtained a sufficiently high accuracy for the hyperfine constant A and for nuclear g_I -factor of the stable isotope ^9Be , 10^{-8} and 10^{-6} , respectively [9].

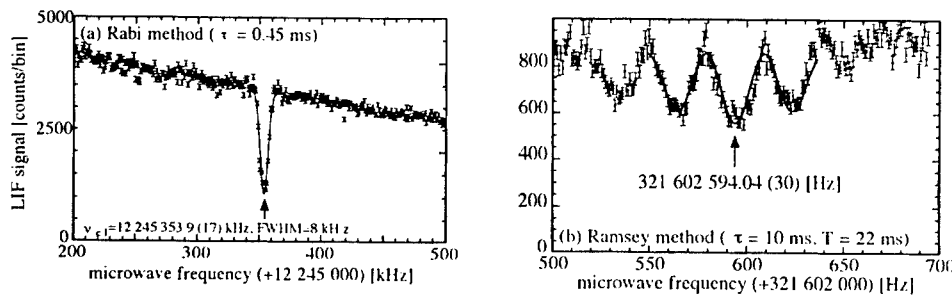


FIGURE 1. Electron spin flip resonance (left) and nuclear spin flip resonance (right) spectra of the ground state hyperfine structure of $^9\text{Be}^+$ obtained by laser microwave multiple resonance spectroscopy in an external magnetic field.

In order to perform such trap experiment, a new scheme to decelerate energetic unstable nuclear ion beams and to cool them efficiently has to be developed. We have been working on the development of an rf ion guide system for this purpose.

PRINCIPLE

The rf ion guide system was proposed to obtain slow or trapped radioactive nuclear ions which are primarily produced by a projectile fragment separator. The energetic ion beams from the fragment separator are energetically degraded by passing through a degrader plate. The medium-energy ion beam thus obtained is then injected into a large He gas cell to thermalize the ions. The stopped ions have to be quickly extracted to the vacuum and transferred to the downstream instruments. A schematic diagram of the entire system is shown in Fig. 2. The ordinary ion guide system has been used for a kind of a target ion-source unit of an isotope separator on-line (IGISOL) [10]. Reaction products recoiling out from the target are mostly in singly charged state when stopped in the He gas and extracted to the vacuum. In the ordinary ion guide system, the transport of ions in the cell is carried out only by the gas flow. The use of a large cell to stop relatively high energy ion beams, however, would take much more time. Possible loss processes such as charge exchange and diffusion to the wall become effective.

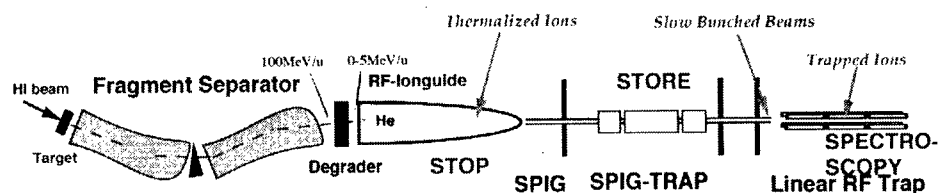


FIGURE 2. Overview of the proposed scheme

Due to the ion charge, the thermalized ions in the gas must be manipulated by an electric field. However, if a simple static electric field is applied, the ions would be lost at the cathode since the average ion motion under such high-pressure just follows the electric lines of force. There are two possible solutions to avoid the losses at the cathode electrode. One way is to apply a gas flow and the other way is to use an rf barrier field. The former is only applicable at the region very close to the exit where a significant gas flow speed is expected. In the latter, the cathode electrode is replaced by a series of lined ring electrodes on which rf voltages are applied. The electrodes produce a local rf gradient field on the surface. The average force due to the rf gradient field becomes repulsive against the electrode (Fig. 3). The fundamental principle is the same

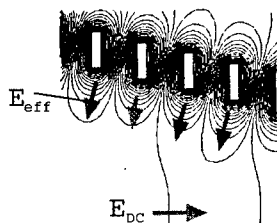


FIGURE 3. rf gradient field produced by a series of ring electrodes.

as an rf quadrupole ion trap developed by W. Paul in 1953. The first experimental test of this structure for manipulating charged micro-particles in an atmospheric pressure

air was performed by Masuda et al. in early 1970s, they called *electric field curtain* or *rf hopper* [11]. They aimed at industrial applications such as an ink-jet printer. We proposed to incorporate this *rf funnel* structure into the ion-guide gas cell to manipulate singly charged radioactive nuclear ions [12, 13].

Simulation

In order to understand the detail of the rf ion guide scheme, we performed several ways of ion motion analysis. The fundamental equation of motion is

$$m\ddot{\mathbf{r}} = e\mathbf{E}(r, t) \quad (3)$$

where m is the mass of ion and \mathbf{E} is the electric field (a function of coordinate and time). The first method is a microscopic Monte Carlo simulation which could start from this equation. The presence of a gas is taken into account by including classical potential scattering at each collision between ion and gas molecules. The scattering angle in the center of mass system is

$$\theta_{CM}(b, E) = \pi - 2 \int_{R_{min}}^{\infty} \frac{b}{r^2} \frac{dr}{\sqrt{1 - (b/r)^2 - V(r)/E}} \quad (4)$$

where b is the impact parameter, E the relative energy, and R_{min} the root of $1 - (b/R_{min})^2 - V(R_{min})/E = 0$. We have chosen a scattering potential accordingly

$$V(r) = \frac{\varepsilon}{2} \left[(1 + \gamma) \left(\frac{r_m}{r} \right)^{12} - 4\gamma \left(\frac{r_m}{r} \right)^6 - 3(1 - \gamma) \left(\frac{r_m}{r} \right)^4 \right]. \quad (5)$$

The parameters γ , ε and r_m were taken from the literature [14].

The dc and rf electric field maps were calculated independently by the POISSON [15] code, obtaining the total electric field as a function of time:

$$\mathbf{E}(r, t) = \mathbf{E}_{dc}(r) + \mathbf{E}_{rf}(r) \cos(\Omega t). \quad (6)$$

Typical ion trajectories are depicted in Fig. 4. The figure shows a part of the cell which is close to the exit. The electrode structure consists of a nozzle part and a large funnel part. The nozzle part is made of 70 ring electrodes with an interval of 0.3 mm. It has an aperture of 0.4 mm at the exit and an aperture of 11.2 mm at the top. The large funnel part follows at the top of the nozzle part. The interval of each electrode in this part is 0.5 mm and the aperture at the bottom is 10 mm. One trace of simulation with a 500 MHz Alpha processor required several minutes of computational time.

The microscopic simulation clearly shows the transport of ions in the rf ion guide. However, an analytical approach is more helpful to understand the various physical processes. We employed the *mobility* (μ) of ions in the gas to simulate the effect of multiple collisions as a frictional force. The equation of motion is

$$m\ddot{\mathbf{r}} + \frac{e}{\mu} \dot{\mathbf{r}} = e\mathbf{E}(r, t). \quad (7)$$

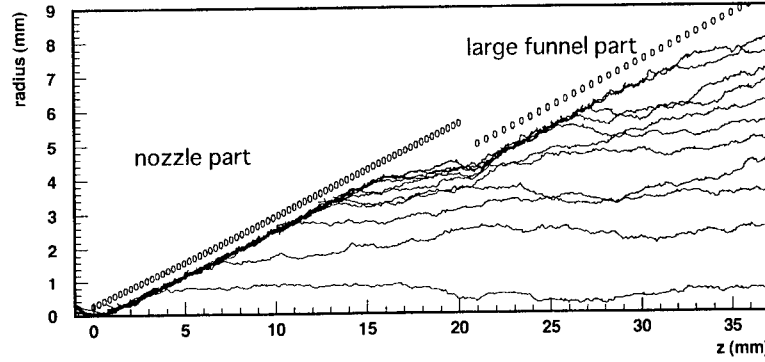


FIGURE 4. Typical ion trajectories by microscopic simulation. ^8Li ions in 30 Torr He gas, rf amplitude 80 V, rf frequency 10 MHz, dc gradient field 12 V/cm.

If we define the velocity relaxation time as $\tau_v = m\mu/e$, the equation becomes

$$\dot{r} + \frac{1}{\tau_v} \dot{r} = \frac{e}{m} (\mathbf{E}_{dc}(r) + \mathbf{E}_{rf}(r) \cos(\Omega t)). \quad (8)$$

This equation permits two different ways of analysis. If we assume that the field very close to the electrode is a quadrupole field, Eq. (8) is simplified in a Mathiu equation,

$$u'' + 2pu' + (a - 2q \cos 2\tau)u = g \quad (9)$$

with the non-dimensional parameters $a = 8eV_{dc}/mr_0^2\Omega^2$ being the index of dc offset $q = 4eV_{rf}/mr_0^2\Omega^2$ being the index of rf field strength $p = e/m\mu\Omega = 1/\tau_v\Omega$ being the index of gas pressure $g = 4eE_{dc}/m\Omega^2$ being the index of external force and $\tau = \Omega t/2$. The terminal voltage of the assumed quadrupole electrode is assigned as V_{rf} and V_{dc} and the half distance of the electrode is assigned as r_0 . The stability analysis of an ordinary Mathiu equation could be performed using this equation. Details of this analysis will be reported elsewhere [16].

Another way of to analyze Eq. (8) is the pseudo potential approach. The rf electric field is averaged over a cycle to deduce the strength of the effective electric field due to the rf gradient field. We omit the static field in Eq. (8) and split the motion of an ion into a slow average motion \bar{r} and a small oscillation motion $\rho(t)$ as

$$r = \bar{r} + \rho(t) = \bar{r} + c\mathbf{E}_{rf}(r) \cos(\Omega t + \beta). \quad (10)$$

The coefficient c is deduced by inserting the derivative of Eq. (10) into Eq. (8), then the small oscillation is

$$\rho(t) = -\frac{e}{m\Omega} \frac{\mathbf{E}_{rf}(r)}{\sqrt{\Omega^2 + 1/\tau_v^2}} \cos(\Omega t + \beta), \quad \tan \beta = \frac{1}{\tau_v^2 \Omega^2}. \quad (11)$$

The average force \bar{F} due to the gradient rf electric field is

$$\bar{F}(\bar{r}) = e \langle \mathbf{E}_{\text{rf}}(\bar{r}) \cos \Omega t + [\nabla |_{r=\bar{r}} \mathbf{E}_{\text{rf}}(r)] \rho(t) \cos \Omega t \rangle_{\text{av}} = -\nabla E_{\text{rf}}^2(\bar{r}) \frac{e^2}{4m(\Omega^2 + 1/\tau_v^2)}. \quad (12)$$

Eq. (12) is simplified in two extreme cases, the vacuum limit and the high pressure limit, respectively

$$\bar{F}(\bar{r}) = \begin{cases} -\nabla E_{\text{rf}}^2(\bar{r}) \frac{e^2}{4m\Omega^2}, & \text{for } \Omega^2 \tau_v^2 \gg 1 \quad (\text{vacuum}) \\ -\nabla E_{\text{rf}}^2(\bar{r}) \frac{e^2}{4m} \tau_v^2, & \text{for } \Omega^2 \tau_v^2 \ll 1 \quad (\text{high pressure}). \end{cases} \quad (13)$$

If we assume again a quadrupole field close to the electrode, the average force in high pressure limit is

$$\bar{F}_{\text{hp}} = -\frac{e^2}{4m} \tau_v^2 \frac{8V_{\text{rf}}^2}{r_0^3} \left(\frac{r}{r_0} \right) = -m\mu^2 \frac{V_{\text{rf}}^2}{r_0^3} \left(\frac{r}{r_0} \right). \quad (14)$$

If we assume the mobility being simply proportional to the reciprocal of the pressure, heavier ions in lower pressure gas are manipulated by weaker rf field. It should be noted, however, that the pseudo potential analysis does not provide any information about the stability.

EXPERIMENT

We first tested the rf ion-guide system off-line and then constructed a proof of the principle (POP) system for on-line test experiments. The on-line test was performed at the RIKEN projectile fragment separator RIPS which provides us a 70-MeV/u ^8Li ion beam with an intensity of $\sim 10^6$ atoms/s from a primary beam of 70-MeV/u ^{13}C and a production target of ^9Be . We choose ^8Li for the test ion beam instead of ^{11}Be , since the detection of ^8Li , which emits two alpha particles followed by the β -decay, is efficient and reliable.

The fragment separator consists of two dipole magnet and an energy degrader in between the two magnets. The first magnet analyzes for A/Z of the fragment ions and the second one for $\sim A^{2.5}/Z^{1.5}$, since the dependence of energy loss in the degrader is different for Z and A . The separator thus provides pure isotopic ions in many cases. Although there are many impurity ions, we used only a half part of the separator. An advantage of using the half part is that we can put our system at the momentum dispersive focal point. It allows us to use a wedge shaped energy degrader for mono-energetic deceleration. The impurity ions, on the other hand, can be eliminated by a so called range separation; heavier ions such as $^{10,11}\text{Be}$ stop in the degrader and lighter ions such as ^3H just pass through the gas cell.

Apparatus

In the off-line test [17], multiple metallic plates were used to form the rf electrodes. The distance between the electrodes was 2.5 mm. More than 50 % transmission effi-

ciency was achieved for Ta ions under the conditions of 30 Torr He pressure and an rf amplitude of 50 V. A pressure of 30 Torr was too low for practical experiments. We therefore set the target pressure 150 Torr, which corresponds to the stopping capabilities of 5 MeV/u for medium to heavy ions and 2.5 MeV/u for very light ions, if the depth of the cell is 2 m. To operate the rf ion guide mechanism under such high pressure, decreasing r_0 is the most effective way while an increase of the voltage is limited by discharge problems. According Eq. (14), a transport of Li ions in 150 Torr He gas could be realized if a higher rf amplitude (~ 150 V) is achieved and a fine structure electrode assembly with a distance of 0.3 mm or 0.5 mm between electrodes is fabricated. This type of electrode assembly was fabricated with a flexible printed circuit board.

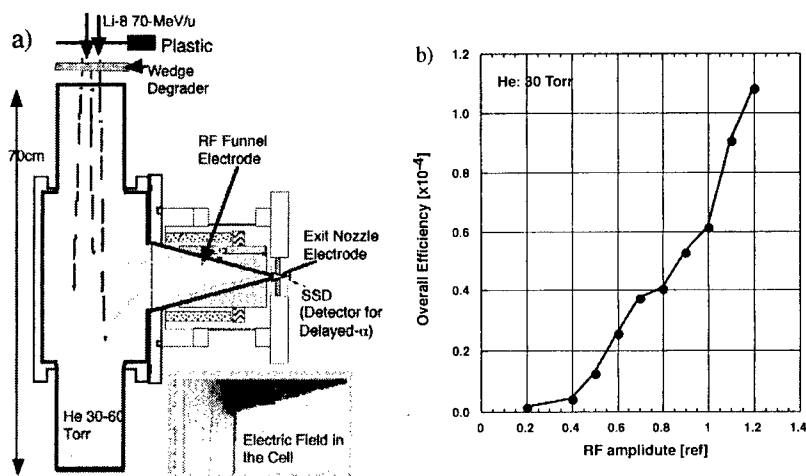


FIGURE 5. Experimental setup of the POP system (a). Overall efficiency plotted as a function of applied rf amplitude (b). Gas pressure was 30 Torr, dc field gradient 10 V/cm, rf amplitude about 40 V at ref=1.0, rf frequency 10 MHz.

A schematic diagram of the POP setup is shown in Fig. 5a. The gas cell is made of a simple vacuum duct with diameter of 10 cm and length of 70 cm. The duct is orthogonally connected to the rf funnel structure of 10 cm aperture. The stopped ^8Li ions are transported by static electric field, which penetrates from the aperture, to the funnel part where the rf barrier field protects ions from the collision to the electrodes. We took the orthogonal geometry in order to avoid the direct implantation of ^8Li ions into the detector and also to make sure that the ions are transported by the electric field, not only from the region very close to the exit but also from the region very far from the exit.

Results and discussion

Figure 5b shows an experimental result of transporting ^8Li ions. We define the overall efficiency as a ratio of detected counts of delayed alpha particles from ^8Li to the number of ^8Li ions output from the RIPS. The overall efficiency was plotted as a function of the applied rf amplitude. The dc field was fixed to 10 V/cm at the center of the funnel structure electrode assembly. We could clearly see the effect of rf field applied in the ion guide gas cell and obtained a typical overall efficiency of 10^{-4} at a condition of the He gas pressure of 30 Torr and rf amplitude of 40 V. We split the efficiency into two components: First the gas stopping efficiency which indicates how much fraction of injected ^8Li ions can be stopped in the volume of the cell, and, second, the ion transport efficiency by the electric field. We put a collimator in front of the cell to deduce the radial acceptance of the cell which was obtained to be 28 %. Combined with a range calculation by the TRIM code [18], we obtained the stopping efficiency of 0.43 % and thus the transport efficiency of 2.4 %.

We compared the yield at different gas pressures of 30 Torr and 60 Torr. The yield at 60 Torr was lower than at 30 Torr. It is considered to be due to the fact that the rf amplitude was too low for transporting ^8Li ions in He gas of 60 Torr. We also tested the yield dependence on the length of the cell. The longer cell showed a higher yield than the shorter one. This indicates that even if ions are stopped in the region very far from the exit were transported by the electric field.

The overall efficiency of 10^{-4} of the present POP system was limited by the known reasons. The gas stopping efficiency could be increased up to 10 % range simply by increasing the size of cell and possibly by increasing the pressure. The ion transport efficiency could be increased also towards the 10% range by increasing the rf amplitude.

Based on the experience with the POP system we are now constructing a new system. The new gas cell is 40 cm in diameter and 2 m in length. It is capable of in-line extraction as well as orthogonal extraction. The rf system has been extensively modified. In the POP system, rf divider circuits were placed outside the cell and many long cables transported the power through a feedthrough resulting a large capacity and heat dissipation. The new rf electrode is made of a flat doughnut form plate with an outer diameter of 25 cm and an inner hole diameter of 14 mm in addition to the small funnel structure at the nozzle part. The effective aperture of 25 cm causes stronger penetration field in the whole area of the cell. The rf divider circuits are soldered on the back surface of the doughnut plate and the matching coil has a water cooling capability. This reduces the capacity as well as the required power. Typical operating parameter conditions are 10 MHz and 150 V. This can be achieved by applying an rf power of about 30 W.

CONCLUSION

We have tested the rf ion-guide system for collecting energetic radioactive beam from a projectile fragment separator. The proof of the principle model has a compact sized gas cell with a diameter of 10 cm and a length of 70 cm with an rf funnel structure of 10 cm aperture and a nozzle structure of 0.5 mm aperture: the model was shown to be effective

for collection of ^8Li . The overall efficiency of the compact system was 10^{-4} with a gas stopping efficiency of 0.43% and a transporting efficiency of 2.4%. Both efficiency must be improved by increasing the size of the cell and amplitude of the applied rf voltage.

We conclude that the aimed goal of an overall efficiency of 1 % should be feasible. It should be noted that the overall efficiency of an ordinary ISOL type target ion-source system rarely exceeds 1 % range for many elements, while the combination of a fragment separator and the rf ion guide system is, in principle, independent to the chemical property of the nuclides.

We plan to perform the hfs spectroscopy experiment for ^{11}Be with the new rf ion-guide system within a year. A low energy radioactive beam experimental facility based on this technique will be prepared in the RIKEN RI-beam factory.

ACKNOWLEDGMENT

We would like to thank Mr. Y. Chiba for useful suggestions concerning the rf system of the new setup. We also thank the crew of the RIKEN accelerator facility for providing the beam for the on-line test experiment. The project is financially supported by Grants-in-Aid for Scientific Research from Japan Society for the Promotion of Science.

REFERENCES

1. <http://ribfweb1.riken.go.jp/>.
2. M. Wada, H. Xu, J. Tanaka, H. Kawakami, I. Katayama, K. Okada, and S. Ohtani, *Hyp. Inter.* **81** (1993) 161.
3. A. Bohr and V. F. Weisskopf, *Phys. Rev.* **77**, 94 (1950).
4. T. Fujita, K. Ito, T. Suzuki, *Phys. Rev. C* **59**, 210 (1999).
5. M. Wada, K. Okada, H. Wang, K. Enders, F. Kurth, T. Nakamura, S. Fujitaka, J. Tanaka, H. Kawakami, S. Ohtani and I. Katayama, *Nuclear Physics A* **626**, 365c (1997).
6. S. Fujitaka, M. Wada, H. Wang, J. Tanaka, H. Kawakami, I. Katayama, K. Ogino, H. Katsuragawa, T. Nakamura, K. Okada, and S. Ohtani, *Nucl. Instrum. and Meth. in Phys. Res. B* **126**, 386 (1997).
7. K. Okada, M. Wada, T. Nakamura, R. Iida, S. Ohtani, J. Tanaka, H. Kawakami, I. Katayama, *J. Phys. Soc. Japan* **67**, 3073 (1998).
8. T. Nakamura, S. Ohtani, K. Okada, M. Wada, I. Katayama and H. A. Schuessler, *J. Appl. Phys.* **89**, 2922 (2001).
9. T. Nakamura, M. Wada, K. Okada, I. Katayama, S. Ohtani, and H. A. Schuessler, submitted to *Opt. Comm.*
10. J. Ärje, J. Äystö, H. Hyvönen, P. Taskinen, V. Koponen, J. Honkanen, K. Valli, A. Hautojärvi, and K. Vierinen, *Nucl. Instr. and Meth. A* **247**, 431 (1986).
11. S. Masuda, K. Fujibayashi, K. Ishida, *Adv. in Static Electricity*, pp 398-414, Auxillia SA, Brussels, 1970.
12. M. Wada and I. Katayama, presented in the *Int. Workshop on Ion Guide Isotope Separator On-Line (IGISOL-6)*, Dubna 1997, unpublished.
13. I. Katayama, M. Wada, H. Kawakami, J. Tanaka, K. Noda, *Hyper. Inter.* **115**, 165 (1998).
14. E.A. Mason et al., *Phys. Rev.* **112**, 445 (1958).
15. <http://laacg1.lanl.gov/laacg/services/possup.html>.
16. M. Wada et al., in preparation.
17. M. Wada et al., *RIKEN Review*, **31**, 56 (2000).
18. <http://www.srim.org>.

System of Slow Highly Charged Ion Beam Generation Using a Cold Positron Plasma Trap at RIKEN

Akihiro Mohri*, Takao M. Kojima*, Nagayasu Oshima*†,
Megumi Niigaki*† and Yasunori Yamazaki*†

* Atomic Physics Laboratory, The Institute of Physical and Chemical Research (RIKEN),
Wako 351-0198, Japan

† Institute of Physics, Graduate School of Arts and Sciences, University of Tokyo,
Tokyo 153-8902, Japan

Abstract. A system to generate ultra-slow beams of highly ionized ions (HCIs) is under construction at RIKEN for studying collision processes of slow HCIs with atoms, molecules and surfaces. HCIs beams produced with an ECR ion source are transported to a multi-electrode trap, which can include several local harmonic potential wells enabling to confine different nonneutral plasmas of oppositely charged particles. Injected HCIs are decelerated by a dense electron plasma and then, to evade their recombination with electrons, cooled further with a positron plasma under cyclotron radiation cooling. This electron plasma also works as the damper of slow positrons at their loading into the trap. The cold HCIs are finally extracted from the trap as an ultra-slow beam with well-defined energy and used for slow collision experiments.

INTRODUCTION

Production of highly charged ions (HCIs) of ultra low velocities is expected to give an effective means for studies of interaction processes of slow HCIs with matter [1]. A new project to generate very slow HCI beams by using a nonneutral plasma trap has been started at RIKEN. Since different nonneutral plasmas as electrons, positrons and HCIs should be manipulated in the trap, a multi-ring electrode trap [2] is adopted, which can produce a variety of axially symmetric configurations of electric field.

The following is a rough sketch to generate a cold HCI beam using the trap. A dense electron plasma is formed in the trap for a start. Subsequently, slow positrons are injected into the trap and stacked subject to collisional damping by the electrons. Non-adiabatic process employed here is Coulomb collisions between electrons and positrons. At that phase, the electron plasma and the positron plasma are simultaneously confined in different regions of the trap and they are cooled by cyclotron radiation. An HCIs beam is then transported from an ECR ion source to the trap and captured in it by changing its potential barrier. The trapped HCIs are mainly

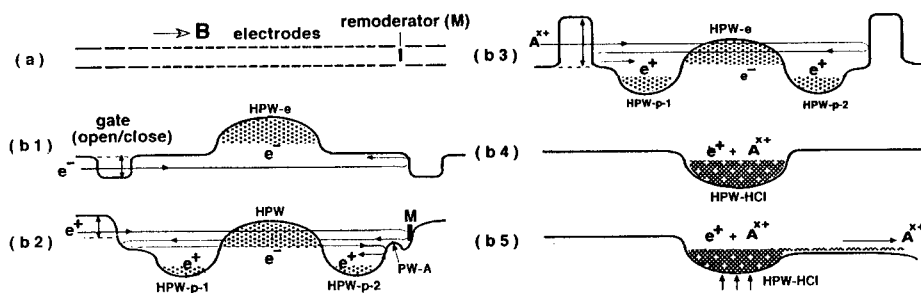


Figure 1. (a) Alignment of electrodes of the trap. (b1 - 5) Potential configurations in operational stages. (b1) Loading of electrons, (b2) Stacking of positrons, (b3) Injection and deceleration of HCl beam, (b4) Positron cooling of HCl, (b5) Extraction of an ultra-slow HCl beam. HPW indicates the portion of a harmonic potential well, and PW-A is a low potential hill.

cooled down by the electrons at the beginning. When the energies of HCl become lower, they are separated from the electrons to fall into the positrons, evading recombination loss of HCl. After the HCl thermally equilibrate with the cold positrons, they are extracted as a cold beam with a well-defined energy.

This report discusses the fundamental procedure mentioned above, in addition to a brief description of the trap.

Trap

A sketch of the trap is shown in Fig.1(a). Twenty seven ring electrodes of 3.8 cm inner diameter are aligned in the bore of a superconducting solenoid, which generates uniform magnetic field of 5 T over the axial length of 50 cm. Installation of many electrodes enables to form different configurations of electrostatic potential necessary for the manipulation. Two of the electrodes are cut into 4 sectors to be used for compression and diagnosis of trapped plasmas. All beams of electrons, positrons and HCl are injected into the trap from the one side. On the down stream side, a removable tungsten plate of single crystal is installed to remoderate the incoming positrons.

HCl of the charge state q are injected into the trap with energies of about $3 \text{ keV}/q$ and then cooled. To avoid their charge-exchange losses with residual gas molecules, the vacuum pressure of the trap is required to be 10^{-9} Pa or lower [3]. This ultra-high vacuum is realized by keeping the trap at the temperature less than 10 K. Such an environment also helps the radiation cooling of electrons and positrons.

Stacking of Electrons and Positrons

An electron gun is set at an off-axial position outside the trap to ensure the axial beam paths of positrons and HCl. The emitted electron beam launches onto the axis

making $E \times B$ drift motion, which is induced by applying an electric field perpendicular to the leaked magnetic field from the main SC-solenoid. The beam electrons are stacked by raising the gate potential as shown in Fig.1(b1). They finally settle in the central harmonic potential well (HPW-e) and become colder due to cyclotron radiation cooling. This cold electron plasma is spheroidal, characterized by the parameters as the radius a , the half axial length of b and the density n_e . Although there are a lot of choices of these parameters, later discussions will be made using a spheroidal electron plasma with $a=0.25$ mm, $b=10$ cm and $n_e=1 \times 10^{11}$ cm $^{-3}$. After the electron plasma is formed, the potential distribution is rearranged to add two harmonic wells: HPW-p-1 and HPW-p-2 to trap positron plasmas on the both sides of the electron plasma (Fig.1(b2)).

A slow positron beam is produced by combining a solid Ne moderator with a positron source of 40 mCi ^{22}Na [4,5]. The attainable beam intensity is about 10^7 e $^+$ /s. It is guided toward the trap with a magnetic duct. On reaching the SC-solenoid, the beam is once accelerated up to ~ 1 keV to get over the magnetic mirror present there. In the trap, the beam radius is $r_{e+}=0.1$ mm, and its energy parallel to the magnetic field spreads to ~ 1 keV. To reduce this energy spread, the beam positrons are implanted into the tungsten remoderator shown in Fig.1(b2). About 30 % of the implanted positrons are expected to emerge backward from the remoderator with the energy of 2~3 eV. Before this implantation, the beam once passes through the electron plasma but the caused energy loss is small because of high beam energy.

Figure 2 shows energy decay of positrons through the electron plasma of $n_e=1 \times 10^{11}$ cm $^{-3}$ as a function of their penetrated depth d . Here, the decay is estimated from the longitudinal momentum change of positrons moving in the electron plasma [6], since the loss of longitudinal energy is essential when we consider the axial motion in the potential well. The hatched lines in the figure indicate one path length of positron

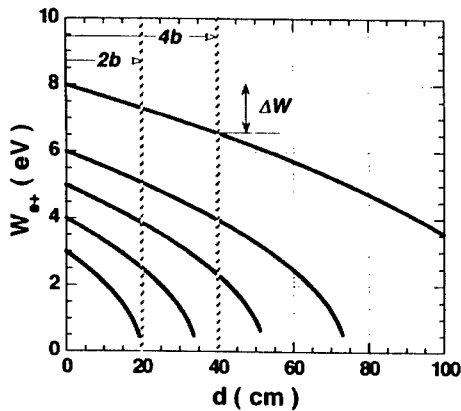


Figure 2. Decrease of positron beam energy W_{e+} as a function of penetration depth d for $n_e=1 \times 10^{11}$ cm $^{-3}$.

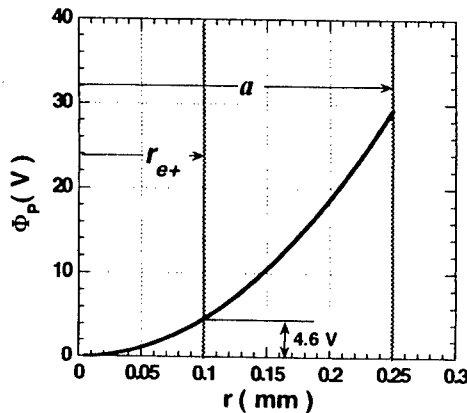


Figure 3. Internal potential of the plasma on the midplane $\Phi_p(r)$ for the case $a=0.25$ mm and $n_e=1 \times 10^{11}$ cm $^{-3}$.

through the plasma $2b=20$ cm and the double one $4b=40$ cm. The plasma potential radially increases, as is shown in Fig.3. We express this variation as $\Phi_p(r)$, where $\Phi_p(0)=0$. Let the potential of the remoderator and the energy of re-emitted positron be Φ_M and W_M , respectively, then the incident positron energy into the plasma is written by $W_{IN}(r)=\Phi_M+W_M-\Phi_p(r) > 0$. Incident positrons returning back after twice passes through the plasma lose their energies by ΔW . If $\Delta W > W_M$, the positron is kept off from re-entering the remoderator. Reduction of ΔW may relax requirements for n_e and b of the electron plasma. When a low potential hill Φ_A (PW-A in Fig.1) is added just in front of the remoderator such that $\Phi_M < \Phi_A < (\Phi_M + W_M)$, ΔW is reduced by $(\Phi_A - \Phi_M)$, so that $\Delta W > W_M - (\Phi_A - \Phi_M)$.

For the example electron plasma, Φ_p varies from 0 to 4.6 V within the radius of the incident positron beam r_{e+} (Fig.3). Also, W_M is 2-3 eV as mentioned above. When we set $\Phi_A = 4.5$ V and $\Phi_M = 2.6$ V, all re-emitted positrons can pass the potential hill PW-A, since $\Phi_A < (\Phi_M + W_M)$. In this case, W_{IN} is distributed in a range of 0-5.6 eV. As is seen in Fig.2, incident positrons of 5.6 eV return back with the energy ~ 3 eV and they are reflected by PW-A. They are again damped by the electron plasma. In this way, all of the re-emitted positrons are either sufficiently slowed down or stopped in the plasma. They are expected to finally settle in the harmonic wells: HPW-p1 and HPW-p2 in Fig.1. The positrons with the total number $N_{e+} \approx 1 \times 10^8$ are estimated to be stacked within 100 s.

The harmonic wells for positrons are formed by applying allocated voltages on the electrodes through resistors with high impedances, so that the electrodes work as a resistive wall. Besides, once some slow positrons accumulate in these wells, they damp positrons incoming later. Such a damping mechanism and application of rf field may contribute to make the positron stacking more efficient [7].

Cooling of HCIs

Deceleration of HCI beam by Electron Plasma

We shall start our discussions from the situation that HCIs of charge state q are just trapped between the potential barriers set on the both ends of the main trap as shown in Fig.1(b3). The dense electron plasma interacts with the HCIs through Coulomb collisions. Let the beam energy, the density and the total number of HCIs be W_{HCI} , n_{HCI} and N_{HCI} , respectively. The ratio of $2b$ to the length of the HCI trap is noted by α . The HCIs lose their energies by heating the electrons, while the electrons are cooled by cyclotron radiation. The cooling time used here is empirically obtained from experiments on ASACUSA-Trap [8] which is now in operation at CERN [9]. This

time is expressed as $\tau_R \approx 6/B^2$ s where B is in Tesla. Neglecting interactions among HCIs, we formulate the rates of change in W_{HCl} and electron temperature T_e as [6]

$$\frac{dW_{\text{HCl}}(t)}{dt} = -\alpha F(n_e, T_e(t), q, W_{\text{HCl}}(t), \beta), \quad (1)$$

$$\frac{dT_e(t)}{dt} = \frac{2}{3} \frac{N_{\text{HCl}}}{k_B N_e} \alpha F(n_e, T_e(t), q, W_{\text{HCl}}(t), \beta) - \frac{T_e(t)}{\tau_R}, \quad (2)$$

where β and k_B are the reduced mass and Boltzmann constant. The function F includes Coulomb logarithm and velocity of HCl, which are all given by the denoted variables. Solving these equations, we can find the time evolutions of W_{HCl} and T_e .

The case of Ar^{8+} is taken as an example. The initial condition at $t=0$ is set as follows; $B=5$ T, $N_e=2.7 \times 10^9$, $n_e=1 \times 10^{11} \text{ cm}^{-3}$, $T_e=0.01$ eV, $N_i=1 \times 10^7$, $W_{\text{HCl}}=10$ keV, and $\alpha=0.2$. Figure 4 shows the results. Immediately after the start of damping, the beam energy decreases fast, while T_e rapidly rises. Then, T_e reaches its peak of 18 eV and smoothly decreases with time. On the other hand, W_{HCl} continuously gets lower toward $k_B T_e$. The deceleration of 10 keV Ar^{8+} is almost finished within 0.3 s.

The HCl beam also heats up the positrons which are being cooled by cyclotron radiation. However, the coupling is weak since the positron density n_{e+} is much lower than n_e . Here dominates the radiation cooling. When the positron total number is $N_{e+}=10^8$, the positron temperature T_{e+} rapidly rises but it saturates at 2.7 eV.

When both of W_{HCl} and T_e decrease to a few eV, the electrons are exhausted from the trap by changing the potential profile as shown in Fig.1(b4). This electron removal is necessary to evade HCl-electron recombination at lower T_e . By this potential change,

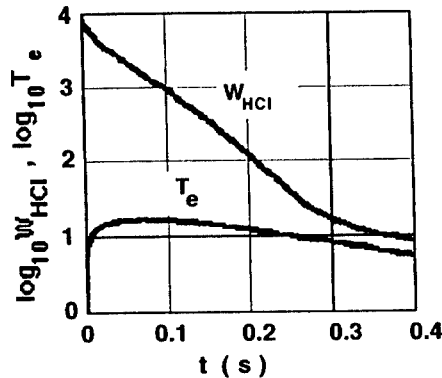


Figure 4. Time evolutions of W_{HCl} and T_e during the deceleration of HCIs in the electron plasma of $n_e=1 \times 10^{11} \text{ cm}^{-3}$. Energy is in eV.

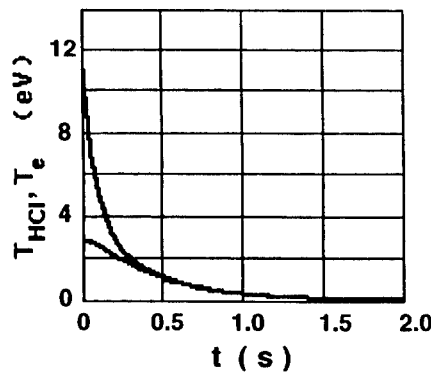


Figure 5. Time variations of W_{HCl} and T_{e+} of the mixed plasma, where $N_{\text{HCl}}=1 \times 10^7$, $T_{\text{HCl}}=12$ eV, $n_{e+}=1 \times 10^9 \text{ cm}^{-3}$, and $T_{e+}=2.7$ eV at $t=0$.

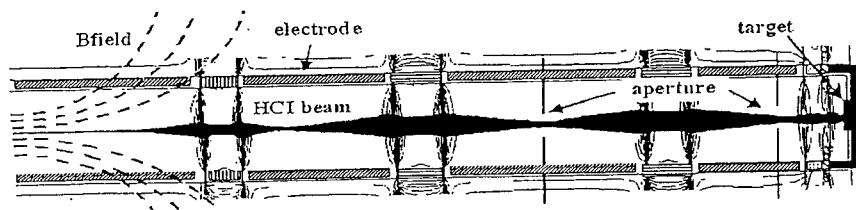


Figure 6. Beam line consisting of Einzel lenses for extraction of ultra-slow beams.

the HCIs and the positrons are mixed in the newly formed trap: HPW-HCI shown in Fig.1.

Positron Cooling and Extraction of HCIs

The HCIs in HPW-HCI becomes colder through the temperature equilibration with the positrons which are under cyclotron radiation cooling. The time evolution of the HCI temperature T_{HCI} is easily estimated by adding a radiation loss term to usual temperature relaxation equations. To clearly demonstrate the cooling, we choose the initial T_{HCI} to be somewhat as high as $T_{\text{HCI}}=12$ eV. The other parameters are $B=5$ T, $N_{e^+}=1 \times 10^8$, $T_{e^+}=2.7$ eV, $n_{e^+}=1 \times 10^9 \text{ cm}^{-3}$ and $N_{\text{HCI}}=1 \times 10^7$. These values correspond to the situation at 0.2 s in Fig.4. The estimated time variations of T_{HCI} and T_{e^+} are shown in Fig.5. Temperature equilibration between the HCIs and the positrons finishes within 0.3 s and, after then, the equilibrated temperature decreases to that determined either by the environmental noise temperature or by the wall temperature. Thus, there are produced cold HCIs.

The cold HCIs are finally extracted as an ultra-slow beam from the trap set in 5 T magnetic field [10]. A beam line consisting of Einzel lenses is used for the extraction. Figure 6 shows the arrangement of lenses and the HCI beam trajectories in the line. Two lenses at the exit of the trap accelerate HCIs to suppress the spatial beam divergence caused by the strong magnetic field gradient. The other lenses take parts to make nodes of the trajectories and also to decelerate and focus the beam. Disks with small apertures are installed at these node positions, which enable differential pumping of gas which is coming back from the region of atomic collision experiments.

Present Status and Examination of Scenario

A scenario to generate ultra-slow HCIs has been described and the system is near completion at RIKEN. Realization of the scenario has been checked at each stage of

the assembling. The SC magnet stably works to generate 5 T and the trap housed in the inner bore can be cooled down to 9 K. To increase the production efficiency of a slow positron beam, several different structures near the ^{22}Na positron source have been examined experimentally [11]. At present, the HCI source is supplying HCI beams to the other experimental devices for atomic physics.

A dense electron plasma is requisite for damping remoderated slow positrons in order to realize the scenario. When a spheroidal electron plasma is slim enough, its density can be high with the small total number of electrons. No deep harmonic potential well is necessary in this case and also image charge effects caused by the surrounding walls are small. Formation of such a plasma was experimentally checked at $B=5\text{ T}$. A long harmonic potential well of 46 cm length and 60 V well depth was made in the central region of the trap. Very slender plasmas were formed in the well. Their typical parameters were $N_e=1.9\times 10^8$, $a\sim 0.07\text{ mm}$, $2b\sim 25\text{ cm}$ and $n_e\sim 7\times 10^{10}\text{ cm}^{-3}$. The confinement time was about 8 hours. These results suggest that the electron plasma of $n_e=1\times 10^{11}\text{ cm}^{-3}$ in the example mentioned above, is easily producible. However, very fine adjustment of the plasma parameters is necessary since we have to accurately set a small potential difference between the plasma and the tungsten remoderator. To make the adjustment easier, alternative potential configurations and operational schemes are now under study.

REFERENCES

1. *Production of Ultra Slow Highly-Charged Ions*, edited by Y. Yamazaki, RIKEN, *RIKEN Rev.* **31**, Wako, 2000.
2. Mohri, A., Higaki, H., Tanaka, H., et al., *Jpn J. Appl. Phys.* **37**, 664-670 (1998).
3. Kojima, T. M., et al., *RIKEN Rev.* **31**, edited by Y. Yamazaki, RIKEN, Wako, 2000, pp.70-73.
4. Surko, C. M., Leventhal, M., and Passner, A., *Phys. Rev. Lett.* **62**, 901-904 (1989).
5. Murphy, T. J., and Surko, C. M., *Phys. Rev. A.* **46**, 5696-5705 (1992).
6. Sivukhim, D. V., *Rev. of Plasma Physics*, edited by M. A. Leontovitch, Consultant Bureau, New York, 1966, pp.93-241.
7. Mohri, A., Yuyama, T., Tanaka, H., et al., *Jpn. J. Appl. Phys.* **39**, 6726-6731 (2000).
8. Higaki, H., et al., to be submitted to *J. Appl. Phys.*.
9. Yamazaki, Y., *Nucl. Instrum. Methods*, **B154**, 174-184 (1999).
10. Niigaki, M., Ohshima, N., Kojima, T. M., and Yamazaki, Y., "Extraction System for ultra-slow highly-charged ions from a trap in a strong magnetic field", in *22nd International Conference on Photonic, Electronic, and Atomic Collisions (XX-II ICPEAC)*, edited by S. Datz, et al., Rington Press Inc., Princeton, 2001, p. 689.
11. Oshima, N., Kojima T. M., et al., "Production scheme of a slow highly charged ion beam using a positron cooling technique" in *XX-II ICPEAC*, edited by S. Datz, et al., Rington Press Inc., Princeton, 2001, p. 681.

Proposed Non-neutralized Two-Fluid Plasma Experiment

Haruhiko Himura, Zensho Yoshida, Masayuki Fukao,
Junji Morikawa, and Yuichi Ogawa

*University of Tokyo, Department of Advanced Energy,
Graduate School of Frontier Sciences, Hongo, Tokyo 113-0033, Japan*

Abstract. An experimental test of generating ion flow under a complete charge non-neutral condition is proposed. On the experiment, a quasi-neutral plasma is injected into a pure electron plasma which is confined in a Malmberg type trap. So far, the device named BX-U (Beam Experiment Upgrade) confines only electrons having density of $10^{11-12} \text{ m}^{-3}$ for $\sim 0.3 \text{ s}$ with $B_z \sim 50 \text{ G}$. After completing a plasma gun, the first series of a two-fluid plasma experiment will be initiated.

I INTRODUCTION

A possibility of extremely high- β equilibrium (β can exceed unity) with a strong sheared flow was theoretically pointed out, which was based on the double-curl Beltrami field [1]. In fact, under some theoretical and simulation works obtain several high- β solutions in both cylindrical and toroidal geometry. The requirement to this high- β equilibrium is to maintain two-fluid effects with the large velocity field whose magnitude is comparable to that of the magnetic field in the plasma. Another significant feature of the high- β equilibrium is that the thermal pressure of plasmas is sustained by the hydrodynamic pressure of the strong shear flow, alleviating the strength of magnetic fields to confine the plasmas which offers attractive benefits including the lowest construction costs among toroidal fusion systems.

To generate such a fast flow in a plasma, a charge non-neutral condition has been proposed [2] which inherently produces a strong self-electric field \mathbf{E} inside the plasma, causing a fast $\mathbf{E} \times \mathbf{B}$ sheared flow if we apply an appropriate magnetic field \mathbf{B} . Then the question is asked on how such a non-neutralized plasma can be produced in laboratory experiments. Although several methods can be considered, we have proposed to add a charge neutral plasma to a pure electron plasma. If the two plasmas are well mixed together, a perpendicular

ion flow would be driven inside the two-fluid plasma due to \mathbf{E} . Furthermore, if the flow is fast enough in the electrically non-neutralized plasma, the structure of \mathbf{B} may exhibit a diamagnetic profile, which is required to attain a high- β value, as the theory [1] points out.

In order to explore this way, we have conducted experiments on a toroidal machine Proto-RT [3] and recently, upgraded a small linear device. This machine, named BX-U (Beam Experiment Upgrade), is based on the Malmberg type trap [4] and equipped with a Marshall type plasma gun [5] at the end of the downstream of the device. The goal of BX-U is to demonstrate a fast azimuthal ion rotational flow which is perpendicular to \mathbf{B} under the charge non-neutral condition and investigate fundamental physics of the non-neutralized two-fluid plasmas especially with the focus on the transport phenomenon related to the flow damping. A description of the BX-U device is explained in Sec. II. The first experimental data of pure electron plasmas and a summary are given in Sec. III and IV, respectively.

II APPARATUS OF THE BX-U DEVICE

BX-U is a Malmberg type linear trap which is being constructed to investigate the fundamental plasma physics of (1) charge non-neutralization, (2) rotational ion flow induced by \mathbf{E} , and (3) frictional damping of the ion flow. The primary objective of BX-U is to attain an enough confinement time (~ 1 s) of pure electron plasmas as a target plasma. Also, the degradation of confinement properties of the electron plasmas caused by an effective frictional force is studied.

Figure 1 shows a photograph of the BX-U device. It has a 15.0 cm inner diameter and 209 cm long vacuum chamber. Most of the vessel is made of 5.0



FIGURE 1. A photograph of the Beam Experiment Upgrade (BX-U). BX-U is one of Malmberg type traps with a plasma gun. This device is being constructed to investigate fundamental physics of electrically nonneutralized plasmas in a linear device on which difficulties encountered on experiments and data analyses in a toroidal geometry are eliminated.

mm thick aluminum (5052B). The device mainly consists of three parts: (1) the electron plasma source, (2) the central confinement region, and (3) the end region. A baking is available to obtain lower pressure, however, the vessel is usually pumped down by only a 250 liter turbo molecular pump and the pressure is about 6×10^{-9} Torr for the present experimental research.

The source region has originally been designed for a new plasma gun which is developed as a modified Marshall gun [5] having an electron source inside the inner electrode. However, only the electron source is so far placed there and the coaxial gun will be installed at the end region to avoid experimental difficulties. Regarding to the electron source, a five turns flat spiral Th-W wire is used. The diameter of the cathode is about 2.5 cm. And, it is directly heated with 12.0 A heater current to emit thermal electrons. About 0.5 cm away from the filament, a metal grid is located as an anode. The acceleration voltage is variable, but usually being set at -40 V. Thus, the space charge limited current from the e-gun is calculated to be about 15 mA enough to supply electrons to the central confinement region.

The central confinement region contains five cylindrical electrodes which produces a potential well to confine electrons. Each of them has 11.2 cm outer and 10.0 cm inner diameters and 9.5 cm long. All of them are made of copper (C1020B-F). Inside the vessel, these electrodes are electrically isolated from the vessel and axially aligned with 0.5 cm gap. Thus, it allows to externally supply independent voltage to each ring to form a negative potential well to trap electrons. The voltage is so far energized from the end region by DC power supplies through bus-bars with ceramic tube covers.

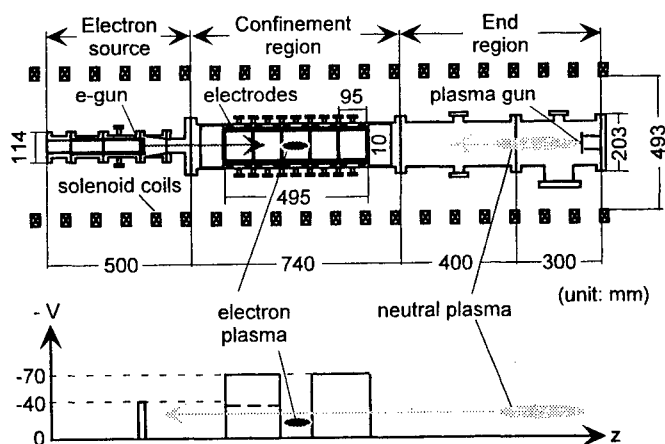


FIGURE 2. Axial profiles of negative potential to trap electron plasmas in the grounded cylindrical tube (the central confinement region) in BX-U. The electrons are injected through the front gate on which the bias voltage is electrically shuttered for 200 times every 2 ms interval.

In the end region, a Marshall type plasma gun will be installed to inject a neutral plasma into a pure electron plasma. However, for the purpose of the first experiments on the confinement properties of pure electron plasmas in BX-U, a metal plate has been so far placed there to detect the electron particle flux which flows out from the central confinement region after opening the potential barrier on the last electrode. By properly programming the gate opening time, the time history of total charge Q of the electron plasmas can be measured, which also provides the confinement time of the electron plasmas.

The Marshall type gun was originally developed for a study of cross-field plasma injection into an axisymmetric mirror machine with an internal ring [6]. The outer and inner diameters of the gun are 3 cm and 1 cm, respectively. Also, the length of the muzzle of it is 10 cm. A tiny magnetically acting valve is used in the middle of the inner electrode. To fire the gun, we will feed a power through an ignitron with 20 kV 9 μ F capacitor banks.

On BX-U, the axial solenoidal field is produced by a set of 14 pancake-shaped coils which are energized by a DC power supply. The strength of the field is available up to ~ 0.3 kG. Thus, the value of the Brillouin density limit on BX-U is calculated to be in the range between 5×10^{14} and $8 \times 10^{15} \text{ m}^{-3}$.

III FIRST DATA OF PURE ELECTRON PLASMAS

Since the device was completed in spring of 2000 except the plasma gun, we performed the first experiments to confine pure electrons in a negative potential well. Thermal electrons are extracted from the spiral Th-W cathode and accelerated up to ~ -40 V. The value of both the front and end gates is set precisely at -70 V for this experiment, while the center electrode is grounded to form a negative potential well shown in Fig. 2. When the negative potential of the front gate is down to ~ -40 V for ~ 0.4 ms every 2 ms interval, the thermal electrons enter the grounded cylindrical tube. This scheme is electrically repeated for 200 times to provide enough electrons. During the injection, the end gate is biased strongly negative (-70 V) to reflect the electrons.

At the first series of experiments, the time history of Q is measured as a function of axial magnetic field strength B_z . As seen from the data in Fig. 3, the confinement time τ_N of electron plasmas is about 0.3 s for $B_z \sim -50$ G if we define τ_N as $1/e$ folding time of Q .

Since the electron-neutral collision time can be calculated to be 0.3 s for the present background pressure, the observed τ_N seems to be governed by the classical binary collisions, suggesting that the BX-U device works well. However, when the strength of B_z is increased up to 150 G, τ_N decreases to 0.1 s, which is inconsistent with the empirical law observed in past Malmberg trap experiments [7]. The reason is unknown, but it should be attributed to

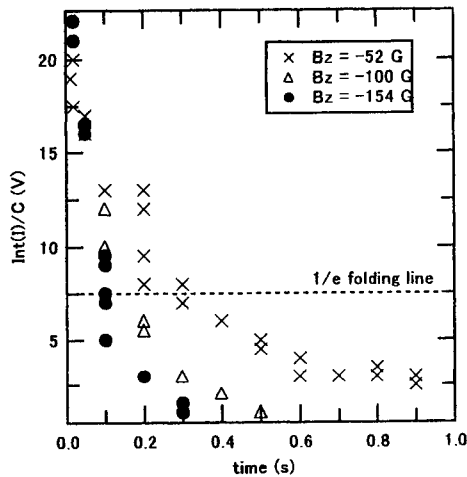


FIGURE 3. Time history of the total charge Q of trapped electrons in the grounded cylindrical tubes for the three different cases of axial magnetic field strength B_z . The value of Q is measured at the metal plate located in the end region. The data show that the confinement time τ_N is about 0.1 – 0.3 s, however, it becomes shorter with stronger B_z .

some error of experimental setting such as the axial alignment of electrodes of the electron gun. Another possibility of the deterioration may be due to the large ratio of plasma radius to wall radius, which is 0.3 in this experiment. In fact, larger plasmas suffer much effect of the image charge induced on the wall which is one of key parameters to determine the stability property of electron plasmas. Thus, it might cause some macro instability such as the diocotron mode because the cyclotron frequency becomes faster for the stronger B_z cases.

IV SUMMARY

A linear device, named BX-U (Beam Experiment Upgrade), has been constructed at the University of Tokyo. BX-U is one of the Malmberg type trap which creates a potential well with five cylindrical electrodes. The most significant feature of BX-U is that the device is equipped with a modified Marshall gun in order to inject a neutral plasma into a pure electron plasma. It thus offers an opportunity to explore a new regime of non-neutral plasma physics on which both ion and electron fluids are interacted each other under a charge non-neutral condition. The goal of BX-U is to investigate fundamental physics of ion perpendicular flow and the related phenomena of an electrically non-neutralized two-fluid plasma in a cylindrical geometry.

At the first series of experiments on BX-U, pure electron plasmas are confined in negative potential well. The confinement time is about 0.3 s for weak

B_z cases (~ 50 G). Since this time is comparable with the electron-neutral collision time (~ 0.2 s), the confinement properties of BX-U may be governed by the classical diffusion. However, the confinement time becomes shorter with stronger B_z . This seems to be inconsistent with the observations in past experiments on the Malmberg type trap. Further experiments are required to clarify the result.

ACKNOWLEDGMENTS

This work was supported in part by a Grant-in-Aid from the Japan Society for the Promotion of Science, No. 11780343.

REFERENCES

1. Mahajan, S. M. and Yoshida, Z., Phys. Rev. Lett. **81**, 4863 (1998).
2. Yoshida, Z. *et al.*, Fusion Energy 1998, IAEA-CN-69/ICP/10(R).
3. Himura, H. *et al.*, Phys. Plasmas **8** (10) (2001).
4. Malmberg, J. H. and deGrassie, J. S., Phys. Rev. Lett. **35**, 577 (1975).
5. Krall, N. A. and Trivelpiece, A. W., *Principles of plasma physics*, San Francisco Press, San Francisco, CA, 1986, pp.32.
6. Asano, S., Ihara, M., and Fukao, M., J. Phys. Soc. Jpn. **58**, 1265 (1989).
7. Driscoll, C. F. and Malmberg, J. H., Phys. Rev. Lett. **50**, 167 (1983).

Quadrature Detection for the Separation of the Signals of Positive and Negative Ions in Fourier Transform Ion Cyclotron Resonance Mass Spectrometry

Lutz Schweikhard¹, Jared J. Drader², Stone D.-H. Shi²,
Christopher L. Hendrickson², and Alan G. Marshall^{2,3}

¹ *Inst. f. Physik, Ernst-Moritz-Arndt-Universität, D-17487 Greifswald, Germany*

² *National High Magnetic Field Laboratory, Tallahassee, FL 32310, U.S.A.*

³ *Department of Chemistry, Florida State University, Tallahassee, FL 32306, U.S.A.*

Abstract. Positive and negative ions may be confined simultaneously in a nested open cylindrical Malmberg-Penning trap. However, ion charge sign cannot be distinguished by conventional dipolar (linearly-polarized) detection with a single pair of opposed electrodes. Here, the signals from each of two orthogonal pairs of opposed detection electrodes are acquired simultaneously and stored as real and imaginary parts of mathematically complex data. Complex Fourier transformation yields separate spectra for positive and negative ions. For a fullerene sample, experimental quadrature detection yields C_{60}^+ and C_{60}^- signals separated by ~ 1440 u rather than by the mass of two electrons, ~ 0.001 u in conventional dipolar detection.

INTRODUCTION

Both anionic and cationic particles may be trapped simultaneously in Penning-like ion traps by either nested trapping geometries [1] or dynamic trapping, i.e. the combination with an rf trapping field [2]. These investigations have also been extended to Fourier transform ion cyclotron resonance (FT-ICR) mass spectrometry (see ref. e.g. [3,4] and [5], resp.). Under such trapping conditions the conventional FT-ICR detection scheme does not distinguish between positive ion signals and negative ion signals.

To overcome this shortcoming we have implemented quadrature detection to distinguish the ion polarity. Quadrature detection not only determines the ion cyclotron frequency but also the sense of cyclotron rotation for each ion signal. Positive and negative ions may then be easily identified based on the opposite senses of their cyclotron rotation. As an example, positively and negatively charged fullerenes, C_{60}^+ and C_{60}^- , produce signals at $m/z = +720$ and -720 for a total separation of 1440 u compared to a difference of just about $1/1000$ u in the absolute values due to the mass of the two electrons. Thus, in this particular case, the signal separation is increased by six orders of magnitude.

EXPERIMENTAL SETUP AND PROCEDURE

All experiments were performed with a 6 tesla FT-ICR mass spectrometer described elsewhere [6]. A heated solids probe was inserted into the source region of the vacuum system. After the C_{60} sample was heated to $\sim 475^\circ\text{C}$, the volatilized fullerene gas was pulsed into the analyzer region by opening a mechanical shutter.

In the present work ions were formed by application of a 100 eV electron beam through the trap volume. The FT-ICR analyzer region was equipped with a modified 2 1/4" diameter open cylindrical cell. To create the nested trapping potential each trapping electrode was axially segmented into two pieces.

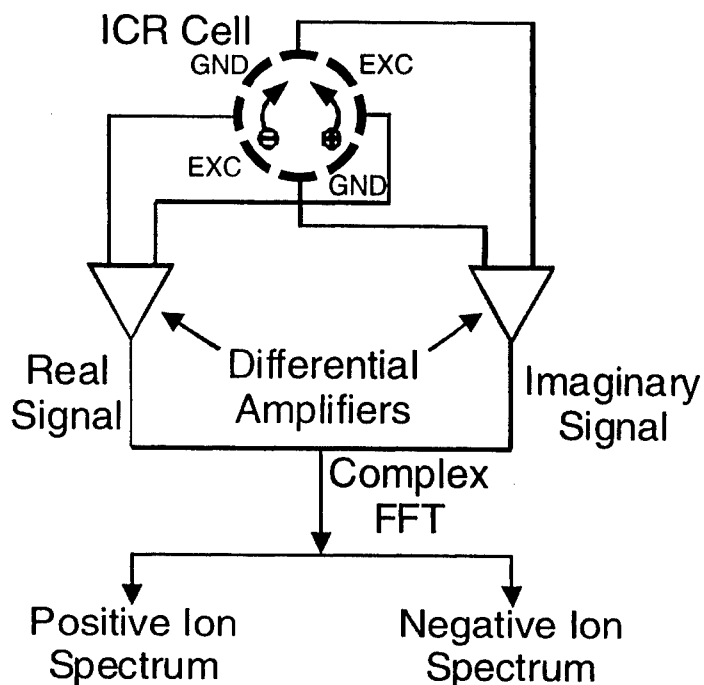


FIGURE 1. Wiring of ICR cell and data processing for quadrature detection FT-ICR MS.

For quadrature detection the excitation and detection electrodes were segmented into a total of eight electrodes. Two pairs of opposed electrodes were used for the two channels of quadrature detection (Fig. 1). Dipolar excitation was performed on two electrodes while the remaining two electrodes were grounded. As in conventional FT-ICR MS, the signal from each pair of detection electrodes was differentially amplified. A MIDAS data station [7] was modified to incorporate two HP E1437A modules (Hewlett Packard, Palo Alto, CA) to digitize the two ICR transient signals simultaneously for storage as real and imaginary components of mathematically complex data. The MIDAS analysis software was modified to process this data and display both positive and negative ion spectra.

RESULTS AND DISCUSSION

Quadrature detection distinguishes the sense of ion rotation for a given ion polarity. The sense of rotation is manifested as a signal at positive or negative frequency in the complex Fourier transform spectrum of the quadrature time-domain data. An example of quadrature detection for simultaneous storage and detection of cationic and anionic fullerenes is given in Figures 2 and 3. Figure 2 shows the transients from each of the two pairs of electrodes and the resulting frequency spectrum after a complex Fast Fourier Transform (FFT) of this data, as well as the corresponding mass-to-charge ratio spectra.

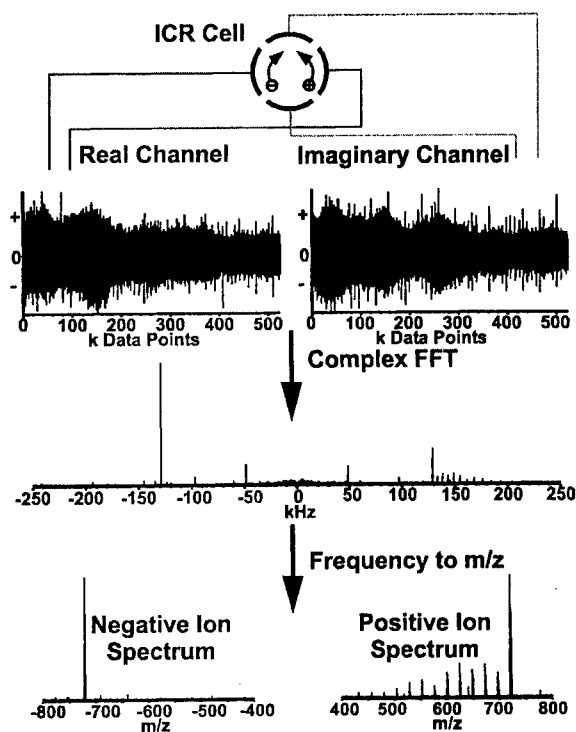


FIGURE 2. From top to bottom: Schematic wiring, transients, frequency spectrum and mass spectra from quadrature detection FT-ICR MS of fullerenes. (For details see text.)

In Fig. 3 these mass spectra (middle and bottom) are compared to the corresponding spectrum (top) acquired as before, but with complex FT of only the real time-domain data. A strong C_{60} signal at $m/z = 720$ and several species corresponding to $n C_2$ ($n = 1 - 12$) losses are present. Quadrature detection reveals that most of the fullerene signal at $m/z = 720$ is due to anionic and only a small fraction to cationic fullerenes. Because C_{60}^+ and C_{60}^- differ in mass by only two electrons, a resolving power of 720,000 is necessary to distinguish the two species with dipolar detection. In the quadrature detection mode, however, there is no problem in distinguishing the same species.

The same holds for the smaller fullerenes (dissociation fragments). The positive ion mass spectrum indicates the well-known pattern due to sequential C_2 losses (For a recent review on the mass spectrometry of fullerenes see e.g. [8]). No fragments, however, do appear in the anions' mass spectrum, since C_{60}^- more readily loses its excess electron than a carbon dimer [9] and the neutral product, C_{60} , is no longer stored nor detected by FT-ICR MS.

Furthermore, electronic noise peaks are more easily identified than by conventional detection because they tend to appear in the spectra of ions of both polarities.

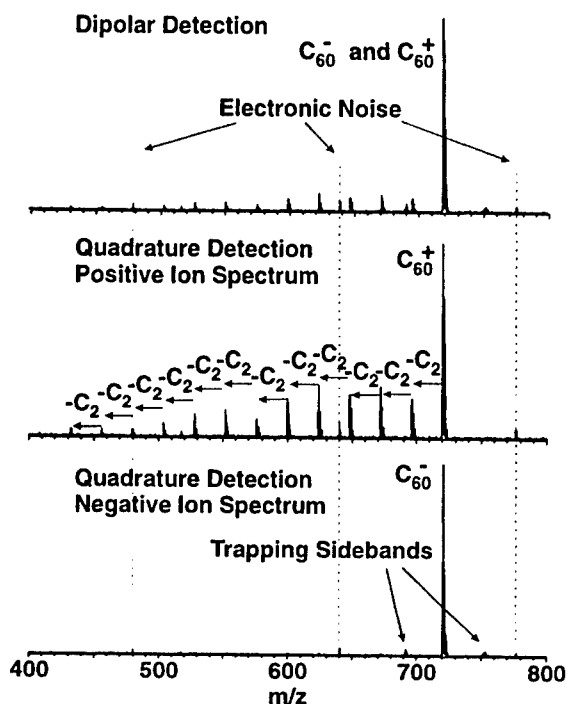


FIGURE 3. Fullerene FT-ICR mass spectra. Top: Spectrum in dipolar detection mode, i.e. the transient from only one pair of opposed detection electrodes, generated by Fourier transform processing of real time-domain data. Middle and bottom: Evaluation of the full "complex" transient yields separate mass spectra for positive and negative ions.

It may be noted, that there is a second, closely related method to distinguish the polarity of simultaneously stored ions, namely by the application of quadrature (i.e., circularly-polarized) excitation [10, 11]. In this case only ions of one polarity, either the cations or the anions, are excited and thus only their FT-ICR signal appears in conventional dipolar detection. However, in order to extract all of the information, the mass measurement has to be performed twice (once for each polarity) whereas dipolar excitation/quadrature detection results in the full information after one measurement. (In principle, the dipolar and quadrupolar excitation and detection schemes can be used in any combination – depending on the experimental results of interest.) A

further advantage of the use of two simultaneous transients instead of one is an increased signal-to-noise ratio of the FT-ICR MS spectra.

Finally, the present "physical" quadrature detection may be conducted in either "direct" or "heterodyne" mode. In heterodyne mode, a similar factor of $2^{1/2}$ enhancement in signal-to-noise ratio may be realized (versus single-phase heterodyne) by so-called "digital" quadrature heterodyne-mode detection [12], in which the signal from a given pair of opposed detection electrodes is multiplied by digital sine or cosine waveforms and stored as real and imaginary data. "Digital" quadrature heterodyne detection distinguishes signals whose cyclotron frequencies are above or below the reference frequency. However, "physical" quadrature detection is required to distinguish the sense of ion cyclotron rotation (and thus ion polarity).

CONCLUSIONS

We have demonstrated the experimental implementation of quadrature detection to distinguish positive ions from negative ions in a nested FT-ICR ion trap. The use of quadrature detection circumvents the problem of identifying ions with the same mass but opposite charge. In particular, cationic and anionic fullerenes, C_{60}^+ and C_{60}^- , at $m/z = 720$ may be differentiated without the need to resolve their mass difference of just two electrons.

ACKNOWLEDGMENTS

This work was supported by the NSF High Field FT-ICR Facility CHE-94-13008), Florida State University, and the National High Magnetic Field Laboratory in Tallahassee, Florida.

REFERENCES

1. Gabrielse, G., Rolston, S.L., Haarsma, L., and Kells, W., *Phys. Lett. A* **129**, 38-42 (1988).
2. Schermann, J.P., and Major, F.G., *Appl. Phys.* **16**, 225-230 (1978).
3. Vartanian, V. H., and Laude, D. A., *Org. Mass Spectrom.* **29**, 692-694 (1994).
4. Malek, R., and Wanczek, K. P., *Rapid Comm. Mass Spectrom.* **11**, 1616-1618 (1997).
5. Gorshkov, M.V., Guan, S., and Marshall, A. G., *Rapid Commun. Mass Spectrom.* **6**, 166-172 (1992).
6. Drader, J. J., Bonneau, R. A., Hendrickson, C. L., and Laude, D. A., in "45th Amer. Soc. Mass Spectrom. Conf. on Mass Spectrometry & Allied Topics", Palm Springs, CA, 1997, p 867.
7. Senko, M.W., Canterbury, J.D., Guan, S., Marshall, A. G., *Rapid Commun. Mass Spectrom.* **10**, 1839-1844 (1996).
8. Lifshitz, C., *Int. J. Mass Spectrom.* **200**, 423-442 (2000).
9. Jaffke, T., Illenberger, E., Lezius, M., Matejcek, S., Smith, D., Mrk, T.D., *Chem. Phys. Lett.* **226**, 213-218 (1994).
10. Guan, S., Gorshkov, M.V., Alber, G.M., and Marshall, A.G., *Chem. Phys. Lett.* **198**, 143-148 (1992).
11. Schweikhard, L., and Marshall, A.G., *J. Am. Soc. Mass Spectrom.* **4**, 433-452 (1993).
12. Drader, J.J., Shi, S.D.-H., Blakney, G.T., Hendrickson, C.L., Laude, D. A., and Marshall, A.G., *Anal. Chem.* **71**, 4758-4763 (1999).

Charge-changing reactions and their influence on the ion motion in a Penning trap

A. Herlert*, L. Schweikhard† and M. Vogel*

*Institut für Physik, Johannes Gutenberg-Universität Mainz, D-55099 Mainz, Germany

†Institut für Physik, Ernst-Moritz-Arndt-Universität Greifswald, D-17487 Greifswald, Germany

Abstract. Charge-changing reactions can lead to a significant change of the ion motion which may result in the loss of the ions from the trap. For the present experiments singly charged gold clusters from an external laser vaporization source have been transferred into a Penning trap and transformed into dianions by use of an electron bath of simultaneously stored electrons. The dianions have been investigated by collisional activation and laser excitation where electron emission has been observed as a cooling mechanism. Electron emission doubles the value of the cyclotron radius and in addition, the ions acquire a finite magnetron radius. This leads to an extension of the radial distance of the ion motion from the trap's axis by a factor of about three.

INTRODUCTION

The Penning trap is a versatile tool for the investigation of charged particles [1], including atomic clusters. Recently, it has been shown that the trap can be employed for the production of multiply charged anionic metal clusters [2–4]. The properties of these new particles are currently examined by use of laser excitation and collisional activation. As will be shown, especially in the latter case care has to be taken when charge-changing reactions are involved. These can lead to significant changes of the motion of the trapped ions and may cause their loss from the trap. In the following the influence of electron emission from doubly charged gold cluster anions in case of collisional activation is described in more detail.

ION MOTION IN THE PENNING TRAP

We start with a brief review of the basics of a Penning Trap [1]. For axial ion confinement in a harmonic potential, a potential U_0 is applied between a ring electrode and two endcap electrodes, all of which have a hyperbolic shape. A particle of mass m and charge q is therefore trapped and performs an axial oscillation (trapping motion) at the frequency

$$\omega_z = \sqrt{\frac{qU_0}{md_0^2}} \quad (1)$$

where the trap dimension d_0 is defined as in ref. [1]. Radial confinement is achieved by use of a homogeneous magnetic field \vec{B} where the field lines are parallel to the

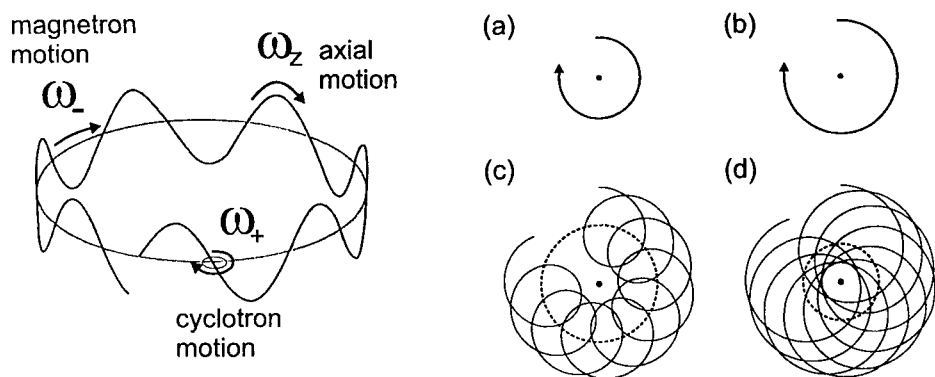


FIGURE 1. Left: Motional modes of an ion in a Penning trap. Right: Radial ion motion in the Penning trap: (a) only cyclotron motion, $\rho_- = 0$, (b) only magnetron motion, $\rho_+ = 0$, (c) $\rho_+ < \rho_-$ and (d) $\rho_+ > \rho_-$. The dotted line in (c) and (d) indicates the guiding center of the cyclotron orbits (e.g. the magnetron orbit).

electrodes' symmetry axis. In the absence of the electric potential the ion performs a cyclotron motion at the frequency

$$\omega_c = \frac{qB}{m}. \quad (2)$$

But the crossed electric and magnetic fields lead to a splitting of the radial motion into two modes (see Fig. 1 (left)): the high frequency cyclotron motion at the reduced cyclotron frequency

$$\omega_+ = \frac{\omega_c}{2} + \sqrt{\left(\frac{\omega_c}{2}\right)^2 - \frac{\omega_z^2}{2}} \quad (3)$$

and the low frequency magnetron motion (drift motion) around the trap axis at the frequency

$$\omega_- = \frac{\omega_c}{2} - \sqrt{\left(\frac{\omega_c}{2}\right)^2 - \frac{\omega_z^2}{2}}. \quad (4)$$

The amplitudes and phases of the three harmonic motional modes (axial, cyclotron and magnetron) are independent of each other and are only determined by the "initial conditions". In Fig. 1 (right) four different trajectories are shown in a projection on the radial plane.

METAL CLUSTER DIANIONS: EXPERIMENTAL RESULTS

A detailed description of the experimental setup has been given elsewhere [5–7]. Singly charged metal cluster anions of various sizes are produced in an Smalley-type laser vaporization source [8, 9] and transferred into a Penning trap. After in-flight-capture the cluster size of interest is selected by radial ejection of all unwanted ions from the trap. An external electron beam is applied while argon gas is pulsed into the trap volume. Thus,

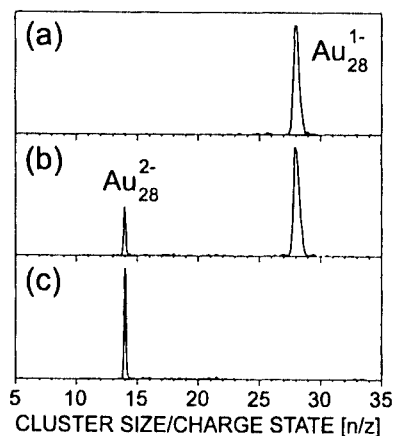


FIGURE 2. TOF spectra of the experimental sequence of dianion production: (a) selection of singly charged cluster anions, (b) application of electron bath, (c) selection of dianions.

by ionization low energy electrons are produced which stay trapped. The simultaneously stored cluster anions are therefore subjected to an electron bath and electrons may attach producing cluster dianions [2, 3]. Note, that the trap allows the simultaneous storage of electrons and negatively charged gold clusters (e.g. Au_{28}^{1-} with $n=28$ atoms), while the mass-over-charge ratio of these particles differs by seven orders of magnitude. In a second selection step an ion ensemble of specific charge state can be prepared for further experiments. Finally, the trap is emptied by axial ejection into a drift section and

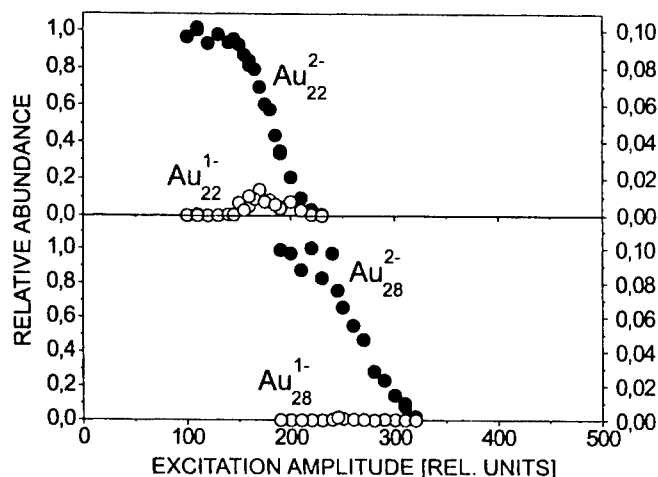


FIGURE 3. Relative abundance of gold cluster dianions Au_{22}^{2-} (top, full circles) and Au_{28}^{2-} (bottom, full circles) as a function of collisional activation. Note, that for the singly charged cluster anions the scale is decreased by one order of magnitude.

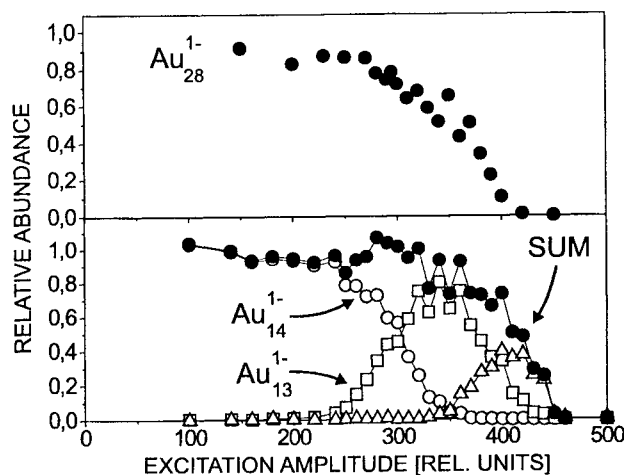


FIGURE 4. Relative abundance of cluster anions Au_n^{1-} after collision induced dissociation of Au_{28}^{1-} (top) and Au_{14}^{1-} (bottom). For the latter open circles represent $n = 14$, open squares $n = 13$, open triangles $n < 13$ and full circles the sum of all ion signals.

reactions during the storage period are analyzed by time-of-flight mass spectrometry. In Fig. 2 several spectra of the production sequence are shown for the case of Au_{28}^{2-} : (a) capturing and size selection, (b) after reaction with the electron bath and (c) selection of dianions.

In order to study the properties of the size and charge-state selected gold-cluster dianions, collisional activation is applied as previously investigated for singly charged species [10]. The ring electrode of the Penning trap is segmented to perform a dipolar rf-excitation at the reduced cyclotron frequency ω_+ . This leads to an increase of the radius ρ_+ of the cyclotron motion (proportional to the amplitude of the rf-excitation) and therefore to an increase of the kinetic energy of the cluster dianions. When argon gas is pulsed into the trap volume the dianions collide with the gas atoms and part of

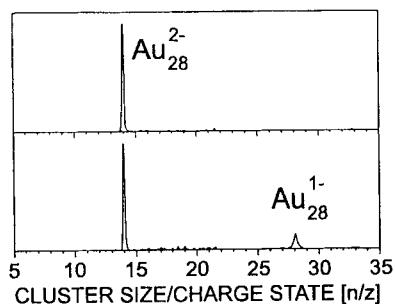


FIGURE 5. TOF spectra before (top) and after (bottom) photoexcitation of selected gold cluster dianions Au_{28}^{2-} .

the kinetic energy is transformed into internal excitation energy. In Fig. 3 the relative abundance of Au_{22}^{2-} (top) and Au_{28}^{2-} (bottom) is plotted as a function of the excitation of the cyclotron radius. The dianion signal (full circles) disappears, but almost no product signal is observed, in particular with respect to singly charged cluster anions (open circles). For comparison Fig. 4 shows the analog result for CID measurements of Au_{28}^{1-} and Au_{14}^{1-} , i.e. of singly charged gold-cluster anions of the same mass and cyclotron frequency as Au_{28}^{2-} , respectively. Compared to these measurements on singly charged cluster anions the Au_{28}^{2-} signal is disappearing at a much smaller cyclotron radius.

In case of photoexcitation, the cluster dianions remain in the center of the trap volume when they are excited with a single pulse of a frequency tripled Nd:YAG laser ($\lambda = 355 \text{ nm}$). In Fig. 5 the spectra before (top) and after the excitation (bottom) of Au_{28}^{2-} are shown. Only the singly charged species Au_{28}^{1-} appear in the spectrum as a product signal, which is interpreted as the result of electron emission.

EXPLANATION: THE EFFECT OF CHARGE-CHANGING REACTIONS

In order to explain these observations the influence of the electron loss on the ion motion is studied in more detail. Consider the simple initial conditions of a finite cyclotron radius ρ_+ and no magnetron motion ($\rho_- = 0$) for an ion of mass m and charge state $z = -2$. The loss of an electron changes the charge state from $z = -2$ to $z' = -1$ and therefore cuts the cyclotron frequency by a factor of almost two ($\omega'_+ \approx \omega_+/2$). But there is no significant change of the velocity, $v' \approx v$, thus

$$v' \approx \omega'_+ \rho'_+ \approx \omega_+ \rho_+ \approx v. \quad (5)$$

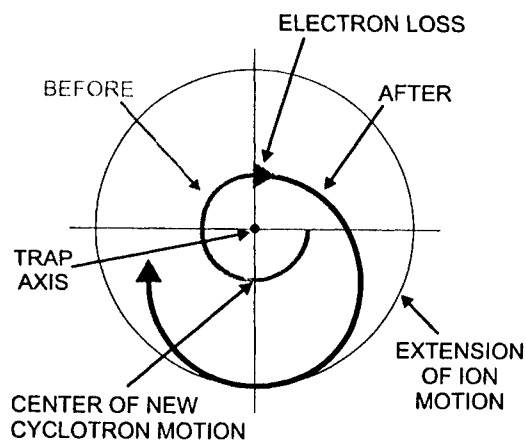


FIGURE 6. Radial ion motion of a dianion which loses an electron for the initial conditions of a finite cyclotron radius ρ_+ and no magnetron motion ($\rho_- = 0$).

Therefore, the loss of charge leads to an instantaneous increase of the cyclotron radius ρ_+ by a factor of about two:

$$\rho'_+ \approx 2\rho_+. \quad (6)$$

At the same time the center of the ion motion is shifted and the magnetron radius is increased from $\rho_- = 0$ to $\rho'_- \approx \rho_+$. Thus, the maximum extension of the radial ion motion $\rho'_+ + \rho'_-$ is about three times as large as before the loss of the electron (see Fig. 6). However, the Penning trap has finite radial dimensions. Thus, after the electron loss the ion will collide with the ring electrode, if its initial cyclotron radius exceeds 1/6 of the free diameter of the ring electrode.

In conclusion, charge-changing reactions may lead to drastic changes of the ions' motion in a Penning trap. In particular, the decrease of the charge state can result in severe ion loss.

ACKNOWLEDGMENTS

This work was supported by the Deutsche Forschungsgemeinschaft and by the EU networks "EUROTRAPS" and "CLUSTER COOLING". We further thank the Materials Science Research Center at Mainz and the Fonds der Chemischen Industrie.

REFERENCES

1. Brown, L. S., and Gabrielse, G., *Rev. Mod. Phys.* **58**, 233-311 (1986).
2. Herlert, A., Krückeberg, S., Schweikhard, L., Vogel, M., and Walther, C., *Physica Scripta* **T80**, 200-202 (1999).
3. Schweikhard, L., Herlert, A., Krückeberg, S., Vogel, M., and Walther, C., *Philos. Mag. B* **79**, 1343-1352 (1999).
4. Yannouleas, C., Landman, U., Herlert, A., and Schweikhard, L., *Phys. Rev. Lett.* **86**, 2996-2999 (2001).
5. Schweikhard, L., Becker, St., Dasgupta, K., Dietrich, G., Kluge, H.-J., Kreisle, D., Krückeberg, S., Kuznetsov, S., Lindinger, M., Lützenkirchen, K., Obst, B., Walther, C., Weidele, H., and Ziegler, J., *Physica Scripta* **T59**, 236-243 (1995).
6. Schweikhard, L., Krückeberg, S., Lützenkirchen, K., and Walther, C., *Eur. Phys. J D* **9**, 15-20 (1999).
7. Schweikhard, L., Herlert, A., and Vogel, M., "Metal Clusters as Investigated in a Penning Trap," in *The Physics and Chemistry of Clusters (Proceedings of the Nobel Symposium 117)*, edited by E. E. B. Campbell and M. Larsson, World Scientific, Singapore, 2001, pp. 267-277.
8. Powers, D. E., Hansen, S. H., Geusig, M. E., Puiu, A. C., Hopkins, J. B., Dietz, T. G., Duncan, M. A., Langridge-Smith, P. R. R., and Smalley, R. E., *J. Phys. Chem.* **86**, 2556-2560 (1982).
9. Weidele, H., Frenzel, U., Leisner, T., and Kreisle, D., *Z. Phys. D* **20**, 411-412 (1991).
10. Weidele, H., Vogel, M., Herlert, A., Krückeberg, S., Lievens, P., Silverans, R. E., Walther, C., and Schweikhard, L., *Eur. Phys. J. D* **9**, 173-177 (1999).

SECTION 9

TOROIDAL GEOMETRY

Flowing Electron Plasmas as Modified Current Source

Haruhiko Himura, Chihiro Nakashima, Haruhiko Saito,
Zensho Yoshida, Junji Morikawa, and Masayuki Fukao

*University of Tokyo, Department of Advanced Energy,
Graduate School of Frontier Sciences, Hongo, Tokyo 113-0033, Japan*

Abstract. Probing of streaming electron plasmas with finite temperature is studied. Due to the fast flow of the electron plasmas, the characteristic curve spreads out significantly and exhibits a long tail. Another significant feature of the characteristic is that it determines a floating potential where the current equals zero, despite there being very few ions in the electron plasma. A high impedance probe, which is popularly used to determine the space potential of electron plasmas, outputs the potential. The method is available only for plasmas with density much smaller than the Brillouin limit.

I INTRODUCTION

There has been considerable interest both experimentally and theoretically in toroidal nonneutral plasmas, which are relevant to heavy ion accelerators [1], sources of highly stripped heavy ions [2], and thermonuclear fusion reactors [3]. These concepts are based totally on the electrostatic confinement of ions in a deep potential cavity. For this purpose, a background cloud of magnetized electrons has been considered to be a candidate to form the negative well. Another significant feature of the background electrons is that a strong electric field \mathbf{E} intrinsically forms due to their space charge. This field can produce strong $\mathbf{E} \times \mathbf{B}$ shear flows if we apply an appropriate magnetic field \mathbf{B} . This property may be applied to produce two-fluid high- β plasmas [4] which possess diamagnetic structures formed by the hydrodynamic pressure of the significant shear flows. In fact, sample equilibria of the hydrodynamic (relaxed) states resemble field-reversed configurations [5] and H-mode tokamaks [6]. Thus, studies on flowing plasmas have attracted considerable interest in experimental plasma physics.

One of the key parameters which characterizes nonneutral plasmas is the space potential ϕ_p or, equivalently, number density n . This value is easily

obtained in nonneutral plasmas with cylindrical geometry, which have an axial magnetic field providing radial confinement and applied potentials providing axial confinement. After a variable confinement time, a dump gate is pulsed to ground potential, which allows the remaining electrons to stream out axially along the field lines for collection and analysis. However, in axisymmetric toroidal plasmas, this method cannot be applied because the field line is closed.

In all earlier experiments on toroidal electron plasmas, ϕ_p was determined by a Langmuir probe terminated across a high impedance attenuator. In this method, no current flows in the electric circuit of the probe, i.e. the electron plasma outputs a constant voltage to the probe just like a voltage source in electronics. However, this raises a question. Generally, a neutral plasma behaves as a current source for probe measurements where a current-voltage ($I - V$) characteristic, consisting of both electron and ion currents, is observed. Moreover, at $V = \phi_p$, I is never zero and the value of I is determined almost completely by electrons. These facts suggest strongly that even in electron plasmas, there should be a current-voltage characteristic which consists entirely of only electrons. Also, I should not be zero at $V = \phi_p$ in electron plasmas, which points out the need for attention to the high impedance method that causes ϕ_p to be overestimated.

This paper answers the question clearly. On experiments in the Proto-RT (Prototype Ring Trap) device [7], current-voltage characteristics of toroidal electron plasmas are measured for the first time. Similar to neutral plasmas, a current-voltage characteristic is established. However, no exponential dependence of I against V appears in the retarding region. Due to the effect of fast flow of electron plasmas, the measured characteristic spreads out significantly, exhibiting a long tail. These properties are interpreted by a calculation of particle flux collected to the probe. With regard to obtaining the value of ϕ_p , an emissive probe which is considered to be more adequate in determining ϕ_p is applied to electron plasmas for the first time. Remarkably, the probe always outputs higher voltage (Φ_E) than the voltage (Φ_H) measured by the same probe with no filament current ($|\Phi_E| < |\Phi_H|$). Here, one notes that for the latter case, the probe works as a high-impedance probe. We show that the disagreement would become relatively small when the flow energy is much smaller than the electrostatic potential energy of electron plasmas, which corresponds to the condition of $n \ll n_B$, where n_B is the Brillouin limit on number density. Another significant feature of the current-voltage characteristic of an electron plasma is that a floating potential ϕ_f , where $I = 0$, is determined, although ideally $\phi_f = -\infty$ because there are no ions. And, $I \neq 0$ at Φ_E , while $I = 0$ at Φ_H as seen in neutral plasmas.

The remainder of this paper is organized as follows. In Sec. II, experimental data of toroidal electron plasmas are presented. Interpretation of the measured current-voltage characteristics and several other phenomena related to this are given in Sec. III and IV. Finally, a summary is given in Sec. V.

II EXPERIMENTAL RESULTS

Experiments are conducted on the Prototype Ring Trap device (Proto-RT). Since the Freon cooling system was completed, we have performed initial experiments to confine energetic electrons in X point, Spherator-like, and dipole-like closed configurations.

A Potential measurements

Since the magnetic surfaces are closed in toroidal plasmas, passive probing is a key method to diagnose the plasmas. To focus attention on it, we have intensively studied pure electron plasmas confined in dipole-like configurations shown in Ref. [7]. The electron gun is fixed on the symmetry plane ($z = 0$), and the radial position of the gun is at $r = 50$ cm. The angle of the injected electrons with respect to the magnetic field is 90 degrees. The electrons circulate in the clockwise direction, which is opposite to the direction of equilibrium rotating flow.

Figure 1 shows time histories of an emissive probe signals at $r = 43$ cm for the case of $I_{tr} = 30$ A with/without a filament current I_{fil} . Substantial difference between the values of Φ_E and Φ_H can clearly be recognized. For the $I_{fil} \sim 1.1$ A case (with emission), the value of Φ_E is -52 V and constant during the discharge. In these experiments, we took at least three data sets at each position to determine the scattering of the data. The accuracy of

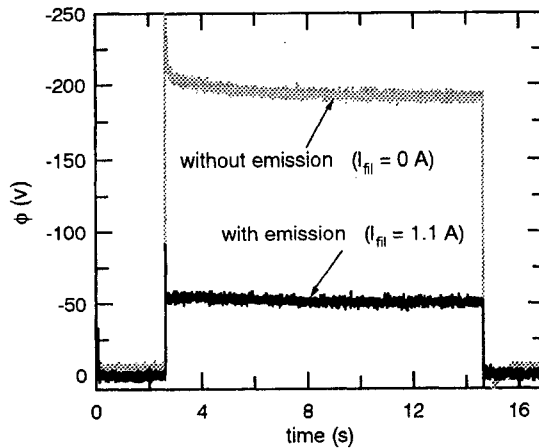


FIGURE 1. Time evolution of measured voltages by an emissive probe with completely the same conditions except for the filament current I_{fil} . Without I_{fil} , the probe works as a high-impedance probe which measures the voltage for $I_p = 0$. The difference between Φ_H and Φ_E is rather large, showing that the high-impedance method does not apply for determining ϕ_p .

the data was good and within 3 %, probably due to the completely static experiments. Also, Φ_E increased little with larger I_{fil} . Thus, we conclude that even in toroidal electron plasmas, emissive probes work like conventional ones in neutral plasmas, and the value of Φ_E gives ϕ_p of toroidal electron plasmas within experimental error.

On the other hand, for the $I_{fil} \sim 0$ A case (without emission), the value of Φ_H is -194 V which is about 3.7 times larger than Φ_E . Also, it gradually increases from -205 (at $t \sim 3$ s) to -190 V (at $t \sim 15$ s). Since the probe in this case inherently acts as a high-impedance probe, this result means that a high-impedance probe cannot measure ϕ_p of Proto-RT electron plasmas, contrary to past experiments on toroidal electron plasmas in which ϕ_p was determined with high-impedance probes.

B Current-Voltage characteristics

Since the Φ_H measurement has popularly been used to determine ϕ_p in experiments on toroidal electron plasmas, a question arises on what Φ_H is in Proto-RT. To answer this question, we installed a directional probe to measure a current-voltage characteristic of Langmuir probe and the primary direction of electron flow in the plasmas.

Usually it is very difficult to detect the perpendicular motion of electrons by a probe because the parallel thermal motion of electrons is still faster in strong **B** even if they drift across **B**. However, on Proto-RT the strength of **B** is relatively weak ($B_p \sim 30$ G). Since the strength of the radial electric field E_r can be calculated to be ~ 10 V/cm for the dipole-like configuration, the perpendicular flow velocity v_d ($\sim E_r/B_p$) is thus expected to be $\sim 3 \times 10^5$ m/s. On the other hand, the parallel thermal velocity can be calculated $\sim 10^6$ m/s for $T_e \sim 10$ eV which is comparable to v_d , suggesting that the probe can distinguish the perpendicular flow.

Figure 2 shows typical current-voltage characteristic taken from the directional probe at $r = 43$ cm for the dipole-like configuration. Substantial difference in the collected current can be recognized between the upstream perpendicular- (black circle) and the downstream perpendicular (white circle) direction. This flow direction corresponds to the $-\nabla\phi_p \times \mathbf{B}$ direction, not to the direction of the injected beam from the gun. Thus, this result indicates the existence of equilibrium flow inside the magnetic surfaces.

It may then be considered that the total current plotted in Fig. 2, which is the sum of all the currents of the four independent probes, approximately shows a current-voltage characteristic of a cylindrical probe in toroidal electron plasmas. And, as recognized on the plotted curve, Φ_H indicates the 'floating' potential ϕ_f where $I_p \sim 0$, although ideally $\phi_f \rightarrow -\infty$ because there are no ions in electron plasmas.

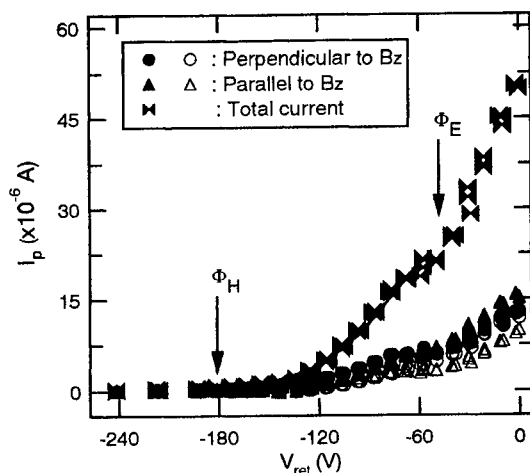


FIGURE 2. Current-voltage characteristics measured by a directional probe with four electrodes at $r = 43$ cm for the dipole-like configuration; two of them (denoted by circles) are turned toward the azimuthal direction of machine axis (perpendicular to magnetic field lines), while the others (denoted by triangles) are turned toward the z direction (along magnetic field lines): black circle: θ_- , white circle: θ_+ , black triangle: z_+ , and white triangle: z_- . The primary direction of perpendicular flow v_f corresponds to the $-\nabla\phi_p \times \mathbf{B}$ direction, strongly suggesting the existence of equilibrium flow. Thus, the total current, which is the sum of all the currents of the four independent electrodes of the directional probe, reflects the characteristic of a cylindrical probe in electron plasmas. As is apparent, Φ_H indicates the *floating potential* V_f , although ideally $V_f = -\infty$ in pure electron plasmas.

Another significant feature of the measured characteristic is that in decreasing the probe potential, I lessens not exponentially but gradually. And the value of I at $V = \Phi_E (\sim \phi_p)$ is finite and never equals 0, as recognized from the plotted data in Fig. 2.

III CALCULATION OF CURRENT-VOLTAGE CHARACTERISTICS OF FLOWING ELECTRON PLASMAS

To study the current collection characteristics of the probe, we consider the sheath configuration around the probe in flowing electron plasmas. As in neutral plasmas, Debye shielding of the electrostatic potential is realized even in pure electron plasmas. However, the shape of the sheath around the probe may be no longer cylindrical due to such a large value of v_f . Although there has been work on electric probes in flowing (neutral) plasmas, no sufficiently precise model is available which can justify empirically or theoretically any

other sheath shape. Thus, as a first-order approximation, a cylindrical sheath is assumed around the probe. We assume a cylindrical sheath in a rectangular coordinate system (x, y, z) which is fixed in the laboratory frame, shown in Ref. [7]. Let v_x, v_y, v_z be the electron velocity components in this frame, and v'_x, v'_y, v'_z be the electron velocity in a rectangular coordinate system in the moving frame with speed v_f and parallel to the laboratory frame. Choosing the y axis along the axis of the cylinder and θ the angle between the \mathbf{v}_f vector and the y axis, then the transformation equations between the velocity components in the two coordinates are

$$v_x = v'_x + v_f \sin \theta \cos \beta, \quad v_y = v'_y + v_f \cos \theta, \quad v_z = v'_z + v_f \sin \theta \sin \beta \quad (1)$$

where β is the azimuthal angle of \mathbf{v}_f with respect to the x axis.

Assuming that the plasma is in a state of thermal equilibrium on a magnetic surface, then the Boltzmann distribution of the rotating axisymmetric plasmas in the moving frame takes the form

$$f = n_0 \left(\frac{m}{2\pi\kappa T} \right)^{3/2} \exp\left(-\frac{H'}{\kappa T}\right) \quad (2)$$

where n_0 , m , κ , and T are number density, electron mass, Boltzmann's constant, and temperature, respectively. The particle energy H' in the moving frame is given by

$$\begin{aligned} H' &= H - \omega P_\theta \\ &= \frac{1}{2}mv^2 + q\phi - \omega P_\theta \\ &= \frac{1}{2}mv^2 + q\phi - \omega r(mv_\theta + qA_\theta), \end{aligned} \quad (3)$$

where q , ϕ , P_θ , ω , and A_θ are charge, electric potential, canonical angular momentum, angular velocity, and the theta component of the vector potential. From eqs. (2) and (3), the distribution function can be rewritten as

$$\begin{aligned} f &= n_0 \left(\frac{m}{2\pi\kappa T} \right)^{3/2} \exp\left[-\frac{1}{\kappa T} \left\{ \frac{m}{2}(\mathbf{v} - \omega r \hat{\theta})^2 + q\phi - \frac{m}{2}\omega^2 r^2 - qA_\theta \omega r \right\}\right] \\ &= n_0 \left(\frac{m}{2\pi\kappa T} \right)^{3/2} \exp\left[-\frac{1}{\kappa T} \left\{ \frac{m}{2}(\mathbf{v} - \omega r \hat{\theta})^2 + q\phi - C(r) \right\}\right] \\ &\equiv n' \left(\frac{m}{2\pi\kappa T} \right)^{3/2} \exp\left[-\frac{1}{\kappa T} \left\{ \frac{m}{2}(\mathbf{v} - \omega r \hat{\theta})^2 + q\phi \right\}\right], \end{aligned} \quad (4)$$

where $n' = n_0 \exp(C(r)/\kappa T)$. This distribution function may be modified in a way which is determined by the linear transformations of the velocity components given in eq. (1). Thus, for the laboratory frame, a new distribution $F(v_x, v_y, v_z, \beta)$ at the sheath edge can be written as

$$F = n' \left(\frac{m}{2\pi\kappa T} \right)^{3/2} \exp \left[-\frac{1}{\kappa T} \{ (v_x - v_f \sin\theta \cos\beta)^2 + (v_y - v_f \cos\theta)^2 + (v_z - v_f \sin\theta \sin\beta)^2 + q\phi \} \right]. \quad (5)$$

Here, we consider an infinitesimal strip of area $Lad\beta$ on the sheath surface which is normal to the x axis, where a is the sheath radius. The particle number of electrons N , with velocity ranges between v_x and $v_x + dv_x$, v_y and $v_y + dv_y$, and v_z and $v_z + dv_z$, which are expected to cross the infinitesimal area per unit time is given by

$$N = v_x F dv_x dv_y dv_z Lad\beta, \quad (6)$$

where L is the length of the cylinder. Therefore, on multiplying eq. (6) with q and integrating between proper limits, the current collected by the cylindrical probe in electron plasmas is described by

$$I = Laq \int_{\beta=0}^{2\pi} \int_{v_x=0, v_1}^{\infty} \int_{v_y=-\infty}^{\infty} \int_{v_z=-p}^p v_x F dv_x dv_y dv_z d\beta. \quad (7)$$

The lower limit of v_x is zero for $V_{ret} > \phi_p$ and is $v_1 = \sqrt{2qV_{ret}/m}$ for $V_{ret} < \phi_p$. The case where $V_{ret} > \phi_p$ is the 'accelerated current', and the case where $V_{ret} < \phi_p$ is the 'retarded current' in conventional probe theory. The limits of v_y from $-\infty$ to ∞ follow from the assumption that $L \gg r$ for cylindrical probe, where r is the probe radius. For the limits of v_z (tangential component), p must satisfy $p = \sqrt{\gamma^2(v_x^2 + 2qV_{ret}/m)}$ where $\gamma^2 = r^2/(a^2 - r^2)$. This is obtained by applying the laws of conservation of energy and angular momentum to the electron trajectory in the sheath. In toroidal electron plasmas, the Debye length λ_D is 1–10 cm due to the low n_0 . Accordingly, the value of a ($\geq 4\lambda_D$ at least) is approximately 4–40 cm. On the other hand, r is typically less than 0.5 mm. Hence, $a/r \rightarrow \infty$ ($\gamma \rightarrow 0$) is a fairly good approximation for electron plasmas, and this condition corresponds to the case of orbital-motion-limited (OML) current. Thus, the final form of eq. (7) for electron plasmas normalized by $I_d = qn'v_{th}S$ (S is the collector area.) is given by

$$I = \frac{2}{\sqrt{\pi}} \exp(V_0 - \alpha^2) \sum_{n=0}^{\infty} \frac{\alpha^n}{n! V_0^{n/2}} \Gamma\left[n + \frac{3}{2}, V_0\right] J_n(2\alpha V_0^{1/2}) \quad (V_0 > 0)$$

$$= \exp(V_0 - \alpha^2) \sum_{n=0}^{\infty} \frac{(2n+1)! \alpha^n}{(n!)^2 2(2n)(-V_0)^{n/2}} I_n[2\alpha(-V_0)^{1/2}], \quad (V_0 < 0) \quad (8)$$

where $V_0 = q(V_{ret} - \phi_p)/\kappa T$, $\alpha = (v_f/v_{th})\sin\theta$, and Γ , J_n , and I_n are the incomplete gamma, Bessel, and modified Bessel functions, respectively.

The $I-V$ characteristics shown in Fig. 3 correspond to typical experiments for the $\theta = 90$ deg. case, in which the values of v_f/v_{th} are 0 (no flow), 1, and 2. Considerable differences can clearly be seen among them. For the case

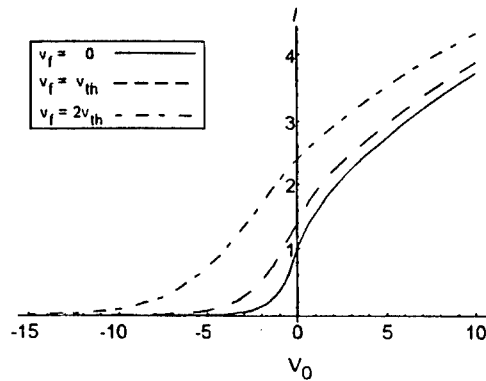


FIGURE 3. The calculated $I - V$ characteristics of electron plasmas in the OML limit for the case of $v_f/v_{th} = 0, 1$, and 2 . The value of θ is 90 degrees for this calculation. The horizontal axis denotes $V = V_{ret} - \phi_p$ therefore, ϕ_p is fixed at $V = 0$. On the other hand, the value of I is normalized by the probe current for $v_f/v_{th} = 0$ (no flow) case. As v_f increases, no exponential dependence appears in the retarding region ($V < 0$), although the plasma is assumed to be in a state of thermal equilibrium in the moving frame. This property causes a long tail in the measured profiles observed in the laboratory frame, and moreover, I significantly increases when $v_f \neq 0$ because of the existence of flow flux.

of $v_f/v_{th} = 0$, the value of I in the retarding region ($V_0 < 0$) decreases exponentially, as in stationary plasmas. However, as v_f increases, the decay of I at $V_0 < 0$ changes gradually and is no longer an exponential curve. This brings about a longer tail, as recognized in the characteristic curve, despite T remaining constant. Moreover, the value of I increases for any V_0 .

IV APPLICABILITY OF HIGH IMPEDANCE METHOD

As mentioned in the previous section, the value of Φ_H is unstable in pure electron plasmas, which calls for careful attention to the high impedance method. However, practically, the Φ_H measurement may be applied to estimate ϕ_p roughly for electron plasmas in which $\Phi_H/\Phi_E \rightarrow 1$ since the error bar of ϕ_p caused by the Φ_H method becomes relatively small for this case. This corresponds to the condition where the thermal energy $mv_{th}^2/2$ is as large as the flow energy $mv_f^2/2$, and the electrostatic energy $q\phi_p$ is much greater than $mv_f^2/2$: $q\phi_p \gg mv_{th}^2/2 \geq mv_f^2/2$.

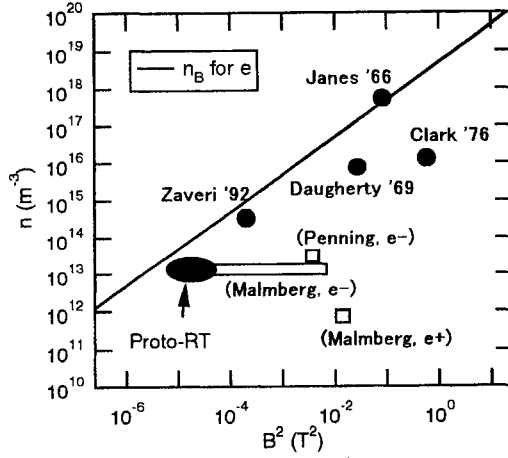


FIGURE 4. Typical plasma parameters (n and B^2) of nonneutral plasma experiments. The black circle shows the region for toroidal experiments on electrons, while the white square does so for linear experiments on electrons, positrons, and ions. The solid line indicates the Brillouin density limit n_B for pure electron plasmas. As recognized, n of toroidal electron plasmas is higher than that of cylindrical plasmas. Some of them are close to n_B , in such cases, the difference between Φ_H and Φ_E clearly appears because $\Lambda \rightarrow 1$.

The above condition is satisfied when the plasma density n is much smaller than the Brillouin limit on number density n_B at which the value of ω_p^2/ω_c^2 equals $1/2$, where ω_p and ω_c are the plasma and cyclotron frequencies, respectively. Assuming $v_f \sim E/B$, then the ratio of $mv_f^2/2$ to $q\phi_p$ can be calculated as

$$\Lambda = \frac{mv_f^2/2}{q\phi_p} = \frac{q^2 E^2 / 2m\omega_c}{q\phi_p} \sim \frac{q}{2m} \frac{\phi_p}{\ell^2 \omega_c^2} \sim \frac{q}{2m} \frac{qn}{\epsilon_0 \omega_c^2} = \frac{1}{2} \frac{\omega_p^2}{\omega_c^2}. \quad (9)$$

Hence, if $n \ll n_B$, then $\Lambda \ll 1/4$. Thus, the error bar of ϕ_p caused by the Φ_H method becomes relatively small. Actually, this would hold in most electron plasmas confined in a linear device, although no probe measurements have been applied to them so far.

On the other hand, for the case of $n \sim n_B$, the value of $mv_f^2/2$ becomes comparable to that of $q\phi_p$, which brings about a larger error bar. This situation is easily realized in toroidal electron plasmas. In fact, n of toroidal electron plasmas can locally exceed n_B . Figure 4 shows typical regions of n versus the value of B^2 for past experiments on both toroidal (black circle) and linear (white square) devices (see Ref. [7] for the detail). As can be recognized from the black circle, values of n of most toroidal electron plasmas are close to n_B , and actually the data seem to exceed n_B . This means that the error bar caused by the Φ_H measurement must hardly be small in those experiments.

In fact, on Proto-RT experiments, the error bar is about -150 V which is three times as large as ϕ_p (~ -50 V), as seen in Fig. 4.

V SUMMARY

Current-voltage characteristics of a cylindrical probe are measured in electron plasmas. Similar to a neutral plasma, a current-voltage characteristic is completely established. However, because of fast flow, the characteristic curve significantly spreads out, exhibiting a long tail. This feature can almost be interpreted completely by a calculation of collected currents to the probe. As a first approximation, a cylindrical sheath is assumed to form around the probe even though the probe is immersed in flowing plasmas. The results indicate that the distribution function observed by a probe fixed in the laboratory frame is always a non-Maxwellian even if the rotating plasmas are completely relaxed to a state of thermal equilibrium. This holds even for cold electron plasmas in which a larger value of v_f/v_{th} is attained, causing the characteristic curve to become more broadened.

The space potential ϕ_p of electron plasmas is measured by an emissive probe, which basically works even in flowing electron plasmas. The negative potential Φ_E measured by the emissive probe is always higher than Φ_H : $|\Phi_E| < |\Phi_H|$, which points out the need for attention when the high impedance method is utilized to determine ϕ_p of electron plasmas. However, practically, the Φ_H measurement is still available for plasmas in which $\Phi_H/\Phi_E \rightarrow 1$, namely, electrostatic energy ($q\phi_p$) \gg flow energy ($mv_f^2/2$). Since the ratio of $mv_f^2/2$ to $q\phi_p$ can approximately be written as $\omega_p^2/2\omega_c^2$, the condition is satisfied when $n \ll n_B$ ($\Leftrightarrow \omega_p^2/2\omega_c^2 \ll 1/4$) where n_B is the Brillouin limit on number density.

ACKNOWLEDGMENTS

This work was supported in part by a Grant-in-Aid from the Japan Society for the Promotion of Science, No. 09308011 and No. 11780343.

REFERENCES

1. Janes, G. S. *et al.*, Phys. Rev. **145**, 925 (1966).
2. Daugherty, J. D. *et al.*, Phys. Rev. Lett. **20**, 369 (1968).
3. Stix, T. H., Phys. Rev. Lett. **24**, 135 (1970).
4. Himura, H. *et al.*, *accepted for publication in Fusion Energy 2000, 18th IAEA Fusion Energy Conference, Italy*, (IAEA, 2001) IAEA-CN-77-ICP/14.
5. Steinhauer, L. C. and Ishida, A., Phys. Plasmas **5**, 2609 (1998).
6. Mahajan, S. M. and Yoshida, Z., Phys. Plasmas **7**, 635 (2000).
7. Himura, H. *et al.*, Phys. Plasmas **8** (10) (2001).

Electron Plasma Confinement in a Partially Toroidal Trap

M.R. Stoneking, P.W. Fontana, R.L. Sampson, and D.J. Thuecks

Department of Physics, Lawrence University, Appleton, WI 54911

Abstract. A new experiment seeks to examine equilibrium, stability, and confinement properties of toroidal electron plasmas. Electron plasmas with density about $3 \times 10^6 \text{ cm}^{-3}$ are trapped for $\sim 100 \mu\text{s}$ in a "partially" toroidal (or 'C'-shaped) trap ($B \approx 200 \text{ G}$). Large amplitude oscillations are observed in the 100 kHz frequency range. The oscillation frequency is proportional to $1/B$ and depends on the applied horizontal electric field, but not on the amount of charge in the trap. Some evidence points toward the ion resonance instability as the cause of these oscillations.

INTRODUCTION

Theory supports the expectation that equilibria exist for nonneutral plasmas in a toroidal magnetic field [1, 2, 3, 4]. Under certain restrictions, the equilibria are also expected to be stable [5, 6, 7]. Experiments confirm the existence of equilibria [8, 9, 10, 11], but to date, no experiment has tested the theory closely.

In this paper we report first measurements from a new experiment that seeks to explore toroidal equilibrium, stability and confinement of pure electron plasmas. Controlled injection of charge into the toroidal field is a significant initial hurdle to successful trapping of a nonneutral plasma. Past experimenters focused significant effort toward solving this problem [8, 9, 10, 11], but none of them achieved the kind of reproducible initial charge distributions routinely obtained in cylindrical traps. The present experiment provides controlled charge injection by limiting the confinement region to a 'C'-shaped segment of the torus. Charge is loaded directly onto field lines tied to the *partially* toroidal trapping region.

TOROIDAL EQUILIBRIUM

A toroidal magnetic field is nonuniform in magnitude and possesses curvature. The field can be written as

$$\mathbf{B} = \frac{B_o R_o}{R} \hat{\phi}, \quad (1)$$

where R is the distance from the major axis (major radial coordinate), R_o is the major radius of the plasma, B_o is the magnetic field at the center of the plasma, and $\hat{\phi}$ is the unit vector in the toroidal (azimuthal) direction. In the absence of other fields, charged particle guiding centers drift in the z -direction (vertically in most experimental configurations) due to the ∇B -drift and the curvature-drift. Circulation in the poloidal

plane superimposed on the cross-field drifts can close the drift orbits. In the tokamak (and other toroidal quasineutral plasma devices), poloidal circulation of particles is ensured by giving the field a rotational transform, a poloidal field component generated by a toroidal plasma current. Field lines are then toroidal helices and particles circulate in the poloidal plane as a result of flow parallel to \mathbf{B} .

By contrast, the hope for establishing closed drift orbits in a toroidal *nonneutral* plasma rests on the presence of the space charge electric field. A toroidal nonneutral plasma circulates in the poloidal plane because the space charge electric field provides a poloidal $\mathbf{E} \times \mathbf{B}$ drift. In a purely toroidal magnetic field, the single particle total energy (in the drift orbit approximation) can be written as

$$U(R, z) = qV(R, z) + \frac{L_z^2}{2mR^2} + \frac{\mu B_o R_o}{R}, \quad (2)$$

where q and m are the particle's charge and mass respectively, V is the electrostatic potential, L_z is the component of the angular momentum about the symmetry axis (z-axis), and μ is the particle's magnetic moment. The first term in Eq. 2 is the potential energy, the second is kinetic energy associated with motion parallel to \mathbf{B} , and the last term is kinetic energy associated with the gyro-motion perpendicular to \mathbf{B} . Total energy, angular momentum and magnetic moment are all conserved. As the particle $\mathbf{E} \times \mathbf{B}$ drifts around from the low field (outboard) side of the poloidal plane to the high field (inboard) side, both kinetic energy terms increase at the expense of electrostatic potential energy. The particle moves down the potential energy hill. Closed drift orbits will exist only if the electrostatic potential energy is greater than the change in the particle's kinetic energy as it goes from outboard to inboard. A rough criterion for closing the drift orbits in a toroidal nonneutral plasma is therefore, $qV_s > kT$, where V_s is the space charge potential of the plasma, and kT is the temperature (times Boltzmann's constant).

Consider the difference between charged particle drift orbits in the presence of a substantial space charge and orbits in a field with a rotational transform but no space charge. If the magnetic field possesses a rotational transform, the single particle energy cannot be written in the form of Eq. 2. The (canonical) angular momentum includes a term due the magnetic vector potential (or equivalently the poloidal magnetic flux) and therefore kinetic energy associated with parallel motion, when expressed in terms of the conserved canonical angular momentum, is z- as well as R-dependent. As charged particles flow along the magnetic field from the low field side to the high field side, they gain perpendicular kinetic energy (μ is conserved) at the expense of parallel kinetic energy ($V \approx 0$). Particles with insufficient parallel kinetic energy on the low field side are reflected at the point where parallel kinetic energy vanishes. These are the so-called "trapped particles" in the tokamak with "banana"-shaped drift orbits. In the toroidal *nonneutral* plasma the energy exchange is between electrostatic potential energy and kinetic energy as opposed to an exchange between parallel and perpendicular kinetic energy. Therefore, there are no banana orbits in the nonneutral case.

The equilibrium momentum equation for the electron fluid, neglecting electron inertia and thermal effects, is

$$\mathbf{J} \times \mathbf{B} = -ne\nabla V, \quad (3)$$

where n is the electron density and e is the elementary charge. The cold electron fluid $\mathbf{E} \times \mathbf{B}$ drifts along equipotential contours. Because the plasma is nonneutral, the drift results in a current, \mathbf{J} , which when crossed into the magnetic field, \mathbf{B} , balances the electrostatic self-repulsion of the plasma. By writing the momentum equation in the form of Eq. 3, its similarity to the magnetohydrodynamic (MHD) equilibrium momentum equation is evident, $\mathbf{J} \times \mathbf{B} = \nabla p$. In MHD theory the diamagnetic current crossed into the magnetic field balances the pressure gradient force. The thermal pressure plays a role in MHD equilibrium theory that is nearly analogous to the electrostatic potential energy density for the electron fluid. Combining Eq. 3 with the steady-state continuity equation and using the form for the toroidal magnetic field (Eq. 1), the electron density can be written as [1]

$$n = \frac{f(V)}{R^2}, \quad (4)$$

where $f(V)$ is an arbitrary function of the potential. Evidently, the electron density must vary along an equipotential contour as $1/R^2$. This result can also be obtained by conserving the number of electrons in a magnetic flux tube ("frozen flux") as the fluid element associated with the flux tube $\mathbf{E} \times \mathbf{B}$ drifts around in the poloidal plane. The area of the flux tube is proportional to R ($A \propto 1/B \propto R$) and the length of the flux tube is also proportional to R ($L = 2\pi R$), leading to Eq. 4. Substituting Eq. 4 into Poisson's equation yields a partial differential equation for the electrostatic potential [1] (this equation is the analog of the Grad-Shafranov Equation [12] for toroidal MHD equilibrium).

In the MHD description of toroidal plasma equilibrium, force balance in the major radial (\hat{R}) direction must be considered [13]. For example, a toroidal plasma current leads to a magnetic "hoop force" directed away from the z-axis. Also, since the pressure gradient has more surface area to act against on the outboard side, there is an outward force known as the "tire tube" force. Equilibrium is provided by a "vertical" (z-directed) magnetic field, oriented such that the $\mathbf{J} \times \mathbf{B}$ force is inward (toward the z-axis), where \mathbf{J} is the toroidal plasma current. The vertical field can be generated passively by surrounding the plasma with a conducting shell, so that as the plasma expands in the \hat{R} direction image currents arise to provide the vertical magnetic field necessary to establish equilibrium. More commonly the vertical field is applied actively using a set of vertical field coils. The position (and shape) of the plasma equilibrium can be controlled in this way. There are analogous "toroidal" forces for an electron plasma [3]. Electrostatic self-repulsion is the source of a "hoop force," because a charged hoop tends to expand. The electrostatic force also has a larger surface area to act against on the outboard side of a finite aspect ratio torus leading to an electrostatic "tire tube" force. In electron plasmas a *horizontal electric field* plays the role of the MHD vertical magnetic field. An electric field in the $+\hat{R}$ direction exerts an inward force on the plasma opposing the outward hoop and tire tube forces. Bhattacharyya and Avinash [5] investigated not only the required magnitude of the horizontal electric field, but the index of variation in the horizontal field required to avoid certain macroscopic instabilities (involving axisymmetric rigid displacements). The experimental design discussed below incorporates horizontal field electrodes that permit a test of theoretical predictions like those of Bhattacharyya and Avinash.

EXPERIMENTAL DESIGN

The experiment makes use of a novel "partially" toroidal design. Sacrificing some of the symmetry of a completely toroidal trap, charge is injected directly onto field lines tied to the trapping region. The trapping region consists of a 'C'-shaped 335° toroidal arc whose ends are defined by the presence of two grids (Fig. 1). Electrons are injected and trapped by application of suitably timed gate pulses to these grids, in a manner similar to the trapping of nonneutral plasmas in cylindrical Penning-Malmberg traps. During the injection phase, the grid furthest from the electron source (referred to hereafter as the "collector grid") is biased to reflect electrons. Trapping begins when the near grid (referred to hereafter as the "source grid") is biased to shut off the source and isolate the trapped population. After a specified "hold time," the trap is dumped onto a collector by removing the bias from the collector grid. The electron source and the collector are located back-to-back between the two grids, but are not shown in Fig. 1.

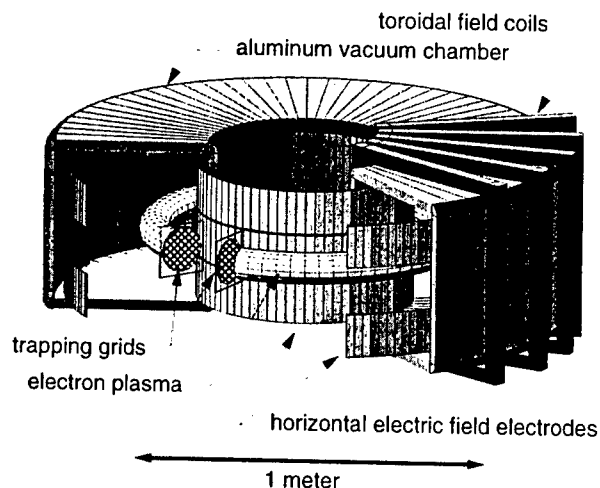


FIGURE 1. Cutaway view of toroidal vacuum chamber showing the trapping grids, horizontal electric field electrodes, a representative set of toroidal field coils and the electron plasma (the electron source and collector reside back-to-back between the grids but are not shown).

The vacuum chamber for this experiment is a 3 cm thick aluminum chamber with a square poloidal cross section [14]. The major radius of the chamber is 50 cm and the poloidal cross-section has inner dimensions of 44 cm by 44 cm. Base pressures of $\sim 2 \times 10^{-7}$ Torr are achieved with a 700 l/s turbomolecular pump, but the pressure rises to $\sim 10^{-6}$ Torr when the tungsten filament (electron source) is heated to its emitting temperature of 1900 K. The toroidal magnetic field coil is composed of 96 turns of 4/0 cable bundled on the outboard side into 24 evenly spaced bundles of 4 turns each. Two interleaved sets of 12 bundles, connected in series, are wound with opposing helicity ensuring that the net toroidal current is zero. The maximum field at the center of the plasma is $B_\theta \approx 196$ Gauss when the coil is energized with 440 A. The field can be maintained for 30 seconds or more and re-established about every minute without heating the coils significantly.

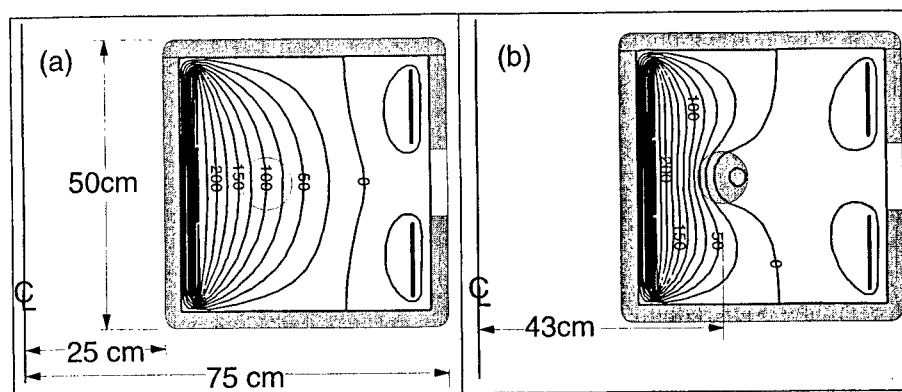


FIGURE 2. A poloidal cross-section of the torus showing (a) the vacuum equipotential contours when +250 V is applied to the inner hoops and -50 V to the outer hoops (contours are spaced every 25 V, open circle indicates location of plasma), and (b) the equipotential contours in the presence of an electron plasma (shaded circle) with average density $3.1 \times 10^6 \text{ cm}^{-3}$.

The electron source is a pancake spiral with 22 turns of 0.5 mm diameter pure tungsten wire. The spiral has a radius of 4.5 cm, the minor radius of the resulting plasma. The center of the filament and the target major radius of the plasma is 43 cm from the major (or z-) axis, a location where the toroidal field ripple is a minimum. Consequently, the plasma is not centered in the chamber, but is 7 cm inboard of the chamber's major radius. The center of the filament is biased to -100 V with respect to its edge, drawing 10.2 A of heating current. The edge of the filament is biased independently with respect to the grounded vacuum chamber. Electrons are drawn from the hot filament by the grounded source grid, a 52% transparent stainless steel grid located 4 cm from the filament. A -250 V potential applied to the source grid suppresses electron flow from the source to the trapping region or vice versa. The collector grid is 252 cm from the source grid as measured along the field. A -300 V potential applied to the collector grid prohibits electron flow from the trapping region to the collector and when +100 V is applied to the grid, the trap contents are dumped. The collector is an aluminum plate biased to +150 V. Collector current is measured with a 1 k Ω sampling resistor.

Five internal stainless steel hoops serve as horizontal electric field electrodes. Three hoops hug the inner wall of the vacuum chamber and the other two are placed above and below the midplane near the outer wall as shown in Fig. 2. Most of the ports are on the outer midplane and the gap between the outer hoops permits diagnostic access, a high conductivity path for pumping, and visual sight lines for inspection of the filament assembly. A typical vacuum equipotential calculation in the poloidal plane is shown in Fig. 2a. While the five hoops can be biased independently, providing control of both the field magnitude and variation across the location of the plasma, for the work reported here the three inner hoops are biased together and the two outer hoops are biased together.

The collector permits diagnosis of the charge remaining in the trap after a specified hold time; however, the measurement requires the destruction of the plasma. An in-

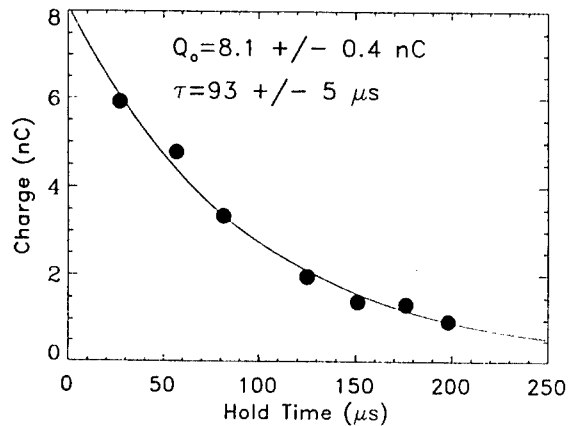


FIGURE 3. Charge (adjusted for trapping grid transparency) dumped onto detector after holding the trap shut for various intervals (circles), and an exponential fit to the data (solid line).

sertable five tip probe can access the plasma *in situ*. The five stainless steel probe tips (1 mm diameter by 3 mm long) are spaced 1.5 cm apart vertically with the middle tip on the midplane. In the work reported here the probe was fixed in position with the middle probe tip 2.5 cm outside the plasma (outboard side). The tips were connected to ground across 11 kΩ, and the flow of image charges across the resistor in response to plasma motion is the signal of interest.

MEASUREMENTS AND RESULTS

To measure the charge confinement time, the trapping grids are cycled through a fill-hold-dump sequence a number of times with different hold times. For each sequence the pulse on the detector is integrated and adjusted for the known transparency of the trapping grid to obtain the total charge leaving the trap. To our knowledge this is the first time the confinement time for a toroidal nonneutral plasma has been measured by the same direct method used in cylindrical Penning-Malmberg traps. Typical results are shown in Fig. 3 (The magnetic field was 196 G at $R = R_o = 43$ cm, the inner hoops were biased to +250 V and the outer hoops to -50 V). The charge remaining in the trap decays with a $93 \pm 5 \mu\text{s}$ exponential decay time. By extrapolating the fit back to zero hold time, the maximum trapped charge can be obtained, 8.1 ± 0.4 nC. The trapped charge corresponds to $\sim 5 \times 10^{10}$ electrons and a mean electron density of $(3.1 \pm 0.1) \times 10^6 \text{ cm}^{-3}$.

The electrostatic potential in the presence of an electron plasma with average density of $3.1 \times 10^6 \text{ cm}^{-3}$ is shown in Fig. 2b. The region of closed potential contours is small compared to the plasma size. Since cold electrons will $\mathbf{E} \times \mathbf{B}$ drift along equipotential

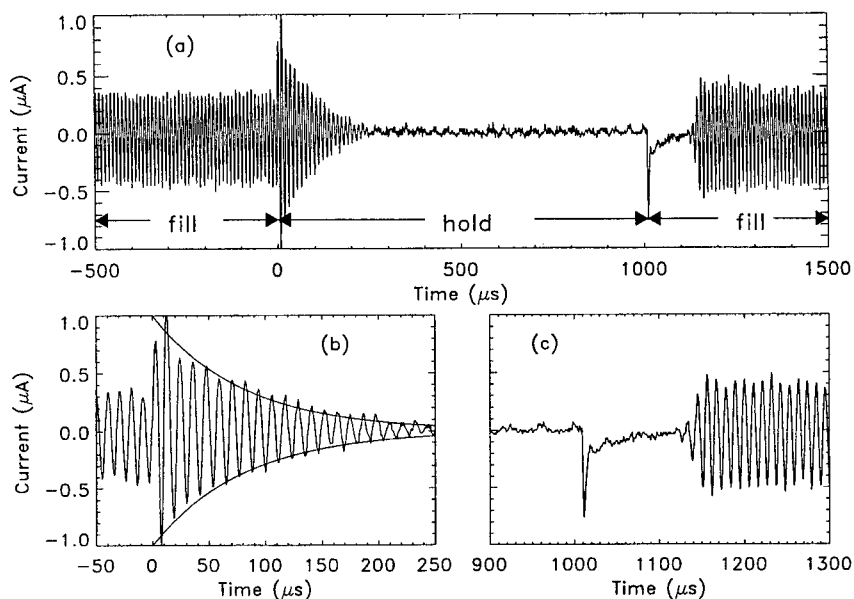


FIGURE 4. Probe signal showing the rate of image charge flow to/from the probe tip (a) while the trap is alternately filled and trapped (trap closes at $0\ \mu\text{s}$), (b) for times early in the hold phase with an $80\ \mu\text{s}$ exponential decay envelope superimposed on the signal, and (c) for times after the trap is opened showing $\sim 120 - 150\ \mu\text{s}$ delay before oscillations reappear.

contours, the region of closed drift orbits for a cold plasma is small. To obtain closed drift orbits that coincide with the location and size of the plasma, substantial curvature drift (or ∇B -drift) effects must be included. Typical electron energies must be 100-200 eV to produce drift orbits consistent with the observed location of the plasma. This energy range is consistent with the acceleration energy given to electrons as they leave the filament, because the center of the filament is at $-200\ \text{V}$ with respect to ground and the $0\ \text{V}$ contour passes near the center of the plasma in this case (Fig. 2b).

Under nearly the same experimental conditions used to obtain the confinement time data in Fig. 3, the flow of image charge signal to and from a probe tip near the plasma is displayed in Fig. 4a. The collector grid was maintained at a steady $-400\ \text{V}$ while $1\ \text{ms}$ long ($-250\ \text{V}$) pulses were applied to the source grid. Instead of a fill-hold-dump cycle, this constitutes a fill-hold-fill-hold-... sequence. The hold time is long enough to permit all of the charge to escape before the trap is filled again. There are three features to note in Fig. 4. First, during the fill phase of the cycle ($t < 0\ \mu\text{s}$), prior to application of negative trapping bias to the source grid, a large amplitude oscillation is detected on the image charge signal to the probe. The power spectrum for the signal during this phase (Fig. 5a) is dominated by a narrowband feature and its harmonics. Second, when the trap is closed ($t = 0\ \mu\text{s}$), the oscillation grows to larger amplitude very quickly and

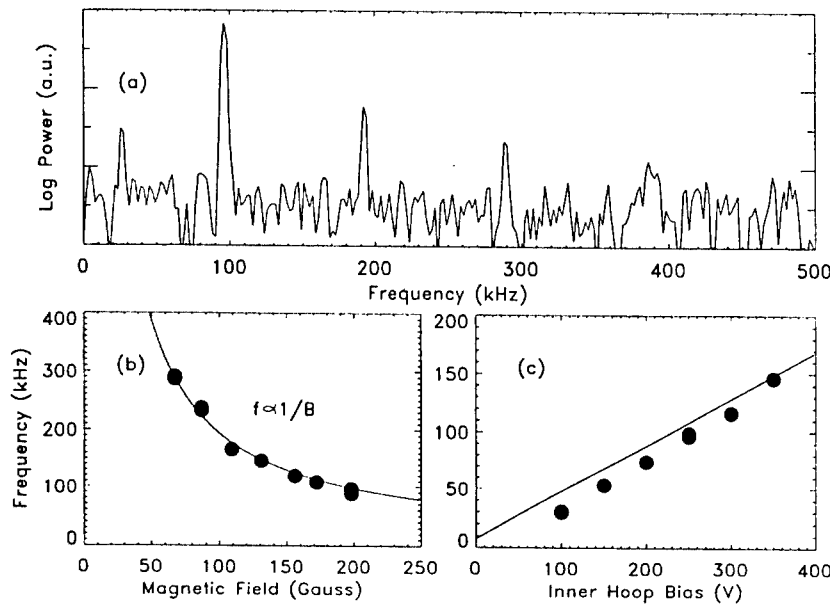


FIGURE 5. The oscillations detected on the probe tip have (a) a power spectrum during fill phase that is dominated by a ~ 100 kHz feature and its harmonics, (b) a fundamental frequency (circles) that is proportional to $1/B$ (solid line is a fit to $1/B$), and (c) a frequency (circles) roughly proportional to the applied horizontal electric field (solid line is E_R/RB_0 , where E_R is the calculated vacuum horizontal field).

then decays. The amplitude envelope decays exponentially with a time constant ($\sim 80 \mu\text{s}$, Fig. 4b) comparable to the confinement time obtained by dumping the trap contents onto the detector (Fig. 3). Note, however, that the oscillation frequency remains constant as the amplitude decays. Third, when the trap is opened again ($t \approx 1000 \mu\text{s}$), there is delay of about $120 - 150 \mu\text{s}$ before the oscillation sets in again (Fig. 4c).

The exponential decay of the oscillation amplitude provides a rapid, alternate method of measuring the confinement time while changing other control variables. Figure 6 shows the decay time constant for the oscillation amplitude as the magnetic field is varied from 67 G to 198 G. The confinement time (as measured by the decay time for the low frequency oscillations) scales roughly as $B^{3/2}$. The scaling differs from the B^2 scaling observed in cylindrical traps both when losses are due to collisions with neutrals [15] and when losses are due to trap asymmetries [16].

The observed low-frequency oscillations are evidently not a straightforward modification of the diocotron modes seen ubiquitously in cylindrical nonneutral plasmas. The longest wavelength diocotron wave (azimuthal mode number $m_\theta = 1$) has a frequency that is proportional to the total charge (per unit length), and shorter wavelength modes have frequencies that are (roughly) proportional to the charge density [17]. The oscillations observed in this experiment maintain a fixed frequency as the plasma decays,

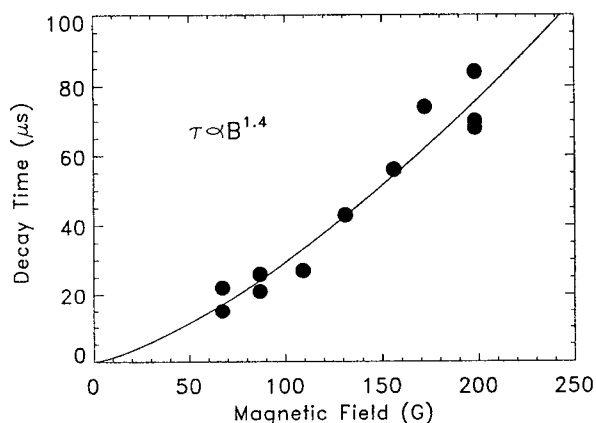


FIGURE 6. The decay time constant for the oscillation amplitude (circles) versus magnetic field, and a power law fit (solid line) with exponent 1.4 ± 0.1 .

indicating that the frequency does not depend on the total charge. It is possible that the charge density remains constant as the plasma sheds electrons from its outer surface and that the observed oscillation is a diocotron wave with $m_0 > 1$. It seems more likely however, that the presence of the applied horizontal electric field introduces a new mode of oscillation not present in the cylindrically symmetric trap. Bhattacharyya and Avinash [5] predict a mode with characteristic frequency in the range of E_R/RB_0 , where E_R is the magnitude of the vacuum horizontal electric field. The experimentally measured frequency is proportional to $1/B$ (Fig. 5b), and is nearly proportional to E_R (Fig. 5c). Bhattacharyya and Avinash model the plasma with a charged hoop, neglecting the internal structure of the plasma, and consider only modes of oscillation involving rigid axisymmetric displacements. The magnitude of the horizontal electric field required experimentally to trap electrons (~ 925 V/m) is much larger than their model predicts for the same total charge (~ 140 V/m) and the index of variation for the field would make the mode unstable with a purely imaginary frequency. The model evidently needs to be extended to explain our observations.

The $120 - 150 \mu$ s delay before the oscillations reappear after opening the trap (Fig. 4c) suggests that the catalyst for growth of the oscillations is the accumulation of ions. The neutral pressure (measured with a standard hot filament ion gauge) is in the range $1 - 2 \times 10^{-6}$ Torr during these experiments. The residual gas is a mix of molecular hydrogen, water vapor and molecular nitrogen. A typical room temperature proton produced by electron impact ionization of residual gas will drift out of the trap on a $\sim 500 \mu$ s timescale, hence on the timescale of the experiments reported here ions are, for all practical purposes, confined. An order of magnitude calculation suggests that a significant ion population ($\sim 10\%$ of n_e) could accumulate in 100μ s. When the ion orbit frequency resonates with a mode of the electron plasma, the ion resonance instability

sets in [18, 19]. The negative energy electron mode grows by pumping up the ion orbits. At this time we do not have a quantitative understanding of the oscillation frequency or spatial structure.

CONCLUSIONS

Electron plasmas with confinement times as long as $100\ \mu\text{s}$ ($B \approx 200\ \text{G}$) and densities $n \approx 3 \times 10^6\ \text{cm}^{-3}$ are produced in a partially toroidal trap. Successful trapping requires application of a horizontal electric field as predicted by Bhattacharyya and Avinash [5], although the magnitude of the applied field is significantly larger than theory predicts for a high aspect ratio electron plasma. Drift orbit calculations suggest that typical electron energies are in the range of 100-200 eV. The confinement time is found to scale with magnetic field as $\tau \propto B^{1/2}$, weaker than the B^2 scaling seen in cylindrical traps [15, 16]. Low frequency oscillations are observed with a frequency roughly proportional to E_R/B , where E_R is the vacuum applied horizontal electric field. Some indications point toward the ion resonance instability as the cause of these oscillations [18, 19].

ACKNOWLEDGMENTS

The authors acknowledge the contributions of Angela Kopp. The project is funded by Lawrence University and by grants from Research Corporation (Award No. CC4593) and the U.S. Department of Energy (Grant No. DE-FG02-98ER54503).

REFERENCES

1. Daugherty, J.D. and Levy, R.H., *Phys. Fluids* **10**, 155 (1967).
2. Elsässer, K., Yu, M.Y., and Shukla, P.K., *Phys. Lett. A* **152**, 59 (1991).
3. Avinash, K., *Phys. Fluids B* **3**, 3226 (1991).
4. Hurricane, O.A., *Phys. Plasmas* **5**, 2197 (1998).
5. Bhattacharyya, S.N. and Avinash, K., *Phys. Fluids B* **4**, 1702 (1992).
6. Bhattacharyya, S.N. and Avinash, K., *Phys. Lett. A* **171**, 367 (1992).
7. O'Neil, T.M. and Smith, R.A., *Phys. Plasmas* **1**, 2430 (1994).
8. Daugherty, J.D., Eninger, J.E., and Janes, G.S., *Phys. Fluids* **12**, 2677 (1969).
9. Clark, W., Korn, P., Mondelli, A., and Rostoker, N., *Phys. Rev. Lett.* **37**, 592 (1976).
10. Puravi Zaveri, John, P.I., Avinash, K., and Kaw, P.K., *Phys. Rev. Lett.* **68**, 3295 (1992).
11. Khirwadkar, S.S., John, P.I., Avinash, K., and Kaw, P.K., *Phys. Rev. Lett.* **71**, 4334 (1993).
12. Freidberg, J.P. *Ideal Magnetohydrodynamics*, Plenum Press, New York, 1987, pp.75-83.
13. *Ibid.*, p.111.
14. The vacuum chamber was formerly used in the Tokapole II experiment. See for example, Biddle, A.P., *et. al.*, *Nucl. Fusion* **19**, 1509 (1979).
15. deGrassie, J.S. and Malmberg, J.H., *Phys. Fluids* **23**, 63 (1980).
16. Driscoll, C.F. and Malmberg, J.H., *Phys. Rev. Lett.* **50**, 167 (1983).
17. Davidson, R.C. *Physics of Nonneutral Plasmas*, Addison-Wesley, Redwood City, CA, 1990, p. 304.
18. Levy, R.H., Daugherty, J.D., and Buneman, O., *Phys. Fluids* **12**, 2616 (1969).
19. Peurrung, A.J., Notte, J., and Fajans, J., *Phys. Rev. Lett.* **70**, 295 (1993).

Comparative experimental study of large-scale fluctuations in a toroidally magnetized low- β plasma

O. Grulke*, F. Greiner[†], T. Klinger* and A. Piel[†]

*MPI for Plasmaphysics, EURATOM Association, D-17491 Greifswald, Germany

[†]IEAP, Christian-Albrechts-University, D-24098 Kiel, Germany

Abstract. A comparative experimental study of large-scale space-time structures embedded into the broad-band multi-scale turbulent plasma fluctuations of the purely toroidally magnetized experiment TEDDI is presented. Two different plasma sources are compared: Plasma can be produced either by a thermionic discharge or by inductive heating by a helicon antenna. Turbulent plasma potential and plasma density fluctuations were analyzed by conditional averaging. It turned out that large-scale space-time structures develop on both plasmas, which propagate with local $E \times B$ drift. A contribution of diamagnetic drifts is not observed. In the thermionic discharge dipole-like density structures are found, in the helicon discharge the detected structures are generally of monopole-like shape and are considerably sized when compared to the thermionic discharge. Direct measurements of the fluctuation induced transport can be related to the specific properties of the detected large-scale fluctuation structures. It is concluded that the injection of the negative space charge via the heated filament greatly alters the properties of the turbulent fluctuations. Although the basic statistical properties are substantially unaffected by the plasma source a strong influence on the formation of large-scale fluctuation structures and the associated transport is found.

INTRODUCTION

It is a well known feature of turbulent systems that they develop large-scale space-time fluctuation structures. Fluctuation structures can be observed not only in plasmas but also in turbulence in neutral fluids, atmospheric turbulence etc. In plasmas the formation and properties of space-time fluctuation structures have been attracting great attention because they are suggested to contribute significantly to the fluctuation induced transport perpendicular to the magnetic field. The large fluctuation amplitudes can lead to large transport events and the large spatial extent of the structures leads to transport over large radial distances.

Experimentally, investigations of large-scale fluctuation structures were conducted in linear [1, 2, 3, 4] as well as in toroidal magnetic field geometry [5, 6, 7].

In linear geometry long-living large-scale monopole-like structures embedded into the turbulent plasma fluctuations were detected. In toroidal geometry large-scale fluctuation structures were also found but with different basic properties. Here, the detected structures have dipole-like shape. The interpretation of this difference is complicated because the effect of the magnetic field geometry in the toroidal devices are generally strongly entangled with effects arising from charge sources present to produce the plasma in

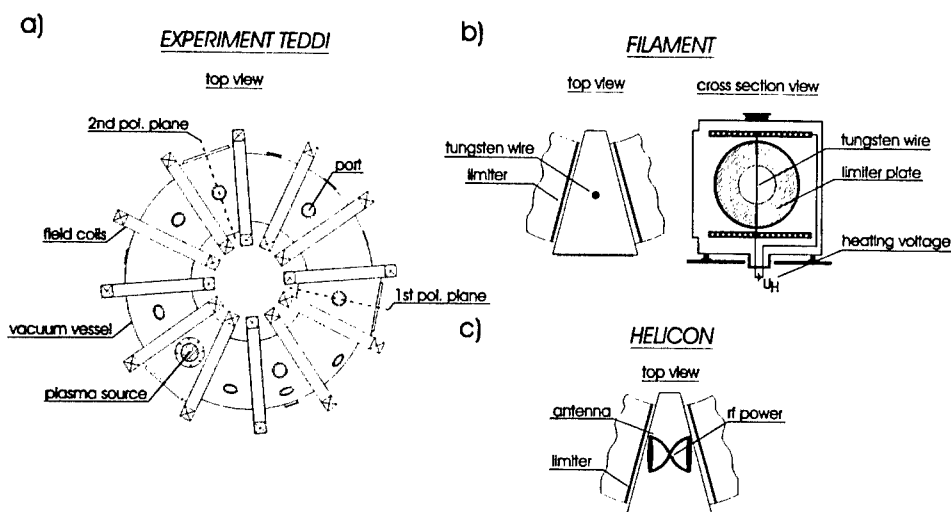


FIGURE 1. Schematic drawing of the TEDDI device (a) together with the two plasma sources, the filament source (b) and the helicon source (c).

these campaigns. Based on numerical simulations it was suggested that the formation of dipole-like structures can be mainly attributed to the presence of the charge source [8, 9]. To separate the geometry from plasma source effects an experimental study conducted in a device with simple toroidal magnetic field geometry is presented, in which two different plasma sources are used. First, plasma can be produced by the injection of highly energetic electrons, which is the standard method for plasma production in such devices. Alternatively, plasma can be produced 'quasineutral' by inductive heating without the injection of net charge.

This paper is organized as follows: After the introduction of the experimental setup the diagnostics and data analysis method of conditional averaging are briefly described. Subsequently the experimental results of conditional averaging for both plasmas and direct measurements of the fluctuation induced transport are presented. Finally, the results are summarized and conclusions are drawn.

EXPERIMENTAL SETUP

The experiments were conducted in the toroidal plasma device TEDDI [10, 11, 12]. A schematic drawing of the device and the plasma sources is shown in Fig. 1. It consists of a toroidal vacuum chamber with three wedge-shaped segments, where the plasma

TABLE 1. Device and typical plasma parameters valid for the filament and helicon operation.

Parameter	Value
large device radius	0.3 m
small device radius	0.1 m
neutral Argon gas pressure	$3.2 \cdot 10^{-2}$ Pa
magnetic field	0.15 T
plasma density	$1 \cdot 10^{16} \text{ m}^{-3}$
electron temperature	4 eV
ion temperature	0.03 eV
filament operation:	
discharge voltage	100 V
discharge current	0.2 A
helicon operation:	
rf frequency	28MHz
rf power	200W

source is placed and measurements of poloidal cross sections are performed. The device is magnetized by 12 planar poloidal magnetic field coils. Consequently, the magnetic field is purely toroidal. The typical magnetic field strength on the device axis is 0.15T. Plasma can be produced by two completely different discharge mechanisms: by direct injection of high energetic electrons (filament discharge) or by inductive coupling (helicon discharge). For the filament discharge (Fig. 1(b)) a tungsten wire is inserted into the vacuum vessel. The wire is directly heated by a DC current and the emitted electrons are accelerated between the negatively biased filament and the grounded poloidal limiters placed on both sides of the source region. Plasma is produced by ionizing collisions between the primary electrons and the Argon neutral gas background.

Alternatively, the plasma can be produced inductively. For this discharge mode a helicon antenna [13] (double-half-turn right-helical antenna) is installed at the position of the filament (Fig. 1(c)). Measurements of the magnetic wave field suggest that a helicon $m = 1$ mode is driven by the antenna at a rf-frequency of 10-30MHz [10]. With a rf-power of 200W similar plasma density and electron temperature are obtained when compared to the filament discharge.¹ The basic device and plasma parameters are compiled in Tab. 1. The important difference between the two discharge types is that a strong negative source of charge is present in the filament generated plasma whereas plasma production is 'quasineutral' in the helicon discharge. This difference facilitates for direct investigation of the influence of net sources of charge on the formation and properties of large-scale fluctuation structures.

¹ It should be noted that helicon discharge in this context does not indicate the very efficient antenna-plasma coupling that leads to 100% ionization degree [14]

DIAGNOSTICS AND DATA ANALYSIS

Measurements are performed with electric probes exclusively. Equilibrium plasma parameter profiles are obtained by evaluation of Langmuir probe characteristics. For density fluctuation measurements Langmuir probes are negatively biased and the ion saturation current fluctuations are taken as proportional to density fluctuations. For plasma potential fluctuations emissive probes are used, which are fairly insensitive against hot electron components [15, 16]. Fluctuation induced transport measurements are performed with triple probes.

Large-scale fluctuation structures are extracted out of the noise-like turbulent fluctuations by the statistical method of conditional averaging (CA). In its simplest form CA is based on two simultaneously recorded time series: On fluctuation time series Φ_{ref} is recorded at a fixed spatial point \vec{r}_0 and acts as the reference signal for the analysis. Another fluctuation time series Φ_{pos} is recorded at an arbitrary second spatial position $\vec{r}_0 + \Delta\vec{r}$, here called the positioned signal. By a predefined condition ρ on Φ_{ref} characteristic events in the time series are detected. Together with a time interval $\Delta\tau$ around these time instants t_i an ensemble of sub-time series out of Φ_{mov} of length N are collected, which are taken as statistical independent realizations of a random process. Consequently, ensemble averaging of the sub-time series extracts the part of fluctuations, which is consistently repeated in the sub-time series (coherent part) whereas the incoherent fluctuations are suppressed. The procedure reads:

$$\Phi_{\text{con}}(\vec{r}_0 + \Delta\vec{r}, \tau) = \frac{1}{N} \sum_{i=1}^N [\Phi_{\text{pos}}(\vec{r}_0 + \Delta\vec{r}, t_i + \tau) | \Phi_{\text{ref}}(\vec{r}_0, t_i) = \rho] . \quad (1)$$

The idea of conditional average is as follows: If a large-scale fluctuation structure passes the position of the reference probe, it produces a specific signal pattern in Φ_{ref} , which is detected by the condition ρ . If the structure, depending on its lifetime and propagation, reaches the positioned probe, a similar signal pattern is produced in Φ_{pos} . By taking the time instants t_i as the reference time for the analysis, the phase relation of structures occurring in the reference and positioned signal is conserved and ensemble averaging extracts the structure from the superimposed random turbulent background fluctuations. To obtain a confidence level for CA a conditional deviation is defined as the standard deviation at each time lag $\tau \in \Delta\tau$ of the difference between the conditionally averaged structure and the single realization of the sub-time series. This quantity is normalized to the standard deviation of the reference signal

$$\sigma_{\text{CA}}(\vec{r}_0, \tau) = \frac{\sigma([\Phi_{\text{con}}(\vec{r}_0, \tau) - \Phi_{\text{ref}}(\vec{r}_0, t_i + \tau)]_{i=1 \dots N})}{\sigma(\Phi(\vec{r}_0, t))} . \quad (2)$$

A value of σ_{CA} well below unity indicates that the single realizations are reproducible whereas values close to one indicates that the single realizations strongly deviate from the average result.

For the current analysis an amplitude condition of 1σ together with a rising slope condition is used. The slope condition ensures that events are always found on the same slope of the fluctuation signal and artificial phase shifts due to the finite widths of the fluctuations are avoided.

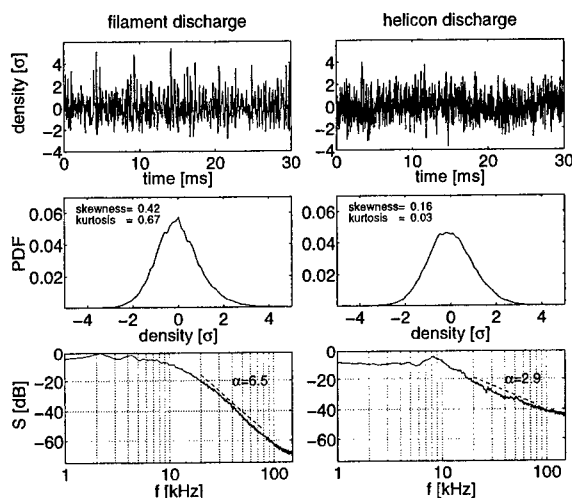


FIGURE 2. Density fluctuations (top row) with the respective probability distribution function (middle row) and power spectral densities (bottom row) for the filament (left column) and the helicon discharge (right column)

EXPERIMENTAL RESULTS

Basic statistical properties of turbulent fluctuations

In Fig. 2 time series of plasma density fluctuations are shown for both discharges together with their probability distribution function (PDF) and their power spectral density. The density fluctuations in both discharges show an irregular behavior. In the filament discharge fluctuation are slightly burst-like, whereas in the helicon discharge the density fluctuation show a noisy behavior. This is also expressed by the PDF, which is peaked and asymmetric for the filament discharge. This is quantified by the non-zero higher moments skewness and kurtosis (note that a Gaussian distribution has $s=0$, $k=0$ in this representation). In the helicon discharge the PDF is of almost perfect Gaussian shape. Both power spectral densities show a power law decrease $S(f) \propto f^{-\alpha}$ over one frequency decade, which indicates that both plasma are in a fully developed turbulent state [17]. The decrease is stronger in the filament plasma with a spectral index of $\alpha = 6.5$ whereas in the helicon plasma the spectral index is $\alpha = 2.9$.

Conditional averaging results

In Fig. 3 typical results of CA of the reference and positioned probe are presented for both discharge types. The reference signals show a pronounced positive fluctuation structure, which is mainly induced by the positive amplitude condition met at $\tau = 0$. The temporal width of the pattern is larger for the filament plasma when compared to the

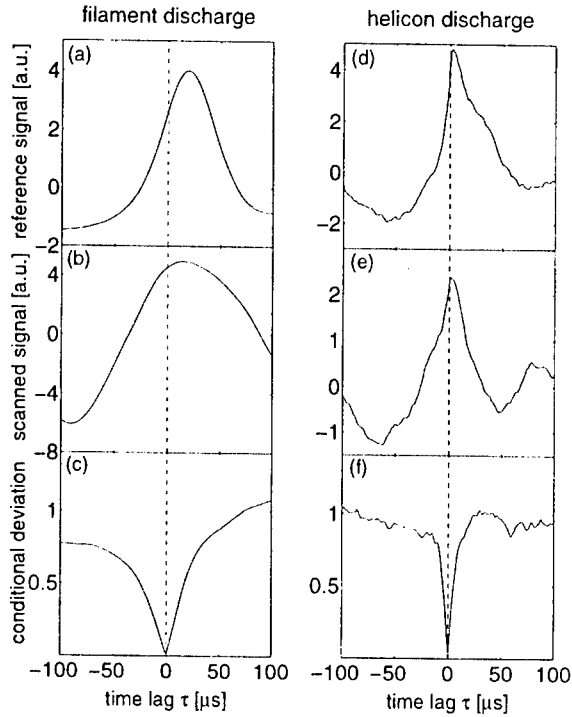


FIGURE 3. Conditional averaging signal at a single spatial point. Shown are the conditionally averaged reference signals (a), (d), the conditionally averaged positioned signals (b), (e), and the respective conditional deviations as defined in Eq. 2 (c), (f) for the filament and the helicon discharge

helicon plasma. Stronger differences are found in the positioned signal. Here, a dipole-like behavior is observed in the filament plasma with negative and positive amplitudes of similar magnitude. In the helicon plasma the conditionally averaged positioned signal shows a positive amplitude fluctuation with only little adjacent minima. The conditional deviation is zero at the time instant where the condition is fulfilled and increases with increasing absolute value of the time lag τ . It is noticeable that the temporal confidence interval is larger in the filament plasma than in the helicon plasma.

To obtain space-time information of large-scale fluctuation structures measurements of density fluctuations are performed in a two-dimensional section perpendicular to the magnetic field lines. The results are shown in Fig. 4 for the filament generated plasma and in Fig. 5 for the helicon plasma.

Filament discharge. In Fig. 4 the results of CA of density fluctuations for a complete poloidal section are shown in normalized values. The time interval extends over $160\mu s$. The cross at $\tau = 0$ indicates the position of the reference probe. Large-scale minimum fluctuation structures with adjacent maximum structures are found in the complete time window under consideration. Thus, the observed structure always appear in a dipole-like configuration. The minimum structure propagates radially outwards during the first

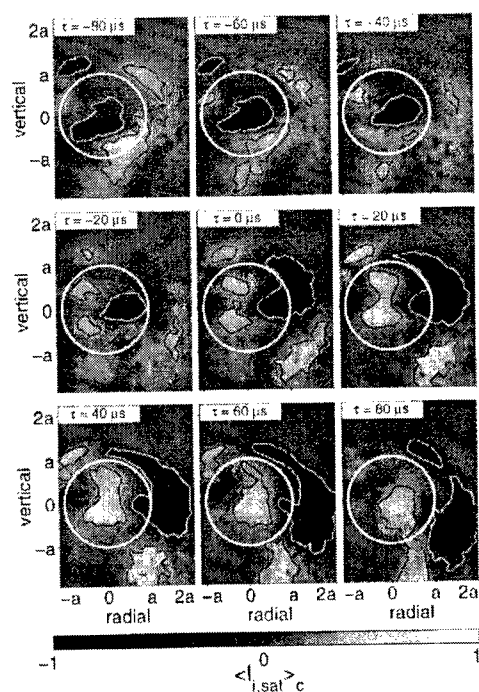


FIGURE 4. Conditional averaging results in a two-dimensional plane for density fluctuations in the filament discharge. The ambient magnetic field points into the plane. The solid white circle indicates the inner limiter radius. Minimum and maximum structures are emphasized by white and black contour lines, respectively, which represent a level of 30% of the peak amplitudes. The labeling of the radial and vertical axes are in units of the inner limiter radius a .

half of the time window $\tau = -80 \dots 0 \mu\text{s}$ and poloidally during the second half from $\tau = 0 \dots 80 \mu\text{s}$. The same propagation properties are found for the maximum structure. Comparison of the propagation properties with the equilibrium potential profile yields that the propagation of the structures is fully determined by background $\mathbf{E} \times \mathbf{B}$ drift, which is well distinguishable from diamagnetic drifts due to the strongly asymmetric plasma potential and plasma pressure profiles [10, 12]. The lifetimes of the detected structures are larger than the chosen time interval and the spatial extent are of the order of the plasma radius.

Helicon discharge. A different picture is obtained in the helicon discharge. The results of conditional averaging are shown in Fig. 5 in the same representation as Fig. 4. Here a negative density fluctuation structure develops at $\tau = 0 \dots 80 \mu\text{s}$, propagates radially towards the device center and decays at $\tau = -20 \mu\text{s}$. At the same time a maximum structure rapidly grows at $\tau = -20 \dots 0 \mu\text{s}$, is turned at the center of the device and decays at $\tau = 40 \dots 60 \mu\text{s}$. It is visible that both structures do not exist simultaneously. Thus, the structure are of monopole-like shape. The lifetime is significantly reduced and the structures are sized when compared to the structures found in the filament plasma.

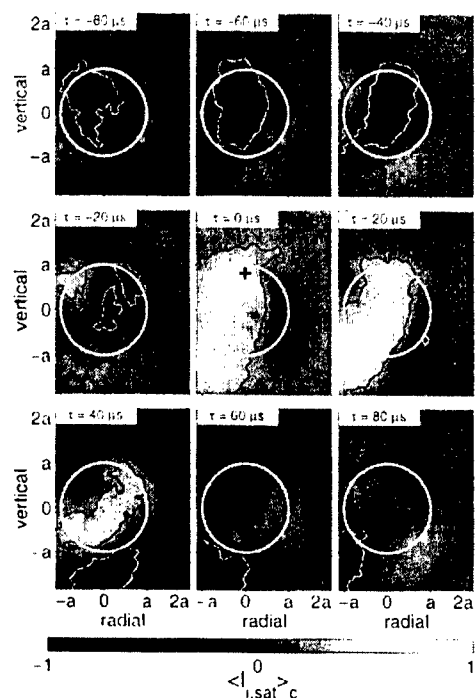


FIGURE 5. Conditional averaging results of density fluctuations for the helicon plasma in the same representation as Fig. 4

Fluctuation induced transport

An important parameter for the fluctuation induced transport associated with space-time fluctuation structures is the phase relation between plasma potential and plasma density fluctuations. To obtain the phase information for the large-scale fluctuation structures under investigation the CA procedure was repeated in the two-dimensional spatial domain with plasma potential fluctuations as reference signal. Similar structures were found as shown in Figs. 4 and 5, but phase shifted by $\approx \pi/2$, which results in a strong fluctuation induced transport caused by the structures [12]. Fig. 6 shows the two-dimensional amplitude coherence between plasma potential and plasma density fluctuations, the directly measured fluctuating transport at the plasma outside, and its probability distribution function. The amplitude coherence show a broad structure, which strongly suggests, that the formation of structures is based on a MHD instability [18]. This is consistent with the observed large phase shift between plasma density and plasma potential fluctuations. The fluctuating transport and their respective PDF's for the filament and helicon plasma show significant differences. In the filament generated plasma the transport is burst-like with large transport events directed outwards. The PDF is peaked and asymmetric towards large transport events. In the helicon plasma a more noise-like transport is observed with a symmetric PDF. This can be directly related to

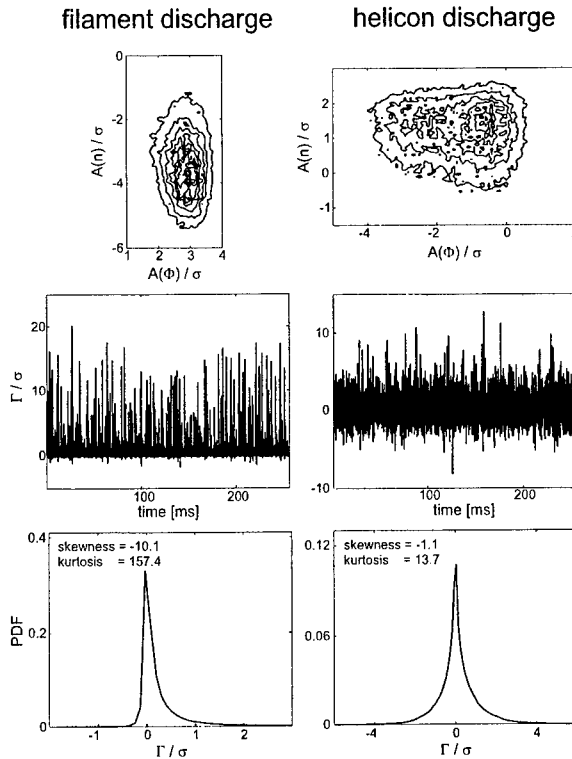


FIGURE 6. Two-dimensional amplitude probability distribution function between plasma density and plasma potential fluctuations (top row), time series of the measured fluctuation induced transport (middle row) and the respective PDF (bottom row).

the dynamical properties of the observed large-scale structures. In the filament plasma the spatial region of existence of structures is mainly outside and the phase relation between density and potential structures lead to a transport caused by these structures that is directed outwards. This strongly suggests that the large transport events are associated with these structures. In the helicon plasma structures exist in the plasma center and the phase shift between plasma density and plasma potential fluctuations is such that the resulting transport is directed towards the device center [12]. Consequently, no exposed large transport events are found and the PDF is symmetric.

CONCLUSIONS

The presented experimental study was addressed to the question, what determines the specific properties of large scale turbulent fluctuation structures. By operating the device with two completely different plasma sources geometry effects could be separated from source-induced effects. Large-scale structures were found in both plasmas, which

propagate with local background $E \times B$ drift. In contrast to linear magnetic field geometry, where generally small phase shifts between large-scale plasma potential and plasma density fluctuations are observed, the magnetic curvature in toroidal magnetic field geometry leads for both plasma sources to a large phase shift of $\pi/2$. This is consistent with numerical simulations, which includes both, curvature driven instabilities and drift waves, and measurements of the amplitude coherence between plasma density and plasma potential fluctuations. But the plasma source has a great influence on the specific shape and lifetime of structures. If negative space charge is injected into the plasma by the filament, structures generally appear dipole-like and have long lifetime. In the helicon discharge, where plasma is produced quasineutral, the structures are of monopole-like shape and their lifetime is considerably reduced when compared to the filament generated plasma. Specific features of the measured fluctuation induced transport can be attributed to the large-scale structures. In the filament plasma the propagation and phase shift of structures lead to transport events that dominate the transport time series. In the helicon plasma no significant contribution to the transport radially outwards due to the detected structures is expected and consistently the measured transport is more noise-like.

The results indicate that it is not sufficient to include only the magnetic geometry in the interpretation of particular properties of turbulent plasma fluctuations. As it was explicitly demonstrated for large-scale fluctuation structures, the plasma source can strongly alter the turbulent fluctuations and the associated transport.

REFERENCES

1. Huld, T., Nielsen, A. H., Pécseli, H. L., and Rasmussen, J. J., *Phys. Fluids B*, **3**, 1609–1625 (1991).
2. Pécseli, H. L., Coutias, E. A., Huld, T., Lynov, J. P., Nielsen, A. H., and Rasmussen, J. J., *Plasma Phys. Controlled Fusion*, **34**, 2065–2070 (1992).
3. Nielsen, A. H., Pécseli, H. L., and Rasmussen, J. J., *Physica Scripta*, **51**, 633–637 (1995).
4. Grulke, O., Klinger, T., and Piel, A., *Phys. Plasmas*, **6**, 788–796 (1999).
5. Endler, M., Giannone, L., Holzhauser, E., Niedermeyer, H., Rudyj, A., Theimer, G., Tsois, N., and ASDEX Team, *Nucl. Fusion*, **35**, 1307–1339 (1995).
6. Øynes, F. J., Pécseli, H. L., and Rypdal, K., *Phys. Rev. Lett.*, **75**, 81–84 (1995).
7. Joseph, B. K., Jha, R., Kaw, P. K., Mattoo, S. K., Rao, C. V. S., Saxena, Y. C., and the ADITYA team, *Phys. Plasmas*, **4**, 4292–4300 (1997).
8. Rypdal, K., Fredriksen, H., Paulsen, J. V., and Olsen, O. M., *Physica Scripta*, **T63**, 167–173 (1996).
9. Rypdal, K., Garcia, O. E., and Paulsen, J.-V., *Phys. Rev. Lett.*, **79**, 1857–1860 (1997).
10. Greiner, F., Grulke, O., Lechte, C., and Piel, A., “RF-plasma in a simple magnetized torus”, in *Proc. 2000 Int. Congress on Plasma Physics*, Quebec City, Canada, 2000, vol. 1, pp. 140–143.
11. Grulke, O., Greiner, F., Klinger, T., and Piel, A., “Spatiotemporal analysis of electrostatic fluctuations in a simple magnetized torus”, in *Proc. 2000 Int. Congress on Plasma Physics*, Quebec City, Canada, 2000, vol. 1, pp. 284–287.
12. Grulke, O., Greiner, F., Klinger, T., and Piel, A., *Plasma Phys. Controlled Fusion*, **43**, 525–542 (2001).
13. Light, M., and Chen, F. F., *Phys. Plasmas*, **2**, 1084–1093 (1995).
14. Chen, F. F., *Phys. Plasmas*, **3**, 1783–1793 (1996).
15. Wang, E. Y., Hershkovitz, N., Intrator, T., and Forest, C., *Rev. Sci. Instrum.*, **57**, 2425–2431 (1986).
16. Hershkovitz, N., and Cho, M. H., *J. Vac. Sci. Technol. A*, **6**, 2054–2059 (1988).
17. Frisch, U., *Turbulence: The Legacy of A. N. Kolmogorov*, Cambridge University Press, 1995.
18. Scott, B., *Phys. Plasmas*, **7**, 1845–1856 (2000).

Design of a toroidal device with a high temperature superconductor coil for non-neutral plasma trap

Yuichi Ogawa*, Junji Morikawa*, Hitoshi Nihei[#], Daisaku Ozawa[#],
Zensho Yoshida[%], Toshiyuki Mito^{\$}, Nagato Yanagi^{\$} and Masataka
Iwakuma[&]

**High Temperature Plasma Center, The University of Tokyo, Bunkyo-ku, Tokyo 113-8656, JAPAN*

#School of Engineering, The University of Tokyo, Bunkyo-ku, Tokyo 113-8656, JAPAN

%School of Frontier Science, The University of Tokyo, Bunkyo-ku, Tokyo 113-8656, JAPAN

\$National Institute for Fusion Science, Toki, Gifu 509-5292, JAPAN

&School of Engineering, Kyushu University, Higashi-ku, Fukuoka 812-8581, JAPAN

Abstract. The non-neutral plasma confinement device with a floating internal coil is under construction, where the high temperature superconductor (HTS) Ag-sheathed BSCCO-2223 is employed as the floating coil. We have two topics with this device; one is a trap of a non-neutral plasma consisting of one species, and another is an exploration of a high beta plasma based on two-fluid MHD relaxation theory. In the latter case the plasma should be non-neutralized in order to drive the plasma flow in the toroidal direction. The expected plasma parameters are discussed. Key elements of engineering issues have already developed. In addition, we have fabricated a small HTS coil and succeeded in levitating it within an accuracy of 25 ~ 30 μm for 4 min or more.

INTRODUCTION

An internal coil device with a normal conductor (called Proto-RT) has been constructed, and trapping/confinement of non-neutral plasmas in a toroidal device has been intensively promoted [1]. There are, however, some restrictions for the normal conductor device; i.e., the current feeder and the coil support are intersecting with the magnetic surface, resulting in the deterioration of the plasma confinement. In addition, the high magnetic field seems not to be easy, because of the low current density of the normal conductor. To overcome these issues we are now constructing a toroidal device with a floating coil wound with a superconductor, called Mini-RT.

We adopt a high temperature superconductor (HTS) wire for the floating coil, expecting easy/reliable operation and maintenance. In addition, the HTS coil is preferable for plasma experiments, because long pulse and/or high power heating experiments might be available due to the high thermal stability and large heat capacity of the HTS wire.

In this Mini-RT device, we are expecting to study two topics; one is a trap of a pure electron (or positron) plasma in a toroidal device. From the viewpoint of trapping experiments, the strong magnetic field might make it possible to confine relatively high energy charged particles.

Another purpose is an exploration of a new type of MHD relaxation by producing a non-neutralized plasma. Recently, Mahajan-Yoshida has found a new relaxation state by taking a two-fluid effect into account, and pointed out the possibility of a new type of high beta plasma [2]. To explore this new relaxation theory, the toroidal device with an internal coil is suitable, where the high beta plasma would be confined with the dynamic pressure of the plasma flow in toroidal direction. The toroidal plasma flow can be driven by the radial electric field by the $E \times B$ force. We are expecting to produce the radial electric field by producing a non-neutralized plasma.

In this manuscript, the design of the internal coil device called Mini-RT is described, and expected plasma parameters are discussed. Test of HTS wire has been started, and levitation experiments with a small HTS coil have been successfully carried out [3]. This is a first challenge to apply the HTS coil for plasma confinement devices, as well as the levitation experiment of the HTS coil.

DESIGN OF A FLOATING COIL DEVICE (MINI-RT)

Schematic drawing of the internal floating coil device Mini-RT is shown in Fig. 1, where a vacuum chamber is 0.5 m in radius and ~ 0.7 m in height. A levitation coil is

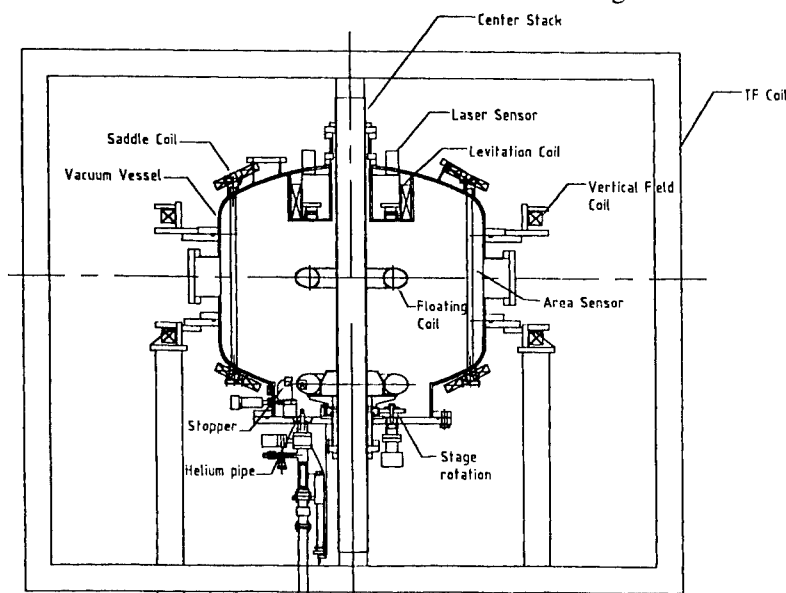


FIGURE 1. Schematic Drawing of the internal coil device Mini-RT, where a floating coil are re-cooled and charged at the bottom of the torus.

put at the top of the vacuum vessel. Since the floating coil is unstable to the vertical motion, the levitation coil current is feedback-controlled to keep the floating coil position. The floating coil is re-cooled at the bottom of the vacuum vessel through the demountable pipe, and the coil current is recharged, as well.

The HTS wire is Ag-sheathed BSCCO-2223. The specification of the floating coil is listed in Table 1.

TABLE 1. The Specification of the Floating Coil Made of HTS Wire.

Parameters	Values
Major and minor radii	$R = 0.15$ m and $a = 0.028$ m
Operation current of the coil	$I_{op} = 115$ A
Magneto-motive force (total coil current)	$I_{tot} = 50,000$ A (435 turns)
Critical current of the HTS wire	$I_c = 108$ A at 77 K, s.f., $1 \mu\text{V}/\text{cm}$
Residual voltage and inductance of the coil	$R_\Omega = 1.66 \times 10^{-5}$ V, $L = 0.091$ H
Decay constant of the coil current	$\tau = 174.4$ hours at 20 K
Weight of the coil	$W \sim 20$ kg

The maximum magnetic field strength appears at the surface of the coil and is that $B_z = 0.75$ T and $B_r = 0.57$ T. To evaluate the residual voltage of the HTS wire, it is assumed that the n -value defined by $V = V_c (I/I_c)^n$ is 10. Operation temperature of the HTS wire is initially 20 K, and increases up to ~ 40 K. Taking the decrease of the decay constant of the coil current at the elevated temperature into account, we expect to keep the floating coil during a few hours for plasma experiments. In this floating coil system we need no quench protection system.

In addition to the floating coil, there are other magnetic field coils made of normal conductors. With the combination of the levitation coil, the nested magnetic field lines can be produced as shown in Fig. 2(a). To levitate the floating coil, the coil

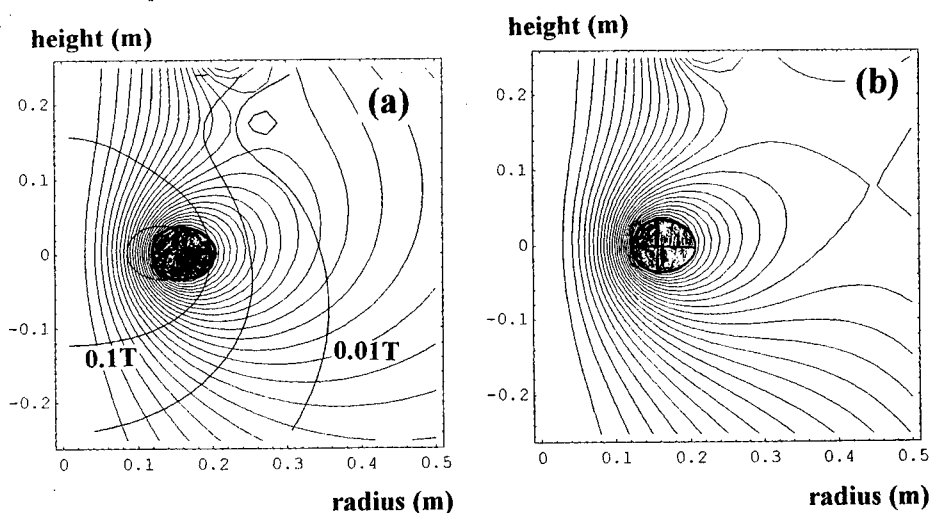


FIGURE 2. Magnetic field configuration (a) only with the levitation coil and (b) the levitation and vertical coils. The contour of the magnetic field strength is also shown in the case (a).

current of the levitation coil is 15.3 kA·turn. We should pay attention to the clearance at the inner side of the torus; e.g., the distance between the separatrix magnetic field line and the inner surface of the coil is 22 mm. This clearance is sufficiently large for electrons; i.e., the Larmor radius of electrons with the energy of 100 keV is 3 mm at the inner side of the torus ($B = 0.35$ T), but is marginal for ions.

A pair of the vertical field coil made of the normal conductor is put outside the vacuum vessel so as to modify the magnetic surface. In Fig. 2(b) the closed magnetic surface with the separatrix outside of the torus is also presented, where the coil current of the vertical field coil is 2.7 kA·turn.

PLASMA PARAMETERS EXPECTED IN A MINI-RT DEVICE

In order to produce non-neutral (or non-neutralized) plasmas, the injection of electrons through the separatrix has been proposed, where the inward diffusion of electrons is expected at the separatrix, by taking the chaotic motion of electrons at the magnetic null point into account [4]. In a Proto-RT device, the production of a non-neutral plasma with a potential of a few hundreds of eV has been succeeded [1]. In a Mini-RT device, we expect to apply this technique, as well.

We are planning to produce a neutral plasma in the range of $n \sim 10^{16-17} \text{ m}^{-3}$ with 2.45 GHz Electron Cyclotron Heating system. As shown in Fig. 2(a), the contour of the magnetic field strength of 0.1 T is located around the outer side of the floating coil. We expect the neutral plasma will be produced in the neighborhood of the contour of $B = 0.1$ T. Since the ECH could produce high energy electrons more than a few tens keV [5,6], this might be helpful to produce a high beta plasma. In addition, some part of the extremely high energy electrons might escape from the magnetic surface through the separatrix region. This might yield a bulk plasma to non-neutralize.

Mahajan-Yoshida has found a MHD relaxation state in two-fluid plasmas, and derived the following Beltrami/Bernoulli condition [2]; i.e., $\beta + (V_P / V_A)^2 = \text{constant}$, where β is the ratio of the plasma pressure to the magnetic pressure, and the velocities V_P and V_A are plasma flow velocity and Alfvén velocity, respectively. When the plasma velocity is increasing as the plasma radius, high beta plasmas can be confined at the core region of the plasma column. If the radial electric field is introduced in the torus plasma with the internal coil, the so-called $E \times B$ drift velocity is an increasing function of the plasma minor radius. This is the reason why the internal coil device is suitable for studying high beta plasmas based on two-fluid MHD relaxation theory.

By assuming that $\beta = 0$ at the plasma surface, the relation between the plasma beta value and the radial electric field can be derived as follows;

$$\frac{E}{B} = \sqrt{\frac{B^2}{\mu_0 n_i m_i}} \sqrt{\beta}, \quad (1)$$

where n_i and m_i are ion density and mass, respectively. This gives plasma parameters necessary for studying high beta plasmas, and typical values are listed in Table 2.

TABLE 2. Typical Plasma Parameters to study High Beta plasma Experiments.

Beta Value and Magnetic Field	Plasma Density and Temperature	Radial Electric Field
100 % at $B = 0.1$ T	$n = 10^{16} \text{ m}^{-3}$ and $T = 1240$ keV	2200 kV/m
100 % at $B = 0.1$ T	$n = 10^{17} \text{ m}^{-3}$ and $T = 124$ keV	690 kV/m
10 % at $B = 0.1$ T	$n = 10^{17} \text{ m}^{-3}$ and $T = 12.4$ keV	220 kV/m
100 % at $B = 0.01$ T	$n = 10^{17} \text{ m}^{-3}$ and $T = 124$ keV	6.9 kV/m
10 % at $B = 0.01$ T	$n = 10^{17} \text{ m}^{-3}$ and $T = 1.24$ keV	2.2 kV/m

The low density plasma needs a high plasma temperature and a large radial electric field. We might expect a high beta plasma at the outer region of the plasma column, because the magnetic field strength drastically decreases, as shown in Fig. 2(a).

It is not so easy to predict the plasma confinement time in this internal coil device. Here we roughly estimate the energy confinement time necessary to achieve these plasma parameters. When the ECH power is assumed to be 10 kW, the energy confinement time to achieve the plasma with $\beta = 100\%$ is estimated to be 4.1 msec.

ENGINEERING PROGRESS OF THE HTS COIL

We employ the method to drive the HTS coil current through the demountable electrode. This has some advantages in comparison with the induction drive; e.g., the induction coil is not necessary, and the power supply system becomes quite simple. However, it is necessary to introduce the persistent current switch (PCS) made of the HTS wire in the floating coil. There are few experiences of the PCS with the HTS wire in the past. We use the Mn-doped HTS wire, which gives high electric resistance at the elevated temperature. We have measured the characteristics of the Mn-doped HTS wire, and confirmed the performance as the PCS for the floating coil.

The levitation of the HTS coil is another important issue. We cannot expect the pinning effect for the HTS coil, because the HTS wire is composed of multi-filaments, in comparison with the bulk HTS material. The feedback control is, therefore, indispensable. In addition, we particularly pay attention to the position control of the floating coil, because the fluctuation of the coil position induces an error field, resulting in the disturbance of the magnetic surface for the plasma confinement. In plasma experiments, the position of the floating coil should be controlled within a sufficiently high accuracy (e.g., less than 100 micrometers).

We have fabricated a small HTS coil (4 cm in radius and 2.6 kA·turn) and carried out the levitation experiment [3]. The coil is covered with the casing made of polycarbonate and immersed in liquid nitrogen. The total weight is approximately 321 g with liquid nitrogen. The HTS coil current is induced by the field-cooling method.

Figure 3 shows the levitation experimental setup using the reflection method. Nitrogen vapor can be seen, because the HTS coil immersed in liquid nitrogen is open. The laser light injected from the bottom of the HTS coil is sometimes interrupted by this nitrogen vapor, making the position control worse. The detected signals of the floating coil position are transferred to the feedback system, which is composed of a proportional and differential feedback control (the so-called PD feedback control).

The position data of the HTS coil is shown in Fig. 4, where the coil position is artificially changed so as to examine the dynamic response of the coil. The HTS coil position can successfully be controlled within an accuracy of 25–30 μm , and levitated for 4 min or more.

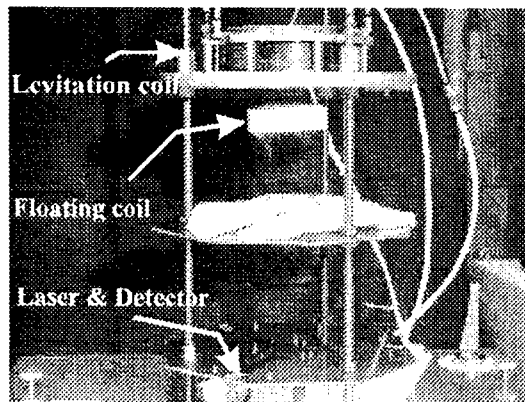


FIGURE 3. Setup of levitation experiment of a small HTS coil. Laser light is irradiated from the bottom, and reflected light is measured at the bottom by the CCD camera.

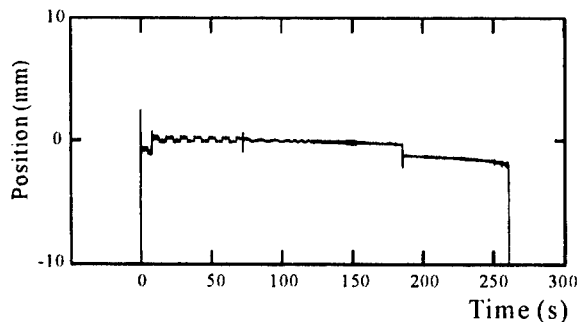


FIGURE 4. Feedback control experiments of the HTS floating coil. The coil position is artificially changed, in order to examine the dynamic response of the floating coil.

REFERENCES

1. Yoshida, Z., Ogawa, Y., Morikawa, J., Himura, H., Kondo, S., Nakashima, C., Kakuno, S., Iqbal, M., Volponi, F., Shibayama, M., Tahara, S., "Toroidal magnetic confinement of non-neutral plasmas" in *Non-Neutral Plasma Physics III*, edited by J.J. Bollinger, AIP Conference Proceedings 498, New York: American Institute of Physics, 1999, pp. 397-404.
2. Mahajan, S.M., and Yoshida, Z., *Phys. Rev. Letters* **81**, 4863-4866 (1998).
3. Morikawa, J., *Jpn. J. Appl. Phys.* in print.
4. Yoshida, Z., Asakura, H., Kakuno, H., Morikawa, J., Takemura, K., Takizawa, S. and Uchida, T., *Phys. Rev. Letters* **81**, 2458-2461 (1998).
5. Ikegami, H., Ikezi, H., Hosokawa, M., Tanaka, S. and Takayama, K., *Phys. Rev. Letters* **19**, 778-780 (1967).
6. Warren, H.P. and Mauel, M.E., *Phys. Rev. Letters* **74**, 1351-1354 (1995).

Injection of electrons into a toroidal trap using chaotic orbits near magnetic null

Chihiro Nakashima, Zensho Yoshida[†], Haruhiko Himura[†],
Masayuki Fukao*, Junji Morikawa* and Haruhiko Saitoh[†]

*Graduate School of Engineering,
Graduate School of Frontier Sciences[†],
High Temperature Plasma Center*,
The University of Tokyo
7-3-1 Hongo, Bunkyo-ku, Tokyo 113-0033, Japan*

Abstract. A new method of injecting electrons across magnetic field has been studied. The electrons, launched near an X-point of magnetic separatrix, describe chaotic (non-integrable) orbits and are trapped inside the separatrix; probe measurements show several tens volts of the floating potential inside the separatrix. For the production of higher density electron plasmas, a new electron gun with a LaB₆ cathode has been developed. The gun generates a floating potential of the order of 10³ V. The electron density is calculated to be of the order of 10¹⁴ m⁻³, which is close to the Brillouin density limit.

I INTRODUCTION

Recently, a new type of toroidal magnetic trap has been developed aiming at production of antimatter plasmas [1] and high- β fusion plasmas [2,3]. One of the key issues in developing a nonneutral plasma trap is how we can inject particles into the trapping region. In linear systems, particles are injected along magnetic field lines by opening the plugging electric potential. This method cannot be used in a toroidal system that does not have open ends of field lines. In earlier toroidal experiments, some different methods of injection, such as use a rising toroidal magnetic field ('inductive charging method' [4]) or use a drift motion of particles [5] were invented.

Our mission is to put the particle source at possible outside the trapping region and inject particles across the closed magnetic surfaces. One of the merits of toroidal geometry is that the connection lengths (the lengths between the source and sinks of the particles) can be made much longer than the size

of the device when particles describe chaotic orbits [1]. Continuous injection of particles through the long orbits enables steady state operation of the trap.

II INJECTION OF ELECTRON BEAM THROUGH CHAOTIC ORBITS

Experiments on electron beam injection into a toroidal system were performed on the Proto-RT device shown in Fig.1(a). Particles are trapped primarily by a stationary poloidal magnetic field (B_p) with a separatrix (shown in Fig.1(a)), that is produced by combination of a dipole field generated by an internal ring conductor and a vertical field. We can also add a stationary toroidal magnetic field (B_t) to produce magnetic shear. The combination of B_p and B_t can also adjust the orbits of injected electrons to increase the connection lengths [6]. Electrons are accelerated up to 2 keV. Electron beam current is about 10 mA. Electrostatic probes are inserted into the plasma on the horizontal plane ($Z = 0$). Each cylindrical probe has 1.0 mm diameter and 1.5 mm length. The floating potential (Φ) is estimated at high-impedance of order $10^{-9} \Omega$.

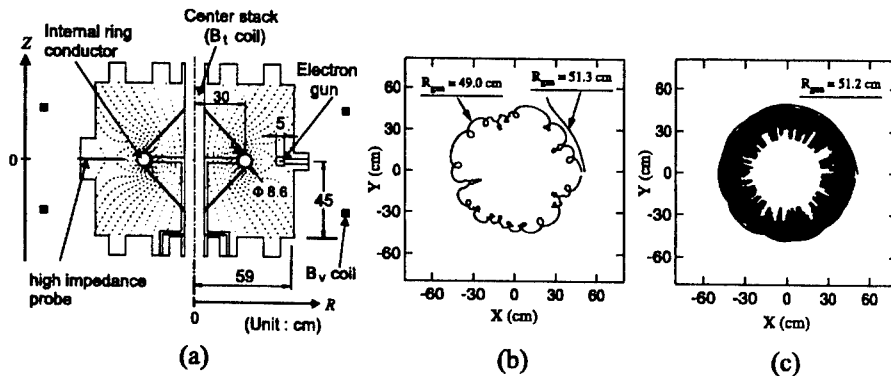


FIGURE 1. (a) Schematic view of the Proto-RT device. (b) Typical orbits of electrons emitted from inside ($R_{gun} = 49.0$ cm) and outside ($R_{gun} = 51.3$ cm) the trapping region (c) A typical orbit (toroidal projection) of electrons emitted from near an X-point ($R_{gun} = 51.2$ cm)

For the optimization of injection, we have analyzed the particle orbit numerically. In Fig.1(b) and (c), we compare orbits (toroidal projections) starting from different positions: $R_{gun} = 49.0$ cm, 51.3 cm and 51.2 cm. In Fig.1(b), when the electron source is placed inside the separatrix ($R_{gun} = 49.0$ cm) the electron moves in the toroidal direction and comes back to the electron source.

When the source is placed outside the X-point ($R_{gun} = 51.3$ cm) the electron is not injected and lost immediately. In Fig.1(c), when the source is placed near the X-point ($R_{gun} = 51.2$ cm) the electron describes a chaotic and long orbit before it comes back to the source.

We inject electron beam into the Proto-RT using parameters determined by the numerical orbit analysis. In Fig.2(a), we show the floating potential (Φ) measured at $R = 42.0$ cm (inside the separatrix) as a function of the radial position of the electron gun. Two cases of magnetic field configurations are compared. The black points show the potential Φ in an optimized magnetic field ($B_p > 0$) based on the orbit calculations. In this case, the maximum value of the Φ is about -65 V when the gun is deeply inserted into the trapping region ($R_{gun} = 42.0$ cm). When $R_{gun} = 51.0$ cm (near the X-point) the value of the Φ is about -35 V (~ 50 % of the maximum value). If the sign of the poloidal magnetic field is flipped ($B_p < 0$), the Φ decreases (white square markers). In this case, the value of the Φ is about -10 V when the gun is located inside the separatrix ($R_{gun} \lesssim 47$ cm). Figure 2(b) shows the loss current collected by the grounded casing of the electron gun as a function of the radial position of the gun (for $B_p > 0$). The maximum value of the loss current is ~ 1 mA (~ 10 % of the total emission), when the gun is deeply inserted inside the separatrix. When the gun is located near the X-point, the loss current decreases, due to the effect of the chaotic orbits (like Fig.1(b)). In this case, the value of the loss current is ~ 0.02 mA (less than 1 % of the total emission and only ~ 2 % of the maximum value, which is compared with the decrease in the Φ in Fig.2(a)).

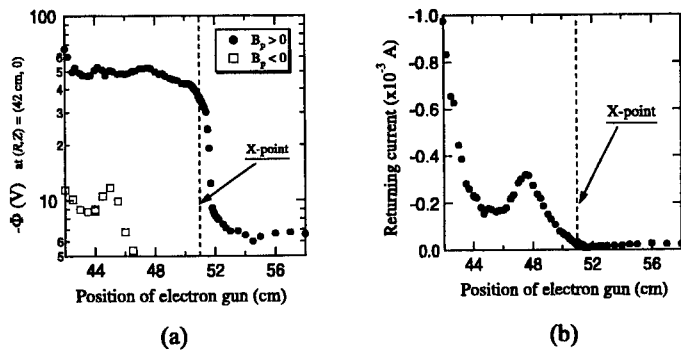


FIGURE 2. (a) Measured floating potential at $R = 42.0$ cm as a function of the radial position of the electron gun for the optimized magnetic configuration (black points). If the sign of the B_p is flipped (white square markers), the potential decreases. (b) Measured loss current collected by the casing of the electron gun vs. the radial position of the gun

Radial floating potential profiles are measured by high-impedance probes.

In Fig.3(a), we show the potential profiles at three different toroidal positions (60° , 180° and 300° from the electron gun) on the horizontal plane ($Z = 0$). Here, the electron gun is placed near the X-point ($R_{gun} = 51.2$ cm). The potential profiles have approximately broad parts inside the trapping region ($36 \text{ cm} \lesssim R \lesssim 51 \text{ cm}$). Toroidally asymmetric peaks are considered to be corresponding to the beam. In Fig.3(b), we show the potential profiles for different B_t . When the toroidal magnetic field is weak ($\lesssim 20$ G), the potential build up inside the trapping region with broad equilibrium profiles. The maximum value of the potential is about -40 V (at $R \sim 41$ cm), when $B_t \sim 3.4$ G. For larger B_t ($\gtrsim 50$ G) we observe only beams near the X-point because electrons are magnetized by the strong B_t and they cannot be injected.

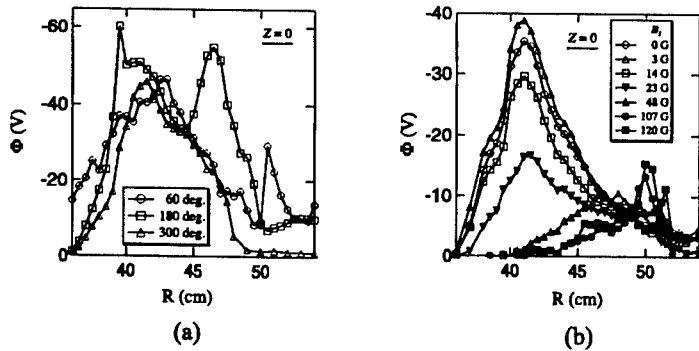


FIGURE 3. (a) Measured radial floating potential profiles at three different toroidal positions (60° , 180° and 300° from the electron gun) on the horizontal plane ($Z = 0$). (b) Measured radial floating potential profiles for the different B_t .

We discuss the experimental results comparing with the numerical orbit analysis. Figure 4(a) shows the calculated staying time of beam electrons as a function of the initial position. The calculation is terminated when the electron hits the source or the boundary. In the Proto-RT experiment, the divergence angle of the electron beam is about 20° . To estimate average orbit lengths, we compare different injection angles: 0° , $\pm 5.7^\circ$ and $\pm 11.3^\circ$ with respect to the horizontal plane. When the source is located inside the separatrix ($R_{gun} \lesssim 48$ cm), magnetized electrons return to their source after a few gyrations with the staying time of $\sim 1 \mu\text{sec}$. When the source is placed in the weak field region ($48 \text{ cm} \lesssim R_{gun} \lesssim 51 \text{ cm}$) electrons come back to their source or escape from the trapping region through the X-point. In this case, the staying time has a very strong and almost random dependence on the initial condition of the orbit because of the chaos of the electron motion. In Fig.4(b), we summarize the results of calculations with diverse injection conditions, which is compared with the experimental result in Fig.2(a).

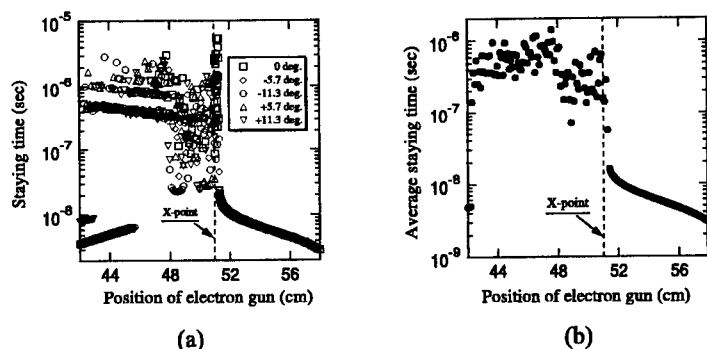


FIGURE 4. (a) Calculated staying time of beam electron vs. initial position of injection for different horizontal angle: 0° , $\pm 5.7^\circ$ and $\pm 11.3^\circ$ (b) Calculated average staying time of beam electrons (from the results in Fig.(a))

III PRODUCTION OF DENSE TOROIDAL ELECTRON PLASMAS

In order to produce higher density electron plasmas, we have developed an electron gun with a LaB₆ cathode. The beam current is ~ 720 mA. In Fig.5(a), radial floating potential profiles for different toroidal positions (60° and 180° from the electron gun) are plotted. The potential has broad profiles, which are approximately symmetric in the toroidal direction. The maximum value of the potential is about 2 kV (at $R = 36$ cm), which is near the acceleration voltage of the electron gun. Figure 5(b) shows the probe characteristics obtained at $R = 44$ cm. From the data, the electron temperature is estimated to be ~ 72 eV and the calculated electron density is $\sim 6 \times 10^{14} \text{ m}^{-3}$. The electron density can be related with the potential by the Poisson equation that is approximated by $n_e \approx 4\epsilon_0\Phi/ea^2$ (a is the minor radius). Using experimental values $a \sim 0.05$ m and $\Phi \sim -890$ V, we obtain $n_e \sim 10^{14} \text{ m}^{-3}$. This discrepancy (by factor ~ 6) may be due to the cancellation of the space potential by induced image charges on the internal ring conductor of the Proto-RT. On the other hand, the Brillouin density limit (n_B) is estimated to be $\sim 2 \times 10^{14} \text{ m}^{-3}$ using $n_B = \epsilon_0 B^2/2m_e$ (in a cylindrical model) when $B \sim 60$ G (at $R = 40$ cm).

IV SUMMARY

We have studied the injection conditions of electrons into a toroidal magnetic trap. Development of a particle injection scheme is an essential issue in the study of toroidal nonneutral plasmas. We found appropriate conditions to inject non-magnetized electrons near the edge of the trapping region. The

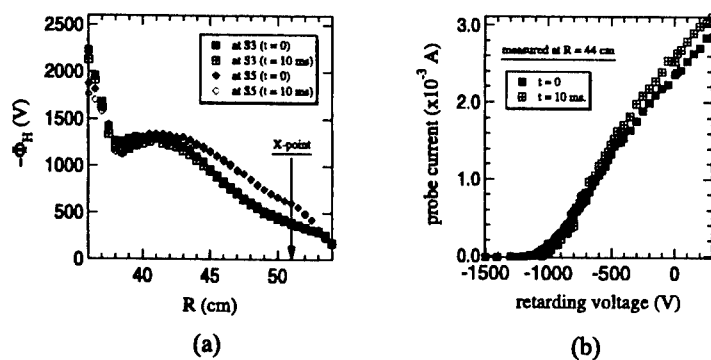


FIGURE 5. (a) Measured radial potential profiles for different toroidal positions: 60° and 180° from the electron gun. (b) Measured I-V characteristics at $R = 44$ cm.

current returning back to the gun can be minimized less than 1 % of the emitted current due to the effect of the chaotic orbits. A large-current (~ 720 mA) electron gun has been developed, which successfully produces the high density (near the Brillouin density limit) electron plasmas of the order of 10^{14} m^{-3} .

ACKNOWLEDGMENTS

The authors are grateful to Prof. T.M. O'Neil, UCSD nonneutral plasma group, Prof. Y. Ogawa and Dr. S. Kondoh for their discussions. This work was supported by Grant-in Aid for Scientific Research from the Japanese Ministry of Education, Science and Culture No. 09308011. The work of CN was supported by Research Fellowships of the Japan Society for the Promotion of Science (JSPS) for Young Scientists.

REFERENCES

1. S. Kondoh and Z. Yoshida, Nucl. Instr. and Meth. in Phys. Res. A **382** 561 (1996).
2. S. M. Mahajan and Z. Yoshida, Phys. Rev. Lett. **81**, 4863 (1998).
3. Z. Yoshida, *et al.*, in *Proceedings of Non-neutral Plasma Physics III, AIP Conf. Proc. No. 498*, p. 398 (AIP, New York, 1999).
4. J. D. Daugherty, J. E. Eninger, and G. S. Janes, Phys. Fluids **12**, 2677 (1969).
5. S. S. Khirwadkar, *et al.*, Phys. Rev. Lett. **71**, 4334 (1993).
6. C. Nakashima, *et al.*, in *Proceedings of Non-neutral Plasma Physics III, AIP Conf. Proc. No. 498*, p. 411 (AIP, New York, 1999).

Relaxed states in plasmas — non-neutral and diamagnetic plasmas

Z. Yoshida and H. Saitoh

*Graduate School of Frontier Sciences, The University of Tokyo,
Hongo, Tokyo 113-0033, Japan*

Abstract. The aim of this paper is to present a unified representation of relaxed states generated in various type of plasma systems. Self-organization of structure is the central theme of the recent theory of relaxation phenomena. Invoking fluid mechanical models, many authors have discussed various relaxed states that constitute a special class of macroscopic equilibria (force-balance states). The present theory, however, starts from a kinetic model of relaxed state, which encompasses a variety of structures including both electrostatic and electromagnetic configurations. This model also describes the macroscopic relaxed state characterized by the Beltrami and (generalized) Bernoulli conditions, which gives strong diamagnetism.

I INTRODUCTION

Plasmas, viewed as a fluid, can produce a variety of structures. In the ideal (dissipation-less) model of fluid mechanics, the equilibrium (force-balance) equations may have infinite number of solutions, because the hyperbolic part of the partial differential equation demands Cauchy data that specify the profiles of internal fields. To select a physically realized structure from the total set of ideal equilibrium solutions, we invoke the effect of small dissipations. In approximately collision-less plasmas, it is believed that the effect of dissipation does not modify the equilibrium structure, while it chooses a most preferential profile that can minimize the influence of the dissipation. This stands reason to start from an ideal model, and then search for a relaxed state.

Many authors have discussed various relaxed states that constitute a special class of macroscopic (fluid mechanical) equilibria. The pioneering work in this context was J.B. Taylor's model of the RFP (reversed-field pinch) plasma [1]. The present paper, however, presents a kinetic model of self-consistent relaxed states that are characterized by some rugged constants of motion. Both

electrostatic and magnetic confinements are discussed on a unified basis. This model also derives the macroscopic relaxed state characterized by the Beltrami and (generalized) Bernoulli conditions, which gives strong diamagnetism.

II KINETIC EQUILIBRIA

A Steady states in kinetic theory and relaxed states

We begin with formulating the equilibrium (steady state) in the phase space of kinetic theory that is spanned by \mathbf{x} (coordinate) and \mathbf{p} (canonical momentum). Let $f(\mathbf{x}, \mathbf{p}, t)$ be the distribution function. We consider a collision-less plasma. The evolution of f obeys the Liouville equation (Vlasov equation)

$$\partial_t f + \{H, f\} = 0, \quad (1)$$

where H is the Hamiltonian of a test particle moving in a mean field, and $\{, \}$ is the Poisson bracket. The mean field \mathbf{A} and ϕ must be consistent to f through Maxwell's equations. We consider a stationary state, we assume that H is independent to t . Then, a steady state for (1) satisfies

$$\{H, f\} = 0. \quad (2)$$

The stationary equation (2) has infinite number of solutions. Let a_j be a time-independent quantity that commutes with H , i.e., $\{H, a_j\} = 0$. The H itself satisfies this condition. Suppose that we know N of such quantities (constants of motion). Using them, we generate a distribution (F is an arbitrary smooth function)

$$f = F(a_1, \dots, a_N). \quad (3)$$

If N is equal to the degree of freedom, the system is "integrable", and (3) gives the complete solution. Our motivation in this work, however, is to find a special class of solutions that are robust (rugged) against various perturbations destroying the invariance of fragile constants of motion. Only a small number of them are robust in a sense that the ensemble averages (or the total sums) of such quantities are conserved.

The most robust steady state is the Boltzmann distribution

$$f = Z^{-1} e^{-\beta H} \quad (4)$$

where Z (normalization factor) and β (inverse temperature, or a Lagrange multiplier) are positive constants. We obtain this equilibrium by maximizing the entropy over an ensemble that is characterized by a given total energy (i.e., a constant-energy set). If we invoke another constant G (in an ensemble

average sense), we must maximize the entropy on the ensemble defined both by H and G . With restricting the totals of H and G , we obtain

$$f = Z^{-1} e^{-\beta H - \gamma G}, \quad (5)$$

where γ is the second Lagrange multiplier. Including some additional constants of motion, we obtain a maximum entropy solution that is more restricted than the Boltzmann equilibrium. Such a solution remains in equilibrium as far as the additional constraints work.

B Equilibrium with momentum conservation

A symmetry of the system warrants the conservation of the corresponding canonical momentum. Suppose that the Lagrangean L is independent of a coordinate x_0 , as well as t . Then, the Hamiltonian H and the momentum $p_0 = \partial L / \partial x'_0$ are conserved ($'$ is the time derivative). With an arbitrary constant C , we define

$$\hat{H} = H - C p_0, \quad (6)$$

and consider a distribution [see (5)]

$$f = Z^{-1} e^{-\beta \hat{H}} = Z^{-1} e^{-\beta(H - C p_0)}. \quad (7)$$

This solution of (2) has the following important connotation that provides a physical meaning for the parameter C .

When we discuss a distribution function f , we consider an ensemble of particles, which is characterized by the sum of the Hamiltonian over the all particles. We invoke the conservation of the total energy, but not the energy of each particle. We apply the same framework for the momentum p_0 in (7). We do not assume the conservation of H or p_0 for each particle, while we consider an ensemble determined by the totals of these quantities. Then, the physical meaning of \hat{H} becomes essential. Indeed, we can interpret \hat{H} as the Hamiltonian on a moving frame, and hence, $f = Z^{-1} e^{-\beta \hat{H}}$ is an invariant of the collision operator (the average momentum is unchanged by collisions). This robustness of p_0 warrants the use of p_0 in determining the ensemble.

Let us revisit the change of variables in general inhomogeneous coordinate transform, and see the relation between H and \hat{H} . Let \mathbf{U} be a certain temporary-constant velocity field. We write the velocity \mathbf{v} of the laboratory frame as

$$\mathbf{v} = \tilde{\mathbf{v}} + \mathbf{U}, \quad (8)$$

and set $\tilde{\mathbf{x}}' = \tilde{\mathbf{v}}$. The Lagrangean of a charged particle (q : charge, m : mass) can be written as

$$L = \frac{m}{2} |\tilde{\mathbf{v}} + \mathbf{U}|^2 + q(\tilde{\mathbf{v}} + \mathbf{U}) \cdot \mathbf{A} - q\phi.$$

The canonical momentum and the Hamiltonian are

$$\tilde{\mathbf{p}} = \frac{\partial L}{\partial \tilde{\mathbf{v}}} = m(\tilde{\mathbf{v}} + \mathbf{U}) + q\mathbf{A} = m\tilde{\mathbf{v}} + q\tilde{\mathbf{A}}, \quad (9)$$

$$\tilde{H} = \frac{1}{2m} |\tilde{\mathbf{p}} - q\tilde{\mathbf{A}}|^2 - \frac{m}{2}U^2 + q\tilde{\phi} = \frac{m}{2}\tilde{v}^2 - \frac{m}{2}U^2 + q\tilde{\phi}, \quad (10)$$

where

$$\tilde{\mathbf{A}} = \mathbf{A} + \frac{m}{q}\mathbf{U}, \quad \tilde{\phi} = \phi - \mathbf{U} \cdot \mathbf{A}. \quad (11)$$

The effective vector potential $\tilde{\mathbf{A}}$ includes an additional term that yields the Coriolis force. The scalar potential $\tilde{\phi}$ has received the (nonrelativistic) Lorentz transform. In (10), $-mU^2/2$ is the centrifugal potential. The transform of the Hamiltonian and the momentum can be written as

$$\tilde{H} = H - \mathbf{U} \cdot (m\mathbf{v} + q\mathbf{A}) = H - \mathbf{U} \cdot \mathbf{p}, \quad (12)$$

$$\tilde{\mathbf{p}} = \mathbf{p} \equiv m\mathbf{v} + q\mathbf{A}. \quad (13)$$

Suppose that a component p_0 of the momentum is a constant of motion. Comparing (6) and (12), we observe

$$\tilde{H} = H - Cp_0 = \hat{H}, \quad (14)$$

which implies that \hat{H} is the Hamiltonian in the moving coordinate, and C is the velocity (or the angular velocity if we define $\tilde{\mathbf{p}}$ with respect to an angle) of the frame. Hence, the solution (7) represents the "thermal equilibrium" in the moving frame. Let us review some well-known examples. The Hamiltonian H includes the potentials ϕ and \mathbf{A} that must be self-consistently determined by the field equation including f .

(1) *Electrostatic equilibrium*

When the magnetic field produced by the internal current is negligibly small in comparison with the externally applied magnetic field, we can use the electrostatic model; \mathbf{A} is a prescribed field, while ϕ is determined by the Poisson equation

$$-\Delta\phi = \frac{q}{\epsilon}n. \quad (15)$$

Using (10), the density n is given by

$$n(\mathbf{x}) = \int f(\mathbf{x}, \mathbf{v}) d\mathbf{v} = n_0 e^{-\beta(-mU^2/2 - q\mathbf{U} \cdot \mathbf{A} + q\phi)}, \quad (16)$$

where $n_0 = Z^{-1} \int e^{-\beta m v^2/2} d\mathbf{v}$.

Here, we review the well-known "thermal equilibrium" of a cylindrical single-species plasma confined in a homogeneous magnetic field ($\mathbf{B} = B\mathbf{e}_z$). Let r - θ - z denote the cylindrical coordinates. By the symmetry $\partial/\partial\theta = 0$, the canonical angular momentum $p_\theta = \partial L/\partial\theta' = mrv_\theta + qrA_\theta$ is conserved. Hence, $\hat{H} = H - \omega p_\theta$ ($\omega = \text{constant}$) is a constant of motion. This \hat{H} is the Hamiltonian in a rigid rotation frame. Indeed, setting $\mathbf{U} = \omega r\mathbf{e}_\theta$ (ω is the angular velocity of the rigid rotation), (10) reads

$$\tilde{H} = \frac{m}{2}\tilde{v}^2 - \frac{m}{2}(r\omega)^2 - qr\omega A_\theta + q\phi = \hat{H}. \quad (17)$$

The equilibrium $f(\hat{H}) = Z^{-1}e^{-\beta\hat{H}}$ represents a drift Maxwellian with a constant angular velocity ω . Here, we seek a solution that has a constant density inside the plasma, i.e.,

$$\hat{H} = \frac{m}{2}\tilde{v}^2 = \frac{1}{2m}|\tilde{\mathbf{p}} - q\tilde{\mathbf{A}}|^2. \quad (18)$$

The vector potential for the homogeneous longitudinal magnetic field is $\mathbf{A} = (rB/2)\mathbf{e}_\theta$. For the distribution function $f(\hat{H}) = Z^{-1}e^{-\beta\hat{H}}$ with the Hamiltonian (18), the density n is constant for the radius $r < a$. Then, the potential is $\phi = -(qn/4\epsilon_0)r^2$ [2]. To satisfy (18), we demand $-(m/2)(r\omega)^2 - qr\omega A_\theta + q\phi = 0$ [see (17)], which reads as the familiar equilibrium condition

$$\omega^2 + \omega_c\omega + \frac{1}{2}\omega_p^2 = 0, \quad (19)$$

where $\omega_c = qB/m$ and $\omega_p^2 = nq^2/m\epsilon_0$.

(2) Electromagnetic equilibrium

Next, we discuss magnetic confinement solutions. Let us consider a slab plasma with $\mathbf{B} = B_z(x)\mathbf{e}_z$. We assume that the system is homogeneous with respect to y ($\partial/\partial y = 0$), so that the canonical momentum $p_y = my' + qA_y(x)$ is conserved. We consider $\hat{H} = H - cp_y$ and the equilibrium distribution $f(\hat{H}) = Z^{-1}e^{-\beta\hat{H}}$, which gives the drift Maxwellian with a constant velocity $\mathbf{U} = c\mathbf{e}_y$. Here, (10) reads

$$\tilde{H} = \frac{m}{2}\tilde{v}^2 - \frac{m}{2}c^2 - qcA_y + q\phi = \hat{H}.$$

We note that this \hat{H} depends on x . From the distribution function $f(\hat{H})$, we can calculate the density of each species. For appropriate parameters, the charge-neutrality can be achieved, and hence, ϕ can be set zero self-consistently. The drift Maxwellian yields a finite current. The magnetic field produced by this current must be consistent to the vector potential $A_y(x)\mathbf{e}_y$ in \hat{H} . Setting $B_z = B_0 \tanh(x/\ell)$, we can find a self-consistent solution that is called the Harris sheet [3]. The magnetic pressure B_z^2 has a dip around $x = 0$, where the pressure is confined. This equilibrium is based on the conservation of the momentum p_y . Similar calculations in cylindrical coordinates lead to the Bennet pinch equilibrium.

C Equilibrium with adiabatic constants and Beltrami-Bernoulli conditions

As the analysis in the previous section shows, a shear flow is not obtained from the model of momentum conservation. Here we examine an adiabatic invariant model to find an equilibrium with a shear flow. Let us first consider a certain velocity field \mathbf{U} and define a moving coordinate by (8). Here we assume that \mathbf{U} depends only on x , and

$$\mathbf{U} \cdot \nabla x = 0. \quad (20)$$

The transform of coordinates does not bring about temporal variation in any field. The equation of motion associated with the Hamiltonian \tilde{H} of (10) reads

$$\frac{d}{dt} \tilde{x}_j = \frac{\partial}{\partial \tilde{p}_j} \tilde{H} = \frac{1}{m} (\tilde{p}_j - q \tilde{A}_j), \quad (21)$$

$$\frac{d}{dt} \tilde{p}_j = -\frac{\partial}{\partial \tilde{x}_j} \tilde{H} = \frac{-1}{m} \sum_{\ell} (\tilde{p}_j - q \tilde{A}_j) \frac{\partial}{\partial \tilde{x}_j} \tilde{A}_{\ell} - \frac{\partial}{\partial \tilde{x}_j} \left(\frac{-m}{2} U^2 + q\phi \right), \quad (22)$$

or, in the form of Newton's equation (with $\partial \tilde{A}/\partial t = 0$),

$$m \frac{d}{dt} \tilde{\mathbf{v}} = q \left[-\tilde{\nabla} \phi + \tilde{\mathbf{v}} \times (\tilde{\nabla} \times \tilde{\mathbf{A}}) \right] + \frac{m}{2} \tilde{\nabla} U^2. \quad (23)$$

In (23), the Lorentz force includes the Coriolis force. We define a generalized magnetic field by $\tilde{\boldsymbol{\Omega}} = \tilde{\nabla} \times \tilde{\mathbf{A}}$. We assume that $\tilde{\boldsymbol{\Omega}}$ is a smooth and strong field.

Here we introduce an essential assumption

$$\tilde{\boldsymbol{\Omega}} = a\mathbf{U}, \quad (24)$$

where a is a certain constant. We denote \perp and \parallel , respectively, the perpendicular and parallel directions with respect to $\tilde{\boldsymbol{\Omega}}$. For "magnetized particles", the generalized magnetic moment $\tilde{\mu} = \tilde{v}_{\perp}^2 / |\tilde{\boldsymbol{\Omega}}|$ is an adiabatic invariant. By (20) and (24), we have $\tilde{\nabla}_{\parallel} = 0$ for every scalar field, and hence, the potential force in (23) does not have a parallel component. Therefore, \tilde{v}_{\parallel} is a constant of motion, and gyration average of the kinetic energy $m\tilde{v}^2/2$ does not change. Conservation of both \tilde{v}^2 and \tilde{v}_{\parallel} yields the constancy of \tilde{v}_{\perp}^2 , which, together with $\tilde{\mu} = \text{constant}$, imply that $|\tilde{\boldsymbol{\Omega}}|$ is constant (in gyration average) through the motion of particles. By (24), $|\tilde{\mathbf{U}}|$ is also constant in gyration average. Combining these adiabatic invariants, we observe that $\mathbf{U} \cdot \tilde{\mathbf{v}} = (v^2 - \tilde{v}^2 - U^2)/2$ is an adiabatic invariant.

Using this adiabatic constant, we define

$$\hat{H} = H - m\mathbf{U} \cdot \tilde{\mathbf{v}} = H - \mathbf{U} \cdot (\mathbf{p} - \bar{\mathbf{p}}), \quad (25)$$

where $\bar{\mathbf{p}} = m\mathbf{U} + q\mathbf{A}$. We may rewrite (25) as

$$\hat{H} = \frac{m}{2}\tilde{v}^2 + \frac{m}{2}U^2 + q\phi = \frac{m}{2}|\mathbf{v} - \mathbf{U}|^2 + \varphi,$$

where $\varphi = mU^2/2 + q\phi$ is the effective potential. The equilibrium define by \hat{H} reads

$$f(\hat{H}) = Z^{-1}e^{-\beta\hat{H}} = Z^{-1}e^{-\beta(m|\mathbf{v}-\mathbf{U}|^2/2+\varphi)}, \quad (26)$$

which is a drift Maxwellian with a shear flow velocity \mathbf{U} . We note that (24) is the determining equation for \mathbf{U} , which corresponds to the "Beltrami condition" of vortex dynamics systems [4].

The effective potential φ determines the density;

$$n = \int f \, dv = n_0 e^{-\beta\varphi} \quad (n_0 = Z^{-1} \int e^{-\beta m \tilde{v}^2/2} \, dv).$$

The pressure $p = nkT$ ($kT = 1/\beta$) satisfies the Bernoulli-like condition

$$\nabla p + n\nabla\varphi = \nabla p + n\nabla(mU^2/2 + q\phi) = 0. \quad (27)$$

We note that the Beltrami and Bernoulli conditions recover the fluid mechanical equilibrium model of diamagnetic (high-beta) structures [4,5].

III TOROIDAL EQUILIBRIUM OF NON-NEUTRAL PLASMAS

A Constant-density equilibrium in a straight annular geometry with sheared magnetic field

In this section, we discuss a more specific subject aiming at development of a new-type of non-neutral plasma trap. We consider a toroidal internal ring system that can produce a magnetic shear configuration [6]. To understand the basic property of such a configuration, we start with the analysis of an annular electron plasma column ($a < r < b$) confined by both longitudinal (B_z) and poloidal ($B_\theta = B_p a/r$) magnetic fields (B_z and B_p are constants). The core region of $r < a$ is occupied by a conductor that carries a longitudinal current to produce the poloidal magnetic field. The combination of B_z and B_θ produces a magnetic shear configuration with spiral field lines. The vector potential of the magnetic field is $\mathbf{A} = {}^t(0, (B_z/2)r, -B_p a \log r)$. The scalar potential ϕ is given by the Poisson equation (15). Here, we seek for a solution with a constant density. Let us consider a rigid motion of the plasma; $\mathbf{U} = {}^t(0, \omega r, U_z)$, where ω is the constant angular frequency of the poloidal rotation and U_z is

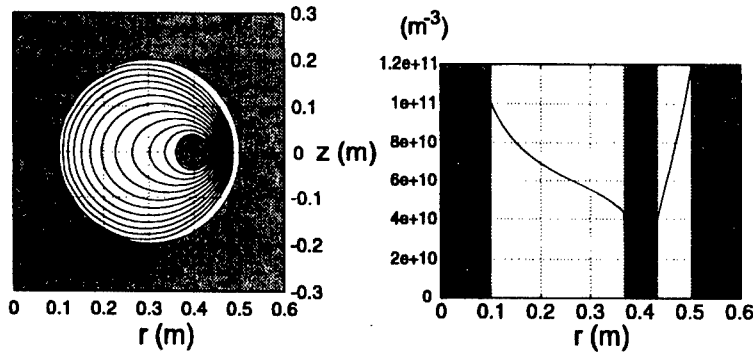


FIGURE 1. Toroidal thermal equilibrium of non-neutral plasma.

the constant longitudinal velocity. To obtain a constant-density equilibrium, we demand $-\frac{m}{2}U^2 - q\mathbf{U} \cdot \mathbf{A} + q\phi = 0$ [see (10)], which reads

$$-\frac{m}{2} \left(\omega^2 + \frac{qB_z}{m} \omega + \frac{q^2 n_0}{2m\epsilon_0} \right) r^2 + q(B_p a U_z + c_1) \log r + qc_2 - \frac{m}{2} U_z^2 = 0.$$

The coefficients of r^2 terms yield the conventional equilibrium condition (19), where the ω_c is determined by the longitudinal magnetic field ($\omega_c = qB_z/m$). The coefficients of $\log r$ terms yields $c_1 = -B_p a U_z$.

For this equilibrium, the longitudinal magnetic field B_z plays the principal role to confine the plasma, as in the previous cylindrical equilibrium. The poloidal magnetic field B_θ and the longitudinal flow U_z produces an electric field on the plasma, while it does not work to confine the plasma. Indeed, B_p and U_z determines the coefficient c_1 of the electric field, but they are not related to the density n_0 . However, the poloidal magnetic field, producing a magnetic shear, has an important function to stabilize the diocotron (Kelvin-Helmholtz) instability [7].

B Generalized thermal equilibrium in a toroidal geometry with magnetic shear

In a toroidal system, the toroidal symmetry gives the constancy of the toroidal canonical angular momentum. We denote the cylindrical coordinate by (r, ϑ, z) . The toroidal angle ϑ parallels the longitudinal direction z in the previous subsection. The poloidal angle is no longer an ignorable coordinate, and hence, we cannot assume the conservation of the poloidal angular momentum (which played the essential role to produce the constant density

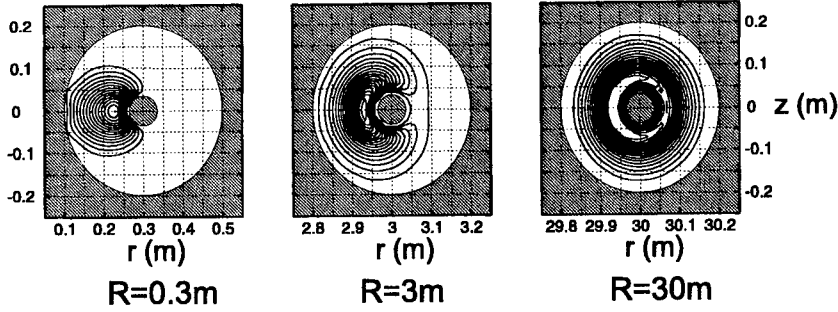


FIGURE 2. Toroidal equilibrium of non-neutral plasma base on the drift model.

equilibria in Secs. II B and III A). Here we consider a more general (non-constant density) solution of the nonlinear Poisson equation (15)-(16) with setting $\mathbf{U} = r\Omega\mathbf{e}_\vartheta$ (Ω is the angular frequency of the toroidal rotation). Writing the magnetic field as $\mathbf{B} = \nabla\psi \times \nabla\vartheta + B_\vartheta r\nabla\vartheta$, the transformed Hamiltonian is

$$\tilde{H} = H - \Omega p_\vartheta = \frac{m}{2}\tilde{v}^2 - \frac{m}{2}(r\Omega)^2 - q\Omega\psi + q\phi.$$

We normalize the variables as $x/\lambda_D = \hat{x}$, and $\beta q\phi = \hat{\phi}$, where λ_D is the Debye length. The nonlinear Poisson equation now reads

$$-\hat{\nabla}^2\hat{\phi} = \exp\{-\hat{\phi} + \beta[m(r\Omega)^2/2 + q\Omega\psi]\}. \quad (28)$$

When $\Omega = 0$, (28) is just the Debye shielding equation. The plasma flow (rotation) has the effect of charge neutralization. To confine a high-density plasma with low temperature ($\lambda_D \ll \ell$), Ω and magnetic field must be carefully chosen, because $e^{-\hat{\phi}}$ becomes a very small number, and the density tends to localize near the boundary, producing a sheath. In Fig. 1, we show an example of thermal equilibrium with $T_e = 10\text{eV}$ and $n_0 = 10^{11}\text{m}^{-3}$. When we diminish the temperature, equilibrium density becomes strongly localized near the boundaries.

Another model of non-neutral plasma equilibrium considers a drift motion of magnetized particle. For a low density magnetized non-neutral plasma ($\omega_c/\omega_p \gg 1$), we can use the $\mathbf{E} \times \mathbf{B}$ approximation of the flow velocity [8]; $\mathbf{u} = -\nabla\phi \times \mathbf{B}/B^2$. The macroscopic continuity equation in a steady state reads $\nabla \cdot (n\mathbf{u}) = -[\nabla\phi \times \nabla(n/B^2)] \cdot \mathbf{B} = 0$. When the magnetic field has a component perpendicular to $\nabla\phi$, this relation demands $n = B^2 F(\phi)$, where F is a certain smooth function. Using this n in the Poisson equation (15), we can find equilibrium solution. In comparison with (16), this model can produce a larger variety of solutions. Figure 2 shows typical equilibrium solutions with

different aspect ratios [9]. Because the drift velocity decreases as B increases, the equilibrium density shifts towards a higher field region (paramagnetism).

ACKNOWLEDGMENTS

The authors are grateful to Swadesh M. Mahajan for his comments and suggestions. This work was partially supported by Toray Science Foundation.

REFERENCES

1. J.B. Taylor, Rev. Mod. Phys. **58**, 741 (1986).
2. In a real experiment, finite-length confinement is produced by superposing an appropriate external electric field to adjust the potential to be $\phi \propto r^2$ inside the plasma. This can be done when we apply an electric field that has hyperbolic field lines to a spheroidal plasma; F. M. Penning, Physica (Amsterdam) **3**, 873 (1936).
3. E. G. Harris, Nuovo Cimento **23**, 115 (1962).
4. S.M. Mahajan and Z. Yoshida, Phys. Rev. Lett. **81**, 4863 (1998).
5. Another type of high-beta equilibrium is obtained by considering a large variation of a confining magnetic field. A neutral plasma confined in a dipole magnetic field (such as a stellar magnetic field) has two important adiabatic constants; the magnetic moment μ (associated with cyclotron motion) and the longitudinal invariant J_{\parallel} (associated with mirror bounce motion). To explain a high-beta plasma trapped by a stellar dipole field, An equilibrium of the form of $f(\mu, J_{\parallel}) = Z^{-1} e^{-\beta_1 \mu - \beta_2 J_{\parallel}}$ can have a very large density gradient; see A. Hasegawa, Comments Plasma Phys. Controll. Fusion **11**, 147 (1987).
6. Z. Yoshida *et al.*, in *Non-Neutral Plasma Physics III* (American Institute of Physics, 1999), 397.
7. S. Kondo, T. Tatsuno, and Z. Yoshida, Phys. Plasmas **8**, 2635 (2001).
8. J. D. Daugherty, J. E. Eninger, G. S. Janes, Phys. Fluids **12**, 2677 (1969).
9. H. Saitoh, Z. Yoshida, and C. Nakashima, Rev. Sci. Instrum. (to be published).

NNP-2001 Roundtable Discussion

Chuck Roberson, Chair
Office of Naval Research

This is the time in a meeting when we ask, "What is the future of non-neutral plasma physics?" This means it is the part of the meeting where there are more unknowns than boundary conditions. To address these questions I have asked the former conference chairs to be on this panel. Joel Fajans had to leave early, and Cliff Surko has volunteered to fill in for him.

The approach I want to adopt at this Roundtable discussion is a little different than we have done in the past. By any measure you wish to choose, the non-neutral plasma physics research program has been a scientific success. I have asked this panel of former conference chairs to address the following question: "What did we do right that made this program such a success?" Clearly the circumstances had to be right, and there had to be enough willing and able people to make this happen. The people at this table have played a vital role in this process.

Since I was the first Chair, I will start.

This program began, for me, when John Malmberg came to the Office of Naval Research with a proposal. They had done some preliminary experiments at U. C. San Diego to make the first thermal equilibrium plasma. However the transport was limited by asymmetries. I was a little surprised at this proposal, but he insisted this work was the key to the future of fundamental plasma research. I funded the proposal. He and Fred Driscoll built a new experiment, and demonstrated the first thermal equilibrium in a pure electron plasma.

When I presented these results in our reviews, there were some surprising reactions. A thermal equilibrium is easy for solids, liquids and gases, but for the fourth state of matter, a plasma, one normally needs an energy source to maintain it or else the electrons and ions recombine. Single component plasmas are the key, and the rigid rotor equilibrium the solution. The pure electron plasma in a rigid rotor equilibrium is the simplest thermal equilibrium plasma. It is what some have called a plasma equivalent to the hydrogen atom of atomic physics.

These results and some laser cooling of pure ion plasmas by the NIST Boulder group provided the stimulus for a new initiative at ONR in non-neutral plasmas.

With the benefit of hindsight, I realize what a major role this first non-neutral plasma physics meeting played in the success of this program. As someone has put it, the stars were aligned. The National Research Council was in the process of starting the Plasma Science Committee. When looking for a site to hold the meeting, the NRC made an offer we could not refuse — a conference room in the National Academy building. We ran the meeting as a symposium. The first day was devoted to non-neutral plasmas in traps and the second day to beams. The welcome address was given by Bruce Robinson, Director of the Contract Research Program at ONR. Bruce began his career as a plasma physicist. Many of the people came from funding agencies, attracted by the NRC Plasma Science Committee connection. Nearly a

third of the people were from the Naval Research Laboratory, who had a strong interest in beams. There was a sense of a revival of fundamental plasma physics, and I think the emphasis on basic plasma physics has served this community well over the intervening years.

Let me now ask Tom O'Neil for his perspective.

Tom O'Neil: In earlier conversation Chuck posed 4 questions: Where have we been? Where are we going? What have we done right in the past? And how can we replicate that in the future?

It seems to me that the easiest of these questions is, "Where have we been?" Of course, this question is like the Japanese movie *Roshomon* — everyone has a different perspective on the same events. But I'll give you mine to start with. Non-neutral plasma physics extends back a long time before these conferences got started. Ron Davidson coined the name many years earlier. When Chuck Roberson organized the first conference of this community, he gathered together a group of people that were focused on Penning traps, together with some people doing more traditional non-neutral plasma physics, such as radiation sources, relativistic beams, and energetic non-neutral plasmas.

The second conference focused more on trap physics. The Malmberg group was doing basic plasma physics with pure electron plasmas in Penning traps. Cliff Surko had developed a scheme for accumulating positrons. Dave Wineland and John Bollinger were doing very elegant atomic physics experiments with trapped pure ion plasmas. And Gerry Gabrielse had this crazy idea of using nested traps to produce antihydrogen. Thus, a community grew that was interested in understanding the physics of plasmas in Penning traps, in improving the confinement of Penning traps, and in doing a wide range of novel many-bodied physics in these Penning traps.

It seems to me that this community has succeeded far beyond our wildest dreams. I would simply have laughed 20 years ago if you had told me that we would learn how to confine non-neutral plasmas for arbitrarily long times, which we now do. Or that we could routinely confine plasmas in a state of thermal equilibrium that is very controllable, but we can now sweep the thermal equilibrium through the full range of allowed states. Or that we could cool these plasmas to make liquids and crystals, but we now study the rich and interesting interplay between various different crystal structures, and these structures are understood theoretically and in good correspondence with experiment.

Nor could anybody anticipate that pure electron plasmas are excellent vehicles for studying 2D fluids, but we now do high-precision experiments unmatched by water tank experiments, and the experiments exhibit a great visual attraction and surprises like vortex crystals. The list goes on and on — there is also a whole new range of transport phenomena that are understood in detail and in correspondence with experiments.

So I think this activity has been way more successful than we had any right to expect it to be in the beginning. Why was that?

We were lucky in several ways. First of all, the confinement and control of non-neutral plasmas in Penning traps is governed by powerful theorems. We learned from Ron Davidson's book that you could have these plasmas in thermal equilibrium, and that's been a key to a lot of progress; it made possible great understanding, great control. Any system that's close to thermal equilibrium is highly controllable; you can make small perturbations in a controlled way and understand the results.

Also, I think we were lucky that the physics turned out to be richer than many people anticipated. An early criticism of this program was that a single species plasma in a very simple confinement geometry will not be rich in terms of physics. But I think we hit a sweet spot between an over-simplified system and a system that is so rich and complicated that you haven't got a chance of understanding it (which much of plasma physics is, by the way). Of course, new and interesting results continue to be produced.

Then it seems to me that connections were made to other areas through the underlying physics; for example, strong correlation led to many connections. John Schiffer suggested that we would find strongly correlated plasmas in storage rings; that brought in the storage ring community. Also there's all this elegant work with Paul traps on crystals.

There were other connections; for example, continuing efforts to transfer this good confinement in Penning traps to other geometries, such as to toroidal geometries. Another connection is through three-body recombination that became of interest through the attempts to produce anti-hydrogen. We also saw Tom Killian's recombination experiments described at this conference. And so, many connections have been made through the physics, and I think that has broadened the community.

I particularly like that because one of the things we tried for at all stages is to have good physics problems. As Dave Crandall described at the end of our first conference: "You guys are doing physics with sex appeal." And I think we saw several new experiments described this week here that have sex appeal. That's how we have been able to hold our own alongside much larger communities, like the fusion community. Because of the interesting physics problems, this community has done well in terms of recognition from the whole plasma community.

I'll mention a couple of things that I think are crucial in this community. I think it's crucial that we have brought together physicists from different fields — from plasma physics and atomic physics first of all. The progress that I talked about just would not have been possible from plasma physicists alone, or from atomic physicists alone. It was absolutely crucial that we interacted closely, collaborated, traded post-docs, and so on. And I hope that that continues, and continues with new people coming into the field.

I think it's been crucial that there was an effort and a strong commitment to match theory and experiment. We worked very hard on Penning traps to match theory and experiment, and I think if we can transfer that to other programs, for example these laser-produced ultra-cold neutral plasmas, I think that would be important for the

development of those areas.

What are future directions? I can speak only for myself. I find interesting connections these days with neutral plasmas. I think that the program to produce anti-hydrogen poses a wide range of fascinating physics challenges in terms of stability of nested traps. Also, there are interesting problems with sympathetic cooling, when you have an electron and an ion species right next to each other but rotating in opposite directions. The experiments on ultra-cold neutral plasmas produced by photoionization I think are fascinating — so for me those are interesting directions.

Ron Davidson: We may have all had slightly different interpretations of Dr. Roberson's questions, but perhaps not.

Let me say a few words about the 2001 Workshop. Comparing with the Workshop in 1988, I think it is clear that there's been an enormous diversification of activities, including a large international effort. I believe about 30% of the institutions represented here are foreign institutions.

For completeness, I've listed the areas of research by going through the presentations for the past several days. They include: positron plasmas and sources; anti-matter plasmas and anti-hydrogen traps; ion traps, including high charge states; collective processes; nonlinear vortex dynamics; transport, including collisional, asymmetry-induced, and pressure-induced; coherent radiation generation; free electron lasers; microwave tubes; accelerator physics; intense beams and non-neutral charge bunches; strongly coupled plasmas; Coulomb crystals; dusty plasma crystals; ion clusters; Coulomb ordered strings (strongly coupled plasmas has been a large area of growth — I believe we had a full day of presentations on this topic area); ultra-cold neutral plasmas; various trap configurations, including the standard configurations — Malmberg, Penning and Paul; research in toroidal traps; an ion trap resonator — a very interesting paper; non-neutral beams and accelerator physics in which you have a periodic quadrupole field configuration; and also novel trap configurations like the ones that Ordonez and Dubin are looking at for anti-hydrogen.

Dr. Roberson also asked the question, "How did we get here?" And I would say to a large extent the U.S. effort has flourished due to the ONR, that is to say Dr. Roberson's encouragement of a program in non-neutral plasmas which features curiosity-driven research. And while it started with certain special areas of investigation, it could well be that had it started with other topics, we'd still all be here today at this exciting Workshop. The main point is that the field has flourished because of the emphasis on basic research, or curiosity-driven research. It's also true that the NSF has provided some level of support for non-neutral plasmas for many years, and what I find encouraging is that more recently the Office of Fusion Energy Sciences is providing support for non-neutral plasma research as well. In fact several of the presentations here are new initiatives supported by DOE. Some areas of increased emphasis are clearly evident from this Workshop — strongly coupled plasmas and anti-matter plasmas. This is very good, because these areas of

intersection with other areas of physics are highly visible, and I think very highly regarded by the physics community. To the degree that we can succeed in these areas, this will be very beneficial to the field overall.

Increased recognition of non-neutral plasma physics by other subfields of physics requires continued attention, and we need to accomplish this through seminars and colloquia, and certainly, within the community, through peer-reviewed publications and review articles. It is important in addition to have feature articles in *Physics Today*, *Science* and *Nature*, whenever possible, and there have certainly been some exciting results at this Workshop that are worthy of such broad exposure.

Now how do we ensure an even stronger future? Several points come to mind: we need to continue to have a strong student involvement and recruitment of bright young talent into the program; continue to encourage curiosity-driven research, not always knowing where it's going to lead; strengthen interdisciplinary activities — this is now a real hallmark of this Workshop, and non-neutral plasma physics overall; capitalize on successes in critical mass areas; identify new application areas; and identify new regimes of physics investigation, e.g., experimental studies closer to Brillouin flow conditions in weakly-coupled non-neutral plasmas.

This area of Brillouin flow was also identified in the minutes of the 1988 Workshop. It's certainly true in the strongly coupled regime, and scientists have been looking at crystalline plasmas near the Brillouin flow limit. It's also true in accelerator physics; for example for heavy ion beam fusion you're very close to the equivalent Brillouin flow condition. To the extent possible, I believe it is important to do more laboratory experiments at higher space-charge intensity. This was also a point I made at the 1988 Workshop for the case of weakly coupled plasmas. This is a very rich area of physics, and the simplified models that people have used at low density don't apply. For example, the flow is no longer incompressible, and vortex structures will change character completely from the low-density regime.

John Bollinger: I'll be very brief here, because what do you say after Tom and Ron have really said it all? I guess I focused on, when Chuck asked me, the question, "What are we doing right?" If we can recognize what we're doing right, then perhaps we can do things right in the future.

I think it starts with the good science and the high standards that are set here at UCSD, which we all try to aspire to. But from my point of view, what's been a lot of fun and very interesting working in this field has been the cross-fertilization. First there is the cross-fertilization between theory and experiment, and I think Tom already mentioned this. There are theorists in this field who work closely with the experimentalists, and of course Tom O'Neil and Dan Dubin are good examples, but also Ron Davidson and Rainer Hasse. There are people who do both, such as Roy Gould, and then there are some experimentalists who do theory such as John Schiffer; so this makes it a very vital field.

The cross-fertilization between different fields is particularly important to me. I could mention a number of examples where that's really worked out surprisingly

well. The rotating wall technique is a good example. Most of you know we had this technique of using lasers to control the rotation frequency in our laser-cooled ion plasmas, and it gave us good control. But it's not nearly as precise as we got with the rotating wall technique, and it was a post-doc, Pei Huang from the UCSD group, who brought that with him when he came to work with us.

The interaction with the ion storage ring community I find very interesting, and now recently the cold neutral plasmas. Once again that's making a connection with the atomic physics community. One problem with cross-fertilization is that we all speak a little bit different language. Around the second day of this workshop, someone asked me what a diocotron mode was. He suggested that it might make sense to have a tutorial talk. I don't know how we find the time and space for that, but if cross fertilization is what we want to emphasize, that might be something to think about for future meetings.

Finally, I think an important aspect of this field which can help maintain its vitality is the interesting applications. Anti-matter physics is fascinating to everyone. And it's not just a fascinating application; there's good science there as well. With the trapped ion work, there are the clocks. With the Penning traps we're now receiving very impressive competition from the single ion optical standards, however we can also pursue applications in quantum information. The fact that we can even tie into the field of quantum information relies on having the rotating wall and being able to localize our ions and address them.

In summary, I believe one of the things Chuck is interested in is, how do we keep the ball rolling? I think good science is one of them, but sometimes good science seems a little stale to the people we need to convince that this work is worth funding. However I believe cross-fertilization and the applications can keep providing us with good ideas and keep the field fresh.

Fred Driscoll: In putting the program together for this meeting, one thing that impressed me is that the field has matured to where there are lots of what I call "devices". That is, there are lots of very sophisticated apparatuses that *use* non-neutral plasmas, rather than *study* non-neutral plasmas. These devices are important in the pursuit of anti-matter, atomic physics, spectroscopy, cyclotron resonance, and beam physics. Because of this broad range of physics interests, we're evolving to a community of "users" of non-neutral physics; that is, the applications are now just as exciting as the basic science.

I would suggest, however, that the strategy of pursuing basic, device-independent physics has guided this community well in the past, and is an appropriate perspective for the future. I would say that we now have a fairly broad and coarsely complete picture of non-neutral plasma physics, of what goes on in these systems. "Coarsely complete" ranges from quantitative to qualitative in being able to describe and predict the operation of these devices.

From my experimentalist's perspective, what this broad community of device developers needs are user-friendly, physics-based scaling laws. Scaling laws have kind of a bad reputation because they often cover up a lot of ignorance, being specific

to particular devices; but here I think we really are getting to the point where much of our working knowledge is physics-based.

Thus, I look forward to a time when we fully understand the various regimes of plasma loss, so that anybody who builds a non-neutral plasma device can predict how it will operate. We understand quite well that these losses are due to external “trap asymmetries”. At present, we have broad characterizations of the loss rates for the 4 or 5 types of traps that have been studied, and an understanding of the physics of several individual loss processes. But I would hope that we will fully integrate the experimental results into a global perspective (and scaling laws) that includes temperature, density, magnetic field, and length — this has been partially done — but also including size, construction techniques, and geometry — including toroidal geometry, if you’re really optimistic.

Along these lines, Eli Sarid presented at this conference what might well be a new transport mechanism at low plasma density. I think we have to work hard to ask how this new effect fits in with Jason Kriesel’s “2-regime” results, which characterize the loss rate in terms of the Rigidity, defined as the bounce rate along the magnetic field compared to the plasma rotation rate.

Also at this conference, Andrey Kabantsev reported what I think will be a developing field of “trapped particle asymmetry” modes, and how they contribute to particle transport. I think this research direction will be fruitful, connecting to the “sloshing particles” previously discussed by Grant Hart in connection with the diocotron mode and magnetic field tilt.

So what I’m suggesting is that we’re getting to the point where our understanding will evolve from individual effects to a global physics view of how these effects fit together. We will then be able to present the physics results to people who are users, who do not want to spend their careers learning plasma physics. A user wants to ignore plasma physics as much as possible; he just wants the device to work. This user will be able to incorporate a unified physics perspective much more readily than a collection of individual effects.

Chuck Roberson mentioned that the ONR funding initiative got started based on the physics of internal transport of particles, heat, and angular momentum. Here, I think the strategy of pursuing basic device-independent physics has been a stunning success. For example, when the experimental data on test-particle diffusion disagreed with the Dubin-O’Neil transport theories describing “long-range collisions”, it led to an understanding of a new device-independent collisional effect of “velocity caging”.

Similarly, the transport theories were done separately in the 2D and 3D regimes, but now a more global perspective is emerging based on the parameter N_b , which is the number of bounces that a particle takes before it is separated from its neighbor by the shear in the plasma rotation. The parameter N_b is actually quite analogous to the Rigidity parameter, except that N_b is appropriate to the rotating frame where internal transport takes place. Both parameters are just the number of particle bounces before theta-separation becomes important, i.e. just f_{bounce} over the shear or the rotation.

From this perspective, there's the 3D regime, characterized by low rigidity and low number of bounces, and the 2D regime, where these parameters are pushing up into the 10^5 range. This simplifies the global picture significantly.

Thus, part of the organizing picture that I think we will be developing is the idea that 2D vs 3D is the same as shear reduction of transport. That is, the onset of shear effects is really the transition between the 2D and the 3D regimes. I think once we get that picture filled in, and fit perhaps internal and external transport into it, we will have made quite a bit of progress.

One thing that has characterized this community is that we are doing experiments and comparing them directly and quantitatively to theory, with the expectation of full agreement. Here, you cannot ignore the ends or boundaries of the devices. In characterizing the 10 year history of "end effects", I'd say that getting physics right including all boundaries is very hard.

Take, for example, the relation between the plasma physicist's diocotron mode, where the plasma orbit is driven by image charges with small end corrections; and the atomic physicist's magnetron mode, which is driven by containment fields with small image charge corrections. It's taken quite a while, starting perhaps with Kevin Fine's diocotron "end corrections" work, to relate the plasma and atomic physics regimes. But overall, we're developing a less narrow, more global picture of these devices and fitting the physics into one picture.

Along similar lines, we're now beginning to understand the non-2D-fluid end effects such as velocity-dependent theta smearing in the ends which Joel Fajans introduced with his Lambda parameter some 8 years ago. The dynamics of single particles in the end containment fields is straightforward, but things get substantially harder when dealing with multiple particles and simultaneous collisions. Thus, there are still outstanding puzzles, such as the 2D viscosity results described by Jason Kriesel — that's where the theory and experiment are not yet fitting together. I suspect that significant advances in our understanding of basic collision theory will result from efforts to incorporate end effects in theories of viscosity.

And finally, one example of a long-term problem relating to end effects is the exponential instability of the $m_\theta = 1$ mode, where end effects cause deviation from the 2D fluid perspective. It's a problem that includes the hardest parts of finite geometry and collective effects. There are now 10 years of experiments and theory, with lots theory effects being partially understood, yet a satisfying resolution remains elusive. This maze of effects was jokingly characterized in one of this week's talks as the "6 levels of hell." But really, what is one man's hell is another man's heaven, because it says there is very rich physics in here, and it's our job to develop a full and workable understanding.

At the end of the day, however, we want to develop our understanding to the point where experimentalists from various fields of physics can use the results with confidence. That is, these users need physics-based scaling laws, where individual effects fit into a bigger picture, with boundaries defined in physics terms rather than

in device-specific jargon. I think that's the challenge, and that we're making good progress.

Cliff Surko: First the past: The beginnings of the field were before my time working in non-neutral plasmas. My impression is that the field began with a simplicity that was unprecedented in the plasma physics of the day, but maybe not in early plasma physics. About the time that Malmberg, O'Neil and Driscoll and Bollinger and Wineland were beginning to do things in this area, almost all of plasma physics was focused on applications. What that meant was that, for one reason or another, it was very hard in most of the field to actually focus on a problem, throw away anything extraneous, and bore in and kill it. Non-neutral plasmas was the one area where one could do just that. The experiments were relatively simple and inexpensive, which led to great flexibility. When they started, it was natural to focus on the simplest things around. This led to several key results, for example, to the famous thermal equilibrium states and ion crystals.

You then had an experimental base and a tradition that set the stage for many things. When you look at the field at that stage, it is useful to make analogy, not with plasma physics in the 70's and 80's, but with condensed matter and atomic physics, where typically you would never be satisfied with factor of two agreement, or agreement over a small parameter range. Typically, theory would stimulate experiment (or vice versa), and then progress would go iteratively until you really solved the problem. At the end of the day, you knew what you knew, and you knew what you didn't know. And so this style in non-neutral plasma research set the stage for a whole bunch of things — things we've seen at this meeting — such as connections to FELs and lasers, the beautiful electron fluid experiments, antimatter plasma experiments, and a whole host of other spinoffs.

That's the past. The present — well, I guess I'd characterize the present as the stage where we are focusing on more refined questions, typically in more complicated systems. This has a good part and a bad part. It's hard in a short period of time to come up with a completely revolutionary idea or result. There are pleasing, nice results, but again you're a little bit more in the mode of focusing on details — there are more things in the models, more things in the experiments, etc. The other side of this is that, as has been discussed, many applications are being successfully exploited. I look at the last two meetings as a manifestation of this evolution. People from all sorts of fields are coming together to talk and share ideas and share problems, and that's really very positive. I feel compelled to add to these comments the last line on the viewgraph: while there are applications, I guess I'd say that there are no killer applications yet — we're still waiting for that. That's not necessarily bad, but at least in my view, that's where we're at.

Now the future. That's always hardest — well, maybe it's really easiest because people (at least optimistically) will forget what you say if it's wrong. We clearly want to exploit our successes. To me (and I thought I was agreeing with everybody in this discussion today), comments in the last talk touched on the one thing I would

look at differently. It seems to me that our strength is not likely to lie in developing scaling laws. Really, our successes have been, and probably will continue to be, more in the style of really going to the core of something until you understand it. And so I would hope that as we continue to expand and pursue a wider variety of applications, we keep one of the most important things we bring to the whole enterprise, which is this tradition of rigorous, first-principles science. It's quite fine to develop scaling relations and other engineering tools, but I think one doesn't want to forget this other side of things.

Regarding other points, Ron mentioned something in different language, that I list as outreach — the importance of carrying our scientific message to other communities in this scientific world of ours, a world where things are now much more interdisciplinary, and there's much more competition for resources. We need a suitable forum in which to present our results. We need to consistently confront the fact that we can't just float along on our own. The fact that there are so many people from different areas at this meeting is very positive in this regard.

How about directions for the future? There are many interesting directions — you know my great enthusiasm for antimatter physics, for example. But I don't think the specifics are so important. Like all guesses at future directions, sometimes they work out and sometimes they don't. An example is focusing on cross-field transport in single component plasmas as early as the 70's — and here it's still around more than 20 years later. My "hot direction" may come to naught — but with all we know about single-component plasmas, investigating the evolution from single-component plasmas, to partially neutral plasmas, and then (optimistically) toward neutral plasmas, is a problem that I think is natural for us to pursue. And of course, it has widespread applications — in tokamaks, electron-positron plasmas, antiproton-positron plasmas, and a host of other situations. Maybe some of them will be very successful (and some of them won't, of course). We'll just have to see about that.

I covered this earlier, but, if there were one overarching message I'd like to leave you with, it is to keep the focus. We should continue to maintain a broad enterprise, we should continue to pursue applications, but on the other hand, I think the right strategy for us is keeping the community focusing on non-neutral plasmas, boring in on (model) problems and nailing them.

Chuck Roberson: Let me make a few more comments to wrap up.

At the first workshop we didn't have any of these results with vortex dynamics or the minivortex convergence and the 2D fluid dynamics. These beautiful experiments emerged immediately afterwards. We really started with what some people call the hydrogen atom of plasma physics. If you start with something that simple, you're going to go in all kinds of directions.

I'm always looking for something that has a Navy hook to it, and I thought the vortex dynamics was really something I could brag about because we have lots of activities in fluid dynamics and the Navy lives in the sea. At one time I got carried away and claimed we could do better fluid dynamics in something the size of a beer

can with a number of particles about equal to the population of the U.S. than you could in all the seven seas of the world. For the most part, I got blank looks. Fred and Joel sent me lots of supporting viewgraphs, and I connected with a few people in the organization who knew what we were talking about from the physics point of view, so I felt good about it.

Of course we had the clocks; the motivation from the beginning for funding the Wineland and Bollinger group was because of the clocks, and the Navy has a critical need for clocks other than the national standards. That's something I've always found extremely remarkable, that we were doing plasma physics and talking about accuracies of one part in 10^{16} or 10^{18} .

John Bollinger tells us the Ion Penning traps have opened a new approach to quantum computing. A critical element of that has been the rotating wall. That's given him the control to make these rotating crystallized disks, and that came out of this group.

As Cliff says, there are no killer Apps, but the kind of developments Rod Greaves is starting to work on is in that direction. This is an outgrowth from things in Cliff's lab. Rod's work is funded with SBIRs and trying to find a way to commercialize these trap-based positron sources.

At this meeting there are clearly a lot of trap-based sources emerging. People are using these traps to load the particles, especially if they're very exotic particles. They can do things to them in the traps, cool them and compress them, then take them out and use them. That seems to be becoming an intermediate stage more and more in particle sources.

The category of non-neutral plasmas in traps has led us to many extremes. We funded the smallest experiment at the Princeton Plasma Physics Laboratory, a Malmberg-Penning trap to take advantage of the predictability of the expansion rate of the rigid rotor equilibrium with a neutral gas.

Perhaps the most extreme is the effort to make antihydrogen at CERN. The work involves particle, atomic and plasma physics. There are two very talented and competitive groups pursuing this effort. A special accelerator facility has been constructed to produce anti-protons. Since the main accelerator at CERN will be down a few years for upgrades, this is now an extremely high visibility effort.

Recently Ron Davidson has started a new effort with Paul Traps to simulate intense beam propagation through a periodic focusing quadrupole field. This is an example of the "beams at rest" kind of thing these traps are capable of. A lot of the beam dynamics can be studied in the traps without building an accelerator.

We have focused on non-neutral plasmas in traps since the first Non-neutral meeting. However we have adopted a policy of inviting someone from the beams community to report on interesting developments in that field. At the Boulder meeting we heard about the use of plasma wave echoes as a nondestructive diagnostic in a storage ring. This came some 30 years after the pioneering work by Gould, Malmberg and O'Neil.

At the Princeton conference we heard about the first free electron laser experiments to exceed a kilowatt average power. This experiment used the

superconducting accelerator technology developed at the Jefferson Laboratory. The most expensive element in accelerator based radiation sources (FELs) is the accelerator and the most critical element for scaling to short wavelengths is a high quality high current electron beam. Recently some pioneering experiments in the high (exponential) gain FELs have been carried out at short wavelengths where nonlinear saturation is reached in a single pass. These single pass FELs offer the possibility of high power coherent free electron radiation sources without mirrors. This has led to proposals by SLAC and DESY to make 1 Angstrom X-ray sources based on the high gain FELs.

The paper presented at this meeting by Bahaman Hafizi on Kinetic Effects in High Gain Free Electron Lasers explores the similarity between beam quality in the two stream instability and high gain FELs. The scaled thermal velocity developed by O'Neil and Malmberg for the transition from the two stream instability to the bump on tail instability can be generalized and used as a measure of free electron laser beam quality in high gain FELs.

Thus, I think we can all be proud of both the basic enabling science and the sophisticated applied science which has developed around non-neutral plasmas. I look forward to the mix of progress and surprises at the next Non-Neutral Plasma Workshop.

List of Participants

Friedhelm Ames
Sektion Physik der LMU Munchen
Am Coulombwall 1
D-85748 Garching
GERMANY
Friedhelm.Ames@cern.ch

Marco Amoretti
Dipartimento di Fisica & Infm.
Univ. degli Studi di Milano
Via Celoria 16
20133 Milano
ITALY
amoretti@mi.infn.it

Francois Anderegg
Univ. of California, San Diego
IPAPS 0319
9500 Gilman Drive
La Jolla CA 92093-0319
fanderegg@ucsd.edu

Daniel Bahr
2103 Folwell Dr. SW
Rochester MN 55902
dnbahr@2hotmail.com

Stephan Barlow
Pacific Northwest National Lab
P.O. Box 999 (K8-88)
Richland WA 99352
se_barlow@pnl.gov

Levi Barnes
UCSD Physics Dept. 0319
9500 Gilman Drive
La Jolla CA 92093-0319
levi@physics.ucsd.edu

Dan Barnes
P.O. Box 1663, B-259
Los Alamos National Laboratory
Los Alamos, NM 87545
dbarnes@lanl.gov

Reinhold Blumel
Dept. of Physics
Wesleyan University
265 Church Street
Middletown CT 06459-0155
rblumel@wesleyan.edu

Georg Bollen
Michigan State University / NSCL
South Shaw Lane
East Lansing MI 48824-1321
bollen@nscl.msu.edu

John Bollinger
NIST, MS 847.10
325 Broadway
Boulder CO 80303-3328
john.bollinger@nist.gov

Steven J. Buckman. Associate Director
Research School of Phys. Sci. & Engr.
Institute of Advanced Studies
The Australian National University
Canberra, AUSTRALIA
stephen.buckman@anu.edu.au

Yongbin Chang
Univ. of North Texas
Physics Dept. RM 110
Denton TX 76203-1427
cao@unt.edu

Noel Corngold
CalTech 128-95
1201 E. California Blvd.
Pasadena CA 91125
nrd@cco.caltech.edu

Jose Correa
Univ. of North Texas
Physics Dept. RM 110
Denton TX 76203-1427
cao@unt.edu

James Danielson
University of California, San Diego
Department of Physics 0319
9500 Gilman Drive
La Jolla CA 92093-0319
jdanielson@ucsd.edu

Ronald Davidson
Princeton Plasma Physics Laboratory
P.O. Box 451
Princeton NJ 08543
rdavidson@pppl.gov

Gian Luca Delzanno
Los Alamos National Laboratory
Mail Stop C-305
Los Alamos NM 87545
delzanno@lanl.gov

Michael Drewsen
Institute of Physics and Astronomy
University of Aarhus
Ny Munkegade
DK-8000 Aarhus C
DENMARK
drewsen@ifa.au.dk

C. Fred Driscoll
University of California, San Diego
Physics Dept. 0319
9500 Gilman Drive
La Jolla, CA 92093
fdriscoll@ucsd.edu

Daniel Dubin
University of California in San Diego
Dept of Physics 0319
9500 Gilman Drive
La Jolla CA 92093
dhubin@ucsd.edu

Philip Efthimion
Princeton Plasma Physics Laboratory
P.O. Box 451 / MS 34
Princeton NJ 08543
pefthimion@pppl.gov

Dennis Eggleston
Occidental College, Physics Dept.
1600 Campus Road
Los Angeles CA 90041
eggleston@oxy.edu

Udo Eisenbarth
Max-Planck-Institut fuer Kernphysik
Saupfercheckweg 1
69117 Heidelberg
GERMANY
u.eisenbarth@mpi-hd.mpg.de

Jennifer Ellsworth
175 S. West Street
Geneva NY 14456
jle59@columbia.edu

Joel Fajans
Physics Department
UC Berkeley
151 LeConte Hall
Berkeley CA 94720
joel@plasma.berkeley.edu

K. Yoshiki Franzen
c/o Prof. Y. Yamazaki
Institute of Physics / Univ. of Tokyo
3-8-1 Komaba Meguro-ku
Tokyo 153-8902 JAPAN
kyf@radphys4.c.u-tokyo.ac.jp

Gerald Gabrielse
Harvard University, Physics Dept.
17 Oxford Street
Cambridge, MA 02138
gabrielse@physics.harvard.edu

Steve Gilbert
UCSD Physics Dept 0319
9500 Gilman Drive
La Jolla CA 92093-0319
sjgilbert@ucsd.edu

Erik Gilson
Princeton Plasma Physics Laboratory
P.O. Box 451, M.S. 17
Princeton NJ 08543-0541
egilson@pppl.gov

Dirk David Goldbeck
Max Planck Institute
Cosimastr. 162
81927 Munchen
GERMANY
ddg@mpe.mpg.de

Daniel Gordon
Naval Research Laboratory (6790)
4555 Overlook Ave. SW
Washington DC 20375
gordon@ppdu.nrl.navy.mil

John Goree
University of Iowa
Dept of Physics and Astronomy
Iowa City IA 52242
john-goree@uiowa.edu

Roy Gould
Cal Tech
MS 128-95
Pasadena CA 91103
rwgould@caltech.edu

Rod Greaves
First Point Scientific, Inc.
5330 Derry Avenue, Suite J
Agoura Hills, CA 91301
greaves@firstpsi.com

Olaf Grulke
MPI for Plasma Physics
Wendelsteinstrasse 1
17491 Greifswald
GERMANY
grulke@ipp.mpg.de

Bahman Hafizi
Icarus Research Inc.
P.O. Box 30780
Bethesda MD 20824-0780
solcat9@aol.com

Grant Hart
Brigham Young University
Dept. of Physics & Astronomy
Provo UT 84602
grant_hart@byu.edu

Rainer Hasse
GSI Darmstadt
Planckstr. 1
D-64291 Darmstadt
GERMANY
r.hasse@gsi.de

Yasuaki Hayashi
Kyoto Institute of Technology
Matsugasaki, Sakyo-ku
Kyoto 606-8585 JAPAN
hayashi@dj.kit.ac.jp

Terry Hilsabeck
Department of Physics 0319
University of California, San Diego
9500 Gilman Drive
La Jolla CA 92093-0319
thilsabeck@ucsd.edu

Haruhiko Himura
University of Tokyo
Graduate School of Frontier Sciences
7-3-1 Hongo, Bunkyo Ward
Tokyo 113-0033
JAPAN
himura@k.u-tokyo.ac.jp

Joe P. Holder
Lawrence Livermore National
Laboratory
P.O. Box 808, Mail Stop L-280
Livermore CA 94550
Holder4@llnl.gov

Eric Hollmann
Center for Energy Research
UCSD M/C 0417
9500 Gilman Drive
La Jolla CA 92093-0417
ehollmann@ucsd.edu

Al Hyatt
General Atomics
P.O. Box 85608
San Diego CA 92186
al.hyatt@gat.com

Toshiyasu Ichioka
The University of Aarhus
Inst. of Physics & Astronomy
Ny Munkegade, Bygn. 520
DK 8000 Aarhus C
DENMARK
itchy@radphys4.c.u-tokyo.ac.jp

Kiyokazu Ito
Plasma Lab/Fac. Integrated Human
Studies
Kyoto University
Sakyoku, Kyoto 606-8501
JAPAN
n50116@sakura.kudpc.kyoto-u.ac.jp

Thomas Jenkins
Princeton Plasma Physics Laboratory
MS 30, P.O. Box 451
Princeton NJ 08543
tjenkins@pppl.gov

Gene Jerzewski
UCSD Physics Dept. 0319
9500 Gilman Drive
La Jolla CA 92093-0319
gjerzewski@ucsd.edu

Lars V. Jorgensen
University of Wales, Swansea
Department of Physics
Singleton Park
Swansea SA2 8PP
UNITED KINGDOM
Lars.Vorming.Jorgensen@cern.ch

Andrey Kabantsev
Department of Physics 0319
University of California, San Diego
9500 Gilman Drive
La Jolla CA 92093-0319
aakpla@physics.ucsd.edu

Thomas Killian
Rice University
Physics and Astronomy, MS 61
6100 Main Street
Houston TX 77005
killian@rice.edu

Yasuhito Kiwamoto
Kyoto University
Yoshida, Sakyo-ku
Kyoto 606-8501 JAPAN
m52279@sakura.kudpc.kyoto-u.ac.jp

Niels Kjaergaard
Optics and Fluid Dynamics Dept.
Riso National laboratory
P.O. Box 49
DK-4000 Roskilde
DENMARK
niels.kjaergaard@risoe.dk

Shigeo Kondo
The University of Tokyo
Graduate School of Frontier Sciences
7-3-1 Hongo, Bunkyo-ku
Tokyo 113-0033 JAPAN
kon@plasma.q.t.u-tokyo.ac.jp

Jason Kriesel
NIST -- MS 847
325 Broadway
Boulder CO 80303
kriesel@boulder.nist.gov

Naofumi Kuroda
Institute of Physics, Univ. of Tokyo
c/o Prof. Yamazaki
3-8-1 Komaba Meguro-ku
Tokyo 153-8902 JAPAN
kuroda@radphys4.c.u-tokyo.ac.jp

Stanislav Kuzmin
UCSD Physics Dept 0319
9500 Gilman Drive
La Jolla CA 92093-0319
skuzmin@physics.ucsd.edu

Giovanni Lapenta
Los Alamos National Lab., MS C305
Los Alamos, NM 87545
lapenta@lanl.gov

Wallace Manheimer
Department of the Navy - Code 6707
Naval Research Laboratory
4555 Overlook Ave. SW
Washington DC 20375-5320
manheime@ccsalpha2.nrl.navy.mil

Joan Marler
UCSD Physics Dept. 0319
9500 Gilman Drive
La Jolla CA 92093-0319
jmarler@physics.ucsd.edu

Gerrit H. Marx
GSI - Darmstadt
Planckstr. 1
D-64291 Darmstadt
GERMANY
g.marx@gsi.de

Grant Mason
Brigham Young University
Dept. of Physics & Astronomy
[N249 ESC]
Provo, UT 84602
masong@einstein.byu.edu

Kirby Meyer
Synergistic Technologies
127 East Gate Drive, Suite 203
Los Alamos NM 87544
kirby@synergistictech.com

Travis Mitchell
223 Sharp Lab
Dept. of Physics & Astronomy
Univ. of Delaware
Newark DE 19716
tbmitche@udel.edu

Akihiro Mohri
Institute of Physical and Chemical
Research
Ichijoji Matsubaro-cho 105
Sakyo-cu
Kyoto 606-8156
JAPAN
akimohri@ip.media.kyoto-u.ac.jp

Kyle Morrison
Princeton Plasma Physics Laboratory
MS 17, Box 451
Princeton NJ 08540
kmorrison@pppl.gov

Chihiro Nakashima
University of Tokyo
High Temperature Plasma Ctr Room
0033
2-11-16 Yayoi, Bunkyo-ku
113-8565 Tokyo
JAPAN
nakasima@plasma.q.t.u-tokyo.ac.jp

Takeshi Nakata
Brigham Young University
392 N. Seven Peaks Blvd. #323
Provo UT 84606
mtn2@email.byu.edu

Thomas O'Neil
UC San Diego
Physics Dept. 9500 Gilman Dr.
La Jolla CA 92093
toneil@ucsd.edu

Yuichi Ogawa
High Temperature Plasma Center
The University of Tokyo
2-11-16 Yavoi, Bunkyo-ku
113-8656 Tokyo
JAPAN
ogawa@plasma.q.t.u-tokyo.ac.jp

Carlos Ordonez
University of North Texas
Physics Dept., RM 110
Denton, TX 76203-1427
cao@unt.edu

Garrett Otto
Massachusetts Institute of Technology
PSFC NW16-160
77 Massachusetts Avenue
Cambridge MA 02139
glotto@mit.edu

Thomas Pasquini [c/o Joel Fajans]
UC Berkeley Physics Dept MS-7300
151 LeConte Hall
Berkeley CA 94720-7300
Thomas.A.Pasquini.00@
alum.dartmouth.org

Stephen Paul
Princeton Plasma Physics Laboratory
P.O. Box 451 / MS 17
Princeton NJ 08543
spaul@pppl.gov

Bryan Peterson
Brigham Young University
Dept. of Physics & Astronomy
[N355 ESC]
Provo UT 84602-4668
bryan_peterson@byu.edu

Robert Pollock
Indiana University
Swain Hall West
Bloomington IN 47405-7105
pollock@iucf.indiana.edu

Roberto Pozzoli
University of Milan
Physics Department
Via Celoria 16
20133 Milano
ITALY
roberto.pozzoli@mi.infn.it

Richard Quinn
Max Planck Institute
Erddinger Platz 7
Garching 85478
GERMANY
raq@mpe.mpg.de

Qudsia Quraishi
University of Colorado at Boulder
Department of Physics
Campus Box 390
Boulder CO 80309-0390
qudsia.quraishi@colorado.edu

Georg Raithel
Physics Department
4223 Randall Lab.
University of Michigan
Ann Arbor MI 48109-1120
graithel@umich.edu

Neil Rasband
Brigham Young University
Dept. of Physics
Provo UT 84602
rasband@beethoven.byu.edu

Paolo Ricci
Politecnico di Torino
Dipartimento di Energetica
C.So Duca Degli Abruzzi 24
10100 Torino
ITALY
riccipaolo@libero.it

Kevin Rigg
UCSD Physics 0319
9500 Gilman Drive
La Jolla CA 92093-0319
krigg@physics.ucsd.edu

Charles Roberson
Office of Naval Research
Physical Science Div, Code 331
800 N. Quincy St.
Arlington VA 22217
robersc@onr.navy.mil

Scott H. Robertson
University of Colorado at Boulder
Department of Physics
Campus Box 390
Boulder CO 80309-0390
robertso@stripe.colorado.edu

Federico Rocchi
Bologna University
c/o Lab. di Montecuccolino
via del Colli 16
40136 Bologna (BO)
ITALY
federico.rocchi@mail.ing.unibo.it

Massimiliano G. Rome
dipartimento di Fisica
Universita degli studi di Milano
via Celoria, 16
20133 Milano
ITALY
rome@mi.infn.it

Akio Sanpei
Plasma Lab/Fac. Integrated Human
Studies
Kyoto University
Sakyoku, Kyoto 606-8501
JAPAN
n50117@sakura.kudpc.kyoto-u.ac.jp

Eli Sarid
Physics department
NRCN
P.O. 9001
Beer Sheva 84190
ISRAEL
esarid@netvision.net.il

Tobias Schatz
Sektion Physik der LMU Munich
Am Coulombwall 1
85748 Garching
GERMANY
tschaetz@physik.uni-muenchen.de

Martin Schauer
Los Alamos National Laboratory
MS H803
Los Alamos NM 87545
schauer@lanl.gov

David Schechter
Nat'l Center for Atmospheric
Research/ASP
P.O. Box 3000
Boulder CO 80307
daspla@net.asp.ucar.edu

John Schiffer
Argonne National Laboratory
Physics Div. - Bldg. 203
9700 S. Cass Avenue
Argonne IL 60439-4843
schiffer@anl.gov

Pit Schmidt
UCSD Physics Dept 0319
9500 Gilman Drive
La Jolla CA 92093-0319
Pit.Schmidt@physics.ucsd.edu

Ulrich Schramm
Sektion Physik der LMU Munich
Am Coulombwall 1
85748 Garching
GERMANY
ulrich.schramm@physik.uni-
muenchen.de

Lutz Schweikhard
Ernst-Moritz-Arndt-Univ. Greifswald
Inst. f. Physik, Domstr. 10a
D-17487 Greifswald
GERMANY
lutz.schweikhard@physik.uni-
greifswald.de

Luca Serafini
Dipartimento di Fisica
University of Milan
Via Celoria 16
20133 Milano
ITALY
luca.serafini@mi.infn.it

Nobuyasu Shiga
UCSD Physics 0319
9500 Gilman
La Jolla CA 92093-0319
shiga@physics.ucsd.edu

Matthew R. Stoneking
Lawrence University
115 South Drew Street
Appleton WI 54911
matthew.r.stoneking@lawrence.edu

Ronald R. Stowell
Princeton Plasma Physics Laboratory
P.O. Box 451
Princeton NJ 08543
rstowell@pppl.gov

James Sullivan
UCSD Physics 0319
9500 Gilman Drive
La Jolla CA 92093-0319
sullivan@physics.ucsd.edu

Clifford Surko
UCSD Physics Dept. 0319
9500 Gilman Drive
La Jolla CA 92093
csurko@physics.ucsd.edu

Endre Takacs
Natl. Inst. of Standards & Technology
Bldg. 221, Room B228
Gaithersburg MD 20899
etakacs@nist.gov

Teruo Tamano
2-18-16 Umezono
Tsukuba, Ibaraki 305-0045
JAPAN
tamano@mail1.accsnet.ne.jp

Mark Tinkle
Dynamics Technology, Inc.
21311 Hawthorne Blvd., Suite 300
Torrance CA 90503-5691
mtinkle@dynatec.com

Damon Todd
Indiana University Cyclotron Facility
2401 Mile 8 Samson Rd.
Bloomington IN 47403
datodd@indiana.edu

Hiroo Totsuji
Okayama University
Tsushimanaka 3-1-1
Okayama 700-8530
JAPAN
Totsuji@elec.okayama-u.ac.jp

Alexander A. Vedenov
RRC Kurchatov Institute
1 Kurchatov Square
Moscow 123182 RUSSIA
vedenov98@hotmail.com

Michiharu Wada
Atomic Physics lab.
RIKEN Institute
2-1, Hirosawa, Wako, Saitama
351-0198 JAPAN
mw@riken.go.jp

Zensho Yoshida
University of Tokyo
Hong, Bunkyo-ku
Tokyo 113-0033 JAPAN
yoshida@k.u-tokyo.ac.jp

Jonathan Yu
UCSD Physics Dept 0319
9500 Gilman Drive
La Jolla CA 92093-0319
jonyu@physics.ucsd.edu

Daniel Zajfman
Department of Particle Physics
Weizmann Institute
76100 Rehovot ISRAEL
fndaniel@wicc.weizmann.ac.il

Milenko Zuzic
Max Planck Institute for
Extraterrestrial Physics
Giessenbachstrasse, 85748 Garching
GERMANY
zuzic@mpe.mpg.de

Günter Zwicknagel
Institut für Theoretische Physik II
Universität Erlangen
Staudtstr. 7
D-91058 Erlangen
GERMANY
zwicknagel@theorie2.physik.uni-
erlangen.de

AUTHOR INDEX

A

Amarant, B., 565
 Ames, F., 609
 Amoretti, M., 45, 459, 603
 Ananthamurthy, S., 360
 Anderegg, F., 253, 353, 401
 Angelescu, C., 360
 Aretiev, A. V., 317

B

Barlow, S. E., 519, 525
 Barnes, D. C., 596
 Barnes, L. D., 24
 Beck, D., 609
 Beiersdorfer, P., 174
 Bettega, G., 603
 Biswas, D., 360
 Blümel, R., 509
 Bollen, G., 609
 Bollinger, J. J., 63, 111, 121
 Bowden, N. S., 51
 Buckman, S. J., 24

C

Carraro, C., 45
 Carrillo, B., 369
 Cavaliere, F., 603
 Cavenago, M., 603
 Chang, Y., 544, 544
 Charlton, M., 35
 Church, D. A., 164
 Collier, M. J. T., 35
 Coppa, G. G. M., 323, 531
 Correa, J. R., 544

D

D'Angola, A., 323
 Danielson, J. R., 253, 353
 Davidson, R. C., 73, 298, 305, 416, 576
 De Luca, F., 603

Delzanno, G. L., 323, 329, 486
 Dilling, J., 615
 Dolliver, D. D., 590
 Drader, J. J., 647
 Drewsen, M., 135, 145
 Driscoll, C. F., 253, 277, 347, 353, 388, 401
 Dubin, D. H. E., 111, 121, 253, 388, 401, 582
 Durkin, D., 459
 Dutta, S. K., 89

E

Efthimion, P. C., 576
 Eggleston, D. L., 369
 Estrada, J., 51

F

Fajans, J., 378, 422, 433, 453, 459
 Feldbaum, D., 89
 Finn, J. M., 329, 486
 Fontana, P. W., 671
 Forstner, O., 609
 Franzen, K. Y., 79
 Fukao, M., 641, 661, 697
 Fukuyama, Y., 625

G

Gabrielse, G., 51
 Gilbert, S. J., 24
 Gillaspy, J. D., 151
 Gilson, E. P., 378, 422, 576
 Gordon, D. F., 218
 Gould, R. W., 253, 263
 Greaves, R. G., 3, 10
 Greiner, F., 681
 Gruber, L., 164
 Grulke, O., 681
 Grzonka, D., 51

H

Habs, D., 235, 609
Hafizi, B., 209, 218
Hart, G. W., 271, 341
Hasse, R. W., 245
Hayashi, Y., 191
Heber, O., 565
Hendrickson, C. L., 647
Herlert, A., 652
Higaki, H., 79
Hilsabeck, T. J., 277
Himura, H., 641, 661, 697
Holder, J. P., 164
Hori, M., 79
Hornekær, L., 135
Huber, G., 609

I

Ichioaka, T., 79
Ishida, Y., 625
Itano, W. M., 63, 111
Ito, K., 464, 474, 480
Iwakuma, M., 691

J

Jelenković, B. M., 63
Jenkins, T. G., 298, 305, 416
Jensen, F., 135
Jørgensen, L. V., 35

K

Kabantsev, A. A., 277
Kambara, T., 625
Kanai, Y., 625
Katanuma, I., 556
Katayama, I., 625
Kawakami, H., 625
Killian, T. C., 96
King, L. B., 121
Kishimoto, T., 181, 201
Kiwamoto, Y., 464, 474, 480
Kjærgaard, N., 135, 145
Klinger, T., 681

Kluge, H.-J., 615
Kojima, T. M., 625, 634
Komaki, K., 79
Kondoh, S., 311
Kotelnikov, I. A., 317
Kriesel, J. M., 121
Kubo, T., 625
Kulin, S., 96
Kuroda, N., 79
Kuzmin, S. G., 102

L

Lagomarsino, V., 45
Lapenta, G., 323, 329, 486
Lim, M. J., 96

M

Majeski, R., 576
Manuzio, G., 45
Marcus, P., 433
Marler, J. P., 24
Marshall, A. G., 647
Marx, G., 615
Mason, G. W., 287
Matsuo, Y., 625
Michishita, T., 464
Mitchell, T. B., 63, 111, 121
Mito, T., 691
Mohri, A., 634
Møhlhave, K., 135, 145
Molinari, V. G., 513
Morikawa, J., 641, 661, 691, 697
Morrison, K. A., 298, 305, 416
Morrow, N. V., 89
Mortensen, A., 135
Mukherjee, M., 615

N

Nakai, Y., 625
Nakamura, T., 625
Nakashima, C., 661, 697
Nakata, M. T., 271
Newbury, A. S., 63
Nihei, H., 691

Niigaki, M., 634
Nikolaev, E. N., 537
Noda, K., 625

O

Oelert, W., 51
Ogawa, Y., 641, 691
Ohtani, S., 625
Ohyama, H., 625
Okada, K., 625
O'Neil, T. M., 102, 277
Ordonez, C. A., 544, 544, 590
Oshima, N., 625, 634
Oxley, P., 51
Ozawa, D., 691

P

Paasche, P., 360
Pariev, V. I., 329
Pasquini, T., 453
Paul, S. F., 298, 305, 416
Pedersen, H. B., 565
Peterson, B. G., 271, 341
Piel, A., 681
Pollock, R. E., 223
Pozzoli, R., 317, 459, 603

Q

Qin, H., 576
Quint, W., 615
Quraishi, Q., 407

R

Rahaman, S., 615
Raithel, G., 89
Rappaport, M. L., 565
Rasband, S. N., 335
Reisinger, K., 609
Ricci, P., 531
Rigg, K., 353
Roberson, C. W., 209, 218
Robertson, S., 407

Rocchi, F., 513
Rodriguez, D., 615
Rolston, S. L., 96
Romé, M., 317, 459, 603

S

Saito, H., 661
Saitoh, H., 697, 703
Sampson, R. L., 671
Sanpei, A., 464, 474, 480
Sarid, E., 422, 433
Schätz, T., 235
Schauer, M. M., 596
Schechter, D. A., 443
Schepers, G., 51
Schiffer, J. P., 127
Schmidt, P., 24, 609
Schneider, D., 164
Schramm, U., 235
Schweikhard, L., 174, 647, 652
Sefzick, T., 51
Shi, S. D.-H., 647
Shiga, N., 253, 353
Sikler, G., 615
Soga, Y., 464, 480
Speck, A., 51
Spencer, R. L., 287, 335
Sprangle, P., 218
Squires, T., 51
Stoneking, M. R., 671
Storry, C. H., 51
Stowell, R., 73
Sullivan, J. P., 24
Sumini, M., 513
Surko, C. M., 10, 24
Swanson, K., 519

T

Takács, E., 151
Tamano, T., 556
Tan, J. N., 51
Tarisien, M., 615
Tatsuno, T., 311
Taylor, A. E., 519
Teodorescu, C., 433
Testera, G., 45

Thommesen, A. M., 135
Thuecks, D. J., 671
Tinkle, M. D., 525
Todd, D. S., 223
Toepffer, C., 499
Torii, H. A., 79
Totsuji, C., 181, 201
Totsuji, H., 181, 201
Träbert, E., 174
Tsuruta, K., 181, 201

U

Uhlmann, N., 229
Umstadter, K. R., 596

V

Valenzuela, T., 360
van der Werf, D. P., 35
Variola, A., 45
Vedenov, A. A., 537
Videsen, Z., 135
Vogel, M., 652

W

Wada, M., 625
Walch, B., 407

Walz, J., 51
Wang, Z., 79
Watson, T. L., 35
Weber, C., 615
Werth, G., 360
Wessels, M., 51

Y

Yamazaki, Y., 79, 625, 634
Yanagi, N., 691
Yesley, P., 51
Yoneda, S., 79
Yoshida, A., 625
Yoshida, Z., 311, 641, 661, 691, 697,
703
Yu, J. H., 277, 347
Yuyama, T., 464

Z

Zajfman, D., 565
Zwicknagel, G., 229, 499